Luigi De Luca
Toru Shimada
Valery P. Sinditskii
Max Calabro *Editors*

Chemical Rocket Propulsion

A Comprehensive Survey of Energetic Materials

Springer Aerospace Technology

More information about this series at http://www.springer.com/series/8613

Luigi T. DeLuca • Toru Shimada
Valery P. Sinditskii • Max Calabro
Editors

Chemical Rocket Propulsion

A Comprehensive Survey of Energetic
Materials

🐎 Springer

Editors
Luigi T. DeLuca
Space Propulsion Laboratory (SPLab)
Department of Aerospace Science
   and Technology
Politecnico di Milano
Milan, Italy

Valery P. Sinditskii
Department of Chemical Engineering
Mendeleev University
   of Chemical Technology
Moscow, Russia

Toru Shimada
Institute of Space and Astronautical
   Science (ISAS)
Japan Aerospace Exploration
   Agency (JAXA)
Sagamihara, Japan

Max Calabro
The Inner Arch
Poissy, France

Preface

This book deals with energetic materials and their application to chemical rocket propulsion as initially discussed at the 12th IWCP titled "New Energetic Materials for Space Exploration." This event was held at Politecnico di Milano (PoliMi), Campus Bovisa, Milan, Italy, 9–10 June 2014 and was attended by about 200 participants from 20 countries. In total, 37 technical papers were offered, including 28 oral presentations and 9 poster papers. The Workshop was a unique gathering and opportunity, where participants could freely discuss the future of chemical rocket propulsion for access to, and exploration of, space. Distinguished scientists and propulsion engineers from academia, government, and industry were invited to attend. The official Group Photo of the Milan Workshop is shown as Fig. 1.

This book includes selected technical papers of high-quality presented at the Workshop, with several additional papers invited from the relevant international scientific community. All papers were accepted for publication only after passing a careful and severe peer review process by two to five anonymous international experts, according to the same comprehensive procedures employed by the most qualified archival publications. Every printed paper has a DOI reference. Therefore, this volume should not be considered an unfiltered collection of conference proceedings but rather an advanced supplemental reading for graduate students, lecturers, researchers, and scientists in academia or research centers, engineers, and industrialists.

The International Workshop on Combustion and Propulsion (IWCP) series was started in 1990 by the Space Propulsion Laboratory (SPLab) of Politecnico di Milano as an attempt to bridge the gap between researchers of the Eastern and Western blocs, which were until that time rigidly separated, in the broad areas of combustion applications for propulsion and rocket propulsion. Conveniently located between the two big countries, Italy has kept communication channels open between American and Russian scientists, even during the hard times of global competition. The IWCP series intends to promote free technical discussion and knowledge exchange in a relaxed atmosphere. The meeting format was built in order to favor detailed discussions among leading international researchers on selected areas of interest, rather than formal presentations of final results by registered authors on

a wide range of topics. Plenary Lectures by outstanding speakers are meant to offer a critical survey of specific themes and pave the way to detailed contributions from the authors as well as general discussions within the audience. For quality assurance, participation of lecturers/speakers/observers is normally restricted to a small number of invited people internationally selected for their demonstrated technical competence but also innovative vision or provocative approach. Serious efforts are made to ensure that the results are readily and easily available to a wide range of international readers, and the level of technical accuracy at all stages, from paper presentations to written diffusion of results, is set at the highest professional standards.

Although some of these features may have been diluted or adapted during the years, the basic flavor has been kept. The attendance of worldwide renowned authors in the meetings and timeliness of topics contained in the IWCP collection of events prove the effectiveness and success of the series in advancing energetic material combustion and rocket propulsion understanding.

The 12th IWCP addressed the current status in the field of energetic materials, from the viewpoint both of formulation and related topics from rocket propulsion to other applications. The workshop also looked for inspiring perspectives in a number of areas related to the energetic materials specifically used in chemical rocket propulsion.

Subsequently, the book will:

- Survey the current international status of energetic materials for propulsion
- Identify new promising ingredients for novel energetic materials formulation
- Provide an insight into powerful new energetic formulations under study at world-wide advanced laboratories
- Provide some rarely accessible information from Russian and Chinese sources
- Recommend future directions for a wide range of themes, from chemical propulsion to applications, resorting to energetic materials
- Offer the advantage of a common source for several topics treated in the book but scattered in the open literature
- Discuss little-known propulsion topics such as gel propulsion, catalytic techniques, and nanosized ingredients

The book is meant to offer a comprehensive survey of chemical rocket propulsion from the energetic materials viewpoint. Thus, the whole "life-cycle" of energetic materials is covered: from their conceptual formulation to practical manufacturing, including theoretical and experimental ballistics as well as performance properties, laboratory-scale and full system-scale, management (handling, storage, ageing, hazards, impact, disposal, remediation), and so on. Each of the chapters shall focus on one of main aspects, without however overlooking possible interactions with the remaining issues. All topics are considered from a broad international viewpoint. In order to offer readers a comprehensive survey of current technical problems, a fine selection of accomplished experts from the pioneering era of space propulsion

as well as of current technologists from some of the most advanced international laboratories was put together and agreed to support this editorial initiative.

The whole collection of **45** accepted papers is structured in the following **11** book chapters with a common target of "advancing chemical propulsion systems by addressing all aspects of propellants" (as expressed by an anonymous reviewer).

The book is opened by a collective introductory chapter that provides a consistent theme for the volume and shows how distinctly different chapters fit into this theme and cooperate to reach a common final goal. Such chapter was assembled by collecting well-focused essays by internationally recognized experts in the covered area, who briefly introduce each chapter. This introductory chapter will also help in arousing the interest of potential readers and will hopefully prompt them to look into individual chapters or papers.

It is our great pleasure to thank the following international reviewers for their substantial help in raising the quality of the book. Without their efforts, the publication of this volume would have been impossible:

Shalini Anand, *Hiroshi Aoki*, *Hiroya Asakawa*, *Valery A. Babuk*, *M. Balduccini*, *Yann Batonneau*, *L. Boccaletto*, *Manfred A. Bohn*, *Ch. Bonhomme*, *Ch. Bonnal*, *Max Calabro*, *Leonard H. Caveny*, *S. Mary Celin*, *N. Cesco*, *Helmut Ciezki*, *Adam S. Cumming*, *B. D'Andrea*, *E. D'Aversa*, *W.P.C. de Klerk*, *Luigi T. DeLuca*, *Y. Fabignon*, *Go Fujii*, *Luciano Galfetti*, *S. Gallier*, *A. Gany*, *N.G. Glumac*, *T.I. Gorbenko*, *J.F. Guéry*, *Dietrich Haeseler*, *Oskar J. Haidn*, *Stephen D. Heister*, *Keiichi Hori*, *N. Ierardo*, *Charles Kappenstein*, *Arif Karabeyoğlu*, *Thomas M. Klapötke*, *M.J. Klopfstein*, *A. Korotkikh*, *Bernard M. Kosowski*, *C.J. Lee*, *David Lempert*, *Filippo Maggi*, *Anthony P. Manzara*, *K. Menke*, *Harunori Nagata*, *Ichiro Nakagawa*, *Benveniste Natan*, *A. Neri*, *J. Neutz*, *O. Orlandi*, *Bryan A. Palaszewski*, *D. Pavarin*, *Wei Qiang Pang*, *P. Pempie*, *Alla N. Pivkina*, *S. Peters*, *S. Petitot*, *Sergey A. Rashkovskiy*, *Takashi Sakurai*, *Keisuke Sawada*, *H. Schöyer*, *Toru Shimada*, *Y.J. Shu*, *Irina L. Simakova*, *Valery P. Sinditskii*, *Haridwar Singh*, *V.I. Trushlyakov*, *Ruth Tunnell*, *D. Yagodnikov*, *N. Wingborg*, *Q.L. Yan*, *Vladimir E. Zarko*, *Feng Qi Zhao*.

In addition, the technical language of many non-native English authors was polished by *Dr. Adam S. Cumming*, *Dr. Anthony P. Manzara*, *Mr. Bryan A. Palaszewski*, and *Dr. Ruth Tunnell*, who deserve special thanks for their patient and generous assistance in the phase of paper revision. We would also like to thank all the authors for their paper contribution and collaboration in following the format specified by Springer International Publishing AG. Finally, special thanks are due to *Ms. Charlotte Cross* for her continuous assistance in the many publishing issues we had to face.

Further high-quality presentations were made at the Workshop by I.G. Assovskiy (Semenov Institute of Chemical Physics, Russia), P. Bellomi (Avio, Italy), E. Bucci (Avio, Italy), Helmut Ciezki (DLR, Germany), Charles Kappenstein (University of Poitiers, France), Bernard M. Kosowski (MACH I, USA), K.K. Kuo (Pennsylvania State University, USA), Z. Mansurov (Institute of Combustion Problems, Kazakhstan), M. Persson (ECAPS, Sweden), S. Schlechtriem (DLR, Germany),

and N. Wingborg (FOI, Sweden). Unfortunately, these contributions could not be included in the book, but the authors are greatly thanked for their active participation. In addition to the several chapter authors listed in the Table of Contents, further short contributions were provided by Dr. Chaoyang Zhang (China Academy of Engineering Physics, Mianyang, Sichuan, China), Dr. Qinghua Zhang (China Academy of Engineering Physics, Mianyang, Sichuan, China), and Dr. Hao Feng (Xi'an Modern Chemistry Research Institute, Xi'an, Shaanxi, China).

This book was started at Politecnico di Milano, Milan, Italy, by one of the editors (Luigi T. DeLuca), continued after his retirement at Konkuk University, Seoul, Korea, and finally completed at Nanjing University of Science and Technology, Nanjing, China. Sincere thanks are due to both Konkuk University and Nanjing University of Science and Technology for providing an excellent atmosphere and all needed professional support. This opportunity is taken to thank also Ms. I. Palmucci, Mr. D. Trache, Dr. Wei Qiang Pang, and Mr. Giovanni Colombo for their valuable and continuous assistance during the entire Workshop organization and conduction.

We sincerely wish that this joint international effort will help all readers to gain a better understanding of the puzzling intricacies and appealing secrets of energetic materials as well as of the perplexing difficulties but also fascinating horizons of space propulsion!

Sic itur ad astra (Virgil, Aeneid Book IX, line 641, 19 BC)

30 September 2015   The Volume Co-Editors

Milan, Italy   Luigi T. DeLuca
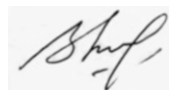

Sagamihara, Japan   Toru Shimada

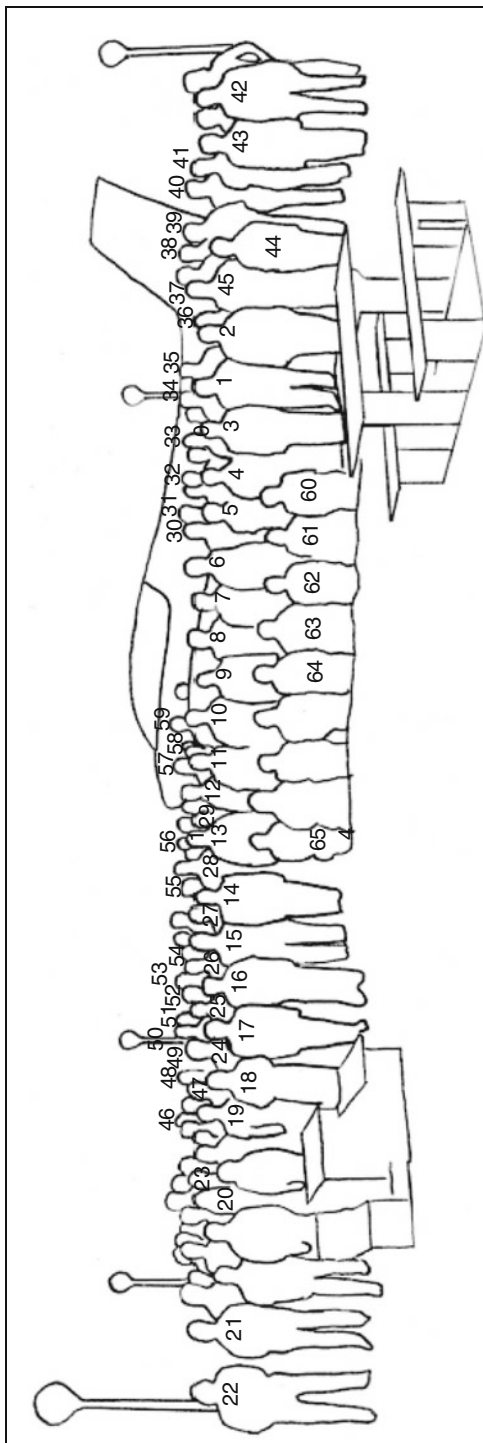Moscow, Russia   Valery P. Sinditskii

Poissy, France   Max Calabro

Fig. 1 Group Photo 12th IWCP Workshop, PoliMi, Campus Bovisa, Milan, Italy, 9–10 June 2014

12th IWCP Workshop – Identity of book contributors (editors, authors, and reviewers) and selected Workshop participants

(41) A. Annovazzi, (47) I.G. Assovskiy, (5) Valery A. Babuk, (62) L. Balasubramanyam, (21) P. Bellomi, (34) Manfred A. Bohn, (46) C. Bombardieri, (36) E. Bucci, (2) M. Calabro, (58) C. Carmicino, (3) Shri M. Chandradathan, (30) Helmut Ciezki, (42) Giovanni Colombo, (59) Adam S. Cumming, (57) N. de Backer, (1) Luigi T. DeLuca, (45) A. Di Biase, (29) L. Fanton, (50) Marco Fassina, (51) A. Franzin, (39) G. Fundarò, (43) Luciano Galfetti, (33) Volker Gettwert, (24) Keiichi Hori, (63) S.R. Jangoan, (60) Charles Kappenstein, (37) Marcos A. Kettner, (27) Koki Kitagawa, (28) M. Kobald, (15) Bernard M. Kosowski, (11) K.K. Kuo, (12) C.J. Lee, (4) S. Magham, (6) Z. Mansurov, (35) G. Marra, (20) O. Martos, (64) S. Muttangi, (55) F. Nasuti, (49) M. Negri, (14) O. Orlandi, (19) Wei Qiang Pang, (54) D. Pastrone, (40) M. Persson, (17) G. Platova, (16) Yulii Platov, (38) F. Pochetti, (23) Z. Qin, (44) H. Raina, (10) Sergey A. Rashkovskiy, (52) JAFF Rocco, (53) L. Rocco Jr., (25) R.Q. Shen, (22) T. Sgobba, (13) Toru Shimada, (7) Irina L. Simakova, (8) Valery P. Sinditskii, (9) Haridwar Singh, (61) Y. Sundhari, (48) Pietro Tadini, (65) Y. Sundhari, (26) Alexander B. Vorozhtsov, (31) Volker Weiser, (32) N. Wingborg, (18) Q.L. Yan, (56) Y.F. Zhao

Contents

Short Biography

Luigi T. DeLuca
Professor of Aerospace Propulsion
Space Propulsion Laboratory, *Politecnico di Milano*, *Milan*, *Italy*

Timeline

- 2014: Retired (maximum age) with a 2-year part-time extension, Politecnico di Milano, Milan, Italy
- 1989: Full Professor of Aerospace Propulsion, Politecnico di Milano, Milan, Italy
- 1983: Associate Professor of Aerospace Propulsion, Politecnico di Milano, Milan, Italy
- 1976: Ph.D. Aerospace and Mechanical Sciences, Princeton University, Princeton, NJ, USA, under the supervision of Prof. Martin Summerfield
- 1973: Assistant Professor of Aerospace Propulsion, Politecnico di Milano, Milan, Italy
- 1967: Laurea Aeronautical Engineering, Politecnico di Milano, Milan, Italy

Accolades

- 2015 Fall: Visiting Professor NUST (Nanjing University of Science and Technology), Nanjing, China
- 2015 Spring: Visiting Professor Konkuk University, Seoul, Korea
- 2014: Honorary Fellowship by High-Energy Materials Society of India (HEMSI), India
- 2013: Guest Professor NUST (Nanjing University of Science and Technology), Nanjing, China
- 2010: Honorary Professor OmSTU (Omsk State Technical University), Omsk, Russia
- 1998: Visiting Scholar, Kyushu Institute of Technology, Japan
- 1997: Visiting Scientist, CalTech, Pasadena, CA, USA
- 1993: Visiting Scholar, Brigham Young University, Provo, UT, USA
- 1977: Visiting Scientist, Princeton University, Princeton, NJ, USA

Toru Shimada
Professor of Space Flight Systems
JAXA/ISAS Japan Aerospace Exploration Agency, *Sagamihara*, *Japan*

Timeline

- 2006–Present: Professor, Institute of Space and Astronautical Science, JAXA
- 2006–Present: Visiting Professor, University of Tokyo, Graduate School of Engineering
- 2007–2003: Technical Manager of MuV Launch Vehicle Project, JAXA
- 2006–2000: Associate Professor, Institute of Space and Astronautical Science, JAXA
- 2000–1985: Senior Engineer, Aerospace Division, Nissan Motor Co., Ltd.
- 1985: Doctor of Engineering, University of Tokyo (Aeronautics)
- 1982: Master of Engineering, University of Tokyo (Aeronautics)
- 1980: Bachelor of Engineering, Kyoto University (Aeronautical Engineering)

Research

- Flow dynamics inside solid/hybrid rocket motor combustion chambers and nozzles including internal ballistics, multiphase flows, ablation phenomena of nozzle TPS, combustion instability, fuel/propellant regression rate modeling, CFD for combustive, swirling, and turbulent flows.
- R&D for low-cost launch vehicle systems dedicated for nano/micro satellites, using hybrid rocket engines

Valery P. Sinditskii
Professor and Head of Department of Chemical Engineering
Mendeleev University of Chemical Technology, *Moscow*, *Russia*

Timeline

- 2008–Present: Dean of Chemical Engineering Department at Mendeleev University of Chemical Technology of Russia
- 1999–Present: Professor, Mendeleev University of Chemical Technology of Russia
- 1999–Present: Head of Chair, Mendeleev University of Chemical Technology of Russia
- 1999–1997: Associate Professor, Mendeleev University of Chemical Technology of Russia
- 1997–1984: Senior Researcher, Mendeleev University of Chemical Technology of Russia
- 1984–1981: Researcher, Mendeleev University of Chemical Technology of Russia
- 1981–1976: Ph.D. in Chemistry, Academy of Science of USSR
- 1976: Graduated from Moscow State University, Department of Chemistry

Research

Energetic materials, synthesis, combustion, thermal decomposition, and application

Accolades

- 2013: Foreign honorary member of the High-Energy Materials Society of India
- 2012: Visiting professor of Beijing Institute of Technology, China
- 2010–Present: Associate editor of "International Journal of Energetic Materials and Chemical Propulsion"
- 2010–Present: Editorial board of "Combustion, Explosion, and Shock Waves"
- 2002–Present Editorial board of "Central European Journal of Energetic Materials"

Max Calabro
Consultant
Mechanical Engineer INSA, Lyon

Timeline

- 2004–Present: Consultant at "The Inner Arch" S.A.R.L.
- 2003–2002: ONU Inspector in Baghdad (UNMOVIC)
- 2002–1965: EADS

    – 2002–1985: Chairman of the Steering Committee for Propulsion R&D
    – 2001–1990: Head of the Propulsion Department
    – 1982: In charge of Propulsion Design Team
    – 1972: Management of rocket motor design and development
    – 1973–1969: Studies on propulsion design for civil launchers and military satellites propulsion system design
    – 1969–1965: Development of the cryogenic engine HM 4, ancestor of the HM7B

Memberships

- IAF (International Astronautic Federation) IPC Member
- Fellow Member and Vice-President of European Conference for Aerospace Sciences (EUCASS)
- AIAA: Associated Fellow and SRTC Emeritus Member
- Member of IAA (International Astronautical Academy)
- AAAF Emerit. Member

Part I
An Introduction to Energetic Materials for Propulsion

An Introduction to Energetic Materials
for Propulsion

Luigi T. DeLuca, Toru Shimada, Valery P. Sinditskii, Max Calabro, and
Anthony P. Manzara

Abstract This chapter is a general introduction to the overall organization of the
book and its main topics. Contributions to the volume were collected from authors
of 13 countries including those most engaged in space exploration missions. This
chapter was assembled with the support of many of the volume contributors and
other internationally qualified experts in the field of energetic materials. Highlights
of the state-of-the-art and future needs are outlined in a number of areas extending
from the classical applications of chemical propulsion (solid, liquid, hybrid, gel)
to the collateral areas of unconventional applications and energetic materials Life-
Cycle Management. Prospective new energetic materials and new concepts in
chemical propulsions are discussed as well as practical problems related to quality
control, aging, hazards, impact, disposal, and remediation of the energetic materials
in use today or in the near future. For every chapter, a short introduction is given

A collection of essays coordinated by Luigi T. DeLuca, Toru Shimada, Valery P. Sinditskii,
Max Calabro, and Anthony P. Manzara.

L.T. DeLuca (✉)
Space Propulsion Laboratory (SPLab), Department of Aerospace Science and Technology,
Politecnico di Milano, 20156 Milan, Italy
e-mail: luigi.deluca@polimi.it

T. Shimada
Institute of Space and Astronautical Science (ISAS), Japan Aerospace Exploration Agency
(JAXA), Sagamihara 252-5210, Japan
e-mail: shimada.toru@jaxa.jp

V.P. Sinditskii
Department of Chemical Engineering, Mendeleev University of Chemical Technology,
9 Miusskaya Sq., 125047 Moscow, Russia
e-mail: vps@rctu.ru

M. Calabro
The Inner Arch, 4, rue Saint Sébastien, 78300 Poissy, France
e-mail: max.calabro@innerarch.eu

A.P. Manzara
MACH I, King of Prussia, PA 19406, USA
e-mail: tony@machichemicals.com

of each included paper in order to help the reader to identify the contributions most suitable for their specific needs or interests. The final book chapter is dedicated to an historical survey of the Russian developments in solid rocket propulsion. No matter how impressive from both a theoretical and experimental viewpoint, for a variety of reasons, they are still little known, if not misunderstood, beyond the national barriers.

Nomenclature

ADN	Ammonium dinitramide
AFM	Atomic force microscopy
AFM-315	HAN-based green liquid monopropellant (by AFRL)
AFOSR	Air Force Office of Scientific Research
ALD	Atomic layer deposition
ALICE	Aluminum ice
AP	Ammonium perchlorate
BAMO	3,3′-bis(azidomethyl) oxetane
BFF	3,4-bis(3-fluorodinitro-methyl furazan-4-oxy)furazan
CCP	Condensed combustion products
CFD	Computational fluid dynamics
CL-20	2,4,6,8,10,12-hexanitro-2,4,6,8,10,12-hexaazaisowurtzitane
CMDB	Composite modified double base
CNSA	China National Space Administration
CSS	Canopy severance system
DCPD	Dicyclopentadiene
DLR	German Aerospace Center (Deutsches Zentrum für Luft- und Raumfahrt)
EIL	Energetic ionic liquids
EM	Energetic materials
EMGI	Energetic materials genome initiative
EPDM	Ethylene propylene diene monomer (M-class) rubber
ESA	European Space Agency
FLOX	Fluorine liquid oxygen
FLSC	Flexible linear-shaped charges
GAP	Glycidyl azide polymer
GINC	Graphene–iron oxide nanocomposite
GUDN	N-guanylurea-dinitramide
HADNMNT	2-dinitromethyl-5-nitrotetrazole
HAN	Hydroxylammonium nitrate
HATO	Hydroxylammonium 5,5′-bistetrazole-1,1′-diolate (also TKX-50)
HEDM	High-energy density material
HEMRL	High-Energy Materials Research Laboratory
HMX	Cyclotetramethylenetetranitramine or High-Melting eXplosive (also known as octogen or Her Majesty eXplosive)
HNF	Hydrazinium nitroformate

HNS	Hexanitro stilbene
HTP	High-test (hydrogen) peroxide
HTPB	Hydroxyl-terminated polybutadiene
HTPE	Hydroxyl-terminated polyether
HTV	H-II transfer vehicle
ICBM	Intercontinental ballistic missile
IRFNA	Inhibited red fuming nitric acid
ISS	International Space Station
ITE	Integral throat entrance
JAXA	Japan Aerospace Exploration Agency
KARI	Korea Aerospace Research Institute
KSLV	Korea space-launch vehicle
L/D	Length-to-diameter ratio
LAS	Launch abort system
LES	Large-eddy simulation
LFI	Low-frequency instability
LH2	Liquid hydrogen
LMP-103S	ADN-based green liquid monopropellant (by Eurenco and ECAPS)
LNG	Liquefied natural gas
LOx	Liquid oxygen
LT	Low-melting temperature
MEMS	Microelectromechanical systems
MGI	Materials genome initiative
MIC	Metastable intermolecular composites
MLD	Molecular layer deposition
MMH	Monomethylhydrazine
MON	Mixed oxides of nitrogen
MURI	Multidisciplinary University Research Initiative
NASA	National Aeronautics and Space Administration
NC	Nitrocellulose
NG	Nitroglycerine
NIOSH REL	National Institute Occupational Safety and Health Recommended Exposure Limits
NTO	Nitrogen tetroxide (in liquid rocket propulsion)
NTO	5-Nitro-1,2,4-triazol-3-one (in solid rocket propulsion)
O/F	Oxidizer-to-fuel ratio
PBAN	PolyButadiene acrylic acid AcryloNitrile
PETN	Pentaerythritol tetra nitrate
PTFE	Polytetrafluoroethylene
R&D	Research and Development
RAP	Rocket-assisted projectile
RD	Ракетный Двигатель (rocket engine)
RDX	Cyclotrimethylenetrinitramine or Research Department eXplosive (also known as hexogen, cyclonite, T4, Royal Demolition Explosive)

RP1	Rocket propellant-1 (also refined petroleum-1)
SDI	Strategic defense initiative
SEM	Scanning electron microscopy
SLS	Space launch system
SNPE	Société Nationale des Poudres et des Explosifs (1971–2013)
SOFT	Swirling oxidizer flow type
SPFE	Solid propellant fire extinguishers
SRB	Solid rocket booster
SRM	Solid rocket motor
SSME	Space shuttle main engines
STANAG	NATO standardization agreement
T/W	Thrust over weight ratio
TATB	Triaminotrinitrobenzene
TB	Technical bulletin
TDI	2,4-toluene diisocyanate
TKX-50	Hydroxylammonium 5,5′-bistetrazole-1,1′-diolate (also HATO)
TOW	Tube-launched optically tracked, wire-guided
TRL	Technology readiness level
TRW	Thompson Ramo Wooldridge company (acquired by Northrop Grumman in 2002)
UDMH	Unsymmetrical dimethyl hydrazine
UH25	75 % UDMH + 25 % $N_2H_4xH_2O$ (hydrazine hydrate)
USSR	Union of Soviet Socialist Republics
WFNA	White fuming nitric acid

1 Background and Volume Introduction

This chapter [1] is a general introduction to the topics discussed in the remaining ten chapters of the book. It comprises 12 sections and was assembled with the support of many of the volume contributors and other internationally qualified experts in the field of energetic materials for propulsion. An exhaustive graphical summary of the current state-of-the-art in propulsion is illustrated in Fig. 1 by NASA. Using different colors, the graph also discriminates categories of engines having a different technology readiness level (TRL). Chemical propulsion, together with electrothermal and electrostatic, enjoys the highest TRL (7–9, i.e., fully operational systems). In addition, straight lines parameterized in power density (kW/kg), over the range 10^{-2}–10^{+4}, clearly show chemical engines advantaged with respect to electrical engines. Today chemical propulsion is the only way to access space, and this will remain true for decades to come. The chemical propulsion options include two technologies considered already mature (solid and liquid) and two technologies potentially very interesting (hybrid and gel). The NASA plot in Fig. 1 underlines the uniqueness of the current chemical propulsion, being the ratio T/W > 1, but also
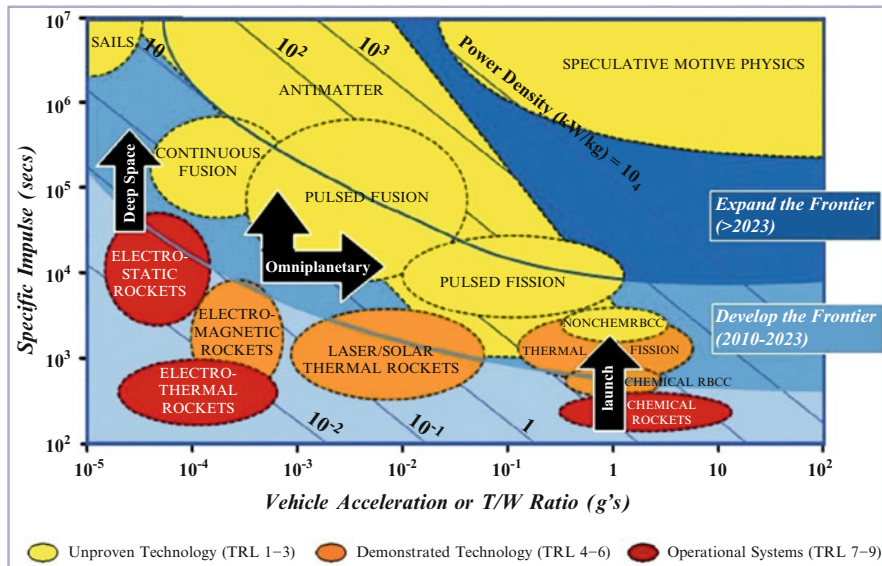
Fig. 1 NASA state of the art in propulsion, in terms of gravimetric specific impulse I_s vs. vehicle acceleration or thrust/weight T/W ratio, for several classes of devices (Courtesy of NASA)

the modest specific impulse as compared to any other propulsion device. The main approach to improve specific impulse is to resort to suitable ingredients from the broad class of high-energy density materials (HEDM).

1.1 Sections of This Chapter

Within this framework, general highlights and future needs are outlined in the New Ingredients for Chemical Propulsion (Sect. 2, [2–7]); Metals as Energetic Fuels for Chemical Propulsion (Sect. 3, [8–12]); Solid Rocket Propellant Formulation (Sect. 4, [13–17]), Liquid Rocket Propulsion (Sect. 5, [18–21]); Hybrid Rocket Propulsion (Sect. 6, [22–25]); New Concepts in Chemical Propulsion (Sect. 7, including Catalysis, [26–29]); Life-Cycle Management of Energetic Materials, including aging, hazards, impact, disposal, and remediation problems (Sect. 8, [30–35]); Rocket Propulsion Systems (Sect. 9, [36–38]); Applications of Energetic Materials (Sect. 10, [39–41]); History of Solid Rocket Propulsion in Russia (Sect. 11, [42–45]); and Gels for Rocket and Ramjet Propulsion (Sect. 12, [12, 21]). For a matter of convenience, these last two papers were incorporated in the previous chapters. Whether good or bad, the current space programs are based on the solid and liquid propellants discussed in this volume; see, for example, Fig. 2.
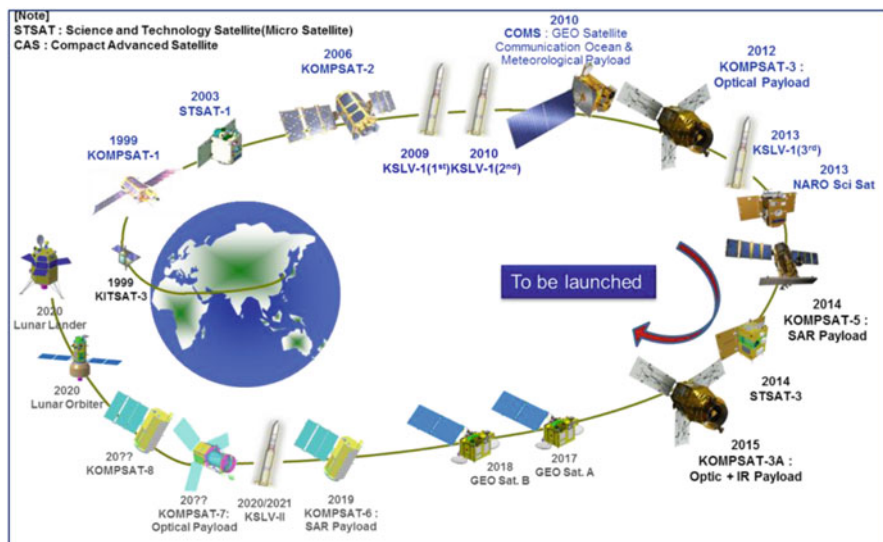
Fig. 2 Korean strategic plan for space exploration over the years 1999–2020 as of May 2015 (Courtesy of KARI)

2　New Ingredients for Chemical Propulsion[1]

Mankind has reached space, walked on the moon, sent exploration rovers to Mars and probes to deep space. The requirements of rocket propulsion for such undertakings grow with the rising distances and complexities of the missions. Therefore, research for new ingredients that fulfill present and future new requirements is constantly furthered by both military and civilian institutions. These requirements include first and foremost compounds which are more environmentally acceptable particularly for surface and atmosphere applications – missiles, low Earth orbit probes, or just for greater launch distances. This again requires that the synthesis process, the storage, and also the combustion products should be "greener" or more environmentally sound. Smoke reduction is not solely associated with this topic, because both primary and secondary smokes also adversely affect guidance and control systems. Increased range requires more powerful and generally enhanced materials, particularly for space saving. Therefore, more effective HEDMs are needed. Last but not least, more cost-effective compounds are required for driving of any rocket or missile. Until now thermochemical-propelled rockets are the only ones allowing space access, while nuclear, electric, and radiant (beamed energy or solar) propulsion systems – while suitable for in-space navigation – are for different reasons unable to perform space access to low Earth orbit.

---

[1]Coordinated by Marcos A. Kettner and Thomas M. Klapötke.

On the one hand, considerable effort is being spent on the improvement and perfecting of the propulsion systems themselves which are designed exclusively for the ingredients they work with – an engineer's challenge. On the other hand, the research for new ingredients for rocket propulsion is a challenge for chemistry. This effort focuses on the design of novel high-tech materials for fuels, oxidizers, polymer matrices, plasticizers, and further additives for liquid, solid, gelled, and hybrid propellant systems. The main focus remains on higher performance while ensuring they are environmentally more acceptable and economically acceptable materials compared with conventional propellant ingredients or compositions (e.g., in terms of cost efficiency, since raw materials represent less than 5 % of the cost of a solid stage). This development area particularly concerns the ingredient families that are known to be toxic or harmful and also the conventional nonenergetic ingredients that need to be replaced to achieve more energy. A major constraint for solid and hybrid propellants in particular is to remain safe (class 1.3), and so many new candidate energetic ingredients will be discarded, making production-ready improvements rare.

Several families of HEDM propellants were identified, such as formulations based on high-nitrogen compounds (see details in Sect. 7), octanitrocubane $C_8(NO_2)_8$, metallic hydrogen, atomic radicals, metastable helium, and so on. However, most of them are still far from being practically usable in the short range due to severe difficulties in large-scale manufacture, prolonged storage, acceptable safety, and cost considerations. This chapter provides an overview of the requirements and challenges in the design of new ingredients currently tested at laboratory level to a significant extent in view of possible field applications. With the development of nano-materials (with a diameter around 100 nanometers (nm) as the favorite size for rocket propulsion), burning rates are increased, and burning efficiency may be improved; however, a decrease of active metal content and an increase in particle clustering during manufacture are also observed. For higher-energy and improved burning rate dependences, metallic hydrides such as alane are being studied as new fuels in the solid propellants sector. Novel perchlorate-free oxidizers such as ammonium dinitramide (ADN) and hydroxylammonium nitrate (HAN) are being examined, as are polynitro compounds which are being discussed as oxidizers or oxygen-rich energetic fillers. Furthermore, new explosive additives, like CL-20, and high-nitrogen-containing compounds, like tetrazoles or tetrazines, are being investigated for eco-friendly missile propellant mixtures which easily exceed the energy of conventional additives like RDX and HMX. On the contrary, other compounds such as HNF, initially very promising, have lost their appeal following extensive experimental testing. Metal oxides like MgO, B_2O_3, NiO, or CuO as new catalysts are being studied or are already in use and allow the accurate adjustment of the burning rate of propellant formulations. The continuing investigation of energetic polymers which also incorporate curing agents and plasticizers should result in new materials and matrices for solid and hybrid propulsion systems with improved sensitivities and compatibilities with the other propellant ingredients while not decreasing the energy content of the formulations. In the field of liquid propellants, ammonium dinitramide-based liquids such as

LMP-103S and hydroxylammonium nitrate-based AFM-315 are proven to be superior in terms of specific impulse, density, and toxicity. For cryogenic propellants including LOx, LH$_2$, or FLOX, new laser ignition systems, chamber wall materials, and geometries are being developed to give better throttling, better efficiency of the engine, and better safety in handling. The use of gels in rocket systems allows the addition of energetic metal particles and also catalyst/reactive particles to obtain hypergolic ignition of conventional, nontoxic fuels and oxidizers. New gelling agents and the introduction of nano-sized metals enhance the advantages of gelled hydrocarbon-based fuels for ramjets even more.

Due to the large number of active investigations at various international locations, Chap. 2 is especially focused on solid propellants and solid fuels. It goes into detail on substitute compounds for conventional toxic or inert ingredients such as ammonium perchlorate, lead-based materials, or nonenergetic polymers. Some state-of-the-art compounds are presented and discussed in new formulations, but also novel ingredients and mixtures for solid composite propellants will be discussed.

2.1 Full Papers of This Part

Part II comprises six papers (2–7). The search for new materials and their possible use in propulsion are illustrated by the papers by Kettner and Klapötke, Sinditskii et al., Singh, Karabeyoğlu, Fan et al., and Zhai et al.

The paper by Kettner and Klapötke contains valuable information on new perchlorate-free oxidizers for potential use in chemical rocket propulsion. The paper covers the synthesis methods and properties of trinitromethyl containing oxidizers from the following chemical classes: orthocarbonates, 2,5-disubstituted tetrazoles, bi-1,2,4-oxadiazoles, 2,2,2-trinitroethyl carbamates, and corresponding nitrocarbamates. Considerable recent attention has been focused on research and development of high-nitrogen energetic materials. The purpose of the paper by Sinditskii et al. is to analyze possible application areas of different types of 1,2,4,5-tetrazine-based energetic materials reasoning from their peculiar combustion and thermal decomposition properties. Characteristic features and drawbacks of tetrazine-based energetic materials are considered. The paper by Haridwar Singh is devoted to components of solid propellants which can increase their performance and make them environmentally friendly. Finally, in the paper by Arif Karabeyoğlu, attention is focused on approaches to using performance additives (metals, metal hydrides, or boron compounds) to enhance the regression rate of hybrid rocket solid fuels.

Two additional papers by Fan et al. and Zhai et al. discuss the synthesis and characterization of such high-nitrogen energetic materials as tetrazole salts and furazan derivatives. The paper by Fan et al. makes efforts to introduce tetrazole salts as energetic ingredients for rocket propulsion. Results are presented from the study of two hydroxylammonium salts of 2-dinitromethyl-5-nitrotetrazole (HADNMNT) and 5,5′-bistetrazole-1,1′-diole (TKX-50, HATO), which are positioned as a non-

chlorine oxidizer and high-energy filler for solid composite propellants. It is found that the composite propellants containing HATO offer the advantages of high-burning rate and low sensitivity to mechanical stimuli. Investigations by Zhai et al. show that energetic plasticizers are important constituents of rocket and gun propellants, which aid in improving the mechanical properties of propellant grains. Furazanyl ether compounds have attracted a considerable amount of attention as energetic plasticizers for solid propellants due to their high-energy density, good thermal stability, and positive heat of formation. In this paper, a novel fluorodinitromethyl-containing molecule 3,4-bis(3-fluorodinitro- methyl furazan-4-oxy)furazan (BFF) is synthesized, and its properties are presented. In many aspects, such as density, sensitivity, and detonation parameters, it is far superior to nitroglycerine (NG).

3 Metals as Energetic Fuels for Chemical Propulsion[2]

Propellants for rocket and ramjet propulsion should have high-energy characteristics as much as possible, i.e., providing a high specific impulse (I_s). In this connection, as a rule, metal particles are used as energetic additives in the composition of propellants (for rocket motors) and fuels (for ramjet motors). Attractive features of these substances are their high calorific value and density. Their use leads to an increase in the calorific value of the propellant per unit mass and volume, which results in a reduced mass and size of the propulsion system.

The exotic metallic hydrogen would allow achieving I_s values in the range 500–2000 s, but its implementation is too far from being practically feasible (for details, see Sect. 7). The most attractive high-energy components of the specified type are beryllium and aluminum for rockets and boron for ramjets. However, only aluminum has widespread use. Its advantages are wide availability, ease of handling, good compatibility with the major components of propellant, and cost. The application of beryllium and its compounds is banned due to their high toxicity. In addition, the cost of beryllium is two orders of magnitude higher than that of aluminum.

An obvious negative consequence of the use of aluminum is the formation of condensed combustion products (Al_2O_3), which results in loss of specific impulse and to overcomplicated intrachamber processes. Similar problems are faced with metallic fuels in general. However, the presence of condensed-phase combustion products has also positive consequences associated with the suppression of motor combustion instability.

An effective tool for improving the quality of propellants is the introduction of metals in the form of hydrides. The presence of hydrogen in the composition of these substances leads to increased calorific content and specific impulse without

---

[2]Coordinated by Valery A. Babuk.

increasing the temperature of the combustion products. Another advantage is the lower concentration of water content in the combustion gases thus making the erosion of the nozzle much lower and probably also the need of internal thermal insulation, by lowering carbon oxidation by the classical water gas reaction. A difficulty is the well-known trend of hydrogen to separate from the metal, making the molecule unstable over the periods of time typically needed for field applications. Stabilized alane (AlH_3) is a common product in Russia, but it is not commercially available.

The use of metallic additives requires the study of various aspects of the behavior of these substances in combustion process. It is possible to identify the following phenomena whose understanding and study are extremely important for a successful implementation of performance additives:

1. *Metal ignition*. The study of the ignition of the metal, as a rule, consists of determining the ignition temperature, which enables the determination of the spatial position of the zone of ignition in the area of combustion. This temperature depends on the properties of the protective oxide film, the oxidation potential of the environment, and the conditions of interaction of this environment with the metal particles.
2. *The formation of condensed products and agglomeration process on the surface layer of burning propellant*. Condensed products appear as a result of metal combustion and the completion of the agglomeration process. The properties of these products depend on the propellant composition and on the conditions of their combustion. Information must be obtained about the influence of various factors on the particle size, chemical composition, and internal structure of these products.
3. *The process of metal combustion*. The description of the burning process of metal particles is important to describe the kinetics of combustion (combustion time of the particles) and to determine the properties of the combustion products.
4. *The influence of metal combustion on the propellant combustion process in general*. Ignition and burning of the metal particles in the surface layer have a significant impact on the conditions of ignition and the burning rate law of the actual propellant. The properties of the metal fuel and its required quantity are influenced by the burning rate of the propellant and its dependence on the initial temperature and pressure.
5. *Two-phase (2P) flow loss*. This is by far the most important loss associated with all metalized solid propellants and thus an issue of crucial importance for the actually delivered performance. The final result will depend on not only the combustion details near the surface layer but also the hydro- and fluid-dynamics phenomena involving droplets and particles in the nozzle throat region. Empirical rules to assess the loss are well-known for conventional formulations, but high-energy or innovative formulations require further detailed study. In general, for near-surface phenomena, one should decrease the amount of condensable

products in the combustion chamber, the fraction of CCP going to agglomeration, and, most importantly, the average size and size distribution of the resulting agglomerates. As to agglomerate formation, decreasing the particle ignition temperature and increasing heat release at or removing heat release closer to the burning surface would help. These effects are possible by shortening the background flame thickness, using more reactive metal particles (nAl, MgB, Ni coating, and so on), ball milling of conventional μAl to create nano-sized inclusions, encapsulating nano-ingredients and aluminum "alloys" with PTFE, and more. The final outcome will anyway depend on the nozzle throat effects.

6. *Slag formation loss*. This is a phenomenon of accumulation of condensed products on motor elements, which leads to a drop in the rocket motor mass perfection (ratio of rocket inert mass and propellant mass). The occurrence and importance of this phenomenon mainly depend on the characteristics of the agglomeration process (the degree of involvement of the initial metal to agglomeration, agglomerate size, their structure, and chemical composition).

3.1   Full Papers of This Part

Part III comprises five papers (8–12) authored by DeLuca et al., Vorozhtsov et al., Weiser et al., Zhao et al., and also Gafni et al. The basic mechanisms of metal burning are reviewed and the prospects of using new metallic formulations (based on nano-sized ingredients, chemically or mechanically activated Al, stabilized alane, etc.) are discussed. The paper by Vorozhtsov et al. describes some of the opportunities and challenges in using nanomaterials in formulations. Although nanomaterials have potential, there is still considerable research required to exploit or even confirm that potential. The paper by Zhao et al. discusses the ignition delay of nano-metalized propellants subject to thermal radiation pulses, showing that there is a critical level of laser power density in the ignition of surface-coated aluminum nano-sized powders. The last paper by Gafni et al. discusses the application of aluminized gel fuels to ramjet propulsion.

4   Solid Rocket Propellant Formulation[3]

Solid rocket propellants are classified as composite or high energy and may be in the subclasses of metalized or minimum smoke. Hybrid rocket propellants and air-breathing solid rocket ramjets are not considered under this heading.

---

[3]Coordinated by Anthony P. Manzara.

There are a number of current goals for solid rocket propellant improvements (see underlined headers):

Ingredients. Common solid propellants are formulated using oxidizers, typically AP, binders such as HTPB, cross-linkers such as polyisocyanates, and plasticizers such as DOA in the workhorse composite type. Optionally additional fuel such as Aluminum is added. There also are classes of additives generally used in solid rocket propellant formulations. These materials include burn rate catalysts used to tailor the ballistics for particular requirements, bonding agents to improve the mechanical properties, antioxidants to improve the storage life, dispersants to improve the processing characteristics, metal deactivators to improve pot life, opacifiers to improve heat transfer from the flame zone to the unburned propellant, and acoustic stabilizers to improve oscillatory ballistic behavior. Such materials are typically used at levels of less than 1 % of the formulation. Many writers omit these materials from their discussion of formulations due to concern for proprietary or security interests.

Higher performance either I_s or density I_v. There has been a gradual improvement in the performance of composite solid propellants made from conventional ingredients (AP, Al, HTPB, ester plasticizer) and high-energy propellants made from conventional ingredients (AP, Al, RDX, HMX, polyester or polyether binder, nitrate ester plasticizer). Over the past 40 years, the performance characteristics of these two types have each been approaching its own asymptotic level. Creative use of bonding agents, urethane cure catalysis, and burn rate catalysts have allowed formulators to gradually improve the propellants both with respect to mechanical properties and with respect to energy. But there are limits to the gains to be made in this way, due to the fundamental properties of the ingredients. It is possible that another second or two of I_s can be achieved by better processing techniques or the use of additives to improve processing success or mechanical properties. But significant growth in solid rocket performance will depend on the availability and proper formulation of new ingredients. Materials such as nano-Aluminum, AlH_3, CL-20, ADN, energetic binders, and alternative binder systems based on poly-DCPD have been shown to give higher performance in some formulations, but they have not been incorporated in many standard systems, due to cost issues, uncertainty about suitability under some conditions, and incomplete development of the specific formulation techniques required. There is also a bias against using new "unproven" ingredients when a combination of familiar materials can be formulated to meet the new requirements.

Lower "signature" of the exhaust. Metalized (usually taken to mean aluminum containing) rocket propellants produce a higher I_s but also copious white smoke that marks the launch point and may interfere with control signals. Originally rocket motors were classified as "smokeless" or "minimum smoke" if their exhaust products were not visible (no condensation) and "reduced smoke" if the condensation was not immediate or not always obvious (e.g., HCl in moist air). Small amounts of certain propellant additives used to prevent combustion instability (such as aluminum, aluminum oxide, silicon carbide, etc.) will

produce visible trails. More recently, other exhaust signature-producing materials became important in certain applications, such as materials that block radar signals, interfere with seeker performance, or emit infrared light which indicates the fact of a launch and may even cue an antimissile response. There are some requirements to reduce the presence of certain chemical elements in a propellant because of their tracking value in the rocket exhaust.

Lower sensitivity and lower hazard ratings in processing and in final configuration. There has been a sustained effort over the past 25 years to reduce the hazards of finished motors from the 1.1 explosive level to 1.3 or to even safer classifications. The related issue of reduced hazards during processing has had less visibility but remains a matter of concern in the industry. Regulatory regimes to measure and control rocket motor hazards have been introduced, such as the TB 700-2 and STANAG guidelines. Much progress has been made in understanding the effects of changes in conventional ingredients and formulations on the measured hazard levels of a propellant. Importantly, the hazards of a rocket motor are often related to the amount of confinement created by the motor case, which generally correlates with a more hazardous response to stimuli such as heating (fast cook-off and slow cook-off) and high-rate kinetic events (bullet impact, fragment impact, sympathetic detonation). Advances in rocket motor case materials and construction techniques have allowed previously "too hazardous" combinations of propellant formulation and motor design to be downrated in the finished motors. The original belief that reducing the sensitivity of a motor to the required level would reduce its performance below the required level has been shown to be false in many cases. Good progress has been made in maintaining acceptable performance while approaching or achieving the relevant insensitivity goals. This area is by no means completely resolved, and there are undoubtedly many good innovations yet to be made to further reduce the hazards of rocket motor production, storage, handling, and use.

However, this comment is essentially valid for small tactical missiles. For civilian applications, the complete motor has to be class 1.3 and so avoid any risk of mass detonation under any event (falling down, high-velocity impact, and more).

Longer shelf life under specified storage conditions. For space-launch boosters which are typically fired within 2 years of manufacture, and kept under controlled storage conditions, shelf life is not considered a problem. Yet, this is not granted when using highly hygroscopic new oxidizers. Rocket propulsion elements of strategic weapons (fixed-base ICBM's and submarine-launched missiles) are expected to remain useful for at least a dozen years, when stored at controlled temperature and humidity, and are not subjected to significant vibration or thermal cycling challenges. Tactical propulsion elements, either road mobile or especially air carried, have the most demanding requirements including +65 °C to −45 °C, for example, temperature cycling and extensive vibration testing. Naval shipboard tactical systems typically have slightly less stringent requirements. Much of the approach to resolving issues with these requirements revolves about improving the binder stability upon aging and improving the

original mechanical properties to allow more stress and strain to be experienced without damage to the motor.

Lower cost. Everyone would like the rocket motors to be available at low cost. The major drivers of cost are the long development times required to achieve the requisite performance, the changes in specifications after the development is under way, the need for only small numbers of certain motors which militates against cost-effective procurement and production techniques, the use of specialty ingredients that are procured in small volumes, and the variable nature of annual requirements. This last situation requires that large capacity facilities and workforces be available, but their utilization is often incomplete, hence more costly on a per-item basis. As newer ingredients are being phased in, their cost will be much higher than that of the "legacy" ingredients (AP, Al, HTPB, plasticizers) because their production volume will be much smaller until their use is widespread.

More consistent properties. The use of statistical process control techniques is said to have originated with Congreve in the manufacturing of solid rocket propellant, and their application has brought an improvement in the consistency of the propellants and motors. Some incidents of failure of propellant processing to achieve high-quality results have been traced to variation in the ingredients. In these cases, the ingredients were found to meet the established specifications but to vary in unexpected ways. This problem is of concern across the industry but especially for those ingredients whose production volume is subject to significant annual variation, or made only occasionally, or in a production facility that is not attuned to the concerns of production of ingredients for energetic materials. Another cause of inconsistent performance is the use of formulations with lack of robust response to slight mischarges in ingredient weights or to slight in-spec variations of ingredient properties or lack of robust response to slight processing variations. These causes can be difficult to recognize and even more difficult to design out of a formulation, because they require many multidimensional experiments to define the relevant response surfaces. Typically, a propellant development program does not have sufficient funding to pay for the necessary work up-front.

Environmental concerns. AP is a nearly ideal oxidizing ingredient, considering high oxygen stoichiometry, good stability, absence of phase changes in the temperature range of interest, reasonable density, relatively low rate of moisture absorption, decomposition from the solid state allowing ballistic control via particle size adjustment, and relatively low cost at high-production volumes. But the evolution of HCl as an exhaust species and the mimicry of iodide by perchlorate in biological systems have caused concerns in the environmental community. Other oxidizers have been suggested and tested, but none has stood the test of time as a high-volume "workhorse" oxidizer. Ammonium nitrate has the advantage of low-cost and benign-exhaust products and has been formulated into some useful propellants. But it is much lower in available oxygen and melts before decomposition which eliminates burn rate effects based on particle size. Pure ammonium nitrate exhibits troublesome phase changes, and phase stabilizers have caused other problems. ADN (ammonium dinitramide) does not

evolve chlorine or mimic iodide, but it is still very costly, is inconveniently chemically reactive with some cure systems, melts a bit too low for many applications, and does not exhibit simple ballistic control. The production of nitrate esters leads to significant waste streams that must be treated. Certain burn rate catalysts based on metallic elements may cause toxicity in the exhaust products. Again, a liberal application of development funding may resolve some of these issues, but the pathway from here to a large-volume, low-cost production is not straightforward.

Life-cycle discussion. There has been a lot of talk about the costs and side effects of propellant development and production during their life-cycle, that is, all the way from ingredient synthesis to disposal of motors which are not used. The disassembly of motors with recycling of some ingredients has been demonstrated, particularly AP and Al, some of which has found its way into less-demanding applications. Some high-energy propellant has been recycled into simple explosives. The traditional approach of simply burning the propellant in an open pit is still used, albeit in fewer locations, with more permission required. Some researchers have proposed using thermoplastic binders which allow remixing of the propellant or hydrolysable binders that might be reconstituted into their original form after saponification or binder softening by solvent followed by ingredient separation and reuse. These schemes, for cost-effectiveness, would require large amounts of a single propellant (or of a closely related group of propellants) to be recycled.

4.1 Full Papers of This Part

Part IV comprises five papers (13–17) mainly examining the effects of propellant formulation on the condensed combustion products. The combustion mechanism of composite propellants based on different inert and energetic binders (HTPE, BAMO–GAP) and different oxidizers (AP, HMX, ADN) is thoroughly explored. Based on the synergistic effect of AP on HMX decomposition, a new route for incorporating HMX in composite propellants is proposed by Pivkina et al. The paper by Rashkovskiy et al. describes a new effect: the influence of burning surface curvature on burning rate of solid homogeneous energetic materials (e.g., double-based propellants, energetic binders, etc.) and a role of this effect in combustion of binary compositions based on different energetic binders and different fillers (AP, HMX, CL-20). The paper by Pang et al. is focused on AP-based dual oxidizers for a better control of mainly ballistic properties. By replacing the same fraction of AP by some energetic fillers (ADN, CL-20, GUDN, HMX), the combustion properties were appreciably modified; the compositions with ADN or CL-20 filler show higher performance in terms of specific impulse, heat of explosion, burning rate, and density but also demonstrate more sensitivity to impact and friction. The paper by Pei et al. investigates the energetic and combustion properties of formulations using BAMO–GAP copolymer as energetic binder. The ideal energetic properties

show a remarkable increase when AP and Al particles are replaced by ADN and AlH$_3$, respectively. The addition of catalysts to the composition can increase both the burning rate and surface temperature.

5   Liquid Rocket Propulsion[4]

All pioneers in rocketry, i.e., K. Tsiolkovsky, R. Goddard, W. von Braun, and H. Oberth, have always considered liquid propulsion as the most promising option for earth-to-orbit propulsion. Looking at an ideal rocket engine and assuming a frictionless, 1-D flow of an ideal gas with negligible entry velocity and the heat release in the combustion chamber at constant pressure with adiabatic walls, the thrust can be written as the sum of the momentum part and the pressure part to:

$$F = \dot{m}\, u_e + (p_e - p_a)\, A_e \tag{1}$$

where $u_e =$ the exhaust gas velocity at the exit area A_e; $p_e =$ the exit and $p_a =$ the ambient pressure, respectively. Obviously, for the early phases into the launch (when due to high ambient pressures, the pressure part is limited), the momentum part, i.e., the product of mass flow rate and exhaust velocity provides for main thrust contribution. With limited exhaust velocities, very large thrust levels are only possible with sufficient large propellant mass flow rates, and this is the main reason why many launch vehicles such the Space Shuttle, the ARIANE 5, the ATLAS V, or the H2A have been or are still using large solid propellant boosters for this initial launch phase although their exhaust gas velocities are at least 20 % smaller than those of liquid propellants.

As for all chemical rockets, although large exit velocities are quite favorable, the corresponding expansion in the nozzle may, depending of the height during ascent, result in exit pressures smaller than the ambient pressure which finally yields a smaller thrust coefficient. Aside from high combustion chamber pressure, the key impact factors are sufficient high temperatures, achievable with high-energy density of the fuel; a small isentropic coefficient; and the smallest possible molecular mass of the exhaust gas mixture. It should be mentioned here that already at temperatures below 2500 K, a process starts to play a role which distributes the energy released not only to the transitional states but as well to vibrational and rotational energy states of the molecules, and at somewhat higher temperatures, ionization is initiated, too. All these phenomena lower the overall efficiency since these energies cannot be fully recovered when the hot gases pass through the nozzles to generate the desired thrust.

The impact of the liquid propellant combination and its mixture ratio on the specific impulse is shown in Fig. 3. Obviously, H$_2$/O$_2$ is by far the most efficient propellant pair, while combinations of O$_2$ and hydrocarbons have an almost 30 % lower specific impulse which decreases further with increasing carbon content. Fuels which already contain oxygen atoms, i.e., various alcohols lag further

---

[4]Coordinated by Bryan A. Palaszewski and Oskar J. Haidn.
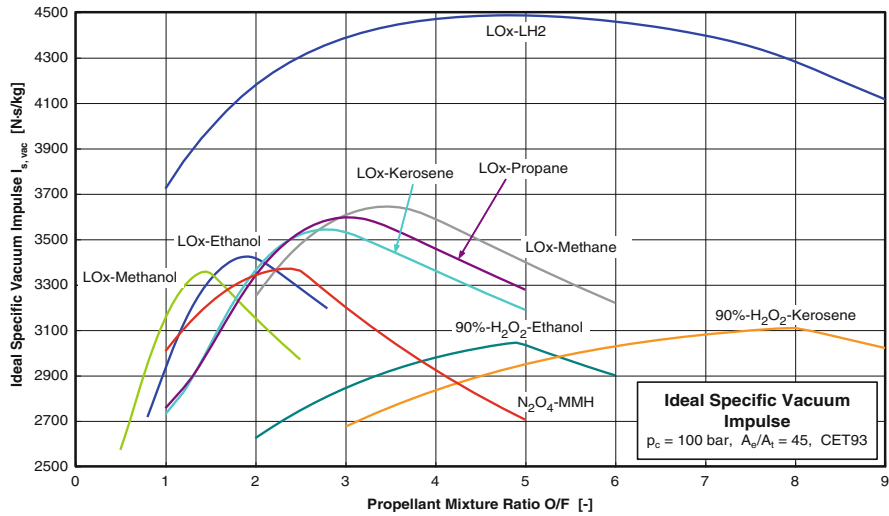
Fig. 3 Ideal specific impulse of various liquid propellant combinations (Courtesy of NATO RTO)

10 % behind and have an almost similar specific impulse as storable propellant combinations. For comparison reasons, the figure includes as well two propellant combinations which apply hydrogen peroxide as oxidizer. With the propellant combination hydrogen/oxygen having a specific impulse which exceeds that of any other practical propellant pair by at least 30 %, it becomes clear that engine designers strive to master the technological problems such as leakage, tightness, thermal transients, and storage which are linked to the application of liquid hydrogen in their engine in order to reduce the necessary fuel mass and increase the payload capability of the launcher. The major disadvantage of H_2/O_2 is the very low density of liquid hydrogen which is considerably smaller than any other liquid fuel and which cannot be compensated by the larger optimum mixture ratio and therefore results in much larger tank sizes for the same mission.

An interesting option from a system and cost point of view could be a launcher which applies only one propellant combination, i.e., LOx/methane. Although it is much less suited for booster applications than LOx/kerosene, it profits from the superior specific impulse at high-altitude operation, and this is one reason why this propellant combination has seen raising interest recently; see also the contribution in this chapter by Asakawa and coworkers.

Depending on the application, the thrust level of liquid propellant rocket engines may either reach values of almost 8000 kN or may be limited to a few mN, with the former thrust level achieved in the Russian RD-170 engine used for booster applications of the Energija launcher; see the contribution of Haeseler and Haidn and the latter value being typical for attitude control thrusters of satellites; see the paper of Fujii and coworkers later in this chapter, respectively. This extremely wide thrust range clearly demonstrates one of the many advantages of liquid propulsion

among which there are the possibilities to continuously regulate the thrust or to shutdown the engine on demand. One consequence of very high thrust levels is an adequately high combustion chamber pressures necessary to keep the rocket engines and pipe dimensions and thus their weight within the size and weight requirements of the launcher. Obviously, these high pressure requirements have severe consequences for the design of the turbomachinery.

Additionally to the propellant combinations and the consequences of their application, a liquid propellant rocket engine features several components and subsystems with critical design and manufacturing challenges. The injection system is one of the most crucial component since it has to fulfill many tasks, i.e., distribution and homogenization of fuel and oxidizer mass flow rates into the injection elements, decoupling of supply system and combustion chamber in order to avoid low frequency instabilities, and atomization and mixing of the propellants in order to achieve the best possible performance but at controlled heat release in order to avoid local overheating the combustion chamber walls. A typical design methodology would foresee to perform several subscale single-element tests in cold and hot flows to determine candidates for full-scale single elements where one would select a few candidates which would be tested further in subscale multi-injector arrangements to determine the most suitable injector configuration. All these subscale data will be used to anchor numerical design tools which will be used for the final full-scale design.

A proper design of a reliable ignition system is critical since a too early or a too late initiation of the ignition system may trigger combustion instabilities and result in a total loss of mission. The most challenging issue in ignition system design is the timing of the ignition sequence. Different propellant propagation velocities, heat transfer to, structural element, and phase changes in case of cryogenic propellants have to be predicted properly to determine the necessary amount of ignition initiation energy and proper timing as well as favorable conditions for ignition and flame propagation inside the combustion chamber. Furthermore, the ignition system has to fulfill the system requirements for weight and size and of course for safety.

With heat loads which may exceed 100 MW/m^2, design and manufacturing of a cooling system with varying channel geometry along the combustion chamber and wall thicknesses of less than 1 mm are major challenges in thrust chamber engineering. The design necessitates a coupled solution of the hot gas side heat transfer, the heat transport inside the combustion chamber walls, and the coolant side heat transfer. Due to the large thermal gradients, plastic deformation occurs which has to be taken into account for an analysis of the cyclic life of the liner. The cooling channel geometry design has to account for the thermal blockage caused by the high heat fluxes and the comparatively drastic change in the fluid properties, i.e., heat capacity, density, and viscosity, which take place at cryogenic temperature and high pressures. Very often Nusselt-type correlations are still applied to describe the heat transfer since a fully numerical solution of the coupled problems is far too complex. Major hurdles are the large differences in the length and time scales, chemical nonequilibrium or finite rate chemistry, the continuous transformation from sub- to supersonic velocities, and still missing models which describe satisfactorily dominating phenomena such as fluid atomization and near-critical fluid

behavior. Additionally, effects such as dissociation due to high temperatures in the combustion chamber and recombination with appropriate heat release in the cooler wall boundary layer, and, finally, catalytic effects at the liner surface are far too complex and time-consuming to allow for a coupled numerical solution.

Finally, turbomachinery design and manufacturing is the principal discipline in liquid propellant propulsion. These systems have to work under extremely high pressure and temperature gradients and rotational speeds which cause tremendous loads to the blades as well as to seals and bearings in general and in particular in hydrogen/oxygen engines where these components have to work in a liquid oxygen environment. The design process itself is an iterative process and requires the interaction of many disciplines, such as hydrodynamics, aerodynamics, mechanics, materials and processes, structural mechanics and analysis, rotor dynamics, thermodynamics, and last but not least instrumentation and testing. The set of requirements, pump discharge pressure and flow rate, pump suction pressure, turbine drive cycle and efficiency, fluid properties, throttling range, life, reliability, weight and size, and cost are often contradictive, and the final design is at best a compromise optimum for a specific application. Some of the issues mentioned above are discussed in more detail in the contribution of Haeseler and Haidn.

5.1 *Full Papers of This Part*

Part V includes four papers (18–21). Haeseler and Haidn present a concise summary of relevant Russian contributors (V. Chelomei, V. Glushko, S. Korolev, N. Kuznetsov, M. Yangel), design offices, specific and unique rocket engine technologies, and well-known launch systems. The paper discusses a wide range of engine and launcher developments starting with those systems the Russians worked on during their race to the moon and beyond. The fruits of this work persist in current engines and launch systems, namely, the RD-107/RD-108, RD-253, NK-33 engines, and Soyuz and Proton launch vehicles. The main emphasis of the description of up-to-date rocket engines (RD-170, RD-0120) and new developments (RD-0146) in Russia is put on unique concepts and technologies for propellant injection and ignition, manufacturing and cooling of thrust chamber liners and nozzles, and in particular turbo-pump technologies.

A second paper by Asakawa et al. also reports the status of research and development which has been carried out to realize a liquefied natural gas (LNG) rocket engine with higher performance in Japan. As a fuel of a rocket engine, LNG has better characteristics, i.e., longer storage, lower cost, and nontoxic; hence, LNG rocket engines have been investigated among many countries. A Japanese LNG rocket engine, named LE-8, had been developed by 2009 as the second-stage engine of GX rocket and successfully completed more than 2000 s of its firing tests.

A third paper by Fujii et al. provides recent activities and plans for spacecraft propulsion in JAXA (Japan Aerospace Exploration Agency). Over many years, JAXA launched numerous spacecraft, such as earth observation satellites, geosta-

tionary satellites, and HTV (H-II Transfer Vehicle). This is the spacecraft that carries various cargoes to the ISS in support of the ISS operation and has been launched at a rate of 1 per year since 2009. The propulsion system of the HTV is a bipropellant (MMH and MON-3) system and is equipped with four 500-N engines and twenty-eight 120-N thrusters to control orbit and attitude control.

The future liquid propulsion systems would aim to achieve higher performance, greater payload lift-off capabilities, system miniaturization, and overall reliability and safety. Gel propulsion offers one of the most attractive approaches to transform storable as well as cryogenic propellants to meet advanced mission requirements. The fourth paper authored by Varma focused on the formulation of hydrazine-based gelled fuel systems at reasonably low gellant concentrations, mechanism of propellant gel formation, and optimization of gelation process to produce gels of high quality and consistency. The influence of metallization of gelled fuel with nano- and micron-size metal powders on performance, ignition, and combustion characteristics is discussed. The flow behavior of UDMH-based gelled propellants under low and high shear rate has been emphasized to demonstrate their suitability for gel propulsion engines.

6   Hybrid Rocket Propulsion[5]

In recent years, very lightweight satellites become significantly popular for the purposes of communication, and Earth observation and demands are growing for launching such satellites by dedicated launch systems with high-degree-of-freedom options concerning the launch window, orbits, and other mission and system requirements. The key issue for the realization of such space transportation is economic efficiency. One answer to this question is utilization of nonexplosive rockets that can make economic production and operation possible. Hybrid propulsion is such a solution. On top of its relative simplicity, because of high levels of safety and thanks to the low effect of fuel cracking on the mission achievement and propulsion performance, hybrid rockets can utilize industrial-level raw materials, production methods, and inspection methods. Moreover, quality assurance and control can be done efficiently, and prelaunch safety reviews can also be reasonably reduced.

Hybrid rocket propulsion performance depends on internal flow dynamics with heterogeneous combustion, or in other words, the boundary-layer combustion. Since combustion occurs in the boundary layer over a fuel surface and the fuel regression rate is affected by the heat feedback from the flame, the smaller the length-to-diameter ratio, L/D, of the cavity of the combustion chamber is, the less the combustion efficiency is in the chamber. Besides, the shorter the length of the fuel grain is, the larger the oxidizer-to-fuel ratio, O/F, is. Too large an O/F

---

[5]Coordinated by Toru Shimada.

leads to insufficient extraction of the potential performance of propellant, that is, combination of fuel and oxidizer. In such a sense, the port L/D should be greater than a certain value for a given thrust level. The fuel gasification, or regression, rate depends on the oxidizer mass flux, G_{ox}, typically to the power of 0.6–0.8. This means that the larger the thrust level is, the larger the port L/D should be to keep the same O/F, because the growth of the fuel generation is slower than the oxidizer augmentation rate. Too high of an L/D leads to too heavy structural weights and inefficient loading of the propellant, which reduces the propulsion performance of the system.

For a conventional setting like an axial oxidizer injection with fuels, such as HTPB, polyethylene, and so on, an approach to minimize this problem is to use multiport grain of the fuel. This, however, requires a very complicated design when a high initial thrust is necessary, as in the case of the first stage of a satellite launcher. Because of this dilemma, studies on liquefying fuel, such as paraffin fuel or fuels with metallic or metal hydrides additives, have recently been conducted showing that such fuels can be supplied into the flame zone threefold faster than conventional fuels. Another way of generating and introducing fuel gas faster to the combustion process is to utilize swirling injection of gaseous oxidizer. In order to secure the effect of swirl injection, gaseous oxidizer should be injected in this type of hybrid rockets, which necessitates the prerequisite vaporization of liquid oxidizer before injection. Some promising methods have been proposed and tested.

Critical design issues for in-space propulsion, in general, regard higher mass fraction and higher specific impulse ranges, thus requiring optimization trade studies. For upper stage applications, mastering of restart/multiple firing use is needed.

In addition to system studies, the most promising propellant formulations and arrangements (aluminum loading, high-regression fuel, paraffin, additives, vortex, multiport/multilayer configuration, etc.) should be tested at larger thrust levels to determine propulsion scaling and combustion efficiency. Subscale testing and comprehensive analyses are needed to prepare candidate system(s) for enhanced component demonstrations at higher thrust level. Also, it is worth noting that hybrid rocket combustion is prone to low frequency instabilities (<100 Hz), but the triggering mechanism is not yet fully understood.

6.1   Full Papers of This Part

Part VI includes four papers (22–25). The first paper by Shimada et al. discusses why and how hybrid propulsion can make a dedicated, economic, lightweight satellite launcher possible. In this context, up-to-date technologies being developed in Japan on new fuels like low-melting temperature (LT) fuels and on swirling-oxidizer-flow-type (SOFT) hybrid rockets are described. In addition, challenges are discussed on simultaneous control of thrust and O/F ratio as well as on

CFD computations and visualization diagnostics of the internal ballistics and flow characteristics in hybrid rockets.

A second paper by Park et al. discusses the role of internal flow dynamics in determining regression rate and low-frequency combustion instability (LFI) in hybrid rocket combustion. In this context, large-eddy simulation (LES) and proper orthogonal decomposition (POD) analyses are conducted to investigate how turbulent flow characteristics are affected by wall blowing and/or a diaphragm insertion into combustion chamber, together with discussions on the LFI initiation mechanism.

A third paper by Hu et al. provides the energy performance analyses for paraffin-based fuel and HTPB fuel with different oxidizers to show the effect of these bipropellant combinations, together with measurements on thermal decomposition characteristics and on melting characteristics. In this context, experiments and numerical simulations are conducted to verify the regression rate characteristics of paraffin-based fuel in hybrid engines.

A fourth paper by Galfetti et al., focusing on the regression rate enhancement, analyzes the ballistic response of hydroxyl-terminated polybutadiene (HTPB)- and paraffin-based fuel formulations burning under quasi-steady and transient operating conditions by different diagnostics developed at the Space Propulsion Laboratory (SPLab) of Politecnico di Milano and discusses better formulations in terms of oxidizer mass flux sensitivity reduction, of regression rate enhancement, and of mechanical properties enhancement, together with the ballistic response of HTPB to forced transient conditions considering throttling down events.

7   New Concepts in Chemical Propulsion[6]

In addition to the four full papers presented in Part VII, several well-focused essays by recognized experts in the treated area are collected in this section. The topics were selected for their intrinsic importance or because they are considered quite promising for practical applications. These essays were written by a number of authors, some of which for different reasons could not provide a full paper.

7.1   Advanced Energetic Materials

New concepts in chemical rocket propulsion have been suggested and tested at many thrust levels over many decades. A wide range of advanced chemical propulsion concepts are given in this chapter. Implementation of these more exotic propellants

---

[6]Coordinated by Bryan A. Palaszewski.

is often not practical due to either physical limits of storage, safety considerations, or cost of development.

High-energy oxidizers such as fluorinated compounds include chlorine trifluoride (ClF_3), chlorine pentafluoride (ClF_5), and oxygen difluoride (OF_2). These oxidizers have a long history of testing with most recent testing in the 1980s under the Strategic Defense Initiative (SDI). Stages for interceptors were created for flight testing using hydrazine/ClF5.

Metallic hydrogen is a theoretically dense energetic material (not yet produced on earth). The TRL level is now at level 1 as the characteristics are based on theoretical calculations. The estimated density at ambient conditions is 7 g/cc, ten times LH2. Above a critical temperature, possibly 1000 K, metallic hydrogen will become unstable and recombine to the molecular phase, releasing the energy of recombination, 216 MJ/kg (for reference: $H_2 + O_2$ in the Space Shuttle Main Engine (SSME) releases 10 MJ/kg, LOx/RP1 releases 6 MJ/kg). Ongoing experiments are using diamond anvil cells and short pulse laser technologies to follow the hydrogen melt line toward the conditions for the metallic state. Expected specific impulse (I_s) values are in the 500–2000 s range.

The challenges in implementing are that upgrading of the existing experimental equipment is required for synthesis and characterization of small quantities of metallic hydrogen. Also, scaling up production by many orders of magnitude is required. Engine components must be developed that are compatible with metallic hydrogen. Test engines must be developed to verify expected operations and performance with a variety of diluents and mixture ratios. Potentially, there is a need for tankage that operates at several thousands MPa of pressure.

Atomic boron/carbon/hydrogen propellant has been investigated for many decades. Atomic hydrogen, boron, and carbon fuels are very high-energy density, free-radical propellants. These atoms have been trapped in solid cryogens (neon, etc.) at 0.2–2 mass %. Atomic hydrogen may deliver an $I_s \approx 600$–1500 s. There has been great progress in the improvement of atom storage density over the last several decades. Laboratory studies have demonstrated 0.2 and 2 mass % atomic hydrogen in a solid hydrogen matrix. If the atom storage were to reach 10–15 mass %, the rocket I_s would be 600 to 750 s. The storage of atoms at 10, 15, or 50 mass % is needed for effective propulsion.

High-nitrogen compounds (N_4, N_5^+, N_5^-, N_8, etc.) are potentially the most powerful chemical explosives created in history. Work was conducted on N_5^+ and N_5^- both under the Air Force Office of Scientific Research (AFOSR) High Energy Density Materials (HEDM) Program and in Sweden (N_5^-). Gram quantities of the (N_5^+) ionic salt have been produced in the laboratory [46, 47]. Theoretical studies have shown that these materials may have in-space propulsion applications. There are many challenges to any practical use of these compounds, particularly as these materials are highly shock sensitive. Additional challenges include fabrication, transportation, ground processing, and personnel safety. Presently, there are no integrated vehicle designs that can make use of this possible propellant. Work is continuing in this area both in the USA and worldwide.

7.2 Innovation of Energetic Materials by Materials Genome Initiative[7]

7.2.1 Conception and Significance

Advanced materials are the foundations for the innovation and development of almost all modern industries such as advanced fabrication, information and internet technology, human happiness and benefit, national security, and so on. In order to promote the development efficiency of advanced materials, US President Obama subscribed to the white book entitled "Materials Genome Initiative (MGI)." This initiative hopes to integrate the theoretical, computational, experimental, and database methods to speed up advanced materials fabrication. MGI aims at reducing the whole development period of new materials (from discovery and design and synthesis and fabrication to service and application) from about 20 years in average to half of it, as well as make the cost much lower.

Energetic materials (EM) are one of the key materials for the national defense and the people's livelihood. If the MGI modes were used in the development of EM, the efficiency of EM manufacture would be greatly enhanced, which will benefit the society. This is the so-called EM genome initiative (EMGI). EMG is the basic microstructural genes and their essential correlations which determine the related macro-properties and behaviors; EMGI is the discovery of "genome" which determines the properties of EM, based on which new EMs are designed and synthesized. EMGI emphasizes the exertion of cross effect and the enhancement of cooperation for databases, computations, and experiments by the guidance of theories. The outstanding characteristic is putting all sorts of data into databases and managing them, forming big EM data through multiple iterative operations and obtaining MG; at the same time, by forecasting through theoretical modeling and calculations, as well as the validations of experimental technologies, fabrication efficiency of EM is greatly enhanced. In detail, as demonstrated in Fig. 4, EMG includes atoms, atomic groups, molecules, crystals, crystal/crystal surfaces and interfaces, crystal defects, the relatives, crystal/relative surfaces and interfaces, and so on [48–52]. This can be the cut-in point in the study of EMG. For example, in the scale of molecular structures, the EMGs of low-sensitive EM feature planar conjugation structure, relatively strong intramolecular hydrogen bonds, and large bond-dissociation energy; as for crystal structures, they should have intermolecular hydrogen bond-assisted $\pi-\pi$ stacking [51, 52]. As a matter of fact, finding EMG is not an easy thing, which must be based on large amount of data.

The significances of the EMGI are that EMGI reflects the nature of EMs, EMGI will change the modes of the EM R&D, and EMGI will change the people's traditional closed concepts to be more open. More than 1000 years ago, Chinese invented black powder. EMs proceeded from black powder to premodern EM and

---

[7]Written by Chaoyang Zhang.
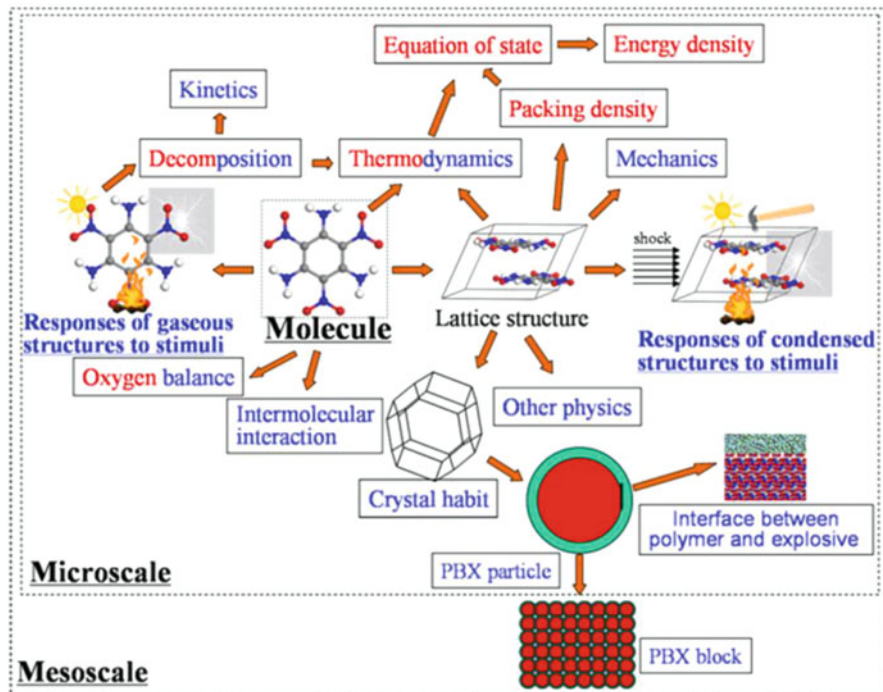
Fig. 4 Typical microstructures of EM, including atoms, molecules, crystals, micro-particles, interfaces, and so on. These structures could be the genes of EMs. One of the tasks of EMGI is to confirm the relationship between these structures and macro-properties and performance

to modern EM periods. Especially for the latest 100 years, EMs have progressed quite greatly. However, the development of EMs has still problems such as the low speed of development, the singleness of the composition and structure, the unsolved energy-sensitivity contradiction, the limitation of energy storage and release, and so on. Using the MGI mode, viz., through the operation of EMGI, the big progress of EMs is hopeful to be realized. MGI emphasizes the application of high-throughput parallel iterations, instead of progressive iterations in traditional trial-and-error methods, changes the research modes from "experience-guided experiments" to new "theory forecasting and experiment validating" gradually, and realizes the "demand design" of materials finally. In the process, experiments, computation, and database are highly integrated, and cross-field information is also highly integrated. Based on the former studies, the EM research also accumulates some bases of EMGI.

7.2.2 A Tentative Plan of EMGI Development

The medium- and long-term goals of EMGI are to achieve the "demand design" and complete digitized fabrication of advanced EM through theoretical computation and digital simulation. The present goal of EMGI is to establish EM innovation, including high-flux computation platform, high-flux fabrication and examination platform, as well as materials database. These basic establishments are linked up with existing integrated computational materials project, and multi-subject intercrossing and syncretizing are realized, so that the process from discovery to application of EM can be speeded up. Thus, EMs with required properties can be designed and synthesized.

In order to achieve these goals, concrete measures should be taken, which include (1) developing computational tools and methods of EMs, reducing the experiments cost and time, and speeding up the design and selection of EMs; (2) developing high-flux experimental tools of EMs, and the candidate EMs are selected and validated; (3) developing and consummating the EM database/informatics tools and managing the data chain of the whole process from discovery to application for EM efficiently; and (4) reforming the enclosed working modes of EM and forming new open and cooperative working modes.

The MGI platform has four parts including (a) database, (b) design and computation, (c) fabrication and characterization, and (d) service and aging evaluation:

(a) EM database. Three parts of works are included: (1) collecting and handling relative basic data of EMs and establishing standards for EM data; (2) selecting design methods and tools for the database and designing database models; and (3) applying software engineering technologies, designing and developing the database system, and managing the platform.

(b) EM design and computation. The relative researches on computational EM science include (1) as for structures, multi-scale and multilevel structures of EM: molecular structure, crystal structure, surface and interface structure, geometric structure of the components, and so on; (2) as for performance, energy, safety, mechanical properties, compatibility, aging performance, and so on; and (3) as for computational methods, molecular simulations, cellular simulations and numeric simulations. In addition, considering the environmental stimuli such as heating and strength, necessary experimental validations are also considered in the computational part. The high-performance computations facing to EMGI and the demand of national advanced equipment include subjects as follows: scientific understanding of EM science, design of EMs, and engineering application and design of EMs. Through the researches above, a high-performance research platform of EMGI science and engineering which includes computational EM theories and methods, EM database, hardware, and software can be formed.

(c) EM fabrication and characterization. The EM fabrication and characterization based on EMGI modes have high-efficient characteristics such as multi-scale, "whole process," and high flux. As for the EM fabrication, three levels are

included, which are contriving of energetic molecules, controlled fabrication of energetic crystals, and fabrication of composite EMs like propellants. Based on the design and computation, suitable platform should be selected to carry out the works, and parallel and batch experiments should be considered for the crystallization and composite EM fabrication. As for energetic molecules, energetic crystals, and energetic composites, analysis technology and methods should be established, molecular structures should be determined, and the analysis standard and method of the crystal phase, surface and interface, composition, thermal properties, and safety should be set up, so that the high-efficient analysis insurance can be provided for the fabrication of EMs. A "whole process" monitoring system should be designed to realize fast analysis.

(d) EM service and aging evaluation. In the study of the aging and compatibility for EMs, we could examine chemical reactivity, thermodynamics, molecular degradation mechanism, and microstructure studies at EM scale and master the microchange mechanism of component materials; at the specimen and component scales, we could carry out studies of testing aging, interfacial property, mass, density, and mechanical property and releasing gas sorts and components; see about the change of the macro-properties and the size effects from specimen to component in the process of aging and compatibility research, and improve the efficiency of aging and compatibility research; meanwhile, we could establish numerical models and achieve the organic combination from microchange mechanism to macro-properties.

Moreover, EMGI theories and their cooperative development with database, computations, and experiments should be noted. The development of EMGI theories is tightly related to that of database, computations, and experiments: theories are the basis and ligament of database and computational and experimental methods, and also guide the whole process of research and development of new EMs.

To summarize, to develop EM using the concepts of genome, new opportunities are hoped to come, and breakthrough is currently possible to be realized at the aspects such as energetic co-crystals and energetic salts. More importantly, EMGI will change the culture and ideas of EM R&D greatly, which will be more open and cooperative. Thus, the efficiency of EM fabrication will be greatly enhanced.

7.3 Surface Engineering of Energetic Materials by Atomic Layer Deposition[8]

Surface properties of energetic materials are important factors to consider for their employments in propellants and explosives. For example, the sensitivities of energetic materials are closely related to their surface compositions and morphologies.

---

[8]Written by Hao Feng.

Surface fabrications are usually necessary for the applications of many energetic materials. For surface fabrication of energetic materials, effective modification of surface properties without too much sacrifice in the energy density is desired. However, due to the lack of efficacious control, conventional surface fabrication techniques, such as mechanical mixing, polymer encapsulation, wet impregnation, etc., can only produce surface coatings of fair qualities, which usually lead to significant loss of the energy density.

In recent years, atomic layer deposition (ALD) has emerged as an effective technology for applying precise, conformal thin films onto high surface area supports [53]. In an ALD process, two gaseous precursors are pulsed alternatively such that each reacts with the surface functional groups generated during the previous pulse to produce a deposition cycle. This unique film growth pattern effectively avoids channel blocking in porous systems and ensures excellent film uniformity on almost any substrate. In addition, ALD is capable of preparing thin films of virtually any thickness down to atomic-level precision [53]. Therefore, this technology is suitable for surface fabrication of some energetic materials.

The first endeavor to fabricate energetic materials by ALD is the synthesis of metastable intermolecular composites (MICs). The objective is to obtain intimate fuel–oxidizer contact by directly coating the oxidizer onto nanometer-sized Al particles. The first attempt to test the possibility of this approach was made by Ferguson et al. [54]. In their work, SnO_2 was deposited on the Al nanoparticles with a fluidized bed ALD reactor. However, due to insufficient reactant exposures, the ALD surface reaction was not saturated, leading to limited film growth and large deviations from the expected oxidizer to fuel ratio. Qin et al. carefully studied the saturation conditions of ALD surface reactions on the Al nanoparticles [55]. With saturated surface reactions, film growth rates comparable to those reported on flat substrates were achieved on the Al nanoparticles. The MICs synthesized under saturated surface reaction conditions exhibited very nice core–shell structures (see Fig. 5). The oxidizer layers deposited on the Al nanoparticles were conformal, and their thicknesses could be precisely controlled by adjusting the number of ALD cycle. In laser ignition experiments, the reaction rates of the core–shell-structured MICs were several times faster than the mixture of nanopowders [55]. The enhanced reaction rate was ascribed to the intimate fuel–oxidizer contact as a result of the exquisite core–shell nanostructure and the excellent conformity of the oxidizer films.

In a recent conference report, ALD was applied to fabricate micro- and nanoparticles of Zr to tackle with its static charge sensitivity problem [56]. By performing ALD of metal oxides or organic polymers to the Zr powder (the process is named molecular layer deposition (MLD) when organic polymers are synthesized in a layer-by-layer thin film growth fashion of ALD), Zr particles could be encapsulated by a uniform, thin layer of Al_2O_3, ZnO, polyamide, or carbon. The thicknesses of the encapsulation layers could be precisely controlled and the mass % of the deposited materials accounted for less than 3 % of the metal particles. The static charge sensitivity of Zr particles could be tuned by varying the type and thickness of ALD coatings. The ALD Al_2O_3 coating exhibited a unique surface-sealing effect:
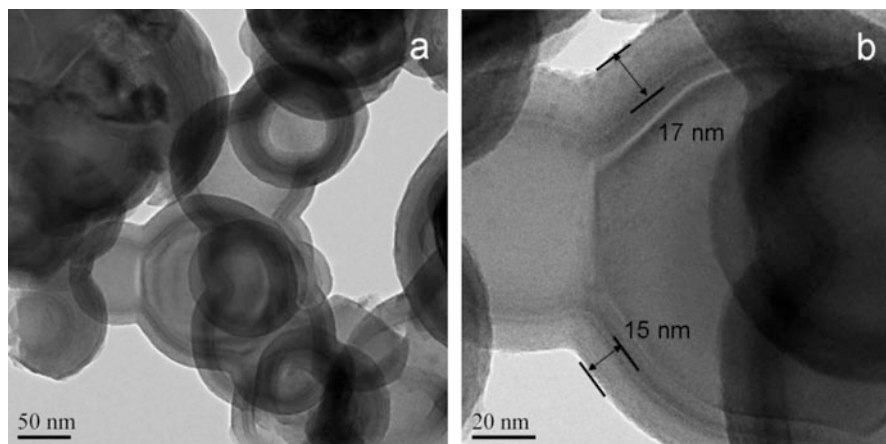
Fig. 5 TEM images of core–shell-structured MIC: **a** Al-core-SnO$_2$-shell nanoparticles synthesized by ALD; **b** magnified TEM image showing the uniform SnO$_2$ layer on the nAl particles (Reprinted with permission from [50], copyright (2013) Springer Science + Business Media Dordrecht)

oxidation of Zr particles at temperatures lower than 700 °C could be suppressed with an ALD Al$_2$O$_3$ coating of a few nanometers.

ALD Al$_2$O$_3$ coatings were also utilized to fabricate the surface of ammonium dinitramide (ADN) [57]. The purpose of the research was to build a water molecule diffusion barrier layer on the surface of ADN to improve its stability in humid air. The surface of ADN could be completely encapsulated by the ALD Al$_2$O$_3$ coating. Under scanning electron microscope, no defects were observed on the ALD Al$_2$O$_3$ film. In an environmental adaptability test, the shapes and topologies of the ALD Al$_2$O$_3$-coated ADN particles were maintained after 48 h of air exposure. However, results from vapor adsorption experiments indicated that the hygroscopicity of ALD Al$_2$O$_3$-coated ADN was not improved. The loss of the surface-sealing effect was attributed to the invisible defects in the ALD Al$_2$O$_3$ film. Since the melting temperature of ADN is very low, the ALD experiment had to be carried out at an even lower temperature, which inevitably led to incomplete surface reactions and, consequently, tiny defects in the Al$_2$O$_3$ film. Therefore, although the ALD Al$_2$O$_3$ coating completely covered the surface of ADN and helped maintain the shapes of spherical ADN particles, the tiny defects in the ALD Al$_2$O$_3$ film could serve as passages for water molecules to infiltrate.

ALD coatings of Al$_2$O$_3$ and ZnO were applied to Octogen (HMX) for the purpose of reducing its sensitivities [58]. The micrometer-sized HMX particles could be completely encapsulated by ALD Al$_2$O$_3$, whereas the surface coverage was not complete when ALD of ZnO was directly applied to HMX. A seed layer of ALD Al$_2$O$_3$ was required to obtain complete encapsulation of HMX by ZnO. Thermal gravimetric analysis indicated that the inorganic coatings were compatible with HMX in that the thermal decomposition behaviors of HMX were not too

much affected by these ALD films. An interesting finding was that the crystal phase transformation of HMX at 193.7 °C could be inhibited by the ALD coatings. Results of the sensitivity measurements revealed that the inorganic ALD coatings could reduce the static charge sensitivity of HMX but could not lower its mechanical sensitivities. Soft organic polymers fabricated by MLD were proposed in the future work to alleviate the mechanical sensitivity problems.

The greatest merit of ALD or MLD is the ability to precisely control the surface structure. With this technology, it is possible to introduce desired physical or chemical properties onto the surface of various energetic materials with the minimum loss of the energy density. In principle, most of the problems related to surface properties of energetic materials could be solved or mitigated by proper treatment to the surface. ALD surface engineering is a powerful tool to provide such high-quality and precisely controlled surface treatment.

As an emerging technology, ALD surface engineering of energetic materials still faces many challenges. First, although most of the ALD and MLD reactions can be carried out at relatively low temperatures (100–200 °C), this temperature range is still too high for many energetic materials. ALD and MLD processes that can be performed at milder conditions are needed for fabrication of more energetic materials. Second, the technology to fabricate large quantities of powder samples by ALD is not mature. Although a few prototypes of rotary ALD reactors and fluidized bed ALD reactors have been developed for this purpose, their best production capacity is not more than 100 g per batch [59, 60]. In addition, many safety issues related to the large-scale ALD fabrication of energetic materials still remain to be explored. Last, but not least, ALD fabrication of energetic materials can be expensive. Besides the investment in the ALD facility, the expenses of ALD precursors are not trivial. Many efforts are needed to lower the costs of ALD processes, including developing cheaper ALD/MLD precursors, promoting efficacy of ALD reactions by improving the reactor design, and installing recovery systems to reuse unreacted precursors.

7.4   Energetic Ionic Liquids for Space Propulsion[9]

Research in energetic materials is now heavily focused on the design and synthesis of novel insensitive energetic materials for rocket propulsion or military applications. The challenges in this field have been concentrated on how to integrate high energy and low sensitivity as well as greenness in one propellant or explosive molecule. Recently, a new class of the so-called "energetic ionic liquid (EIL)" materials has emerged, which are only composed of ions, such as nitrogen-rich cations and energetic fuel-rich anions [61]. Since 2005, a variety of EILs have been developed containing one or more $-NO_2$, $-N_3$, or $-CN$ groups, and their applications

[9]Written by QingHua Zhang.

as chemical propellant fuels or high explosives have been preliminarily explored. Indeed the concept of EILs has provided a great opportunity for developing new ion-type energetic materials, which can make both the property and performance of the target material reasonably customized [62].

The advent of EIL materials is the result of interdisciplinary research between ionic liquid chemistry and energetic materials. Obviously, there are a number of benefits of EILs as novel energetic materials, including (1) the traditional design strategy of ionic liquids which has endowed EILs with a unique modularity character, which can better control the physical, chemical, and energy properties of target energetic materials; (2) the extremely low volatility of EILs which avoids their volatilization problems in uses and therefore reduces safety and environmental concerns; and (3) the low sensitivity of EILs which makes the storage, handling, transportation, and processing much safer and easier [63]. More importantly, by virtue of this EIL concept, the combination of ionic liquid properties (e.g., nonvolatility, high thermal stability, low melting point) with the energetic functions of propellants or explosives (e.g., high-energy density, hypergolicity, high specific impulse, etc.) may lead to a variety of new energetic materials while at the same time improving the related safety and environment issues. In this sense, EILs have provided a new platform for the R&D of new energetic materials, in particular for the hypergolic liquid propellants and melt–pour explosives.

According to different application purposes, EILs can be divided roughly into two main classes: green propellants and novel explosives. In the explosive uses, EILs are mainly designed as the promising explosive melt phase, whose function is to replace TNT in the melt–pour explosives [64]. In the field of chemical propulsion, it is known that highly toxic and volatile hydrazine derivatives are still widely used in both the liquid monopropellant and storable bipropellant systems, especially in those spacecraft control propulsion systems that require pulsing modes of operation and multi-restarts. Along with growing concerns about the environment and safety issues, considerable efforts have been devoted to synthesizing new EILs as green propellants. When compared to hydrazine-type fuels, hypergolic EILs as propellant fuels have some advantageous properties including extremely low volatility, higher loading density (e.g., 0.9–1.2 g cm^{-3}), long-term thermal stability (decomposition temperatures up to 300 °C), short ignition times (down to 2 ms), high specific impulses (I_s comparable to UDMH, i.e., 198 s under standard operating conditions), etc. Since 2008, a wide variety of EILs have been attempted as green hypergolic fuels. In this field, S. Schneider and T. Hawkins from Edwards Air Force Base (USA) are pioneers who have first demonstrated the feasibility of dicyanamide-based EILs as potential hypergolic fuels [65]. Later, J. M. Shreeve' group from Idaho University (USA) has done massive works in the development of new hypergolic EILs, in particular focusing on fuel-rich borane-derived EILs [66]. A typical example is the N-allyl-N,N-dimethylhydrazinium dicyanoborate with a melting point of <−80 °C, a thermal decomposition temperature of 189 °C, a density of 0.93 g cm^{-3}, a viscosity of 35 cP, and an ignition time as short as 4 ms [67]. No doubt that the designable character of EILs makes the achievement of an ideal hypergolic fuel possible, where the property and performance of EILs
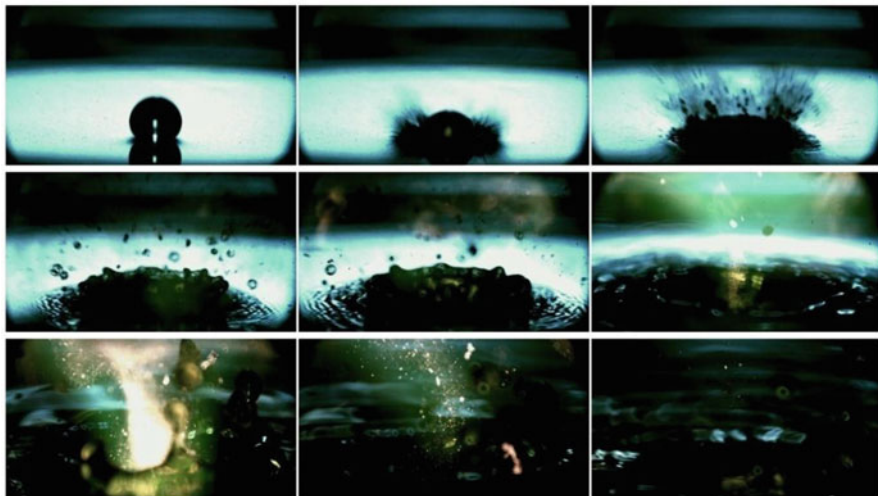
Fig. 6 Hypergolic ignition delay measurement of an EIL fuel drop released from a syringe into a WFNA (white fuming nitric acid) oxidizer

can be task-specifically customized to a level comparable to hydrazine-type fuels, thereby providing a unique architectural platform for future ionic liquid propellant materials. In principle, like hydrazines, EILs can be used as both monopropellants and hypergolic fuels. An example of hypergolic ignition is shown in Fig. 6.

In essence, chemical propulsion is achieved by converting thermal energy of chemical reactions into directed translational energy of combustion products. Therefore, from the viewpoint of practical applications, a number of physical, engineering, economic, and combustion characteristics are of great importance in evaluating the EILs' performance level. Important factors include their normal liquid operating range, energy density, viscosity, ignition time, specific impulse, density, cost, etc. Specifically, a wide liquid operating range, viz., low melting point and high-decomposition temperature, is very desirable for EILs' practical applications, also considering their harsh operating conditions. In particular, in many cases, unexpected thermal decomposition of propellants may cause undesirable product deposition (resulting in local "hot spots" and burnout) and even induce accidental explosion. The high thermal stability of EILs (decomposition temperatures generally higher than 150 °C) solves this problem well. In addition, the density determines the size of the fuel tank. Thus, the EILs which generally have densities >0.9 g cm^{-3} (much higher than 0.793 g cm^{-3} of UDMH) can contribute to higher loading capacity, thereby reducing the structural weight and aerodynamic drag of the vehicle. Short ignition delay and high-combustion efficiency can efficiently eliminate the undesirable product deposition of EILs which may result in local "hot spots" and burnout, avoiding possible accidental explosions in the launch process. Low viscosity is also very desirable for the mass transfer requirements

of EILs during the fuel pumping, pressurization, and ignition and combustion processes, in spite of higher viscosities (>20 cP at 25 °C) of most known EILs than hydrazine-type fuels (*ca.* 0.51 cP at 25 °C). Economic factors of the EILs as rocket fuels are mainly related to the availability of their raw materials and synthesis cost as well as the equipment required for transportation and storage. At this point, high synthesis cost and difficult purification problem of EILs will be one of the most important issues hampering their large-scale application.

Although significant progresses involving EILs have been made in the field of energetic materials, there are many challenges that remain to be overcome. For a long time, most studies have been conducted based on the "try and see" approach, and in-depth studies of EILs on their rational design and high-throughput synthetic technologies are still lacking to date. Future research should focus on a deeper understanding of these interesting EILs materials, in particular the correlations between their structure, property, and performance, which will be of great significance to stimulate their potential applications in industry. Also, more efforts should be devoted to an integrative utilization of multitheories and technologies on a deeper level, e.g., one may make use of computing simulation to achieve the structure screening and property prediction. Systematic studies on large-scale storability, compatibility, and aging are rare. Yet, we believe that this new class of EIL materials as fuels for chemical propulsion is far from fully exploited. As discussed in detail in both [68, 69], EILs represent a new technological field full of opportunities.

7.5   *Catalysts in Chemical Propulsion*[10]

Catalysts in the field of chemical rocket propulsion have been developed along different guidelines:

1. For the chemical synthesis of new energetic materials. Heterogeneous catalysis using solid catalysts can improve the synthesis conditions, reduce the number of reaction steps, and avoid the formation of side products. New developments of the synthesis parameters are necessary for future production scale-up.
2. For the control of the solid propellant burning rate and its pressure dependence, typically by influencing the heat release rate in the condensed phase. Introducing new catalytic nano-materials as rate modifiers in general may permit increased ballistic accuracy (see also the historical survey in 45).
3. For the catalytic decomposition of liquid monopropellants or the ignition of liquid bipropellant mixtures. Less pressure drops and stronger mechanical as well

---

[10]Coordinated by Charles Kappenstein and Valery P. Sinditskii with contributions by WeiQiang Pang and FengQi Zhao.

as thermal resistance are needed to improve the performance of new engines; this can be obtained by using advanced catalytic beds.

4. For the replacement of classical alumina pellets by new structured cellular catalyst supports, as honeycombs, foams, or MEMS; the substrate can be based on ceramic or metal- or nano-sized metal oxide-decorated graphene, such as Fe_2O_3/graphene, TiO_2/graphene, etc. Such new catalyst substrates have been tested for the decomposition of various monopropellants (hydrazine, hydrogen peroxide, nitrous oxide, and ionic liquid-based propellants) and for the ignition of cold hydrogen–oxygen mixtures. Results are available at different levels depending on the application.

With reference to the second topic, due to the strong interest in military applications, attention has mainly been paid to solid rocket propulsion. During the last decades, the main targets for solid propellant development have been to increase energy content, density, and insensitivity while decreasing signature and environmental impact. Energetic materials for missiles and ammunitions demand well-controlled characteristics over a wide range of burning rates and keeping low the pressure exponent values. Combustion catalysts can be added to the basic solid propellant formulation in order to exactly meet this demand. To this end, many types of combustion catalysts were developed, such as metal oxides, organometallic compounds, mixtures of metals, nano-sized combustion catalysts, energetic catalysts, dual-metal catalysts, and more. Because of their unique properties, nano-sized combustion catalysts, energetic catalysts, and dual-metal catalysts have become hot research topics in the field of catalysis for chemical propulsion and have attracted the attention of researchers from all over the world.

For example, thermal decomposition of ammonium perchlorate (AP) by noncrystal nano-sized Fe_2O_3 was shown in [70]. Thermal decomposition of NC/NG and RDX by nano-sized neodymium oxide was discovered in [71]. The interaction of different nano-sized components in the same composition can produce strong synergistic effects leading to higher catalytic activities than that of the single component. In this respect, the catalytic effects of nano-sized $CuO \cdot Cr_2O_3$ composites, nano-$CuFe_2O_4$ powders, and nano-$Bi_2O_3 \cdot SnO_2$ on the thermal decomposition of RDX were compared, and the best catalytic effects were displayed by nano-$CuO \cdot Cr_2O_3$ composites [72]. The effect of nano-sized titanium oxide on thermal decomposition and combustion of HMX was discovered in [73].

Energetic catalysts are compounds which contain both metal atom and energetic groups (nitro-, azido-, azo-, etc.) capable of releasing energy during their decomposition. Availability of such groups in the molecule increases energetic characteristics of the metal-containing material and often endows the compound with ability to burn [74]. Combustion of the energetic catalyst is accompanied by generation of the catalyst practically in the atomic or molecular form, thus increasing efficiency of its action. The efficiency of ferrocene derivatives, the best combustion catalysts of AP-based propellants, is caused by the rapid oxidation of ferrocene by AP to form Fe_2O_3 in the molecular form [75, 76]. Currently, a large number of metal compounds, which can sustain combustion and may act as energetic catalysts, have

been synthesized and studied [77, 78]. However, it should be noted that an increase in the burning rate of propellants can be attributed to not only the catalysis of combustion but also the cratering effect at the burning surface caused by extremely fast decomposition or combustion of particles of the fast-burning additive [79].

Novel energetic composite catalysts for propellant combustion were prepared and tested by Zhao FengQi et al. [80]. It was found that lead salt of 2-hydroxy-3,5-dinitropyridine (2HDNPPb)/copper salt of 2-hydroxy-3,5-dinitropyridine (2HDNPCu) and lead salt of 4-hydroxy-3,5-dinitropyridine (4HDNPPb)/2HDNPCu composite catalysts feature better catalytic effects and a pronounced ability to reduce the pressure exponent of RDX–CMDB propellants. Compared to single energetic lead or copper salts, the mixtures of lead and copper salts of hydroxypyridines have higher catalytic efficiencies at the same content of catalyst.

NTO is an insensitive high explosive, and the metal salts of NTO are considered potential energetic ballistic modifiers for AP/HTPB- and AN/HTPB-based solid propellants. Preparation, characterization, and thermal decomposition of some of the NTO transition metal salts were reported by Singh et al. [81] at HEMRL (Pune). The results show that NTO, $Cu(NTO)_2$, and $Fe(NTO)_3$ enhance the steady burning rates of AP/HTPB-based solid propellants above those of CuO and Fe_2O_3 at equivalent metal concentration. The activity of NTO and its salts is also evident during the condensed-phase thermolysis of the modified propellants. Further systematic analyses by Singh [82] show that the metal ions catalyze oxidation of NTO moiety in the respective compounds, and Cr is the best catalyst among the tested metals. Ferric and chromic compounds are well-known oxidation catalysts, and their NTO salts are quite insensitive toward impact and friction. Thus, these salts are promising high-energy ballistic modifiers for solid propellants.

With reference to topic no. 4, graphene is a special type of carbon having a flat sheet, which is just one atom thick. It has attracted great attention in recent years due to its unique features such as electrical, optical, catalytic, and mechanical properties [83, 84]. Recently, graphene sheets have been successfully used as a substrate that helps to stabilize and disperse nano-sized particles (Fe_3O_4, TiO_2, Fe_2O_3, CdS, CdSe, Co_3O_4, etc.). This dispersion, along with the stabilization of nano-sized particles, helps to enhance the catalytic activity. It has been found that graphene–iron oxide nanocomposites (GINCs) show excellent catalytic activity on the thermal decomposition of AP and significantly increase the burning rate of the associated propellants. It is foreseen that other metal/graphene nanocomposites and graphene-based metal/metal oxides can be used as catalysts for AP and AP-based composite propellants.

Further achievements of research on catalytic combustion of fuels in a fluidized bed have mainly been performed at the Boreskov Institute of Catalysis of the Siberian Branch of the Russian Academy of Sciences for the last 40 years; see, for example [85, 86]. As compared to other types of combustion, a specific feature of catalytic combustion is the predominant oxidation of the fuel on the surface of solid catalysts, with or without a minimum contribution of the open flame. As a result, chemical interactions of fuel components with surface oxygen occur on the catalyst surface, followed by regeneration of the reduced surface by gas-phase oxygen.

The catalyst activity in the course of complete oxidation is largely determined by the bonding energy of surface oxygen. As compared to traditional methods of fuel combustion, the presence of a catalyst alleviates the severe requirements of thermochemical properties for structural materials, reduces heat losses through the walls, simplifies the process control, and eliminates secondary endothermic processes where toxic substances are formed. Moreover, the use of a catalyst decreases the explosion hazard and increases the energy intensity of the processes. As a result, the size and metal consumption of structures can be substantially decreased. The use of a catalyst also reduces the concentration of nitrogen oxides for both thermal oxides (generated from nitrogen contained in air) and fuel oxides (generated by nitrogen-containing fuel components).

7.6   *High-Performance/Low-Cost Solid Rocket Motors*[11]

Solid rocket propulsion allows using a very low-cost hardware, but it is handicapped by its (i) low performance in terms of specific impulse versus liquid rocket propulsion and by (ii) its environmental impact. Work done in the USA and in Germany (Lo, TU Berlin) shows that a frozen mixture of H_2 and O_2 burns as a traditional solid charge by parallel planes. Such a way may combine the high performance of cryogenic propellant with the low cost of solid hardware.

An intermediate and more realistic step is to remain in the domain of the refrigeration industry. Working in this range of temperature allows the use of the classical hardware of solid propulsion with minor adaptations (i.e., composite cases, flex seal): current technologies can be used, without any adaptations, from ambient to $-10\,°C$ initial temperature. Solutions exist and have already been tested using hydrogen peroxide as oxidizer and aluminum or alane with potentially much higher I_s than conventional solids; see work by SNPE (now Safran Herakles) in France [87] and the sounding rocket ALICE in the USA [88].

7.7   *Space Commercialization*

While the technologies described above have many applications, the most recent new space commercialization vehicles may be their first users. With the retirement of the Space Shuttle in the USA, new directions for space exploration have begun. NASA, while mainly focusing on planetary exploration with robots and humans, has begun fostering commercial companies to provide the more near-Earth cargo and personnel deliveries to the International Space Station (ISS). Actually, commercialization of space systems has been evolving over a long

---

[11]Written by Max Calabro.

period, say several decades, but limited to space services (such as systems for telecommunications, Earth observation, meteorological forecasts, navigation, and so on). Only recently reliable and low-cost access to space, a crucial factor for true space commercialization, is becoming a reality. SpaceX, Orbital, and Boeing, along with some newer start-up companies, are providing or developing space vehicles that can deliver cargo or people or both to the ISS. In addition, other companies such as Virgin Galactic (a venture with Great Britain and the USA), are planning for short flights in microgravity for space tourism. All of these applications can benefit from more advanced chemical propulsion: improved propellants with higher specific impulse (I_s) for space tourism, as well as higher density propellants for first-stage applications. The proliferation of commercial launch companies and spaceports, currently taking place in different countries, only makes sense with safe, reliable, and high-performance chemical propulsion.

7.8 Full Papers of This Part

Part VII comprises four papers (26–29), respectively, authored by Palaszewski et al., Zare et al., Shen et al., and Simakova and Parmon. The four papers describe some of the active research areas. The paper by Palaszewski et al. is a welcome NASA roadmap summarizing the current needs and indicating the most promising future directions. The paper by Zare et al. describes new diagnostic techniques useful in overcoming the persistent problems of clustering and oxide-aggregation/agglomeration phenomena affecting burning of metals loaded in energetic materials. Raman spectroscopy, atomic force microscopy (AFM), and scanning electron microscopy (SEM) are used to evaluate the dispersion and clustering behavior of micron- and nanometer-sized Al particles. For nanometer-sized Al particles, the effects of ultrasonic vibration-assisted fabrication procedures on the dispersion and clustering of the particles in HTPB are compared to those of procedures using only mechanical mixing. Several types of dispersing agents are also evaluated for their effectiveness at preventing clustering. The paper by Shen et al. points out new directions in chemical propulsion, explored in China, by augmenting performance by means of an external laser beam impingement; a qualitative portray of the ambitious Chinese Chang'E spacecraft lunar mission is illustrated in Fig. 7. Finally, the paper by Simakova and Parmon presents recent results on the use of palladium-based catalyst for the synthesis of CL-20 molecule. The key step is the transformation of N-bonded benzyl groups (CH_2-C_6H_5), into acetyl groups (CO-CH_3) or formyl groups (CHO), before the final conversion into nitro groups. A careful study of the catalytic reaction conditions leads to a sensibly improved manufacturing technique.
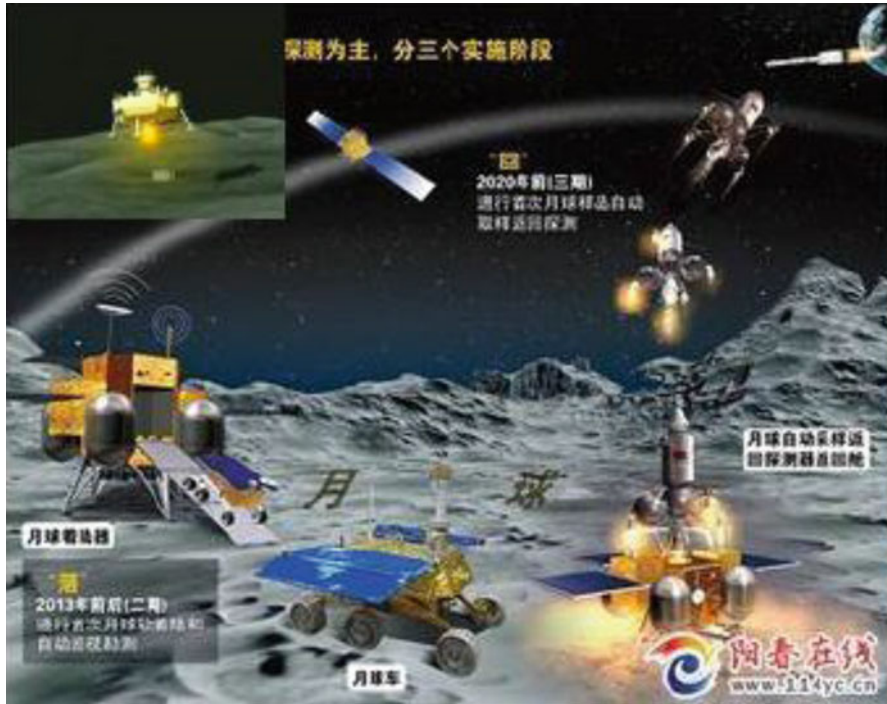
Fig. 7 Qualitative portray of the Chinese Chang'E lunar mission (2004–2020): Chang'E1, 24 Oct 2007; Chang'E2, 01 Oct 2010; Chang'E3, 02 to 14 Dec 2013; Chang'E4, to be launched (Courtesy of CNSA)

8 Life-Cycle Management of Energetic Materials[12]

The term Life-Cycle Management is often used when discussing the processes covering the manufacture, storage, usage and disposal of energetic materials in their various forms and the systems in which they are contained. After manufacture, the terms In-Service Management or In-Service Surveillance are commonly used to describe the processes employed to ensure their safety and suitability for storage and use. The topic has become more prevalent in the last decade and has been a major consideration in the development and use of energetic systems.

There are several aspects to this, and many of these are covered in this chapter, for it is far from as simple as is sometimes thought. The key aspect is contained within the word "life," which must be considered to cover all the aspects of the system, from initial manufacture through to disposal. This wide range does cover the maintenance of the system while in storage or use but must not be limited to

---

[12]Coordinated by Adam S. Cumming.

those intervals. This fact is increasingly being recognized both by scientists and regulators. In some cases this recognition is in response to legislation, which in turn is driven by events.

It should be noted that proper Life-Cycle Management requires a secure and well-understood baseline. Therefore sustainable processing of ingredients, manufacture, and appropriate characterization of the propellant form an essential precursor to effective management (quality control) throughout the entire life-cycle. Failure to take this step introduces what may be hazardous uncertainties.

8.1 Full Papers of This Part

Part VIII comprises six papers (30–35) dealing with specific aspects of Life-Cycle Management such as aging, hazards, impact, disposal, and remediation. After the overview paper by Cumming, contributions are presented following the same logical order.

Individual contributions discuss the management of propellant aging. Tunnell gives an overview in general terms of approaches that have been developed over many years and are backed by considerable amounts of data. Bohn and Cerri provide a specific example related to innovative ADN-based propellants which are being developed by several groups. They focus on new modeling techniques for the loss factor of the elastomer binder in order to assist in managing aging. This should be a widely applicable method.

The drive is to define processes, to acquire more reliable data, to use these data with newer modeling techniques to predict the behavior of propellants, etc. in a range of likely environments. This remains a work in progress. This diagnostic approach can be used to provide not only predictive models for known conditions but, through the basic understanding of processes, can also ensure that costs are minimized.

It should be recalled that with launch and its stresses, the behavior and therefore the risks may change as the energetic material responds to the forces imposed on it. Cracks or changes in material properties produce potential ignition or failure points, and the selection of a material composition and its method of manufacturing should be the subject of an intelligent and knowledgeable choice to minimize these risks. The studies in progress, and those planned, aim to provide useful tools for that estimation, and this work is discussed in the examples.

The understanding is not limited to slow decomposition on aging but can also be applied to the safety issues of the use and in handling. One aspect of this is discussed by Hori in the analysis of causes and implications of thruster accidents. Such an example is only one of the many, and there is a link to the prediction of sensitivity and vulnerability behavior. This is a critical issue for military design but is also important for safe handling of energetic materials in civil use. The name "energetic" indicates that these are materials with an intrinsic risk, a risk that must be managed. Such management is only possible if it is understood sufficiently.

Fig. 8 Optical phenomenon observed in Ekaterinburg following the launch of a Soyuz 2, with the satellite "Meridian", from Plesetsk on 5 May 2011. The picture was taken in twilight and shows the structure of the gas-dust cloud with shock wave fronts, and the track of the engines plume during the exposure (http://my.mail.ru/bk/vesti.ru/video/society/50252.html)

The required understanding would ideally cover the whole range of behavior; hence, the definition of the environment in which these materials operate is important. The regime of interest can be novel or nonstandard, with interesting and possibly important effects. An instance of this kind of consideration is illustrated and discussed by Platov (see Fig. 8). Behavior at ground level may not fully represent the behavior in other environments, which is an often-neglected part of the necessary understanding, and is a further concern in predicting safety and performance. It is worth adding that changing the environment can change the performance behavior. Again understanding and data are required to allow the system to be properly managed.

Finally, Life-Cycle Management requires that not only are the intrinsic properties of the energetic materials from their initial synthesis to their disposal understood and predicted, it also requires that their impact on the external environment be understood and managed. This area has increased dramatically in importance in the last 20 years, and, with the increasing legislative pressure on the manufacture and supply chemicals and ingredients, it will have a dramatic impact on the choice of material and its handling and disposal.

The review by Cumming in the overview paper and the contribution by Anand and Celin provide a concrete example of the processes being developed to manage the impact on the environment of the materials either in actual use or proposed use. In particular, Anand and Celin give an example of explosive waste management using natural degradative capabilities.

This is a complex subject and one that is continually changing as new facts on bioavailability and toxicity become available. Certain materials are at risk of being banned, or if still allowed, may not be useful in their present form. It is clear that there is a need to provide well-designed and well-understood processes to manage the risks to the environment and to people exposed to such materials. Responsible stewardship requires investment in order to firstly understand the processes and secondly to provide enough capability to ensure that the risks are at an acceptable level. There should also be the ability to change and develop the approach to meet new or more stringent demands.

Therefore, Life-Cycle Management in its broadest sense as described in this chapter fundamentally requires the understanding of the material characteristics, the processes affecting them in manufacturing, and their use and disposal (defined as In-Service Management) in order that the risks can be understood well enough to be managed effectively and in a cost-efficient manner.

9 Rocket Propulsion Systems

This section includes two short essays: the first one describes the propulsion issues regarding launch vehicle in general, and the second one describes the issues afflicting SRM systems in particular. For the sake of completeness, readers might wish to consult Sect. 5 dedicated to Liquid Rocket Propulsion as well.

9.1 Launch Vehicle Propulsion[13]

From its very beginning, dating back to the German V2, the propulsion of launch vehicles has not known any revolution except the use of the couple LOx/LH2 and of solid rocket boosters, a technology developed for instant readiness and launch-on-demand characteristics required for certain missiles. Presently, there are at least two reasons to consider a new generation of launch vehicles.

The first reason is always to improve the cost efficiency of the access to space including as consequences:

- Lower environmental impact
- Use of nontoxic propellants

---

[13]Coordinated by Max Calabro.
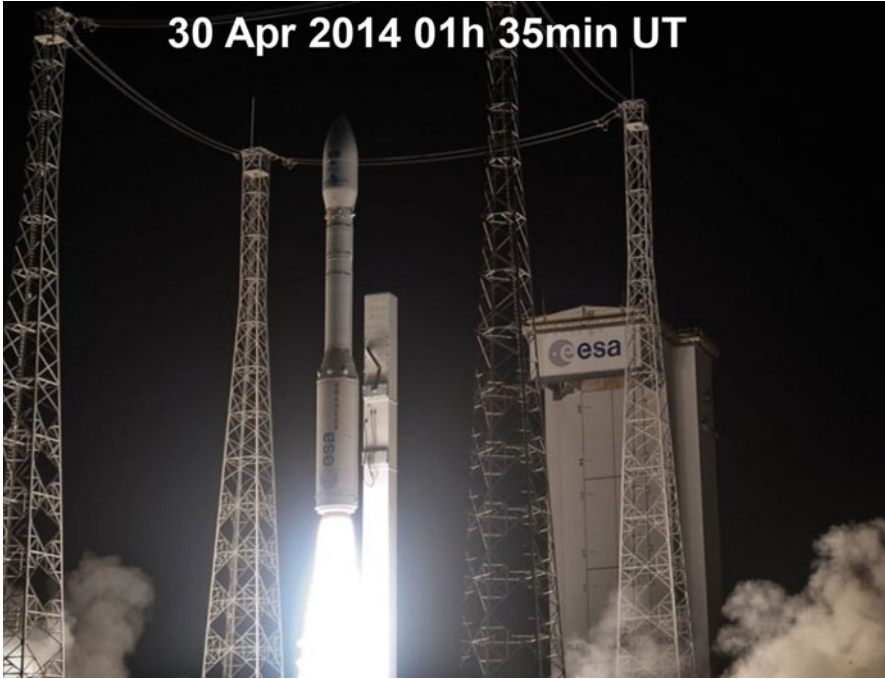
Fig. 9 Third launch of Vega on 30 Apr 2014 (Courtesy of ESA)

- An increase in reliability to avoid, among others, a catastrophic failure during the launch
- Better performance in terms of payload into orbit for a given lift-off mass

Looking at the current panorama of on-service launch vehicles, the smallest ones are using solid propulsion for the booster stages (e.g., Athena, Vega shown in Fig. 9), and heavier launchers are using mainly liquid propulsion, with or without add-on solid boosters, with or without a very large first solid stage. For the upper stage of heavier launchers, the use of LOx/LH2 is now a widespread solution.

A second reason could be the consequences of a catastrophic failure. Even if the launch vehicle has been designed, built, and tested well, it can fail in unforeseen ways. A historical approach would show that failures occur more often during the first flights of a new launch vehicle; nevertheless, after more than 360 flights, on 02 July 2013, a Proton launcher failed just after lift-off. Even if the failure is not the result of the propulsion malfunction, even if it is not occurring close to the launch pad with direct casualties (as Long March failures in 1995 and 1996), the launch vehicle has to be destroyed and will release in the atmosphere clouds of its liquid propellants. As an example, when the flight number 36 of ARIANE 4 had to be destroyed in flight, a toxic and potentially explosive cloud of NTO, UDMH, and

also hydrogen was produced; but risks for the inhabitants of the city of Kourou were avoided by prediction analysis and definition of a safety corridor. It is a key point to preclude future use of propellants such as NTO and UDMH. Furthermore, the family of hydrazine is potentially carcinogenic (NIOSH REL C (ceiling value), that should not be exceeded at any time, is around 0.03 ppm for hydrazine and 0.06 ppm for UDMH); inhalation of NTO vapors are very toxic resulting in lung edemas (NIOSH REL short-term exposure is 1 ppm for NO_2) but with much less stringent regulations. The ARIANE 4 launch vehicle family using NTO/UH25 (75 % UDMH + 25 % $N_2H_4xH_2O$ (hydrazine hydrate)) is no longer in service and was replaced by ARIANE 5 using solid boosters and a cryogenic central core. A version of Soyuz launched from Kourou uses LOx/kerosene.

Some families of launch vehicles are using these storable propellants still today, like Proton and Long March 2 and 3, even if programs to replace them by more friendly propellants are going on (Long March 5 and 7, Angara, Antares, KSLV). Probably only India will use toxic propellants for main stages propulsion in the next decade.

The development of a new generation propulsion technology for launch vehicles needs huge investments (in terms of both material and manpower), so in the relatively short term, such propulsion will use booster stages employing off-the-shelf technologies:

- LOx/kerosene or LOx/LH2
- Solid propellant: HTPB binder, AP, and Al, the best and only blend able to comply with the requirements of safety, burning rate, and cost-effectiveness

In the field of liquid propulsion of expendable launch vehicles, the major trend is for new launchers to employ the Russian technology of staged combustion of LOx/kerosene (e.g., Atlas V, Antares, Long March, KSLV, Angara) and to develop new versions replacing the kerosene by methane or LNG (e.g., RD-192), as all the system studies show an interesting performance increase for this evolution. For reusable vehicles, several LOx/methane engines are under development using the gas-generator cycle more suitable for airplanes (Europe, Japan).

For the postboost vehicle of expendable launchers used for orbital and then deorbit maneuvers of the last stage, the replacement of hydrazine and of the couple MMH/NTO is leading to a larger choice of less toxic potential solutions, for example, monopropellants, like ionic liquids based on ADN or HAN (see also Sect. 7.4), and new bipropellants based on HTP (high-test hydrogen peroxide) or nitrous oxide blends.

In the field of solid propulsion, research is focused on new energetic materials delivering better specific impulse and with lower environmental impact. The challenge is to find a more powerful oxidizer than AP and to find a combination, which complies with the safety requirements (class 1.3), with a controllable burning rate, and cost competitive with the current HTPB propellant.

9.2 Solid Rocket Motor (SRM) Systems[14]

Work also continues at the system level to enhance the performance of solid motors for space, strategic, and tactical propulsion. Technologies for solid motor systems are very mature given the more than 7 decades of development of these systems. Metallic motor cases provide known performance, and work continues to progress to bring higher strength/weight ratio composite materials based mainly on graphite fibers in polymeric matrices. There is a very little funded work specific to solid motors in this area in the USA. Liner and insulation technologies are similarly evolved, but work does continue to remove asbestos-based insulators from some applications; asbestos has already been removed for some time in most European countries. A preferred alternative employs particulate-filled EPDM for many applications. An area of continued emphasis relates to safety and inspection of motors subjected to normal handling and aging, and nondestructive evaluation techniques continue to evolve.

Nozzle technologies are similarly well-developed with carbon/phenolic and carbon/carbon materials that are employed in many current systems. The use of a pintle in the nozzle throat to control motor flow rate and thrust level provides for a throttleable solid motor system and remains a technology that could have broader application in the future, at least for small- or medium-size SRM. For large-size SRM, there is no real need for pintle technology, since propulsive missions for this class of motors are generally fixed for each system by properly designing the solid grain geometry. A pintle, however, could be useful for planetary landings, where thrust has to be decreased without actually stopping (nonstop release of a payload).

For totally new solid propellant formulations, the prediction of nozzle erosion rates and the unknown behavior of the propellant grain create a challenge to ballisticians for the prediction of the first firing test performance. Ceramic coating technologies could play a role in improving nozzle performance in this regard. Solid propulsion also serves a number of gas-generator applications with evolving capability of hot gas valves to provide mechanism for control of thrust vector or gas path on an as-needed basis.

Section 4 of this chapter provides a summary of solid propellant technologies including current work and challenges. NASA continues to look at HTPB as binder alternative to PBAN in future solid booster applications for vehicles such as SLS [89]. There have been some efforts in the USA to develop alternative binder systems based on polydicyclopentadiene (DCPD) [90].

In the USA, much of the recent solid motor work has been focused on applications to the new Space Launch System (SLS) in development by NASA. In recent years, ATK has conducted demonstration and development firings of the five-segment SRB that will provide first-stage thrust for the SLS system. Major

---

[14]Coordinated by Stephen D. Heister.

developments of three motors associated with the launch abort system (LAS) have also been underway [91]. The LAS uses solid propulsion for jettison, attitude control, and the abort itself. The abort and jettison motors represent unusual applications of solid propulsion given that the motors lie above the crew capsule and effectively pull portions of the vehicle away from the booster that lies below. Both of these motors employ four individual nozzles fed by a common combustion chamber presenting unique challenges to distribute the combustion gases uniformly and maintaining stable combustion in the process. Given the requirement to rapidly pull the crew capsule away from the booster during a launch abort, the launch abort motor is a very substantial system generating over 400,000 lbf (1.8 MN) [92]. The attitude control system employs a gas generator feeding eight proportional hot gas valves to provide up to 7000 lbf (30 kN) of control force.

In Europe, the effort is concentrated on improving the mastering of technology (and industrialization) of high-performance monolithic SRB used on large launchers (graphite composite case, EPDM insulation, flexseal, carbon/carbon ITE, HTPB propellant associated to a finocyl grain).

9.3 Full Papers of This Part

Part IX comprises three papers (36–38), respectively, authored by Chandradathan, Calabro, and Yoshida et al. The paper by Chandradathan is an excellent overview of the Indian accomplishments in the area of large solid boosters. The paper by Calabro offers interesting suggestions on how to improve the performance of VEGA, the European light launcher which recently entered into and completed the European fleet of launch vehicles. The paper by Yoshida et al. offers an overview of the efforts being conducted by JAXA in Japan in order to implement a reusable liquid rocket launcher.

10 Applications of Energetic Materials[15]

Energetic materials (EMs) have played a very vital role in improving the economy of many countries. Many engineering projects including space exploration would not have been possible without the use of energetic materials. However, for public opinion, EMs are often seen as a devil, which causes destruction. Now, due to the application of energetic materials, it is possible to mine rich minerals like coal and ores of different kinds from deep within the earth. Demolition and blasting operations are very common in civil engineering. Taming the path of rivers and moving mountains or any other unwanted hurdles for construction work are other

---

[15]Coordinated by Haridwar Singh.

major applications. Oil well blasting charges for oil exploration and the use of gas generators to take out oil even from dead wells are now very common. EMs have also been extensively used as fire extinguishing materials. In agriculture, these materials help in cracking and removing boulders for tree plantation, etc.

The use in surgery for the removal of kidney stones from the bladders of patients and the use of nitroglycerine (NG) and pentaerythritol tetra nitrate (PETN) tablets for control of angina heart pain within medicine are very common applications. EMs have also been used for compacting superconducting powders. Waste EMs can be used for preparing high-altitude fuels and for use where air density is low, as EMs do not require atmospheric air for full combustion. Seat ejection of aircrafts and canopy severance system (CSS) for ejecting pilots under distress are a few other applications in both civil and military industries. Stage separation of space vehicles is achieved through flexible linear-shaped charges (FLSCs), which are based on energetic materials. Soon, explosively driven power generators will be a reality and several devices based on them will be available in the market.

For space exploration, all varieties of propellants have been used: specifically, solid, liquid, and hybrid varieties. For hybrid propellants, the fuel is generally solid and the oxidizer is liquid. In the near future, many space propulsion devices will use gelled propellants. Thermally stable explosives such as TATB (triaminotrinitrobenzene) and HNS (hexanitrostilbene) are used for applications demanding high thermal stability (>300 °C).

Metal forming for improved mechanical properties in metals and for welding dissimilar metals is another very important industrial application. These processes make it less expensive to use cladded plates with thick steel plate outside and a thin exotic metal plate inside the vessels. Today, steel can be hardened by rapid compression, heating, and cooling. Metal forming of specific shapes is possible through the use of EMs. Industrial diamond can be made using high pressure and high temperature produced by shock waves to transform graphite in to small diamond crystals. The application of this technology is increasing, as the products find greater use as abrasive materials. Russia has mastered the technology for the conversion of graphite to make artificial diamonds by using energy obtained from EMs. Thus, EMs have numerous applications in both civil and military sectors and are proving to be boon to human society. These materials are certainly not the devil, as generally visualized.

10.1 Full Papers of This Part

Part X comprises three papers (39–41) describing in more detail several other applications of solid propellants in the civilian sphere. In the paper by Bozic and Jankovski, attention is focused on some civilian applications of solid propellants. The first application is in small weather sounding rockets, used to prevent hailstone formation in turbulent atmospheric conditions, which can damage the crops when they fall to the ground. The second is in gas generators suited for fire suppression applications, called solid propellant fire extinguishers (SPFE), via a combination

of different physical mechanisms like dilution, cooling, and flow rate. The third application of solid propellants is in systems for emergency surfacing of submarines, ships, or any other sinking objects. Mounting a required number of gas-generator units, in or around the sinking object, ensures buoyancy force after the activation of gas generators, which pushes the object to surface regardless of the availability of electric or diesel power.

Different kinds of solid propellants have found additional applications in various devices with special purposes in the automotive and aviation industries, among them pyrotechnic inflators in air bags and various separation mechanisms. In the paper by Date, an overview of the automobile airbag system is given, followed by reviews on the ingredients used for pyrotechnic inflators, and some studies on the combustion behaviors of ammonium nitrate-based gas-generating energetic materials.

Finally, in the paper by Tadini et al., a detailed discussion is carried out on how and why chemical propulsion modules are today the most logical way to address the severe challenges of active removal of space debris. A multiple debris removal scenario is analyzed, by selecting a suitable target, defining disposal reentry trajectory constraints and conceptually designing a compact and autonomous deorbiting kit, powered by chemical rockets. To this end, the characteristics and functionality of solid, liquid and hybrid systems are compared, with particular attention to the advantages of nontoxic propellants and to the preference for cheap solutions for cost reduction.

11 History of Solid Rocket Propulsion in Russia[16]

Solid propellant rockets have reached a major and in many respects efficient stage of development. In Russia, the first option of solid rockets appeared in 1928 when at the proving ground near the city of Leningrad the superiority of rocket-assisted projectile (RAP) was demonstrated in comparison with ordinary artillery shell of the same mass [93, 94]. The motor of this RAP employed the first widely used solid propellant for rocket motors in the world (based on nitrocellulose, NC). This was a pyroxylin–trinitrotoluene propellant invented in 1925 by professor S.A. Brouns (1863–1933) of Mikhailov Artillery Academy (Leningrad). The propellant contained 76 % pyroxylin (a highly flammable mixture of NC), 23.5 % trinitrotoluene (nonvolatile solvent), and 0.5 % centralite (stabilizer).

In 1933, that propellant was replaced with an energetically more efficient double-base propellant N. Its formulation also was invented by S.A. Brouns, and his successor A.S. Bakayev developed the idea of his teacher into a workable system. Accordingly, the first aviation missiles RS-82 and RS-132 (1937) as well as the first field missiles M8 and M13 employed in a salvo firing system (1941) used the

---

[16]Coordinated by Alexey M. Lipanov and Vladimir E. Zarko.

propellant N (colloxylin 57 %, nitroglycerine 28 %, dinitrotoluene 11 %, centralite 3 %, and vaseline 1 %). All of the missiles mentioned above were unguided.

In the initial development, the level of technical output parameters was relatively low. The coefficient of the rocket mass perfection (ratio of rocket inert mass to propellant mass) was equal to 2; the coefficient of motor volume loading was less than 0.7; the specific impulse of the propellant in standard conditions (chamber pressure 4 MPa and nozzle output pressure 0.1 MPa) equaled 202 s. The USSR entered the Second World War with missiles having such technical characteristics.

After the Second World War, the development of solid propellant rockets continued and, in the middle of the 1960s, the development of solid composite propellants was well advanced (see also [45]). The theoretical studies available at that time allowed understanding the key role of the reactions in the condensed phase, the partial evaporation of the components of propellants based on ammonium perchlorate (AP), the role of particle grain size distribution, and more.

During the second half of the twentieth century, as a result of intensive scientific researches and design and technological works, some significant progress has been achieved:

- Guidance was developed for solid propellant missiles of all classes.
- The value of mass perfection coefficient became less than 0.08.
- The value of motor volume loading exceeded 0.93.
- The specific impulse of solid propellants under standard operating conditions exceeded 250 s.

At present, the researchers involved in the development of solid rockets deal with the problems of enhancement of the propellant energy and minimization of specific impulse losses. Those losses arise due to the existence of condensed particles in the combustion products of propellants formed as a result of combustion of aluminum particles. The aluminum is added to propellant formulation to increase the energetic characteristics. The task consists not only in the organization of such movement of condensed particles in the free volume of motor, which minimizes the coagulation of small particles and the formation of slag, but also in the design of propellant formulations which minimize the formation of large-size agglomerates on the burning surface. In particular, the intensity of the metal agglomeration on the burning surface can depend on the properties of liquid-viscous reaction zone at the surface.

Other important directions of works in designing new propellant formulations are the use of active (energetic) binders containing oxygen. In this case, the binder not only has to cover the heterogeneous propellant components (which needs a mass fraction at the level of 0.10–0.12) but effectively contribute in the enhancement of the solid propellant specific impulse. As before, a serious issue is the choice of the burning rate modifiers which allow controlling the burning law and provide increasing as well as decreasing the burning rate while keeping the pressure exponent at the level of 0.3 and lower.

But these are not all the problems. As at display of fireworks, one seeks to demonstrate unexpected coloring of the formed original structures which are

burning down in visibility limits for observing; in the case of ordinary rockets, their performance has to satisfy a set of various requirements and specifications. Thus, when new components are used in a novel formulation, there is a need for carrying out large volumes of research. Therefore, both basic and developmental researches are still actively performed at the present time, as unambiguously confirmed by the papers presented in several chapters of this volume.

11.1 Full Papers of This Part

Part XI comprises four papers (42–45). The opening paper by DeLuca underlines the highlights of the overall solid propulsion history, while the remaining three papers deal specifically with the Russian developments in solid rocket propulsion. The paper by Lipanov and Zarko offers a general overview, historical as well as technical, of the Russian efforts and is an ideal continuation of previous papers published by the senior author [93, 94], who was one of those who substantiated the necessity of solid propulsion research activities in the Soviet Union. Two more papers are historical essays dedicated to peculiar aspects of the Russian heritage in the area of solid rocket propulsion.

The first is devoted to the heritage of the Semenov Institute of Chemical Physics, Moscow Russia, established in 1931 under the direction of N.N. Semenov, a Nobel Prize Winner in Chemistry (1956). Among the several international institutions, which during the modern times dedicated substantial and systematic efforts to research in the broad area of energetic materials from a number of viewpoints (physics and chemistry of combustion, shock waves and detonation, synthesis and manufacturing, cost and safety, and so on), the Semenov Institute of Chemical Physics was able to achieve and maintain a leading position at worldwide level. This school could count on world famous scientists, such as notably N. N. Semenov, Ya.B. Zel'dovich, D. Frank-Kamenetskiy, A.F. Belyaev, P.F. Pokhil, K.K. Andreev, and many others. An official presentation of the Semenov Institute of Chemical Physics was written by a team led by the current director of the institute (Academician Alexander A. Berlin) emphasizing the specific contributions to understanding of energetic materials combustion by N.N. Semenov, Ya.B. Zel'dovich, and A.F. Belyaev.

The second paper is a more personal collection of private events recorded by George B. Manelis and collected by David Lempert. For years the deputy of N.N. Semenov in the committee on military–industrial complex, George B. Manelis was in turn a well-known expert in the area of energetic materials for solid propulsion. It is a vivid portrayal of the life of Russian scientists in the middle part of the previous century, and the volume editors deliberately tried to keep as much as possible the Russian flavor of the manuscript.

12   Gels for Rocket and Ramjet Propulsion[17]

The research on gel propulsion started in the late 1980s in NASA, mainly by Bryan A. Palaszewski, and at TRW and Aerojet. Gels were characterized as non-Newtonian fluids, and their atomization properties were studied. Little was known then, because the propulsion community lacked the basis necessary to deal with the complex issues of these propellants. Gels were identified as being capable of providing answers to safety issues, as well as having performance advantages; therefore, they received significant research attention.

Gels are defined as liquids whose rheological properties can be altered by the addition of gelling agents; they behave as solids while at rest and can be atomized and burn like liquids during operation. This semisolid character provides safety since, in case of accident, the leakage rate is limited, if at all. The existence of yield stress allows the dispersion of metal particles with almost no sedimentation, thus increasing both the propellant energetic potential and energy density.

In the mid-1990s and 2000s, in basic studies that were conducted at the Technion, Israel, and led by Natan, three sides of the scientific triangle for gel propellants were defined: rheology, atomization, and combustion. All these areas were studied and provided a first good insight to the issues involved. The rheological properties of the gel fluids were proved to play a most significant role in the flow in pipes and injectors, in atomization, and also in combustion. Novel injectors were developed to decrease the feeding pressure and achieve fine atomization. The combustion of gel fuels droplets was studied using inorganic and organic gellants. The combustion mechanism of gel fuels was investigated experimentally and theoretically and new phenomena were revealed.

In March 1999, a TOW missile using carbon-loaded gelled MMH and gelled IRFNA was successfully launched by TRW (USA) in a first flight test. This was a very important test that proved the concept of gel propulsion.

Cooperation between DLR Germany and Technion, Israel, that started in 2000 opened the road to further scientific achievements. The group of DLR, led by Roland Pein (until his retirement) and Helmut Ciezki, obtained understanding of the atomization regimes (formation of sheets, ligaments, threads, and droplets) based on the rheological properties, the jet velocity, and the generalized Reynolds and Weber numbers. The DLR group also studied the rheological properties of gels using various gelling agents.

In Rafael, Israel, research, led by Shai Rahimi and Arie Peretz, contributed in preparation and characterization of hydrazine-based gel propellants.

In India, several researchers (Varma, Mishra, Varghese, and others) studied the rheology and synthesis of certain gel propellants, providing mainly information on the various properties.

---

[17]Coordinated by Benveniste Natan.

In Germany, significant progress was achieved by Ulrich Teipel, Volker Weiser, and coworkers in Fraunhofer Institute for Chemical Technology using gelled nitromethane as a monopropellant. Moreover, Karl Naumann reports that in 2009 a gel monopropellant rocket was successfully launched by Bayern Chemie.

In 2008, in the USA, two MURI awards were given to leading universities to conduct basic research on gels. In Purdue University, the team led by Stephen D. Heister combining scientists from several disciplines such as William Anderson, Steve Son, Timothee Pourpoint, Osvaldo Campanella, and Paul Sojka conducted significant studies on all the gel propellant-related subjects. The impact of this team was quite important. At Pennsylvania State University, Richard Yetter studied the atomization characteristics of gel fuels.

China also entered lately the area of gel propulsion focusing on research issues.

In Israel, the idea of hypergolic ignition of gelled kerosene that contains catalyst/reactive particles with hydrogen peroxide was proposed. These propellants are nontoxic, and hypergolic ignition can be obtained only due to gelation that allows particle suspension. This can be used also in space application as a hydrazine alternative.

The issue of a metalized gel fuel ramjet engine was investigated in Germany and Israel. Gelled kerosene allows the suspension of metal particles, such as boron, that under certain conditions can burn efficiently inside the motor. A theoretical assessment of the performance of such an engine, boosted by a solid rocket motor, shows that an air-to-surface 1500 kg (total) missile can reach a range of 1000 km within 20 min obtaining I_s of 2000 s.

The question is where the future takes us.

Gel propulsion has not yet reached maturity. Additional research has to be conducted; however, the time for demonstrators has come. In several countries, gelled hydrazine for rocket applications will be employed, increasing safety and exploiting the hypergolicity advantages; however, Europe is trying to avoid the use of hydrazine at all. Gelled monopropellants will be used too. Most probably, in the near future, we will see applications of nontoxic, hypergolic gel propellants. The gel fuel ramjet engine using boron seems also to be very promising.

Regarding space exploration, gelled cryogenic propellants have mainly been tested in laboratory experiments and have not yet flown in a space representative environment. Cryogenic fluid management, including boil-off and the corresponding shift in gellant loading in the fuel are the issues to be addressed. Storable NTO/MMH/Al, LOx/RP-1/Al, and cryogenic LOx/LH2/Al are the primary candidates to be investigated. Gelling the cryogenic fuels with the aluminum particles is certainly a challenge. Large-scale (up to 5000 N thrust) RP-1/Al and hydrogen/Al engine and component testing must be conducted.

Eventually, gel propulsion will find its place among solid, liquid, and hybrid propulsion.

12.1 Full Papers

For a matter of convenience, the two accepted papers dealing with gel propulsion are, respectively, included in Part. III (Aluminized Gel Fuel Ramjet by Gafni et al.) and Part V (UDMH gel by Varma).

References

1. DeLuca LT, Shimada T, Sinditskii VP, Calabro M, Manzara AP (2016) An introduction to energetic materials for propulsion. In: DeLuca LT, Shimada T, Sinditskii VP, Calabro M (eds) Chemical rocket propulsion: A comprehensive survey of energetic materials. Springer, Cham
2. Kettner MA, Klapötke TM (2016) Synthesis of new oxidizers for potential use in chemical rocket propulsion. In: DeLuca LT, Shimada T, Sinditskii VP, Calabro M (eds) Chemical rocket propulsion: A comprehensive survey of energetic materials. Springer, Cham
3. Sinditskii VP, Egorshev VY, Rudakov GF, Filatov SA, Burzhava AV (2016) High-nitrogen energetic materials of 1,2,4,5-tetrazine family: thermal and combustion behaviors. In: DeLuca LT, Shimada T, Sinditskii VP, Calabro M (eds) Chemical rocket propulsion: A comprehensive survey of energetic materials. Springer, Cham
4. Singh H (2016), Survey of new energetic and eco-friendly materials for propulsion of space vehicles. In: DeLuca LT, Shimada T, Sinditskii VP, Calabro M (eds) Chemical rocket propulsion: A comprehensive survey of energetic materials. Springer, Cham
5. Karabeyoğlu A (2016) Performance additives for hybrid rocket engines. In: DeLuca LT, Shimada T, Sinditskii VP, Calabro M (eds) Chemical rocket propulsion: A comprehensive survey of energetic materials. Springer, Cham
6. Xuezhong Fan, Fuqiang Bi, Min Zhang, Jizhen Li, Weiqiang Pang, Bozhou Wang, Zhongxue Ge (2016) Introducing tetrazole salts as energetic ingredients for rocket propulsion. In: DeLuca LT, Shimada T, Sinditskii VP, Calabro M (eds) Chemical rocket propulsion: A comprehensive survey of energetic materials. Springer, Cham
7. Lianjie Zhai, Bozhou Wang, Xuezhong Fan, Fuqiang Bi, Jizhen Li, Weiqiang Pang (2016). Synthesis and characterization of 3,4-bis(3-fluorodinitromethylfurazan-4-oxy)furazan. In: DeLuca LT, Shimada T, Sinditskii VP, Calabro M (eds) Chemical rocket propulsion: A comprehensive survey of energetic materials. Springer, Cham
8. DeLuca LT, Maggi F, Dossi S, Fassina M, Paravan C, Sossi A (2016) Prospects of aluminum modifications as energetic fuels in chemical rocket propulsion. In: DeLuca LT, Shimada T, Sinditskii VP, Calabro M (eds) Chemical rocket propulsion: A comprehensive survey of energetic materials. Springer, Cham
9. Vorozhtsov AB, Zhukov A, Ziatdinov M, Bondarchuk S, Lerner M, Rodkevich N (2016) Novel micro- and nano-fuels: production, characterization, and applications for HEMs. In: DeLuca LT, Shimada T, Sinditskii VP, Calabro M (eds) Chemical rocket propulsion: A comprehensive survey of energetic materials. Springer, Cham
10. Weiser V, Gettwert V, Franzin A, DeLuca LT et al. (2016) Combustion behavior of aluminum particles in ADN/GAP composite propellants. In: DeLuca LT, Shimada T, Sinditskii VP, Calabro M (eds) Chemical rocket propulsion: A comprehensive survey of energetic materials. Springer, Cham
11. Fengqi Zhao, Ergang Yao, Siyu Xu, Xin Li, Huixiang Xu, Haixia Hao (2016) Laser ignition of aluminum nanopowders for solid rocket propulsion. In: DeLuca LT, Shimada T, Sinditskii VP,

Calabro M (eds) Chemical rocket propulsion: A comprehensive survey of energetic materials. Springer, Cham

12. Gafni G, Kuznetsov A, Natan B (2016) Experimental investigation of an aluminized gel fuel ramjet combustor. In: DeLuca LT, Shimada T, Sinditskii VP, Calabro M (eds) Chemical rocket propulsion: A comprehensive survey of energetic materials. Springer, Cham

13. Babuk VA (2016) Propellant formulation factors and properties of the condensed combustion products. In: DeLuca LT, Shimada T, Sinditskii VP, Calabro M (eds) Chemical rocket propulsion: A comprehensive survey of energetic materials. Springer, Cham

14. Jiangfeng Pei, Fengqi Zhao, Ying Wang, Siyu Xu, Xiuduo Song, Xueli Chen (2016) Energy and combustion characteristics of composite propellants based on BAMO-GAP copolymer. In: DeLuca LT, Shimada T, Sinditskii VP, Calabro M (eds) Chemical rocket propulsion: A comprehensive survey of energetic materials. Springer, Cham

15. Pivkina A, Muravyev N, Monogarov K, Ostrovsky V, Fomenkov I, Milyokhin YuM, Shishov NI (2016) Synergistic effect of ammonium perchlorate on HMX thermal stability and combustion behavior of compositions with active binder. In: DeLuca LT, Shimada T, Sinditskii VP, Calabro M (eds) Chemical rocket propulsion: A comprehensive survey of energetic materials. Springer, Cham

16. Rashkovskiy SA, Milyokhin YuM, Fedorychev AV (2016) Combustion of solid propellants with energetic binders. In: DeLuca LT, Shimada T, Sinditskii VP, Calabro M (eds) Chemical rocket propulsion: A comprehensive survey of energetic materials. Springer, Cham

17. Weiqiang Pang, DeLuca LT, Huixiang Xu, Xuezhong Fan, Fengqi Zhao, Wuxi Xie (2016) Effects of dual oxidizers on composite solid propellant burning. In: DeLuca LT, Shimada T, Sinditskii VP, Calabro M (eds) Chemical rocket propulsion: A comprehensive survey of energetic materials. Springer, Cham

18. Haeseler D, Haidn OJ (2016) Russian technologies in liquid rocket engines. In: DeLuca LT, Shimada T, Sinditskii VP, Calabro M (eds) Chemical rocket propulsion: A comprehensive survey of energetic materials. Springer, Cham

19. Asakawa H, Nanri H, Aoki K, Kubota I, Mori H, Ishikawa Y, Kimoto K, Ishihara S, Ishizaki S (2016) The status of the research and development of LNG rocket engines in Japan. In: DeLuca LT, Shimada T, Sinditskii VP, Calabro M (eds) Chemical rocket propulsion: A comprehensive survey of energetic materials. Springer, Cham

20. Fujii LG, Hatai K, Masuoka T, Nagata T, Masuda I, Kagawa H, Ikeda H (2016) Research and development activities on JAXA's spacecraft propulsion. In: DeLuca LT, Shimada T, Sinditskii VP, Calabro M (eds) Chemical rocket propulsion: A comprehensive survey of energetic materials. Springer, Cham

21. Varma M (2016) High shear rheometry of UDMH gel. In: DeLuca LT, Shimada T, Sinditskii VP, Calabro M (eds) Chemical rocket propulsion: A comprehensive survey of energetic materials. Springer, Cham

22. Shimada T, Yuasa S, Nagata H, Aso S, Nakagawa I, Sawada K, Hori K, Kanazaki M, Chiba K, Sakurai T, Morita T, Kitagawa K, Wada Y, Nakata D, Motoe M, Funami Y, Ozawa K, Usuki T (2016) Hybrid propulsion technology development in Japan for economic space launch. In: DeLuca LT, Shimada T, Sinditskii VP, Calabro M (eds) Chemical rocket propulsion: A comprehensive survey of energetic materials. Springer, Cham

23. Kyung-Su Park, Yang Na, Changjin Lee (2016) Internal flow characteristics and low frequency stability in hybrid rocket combustion. In: DeLuca LT, Shimada T, Sinditskii VP, Calabro M (eds) Chemical rocket propulsion: A comprehensive survey of energetic materials. Springer, Cham

24. Songqi Hu, Guanjie Wu, Noor Fatima Rashid (2016) Performance analysis of paraffin fuels for hybrid rocket engines. In: DeLuca LT, Shimada T, Sinditskii VP, Calabro M (eds) Chemical rocket propulsion: A comprehensive survey of energetic materials. Springer, Cham

25. Galfetti L, Boiocchi M, Paravan C, Toson E, Sossi A, Maggi F, Colombo G, DeLuca LT (2016) Paraffin blends and energetic additives for regression rate enhancement in hybrid rocket propulsion. In: DeLuca LT, Shimada T, Sinditskii VP, Calabro M (eds) Chemical rocket propulsion: A comprehensive survey of energetic materials. Springer, Cham

26. Palaszewski BA, Meyer M, Johnson L, Goebel D, White H, Coote D (2016) NASA in-space propulsion systems roadmap. In: DeLuca LT, Shimada T, Sinditskii VP, Calabro M (eds) Chemical rocket propulsion: A comprehensive survey of energetic materials. Springer, Cham
27. Zare A, Harriman T, Lucca DA, Roncalli S, Kosowski BM, Paravan C, DeLuca LT (2016) Mapping of aluminum particle dispersion in solid fuel formulations. In: DeLuca LT, Shimada T, Sinditskii VP, Calabro M (eds) Chemical rocket propulsion: A comprehensive survey of energetic materials. Springer, Cham
28. Ruiqi Shen, Lizhi Wu, Zhao Qin (2016) New concept of laser-chemical hybrid propulsion. In: DeLuca LT, Shimada T, Sinditskii VP, Calabro M (eds) Chemical rocket propulsion: A comprehensive survey of energetic materials. Springer, Cham
29. Simakova IL, Parmon VN (2016) New catalytic aspects in the synthesis of a promising energetic material. In: DeLuca LT, Shimada T, Sinditskii VP, Calabro M (eds) Chemical rocket propulsion: A comprehensive survey of energetic materials. Springer, Cham
30. Cumming AS (2016) Environmental aspects of energetic materials use and disposal. In: DeLuca LT, Shimada T, Sinditskii VP, Calabro M (eds) Chemical rocket propulsion: A comprehensive survey of energetic materials. Springer, Cham
31. Tunnell R (2016) Overview and appraisal of analytical techniques for ageing of solid rocket propellants. In: DeLuca LT, Shimada T, Sinditskii VP, Calabro M (eds) Chemical rocket propulsion: A comprehensive survey of energetic materials. Springer, Cham
32. Bohn MA, Cerri S (2016) Ageing behavior of ADN solid rocket propellants using their glass-to-rubber transition characteristics. In: DeLuca LT, Shimada T, Sinditskii VP, Calabro M (eds) Chemical rocket propulsion: A comprehensive survey of energetic materials. Springer, Cham
33. Hori K (2016) Lessons learnt in the thruster tests of HAN. In: DeLuca LT, Shimada T, Sinditskii VP, Calabro M (eds) Chemical rocket propulsion: A comprehensive survey of energetic materials. Springer, Cham
34. Platov Yu, Nikolayshvili S (2016) Optical phenomena in the upper atmosphere associated with the operation of rocket engines. In: DeLuca LT, Shimada T, Sinditskii VP, Calabro M (eds) Chemical rocket propulsion: A comprehensive survey of energetic materials. Springer, Cham
35. Anand S, Mary Celin S (2016) Green technologies for the safe disposal of energetic materials in the environment. In: DeLuca LT, Shimada T, Sinditskii VP, Calabro M (eds) Chemical rocket propulsion: A comprehensive survey of energetic materials. Springer, Cham
36. Chandradathan SM (2016) Challenges in manufacturing large solid boosters. In: DeLuca LT, Shimada T, Sinditskii VP, Calabro M (eds) Chemical rocket propulsion: A comprehensive survey of energetic materials. Springer, Cham
37. Calabro M (2016) Evaluating the interest of new solid propellants for the VEGA launch vehicle. In: DeLuca LT, Shimada T, Sinditskii VP, Calabro M (eds) Chemical rocket propulsion: A comprehensive survey of energetic materials. Springer, Cham
38. Yoshida M, Kimura T, Hashimoto T, Moriya S, Takada S (2016) Overview of research and development status of reusable liquid rocket engines. In: DeLuca LT, Shimada T, Sinditskii VP, Calabro M (eds) Chemical rocket propulsion: A comprehensive survey of energetic materials. Springer, Cham
39. Bozic V, Jankovski B (2016) Some civilian applications of solid propellants. In: DeLuca LT, Shimada T, Sinditskii VP, Calabro M (eds) Chemical rocket propulsion: A comprehensive survey of energetic materials. Springer, Cham
40. Date S (2016) Novel ammonium nitrate based formulations for airbag gas generation. In: DeLuca LT, Shimada T, Sinditskii VP, Calabro M (eds) Chemical rocket propulsion: A comprehensive survey of energetic materials. Springer, Cham
41. Tadini P, Tancredi U, Grassi M, Pardini C, Anselmo L, Shimada T, DeLuca LT (2016) Active debris removal by chemical propulsion modules. In: DeLuca LT, Shimada T, Sinditskii VP, Calabro M (eds) Chemical rocket propulsion: A comprehensive survey of energetic materials. Springer, Cham
42. DeLuca LT (2016) Highlights of solid rocket propulsion history. In: DeLuca LT, Shimada T, Sinditskii VP, Calabro M (eds) Chemical rocket propulsion: A comprehensive survey of energetic materials. Springer, Cham

43. Lipanov AM, Zarko VE (2016) Survey of solid rocket propulsion in Russia. In: DeLuca LT, Shimada T, Sinditskii VP, Calabro M (eds) Chemical rocket propulsion: A comprehensive survey of energetic materials. Springer, Cham

44. Berlin AA, Frolov YV, Isaevich YG (2016) The contribution of the Semenov Institute of Chemical Physics to the science of combustion: a historical review. In: DeLuca LT, Shimada T, Sinditskii VP, Calabro M (eds) Chemical rocket propulsion: A comprehensive survey of energetic materials. Springer, Cham

45. Manelis GB (2016) The Russian missile saga: personal notes from a direct participant. In: DeLuca LT, Shimada T, Sinditskii VP, Calabro M (eds) Chemical rocket propulsion: A comprehensive survey of energetic materials. Springer, Cham

46. Ostmark H, Wallin S (2003) Detection of pentazolate anion (cyclo N5-) from laser ionization and decomposition of solid p-dimethylaminophenyl pentazolate. J Chem Phys Lett 379: 539–546

47. Vij A, Wilson WW, Vij V, Tham FS, Sheehy JA, Christe KO (2001) Polynitrogen chemistry. Synthesis, characterization, and crystal structure of surprisingly stable fluoroantimonate salts of N5+. J Am Chem Soc 123(26):6308–6313

48. Zhang CY, Shu YJ, Huang YG, Zhao XD, Dong H (2005) Investigation of correlation between impact sensitivities and nitro group charges in nitro compounds. J Phys Chem B 109:8978–8982

49. Zhang CY, Wang XC, Huang H (2008) π-stacked interactions in explosive crystals: buffers against external mechanical stimuli. J Am Chem Soc 130:8359–8365

50. Zhang CY (2009) Review of the establishment of nitro group charge method and its applications. J Hazard Mater 161:21–28

51. Ma Y, Zhang A, Xue XG, Jiang DJ, Zhu YQ, Zhang CY (2014) Crystal packing of impact-sensitive high-energy explosives. Cryst Growth Des 14:6101–6114

52. Ma Y, Zhang A, Zhang CH, Jiang DJ, Zhu YQ, Zhang CY (2014) Crystal packing of low-sensitivity and high-energy explosives. Cryst Growth Des 14:4703–4713

53. George SM (2010) Atomic layer deposition: an overview. Chem Rev 110:111–131

54. Ferguson JD, Buechler KJ, Weimer AW, George SM (2005) SnO_2 atomic layer deposition on ZrO_2 and Al nanoparticles: pathway to enhanced thermite materials. Powder Technol 156(2/3):154–163

55. Qin L, Gong T, Hao H, Wang K, Feng H (2013) Core-shell structured nanothermites synthesized by atomic layer deposition. J Nanopart Res 2150:1–15

56. Feng H. Surface engineering of metal nanoparticles by atomic layer deposition and molecular layer deposition. 2015 Inter. Autumn seminar on propellants, explosives and pyrotechnics, Tsingtao, China, 16–18 Sept 2015

57. Gong T, Qin L, Yan R, Hu L, Ji Y, Feng H (2014) Alumina thin film coated ammonium dinitramide fabricated by atomic layer deposition. J Inorg Mater 29(8):869–874

58. Qin L, Gong T, Hao H, Wang K, Feng H (2015) Influences of metal oxide encapsulation by atomic layer deposition on the sensitivities of octogen. Chem J Chin Univ 36(3):420–427

59. Hakim LF, Blackson J, George SM, Weimer AW (2005) Nanocoating individual silica nanoparticles by atomic layer deposition in a fluidized bed reactor. Chem Vap Depos 11: 420–425

60. McCormick JA, Cloutier BL, Weimer AW, George SM (2007) Rotary reactor for atomic layer deposition on large quantities of nanoparticles. J Vac Sci Technol A 25(1):67–74

61. Qinghua Zhang, Shreeve J'n M (2014) Energetic ionic liquids as explosives and propellant fuels: a new journey of ionic liquid chemistry. Chem Rev 114:10527–10574

62. Qinghua Zhang, Shreeve J'n M (2013) Ionic liquid propellants: future fuels for space propulsion. Chem Eur J 19:15446–15451

63. Sebastiao E, Cook C, Hu A, Murugesu M (2014) Recent developments in the field of energetic ionic liquids. J Mater Chem A 2:8153–8173

64. Klapötke TM, Mayer P, Schulz A, Weigand JJ (2005) 1,5-diamino-4-methyltetrazolium dinitramide. J Am Chem Soc 127:2032–2033

65. Schneider S, Hawkins T, Rosander M, Vaghjiani G, Chambreau S, Drake G (2008) Ionic liquids as hypergolic fuels. Energy Fuel 22:2871–2872
66. Zhang Y, Gao H, Joo Y-H, Shreeve J'n M (2011) Ionic liquids as hypergolic fuels. Angew Chem Int Ed 50:9554–9562
67. Zhang Y, Shreeve J'n M (2011) Dicyanoborate-based ionic liquids as hypergolic fluids. Angew Chem Int Ed 50:935–937
68. Fahrat Kamal, Batonneau Yann, Brahmi Rachid, Kappenstein Charles (2011) Application of ionic liquids to space propulsion, applications of ionic liquids in science and technology. In: Handy S (ed) ISBN: 978-953-307-605-8, InTech, doi: 10.5772/23807. Available from: http://www.intechopen.com/books/applications-of-ionic-liquids-in-science-and-technology/application-of-ionic-liquids-to-space-propulsion
69. Klapötke TM (2015) Chemistry of high-energy materials, 3rd edn. Walter de Gruyter GmbH, Berlin/Boston, pp 221–224, Chapter 9.3.3 Ionic Liquids
70. Ma ZY, Li FS, Ye MQ et al. (2004) Structure and property characterization of nanoparticles of ferric oxide/oleic acid composites. J Nanjing Univ Sci Technol 25(4): 436–444
71. Xu H, Cai HH, Luo ZK et al. (2003) Preparation and catalytic properties of nano neodymium oxide. J Inorg Chem 19(6):627–630
72. Hong WL, Liu JH, Tian DY, et al. (2003) Catalysis of nanocomposite $CuO \cdot Cr_2O_3$ on thermal decomposition of RDX. J Propuls Technol 24(1):83–86
73. Muravyev N, Pivkina A, Schoonman J, Monogarov K (2014) Catalytic influence of nanosized titanium dioxide on the thermal decomposition and combustion of HMX. Int J Energ Mater Chem Propuls 13(3):211–228
74. Fogelzang AE, Sinditskii VP, Egorshev VY, Serushkin VV (1995) Effect of structure of energetic materials on burning rate. In: Brill TB, Russell TP, Tao WC, Wardle RB (eds) Decomposition, combustion, and detonation chemistry of energetic materials, MRS proceedings, vol 418. Materials Research Society, Pittsburgh, pp 151–161
75. Sinditskii VP, Chernyi AN, Marchenkov DA (2014) Mechanisms of combustion catalysis by ferrocene derivatives. 1. Combustion of ammonium perchlorate and ferrocene. Combust Explosion Shock Waves 50(1):51–59
76. Sinditskii VP, Chernyi AN, Marchenkov DA (2014) Mechanism of combustion catalysis by ferrocene derivatives. 2. Combustion of ammonium perchlorate-based propellants with ferrocene derivatives. Combust Explosion Shock Waves 50(2):158–167
77. Sinditskii VP, Fogelzang AE (1997) Energetic materials based on coordination compounds. Russ J Chem 41:74–80
78. Sinditskii VP, Egorshev VY, Serushkin VV (2000) Design and combustion behavior of metal-containing energetic materials. Proc. Sino-Russian Inter. Academic Conference on 60th Anniversary of the Founding of BIT, Beijing, 20–21 Sept 2000, pp 174–190
79. Fogelzang AE, Denisyuk AP, Serushkin VV, Egorshev VY, Sinditskii VP, Margolin AD (2000) Burning behavior of composite propellants with fast-burning inclusions. J Propuls Power 16(2):374–376
80. Zhao FQ, Gao HX, Luo Y et al. (2007) Effect of novel energetic composite catalysts on combustion properties of minimum smoke propellant. Chin J Explos Propellants 30(2):1–5
81. Singh G, Felix SP (2003) Studies of energetic compounds, part 29: effect of NTO and its salts on the combustion and condensed phase thermolysis of composite solid propellants, HTPB-AP. Combust Flame 132:422–432
82. Singh G, Felix SP (2003) Studies on energetic compounds: part 36: evaluation of transition metal salts of NTO as burning rate modifiers for HTPB-AN composite solid propellants. Combust Flame 135(1–2):145–150
83. Dey A, Nangare V, More PV et al (2015) A grapheme titanium dioxide nanocomposite (GTNC): one pot green synthesis and its application in a solid rocket propellant. RSC Adv 5:63777–63785
84. Dey A, Athar J, Varma P et al (2015) Graphene-iron oxide nanocomposite (GINC): an efficient catalyst for ammonium perchlorate (AP) decomposition in and burn rate enhancer for AP based composite propellant. RSC Adv 5:1950–1960
85. Boreskov GK (1986) Heterogeneous catalysis. Nauka, Moscow [in Russian]

86. Parmon VN, Simonov AD, Sadykov VA, Tikhov SF (2015) Catalytic combustion: achievements and problems. Combust Explosion Shock Waves 51(2):143–150
87. Franson C, Orlandi O, Perut C, Fouin G, Chauveau C, Gokalp I, Calabro M (2007) Al/H_2O and Al/H_2O/H_2O_2 frozen mixtures as examples of new composite propellants for space application. EUCASS, Brussels
88. Risha GA, Connell TL, Jr, Weismiller M, Yetter RA, Sundaram DS, Yang V, Wood TD, Pfeil MA, Pourpoint TL, Tsohas J, Son SF. Novel energetic materials for space propulsion. AFOSR, Final Report No. FA9550-07-1-0582, 30 Apr 2011
89. NASA technology roadmaps TA 1: launch propulsion systems (2015)
90. Heister SD, Austin BL, Corpening J (2012) U.S. Patent 8,192,567 B2
91. http://www.nasa.gov/sites/default/files/files/orion_las_fact_sheet.pdf
92. https://youtu.be/JLdP-L7D58g
93. Lipanov AM (2002) Brief history of development of solid propellant rockets in Russia in XX century. Inst Appl Mech, Ural Div Russ Acad Sci, Izhevsk, pp 84
94. Lipanov AM (2003) Historical survey of solid-propellant rocket development in Russia. J Prop Power 19(6):1067–1088

Part II
New Ingredients for Chemical Propulsion

Synthesis of New Oxidizers for Potential Use in Chemical Rocket Propulsion

Marcos A. Kettner and Thomas M. Klapötke

Abstract The currently used oxidizer for solid rocket propellants – ammonium perchlorate (AP) – has been detected as hazardous to human's thyroid gland, amphibian pigmentation and growth, and a large number of maritime life forms. Presently used or tested perchlorate-free alternatives like ammonium nitrate or ammonium dinitramide overcome these harms while showing up new problems like polymorphism, hygroscopicity, or a low thermal stability. Therefore, research is further driven toward environmentally more acceptable and strong oxidizers. One strategy is the synthesis of neutral CHNO-based materials for full or partial replacement of AP. Here we report about several new compounds with positive oxygen balance that were synthesized within our group over the last few years. The main focus is on the syntheses of molecules containing the trinitromethyl functionality due to the high oxygen content of this group. In addition the analogue fluorodinitromethyl derivatives were investigated for comparison. The prepared materials were chemically characterized, and in addition the sensitivities toward impact, friction, and electrostatic discharge were determined experimentally. Furthermore, the performances regarding the specific impulse of aluminized mixtures of the compounds were calculated using the Explo5 computer code.

1 Solid Rocket Propellants

Chemical rocket propulsion systems can principally be classified as liquid, solid, hybrid, and gel propellant systems, which basically differ in the state of matter of the fuels, oxidizers and other ingredients, and therefore also in the rocket tank architectures. Solid propulsion systems are preferred over liquid and hybrid propellants owing to their high simplicity, reliability, and commonly lower costs, although in general they cannot be throttled or operated in pulsed mode [1].

M.A. Kettner • T.M. Klapötke (✉)
Department of Chemistry, Energetic Materials Research, Ludwig-Maximilian University of Munich, 81377 Munich, Germany
e-mail: tmk@cup.uni-muenchen.de

Solid propellants are distinguished into two major classes: *composite* and *double-base propellants*. Composite propellants are based on a physical mixture of a metal powder such as aluminum (rocketry) or magnesium (pyrotechnics) and a solid oxygen carrier or *oxidizer* like ammonium perchlorate (AP), which provides oxygen for the appropriate combustion of the fuel in an oxygen-deficient environment. The main fuel and oxidizer are embedded in a rubberlike binder such as polybutadiene derivatives that determines the propellants burning properties, protects the ingredients, and acts as secondary fuel. Essentially all large solid rocket boosters use ammonium perchlorate composite propellants (APCPs). Double-base propellants in contrast are used in smaller propellant charges like hand guns or mortars. They are usually comprised of nitrocellulose and nitroglycerin. To prevent the increased erosion and muzzle flash caused by these mixture, nitroguanidine is added for the reduction of the combustion temperature giving triple-base propellants. These are used in large caliber weapons [2].

The oxygen balance Ω is defined as the ratio of oxygen contained in a material to the amount of oxygen required for complete oxidation of the material. In general an oxidizer is a material with a positive value for Ω, which describes the ability of a CHNOX material (X = halogen) to form additional O_2 (beside H_2O, N_2, HX, CO, or CO_2) during its assumed ideal combustion. The oxygen balance Ω can easily be calculated from the sum formula $C_xH_yN_aO_nX_z$ (X = Cl, F) according to Eqs. 1 and 2 assuming the formation of CO_2 or CO [2]:

$$\Omega_{CO_2} = nO - 2xC - \frac{1}{2}(y - zX)H \cdot \left(\frac{1600}{M}\right) \tag{1}$$

$$\Omega_{CO} = nO - xC - \frac{1}{2}(y - zX)H \cdot \left(\frac{1600}{M}\right) \tag{2}$$

Since the combustion temperature T_C is significantly increased when aluminum (ΔH_C (Al) $= -834$ kJ·mol^{-1}) [3] is used as fuel (ΔH_f^0 (Al$_2$O$_3$) $= -1676$ kJ·mol^{-1}) [4], Ω_{CO} is predominant due to the Boudouard equilibrium. Generally every individual propellant formulation needs a determination of its actual experimentally measured combustion products for the exact identification of the oxygen balance, but the value ranges between the theoretical Ω_{CO} and Ω_{CO2} according to an ideal combustion. In the following for all carbon-containing molecules, both values will be specified.

The performance of a propellant mixture depends on its specific impulse I_s [5]. It can be described according to Eq. 3 as a function of thrust F during the burning time t_b divided by the propellant mass m and the earth gravity factor g_0 for standardization. Therefore, its unit is seconds. For the chemistry it is more important that I_s is proportional to the square root of the combustion temperature T_C divided by the average molecular mass of the gaseous combustion products M according to Eq. 4 [2]:

$$I_s = \frac{1}{m \cdot g_0} \int_0^{t_b} F(t) \mathrm{d}t_b \tag{3}$$

$$I_s \propto \sqrt{\frac{T_C}{M}} \tag{4}$$

2 Ammonium Perchlorate: Uses and Hazards

As mentioned above APCPs are common in all rocketry. Currently AP is the mostly used oxidizer for solid rocket boosters [1, 6]. It has an oxygen balance Ω of 34 %, and the common used mixtures with 15–20 % aluminum embedded in 10–15 % polybutadiene binders (CTPB, PBAN, HTPB) achieve specific impulses I_s of 262 s (70 % AP, 16 % Al, 14 % PBAN), which corresponds to a vacuum specific impulse of about 285 s [1, 7]. Beside high-power and amateur rocketry, and due to its simplicity, reliability, and high I_s, APCPs are also used for pyrotechnic devices like warning flares (USA) and fireworks and find application in airbag inflators and aircraft injection seats. AP can additionally be formed as impurity during production of agricultural fertilizers. Owing to its high stability and solubility in water, it has been widely distributed in surface and groundwater systems worldwide, but particularly in the southwestern USA due to its multiple applications [2, 8].

Only few incidents are known that can be ascribed to the use of AP, which again reflects the reliability of this material on the one hand, but also displays its explosive hazard on the other hand: (1) the "Challenger Tragedy" in 1986, which is only indirectly connected, because the reason was a fracture in the sealing ring of one of the space shuttle boosters [9]; (2) the "PEPCON Disaster" in 1988 in Henderson, Nevada, USA, can directly be connected to the explosive hazard and oxidizing properties of AP, which was stored in amounts of about 4000 t near the production site [10]; and (3) the explosion of an unmanned Delta II rocket with nine solid boosters in 1997, which again can be attributed to a defective rocket assembling [11].

Besides these incidents, unfortunately this very low-priced salt AP has also been detected as toxic, which is even worse considering its good solubility. In vertebrates the perchlorate anion competes with iodide in the binding sides of the thyroid gland due to a similar diameter (iodide 2.11 Å, perchlorate 2.25 Å) [12]. This leads to dysfunction and affects both growth and development of humans and animals. Also amphibians' normal pigmentation and growth is disturbed by the exposure to AP. Furthermore, AP also might be toxic to a large number of maritime life forms of unknown magnitude [13]. Further problems are caused by the APCPs combustion products. Hydrogen chloride (HCl) is formed in very large quantities during combustion, which causes acid rain formation and ozone degradation [14]. The launching of the Ariane 5 rocket, for instance, generated about 270 tons of concentrated HCl beside Al_2O_3. Furthermore, these primary and secondary smokes

affect guidance and control systems adversely. Additionally for tactical missiles the aspect of a visible and detectable expulsion is unfavorable. For example, the standard MIM-104A *Patriot* rocket or the first AGM-114A *Hellfire* missiles used APCP-based motors until being replaced by smoke-reduced propellants [15].

Perchlorate-free alternatives, which presently are in testing procedures, overcome most of these harms, but bring up new problems: while ammonium nitrate (AN) has a high Ω of 20.0 % and has definitely the advantage of very low costs, the salt shows slight hygroscopicity, and its various polymorphs result in burning rate problems due to cracks in the propellant formulation. So-called phase-stabilized AN might be able to overcome the latter, but as a fact AN-based propellants cannot provide the high energy produced by APCPs. Ammonium dinitramide (ADN) shows a very high Ω of 25.8 %, but its low thermal stability ($T_{dec} = 127$ °C) is a problematic issue for application. Currently 1 kg of ADN costs about 4000 Euro [16]. Another expensive research chemical is hydrazinium nitroformate (HNF) containing one carbon atom with a high Ω_{CO} of 21.8 % and a moderate Ω_{CO2} of 13.1 %. In compositions it burns very rapidly and with a very high combustion efficiency, but also this material suffers from a low thermal stability ($T_{dec} = 129$ °C) and additionally a high friction sensitivity. Furthermore, the use of the hydrazinium cation may be critical due to the eventual release of highly cancerogenic hydrazine as a consequence of thermal stress or alkaline reaction conditions. Hydroxylammonium salts such as the research compound hydroxylammonium nitrate (HAN) increase the oxygen content of various ammonium and hydrazinium salts, but also hydroxylamine if released from the salt shows a mutagenic impact, which can convert the nucleic acid cytosine into uracil within the DNA (however, as uracil does not appear in the DNA, such errors are easily recognized and repaired by DNA repair mechanisms). Hence, AP currently has no fielded alternatives; this is why scientific research is further driven toward environmentally more acceptable and strong oxidizers as replacement or for the reduction of the AP ratio in solid rocket propellants.

3 Requirements, Strategy Development, and Building Blocks for the Design of New Oxidizers

The challenge in the development of new and advanced oxidizers is – as it is for all energetic materials research – to find a good balance between performance and physical properties, in this case between high specific impulse and high oxygen balance on the one hand and good thermal stabilities and low mechanical sensitivities on the other hand. Furthermore, it has to be considered that for every individual problem (big rocket or small missile motor), designed solutions are required.

The primary aspects that need to be considered in the development of new oxidizers include low costs, simplicity of synthesis, high performance, and low hazards.

Table 1 Possible oxygen sources derived from (mineral) acids for the design of new oxidizers

	Sum formula	Drawback
Carbonates	CO_3^{2-}	Non-energetic
Sulfates	SO_4^{2-}	Non-energetic
Perchlorates	ClO_4^-	Toxicity
Periodates	IO_4^-	Weight
Peroxides	O_2^{2-}	Low stability/explosive
Ozonides	O_3^-	Low stability/explosive
Nitrate esters/nitrates	NO_3^-	Low stability/hygroscopicity
Dinitramides	$N(NO_2)_2^-$	Low stability/costs
Xenates	XeO_4^-	Weight/costs
Nitro compounds	$C-NO_2$	Various

Additionally, in our group at the Ludwig-Maximilian University of Munich, some internal benchmark requirements were defined, which a novel oxidizer should fulfill [2]:

- High density ρ (close to 2 g·cm^{-3})
- High oxygen balance (Ω_{CO} >25 %)
- High thermal stability (T_{dec} >150 °C)
- Low sensitivities (*impact*: 4 J, *friction*: 80 N, *electrostatic discharge*: 0.1 J)
- Compatibility with aluminum, AP, and binder system
- Minimum number of synthesis steps

For the design of new oxygen carriers in a first step, several possible oxygen sources were taken into consideration. The listed anions derived from (mineral) acids (Table 1) show defined drawbacks and would form salts, which usually are soluble in water. Neutral nitro compounds certainly also show various drawbacks, but these can be manipulated and limited by using different stabilizing carbon backbones. In contrast to salts, they usually are only slightly or non-soluble in water. Furthermore, poly-nitro moieties like dinitromethyl and trinitromethyl groups in neutral molecules might be stabilized by a carbon backbone in contrast to dinitromethanide and nitroformate salts, where these anions seem to influence the thermal stability (compare HNF). Therefore, neutral CHNO-based poly-nitro compounds were the basic approach toward new oxidizers in our group in the last few years [17].

But, when increasing the oxygen content of a molecule with nitro groups, one cannot just introduce nitro groups into a system and expect that it remains stable. This can easily be displayed when looking at the row of nitromethanes and higher homologues. These compounds are either liquids or not stable at ambient temperature. Additionally, tetranitromethane, the representative with highest nitro group content in this row, is a quite toxic material. Looking at higher homologues of per-nitrated compounds, for instance, hexanitroethane, these show very high oxygen balances Ω, but very low long-term stabilities and high vapor pressures.
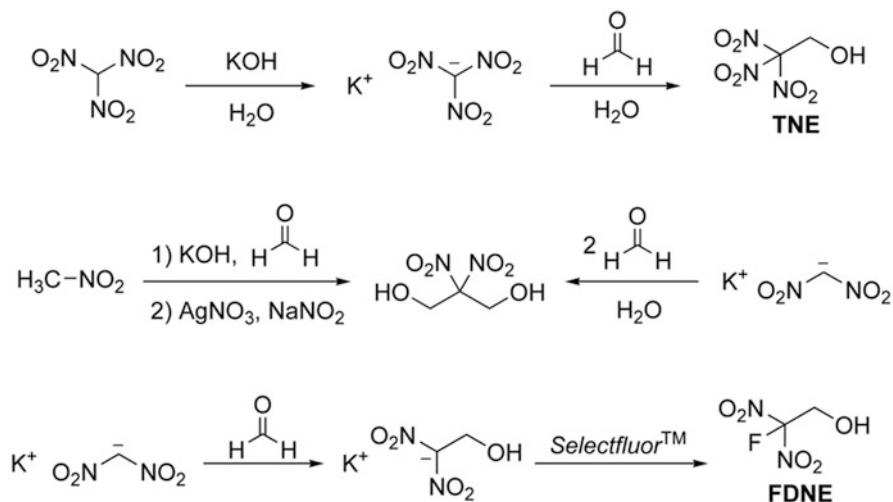
Fig. 1 Scheme of the facile synthesis of 2,2,2-trinitroethanol (TNE) from nitroform (*top*) [18], two synthetic routes toward 2,2-dinitropropane-1,3-diol from nitromethane or potassium dinitromethanide (*middle*), [19] and the synthesis of 2-fluoro-2,2-dinitroethanol (FDNE) from potassium dinitromethanide [20]

Hence, per-nitrated compounds are very problematic. But as mentioned before, the dinitromethyl and trinitromethyl group may be considered as oxygen-rich building blocks for the design of new neutral oxidizer molecules, due to their high oxygen contents and densities [17].

From an aqueous solution of nitroform with formaldehyde, 2,2,2-trinitroethanol (TNE) can be synthesized easily in two steps. In contrast to nitroform, which is only stable in aqueous solution, TNE can be purified as a crystalline solid and represents a very useful and stable precursor in the synthesis of new oxidizers [18]. The analogue precursor with two reaction sides for further derivatization is 2,2-dinitropropane-1,3-diol, which can easily be synthesized from nitromethane or potassium dinitromethanide [19]. One further building block of interest is 2-fluoro-2,2-dinitroethanol (FDNE) due to its enhanced thermal stability compared to that of TNE. It may be introduced instead of TNE for structural investigations and saver working, but nevertheless, it represents an energetic poly-nitro containing moiety. If fluorine is formed during combustion, it might also act as strong oxidizer. The synthesis of FDNE is realized starting from potassium dinitromethanide and using *Selectfluor*™ (Fig. 1) [20].

Taking into consideration all thoughts mentioned above, the main strategy that is focused on are covalent aliphatic poly-nitro compounds containing the dinitromethyl or trinitromethyl groups due to the high oxygen balance of these moieties. Advantages of such CHNO compounds are the insolubility in water and that the combustion products H_2O, N_2, CO/CO_2, and O_2 are harmless (of course, fluorinated combustion products of fluorodinitromethyl containing materials are excluded from

this strategy). Drawbacks of such materials may be the vapor pressure, sensitivity, and thermal stability, but these have to be determined experimentally.

4 Synthesized Materials

The main focus in our group is on the syntheses of molecules containing the dinitromethyl, trinitromethyl, or -ethyl moieties owing to their high oxygen content and heat of formation. Combining these with various connecting carbon backbones, heterocyclic systems, and other energetic groups including mainly nitramines led to a large quantity of new compounds and also revalidation of some literature known compounds in the past years, some of these in collaboration with other groups (Fig. 2).

For almost every material containing the trinitromethyl group, its fluorodinitromethyl derivative has also been synthesized. Some mixed molecules with both of these moieties have also been prepared (Fig. 6l, n, o) [31, 32]. These fluorine-containing materials do not only serve as model compounds for saver working and increasing the thermal stability but could also be considered as solid energetic oxidizers for outer space applications or explosives for agent-defeat weapons due to the fluorinated toxic combustion products. In the following, there will be gone

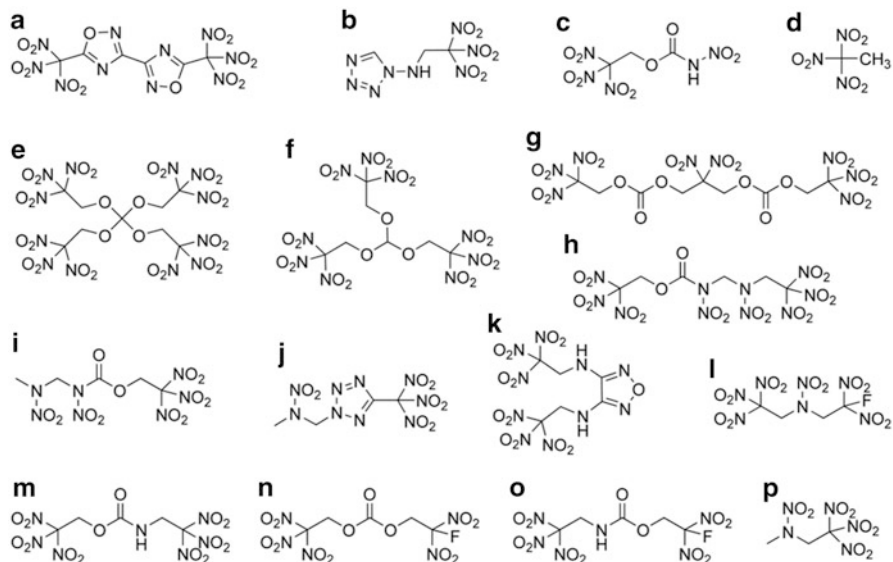**Fig. 2** Selected compounds that were synthesized and investigated within our group over the past years. Their according literature references: (**a**) [21], (**b**) [22], (**c**) [23], (**d**) [24], (**e**) [25], (**f**) [25], (**g**) [26], (**h**) [27], (**i**) [28], (**j**) [29], (**k**) [30], (**l**) [31], (**m**) [32], (**n**) [32] (**o**) [32], (**p**) [33]

into detail about some of the most outstanding candidates with different backbones and varying number of trinitromethyl groups. Their analogue fluorodinitromethyl derivatives will be presented in direct comparison.

For all compounds, the single crystal X-ray structures were measured. Due to their energetic character, their sensitivities toward impact (IS), friction (FS), and electrostatic discharge (ESD) were determined at defined grain sizes according to the standards of the German Federal Institute for Materials Research and Testing (BAM) [34]. This includes the method "one out of six" measurements, where the material is allowed to decompose or explode for the value given as sensitivity. The melting and decomposition point were determined by differential scanning calorimetry (DSC) at a heating rate of 5 °C·min^{-1}. Additionally the room temperature densities ρ_{RT} were measured by means of a pycnometer, and all heats of formation ΔH_f^0 were calculated at the CBS-4M level of theory [35]. By means of the last two values, the detonation parameters of the neat compounds were computed with the EXPLO5 (version 6.02) computer code [36] as well as all propulsion parameters for formulations of the compounds with aluminum and polybutadiene acrylonitrile (PBAN) as binder. The formulation used in the solid rocket boosters of the NASA Space Shuttle program (70 % AP and 16 % aluminum in 14 % PBAN) [37] serves as AP reference as it is imperative in this project to replace this component. PBAN ratio is kept at 14 % because the maximum solid loading of this polymer is given with 86 % in the literature [7]. In some cases also the ratio oxidizer/aluminum needs to be varied to achieve the maximum value for the specific impulse I_s. Furthermore, formulations with different ratios of AP and ADN were calculated to investigate the influence on I_s when the new compounds are used as additives (10 %), in 50/50 mixtures, or AP respectively ADN are used as additives (10 %).

4.1   Orthocarbonates [25, 38]

Starting with the largest candidate with four trinitroethyl groups, the class of orthocarbonates is presented. Owing to the high amount of trinitromethyl and also fluorodinitromethyl groups that can be introduced into such molecule, this class seems to be perfect for the achievement of very high oxygen balances. Both materials were known since the late 1960s, but only very few analytical information was given in those articles [39]. The syntheses were performed as catalyzed condensation reactions of TNE or FDNE with tetrachloromethane and furnished the desired tetrakis(2,2,2-polynitroethyl) orthocarbonates **1** and **2** in moderate yields (Fig. 3).

Single crystals suitable for X-ray structure determination were obtained from tetrachloromethane (Fig. 4). During the low temperature measurements in both materials **1** and **2**, solid phase transitions were observed. By means of DSC measurements, the exact transition temperatures could be determined: compound **1** shows transition when heating at 34 °C and when cooling at −16 °C, just in the
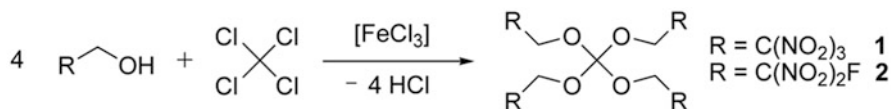
Fig. 3 The catalyzed condensation reactions toward TNE-OC (**1**) and FDNE-OC (**2**) [25, 38]
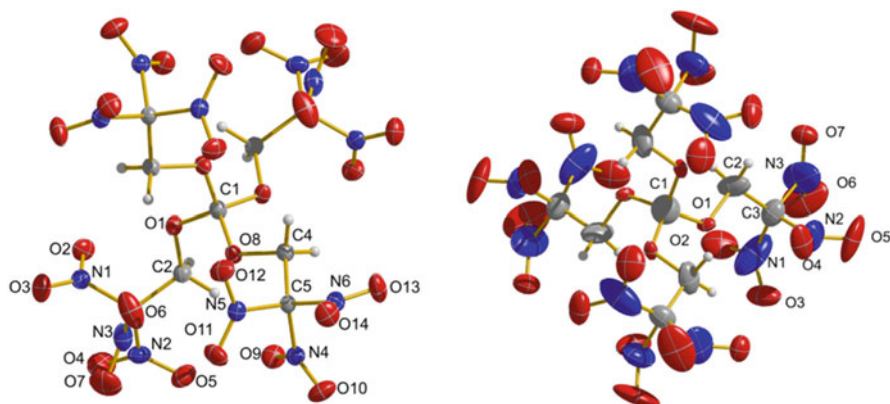
Fig. 4 Crystal structure of the two phases of orthocarbonate **1**. *Left*: low temperature **α-1**; *right*: ambient temperature **β-1**. Thermal ellipsoids shown at the 50 % probability level [25]

range of room temperature. Compound **2** shows a sharper range when heating at −22 °C and when cooling at −26 °C. These phase transitions might be due to the dimensions of the molecules, which have large degrees of freedom, but also due to different packing within the structures. They are problematic since the oxidizer is the highest ratio ingredient in propellant mixture, and consequently they can cause burning rate problems due to micro-cracks in a propellant formulation as it is known for AN [25].

Table 2 shows the physical–chemical properties determined for these materials. While compound **1** shows a considerable high sensitivity toward impact and is moderate toward friction, compound **2** shows sensitivities in the desired range. As mentioned before, the thermal stability gets improved by substitution of one nitro group with a fluorine atom, but also the melting point is decreased due to extensive nonclassical hydrogen bonding within the structure. Therefore, the melting range is much larger.

The oxygen balance of compound **1** exceeds the requirement by more than 7 % which should be at least 25 % (assuming the formation of CO), while compound **2** almost achieves this value. Burning in a vacuum at low temperature secures the necessary oxygen content for a complete combustion ($\Omega_{CO2} = 0.0$ %). The densities of both materials are in a good range near to 2.00 g·cm^{-3}. The calculated heats of formation display the expected trend: while orthocarbonate **1** shows a rather negative value, the contribution of the C–F bonds is obvious in view of the value for compound **2**.

Table 2 Physical–chemical properties and calculated detonation and propulsion parameters of orthocarbonates **1** and **2**

	1	2	Requirement
Formula	$C_9H_8N_{12}O_{28}$	$C_9H_8N_8O_{20}F_4$	–
Weight [g·mol^{-1}]	732.22	624.20	–
Sensitivities according to BAM standard methods (1 out of 6)			
IS [J]	1	9	>4
FS [N]	96	192	>80
ESD [J]	0.20	0.25	>0.10
Grain size [μm]	<500	<500	–
Thermal analysis according to DSC measurements (T_{onset})			
T_{melt} [°C]	161	110	–
T_{dec} [°C]	191	216	150
Combined nitrogen and oxygen content, oxygen balance, and density at room temperature			
N + O [%]	84.13	69.21	–
Ω_{CO} [%]	32.8	23.1	>25.0
Ω_{CO2} [%]	13.1	0.0	–
ρ_{RT} [g·cm^{-3}]	1.81	1.84	±2.00
Enthalpy and internal energy of formation at the CBS-4M level of theory			AP
ΔH_f^0 [kJ·mol^{-1}]	−748	−1640	−296
ΔU_f [kJ·kg^{-1}]	−940	−2548	−2433
Detonation parameters (EXPLO5, V6.02)			
$-\Delta U_{EX}$ [kJ·kg^{-1}]	5167	4538	1422
T_{EX} [K]	3961	3774	1735
p_{CJ} [kbar]	278	367	158
D_V [m·s^{-1}]	8224	8381	6368
V_0 [L·kg^{-1}]	734	677	885
Isobaric combustion parameters (EXPLO5, V6.02), specific impulse (Oxidizer/Al/PBAN binder), T_C [K] in parenthesis			
I_s (neat) [s]	243 (3231)	249 (3245)	157 (1403)
I_s (70/16/14) [s]	266 (3525)	246 (2805)	262 (3380)
Specific impulse (Oxidizer/AP/Al/PBAN binder), T_C [K] in parenthesis			
I_s (60/10/16/14) [s]	265 (3502)	248 (2915)	–
I_s (35/35/16/14) [s]	264 (3447)	258 (3207)	–
I_s (10/60/16/14) [s]	262 (3399)	261 (3341)	–
Specific impulse (Oxidizer/ADN/Al/PBAN binder), T_C [K] in parenthesis			
I_s (60/10/16/14) [s]	267 (3498)	250 (2855)	–
I_s (35/35/16/14) [s]	268 (3409)	262 (3179)	–
I_s (10/60/16/14) [s]	270 (3320)	268 (3261)	–

The calculated detonation parameters show two compounds with rather good performance data in the range of the values calculated for PETN (pentaerythrithyl-tetranitrate, $\rho_{RT} = 1.78$ g·cm^{-3}, $D_V = 8404$ m·s^{-1}, $p_{CJ} = 309$ kbar). Considering these orthocarbonates as ingredients for propellant formulations, it is noticeable

that compounds **1** and **2** with their carbon backbone already achieve rather high values for the specific impulse I_s as neat compounds. The propellant formulation of compound **1**, with the same ratio as the boosters for the Space Shuttle had (70/16/14) [37], achieves a superior value for I_s with a slightly higher combustion temperature T_C than the original AP formulation. In contrast the analogue mixture of the fluorine containing derivative **2** is far from the value of the AP formulation (262 s). When adding AP to the formulation of compound **2** with rising AP content, the I_s increases, while when doing so with the formulation of compound **1**, the I_s decreases. However, the I_s of the TNE derivative **1** can even be improved when adding ADN to the mixture. The formulation of a 1:1 mixture of ADN with compound **1** achieves a I_s of 268 s. The theoretical maximum value for I_s of the ADN/Al/PBAN mixture is 273 s ($T_C = 3396$ K) at a 65/21/14 ratio.

In comparison the trend between the TNM compound **1** and the fluorine containing derivative **2** becomes obvious. Although the TNM compound shows a very high oxygen balance and a superior specific impulse than AP in a formulation with aluminum, it's very high impact sensitivity of 1 J makes this compound rather inoperative. The fluorine-containing compound in contrast shows a lower specific impulse than that of AP, while the sensitivities are in a good range, and thermal stabilities are improved compared to the TNE derivative **1**.

4.2 2,5-Disubstituted Tetrazoles [29]

Tetrazole derivatives have an important rank in energetic research as they are stable five-membered ring systems with high nitrogen contents and high positive heats of formation. Often they are considered for gas generating applications [2]. 5-(Polynitro-methyl)tetrazoles and salts thereof show very high mechanical sensitivities in previous publications, thus too sensitive for processing propellant formulations [40]. For the reduction of the sensitivities, the alkylation of the tetrazole ring was investigated. A secondary nitramine group was chosen to maintain the energetic character of the molecules and to investigate the interaction of this moiety with the polynitromethyl groups. The syntheses of 2-(2-nitro-2-azapropyl)-5-(trinitromethyl) tetrazole **3** and 2-(2-nitro-2azapropyl)-5-(fluoro-dinitromethyl)tetrazole **4** were carried out using the ammonia salts of the parent 5-(polynitromethyl)tetrazolates in anhydrous acetone. The precipitation of ammonium chloride drives the reaction, which results in rather high yields of 80 % (Fig. 5).
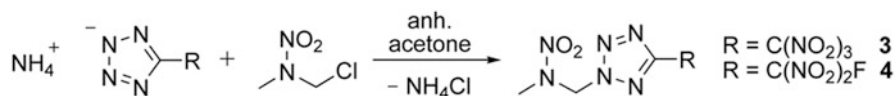

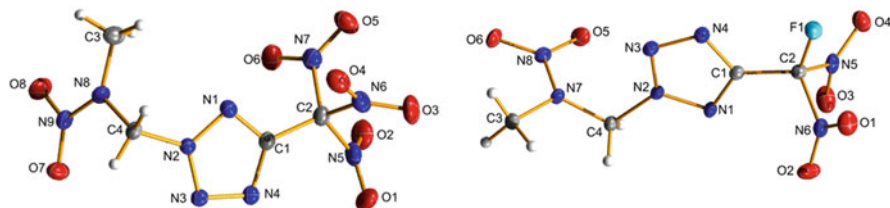**Fig. 5** Syntheses of the alkylated tetrazoles **3** and **4** [29]

Fig. 6 Crystal structures of the polynitrotetrazoles **3** and **4**; thermal ellipsoids shown at the 50 % probability level [29]

Single crystals suitable for X-ray measurements were obtained from a methanol/dichloromethane mixture and the crystal structures were determined at 100 K. The densities at this temperature were in the range of 1.83 g·cm^{-3} (Fig. 6).

Table 3 shows the physical–chemical properties determined for these materials. The impact sensitivities of 2–3 J could barely be decreased by the alkylation compared to the starting materials (impact = 1–2 J) and are rather similar among each other. This is noticeable since this result stands in contrast to Kamlet's theory [41], that TNM containing materials are more sensitive toward impact than their FDNM containing analogues, due to the restricted rotation of the C–NO$_2$ bonds [41]. In contrast the friction sensitivity for both compounds **3** and **4** was improved by the alkylation [29]. However, both compounds reveal too high sensitivities for application. With regard to thermal stabilities, the expected trend between TNM and FDNM containing materials is again observed: a much lower melting point and rather high decomposition point for the fluorine containing derivative **4** was determined by DSC measurements. While the trinitromethyl derivative **3** shows a positive value for Ω_{CO}, compound **4** is no oxidizer according to the definition. The calculated heats of formation are positive for both molecules as expected for tetrazole derivatives, but about three times higher for the trinitromethyl derivative **3**. The detonation parameters of **3** and **4** calculated with the density measured at room temperature are comparable with those calculated for RDX (1,3,5-trinitroperhydro-1,3,5-triazine, $\rho_{RT} = 1.80$ g·cm^{-3}, $D_V = 8838$ m·s^{-1}, $p_{CJ} = 343$ kbar). When considering an isobaric combustion of formulations using compounds **3** and **4** as oxygen carriers, the mixture that achieves the maximum I_s values of 256 s (**3**) and 246 s (**4**) was found when reducing the aluminum content to 10 % (76/10/14). In a 1:1 mixture of compound **3** with AP, that means by replacing half of the AP in the original Space Shuttle mixture, the same value for I_s of 262 s is achieved [37]. If compound **3** is considered as additive (10 %) to the AP mixture, the I_s increases to 264 s. When mixing compound **3** with ADN, with increasing ADN content, the formulations reach I_s values up to 270 s. The fluorine containing derivative **4** with a negative oxygen balance is far from giving the mixtures any advantages. However, both compounds **1** and **3** are not suitable for processing propellant charges owing to their high sensitivities.

Table 3 Physical–chemical properties and calculated detonation and propulsion parameters of tetrazoles **3** and **4**

	3	4	Requirement
Formula	$C_4H_5N_9O_8$	$C_4H_5N_8O_6F$	–
Weight [g·mol^{-1}]	307.14	280.13	–
Sensitivities according to BAM standard methods (1 out of 6)			
IS [J]	3	2	>4
FS [N]	40	36	>80
ESD [mJ]	0.10	0.10	>0.10
Grain size [μm]	100–500	100–500	–
Thermal analysis according to DSC measurements (T_{onset})			
T_{melt} [°C]	87	46	–
T_{dec} [°C]	134	184	150
Combined nitrogen and oxygen content, oxygen balance, and density at room temperature			
N + O [%]	82.71	74.27	–
Ω_{CO} [%]	7.8	−2.9	>25.0
Ω_{CO2} [%]	−13.0	−25.7	–
ρ_{RT} [g·cm^{-3}]	1.75	1.83	±2.00
Enthalpy and internal energy of formation at the CBS-4M level of theory			AP
ΔH_f^0 [kJ·mol^{-1}]	314	98	−296
ΔU_f [kJ·kg^{-1}]	1111	439	−2433
Detonation parameters (EXPLO5, V6.02)			
$-\Delta U_{EX}$ [kJ·kg^{-1}]	6016	5394	1422
T_{EX} [K]	4291	3783	1735
p_{CJ} [kbar]	334	342	158
D_V [m·s^{-1}]	8704	8773	6368
V_0 [L·kg^{-1}]	774	728	885
Isobaric combustion parameters (EXPLO5, V6.02), (Oxidizer/Al/PBAN binder), T_C [K] in parenthesis			
I_s (neat) [s]	273 (3551)	259 (3328)	157 (1403)
I_s (70/16/14) [s]	253 (2828)	244 (2775)	262 (3380)
I_s (76/10/14) [s]	256 (2760)	246 (2563)	257 (3228)
(Oxidizer/AP/Al/PBAN binder), T_C [K] in parenthesis			
I_s (60/10/16/14) [s]	254 (2816)	246 (2641)	–
I_s (35/35/16/14) [s]	262 (3156)	253 (2872)	–
I_s (10/60/16/14) [s]	264 (3344)	262 (3305)	–
(Oxidizer/ADN/Al/PBAN binder), T_C [K] in parenthesis			
I_s (60/10/16/14) [s]	256 (2850)	247 (2721)	–
I_s (35/35/16/14) [s]	265 (3019)	259 (2840)	–
I_s (10/60/16/14) [s]	270 (3268)	269 (3229)	–

4.3 Bi-1,2,4-Oxadiazoles [21]

A further development in the investigation of polynitroazole oxidizers is the class of oxadiazoles, for instance, bi-1,2,4-oxadiazoles. Similar to the alkylation of tetrazoles, bi-heterocyclic compounds overcome the problem of the acidities associated with cyclic nitroazoles and might also reduce their high mechanical sensitivities. Moreover, the class of oxadiazoles contains one oxygen atom within the ring, thus increasing the oxygen balance compared to tetrazole derivatives. The following presented bi-3,3′-(5-trinitromethyl-1,2,4-oxadiazole) **5** and bi-3,3′-(5-fluorodinitromethyl-1,2,4-oxadiazole) **6** are also examples for hydrogen atom free poly-nitro derivatives. Both compounds can be synthesized starting from diammonium bi-3,3′-(5-dinitromethylide-1,2,4-oxadiazole) by fluorination (**6**) or non-oxidative nitration with nitronium tetrafluoroborate (**5**). Since the later reaction resulted in low yields, a much cheaper synthesis route was developed via decarboxylative nitration of the according free carbonic acid furnishing high yields and purities (Fig. 7) [21].

Single crystals suitable for X-ray diffraction of compounds **5** and **6** were obtained from diethyl ether or dichloromethane (Fig. 8). Both materials reveal remarkable high densities in the desired range of 2.00 g·cm^{-3} at 100 K. These high densities might be explained by multiple attractive intra- and intermolecular contacts that distances were found to be clearly under the sum of van der Waals radii.

Table 4 shows the physical–chemical properties determined for these bi-1,2,4-oxadiazoles **5** and **6**. Looking at the sensitivities and thermal stabilities first, it can
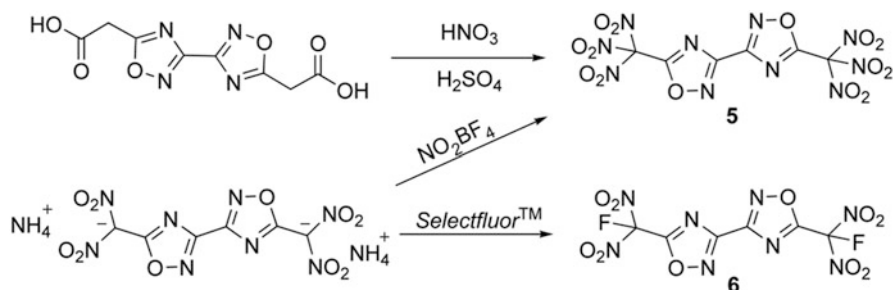

Fig. 7 Syntheses of the bi-1,2,4-oxadiazoles **5** and **6** starting from bi-3,3′-(5-acetato-1,2,4-oxadiazole) and diammonium bi-3,3′-(5-dinitromethylide-1,2,4-oxadiazole) [21]
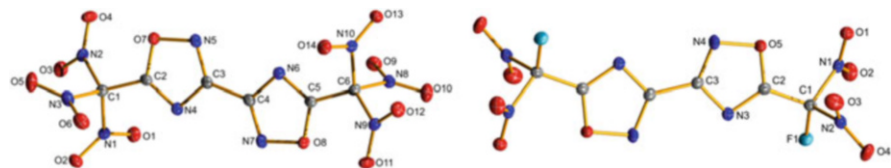

Fig. 8 Crystal structures of the bi-1,2,4-oxadiazoles **5** and **6**; thermal ellipsoids shown at 50 % probability level [21]

be noticed that the sensitivities are in a good range compared to the requirement. The sensitivity toward impact is 10 J for both compounds. Similar to the finding of the tetrazole derivatives **3** and **4**, this result stands in contrast to the theory established by

Table 4 Physical–chemical properties and calculated detonation and propulsion parameters of bi-1,2,4-oxadiazoles **5** and **6**

	5	6	Requirement
Formula	$C_6N_{10}O_{14}$	$C_6N_8O_{10}F_2$	–
Weight [g·mol^{-1}]	436.12	382.11	–
Sensitivities according to BAM standard methods (1 out of 6)			
IS [J]	10	10	>4
FS [N]	80	192	>80
ESD [mJ]	0.80	1.00	>0.10
Grain size [μm]	<100	<100	–
Thermal analysis according to DSC measurements (T_{onset})			
T_{melt} [°C]	119	67	–
T_{dec} [°C]	124	151	150
Combined nitrogen and oxygen content, oxygen balance, and density at room temperature			
$N + O$ [%]	83.48	71.20	–
Ω_{CO} [%]	29.3	16.8	>25.0
Ω_{CO2} [%]	7.3	−8.4	–
ρ_{RT} [g·cm^{-3}]	1.94	1.96	±2.00
Enthalpy and internal energy of formation at the CBS-4M level of theory			AP
ΔH_f^0 [kJ·mol^{-1}]	62	−362	−296
ΔU_f [kJ·kg^{-1}]	210	−884	−2433
Detonation parameters (EXPLO5, V6.02)			
$-\Delta U_{EX}$ [kJ·kg^{-1}]	5551	3950	1422
T_{EX} [K]	4356	3355	1735
p_{CJ} [kbar]	337	309	158
D_V [m·s^{-1}]	8830	8568	6368
V_0 [L·kg^{-1}]	675	676	885
Isobaric combustion parameters (EXPLO5, V6.02), specific impulse (Oxidizer/Al/PBAN binder), T_C [K] in parenthesis			
I_s (neat)	246 (3466)	238 (3474)	157 (1403)
I_s (70/16/14)	249 (2945)	234 (2890)	262 (3380)
I_s (76/10/14)	256 (3338)	236 (2732)	257 (3228)
Specific impulse (Oxidizer/AP/Al/PBAN binder), T_C [K] in parenthesis			
I_s (60/10/16/14)	251 (3142)	238 (2797)	–
I_s (35/35/16/14)	261 (3407)	252 (3121)	–
I_s (10/60/16/14)	262 (3394)	260 (3347)	–
Specific impulse (Oxidizer/ADN/Al/PBAN binder), T_C [K] in parenthesis			
I_s (60/10/16/14)	254 (3034)	240 (2837)	–
I_s (35/35/16/14)	266 (3357)	256 (2978)	–
I_s (10/60/16/14)	269 (3317)	268 (3269)	–

Kamlet mentioned above [21, 41]. The trend in the thermal stabilities is continued when comparing FDNM and TNM containing materials. The decomposition temperature of compound **5** is 124 °C, just in the range of ADN. Therefore, it does not meet the requirement, while the oxygen balance of this material exceeds the required value. The densities at room temperature are remarkably high. The oxygen balance Ω_{CO} of the fluorine-containing material is positive. The calculated heats of formation exemplarily show the effect of introducing C–F bonds into this class of heterocyclic system: while the value for the TNM derivative **5** is positive, the fluorine derivative shows a negative heat of formation.

The calculated detonation parameters show rather good performances for both compounds in the range of RDX (1,3,5-trinitroperhydro-1,3,5-triazine, $\rho_{RT} = 1.80$ g·cm^{-3}, $D_V = 8838$ m·s^{-1}, $p_{CJ} = 343$ kbar) and PETN (pentaerythrithyl-tetranitrate, $\rho_{RT} = 1.78$ g·cm^{-3}, $D_V = 8404$ m·s^{-1}, $p_{CJ} = 309$ kbar) [36]. Considering an isobaric combustion, the propellant mixtures with the highest values for I_s are obtained when the aluminum ratio is set to 10 % (76/10/14). The I_s of the TNM compound **5** is slightly lower than the maximum I_s of the AP formulation, and I_s values for the FDNM derivative **6** are considerably lower (20–30 s). When 50 % of AP is replaced by compound **5** in the formulation with 16 % aluminum, a I_s of 261 s is achieved with a slightly higher combustion temperature T_C in the combustion chamber. Mixing compound **5** with ADN (1:1) leads to higher values for I_s as shown before. The fluorine containing oxadiazole derivative **6** shows the same tendencies when mixing with AP or ADN in the I_s values, but in contrast to the trinitromethyl derivative **5,** these are considerably lower.

4.4   Carbamates and Nitrocarbamates [28]

Carbamate derivatives have been studied intensively within our group. This building block shows an increased oxygen content compared to urea and also offers the opportunity to be further nitrated at the nitrogen atom, thus increasing the oxygen content further without becoming that unstable toward hydrolysis like nitrourea derivatives tend to. Unfortunately it has been experienced that bis-*O,N*-(2,2,2-trinitroethyl)-carbamate cannot be further nitrated, which was interpreted by a lack of electron density in the N–H position caused by the electron withdrawing character of the trinitroethyl moiety according to quantum chemical calculations [35]. Instead, a secondary nitramine moiety was attached at this side of the carbamate unit simply by the addition reaction of TNE or FDNE to 2-nitro-2-azapropyl isocyanate which yielded the desired carbamates **7** and **8**. The subsequent nitration was achieved by standard nitration methods furnishing the nitrocarbamates **9** and **10** (Fig. 9) [28].

Figure 10 shows the X-ray crystal structures of the carbamate derivatives **7** and **8** and the nitrocarbamate **9**. Remarkable is the high density of the nitrocarbamate **9** which might be explained due to an intramolecular interaction between the two
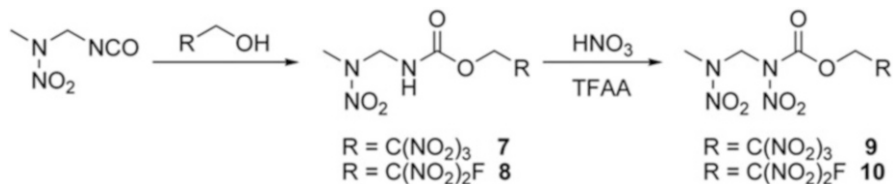
Fig. 9 Syntheses of carbamates **7** and **8** via addition reaction to 2-nitro-2-azapropyl isocyanate and subsequent *N*-nitration yielding the nitrocarbamates **9** and **10**
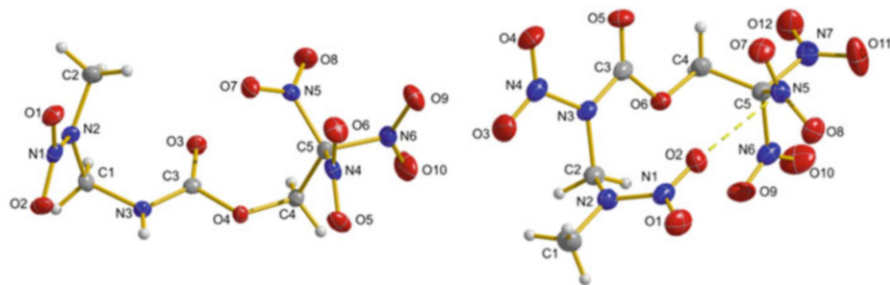
Fig. 10 Crystal structures of the carbamate **7** and the nitrocarbamate **9**; thermal ellipsoids shown at 50 % probability level [28]

opposite sides of the nitrocarbamate ($O_2 \cdots N5$ 2.949(2) Å), so that the molecule is folded.

Table 5 summarizes the physical–chemical properties of the carbamates **7** and **8** and nitrocarbamates **9** and **10**. Having a look at the sensitivities, the differences that occur only by introducing the additional nitro group to the carbamate unit become obvious. While compounds **7** and **8** can be classified as insensitive and less sensitive, the nitrocarbamates **9** and **10** are sensitive toward impact and friction; however, they are in an acceptable range for the requirements. The thermal stabilities of the carbamates are considerably higher than for the nitrocarbamates. The maximum decomposition temperature of all of these compounds is observed for the fluorine containing carbamate **8** at 219 °C, while the maximum melting point is found for the carbamate **7** at 135 °C. Taking into account the oxygen balances of these compounds, only the nitrocarbamate **9** can be considered as oxygen carrier for propellant formulations.

The calculated detonation parameters reveal good performances for all compounds with the expected trends when comparing among each other. The lowest values were obtained for the FDNE containing carbamate **8**, which are in the range of those calculated for picric acid ($\rho_{RT} = 1.77$ g·cm^{-3}, $D_V = 7685$ m·s^{-1}, $p_{CJ} = 251$ kbar) [36]. Best detonation parameters were found for the TNE containing nitrocarbamate **9**, which were found to be in the range of RDX (1,3,5-trinitroperhydro-1,3,5-triazine, $\rho_{RT} = 1.80$ g·cm^{-3}, $D_V = 8838$ m·s^{-1}, $p_{CJ} = 343$ kbar) [36]. Considering an isobaric combustion for all compounds

Table 5 Physical–chemical properties and calculated detonation and propulsion parameters for carbamates **7** and **8** and nitrocarbamates **9** and **10**

	7	8	9	10	Required
Formula	$C_5H_8N_6O_{10}$	$C_5H_8N_5O_8F$	$C_5H_7N_7O_{12}$	$C_5H_7N_6O_{10}F$	–
Weight [g·mol^{-1}]	312.15	285.14	357.15	330.14	–
Sensitivities according to BAM standard methods (1 out of 6)					
IS [J]	30	>40	6	8	>4
FS [N]	240	324	120	144	>80
ESD [mJ]	0.08	0.50	0.20	0.30	>0.10
Grain size [μm]	<100	<100	<100	<100	–
Thermal analysis according to DSC measurements (T_{onset})					
T_{melt} [°C]	135	70	92	62	–
T_{dec} [°C]	183	219	147	158	150
Combined nitrogen and oxygen content, oxygen balance, and density at room temperature					
$N + O$ [%]	78.18	69.45	81.21	73.92	–
Ω_{CO} [%]	5.1	−2.8	15.7	9.7	>25.0
Ω_{CO2} [%]	−20.5	−30.9	−6.7	−14.5	–
ρ_{RT} [g·cm^{-3}]	1.74	1.71	1.82	1.77	±2.00
Enthalpy and internal energy of formation at the CBS-4M level of theory					AP
ΔH_f^0 [kJ·mol^{-1}]	−449	−654	−316	−531	−296
ΔU_f [kJ·kg^{-1}]	−1343	−2199	−794	−1517	−2433
Detonation parameters (EXPLO5, V6.02)					
$-\Delta U_{EX}$ [kJ·kg^{-1}]	5018	4318	5949	5058	1422
T_{EX} [K]	3494	3133	4061	3605	1735
p_{CJ} [kbar]	283	264	328	299	158
D_V [m·s^{-1}]	8118	7820	8706	8234	6368
V_0 [L·kg^{-1}]	754	735	751	722	885
Isobaric combustion parameters (EXPLO5, V6.02), specific impulse (Oxidizer/Al/PBAN binder) [s], T_C [K] in parenthesis					
I_s (neat)	246 (3014)	224 (2403)	262 (3353)	253 (3222)	157 (1403)
I_s (70/16/14)	247 (2507)	239 (2457)	255 (2818)	247 (2653)	262 (3380)
Specific impulse (Oxidizer/AP/Al/PBAN binder) [s], T_C [K] in parenthesis					
I_s (60/10/16/14)	248 (2563)	241 (2454)	256 (2879)	249 (2672)	–
I_s (35/35/16/14)	256 (2985)	249 (2719)	262 (3211)	258 (3051)	–
I_s (10/60/16/14)	261 (3286)	260 (3243)	262 (3339)	261 (3307)	–
Specific impulse (Oxidizer/ADN/Al/PBAN binder) [s], T_C [K] in parenthesis					
I_s (60/10/16/14)	250 (2626)	243 (2466)	258 (2842)	251 (2727)	–
I_s (35/35/16/14)	260 (2927)	254 (2719)	266 (3180)	261 (2992)	–
I_s (10/60/16/14)	268 (3203)	267 (3160)	269 (3259)	268 (3226)	–

(**7–10**), the propellant formulation with aluminum and binder that reveal the highest values for I_s have the same ratios as the reference formulation with AP (70/16/14) [37].

As expected the highest I_s of 255 s in this formulation is accomplished by the TNE containing nitrocarbamate **9** which also shows the highest oxygen balance. By replacing 50 % of AP with compound **9** in the reference formulation, the I_s of 262 s is maintained, while T_C remains at the same level. Mixing compound **9** with increasing amounts of ADN again leads to higher I_s values up to 269 s. Although compound **9** does not meet all requirements such as oxygen balance and thermal stability, the class of nitrocarbamates seemed to be a good basis for further investigations on the design of oxidizers for solid composite propellants.

4.5 2,2,2-Trinitroethyl Carbamate and -Nitrocarbamate [23]

Based on the previous shown drawbacks in the investigations on carbamate derivatives as linkers for different poly-nitro building blocks, an even smaller molecule was considered for investigation. It displays the smallest derivative synthesized in our group containing only one TNE group in combination with a nitrocarbamate unit, namely, 2,2,2-trinitroethyl nitrocarbamate **12**. A very cheap synthetic route yielding TNE-chloroformate was established by reacting TNE with gaseous phosgene. TNE-chloroformate can be isolated and offers a further oxygen-rich building block toward new TNE containing oxidizers that are based on carbonate and carbamate backbones [32]. Treatment of TNE-chloroformate with aqueous ammonia yields TNE-carbamate **11** [42]. A less hazardous synthesis route for the carbamate **11** is given by the reaction of TNE with chlorosulfonyl isocyanate [23]. It skips the involved toxic synthesis step using phosgene, and the aqueous workup of the reaction mixture enables the formation of the carbamate **11** in "one-pot." The subsequent nitration of **11** furnishes the nitrocarbamate **12** in quantitative yield (Fig. 11).

The X-ray crystal structures of compounds **11** and **12** are shown in Fig. 12. Remarkable in both compounds **11** and **12** is the almost perfect planarity around the carbamate and nitrocarbamate unit. Moreover, even though the measurements were
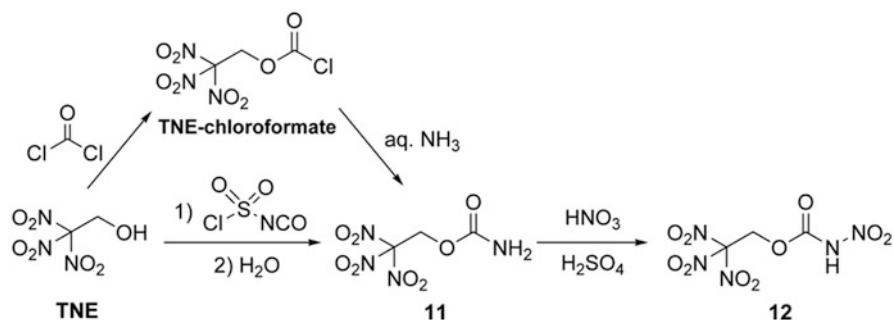

Fig. 11 Two syntheses routes toward TNC (**11**) and TNC-NO$_2$ (**12**) starting from TNE [23]
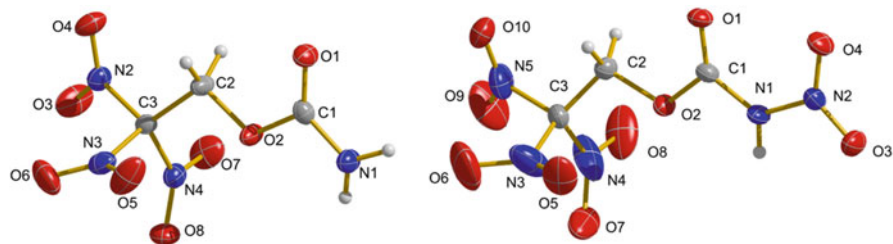
Fig. 12 Crystal structures of TNC (**11**) and TNC-NO$_2$ (**12**); thermal ellipsoids shown at the 50 % (*left*) and 30 % (*right*) probability level [23]

carried out at different temperatures, compound **11** shows up the higher density. This might be explained by consideration of several intermolecular interactions observed within the crystal structure. The reason for the different measurement temperatures is due to a solid phase transition of the nitrocarbamate **12** at −62 °C, thus in an unproblematic range.

Table 6 summarizes the physical–chemical properties determined for compounds **11** and **12**. The trend when comparing the sensitivities of the carbamate and the nitrocarbamate is obvious again: while compound **11** can be classified as insensitive toward impact, the nitrocarbamate **12** is sensitive toward this external stimulus. Unexpectedly the sensitivities toward friction behave the other way round. Both compounds meet the requirement in terms of the thermal stability, and the difference between the decomposition points is smaller than observed for the previous compounds **7**–**10**. The oxygen balances of both the carbamate and the nitrocarbamate are in a good range to provide oxygen while combustion, but compound **12** exceeds the requirement by far, such as the orthocarbonate derivative **1**. The calculated detonation parameters reveal a higher performance for the carbamate **11** compared to the nitrocarbamate **12**. One reason for this finding is the higher density of **12** that affects the detonation parameters advantageously.

When considering compounds **11** and **12** as oxidizers in propellant formulations with aluminum and PBAN binder, the original Space Shuttle mixture ratio using 70 % of oxidizer with 16 % aluminum [37] achieves the highest values for I_s. The formulation of the nitrocarbamate **12** almost equals the I_s of the reference formulation with AP, and combining AP with compound **12** does not further increase this value of 261 s. An increase of the I_s is only accomplished by mixing the compound with ADN. Due to the easy and cheap synthesis of the nitrocarbamate **12**, it is a very good candidate for further investigations including long-term thermal analysis, testing of its compatibilities with different binder systems, single crystal growth to obtain defined shapes, and eventual polymer coating of those for the enhancement of its properties and performance.

Table 6 Physical–chemical properties and calculated detonation and propulsion parameters of compounds **11** and **12**

	11	12	Requirement
Formula	$C_3H_4N_4O_8$	$C_3H_3N_5O_{10}$	–
Weight [g·mol^{-1}]	224.09	269.08	–
Sensitivities according to BAM standard methods (1 out of 6)			
IS [J]	>40	10	>4
FS [N]	64	96	>80
ESD [mJ]	0.15	0.10	>0.10
Grain size [μm]	<500	500–1000	–
Thermal analysis according to DSC measurements (T_{onset})			
T_{melt} [°C]	91	109	–
T_{dec} [°C]	169	153	150
Combined nitrogen and oxygen content, oxygen balance, and density at room temperature			
N + O [%]	82.12	85.49	–
Ω_{CO} [%]	21.4	32.7	>25.0
Ω_{CO2} [%]	0.0	14.9	–
ρ_{RT} [g·cm^{-3}]	1.82	1.72	±2.00
Enthalpy and internal energy of formation at the CBS-4M level of theory			AP
ΔH_f^0 [kJ·mol^{-1}]	−459	−366	−296
ΔU_f [kJ·kg^{-1}]	−1960	−1277	−2433
Detonation parameters (EXPLO5, V6.02)			
$-\Delta U_{EX}$ [kJ·kg^{-1}]	5286	4426	1422
T_{EX} [K]	3781	3601	1735
p_{CJ} [kbar]	302	231	158
D_V [m·s^{-1}]	8525	7685	6368
V_0 [L·kg^{-1}]	761	750	885
Isobaric combustion parameters (EXPLO5, V6.02), specific impulse (Oxidizer/Al/PBAN binder) [s], T_C [K] in parenthesis			
I_s (neat)	246 (3114)	232 (3032)	157 (1403)
I_s (70/16/14)	248 (2780)	261 (3420)	262 (3380)
Specific impulse (Oxidizer/AP/Al/PBAN binder) [s], T_C [K] in parenthesis			
I_s (60/10/16/14)	251 (2945)	261 (3410)	–
I_s (35/35/16/14)	257 (3171)	261 (3396)	–
I_s (10/60/16/14)	260 (3327)	261 (3385)	–
Specific impulse (Oxidizer/ADN/Al/PBAN binder) [s], T_C [K] in parenthesis			
I_s (60/10/16/14)	252 (2910)	262 (3404)	–
I_s (35/35/16/14)	261 (3126)	266 (3354)	–
I_s (10/60/16/14)	268 (3244)	269 (3305)	–

5 Summary, Conclusions, and Continuing Investigations

Four rather different molecule classes have been presented as backbones for diverse poly-nitro moieties. The resulting neutral compounds have been discussed in detail concerning their properties as oxygen carriers in solid rocket propellants. They all

show up advantages as well as disadvantages for the suitability in such applications. The fluorine-containing materials have been proven to be inferior compared to their analogue trinitromethyl derivatives in terms of performance (I_s), but they meet the requirements of high thermal stabilities and low sensitivities better than the trinitromethyl compounds. However, the concept that is followed with these neutral CHNO (F) compounds seems to be a promising way to achieve the specific impulse of ammonium perchlorate [17]. Some of the presented derivatives that arise from this strategy even exceed this value, but fail to meet other requirements such as low sensitivities. Preliminary combustion tests of the nitrocarbamates **9** and **12** showed well burning in formulations with micron-sized aluminum. Therefore, this strategy will be pursued in our group, and searching for new backbones connecting poly-nitro groups will be continued for the design of new energetic oxidizers.

The quest for novel oxygen sources for chemical propulsion keeps busy research groups worldwide. Finding green, high-performing replacements for AP is also a national top priority in the USA. In this diversity of outstanding scientists, also other strategies are being followed. For instance, Karl O. Christe from the University of Southern California should be mentioned, who pursues an ionic concept. His technical approach is based on large oxygen-rich anions, such as borates substituted by poly-nitro moieties, in combination with fuel cations [43]. Andrei A. Gakh from the Oak Ridge National Laboratory synthesized the hexani-troisobutene (HNB) dianion in 2000, which represents a higher carbon homologue to the trinitromethanide anion [44]. Also Jean'ne M. Shreeve from the University of Idaho focuses on energetic materials based on poly-nitro compounds [45]. Co-workers now discovered a novel trinitromethyl derivative by nitration of the insensitive explosive FOX-7 (diaminodinitroethylen), namely, tetranitroacetimidic acid (TNAA), [46] which formally is 2,2,2-trinitroethyl nitrocarbamate **12** minus formaldehyde (Fig. 13).

Nevertheless, with regard to the reference compound ammonium perchlorate, which is the ingredient to be substituted, it needs to be distinguished that this compound is an ionic material with perfect appearing properties, except its toxicity. In the many years it has been used in rocketry, the application designs also converged to the properties of AP step by step until dependency. This is why it is difficult to replace such compound, and all other disciplines connected with rocketry such as engineering need to open up for new materials with different
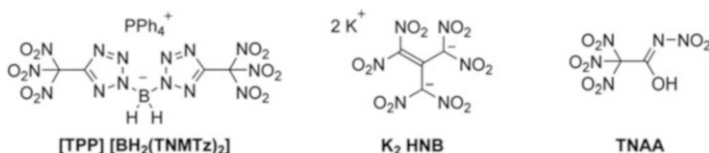

Fig. 13 *Top*: worldwide ongoing investigations on novel oxygen carriers: tetraphenylphosphonium bis-B,B-(5-trinitromethyltetrazolyl)borate [PPh$_4$] [BH$_2$(TNMTz)$_2$] [43], dipotassium hexanitroisobutene (K$_2$ HNB) [44], tetranitroacetimidic acid (TNAA) [46]

properties and behavior and design novel strategies for rocket motors for upcoming new ingredients.

References

1. Sutton GP (2001) Rocket propulsion elements, 7th edn. Wiley, New York
2. Klapötke TM (2012) Chemistry of high-energy materials, 2nd edn. de Gruyter, Berlin
3. Akhavan J (2004) The chemistry of explosives, 2nd edn. The Royal Society of Chemistry, Cambridge
4. NIST Chemistry WebBook (2014) http://webbook.nist.gov/cgi/cbook.cgi?ID=C1344281& Mask=2#Thermo-Condensed. Accessed 26 Nov 2014
5. Kubota N (2002) Propellants and explosives. Wiley-VCH, Weinheim
6. Cooper PW (1996) Explosives engineering, 1st edn. Wiley-VCH, Weinheim
7. (a) Ang HG, Pisharath S (2012) Energetic polymers, 1st edn. Wiley-VCH, Weinheim; (b) Moore TL (1997) Assessment of HTPB and PBAN propellant usage in the US, American Institute of Aeronautics and Astronautics
8. (a) Gu B, Coates JD (2006) Perchlorate: environmental occurrence, interactions and treatment. Springer Verlag, New York; (b) Motzer WE (2001) Perchlorate: problems, detection, and solutions. Environ Forensic 4(2):301–311
9. Rogers WP (1986) Report of the Presidential Commission on the Space Shuttle Challenger Accident, Commission report
10. Routley JG (1988) Fire and explosions at Rocket Fuel Plant in Henderson, Nevada, Report 021 of the Major Fires Investigation Project conducted by TriData Corporation under contract EMW-8-4321 to the United States Fire Administration, Federal Emergency Management Agency
11. CNN interactive (2014) Unmanned rocket explodes after liftoff, Jan. 17th 1997 http://edition. cnn.com/TECH/9701/17/rocket.explosion. Accessed 26 Nov 2014
12. Holleman AF (1995) Lehrbuch der Anorganischen Chemie, 101st edn. de Gruyter, Berlin
13. (a) McLanahan ED et al (2007) Low-dose effects of ammonium perchlorate on the hypothalamic-pituitary – thyroid axis of adult male rats pretreated with PCB126. pp 308–317; (b) Tarone RE, Lipworth L, McLaughlin JK (2010) The epidemiology of environmental perchlorate exposure and thyroid function: a comprehensive Review. pp 653–660; (c) Dumont J (2008) The effects of ammonium perchlorate on reproduction and development of amphibians, SERDP Project ER-1236

14. Makhijani A, Gurney KR (1995) Mending the ozone hole: science, technology, and policy. Institute for Energy and Environmental Research. MIT press, Boston

15. Taylor JWR, Munson K (1981) Jane's all the world's aircraft 1981–82. Jane's Publishing Company Limited, London

16. Eurenco Bofors AB (2008) Karlskoga

17. Göbel M, Klapötke TM (2009) Development and testing of energetic materials: the concept of high densities based on the trinitroethyl functionality. Adv Funct Mater 19:347–365

18. (a) Marans NS, Zelinski RP (1950) 2,2,2-trinitroethanol: preparation and properties. J Am Chem Soc 72(11):5329–5330; (b) Göbel M, Klapötke TM (2007) 2,2,2-trinitroethanol. Acta Crystallogr C C63:562–564

19. Herzog L, Gold MH, Geckler RD (1951) The chemistry of aliphatic dinitro compounds. I. The Michael reaction. J Am Chem Soc 73:749–751

20. (a) Duden P, Ponndorf G (1905) Über aci-Dinitro-Alkohole. Ber Dtsch Chem Ges 38:2031–2036; (b) Klapötke TM, Krumm B, Moll R (2013) Polynitroethyl- and fluorodinitroethyl substituted boron esters. Chem Eur J 19:12113–12123

21. (a) Kettner MA, Klapötke TM (2014) 5,5'-Bis-(trinitromethyl)-3,3'-bi-(1,2,4-oxadiazole): A Stable Ternary CNO-compound with high density. Chem Commun 50(18):2268–2270; (b) Kettner MA, Karaghiosoff K, Klapötke TM, Sućeska M, Wunder S (2014) 3,3'-Bi-(1,2,4-oxadiazoles) featuring the fluorodinitromethyl and trinitromethyl groups. Chem Eur J 20:7622–7631

22. Klapötke TM, Piercey DG, Stierstorfer J (2012) Amination of energetic anions: high-performing energetic materials. Dalton Trans 41:9451–9459

23. (a) Axthammer QJ, Klapötke TM, Krumm B, Moll R, Rest SF (2014) The energetic nitrocarbamate $O_2NN(H)CO[OCH_2C(NO_2)_3]$ derived from phosgene. Z Anorg Allg Chem 640:76–83; (b) Axthammer QJ, Krumm B, Klapötke TM (2015) Synthesis of energetic nitrocarbamates from polynitro alcohols and their potential as high energetic oxidizers. J Org Chem 80(12):6329–6335

24. Klapoetke TM, Krumm B, Moll R, Penger A, Sproll SM, Berger RJF, Hayes SA, Mitzel NW (2013) Structures of energetic acetylene derivatives $HC{\equiv}CCH_2ONO_2$, $(NO_2)_3CCH_2C{\equiv}CCH_2C(NO_2)_3$ and trinitroethane, $(NO_2)_3CCH_3$. Z Naturforsch B 68:719–731

25. Klapötke TM, Krumm B, Moll R, Rest SF (2011) CHNO based molecules containing 2,2,2-trinitroethoxy moieties as possible high energy dense oxidizers. Z Anorg Allg Chem 637:2103–2110

26. Klapötke TM, Krumm B, Rest SF, Sućeska M (2014) Polynitro containing energetic materials based on carbonyldiisocyanate and 2, 2-dinitropropane-1, 3-diol. Z Anorg Allg Chem 640:84–92

27. Baumann A, Erbacher A, Evangelisti C, Klapötke TM, Krumm B, Rest SF, Reynders M, Sproll V (2013) Multiply nitrated high-energy dense oxidizers derived from the simple amino acid glycine. Chem Eur J 19(46):15627–15638

28. Aas B, Kettner MA, Klapötke TM, Suceska M, Zoller C (2013) Asymmetric carbamate derivatives containing secondary nitramine, 2,2,2-Trinitroethyl, and 2-Fluoro-2,2-dinitroethyl moieties. Eur J Inorg Chem 35:6028–6036

29. (a) Feierfeil J, Kettner MA, Klapötke TM, Sućeska M, Wunder S (2014) Proceeding of the 17th seminar on new trends in research of energetic materials (NTREM), Pardubice, 9–11 Apr 2014; (b) Kettner MA, Klapötke TM (2015) New energetic polynitrotetrazoles. Chem Eur J 21(9):3755–3765

30. Chavez D, Klapötke TM, Parrish D, Piercey DG, Stierstorfer J (2014) The synthesis and energetic properties of 3,4-Bis(2,2,2-trinitroethylamino)furazan (BTNEDAF). Propellants Explos Pyrotech 39:641–648

31. Klapötke TM, Krumm B, Rest SF, Reynders M, Scharf R (2013) (2-Fluoro-2,2-dinitroethyl)-2,2,2-trinitroethylnitramine: a possible high-energy dense oxidizer. (2013) Eur J Inorg Chem 34:5871–5878

32. Klapötke TM, Krumm B, Moll R, Rest SF, Schnick W, Seibald M (2013) Asymmetric fluorodinitromethyl derivatives of 2,2,2-trinitroethyl N-(2,2,2-trinitroethyl)carbamate. J Fluor Chem 156:253–261

33. Klapötke TM, Krumm B, Scherr M, Spieß G, Steemann FX (2008) Facile synthesis and crystal structure of 1,1,1,3-tetranitro-3-azabutane. Z Anorg Allg Chem 634:1244–1246

34. (a) Bundesanstalt für Materialforschung (BAM) (2008) http://www.bam.de; laying down the test methods pursuant to Regulation (EC) No. 1907/2006 of the European Parliament and of the Council on the Evaluation, Authorization and Restriction of Chemicals (REACH), ABl. L 142; (b) NATO standardization agreement (STANAG) on explosives, impact tests, no. 4489, 1st edn, 17 Sept 1999; (c) NATO Standardization Agreement (STANAG) on explosives, friction tests, no. 4487, 1st edn, 22 Aug 2002; (d) Klapötke TM, Krumm B, Mayr N, Steemann FX, Steinhauser G (2010) Hands on explosives: safety testing of protective measures. Saf Sci 48:28–34

35. (a) Montgomery JJA, Frisch MJ, Ochterski JW, Petersson GA (2000) A complete basis set model chemistry. VII. Use of the minimum population localization method. J Chem Phys 112:6532–6542; (b) Ochterski JW, Petersson GA, Montgomery JJA (1996) A complete basis set model chemistry. V. Extensions to six or more heavy atoms. J Chem Phys 104:2598–2619

36. (a) Sućeska M (2014) EXPLO5, Version 6.02, Zagreb; (b) Sućeska M (1991) Calculation of the detonation properties of C-H-N-O explosives. Propellants Explos Pyrotech 16:197–202; (c) Sućeska M (1999) Evaluation of detonation energy from EXPLO5 computer code results. Propellants Explos Pyrotech 24:280–285; (d) Suceska M, Ang HG, Chan HY (2011) Modification of BKW EOS introducing density-dependent molecular covolumes concept. Mater Sci Forum 673:47–52

37. NASA, Space shuttle news reference, 2-20–22-21, http://de.scribd.com/doc/17005716/NASA-Space-Shuttle-News-Reference-1981; (b) NASA, press release: STS-122 The Voyage of Columbus, 2008, pp 82–84, http://www.nasa.gov/pdf/203212main.sts122 presskit2.pdf

38. Klapötke TM, Krumm B, Moll R, Rest SF, Sućeska M (2014) Fluorodinitroethyl ortho-carbonate and -formate as potential high energy dense oxidizers. Z Naturforsch B 69:8–16

39. (a) Kamlet MJ, Shipp KG, Hill ME (1968) US Patent 3388147; (b) Sheremetev AB, Yudin IL (2005) Synthesis of 2-R-2,2-dinitroethanol orthoesters in ionic liquids. Mendeleev Commun 15:204–205; (c) Mueller KF, Renner RH, Gilligan WH, Adolph HG, Kamlet MJ (1983) Thermal stability/structure relations of some polynitroaliphatic explosives. Combust Flame 50:341–349; (d) Hill ME (1967) US Patent 3306939; (e) Hill ME, Shipp KG (1970) US Patent 3526667

40. (a) Grakauskas V, Albert AH (1981) Polynitroalkyltetrazoles. J Heterocycl Chem 18:1477–1479; (b) Fokin AV, Studnev YN, Rapkin AI, Komarov VA, Verenikin OV, Potarina TM (1981) Synthesis and some properties of 5-fluorodinitromethyl- and 5-difluoronitromethyltetrazoles. Izv Akad Nauk SSSR Ser Khim 7:1592–1595; (c) Christe KO, Haiges R (2013) Energetic high-nitrogen compounds: 5-(Trinitromethyl)-2H-tetrazole and -tetrazolates, preparation, characterization, and conversion into 5-(dinitromethyl) tetrazoles. Inorg Chem 52:7249–7260

41. (a) Kamlet MJ (1959) NAVORD Rep. 6206, US Naval Ordnance Lab, Whiteoak; (b) Agrawal JP, Hodgson RD (2006) Organic chemistry of explosives, 1st edn. Wiley, Chichester, p 33

42. Luk'yanov OA, Pokhvisnena GV (1991) (2,2,2-Trinitroethoxy)acetic acid and its derivatives. Izv Akad Nauk SSSR Ser Khim 11:2545–2548

43. (a) Haiges R, Jones CB, Christe KO (2013) Energetic Bis(3,5-dinitro-1H-1,2,4-triazolyl)dihydro- and dichloroborates and Bis(5-nitro-2H-tetrazolyl)-, Bis(5-(trinitromethyl)-2H-tetrazolyl)-, and Bis(5-(fluorodinitromethyl)-2H-tetrazolyl)dihydroborate. Inorg Chem 52:5551–5558; (b) Belanger-Chabot G, Rahm M, Haiges R, Christe KO (2013) [BH$_3$C(NO$_2$)$_3$]−: the first room-temperature stable (trinitromethyl)borate. Angew Chem Int Ed, 52:11002–11006; (c) Haiges R, Christe KO (2013) Energetic High-nitrogen compounds: 5-(trinitromethyl)-2h-tetrazole and - tetrazolates, preparation, characterization, and conversion into 5-(dinitromethyl) tetrazoles. Inorg Chem 52:7249–7260

44. Khutoretsky VM, Matveeva NB, Gakh AA (2000) Hexanitroisobutene dianion salts. Angew Chem Int Ed 39(14):2545–2547

45. (a) Yin P, Parrish DA, Shreeve JM (2014) Bis(nitroamino-1,2,4-triazolates): N-bridging strategy toward insensitive energetic materials. Angew Chem Int Ed 53:12889–12892; (b) Thottempudi V, Zhang J, He C, Shreeve JM (2014) Azo-substituted 1,2,4-oxadiazoles as insensitive energetic materials. RSC Adv 4:50361–50364
46. Vo TT, Parrish DA, Shreeve JM (2014) Tetranitroacetimidic acid: a high oxygen oxidizer and potential replacement for ammonium perchlorate. J Am Chem Soc 136(34):11934–11937

High-Nitrogen Energetic Materials of 1,2,4,5-Tetrazine Family: Thermal and Combustion Behaviors

Valery P. Sinditskii, Viacheslav Yu. Egorshev, Gennady F. Rudakov, Sergey A. Filatov, and Anna V. Burzhava

Abstract Considerable recent attention has been focused on research and development of high-nitrogen energetic materials. Among polynitrogen energetic materials, 1,2,4,5-tetrazine derivatives are of particular interest owing to their high density, thermostability, and remarkable insensitivity to electrostatic discharge, friction, and impact. The purpose of the present work is to analyze possible application areas of different types of tetrazine-based energetic materials reasoning from their peculiar combustion properties. Study of thermal stability of tetrazine derivatives has shown that, in most cases, the stability of the substance is determined by decomposition of the less stable substitute rather than the tetrazine cycle itself. Combustion and thermocouple-aided studies have revealed that tetrazines are mostly low-volatile substances with high burning surface temperatures that, in turn, predetermine the condensed-phase combustion mechanism. The lack or low content of oxygen in tetrazine-based energetic materials results in formation of high-enthalpy species among combustion products, thus preventing from full release of energy stored in the material.

1 Introduction

Energetic materials that burn at the expense of energy derived from positive heat of formation rather than oxidation of the carbon backbone have recently attracted attention not only as explosives but also as components of gas-generating and propellant compositions because they are capable of producing relatively high specific impulse despite low combustion temperature [1]. 1,2,4,5-Tetrazine (also known as s-tetrazine) derivatives are among these compounds. 1,2,4,5-Tetrazines are unique heterocyclic compounds containing the maximum number of nitrogen atoms in the cycle among the stable azines. Introduction of nitrogen atoms in the

V.P. Sinditskii (✉) • V.Yu. Egorshev • G.F. Rudakov • S.A. Filatov • A.V. Burzhava
Department of Chemical Engineering, Mendeleev University of Chemical Technology, Moscow 125047, Russia
e-mail: vps@rctu.ru

$$H_2N-\underset{}{\text{(benzene ring)}}-NH_2$$

$$\Delta H_f^0 = 1.5 \text{ kcal/mole (14 kcal/kg)} \quad \Delta H_f^0 = 71.2 \text{ kcal/mole (635 kcal/kg)}$$

Scheme 1

$$R-\underset{N-N}{\overset{N=N}{\text{(tetrazine ring)}}}-R \longrightarrow N_2 + 2\,RCN$$
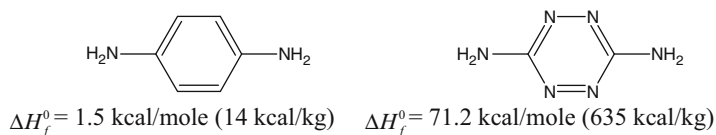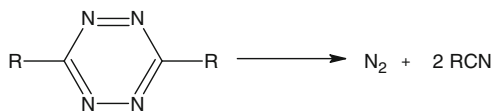
Scheme 2

molecule leads to an increase in the enthalpy of formation. As it can be seen from Scheme 1, the tetrazine ring even without explosophoric groups has a high enough enthalpy of formation, providing TNT coefficient as large as 0.6.

Decomposition mechanism of photochemically excited 1,2,4,5-tetrazines, proposed by Hochstrasser in 1975, consists of the triple concerted dissociation [2] (Scheme 2).

It was theoretically proved by Schaefer in 1986 [3]. In 2000, J. Oxley et al. [4] investigated the thermal decomposition of a large number of tetrazine derivatives and found out that thermal decomposition might follow this pathway, but it was not concerted and not the only pathway. It was shown that the tetrazines exhibit two principal modes of decomposition: elimination of N_2 from the tetrazine ring followed by cleavage of the remaining N-N bond and loss of the substituent group, in some cases assisted by proton transfer. Tetrazine ring possesses high thermal stability; elementary representatives, for example, diaminotetrazine, decompose at temperatures over 300 °C.

It was discovered that some of tetrazine derivatives can be surprisingly insensitive toward destructive stimuli such as impact, friction, and electrostatic discharge. Furthermore, some of these compounds display interesting explosive performance and extraordinary combustion properties: high burning rates and a weak dependence of the burning rate on the pressure. The latter was attributed to the occurrence of the leading combustion reaction in the condensed phase [5] that is not quite correct. The low dependence of the burning rate on the pressure is typical of the systems with the invariable surface temperature, for example, of some thermites. If the temperature of the burning surface (the place of the leading combustion reaction) is defined by boiling, it grows with pressure, and, correspondingly, the exponent in the combustion law can change in a wide interval and even exceed unity.

Due to their remarkable properties, tetrazine-based energetic materials have been proposed for using in various fields: insensitive "green" explosives, components of powders and solid rocket propellants, gas-generating and fire-fighting compositions, monopropellants, and fuel components for microengines.

In recent years, there have been a number of reviews, dedicated to s-tetrazines as building blocks for new functional molecules, including energetic materials [1, 6]. However, an analysis of the combustion behaviors of tetrazines, their place among other energetic materials, has not been carried out yet. The purpose of the present work was to analyze burning behavior of these compounds, try to establish a connection between their physicochemical properties and combustion mechanism, and propose possible application areas of different types of tetrazine-based energetic materials reasoning from their peculiar combustion properties.

A wide range of derivatives of 1,2,4,5-tetrazine have been synthesized to date. They can be conventionally divided into four groups: (1) compounds that contain no oxidizing elements in the molecule (CHN-tetrazines), (2) compounds that contain active oxygen in the molecule (CHNO-tetrazines), (3) salts of tetrazine derivatives with oxidizing acids, and (4) salts of tetrazine derivatives with metals and coordination compounds with metal nitrates and perchlorates.

2 General Schemes of Synthesis of Substituted s-Tetrazines

s-Tetrazines have long been discovered; the first report dates back to the end of the nineteenth century. A convenient method for the synthesis of symmetrically disubstituted tetrazine, containing alkyl, aryl, or hetaryl moieties, is the Pinner method, which comprises cycling the corresponding nitriles under the action of hydrazine followed by oxidation of the intermediate dihydrotetrazine [7] (Scheme 3).

The tetrazine chemistry reached its peak after the 1990s, when American researchers from Livermore Laboratory have proposed a method of synthesis of 3,6-bis(dimethylpyrazolyl)tetrazine from available and cheap starting materials – triaminoguanidine and acetylacetone [1, 8]. Dipyrazolyltetrazines are remarkably versatile starting synthons for preparation of a huge number of tetrazines by simply using nucleophilic displacement of the pyrazolyl groups by various nucleophiles (Scheme 4).

Dimethylpyrazolyltetrazine reacts with weakly based hetarylamines such as aminofurazans, aminoimidazoles, aminotriazoles, aminotetrazoles, or aminotetrazines to afford 3-hetaryl-amino-s-tetrazines [9]. Dipyrazolyltetrazine can react to form monosubstituted products, which, in turn, can be transformed to derivatives of annulated azolotetrazines: triazolotetrazines and tetrazolotetrazines (Scheme 5).

Scheme 3

Scheme 4

R_1=H, R_2=H, NHCONH$_2$, triazol-3-yl, tetrazol-5-yl
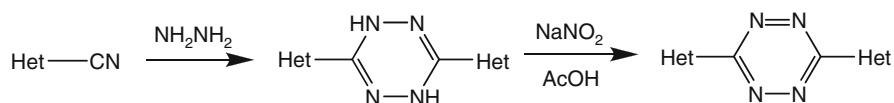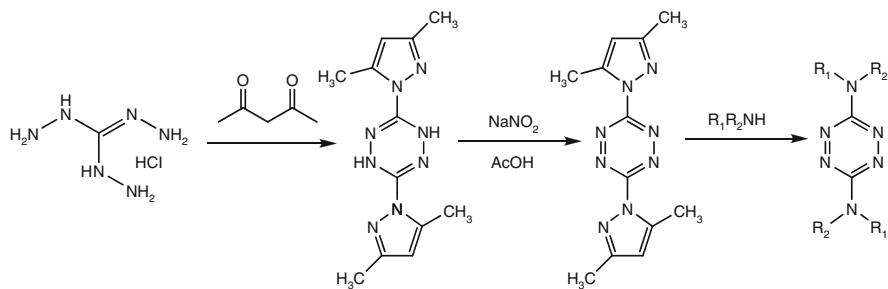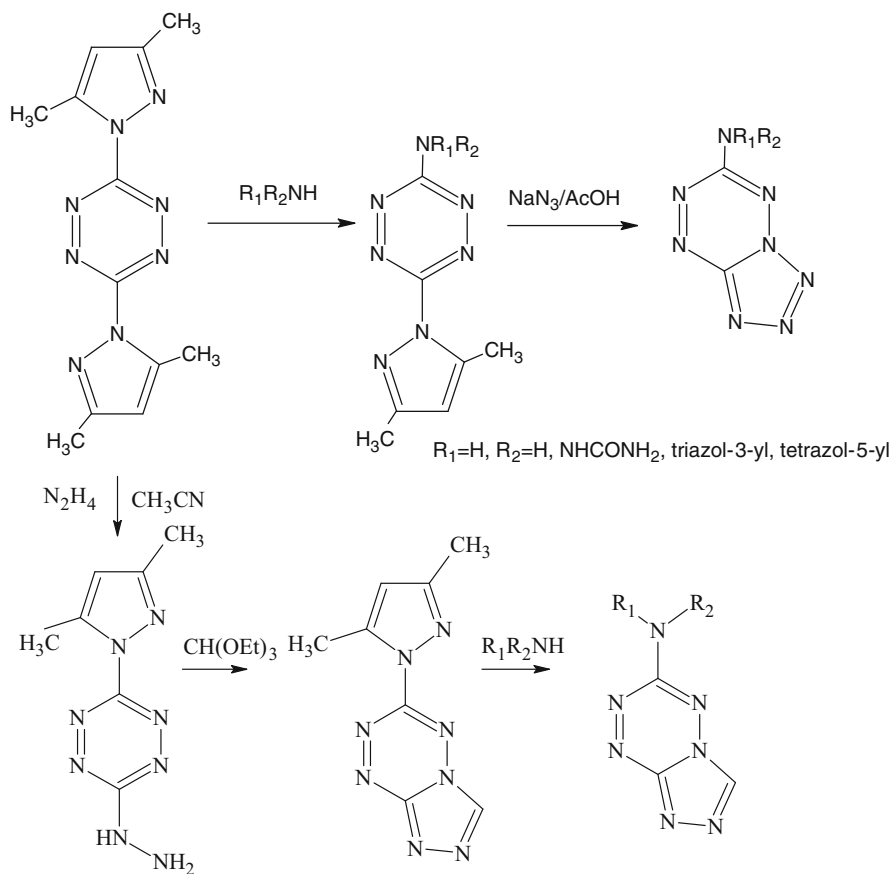
Scheme 5

3　Energetic Materials Based on CHN-Tetrazines

The main representatives of tetrazine-based energetic materials without active oxygen are shown in Scheme 6. As it can be seen from the Scheme and Table 1, the introduction of endothermic substituents, such as hydrazine, tetrazole, or diazo group in the tetrazine cycle leads to energetic materials with the enthalpy of formation up to 900–1000 kcal/kg. Such high-energy content makes these materials explosive with detonation velocity of about 7500 m/s and more.

Dihydrazino-tetrazine (DHT) was previously calculated to perform well in both rocket and gun propellant applications [12]. DHT is described as a highly energetic fuel having a heat of formation measured as 128 kcal/mol or 900 kcal/kg [9]. The hot flame and carbon-free combustion of DHT have made it ideal for a new generation of reduced-toxicity fireworks [10].

3,6-Dihydrazino-1,2,4,5-tetrazine (DHT)

3,3'-Azobis(6-amino-1,2,4,5-tetrazine) (DAAT)

3,6-Bis(tetrazol-5-amino)-1,2,4,5-tetrazine (BTATz)

3,6-Bis(tetrazol-5-yl)-1,2,4,5-tetrazine (BTT)
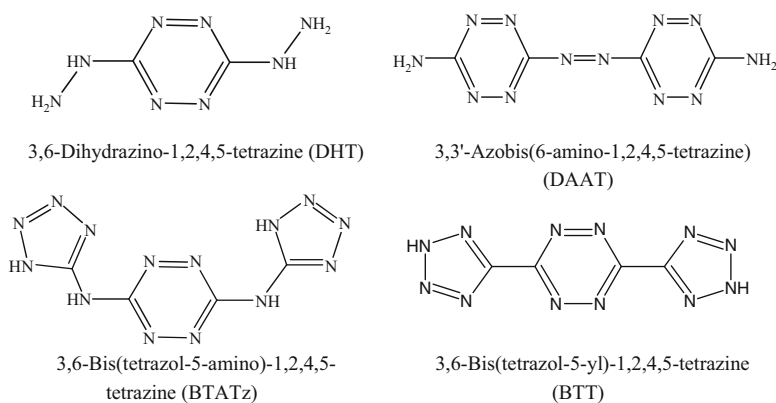
Scheme 6

Table 1　Some physicochemical properties of main CHN-tetrazines

Compound	Density (density of pressed sample), g/cm³	ΔH_f^0, kcal/mol (kcal/kg)	DSC exotherm, °C (heat effect, kcal/kg)	Detonation velocity, m/s (density, g/cm³)
DHT	1.69 [17] (1.59)	128 (900) [11]	164 (307) and 307 (196) [4][b]	7540 (1.56) [18]
DAAT	1.78 [19]	206 (936) [13, 21]	>252 [15]	7400 (1.65) [14]
	1.76 (1.65) [20]	247 (1123) [14]	320 (714) [14]	7900 (1.78) [22]
BTATz	1.76 [23]; 1.742 [24] (1.71)	211 (850) [25]; 170 (685)[a] [26]	264[c] [12]; 320 (374) [27]	7520[a] (1.76) [12]
BTT	1.68 [28]	224 (1026) [22]	235 (633) [22]	7950[a] (1.68)

[a]Estimation
[b]Two-stage decomposition
[c]DSC onset

Experimental test of 3,3′-azobis(6-amino-1,2,4,5-tetrazine) (DAAT) with 5 mass % Kel-F 800 binder yielded a detonation velocity of 7400 m/s at a pellet density of 1.65 g/cm^3, the detonation velocity at TMD (1.78 g/cm^3) was extrapolated to reach 7900 m/s. A density of 1.76–1.78 g/cm^3 was measured by gas pycnometry [13, 14] which is somewhat lower than the value reported by Hiskey et al. (1.84 g/cm^3, Ref. [13]). Sensitivity properties of DAAT demonstrate that the material is relatively insensitive to impact and resistant to initiation by electrical discharge and friction.

Bis(tetrazolylamino)tetrazine (BTATz) was treated as the key component for new generation propellants [12, 17], fire suppressing gas generators [11, 12], and automobile airbags [13]. BTATz can sustain burning when packed in glass tubes as small as 250 μm in diameter [12], which may well find an application as monopropellant for microthrusters [14, 15]. In addition, BTATz is ballistic modifier for propellants: adding 22 % BTATz to ammonium dinitramide (ADN) leads to 1.5 times increase in the burning rate and reduces the pressure exponent [18]. As a substitute of hexogen (RDX) in the composite modified double-base (CMDB) propellant, BTATz can improve the burning rate and reduce the pressure exponent [16].

As with DAAT, 3,6-bis(tetrazol-5-yl)-1,2,4,5-tetrazine (BTT) also can be described as low-sensitive energetic material. The high-nitrogen content of this energetic material makes it highly attractive as a component for energetic applications like gas-generating airbag formulations.

As it was noted above, the thermal stability of the tetrazine ring is quite good. The pure DAAT was found to be thermally stable up to melting point 252 °C [13, 15]. BTATz is also thermally stable substance, demonstrating DSC exotherm maximum at 320 °C [21]. It is interesting to note that BTT which is similar to BTATz, but free of NH-bridges between heterocycles, shows much less temperature of DSC exotherm [22]. DHT decomposes in two steps, demonstrating exotherms at 164 and 307 °C [4]. The low thermal stability of DHT has been explained by primary decomposition of the exocyclic substituent or by its loss [4]. This explanation is not quite obvious, since the hydrazine moiety is stable enough.

In our lab, we studied two compounds from this class, DHT and BTATz [20]. The experiments on thermal decomposition of DHT under isothermal conditions were carried out in thin-walled glass manometers of the compensation type (the glass Bourdon gauge) in the temperature interval of 110–130 °C. There is a sharp rise of the gas release curves preceded by a section with small decomposition rate, which is typical for decomposition with self-acceleration. The reason for such a behavior is topochemistry. Most likely, the section of fast gas release is associated with the DHT decomposition on the crystal defects. The rate constants were evaluated from experimental data using a model of first-order reaction with self-acceleration. The difference in rate constants between first-order reaction and self-acceleration is two orders of magnitude. Taking into account complex behavior of DHT decomposition, the rate constants obtained under DSC nonisothermal conditions should be considered as formal.

Scheme 7
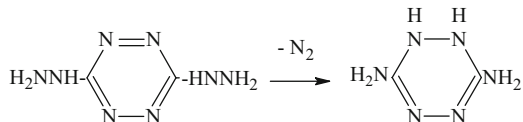
Maximum gas release at DHT decomposition at 110–130 °C is not big (208 cm^3/g or 1.32 mol of gas per one mole of DHT), which is close to data of work [29] (0.79–0.83 mol/mol). It has been determined that the first stage of DHT decomposition is not the loss of the exocyclic hydrazine moiety but the redox process, in which the tetrazine ring is reduced by the hydrazine groups to form diaminodihydrotetrazine and molecular nitrogen [20] (Scheme 7).

This is because the tetrazine is the electron-poorest aromatic system that makes the tetrazine ring a strong electron attractor. The easy reduction of tetrazines was reported by Stone et al. as soon as 1963 [30]. Decomposition of the formed diaminodihydrotetrazine occurs at higher temperatures during the second stage.

BTATz is a much more thermally stable substance. Its decomposition under isothermal conditions in the temperature interval of 250–285 °C follows a first-order reaction to high extent of decomposition, and no self-accelerations is observed. Maximum gas release at BTATz decomposition is 280 cm^3/g or 3 mol of gaseous products per one mole of BTATz. The study of BTATz decomposition allows assumption that the decomposition involves all three heterocyclic rings. The rate constants obtained in different works [21, 31] in isothermal and nonisothermal conditions are in a good agreement with each other. All rate constants obtained in the our work [20] in the interval of 250–334 °C are well described by the Arrhenius equation with activation energy of 57.5 kcal/mol: $k = 2.0 \cdot 10^{19} \exp(-28900/T)$, s^{-1}.

The kinetic parameters of BTATz decomposition proved to be rather high for typical first-order reaction. Decomposition reactions of the tetrazole ring include preliminary isomerization of 1H-tautomer in 2H-tautomer with subsequent elimination of a molecule of nitrogen by means of the concert mechanism [32, 33] or isomerization of 1H-tautomer of tetrazole in azidoimine with subsequent elimination of molecular nitrogen from the azido group [34-36]. Because of preliminary isomerization, the observable activation energy is higher than the activation energy of nitrogen elimination reaction itself.

According to Son et al. [37], DHT has a high burning rate, slightly <50 mm/s at 10 MPa. In our experiments [20], DHT in the form of samples, pressed into 4-mm acrylic tubes, is capable of stable burning starting from a pressure of 0.2 atm (Fig. 1). Pressure dependence of the burning rate is described by two laws ($r_b = 3.63p^{0.69}$; $r_b = 2.04p^{0.67}$) for different pressure intervals (0.02–2 MPa and 4–10 MPa, respectively), which are divided by the combustion instability region. Literature data agree with ours at high pressures only. The difference at low pressures is likely to be connected with some admixtures to the samples, for example, trace amounts of a volatile solvent, acting as the coolant.

BTATz also demonstrates high burning rates. Available data on burning rates of BTATz vary over a wide range. Addition of binder and mode of purification

Fig. 1 Comparison of DHT burning rates measured in [20] (*1*, *points*) and [37]: DHT + 3 % estane (*2*), pure DHT (*3*)
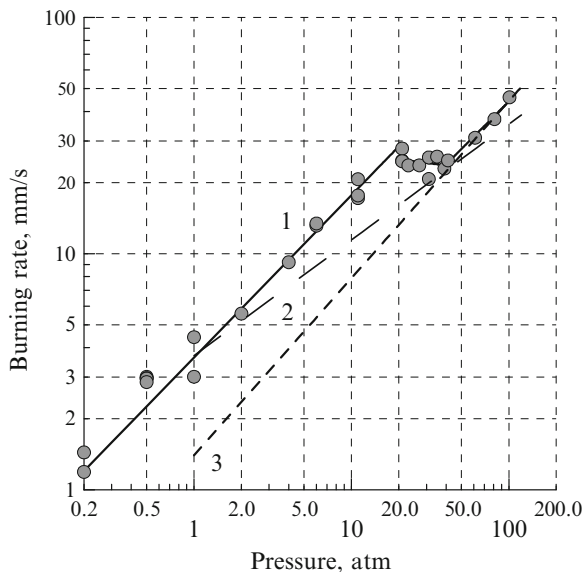
Fig. 2 Comparison of burning rates of BTATz samples obtained in different labs: data of [20] (*1*, *solid line* and *points*), data of [18] (*2*, *3*, *4*, *points* and *dashed lines*), data of [37] (*5*, *dashed line*)
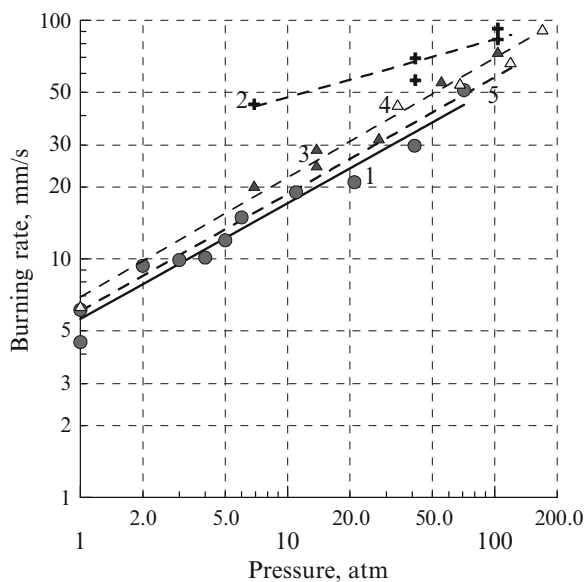
both exert effect on the burning rate [18, 37]. A comparison of results obtained in the present work ($r_b = 5.6p^{0.49}$) with available data on burning rates of BTATz is presented in Fig. 2. Our burning rates are practically coincident with those for BTATz with 3 % of binder Kel-F [37] and slightly lower than data for samples of BTATz thoroughly washed by alcohol (points 3 and 4 in Fig. 2) [18]. Surprisingly, the maximum burning rates were observed in combustion of BTATZ samples treated with dimethylformamide (points 2 in Fig. 2).

Fig. 3 Temperature distribution in the combustion wave of BTATz at pressures 0.2 atm (*1*) and 4 atm (*2*)
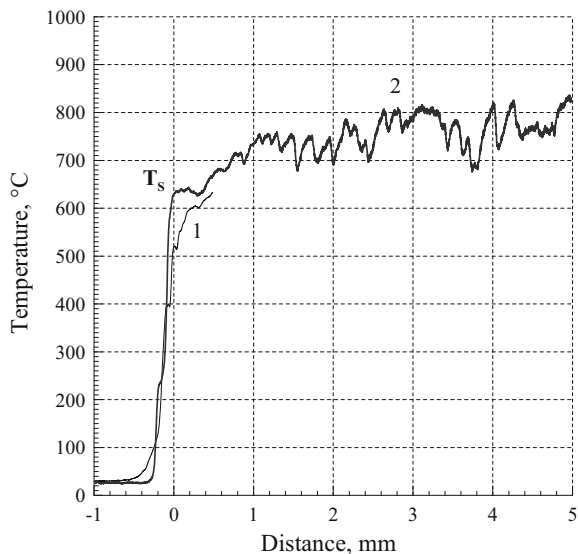
Fig. 4 Temperature distribution in the combustion wave of DHT at pressures 0.2 atm (*1*) and 0.5 atm (*2*)
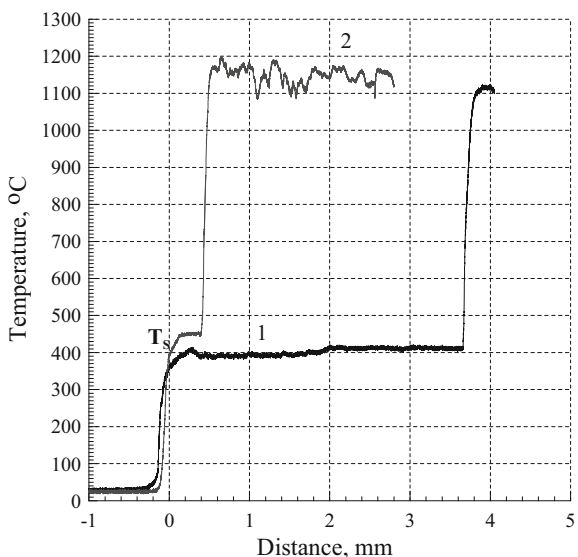
Temperature profiles in the BTATz and DHT combustion wave were obtained with the help of thin tungsten-rhenium thermocouples at low pressures [20]. Both compounds burn with little or no luminous flame, indicating low flame temperatures. Indeed, the maximum measured flame temperature of BTATz does not exceed 800 °C (Fig. 3), which is 1060 °C less than the adiabatic temperature. Combustion of DHT proceeds in two-stage regime: there is a region between the surface and flame with a weak growth of temperature (Fig. 4).

Fig. 5 Surface temperature against pressure for BTATz, DHT, and HMX
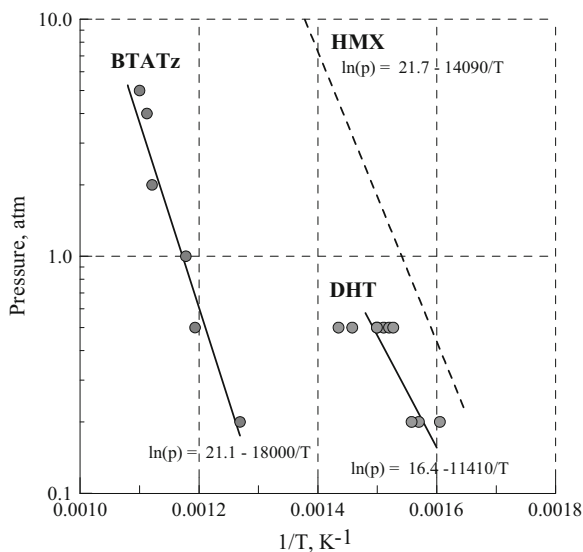
The maximum measured flame temperature is also less than the adiabatic temperature, which is caused by formation of high-energy products in the flame, such as endothermic nitrile derivatives. The thermocouple measurements show that condensed-phase reactions play a dominant role in combustion of DHT and BTATz.

The effect of pressure on the measured surface temperatures of DHT and BTATz is shown in Fig. 5 in comparison with HMX [38]. Both tetrazines have surface temperatures significantly higher than those for such low-volatile substance as HMX. DHT is a low-volatile substance with boiling temperature of about 425 °C and heat of vaporization of 22.7 kcal/mol. BTATz is a nonvolatile substance with boiling temperature of about 580 °C and heat of vaporization of 35.8 kcal/mol.

Comparison of surface temperatures of various explosives at atmospheric pressure shows that temperatures of DHT and BTATz are, respectively, 50 and 200° higher than the surface temperature of HMX (Fig. 6). It is believed that so high temperatures of the rate-limiting combustion zone are responsible for the observed high burning rates of the tetrazines.

The DHT decomposition mechanism allows explanation of its combustion behavior. Since DHT combustion is controlled by a reaction in the condensed phase, one can derive kinetic parameters of this reaction if the residence time of the substance at the burning surface is known [39, 40]. Kinetics of the leading reaction of DHT combustion at low pressures $\left(k = 10^{12.26} \exp\left(-15850/T\right), \text{ s}^{-1}\right)$ coincide with kinetics of initial reaction of the first decomposition stage (Fig. 7).

The heat effect of this reaction averages about 280 cal/g. Since the surface temperature grows with pressure, at pressures above 2 MPa, the reaction heat effect becomes comparable with the heat required for warming up the condensed phase to the surface temperature and melting. The further increase of pressure results in occurrence of heat instability. At pressures higher than 4 MPa, the

Fig. 6 Comparison of burning surface temperatures (in °C) of various explosives at atmospheric pressure
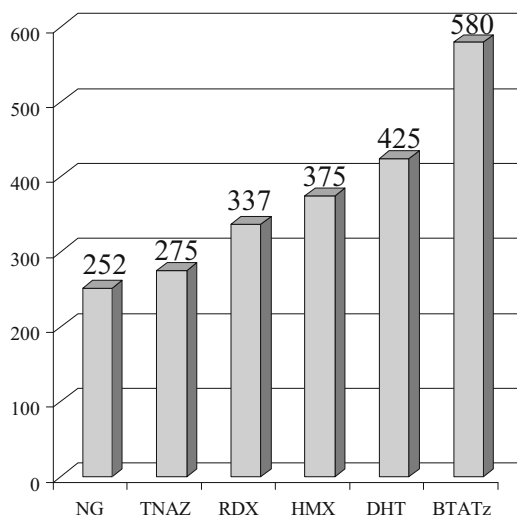
Fig. 7 Comparison of rate constants of initial reaction of the first (*1*) and second (*2*) decomposition stages and kinetics of the leading reaction of DHT combustion at low (*3*) and high (*4*) pressures
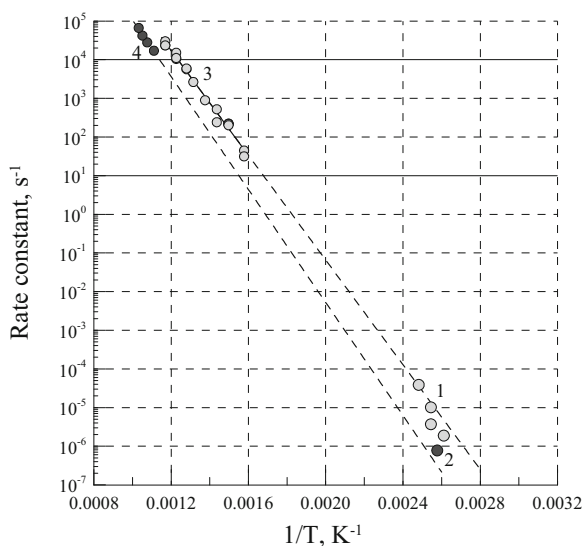
instability disappears. The burning rate at high pressures is obviously controlled by decomposition kinetics $\left(k = 10^{12.33} \exp\left(-16830/T\right),\ \mathrm{s}^{-1}\right)$ of the second stage with total heat effect of approximately 575 cal/g.

The comparison of the obtained rate constants of the leading reaction of combustion with rate constants of BTATz decomposition is shown in Fig. 8. As can be seen in the Figure, the kinetic parameters derived from the combustion model, $k\left(s^{-1}\right) = 10^{10.44} \exp\left(-16150/T\right)$, considerably differ from kinetics of decomposition BTATz in the condensed phase. The slope of dependence *lnk* vs. *1/T* for the leading reaction of combustion strongly differs from the slope of a

Fig. 8 Comparison of
decomposition kinetics of
BTATz (*1–4*), aminotetrazole
(*5*) [41], and kinetics of
leading reaction of BTATz
combustion (*6*) [20]: *1* and *2*
[20], *3* [21], *4* [31]
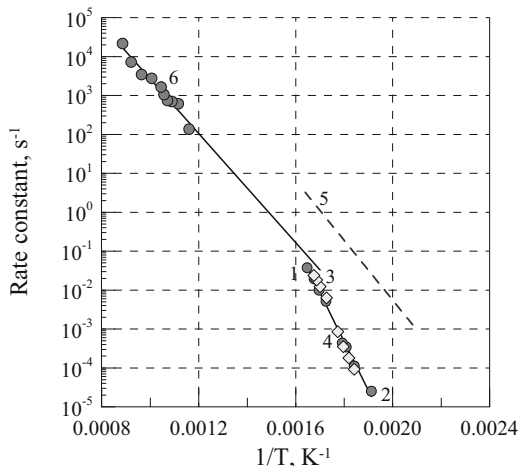
straight line *lnk* (*1/T*) for reaction of BTATz in the condensed phase and is close to the slope of *lnk* (*1/T*) dependence for the decomposition reaction of 5-AT [41]. As mentioned above, the decomposition of tetrazole ring includes preliminary reactions of isomerization. At high temperatures, which are realized at the burning surface of BTATz, all these preliminary reactions have been already finished, and there is only decomposition of the last product of isomerization reaction. The similar situation was observed at study of decomposition kinetics of 5-nitro-1,2,4-triazol-3-one (NTO) in a wide interval of temperatures [42]. The activation energy of the leading combustion reaction of BTATz (32.1 kcal/mol) is in a good agreement with calculated activation energy of azidoimine decomposition (∼28 kcal/mol) [33, 34].

A comparison of the rate constants of the leading reaction of BTATz combustion $\left(k = 2.8 \cdot 10^{10} \cdot \exp\left(-16150/T\right), \text{ s}^{-1}\right)$ with rate constants of 5-aminotetrazole decomposition ($k = 1.3 \cdot 10^{13} \cdot \exp\left(-17680/T\right), \text{ s}^{-1}$ [41]) shows (Fig. 8) that combination of two heterocyclic systems has resulted in increasing stability of aminotetrazole moiety.

The data obtained make it possible to explain low pressure index for combustion of DHT and BTATz. If the rate-limiting reaction occurs in the condensed phase, the pressure index will be dependent on the ratio of activation energy of the reaction to heat of evaporation [40]. This ratio for DHT and BTATz is correspondingly equal to 0.69 and 0.45 that is in a good agreement with experimental pressure index (0.69 and 0.49, respectively).

In combustion of CHN-tetrazines, the formation of high-energy products in the flame, such as endothermic nitrile derivatives, occurs that results in lowering of measured flame temperatures as compared with adiabatic values. Most likely it was the main reason for the measured specific impulses being of approximately 14 % of the theoretical one in a study on possible application of BTATz in micropropulsion systems [14].

4 Energetic Materials Based on CHN-Tetrazines Annulated with Azoles

Azoloannulated tetrazines are of current interest as energetic materials. Of all the possible azolo[1,2,4,5]tetrazines, derivatives of [1,2,4]triazolo[4,3-b]-s-tetrazine and tetrazolo[1,5-b]-s-tetrazine are of particular interest. The main method of synthesis of [1,2,4]triazolo[4,3-b]-s-tetrazines is condensation of hydrazine derivatives of tetrazine with orthoesters of carboxylic acids [43, 44].

The derivatives of tetrazolo[1,5-b][1,2,4,5]tetrazine can be synthesized by treatment of 3-hydrazine-[1,2,4,5]tetrazines by nitrous acid [1] or by substitution of leaving groups in the tetrazine cycle with sodium azide [1, 45]. All the tetrazolo[1,5-b][1,2,4,5]tetrazines demonstrate the azido-tetrazole tautomerism, with the azido form being predominant [45-47]. However, substituted 6-amino-tetrazolo[1,5-b]-1,2,4,5-tetrazines and their salts in the solid states were shown to exist in the tetrazole form at ambient and elevated temperatures [48, 49]. A reason for such a behavior is, apparently, the donor properties of substituted 6-amino group, since it is known that the open-ring azidoimine form is favored by electron-withdrawing groups and the tetrazole form is favored in the presence of electron-donating groups [50].

Some representatives of azolotetrazine-based energetic materials are shown in Scheme 8. As shown from Table 2, all of them possess high positive enthalpy of formation, for some of them it is higher than 1000 kcal/kg.

Licht and Ritter [51] synthesized 6-amino-tetrazolo[1,5-b]-1,2,4,5-tetrazine (ATTz) (deflagration point ~200 °C), by the diazotization of 3,6-diamino-1,2,4,5-tetrazine with NaNO$_2$, followed by reacting the non-isolated diazonium salt compound with NaN$_3$. They found that the tetrazolotetrazine ATTz should be

6-Aminotrizolo[1,5-b]-1,2,4,5-tetrazine (ATrTz)

6-Aminotetrazolo[1,5-b]-1,2,4,5-tetrazine (ATTz)

2-Tetrazolo[1.5-b]-1,2,4,5-tetrazine-6-hydrazine carboxamide (STTz)

6-(Tetrazolyl-5-amino)tetrazolo[1,5-b]-1,2,4,5-tetrazine(TzATTz)
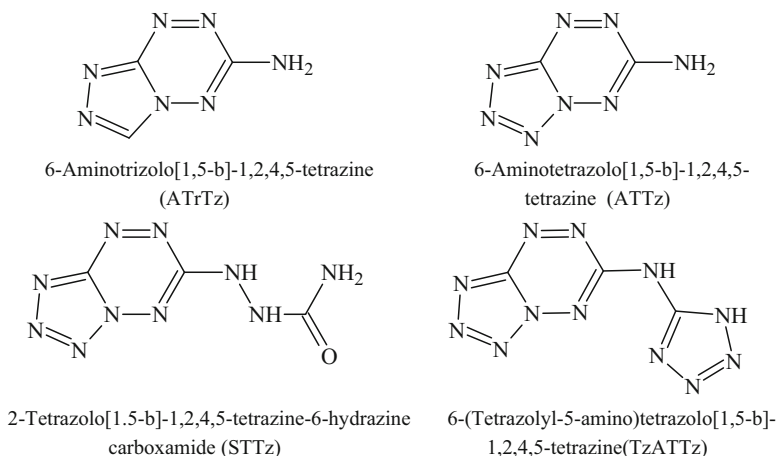
Scheme 8

Table 2 Some physicochemical properties of main CHN-azolotetrazines

Compound	Density (density of pressed strand), g/cm^3	ΔH_f^0, kcal/mol (kcal/kg)	DSC exotherm, °C (heat effect, kcal/kg)	Detonation velocity, m/s (density, g/cm^3)
ATrTz	1.60 [52]	116 (847)[a]	300 (159) [53]	7200 (1.60)[c] [52]
		148 (1080)[b] [52]		
ATTz	1.68 [52]	146 (1060)[a] [54]	203 (948) [54]	7970 (1.68)[c] [52]
	(1.6) [54]	175 (1268)[b] [52]		
STTz	1.84 (1.43) [54]	114 (584)[a] [54]	215 (758) [54]	7720 (1.84)[c] [54]
TzATTz	(1.52) [54]	221 (1077)[a] [54]	188 (937) [54]	7390 (1.52)[c] [54]

[a]Estimation
[b]Gas phase, DFT calculation
[c]Calculation

regarded as a primary explosive because of its distinct shock and friction sensitivity and strongly exothermal decomposition in the thermal analysis.

According to work [54], ATTz possesses good initiating properties. The minimum initiating charge of ATTz for RDX in detonator No. 8 brass caps was found to be <0.05 g. It is notable that sensitivity of triazolotetrazines to mechanical stimuli is significantly less than sensitivity of tetrazolotetrazines.

According to calculations at the B3LYP/6-311G** level, the introduction of annulated azole cycle leads to increase in the length of N-N and C-N bonds in the tetrazine cycle and decrease in the bond order in comparison with simple representative, diaminotetrazine, leading to reduction in the thermal stability of azolotetrazines. Indeed, DSC exotherm of 6-aminotrizolo[1,5-b]-1,2,4,5-tetrazine (ATrTz in Table 2) is observed at lower temperature (300 °C) than DSC exotherm of diaminotetrazine (347 °C) [4], although remaining still thermally stable. Despite the fact that calculated bond lengths and bond orders of ATrTz and ATTz are close, the latter substance is less stable; according to DSC data, the maximum of ATTz exotherm is observed at considerably lower temperatures (∼200 °C).

The experimental data on thermal decomposition of ATrTz and ATTz under isothermal conditions in the temperature interval of 230–260 and 165–180 °C, respectively, are shown in Figs. 9 and 10. The decomposition of both substances follows the reaction of first order up to high extents of the decomposition.

Maximum gas release at ATrTz decomposition is not large (∼130 cm^3/g or 1 mol of gases per 1 mol of ATrTz). The decomposition of ATTz at 165–180 °C produces up to 335 cm^3/g or 2 mol of gaseous products per 1 mol of ATTz, which corresponds to destruction of both tetrazole and tetrazine cycles.

As the decomposition of both ATrTz and ATTz follows a first-order reaction until high extent of decomposition, the kinetic data obtained under nonisothermal conditions (DSC) can be compared with corresponding data obtained under isothermal conditions. As Fig. 11 shows, all the kinetic data for both substances are well described by straight lines in wide temperature

Fig. 9 *Curves* of the gas release in decomposition of ATrTz at different temperatures. *Lines* are fittings; *points* are experimental data
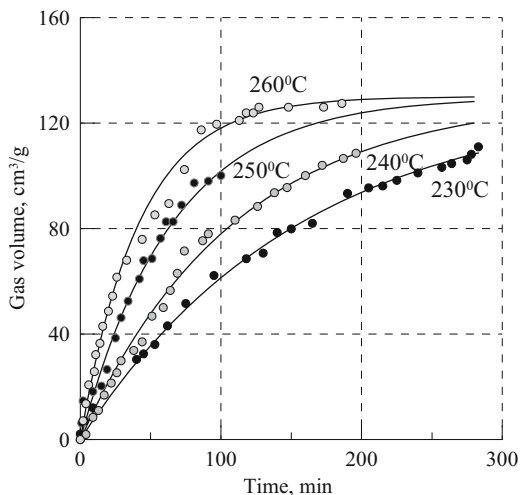
Fig. 10 *Curves* of the gas release in decomposition of ATTz at different temperatures. *Lines* are fittings; *points* are experimental data
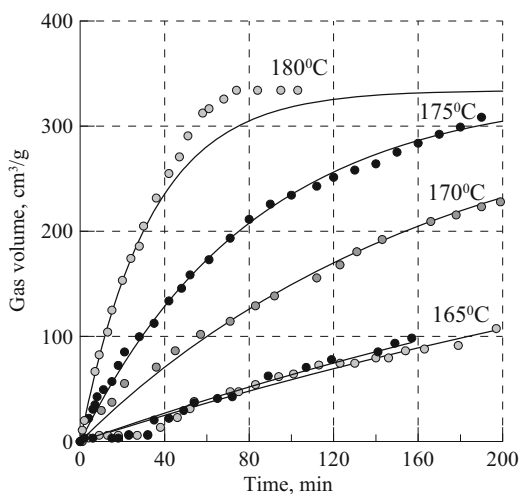
intervals: $k\,(230 - 328\;\,°\text{C}) \;=\; 5.8 \cdot 10^{10}\exp\left(-17205/T\right),\;\,\text{s}^{-1}$ for ATrTz and $k\,(164 - 221\;\,°\text{C}) = 1.3 \cdot 10^{25}\exp\left(-29750/T\right),\;\,\text{s}^{-1}$ for ATTz.

As might be expected from results of calculation at the B3LYP/6-311G ** level, the simplest representatives of azolotetrazines, ATrTz and ATTz, have rate constants of decomposition higher than rate constants of decomposition of the simplest tetrazine – diaminotetrazine [4].

Many researches are apt to relate thermal stability of energetic material to the activation energy. A comparison of thermal stabilities of tetrazolotetrazine and triazolotetrazine shows that such approach is not always correct. Tetrazolotetrazine, being considerably less stable than triazolotetrazine (e.g., ATrTz and ATTz decomposition rate constants at 500 K differ each other by more than three orders of

Fig. 11 Comparison of thermal stability of triazolotetrazine ATrTz and tetrazolotetrazine ATTz, obtained by different methods. *Lines* are fittings through both isothermal and nonisothermal experimental points
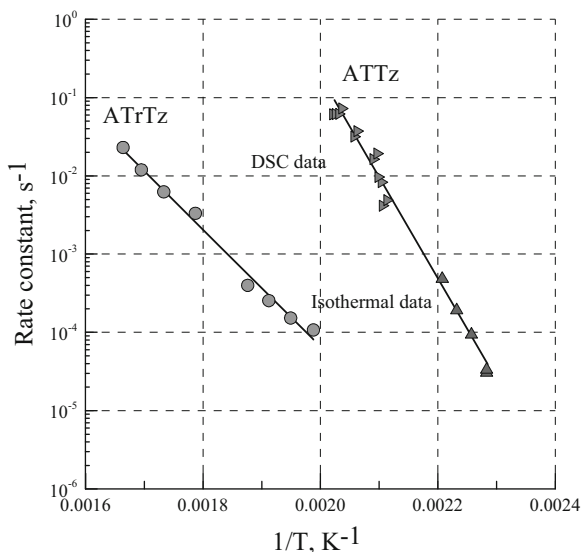
magnitude), possesses at the same time a very high value of the activation energy 57.5 kcal/mol, and, vice versa, stable triazolotetrazine shows a rather low activation energy of 34.2 kcal/mol.

The abovementioned activation energies do not relate to any elementary decomposition stage but are characteristics of more complex transformation. It is well known that higher temperatures generally favor the azide form [47, 55]. In the case of tetrazolotetrazines, for example, BTATz [20], this transformation includes preliminary isomerization into the azide followed by its decomposition. Apparently, the decomposition of the azido group induces simultaneous decomposition of the tetrazine ring:
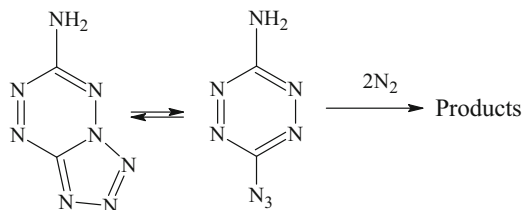
As a result, the observed activation energy is a sum of activation energies of these two elementary stages:

$$E_{obs} = E_{isom} + E_{dec}$$

Low activation energies of decomposition of triazolotetrazines can be linked with concerted mechanism of decomposition of the tetrazine cycle as it has been postulated in the case of photochemically excited 1,2,4,5-tetrazines [2, 3]. Here, elimination of nitrogen takes place synchronously with recombination of formed radicals [56] to give one kinetically indistinguishable stage:
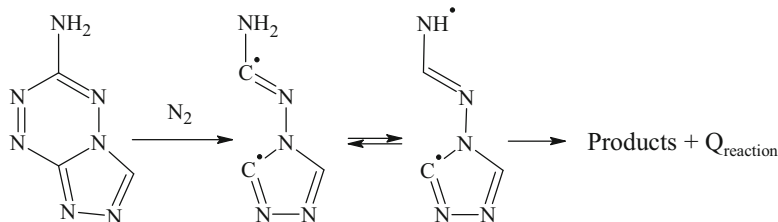
As a result, the observed activation energy is a difference between activation energy of bond rupture and heat effect of the subsequent radical reaction:

$$E_{obs} = E_{dec} - Q_{reaction}$$

Annulated tetrazolotetrazines appeared to burn faster than similarly structured open tetrazine derivatives. For example, tetrazolotetrazine with aminotetrazole substituent (TzATTz) burns four to seven times faster than its structural analog BTATz (Fig. 12).

Fig. 12 Comparison of burning rates of similarly structured tetrazolotetrazines
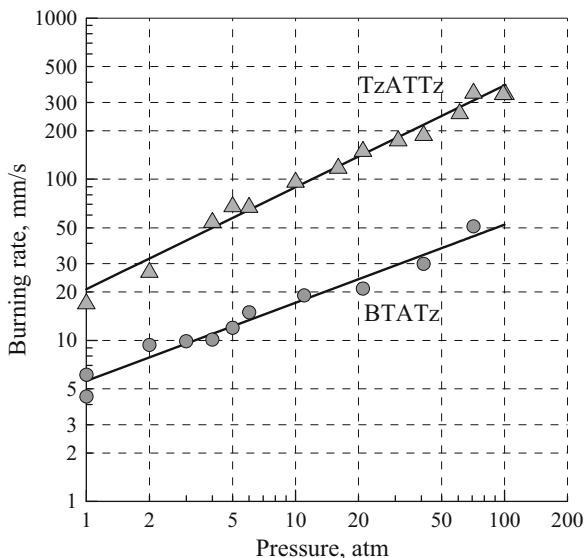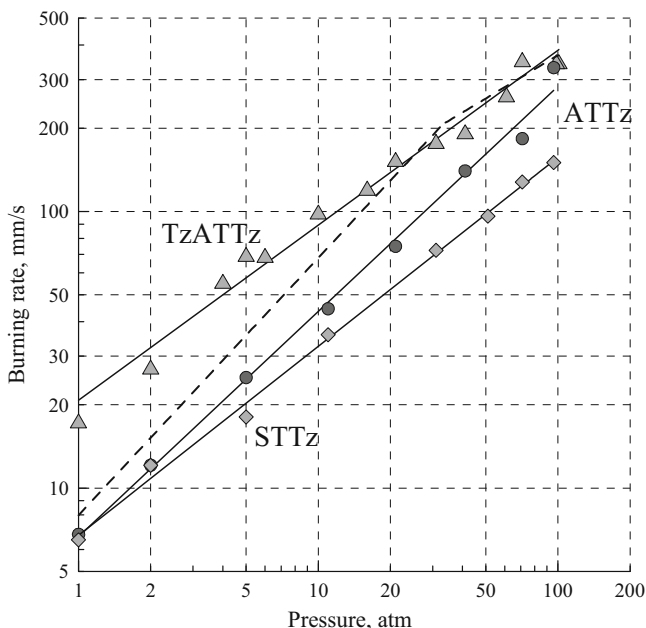
Fig. 13 Comparison of burning rates of tetrazolotetrazines and primary explosive tetrazene (*dashed line*)

High burning rates of many of tetrazolotetrazines allow considering these materials as potential primary explosives. Figure 13 shows a comparison of burning rates of some of tetrazolotetrazines with burning rates of a well-known initiating explosive tetrazene.

Because of high burning rates, temperature profiles in the combustion of tetrazolotetrazines can hardly be obtained with the help of thin thermocouples. However, supposing that the surface temperature (i.e., boiling point) of annulated azolotetrazines has changed little in comparison with ordinary tetrazines, it is reasonable to assume that higher burning rates of tetrazolotetrazines are stipulated by their lower thermal stability.

5   Energetic Materials Based on CHNO-Tetrazines

The best energetic performance can be reached if endothermic tetrazine cycle and active oxygen are joined together in one molecule. As shown in Scheme 9 and Table 3, the enthalpies of formation of CHNO-tetrazines containing nitroamino groups are lower than enthalpies of formation of CHN-tetrazines. Nevertheless, the calculated detonation velocities of CHNO-tetrazines are comparable to those of such explosives as RDX and HMX. However, all attempts to synthesize 3,6-

3,6-Dinitro-1,2,4,5-tetrazine (DNT)   3-Amino-6-nitro-1,2,4,5-tetrazine-2,4-dioxide
(ANTDO)

N-Nitro-3,6-diamino-1,2,4,5-tetrazine   N,N'-Dinitro-3,6-diamino-1,2,4,5-tetrazine
(ANAT)   (DNAT)
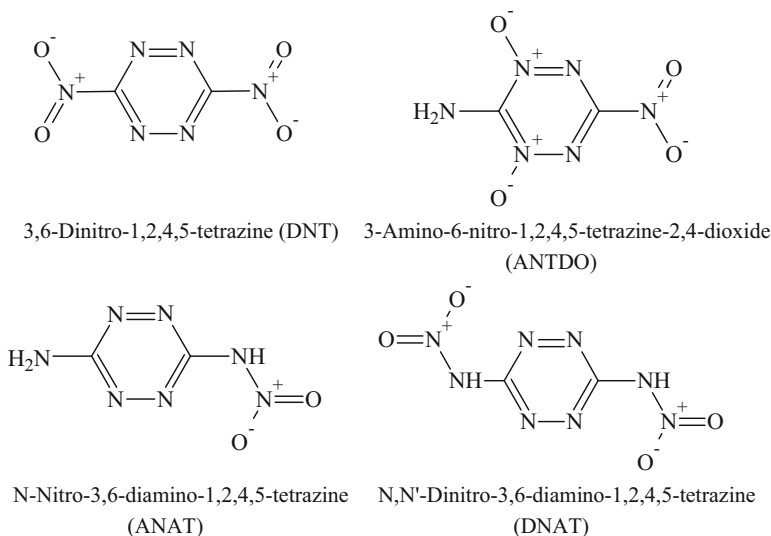
Scheme 9

Table 3 Some physicochemical properties of main CHNO-tetrazines

Compound	Density, g/cm^3	ΔH_f^0, kcal/mol (kcal/kg)	DSC exotherm, °C	Detonation velocity, m/s (density, g/cm^3)
DNT	1.88 [57]	128 (744)^a [57]	Too unstable to isolate [8]	9380 (calc.) (1.88) [57]
		60 (350)^b		
ANTDO	1.92 [58]	53.4 (307) [58]	110 [8]	9120 (calc.) (1.92)
			192 [58]	
ANAT	1.82 [59]	105 (671)^a [59]	164 [1, 59]	8230 (calc.) (1.82) [57]
DNAT	1.83 [57]	135 (670)^a [57]	Unstable [60]	9150 (calc.) (1.83) [57]

^{a}Gas phase, DFT calculation
^{b}Estimation

dinitro-1,2,4,5-tetrazine (DNT) failed due to extreme hydrolytic and thermal instability [8].

According to calculations at the B3LYP/6-311G** level [57], the substitution of amino group for nitro group leads to increase in the lengths of N-N and C-N bonds in the tetrazine ring and to decrease in their bond order in comparison with diaminotetrazine, but the least stable bond is the bond between nitro group and the tetrazine ring. It should be noted that according to work [58], tetrazine mononitro derivatives, 3-amino-6-nitro-1,2,4,5-tetrazine and its 2,4-dioxide, have

quite a satisfactory thermal stability: substantial decomposition is observed at temperatures higher than 190 °C.

The stability of nitroamino derivatives is not much better. N,N′-Dinitro-3,6-diamino-1,2,4,5-tetrazine (DNAT) was readily hydrolyzed back to starting material in contact with traces of moisture [1]. It is known that nitroamines, containing electron-withdrawing groups like NO_2 and F, have weak hydrolytic and thermal stability [34]. In this connection, it is not surprising that nitroamines, containing such a strong electron attractor as the tetrazine ring, possess unsatisfactory thermal stability. Nevertheless, unlike nitrotetrazines, the stability of nitroaminotetrazines can be increased by transforming them into anionic form. Thus, some salts of N-nitro-3,6-diamino-1,2,4,5-tetrazine (ANAT) are described as relatively dense (>1.55 g/cm^3) materials, exhibiting relatively good thermal stability (T_d >148 °C) [59].

Another way to incorporate the active oxygen into the tetrazine molecule is to obtain N-oxide fragment in the cycle or to introduce the nitro group into the side chain (Scheme 10 and Table 4). However, such approach does not allow obtaining energetic materials with well-balanced oxidizer/fuel ratio.

In 1993, Coburn et al. [8] reported the synthesis of 3,6-diamino-1,2,4,5-tetrazine-1,4-dioxide (LAX-112), an example of a cycloaromatic energetic material without oxidizing nitro groups. LAX-112 has relatively high heat of formation, good density, and detonation velocity that initially led to a much higher predicted performance than measured. This tetrazine compound was extensively evaluated as an insensitive explosive in the early 1990s. Then, LAX-112 was considered as fuel for solid-fuel digital microthrusters [16]; however, slow burning rates and formation of solid particles during combustion prevented further studying it as a monopropellant.

3,6-Diamino-1,2,4,5-tetrazine-1,4-dioxide
(LAX-112)

3,3′-Azoxybis(6-amino-5-N-oxide-s-tetrazine) (DAATO3.5)

3,6-Bis(nitroguanidine-1,2,4,5-tetrazine
(NQ2Tz)

Triaminoguanidinium salt
of 3,6-bis(nitroguanidine)-1,2,4,5-tetrazine
(TAG2NQ2Tz)
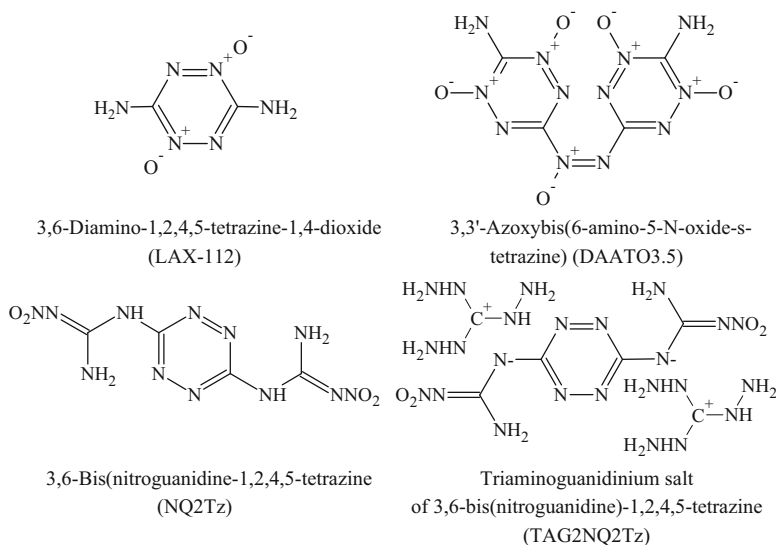
Scheme 10

Table 4 Some physicochemical properties of main CHNO-azolotetrazines

Compound	Density (density of pressed sample), g/cm^3	ΔH_f^0, kcal/mol (kcal/kg)	DSC exotherm, °C	Detonation velocity, m/s (density, g/cm^3)
LAX-112	1.85 [51]	48 (330) [51]	220 [8]	8786 (calc.)(1.85) [51]
			266 [51]	
DAATO3.5	1.88 [16]	131 (440)[a] [26]	177[a] [16]	9000 (calc.)(1.88) [16]
NQ2Tz	1.76 (1.70) [62]	93 (330) [62]	269 [63]	7840 (1.7) [63]
TAG2NQ2Tz	1.61 (1.51) [62]	300 (606) [62]	175 [63]	7620 (1.51) [63]
		153 (309) [67]		

[a]For a mixture of compounds

In the effort to improve the density and explosive performance of DAAT, Los Alamos chemists [16] obtained a mixture of various N-oxides of DAAT with an average oxygen content of approximately 3.5. This mixture of N-oxides, which was called DAATO3.5, has the calculated detonation velocity (at measured density of 1.88 g/cm^3) of 9.0 km/s [16]. DAATO3.5 proved to be sensitive to friction and spark. The density of DAATO3.5 was found to be relatively high; however, it could not be pressed to densities >80 % of theoretical maximum density (TMD), which was attributed to unusual morphology.

DAATO3.5 with an addition of 5 % polyvinyl alcohol and 1 % triethylene glycol (6.35-mm diameter, 1.52 g/cm^3 pressed pellet) burns at high rates (r_b at 10 MPa is 58.6 mm/s) and shows low dependence on pressure ($r_b = 16.9P^{0.27}$, P in atm); both parameters are desirable in high-performance propellant applications [26]. Because it was not possible to press neat DAATO3.5 without a binder and because binders generally suppress burn rates, it may be expected that the burn rate of pure DAATO3.5 is higher than that published.

A 6:2:1 mixture of nitro compound 3,6-bis-(3-nitrofurazan-4-ylamino)-s-tetrazine with mono- and di-N-oxides in tetrazine ring was synthesized by oxidation of 3,6-bis(3-aminofurazan-4-ylamino)-s-tetrazine [61]. In analogical way, the triazolotetrazine-substituted aminofurazan was oxidized into the nitro analog. A mixture of triazolotetrazine-substituted diaminoazofurazan and diaminoazoxyfurazan as by-products was formed. The synthesized nitro compounds are strong NH-acids. The acidity of these compounds allows a large variety of energetic salts to be prepared.

3,6-Bis(nitroguanidine)-1,2,4,5-tetrazine (NQ2Tz) and its triaminoguanidinium salt (TAG2NQ2Tz) were studied as promising components in gas-generating and propellant applications because they have low pressure indexes [62, 63]. Compound NQ2Tz has a DSC onset of 228 °C, with fast decomposition at 269 °C, and a gas pycnometry density of 1.76 g/cm^3. The heat of formation was measured using combustion calorimetry, and a value of 93 kcal/mol was obtained [63]. Compound TAG2NQ2Tz has a density of 1.61 g/cm^3 as determined by gas pycnometry. The

thermal stability of triaminoguanidinium salt is lower than NQ2Tz as determined by DSC analysis. The onset of decomposition begins at 166 °C, with a fast exotherm at 175 °C. Compound TAG2NQ2Tz was determined by combustion calorimetry to have a very high heat of formation of 300 kcal/mol. Such a high value of enthalpy is somewhat doubtful. Indeed, simple summation of enthalpies of formation of TAG2NQ2Tz composing fragments – triaminoguanidine (68.8 kcal/mol [64]) and NQ2Tz (93 kcal/mol [62]) – gives a considerably lower value of 230.6 kcal/mol. Taking into account the heat of salt formation (∼39 kcal/mol, an estimate from enthalpies of formation of triaminoguanidinium nitrate -12.0 kcal/mol [65], liquid nitric acid -41.6 kcal/mol [66], and triaminoguanidine), the resulting enthalpy of TAG2NQ2Tz formation is calculated as ∼153 kcal/mol, i.e., almost twice as less as published in [62].

As indicated in work [63], both NQ2Tz and TAG2NQ2Tz exhibit very low pressure dependence during combustion; the former has been shown to demonstrate the lowest pressure exponent known in the literature for a neat material. The combustion study of NQ2Tz pressed into 4-mm i.d. plexiglass tubes to a density of 1.6 g/cm^3 has shown that NQ2Tz burning rate is very sensitive to impurities [67]. At low pressures, including subatmospheric region, it burns in flameless mode with a large scatter of burning rates. A luminous flame appears at pressures higher than 20 atm. A comparison of burning rates of NQ2Tz measured in different labs (Fig. 14) shows that burning rates are different and that the pressure index obtained
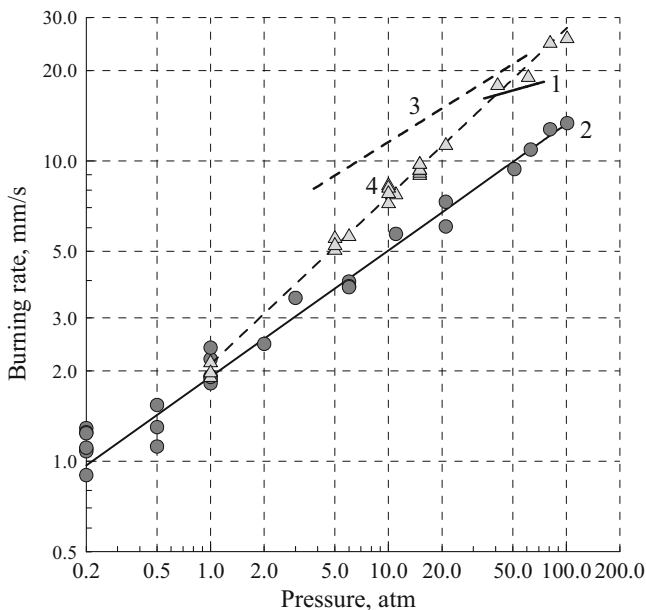
Fig. 14 Comparison of burning rates of NQ2Tz (*1*, *2*) and TAG2NQ2Tz (*3*, *4*), obtained in different labs: *1*, *3* – work [63]; *2*, *4* – work [67]

Fig. 15 Typical temperature profiles for NQ2Tz at different pressures
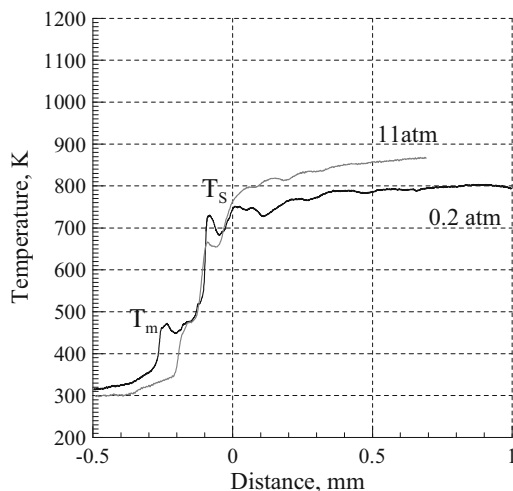
in our lab ($r_b = 1.91P^{0.42}$) [67] is significantly larger that pressure index published in [63] ($r_b = 8.97P^{0.16}$). Nevertheless, it is still less than the pressure index of HMX.

TAG2NQ2Tz pressed into 4-mm plexiglass tubes to a density of 1.55 g/cm^3 burns a little faster than the parent NQ2Tz compound. Combustion of the triaminoguanidine salt proceeds without luminous flame at all pressures up to 100 atm. As with NQ2Tz, the pressure exponent of the salt measured in our lab [67] ($r_b = 2.1P^{0.56}$) appeared to be significantly more than published one ($r_b = 4.92P^{0.37}$). A possible reason for such different combustion behaviors is likely purity of the materials and different sample preparation technique for burning rate tests.

Temperature profiles in the NQ2Tz and TAG2NQ2Tz combustion waves were obtained with the help of thin tungsten-rhenium thermocouples at low pressures, where both compounds burn without luminous flame. The maximum measured flame temperature of NQ2Tz in the pressure interval of 0.2–11 atm does not exceed 900 °C (Fig. 15), which is 1210 °C less than the adiabatic temperature. Reactions in the NQ2Tz flame do not reach their thermodynamic equilibrium (2115 K) even at 50 atm, resulting in the measured combustion temperature being no more than 1700 K. The temperature gradient above the surface is low ($\sim$4000 K/cm).

Unlike NQ2Tz, the temperature gradient above the burning surface of the triaminoguanidinium salt (Fig. 16) is much higher. A considerable heat flow from the gas phase is spent on warming up the dispersed substance over the burning surface, thus not affecting the heat balance of the condensed phase and leaving the dominant role for the condensed phase.

Thus, the thermocouple-aided measurements show that condensed-phase reactions play a dominant role in combustion of both NQ2Tz and TAG2NQ2Tz. As with NQ2Tz, the maximum measured flame temperature (910–1035 K) for TAG2NQ2Tz in the pressure range of 0.7–15 atm is less than adiabatic temperature (1590 K). This difference is caused by formation of high-energy products in the flame, such as

Fig. 16 Typical temperature profiles for TAG2NQ2Tz at different pressures
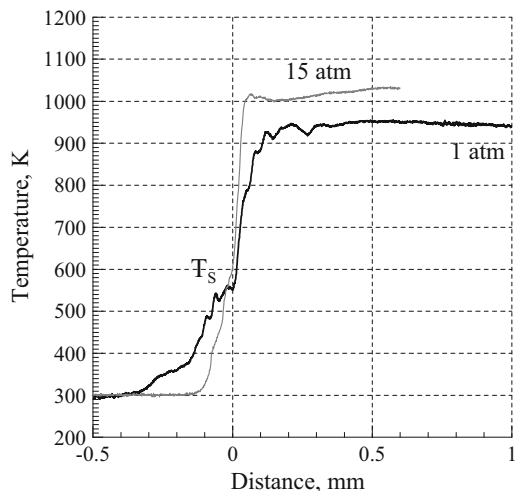
Fig. 17 Surface temperatures vs. pressure for NQ2Tz (*1*) and TAG2NQ2Tz (*2*)
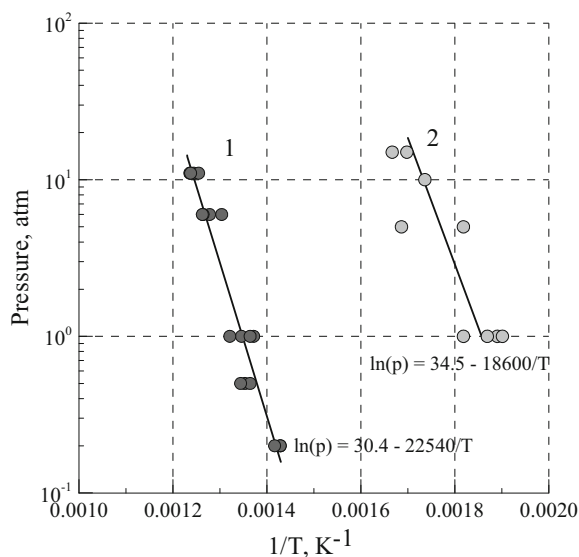
endothermic nitrile derivatives, favored by deficiency of oxygen in both molecules. Besides, T-Jump/FTIR spectroscopy indicates that NO_2 and N_2O are formed in the gaseous products from the flash pyrolysis of NQ2Tz [68].

NQ2Tz is a low-volatile substance with boiling temperature of about 743 K and heat of vaporization of 44.8 kcal/mol. The surface temperatures of TAG2NQ2Tz are within the interval of 530–600 K (Fig. 17) that is considerably lower than the surface temperature of the parent NQ2Tz acid (705–805 K). NQ2Tz possesses weak acidic properties, and, therefore, the dissociation temperature of the salt cannot be very

high. After dissociation of the salt and evaporation of volatile triaminoguanidine, the remaining NQ2Tz acid evaporates in the flame at higher temperatures.

The experiments on thermal decomposition of NQ2Tz under isothermal conditions have been carried out at temperatures 200–240 °C. The curve of gas evolution is described by the first-order reaction to high extents of decomposition. The final volume of gases is 320 cm^3/g (4.1 mol/mol). In $lnk – 1/T$ coordinates, the experimental points are fitted by a straight line as $k = 5.4 \cdot 10^{12} \exp{(-19140/T)}$, s^{-1}. The nonisothermal kinetics derived from DSC analysis is in a good agreement with the above kinetic equation for isothermal decomposition. According to T-jump/FTIR spectroscopy [68], the evolution of NO_2 indicates that $N-NO_2$ homolysis in nitroguanidine substituent is a trigger reaction of decomposition process. It is interesting to note that a comparison of the decomposition rate constants of NQ2Tz with those of nitroguanidine (NQ) ($k = 5.9 \cdot 10^9 \cdot \exp{(-14188/T)}$, s^{-1} [69]) indicates that bonding of the tetrazine ring to nitroguanidine has resulted in increasing stability of nitroguanidine moiety.

TAG2NQ2Tz has a considerably lower stability than NQ2Tz: the peak of exothermal decomposition in the DSC curves is observed at 197–230 °C depending on the heating rate. Experiments on thermal decomposition of TAGNQ2Tz under isothermal conditions have been carried out at 150–160 °C. The curves of gas evolution have a significant induction period which decreases with temperature. A sharp rise in the decomposition rate begins after the induction period is over. The final volume of released gases is 365 cm^3/g ($\sim$8 mol/mol). The experimental points can be satisfactorily described by a kinetic equation with autocatalysis to give the following rate constants: $k_1 = 1.9 \cdot 10^{15} \exp{(-21090/T)}$, s^{-1} and $k_2 = 3.1 \cdot 10^{17} \exp{(-19460/T)}$, s^{-1}. Composition of formed gases [68] indicates that the TAG cation dramatically affects the decomposition pathway. The formation of large amounts of NH_3 suggests that bond cleavage in the TAG cation is the dominant reaction of the thermal decomposition of TAG2NQ2Tz.

As burning rates of NQ2Tz and TAG2NQ2Tz are defined by chemical reactions in the condensed phase, the kinetics of the leading reaction on combustion can be derived from the burning rates and data of thermocouple measurements [39, 40]. A comparison of thus obtained rate constants of the leading reaction with decomposition rate constants in DSC and manometric experiments is shown in Fig. 18. A good correspondence between the kinetics of the leading combustion reaction and the kinetics of decomposition, defined at considerably lower temperatures, is observed for NQ2Tz. In the case of TAG2NQ2Tz, the kinetics of the leading combustion reaction coincides with the kinetics of decomposition acceleration, extrapolated to the high-temperature range. At high temperatures, the substance on the burning surface is in the molten state. The coincidence of combustion kinetics and the auto acceleration shows that the reason for the acceleration of decomposition is submelting of the sample.

Thus, the experiments have shown that the combustion mechanism of both substances is based on the reactions in the condensed phase and their burning rates are defined by the decomposition kinetics at the surface temperatures.

Fig. 18 Comparison of rate constants of the leading reaction on combustion and rate constants of decomposition under nonisothermal (*DSC*) and isothermal conditions for NQ2Tz (*1*) and TAG2NQ2Tz (*2*). *Line 1* is fitting of NQ2Tz isothermal decomposition data, *line 2* is kinetics of the leading reaction of TAG2NQ2Tz combustion, and *line 3* is rate constants of NQ decomposition
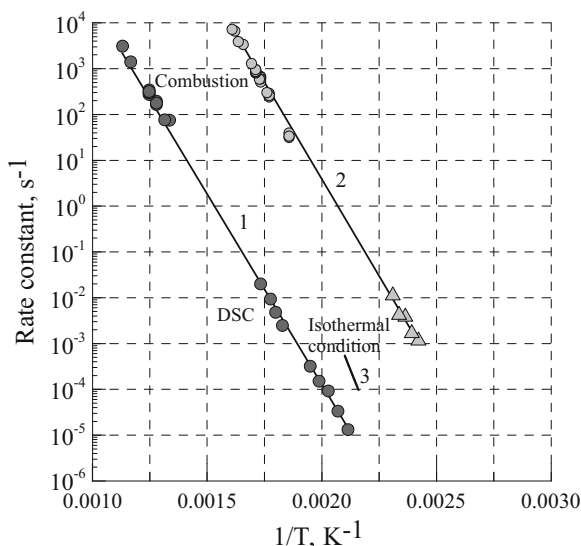
6 Salts of Substituted Tetrazines with Oxidizing Acids

Active oxygen can be introduced into the molecule by synthesizing tetrazine salts with such inorganic oxidizing acids as nitric and perchloric ones. In this case, the tetrazine molecule must contain some substituent groups of basic nature, for example, hydrazine or guanidine.

Several energetic salts of DHT were synthesized including bisdinitramide, diperchlorate, dinitrate, and 4,4′,5,5′-tetranitro-2,2′-biimidazolate, all having fairly low drop weight impact values and decomposition points [1]. Other tetrazine-based explosives of this class include nitrate and perchlorate salts of 3,6-diguanidino-s-tetrazine (DGT) [16, 19] (Scheme 11).

The reaction of salt formation reduces the total enthalpy of formation of the compounds. The heat of formation of DGT was determined to be 47 kcal/mol. The heat of formation of DGTN and DGTP was estimated on the base of thermodynamic data for guanidine, guanidine nitrate, and guanidine perchlorate [19]. Enthalpies of formation of DHTN and DHTP (Table 5) were calculated in similar way. However, due to good oxidizer/fuel ratios and high densities of these compounds, they possess high detonation velocities: 7.5 km/s and higher (Table 5). Among these substances, one can find insensitive explosives.

The use of different heterocycles containing nitro groups and acting as acids in the reaction with DHT, such as 5-nitrotetrazole, 3-amino-5-nitrotriazole, or 4,4′,5,5′-tetranitro-2,2′-bisimidazole [72], helps to increase enthalpies of formation of the salts, but at the same time decreases the oxidizer/fuel ratio. As the result, the salts proved to possess energetic characteristics not exceeding characteristics of RDX.

Nitrate of 3,6-dihydrazino-s-tetrazine
(DHTN)

Perchlorate of 3,6-dihydrazino-s-tetrazine
(DHTP)

3,6-Diguanidino-1,2,4,5-tetrazine nitrate
(DGTN)

3,6-Diguanidino-1,2,4,5-tetrazine perchlo-
rate (DGTP)
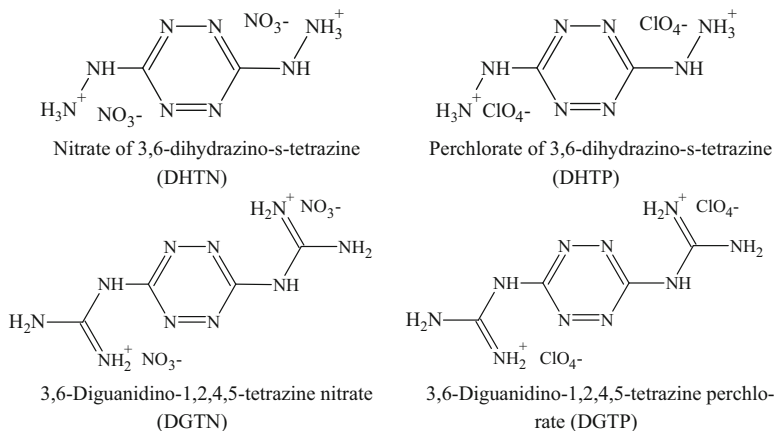
Scheme 11

Table 5 Some physicochemical properties of salts of substituted tetrazines with oxidizing acids

Compound	Density (density of pressed strand), g/cm^3	ΔH_f^0, kcal/mol (kcal/kg)	DSC exotherm, °C (heat effect, kcal/kg)	Detonation velocity, m/s (density, g/cm^3)
DHTN	1.80 [1]	−30 (−112)^a	117 [1], 161 (1200)	8300 (1.65)^c
	(1.65) [70]		[29], 156 [70]	
DHTP	1.96 (1.76) [1]	6 (18)^a	200 [1], 191 (67) and 288 (355) [29]	7520 (1.76)^c
DGTN	1.72 (1.6) [16]	−61 (−189)^a [19]	226^b [16]	7310 (1.6) [16, 19]
			276 (200) [73]	
DGTP	1.905 (1.79) [16, 19]	−30 (−75)^a [19]	265^b [16]	8070 (1.79) [16, 19]
	1.977 (at 93 K) [71]		272 [71]	

^{a}Estimation
^{b}DSC onset
^{c}Calculation

The thermal stability of DHT salts has been examined in [29]. It has been shown that the salts exist in the reversible equilibrium with the parent base and acid; thus, in several cases, the decomposition rate of the parent DHT and the salt are essentially identical. The thermal stability of DHT salts strongly depends on the acidity of the corresponding acid [72]. When strong acids are used, the thermal stability is enhanced.

Burning rate behaviors and temperature profiles have been investigated for salts of 3,6-diguanidino-1,2,4,5-tetrazine with perchloric and nitric acids [73] (Fig. 19). The burning rate-pressure dependences for pressed samples of DGTN and DGTP are expressed in the pressure interval of 1–100 atm as $r_b = 0.535p^{0.816}$ and $r_b = 0.92p^{0.906}$, respectively. Both salts burn faster than HMX: 1.3 times for

Fig. 19 Comparison of
burning rates of DGTP,
DGTN, HMX, and AP
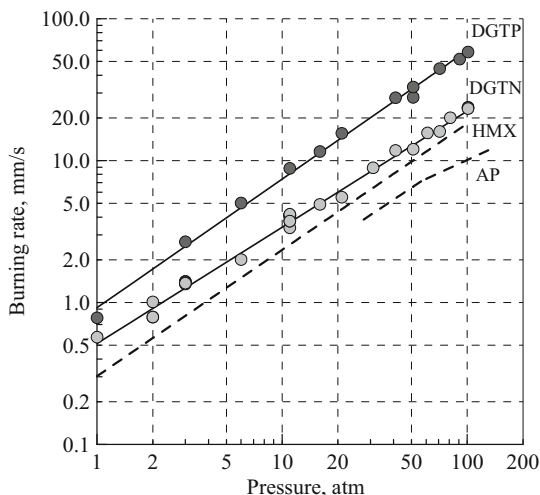
nitrate and 3 times for perchlorate. Comparing DGTP with ammonium perchlorate, one can see a six-time increase in the burning rate, which is not surprising, since the combustion temperature of DGTP is two times higher than the combustion temperature of AP. It should be noted that the burning rates of DGTP are relatively moderate among other energetic salts of perchloric acid. For example, the burning rate of both 1,5-diaminotetrazole perchlorate [74] and carbohydrazide perchlorate [75] approaches 150 mm/s at pressure of 100 atm.

Temperature profiles in the DGTN combustion wave were studied with the help of thin tungsten-rhenium thermocouples at pressures of 0.5, 1, 3, and 11 atm (Fig. 20). At low pressures, temperature profiles demonstrate the absence of high-temperature flame. At pressure 100 atm, the maximum flame temperature T_f does not exceed 900 °C. It is much lower than the calculated adiabatic flame temperature (1396 °C), and the observed 460° difference cannot be connected with radiant heat losses by the thermocouple.

Flameless combustion makes it easy to determine the surface temperature up to 100 atm (Fig. 21). All experimental points give the dependence of DGTN vapor pressure on temperature as $\ln(P) = 10860/T + 16.07$, allowing estimation of the heat of vaporization as 64.8 kcal/mol. Comparison of effect of pressure on the surface temperatures of TAGN [76], DGTN, and AN [77] shows that DGTN surface temperature is close to TAGN surface temperature but is higher than AN surface temperature. The surface temperatures of DGTN and TAGN are close, which, in our opinion, is caused by the close basicity of guanidine fragments in both molecules.

According to DSC analysis, DGTN shows no melting point and exhibits one intense exotherm between 272 and 280 °C at heating rate 4–16 °C/min. Kinetic data of thermal decomposition of DGTN were calculated by Kissinger's equation, suggesting the first reaction order. The calculation gives unrealistically high activation energy (∼76 kcal/mol), which is likely due to fact that the decomposition does not obey the first order.

Fig. 20 Typical temperature profiles of DGTN at 0.5, 1, 3, and 11 atm
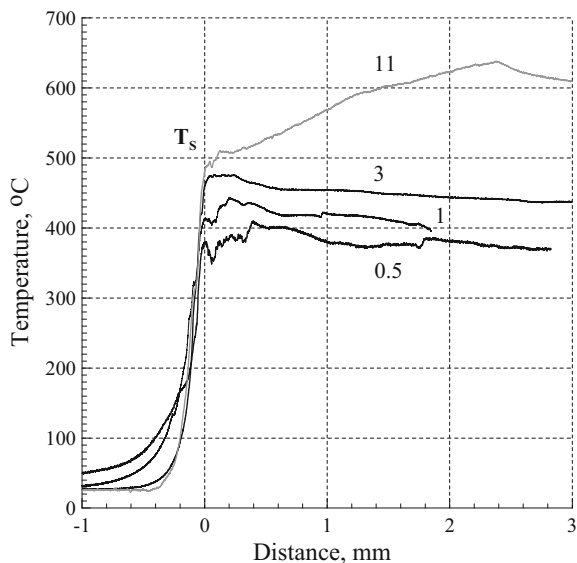
Fig. 21 Effect of pressure on the surface temperatures of TAGN, DGTN, and AN
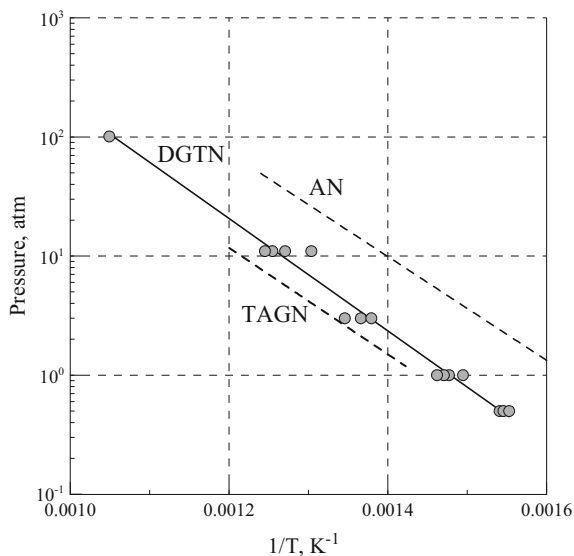
Flameless combustion of DGTN in a wide range of pressures clearly testifies the leading role of reactions in the condensed phase. Therefore, one can use the experimental data on the burning rates and surface temperatures to extract kinetic parameters of the leading combustion reaction. Kinetic parameters of DGTN decomposition derived from the condensed-phase combustion model, $k\,(\mathrm{s}^{-1}) = 10^{13.14}\exp\left(-37200/RT\right)$, are in a good agreement with rate constants obtained

Fig. 22 Comparison of rate constants of the leading reaction of DGTN combustion (*1*) and rate constants of DGTN decomposition derived from DSC measurements (*2*) with kinetic parameters of DGT (*3*) and GuN (*4*) decomposition
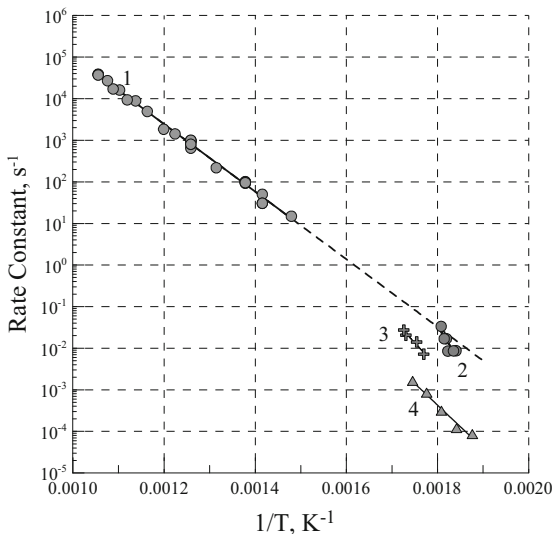
by Kissinger's method from DSC curves (Fig. 22). It should be noted that the leading combustion reaction acquires more realistic activation energy (37 kcal/mol) if calculated over a wide temperature range. As can be seen from the figure, DGTN is significantly less stable than guanidinium nitrate GuN [78]. The comparison of rate constants of DGTN and GuN shows that the introduction of tetrazine ring into guanidine molecule decreases thermal stability of the salt. This is in correspondence with the abovementioned facts [29, 72] that the decrease in the salt stability is caused by decreasing strength of the acid. The tetrazine ring is an electron-withdrawing substituent, and, consequently, it reduces the basic properties of guanidine. The weaker the bond strength between acid and base, the more shifted the equilibration toward free acid and base, which possesses lower thermal stability than the initial salt.

Thus, the investigation carried out allow conclusion that the mechanism of DGTN combustion is similar to that of other onium salts, such as ammonium nitrate, perchlorate, and dinitroamidate [79]. The surface temperature on combustion of DGTN is controlled by reaction of dissociation as well. The burning rate of DGTN is determined by processes in the condensed phase.

7 Coordination Compounds of Tetrazine

Tetrazine-based energetic materials can be obtained in synthesis of coordination compounds of metal perchlorates or nitrates by using the tetrazine ring as the ligand. The presence of at least four nitrogen donor atoms in tetrazine and its derivatives allows for potentially rich coordination chemistry. The most common arrangement

Dihydrazino-s-tetrazine nickel(II) Nitrate
[Ni(DHT)(NO₃)₂]

Tris(dihydrazino-s-tetrazine)dinickel(II)
Perchlorate [Ni₂(DHT)₃](ClO₄)₄
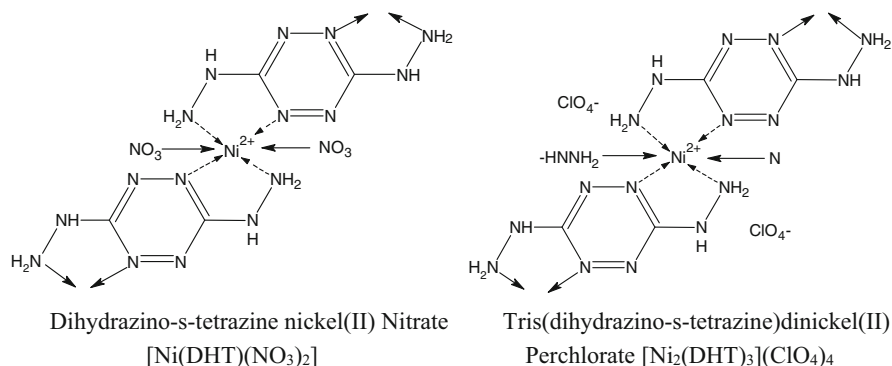
Scheme 12

Table 6 Some physicochemical properties of explosive coordination compounds of tetrazine

Compound	Density (density of pressed sample), g/cm^3	ΔH_f^0, kcal/mol (kcal/kg)	DSC exotherm, °C	Flame temperature at 100 atm, K
[Ni(DHT)(NO₃)₂]	(1.85)	29 (90)	130	3040
[Ni₂(DHT)₃](ClO₄)₄	–	258 (275)	242	3290
[Cu₂(DPT)₃](ClO₄)₄	(1.65)	175 (174)	302	2250
[Ni(DPT)(ClO₄)₂]	(1.57)	79 (164)	332	2400

with tetrazine itself involves it as a bridging ligand via the one and four positions. Discrete dinuclear complexes or linear coordination oligomers and polymers may result [80]. Basicity, and therefore coordination ability of tetrazine cycle, is low, that is why stable complexes can be better obtained if one uses tetrazines with donor substitutes. In this regard, most interesting compounds, from energetic point view, are dihydrazino-s-tetrazine and diguanidino-s-tetrazine. However, complexing of diguanidino-s-tetrazine with metal perchlorate results in hydrolysis of guanidine groups. Dihydrazino-s-tetrazine forms coordination compounds with nickel nitrate and perchlorate (Scheme 12). The nitrate complex still proved to be thermally unstable: its ignition temperature was as low as 130 °C, and the perchlorate complex was prone to spontaneous explosion [70] (Table 6).

Therefore, stable coordination compounds with tetrazines have been synthesized from the well-known pyridyltetrazines. The most frequently used tetrazine ligand 2,2′-bispyridyltetrazine usually acts as transoid symmetrically bis-chelating ligands [80]. In our lab, explosive complex compounds of 3,6-di(2-pyridinyl)-1,2,4,5-tetrazine (DPT) with nickel and cobalt perchlorates have been obtained and studied [70].

Explosive coordination compounds (CC) can be considered as model propellants containing the catalyst, which is the central metal ion; fuel, which is the ligand; and oxidizer, which is the anion, all mixed at the molecular level. For this reason, the

Fig. 23 Burning behaviors of complex perchlorates: (*1*) [Cu$_2$(DPT)$_3$(ClO$_4$)$_4$], (*2*) [Ni(DPT)(ClO$_4$)$_2$], (*3*) DPT·2HClO$_4$, (*4*) [Cu(PhDA)$_2$](ClO$_4$)$_2$, and (*5*) [Ni(PhDA)$_3$](ClO$_4$)$_2$
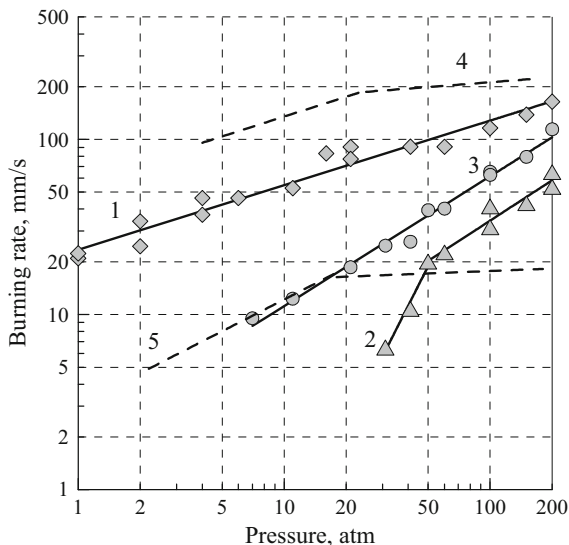
study of CC combustion allows one to avoid problems of interpretation of results associated with inhomogeneity of the catalyst distribution and particle size effect. The effect of the metal atom nature on combustion of a coordination compound can be estimated by comparing its burning rates with burning rates of the corresponding metal-free system containing the same fuel and oxidizer [74, 81].

The leading reactions in combustion of coordination compounds of DPT as well as DPT salt with perchloric acid (DPT·2HClO$_4$) was assumed to proceed in the gas phase because of low decomposition depths in the condensed phase and high flame temperatures [70]. By its chemical nature, this leading reaction is a redox transformation. It is interesting to note that burning rates of [Cu$_2$(DPT)$_3$](ClO$_4$)$_2$ appeared to be much higher than burning rates of DPT·2HClO$_4$ that has been naturally explained by high efficiency of copper ion acting as the catalyst. In its turn, nickel does not show any catalytic activity in its perchlorate complex with DPT (Fig. 23).

The burning rates of complexes with energetic tetrazine ligands turned out to be close or even slower than burning rates of analogous complexes with non-energetic phenylenediamine (PhDA). This fact suggests that the activity of tetrazine derivatives in redox reactions is low.

As an example, the reduced reactivity of tetrazine derivatives can be illustrated by comparison of burning rates for complexes of DHT and hydrazine with nickel nitrate, which is as replacement of lead azide in a new type of detonators [82]. It is evident that, despite a significant difference in the combustion temperatures of [Ni(DHT)(NO$_3$)$_2$] (3040 K) and [Ni(N$_2$H$_4$)$_3$(NO$_3$)$_2$] (2500), both complexes have the same burning rates (Fig. 24).
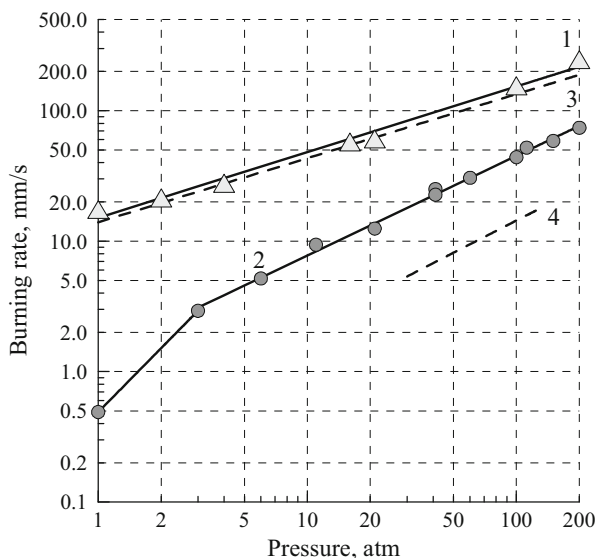
Fig. 24 Burning behaviors of complex nitrates: (*1*) [Ni(DHT)(NO$_3$)$_2$], (*2*) DHT·2HNO$_3$, (*3*) [Ni(N$_2$H$_4$)$_3$](NO$_3$)$_2$, and (*4*) N$_2$H$_4$·HNO$_3$

8 Conclusions

High enthalpy of formation and good thermal stability of tetrazine cycle allow producing tetrazine-based energetic materials, which can be used as insensitive, thermostable, environmentally friendly explosives, components of fast-burning propellants, gas-generating compositions, and nonmetal primary explosives.

A drawback of tetrazines is their poor solubility in organic solvents along with the tendency to give solvates, which makes obtaining these substances in pure form difficult.

Investigation of the thermal stability of tetrazine derivatives has shown that the least stable group in the molecule is usually the substituent in the tetrazine cycle which decomposition controls decomposition of whole molecule. Electron-withdrawing properties of the tetrazine cycle, in its turn, tend to increase thermal stability of the substituents.

Study of combustion behavior along with thermocouple-aided measurements has shown that most of tetrazines are low-volatile substances with high surface temperatures, which determines a dominant role of the condensed phase in combustion of many tetrazine derivatives.

The tetrazine cycle shows low reactivity in redox reactions, leading to rather moderate burning rates of its salts with oxidizing acids and coordination compounds despite high energetic characteristics.

The absence of oxygen or low-oxygen content in the tetrazine-based energetic materials leads to formation of high-enthalpy species (nitriles) in the combustion products, resulting in the incomplete heat release.

References

1. Chavez DE, Hiskey MA (1999) 1,2,4,5-Tetrazine based energetic materials. J Energy Mater 17(4):357–377
2. Hochstrasser RM, King DS (1975) Isotopically selective photochemistry in molecular crystals. J Am Chem Soc 97(16):4760–4762
3. Scheiner AC, Scuseria GE, Schaefer HF III (1986) Mechanism of the photodissociation of s-tetrazine: a unimolecular triple dissociation. J Am Chem Soc 108(26):8160–8162
4. Oxley J, Smith J, Zhang J (2000) Decomposition pathways of some 3,6-substituted s-tetrazines. J Phys Chem A 104:6769–6777
5. Chavez DE, Hiskey MA, Huynh MH, Naud DL, Son SF, Tappan BC (2006) The combustion products of novel high-nitrogen energetic materials. J Pyrotech 23:70–80
6. Clavier G, Audebert P (2010) s-Tetrazines as building blocks for new functional molecules and molecular materials. Chem Rev 110(6):3299–3314
7. Pinner A (1893) Action of hydrazine on imido-ethers. Ber Dtsch Chem Ges 26:2126–2135
8. Coburn MD, Hiskey MA, Lee KY, Ott DG, Stinecipher MM (1993) Oxidations of 3,6-diamino-1,2,4,5-tetrazine and 3,6-bis(S, S-dimethylsulfilimino)-1,2,4,5-tetrazine. J Heterocycl Chem 30(6):1593–1595
9. Sheremetev AB, Palysaeva NV, Struchkova MI, Suponitsky KY (2012) A mild and efficient synthesis of 3-hetarylamino-s-tetrazines. Mendeleev Commun 22(6):302–304
10. LoPresti V (2003) Versatile explosives, Los Alamos Res Q. Summer:4–12
11. Fallis S, Reed R, Lu YCh, Wierenga PH, Holland GF (2000) Advanced propellant/additive development for fire suppressing gas generators. Proceedings of the halon options technical working conference, pp 361–370
12. Fallis S, Reed R, McCormick JL, Wilson KA, Holland GF (2001) Advanced propellant/additive development for fire suppressing gas generators: hybrid systems. Proceedings of the halon options technical working conference, Albuquerque, pp 364–372
13. Enerson JR, Lucius JH, Battat D, Battat E, Mackal G (2009) Apparatus and method for using tetrazine-based energetic material. US Patent 20090301601
14. Ali AN, Son SF, Hiskey MA, Naud DL (2004) Novel high nitrogen propellant use in solid fuel micropropulsion. J Prop Power 20(1):120–126
15. Wu XZ, Dong PT, Li ZZ, Li SG, Liu QH, Xu C, Wan H (2009) Design, fabrication and characterization of a solid propellant microthruster. Proceedings of the 4th IEEE international conference on nano/micro engineered and molecular systems, pp 476–479
16. Yi JH, Zhao FQ, Wang BZ, Liu Q, Zhou C, Hu RZ, Ren YH, Xu SY, Xu KZ, Ren XN (2010) Thermal behaviors, nonisothermal decomposition reaction kinetics, thermal safety and burning rates of BTATz-CMDB propellant. J Hazard Mater 181(1–3):432–439
17. Chavez DE, Hiskey MA (1998) High nitrogen pyrotechnic compositions. J Pyrotech 7:11–14
18. Hiskey MA, Chavez DE, Naud DL (2001) Insensitive high-nitrogen compounds. Report LA-UR-01−1493, pp 1–10
19. Hiskey MA, Chavez DE, Naud D (2002) Preparation of 3,3′-azobis (6-amino-1,2,4,5-tetrazine). US Patent 6342589
20. Kerth J, Löbbecke S (2002) Synthesis and characterization of 3,3′-azobis (6-amino-1,2,4,5-tetrazine) DAAT – A new promising nitrogen-rich compound. Prop Exp Pyrol 27(3):111–118

21. Chavez DE, Hiskey MA, Gilardi RD (2000) 3,3′-Azobis (6-amino-1,2,4,5-tetrazine): a novel high-nitrogen energetic material. Angew Chem 112(10):1861–1863
22. Naud DL, Hiskey MA, Kramer JF, Bishop R, Harry H, Son S.F. Sullivan G (2002) High-nitrogen explosives. Proc. 29th Inter. Pyro Seminar. Westminster, 14–19 July
23. Hiskey MA, Chavez DE, Naud DL (2002) Propellant containing 3,6-bis(1H-1,2,3,4-tetrazol-5-ylamino)-1,2,4,5-tetrazine or salts thereof. US Patent 6458227
24. Atwood AI, Bui DT, Curran PO, Ciaramitaro DA, Lee KB (2002) Burning rate studies of energetic materials. Proceedings of the 8th international workshop on Comb Prop Naples, Italy. pp 1–11
25. Chavez DE, Hiskey MA, Naud DL (2004) Tetrazine explosives. Prop Exp Pyro 29(4):209–215
26. Sinditskii VP, Egorshev VY, Rudakov GF, Burzhava AV, Filatov SA, Sang LD (2012) Thermal behavior and combustion mechanism of high-nitrogen energetic materials DHT and BTATz. Thermochim Acta 535:48–57
27. Saikia A, Sivabalan R, Polke BG, Gore GM, Singh A, Subhananda RA, Sikder AK (2009) Synthesis and characterization of 3,6-bis(1H-1,2,3,4-tetrazol-5-ylamino)-1,2,4,5-tetrazine (BTATz): novel high-nitrogen content insensitive high energy material. J Hazard Mater 170:306–313
28. Loebbecke S, Schuppler H, Schweikert W (2003) Thermal analysis of the extremely nitrogen-rich solids BTT and DAAT. J Therm Anal Calorim 72(2):453–463
29. Oxley JC, Smith JL, Heng C (2002) Thermal decomposition of high-nitrogen energetic compounds – dihydrazido-s-tetrazine salts. Thermochim Acta 384:91–99
30. Stone EW, Maki AH (1963) ESR study of polyazine anions. J Chem Phys 39:1635–1642
31. Xing XL, Zhao FQ, Xue L, Yi JH, Pei Q, Hao HX, Xu S, Gao HX, Hu RZ (2009) Study on thermal behavior of 3, 6-bis(1H-1,2,3,4-tetrazol-5-ylamino)-1,2,4,5-tetrazine (BTATz) by using microcalorimeter. Proceedings of the 8th international autumn seminar on Prop Exp Pyro. Kunming, 22–25 Sept. pp 158–160
32. Kiselev VG, Gritsan NP (2009) Theoretical study of the 5-aminotetrazole thermal decomposition. J Phys Chem A 113(15):3677–3684
33. Kiselev VG, Cheblakov PB, Gritsan NP (2011) Tautomerism and thermal decomposition of tetrazole: high-level ab initio study. J Phys Chem A 115(9):1743–1753
34. Manelis GB, Nazin GM, Rubtsov YI, Strunin VA (2003) Thermal decomposition and combustion of explosives and propellants. Taylor and Francis, London
35. Prokudin VG, Poplavsky VS, Ostrovskii VA (1996) Mechanism of the monomolecular thermal decomposition of 1,5- and 2,5-disubstituted tetrazoles. Russ Chem Bull 45(9):2094–2100
36. Prokudin VG, Poplavsky VS, Ostrovskii VA (1996) Mechanism of the monomolecular thermal decomposition of tetrazole and 5-substituted tetrazoles. Russ Chem Bull 45(9):2101–2104
37. Son SF, Berghout HL, Bolme CA, Chavez DE, Naud DL, Hiskey MA (2000) Burn rate measurements of HMX, TATB, DHT, DAAF, and BTATz. Proc Comb Inst 28:919–924
38. Sinditskii VP, Egorshev VY, Berezin MV, Serushkin VV (2009) Mechanism of HMX combustion in a wide range of pressures. Comb Exp Shock Waves 45(4):461–477
39. Sinditskii VP, Egorshev VY, Serushkin VV, Levshenkov AI, Berezin MV, Filatov SA, Smirnov SP (2009) Evaluation of decomposition kinetics of energetic materials in the combustion wave. Thermochim Acta 496(1):1–12
40. Sinditskii VP, Egorshev VY, Serushkin VV, Levshenkov AI, Berezin MV, Filatov SA (2010) Combustion of energetic materials governed by reactions in the condensed phase. Int J Energy Mater Chem Prop 9(2):147–192
41. Lesnikovich AI, Ivachkevich OA, Levchik SV, Balabanovich AI, Gaponik PN, Kulak AA (2002) Thermal decomposition of aminotetrazoles. Thermochim Acta 388:233–251
42. Sinditskii VP, Smirnov SP, Egorshev VY (2007) Thermal decomposition of NTO: explanation of high activation energy. Prop Exp Pyro 32(4):277–287
43. Chavez DE, Hiskey MA (1998) Synthesis of the bi-heterocyclic parent ring system 1,2,4-triazolo[4,3-b][1,2,4,5]tetrazine and some 3,6-disubstituted derivatives. J Heterocycl Chem 35(6):1329–1332

44. Rusinov GL, Ganebnykh IN, Chupakhin ON (1999) Synthesis of triazolo[4,3-b][1,2,4,5] tetrazines. Russ J Org Chem 35:1350–1354
45. Ershov VA, Postovskii IY (1971) Chemistry of sym-tetrazine. Chem Heterocycl Comp 7(5):668–671
46. Huynh MHV, Hiskey MA, Chavez DE, Naud DL, Gilardi RD (2005) Synthesis, characterization, and energetic properties of diazido heteroaromatic high-nitrogen C-N compound. J Am Chem Soc 127:12537–12543
47. Hammerl A, Klapötke TM, Rocha R (2006) Azide–tetrazole ring-chain isomerism in polyazido-1,3,5-triazines, triazido-sheptazine, and diazidotetrazines. Eur J Inorg Chem: 11:2210–2228
48. Karpenko VO, Rudakov GF, Zhilin VF (2011) Synthesis of 6-amino-tetrazolo[1,5-b]-1,2,4,5-tetrazine. Adv Chem Chem Technol (in Russian) 25(12):61–64
49. Kozlov IB, Karpenko VO, Rudakov GF, Zhilin VF (2012) Features azidotetrazole tautomerism in the salts of 6-(tetrazol-5-yl)tetrazolo[1,5-b] -1,2,4,5-tetrazine. Adv Chem Chem Technol (in Russian) 26(2):109–111
50. Elguero J, Claramunt RM, Summers AJH (1978) The chemistry of aromatic azapentalenes. Adv Heterocycl Chem 22:183–320
51. Licht HH, Ritter H (1994) New energetic materials from triazoles and tetrazines. J Energy Mater 12(4):223–235
52. Wei T, Zhu WH, Zhang JJ, Xiao HM (2010) DFT study on energetic tetrazolo-[1,5-b]-1,2,4,5-tetrazine and 1,2,4-triazolo-[4,3-b]-1,2,4,5-tetrazine derivatives. J Hazard Mater 179:581–590
53. Sinditskii VP, Burzhava AV, Rudakov GF, Zacharova DA (2015) Thermal decomposition of triazolo- and tetrazolotetrazines. In: Frolov SM (ed) Combustion and explosion. Torus Press, Moscow, pp 453–460
54. Rudakov GF, Egorshev VY (2014) Synthesis and properties of derivatives of 6-amino-tetrazolo[1,5-b][1,2,4,5]Tetrazine. Proceedings of the 9th international high energy materials conference, HEMSI. Thiruvananthapuram, pp 759–762
55. Henry RA, Finnegan WG, Lieber E (1955) Kinetics of the isomerization of substituted 5-aminotetrazoles. J Am Chem Soc 77(8):2264–2270
56. Kim R, Pedersen S, Zewail FH (1995) Direct femtosecond observation of the transient intermediate in the α-cleavage reaction of $(CH_3)_2CO$ to $2CH_3 + CO$: resolving the issue of concertedness. J Chem Phys 103(1):477–480
57. Wei T, Zhu WH, Zhang XW, Li YF, Xiao HM (2009) Molecular design of 1,2,4,5-tetrazine-based high-energy density materials. J Phys Chem A 113:9404–9412
58. Ovchinnikov IV, Makhova NN (2008) Synthesis of 3-amino-6-nitro-1,2,4,5-tetrazine and its 2,4-dioxide. Proceedings of the 11th seminar of the new trends in research of energetic materials, Pardubice, 10–12 April. pp 713–718
59. Singh RP, Gao HX, Meshri DT, Shreeve JM (2007) Nitrogen-rich heterocycles. Struct Bond 125:35–83
60. Xizeng Z, Ye T (1987) Synthesis and properties of tetrazine explosives, Proc Inter Sym on Pyro Exp. China Academic Publishers, Beijing, p 241
61. Sheremetev AB, Palysaeva NV, Struchkova MI (2010) The first synthesis of 3-nitro-4-[(s-tetrazin-3-yl)amino]furazans. Mendeleev Commun 20(6):350–352
62. Chavez DE, Hiskey MA, Gilardi RD (2004) Novel high-nitrogen materials based on nitroguanyl-substituted tetrazines. Org Lett 6(17):2889–2891
63. Chavez DE, Tappan BC, Hiskey MA, Son SF, Harry H, Montoya D, Hagelberg S (2005) New high-nitrogen materials based on nitroguanyl-tetrazines: explosive properties, thermal decomposition and combustion studies. Prop Exp Pyro 30(6):412–417
64. Dorofeeva OV, Ryzhova ON, Sinditskii VP (2015) Enthalpy of formation of guanidine and its amino and nitro derivatives. Struct Chem 26(5–6):1629–1640
65. Matyushin YN, Kon'kova TS, Titova KV, Rosolovskii VY, Lebedev YA (1982) Enthalpies of formation of triaminoguanidinium chloride, nitrate, and perchlorate. Russ Chem Bull 31(3):446–449

66. Wagman DD, Evans WH, Parker VB, Schumm RH, Halow I, Bailey SM, Churney KL, Nuttall RL (1982) The NBS tables of chemical thermodynamic properties. J Phys Chem Ref Data 11(Suppl. 2):1–392
67. Sinditskii VP, Hoang CH, Filatov SA, Rudakov GF (2012) Decomposition and combustion of polynitrogen energetic materials based on nitroguanyltetrazine. In: Frolov SM (ed) Combustion and explosion, vol 5. Torus Press, Moscow, pp 269–275
68. Tappan BC, Son SF, Ali AN, Chavez DE, Hiskey MA (2007) Decomposition and performance of new high nitrogen propellants and explosives. Int J Energy Mater Chem Prop 6(2):255–268
69. Lee PP, Back MH (1989) Thermal decomposition of nitroguanidine. Thermochim Acta 141:305–315
70. Levshenkov AI, Akhapkina LE, Shebeko AA, Rudakov GF, Sinditskii VP (2011) Synthesis and combustion study of coordination compounds based on 1,2,4,5 tetrazine derivatives. In: Frolov SM (ed) Combustion and explosion, vol 4. Torus Press, Moscow, pp 298–303
71. Li ZM, Xie SH, Zhang JG, Feng JL, Wang K, Zhang TL (2012) Two high nitrogen content energetic compounds: 3, 6-diguanidino-1,2,4,5-tetrazine and its diperchlorate. J Chem Eng Data 57(3):729–736
72. Klapötke TM, Preimesser A, Schedlbauer S, Stierstorfer J (2013) Highly energetic salts of 3,6-bishydrazino-1,2,4,5-tetrazine. Cent Eur J Energy Mater 10(2):151–170
73. Sinditskii VP, Serushkin VV, Egorshev VY, Rudakov GF, Filatov SA, Smirnov SP, Nguen BN (2012) Comparative study of combustion mechanism of guanidine salts: triaminoguanidine and 3,6-diguanidino-1,2,4,5-tetrazine nitrates. Proceedings of the 15th seminar of the new trends in research of energetic materials. Pardubice, 18–21 April, Part I. pp 271–279
74. Sinditskii VP, Egorshev VY, Dutova TY, Dutov MD, Zhang TL, Zhang JG (2011) Combustion of derivatives of 1,5-diaminotetrazole. Comb Exp Shock Waves 47(1):36–44
75. Fogelzang AE, Sinditskii VP, Egorshev VY, Serushkin VV (1995) Effect of structure of energetic materials on burning rate. In: Decomposition, combustion and detonation chemistry of energetic materials. MRS Symp Proc 418, 27–30 Nov. Boston, pp 151–161
76. Serushkin VV, Sinditskii VP, Egorshev VY, Filatov SA (2013) Combustion mechanism of triaminoguanidine nitrate. Prop Exp Pyro 38(3):345–350
77. Sinditskii VP, Egorshev VY, Levshenkov AI, Serushkin VV (2005) Ammonium nitrate: combustion mechanism and the role of additives. Prop Exp Pyro 30(4):269–280
78. Oxley JC, Smith JL, Naik S, Moran J (2009) Decompositions of urea and guanidine nitrates. J Energy Mater 27:17–39
79. Sinditskii VP, Egorshev VY, Serushkin VV, Filatov SA (2012) Combustion of energetic materials controlled by condensed-phase reactions. Comb Exp Shock Waves 48(1):81–99
80. Kaim W (2002) The coordination chemistry of 1,2,4,5-tetrazines. Coord Chem Rev 230:127–139
81. Sinditskii VP, Fogelzang AE (1997) Design of explosive coordination compounds. Ross Khim Zh 41(4):74–80
82. Zhu SG, Wu YC, Zhang W, Mu JY (1997) Evaluation of a new primary explosive: nickel hydrazine nitrate (NHN) complex. Prop Exp Pyro 22(6):317–320

Survey of New Energetic and Eco-friendly Materials for Propulsion of Space Vehicles

Haridwar Singh

Abstract The advent and use of advanced eco-friendly energetic materials to obtain higher and higher energy and reduced vulnerability, improved mechanical properties along with reduced signature profile and extended useful life has assumed very high importance these days. Use of new powerful and green oxidizers like ADN, HNF and ammonium ozonide along with energetic binders like GAP, BAMO and BAMO-THF copolymer can boost specific impulse (I_s) to more than 320 s. Inclusion of energetic plasticizers like tetra azido malonate and tetra azido glutarate can enhance energy further. Likewise, inclusion of nitrogen-rich compounds like nitro guanidinium azides, N8, N10, etc., can boost energy further on higher side. Addition of nano metal powders and nano metal hydrides is likely to enhance burn rates significantly. Thus, there is need to generate reliable exhaustive technical data on the utility of new eco-friendly materials reported recently to obtain unthinkable boost in energy and burn rates.

Nomenclature

ADN	Ammonium DiNitramide
AMMO	3-AzidoMethyl 3-Methyl Oxetane
AN	Ammonium -Nitrate
AP	Ammonium Perchlorate
BAMO	3,3'-Bis(AzidoMethyl) Oxetane
BAMO-THF	Copolymer of 3,3'-Bis(AzidoMethyl) Oxetane and TetraHydroFuran
BDNPA/F	Eutectic Mixture of Bis(2,2-DiNitroPropyl)Acetal/Formal
BP	Boiling Point
Bu-NENA	n-Butyl-NitratoEthylNitrAmines
BTTN	ButaneTriol TriNitrate
CMDB	Composite Modified Double-Base

H. Singh (✉)
High Energy Material Research Laboratory (HEMRL), Sutarwadi, Pune 411021,
Maharashtra, India
e-mail: sharidwar@gmail.com

CP	Composite Propellant
CL-20	2,4,6,8,10,12 - hexanitro- 2,4,6,8,10,12-hexaazaisowurtzitane
DEGBAA	DiEthylene Glycol Bis Azido Acetate
DEGDN	DiEthylene Glycol DiNitrate
DNAPE	DiAzido 3-Nitraza Pentane
DNP	DiNitro Piperazine
DOA	DiOctyl Adipate
DOP	DiOctyl Phatalate
EGBAA	Ethylene Glycol Bis Azido Acetate
GAP	Glycidyl Azide Polymer
HE	High Explosives
HEMRL	High-Energy Materials Research Laboratory
HMX	Cyclotetramethylenetetranitramine, High Melting Explosive (also known as Octogen, Her Majesty's Explosive)
HNC	High-Nitrogen rich Compounds
HNB	HexaNitroBenzene
HNF	Hydrazinium NitroFormate
HTPB	Hydroxyl-Terminated PolyButadiene
HTPBCP	Co-polymer of Hydroxyl Terminated PolyButadieneandCaProlactone
HTPE	Hydroxyl-TerminatedPolyEether
MP	Melting Point
NC	NitroCellulose
NG	NitroGlycerine
NIMMO	3-NitratoMethylMethylOxetane
OB	Oxygen Balance
ONC	OctaNitroCubane
PEP	Propellant Evaluation Program
PETN	PentaErythritol Tetra Nitrate
PGN	PolyGlycidyl Nitrate
PolyGlyn	Polymer of 2-NitratoMethylOxirane
PSAN	Phase Stabilized Ammonium Nitrate
R&D	Research and Development
RDX	Cyclotrimethylenetrinitramine, Research Department eXplosive (also known as Hexogen, Cyclonite, T4, Royal Demolition Explosive)
TATB	TriAmino Trinitro Benzene
TDI	2,4-Toluene diisocyanate
TEGDN	TryEthylene Glycol DiNitrate
TMETN	TryMethylol EthaneTriNitrate
TNAZ	TriNitro AZitidine
VOD	Velocity Of Detonation

1 Introduction

The advent of advanced energetic materials has laid emphasis on the use of energetic ingredients that impart enhanced performance and reduced vulnerability. Improved mechanical properties, reduced signature profile, extended useful life as well as negligible environment effect during manufacture, usage, storage and disposal are other design considerations before choosing a propellant for a particular application. Solid rocket propellants are preferred over liquid and hybrid propellants, in view of their simplicity, reliability, lower cost of propulsion system and ready-to-use system availability. Among solid rocket propellants, both double-base propellants based on NC (nitrocellulose) and NG (nitroglycerine) as major ingredients along with stabilizers, ballistic modifiers and suitable additives to impart special properties to propellant and composite propellants (CP) based on AP-HTPB-Al have been extensively used for both space and military applications [1–6]. However, composite propellants containing AP and Al produce both primary and secondary smokes, which affect guidance and control systems adversely. In addition, AP-based propellants pollute atmosphere due to the formation of hydrochloric acid (HCl) in exhaust products. Furthermore, AP is known to affect functioning of the thyroid gland. Launch of space vehicles produces about 580 tons of conc. HCl and heavy toxic metal oxides. This contaminates stratosphere (30–50 km) above earth including land and water sources. Exhaust plumes could be deposited up to 10 km from launch pad. Space shuttle emits 100 ton HCl from two solid straps on boosters. Launch of nine satellites and six Titan class vehicles will result in stratospheric acidic rain of the order of 0.01 % and ozone depletion of the order of 0.024 % [7]. Figure 1 depicts where we are today with respect to smoke level, whereas Fig. 2 indicates where we should be today and in the future.

Most of earlier approaches on development of eco-friendly propellants were based on ingredient substitution, where toxic materials were replaced with eco-friendly materials. However, it must be also noted that there is no rocket, which is totally clean. This new class of eco-friendly advanced propellants are called *green/clean or alternate propellants*.

2 Powerful Oxidizers

AP has been used as a work horse oxidizer for both conventional and advanced composite propellants all over the globe. Initially, AP was partly replaced with PSAN (phase stabilized ammonium nitrate) to obtain reduced smoke or less smoky propellants. However, this approach produced moderate burning rates and low energy. Present-day requirement is higher and higher energy with clean combustion products. This means propellants with I_s (specific impulse) of >300 s

Fig. 1 Smoky exhaust products

Fig. 2 Smokeless exhaust products

Table 1 Properties of conventional and advanced oxidizers

Oxidizers	AP	AN	RDX	HMX	CL-20	ADN	HNF
Molecular mass, g/mol	117.7	80	222	296	438	124	183
Density, g/cm^3	1.95	1.72	1.805	1.91	2.04	1.81	1.86
Enthalpy of formation kJ/mol	-296	-396	$+70$	$+84$	$+372$	-150	-72
Melting point, °C	235	169	>170	282	>195	93	>115
Decomposition point, °C	235	210	204	287	N/A	134	>115
Oxygen balance, %	34	20	-21.6	-21.6	-10.9	25.8	13.0
Impact sensitivity, cm	15	>49	7.5	7.4	2.5	3.7	3
Friction sensitivity, N	>100	353	120	120	124	>350	20

and with environmentally benign products of combustion. However, this is not possible by using conventional oxidizers, inert binders, non-energetic plasticizers and conventional energetic additives like RDX and HMX. Hence, there is a need to use powerful eco-friendly oxidizers, energetic binders, energetic plasticizers and super energy additives like CL-20 (hexa nitro hexa aza isowurtzitane), ONC (octa nitro cubane), HNCs (high nitrogen-rich compounds), etc. Essentially, green propellant development demands not only the use of eco-friendly energetic materials but also hazard reduction, prevention of toxic release during manufacture and handling, storage and usage without compromising on performance. Inclusion of nitramines like RDX and HMX although produces higher energy with smokeless exhaust products, however, produces low burn rates with higher pressure index values (n). We have reported that inclusion of DNP (di-nitro piperazine) along with lead aromatic salts of organic acids produces plateau effect ($n = 0.1-0.2$) in nitramine-based propellants [8]. It has been reported that a propellant composition having, in mass %, 20 % AP (2 μm size), 45 % HMX, 12 % GAP (glycidyl azide), 18 % TMETN and 4.5 % catalyst gave I_s of 242 s. In this case, HCl content was reduced to 4 %. It was also reported by Russians in 1993 that I_s increases by 8 s with the inclusion of ADN (ammonium dinitramide) in place of AP. So, ADN-based propellants are much in demand these days. Properties of new and conventional oxidizers are given in Table 1 above for ready reference.

We have reported that hydroxyl-terminated copolymer of caprolactone and poly butadiene (HTPBCP), which has high NG solubility, can produce I_s >260 s at 68 % solid loading [9]. We have also found that another propellant composition containing 25 % HTBCP and 20 % HTPB (fuel rich) gave I_s of 900 s in ramjet mode (secondary chamber). Further, we have reported that a fuel-rich propellant containing 70 % zirconium, 18 % AP and 12 % HTPB produced stable combustion even in low-pressure region and gave a burn rate of 7 mm/s at and 7 MPa pressure like conventional composite propellants [10]. By using eco-friendly oxidizers like ADN and HNF (hydrazinium nitro format) with energetic binders like GAP (glycidyl azide polymer), it is possible to obtain I_s >300 s. In addition to ADN (MP-90 °C; density, 1.82 g/cm^3; OB 25.8 %) and HNF (MP, 295 °C; density, 1.90 g/cm^3; OB 13.1 %), other potential oxidizers include ammonium azonide

(NH_4O_3) and ammonium superoxide (NH_4O_2). However, so far no R&D work has been reported on azonides and superoxide-based propellants. HNF is very friction sensitive (2 kg). However, by suitable energetic polymeric coating, we have been able to increase its friction insensitivity to 9 kg level. Now, propellant can be processed. For powerful oxidizers, compounds with low bond energy and high heat of formation are essential. Compounds with groups like N-O, Cl-N and Cl-O bonds are of interest. However, as mentioned earlier, compounds with –Cl –O bond pollute the atmosphere [11–17].

3   Energetic Binders

Earlier innovations in the introduction of NC-NG as binder for composite modified double-base propellants (CMDB) are indication of the advantage of binders containing 0-NO_2 groups. Likewise, introduction of azido group (N_3), which contributes heat release of 355 kJ/N_3 unit, has been considered as a choice to obtain energetic binders. In the family of energetic binders, GAP (glycidyl azide polymer), BAMO (bis azido methyl oxetane), PGN (poly glycidyl nitrate) and their copolymers are very attractive. Low molecular mass azido compounds such as 1,7 diazido 2, 4, 6 trinitraza heptane and 1, 3 diazido 2-nitraza propane in solid propellants widened the scope of use of azido compounds as energetic binders. Properties of a few selected energetic binders are given in Table 2.

It can be seen that BAMO has higher density, low glass transition temperature (T_g) and high impact insensitivity. However, it is semi-solid and hence cannot take higher solid loading of oxidizers and metallic fuels in propellant formulations. To overcome this limitation, we have synthesized BAMO-THF copolymer (mol. mass 2200, T_g – 50 °C, OH value 63). It has been reported that poly-NIMMO and poly-AMMO produce lower burn rates than GAP and have ageing-related problems. While evaluating energetic binders, we have found that a propellant composition containing 60 % RDX and GAP/TMETN as binder and plasticizer produced burn rate of 15 mm/s, whereas another composition containing 60 % CL-20 (hexanitoro-hexa-aza-isowurtzitane) with GAP gave a burn rate of 20 mm/s. Thus, CL-20 has an edge over RDX and HMX. Chlorine-free propellants eliminate both primary smoke of metallic oxides and secondary smoke of aerosol formed by

Table 2 Energetic binders

Binder	Density, g/cm^3	T_g, °C	Impact sensitivity, cm
GAP	1.3	−50	>170
Poly glyn	1.42	−35	>200
Poly NIMMO	1.26	−30	>90
Poly AMMO	1.06	−35	>90
Poly BAMO	1.3	−45	>200

condensed water of the atmosphere (exhaust plume). We have also found that GAP-based fuel-rich propellants produce self-sustained burning without any oxidizer and can achieve I_s >1200 s in ramjet mode (secondary chamber). Thus, among energetic plasticizers, nitro-, nitrato-, and azido-containing compounds are getting the researchers' attention [18–25].

Nitrated HTPB has also been considered as potential energetic binder. Nitration of HTPB has been achieved with N_2O_5. The level of nitration has bearing on thermal stability and mechanical properties of final product. HTPB nitrated to 10 % level produces very good compromise on energetics and mechanical properties and is compatible with energetic plasticizers.

4 Energetic Plasticizers

The function of plasticizer is to modify mechanical properties of polymeric binder by making polymer chain more flexible. Thus, mixed viscosity of propellant is reduced and propellant processing becomes easier. Moreover, plasticizer can improve burn rates and oxygen balance of propellant formulations. Introduction of energetic plasticizer as a replacement of inert or conventional plasticizers like DOA, DOP, triacetin, etc., is another approach to enhance energy. A number of approaches have been followed in the development of energetic plasticizer. Azide-based plasticizer is a very important class. Ethylene glycol-bis azido acetate (EGBAA), di ethylene glycol – bis azido acetate (DEGBAA) are typical examples. The ester group in energetic plasticizer has superior lubricating effect. They have also low vapour pressure and have high BP, low viscosity and good processability. Low molecular mass GAP is a well-known plasticizer, which has been extensively used in gun and rocket propellants, high explosives, etc. Thus, energetic plasticizers range from nitrate esters, azido compounds, azido esters to N-nitramines [26–31].

List of a few potential energetic plasticizers is given in Table 3.

This list is just illustrative and not exhaustive. DNAPE (diazido 3-nitraza pentane) has been found to be highly promising for advanced gun propellant formulations. Like nitramines (RDX and HMX), other powerful high explosives (HEs) have been found to be effective in boosting energy of advanced solid propellants further.

Table 3 Potential energetic plasticizers

Plasticizers	Density, g/cm^3	OB, %	Impact sensitivity, cm
TMETN	1.46	−34.5	8.8
BTTN	1.52	−16.6	4.7
Bu-NENA	1.20	−10.4	–
BDNPA/F	1.39	–	96
TEGDN	1.39	−58	–
DEGDN	1.38	−41	–

5 Energetic Additives

Energetic additives are added to boost energy of propellant further. RDX and HMX have been extensively used in the past. List of some of very powerful additives, which are high explosives in nature, are given in Table 4. These additives are expected to boost energy significantly.

We have found that CL-20 with high molecular mass GAP (mol. mass 2700) produces 5 s higher I_s as compared to HMX-based formulations, and burn rate of 20 mm/s was obtained for this composition at 7 MPa pressure. We have also reported that a propellant composition containing 30 % HNF, 30 % NC and 40 % NG gave burn rates of 30 mm/s at 7 MPa. Likewise, another composition with 40 % HNF, 20 % NC and 40 % NG produced burn rate of 36 mm/s at 7 MPa pressure [32–34]. BDNPA/F with TEGDN could provide improved low temperature properties. HNF is reported to oxidize HTPB. It attacks double bond of HTPB matrix. Thermal decomposition study of ADN indicates that it melts at 94.5 °C and its exothermic decomposition commences at 184 °C. Major products of decomposition include NH_3, H_2O, NO, N_2O, NO_2, HNO_3, etc. Total heat release during decomposition of ADN is of the order of 240 kJ/mol. HNF decomposes at 123 °C. We have also reported that while HNF melts at 124 °C, complete decomposition takes place at 200 °C with release of 27 kcal/mol. energy. TG curve of HNF shows exothermic decomposition at 134 °C. Sixty percent decomposition takes place over a temperature range of 116–130 °C, whereas another 30 % decomposition occurs over a temperature range of 136–166 °C [32–37].

Nitro furazyl compounds have been shown to be attractive as high energy fillers for advanced rocket propellants. David et al. have synthesized high-nitrogen energetic materials such as 3,3 azo bis (6-amino 1,2,4,6 tetrazine), which has a heat of formation of +872 kJ/mol. Trinitroazitidine (TNAZ) is also of high interest as oxidizer cum energetic filler, as it has excess oxygen available for oxidation. It has low MP of 100 °C with good thermal stability (200 °C) and moderate density of 1.84 g/cm^3 and has low sensitivity.

Advent of nano materials has revolutionized the development of advanced solid propellants, explosives and pyrotechnics. Nanosized materials improve the burning

Table 4 Energetic additives to boost energy

Additives	Density, g/cm^3	VOD, m/s	DP, GPa
RDX	1.86	8600	34
HMX	1.91	9100	39
HNB	2.00	9400	42
CL-20	2.1	9400	42
Hepta nitro cubane	1.98	9800	46
ONC	2.0	10,000	47
TATB	1.89	9100	–
HNCs – N8	2.65	15,000	137
- N60	2.67	17,300	196

Table 5 Energy potential of advanced propellants

Composition	I_s, (s)	Density, g/cm^3
AP-HTPB-AI	250	1.70
HNF-GAP (12)-AI	270	–
ADN-GAP	304	–
HNF-BAMO	310	–
HNF-GAP	308	–
ADN-GAP (70:30)	301	1.62
ADN-GAP (80:20)	313	1.67
ADN-Al-GAP (70:10:20)	327	1.73
ADN-Al-GAP (60:20:20)	335	1.78

efficiency of propellants, and non-detectable agglomerates are formed. Higher mechanical properties and reduced slag formation with low signature of propellants are due to small size of oxidized Al nano flakes. It has also been reported that by inclusion of nano materials, burn rates can be increased up to ten times and low-pressure index values can be obtained. DeLuca has reported that rapid combustion of nano Al flakes enhances surface heat release, resulting in higher burn rates. Energy of activation for thermal decomposition of nano powders is much lower than micron-sized metallic powders. Nano-RDX doubles burn rates as compared to micron-sized RDX. While micron-sized RDX gave burn rate of 10 mm/s, nano-RDX produced burn rate of 17 mm/s. Babuk et al. have reported a burn rate increase and a reduction of pressure index values by inclusion of 100 nm Al. Li et al. found that high-temp. decomposition of AP-HTPB propellant is decreased by 15 °C by inclusion of nano materials and nano Ni and nano copper oxide promote decomposition of AP. It has been also found that Cu-Ni-B-based nano composites are more effective catalyst than copper, nickel and boron separately [37–41].

Energy potential of advanced propellants based on powerful oxidizers, energetic binders and energetic plasticizers is given in Table 5.

It is clear from the results presented in the table above that HNF-GAP/BAMO with nano Al or AlH$_3$ is a very attractive propellant candidate to obtain both super energy and clean exhaust products. Likewise, HNCs like N$_8$, N$_{10}$ and N$_{60}$ are expected to boost energy drastically.

Nozzle, liner, insulator and inhibitor also contribute to rocket motor exhaust products. Silicon-based resins are being developed to meet the requirement of non-smoky inhibitor. Energetic oxidizers with conventional binders like HTPB/CTPB may not produce attractive energy, but with energetic binders, energetic plasticizers and energetic additives, energy will go up in an impressive way to more than 330 s. During our search for a powerful energetic plasticizers, we found that two novel tetra azido ester plasticizers, namely, tetra azido malonate and tetra azido glutarate, produced very impressive performance (PEP-2013). These energetic plasticizers are stable up to 200 °C and release heat of 1752.8 and 1774.3 J/g, respectively. Both the plasticizers are impact and friction insensitive with ignition temperatures of more than 250 °C. They are expected to produce

flame temperature of 3164 and 3243 K, respectively, with linear burn rate coefficient of 0.117. Propellants based on these energetic plasticizers produced increase in energy by 100 J/g. Increase in energy level is attributed to the presence of four azido groups in both azido esters [39]. One azido group contributes 357 kJ/mol of energy. Higher energy is also due to positive heat of formation of azido esters ($+581.6$ and $+550.7$ kJ/mol). Weiser has reported that ADN (60 %) – GAP (20 %) – and Al (16 %)-based propellant gave I_s of 293 s (vac.) with density of 1.64 g/cm^3 (41). This propellant produced burn rate of 25 mm/s at 7 MPa pressure. Both CuO and NiO increased burn rates of advanced propellants significantly and produced plateau effect ($n = 0.13$) in 50–100 kg/cm^2 pressure range.

One can expect that inclusion of tetrazoles, triazoles, azitidines and guanidinium azide derivatives as powerful additives can produce considerably higher energy along with clean exhaust products. Further, demands for insensitive and powerful propellants will increase in days to come. In addition, reduction in manufacturing cycle (continuous process), selection of super energy additives, use of nanomaterials, and strict online quality control will assume high importance in years to come. It has been reported that nano-HMX produces higher performance than micron-sized HMX along with improved safety, as impact, friction and shock sensitivity improve considerably with nano-HMX. Hence, one can expect better performance with nano-HMX in high-energy propellants. Nano-RDX, HMX, PETN and TATB have been prepared recently. However, information on comparative effect of nano high explosives versus micron-sized high explosives (HEs) is scanty. Hence, this field is open for more and more R&D work. Amongst HNCs, N_4, N_5, N_8, N_{10}, etc., appear to be viable target molecules to obtain higher energy. N_8 is expected to produce VOD of 15 km/s with density of 2.65 g/cm^3. When realized in large quantity, these materials will change high-energy propellant scene significantly. Nitrogen is a highly benign material. Thus, by inclusion of HNCs, both the objectives of higher energy and eco-friendly combustion products can be met.

Super thermites consisting of metal powder and metal oxides of less than 100 nm produce very high reactivity and are the subject matter of current research. Al-MoO, Al-Teflon and Al-Iodine pentoxide are receiving high attention, both for military and civil applications. Their reaction liberates very high heat, which can be used for various applications.

6   Conclusions

Nanosized oxidizers, energetic binders, energetic plasticizers along with nanosized powerful additives will boost energy very significantly with environment benign exhaust products. Hence, there is lot of scope for innovative R&D work in this challenging area [42].

References

1. Gonser BW (1968) Modern materials; advances in development and applications, vol 6. Academic, New York
2. Shorr M, Zaehringer AJ (1967) Solid rocket technology. Wiley, New York
3. Gold RF (1969) Propellant manufacture, hazards and testing, vol 88, Advances in chemistry. American Chemical Society, Washington, DC
4. Warren FA (1970) Solid propellant technology, vol 10, AIAA selected Reprint. AIAA, Washington, DC
5. Kuo KK, Summerfield M (1984) Progress in astronautics and aeronautics, vol. 90. Fundamental of solid propellant combustion. AIAA, New York
6. Williams FA, Barrère M, Huang NC (1969) Fundamental aspects of solid propellant rockets, AGARDograph 116. Technivision Services, Slough
7. Singh H (2008) Advanced green, clean or alternate rocket propellants. International workshop on processing of composite propellants, H.E.M.R.L, Pune, Oct 18–20
8. Pundlik SM et al (2000) Influence of dinitro pipeazine on the pressure index of extruded double base propellants. J Energetic Mater 18:61–82
9. Bhatt VK et al (1995) Studies on block co-polymer based fuel rich propellants. International workshop on chemical gas dynamics and combustion of energetic materials ,TW95. June 1995
10. Singh H (2013) Emerging trends of R&D in the field of High Energy Materials. 9th international seminar on high energy materials and eco-friendly green applications, Simahara, Kanagawa, 7–9 Oct
11. Borman S (1994) Advanced energetic materials for military and space applications. Chem Eng News 72:18–22
12. Hormuz P, Mama (1996) Solid rocket propellants – latest developments promise significant advances, Spaceflight, vol 38, The British Interplanetary Magazine, London, UK
13. David E et al (2000) A novel high nitrogen energetic material. Angew Chem Int Ed 39(10):1791–1793
14. Chakravarthy SR (1998) Characterization of heterogeneous solid propellants. In: Krishnan S et al (eds) Propellant and explosives technology. Allied Publishers Limited, New Delhi (chapter 3)
15. Pak ZP (1993) Some ways to higher environmental safety of solid rocket propellant applications. AIAA paper 93- 1755
16. Schoyer HFR et al (1995) High performance propellants based on hydrazinium nitro- formate. J Propuls Power 11:856–869
17. Schoyer HFR et al (1995) Advanced solid propellants based on HNF – a status report
18. Frenkel MB et al (1992) Historical development of glycidyl azide polymer. J Propuls Power 8:560–563
19. Vandenburg FJ (1972) Polymers containing azido methyl side chains, US Patent 3,645,317
20. Ahad E (1992) Preparation and uses of branched hydroxyl terminated azide rubbers, US Patent 5,130,381
21. Nair JK et al (2000) Synthesis and characterization of BAMO, its precursor, polymer and co-polymer with THF. In: Proceedings 3rd international conference on high energy materials, Thiruvananthapuram
22. Frenkel MB et al (1981) Synthesis of energetic compounds, CPIA Pub.340, Jannaf propulsion meeting, England
23. Nazare AN et al (1997) Burn rate studies of gas generator propellants containing AP/RDX. Chapter in book, "Challenges in propellant and combustion – 100 years after Noble", Published by Begell House
24. Sanghavi RR et al (2001) Studies on thermoplastic elastomers based propellant compositions. J Energetic Mater 19:79–95
25. Kumari D (2014) Ph.D. thesis, Synthetical approaches to novel azido esters and their applications in LOVA propellants, D.I.A.T., Pune

26. Kumari D, Yamajala KDB, Singh H, Sanghavi RR, Asthana SN, Raju K, Banerjee S (2013) Application of azido ester as energetic plasticizer for LOVA propellants formulations. Propellants Explos Pyrotech 38:805–809
27. Singh H, Shekhar H (2005) Science and technology of solid rocket propellants, Print well, India
28. Agrawal JP, Singh H (1993) Propellants Explos Pyrotech 18:106–110
29. Ghosh K, Pant CS, Sanghavi R, Adhav S, Singh H (2009) Studies on triple base gun propellant based on two energetic azido esters. J Energ Mater 27:40–50
30. Frankel MB et al (1984) US Patent 44,328,17
31. Sayles DC (1991) US Patent 5059260
32. Dendage PS et al (2003) Ecofriendly energetic oxidizers HNF and propellants based on HNF. J Indian Chem Soc 80:563–568
33. Dendage PS et al (2000) Thermal decomposition of HNF and propellants based on HNF. In: Proc 3rd international conference on high energy materials, VSSC, Trivandrum, 6–8 Dec
34. Nair UR et al (2004) Studies on advanced CL-20 based CMDB propellants. J Propuls Power 20:952–955
35. Singh H (2005) Current trends of R&D in the field of high energy materials. Proc int. seminar on high energy material. Japan Explosive Society, Tokyo
36. Talawar MB et al (2005) Novel ultra high energy materials. Combust Explosion Shock Waves 141:264–277
37. Gartner J (2005) Military reloads with nanotech. Technol Rev MIT, USA. Accessed May 2014
38. Brown M (2010) Nanofibres defuse explosives. Chem World, R Soc Chem, Cambridge, UK. Accessed May 2014
39. Granier J (2009) Combustion characteristic of Al nano particles and nano composites, Ph.D. thesis, D.I.A.T., Pune
40. Roberts G, Dreger A (2010) Advanced pyrotechnic or advanced materials discovered in WTC dust, ACS new service weekly
41. Dadson B (2012) Most powerful military explosive for use, ACS new science weekly
42. Weiser (2013) ADN based propellants, 9th International high energy materials (HEMs) workshop, Sagamihara, Kanagawa, Japan

Performance Additives for Hybrid Rockets

Arif Karabeyoğlu

Abstract Addition of performance-improving materials in the solid hydrocarbon fuels of hybrid rockets has been studied extensively both in academia and also in the industry. The primary motivation has been to improve the specific impulse, density impulse, and regression rate performance of the propulsion system. Despite the fact that hybrid rockets are particularly suitable for the inclusion of performance additives, which are typically in solid phase, successful implementation has been quite difficult to achieve. In this paper, we evaluate the feasibility of using performance additives with the following primary objectives: (a) develop a comprehensive survey of fuel additives (and the best binders) for hybrid rockets in order to establish the state of the art in the field, (b) rank these additives based on performance and a number of important practical factors, and (c) recommend a subset of promising additives for further evaluation. Even though, this feasibility study primarily makes use of the information in the open literature, new thermochemical calculations has also been conducted in order to establish the theoretical performance of various propellant systems operating at a common reference state (i.e., chamber pressure, nozzle expansion ratio, etc.).

Nomenclature

Alex	ALuminum EXploded
DCPD	DiCycloPentaDiene
FLOX	Fluorine Liquid Oxygen
GOx	Gaseous Oxygen
HTPB	Hydroxyl-Terminated PolyButadiene
ICBM	InterContinental Ballistic Missile
LGCP	Long Grain Center-Perforated
LOx	Liquid Oxygen

A. Karabeyoğlu (✉)
Mechanical Engineering Department, KOÇ University, İstanbul 34450, Turkey

SPG Inc., San Mateo, CA 94402, USA
e-mail: akarabeyoglu@ku.edu.tr

MON	Mixture of Oxides of Nitrogen
NTO	diNitrogen TetrOxide
O/F	Oxidizer to Fuel ratio
ORPHEE	Operative Research Project on Hybrid Engine in Europe
pDCPD	polyDiCycloPentaDiene
PBAN	PolyButadiene acrylic acid AcryloNitrile
PMMA	PolyMethylMethacrylate
PSU	Pennsylvania State University
PU	PolyUrethane
SF	Solid Fuel
SFRJ	Solid Fuel RamJet
SPG	Space Propulsion Group
USAF	United States Air Force
UTC	United Technologies
XTC	X-ray Translucent Casing

1 Identification of the Important Fuel Properties

For most applications, the primary objective of the propellant formulation activity (including the identification of best fuel additives) for a rocket is to either maximize performance or to minimize the life cycle cost of the system. Depending on the particular application, one of the following can be the cost function for optimizing a performance-driven system: (1) payload mass/gross mass, (2) payload mass/available volume, or (3) range/gross mass or range/available volume. The applications that are driven by cost minimization typically have the following cost functions: (1) cost/payload mass, (2) cost/range, or (3) cost/(payload mass + range). It is important to note that for most practical applications, cost is the primary driver. For example, for a launch vehicle, cost per unit mass of payload is the parameter of interest.

1.1 Advantages and Disadvantages of Using Performance Additives

General advantages and disadvantages of including performance additives in the fuel are summarized in Table 1. As one can see in the table, performance additives introduce a large number of potential disadvantages, and the suitability of an additive depends heavily on the specifics of a selected application.

For example, a system for which the recurring cost is critical (such as tactical missiles), using an expensive fuel additive such as AlH_3 is not an acceptable option. Even for launch vehicle applications, for which the I_s performance is crucial, one needs to evaluate the launch cost per unit mass of payload as a function of

Table 1 Advantages and disadvantages of energetic additives

Advantages	Disadvantages
Improved theoretical I_s	Increased cost of materials/processing
Improved fuel density	Poor availability
Reduced oxidizing agents	Sensitivity to moisture/air
Attenuation of acoustic modes	Finite shelf life
Increased mass generation	Slower chemical kinetics
	Two-phase losses in the nozzle
	Negative impact on mechanical prop
	Added hazard

the additive concentration. For most performance additives, the payload capacity increase associated with the I_s improvement is wiped out by the increase in the cost of materials and processing. However for certain classes of applications, such as in-space missions, performance consideration supersedes the cost issue.

1.1.1 Critical Properties of Fuels with Performance Additives

A list of critical properties of performance additives, which propulsion engineers need to consider at the propellant formulation stage of the design cycle, is given for hybrid rockets:

(a) Delivered I_s improvement: Theoretical I_s improvement, which can be simply predicted by thermochemical calculation codes, should be estimated in the first evaluation. However the effects of additives on the oxidizer to fuel ratio (O/F) shift, combustion efficiency, and nozzle efficiency (two-phase flow losses) need to be considered as well. The quantification of losses due to O/F shift involves the internal ballistic calculations in the hybrid motor. For most systems c* efficiency drop due to O/F shift is very small. Combustion efficiency needs to be determined based on subscale and full-scale motor tests. If available, data from older programs can be helpful. The mass fraction of condensed phase at the nozzle entrance, as predicted by thermochemical calculations, would be a good first indicator for the two-phase flow losses.
(b) Density impulse improvement: Addition of high-density energetic additives can potentially reduce the volume of the propulsion system. Note that optimum O/F for density impulse is different than the O/F that maximizes I_s.
(c) Availability: From a direct procurement perspective, long-term availability of the additive in the nation or ease of importing is a critical consideration. Production technology base and availability of the feedstock in the nation are important factors, if direct procurement is not feasible.
(d) Cost: Cost is always a primary driver in the selection of additives. Price per mass of the additive material and other logistical cost factors (changes in safety procedures, transportation, handling, storage, processing of the propellant) need to be included in the selection process.

(e) Hazard: Acute or chronic toxicity or carcinogenic nature of the additive, sensitivity to moisture and oxygen in the environment, and potential for violent chemical decomposition leading to an explosion are important hazard modes as cost drivers.

(f) Lifetime: Shelf life in storage (aging in the storage) and shelf life in binder (aging in the motor) are critical practical considerations.

(g) Ballistic effects: The following are important effects on the ballistic behavior that the designer must take into account: (1) effect on fuel regression rate, (2) effect on fuel mass generation rate, (3) possible introduction of pressure dependency to the regression rate, (4) effect on fuel mechanical properties (ductility, viscoelastic properties, etc.) (5) compatibility with the liner materials, (6) slag formation and accumulation of metal oxides in the motor, (7) effect on motor stability (especially acoustic modes), (8) mass fraction of oxidizing agents in the nozzle, (9) influence on nozzle erosion rate by changes in the concentration of the oxidizing agents in the nozzle flow, and (10) shift in optimum O/F.

2 Identification of Candidate Materials

The oxidizers, performance additives, and binders which are included in this study are described in the following paragraphs.

2.1 Oxidizers

LOx Liquid oxygen is arguably the most potent practical oxidizer in the field of rocket propulsion. It is readily available and affordable and delivers high performance. The only issue is the lack of storability under earth conditions. This is classified as a high-energy oxidizer for the purposes of this study.

N_2O_4 (NTO) Dinitrogen tetroxide (NTO) is an earth-storable, high-density oxidizer that delivers moderate I_s performance. NTO was extensively used in earlier ICMB's and launch vehicles (such as the Titan system) but became unpopular due to its toxic and nongreen nature. We include NTO in the studies in order to evaluate the influence of performance additives for a high-density oxidizer with moderate I_s capability.

N_2O Nitrous oxide is also a practical oxidizer with self-pressurization characteristics, good availability, and reasonable cost. However it is a low-energy oxidizer (low oxygen mass in the molecule) and also has low density when used under self-pressurizing conditions.

2.2 Performance Additives

The field of possible performance additives for rockets is quite extensive. Even though we have included a reasonable number of chemicals in this study, it still is a small fraction of all possibilities. The following strategy has been adapted in the selection process:

(a) This is not a purely academic study. Our approach is on the practical side and we are primarily interested in finding additives that can be implemented in operational systems after a relatively brief development period.
(b) Exotic materials have not been included due to their lack of availability, extreme hazards, etc.
(c) Highly toxic materials such as Beryllium and its compounds are excluded.
(d) We have selected the most promising and most practical members of each of the following group of additives: (1) metals, (2) metal hydrides, (3) boron compounds, and (4) strained hydrocarbons. Boron, which is a metalloid, is grouped together with metals.
(e) Micron- and nano-sized versions will be compared in a qualitative manner.

The following additives are selected for consideration in this study: (1) metals (micron-sized), such as Al, B, and Mg; (2) metals (nano-sized), such as Al and B; (3) metal alloys, such as Mg_xB_y; (4) metal hydrides, such as $LiAlH_4$, AlH_3, MgH_2, and $LiBH_4$; (5) boron compounds, such as $B_{10}H_{14}$ and NBH_6; and (6) organic molecules, such as two strained hydrocarbons, cubane, and iyvane [8].

2.3 Fuel Binders

Even though the primary thrust of this work is on the performance additives, we have also conducted a comparative study on some of the most popular binders used in hybrid rockets.

Paraffin Waxes Binders that are based on paraffin waxes [1] have the following inherent advantages:

Hydrophobic: This is a critical property, since a large number of performance additives are sensitive to moisture in the air.
Low cost: Paraffin waxes are quite cost-effective. Commonly used waxes cost less than 2–3 \$/kg.
Readily available: A wide range of paraffin waxes can be purchased in the open market.
High performance: Normal alkanes have the best H/C ratio of all hydrocarbons. Paraffin waxes do not contain any oxygen in the molecule which also helps with the I_s performance.

High regression rate: The liquid entrainment mechanism results in regression rates three to five times faster than the classical polymeric fuels. This leads to the design of single circular fuel grains which results in excellent fuel utilization, typically better than 98 %.

Green and nontoxic: Paraffin waxes are green fuels. They are not toxic. The primary combustion products are CO_2 and water.

Inert/infinite life time: Due to the fully saturated nature of paraffin waxes, they are resistant to chemical attacks. Their shelf life is practically infinite.

Extensive experience base: Paraffin-based fuels have been invented in the late 1990s. A wide range of programs in the United States, Japan, Europe, Brazil, China, and other countries have been based on paraffin-based fuels. Paraffin-based motors as large as 0.6 m in diameter have been tested successfully in the past.

HTPB HTPB is an elastomeric material which is also commonly used as hybrid rocket fuel in the world. Its wide use in hybrids (compared to other polymers including other elastomers) is primarily based on convenience. HTPB, as a solid rocket binder, is readily available and a well-known material to the researchers in this field, who primarily come from a solid rocket background. One important technical advantage of HTPB is that it is one of the fastest burning polymeric fuels used in the hybrid rockets. The existence of the hydroxyl end groups and the non-hydrophobic nature of HTPB make it a problematic binder for certain performance additives (such as metal hydrides).

Other Polymers Some other polymers shall also be considered in this study. Polymethylmethacrylate (PMMA) is a commonly used polymer in hybrid rockets (especially in the early history). The big issue with PMMA is the fact that it contains a large mass fraction of oxygen on the molecule, which leads to a reduction in the I_s performance. The other interesting polymer which is worth looking into is polydicyclopentadiene (pDCPD). This polymer has been shown to be compatible with lithium aluminum hydride.

3 Literature Search: Hybrid Rocket Fuel Additives

A comprehensive literature search has been conducted on the performance fuel additives for hybrid rockets. The primary results and conclusions from the literature are discussed in the following paragraphs.

Since most energetic fuel additives are in solid phase under ambient conditions and all high-energy oxidizers are naturally in the liquid phase, hybrid rockets are the best type of chemical systems to achieve very high performance levels (at least theoretically). One of the early papers that address the high-performance potential of hybrids is presented by Rocketdyne engineers [2]. This study covered an evaluation of a high-performance tripropellant system based on the combination $F_2/Li/H_2$. The objective was to verify the extremely high performance that can be achieved by this propellant combination. The investigation had theoretical studies along with motor

testing activities. The paper shows a tremendously high theoretical I_s value of 542 s for this tripropellant system for a chamber pressure of 500 psi (about 3.4 MPa) and an area ratio of 60:1. Note that close to 100 % c* efficiency values have been achieved in motor tests with the F_2 oxidizer for all operating conditions, indicating that the delivered I_s would be fairly close to its theoretical value. Note that for this particular work, lithium was injected in the liquid phase. In the early 1970s, the Chemical Systems Division of UTC tested Li/LiH/PBAN/FLOX combination (true hybrid since Li/LiH/PBAN was the solid fuel) at thrust levels up to 40 klbf (about 178 kN). The motors developed over 400 s of measured I_s.

An excellent review of metals and other performance additives for hybrid rocket fuels is given by Risha et al. [3]. In this review article, the focus was on the effect of additives on the fuel regression rate. As discussed earlier in this report, in our perspective, the primary goal of the energetic additives is to improve I_s and density impulse performance, not to enhance the fuel regression rate. In the following paragraphs, we summarize the important points made by Risha et al.

Metallic additives improve the heat of combustion and the adiabatic flame temperature. The increased gas phase temperature and radiating particles are expected to increase the regression rate. The I_s performance of the rocket motor would also improve as a result of higher combustion product temperature. However molecular weight, two-phase flow losses, combustion efficiency are equally important factors in establishing the I_s performance. Thus in our opinion strategies used to improve the regression rate and I_s performance are not necessarily common.

Gravimetric and volumetric heats of oxidation for metallic additives, along with the HTPB binder, are given in the paper. As discussed in the paper, Be is the best metal additive in terms of gravimetric heat release. Despite this fact, Be is not widely used due to its highly toxic nature. The concentration has historically been on aluminum and boron. In our opinion, the gravimetric performance given for per fuel mass basis is not a good indicator of performance for rocket motors. Heat release per unit propellant mass (includes oxidizer mass as well as fuel mass) is believed to be a better parameter. Energy of combustion per unit propellant mass for light elements has been plotted for combustion with oxygen in Fig. 1. It is interesting to note that, on propellant mass basis, lithium outperforms boron. The volumetric performance of metals is more impressive than the gravimetric performance due to their higher densities compared to the polymeric baseline fuel HTPB.

US Air Force had a significant program on hybrid rocket fuel additives in the 1960s. The Sandpiper Target Drone (an operational hybrid system) actually had 10 % Mg powder (by mass) in PMMA fuel binder. The mix was successfully burned with the MON-25 (mixtures of oxides of nitrogen) oxidizer. They have also tested other metal powders such as Al, B, and even Be but did not incorporate in an operational system.

Most of the early effort was conducted using micron-sized particles. Recently nano-sized particles have been included in the studies. The advantages of the nano-sized particles are shorter ignition delay, shorter burn time and better combustion efficiency, higher particle-specific surface area, and greater flexibility in designing
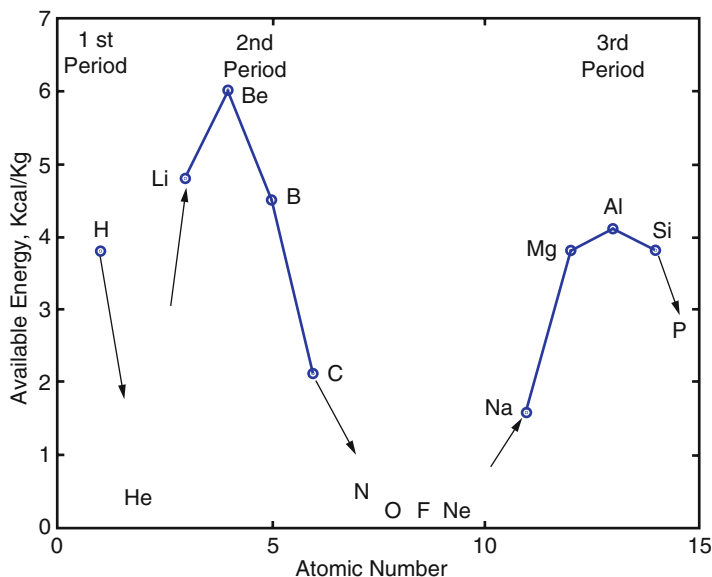
Fig. 1 Available energy per unit mass of propellant. Oxidizer is oxygen

fuel systems with desired physical properties. The nano-sized particles also have significant disadvantages including higher cost, higher oxide mass fraction (if not coated), and difficult processing.

With the exception of the following flight programs, all of the research conducted with energetic additives was limited to ground testing.

- Sandpiper Target Missile (USAF): Long-burning sustainer motor. Thus, despite the slow regression rate (10 % Mg in PMMA fuel), a single circular port design was implemented.
- Lockheed Martin's Hyser sounding rocket: >40 % Al in HTPB. 60,000 lbf (about 265 kN) thrust multiport motor burning with LOx.

Lithium-Based Particle Additives Lithium is a highly reactive, light alkali metal. The volumetric heat release is low compared to the other metallic additives due to its low density. One of the research programs using Li-based additives was conducted by Smoot and Price [4]. LiH at concentrations up to 90 % by mass (butyl rubber binder) has been burned in small-scale motors. The oxidizer was FLOX (F_2 concentration optimized based on fuel composition). The chamber pressures were lower than the typical practical range of operation which leads to a high level of pressure dependency (out of the diffusion-limited regime). Increase in the LiH additive concentration has improved the regression rate. But the author of this paper believes that a good part of this increase is related to the increase in the F_2 concentration in the FLOX oxidizer (as LiH % is increased, F_2 concentration has also been increased to optimize the propellant). A similar study has been conducted

by Osmon [5] using $LiAlH_4$ and 90 % H_2O_2. The binder was PE polymer. The pressure levels for these tests were more realistic. An impressive $LiAlH_4$ loading of 95 % by mass has been achieved in this study.

Aluminum-Based Particle Additives Aluminum is a very practical fuel additive, which is relatively benign and abundant (thus cost-effective) and delivers reasonable performance improvement with low-energy oxidizers. Thus, Al has been studied extensively in the micron- and nano-sizes with different particle shapes and concentration levels. In the 1960s, UTC in Sunnyvale California has fired eight motors with Al powders [6]. Different oxidizer/fuel compositions have been tested. Unfortunately the reported data is incomplete to make a full evaluation of the test results.

Strand [7] has studied the combustion of aluminized HTPB in a slab burner configuration. A double-slab configuration has shown 40 % higher regression rate compared to a single slab, indicating the importance of radiation for the aluminized fuel grains. Note that the difference between the single- and double-slab configurations for neat HTPB was negligible. Fuel grains containing 40 % aluminum powder with mean particle size ranging from 40 to 95 μm have been tested. The low-flux test conditions along with high radiation levels associated with aluminized fuel grains made the regression rate strongly dependent on the chamber pressure. It has been shown that the particle size did not have an effect on the regression rate.

George et al. [8] has studied the effect of aluminum addition in the HTPB grains in the 1990s. Al particle size was 28 μm and additive concentration was approximately 20 % by weight. It has been estimated that addition of aluminum has reduced the combustion efficiency from 93 to 89 %, indicating incomplete combustion for the aluminum particles in the motors with grain lengths ranging from 25 to 40 cm.

Boron-Based Particle Additives In this category, high-purity boron and boron-containing molecules such as decaborane has been studied. The major advantage of boron is its high combustion energy per unit mass/volume and its relative abundance. The largest issue with boron is related to its difficulty to ignite, which could potentially lead to poor combustion efficiencies. Under a contract from USAF, UTC has studied the combustion of boron in solid fuels. A total of six motors have been fired with 20 % B (by mass) in the solid fuel. Unfortunately the reported data is inadequate to establish a regression rate law. Due the high gravimetric heat output, boron is a very effective fuel additive for SFRJ systems. In fact it is much more effective as a SFRJ fuel additive compared to a hybrid rocket fuel additive.

Environmental aspects are divided into three groups: (1) atmospheric, (2) noise, and (3) other impacts (such as emissions associated with the manufacturing process). The atmospheric effects can be evaluated based on the exhaust products. Due to the lack of chlorine-based compounds, hybrids and liquids have distinct advantage in this category compared to solid rocket motors. Regarding the addition of performance additives, the effect of metal oxides on the greenhouse effect and

ozone depletion needs to be understood. Even though this effect is believed to be small, there is no significant research conducted to support this statement.

Lips et al. [9–11] of German Research and Development for Air and Space Travel has studied the combustion of highly aluminized (and other metals as well) fuel grains with FLOX oxidizer. The following parameters have been studied:

Effect of Binder Type Lips looked into five different polymers as binders and found that the type of binder used in the test had a significant effect on the fuel regression rate. The aluminum loading was 60 % by mass and the oxidizer contained 40 % F_2 by mass. It has been determined that polymers that are forming a char layer burned faster.

Effect of Metal Additive Type Pure Al, Si, B, and Mg and 97 % A and l/3 % Mg have been tested at 60 % level in PU binder. Surprisingly, the type of metal additive had a small effect on the regression rate.

Effect of Particle Size The particle size (micron size) also had a small effect on the regression rate. Increasing the mean Al particle size from 32 to 200–250 μm did not significantly change the regression rate.

Effect of Metal Additive Concentration Increasing the Al concentration from 40 % to 60 % has increased the regression rate by almost 40 %. Further increase in the concentration did not have much influence on the regression rate. The reason for this saturation effect is believed to be related to the agglomeration of aluminum on the surface. Note that agglomeration would reduce the heat release and heat transfer to the surface.

Effect of Oxidizer Type Increasing the F_2 in the oxidizer had a very strong effect on the regression rate. Going from 0 % F_2 to 100 % F_2 has increased the regression rate by threefold. This is believed to be caused by two factors: (1) AlF_3 has a low sublimation temperature (1550 K) leading to no accumulation of the condensed combustion products on the surface as opposed to Al_2O_3 which is expected to be in the liquid phase in the motor and (2) higher heat of combustion with F_2.

The Penn State group has been very active in the field of energetic additives for hybrid rockets. The works of Kuo, Risha, Evans, and Boyer [12–15] are briefly summarized in the following paragraphs.

Tests were conducted at laboratory scale using a two-dimensional slab burner (with quartz windows) and also in a tube burner configuration. Gaseous oxygen is the primary oxidizer used in the tests. The binder was HTPB for most tests. A nano-sized aluminum powder (Alex) with 100–150 nm mean particle size has been used in one of the early series of tests. Addition of Alex powder at 20 % level has increased the regression rate and mass generation rate over neat HTPB by 43 % and 70 %, respectively. Addition of micron-sized aluminum particles at 20 % level has resulted in much lower improvement in the regression rate (about 12 %) and mass generation rate (40 %) compared to the nano-aluminum-based formulation. In the case of Alex additive, the nano-sized particles are shown to ignite close to the fuel surface, thus

significantly improving the heat transfer. For the micron-sized particles, the ignition takes place away from the fuel surface, limiting heat transfer rate.

The tubular hybrid motor tests have been conducted at two different scales. The smaller one, the LGCP system, could accommodate fuel grains that are 40.6 cm long. The longer system, XTC, has a grain length capability of about 120 cm. The XTC system used a thermoset plastic casing allowing for X-ray imaging of the burning surface.

A large number of tests have been conducted using the small tubular system. A total of 19 fuel formulations have been tested. It has been determined that particle size, particle shape, and coating on the aluminum powder had significant influence on the regression rate and combustion efficiency of the system.

The two formulations that have shown the largest regression rate improvement are (a) SF-12: 13 % micron-sized aluminum powder and (b) SF-13: 13 % Viton-A-coated Alex particles. It is very interesting to realize the same level of improvement with micron-sized and nano-sized particles at the same concentration. There is no obvious explanation for this observation. The Viton-coated Alex formulations have burned faster than the uncoated formulations. Note that Viton is a fluorinated elastomer and the released fluorine atoms during the pyrolysis of the polymer are believed to enhance the ignitability of the metal surface. Fuels loaded with Alex powder more than 13 % have presented unstable combustion behavior. This is believed to be related to the formation of a molten layer on the fuel surface and sloughing of this layer periodically.

Burning of metallized formulations with the less energetic oxidizer N_2O have led to lower regression rates compared to GOx. Note that similar trends have been observed with non-metallized formulations in other programs.

Paraffin has also been tested as an alternative binder. Tests conducted by Evans et al. at PSU [16] with paraffin (loaded with carbon black) have shown regression rates higher than the ones given by the Stanford group. This difference is believed to be related to (1) differences in the paraffin wax and (2) possible differences in the data reduction methodologies (averaging technique for oxidizer mass flux). Silberline aluminum flakes have been used with paraffin. Thirteen percent flake concentration resulted in an approximately 30 % improvement in the regression rate. The two-dimensional nature of the Silberline additive is believed to be critical in keeping the viscosity of the melt layer low. The entrainment mechanism removes the particle-loaded droplets off the surface in the case of paraffin-based fuels. For HTPB binder, the aluminum particles are collected on the surface (forming agglomerates) until they are sloughed off the surface.

The Viton-coated nano-Al particles delivered better c^* and I_s efficiencies than the uncoated systems. This shows the positive influence of Viton products on ignition kinetics. Formulations with nano-sized particles have delivered better efficiencies than micron-sized systems. This can be explained with the d^2 law for the burning time of particles.

Scaling up to the XTC (larger tubular burner) system has resulted in the reduction of regression rate for neat HTPB. In the large-scale experiments, no regression rate improvement has been observed with the addition of 13 % Silberline powder.

Note that the same formulation resulted in a 30 % increase in the regression rate in the small-scale testing. Accumulation of molten metal on the burning surface and periodic sloughing has been speculated to be the reason for the lack of improvement at large scales. As far as the author of this paper is concerned, there is no satisfactory explanation for this phenomenon, indicating complex (and possibly scale-dependent) nature of combustion with metallic additives. The formulations with metallic additives did not follow a power law type regression rate.

In the early 2000s, Ronald Humble [17, 18] has published papers looking into a new binder (dicyclopentadiene – DCPD) and a new promising performance additive (Li_3AlH_6) for hybrid rockets. The pDCPD polymer has a number of useful features for its use in hybrid rockets. Its high heat of formation (+230 kJ/mol) leads to an I_s performance slightly better than RP-1 and HTPB. With this polymer, a wide range of mechanical states are accessible depending on the chain length and cross-linking. The hydrophobic nature makes it suitable for use with metal hydrides. Density of pDCPD is slightly higher than HTPB (specific density is 0.97). It has been determined that the biggest issue with this binder was its low regression rate (about 50 % of HTPB). Humble also used a less common metal hydride Li3AlH6, which he claimed that it had a very large positive heat of formation leading to excellent I_s performance. Note that this performance prediction is based on the estimated heat of formation, and the impressive I_s improvement with this hydride (or its high heat of formation) has not been demonstrated in any motor testing.

A more recent work on pDCPD and the more conventional hydride $LiAlH_4$ is discussed in [19]. The oxidizer was 98 % hydrogen peroxide and the initial port diameter of the fuel was 4.09 cm. The main conclusions from this study were (1) the higher regression rate of neat pDCPD was comparable to low-density PE and (2) poor combustion efficiencies for fuels containing the metal hydride (I_s efficiency dropped by more than 10 percentage points).

The possibility of using ammonia borane (NH_3BH_3) as a fuel additive for hybrid rockets has been considered by Weismiller et al. [20]. In this study, addition of ammonia borane into a paraffin-based binder has been investigated experimentally. Gaseous oxygen is selected as the oxidizer and the tests were conducted in a laboratory-scale tube burner (with 5.5 in grain diameter). Ammonia borane is included in the paraffin binder in the powder form. The specimens were prepared by casting into a stationary mold. The inclusion of ammonia borane in the 10 % level moderately improved the regression rate. But concentrations over 20 % by mass have resulted in a reduced improvement or even a decrease in the linear burn rate of the fuel. The c* efficiency was claimed to be close to 100 % for all formulations. But the I_s efficiency is shown to be only 60 %. A nozzle efficiency of 60 %, especially for neat paraffin formulations, is too low to believe. We suspect that the c* efficiency estimation (or measurement) is at fault. Note that ammonia borane is being investigated extensively as a promising hydrogen storage medium. Details associated with its synthesis, safety, and performance are discussed in [21].

An effective optical method has been developed to observe the combustion of a variety of fuel grains without and with metallic additives by Prof. Luigi T. DeLuca of Politecnico di Milano [22]; further data are reported in Chap. 25 of this book. In this method, the combustion zone has been tracked visually over time to determine the fuel regression rate of cylindrical fuel grains, mostly with a circular central port of 4 mm initial port diameter and 30 mm length. Using this technique, accurate time histories of the regression rates for neat HTPB, neat paraffin, and metallized formulations have been obtained. The measured data did not follow a classical power law burn rate behavior especially in the early portion of the tests. We suspect that this is due to the extremely small port diameters existed in the early parts of the combustion tests. Similar effects were observed by Evans et al. at Penn State, testing the XTC system with 2.5 in (63.5 mm) port previously mentioned; for details, see Fig. 12 and Fig. 6 of [3] and [16] respectively, Fig. 11-13 of AIAA 2004-3821, and Fig. 6 of AIAA 2005-3909. Similar results were also obtained in the experimental investigations by Zhao Qin, PhD Thesis, NUST, 2015 and Tang Yue, Ph.D. under way, NUST in China. Testing with various Alex additives in HTPB baseline has shown a regression rate improvement in the 20–45 % range. The coated Alex powders (Fluorel + ester and ester coated) have resulted in higher improvements and also more uniform burn rate improvements over time.

A comprehensive review of the European ORPHEE program (a hybrid rocket research project) has been given by Carmicino et al. [23]. In this program, two performance additives (MgH_2 and nano-Al) have been tested in the HTPB binder using a laboratory-scale burner. The nano-Al was an Alex type powder (uncoated with an average diameter of 50 nm) and MgH_2 was obtained from Sibthermochim Russian Federation (mean diameter of 47 μm). MgH2 was added at the 5 % (by mass) level and the nano-Al was at the 15 % concentration by mass. Oxidizer was gaseous oxygen. Motor testing has shown that addition of the powders did not improve the regression rate of the HTPB-based fuel. Testing with the aluminum power also generated some low-frequency instabilities. This is speculated to be related to the accumulation and discharge of the slag forming on the nozzle throat. The unrealistically high c* efficiencies for the aluminized fuel grains are also attributed to the slag coating of the nozzle throat. Tests conducted using the MgH_2 powder have resulted in 5 % drop in the c* efficiency compared to the neat HTPB.

Combustion of $LiAlH_4$-loaded paraffin grains has been investigated by Larson et al. [24]. In this study, $LiAlH_4$ concentrations up to 28 % by mass have been burned with gaseous oxygen in a small laboratory tube burner. A detailed description of the casting process (for the powder containing paraffin fuel grains) is included in the paper. Evidently, multilayer spin casting method employed for the production has resulted in good-quality fuel grains. Tests were conducted at low chamber pressures and they had short steady-state durations (due to long ignition transients and long oxidizer lines that needed to be purged at the end of the test). We believe that these undesirable virtues compromised the accuracy of the regression rate data. It is also reported that a large quantity of unburned paraffin and $LiAlH_4$ were accumulated in the post-combustion chamber area. This mass was measured and used to correct

the regression rate estimation. The authors have stated that including the hydride additive up to the 28 % level did not conclusively change the regression rate of the fuel.

A good review of the nano-sized energetic additives has been given from the Russian perspective in [25]. It is believed that compatibility of the additive with the binder and aging are the two major challenges that need to be overcome.

Effect of Alex particle addition to HTPB has been investigated in [26]. The oxidizer was gaseous oxygen and a very small burner has been used in the tests. Reasonably high regression rate improvements have been realized with the well-dispersed formulation H0-Alex at low-oxidizer fluxes. The improvement was much less at increased flux levels most likely due to the reduction of concentration oxidizer beneath the flame zone.

Another recent study on metal hydride additives for solid and hybrid rocket systems has been conducted by Maggi et al. [27]. This is a theoretical study that has considered the performance gain associated with the addition of eight different metal hydrides in HTPB binder. The oxidizer for the case of hybrid rockets was limited to liquid oxygen. AlH_3 was the only hydride that has generated an appreciable gain in performance. A short but quite useful discussion on the emission issues has also been included in this paper.

4 Thermochemical Calculations

In this section, the results of thermochemical calculations conducted specifically for the direct comparison of the selected propellants will be discussed. New calculations (as opposed to limited data from the literature) were essential to compare different systems under identical operational conditions.

All of the hybrid rocket calculations discussed in this study have been conducted for the chamber pressure of 500 psi (34 atm), nozzle area ratio of 70:1. Shifting equilibrium and vacuum expansion is assumed. Important properties of all ingredients used in the thermochemical calculations have been listed in [28].

4.1 Results

Since most hybrid rockets utilize binders with high H/C ratio (such as paraffin waxes), even with no fuel additives, hybrids deliver good I_s performance (comparable to hydrocarbon-based liquids). Moreover, unlike liquid engines, easy implementation of metal additives into the solid matrix makes it possible to improve the I_s performance significantly for hybrid rockets.

Performance of chemical rockets is best displayed and compared in the specific impulse (I_s) and density impulse (I_v) space. I_s-I_v pairs have been plotted in Fig. 2
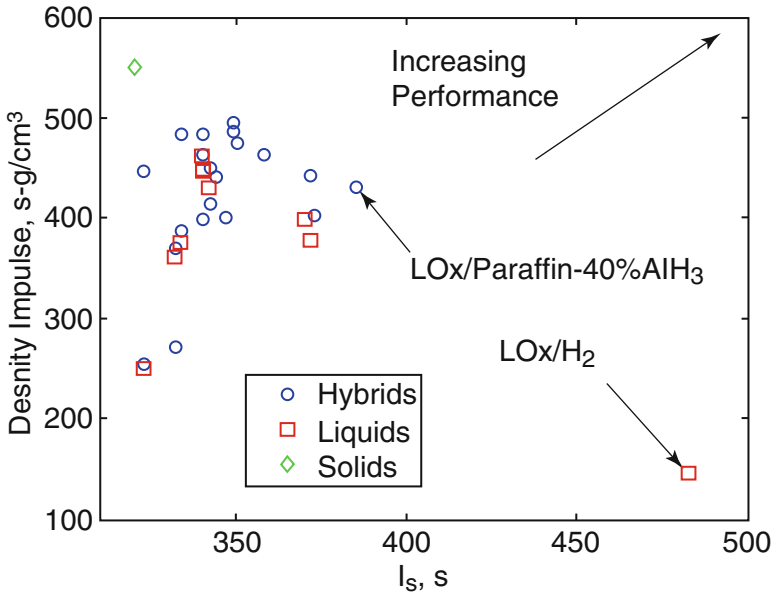
Fig. 2 Vacuum I_s as function of O/F for various hybrid systems

for solid, liquid, and hybrid rocket propellants. The figure show that hybrids loaded with performance additives do significantly better than hydrocarbon-based liquids.

4.1.1 Effect of Additive Type

The effect of additive type on the theoretical I_s performance and optimum O/F has been investigated for the selected additive materials. The results are summarized for metals, metal hydrides, boron compounds, and strained hydrocarbons in the following sections. Note that in this section, additive concentration is selected to be 40 % by mass for all additives. This is believed to be a conservative value for solid loading in practical systems. Paraffin wax with the chemical formula $C_{32}H_{66}$ has been selected as the binder for this part of the study. Results for three oxidizers have been obtained: (1) high-performance oxidizer, LOx, (2) intermediate-performance oxidizer, NTO (N_2O_4), and (3) low-performance oxidizer, N_2O. Results with neat paraffin have also been included in the tables for easy comparison purposes.

Metals and Metal Alloys Aluminum, boron, magnesium, and a specific Mg_xB_y (25 Mg, 75 % B by weight) alloy have been investigated as performance additives for hybrid rocket systems. It is shown that addition of metals with the high-performance oxidizers did not help the performance. In fact the optimum I_s has reduced slightly for all additives. This is due to the increased dissociation effect at elevated temperatures and the increase on the average molecular weight of the combustion products. One important effect of metal addition is the reduction in

the optimum O/F which might be beneficial for certain applications (i.e., systems demanding less liquid mass). Unlike LOx, significant improvements have been achieved by the addition of metals for the lower-energy oxidizers NTO and N_2O. Addition of aluminum generated the best performance followed by boron, MgxBy alloy, and magnesium, respectively.

Metal Hydrides Unlike the metallic additives, hydrides have increased the performance for all systems, including the high-energy oxidizer, LOx. A drop in the optimum O/F is also observed for metal hydride additives. The performance increase is a direct consequence of inclusion of hydrogen in the molecules, unlike the pure metals. AlH_3 proved to be the best performing additive, whereas MgH_2 generates the least performance improvement.

Boron Compounds Two promising boron compounds, ammonia borane (NBH_6) and decaborane ($B_{10}H_{14}$), have also been studied as additives. Both materials were quite effective in improving the I_s performance for all oxidizers. Reduction in the optimum O/F was mild for these materials.

Strained Hydrocarbons Finally two hydrocarbons with strained bonds (high heat of formation) have been studied. Their effect on the I_s performance proved to be quite limited due to the low H/C ratio for these materials.

All additives included in the study have been summarized in Tables 2 and 3. Metal hydrides and boron compounds are the winners of the selected group of

Table 2 All additives I_s summary table

Additive (40 %)	High-energy oxidizer, LOx		Medium-energy oxidizer, NTO		Low-energy oxidizer, N_2O	
	I_s*, s	ΔI_s*, s	I_s*, s	ΔI_s*, s	I_s*, s	ΔI_s*, s
Neat	367.1	0	337.3	0	318.9	0
Metals						
Al	366.5	−0.6	343.6	+6.3	327.7	+8.8
B	363.6	−3.5	339.0	+1.7	324.0	+5.1
Mg	360.0	−7.1			324.5	+5.6
Mg1B₃	361.5	−5.6	338.3	+1.0	323.7	+4.8
Metal hydrides						
AlH₃	379.1	+12.0	351.2	+13.9	330.5	+12.0
MgH₂	368.4	+1.3	343.5	+6.2	325.9	+7.0
LiAlH₄	372.8	+5.7	346.5	+9.2	328.1	+9.2
LiBH₄	373.9	+6.8	342.9	+5.6	323.4	+4.5
Boron compounds						
NBH₃	377.2	+10.1	345.7	+8.4	324.7	+5.8
B₁₀H₁₄	376.3	+9.2	346.9	+9.6	327.4	+8.5
Strained hydrocarbons						
Cubane	372.3	+5.2	342.3	+5.0	322.9	+4.0
Ivyane [8]	369.7	+2.6	339.7	+2.4	320.9	+2.0

Table 3 All additives I_v summary table

Additive (40 %)	High-energy oxidizer, LOx I_v, 10^5 kg s/m^3	ΔI_v, %	Medium-energy oxidizer, NTO I_v, 10^5 kg s/m^3	ΔI_v, %	Low-energy oxidizer, N$_2$O I_v, 10^5 kg s/m^3	ΔI_v, %
Neat	3.954	0	4.737	0	2.489	0
Metals						
Al	4.351	10.05	4.749	0.25	2.618	5.20
B	4.244	7.33	4.702	−0.74	2.551	2.50
Mg	4.108	3.90	–	–	2.563	2.99
Mg$_1$B$_3$	4.203	6.29	4.661	−1.60	2.551	2.47
Metal hydrides						
AlH$_3$	4.253	7.56	4.666	−1.49	2.590	4.06
MgH$_2$	4.123	4.29	4.565	−3.64	2.551	2.48
LiAlH$_4$	3.926	−0.71	4.354	−8.09	2.525	1.44
LiBH$_4$	3.821	−3.37	4.298	−9.26	2.443	−1.84
Boron compounds						
NBH$_3$	3.940	−0.36	4.392	−7.29	2.472	−0.69
B$_{10}$H$_{14}$	4.033	1.99	4.499	−5.01	2.514	1.02
Strained hydrocarbons						
Cubane	4.142	4.75	4.591	−3.08	2.494	0.20
Ivyane [8]	4.050	2.44	4.513	−4.72	2.467	−0.89

additives. The largest improvement was with the AlH$_3$ additive when burned with the NTO oxidizer (13.9 s). The largest I_s performance was with AlH$_3$ additive and LOx oxidizer (379.1 s). Note that the addition of Mg with LOx generated a significant performance decrement.

Density impulse is another performance parameter which would be critical in volume-limited applications. The density impulse for each propellant system has been calculated (at the O/F corresponding to the optimum I_s level) and listed in Table 3. For the LOx oxidizer, all metal additives enhance the density impulse. The gain for aluminum is over 10 %. For metal hydrides, AlH$_3$ and MgH$_2$ generated gains, whereas the Li-based hydrides reduce the I_v performance due to the low-density nature of the additive. The boron compounds did not alter the density impulse performance, whereas the strained hydrocarbons resulted in a modest improvement.

For the NTO oxidizer, all additives (with the exception of Al) have resulted in a drop in the I_v. The reduction in the optimum O/F has led to a drop in the fraction of the dense oxidizer in the overall propellant. Finally the situation for N$_2$O is similar to LOx. The gains are smaller since the optimal O/F is much higher for N$_2$O compared to LOx. Use of Al and AlH$_3$ generate 5.2 % and 4.1 % improvements, respectively.

Table 4 Optimum concentrations for various additives

Additive	Optimum additive, %	I_s, s	OF*
$B_{10}H_{14}$	63	377.9	2.0
$LiAlH_4$	77	380.7	0.9
AlH_3	64	387.4	1.0
$LiBH_4$	100	386.9	2.2
Mg	0	364.5	2.5

4.1.1.1   Effect of Additive Concentration

Certain propellant combinations take an optimum at additive concentration levels less than 100 %. The optimum concentrations for a short list of additives have been summarized in Table 4. The binder is HTPB and the oxidizer is LOx.

As one can see from the table, the optimum is typically at a level well above the practical range of additive concentrations. Effect of additive concentration in the practical range of 0–40 % (by mass) has been investigated with a high-energy and a low-energy oxidizer in reference [28]. Mg was selected as the additive and the binder is the paraffin wax. Monotonic increase in I_s for low-energy oxidizer and monotonic decrease in I_s for high-energy oxidizer has been observed with increasing concentration of the additive. This conclusion can be extended to the other additives included in this study.

4.1.2   Effect of Binder Type

Influence of the binder type on the performance has also been studied. Four commonly used binders, paraffin wax, HTPB, pDCPD, and PMMA, have been included in the study. As the first step, performance of neat binders with different oxidizers has been studied. The results are summarized in [28]. The I_s performance for paraffin, pDCPD, and HTPB materials is very similar. It turns out that pDCPD is slightly higher than the others due to its positive heat of formation. HTPB is the lowest of the three since it is partially oxidized (and also contains small amounts of nitrogen).

PMMA has significantly lower I_s performance, since the molecule contains a large fraction of oxygen. This conclusion would be valid for all binders containing oxygen. Thus in a study concentrating on improving I_s, we did not focus on binders that would reduce the performance. The optimum O/F for PMMA is significantly lower (again due to the large concentration of oxygen in the molecule).

For formulations with fuel additives, the conclusions are similar to the case of neat binder, paraffin/pDCPD/HTPB performing similarly. The interesting point is the large improvement of I_s (21.8 s) with the inclusion of AlH_3 in the case of PMMA as the binder [28].

4.1.3 Combustion Temperature

The combustion temperature is not considered as a performance parameter for rockets. It has an indirect impact on the I_s performance. However combustion temperature can potentially influence the erosion rate of the nozzle and also the ablation rate of the liner materials inside the motor.

The adiabatic flame temperature for various formulations for all three oxidizers has been calculated using the thermochemical calculator [28]. The formulations that are included in the study are 40 % Al and 40 % AlH$_3$ in the paraffin binder. Addition of aluminum generates a substantial temperature increase. Temperature improvement is highest with NTO due to the lower level of the dissociation effects.

4.1.4 Two-Phase Losses and Nozzle Erosion Effect

The actual delivered I_s and I_v performance improvement associated with a given additive will also depend on the two-phase flow losses in the nozzle and the influence on the nozzle erosion. Unfortunately neither one of these critical factors can easily be evaluated without running a comprehensive motor test program. Note that for reliable assessment, motor tests must be conducted at a scale that the essential physics can be captured.

In this section, we will merely consider two important factors that influence the actual performance in a non-ideal nozzle flow situation. Note that this evaluation will only give a general indication of a propellant's (more precisely a selected additive's) performance decrement due to the particular loss mechanism. For simplicity, we will only consider the effect of three additives Al, B, and Mg in a paraffinic binder. The oxidizer is selected to be LOx. Note that these results can be extended to other additives containing the particular metallic atom type.

The first indicator is the mole fraction of the condensed phase products at the nozzle throat. As this fraction goes higher, the two-phase flow losses are expected to increase. As shown in Table 5, for the propellants considered in this study, aluminum and magnesium have high concentrations of condensed phases in the nozzle, whereas the neat binder or the boron-containing formulation has no significant level of condensed species in the nozzle flow (see [28] for the boiling temperatures of the metal oxides). Depending on the additive concentration level, 1–5 % drop in the I_s efficiency is expected for aluminum- and magnesium-containing additives. The drop for boron should be much less.

Table 5 Condensed phase molar fraction at the nozzle and concentration of oxidizing species at the throat. Oxidizer is LOx

Fuel	O/F*	I_s*, s	Condensed phase mole frac	Beta
Neat paraffin	2.86	367.1	0	0.76
Paraffin+40%Al	1.4	366.5	0.11	0.36
Paraffin+40%B	2.1	363.5	0	0.58
Paraffin+40%Mg	1.5	360.0	0.10	0.63

The other big issue that leads to a drop in the I_s of a rocket system is the nozzle erosion. In hybrid rockets, unlike solids, the nozzle erosion is driven by oxidizer attack to the ablative nozzle surface. Thus, as the concentration of the oxidizing species at the nozzle throat (as defined by the parameter beta) increases, the erosion is expected to increase. As shown in Table 5, the addition of aluminum significantly reduces beta since Al_2O_3 uses up a large fraction of the oxygen in the system. Both boron and magnesium have similar effects at a smaller scale. One mitigating factor against this is the increase in the system temperature with the addition of aluminum. Nevertheless, it is expected that the addition of aluminum would reduce the nozzle erosion rate for a LOx-based hybrid rocket motor.

4.1.5 Fuel Cost

One of the most critical aspects of deciding on the selection of a performance additive is its availability and cost. These virtues for the additives considered in this study are given in [28]. The prices are based on the information given by chemical suppliers and bulk prices were used when they were available.

It turns out that Al (in micron size), magnesium, and lithium-based hydrides are quite reasonable in their price and availability. The fact that the price for boron in certain countries might be much lower in the long run must be included in the decision making. Also the cost for materials such as NBH_6 might reduce significantly if its use as a hydrogen storage medium materializes. Despite its favorable characteristics, the phase-stabilized AlH_3 (known as alane) is not readily available in the Western countries. For this reason, we advise against including this material in the follow-on study.

4.1.6 Effect on Regression Rate

The effect of the performance additives on the regression rate of the binder is another factor that needs to be considered. Since there are no satisfactory theoretical models for regression rate, this task also requires empirical data. As discussed in the review section of this paper, the inclusion of high-energy additives is not a good strategy to improve the regression rate. Reference [26] shows that addition of Mg, MgB, or nano-sized aluminum only increases the regression rate in the 10–40 % range. The maximum increase is with nano-aluminum at low-oxidizer fluxes.

5 Ranking of Fuel Additives and Binders

Using the information gathered in the previous sections, an additive merit table has been established (see Table 6). In this table, all additives have been scored from 1 to 5 (1, poor; 5, excellent) based on their performance and a number of issues that relate to their practicality as a propellant ingredient in an operational system.

Table 6 Additive score[b] table

Additive	I_s	I_v	Perf. total	Availability	Cost	Hazard	Storability	Ballistic	Other total
	Performance			Other factors					
Al (micron)	2	5	7	5	5	5	5	2	22
Al (nano)	2	5	7	4	3	3	3	3	16
B	2	4	6	4	3	4	5	1	17
Mg	1	3	4	5	5	5	5	3	23
Mg/B	2	4	6	4	3	5	5	2	19
AlH_3	5	4	9	1	1	3	2	3	10
MgH_2	3	3	6	4	2	4	3	3	16
$LiAlH_4$	4	1	5	4	4	3	3	3	17
$LiBH_4$	4	1	5	4	4	3	3	3	17
NBH_6	5	1	6	3	2	4	4	4	17
$B_{10}H_{14}$	5	2	7	4	4	2	4	4	18
Cubane	3	3	6	2	1	4	3	4	14
Iyvane8[a]	2	2	4	1	1	4	3	4	13

[a]Low confidence evaluation
[b]Scoring: *5* Excellent; *1* Poor

The two performance factors considered are the specific impulse and density impulse. A combined performance score, which is a sum of the two, has also been included in the table. The performance is separated from the other factors in the overall score and evaluation to prevent selecting a high scoring additive which leads to a minimal performance increase (such as Mg). It is also important to consider I_s and I_v performances separately, since for certain applications one of these performance parameters might be dominant.

In terms of I_s improvement (arguably the most important performance parameter for most applications), three additives that scored the best are AlH_3, BNH_6, and $B_{10}H_{14}$. Lithium-based hydrides also performed reasonably well. Benefit associated with the metallic additives (including the metalloid boron) was less than satisfactory.

Regarding the density impulse, Al was the best performer, but boron, Mg/B alloys, and AlH_3 also did well. Lithium-based hydrides and NBH_6 did rather poorly due to their low densities. In terms of total performance, AlH_3 was the clear winner.

The additives have also been scored on the other practical factors including availability, cost, hazard, storability (in binder), and ballistics (ignitability, efficiencies, regression rate). Note that the evaluation on these practical factors is somewhat subjective. The author of this paper used the information in the literature and his experience/judgment for generating the most realistic scorecard. In terms of the practical factors, micron-sized aluminum and magnesium scored the best. AlH_3 has scored the worst due to its lack of availability, outgassing in the binder and its potential high cost. The strained hydrocarbons did not do well either, since they are not commercially available materials. All others clustered around 16–19 points.

The binders considered in this study have also been scored in a similar way (see [28]). The I_s performance is similar for paraffin, HTPB, and pDCPD, whereas it is significantly lower for PMMA. However, PMMA is a denser binder than the others. Due to its superior cost, lifetime, and ballistic (high regression rate) advantages, paraffin is established to be the best binder by a large margin. However, this assumes a paraffinic binder for which the structural and thermal issues have been resolved.

Some of the important points that need to be considered in the additive selection process are as follows: (1) Fuel additives should not be included in order to increase the regression rate of a hybrid rocket motor. They are not effective for this purpose. (2) Full energy capacity of boron cannot be realized in the rocket application, since the boron compounds stay mostly in gas phase in the nozzle. Note that this effect is included in the thermochemical calculations (reflected in the theoretical I_s). (3) Boron-containing additives have a large advantage over aluminum- and magnesium-containing additives in terms of two-phase nozzle losses. Note that there is no condensed phase for boron combustion at the optimum O/F. (4) Aluminum has a positive effect in reducing the nozzle erosion in hybrid rockets (significant reduction in beta). Boron has a smaller influence and magnesium only have a slight advantage over the neat binder.

6   Recommendations for Further Evaluation

We recommend using paraffin for most applications. For systems that require extreme temperature or loading conditions, we recommend pDCPD or HTPB. However, if metal hydrides shall be used, pDCPD is a better binder than HTPB due to the lack of functional groups that promotes hydrogen outgassing. PMMA should only be considered for applications demanding low O/F.

For low-energy oxidizers, we recommend concentrating on micron- and nano-sized aluminum powders. Aluminum is a practical additive, which results in modest I_s improvement for low-energy oxidizers and good I_v increase with all low- and moderate-density oxidizers. AlH_3 is the best additive (in the studied group) from the performance perspective. Due to its lack of availability of its phase-stabilized grade, we do not recommend further studying this material. The only viable program for this substance would be in the synthesis of a commercial version. $LiAlH_4$ and $LiBH_4$ are both practical additives. These materials are readily available, cost-effective, and easy to handle. For applications not requiring high-density impulse, they would be excellent additives (especially in paraffin binder due to its good storability qualities for hydrides). NBH_6 is also a very interesting alternative. If the cost of the material can be reduced, ammonia borane could be a practical additive. For systems and applications for which the toxicity can be tolerated, decaborane is also a good option.

7 Example Case

Recently SPG introduced a design for an affordable ground-based nanosat launcher with all of its three stages based on its existing LOx/paraffin hybrid motors. The payload capability to 500 km polar orbit is 85 kg and the predicted launch cost is approximately \$3.0M. In this section we will evaluate the economic value of including a performance additive in the paraffinic fuel. $LiAlH_4$ is selected as the additive due to its reasonable cost and I_s improvement capability. Specifically, I_s increases by 18 s monotonically up to the $LiAlH_4$ concentration level of 80 % by mass. For the sake of simplicity, we ignore the reduction in c* and nozzle efficiencies and assume that full I_s benefit is retained.

A system study has been conducted to investigate the effect of $LiAlH_4$ addition on the payload performance. We assumed that the same concentration of hydride has been added to all stages. It has been shown that the payload capability increases to 100 kg at an additive concentration level of 55 %. If one considers the cost of the fuel additive, it can be shown that the cost performance of 35.3 k\$/kg for neat paraffin can be decreased to 32.5 k\$/kg. However the additional cost of processing and I_s losses will most likely eliminate this modest cost benefit. Thus, even for a relatively low-cost hydride, realizing an economic benefit is highly unlikely. Unit material cost levels must be further reduced in order to make use of the performance additives beneficial for a cost-driven application.

8 Conclusions

Using performance additives (metals, metal hydrides, or boron compounds) to enhance the regression rate of the hybrid rocket fuels is unproductive. Lack of oxidizer and combustion beneath the flame limits the effectiveness of metal combustion. Even though aluminum is a good additive for energy-deficient oxidizers such as hydrogen peroxide or nitrous oxide, it is not effective in improving the I_s for oxygen systems. Considering nozzle losses, actual performance may even drop appreciably. AlH_3 delivers the best performance improvement, but its lack of availability limits its practical use in the Western world. The long-term storability of AlH_3 in conventional binders such as HTPB is also problematic. Boron does not deliver a significant performance benefit in hybrid rockets. If the incomplete combustion issue is included in the calculations, a performance decrement is likely with boron addition in hybrid systems. Despite its toxicity, decaborane is a promising additive for certain applications requiring high performance such as in-space applications. Ammonia borane can also be helpful to improve the system I_s (assuming that the boron can be burned more readily in the motor).

Use of performance additives with their current high prices is not expected to be beneficial in improving the cost performance even for I_s-driven applications such as launch vehicles. Paraffin is a promising binder due to its high regression rates and other practical advantages.

References

1. Arbit HA, Dickerson RA, Clapp SD, Nagai CK (1968) Combustion characteristics of the fluorine/lithium/hydrogen tripropellant combination: AlAA paper 68–618, AlAA 4th propulsion specialist conference, Cleveland, June 10–14, 1968
2. Karabeyoglu MA, Zilliac G, Cantwell BJ, DeZilwa S, Castellucci P (2004) Scale-up tests of high regression rate paraffin-based hybrid rocket fuels. J Propuls Power 20(6):1037–1045
3. Risha GA, Evans BJ, Boyer E, Kuo KK (2007) Metals, energetic additives, and special binders used in solid fuels for hybrid rockets (Chapter 10). In Chiaverini MJ, Kuo KK (eds) Fundamentals of hybrid rocket combustion and propulsion. AIAA progress in astronautics and aeronautics, vol 218. AIAA, Reston, pp 413–456
4. Smoot LD, Price CF (1966) Regression rates of metalized hybrid fuel systems. AIAA J 4(5):910
5. Osmon RV (1966) An experimental investigation of a lithium aluminum hydride – hydrogen peroxide hybrid rocket. Aerospace Chemical Engineering 62(61):92–102
6. Vickland CW (1967) Experimental investigation of prepackaged hybrid propulsion systems. United Technology Center, Interim Rep. AFRPL-TR-66-268, Sunnyvale, CA, 1 March 1967
7. Strand LD, Jones MD, Ray RL, Cohen NS (1994) Characterization of hybrid rocket internal heat flux and HTPB fuel pyrolysis, AIAA Paper 94-2876, 30thAIAA/ASME/SAE/ASEE Joint propulsion conference, Indianapolis, IN, June 1994
8. George P, Krishnan S, Varkey PM, Ravindran M, Ramachandran L (1998) Fuel regression rate enhancement studies inHTPB/GOXHybrid rocket motors, AIAA paper 98-3188, 38th AIAA/ASME/SAE/ASEE Joint propulsion conference, Cleveland, OH, July 1998
9. Lips HR (1976) Metal combustion in high performance hybrid rocket propulsion systems. AIAA paper 76-640, 12th AIAA and SAE propulsion conference, Palo Alto, CA, July 1976
10. Lips HR (1977) Heterogeneous combustion of Highly Aluminized hybrid fuels. AIAA J 15(6):777
11. Lips HR (1977) Experimental investigation on hybrid rocket engines using highly aluminized fuels. J Spacecr 14(9):539
12. Risha GA, Ulas A, Boyer E, Kumar S, Kuo KK (2001) Combustion of HTPB based solid fuels containing nano-sized energetic powder in a hybrid rocket motor. AIAA paper 2001-3535, 37th AIAA/ASME/SAE/ASEE Joint propulsion conference, Salt Lake City, UT, July 2001
13. Risha GA, Boyer E, Wehrman RB, Kuo KK (2002) Performance comparison of HTPB-based solid fuels containing nano-sized energetic powder in a cylindrical hybrid rocket motor. AIAA paper 2002-3576, 38thAIAA/ASME/SAE/ASEE Joint propulsion conference, Indianapolis, IN, July 2002
14. Risha GA, Boyer E, Evans B, Kuo KK, Malek R (2003) Characterization of nano-sized particles for propulsion applications, synthesis, characterization and properties of energetic/reactive nonmaterials, materials research society symposium – proceedings, vol 800. Material Research Society, Dec. 2003
15. Risha GA, Evans B, Boyer E, Wehrman RB, Kuo KK (2003) Nano- sized aluminum, and boron-based solid-fuel characterization in a hybrid rocket engine. AIAA paper 2003-4593, 39th AIAA/ASME/SAE/ASEE Joint propulsion conference, Huntsville, AL, July 2003
16. Evans B, Favorito NA, Kuo KK (2006) Oxidizer-type and aluminum-particle addition effects on solid-fuel burning behavior. AIAA 2006-4676, 42nd AIAA/ASME/SAE/ASEE Joint propulsion conference and exhibit 9–12 July 2006, Sacramento, CA
17. Humble R (2000) Fuel performance enhancements for hybrid rockets. AIAA 2000-3437, 36th AIAA/ASME/SAE/ASEE Joint propulsion conference and exhibit 16–19 May 2000. Huntsville, AL
18. Humble R (2000) Dicylclopentadiene: a new resin system for making composite tank structures. AIAA 2000-3676, 36th AIAA/ASME/SAE/ASEE Joint propulsion conference and exhibit 16–19 May 2000 Huntsville, AL

19. Corpening J, Palmer RK, Heister SD (2007) Combustion of advanced non-toxic hybrid propellants. Int J Altern Propuls 1(2/3):154
20. Weismiller MR, Connell TL, Jr., Risha GA, Yetter RA (2010) Characterization of Ammonia Borane (NH3BH3) enhancement to a paraffin fueled hybrid rocket system. AIAA 2010-6639, 46th AIAA/ASME/SAE/ASEE Joint propulsion conference and exhibit 25–28 July 2010, Nashville, TN
21. Clane C. Ammonia-borane and related N-B-H compounds and materials: safety aspects, properties and applications, a survey completed as part of a project for the DOE Chemical Hydrogen Storage Center of Excellence, Contract # DE-FC36-05GO15060, Northern Arizona University
22. DeLuca LT, Galfetti L, Maggi F, Colombo G, Paravan C, Reina A, Tadini P, Sossi A, Duranti E (2011) An optical time-resolved technique of solid fuels burning for hybrid rocket propulsion, AIAA 2011-5753 47th AIAA/ASME/SAE/ASEE Joint propulsion conference and exhibit 31 July – 03 August 2011, San Diego, CA
23. Carmicino C, Sorge R, Orlandi O, Blanchard H, Yvart P, Gautier P (2011) Advanced solid fuels for hybrid propulsion: the research activity in Europe, AIAA 2011-5820, 47th AIAA/ASME/SAE/ASEE Joint propulsion conference and exhibit 31 July – 03 August 2011. San Diego, CA
24. Larson DB, Boyer E, Wachs T, Kuo KK, DeSain J, Curtiss TJ, Brady B (2011) Characterization of the performance of Paraffin/LiAlH4 solid fuels in a hybrid rocket system, AIAA 2011-5822, 47th AIAA/ASME/SAE/ASEE Joint propulsion conference and exhibit 31 July – 03 August 2011, San Diego, CA
25. Zarko VE, Talawar MB (2013) Use of nano particles in gas generating and in energetic materials (review), 5th European conference for aeronautics and space sciences (EUCASS)
26. Qin Z, Paravan C, Colombo G, DeLuca LT, Shen RQ (2013) Ignition and combustion of HTPB-based solid fuels loaded with micron-sized metals. 5th European conference for aeronautics and space sciences (EUCASS)
27. Maggi P, Gariani G, Galfetti L, DeLuca LT (2012) Theoretical analysis of hydrides in solid and hybrid rocket propulsion. Int J Hydrog Energy 37:1760
28. Karabeyoglu MA, Ugur Arkun (2014) Evaluation of fuel additives for hybrid rockets and SFRJ systems, AIAA 2014-2771, 50th AIAA/ASME/SAE/ASEE Joint propulsion and energy conference and exhibit 28–30 July 2014, Cleveland, OH

Introducing Tetrazole Salts as Energetic Ingredients for Rocket Propulsion

Xuezhong Fan, Fuqiang Bi, Min Zhang, Jizhen Li, Weiqiang Pang, Bozhou Wang, and Zhongxue Ge

Abstract Two tetrazole salts, hydroxylammonium 2-dinitromethyl-5-nitro-tetrazolate (HADNMNT) and dihydroxylammonium 5,5′-bistetrazole-1,1′-diolate (HATO), were synthesized and characterized. HADNMNT is a new compound, whose structure was determined by ^{15}N NMR experimentally and GIAO calculation, the thermal decomposition temperature, the explosion probabilities of impact sensitivity, and friction sensitivity of which were tested to be 141.9 °C, 96 %, and 100 %, respectively. The detonation parameters of HADNMNT were predicted to be equal to those of 1,3,5,7-tetranitro-1,3,5,7-tetrazocane (HMX). It was found theoretically that HADNMNT is a potential oxidizer for composite propellants to replace ammonium perchlorate (AP), 1,3,5-trinitro-1,3,5-triazinane (RDX), HMX, and 2,4,6,8,10,12-hexanitro-,2,4,6,8,10,12-hexazaisowurtzitane (CL-20). Safety tests for HATO were performed, and results showed that HATO exhibits excellent thermal stability (the decomposition temperature is 230.3 °C, and the volume of the released gas is 0.30 mL·g^{-1} at 100 °C for 48 h) and low mechanical sensitivities (the explosion probabilities of impact sensitivity and friction sensitivity are 16 % and 24 %, respectively). The compatibilities of HATO with hydroxyl-terminated polybutadiene (HTPB), AP, RDX, and aluminum powder (Al) were reexamined to be good, using the vacuum stability test. Results from comparative study of HATO and RDX as ingredient for composite propellant showed that the composite propellant composed HATO offer the advantages of high burning rate and low mechanical sensitivities.

Nomenclature

Acronyms

ADNMNT	Ammonium 2-dinitromethyl-5-nitrotetrazolate
Al	Aluminum powder

X. Fan (✉) • F. Bi • M. Zhang • J. Li • W. Pang • B. Wang • Z. Ge
Xi'an Modern Chemistry Research Institute, Xi'an 710065, Shaanxi, China
e-mail: xuezhongfan@126.com; bifuqiang@gmail.com; 631520072@qq.com;
jizhenli@126.com; nwpu_pwq@163.com; wbz600@163.com; gzx204@sina.com

165

ANT	2-acetonyl-5-nitrotetrazole
AP	Ammonium perchlorate
AT	5-aminotetrazole
CEA	Chemical equilibrium with applications
CL-20	2,4,6,8,10,12-hexanitro-2,4,6,8,10,12-hexaazaisowurtzitane
DSC	Differential scanning calorimetry
GAP	Glycidyl azide polymer
GIAO	Gauge Independent Atomic Orbitals
HADNMNT	Hydroxylammonium 2-dinitromethyl-5-nitrotetrazolate
HATO	Dihydroxylammonium 5,5'-bistetrazole-1,1'-diolate
HATO-HTPB	Composite propellant formulation containing HATO
HDNMNT	2-dinitromethyl-5-nitrotetrazole
HEDMs	High-energy density materials
HMX	1,3,5,7-Tetranitro-1,3,5,7-tetrazocane
HNE	Hexanitroethane
HTPB	Hydroxyl-terminated polybutadiene
HyDNMNT	Hydrazinium 2-dinitromethyl-5-nitrotetrazolate
KBr	Potassium bromide
K-J	Kamlet-Jacobs
NASA	National Aeronautics and Space Administration
NMR	Nuclear magnetic resonance
RDX	Cyclotrimethylenetrinitramine
RDX-HTPB	Composite propellant formulation containing RDX
TNT	2,4,6-Trinitrotoluene

Roman Symbols

D	Detonation velocity
H_{50}	50% Probability of explosion
I_s	Specific impulse
M_c	Molecular mass of combustion products
N	Nitrogen content
n	Pressure exponent
OB	Oxygen balance
P	Detonation pressure
P_F	Explosion probability of fraction sensitivity
P_I	Explosion probability of impact sensitivity
Q_V	Heat of explosion
T_c	Adiabatic flame temperature
T_d	Thermal decomposition temperature
u	Burning rate

Greek Symbols

ΔH_f Heat of formation
ρ Density
Φ Oxygen coefficient

1   Introduction

Tetrazolate-based energetic salts are one of the most recent and exciting high-energy density materials (HEDMs) used in solid explosives, and it continues to get much considerable attractions for researchers all over the world [1–12]. These energetic salts, with higher density, tend to exhibit very low vapor pressure and possess high positive heats of formation and high thermal stabilities [13]. When they are serving as energetic ingredients for rocket propulsion, the properties can be improved by their addition to the propellant formulations such as smokeless combustion, high heats of formation, high propulsive power, and high specific impulse (I_s). Various tetrazole salts, in which each tetrazolate anion pairs with a family of its counterparts through metathetical or protonation reactions, have been reported. Their properties can be carefully tuned via the choice of cations, and hydroxylammonium salt [14] is often found to present higher performance.

2   Hydroxylammonium 2-Dinitromethyl-5-Nitrotetrazolate (HADNMNT)

Recently, Semenov et al. [15] synthesized a new tetrazole with high oxygen balance (10.95 %): 2-dinitromethyl-5-nitrotetrazole (HDNMNT). The acidity of HDNMNT was comparable to that of a strong mineral acid, and its ammonium salt (ADNMNT) and hydrazinium (HyDNMNT) were also synthesized by V. V. Semenov et al. In this work, the properties of hydroxylammonium 2-dinitromethyl-5-nitrotetrazolate (HADNMNT) were investigated.

2.1   Synthesis and Characterization

HDNMNT was synthesized via diazotization substitution, substitution, and nitration hydrolysis, using 5-aminotetrazole (AT) as starting material (Scheme 1) [16]. 1-Chloroacetone is more easily obtained than 1-bromoacetone [17] commercially, so 1-chloroacetone and potassium bromide (KBr) were employed to replace 1-bromoacetone in the substitution reaction to form 2-acetonyl-5-nitrotetrazole (ANT). HADNMNT was finally synthesized from HDNMNT and hydroxylamine through neutralization reaction, and the total yield was 39.3 %.
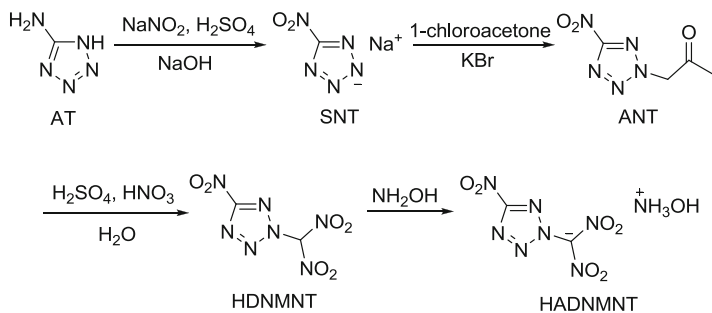
Scheme 1 Synthetic route for HADNMNT

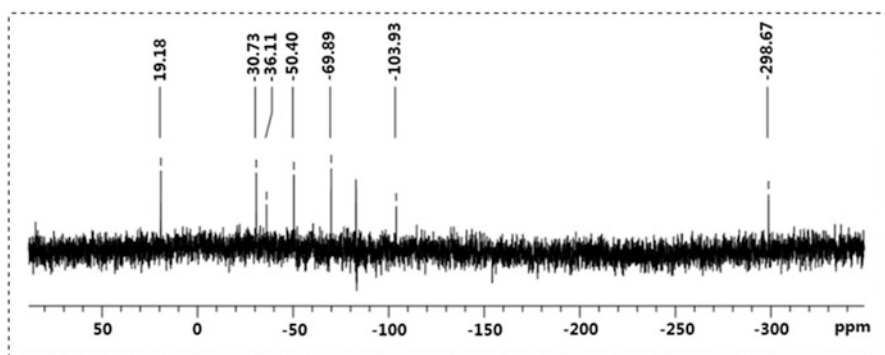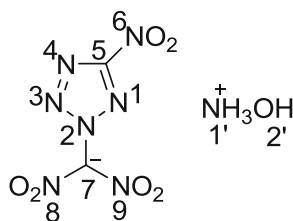**Fig. 1** Atom number of HADNMNT

Fig. 2 ^{15}N NMR spectra of HADNMNT

The structure of HADNMNT (Fig. 1) was investigated using ^{15}N NMR spectroscopy. ^{15}N NMR spectra were recorded on a BRUKER AV500 NMR spectrometer at 25 °C. The chemical shifts are given relative to nitromethane as external standard. Seven well-resolved resonances (Fig. 2) are detected in the ^{15}N NMR spectra for the eight nitrogen atoms because of the symmetry of dinitromethyl group. The assignments were based on comparison with theoretical calculations using Gaussian 09 (GIAO-B3LYP/6-311 + G(2d, p)//B3LYP/6-31G(d, p)) (Table 1). As expected, the nitrogen atoms in nitro groups N6 and N8/N9 peaks appear at δ −30.73 ppm and δ −36.11 ppm, respectively. The nitrogen atom N1 and N4 peaks appear at −69.89 and −50.40, respectively, while the nitrogen atom N2 is shifted toward the higher

Table 1 ^{15}N NMR data of HADNMNT

N atoms	N1	N2	N3	N4	N6	N8/N9
Found	−69.89	−103.93	19.18	−50.40	−30.73	−36.11
Calcd.	−55.66	−90.52	34.55	−43.91	−23.19	−28.71

Fig. 3 The DSC curve of HADNMNT
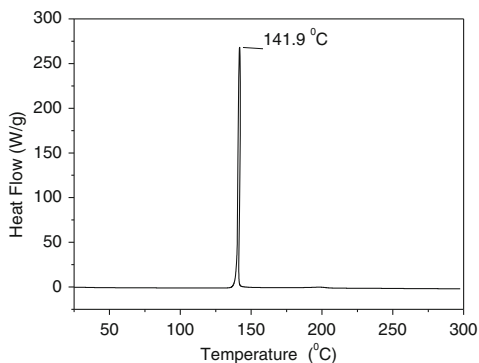
Table 2 The properties of HADNMNT in comparison with RDX and HMX

Compound	Td/°C	N/%	OB/%	ρ/(g·cm^{-3})	$\Delta_f H$/ (kJ·mol^{-1})	D/ (km·s^{-1})	P/GPa	P_I/%	P_F/%
HADNMNT	141.8	44.45	6.35	1.87	299.40	9.240	39.54	96	100
RDX	230.0	37.80	−21.60	1.82	92.6	8.748	34.80	80	76
HMX	286.6	37.80	−21.60	1.91	104.8	9.059	39.20	100	100

field (−103.93 ppm), and the nitrogen atom N3 is shifted toward the lower field (19.18 ppm). It was revealed theoretically and experimentally that the alkylation at N2 could lead to strong shielding at N2 with concomitant deshielding at N3 [18].

2.2 Physical and Chemical Properties

The thermal decomposition temperature (T_d) of HADNMNT was obtained using differential scanning calorimetry (DSC) at 5 °C min^{-1}. The DSC curve (in Fig. 3) shows the exothermic peak temperature at 141.9 °C, corresponding to the decomposition process, which means HADNMNT has the similar thermal stability with ADNMNT and HyDNMNT (130–140 °C).

Density, nitrogen content and oxygen balance of any energetic material are important physical properties. As can be seen in Table 2, the density of HADNMNT is 1.87 g·cm^{-3}, falling in the range of 1.8–2.0 g·cm^{-3} (for new high-energy density compounds), which is higher than that of 1,3,5-trinitro-1,3,5-triazinane (RDX). The nitrogen content and the oxygen balance of HADNMNT (44.45 % and 6.35 %, respectively) are higher than those of RDX and 1,3,5,7-tetranitro-1,3,5,7-tetrazocane (HMX). The calculated heat of formation of HADNMNT

(299.30 kJ·mol^{-1}) is also higher than that of HMX because of the high nitrogen content. By using the values of the heat of formation and the density, detonation velocity and detonation pressure were calculated by Kamlet–Jacobs (K-J) equations [19]. The results show that HADNMNT has much higher detonation velocity and pressure than HMX.

The explosion probability of impact sensitivity (P_I) of the samples was determined by using a WL-1 impact instrument with 10 kg drop weight at 25 cm height on ~50 mg samples. The explosion probability of friction sensitivity (P_F) of the samples was determined by using a WM-1 friction instrument with 90° pendulum angle at 3.92 MPa pressure on ~20 mg samples. In each determination, 25 samples were tested and explosion probabilities were obtained. It was found that the explosion probabilities of impact sensitivity and friction sensitivity of HADNMNT are 96 % and 100 %, respectively, which are higher than those of RDX (80 %, 76 %) and slight lower than those of HMX (100 %, 100 %).

## 2.3   Theoretical Ideal Performance of Composite Propellant Containing HADNMNT

To examine the use of HADNMNT as an ingredient for composite rocket propellants, theoretical performance calculations were performed using the NASA Chemical Equilibrium with Applications (CEA) thermochemical code [20] at 6.86 MPa with an expansion ratio 70:1. Specific impulse (I_s) was used as the performance parameter of merit. Propellants based on 10 mass % of hydroxyl-terminated polybutadiene (HTPB), 5 mass % of aluminum inclusion, and 85 mass % of oxidizers (ammonium perchlorate (AP), RDX, HMX, 2,4,6,8,10,12-hexanitro-,2,4,6,8,10,12-hexazaisowurtzitane (CL-20), and HADNMNT) were considered.

As is shown in Table 3, parts of AP were replaced by HATO, the adiabatic flame temperature (T_c) of the composite propellants increase, and the molecular mass of

Table 3 The effects of mass fraction of HADNMNT on the energetic properties and combustion products of HTPB-based propellants

Content/mass %		Energy characteristics				Mole fraction of combustion product/%					
HADNMNT	AP	Φ	T_c/K	Mc	I_s /(N·s·kg^{-1})	H_2O	CO_2	CO	O_2	N_2	HCl
0	85	1.41	3005	30.1	2331.3	40.5	10.1	0	13.9	10.8	21.0
10	75	1.32	3150	30.0	2407.9	39.4	12.5	0.02	11.3	14.3	18.3
20	65	1.24	3270	29.7	2475.2	38.0	14.9	0.12	8.6	17.9	15.6
30	55	1.16	3372	29.5	2533.7	36.4	17.0	0.51	6.0	21.4	12.9
40	45	1.09	3459	29.1	2584.4	34.6	18.6	1.30	3.9	25.0	10.4
50	35	1.03	3536	28.8	2630.2	32.4	19.4	2.92	2.3	28.5	8.0
60	25	0.97	3606	28.5	2671.1	29.9	19.1	5.36	1.3	31.8	5.7
70	15	0.91	3671	28.1	2708.4	27.4	18.3	8.31	0.7	34.9	3.4
80	5	0.86	3733	27.7	2743.3	24.8	17.0	11.58	0.3	38.0	1.1
85	0	0.84	3764	27.6	2760.0	23.5	16.3	13.28	0.2	39.4	0

Fig. 4 The effect of HADNMNT content on the specific impulse of nitro compound-based composite propellant
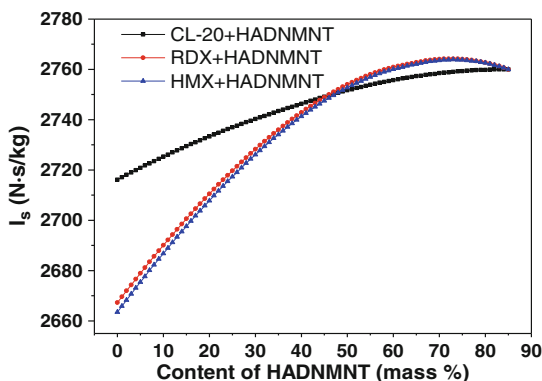

combustion products (M_c) decrease. As a result, the ideal specific impulse of composite propellants increases with an increase in the mass fraction of HADNMNT. When AP is completely replaced by HADNMNT, the propellant has the highest I_s of 2760.0 N·s·kg^{-1} with the least elimination of HCl and H_2O in combustion products.

Replacement of nitro compounds, such as RDX, HMX, and CL-20, by HADNMNT shows different effects to the I_s of composite propellants (Fig. 4). For CL-20-based propellants, following the replacement of CL-20, the I_s increase gradually. For RDX- and HMX-based propellants, it was found that the I_s increase and then decrease with an increase in the mass fraction of HADNMNT in the propellant formulation, and the I_s reach the maximum value of 2764.2 N·s·kg^{-1} and 2763.9 N·s·kg^{-1}, respectively, when the mass fractions of HADNMNT in the propellant formulation are 71 mass % and 73 mass %, respectively.

In summary, HADNMNT is a new tetrazole salt with high positive oxygen balance (6.35 %) and high positive heat of formation (299.30 kJ·mol^{-1}) in the same compound, which make it a potential oxidizer for composite propellants to replace AP, RDX, HMX, and CL-20. The full characterization of the thermal stability and compatibility of HADNMNT needs to be done before its application in propellants.

3 Dihydroxylammonium 5,5′-Bistetrazole-1,1′-Diolate (HATO)

Another hydroxylammonium salt of tetrazole, dihydroxylammonium 5,5′-bistetrazole-1,1′-diolate (HATO), was reported and named as TKX-50 by Fishcher et al. [21–24] The calculated detonation velocity of HATO is found to be higher than that of CL-20, while the impact sensitivity is tested to be less than RDX. Its well performance of both detonation power and safety encouraged us to study its synthetic method, properties, and application in the solid propellants.
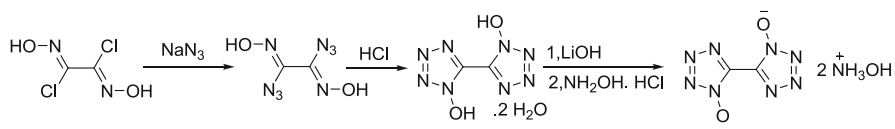
**Scheme 2** Synthetic route for HATO

3.1 Synthesis

Due to the high mechanical sensitivity of the key intermediate diazidoglyoxime, the substitution and cyclization in one step were applied by N. Fishcher and coworkers; however, the followed isolation of dimethylammonium 5,5′-bistetrazole-1,1′-diolate was found to be more complex operations including the evaporation of diethyl ether, water, and DMF. In this work, HATO was synthesized using a modified synthetic method via substitution, cyclization, and metathesis reaction from dichloroglyoxime with a total yield of 81.7 % (Scheme 2) [25].

Wet diazidoglyoxime was experimentally found to be less mechanical sensitive than dry samples, and 5,5′-bistetrazole-1,1′-diol can absorb water to form 5,5′-bistetrazole-1,1′-diol dihydrate. Therefore, a simple and safe synthetic method can be obtained by using the wet product of diazidoglyoxime in the cyclization reaction. Finally, the synthesis of HATO was easily achieved with high yield via metathesis reaction from hydroxyammonium chloride and dilithium 5,5′-bistetrazole-1,1′-diolate, which was generated in situ by the reaction of 5,5′-bistetrazole-1,1′-diol and lithium hydroxide in water.

3.2 Safety Tests

The DSC experiment for HATO was performed under a nitrogen atmosphere with the heating rate of 5 °C·min^{-1}. It was found from Fig. 5 that the peak temperature of exothermal decomposition is at 230.3 °C, which is comparable to that of RDX (230 °C). After heated to 100 °C for 48 h, the volume of the released gas is only 0.30 mL·g^{-1}. The excellent thermal stability maybe attributed to the extensive and strong hydrogen-bonding interactions.

The WL-1 impact sensitivity instrument and WM-1 friction sensitivity instrument were used to determine the mechanical sensitivity of HATO. The results show that the explosion probability of impact sensitivity is 16 % (drop hammer of 10 kg), and the explosion probability of friction sensitivity is 24 %. It can be concluded that HATO possess much lower mechanical sensitivities than RDX (80 % and 76 %) and HMX (100 %, 100 %).

Fig. 5 The DSC curve of HATO
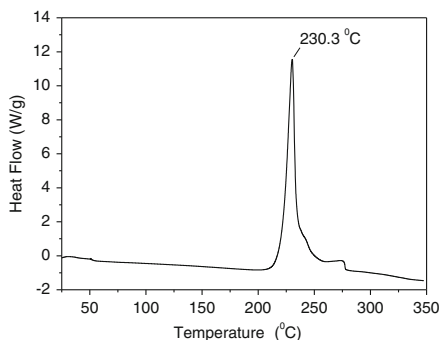
Table 4 The volume of additional gas produced

| Mixture	HATO+HTPB	HATO+AP	HATO+RDX	HATO+Al
ΔV/mL	−0.02	0.12	−0.01	−0.16

3.3 Compatibility

The compatibility study of HATO with some energetic materials and inert materials using DSC method was reported by Huang et al. [26] They found that HATO/hexanitroethane (HNE) possesses good compatibility; HATO and HMX have moderate compatibility; and the compatibility of HATO with 2,4,6-trinitrotoluene (TNT), CL-20, centralite, nitrocellulose (NC), AP, Al, glycidyl azide polymer (GAP), RDX, and HTPB are poor. Based on these results, it can be dedicated that it is dangerous to add HATO to the HTPB-based composite solid propellant formulation. So we reexamine the compatibility of HATO with the components of HTPB-based composite propellants, including HTPB, AP, RDX, and Al, using the vacuum stability test.

In the vacuum stability test, the volume of liberated gas, when the mixture of parts is similar to an explosive and the materials in test are heated at 90 °C for 40 h, is compared to the volume of gas liberated by the energetic material and the material in test when heated separately, in identical conditions. The compatibility is evaluated through the volume of additional gas produced due to the contact between the two components of the mixture. Table 4 presents the volume of additional gas produced, and all of the values are lower than 3 mL, which indicate that there is good compatibility of HATO with HTPB, AP, RDX, and Al.

3.4 Theoretical Performance of Composite Propellant Containing HATO

Prior to laboratory work, the effects of replacement of AP by HATO and Al on the energy characteristics of HTPB-based composite propellant (10 mass % of HTPB, 84 mass % of AP, and 6 mass % of others) were calculated by NASA-CEA code [20].

Fig. 6 The effect of HATO
mass fraction on the ideal
specific impulse of composite
propellant
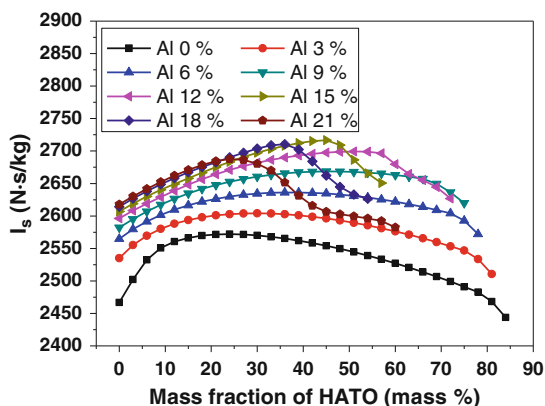
It was theoretically found from Fig. 6 that the I_s of the composite propellant increase and then decrease with an increase in the mass fraction of HATO in the propellant formulation, and the I_s reaches the maximum value of 2572.0 N·s·kg^{-1} when the mass fraction of HATO in the propellant is 24 mass %. When Al is added to the composite propellant, the mass fraction of Al affects the I_s of composite propellant significantly, which has the maximum value of 2717 N·s·kg^{-1} at 10 mass % of HTPB, 15 mass % of Al, 25 mass % of AP, 44 mass % of HATO, and 6 mass % of others.

3.5 Comparative Study of HATO and RDX as Ingredient for Composite Propellant

Based on the results of calculations and preparation processes of the propellant, the composite propellant formulation containing HATO (HATO-HTPB) and RDX (RDX-HTPB) were formulated as follows: HTPB 10 mass %, AP 59 mass %, HATO or RDX 20 mass %, Al 5 mass %, and others 6 mass %. HATO-HTPB and RDX-HTPB propellants were successfully prepared by using the vacuum casting process, and the characteristics, such as energy, combustion, and safety properties of the propellants, were studied.

Density measurements were carried out on a Model AG 104 Mettler Toledo balance at the temperature of (20 ± 2) °C. Heat of explosion measurements was made with a Model ZDHW-2 temperature constant automatic calorimeter. It was shown from Table 5 that the density of HATO-HTPB propellant is 1.628 g cm^{-3}, higher than that of RDX-HTPB formulation. The heat of explosion and the combustion temperature of HATO-HTPB propellant are 4343 kJ·kg^{-1} and 3363.9 K, respectively, which are lower than those of RDX-HTPB compositions. However, the relatively higher nitrogen and hydrogen content of HATO can reduce the molecular mass of combustion products of HATO-HTPB, and the calculated I_s of HATO-

Table 5 The energetic properties of RDX-HTPB and HATO-HTPB propellants

Propellant	$\rho/(g \cdot cm^{-3})$	$Q_v/(kJ \cdot kg^{-1})$	T_c/K	$M_c/(mol \cdot kg^{-1})$	$I_s/(N \cdot s \cdot kg^{-1})$
RDX-HTPB	1.616	4621	3381.9	27.21	2602.4
HATO-HTPB	1.628	4343	3363.9	26.46	2617.2

Table 6 The burning rates and pressure exponents data of RDX-HTPB and HATO-HTPB propellants

Propellant	$u/(mm \cdot s^{-1})$						n		
	2 MPa	5 MPa	10 MPa	15 MPa	20 MPa	22 MPa	2–5 MPa	5–15 MPa	15–22 MPa
RDX-HTPB	12.68	16.92	19.44	20.72	23.33	23.89	0.315	0.184	0.372
HATO-HTPB	14.39	18.69	21.51	23.87	28.99	31.51	0.285	0.223	0.725

Table 7 The mechanical sensitivities of RDX-HTPB and HATO-HTPB propellants

Propellant	H_{50}/cm	$P_f/\%$
RDX-HTPB	85.1	96
HATO-HTPB	102.3	84

HTPB propellant is 2617.2 N·s·kg^{-1}, which is higher than that of RDX-HTPB composition.

The measurements of burning rate and calculated pressure exponent are used to study the combustion characteristics of the composite propellant containing HATO and RDX as parts of oxidizer. The detailed combustion characteristics (burning rates (u) and pressure exponents (n)) of HTPB-based composite propellants at the pressure range of 2–22 MPa are shown in Table 6. It can be seen from the experimental results that the burning rate of HATO-HTPB propellant is higher than that of the RDX-HTPB propellant. For example, at 22 MPa, the burning rate of HATO-HTPB propellant is 31.51 mm·s^{-1}, which is higher than that of the RDX-HTPB propellant (23.89 mm·s^{-1}). The value of pressure exponent (0.725) of HATO-HTPB at the pressure range of 15–22 MPa is advantageously high for throttling and control purposes, but could be problematic from a motor design and sensitivity standpoint.

The mechanical sensitivity of the propellant compositions to impact stimuli was determined by applying the fall hammer method (2 kg drop weight) in a WL-1 impact instrument, and results are given in terms of statically obtained 50 % probability of explosion (H_{50}). Friction sensitivity was measured on a WM-1 friction instrument with 90° pendulum angle at 3.92 MPa pressure on ~20 mg samples. The higher H_{50} is, the lower the impact sensitivity is, while the greater P_f is, the higher the friction sensitivity is. It was shown from Table 7 that the H_{50} of HATO-HTPB propellant is 102.3 cm, higher than that of RDX-HTPB propellant, and the P_f of HATO-HTPB propellant is 84 %, lower than that of RDX-HTPB propellant. As a result of this testing, it appears that HATO-HTPB propellant is safer to handle under normal conditions than RDX-HTPB.

In conclusion, the composite propellant composed HATO offer the advantages of high burning rate and low mechanical sensitivities. The characteristics of easy

preparation, good thermal stability, high energetic performance, low mechanical sensitivity, and good compatibility of HATO make it a promising energetic material to replace RDX.

References

1. Joo Y, Shreeve JM (2009) Energetic mono-, di-, and trisubstituted nitroiminotetrazoles. Angew Chem Int Ed 48:564–567
2. Stierstorfer J, Tarantik KR, Klapötke TM (2009) New energetic materials: functionalized 1-ehyl-5-aminotetrazoles and 1-ethyl-5-nitriminotetrazoles. Chem Eur J 5:5775–5792
3. Klapötke TM, Sproll SM (2009) Alkyl-bridged Bis-5-azidotetrazoles: a safer way of preparation. Eur J Org Chem 74:4284–4289
4. Tao G, Guo Y, Parrish DA et al (2010) Energetic 1,5-diamino-4H-tetrazolium nitro-substituted azolates. J Mater Chem 20:2999–3005
5. Joo Y, Shreeve JM (2010) High-density energetic mono- or Bis(oxy)-5-nitroiminotetrazoles. Angew Chem Int Ed 49:7320–7323
6. Fischer N, Hüll K, Klapötke TM, Stierstorfer J, Laus G, Hummel M, Froschauer C, Wurstb K, Schottenbergerb H (2012) 5,5′-azoxytetrazolates- a new nitrogen-rich dianion and its comparison to 5,5′-azotetrazolate. Dalton Trans 41:11201–11211
7. Tao GH, Parrish DA, Shreeve JM (2012) Nitrogen-rich 5-(1-methylhydrazinyl)tetrazole and its copper and silver complexes. Inorg Chem 51:5305–5312
8. Bonegerg F, Kirchner A, Klapötke TM, Piercey DG, Poller MJ, Stierstorfer J (2013) A study of cyanotetrazole oxides and derivatives thereof. Chem Asian J 8:148
9. Tang Y, Yang H, Wu B, Ju X, Lu C, Cheng G (2013) Synthesis and characterization of a stable, catenated N11 energetic salt. Angew Chem Int Ed 52:4875–4877
10. Klapötke TM, Sabaté CM, Stierstorfer J (2009) Neutral 5-nitrotetrazoles: easy initiation with low pollution. New J Chem 33:136–147
11. Klapötke TM, Mayer P, Sabaté CM (2008) Simply, nitrogen-rich, energetic salts of 5-nitrotetrazole. Inorg Chem 47:6014–6027
12. Li Y, Liu W, Pang S (2012) Synthesis and characterization of 5-nitro-2-nitratomethyl-1,2,3,4-tetrazole: a high nitrogen energetic compound with good oxygen balance. Molecules 17:5040–5049
13. Gao HX, Shreeve JM (2011) Azole-based energetic salts. Chem Rev 111:7377–7436
14. Fischer N, Klapötke T M, Stierstorfer J (2011) The hydroxylammonium cation in tetrazole based energetic materials. In: Proceedings of the 14th seminar on, new trends in research of energetic materials 1, Czech Republic, 13–15 April, pp 128–156
15. Semenov VV, Kanischev MI, Shevelev SA, Kiselyov AS (2009) Thermal ring-opening reaction of N-polynitromethyl tetrazoles: facile generation of nitrilimines and their reactivity. Tetrahedron 65:3441–3445
16. Zhang M, Ge Z, BI F, Xu C, Liu Q, Wang B (2013) Study on the synthesis, thermal performance and quantum chemistry of 2-dinitromethyl-5-nitrotetrazole. Chin J Explos Propellants 36(3):14–19
17. Semenov VV, Ugrak BI, Shevelev SA, Kanishchev MI, Baryshnikov AT, Fainzil'berg AA (1990) Investigation of the alkylation of nitroazoles with α-haloketones by ^{13}C,^{15}N, and ^{14}N NMR. Russ Chem Bull 39:1658–1666
18. Aridoss G, Zhao C, Borosky GL, Laali KK (2012) Experimental and GIAO ^{15}N NMR study of substituent effects in 1H-tetrazoles. J Org Chem 77:4152–4155
19. Kamlet MJ, Jacobs SJ (1968) Chemistry of detonation I. A simple method for calculating detonation properties of CHNO explosives. J Chem Phys 48(1):23–35
20. Gordon S, McBride BJ (1996) Computer program for calculation of complex chemical equilibrium compositions and applications. NASA Reference Publication 1311

21. Fischer N, Fischer D, Klapötke TM, Pierceya DG, Stierstorfera J (2012) Pushing the limits of energetic materials-the synthesis and characterization of dihydroxylammonium 5,5′-bistetrazole-1,1′-diolate. J Mater Chem 22:20418
22. Fischer N, Klapötke TM, Matecic Musanic S, Stierstorfera J, Suceska M (2013) TKX-50. In: 16th new trends in research of energetic materials, Pardubice, pp 574–585
23. Golubev V, Klapötke TM (2014) Comparative analysis of shock wave action of TKX-50 and HMX blasting performance in one-, two- and three-dimensional geometry. In: 17th new trends in research of energetic materials, Pardubice, p 66
24. Golubev V, Klapötke TM (2014) Comparative analysis of shock wave action of TKX-50 and other explosives on various barriers. In: 17th new trends in research of energetic materials, Pardubice, p 67
25. Bi F, Xiao C, Xu C, Ge Z, Wang B, Fan X, Wang W (2014) Synthesis and properties of dihydroxylammonium 5,5′-bistetrazole-1,1′-diolate. Chin J Energ Mater 22(2):272–273
26. Huang H, Shi Y, Yang J, Li B (2015) Compatibility study of dihydroxylammonium 5,5′-bistetrazole-1,1′-diolate (TKX-50) with some energetic materials and inert materials. J Energ Mater 33(1):66–72

Synthesis and Characterization of 3,4-bis (3-fluorodinitromethylfurazan-4-oxy)furazan

Lianjie Zhai, Bozhou Wang, Xuezhong Fan, Fuqiang Bi, Peng Lian, Jizhen Li, and Weiqiang Pang

Abstract A new energetic plasticizer 3,4-bis(3-fluorodinitromethylfurazan-4-oxy)furazan (BFF) was designed and synthesized via a five-step procedure including cyano addition, diazotization, N_2O_5 nitration, KI reduction, and XeF_2 fluorination. The compound was characterized by FT-IR spectroscopy, multinuclear NMR spectroscopy (^{13}C and ^{19}F), elemental analysis, differential scanning calorimetry (DSC), and thermogravimetry-derivative thermogravimetry (TG-DTG). The sensitivity toward impact was determined by standardized impact tests. Furthermore, the heat of formation was calculated with the program package Gaussian 09, and the density was measured using a gas pycnometer at room temperature. Based on the measured density (1.88 g cm^{-3}) and the calculated heat of formation (-111.1 kJ mol^{-1}), impressive values for the detonation parameters such as detonation velocity (8318 m s^{-1}) and pressure (32.0 GPa) were computed using the empirical *Kamlet-Jacobs* equations and compared to those of hexogen (RDX) as well as the most commonly used energetic plasticizer bis(2-fluoro-2,2-diniroethyl)formal (FEFO).

1 Introduction

Furazanyl ether compounds have attracted considerable amount of attention as an ideal backbone for the synthesis of high-energy materials due to their high standard enthalpy of formation, high energy density, good thermal stability, and low melting point, indicating its potential as insensitive high explosives and energetic plasticizers [1–5]. For example, Sheremetev and Wang [6–11] have reported some furazanyl ether compounds showing high energetic performance (Fig. 1), such as bifurazano[3,4-*b*:3′,4′-*f*]furoxano[3″,4″-*d*]-oxacycloheptatriene F(BFFO) (detonation velocity [*D*] = 8600 km s^{-1}, density [*ρ*] = 1.86 g cm^{-3}, characteristic height (H_{50}) =57.5 cm).

L. Zhai • B. Wang (✉) • X. Fan (✉) • F. Bi • P. Lian • J. Li • W. Pang
Xi'an Modern Chemistry Research Institute, Xi'an 710065, Shaanxi, China
e-mail: trihever0210@126.com; wbz600@163.com; xuezhongfan@126.com;
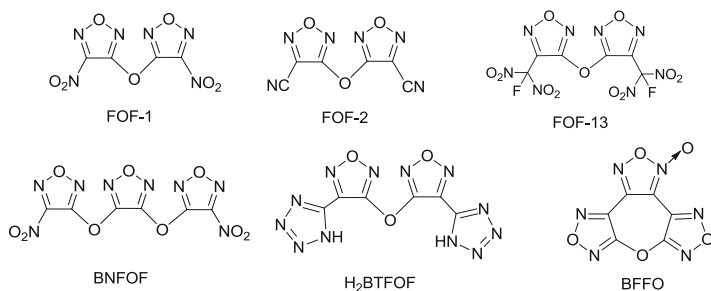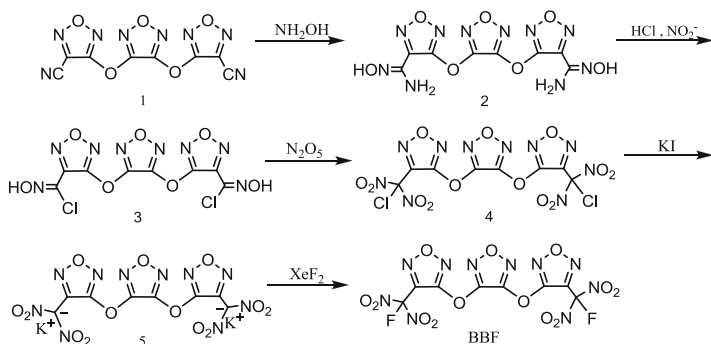bifuqiang@gmail.com; 745377605@163.com; 524305088@qq.com; pangwq204@gmail.com

Fig. 1 Furazanyl ether compounds

Scheme 1 Synthesis of BFF

The fluorodinitromethyl group is an important energetic group that is present in many energetic compounds [12–15]. Most compounds containing fluorodinitromethyl moiety have been found considerably more thermally stable and less sensitive toward external stimuli than the trinitromethyl analogues. Compared with dinitromethyl compounds, most fluorodinitromethyl compounds exhibit high densities, reasonable sensitivities, and good oxygen balance (OB) because of the introduction of F atom. To improve the energetic level and other energetic properties, introducing furazanyl ether as backbone into fluorodinitromethyl group could be an effective method because this fluorodinitromethyl group has rather large density and high detonation velocity and detonation pressure. For example, 3,3′-bis(dinitromethyl)difurazanyl ether (FOF-13) containing fluorodinitromethyl moieties exhibited impressive energetic properties ($T_d > 270$ °C; $\rho = 1.97$ g cm^{-3}; OB $= 0$ %), which prompted us to develop new furazanyl ether compounds containing fluorodinitromethyl group [8].

Continuing our interest in designing and synthesizing new energetic compound and studying the thermal and impact stabilities as well as predicting the detonation properties, we now report the synthesis (Scheme 1) and energetic properties of 3,4-bis(3-fluorodinitromethylfurazan-4-oxy)furazan as a potential energetic plasticizer and high-energy dense oxidizers.

2 Experimental Section

2.1 Instruments and Conditions

Elemental analyses (C, H, and N) were performed on a VARI-El-3 elementary analysis instrument. Infrared spectra were obtained from KBr pellets on a Nicolet NEXUS870 infrared spectrometer in the range of 4000–400 cm^{-1}. Differential scanning calorimetry (DSC) studies were carried out on a Q200 apparatus (TA, USA) with heating rates of 5 K min^{-1}, using dry oxygen-free nitrogen as atmosphere with a flowing rate of 50 mL min^{-1}. The TG-DTG experiment was performed with a SDT-Q600 apparatus (TA, USA) operating at a heating rate of 5 K min^{-1} in a flow of dry oxygen-free nitrogen at 50 mL min^{-1}.

2.2 Synthesis

3,4-bis(3-Aminoximidofurazan-4-oxy)furazan (**2**): A stirred solution of 3,4-bis(3-cyanofurazan-4-oxy)furazan (5.76 g, 20 mmol) and hydroxylamine hydrochloride (2.85 g, 41 mmol) in a solvent mixture of water (55 mL) and isopropanol (25 mL) was stirred at 20 °C; after that, sodium carbonate anhydrous (2.23 g, 21 mmol) was added in batches. The reaction mixture was stirred further for 2 h at 50 °C. The precipitate was filtered, washed with ice-cold water, and dried in vacuum over P_2O_5 to afford **2** (6.74 g, 91.2 %) as a white solid. mp 219−220 °C; ^1H NMR (DMSO-d_6, 500 MHz) δ 10.61 (s, 2H, OH), 6.35(s, 4H, NH_2); ^{13}C NMR (DMSO-d_6, 125 MHz) δ 159.25, 154.20, 142.29, 141.19; IR (cm^{-1}, KBr) 3503, 3487, 3382, 3276, 2893, 1675, 1595, 1576, 1553, 1523, 1439, 1254, 1175, 1034, 967; Anal. calcd for $C_8H_6N_{10}O_7$ (%): C 27.13, N 39.55, H 1.71, found C 26.64, N 39.28, H 1.70.

3,4-bis(3-Chloroximidofurazan-4-oxy)furazan (**3**): To a solution of **2** (5.31 g, 15 mmol) in concentrated hydrochloric acid (55 mL) and water (30 mL), a solution of $NaNO_2$ (2.16 g, 31 mmol) in water (12 mL) was added dropwise at 0 °C. After stirring for 2 h at 0 °C, the reaction mixture was heated to 20 °C for 1.5 h until N_2 evolution stopped. The resulting white precipitate was filtered, washed with cold water twice, and dried in vacuum to yield **3** (5.69 g, 96.5 %) as a white solid. mp 82–83 °C; ^1H NMR (DMSO-d_6, 500 MHz) δ 13.74 (s, 2H, OH); ^{13}C NMR (DMSO-d_6, 125 MHz) δ 158.26, 153.41, 143.23, 123.30; IR (cm^{-1}, KBr) 3583, 3505, 3346, 2832, 2759, 1701, 1605, 1589, 1560, 1528, 1512, 1423, 1301, 1252, 1028, 943; Anal. calcd for $C_8H_2N_8O_7Cl_2$ (%): C 24.45, N 28.51, H 0.51, found C 24.23, N 28.19, H 0.85.

3,4-bis(3-Chlorodinitromethyl furazan-4-oxy)furazan (**4**): To a suspension of **3** (0.75 g, 1.9 mmol) in $CHCl_3$ (50 mL) at 15 °C, N_2O_5 (2.5 g, 23 mmol) was added. The mixture was heated to 45 °C and kept at this temperature for 40 min. The solvent was evaporated and the residue was subjected to preparative TLC on silica

gel to isolate colorless crystals **4** (0.27 g, 28.0 %). mp 79–80 °C; ^{13}C NMR (DMSO-d_6, 125 MHz) δ 159.45, 152.73, 139.27, 113.06; IR (cm^{-1}, KBr) 1602, 1584, 1544, 1501, 1275, 1234, 1030, 981, 816, 786, 621; Anal. calcd for $C_8N_{10}O_{13}Cl_2$ (%): C 18.66, N 27.19, found C 18.40, N 26.95.

Potassium salts of 3,4-bis(3-dinitromethylfurazan-4-oxy)furazan (**5**): To a solution of **4** (1.3 g, 2.5 mmol) in MeOH (18 mL), a solution of KI (2.0 g, 12 mmol) in MeOH (22 mL) was added dropwise at 25 °C. The resulting mixture was stirred for 1 h and triturated with Et$_2$O (20 mL). Precipitate was collected, washed with ice-cold water, MeOH, and Et$_2$O to furnish **5** (0.81 g, 85.7 %) as a yellow solid. dec. 221–222 °C; ^{13}C NMR (DMSO-d_6, 125 MHz) δ 160.54, 153.57, 142.40, 119.58; IR (cm^{-1}, KBr) 1597, 1569, 1552, 1529, 1483, 1312, 1230, 1036, 1000, 743; Anal. calcd for $C_8N_{10}O_{13}K_2$ (%): C 18.36, N 26.76, found C 18.12, N 26.49.

3,4-bis(3-Fluorodinitromethylfurazan-4-oxy)furazan (BFF): To a suspension of **5** (0.35 g, 0.67 mmol) in anhydrous acetonitrile (15 mL), XeF$_2$ (0.46 g, 2.7 mmol) was added under stirring, and reaction mixture was stirred for 60 h at 20 °C. The acetonitrile was evaporated, the residue was treated with water. The white crystals were collected by filtration to afford 6 (0.18 g, 56.2 %) as colorless crystals. mp 48–49 °C; ^{13}C NMR (DMSO-d_6, 125 MHz) δ 159.85, 153.33, 138.03, 114.21; ^{19}F NMR (DMSO-d_6, 470.5 MHz) δ −106.84; ^{15}N NMR (DMSO-d_6) δ −30.11, 1.81, 5.38, 47.45; IR (cm^{-1}, KBr) 1608, 1576, 1545, 1507, 1350, 1309, 1250, 1194, 1033, 982; Anal. calcd for $C_8N_{10}O_{13}F_2$ (%): C 19.93, N 29.05, found C 20.08, N 29.13.

3 Results and Discussion

3.1 Reaction Process

3,4-bis(3-Cyanofurazan-4-oxy)furazan **1** and 3,4-bis(3-aminoximidofurazan-4-oxy)furazan **2** were prepared according to a known procedure [7]. Lukyanov et al. had described the synthesis of chlorodinitromethyl group from chlorooximes by nitration with N$_2$O$_5$ [16–18]. Therefore, when **3** was subjected to N$_2$O$_5$ in chloroform, 3,4-bis(3-chlorodinitromethylfurazan-4-oxy)furazan (**4**) were formed in a low yield (28 %). Compound **4** was further reacted with KI/CH$_3$OH yielding potassium salt of 3,4-bis(3-dinitromethylfurazan-4-oxy)furazan (**5**) in 85.6 % yield. Potassium salt **5** is the most sensitive compound and should be handled with care. In the last step the fluorinating **5** with XeF$_2$ in dry acetonitrile could be accomplished in moderate yields. When acetonitrile contained a little amount of water, the yield of BFF decreased markedly.

3.2 Spectroscopy

Compounds **4**, **5**, and BFF were structurally characterized by FT-IR and NMR spectroscopy. The FT-IR spectrum of **4** showed strong signals at 1602 cm^{-1} (ν_{as}
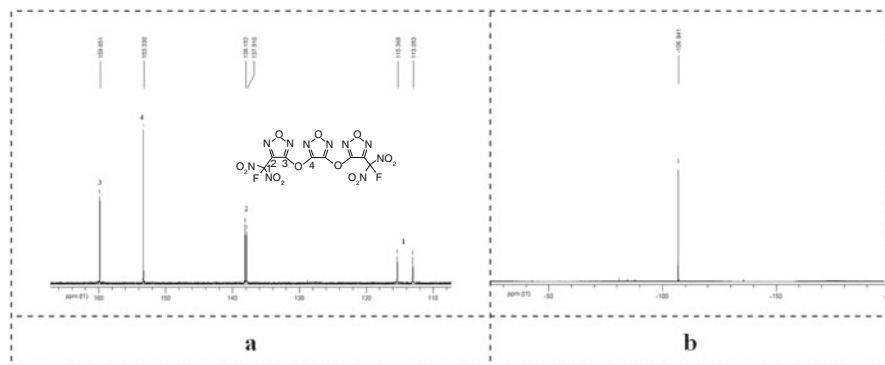
Fig. 2 ^{13}C NMR (**a**) and ^{19}F NMR (**b**) spectra of **BFF**

N–O str.), 1275 cm^{-1} (v_s N-O str.), 621 cm^{-1} (v C–Cl) corresponding to the CCl(NO$_2$)$_2$ moiety. It also showed bonds of strong intensity at 1584, 1544, 1501, 1336, 981 cm^{-1} (furazan ring) and 1234 cm^{-1} (v_{as} ether bond str.), 1030 cm^{-1}(v_s ether bond str.), corresponding to the characteristic absorptions of furazanyl ether [6, 7, 9, 10]. Compound **5** showed strong absorptions from the dinitromethanide anions part at 1483 (v_{as} N–O str.) cm^{-1} and 1230 (v_s N–O str.) cm^{-1}, which were different from those of the CCl(NO$_2$)$_2$ and CF(NO$_2$)$_2$ group. The absorptions for furazanyl ether moiety were observed at 1597, 1569, 1552, 1529, 1312, 1000 cm^{-1} (furazan ring) and 1148, 1036 cm^{-1} (v_{as} and v_s ether bond). BFF showed strong signals at 1608 cm^{-1} (v_{as} N–O str.), 1309 cm^{-1} (v_s N–O str.), 1230 cm^{-1} (v C–F str.) corresponding to the CF(NO$_2$)$_2$ moiety. The absorptions corresponding to the furazanyl ether moiety were observed at 1576, 1543, 1507, 1350, 982 cm^{-1} (furazan ring) and 1194, 1033 cm^{-1} (v_{as} and v_s ether bond).

In the ^{13}C NMR spectroscopy, **4**, **5**, and BFF showed the carbon resonance of the dinitromethyl group at 113–120 ppm because of the electron-withdrawing nature of nitro group; the resonance is shifted toward higher field in the order of **4**, BFF, and **5**. The same trend was observable in the ^{13}C NMR spectra of these compounds for the carbon atom of the furazan ring. Figure 2 shows the ^{13}C NMR and ^{19}F spectra of BFF. The ^{13}C NMR spectrum showed four different signals for the chemically different carbon atoms the molecule. The highly deshielded carbon atoms (C3 and C5) on the furazan ring showed resonances downfield from TMS, at $\delta = 159.85$ and $\delta = 153.33$ ppm, respectively. The resonance signals for C1 ($\delta = 114.21$ ppm) and C2 ($\delta = 138.03$ ppm) showed splitting due to the interaction with F atom, and therefore a doublet signal was observed. The observed coupling constants for $^1J_{13C-19F}$ and $^2J_{13C-19F}$ have values at 290 and 30Hz. These constants are in good agreement with typical values for $^1J_{13C-19F}$ and $^2J_{13C-19F}$ coupling constants [11, 12, 18]. The ^{19}F NMR spectrum showed resonance signals at $\delta = -106.84$ ppm corresponding to the F atoms. The values from elemental analyses (C, H, N) performed on the molecules showed very good correlation with the theoretical values.
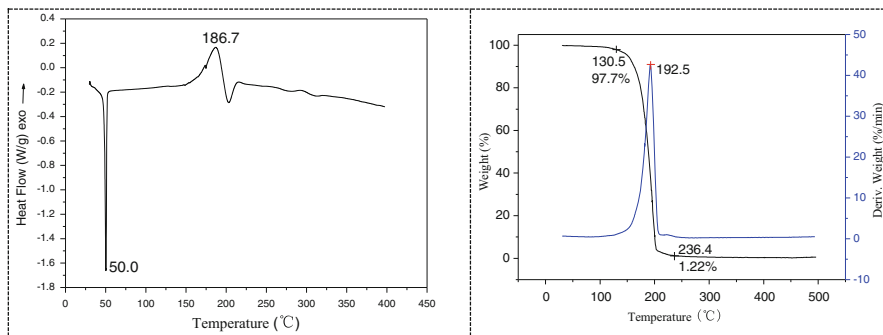
Fig. 3 The DSC (**a**) and TG-DTG (**b**) curves of BFF

3.3   Thermal Analysis

In order to study the thermal decomposition of BFF, the DSC and TG-DTG experiments were carried out under the heating rate of 5 K min^{-1} with flowing dry oxygen-free nitrogen atmosphere. From DSC and TG-DTG curves (Fig. 3), it was found that the thermal behaviors of BFF present multiple stages. The first stage is a typical melting process, and the extrapolated onset temperature and peak temperature are 40.5 °C and 50.0 °C, respectively. When heating temperature is greater than 145 °C, the melting samples begin to slowly evaporate, thus the thermal behavior presents slight endothermic trend, and corresponding TG curve begins to fall. At about 150 °C, the thermal behavior presents an obvious exothermic trend, therefore we believe that BFF begins to decompose at this temperature. Soon after, the thermal behavior presents an obvious endothermic process again, because decomposition heat is less than evaporation heat of melting BFF. Thus, it can be seen that the thermal stability of BFF is good.

3.4   Energetic Properties

Detonation properties of BFF were determined or calculated, and listed in Table 1. The data are compared to these of bis(2-fluoro-2,2-diniroethyl)formal (FEFO) and RDX. The impact sensitivity of BFF was investigated according to the fall hammer method using a 2.0 kg drop hammer on a ZBL-B impact sensitivity instrument. BFF has an impact sensitivity of 11 J, which is less than that of RDX (7.4 J) [19] and similar to that of FEFO (13.5 J) [20]. The density of BFF was measured using a gas pycnometer at room temperature, and its density was 1.88 g cm^{-3} which is even higher than that of 1,3,5-trinitroperhudro-1,3,5-triazine (RDX). Oxygen balance (OB) is an expression that is used to indicate the degree, to which an explosive

Table 1 Detonation properties of BFF

	BFF	RDX [19]	FEFO [20]
Formula	$C_8F_2N_{10}O_{13}$	$C_3H_6N_6O_6$	$C_5H_6F_2N_4O_{10}$
Molar mass	482.1	222.1	320.1
Nitrogen content (%)	28.1	37.8	17.5
Density (g cm^{-3})	1.88	1.800	1.601
Melting point (°C)	50.2	203	14.5
Oxygen balance (%)	−6.6	−21.6	−74.0
Impact sensitivity (J)	11	7.4	15
Enthalpy of formation (kJ mol^{-1})	−111.1	70.63	849.8
Detonation velocity (m s^{-1})	8318	8748	7500
Detonation pressure (GPa)	32	34.9	25

can be oxidized. The oxygen balance of BFF was calculated to be −6.6 %, and this value is better than the OB for RDX (−21.6 %) and TNT (−74.0 %).

Detonation velocity and detonation pressure are another important parameters in evaluating the performance of energetic compounds. These parameters are directly related to the density and the enthalpy of formation. The enthalpy of formation was calculated by *Gaussian 03* program [21]. With the experimental data found for the densities, calculated enthalpy of formation and the empirical formulae for BFF, the detonation velocity and detonation pressure calculated based on *Kamlet-Jacobs* equations are falling in the acceptable range for new high-performance energetic materials. All properties indicate that BFF exhibits good application performances as an energy plasticizer.

4   Conclusions

In this contribution we reported on the synthesis and full structural as well as spectroscopic characterization of 3,4-bis(3-fluorodinitromethylfurazan-4-oxy)furazan (BFF). It is possible to convert 3,4-bis(3-cyanofurazan-4-oxy)furazan to the corresponding fluorodinitromethyl compound via a five-step reaction process, revealing a new synthetic pathway toward new energetic fluorodinitromethyl derivatives. BFF has a predicted detonation velocity of 8318 m s^{-1} and a detonation pressure of 32 GPa while having an impact sensitivity of 11 J and a density of 1.88 g cm^{-3}; thus, it is of lower sensitivity than RDX (impact: 7.4 J) while being significantly more powerful than FEFO ($D = 7500$ m s^{-1}, $P = 25$ GPa); these properties make it suitable as a promising high-energy plasticizer for a solid propellant.

References

1. Sheremetev AB (1995) Chemistry of Furazans fused to five-membered rings. J Heterocycl Chem 32:371–385
2. Badgujar DM, Talawar MB, Asthana SN, Mahulikar PP (2008) Advances in science and technology of modern energetic materials: an overview. J Hazard Mater 151:289–305
3. Wang J, Liv JS, Huang YG, Dong HS (2008) A new high energetic material compound 3, 4-Bis(nitrofurazano)furoxan: synthesis, characterization and properties. New trends in research of energetic materials. Czech Republic, University of Pardubice, pp 182–193
4. Sheremetev AB, Mantseva EV (2001) Hydroxyfurazans: outlook to using. In: 32th international annual conference of ICT, Karlsruhe, vol 103, pp 1–4
5. Sheremetev AB, Kharitonova OV, Mantseva EV, Kulagina VO, Shatunova EV, Aleksandrova NS, Melnikova TM, Ivanova EA, Eman VE, Novikova TS, Lebedev OV (1999) Nucleophilic displacement in furazan series? Reactions with O-nucleophiles. Zh Org Khim 35:1555–1566
6. Sheremetev AB, Kharitonova OV, Mel'nikova TM, Novikova TS, Kuz'min VS, Khmel'nitskii LI (1996) Synthesis of symmetrical difurazanyl ethers. Mendeleev Commun 4:141–143
7. Sheremetev AB, Kulagina VO, Aleksandrova NS, Dmitriev DE, Strelenko YA (1998) Dinitro trifurazans with oxy, azo and azoxy bridges. Propellants Explos Pyrotechnics 23:142–149
8. Sheremetev AB (1998) 3,3-Bis(1-fluoro-1,1-dinitromethyl)difurazanyl ether. In: 29th international annual conference of ICT, Karlsruhe, Germany, vol 58, pp 1–6
9. Fan YJ, Wang BZ, Lai WP, Lian P, Jiang J, Wang XJ, Xue YQ (2009) Synthesis, characterization and quantum chemistry study on 3,3′-Dicyanodifurazanyl Ether (FOF-2). Chin J Org Chem 29:614–620
10. Zhou YS, Xu KZ, Wang BZ, Zhang H, Qiu QQ, Zhao FQ (2012) Synthesis, structure and thermal properties of bifurazano[3,4-b :3′,4′-f] furoxano [3″,4″-d] oxacyclohetpatriene(BFFO). Bull Kor Chem Soc 33:3317–3320
11. Wang XJ, Xu KZ, Sun Q, Wang BZ, Zhou C, Zhao FQ (2014) The insensitive energetic material trifurazano-oxacycloheptatriene (TFO): synthesis and detonation properties. Propellants Explos Pyrotechnics. doi:10.1002/prep.201400148
12. Gidaspov AA., Bakharev VV, Velikanova EV, Tselinsky IV (2009) The fluorination of dnitromethyl-1,3,5-triazines salts with xenon difluoride. New trends in research of energetic materials. Czech Republic, University of Pardubice, pp 539–541
13. Semenov VV, Kanischevy MI, Shevelev SA, Kiselyov AS (2009) Thermal ring-opening reaction of N-polynitromethyl tetrazoles: facile generation of nitrilimines and their reactivity. Tetrahedron 65:3441–3445
14. Klapötke TM, Krumm B, Rest SF, Reynders M, Scharf R (2013) (2-fluoro-2,2-dinitroethyl)-2,2,2-trinitroethylnitramine: a possible high-energy dense oxidizer. Eur J Inorg Chem 2013:5871–5878
15. Kettner MA, Karaghiosoff K, Klapötke TM, Suceska M, Wunder S (2014) 3,3′ -Bi(1,2,4-oxadiazoles) featuring the fluorodinitromethyl and trinitromethyl groups. Chem Eur J 20:7622–7631
16. Lukyanov OA, Zhiguleva TI (1982) New method for preparation of α-chlorodinitro compounds. Bull Acad Sci USSR 31:1270–1271
17. Lukyanov OA, Pokhvisneva GV (1991) 2,2,2-trinitroethyl ethers of 2,2-dinitroalcohols. Bull Acad Sci USSR 40:2439–2444
18. Luk'yanov OA, Pokhvisneva GV, Ternikova TV, Shlykova NI, Shagaeva ME (2011) α-nitroalkyl-ONN-azoxyfurazanes and some of their derivatives. Russ Chem Bull Int Ed 60:1703–1704
19. Gao H, Joo Y-H, Parrish DA, Vo T, Shreeve JM (2011) 1-amino-1-hydrazino-2,2-dinitroethene and corresponding salts: synthesis, characterization, and thermolysis studies. Chem-A Eur J 17:4613–4621

20. Klager K., Rindone R (1987) Development of an efficient way to manufacture Bis (2-fluoro-2,2-diniroethyl) Formal (FEFO). In: Proceedings of the 18th international annual conference of ICT Karlsruhe, vol 28, pp 1–6
21. Gaussian 03, Revision D.01, Frisch MJ, Trucks GW, Schlege HB, Scuseria GE, Robb MA, Cheeseman JR, Montgomery JA, Kudin KN, Burant JC, Millam JM, Iyengar SS, Tomasi J, Barone V, Mennucci B, Cossi M, Scalmani G, Rega N, Petersson GA, Nakatsuji H, Hada M, Ehara M, Toyota K, Fukuda R, Hasegawa J, Ishida M, Nakajima T, Honda Y, Kitao O, Nakai H, Klene M, Li X, Knox JE, Hratchian HP, Cross JB, Bakken V, Adamo C, Jaramillo J, Gomperts R, Stratmann RE, Yazyev O, Austin AJ, Cammi R, Pomelli C, Ochterski JW, Ayala PY, Morokuma K, AVoth G, Salvado P, Dannenberg JJ, Zakrzewski VG, Dapprich S, Daniels AD, Strain MC, Farkas O, Malick DK, Rabuck AD, Raghavachari K, Foresman JB, Ortiz JV, Cui Q, Baboul AG, Clifford S, Cioslowski J, Stefanov BB, Liu G, Liashenko A, Piskorz P, Komaromi I, Martin RL, Fox DJ, Keith T, Al-Laham MA, Peng C, Nanayakkara A, Challacombe M, Gill PMW, Johnson B, Chen W, Wong M, Gonzalez C, Pople JA (2003) Gaussian 03, revision D.01. Gaussian, Inc, Wallingford

Part III
Metals as Energetic Fuels
for Chemical Propulsion

Prospects of Aluminum Modifications as Energetic Fuels in Chemical Rocket Propulsion

Luigi T. DeLuca, Filippo Maggi, Stefano Dossi, Marco Fassina, Christian Paravan, and Andrea Sossi

Abstract The use of metals as high-energy fuels has been for long time a common approach to increase performance of chemical rocket propulsion in general. This effort was initially triggered by theoretical thermochemical considerations, but under real operating conditions, a series of collateral and unforeseen effects occurred, with both positive and negative consequences. After six decades, the use of micron-sized Al is the most common practice at industrial level for solid rocket propulsion in particular. Yet attempts are under way to mitigate some of the most deleterious effects: notably, the two-phase flow losses and slag accumulation taking place in gasdynamic nozzles. In this paper, a range of modified Al powders is discussed, going from nano-sized uncoated to coated Al particles and from chemically to mechanically activated micron-sized Al. These variants are duly characterized and comparatively tested under laboratory burning conditions. Due to page limitations, mainly the class of aluminized composite propellants (ammonium perchlorate/inert binder) and operating conditions often used in space applications are investigated. The reader is cautioned to avoid making generalizations to other formulations and conditions based on this limited dataset. Each of the tested Al variants has its own properties, and implementation in full-scale propulsive systems needs to be carefully evaluated for an overall assessment. The recommended strategy for best results is a dual mode Al mixture, synergistically exploiting each component. Other metal fuels, especially hydrides and boron compounds, are examined as well. New trends, capable of drastically changing the current situation but still in their infancy as of this writing, are briefly discussed at the end of the paper.

L.T. DeLuca (✉) • F. Maggi • S. Dossi • M. Fassina • C. Paravan • A. Sossi
Space Propulsion Laboratory (SPLab), Department of Aerospace Science and Technology, Politecnico di Milano, 20156 Milan, Italy
e-mail: luigi.deluca@polimi.it; filippo.maggi@polimi.it; stefano.dossi@polimi.it; marco.fassina@polimi.it; christian.paravan@polimi.it; andrea.sossi@mail.polimi.it

191

Nomenclature

a	Multiplicative factor in the Vieille steady burning rate law, $(mm/s)/bar^n$
actAl	Activated Al
ADN	Ammonium dinitramide
AFM	Atomic force microscopy
ALEX™	ALuminum EXploded (a trademark by APT, Tomsk, Russia)
AP	Ammonium perchlorate
APT	Advanced Powder Technologies
a_s	Mean surface particle diameter, nm
BET	Brunauer–Emmett–Teller
BPR	Ball-to-powder mass ratio
c	Specific heat, J/g K
CA	Chemical activation
C_{Al}	Active metal content, mass %
CCP	Condensed combustion products
D	particle diameter, cm
EDX	Energy dispersive X-ray analysis
EEW	Electrical explosion of wires
EM	Energetic materials
F-ALEX$_A$	ALuminum EXploded, coated by trihydroperfluoro-undecyl alcohol
F-ALEX$_E$	ALuminum EXploded, coated by ester from esterification of trihydroperfluoro-undecyl alcohol with maleic anhydride
GAP	Glycidyl azide polymer
HEDM	High-energy-density material
HMX	Cyclotetramethylenetetranitramine
HTPB	Hydroxyl-terminated polybutadiene
IARC	International Agency for Research on Cancer
ICP	Inductively coupled plasma analysis
I_s	Gravimetric specific impulse, s
I_v	Volumetric (or density) specific impulse, $s \cdot g/cm^3$
k	Thermal conductivity, J/cm s K
L-ALEX™	ALuminum EXploded, coated by stearic acid
LH_2	Liquid hydrogen
LOx	Liquid oxygen
$\mathcal{M}$	Molecular mass, g/gmole
Mg_xB_y	composite metal made, in mass, by x % Mg and y % B
MM	Mechanical milling
n	Pressure exponent in the Vieille steady burning rate law
nAl	Nano-sized aluminum
NAp.	not applicable
NAv.	not available
O/F	Oxidizer-to-fuel ratio

p	Pressure, bar
P-ALEX™	ALuminum EXploded, coated by palmitic acid process control agent
PDL	Pressure deflagration limit
PTFE	Polytetrafluoroethylene
r_b	Steady burning rate, mm/s
RDX	Cyclotrimethylenetrinitramine
SEM	Scanning electron microscopy
SPLab	Space propulsion laboratory
SRB	Solid rocket booster
SRM	Solid rocket motor
S_{sp}	Specific surface area, m^2/g
TEM	Transmission electron microscopy
TG	Thermogravimetry
T_{melt}	melting temperature, K
T_{vap}	vaporization/decomposition temperature, K
VF-ALEX	ALuminum EXploded, coated by Fluorel™ FC-2175 (copolymer of vinylidene fluoride and hexafluoropropylene made by 3M) and ester
XRD	X-ray diffraction analysis
Δh_f^0	Standard heat of formation, kJ/mole (see Table 1)
Δh_{melt}	melting enthalpy, kJ/mole (see Table 1)
Δh_r	reaction enthalpy, kJ/g or kJ/cm^3 (see Table 1)
Δh_{vap}	vaporization/decomposition enthalpy, kJ/mole (see Table 1)
ΔV	Vehicle velocity increment, m/s
μAl	Micron-sized aluminum
ρ	Density, g/cm^3

1   Background

Although the first suggestion by Tsander to use aluminum as high-energy fuel dates back to 1909, testing of metals, or metallic compounds, started only after the Parson discovery of castable composite propellants in 1942. However, a lot of attempts and efforts were needed before Henderson and Rumble succeeded in adding Al powder, thus significantly increasing the propellant specific impulse in 1955. For historical details, see chapter "Highlights of Solid Rocket Propulsion History" in this book.

As a matter of fact, metals in general burn with marked difficulties due to resistance to ignition, uncertain dynamics of the combustion process in both homogeneous and heterogeneous phase, and unlikely completion of the underlying oxidation reactions. Even larger difficulties are faced by the resulting two-phase mixtures during expansion in the gasdynamic nozzle. The main reason for these difficulties lies in the fact that the condensed-phase reaction products result in two-phase flows where physical aspects dominate over chemistry in combustion chambers and over gasdynamics in nozzles. The associated performance losses could totally be eliminated by employing substances based on F_2 instead of O_2

as the oxidizer, thus yielding volatile rather than condensed combustion products. Unfortunately, both F_2 and its combustion products are extremely toxic and therefore will likely be utilized only in deep space missions.

During combustion, metallic powders release considerable energy due to their high enthalpy of combustion, thus increasing the adiabatic flame temperature and subsequently the propellant gravimetric specific impulse (I_s) in spite of the simultaneous increase of the average molar mass of the combustion products. Metals also increase the propellant density and subsequently the propellant volumetric specific impulse (I_v). Both effects are consistent with primary requirements for space propulsion missions [1, 2]. An unforeseen but very welcome additional effect is the consequent resistance to high-frequency combustion instabilities revealed by metalized formulations. However, concomitant drawbacks were soon discovered: the remarkable increase of adiabatic flame temperature also implies a dangerous increase of thermal fluxes to the motor walls and subsequently an increase of the motor inert mass fraction needed to accommodate more ablative material. A range of detrimental effects takes place in the gasdynamic nozzle, especially in the throat area region, all implying I_s losses due to two-phase flow with subsequent thermal and kinetic nonequilibrium, slag accumulation, nozzle submergence, and nozzle erosion. Also, the emission of a plume consisting of intense primary white smoke of alumina (for Al burning) and electrically charged particles hindering electromagnetic communications is not appreciated by both military bodies and green organizations defending the environment.

Aluminum is one of the most commonly used metal fuels because of its high oxidation enthalpy under a variety of oxidizing atmospheres, high density, low price, good availability, and low oxygen demand. Micron-sized aluminum (μAl) powders have been used for decades in solid propellants to increase the formulation specific impulse and the resistance to high-frequency acoustic instabilities. However, the clustering/aggregation effects of μAl particles, occurring under certain conditions prior to their ignition, favors the deleterious agglomeration phenomena due to inflammation and coalescence by melting. This leads to specific impulse losses due to incomplete metal combustion and two-phase flow effects. In hybrid rocket fuels, μAl has been used, without success, to augment the radiative heat feedback from the flame zone to the gasifying surface, the aim being to increase the regression rate, which is currently one of the limiting factors of these propulsive systems.

Combustion of Al in propulsion applications turns out to be an extremely complex and multifaceted process. Even though most of the Al particles burn as a single particle, either on the burning surface or far from it, a significant fraction of the total Al mass burns as clusters of particles. This is due to a highly intricate mechanism of cohesion, exudation, aggregation, and agglomeration that likely starts in the subsurface region and continues in the convective two-phase flow issued from the surface until all reactions stop at a relatively large distance from the surface. Rarely are these processes finished at the surface. At any rate, the simultaneous occurrence of homogeneous combustion (yielding fine products of reaction) and heterogeneous combustion (yielding coarse products of reaction) eventually gives rise to a bimodal product distribution. While the homogeneous combustion in the

gas phase is believed to be well understood, its heterogeneous counterpart is only poorly known.

An alternative approach of strong interest is to use hydrides instead of the corresponding metals [3]. In this respect, AlH_3 and BeH_2 come out especially attractive and promise significant increase of the ideal gravimetric specific impulse for solid and hybrid propellant rockets. Hybrid rocket engines based on BeH_2 can achieve, at least theoretically, the maximum performance in the field of chemical propulsion, much above that of the current cryogenic couple LH_2/LOx. However, beryllium is not allowed due to its toxicity, and hydrides are in general difficult to synthesize and typically manifest problems of chemical instability. That is, they spontaneously release H_2 after some more or less extended lapse of time.

In general, in a composite formulation, hydrogen release from hydrides is a fast process with respect to the competing binder decomposition and thus acts to sustain and intensify the surrounding flame with prompt and fast hydrogen diffusion. However, metals and metal hydrides are different energetic ingredients and follow different mechanisms during the overall combustion process, even with respect to the basic metal component. In particular, rapid dehydrogenation of metal hydride particles during the combustion process leaves behind a porous metal matrix due to the cavities formed by the gasified hydrogen. The final result is a metallic structure much more reactive than the corresponding solid metal, even if shaped as a micron-sized particle.

Conventional μAl powders have been ineffective in enhancing either the burning rate of solid propellants or regression rate of solid fuels in hybrid propellants. Thus, propellant formulators have directed their attention to suitable variants of the μAl powders such as nano-sized aluminum (nAl) powders, chemically activated μAl powders, mechanically activated μAl powders, boron compounds, and so on with the intent of mitigating the ballistic drawbacks of the conventional μAl powders [4]. This paper will discuss the prospective of μAl powder variants as energetic fuels under laboratory conditions. Agglomeration phenomena are observed near/at the burning surface (incipient agglomeration) and no attempt is made to discuss combustion modeling. The reader is expected to be familiar with the open literature available in this area. Due to page limitations, priority will be given to solid rocket propulsion, focusing on formulations and operating conditions commonly used in space launchers. A companion paper devoted to hybrid rocket propulsion is authored by Karabeyoglu in this volume [5]. A variety of potentially useful additives for improving the regression rate or system performance of hybrid rocket engines was tested and reported in a referenced paper [6].

2 Thermochemical Properties

The use of metal powders in hybrid and solid propulsion pursues different targets. Both gravimetric and volumetric specific impulses can be incremented in solid propellants, depending on the specific additive. The former takes advantage of

combustion enthalpy, while density increment favors the latter one. For hybrid rocket propellants, the addition of metals depresses the gravimetric specific impulse I_s due to the increment of the molar mass of the combustion products. However, density increment represents an important contribution to obtain a higher mass burning rate.

2.1 Metal Fuels

In the open literature Al, Be, B, Li, Mg, Na, Zr, Fe, Cr, and other metals are commonly considered for space applications. The scope of their use can range from increasing enthalpy release, improving either specific impulses or density, or acting as a combustion catalyst. The current industrial state of the art considers the use of micrometric powders. In most cases, there are nanometric alternatives, but several issues related to safety, processing, handling, storing, dispersion, aging, and cost are introduced [7].

Out of this group, there is interest in using Al, B, Mg, and Zr as metal fuels. Beryllium and its derivatives are considered carcinogens by IARC, discouraging their application [8].

Aluminum is one of the most common components in space propulsion. It is an amphoteric metal whose density is 2.70 g/cm^3. The oxidation of Al to the aluminum (III) oxide (alumina, α-Al$_2$O$_3$) generates a heat of reaction of 31.07 kJ/g (83.89 kJ/cm^3) [9]. It features a low toxicity and, as micrometric particles, is relatively safe and easy to compound. Aluminum's positive contribution to ideal performance is calculated for solid propellants, both for its density and for its enthalpy release. The combustion of this material generates condensed products which can be liquid or solid particles, depending on local temperature.

Magnesium is a metal which is fairly easy to ignite and oxidize and has a density of 1.74 g/cm^3. It is considered a low-performance alternative to Al, with lower gravimetric and volumetric heat of reaction, 24.7 kJ/g and 43.0 kJ/cm^3, respectively [10]. Reactivity of Mg is exploited to promote the reaction of other metals which are more reluctant to ignite, such as boron.

Boron is a metalloid with density of 2.34 g/cm^3. Its oxidation to solid boron (III) oxide B$_2$O$_3$ generates a theoretically high value of both gravimetric and volumetric heat of reaction (58.86 kJ/g and 137.73 kJ/cm^3, respectively), making it a good candidate for high energy-density applications [9]. The B$_2$O$_3$ has a boiling point of about 2300 K, so it appears that the full exploitation of B combustion energy release can be obtained only if condensation of the oxide is ensured in the propulsion system [11]. On the other hand, oxide vaporization contributes to the reduction of condensed combustion products and of related specific impulse losses. In actual use, poor particle ignition results in a low combustion efficiency. Recent developments in magnesium–boron alloys enabled rapid particle ignition and efficient combustion [12].

Zirconium has a density of 6.52 g/cm^3 and has mostly been used to increment the density of the propellant. Oxidation to zirconium (IV) oxide (zirconia, ZrO_2) does not provide an attractive gravimetric heat of combustion, which is 12.03 kJ/g. But because of the high density, the volumetric heat release is 78.43 kJ/cm^3 [9].

2.2 Ideal Computed Performance

The performance of solid rocket propellant and hybrid fuel alternatives can be predicted and compared via thermochemical calculations based on the characteristics of the ingredients in the initial composition and their total enthalpy (formation and sensible). Information on combustion products can be obtained, as well. In these calculation techniques, the physical organization of the mixture (e.g., in bricks, micrometric particles, or nanopowders) has no meaning, unless connected to a significant energetic contribution. For example, in the case of nanometric particles, a surface energy may be associated to the size, due to the increasing ratio between superficial and bulk atoms, but this effect is negligible for the range of interest (namely, 100 nm or above) [13, 14]. At the same time, the difference between nominal and real powder composition has to be considered, if passivation layers or surface treatments measurably affect the active metal content.

The following performance data are computed assuming chemical equilibrium in the combustion chamber and, locally, in the nozzle. Reference combustion chamber pressure is 70 bar, nozzle area ratio is 40, and vacuum conditions are assumed. Solid propellant formulations composed of hydroxyl-terminated polybutadiene binder (HTPB, $C_{7.075} H_{10.65} O_{0.223} N_{0.063}$, $\Delta h_f^0 = -58$ kJ/mole) and ammonium perchlorate (AP, NH_4ClO_4, $\Delta h_f^0 = -295.8$ kJ/mole) as oxidizer [15] are compared below. Hybrid rocket performance is evaluated for HTPB binder and liquid oxygen (LOx, $O_{2(l)}$, $\Delta h_f^0 = -13$ kJ/mole), at the boiling point of 90 K [10].

Figure 1 reports volumetric and gravimetric specific impulse for solid propellants having a fixed AP/metal/HTPB formulation of 68/18/14 mass fraction. Figure 2 reports the same data for HTPB/metal hybrid rocket fuels with 90/10 mass fraction. For solid propellants, the aluminum is the metal featuring the highest I_s and I_v. Zirconium has the lowest I_s, but it ranks second for I_v, due to metal density. The other fuels have lower I_v and intermediate I_s. The reader should note that the proposed formulations are not optimal because the stoichiometric oxidizer requirement of the various metals is ignored. AP/metal/HTPB compositions are compared on the basis of equal mass of added metal.

In hybrid rockets, all metals lower the maximum I_s capability, but performance does not change dramatically, with the exception of an oxidizer/fuel shift towards lower value of curve peak. The use of Al or B gives better results than other proposed candidates. The higher density of the metalized polymer fuel improves I_v. The use of Al, B, and Zr enables higher I_v, if compared to Mg and pure HTPB.

The relevant properties of the selected metals (Al, B, Mg, Zr) and of their most common oxides are summarized in Table 1. The volumetric heat release is maximum for B, followed by Al and Zr; while the gravimetric heat release is maximum for B,
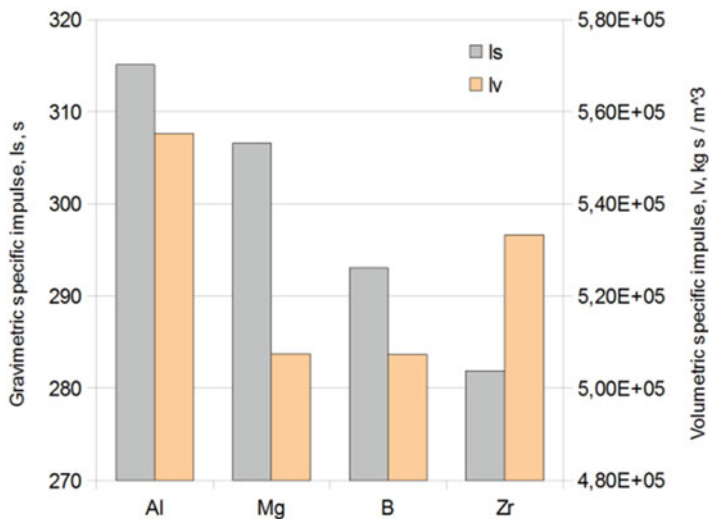
Fig. 1 Solid propellant performance parameters for fixed composition of 68 mass % AP, 14 mass % HTPB, and 18 mass % of metal fuel
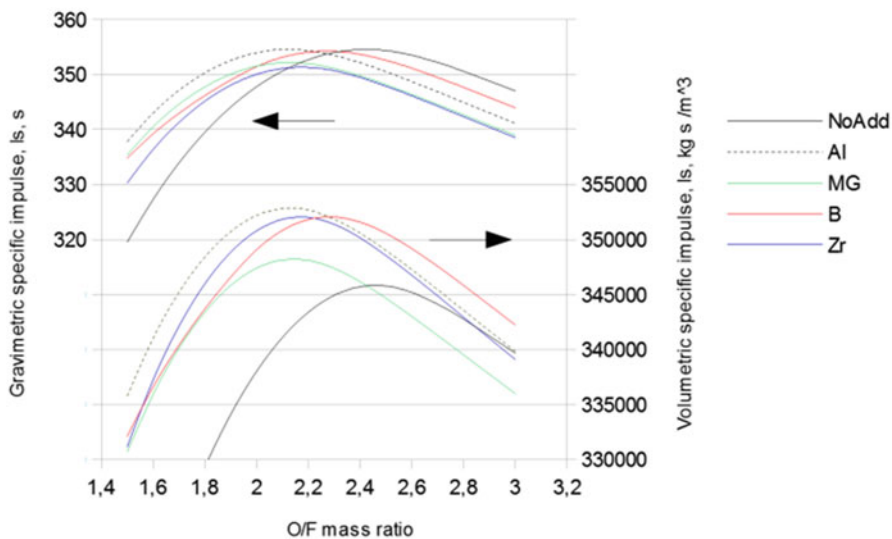

Fig. 2 Hybrid rocket performance parameters for 90 mass % HTPB and 10 mass % metal fuel burning in LO_x

Table 1 Properties of currently used metallic fuels and their most common oxides

Metals and most common oxides	ρ, g/cm^3	$\mathcal{M}$, g/mole	Δh_f^0, kJ/mole	T_{melt}, K	Δh_{melt}, kJ/mole	T_{vap}, K	Δh_{vap}^a, kJ/mole	Δh_r^c, kJ/g	Δh_r^c, kJ/cm^3
Al	2.70	27.0	0	933 [16]	10.7 [16]	2792 [16]	294 [16]	31.07	83.89
Al$_2$O$_3$	3.99	102.0	−2550	2327 [16]	111.1 [16]	3253 [16]	109 [18]	NAp.	NAp.
B	2.34	10.8	0	2348 [16]	50.2 [16]	4273 [16]	480 [16]	58.86	137.73
B$_2$O$_3$	2.55	69.6	−1272	723 [16]	24.6 [16]	2133 [17]	360 [17]	NAp.	NAp.
Mg	1.74	24.3	0	923 [16]	8.5 [16]	1380 [18]	136 [18]	24.70	43.00
MgO	3.60	40.3	−601	3098 [16]	77^d [16]	3430^b [17]	670 [17]	NAp.	NAp.
Zr	6.52	91.2	0	2125 [19]	21.0 [19]	3850 [19]	573 [19]	12.03	78.43
ZrO$_2$	5.68	123.2	−1097	2951 [19]	87.0 [19]	4573 [19]	624 [19]	NAp.	NAp.

^{a} At boiling point
^{b} Metal oxides are subject to vaporization-decomposition phenomena [17]
^{c} O$_2$ reaction
^{d} Unknown with enough accuracy

followed by Al and Mg. The metal melting temperature is much less than that of the corresponding oxide for Al and Mg, while the opposite is true for B. The peculiar properties of B hamper its efficient combustion and nozzle expansion. The interest for Zr in propulsion applications is explained by its large value of density, making possible remarkable ΔV increments of the vehicle velocity [1].

3   nAl Powders

The best-known variant of the conventional μAl powders is the nAl powders first tested by Gen et al. in 1978 [20]. In a flow of oxygen-containing gas, they burned nAl produced by vaporization and consequent condensation of the metal vapors in Argon (as invented by Gen et al. in 1959 [21]). A significant decrease of the CCP (condensed combustion product) size was observed. While the initial expectation of an increased internal energy for nAl powders was disproved (for the typical size of interest in propulsion), it is true that the large specific surface area of nAl makes oxidation rates much higher favoring the heterogeneous metal attack compared to the homogeneous one, because of greatly reduced diffusion lengths.

3.1   Production and Characterization

The knowledge of thermophysical properties of energetic additives prior to their employment in energetic formulations is needed to make reliable assessments about their reactivity and interaction with the external environment. The following paragraphs contain the results of experimental thermophysical investigations carried out on several nAl powders, passivated and coated with various chemical species. For details about tools and diagnostics, see [22].

Today an efficient method for obtaining submicron-sized metal powders is the electrical explosion of wires (EEW) technique, in which electrical energy is almost totally consumed for the metal wire gasification [23]. In the case of Al, the metal powders must be passivated by an inert coating immediately after production, due to their pyrophoric behavior. The passivation process can be done by a slow stream of dry gases (Ar + 0.1 % air) or by means of different chemical substances, other than air. The commercial name for nAl powders passivated by aluminum oxide is ALEX™ [24]. The purpose of coating the metal powders with chemicals is to improve their dispersion inside the matrix, mechanical properties and combustion processes of the final formulation. Specific coatings can be chosen to protect the particle surface from the oxidation by air or atmospheric moisture [25].

In this work, two batches of ALEX™ with nominal size of 50 and 100 nm are considered. They were manufactured by a coating process at lab scale [26] as:

- Stearic and palmitic acid (L-ALEX, P-ALEX)
- Trihydroperfluoro-undecyl alcohol (F-ALEX$_A$)

- Ester from esterification of trihydroperfluoro-undecyl alcohol with maleic anhydride (F-ALEX$_E$)
- Fluorel™ FC-2175 (copolymer of vinylidene fluoride and hexafluoropropylene made by 3M) and ester (VF-ALEX)

Such powders were characterized and tested as energetic additives to evaluate the regression rate enhancement with respect to pure HTPB solid fuel for hybrid rockets [27]. Samples of 50 and 100 nm stearic acid-passivated nAl powders are considered as well, in order to assess the differences between industrial-scale passivated powders and lab-scale powders which are coated after passivation.

3.2 Electron Microscopy Analyses

Uncoated powders display spherical shape of particles, as well as fatty acid-coated nAl (see Fig. 3). The presence of flake-shaped structures in uncoated powders is indicative of possible clustering of particles due to the explosion process and cold cohesive forces between granules or cold sintering processes due to the high specific surface area. Signs of the coating manufacturing process are visible in Fig. 4, in which the incomplete solution of fluoropolymer or its return to the solid state after solvent removal is recognizable.

The different image formation mechanism of TEM with respect to SEM provides different information about coating thickness and nAl particle aggregation to be gathered. It is possible to recognize the thin, brighter layer surrounding the metal core in the case of air-passivated powders (ALEX™ samples). Moreover, the formation of a double shell structure with the coating surrounding the air-passivated particle is clearly visible; see Fig. 5.
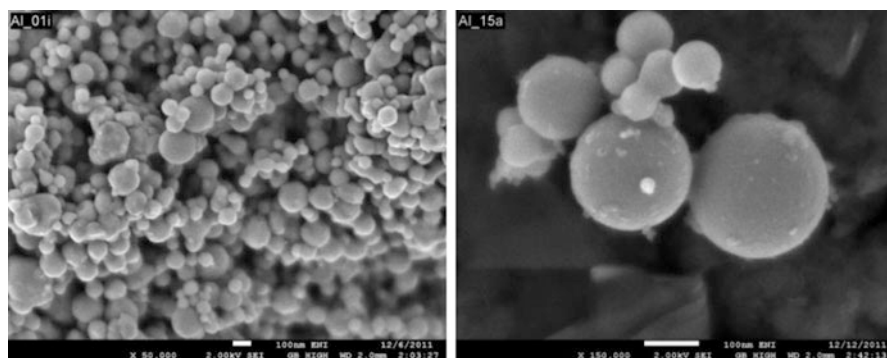
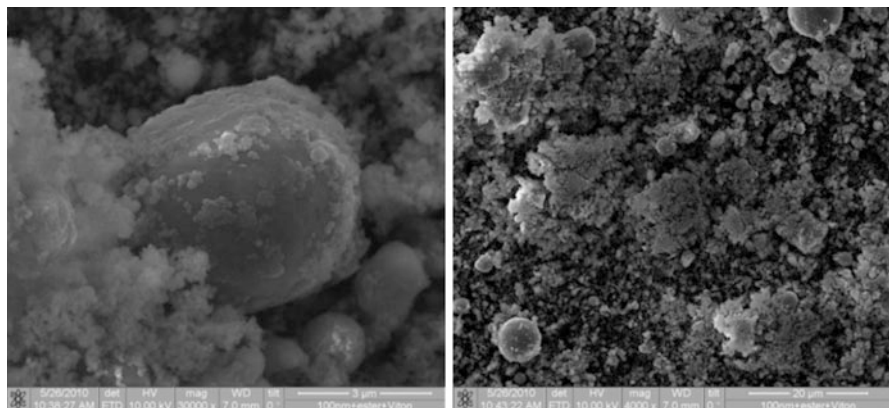**Fig. 3** SEM images of 100 nm ALEX™ (*left*) and 50 nm palmitic acid-coated P-ALEX (*right*)

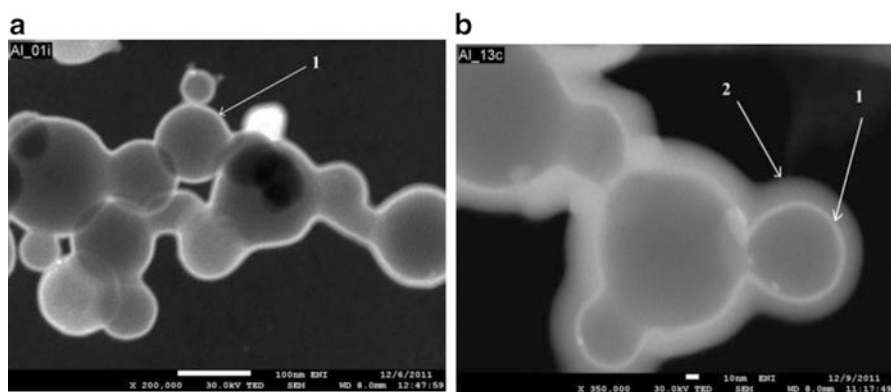**Fig. 4** SEM images of 100 nm Fluorel™ and ester-coated VF-ALEX

Fig. 5 TEM images of nAl [*1* oxide layer; *2* coating layer]: (**a**) 100 nm uncoated ALEX™; (**b**) 50 nm Fluorel™ and ester-coated VF-ALEX

3.3 Physical Analyses

The specific surface area S_{sp} of the nAl powders was evaluated by a BET approach. The active metal content C_{Al} was determined through a volumetric method [28]. Assuming spherical and nonporous particles of density ρ_{Al}, the mean surface particle diameter a_s can be calculated from S_{sp} (Tables 2 and 3), as

$$a_s = \frac{6}{S_{sp}\rho_{Al}} \tag{1}$$

As expected, the BET S_{sp} of 50 nm ALEX™ is greater than that of 100 nm ALEX™. The lowest S_{sp} belongs to Fluorel™ and ester-coated powders, which

Table 2 Physical parameters of 50 nm nAl powders

Powder	BET S_{sp}, m^2/g	a_s, nm	C_{Al}, mass %	ρ_p, g/cm^3
ALEX™	15.7	142	90	2.503
L-ALEX[a]	11.3	197	89	2.329
P-ALEX	13.9	160	71	2.491
VF-ALEX	10.9	204	78	2.559

[a]Stearic acid-passivated

Table 3 Physical parameters of 100 nm nAl powders

Powder	BET S_{sp}, m^2/g	a_s, nm	C_{Al}, mass %	ρ_p, g/cm^3
ALEX™	11.8	188	89	2.522
L-ALEX	9.1	244	70	2.474
P-ALEX	NAv.	NAv.	79	2.448
F-ALEX™	11.3	197	88	2.586
VF-ALEX	6.9	322	78	2.518

is clear evidence of effective coating deposition (and possible effects of particle clustering induced by the coating process itself). An increase of the average particle size related to the coating thickness diminishes the powder specific surface.

The remarkable difference in active Al content, between uncoated ALEX™, stearic acid-passivated L-ALEX, and coated variants, is explained by the presence of a double shell structure for the latter, consisting of a passivating plus a coating layer.

A large amount of data was also provided by DSC and TG traces. A first strong oxidation peak of aluminum and a second less intense oxidation phase above the melting point testify the periodic cracking of the oxide shell surrounding the metal core and the separate oxidation of different particle fractions. These and other data clarify important details about the powder reactivity, as discussed in [22]. However, heating rates are lower by orders of magnitude with respect to those typical of rocket operating conditions. Thus, how to efficiently apply such data to propulsive systems remains a matter of study.

3.4 Suspension Rheology and nAl Dispersion

Heterogeneous solid propellants and solid fuels for hybrid propulsion are formulations containing disperse systems embedded in a binder matrix. The binder is usually an elastomer, typically a polyurethane [29]. Different materials can be considered for this task based on specific requirements such as chemical compatibility or ballistic performance [30]. A commonly used binder in propulsion applications is HTPB. During the propellant/fuel preparation, and after its curing, the rheological behavior of the binder is influenced by the filler addition.

The reduced size and the increased S_{sp} value of nano-sized materials promote their clustering or cold cohesion effects. Due to this effect, the processing of nanomaterial-loaded formulations requires dedicated powder dispersion procedures. The most explored dispersion strategies are based on ultrasonication of particle suspension and use of dispersive agents. For details, see [31, 32] and, in this book, [33].

3.5 nAl Burning in Solid Propellants

Aluminized composite solid rocket propellants loaded with μAl have been studied for decades under a variety of operating conditions, and their ballistics is quite well known; see, for example, [34–36]. Inert binder formulations containing nAl particles, show faster steady burning rates compared with the corresponding propellants containing μAl particles. Nano-sized Al particles manifest a strong reactivity mainly due to their increased specific surface area, notwithstanding the simultaneous decrease of active Al content. Oxidation of nAl is completed very close to/above the burning surface following a form of prompt partial oxidation at/below the burning surface.

The results obtained in previous experimental studies conducted at SPLab can be summarized by the plot in Fig. 6; for details, see [22, 37–43]. Under the common laboratory operating conditions explored for AP/HTPB-based formulations up to
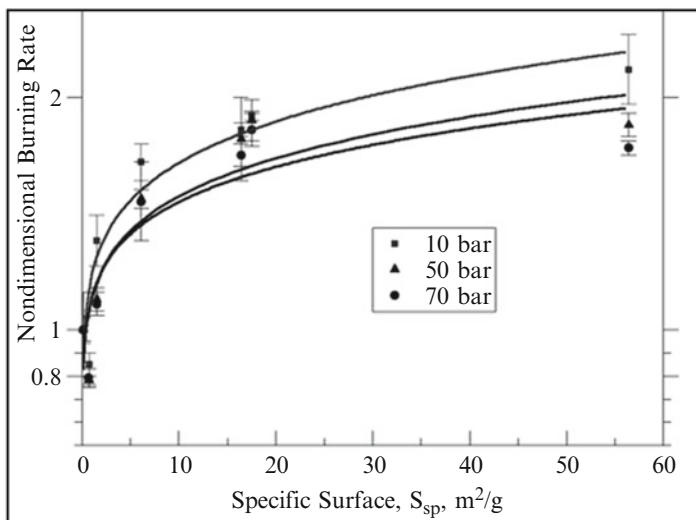
Fig. 6 Normalized steady burning rate vs. BET-specific surface, for solid propellants loaded with nAl powders, showing different sensitivity over the explored S_{sp} range [43]

70 bar, steady burning rates measured for propellants loaded with a variety of Al powders show different sensitivity over the tested S_{sp} range. The observed values are not significantly affected by particles in the micrometric range (say, $S_{sp} \leq 2$ m^2/g), but are strongly increased as the particle size is reduced over the explored nanometric range. The strongest sensitivity in increasing the propellant steady burning rate is noticed for nAl in the range 0.1–0.2 μm (i.e., with S_{sp} in the range 5–20 m^2/g). For the very smallest particles, the appreciable decrease of active metal content hinders a further increase of the propellant steady burning rate in spite of the very fast particle oxidation rate. The maximum propellant steady burning rate increase is by a factor of 2 for S_{sp} approaching 60 m^2/g over the pressure range 10–70 bar. Within the limits of the reported strand burner experiments, pressure exponents in general show only minor changes.

Also for ignition delay, an appreciable decrease is found for solid propellants containing nAl particles in the range 0.1–0.2 μm compared to μAl, while a slight increase was observed for μAl compared to the nonaluminized formulations, due to the increased thermal responsivity $(k \cdot \rho \cdot c)^{1/2}$ of the propellant condensed phase.

3.6 Agglomeration Process

Al particles undergo several events during combustion process. A particular propellant microstructure feature entails the formation of fuel-rich regions, where binder, Al particles, and fine particles of AP are present in high concentrations, confined by coarse AP crystals. These regions, the so-called pockets discussed by Zarko et al. [44] and Cohen [45] or skeleton layer extensively discussed by Babuk et al. in [46–49] and [50] in this book, are where the principal processes connected to Al transformation take place during combustion. An alternative approach has also been developed based on a statistical interpretation of the pockets present in the propellant microstructure [51, 52]; a recent study is due to Maggi et al. [53].

Figure 7 illustrates how Al particles are dispersed into solid propellant and shows μAl more dispersed with respect to nAl. Two-phase flow losses depend on the presence of condensed products during combustion, mainly Al and Al$_2$O$_3$. The sequence of events related to combustion of Al particles is rather complex. The Al powder is first exposed on the burning surface as solid particles coated by molten/decomposed binder and roughly keeping their initial geometry, below the Al melting temperature of 933 K. Then, most of the exposed Al particles burn as single particles, either on the burning surface or far from it, while a significant fraction of them (about one third in the case of Ariane-5 SRB) burns as clusters of particles forming spherical agglomerates of liquid Al and Al$_2$O$_3$ with a solid lobe of Al$_2$O$_3$.

The aggregation/agglomeration phenomena observed near the burning surface appear quite different for nAl formulations compared with μAl formulations. A comparison between the different transformations of μAl and nAl powders during the combustion process is shown in Fig. 8 [38, 40]. Propellants loaded with nAl form aggregates (flakes) with coralline structures and of limited size on the
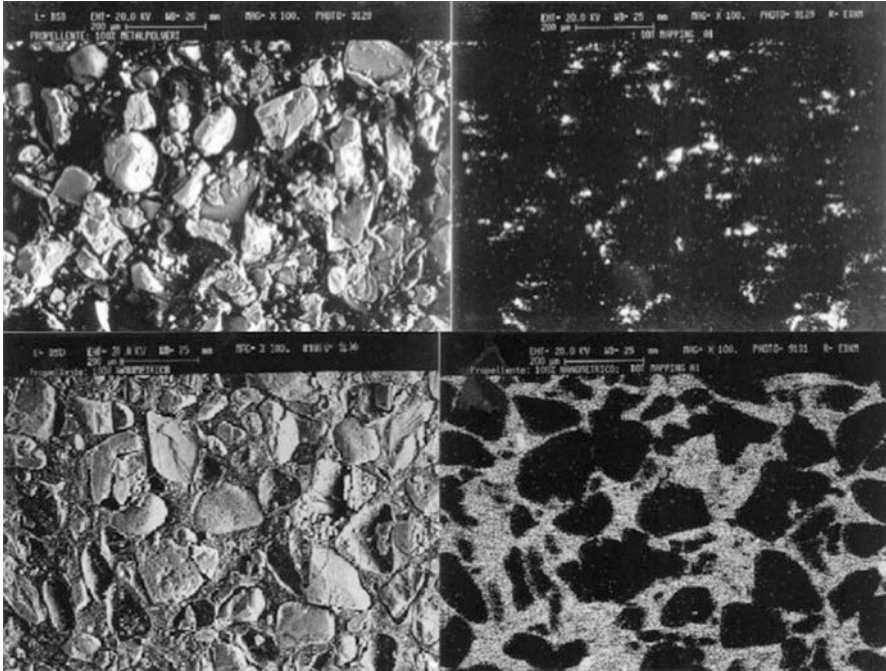
Fig. 7 SEM (*left*) and EDX (*right*) images of solid propellant 68 % AP + 17 % HTPB + 15 % Al. *Top images* show surface dispersion of µAl particles (flakes of 50 µm characteristic size), while *bottom images* show surface dispersion of nAl (uncoated ALEX) [43]
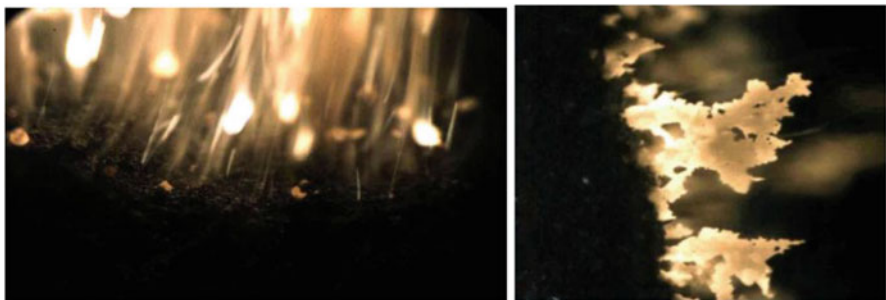

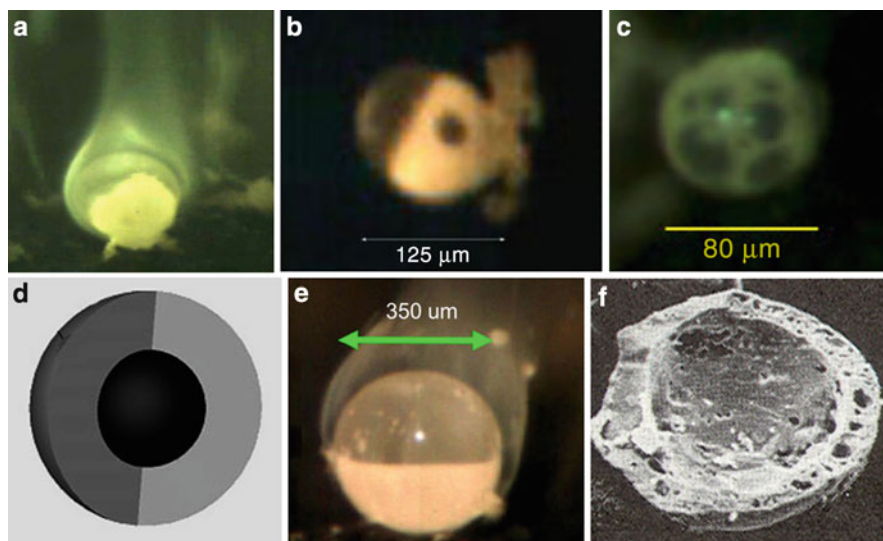**Fig. 8** Agglomeration process for µAl (on the *left*) and nAl (on the *right*) [38]

Fig. 9 Morphology of agglomeration: (**a**) burning oxide cap agglomerate from AP/μAl propellants [38], (**b**, **c**) burning matrix agglomerate [38], (**d**) sketch of metal core coated by an oxide layer [48], (**e**) burning metal cap agglomerate from AN/μAl propellants [38], (**f**) residual hollow shell [54]

burning surface, whereas μAl generates droplets that may reach up to several hundred micrometers near (at or above) the surface. For uncoated nAl burning under subatmospheric pressure, about 80 % γ-Al_2O_3 and δ^*-Al_2O_3 were recovered, while up to 10 % was unburned Al and the remaining CCP consisted of intermediate products, such as Al_2OC and Al_4C_3. A comparative survey of possible agglomerates or CCP shapes is shown in Fig. 9: the oxide cap agglomerate is typical of AP/μAl (image a), the matrix agglomerate is typical of AP/AlH$_3$ (images b and c), the oxide layer coating the metal core is typical of AP/nAl (image d), and the hollow metal cap agglomerate is typical of AN/μAl (images e-f). Systematic analyses on agglomerate size have been carried out by Babuk [46–50], while fundamentals of particle size analysis in solid rocket propulsion were treated by Kraeutle [54]. Further effects are described in this book by Weiser et al. [55].

3.7 Nomenclature for Cohesion, Aggregation, and Agglomeration

To distinguish the different ways that the complex phenomena of; particle clustering manifest themselves, the following nomenclature is used here [22, 42, 43]. The word agglomeration is reserved to the formation of the spherical drops of liquid

metal and oxide in combustion, while the word aggregation is reserved to the formation of the partially oxidized flakes of irregular shape seen at or near the burning surface (an intermediate step between the initial form of the metal and the possible final spherical agglomerates). Agglomerates always imply a loss of the initial particle individuality; aggregates are agglomeration precursors and may keep some semblance of the initial particle individuality. As defined, both agglomeration and aggregation are processes typically occurring at high temperatures during Al burning. In addition, it is convenient to reserve the word cohesion for describing "a portion of a substance cleaving together in a thick nondescript mass" (Webster's Dictionary).

3.8   Comparative Combustion Testing of µAl vs. nAl Formulations

The superior ballistic properties of nAl in terms of steady burning rate, as just summarized, are well known in the open literature. This effect is typically ascribed to the more intense heat release rate near the burning surface compared to that occurring in the corresponding µAl formulations. The minute local space and time scale, however, make very difficult to directly map the heat release rate near the burning surface. But an indirect proof can be obtained by comparing the burning response of solid propellants, featuring the same composition but loaded with different Al particles size (µAl was replaced by nAl), under specific operating conditions:

- Dynamic extinction by fast depressurization
- Static extinction by pressure deflagration limit
- Steady burning near pressure deflagration limit
- Laser radiation ignition

The common formulation of the tested aluminized propellant was AP 68 % + HTPB 17 % + Al 15 %. Two variants were manufactured differing only by the type of Al powder incorporated: 50 µm nominal size µAl (flakes SPLab-06) and 0.150 µm nominal size nAl (air passivated, uncoated SPLab-01a). The data previously collected with an AP 80 % + HTPB 20 % nonmetallized propellant were used as reference. The measured steady-state burning rates for the nAl propellant are higher than for the µAl propellant. For the specific composition tested in this experimental campaign, Vieille's law exponent decreases from 0.56 for the µAl propellant to 0.42 for the nAl propellant. On the contrary, adding µAl to a nonmetallized propellant does not significantly modify the ballistic properties of the propellant; for details see [22].

3.9   Fast Depressurization

The two selected solid propellants were then tested under transient combustion to assess their intrinsic resistance to strong but well-controlled dynamic disturbances. The go/no-go boundary between (continued) combustion and extinction was obtained in the same experimental apparatus. The go/no-go data were plotted in terms of initial depressurization rate vs. initial pressure. A straight line was found to separate the extinction region from the burning region.

If the combustion of nAl formulations truly involves a more vigorous energetic coupling at the burning surface in terms of increased heat feedback, this effect should clearly manifest itself in the experimental results of dynamic extinction boundary by fast depressurization. In fact, testing revealed a great increase of the depressurization rate needed to extinguish the nAl propellant. In the experimental apparatus used in these tests, extinction of the nAl propellant required an exhaust orifice area about four times the one required by the μAl propellant.

In Fig. 10 the dynamic extinction boundaries of the different test propellants in terms of initial depressurization rate vs. initial pressure are reported. Even in this case, the behavior of the μAl propellant and that of the reference non-metallized propellant are comparable, with differences of the order at most of 20 %. However, these differences are negligible if compared to the depressurization rate values associated with the nAl propellant. As a matter of fact, a 400 % increase of the depressurization rate is needed for the nAl composition to achieve extinction.

In contemplating the results presented above, one should also take into account the decrease of condensed-phase characteristic time for the conductive thermal wave. Assuming a constant thermal diffusivity of the condensed phase, the steady burning rate increase leads to a thermal wave characteristic time ≈ 75 % lower.

An additional effect is illustrated in Fig. 11, showing the Al particle distribution on the propellant surface before combustion and after quenching by fast depressurization. This visualization was obtained by superimposing an EDX microanalysis map on the corresponding SEM image. Because of the molten layer of binder during the combustion process, compared to μAl the nAl particles can disperse on the surface more uniformly and compatibly with the AP grain size distribution.

3.10   Pressure Deflagration Limit (PDL)

Pressure deflagration limit (PDL) phenomena are of interest for low-pressure operations in general, ignition, safe storage and transport, controlled extinction phenomena, etc. For a finite sample geometry, burning is no longer self-sustained for pressures below PDL. For a given formulation, the intrinsic value of PDL actually corresponds to a sample of infinite geometry, i.e., unaffected by border effects. In practical terms, the importance of the border effects is assessed by the shape
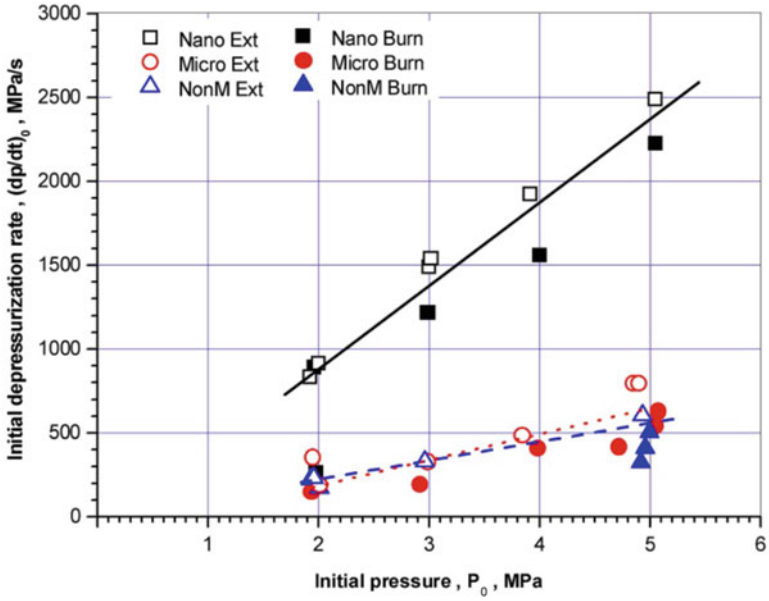
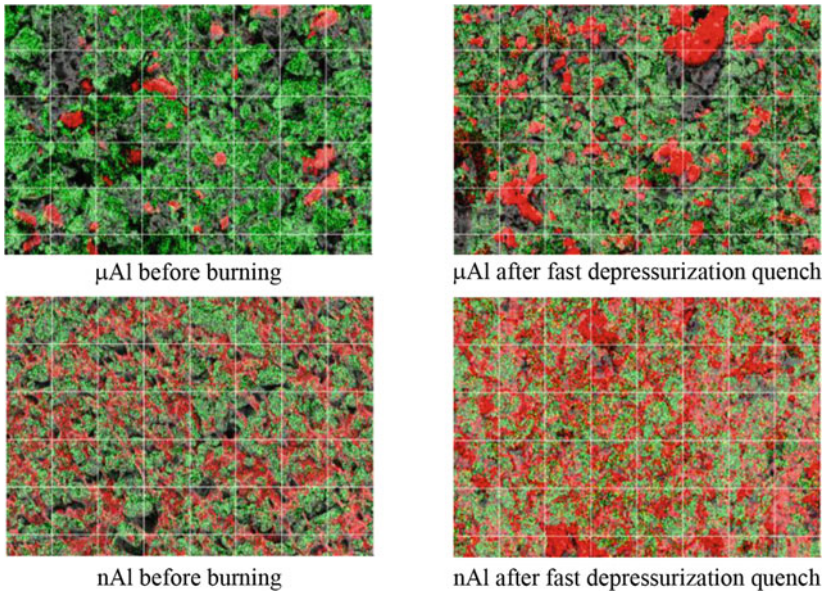**Fig. 10** Dynamic extinction boundaries by fast depressurization of three formulations [56]

μAl before burning

μAl after fast depressurization quench

nAl before burning

nAl after fast depressurization quench

Fig. 11 Morphology and composition maps of unburned (*left*) and quenched (*right*) surfaces of μAl (*top*) and nAl (*bottom*) propellants (Al in *red* and Cl in *green*) [56]
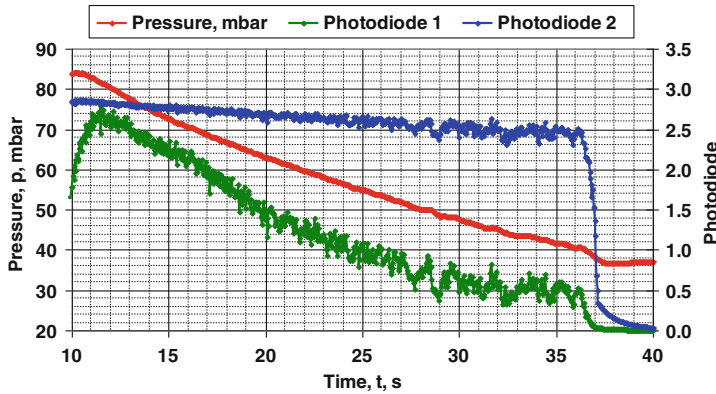
Fig. 12 Photodiodes and pressure transducer signals during PDL testing [56]

factor, defined as the characteristic (area/perimeter) sample cross section ratio. The experimental results obtained at SPLab point out a lower PDL, and thus stronger resistance to static extinction, for propellants using nAl instead of μAl.

Tests were performed in an experimental rig purposely designed for this task; for details see [22]. Propellant samples were ignited at a pressure slightly higher than the expected PDL; the pressure was then smoothly reduced till complete extinction was reached. By direct observation of the signals of the photodiode and pressure transducer (Fig. 12), a peculiar trend can be recognized. The central part of the combustion is characterized by decreasing pressure, while the photodiodes show a reduction of frequency of the oscillating combustion and an increase in amplitude; when the flame extinction is reached, the signal from the photodiode falls to zero, while, at the same time, the pressure curve changes its inclination because no longer there is gas production. The pressure at the sharp slope change is defined as the measured PDL value.

Experimental results indicate that the shape factor dramatically affects the propellant PDL. The lowest PDL value is reached when strands of large cross-sectional area (i.e., large shape factor) are used. Two AP/Al/HTPB propellants were tested, featuring the same 68/18/14 mass % composition and AP particle size distribution (0–71 μm), but different Al particle size (μAl or nAl). The results are reported in Fig. 13: the propellant based on nAl has a lower PDL for all shape factors. This effect also suggests that nAl formulations imply a more vigorous energetic coupling at the burning surface in terms of increased heat feedback, thus requiring less assistance from the gas-phase and a self-sustaining burning region more extended toward lower operating pressures.
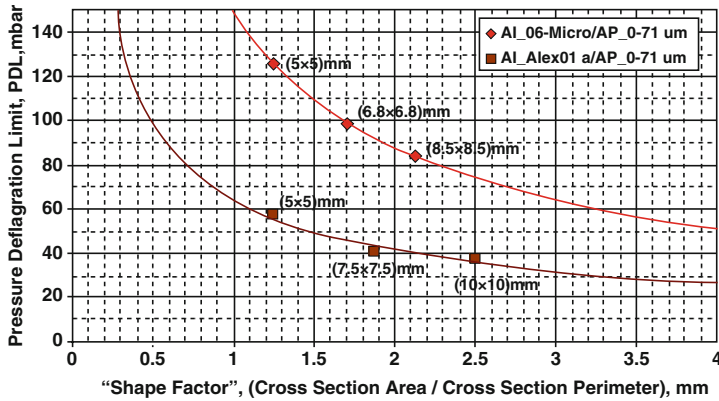
**Fig. 13** PDL vs. shape factor for propellants loaded with μAl vs. nAl [56]

3.11 Subatmospheric Burning

Testing the same aluminized propellants of the previous section under subatmospheric pressure revealed another interesting result; for details see [22]. The nAl formulation is not only faster than the μAl formulation but also less pressure sensitive ($n = 0.52$ for nAl and 0.78 for μAl). This finding supports the hypothesis of less dependence of heat feedback from the gas phase to the condensed phase, as indeed expected for nAl formulations. Moreover, while the μAl formulation near PDL shows the typical self-sustained oscillatory burning associated with intrinsic burning instability, this effect is almost unperceivable in the nAl formulation.

3.12 Laser Radiation Ignition

Finally, the ignition delay under laser radiation was evaluated for a number of formulations ranging from 100 % μAl to 100 % nAl and including intermediate mixtures μAl + nAl [37]. Experimental results show a decrease of the ignition delay for nAl loading (propellant P_02) compared to μAl (propellant P_06) with the ignition boundary slope in the range 1.1–1.3; see Fig. 14. Similar results were found by Arkhipov et al. investigating the effects of particle size distribution on radiant ignition [57, 58]. They observed that nAl ignition is "determined by the possibility of rapid oxidation of aluminum powder particles on the burning surface or in the immediate vicinity of it." They also noticed that oxidation of nAl particles may even occur in the heated layer with the flame appearance accompanied by a loud sound effect, surface layer cracking, its fragmentation, and burnout (called "abnormal" ignition regime with heat supply from a heated block). Further effects associated to nAl radiant ignition are described in this book by Zhao et al. [59].

Fig. 14 Radiant ignition map at 1 bar for several AP 68 % /HTPB, 17 % /Al 15 % formulations showing faster ignition for nAl vs. μAl propellants. P_06 is loaded with 100 % μAl flakes; P_07 with 80 % flakes + 20 % nAl; P_08 with 50 % flakes + 50 % nAl; P_09 with 50 % spheres + 50 % nAl; P_02 with 100 % nAl [37]
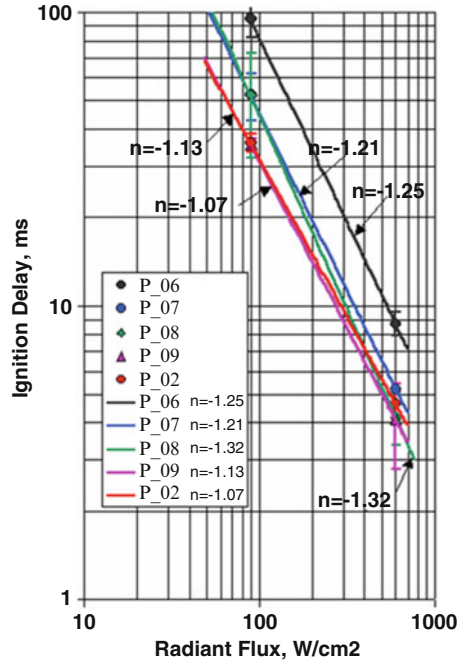
3.13 nAl Summary

Two different mechanisms, metal agglomeration for μAl and metal aggregation (prompt metal oxidation) for nAl, were underlined. Smaller CCP sizes imply reduced specific impulse losses and also reduced particulate damping especially at low pressures, while the damping effects on high-frequency instabilities require further studies [60]. The exact burning response depends on the details of the propellant formulation: in particular, the pressure exponent of steady burning rates has been observed to follow different trends according to the specifics of the composition and operating conditions. This fact suggests that, in addition to the sheer increase of the specific surface, other subtle chemical and physical factors (intermetallic compounds, crystalline structure, etc.) may be important in nAl enhanced reactivity. At any rate, all burning results may be obscured by cold cohesion phenomena of nAl particles. Modern manufacturing techniques of nanometal powders in general are treated by Vorozhtsov et al. in [61, 62] and, in this book, [63].

A comprehensive review of nAl burning in terms of flame structure and combustion modes was recently offered by Sundaram et al. [64]. Burning rate is controlled by mass diffusion, through the gas-phase mixture, for particle diameters greater than a critical value. The critical particle size decreases from 100–1 μm,

as the pressure increases from 1 to 100 bar, thus making chemical kinetics the controlling factor for nAl combustion over the whole pressure range.

4   Activated μAl Powders

Activation represents a viable solution to the need to increase the reactivity of μAl, preserving its intrinsic qualities. The final product is generally kept micrometric and is characterized by a reduced effect on propellant/solid fuel manufacturing, as well as by a good metal content (higher with respect to nAl). Activation treatments can be divided into three categories according to the selected approach:

- Chemical, when powders are treated through chemical substances (e.g., fluorinated compounds). A number of different techniques are available, depending on the specific activation additive.
- Mechanical, when particles are processed by high- or low-energy mills. One of the most widespread approaches in this category is ball milling, in which the activating action on the powder is executed by a certain number of spheres enclosed in a proper vessel.
- Mechanochemical, when two or more materials are mechanically processed to obtain new substances, like intermetallics. Generally speaking, whenever a process changes the composition or the structure of a powder, the treatment can be considered mechanochemical.

By following different strategies, all of the three activation approaches aim at incrementing the powder reactivity.

4.1   Chemical Activation

Chemical activation (CA) can be used to increase the specific surface area of micron-sized powders or to deposit substances, like fluorinated compounds or transition metals, which can increase reactivity on the particle surface. The increment of the particle S_{sp} based on a pitting corrosion procedure, using a solution of water and magnesium chloride, was successfully tested by Rosenband and Gany in [65]. The resulting S_{sp} value, higher than that of standard μAl and similar to that of nAl (10–18 m^2/g), guaranteed a good increase of powder reactivity [65, 66]. A widespread strategy, described in [65, 67, 68], consists in activating Al particles by deposition of metals (such as Ni, Co, and Fe) and complex fluoride compounds. In the latter case, the activation strategy consists in reducing the distance between particles and additive. When complex fluorides are used, the weakening of the protective alumina shell also occurs, promoting a faster diffusion of oxidizer towards the Al core [67, 69].

Chemical treatment processes do not modify particle shape. However, the deposition of the activation substance can alter the superficial texture (see Fig. 15)
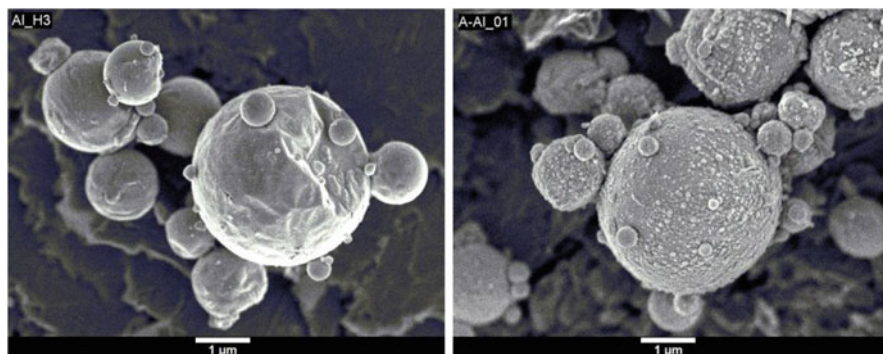
Fig. 15 Standard µAl particles before (*left*) and after (*right*) a chemical activation treatment with complex fluoride

Table 4 Effect of different chemical activation treatments using complex fluoride on powder specific surface area, size, and metal content

ID	Ref. powder	CA-Me	CA-Lo	CA-Hi
Activation intensity	None	Medium	Low	High
D_{43}, µm	5.1	5.5	5.4	5.5
S_{sp}, m^2/g	1.2	2.6	2.2	2.3
Metal content, %	98.3 ± 0.7	93.9 ± 0.9	93.7 ± 0.5	90.5 ± 0.5

with a consequent variation of both the specific surface area and mass-weighted mean diameter of the particles. The effect of a chemical treatment using complex fluoride can be appreciated in Fig. 15, but the exact effect on powder characteristics depends on the specific activation procedure, as reported in Table 4. The metal content, for example, is affected by the activation treatment with a progressive reduction related to the selected additive and to the process duration. In the case of Al activated with a complex fluoride, the metal content depletion is of the order of 5–8 % by mass.

4.2 Mechanical Activation

Mechanical activation aims at incrementing particle reactivity by several ways:

- Particle shape variation
- Additive inclusion, by ball milling techniques
- Distance reduction between particles and additive, for example, employing mechanical mixing techniques

Mechanical milling (MM) is an activation technique consisting in grinding one or more powders by low- or high- energy mills (centrifugal, planetary, or attritor). This approach can be used to produce a series of ingredients, like amorphous powders
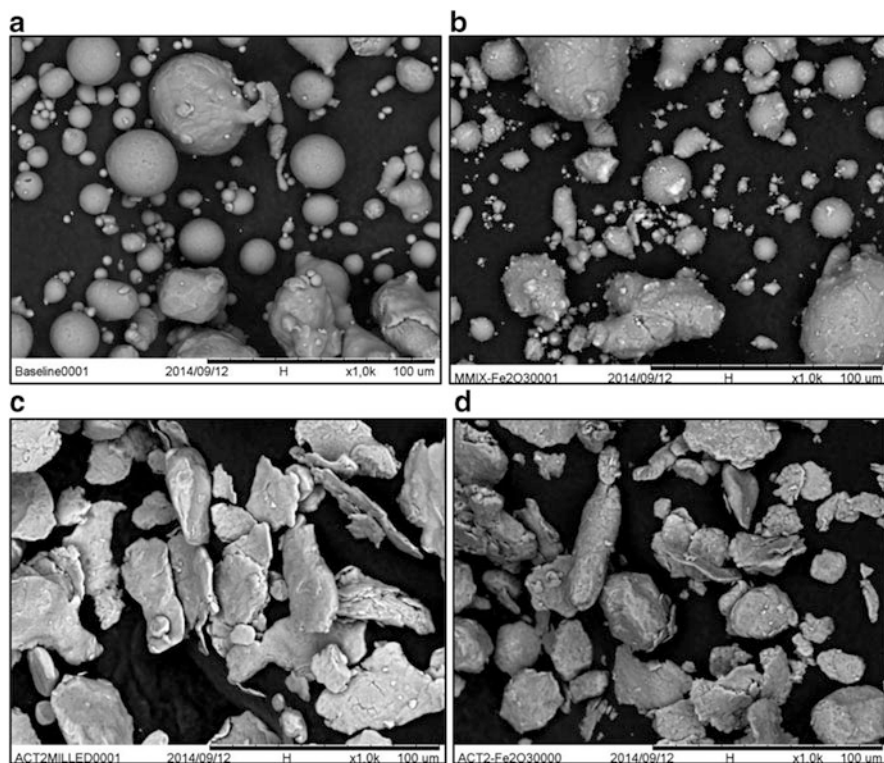
Fig. 16 Effects of different kinds of mechanical activation on a reference μAl. (**a**) Reference Al 30 μm (**b**) Mechanical mixing with Fe_2O_3 (**c**) Mechanical milling (**d**) Mechanical milling with Fe_2O_3

and metal–ceramic composites, or to change the structure of materials [70, 71]. In these cases, the activation is of mechanochemical type. From the standpoint of increasing the effectiveness of aluminum as a propellant fuel ingredient, the most interesting advantage of MM is represented by the enhanced reactivity of the final product, evidenced by a reduction of both ignition temperature and activation energy [72–74]. As with chemical activation, MM leads to a metal content reduction of about 1–2 % for a standard μAl [74]. This loss is associated with the exposure of the Al core to the external environment and is imputable to deformations induced by mechanical stresses applied to particles during the activation treatment. A further loss of elemental metal content is prompted by the presence of an additive, generally added in high mass fractions (10 % or more). The cumulative loss also depends on a series of parameters, like milling time, atmosphere, ball-to-powder mass ratio (BPR), and process control agent (PCA). PCA, in particular, is important to reduce particle–particle and particle–sphere cold welding phenomena. MM strongly affects particle shape and surfacetexture as shown in Fig. 16c, d as compared to Fig. 16a

Table 5 Effect of mechanical activation treatments on powder metal content (volumetric method [28])

ID	μAl-30 μm	MM	MM-Fe$_2$O$_3$	MMx-Fe$_2$O$_3$
Activation	None	Ball milling	Ball milling	Mech. mix
Metal content, %	99.3 ± 0.2	97.5 ± 0.4	94.0 ± 0.9	96.7

Table 6 Ignition temperature for different kinds of activated Al. Two μAl and a 100 nm nAl coated with stearic acid are reported for comparison

ID	Ignition	Ignition temperature, K
μAl – 5 μm	Yes	1155.2 ± 18.0
μAl – 30 μm	No	–
CA – Lo	Yes	870.7 ± 14.5
CA – Me	Yes	904.8 ± 16.2
CA – Hi	Yes	859.0 ± 11.0
MM	[a]	–
MM with Fe$_2$O$_3$	Yes	876.4 ± 12.8
nAl	Yes	771.3 ± 16.3

[a]The specific MM treatment strongly influences this parameter

(reference μAl). Activated powders are characterized by flake-shaped particles and by an irregular external surface. The additive, if present, tends to be entrapped in the granules (see Fig. 16d).

The possibility of activating μAl by mechanical mixing using a low amount of additive (mass fraction < 5 %) has recently been investigated by Dossi [75]. The treatment is capable of retaining the original granule shape and is accomplished using nanometric additives to promote efficient particle coating. Except for some spots, the additive distribution on Al granule surface is homogeneous (Fig. 16b). The treatment promoted an interesting increment of particle reactivity and provided a higher metal content compared with the corresponding powders processed by ball milling (see Table 5).

4.3 Effects of Activation Processes on Powder Reactivity

The capability of mechanical and chemical activation of increasing particle reactivity has been investigated through ignition and TG analyses. A lowering of the ignition temperature has been detected for both chemically and mechanically activated powders, confirming the benefits of these treatments (Table 6). The mechanical treatment brings to a stronger ignition temperature reduction compared with chemical process.

TG traces reported in Fig. 17 confirm what was observed in terms of ignition temperature changes for mechanically activated powders. Milled powders show a significant mass gain in the thermal region of the first oxidation step. Conversely, the ingredient treated with mechanical mixing shows a marked mass increment only during the second oxidation step. At high temperature, the mass gain obtained by
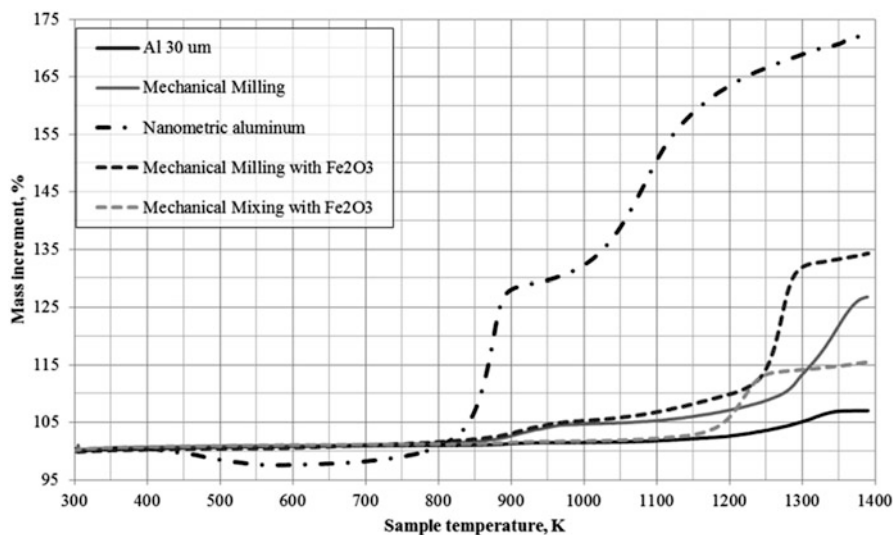
Fig. 17 TG analyses for three mechanically activated Al powders (sample mass: 2 mg; atmosphere: air; heating rate: 10 K/min). The reference Al and a 100 nm nAl coated with stearic acid are reported for comparison

mechanically milled powders is higher than that seen with mechanically mixed ingredients. In this respect, particle morphology variation may play a significant role. Despite a generalized enhancement, all the activated Al materials are characterized by a lower reactivity than nAl as confirmed by the lower mass gain and the delayed oxidation step onsets.

TG analyses of ingredients activated with complex fluoride show an increment of reactivity that is generally higher compared with that shown by mechanically activated powders. However, differences in test parameters and grain size distribution of the reference powder have to be considered. A single major mass gain is located around the Al melting point and is delayed by about 100 K with respect to the onset shown by the μAl-05 powder (Fig. 18). Both mechanical and chemical activation processes are not able to achieve the same results obtained by nAl despite an evident reactivity increment.

4.4 Potentialities of Activated Al Powders in Solid Rocket Propellants

The high reactivity of activated Al can bring about a reduction of condensed combustion product (CCP) size, as shown by Yavor et al. [66], Dossi [75], and Sippel et al. [76], leading to a potential reduction of solid rocket motor performance losses. This possibility is accomplished only if the metal content of the selected
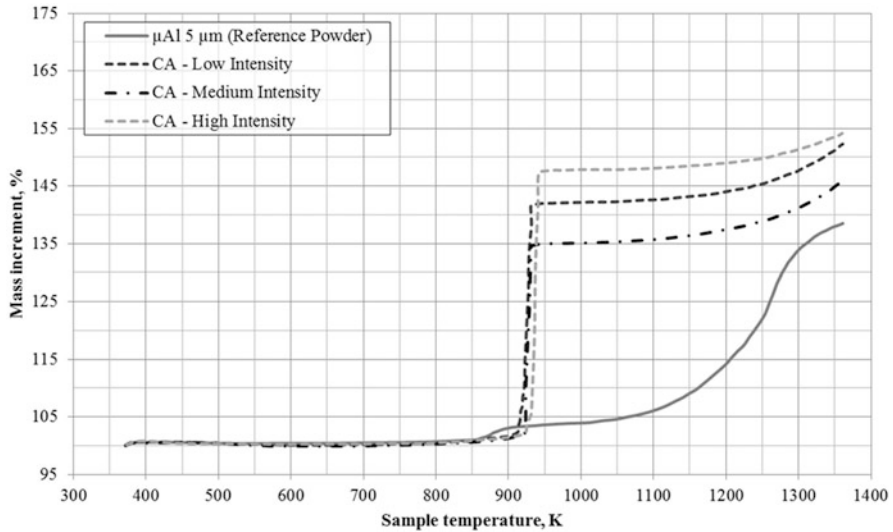
Fig. 18 TG analyses for three chemically activated Al with complex fluoride (sample mass: 9–12 mg; atmosphere: O_2; heating rate: 40 K/min). The reference Al is reported for comparison

Al powder is sufficiently high. In fact, a reduction of Al content of about 15 % is sufficient to jeopardize the performance gain obtainable by eliminating the agglomeration phenomena. Figure 19 shows the ideal I_s calculated for AP/HTPB-based propellants incorporating different metals. The use of activated powders always implies a I_s reduction, but their active Al content guarantees a higher ideal I_s value with respect to nAl. Ingredients processed by MM techniques using a low amount of additive provide a higher I_s value than chemically activated ingredients, approaching that obtained by μAl.

When incorporated into solid propellants, activated ingredients result in an enhancement of the burning rate as shown in Fig. 20. In this respect, mechanically activated powders seem more effective than chemically activated ingredients. However, the positive effect caused by the specific additive (iron oxide) has to be considered. Chemically activated powders provide virtually the same burning rate increment, independent of the treatment intensity. Conversely, the choice of the specific mechanical process seems to control the effect of the powder on the solid propellant burning rate. MM-Fe_2O_3 and MMx-Fe_2O_3, for example, assure a very strong enhancement, similar to nAl or even higher. The effect of particle morphology variation can be observed in the P-MM propellant test results, showing the same burning rate of P-μAl-05 loaded with standard 5 μm Al. The pressure sensitivity is also affected by the activation treatment. Ingredients processed by CA are responsible for an increased propellant pressure exponent, while mechanically activated powders tend to reduce the ballistic exponent or to keep it unaltered. The exact effect depends on the specific ingredient and the precise mechanical activation treatment.
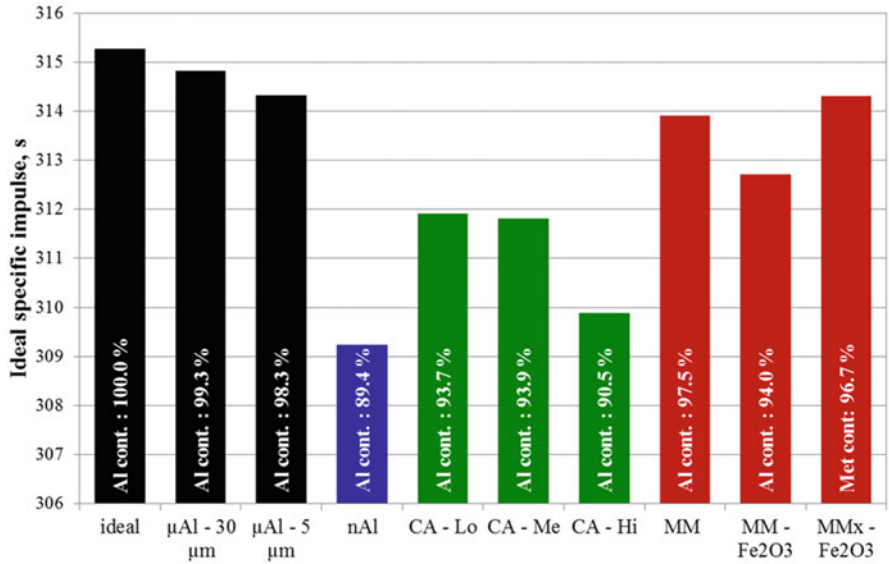
Fig. 19 Effect of different metal powders on ideal specific impulse of AP/Al/HTPB – 68 %/18 %/14 % (in mass) solid propellants. Computations are performed considering a combustion chamber pressure of 70 bar, an expansion ratio of 40, and vacuum conditions
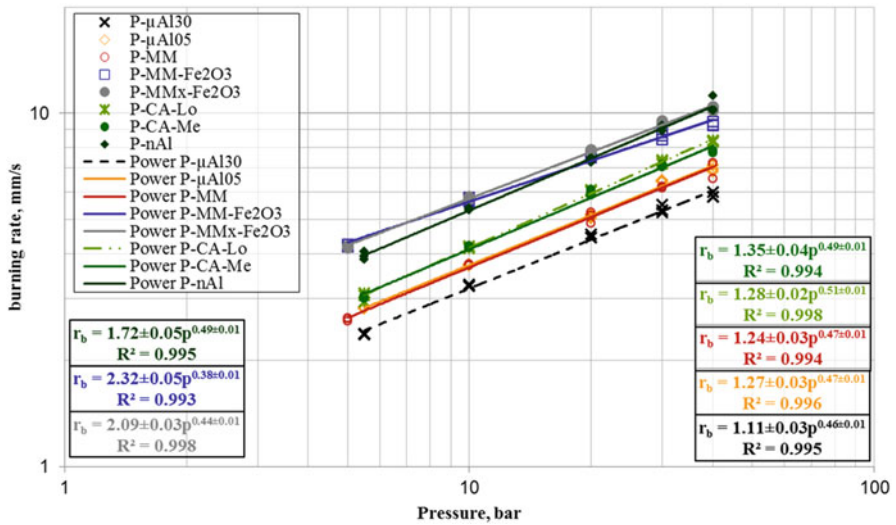

Fig. 20 Effect of different metal fuels on steady burning rate of AP/Al/HTPB – 68 %/18 %/14 % (in mass) solid propellants [56]

5   MgB Dual-Metal Powders

Boron has the highest theoretical energy density ($\sim$59 kJ/g) among the metal or metalloid fuels, with little toxicity and no reactivity issues (such as for Be or Li). This fact makes B a very attractive ingredient for energetic applications. But combustion difficulties (recalled in section "Thermochemical properties") and a reduction up to 5 % of I_s [77] for propellant formulations containing B in place of Al metal conspire to keep B out of solid rocket propellants. Among the many techniques proposed to make B a useful ingredient, a promising one is to resort to dual Al and B metal fuels [77, 78]. In this respect, several Mg_xB_y composite dual-metal powders were tested under laboratory conditions differing by the Mg coating amount (ranging from 10 to 60 % in mass) and B purity. By ICP bulk elemental analysis, boron purity was either 90 % (typically 90–91 % with 5 % max Mg impurity) or 95 % (typically 96 % with 1 % max Mg impurity) and the balance being in both cases oxygenated impurities, moisture, and volatiles. For completeness, pure boron powders were also examined. The theoretical ideal I_s, as well as the adiabatic flame temperature, decrease whenever Al is replaced, totally or partially, by B, Mg, or Mg_xB_y composite metals. A good strategy appears that of a partial replacement, say 3 % of μAl (one sixth of the total μAl load for a standard composite propellant for space propulsion).

Visual inspections of the collected SEM images of the tested metal powders show that Mg_xB_y powders appear larger than the corresponding pure B powders and that 95 % purity B powders appear larger than the corresponding 90 % purity B powders. In addition, all of the tested B powders present an irregular shape different from the near spherical μAl used as a reference metal fuel. B powders present fine particles with no significant cohesion; Mg_xB_y powders feature monomodal distributions with typically $D_{43} \approx 5$ μm, with the exception of $Mg_{60}B_{40}$ ($D_{43} = 20.9$ μm). While Mg_xB_y with 90 % B purity presents no significant cohesion, Mg_xB_y with 95 % B purity may occasionally display visible clumps.

The structure of each Mg_xB_y particle, by X-ray ablation methods, consists of a center of the original Boron input material with a shell of intermetallic material Mg_xB_y which is richer in Magnesium nearest the surface. The approximate surface composition is MgB_2, a brown material which is visually indistinguishable from Boron.

Particle size distributions analyses point out that the tested metal powders tend to pack and stick together into clumps. This trend increases with time, if proper care is not taken during powder storage. But the clumps can be removed by applying a shear stress above some threshold value.

For the listed B_{90}-based dual-metal formulations, Fig. 21 shows that the addition of Mg_xB_y composite metal powders leads to a measurable increase of steady burning rate with respect to the μAl baseline, but not the pure B_{90} baseline. For the tested B_{95}-based formulations, experimental results (not shown) point out that the addition of Mg_xB_y composite metal powders leads to an even more observable increase of steady burning rate with respect to both the μAl baseline and also the pure B_{95}
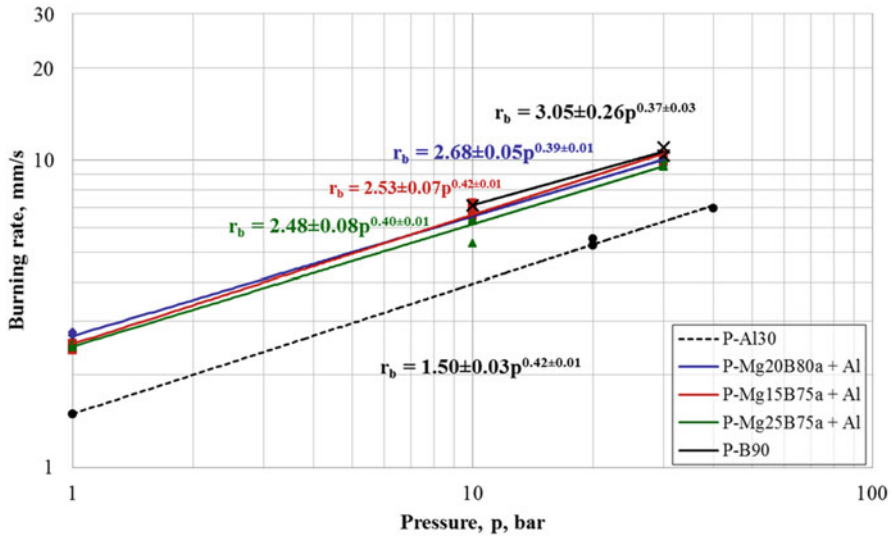
Fig. 21 Comparing steady burning rates of B90-based dual-metal solid propellants: Mg_xB_y addition yields an appreciable increase with respect to the µAl baseline but not with respect to the B90 baseline [81]

baseline. In both cases, the precise content of Mg coating in the range 10–25 % has a minor effect on the propellant burning rate. However, for increasing Mg content, the burning rate gain fades away, for example, when Mg addition reaches 60 %.

Tests to evaluate the incipient agglomeration phenomena were performed under N_2 atmosphere at 5, 10, 20, and 25 bars; some tests were repeated in Ar without noticeable changes. Combustion was performed in a strand burner, recorded by a high-resolution and high-speed video camera for slow motion post-processing and later analyzed with graphic software. For each test, the size of 200 incipient agglomerates was manually measured and the D_{43} mean diameter was then calculated. For all experimental series, the minimum diameter distinctly observable was around 30 µm. As an example, the results obtained for the listed B_{90}-based dual-metal formulations are illustrated in Fig. 22, pointing out a general decrease of the average agglomerate size, especially for 25 % Mg coating.

Ignition temperature of all tested powders was evaluated at SPLab through a specially designed experimental apparatus in air at 1 bar [79]. The ignition temperature is below 800 K for the nAl tested in this work (see Table 6), while for B it is estimated around 1900 K for single particles [78] and down to 1200 K for agglomerates [80]. Further experimental data collected at SPLab [81] point out the beneficial effect of Mg in lowering the Mg_xB_y ignition temperature to the level of nAl.

Comparing the ignition temperature of the tested metal powders with the corresponding adiabatic flame temperature of the pocket at the same pressure, with the metal fuel assumed chemically inert, one observes that the propellant microstructure temperature can be appreciably higher than that of the metal powder
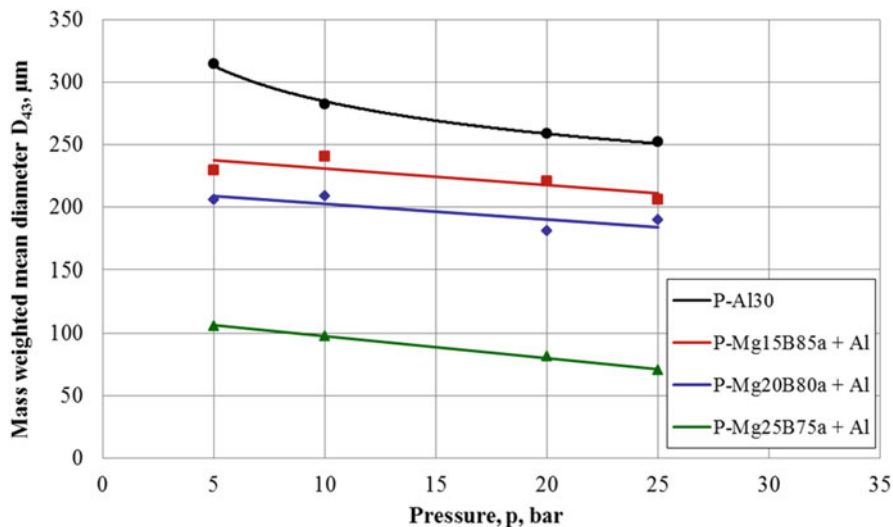
Fig. 22 Average agglomerate size D_{43} vs. pressure of the indicated B90-based dual-metal solid propellants: Mg_xB_y addition with 15–25 % Mg coating causes a general decrease of the average agglomerate size, especially for 25 % Mg coating [81]

ignition. The local exothermicity is then sufficiently high to promote ignition of the metallic powders and induce at least a partial participation in the combustion process, thus strongly increasing the pocket adiabatic flame temperature.

A basic role in these phenomena is played by the propellant microstructure. In general, the conductive thermal wave preceding the burning surface, possibly augmented by exothermic reactions, is able to warm up the metal particles dispersed within the propellant microstructure to temperatures high enough to trigger ignition and a partial oxidation of the metal particles. The intimate mixing with the surrounding decomposition products of the fine AP fractions and binder, favoring a local under-oxidized premixed flame, promotes the formation of partially oxidized and intermediate metallized thin flakes (prompt metal oxidation).

The combination of low metal particle ignition temperature and high pocket adiabatic flame temperature favors at the same time high burning rates (Fig. 21) and small size agglomerates (Fig. 22). Propellant samples containing Mg_xB_y powder with 10–25 % Mg are characterized by high pocket adiabatic flame temperatures and also by low metal particle ignition temperatures. These samples show low values of the incipient agglomerate D_{43} size. In particular, a composite formulation partially replacing μAl with Mg_xB_y at 25 % Mg showed the strongest reduction of the incipient agglomerate mean with respect to the μAl baseline (72 % at 25 bar in Fig. 22).

Whereas all of the tested propellant formulations containing micrometric Al produce agglomerates (spherical drops of liquid metal and alumina in combustion with a distinct oxide cap), no clear agglomeration phenomena could be detected for the propellant formulations containing only the B compounds under examination.

Even if agglomeration occurs, generating burning drops below the optical system resolution or outside the optical system field of view, the combustion process of the B compounds is essentially characterized by the formation of thin flakes (sintered fractal aggregates in the description of [77]).

Depending on steady-state burning rate (i.e., pressure), the type of binder, fine oxidizer size and fraction, metal average size, and distribution, unburned metal may also contribute to the thin flake formation.

6   Comparing Different Metal Powders

A negative effect of Al burning is due to the generation of an appreciable mass fraction of condensed products (ξ_{cc}). The condensed species, originated from the propellant metal particle combustion, are responsible for the two-phase flow losses which cause a downward departure from ideal motor performance. The delivered specific impulse undergoes a few % reduction, due to the interaction between the continuous gas phase and the dispersed phase. Losses are concentrated at the nozzle throat and are only partially recovered during the supersonic expansion; for example, see [22, 82].

6.1   Ballistic Properties

The effects of three different kinds of Al powders on the propellant ballistic properties have been compared in terms of burning rate value and combustion residue size. Regarding particle size distribution, a comparison among a standard μAl powder (μAl-30, 30 μm, spherical shape), a nAl (ALEX, spherical shape) and a mechanically activated Al (MM) is shown in Fig. 23.

Burning rate was evaluated in a standard window strand burner by a high-speed video camera; for details, see [22]. Likewise, condensed combustion products (CCPs) were quenched and collected in a pool filled with tetrachloroethene, in a burner using the same operating conditions (ignition, pressurizing gas, etc.) used for steady burning rate measurements; for details, see [22].

Table 7 shows the main features of the compared Al powders. Particle size distributions are shown in Fig. 23. The results of burning rate evaluations are reported in Table 8, expressed according to Vieille's law ($r_b = ap^n$) over the tested pressure range 10–40 bar. Concerning combustion residuals, a test campaign was

Table 7 Raw Al powder characteristic comparison [83]

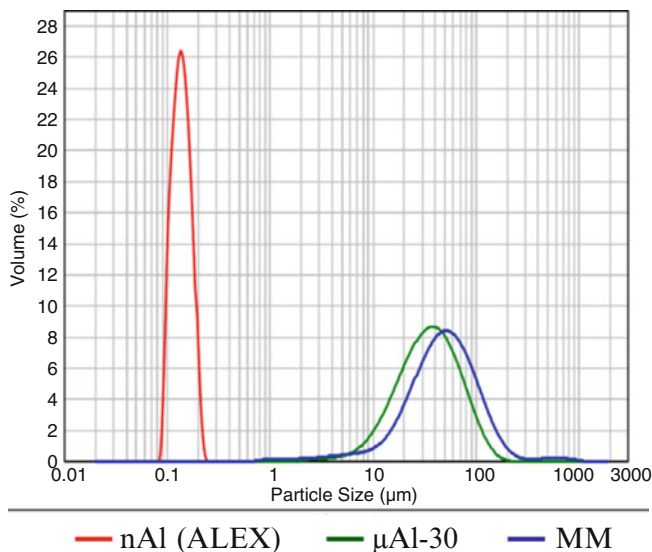| ID	Description	D_{43} μm	Metal content (%)
nAl (ALEX)	Nanometric, spherical, uncoated	0.14	88.7
μAl-30	Micrometric, spherical, uncoated	42.66	99.5
MM	Micrometric, milled	65.02	97.7

Fig. 23 Particle size distributions of the three metal powders compared. Analyses conducted with a laser granulometer Malvern Mastersizer 2000 using the Hydro unit

Table 8 Steady burning rates results [75, 83]

ID	a, $(mm/s)/bar^n$	n	R^2
P-nAl (ALEX)	1.68 ± 0.03	0.50 ± 0.01	0.999
P-μAl-30 μm	1.11 ± 0.03	0.46 ± 0.01	0.995
P-MM	1.24 ± 0.03	0.47 ± 0.01	0.994

conducted to evaluate the particle size with respect to pressure (10 and 30 bar), and an XRD analysis was conducted to identify the phases present in the collected samples.

Table 9 shows the X-ray diffraction (XRD) analysis results. The phases detected are aluminum (Al^0) and aluminum oxide (α-Al_2O_3, γ-Al_2O_3, δ*-Al_2O_3). The phase δ*-Al_2O_3 is typically formed following a violent quenching process of liquid alumina. Aluminum combustion efficiency, defined as the ratio Al_2O_3/Al^0, highlights the different behavior of nAl and μAl powders: over the limited pressure range explored, for increasing pressure it decreases for nAl, while it increases for μAl [83].

In agreement with previous works [79], nAl with respect to μAl increases not only burning rate but also combustion efficiency (see Table 9 and Fig. 24) and moreover makes CCP size smaller. Likewise, the tested milled Al shows better performance than the standard spherical μAl [75, 83].

Table 9 XRD analysis results [75, 83]

ID	p, bar	Al^0, %	α-Al_2O_3, %	γ-Al_2O_3, %	δ*-Al_2O_3, %	Al_2O_3/Al^0
P-nAl (ALEX)	10	0.3	2.6	76.6	20.5	332.3
	30	0.8	3.8	78.4	17.0	124.0
P-μAl-30	10	22.2	2.7	58.8	16.3	3.5
	30	12.3	2.3	67.5	17.9	7.1
P-MM	10	15.6	4.4	61.3	18.7	5.4
	30	8.0	1.4	67.5	23.1	11.5
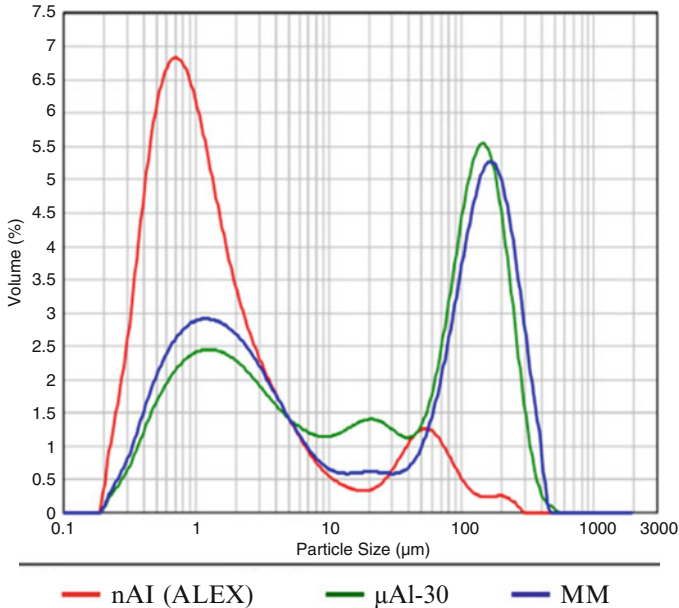
Fig. 24 Particle size distribution of CCP collected at 30 bar. Analyses conducted with a laser granulometer Malvern Mastersizer 2000 using the Scirocco unit

7 Concluding Remarks

Under the common operating conditions tested at SPLab, typical of space propulsion applications, the following trends are observed:

- Concerning nAl ($\rho = 2.520$ g/cm^3), a slight loss of ideal I_s is expected compared with μAl due to decreased active metal content; steady burning rates can increase up to a factor of 2; incipient agglomeration is decreased.
- Concerning Mg_xB_y dual metals ($\rho = 1.450$ g/cm^3), a slight loss of both ideal I_s and density is expected with respect to μAl; steady burning rates can increase up to a factor of 3 with 95 % purity B; incipient agglomeration is strongly decreased.

- Concerning AlH$_3$ ($\rho = 1.476$ g/cm^3), although not commercially available and in spite of its low density, this hydride shows a substantial increase of ideal I$_s$ for both solid and hybrid rocket propulsion. It also features a unique combination of a mild to strong increase of burning rates with a significant decrease of pressure sensitivity; incipient agglomeration is mildly decreased.
- Concerning actAl (ρ variable around that of pure Al, depending on the type and amount of additives), a small increment of the delivered I$_s$ is expected with respect to standard µAl due to good active metal content level combined with appreciable reduction of CCP size.

In terms of industrial applications, no substitute for standard µAl is in use for rocket propulsion. Concerning nAl, extensive experimental and theoretical research activities were carried out internationally covering a variety of energetic applications, including propellants, pyrotechnics, and explosives. After more than 30 years of investigations, no operational systems are reported in use for nAl powders. Loss of active metal; occurrence of cold cohesion or clustering during manufacture, storage, and handling; increased slurry viscosity; possible interactions with the binder system; and so on clearly overcome advantages such as increased burning rate (easily achievable in other ways) and possible reduction of 2P flow losses. Likewise, no operational systems are in use for activated Al and Mg$_x$B$_y$ metals.

Concerning AlH$_3$, an overall assessment appears somewhat elusive. This hydride appears suitable to SRM upper stages and hybrid propulsion in general [84, 85], but no use of it is officially reported. Under low heating rates, AlH$_3$ dehydrogenation temperature is in general around 433 K, while it was measured at 452.7 K for the Russian product, which is anyway much less than the decomposition temperatures of the common binders. Even under combustion tests, this difference brings about a porous metallic structure in the composite propellant matrix, which in turn makes micrometric Al much more reactive by increasing its specific surface area. Details about AlH$_3$ ignition (in terms of 2 % maximum light emission) and combustion properties are discussed in [86–88]. Testing at heating rates of 1×10^5 K/s in air, for pressures ranging from atmospheric to about 70 bar, indicates that the dehydrogenation temperature of 720 K of aluminum hydride is independent of pressure. On the contrary, the ignition temperature is approximately linearly decreasing from the value of 900 K at atmospheric pressure to about 760 K at 4 bar; above 4 bar it maintains approximately constant with an average value of 760 K. The important message is that the ignition temperatures of AlH$_3$ fall in the same low range values typical of nAl (see Table 6), thus confirming the positive effects of the porous metallic structure created by fast dehydrogenation. In turn, these low ignition temperatures eliminate the relatively large standoff distance observed for µAl particle burning in the currently employed metallized formulations. Ultimately, this leads to an appreciable burning rate increase and incipient agglomeration decrease.

While ideal thermochemistry favors Al ($\rho = 2.700$ g/cm^3) as the most suitable metal fuel in terms of gravimetric specific impulse, considerations of the

generated CCP amount and average size point out other promising directions for enhancing the actually delivered specific impulse. The well-known agglomeration phenomena, observed near the burning surface (incipient agglomeration) in the combustion of µAl particles, are drastically modified for some of the evaluated dual-metal formulations. For propellant microstructures using nAl or Mg_xB_y as metallic ingredients, visual inspections of the near burning surface region point to aggregation phenomena (prompt oxidation), without the typical transition to agglomeration, which go much beyond the simple reduction of the particle ignition standoff distance. This essentially heterogeneous burning mechanism yields larger steady-state burning rates and smaller agglomerates of unusual structure, consisting for nAl of a central metal core surrounded by an oxide layer (see Fig. 9d). Both phenomena can be ascribed to the combined effects of large specific surface and low ignition temperature of the metal fuel. Subsurface heating is provided by the conductive thermal wave in the condensed phase, with the possible augmentation by the exothermic reactions of the local premixed flame.

Thus, as of this writing, the recommended approach is to address the attention to dual-metal formulations (µAl–nAl, µAl–Mg_xB_y, etc.) and to identify the optimum compositions, leading to improved ballistic properties under real operating conditions. In particular:

- For µAl–nAl dual-metal formulations, best results are obtained with a partial replacement, around 20–30 % mass of µAl.
- For µAl–Mg_xB_y dual-metal formulations, best results in terms of reduced average agglomerate size are obtained with 25 % Mg coating, while 60 % Mg coating leads to a measurable decrease of steady burning rate.
- For µAl–actAl (either chemically or mechanically) dual-metal formulations, optimization studies are under way and not yet conclusive. However, preliminary studies suggest that actAl powders are a good candidate only for a complete substitution of µAl, if good packing and mechanical properties can be maintained. According to the experimental campaigns executed in past years, µAl–actAl dual formulations are not effective in significantly changing both the burning rate and the agglomerate size of standard aluminized AP-/HTPB-based solid rocket propellants.

Overall, it can be said that the chemistry and physics of the microstructure are important in understanding and controlling the propellant combustion properties and ultimately flight performance. At least two new directions recently appeared capable of drastically modifying, in the long range, the current understanding of metal burning. The first contribution is due to Glorian et al. [89]. Since the Al combustion chemistry in the gas phase is quite well known even under propellant burning conditions, they focused their attention on the elusive details of the combustion chemistries at the surface and surface/gas interface. Depending on the Al particle size especially and a number of additional parameters as well, these chemistries may exert important effects to the overall combustion process. The combustion of nAl in particular (switching from a diffusive to a premixed flame) appears more sensitive to surface reactions than µAl particles. In this respect, surface reactions in

general were carefully studied by quantum chemistry. Basic heterogeneous kinetics describes how molecules interact with metallic surfaces: the first step is adsorption (chemisorption), that is the binding of the adsorbate (atom, radical, molecule) with one or more atoms on the surface. In the pioneering work [89], small adsorbates on Al, such as atoms, were studied experimentally, these species being the simplest intermediates. Adsorption sites, vibrational frequencies, and thermodynamic properties of adsorbed species on an Al surface were calculated using a parameterized density functional method. In spite of a severe lack of experimental information, thermochemical data and kinetic data were developed that can be used to specifically assist modeling surface reactions of Al particle combustion. Considerable efforts are still needed to model the combustion chemistry under the complex operating conditions of segmented solid rocket motors. Eventually, this approach may open the path to a new and more comprehensive understanding of Al and, more generally, metal burning.

An even more drastic prospect is that opened by Komarov and Shandakov [90]. In a thermochemical study conducted under very general conditions, they show that it is possible in principle to get high (computed) I_s by totally avoiding the use of metals or hydrides. The authors show that the basic role of metals or hydrides is simply that of increasing the flame temperature. In the region of oxidizers with a negative heat of formation Δh_f^0, the role of the metal or hydrides in increasing I_s is substantial. But moving into the region of oxidizers with positive Δh_f^0, the role of the metal or hydrides in increasing I_s becomes smaller and may even cause it to decrease! Therefore, by properly combining oxidizers with large enough heats of formation and energetic binders, one can achieve a remarkable I_s increase, compared with current technologies, without the penalties imposed by the use of metals and chlorine (when AP is used as oxidizer); for details see also [91] in this book.

References

1. Williams FA, Barrère M, Huang NC (1969) Fundamental aspects of solid propellant rockets. Technivision Services, Slough, UK. AGARDograph. AGARDograph 116
2. Sakovich GV (1995) Design principles of advanced solid propellants. J Propuls Power 11(4):830–837
3. Maggi F, Gariani G, Galfetti L et al (2012) Theoretical analysis of hydrides in solid and hybrid rocket propulsion. Int J Hydrog Energy 37:1760–1769. doi:10.1016/j.ijhydene.2011.10.018
4. DeLuca LT, Maggi F, Dossi S et al (2013) High-energy metal fuels for rocket propulsion: characterization and performance. Chin J Explos Propellants 36:1–14
5. Karabeyoglu A (2016) Chapter 5: Performance additives for hybrid rocket engines. In: DeLuca LT, Shimada T, Sinditskii VP, Calabro M (eds) Chemical rocket propulsion: a comprehensive survey of energetic materials. Springer International Publishing, Cham
6. Risha GA, Evans BJ, Boyer E, AIAA et al (2007) Metals, energetic additives, and special binders used in solid fuels for hybrid. In: Chiaverini MJ, Kuo KK (eds) Fundamentals of hybrid rocket combustion and propulsion. AIAA, Reston, pp 413–456
7. Gromov AA, Teipel U (eds) (2014) Metal nanopowders: production, characterization, and energetic applications. Wiley-VCH, Weinheim
8. Anon. (1993) Beryllium and beryllium compounds (No. 58), IARC summaries & evaluations. International Agency for Research on Cancer (IARC)

9. Srivastava RD, Farber M (1978) Thermodynamic properties of Group 3 oxides. Chem Rev 78:627–638. doi:10.1021/cr60316a002

10. Chase MWJ (1998) NIST-JANAF thermochemical tables. J Phys Chem Ref Data 9:1–1951

11. Haddad A, Natan B, Arieli R (2011) The performance of a boron-loaded gel-fuel ramjet. In: DeLuca LT, Bonnal C, Frolov S, Haidn OJ (eds) Progress in propulsion physics. EDP Sciences, Paris, pp 499–518. doi:10.1051/eucass/201102499

12. DeLuca LT, Marchesi E, Spreafico M et al (2010) Aggregation versus agglomeration in metallized solid rocket propellants. Int J Energy Mater Chem Propuls 9:91–105

13. Navrotsky A (2003) Energetics of nanoparticle oxides: interplay between surface energy and polymorphism. Geochem Trans 4:34–37. doi:10.1039/b308711e

14. Gromov AA, Maggi F, Malikova EV et al (2014) Combustion synthesis of AlN (Al3O3N), BN, ZrN, and TiN in air and ceramic application. In: Gromov AA, Chukhlomina LN (eds) Nitride ceramics: combustion synthesis, properties and applications. Wiley-VCH, Weinheim, pp 125–163

15. Kubota N (2007) Propellants and explosives: thermochemical aspects of combustion, 2nd edn. Wiley-VCH, Weinheim

16. Lide DR (2007) CRC handbook of chemistry and physics, 88th edn. CRC Press, Boca Raton

17. Glassman I (2008) Combustion, 4th edn. Academic Press/Elsevier, New York

18. Perry RH et al (1997) Perry's chemical engineers' handbook, 7th edn. McGraw Hill, New York

19. Dean JA (1999) Lange's handbook of chemistry, 15th edn. McGraw Hill, New York

20. Gen MY, Frolov YV, Storozhev VB (1978) On combustion of particles of subdispersed aluminum. Combust Explosion Shock Waves 14(5):153–155

21. Gen MY, Ziskin MS, Petrov YI (1959) Investigation of aluminum aerosol dispersion depending on of their formation conditions. Proc Acad Sci USSR (Doklady) 127:366

22. DeLuca LT, Galfetti L, Maggi F et al (2014) Chapter 12: Characterization and combustion of aluminum nanopowders in energetic systems. In: Gromov AA, Teipel U (eds) Metal nanopowders: production, characterization, and energetic applications. Wiley VCH, Wenheim, pp 301–400

23. Kwon YS, Jung YH, Yavorovsky NA et al (2001) Ultra-fine powder by wire explosion method. Scr Mater 44(8–9):2247–2251

24. Advanced Powder Technologies LLC (2015) http://www.nanosized-powders.com. Accessed 31 Mar 2015

25. Kwo YS, Gromov AA, Strokova JJ (2007) Passivation of the surface of aluminum nanopowders by protective coatings of different chemical origin. Appl Surf Sci 253:5558–5564

26. Sossi A, Duranti E, Paravan C, DeLuca LT, Vorozhtsov AB, Gromov AA, Pautova YI, Lerner MI, Rodkevich NG (2013) Non-isothermal oxidation of aluminum nanopowder coated by hydrocarbons and fluorohydrocarbons. Appl Surf Sci 271:337–343. doi:10.1016/j.apsusc.2013.01.197

27. Sossi A, Duranti E, Manzoni M, Paravan C, DeLuca LT, Vorozhtsov AB, Lerner MI, Rodkevich NG, Gromov AA, Savin N (2013) Combustion of HTPB-based solid fuels loaded with coated nanoaluminum. Combust Sci Technol 185(1):17–36. doi:10.1080/00102202.2012.707261

28. Chen L, Song W, Lv J et al (2010) Research on the methods to determine metallic aluminum content in aluminum nanoparticles. Mater Chem Phys 120:670–675

29. Klager K (1984) Polyurethanes, the most versatile binder for solid composite propellants. Am Inst Aeronaut Astronaut. doi:10.2514/6.1984-1239

30. Humble R (2000) Fuel performance enhancements for hybrid rockets. Am Inst Aeronaut Astronaut. doi:10.2514/6.2000-3437

31. Mackay ME, Tuteja A, Duxbury PM et al (2006) General strategies for nanoparticle dispersion. Science 311:1740–1743

32. Reina A, Paravan C, Morlacchi M, Frosi A, Maggi F, DeLuca LT (2013) Rheological and mechanical behavior of coated aluminum loaded nano-composites. In: Haidn OJ, Zinner W, Calabro M (eds) 5th European conference for aerospace sciences (EUCASS 2013), ISBN: 9788494153105, pp 1–14 [5th European conference for aerospace sciences (EUCASS 2013), Munich 1–5 Jul 2013]

33. Zare A, Harriman T, Lucca DA, Roncalli S, Kosowski BM, Paravan C, DeLuca LT (2016) Chapter 27: Mapping of aluminum particle dispersion in solid rocket fuel formulations. In: DeLuca LT, Shimada T, Sinditskii VP, Calabro M (eds) Chemical rocket propulsion: a comprehensive survey of energetic materials. Springer International Publishing, Cham

34. Pokhil PF, Belyaev AF, Frolov YV (1972) Combustion of Metal Powders in Active Media. Nauka, Moscow

35. Price EW (1979) Combustion of aluminum in solid propellant flames, AGARD PEP 53rd Meeting on solid rocket motor technology, Paper 14, AGARD, Paris

36. Price EW (1984) Chap. 9: Combustion of metallized propellants, fundamentals of solid propellants combustion. In: Kuo KK, Summerfield M (eds) AIAA progress in aeronautics and astronautics, vol 90. AIAA, New York

37. Olivani A, Galfetti L, Severini F, Colombo G, Cozzi F, Lesma F, Sgobba M (2002) Aluminum particle size influence on ignition and combustion of AP/HTPB/Al solid rocket propellants, RTO-AVT Fall 2002 Meetings, Aalborg 23–27 Sept 2002

38. DeLuca LT, Galfetti L, Severini F, Meda L, Marra G, Vorozhtsov AB, Sedoi VB, Babuk VA (2005) Burning of nAl composite rocket propellants. Combust Explosion Shock Waves 41(6):680–692

39. DeLuca LT (2007) Burning of aluminized solid rocket propellants: from micrometric to nanometric fuel size. In: Ping H, Yajun W, Shengcai L (eds) Theory and practice of energetic materials, vol 7. Science Press, Beijing, pp 277–289

40. DeLuca LT, Galfetti L (2008) Burning of metallized composite solid rocket propellants: from micrometric to nanometric aluminum size, Asian joint conference on propulsion and power, Gyeongju, 6–8 March 2008

41. DeLuca LT, Galfetti L, Maggi F, Colombo G, Bandera A, Cerri S, Donegà P (2008) Burning of metallized composite solid rocket propellants: toward nanometric fuel size. In: Proceedings of ESA space propulsion, ESA, Crete, 05–08 May 2008

42. DeLuca LT, Bandera A, Maggi F (2009) Agglomeration of aluminized solid rocket propellants. AIAA paper 2009-5439, AIAA, Reston. doi:10.2514/6.2009-5439

43. DeLuca LT, Galfetti L, Colombo G, Maggi F, Bandera A, Babuk VA, Sinditskii VP (2010) Microstructure effects in aluminized solid rocket propellants. J Propuls Power 26(4): 724–733

44. Grigor'ev VG, Kutsenogii KP, Zarko VE (1981) Model of aluminum agglomeration during the combustion of a composite propellant. Combust Explosion Shock Waves 17(4):356–363

45. Cohen NS (1983) A pocket model for aluminum agglomeration in composite propellants. AIAA J 21(5):720–725

46. Babuk VA, Vasilyev VA, Malakhov MS (1999) Condensed combustion products at the burning surface of aluminized solid propellant. J Propuls Power 15(6):783–793

47. Babuk VA, Vasilyev VA, Sviridov VV (2000) Formation of condensed combustion products at the burning surface of solid rocket propellant. In: Yang V, Brill TB, Ren WZ (eds) Solid propellant chemistry, combustion, and motor interior ballistics, vol 185, AIAA Progress in Astronautics and Aeronautics. AIAA, Reston, pp 749–776

48. Babuk VA, Vasilyev VA, Glebov AA, Dolotkazin IN, Galeotta M, DeLuca LT (2004) Combustion mechanisms of AN-based aluminized solid rocket propellants. In: Novel energetic materials and applications, vol 9, IWCP. Grafiche GSS, Bergamo, paper 44

49. Babuk VA, Glebov A, Arkhipov VA, Vorozhtsov AB, Klyakin GF, Severini F, Galfetti L, DeLuca LT (2005) Dual-oxidizer solid rocket propellants for low-cost access to space. In: DeLuca LT, Sackheim RL, Palaszewski BA (eds) In-space propulsion, vol 10, IWCP. Grafiche GSS, Bergamo, paper 15

50. Babuk VA (2016) Chapter 13: Solid propellant formulation factors and properties of condensed combustion products. In: DeLuca LT, Shimada T, Sinditskii VP, Calabro M (eds) Chemical rocket propulsion: a comprehensive survey of energetic materials. Springer International Publishing, Cham

51. Rashkovskiy SA (1998) Metal agglomeration in solid propellants combustion—Part 2: Numerical experiments. Combust Explosion Shock Waves 136(1–6):149–169. doi:10.1080/00102209808924169

52. Gallier S (2009) A stochastic pocket model for aluminum agglomeration in solid propellants. Propellant Explos Pyrotechnics 34(2):97–105. doi:10.1002/prep.v34:2

53. Maggi F, DeLuca LT, Bandera A (2015) Pocket model for aluminum agglomeration based on propellant microstructure. AIAA Journal 53(11):3395–3403. doi:10.2514/1.J053992

54. Kraeutle KJ (1978) Particle size analysis in solid propellant combustion research. In: Boggs TL, Zinn BT (eds) Experimental diagnostics in combustion of solids, vol 63, AIAA Progress in astronautics and aeronautics. AIAA, New York, pp 76–108

55. Weiser V, Gettwert V, Franzin A, DeLuca LT et al (2016) Chapter 10: Combustion behavior of aluminum particles in ADN/GAP composite propellants. In: DeLuca LT, Shimada T, Sinditskii VP, Calabro M (eds) Chemical rocket propulsion: a comprehensive survey of energetic materials. Springer International Publishing, Cham

56. Dondé R, Guarnieri C, Meda L, Marra G, Orsini D, Prato A, Galfetti L, DeLuca LT (2007) Experimental investigations on transient burning of nano-aluminized solid rocket propellants, AAAF conference on changes in aeronautical and space systems, Avignon, 26–28 June 2006

57. Arkhipov VA, Bondarchuk SS, Korotkikh AG, Kuznetsov VT, Gromov AA, Volkov SA, Revyagin LN (2012) Influence of aluminum particle size on ignition and nonstationary combustion of heterogeneous condensed systems. Combust Explosion Shock Waves 48(5):625–635

58. Arkhipov VA, Korotkikh AG (2012) The influence of aluminum powder dispersity on composite solid propellants ignitability by laser radiation. Comb Flame 159(1):409–415

59. Zhao FQ, Yao EG, Xu SY, Li X, Xu HX, Hao HX (2016) Chapter 11: Laser ignition of different aluminum nanopowders for solid rocket propulsion. In: DeLuca LT, Shimada T, Sinditskii VP, Calabro M (eds) Chemical rocket propulsion: a comprehensive survey of energetic materials. Springer International Publishing, Cham

60. Arkhipov VA, Vorozhtsov AB, Shrager ER et al (2004) Acoustic admittance function study for solid propellants containing ultrafine aluminum. In: DeLuca LT, Galfetti L, Pesce-Rodriguez RA (eds) Novel energetic materials and applications. Proceedings of the IX international workshop on combustion and propulsion, Lerici, Italy, 14–18 Sept 2003. Grafiche GSS, Bergamo

61. Komarova M, Vorozhtsov AB (2014) Influence of passivated nanosized aluminum powder on physico-chemical characteristics of metalized compositions combustion. Russ Phys J 57(7):76–80

62. Lerner M, Glaskova E, Vorozhtsov AB, Rodkevich N et al (2015) Passivation of nanosized aluminum powder for use in high energetic materials. Russ J Phys Chem B (Khimicheskaya Foizika, in Russian) 9(1):56–61

63. Vorozhtsov AB, Zhukov A, Ziatdinov M, Bondarchuk S, Lerner M, Rodkevich N (2016) Chapter 9: Novel micro- and nanofuels: production, characterization, and applications for high energy materials. In: DeLuca LT, Shimada T, Sinditskii VP, Calabro M (eds) Chemical rocket propulsion: a comprehensive survey of energetic materials. Springer International Publishing, Cham

64. Sundaram DS, Yang V, Zarko VE (2015) Combustion of nano aluminum particles (review). Combust Explosion Shock Waves 51(2):173–196. © Pleiades Publishing, Ltd., 2015

65. Rosenband V, Gany A (2011) High-reactivity aluminum powders. J Energy Mater Chem Propuls 10(1):19–32

66. Yavor Y, Rosenband V, Gany A (2014) Reduced agglomeration in solid propellants containing porous aluminum. Proc Inst Mech Eng Part G 228(10):1857–1862

67. Hama A, Gany A, Palovuori K (2006) Combustion of activated aluminum. Combust Flame 145(3):464–480

68. Hama A (2010) Method of improving the burn rate and ignitability of aluminum fuel particles and aluminum fuel so modified. US Patent US 7785430 B2

69. Maggi F, Dossi S, Paravan C, DeLuca LT, Liljedahl M (2015) Activated aluminum powders for space propulsion. Powder Technol 270:46–52
70. Zhang DL (2004) Processing of advanced materials using high-energy mechanical milling. Prog Mater Sci 49(3–4):537–560
71. Koch CC, Whittenberger JD (1995) Review mechanical milling/alloying of intermetallics. Intermetallics 4(5):339–355
72. Filimonova VY, Korchagin MA, Evstigneev VV (2009) Anomalous decrease in the activation energy and initiation temperature of a thermal explosion in the mechanically activated composition 3Ni + Al. Dokl Phys 54(6):277–280
73. Shteinberg AS, Lin YC, Son SF, Mukasyan AS (2010) Kinetic of high temperature reaction in Ni-Al system: influence of mechanical activation. J Phys Chem A 114(20):6111–6116
74. Sippel TR, Son SF, Groven LJ (2013) Altering reactivity of aluminium with selective inclusion of polytetrafluoroethylene through mechanical activation. Propell Explos Pyrot 38(2):286–295
75. Dossi S (2014) Mechanically activated Al fuels for high performance solid rocket propellants. PhD Dissertation, Politecnico di Milano
76. Sippel TR, Son SF, Groven LJ et al (2014) Exploring mechanisms for agglomerate reduction in composite solid propellants with polyethylene inclusion modified aluminum. Combust Flame. (162): http://dx.doi.org/10.1016/j.combustflame.2014.08.013
77. Chan ML, Parr T, Hanson-Parr D, Bui T, Mason M (2004) Characterization of a boron containing propellant, In: DeLuca LT, Galfetti L, Pesce-Rodriguez RA (eds) Novel energetic materials and applications, IWCP vol 9, Paper 07. Grafiche GSS, Bergamo
78. Mitani T, Izumikawat M (1991) Combustion efficiencies of aluminum and boron in solid propellants. AIAA J Spacecr Rocket 28(1):79–84
79. Dossi S, Reina A, Maggi F, DeLuca LT (2012) Innovative metal fuels for solid rocket propulsion. Int J Energy Mater Chem Propuls 11(4):299–322
80. Shevchuk VG, Zolotko AN, Polishchuk DI (1975) Ignition of packed boron particles. Combust Explosion Shock Waves 11:189–192
81. DeLuca LT, Galfetti L, Maggi F, Colombo G, Reina A, Dossi S, Consonni D, Brambilla M (2012) Innovative metallized formulations for solid or hybrid rocket propulsion. Hanneng Cailiao/Chin J Energetic Mater 20(4):465–474. doi:10.3969/j.issn.1006-9941.2012.04.018. Presented at the *2011 IASPEP* (International Autumn Seminar on Propellants, Explosives and Pyrotechnics), China
82. DeLuca LT (2011) Energetic problems in aerospace propulsion. Politecnico di Milano, Milan
83. Fassina M (2015) Effects of Al particles shape on solid rocket propellant burning. PhD Dissertation, Politecnico di Milano, Milan, 16 February 2015
84. DeLuca LT, Galfetti L, Severini F, Rossettini L, Meda L, Marra G, D'Andrea B, Weiser V, Calabro M, Vorozhtsov AB, Glazunov AA, Pavlovets GJ (2007) Physical and ballistic characterization of AlH3-based space propellants. Aerosp Sci Technol 11:18–25
85. DeLuca LT, Rossettini L, Kappenstein Ch, Weiser V (2009) Ballistic characterization of AlH₃-based propellants for solid and hybrid rocket propulsion, AIAA Paper 2009–4874
86. Young G, Piekiel N, Chowdhury S, Zachariah MR (2010) Ignition behavior of α-AlH₃. Combust Sci Technol 182:1341–1359
87. Young G, Risha GA, Miller AG, Glass RA, Connell TL, Yetter RA (2010) Combustion of alane-based solid fuels. Int J Energetic Mater Chem Propuls 9(3):249–266
88. Young G, Jacob R, Zachariah MR (2015) High pressure ignition and combustion of aluminum hydride. Combust Sci Technol 187:1335–1350
89. Glorian J, Catoire L, Gallier S, Cesco N (2015) Gas-surface thermochemistry and kinetics for aluminum particle combustion. Proc Combust Inst 35:2439–2446
90. Komarov VF, Shandakov VA (1999) Solid fuels, their properties, and applications. Combust Explosion Shock Waves 35(2):139–143
91. Lipanov AM, Zarko VE (2016) Chapter 43: Survey of solid rocket propulsion in Russia. In: DeLuca LT, Shimada T, Sinditskii VP, Calabro M (eds) Chemical rocket propulsion: a comprehensive survey of energetic materials. Springer International Publishing, Cham

Novel Micro- and Nanofuels: Production, Characterization, and Applications for High-Energy Materials

Alexander B. Vorozhtsov, Alexander S. Zhukov, Mansur Kh. Ziatdinov, Sergey S. Bondarchuk, Marat I. Lerner, and Nikolay G. Rodkevich

Abstract In this paper, the problems of production and characterization of nanosized metals (nanosized aluminum) and microsized metal borides (including aluminum, titanium, magnesium) are discussed. The preferences of application for high-energy materials are presented. Also, the technique for production of nanometals is described which is the electric explosion wire method. The results of characterization of nanometals produced by that method are shown and discussed. To protect an active surface of nanoparticles, the different ways for passivation are suggested. Different polymers including Viton and Fluorel are suggested as passivated agents. The problems of chemical stability and chemical compatibility are discussed. A technique for production of metal borides is also described which is known as self-propagating high-temperature synthesis (SHS) and the subsequent mechanical treatment. The result is microsized borides which have an average size of around 5 μm with a sharp curve for distribution sizes. The purity is enough for use as fuel of high-energy materials. The results of TEM, SEM, X-ray, DSC, and TG analyses are also presented and discussed.

A.B. Vorozhtsov (✉) • A.S. Zhukov • M.Kh. Ziatdinov
Tomsk State University, 634050 Tomsk, Russia

Institute for Problems of Chemical and Energetic Technologies, SB RAS,
659322 Biysk, Russia
e-mail: abv@mail.tomsknet.ru; zhuk_77@mail.ru; ziatdinovm@mail.ru

S.S. Bondarchuk
Tomsk State University, 634050 Tomsk, Russia

Tomsk State Pedagogical University, 634061 Tomsk, Russia
e-mail: isbi@mail.ru

M.I. Lerner
Tomsk Polytechnic University, 634050 Tomsk, Russia
e-mail: lerner@ispms.tsc.ru

N.G. Rodkevich
Institute of Physics Strength and Material Science, SB RAS, 634055 Tomsk, Russia
e-mail: ngradk@ispms.tsc.ru

Acronyms

ALEX	Aluminum explosive (Trade mark)
AS USSR	Academy of Science of the Union of Soviet Socialist Republics
ASD	Aluminum spherical disperse (Russian Trade mark)
CSR	Crystal structure reference (size)
DSC	Differential scanning calorimetry
DTA	Differential thermal analysis (method)
EEW(s)	Electric explosion of wire(s)
EW	Explosion of wire
HEM(s)	High-energy material(s)
LC	Electric circuit consisting of an inductor (L), and a capacitor (C), connected together
nAl	Nanoaluminum
SB RAS	Siberian Branch of Russian Academy of Sciences
SEM	Scanning Electron Microscope
SHS	Self-propagating high-temperature synthesis (of materials)
TEM	Transmission Electron Microscope
TG	Thermogravimetry (mass change study)

1 Introduction

In the last 40 years, high-energy characteristics of composite propellants have been provided by the use of metal powders (mostly aluminum with particle sizes of 5–50 μm) as a fuel component with a mass fraction of 10–20 %. However, several significant disadvantages were discovered during the use of metallized mixed compositions in solid-propellant rocket motors. These include incomplete combustion of aluminum particles, additional two-phase losses of specific impulse, and erosive action of combustion products on the elements of a nozzle block.

Creation of new generation of high-energy materials (HEMs) involves the development of new compounds of fuel binders and oxidizing agents and the use of nanosized powders (nanopowders) with particle sizes a few dozen times smaller than that of commercial powders.

The pioneer work concerned the use of nanopowders as components of fuel compositions and these were conducted in the Institute of Chemical Physics, AS USSR [1]. This research involved aluminum nanopowders and it indicated the possibility of a significant reduction of two-phase flow losses of the specific impulse by means of increasing the combustion efficiency and size reduction of agglomerated products. However, no practical application for this research could be found, and so it was suspended due to an absence of a technological base for the large-scale production of metal nanopowders.

Table 1 Heat of combustion
of energetic metals [7]

Element	Heat of combustion, kJ/g
Li	43.5
B	57.2
Mg	25.1
Al	31.4
Si	32.2
Ti	15.7
Zr	12.0

Recently, new technologies of large-scale metal nanopowder production have been developed and the interest in the use of nanopowders as components of HEM has increased. The problems of ignition and combustion of HEM with aluminum and other metals have been thoroughly investigated in a number of research and development centers and universities in the Russian Federation and abroad. The works of Luigi T. DeLuca, G.J. Pavlovets, Valery A. Babuk, K.K. Kuo, and others [2–6] should be mentioned.

Research has shown that nanopowders could be used as a component of HEM, not only to increase the energy characteristics of the propellant but also to reduce the agglomeration rate, to increase the combustion rate and to control the value of v-index in combustion rate law.

If we compare the heat release of different metals (Table 1), it appears clear that boron and lithium have the best characteristics for this purpose.

Lithium cannot be used due to its toxicity and low processability (low melting point and high chemical activity). Moreover, metallic lithium is rare and very expensive. Therefore, there are no alternatives are to boron regarding exothermicity and availability. The heat of combustion for boron is almost two times higher than that for aluminum and boron has a high availability in nature. However, due to specific properties of its oxide B_2O_3 (high boiling point and high viscosity of oxide melt), the rate of oxidation of elemental boron in fuel composition is unacceptably low. Also boron oxide causes an appreciable agglomeration which is an extremely undesirable phenomenon. Well-known fundamental works by A. Gany and other scientists demonstrate the possibilities of using boron as fuel; however, there are no widespread technologies making it possible to use this element as a component of high-energy materials [8].

Currently the optimal solution for the task of improving the efficiency of metallic additives to fuel compositions would be a full or partial transition to the use of metal borides.

This paper provides an overview of the results following a comprehensive analysis of the properties of different micro- and nanoparticles which can be used as additives for HEM.

2 Results and Discussion

2.1 *Nanoaluminum (nAl)*

2.1.1 Technology of Production by the Method of Electric Explosion of Wire

There are currently more than 20 methods and technologies for the production of ultrafine metal powders. Detailed surveys covering this topic are represented in references [1, 2]. The most promising methods are the electric arc plasma recondensation [3] and electric explosion of wires (EEWs) [4–6, 9].

The EEW method is based on impact destruction of a metal wire in a gas medium under the action of high-density current impulse $(10^6 \div 10^9)$ A/cm^2. The wire heats up to the melting point, melts, and then explodes and falls apart into particles. The simplest way of EEW is the one using an *LC*-contour. The circuit used in ultrafine powder production facilities is presented in Fig. 1. It includes the following basic elements: a high-voltage power supply; storage condenser, C; triggered spark gap, P; inductor, L; a wire, EW; instrument shunt, R_S; and tight stainless steel-blasting chamber.

The typical oscillograms of current and voltage at EEW are represented in Fig. 1. When the voltage is applied to a metal wire, the metal gets hot and melts; this can be seen as a small voltage jump on the oscillogram. At the moment t_1, the metal disintegrates and starts to expand quickly with loss of conductivity. At the moment t_2, the current is absent, it is called current pause, and the expanding explosion products hold residual voltage of the capacitor during this pause. This is followed by the breakdown of the discharge gap and arc ignition.
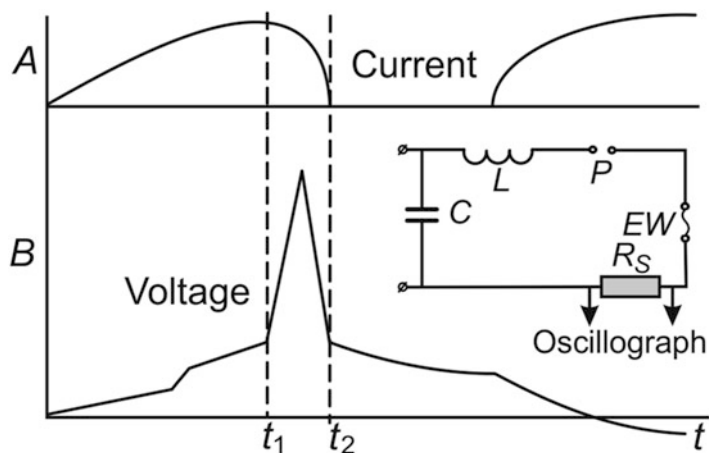
Fig. 1 Electric circuit and oscillograms of current intensity and voltage at EEW

EEW as a method of dispersion of metals is characterized by the following significant features [6]:

- Burst time comprises 10^{-5}–10^{-8} s.
- Power input exceeds 10^{13} W/kg.
- At the moment of explosion, the temperature may reach the value of 10^4 K and higher and the pressure – 10^9 Pa.
- Expansion velocity of explosion products is 1–5 km/s, cooling rate of explosion products being 10^7 K/s.

The size of metal nanopowders formed is determined with process parameters being usually less than 1 μm and specific surface 10–20 m^2/g (measured using a BET method). The powders have a high purity, and the impurity content is determined only by the purity of the metal wire and the quantity of the oxide phase formed when a powder contacts air. The shape of the particles varies from irregular (tens of nanometers in size) to spherical (hundreds of nanometers in size).

EEW method in inert gases is of particular interest. The first samples of aluminum powder obtained through aerosol deposition after electric explosion of wire were produced in Research Institute of High Voltages in 1970s. N.A. Yavorovsky and Yu A. Kotov developed the method of explosion optimization and created more capable facilities to produce sufficient quantities of powders [10]. Nowadays, in Tomsk there are EEW powder production facilities of continuous type for any metals (Al, Cu, Zn, Sn, Ti, Zr, In, Fe, Ni, Mo, W) as well as their alloys with a total production capacity of more than 1 ton of nanopowders per year.

ALEX™ powder produced using described above technology was used as an aluminum nanopowder (nAl) in this research. The particle size characteristics of this powder are described in the following section.

2.1.2 Nanopowder Particle Size Distribution Analysis

As the particle size of aluminum powders used in HEM plays a very important role in all high-temperature processes, let us consider the original method of particle size distribution analysis of ALEX and some regular aluminum powders of Russian trademark ASD (aluminum spherical dispersion). The content of particles of different sizes in a polydisperse system is determined by its integral distribution function of parameter x, which characterizes a size of a single particle (radius, volume, mass, cross section, specific equivalent size for aspheric particles, etc.) [9, 11]; x is considered to be a one-dimensional random variable. The functions of mass distribution $G(x)$ and counting distribution $F(x)$ are the most widely used. Function $G(x)$ is equal to mass of all particles with sizes less than x divided by the total mass of the particle material; function $F(x)$ is equal to number of particles with sizes less than x divided by the total number of particles. The values of $G(x)$, $F(x)$ cannot be obtained experimentally for all values of x. The values G and F are obtained experimentally only for a limited number of x_i (. . . $x_1 < x_2 < x_3$ . . .), where

these functions have positive jumps; G and F are constant between successive values of x_i. The functions $g(x)$ and $f(x)$ represent themselves differential functions of mass and counting distribution.

The analysis of a vast number of sources on particle size composition of various polydisperse systems [12, 13] indicated that all metal powders with unimodal distribution function can be described either with a generalized gamma distribution [14] or a logarithmically normal distribution [15]. A detailed description of the method and the algorithm for the identification of a distribution function of metal powders with a unimodal distribution function is described in paper [16]. The developed approach and corresponding software were tested on aluminum powders ASD-4, ASD-6, and ALEX [5, 17]. Micrographs of aluminum powders ASD-4 and ALEX are represented on Fig. 2. Conductometric analysis (C analysis) was performed for aluminum powders ASD-4, ASD-6 in research [18]. Average diameters calculated using the counting distribution (Fig. 3) are given in Table 2. The values of specific surface area S for aluminum powders under consideration are also shown.
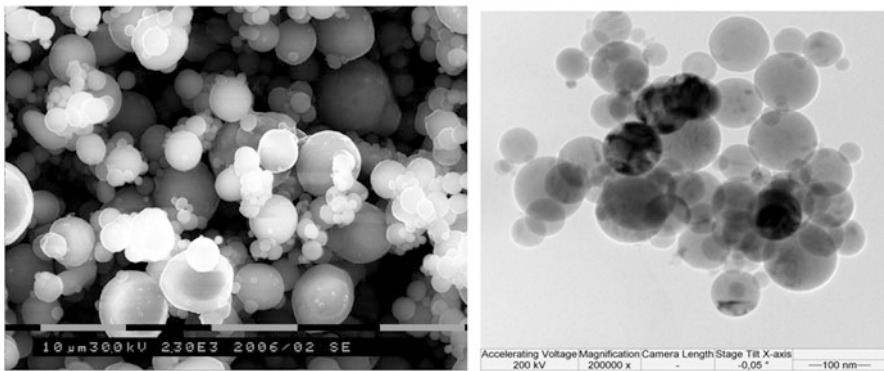
Fig. 2 TEM/SEM picture of aluminum powders ASD-6 (*left*) and ALEX (*right*)
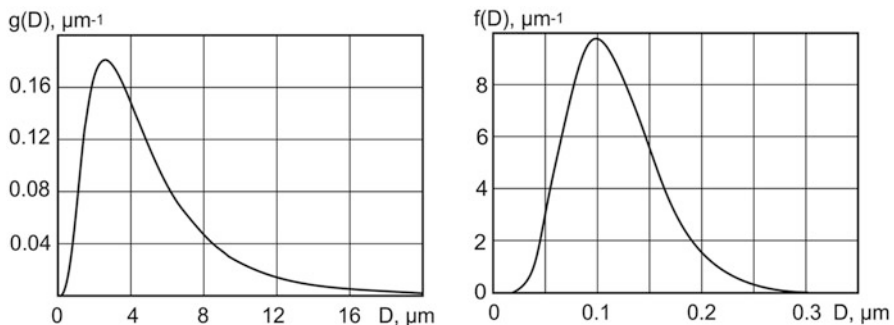
Fig. 3 Distribution functions of aluminum powders ASD-6 (*left*) and ALEX (*right*)

Table 2 Average particle diameters for aluminum powders

Powder type	D_{10}, μm	D_{20}, μm	D_{30}, μm	D_{32}, μm	D_{43}, μm	S, m^2/g
ASD-6 (C analysis)	4.0	4.3	4.5	5.2	6.5	–
ASD-4 (C analysis)	4.3	4.9	5.6	7.4	10.1	–
ASD-4	1.23	1.66	2.28	4.34	7.34	0.512
ASD-6	0.85	1.17	1.60	3.01	4.72	0.739
ASD-8	0.72	0.90	1.09	1.60	2.11	1.389
ALEX	0.12	0.13	0.14	0.16	0.18	13.889

Specific surface area is one of the characteristics of powder particle size distribution. Specific surface area is defined by integral surface area of particles divided by their mass [9]. For globules specific surface area is defined as $S = 6/(\rho D_{32})$ (ρ – density of the material).

2.1.3 Nanopowder Chemical Passivation

Metal nanopowders are highly pyrophoric systems. After synthesis nanopowders exposed to air can ignite as a result of heating caused by metal oxidation with oxygen contained in air. Various passivation methods are used in order to reduce pyrophoricity of nanopowders. Passivation by oxygen-containing atmospheres (air in particular) is a widespread method. In this technique an oxide film is formed on the particle surface which protects the metallic phase from contact with the environment. A major part of existing technologies of metal powder processing are tailored for a certain (usually low) content of oxide phases. Thus, it is necessary to investigate the mechanism of passivation by an oxygen-containing atmosphere and identify dependencies in order to set the optimal parameters for the passivation process so that the chemical activity of nanopowders can be preserved.

Increasing the temperature in the passivation process can lead to sintering of nanoparticles and a change in the nanopowder particle size distribution [19]. This was demonstrated by the experimental measurement of nanopowder electric conductivity as a function of temperature (Fig. 4). During the tests, nanopowders were heated in a flow of argon gas and their electric conductivity was measured. The point of the sharp drop of sample resistance corresponds to the process of sintering of particles and the formation of current contacts between them. The change of resistance, as a function of heating temperature, of layers of non-passivated nAl powder applied from hexane-based paste to ceramic base plate is shown in Fig. 4. As it can be seen, the increase of temperature leads to significant increase of their electric conductivity approximately at 30 °C which is probably associated with sintering of individual nanoparticles. On the basis of obtained data, it may be concluded that sintering of EEW nanopowder is possible at temperatures significantly lower than melting point of the metal.

Aluminum nanopowder with an average particle size of 100 nm which was not exposed to air was used in order to study the process of passivation. The reaction vessel was filled with the powder (volume 25 ml, powder mass 1.75 g) in an inert atmosphere. A gas mixture (O_2 + Ar) was blown through the powder at a specified rate. Powder temperature and active metal content were monitored during the test. Heat exchange with the environment was not considered. Active aluminum content was analyzed using a standard volumetric method.

Dependence of the maximum temperature, T, of nAl powder samples in the process of oxidation in the flow of O_2 + Ar gas mixture is shown in Fig. 5. As can be seen, the samples are heated up to temperatures higher than 30 °C even if the gas flow rate and O_2 concentration in the mixture are low. Thus, on the basis of obtained data, it may be concluded that there is a high probability of sintering of nanoparticles in the process of air passivation of nAl powder.

Active aluminum content in nanopowders also decreases rapidly with the increase of gas flow rate (Fig. 6).

Thus, the passivation of nanopowders with an oxygen-containing gas for the purpose of preservation of particle size distribution of nanopowders and maximum content of active metal is not a promising method.

Fig. 6 Dependence of active aluminum content ω on the flow rate of gas mixture (Ar+O$_2$) V: [O$_2$] concentration in gas mixture – 5 % vol
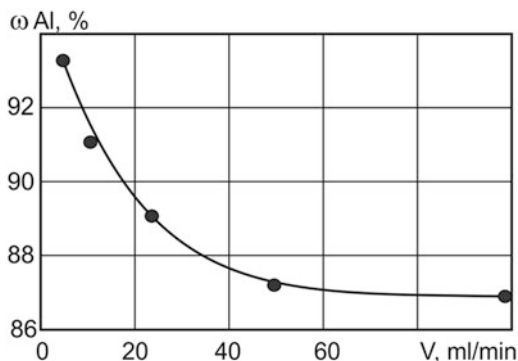
2.1.4 Microencapsulation of nAl Powders

In order to improve the environmental resistance of nanopowders, the method of nanopowders passivation with organic reagents (microencapsulation) — stearic, oleic, and palmitic acids [20, 21] – is used. Adsorption of organic agents forms a protective layer on the surface of nanoparticles, which is more efficient than an oxide layer formed in the process of passivation of nanopowders in an oxygen-containing atmosphere. Adsorption of organic reagents also increases the affinity of metal nanoparticles to organic components of HEM. This has a positive effect on the use of nanopowders as HEM components [22]. Kinetic factors play an important role for HEM in the process of combustion. The use of certain organic agents increases the oxidation rate of nAl powders at high temperatures, which leads to increase of HEM burning rate [23, 24].

In order to perform microencapsulation tests, the following powders were used: nAl powder ALEX passivated in the atmosphere with controlled partial pressure of O$_2$ and non-passivated nAl powders, both produced with EEW in an argon medium. The average particle size for ALEX nanopowder comprised 100 nm, active aluminum content – 92 % by mass and specific surface of nAl powder – 12 m^2/g.

Protective coatings were formed by low-molecular organic compounds capable to form a hydrophobic protective layer on the surface of metal nanoparticles – stearic acid, 8-hydroxyquinoline, glyoxal and polymers: polyethylene glycol adipate (PEGA), vinylidene difluoride and hexafluoropropylene copolymer (Viton™ or Fluorel™) in combination with a monoether (ME) obtained with the interaction of maleic anhydride and 1,1,11-trihydroperfluoroundecyl alcohol [25].

Organic compounds were applied to nAl particles in solution. Twenty grams of nAl powder were suspended in 200 ml of ethyl acetate. This was intensively mixed with a HG-15D homogenizer (5000 rpm, 3 min). There was then a subsequent addition of ethyl acetate solution containing the organic reagent followed by 30 min mixing.

As for Viton coating, the nAl powder suspension was premixed with the solution of 1 g of ME in 10 ml of ethyl acetate with subsequent 30 min mixing and the

Table 3 Characteristics of microencapsulated nAl powders

No	Coating	Sample name	Quantity of organic matter, %	Specific surface, m^2/g
1	W/o coating	ALEX	–	11.8
2	Stearic acid	H-ALEX	3	13.9
3	8-hydroxyquinoline	O-ALEX	0.5	N/A
4	Glyoxal	G-ALEX	1	N/A
5	Stearic acid[a]	L-ALEX	3	11.3
6	PEGA	P-ALEX	1	N/A
7	Viton	VF-ALEX	15	11.0

[a]The coating was applied to non-passivated nAl powder in an inert atmosphere from mineral spirit solution
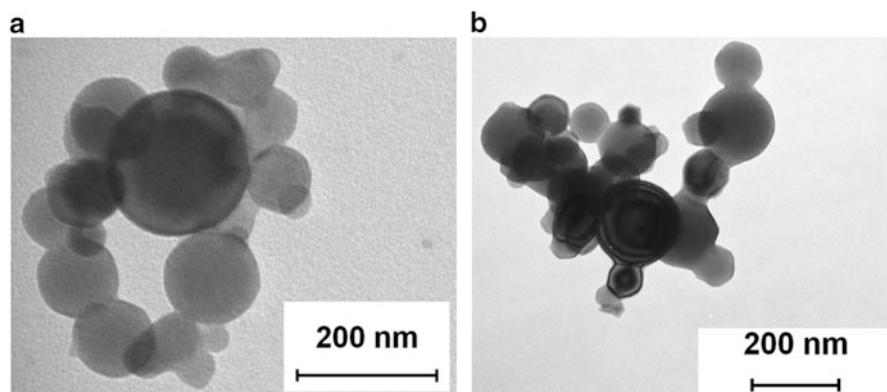
Fig. 7 Characteristic TEM images of microencapsulated nanopowders coated with stearic acid (**a**) and Viton (**b**)

addition of the solution of 2 g of Viton in 50 ml of ethyl acetate followed by additional 30 min mixing.

The solvent was then removed by low-pressure vaporization using IKA RV-10 rotary evaporator. Microencapsulated nanopowders were dried at low pressure, 1 mmHg, over 16 h. Characteristics and TEM images of microencapsulated powders are shown in Table 3 and Fig. 7.

In order to test the barrier properties of protective coating, the samples of microencapsulated nanopowders were exposed to a relative humidity of 90 % and temperature of 25 °C for 180 days. Conversion of nanopowders $\alpha(t)$ was determined on the basis of the change of sample mass and chemical equation of the chemical reaction which takes place (Fig. 8):

$$Al + 3H_2O = Al(OH)_3 + 3/2H_2.$$
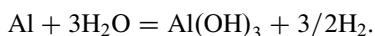
The interaction between the microencapsulated nAl powders and water vapors is significantly slower compared with ALEX. Conversion of microencapsulated nAl particles for the same period of interaction (150 days) is 50–400 times lower than
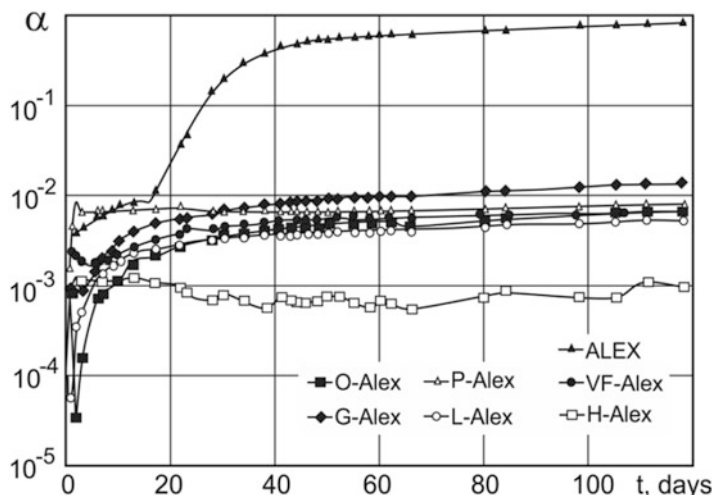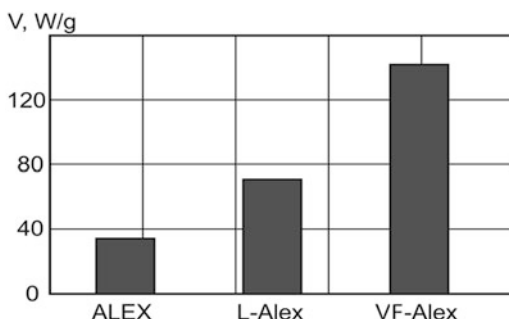
Fig. 8 Kinetic curves of hydrolysis of microencapsulated nanopowders in humid atmosphere: $\alpha = \alpha(t)$

Fig. 9 Heat release rate of nanopowders according to thermal analysis data

that of nAl powder. The value of $\alpha(t)$ after 150 days was less than 0.01 and so the reaction of microencapsulated nAl powders with water vapors during the period of study has not proceeded beyond the induction period. The increase in the mass of these nanopowder samples can be explained by adsorption of water vapor and hydration of oxide layer of nanoparticles rather than chemical reaction.

Thermal analysis of nanopowders has indicated that heat release rate and hence oxidation rate increase in the following sequence: ALEX, L-ALEX, and VF-ALEX (Fig. 9).

Thus, coating of nAl particles with organic compounds at the rate of 0.5–3 % forms a protective layer on the surface of nAl particles which entirely blocks the interaction between nAl particles and water vapors and favors the increase oxidation rate of nanopowders in the process of heating.

Table 4 Heat of combustion of energetic borides

Borides	Heat of combustion, cal/g
AlB_2	9.430
AlB_{12}	12.160
MgB_2	9.050
TiB_2	5.700
$Mg_{0,5}Al_{0,5}B_2$	9.240
ZrB_2	4.230

2.2 Microborides

The use of potentially high boron exothermicity becomes possible if it is used in the form of metal borides which also have high values of the heat of combustion. The oxidation of boron particles unfortunately results in the formation of a solid layer of oxide B_2O_3 and the diffusion of oxygen through this layer is hindered. The oxidation of metal borides does not result in the formation of an oxide layer impenetrable for oxygen. Diffusion of oxygen through the faulted layer of complex oxides is facilitated and the degree and rate of oxidation is increased.

It was found that borides of aluminum and magnesium as well as titanium and zirconium are the most promising (Table 4). Values of the heat of combustion for these borides are given below. Heat of combustion of borides is significantly higher than the values for corresponding metals.

Vacuum-heat technology is used for boride synthesis. At the same time, the formation of borides is associated with significant heat liberation. This energy is often enough for the process in combustion mode according to self-propagating high-temperature synthesis (SHS). Large-scale furnace equipment is not necessary in this case, and most importantly, the synthesized materials have better performance characteristics [26].

At the same time, there are a lot of systems including borides which do not have enough heat release for SHS processes. In such cases there are two possible variants of the SHS process: energy can be pumped in from external sources or energy can be recovered. External energy can be introduced in the form of physical or chemical heat. In case of physical heating, the initial SHS mix is placed into an electric furnace and heated up to the required temperature and then an SHS reaction is initiated. In this case, both layer-by-layer and overall volumetric combustion modes can take place. Preheating of exothermic mix or its part is widely used in metallothermic production of metals and master alloys in particular.

Other possible option of improving the exothermicity of the mix is by introducing additional chemical heat. This method is widely used in aluminothermy in the process of production of complex ferroalloys.

Merzhanov [26] stated the five most typical situations in the process of classification of chemical routes of SHS reactions. One of these types of routes was called "chemically independent routes in thermally coupled systems ("chemical

furnace").'' In these cases chemical reactions proceed independently; however, the heat from the more exothermic reaction provides energy for the less exothermic one.

From the very beginning of the research in the field of combustion synthesis, a lot of promising systems from the practical point of view were determined; however, a self-sustaining process was not possible due to their insufficient exothermicity. The first approach was pumping of additional heat by means of preheating the initial mix in a resistance furnace. It was the production of intermetallides (Ni_3Al, Ni_3Ti, TiFe, Fe_3Al) when the operation of increasing of initial temperature of reaction mix was used for the first time for SHS reactions. The increase of the initial temperature of the mix up to 50–500 °C made it possible to synthesize aluminides of Ni, Co, Ti, Cr, Mo, and other metals in combustion mode. When such furnace SHS technology is used in practice, its characteristic advantages such as no energy consumption, simplicity of equipment, and low time consumption are reduced to zero.

The next step which extended the potential of SH synthesis for low exothermicity systems was the invention of a so-called chemical furnace. This term was coined by V.M. Maslov for the process of synthesis of intermetallides in Nb-Al and Nb-Ge systems. Equiatomic mixture of Ni and Al powders with combustion temperature of 1640 °C was used as a material of "chemical furnace."

The principle of the "chemical furnace" could also be applied to the synthesis of compounds such as WC, NbC, SiC, B_4C, Al_4C_3, VC, Mo_2C, WB, WB_2, and others which do not have enough heat liberation for a general SHS process [27]. In this case, mixtures with higher burning temperatures such as Ti or Zr powders with C or B (Table 5) can be used as materials for a "chemical furnace."

In the case of insufficient heat liberation, the combustion synthesis can be combined with elements of the furnace synthesis. Energy is pre-pumped into the system providing a further combined SHS process. An initial mix of metal and boron is used for the implementation of boride combustion synthesis:
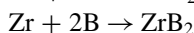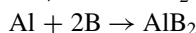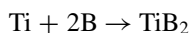
$Ti + 2B \rightarrow TiB_2$
$Al + 2B \rightarrow AlB_2$
$Zr + 2B \rightarrow ZrB_2$

Table 5 Heat of formation of energetic borides

Borides	Heat of formation, cal/g
TiB_2	1006.6
ZrB_2	778.3
TiB_{12}	–
ZrB_{12}	542.8
AlB_2	–
AlB_{12}	–
MgB_2	289.4
MgB_{12}	223.1

A laboratory-scale production technology for borides of Al, Ti, Mg, and other metals including double and mixed compounds has been tested. This has resulted in the synthesized powders having particle sizes of $\delta_{50} \approx 10 \, \mu m$.

Production of borides using the SHS method involves three stages: preparation of the exothermic mix, combustion synthesis, and product processing. The first stage includes operations of batching and mixing of initial powders in stoichiometric proportions and production of cylindrical samples with different diameters.

After this the compressed tablets are placed inside a research SHS reactor with a sealed working chamber which is vacuumized and filled with an inert gas (Ar, He) to provide pressure level of 0.2 MPa. Ignition is then initiated by the application of electric pulse to a tungsten spiral with subsequent formation of a plane combustion front.

At the end of propagation of a combustion synthesis wave and sample cool down, the SHS reactor is depressurized and the sample is processed and analyzed. Particle size distribution and phase composition of the powder produced by milling in a ball mill are determined along with the free boron content. Energy characteristics of the boride powder are then analyzed using DTA (differential thermal analysis) method.

The results of X-ray phase analysis of some synthesized borides are shown in Fig. 10 as an example. Particle size distribution and DTA (Fig. 11) data for AlB_2 were obtained.

According to X-ray phase analysis data, the content of the target phases in the powders studied comprised 88.04 % for $Al_{0,5}Mg_{0,5}B_2$ phase, 93.18 % for AlB_2,
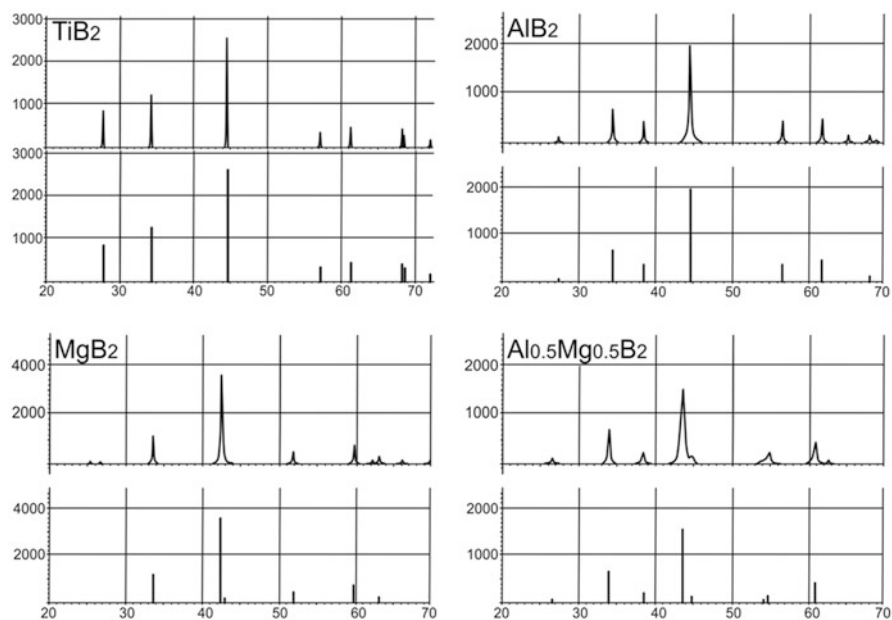

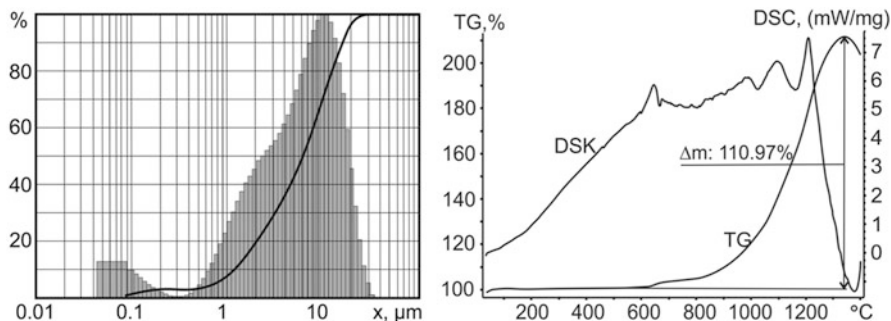**Fig. 10** Typical X-ray images of SHS of energetic borides

Fig. 11 Particle size distribution and DTA analysis data for AlB_2 powder produced by means of SH synthesis

and 98.43 % for TiB_2. The average CSR (crystal structure reference) size for target phases did not exceed 30–40 nm.

The analysis of the particle size distribution in AlB_2 powders has indicated that the average particle size comprises 6.2 μm. The maximum size of the fraction was δ_{99}–24.9 μm. According to DTA data, the sample mass increased $\sim$2.17 times. The increase in the mass was thought to be due to the following reaction

$$2AlB_2 + 3O_2 = Al_2O_3 + B_2O_3$$
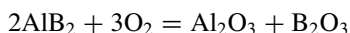
and comprises $\sim$2.26 times. It was also demonstrated that the degree of oxidation was 96 %.

3 Conclusion

This paper has presented the techniques for production of nAl and microborides which can be used as fuels for high energetic materials. The main characteristics of nano- and microparticles have been shown and discussed.

It was found that the EEW method enables pure nAl powders to be produced which have a spherical form of particles (ALEX). According to analysis of particle size composition of nAl powder ALEX, nanopowders have narrow particle size distribution (0.12–0.18) μm and relatively high values of specific surface area (12–14 m^2/g).

It has also been shown that the passivation of nanoparticles with an oxygen-containing gas for the purpose of preservation of particle size distribution of nanopowders and maximum content of active metal was not a viable method.

Synthesis of aluminum borides is one of the most promising areas in the field of development of new energy materials. Self-propagating high-temperature synthesis is the most suitable method for these purposes which makes it possible to produce

ultrapure products with target chemical and phase composition by adjusting the synthesis parameters. Previous studies have indicated that it is possible to produce borides with high content of target phase. According to DTA data, the degree of oxidation of obtained powders exceeds 95 %.

References

1. Morokhov ID, Trusov LI, Chizhik SP (1977) Ultradispersed metal medium. Atomizdat, Moscow. 264 pp. (in Russian)
2. Pavlovets GY, Mazalov YA, Meleshko VY (2001) Modeling and problems of combustion control of heterogeneous condensed systems. Edit.VA RVSN MD RF, Moscow, 289 pp. (in Russian)
3. Gash AE, Simpson RL, Babushkin Y, Lyamkin AI, Tepper F, Biryukov Y, Vorozhtsov A, Zarko V (2004) Chapter 7: Nanoparticles. In: Teipel U (ed) Energetic materials. Particle processing and characterization. WILLEY-VCH Verlag GmbH & Co. KgaA, Weinheim, 590 pp
4. Babuk VA, Vassiliev VA, Sviridov VV (2000) Formation of condensed combustion products at the burning surface of solid rocket propellant. In: Yang V, Brill TB, Ren WZ (eds) Solid propellant chemistry, combustion, and motor interior ballistics. AIAA progress in astronautics and aeronautics, Reston, VA: AIAA, vol 185, pp 749–776
5. Simonenko VN, Zarko VE (1999) Comparative studying the combustion behavior of fine aluminum. Energetic materials: production, processing and characterization. In: Proc. 30-th intern. annual conf. of ICT. Karlsruhe, pp 21–1 – 21–14
6. DeLuca LT, Galfetti L, Severini F, Meda L, Marra G, Vorozhtsov AB, Sedoi VS, Babuk VA (2005) Burning of nano-aluminized composite rocket propellants. Combust Explosion Shock Waves 41(6):680–692
7. Lide DR (ed) (2005) CRC handbook of chemistry and physics. CRC Press, Boca Raton
8. Gany A (1993) Combustion of boron-containing fuels in solid fuel ramjets. Int J Energetic Mater Chem Propuls 2:91–112
9. Gusev AI (1998) Nanocrystalline materials – methods for obtaining and properties. UB RAS, Ekaterinburg. 200 pp. (in Russian)
10. Yavorovsky NA, Kotov YA (1978) Studies of particles formed in electric explosion of wires. Fiz i Khim Obr Mater 4:24–29 (in Russian)
11. Vorozhtsov A, Lerner M, Pavlovets G, Meleshko V, Arkhipov V, Bondarchuk S, DeLuca LT (2004) Advanced technologies of controlled manufacturing and the use of nanometals in high-energy materials (HEM) formulation. In: Proceedings of international workshop on MEMS and nanotechnology integration (MNI): applications, Montreaux, pp 84–85, 10–11 May 2004
12. Burtsev VA, Kalinin NV, Luchinsky AV (1990) Electric explosion and its application in electrophysics devices. Energoatomizdat, Moscow. 228 pp. (in Russian)
13. Arkhipov VA, Bondarchuk SS, Korotkikh AG, Lerner MI (2006) Production technology and dispersion parameters of aluminium nano-powders. Tsvetnie metalli 4:58–64 (in Russian)
14. Sakovich GV, Arkhipov VA, Vorozhtsov AB, Bondarchuk SS, Pevchenko BV (2010) Investigation of combustion of HEM with aluminum nanopowders. Nanotechnologies in Russia 5(1–2):91–107
15. Kouzov PA (1971) Foundation for analysis of dispersity of industry dust and disintegrated materials. Khimiya, Leningrad. 280 pp. (in Russian)

16. Fuks NA (1955) Aerosoles mechanics. Edit. AS USSR Academy of Sciences, Moscow. 352 pp. (in Russian)
17. Arkhipov VA, Bondarchuk SS (1989) Formulations for connection of parameters of particles unimodal distributions in sizes with geometrical characteristics of probability density function, Mechanics of Fast Processes. Edit. TSU Tomsk State University, Tomsk, pp 83–92
18. Arkhipov VA, Bondarchuk SS, Kvesko NG, Trofimov VF (2004) Identification of particles unimodal distributions in sizes. Atmos Ocean Opt 17(5–6):513–516
19. Lerner MI, Saveliev GG, Svarovskaya NV, Galanov AI (2006) Low temperature sintering of electroexplosion nanopowders. Izv Tomsk Polytechn Univ 309(4):69–73. (in Russian)
20. Sossi A, Duranti E, Manzoni M, Paravan C, DeLuca LT, Vorozhtsov AB, Lerner MI, Rodkevich NG, Gromov AA, Savin N (2013) Combustion of HTPB-based solid fuels loaded with coated nanoaluminum. Combustion Science and Technology 185(1):17–36
21. Sossi A, Duranti E, Paravan C, DeLuca LT, Vorozhtsov AB, Gromov AA, Pautova YI, Lerner MI, Rodkevich NG (2013) Non-isothermal oxidation of aluminum nanopowder coated by hydrocarbons and fluorohydrocarbons. Applied Surface Science 271:337–343
22. Vorozhtsov A, Gromov A, Lerner M, Rodkevich N (2010) Characterization and analysis of aluminum nanoparticles passivated with organic layers for energetic applications. Energetic materials for high performance, insensitive munitions and zero pollution: 41 international annual conference of ICT – Karlsruhe, Germany. – June 29 – July 02, 2010. – Karlsruhe, Germany: Fraunhofer ICT. pp 1–10 (90474673)
23. Manelis GB, Nazin GM, Rubtsov YI, Strupin VA (1996) Thermal decomposition and combustion of explosives and gunpowders. Nauka, Moscow. 223 p. (in Russian)
24. Kubota N (2007) Propellants and explosives: thermochemical aspects of combustion. WILEY-VCH Verlag GmbH & Co, Weinheim. 509 p
25. Toroptseva AM, Belogorodskaya KV, Bondarenko VM (1972) Laboratornyj praktikum po khimii i technologii vysokomolekulyarnyh soedinenij (Laboratory course of chemistry and technology of macromolecular compounds). Khimia, Leningrad. 416 p. (in Russian)
26. Merzhanov AG, Mukasyan AS (2007) Solid flame combustion. Torus Press, Moscow. 336 p. (in Russian)
27. Varma A, Rogachev AS, Mukasyan AS, Hwang S (1998) Combustion synthesis of advanced materials: principles and applications. Adv Chem Eng 24:79–226

Combustion Behavior of Aluminum Particles in ADN/GAP Composite Propellants

Volker Weiser, Andrea Franzin, Luigi T. DeLuca, Sebastian Fischer, Volker Gettwert, Stefan Kelzenberg, Sebastian Knapp, Angelika Raab, Evelin Roth, and Norbert Eisenreich

Abstract Propellants containing ADN/GAP are regarded as a promising green alternative to AP/HTPB solid rocket propellants because of avoiding chloric acid emission. The addition of aluminum powder is a classical approach to increase the theoretical specific impulse of composite propellants. The optimum aluminum content is in the range of 16–18 % Al. But propellant formulations with ADN, a chlorine-free oxidizer, and GAP, an energetic binder, generate no chloric acid but more nitrogen on combustion achieving similar performance. Significantly different thermal and chemical conditions occur to the aluminum particles close to the burning surface. This study investigates the combustion behavior of aluminum particles in an ADN/GAP matrix in comparison to AP/HTPB at various pressures up to 15 MPa. The agglomeration of Al particles at the surface and burning behavior of aluminized AP/HTPB propellants has already been investigated and is extended to the ADN/GAP propellants. The temperature measurements close to the propellant surface indicate higher values near the Al boiling point that accelerates the melting of Al particles and influences the agglomeration process. At higher pressure the temperatures are in the magnitude of Al_2O_3 evaporation and decomposition close to 3000 K.

V. Weiser (✉) • S. Fischer • V. Gettwert • S. Kelzenberg • S. Knapp • A. Raab • E. Roth
N. Eisenreich
Fraunhofer-Institut für Chemische Technologie (ICT), Energetic Systems, 76327 Pfinztal, Germany
e-mail: volker.weiser@ict.fraunhofer.de

A. Franzin
Fraunhofer-Institut für Chemische Technologie (ICT), Energetic Systems, 76327 Pfinztal, Germany

Space Propulsion Laboratory (SPLab), Department of Aerospace Science and Technology, Politecnico di Milano, 20156 Milan, Italy

L.T. DeLuca
Space Propulsion Laboratory (SPLab), Department of Aerospace Science and Technology, Politecnico di Milano, 20156 Milan, Italy

1 Introduction

The growing public awareness towards the environment problem, which has driven the last decades of aeronautical research to find a "green fuel," could not leave out the scope of rocket propulsion. The solid propellant formulations, commonly used for space access until today, contain mostly ammonium perchlorate in combination with hydroxyl-terminated polybutadiene (AP/HTPB). One of the main combustion products is hydrogen chloride (HCl) that should be considered as critical pollution, since it contributes to acid rain and causes environmental damage and corrosion around the launch base. The boosters contain this type of solid propellants, burn in the order of tons per second, releasing large quantities of HCl, which can reach more than 20 % of the reaction products at the nozzle. Also aluminum chloride and other intermediate reaction products, which are not more than 2 %, will cause additional serious problems when the huge quantities of expelled mass are considered.

These are the main motivations to develop a new kind of green propellant that possibly will achieve better propulsive performance as well.

Ammonium dinitramide (ADN) seems to be a promising substitute to ammonium perchlorate, as shown in References [1–3], being chlorine-free. Due to its lower oxygen balance of +25.8 %, instead of +34.04 % for AP, an energetic binder is needed to compensate this handicap. The main problem of ADN is its reactivity with some polymeric binders or at least the ingredients of the polymerisation process [2]. To overcome this problem, coated ADN prills shall be used; for details see [4].

An appropriate binder is GAP (glycidyl azide polymer), an energetic polymer treated with bis-propargyl-succinate and isocyanates (Ref. [5]). Using GAP diol less oxidizer is needed and allows higher Al filler contents than HTPB to increase specific impulse.

Thermodynamic calculations of the theoretically delivered mass specific impulse under frozen equilibrium assumption are presented in Fig. 1 to compare the system ADN/GAP/Al with the established system AP/HTPB/Al. The calculations were performed using ICT-Thermodynamic Code for an expansion ratio 70:1 [6]. It is noticeable that the system ADN/GAP/Al features in a significantly higher gravimetric specific impulse with a maximum of 296 s at 59 % ADN, 20 % GAP, and 21 % Al in a wider region of aluminum content in comparison with AP/HTPB/Al (maximum 284 s at 68 % AP, 12 % HTPB and 20 % Al). Even more remarkable is the fact that the compositions with the higher specific impulses are in a region of larger binder contents of 20–30 % instead of 10–20 % for AP/HTPB/Al that will allow to produce such formulations with improved mechanical properties.

The calculations also show that the increment of specific impulse is mainly caused by about 220 K higher adiabatic combustion temperatures, since the variation in the molecular mass of combustion products, considered in the combustion chamber, features in less marked differences as already discussed in [7].

The purpose of this paper is to report investigations of the burning behavior of an ADN/Al/GAP propellant. The decomposition of ADN/GAP takes place at different thermal conditions than AP/HTPB and results in a significantly different
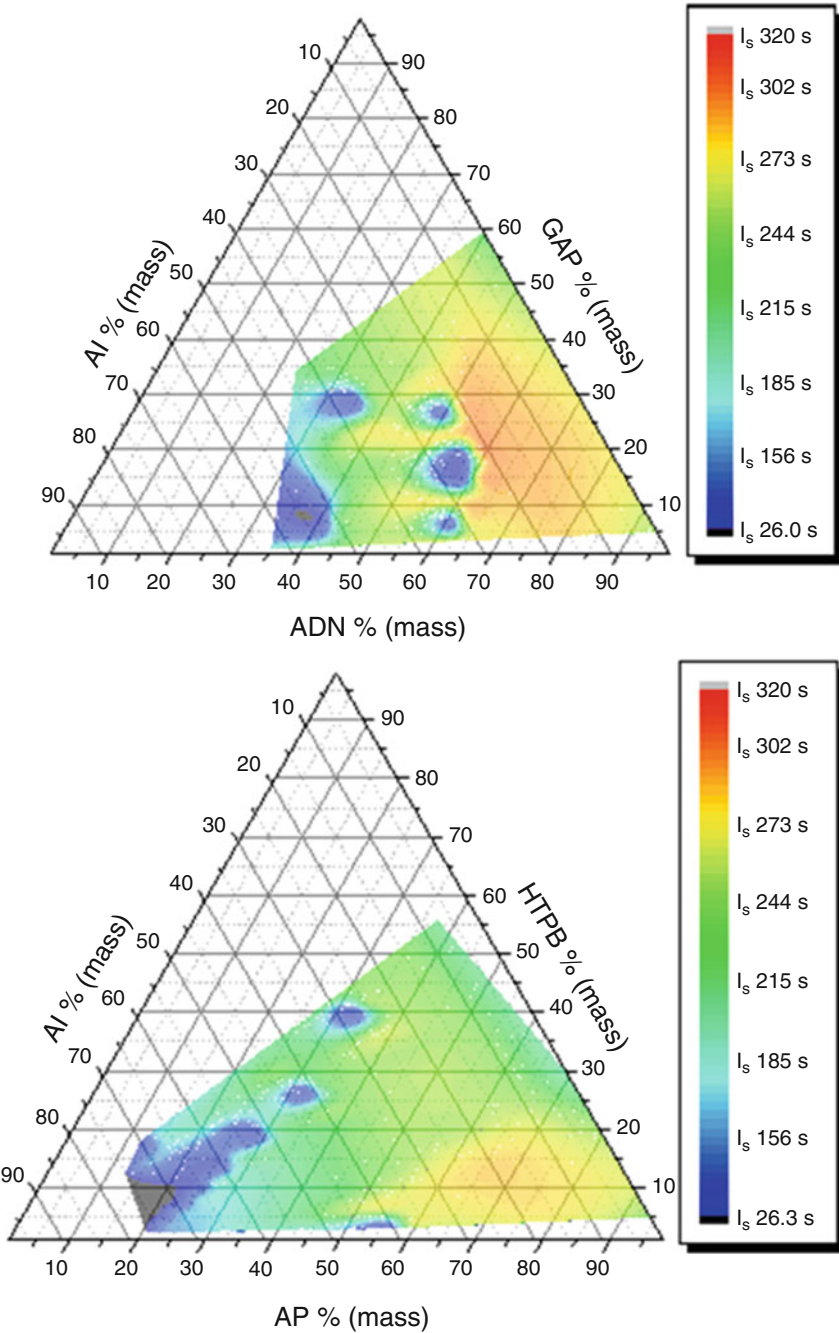
Fig. 1 Comparison between gravimetric specific impulse (frozen equilibrium) of AP/HTPB/Al formulations and ADN/GAP/Al formulations

decomposition product spectrum to oxidize aluminum particles. Based on previous work presented recently [7], this paper describes investigations of the agglomeration of Al particles on the burning surface, the resulting solid residues, the burning rates, and the temperatures depending on the pressure.

2 Experimental

2.1 Tested Formulation

A propellant formulation called H32 was prepared with the composition listed in Table 1 including aluminum particles of 18 μm. Prilled ADN was produced by an emulsion prilling method at ICT, starting from neat ADN delivered by Eurenco Bofors with a particle size distribution for ADN 208 μm of d(0.1) 122 μm, d(0.5) 208 μm and d(0.9) 349 μm and ADN 55 μm of d(0.1) 33 μm, d(0.5) 55 μm and d(0.9) 100 μm [4]. GAP diol prepolymer (Mn = 1685, MW = 1909, equivalent weight 1160 g/mol) was purchased from Eurenco (France) and the isocyanate curing agent Desmodur E305 (equivalent weight 328 g/mol) from Bayer Material Science (Germany); and the alkyne curing agent bis-propargyl-succinate (BPS, equivalent weight 97 g/mol) was synthesised from succinic acid (Merck 822260) and propargyl alcohol (Merck 807050) by ICT. The curing catalyst dibutyltin dilaurate (DBTDL) was bought from Merck Schuchardt (8.20421.0250).

A quite large amount of 16 % aluminum with a mean particle size of 18 μm was chosen to achieve an optimum value of specific impulse of 2695 Ns/kg (4676 Ns/dm^3) for 7–0.1 MPa expansion. The vacuum specific impulse is calculated to 293.7 s using ICT-Thermodynamic Code.

The ingredients were mixed in a planetary centrifugal vacuum mixer (Thinky mixer ARV-310) with 1600 cycles per minute at a pressure of 3500 Pa for 2 min. GAP diol was added into a beaker and mixed with DBTDL and aluminum, followed by ADN prills in a bimodal distribution 70:30 with an average diameter of 208 μm for the coarse prills and 55 μm for the fine prills. The mixture was cooled down to room temperature. E305 and BPS were added together to the dispersion. The mixing and casting of propellant sheets proceeded without any problems. From the sheets, propellant strands of $4 \times 4 \times 35$ mm^3 were cut for combustion tests.

A sample density of 1.641 g/cm^3 was measured using He-pycnometer method. This corresponds to a porosity of 3.70 % related to the measured densities of the individual ingredient.

Table 1 Composition of Al/ADN/GAP

ADN[a]	GAP diol	E305[b]	BPS	Al	DBTDL[c]	NCO/OH[c]
60 %	19.59 %	3.1 %	1.31 %	16 %	0.04 %	0.56

[a]Prills 208 μm and 55 μm – ICT Fraunhofer
[b]Desmodur
[c]Catalysts are not included in final formulation

2.2 Experimental Setup

The combustion behavior was investigated in the ICT window bomb under 0.1, 0.5, 1, 3, 5, 7, 10, 13, and 15 MPa nitrogen. The chimney-type pressure vessel is equipped with four windows where glasses of different types of material can be inserted, to allow spectroscopic investigations in the UV, Vis, NIR, and MIR range. Ignition was performed using a fuse wire enhanced with about 50 mg of a booster mixture. Partially an inhibitor on the lateral surfaces of the strands was used. But no significant difference in the burning rate with and without inhibitor was found.

In order to collect aluminum particles, a SEM sample holder was positioned above the strands inside the window bomb, at various distances (from 5 to 15 mm in dependence on observed flame length) from the upper surface of the strands. To preserve the sample holder from the possible contamination of the booster mixture, the strands were ignited using only the fuse wire. The particle collection was carried out at all pressure levels under investigation.

2.3 Measurement Techniques and Data Evaluation

To visualise the propellant combustion, a 24-bit color high-speed camera (Motion-ProTM X-3, Redlake) equipped with a 105 mm macro lens was used. The maximum resolution is 1280×1024 pixel. It can be used up to a recording frequency of 2000 fps. By reducing the image section, a maximum frequency of 64,000 fps is possible. The procedure reported in [8] was used to determine steady-state, linear burning rates.

To study the size and behavior of the agglomerates near the surface of the burning propellant, the video records were analysed manually picture by picture taking the sizes of all well-defined and detached particles, as explained in [9]. In combination with the optical imaging, an image resolution of about 14 μm per pixel was achieved. The pressure domain of investigation was 0.1, 1, 3, and 5 MPa.

The particles collected on the sample holders were studied using a field emission scanning electron microscope (FE-SEM, Zeiss Supra 55 VP). Elemental composition close to the surface was analyzed by energy-dispersive element analysis (EDX).

While the propellant strand is burning down, material from different flame zones is deposited in layers on the sample holder with material of the flame zone closest to the surface as the lowest layer. In order to investigate also this material, the total sample was transferred head-down to another sample holder.

NIR spectra from 1.0 to 2.2 μm were measured using an MCS 611 PGS-NIR 2.2 spectrometer from Carl Zeiss AG, Germany, equipped with an optical fiber with a temporal resolution up to 70 Hz. The spectra were calibrated using a black body radiator in intensity units versus unit wavelength. To limit the field of view of the spectrometer optics, a 2 mm slit diaphragm was fixed about 15 mm distant from the propellant strand. So a local resolution of about 2–3 mm can be estimated. Each spectrum was analyzed by ICT-BaM code that does not require absolute

spectral radiance to derive temperatures from NIR because it models spectra of gaseous reaction products, soot and continuum radiation only based on their band shapes. The evaluation procedure uses a least squares fit of calculated spectra to the measured ones. The technique is described in [10].

3 Results and Discussion

3.1 Visible Observations and Burning Rate

The propellant strands ignited and burnt steadily at all considered pressure levels. This means pressure deflagration limit (PDL) could not be measured exactly but might be less than or equal to 0.02 MPa, as experimentally realised.

Figure 2 shows pictures that are optimised to visualize hot particles by a strong reduction of exposure time and aperture. At ambient pressure, a small number of distinguishable particles with rounded shape stand on the propellant surface. Occasionally single, mainly larger, particles detach and lift off. With increasing pressure, the number of lift-off particles increases drastically, but the shape of a single particle gets more and more diffuse, and they become smaller. Above 5 MPa the glowing particle density increases to form a cloud because the length of the zone of glowing particles reduces (as is found for flames with increasing pressure). Dark vapor clouds and particles are ejected as well.

At 1 MPa the number of agglomerated particles on the surface increases compared to 0.1 MPa but seems to decrease in number and size with further increasing pressure. Simultaneously, the brightness of the particles reduces compared to the ones lifted off into the flame zone.

Evaluation of most high-speed movies with AVICOR [8] results in linear burning rates as illustrated in Fig. 3 that show regression plots. At higher pressure a coating
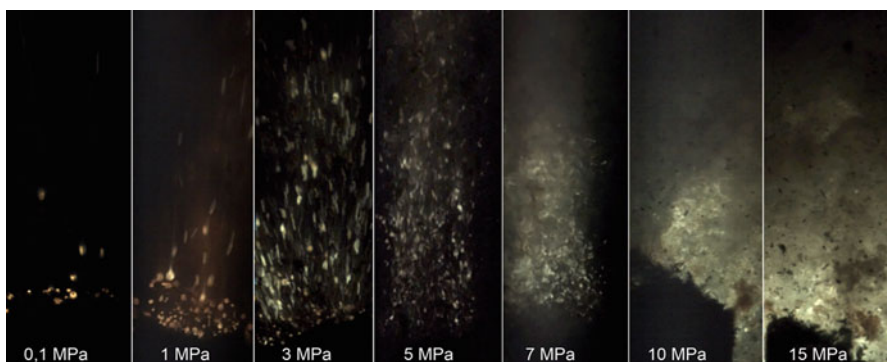

Fig. 2 Selected frames of high-speed movies taken from the combustion of the investigated propellant at various pressure levels
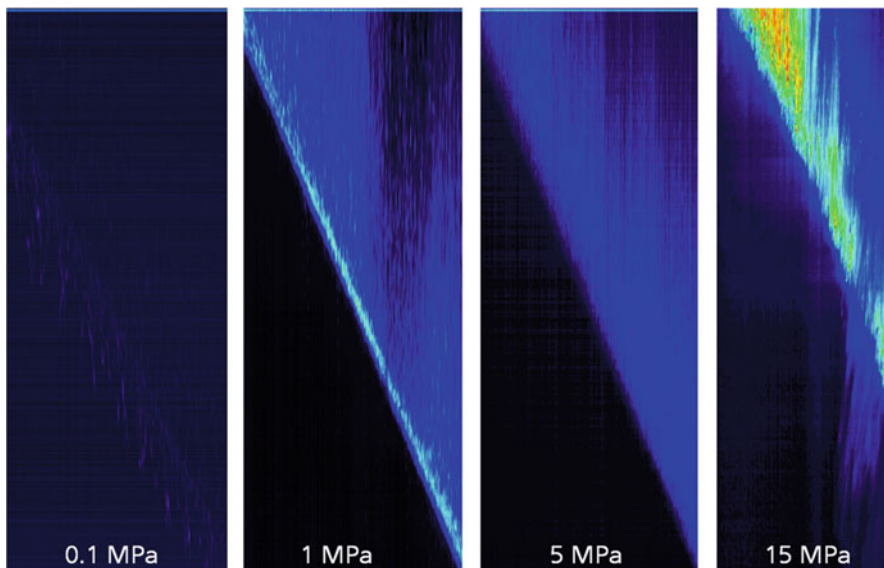
Fig. 3 Regression curves at various pressure levels

consisting of a thin layer of polyurethane was useful to decrease the number of tests failed by lateral combustion. When neglecting failed tests, no other significant differences in burning behavior were found between coated and non-coated strands.

Resulting burning rates are plotted in Fig. 4. On each pressure level 2–6 tests were performed (black dots). Burning rate at 7 MPa is 29.6 mm/s. The mean values of each pressure level can be described in good agreement using a Vieille fit (green line). Vieille fit results in a pre-exponential factor of $A = 8.82 \pm 0.02$ mm/s and a pressure exponent of $n = 0.58 \pm 0.02$ with a coefficient of determination of $R = 0.9956$. The resulting burning rates are quite high for some space applications, but seem applicable to many rocket propulsion applications.

3.2   Spectroscopic Investigations and Temperature

In the wavelength range 0.3–2.15 μm, the spectral emission is dominated by continuum radiation emitted from hot condensed materials. In NIR range water band overlaps the continuum at 1.3–1.6 μm and 1.7–2.1 μm. Additional strong lines at about 769 nm (which is formed from the two lines at 766.4 and 769.8 nm) and 1.17 and 1.25 μm indicate potassium residues in ADN. The strong potassium line is hardly to avoid in engineered propellants especially as ADN is derived from potassium dinitramide. A typical spectrum is plotted in Fig. 5. A view to Fig. 2
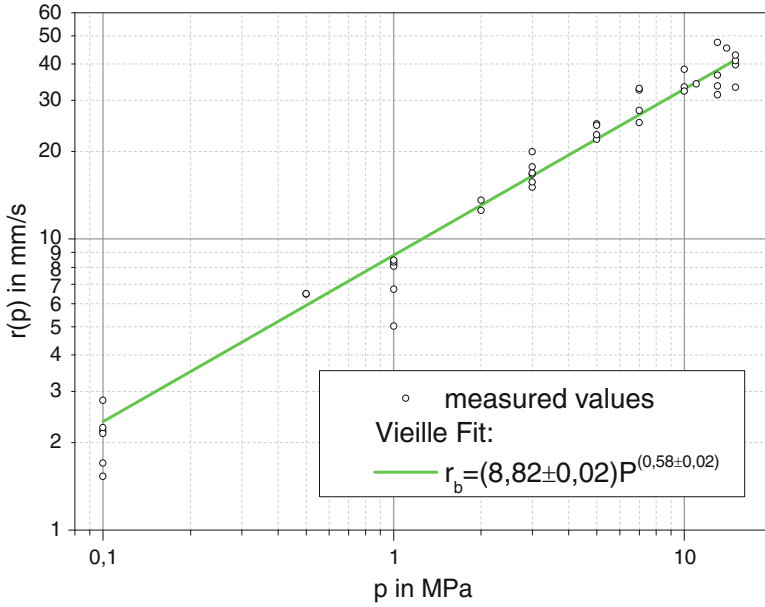
Fig. 4 Burning rate depending on pressure including Vieille analysis
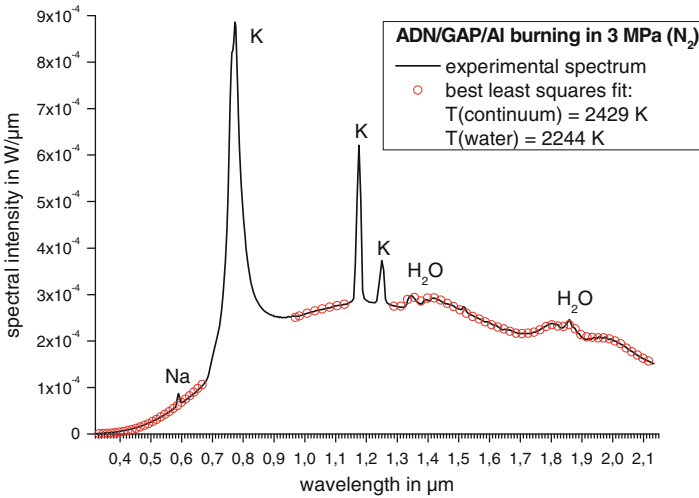

Fig. 5 Characteristic emission spectrum of investigated ADN/GAP/Al propellant including least squares fit by ICT-BaM evaluation combining a *grey* body continuum with water vapour emission with different temperatures

reveals that the reacting particles emit much brighter than the propellant surface so it is obvious that the continuum spectra can be assigned to the emission of the reacting particles. The main emission is therefore from the reacted caps (or shell) at the aluminum particles which is mainly alumina. The water bands are emitted by water vapour and represent the hot flame gases that emit independently from the particles with possibly a different temperature. Therefore an ICT-BaM analysis may evaluate different temperatures for the continuum and the water bands [10]. To calculate the continuum, grey body emission was applied. Particle clouds might tend to grey body continua because of multiple reflections in a particle cloud. It is difficult to identify detailed wavelength dependence of the continuum additional to it [11]. These evaluations by fitting a calculated spectrum (red dots) consisting of a grey body continuum overlapping with water bands assuming different temperatures to each measured one (black line) agree well when omitting the potassium lines as also shown in Fig. 5. However, in many cases the water bands were too weak to evaluate a reliable temperature. Due to the weak signal intensity, large inaccuracies of the water temperature values are expected.

The water vapor temperatures varied about 200 K around 2000 K. The measured temperatures of the hot particles can be considered as much more accurate and are mainly discussed in the following sections. Figure 6 plots the maximum temperatures measured at each test as a function of pressure (red dots). The values increase drastically from about 2000 K at environmental pressure up to values close to 3000 K at pressures above 10 MPa. Figure 6 also presents the adiabatic temperature calculated using ICT-Thermodynamic Code [6] in the same pressure range that increases from 3100 K at 0.1 MPa to 3600 K at 15 MPa (red line). This
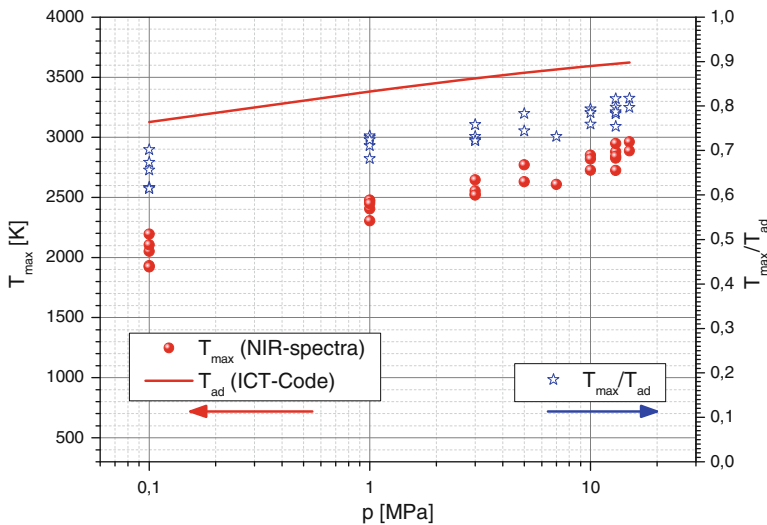

Fig. 6 Comparison of measured maximum temperature and adiabatic temperature calculated by ICT-Thermodynamic Code and their quotient as function of pressure
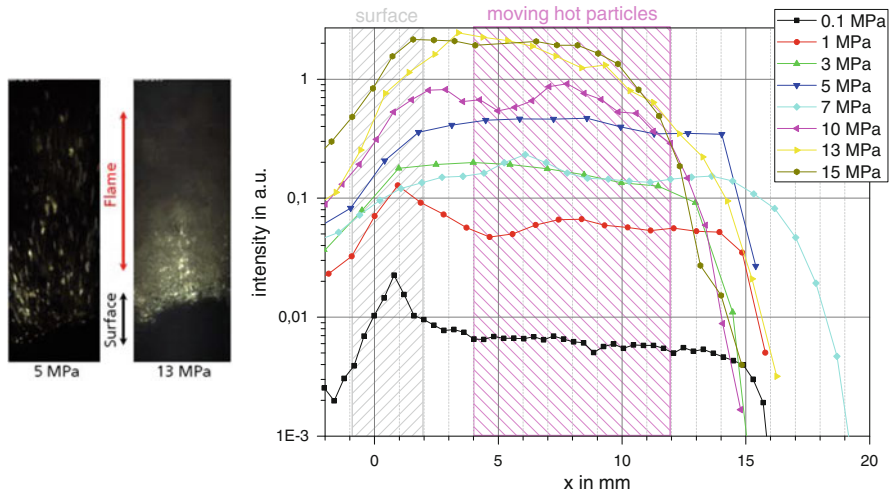
Fig. 7 Axial intensity profiles at various pressure levels

means that the values measured in the window bomb are 30–20 % lower than the theoretical ones, a result which is not unexpected [10]. Regarding the nonadiabatic conditions inside the window bomb and the relatively high absolute temperature values that cause large heat losses, this result seems very reasonable. The ratio of each measured maximum temperature T_{max} to the adiabatic temperature T_{ad} is also plotted in Fig. 6 (blue stars).

Due to the limitation of the field of view of the spectrometer optics using a slit of 2 mm, the single spectrum can be allocated to different zones along the flame. This can effectively be done using the intensity of the spectra series. According to Fig. 2, there should be a steep increase of intensity close to the propellant surface. This can be detected in the course of the integrated spectral intensity as shown in Fig. 7 (left). The profiles are converted from time t to location x scale using the individually measured burning rate r: x = r t. The resolution of the slit of less than 3 mm, as determined above, is in good agreement to the rise of the displayed intensity profiles that should be nearly a jump in reality. So only two flame zones shall be considered: (1) a zone close to the surface where agglomeration takes place and (2) the zone including the moving hot particles. These zones are sketched in Fig. 7. It is assumed that in the second zone, the detached aluminum-rich particles are oxidised by flame gases like water and carbon oxides [12].

At low pressure up to 1 MPa, a peak maximum of intensity is detected close to the surface that can be allocated to the hot particles hovering on the propellant surface. The low intensity of the flame zone may be explained by relatively few particles observed in this range (see Figs. 2 and 7 (right)). With increasing pressure, the peak close to the surface disappears and the maximum intensity is emitted by the flame zone.
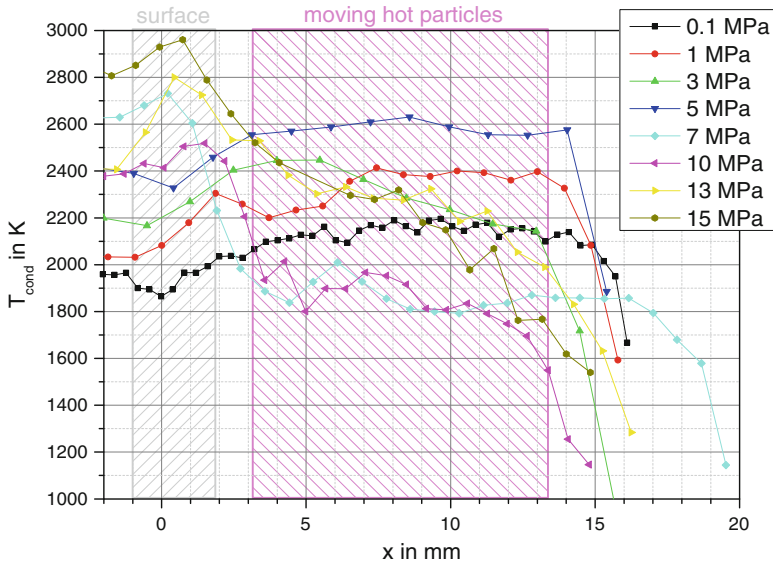
Fig. 8 Axial profiles of continuum temperatures at various pressure levels

The temperature profiles run with an opposing trend. Exemplary curves are shown in Fig. 8. At low pressure up to 5 MPa, the temperatures are lower than the temperature in the flame zone. Above 5 MPa the temperature close to the surface is distinctly higher as inside the flame zone. It is noticeable that independent of pressure, most temperature profiles end at about 15 mm above the surface. This is the position where the particles finish glowing. That means that the velocity of the reaction process increases in a way that it overcompensates the increasing gas flow caused by pressure dependence of burning rate and therefore the flame shifts toward the burning surface. The oxidation zone of the particles shifts in a similar way and produces the temperature maximum close to the surface.

Figure 9 displays the values of measured maximum temperatures in the considered regions as a function of pressure. Close to the surface, the absolute temperature increases drastically from about 1850 K at 0.1 MPa to nearly 3000 K at 15 MPa. Below 5 MPa the temperature of the flame zone is higher and increases from 2200 K at 0.1 MPa to about 2650 K at 5 MPa. Above this pressure, very low values of about 2000 K were observed that increase again above 10 MPa. This might be a result of high optical thickness with increasing particle density that only allows detecting emission from the outer cloud zone.

Fig. 9 Temperatures measured close to the surface and in the flame zone as a function of pressure
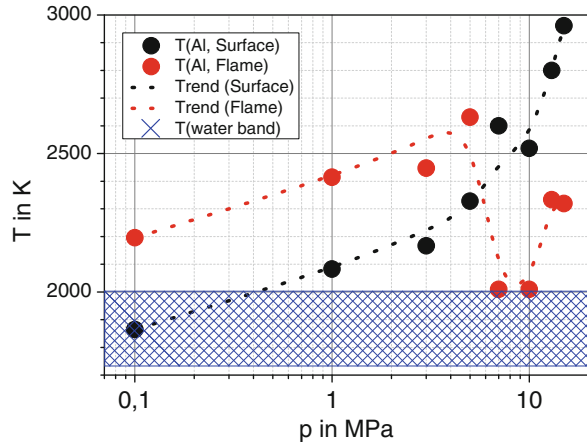
3.3 Agglomeration

Using video analysis, it was possible to measure the mean size of the visible particles at the first appearing on the propellant surface. It seems not strongly affected by pressure. The measured average diameter of this kind of particles is around 80 μm and is the same at 0.1 and 1 MPa. This value is four times larger than the original aluminum particle size in the formulation. These primary particle agglomerations drastically increase in volume before detaching the surface. Visible observations of the agglomerates show a billowing behavior that indicates liquid state of the particles.

The observed aggregation phenomena for the investigated ADN/GAP/Al formulation can be subdivided in the following five steps:

1. Pre-aggregation inside the condensed phase which results in an increase of aluminum particle diameter from 18 μm to the measured 77–78 μm in average.
2. Rising of the pre-aggregated particles on the burning surface and possibly first ignition.
3. Local aggregation with nearest or underlying particles and completion of the transition between aggregates and agglomerates, presenting the well-known oxide cap
4. Rolling of the particles on the burning surface which can result in further aggregation with other rolling particles, but often no aggregation could be observed because of growing volume.
5. When the particles reach a certain diameter, they detach from the burning surface. In many cases the increase of diameter comes along with an increase of brightness that indicates rising temperature. Especially with increasing pressure, some agglomerates are also bloating and seem to boil.

In all observed mixtures, sometimes emerged particles disappear again into pores of the burning strand.

The agglomerates that result from the process of aggregation/agglomeration do not differ so much from the ones observed in AP/HTPB/Al, in fact they seem to be mostly round presenting the same cap of oxide (with some minor exceptions) typical for AP/HTPB/Al propellants (Ref. [13]). After liftoff they show the same turning movement passing the flame zone in a straight line.

The agglomeration size of detaching particles features a quite narrow distribution of diameters with a maximum decreasing with pressure (Fig. 10). In general nearly 2000 particles were metered per histogram. They could be described satisfactorily using a normal distribution for parametric characterisation.

The mean diameters of the analysed detached agglomerates are summarised in Fig. 11 for the investigated sample H32. The agglomerates grow by one order of magnitude with respect to the original size of 18 μm of the aluminum particles. The values decrease from about 265 μm at ambient pressure to less than 150 μm at 5 MPa. This trend is in a good agreement with findings in [14, 15] for the system AP/Al/HTPB.

The sample H32 contains a bimodal size distribution of ADN prills with mean diameters of 208 and 55 μm. In Fig. 11 further results of ADN/Al/GAP formulations with the same composition but with different ADN prill sizes were included [7]. Sample D contains smaller aluminum particles of 5 μm.

As reported in [7] and confirmed by some further investigations of the propellant D and G presented in Fig. 11, the initial dimension of aluminum particles seems not to affect the agglomerate diameter.

The dimension of ADN oxidiser affects the size of agglomerates more significantly. This is also in accordance with observations made for AP/Al/HTPB propellants in [16, 17]. Like depicted in Fig. 11, the biggest ADN prills (H27) correspond to the largest mean size of agglomerates. Although these prills are only 10 % larger (20 μm), the agglomerates are nearly twice as large as those of sample G. Except for 0.1 MPa, the bimodal distribution gives rise at agglomerates which are in between the two monomodal mixtures investigated.

3.4 SEM/EDX Analysis of Collected Particles

Figure 12 presents a selection of SEM images of collected residual particles at different pressures and magnification factors.

Most particles are round. Some especially large particles still feature in an oxide cap that indicates an incomplete combustion (Fig. 12a). This is confirmed by EDX analysis with high aluminum-to-oxygen ratios inside the smaller cap. In general, the ratio of O/Al increases significantly with increasing pressure indicating a more complete oxidation. Some EDX analyses, especially taken at 7 MPa and higher, result in additional contents of nitrogen of 10–20 mol%. In many cases these are accompanied by carbon in the same order of magnitude. It is not clear if the nitrogen
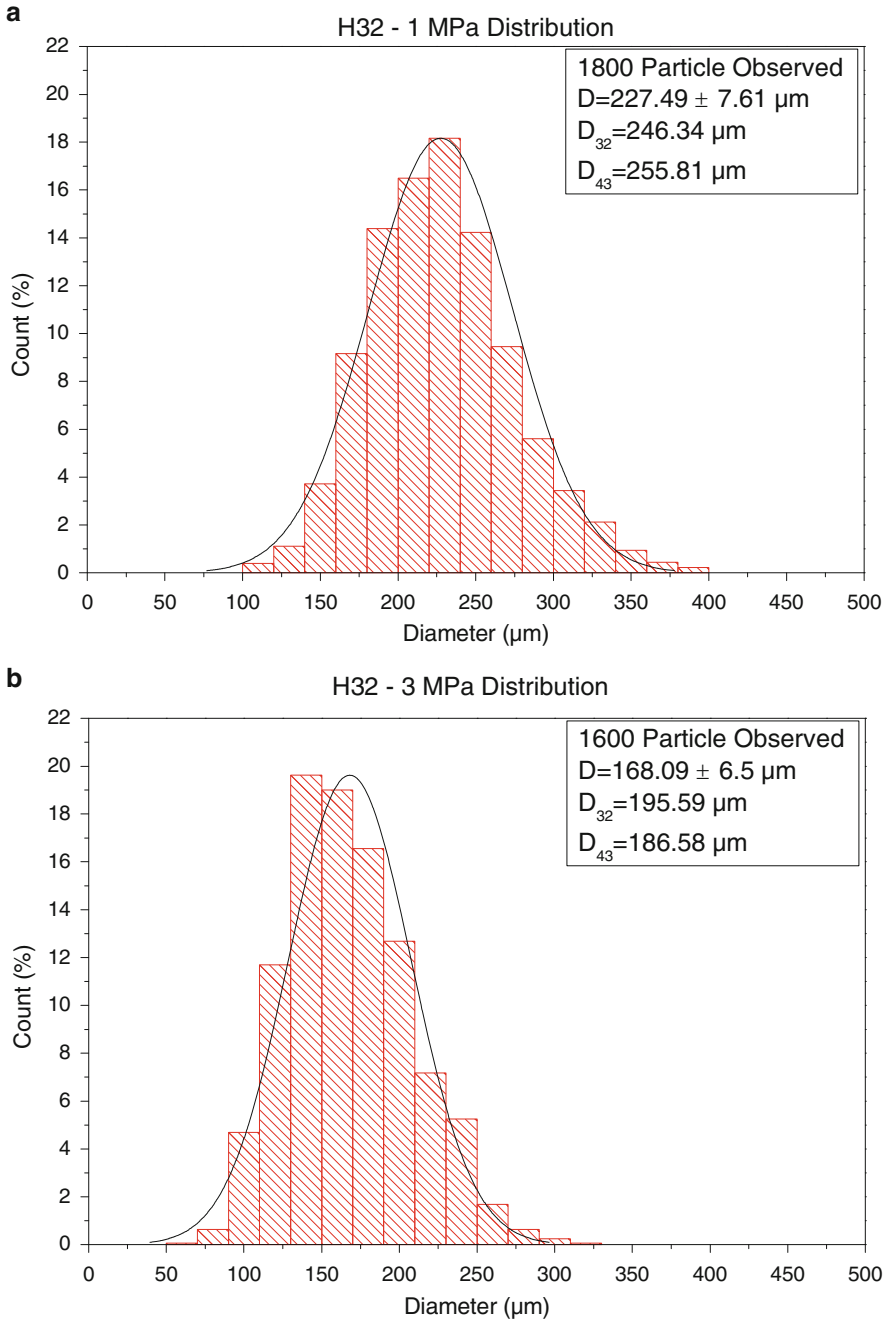
a

b

Fig. 10 Histogram of mean diameter for the propellant H32 at (**a**) 1 MPa and (**b**) 3 MPa
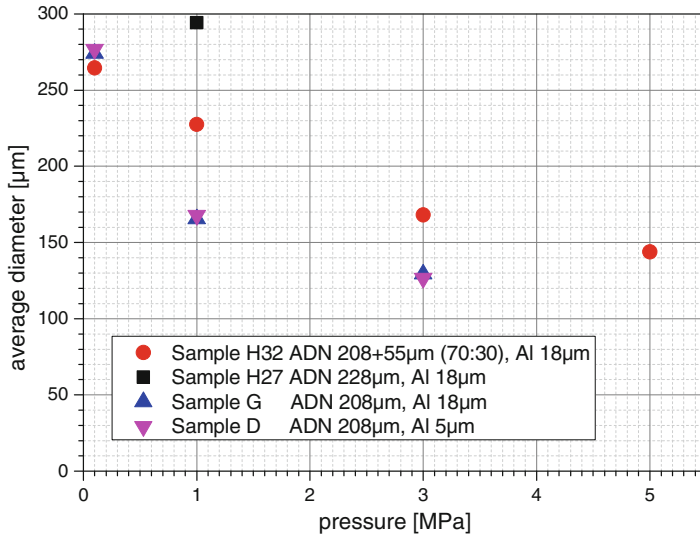
Fig. 11 Mean diameters of agglomerates for different prill sizes of oxidiser

is caused by the components of the formulation (ADN, GAP) or by the reaction with the pressure gas. In the future these investigations will be repeated under argon. But carbon can only be introduced from the GAP binder.

At low pressure 0.1 MPa, many particles with dimensions around 10 μm were found (Fig. 12b). This is in contrast to the agglomeration analysis in Fig. 11. These particles are completely spherical and feature high oxygen content that indicates pure alumina proven by EDX analysis. Maybe small aluminum particles oxidise completely below or at the surface at lower temperatures and are not visible as glowing agglomerates in the movie images. At 0.1 MPa also nanostructures of fluffy material could be observed (Fig. 12). With increasing pressure these structures disappear.

At higher pressure the collected particles consist in spherical sub-particles that look like sintered together to larger aggregates (Fig. 12g, h). This clearly indicates less viscosity probably due to higher temperatures when clashing together.

Most particles collected at all pressure levels show holes, which look like pores formed by gas released from the particle. Also the particles removed from the sample holder's surface feature in a high number of small frozen bubbles inside (Fig. 12d, e). In some cases also broken hollow spheres were found with only a thin oxide shell (Fig. 12f). This is in accordance to observations of Babuk who also found agglomerates including gaseous enclosures for AP/HTPB/Al propellants [18].
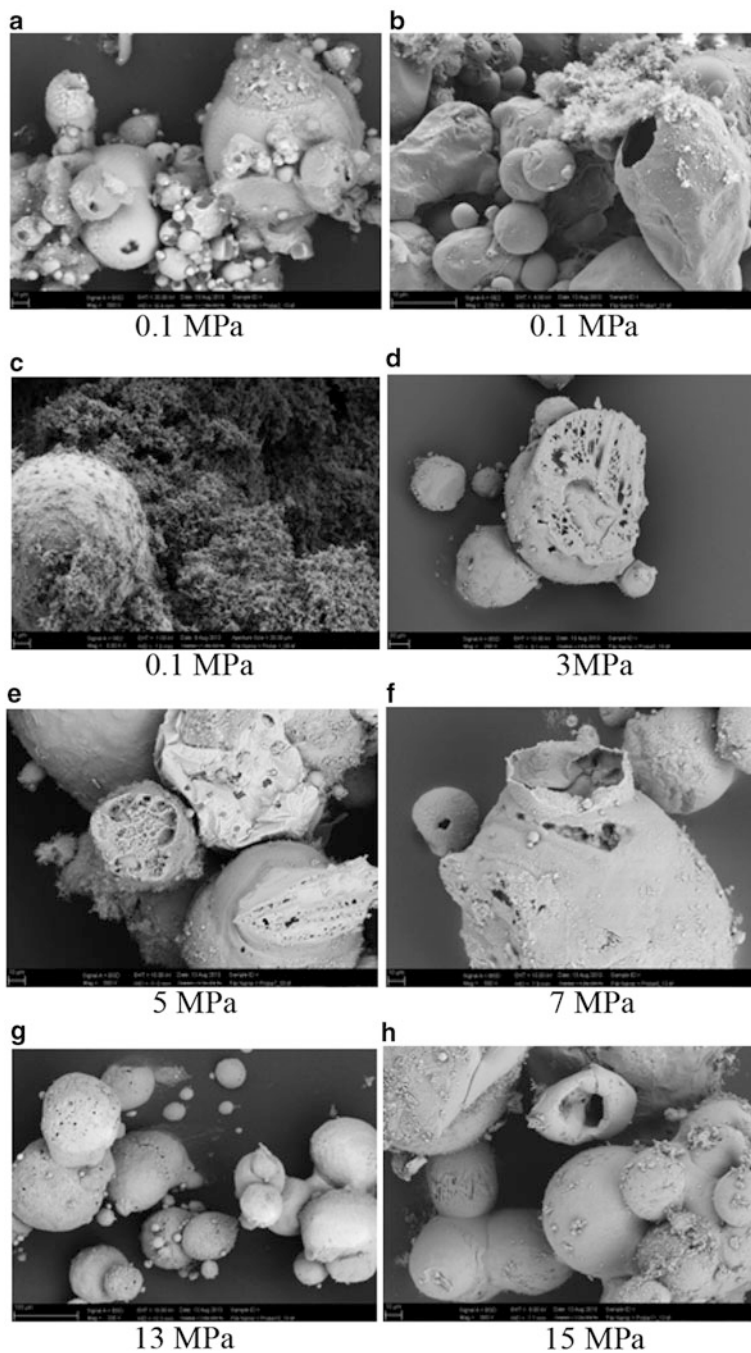
Fig. 12 SEM images of collected products taken at different pressure. (**a**) 0.1 MPa (**b**) 0.1 MPa (**c**) 0.1 MPa (**d**) 3MPa (**e**) 5 MPa (**f**) 7 MPa (**g**) 13 MPa (**h**) 15 MPa

4 Conclusion

The combustion behavior of a formulation including ADN/GAP filled with 16 % aluminum was characterised with a distinct focus on the behavior of agglomerating and reacting aluminum. The propellant features in a pressure-depending burning rate obeying the Vieille's law with a pressure exponent of 0.58 and an A-factor of 8.82 mm/s that is quite high for many applications in space propulsion. Further efforts are necessary to reduce the absolute burning rate. Depending on pressure, very high temperatures up to 3000 K were determined. The agglomeration of reacting aluminum particles behaves similar to the much better investigated system of AP/HTPB/Al. The agglomeration size is mainly influenced by the oxidiser particle size and decreases with increasing pressure. This correlates well with increasing temperatures of the agglomerates close to the surface. The agglomerates do not lift off before reaching a certain size. This contradicts to the physical experience that smaller particles are easier carried as larger ones by a gas flow of a certain velocity and can only be explained assuming a decreasing density during the agglomeration process accompanied by particle oxidation from pyrolysing gases of decomposing ADN/GAP. But the density of pure aluminum of 2.7 g/cm^3 is lower than that of oxidised alumina (Al$_2$O$_3$: 3.94 g/cm^3). So a decreasing density during the oxidation process can only be explained assuming gas enclosures inside the agglomerates like found in the residual particles collected from the flame zone.

Aluminum has a melting point of 934 K and boils at 2743 K at standard pressure. The melting point of alumina (Al$_2$O$_3$) is 2345 K and at about 3250 K it boils and decomposes. The measured temperatures of agglomerates on the surface are in the magnitude of boiling aluminum and could be one explanation of gas bubbles inside the particles by aluminum vapour. But also the internal formation of gaseous AlO should be considered.

These phenomena will be the focus of further investigations.

References

1. Larsson A, Wingborg N (2011) Green propellants based on ammonium dinitramide (ADN). In: Jason Hall (ed) Advances in spacecraft technologies. InTech, Rijeka, Croatia
2. Menke K, Heintz T, Schweikert W, Keicher T, Krause H (2009) Formulation and properties of ADN/GAP propellants. Propellants Explos Pyrotechnics 34:218–230
3. Weiser V, Eisenreich N, Baier A, Eckl W (1999) Burning behaviour of ADN formulations. Propellants Explos Pyrotechnics 24:163–167
4. Heintz T, Pontius H, Aniol J, Birke C, Leisinger K, Reinhard W (2009) Ammonium dinitramide (ADN) – prilling, coating, and characterization. Propellants Explos Pyrotechnics 34:231–238
5. Keicher T, Kuglstatter W, Eisele S, Wetzel T, Krause H (2009) Isocyanate-free curing of glycidyl azide polymer (GAP) with bis-propargyl-succinate (II). Propellants Explos Pyrotechnics 34:210–217

6. Volk F, Bathelt H (1998) User's manual for the ICT-thermodynamic code, vol 1, Bericht 14/88. Fraunhofer-ICT, Pfinztal
7. Weiser V, Franzin A, Gettwert V, DeLuca LT (2013) Combustion of metallised ADN/GAP solid rocket propellants with focus on agglomeration effects. In: 5 EuCASS-Propulsion Physics, Munich, 01–05 July 2013
8. Weiser V, Ebeling H, Weindel M, Eckl W, Klahn T (2004) Non-intrusive burning rate measurement under pressure by evaluation of video data. In: 35th international annual conference of ICT, 29 Jun–2 Jul 2004, Karlsruhe, pp 158-(1-6)
9. DeLuca LT, Galfetti L, Maggi F, Colombo G, Reina A, Dossi S, Consonni D, Brambilla M (2012) Inovative metallized formulation for solid or hybrid rocket propulsion. Chin J Energetic Mater 20(4):465–474
10. Weiser V, Eisenreich N (2005) Fast emission spectroscopy for a better understanding of pyrotechnic combustion behaviour. Propellants Explos Pyrotechnics 30:67
11. Lynch P, Krier H, Glumac N (2010) Emissivity of aluminum-oxide particle clouds: application to pyrometry of explosive fireballs. J Thermophys Heat Transf 24(2):301–308
12. Beckstead MW (2004) A summary of aluminum combustion; NATO Report RTO-EN-023; NATO Research & Technology Organization: Neuilly-sur-Seine, France
13. Babuk VA, Vasilyev VA, Malakhov MS (1999) Condensed combustion products at the burning surface of aluminized solid propellant. J Propuls Power 15(6):783–793
14. DeLuca LT, Marchesi E, Spreafico M, Reina A, Maggi F, Rossettini L, Bandera A, Colombo G, Kosowski BM (2010) Aggregation versus agglomeration in metallized solid propellants. J Energetic Mater Chem Propuls 9(1):91–105
15. Sambamurthi JK, Price EW, Sigman RK (1983) Aluminium agglomeration in solid-propellant combustion. AIAA J 22(8):1132–1138
16. DeLuca LT (2007) Burning of aluminazed solid rocket propellants: from micrometric to nanometric fuel size, vol VI, Theory and practice of energetic materials. IASPEP, Xi'an
17. Cohen NS (1983) A pocket model for aluminium agglomeration in composite propellants. AIAA J 21(5):720–725
18. Babuk VA, Dolotkazin IN, Glebov AA (2005) Burning mechanism of aluminized solid rocket propellants based on energetic binders. Propellant Explos Pyrotechnics 30(4):281–290

Laser Ignition of Different Aluminum Nanopowders for Solid Rocket Propulsion

Fengqi Zhao, Ergang Yao, Siyu Xu, Huixiang Xu, and Haixia Hao

Abstract Aluminum nanopowders (nAl) coated with oleic acid (nAl@OA), perfluorotetradecanoic acid (nAl@PA) and nickel acetylacetonate (nAl@NA) were prepared. The ignition and combustion characteristics of different aluminum nanopowders were studied using the laser ignition system. And the combustion characteristics of hydroxyl-terminated polybutadiene (HTPB)-based composite solid propellants containing different coated aluminum nanopowders were also investigated. The results show that there is a critical power of laser heat flux density in the ignition process of the coated aluminum nanopowders. The ignition delay time of nAl@NA is shorter than that of nAl@PA and nAl@OA, because of the combustion catalysis of nickel acetylacetonate. The burning rate of the propellant sample containing nAl@NA is the highest among all the formulations at different pressure ranges, and the maximum burning rate is up to 26.13 mm·s^{-1} at 15 MPa. The burning rates of propellant samples containing nAl@OA and nAl@PA are almost the same at different pressures and higher than that of the propellant samples containing untreated aluminum nanopowders only at the pressure range of 10–15 MPa. The flame intensity of different propellants at different pressure is not the same. Moreover, the surface coated aluminum nanopowder has a little effect on the combustion flame temperature of solid propellant. The burning surface temperature of propellant increases with an increase in pressure.

1 Introduction

Aluminum nanopowders (nAl) have attracted much interest over the years as reactive additives in explosives [1–3] and propellants [4–7] as well as components of nanocomposite thermite materials [8–10], mostly because of the faster energy release compared to microsized aluminum powders [1]. Hydroxyl-terminated polybutadiene (HTPB)-based composite propellants are widely used for its excellent burning characteristics and good processability and storability. The replacement of

F. Zhao (✉) • E. Yao • S. Xu • H. Xu • H. Hao
Xi'an Modern Chemistry Research Institute, Xi'an 710065, Shaanxi, China
e-mail: zhaofqi@163.com; yaoerg@126.com; xuxy99@163.com; xhx204@163.com;
haohx99@163.com

microsized by aluminum nanopowders in HTTB composite solid propellants is expected to improve the burning rate, reduce pressure exponent, increase specific impulse, reduce nozzle two-phase flow losses, and decrease ignition delay time [11]. Baschung et al. [6] showed that the burning rate of HTPB-based solid fuels can be increased by 70 % with the addition of 20 % mass fraction of nAl. It has been demonstrated by Ivanov et al. [12] that propellants containing nAl exhibit much greater burning rates than the propellants containing regular aluminum powders. In some cases, the burning rate of the propellant with Alex was as much as from 5 to 20 times greater. In addition, ammonium perchlorate (AP)-based propellants containing Alex have been shown to burn cleanly with essentially no residuals, as opposed to a significant amount of condensed-phase particulate and surface residues for AP-based propellants with regular aluminum.

In spite of many benefits associated with the usage of aluminum nanopowders described above, there are significant challenges when moving to the nanoscale. The aluminum nanopowders also suffer from serious drawbacks. Aluminum particles exposed to air undergo rapid aging to produce a 2–6-nm-thick oxide shell [13]. For microsized aluminum particles, this oxide shell may account for <0.5 % of the particle mass, but for aluminum nanopowders with diameters <20 nm, the oxide layer can account for >70 % of the particle mass. For the aluminum nanopowders, this oxide layer results in a much lower energy density. In addition, thicker oxide layers in the particles result in elevated temperatures for ignition [14–16].

Another obstacle associated with the use of aluminum nanopowders is its processability. Processing difficulties are experienced with aluminum nanopowders because of its extremely high specific surface area. The binder is simply, in some cases, incapable of wetting all of the solids. The result can be a crumbly, fragile material unsuitable for use [17]. The aluminum nanopowders also can react more readily with some energetic components, such as RDX [18], and gas products. This minor incompatibility can cause problems in mixes kept in long-term storage. Finally, their electrostatic discharge sensitivity (ESD), and that of mixtures containing the powders, is much higher than that of microsized powders [19].

One way to solve these problems is to coat the nanoparticles with a protective layer of material [20]. Cliff et al. [21] demonstrated that Alex nanopowders coated with palmitic acid decreased the sensitivity of the aluminum powders to humid conditions and slowed down the aging of the powders seriously. Kwon et al. [22] showed that electro-exploded aluminum nanopowders coated with liquids – nitrocellulose (NC), oleic acid ($C_{17}H_{33}COOH$), stearic acid ($C_{17}H_{35}COOH$), and fluoropolymer – can increase the stability to oxidation in air during the storage period and higher reactivity by heating. Jouet et al. [23] also studied the aluminum nanopowders coated with perfluoroalkyl carboxylic acids. It showed that the coating technique appears to prevent the oxidation of the particles in air. Foley et al. [24] found that aluminum nanoparticles capped by transition metal contain less

aluminum oxide than that of aluminum sample not treated with a transition metal when exposure to air at ambient conditions and the nickel-treated sample contained as much or more metallic aluminum as the untreated aluminum sample.

At present, there are few reports on the combustion characteristics of aluminum nanopowders coated with different materials and composite solid propellants containing different coated aluminum nanopowders. Therefore, the objective of this research is to investigate the effect of the coated aluminum nanopowders on the ignition and combustion characteristics of composite solid propellants.

2   Experimental

2.1   Preparation of Coated with Oleic Acid (nAl@OA)

1. A certain amount of aluminum nanopowder ($\sim$50 nm) stored under Ar was added to n-hexane in a nitrogen atmosphere; the solution was then subjected to ultrasonic dispersion for 30 min.
2. A hexane solution containing oleic acid (10 %) was introduced to the abovementioned n-hexane–Al solution, and another 10 min of ultrasonic dispersion was conducted on the solution.
3. The solution was stirred at 60 °C for 12 h in nitrogen atmosphere using a water bath; after that, the solid residues were dried in a vacuum drying oven and grounded using agate mortar to get the aluminum nanopowders coated with oleic acid (nAl@OA).

2.2   Aluminum Nanopowders Coated with Perfluorotetradecanoic Acid (nAl@PA)

1. A certain amount of aluminum nanopowder ($\sim$50 nm) was added to anhydrous diethyl ether in a nitrogen atmosphere; the solution was then subjected to ultrasonic dispersion for 30 min.
2. A Et_2O solution containing perfluorotetradecanoic acid (10 %) was introduced to the abovementioned Et_2O-Al solution, and another 10 min of ultrasonic dispersion was conducted on the solution.
3. The solution was stirred at 60 °C for 12 h in nitrogen atmosphere using a water bath; after that, the solid residues were dried in a vacuum drying oven and grounded using agate mortar to get the aluminum nanopowders coated with perfluorotetradecanoic acid (nAl@PA).

2.3   Aluminum Nanopowders Coated with Nickel Acetylacetonate (nAl@NA)

1. 0.5 g of nickel acetylacetonate was added to 30 ml of glycol dimethyl ether and then stirred to generate a homogeneous solution. After that, the solution was moved to a dropping funnel.
2. In a nitrogen atmosphere, 1.0 g of aluminum nanopowder ($\sim$50 nm) was added to a three-neck flask to mix with 30 mL of ethylene glycol dimethyl ether. Thirty minutes of ultrasonic dispersion was then conducted on the solution to disperse aluminum nanopowder evenly in ethylene glycol dimethyl ether.
3. Upon electromagnetic stirring, the ethylene glycol dimethyl ether–nickel acetylacetonate solution was added slowly to the aluminum–ethylene glycol dimethyl ether solution. During the operation, the temperature was kept at 60 °C and the solution was stirred for 12 h at 60 °C after that.
4. Afterward, the liquid solution was cooled at room temperature and dried in a vacuum drying oven. Finally, the aluminum nanopowders coated with nickel acetylacetonate (nAl@NA) were prepared.

2.4   Preparation of Composite Solid Propellant Samples

The tested propellant compositions are shown in Table 1. A solid propellant formulation containing 70 % of AP, 15 % of Al and 10 % of HTPB, and 4 % of DOA (di-octyl adipate) is prepared by vacuum casting technique. Cross-linking agent, process aids, and burn rate modifiers are introduced in a small percentage (1.0 %) to meet the ballistic requirements [25]. Each propellant is based on a bimodal AP size distribution: coarse particles (68 %) with the average diameter of $\sim$105 µm and fine particles (32 %) with the average diameter of $\sim$13 µm. The average diameter of micronmeter aluminum (mAl) is about 5 µm.

The HTPB composite propellant samples were prepared by mixing thoroughly the ingredients (list in Table 1) in a 2 L vertical kneader. The air bubbles trapped in the propellant slurry while mixing was removed by degassing in a vacuum casting chamber. The slurry was casted into aluminum plates having dimensions about $3 \times 4 \times 15$ cm and then cured in an oven maintained at 70 °C for 7 days.

Table 1   Compositions of HTPB composite solid propellants

No.	Coating materials	HTPB/%	AP/%	mAl/%	nAl/%	Others/%
11HT-0	–	10	70	15	0	5
11HT-1	–	10	70	5	10	5
11HT-2	Oleic acid	10	70	5	10	5
11HT-3	Perfluorotetradecanoic acid	10	70	5	10	5
11HT-4	Nickel acetylacetonate	10	70	5	10	5

2.5 Characterizations

The morphology of the sample was characterized by a FEI Quanta 600 field – emission environment scanning electron microscope (SEM). The composition of the sample was roughly examined by using an OXFORD INCA Penta FET ×3 energy-dispersive X-ray spectroscopy (EDS) attached with SEM. The XRD analysis was conducted on a Rigaku D/Max – 2400 diffractometer with Cu Kα radiation (0.15406 nm). A scanning rate of 4°/min and a step length of 0.02° were adopted. Vibrational characteristics were examined using a Bruker Tensor 27 FTIR spectrometer. The test samples were prepared by cold pressuring mixtures of the powder samples and KBr to form a pellet. The transmission mode was adopted with a resolution of 4 cm^{-1}, the tests were conducted in the wave number range of 4000–400 cm^{-1}, and 32 scans were made and accumulated.

2.6 Equipment Methods and Test Conditions

2.6.1 Laser Ignition Characteristics

The laser ignition characteristics were tested by the laser ignition device (shown in Fig. 1) in air. This system contains CO_2 laser, combustion chamber with two windows, and data acquisition system mainly. The maximum power of CO_2 laser is 120 W, and output wave length is 10.6 μm. The ignition delay time and ignition process can be recorded by the data acquisition system, which contains oscilloscope, computers, photoelectric sensor, and high-speed video.

2.6.2 Combustion Characteristics

Figure 2 is the schematic diagram of combustion test equipment for propellants under 1 MPa. The equipment is composed of sealed burner with four transparent windows, pressure gauge, vacuum gauge, heating device, vacuum pump, high-speed video, and igniter. The different aluminum nanopowders were encased in the paper tube with about 0.5 mm in diameter and 20 mm in length, and then the sample in the combustion was fixed. The combustion flame structure and burning time of samples can be recorded by the high-speed video.

2.6.3 Burning Rate Test Method

The steady burning rates (u) of the propellant strands were measured in N_2 at the initial temperature of 20 °C and the pressure range of 4–15 MPa. The strands were held vertically and ignited electrically with the help of a Nichrome wire at the top. The propellants were cut into samples of $5 \times 5 \times 150$ mm. A thin layer of
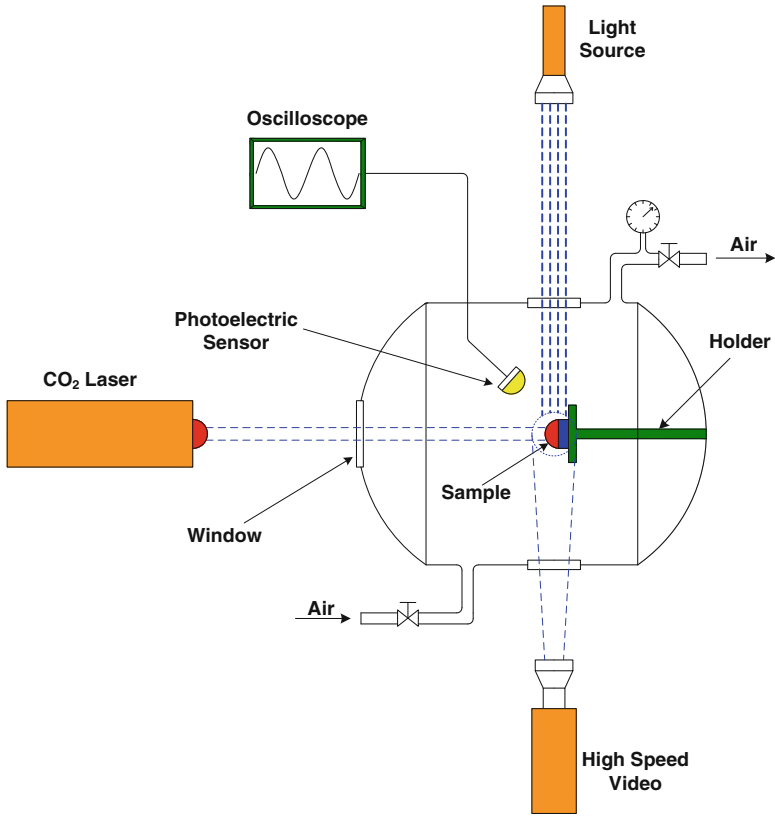
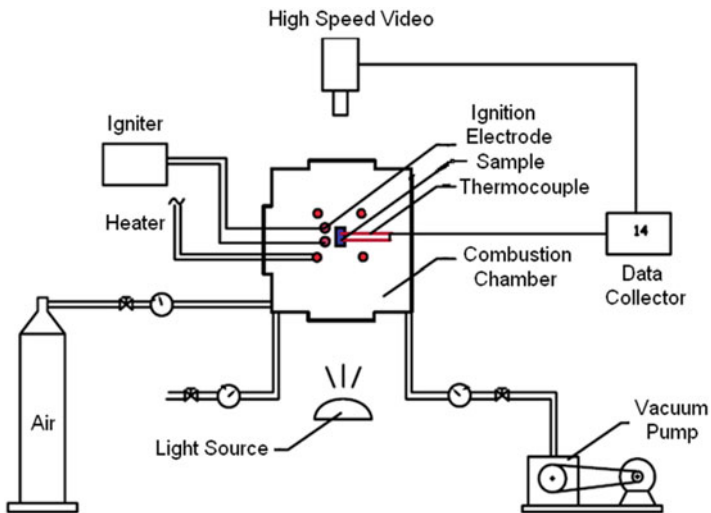**Fig. 1** Schematic diagram of laser ignition device

Fig. 2 Schematic diagram of combustion test equipment for propellants under 1 MPa

inhibitor (polyvinyl alcohol) was coated on the four-side surfaces of the samples to ensure that the burning surface area of the sample remained the same during regression.

2.6.4   Burning Flame Profiles Test Method

In order to investigate the combustion flame structure of the different HTPB propellants, the flame profiles of the different propellants under different pressures were recorded by the single frame amplification photography method. Propellant samples without any side coating were cut into $1.5 \times 4.0 \times 25.0$ mm, then placed vertically on the combustion rack vertically, and sealed in a chamber which was filled with four windows. The combustion chamber was filled with nitrogen gas to reach the objective pressures. In order to ensure the photo quality, the gas should remove immediately by forming a bottom-up flowing nitrogen atmosphere. The ignition source was 20 V DC power. The Φ 0.15 mm nickel–chromium alloy wire was used to the ignition by the process controller. The samples were ignited from the top, and then start the camera to take the flame profiles images at the appropriate time.

2.6.5   Combustion Wave Test Method

The Π type double tungsten–rhenium thermocouple was used to test the combustion wave distribution of the solid propellant. The thermocouple (diameter $= 25\ \mu$m) was embedded in the propellant sample (diameter $= 7$ mm, length $= 120$ mm) whose profile was coated by polyvinyl alcohol solvent as a flame retardant and then exposed to air for drying [26, 27].

The nickel–chromium alloy wire (diameter $= 0.15$ mm) with direct current voltage of 200 V was adopted for ignition. The automatic trigger acquisition system began to record the data output by the thermocouple after the ignition of the propellant. With the sample burning out, the thermocouple approached the burning surface gradually and finally got into the flame zone. In this way, the whole burning process of the propellant was recorded and the combustion wave structure from the condensed-phase surface to gas phase was obtained ultimately.

3   Results and Discussion

3.1   SEM-EDS Analysis

Figure 3 shows SEM images of the pure nAl, nAl@OA, nAl@PA, and nAl@NA. It could be clearly seen from Fig. 3a that the morphologies of the nAl particles
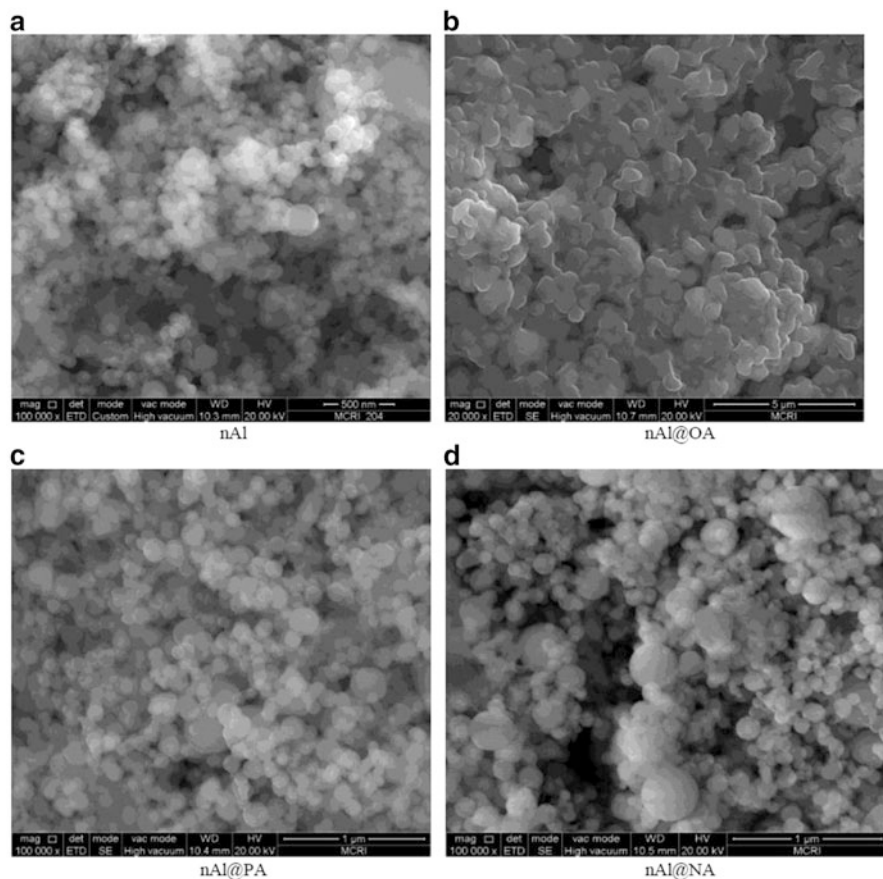
Fig. 3 SEM images of different aluminum nanopowders: (**a**) nAl, (**b**) nAl@OA, (**c**) nAl@PA, (**d**) nAl@NA

were mainly spherical shape with the average diameter of 50 nm. Due to the bonding effect of the oleic acid coated on the surface, as shown in Fig. 3b, the nAl@OA sticked together, the average diameters of particles increased to 200 nm. Figure 3c shows that the nAl@PA particles had a greater dispersion and the unanimous distribution of particle size. This may be due to the long carbon chain of perfluorotetradecanoic acid. The terminal carboxyl group of perfluorotetradecanoic acid can react with the aluminum atoms and form a strong chemical bond [23]. The steric effect of the other end can play a role of dispersant, which makes aluminum nanoparticles separated from each other, so the dispersion of aluminum nanopowders can be improved. Figure 3d shows the uniform particle size distribution of nAl@NA. Its dispersity is also improved, but there are still certain degrees of agglomeration.
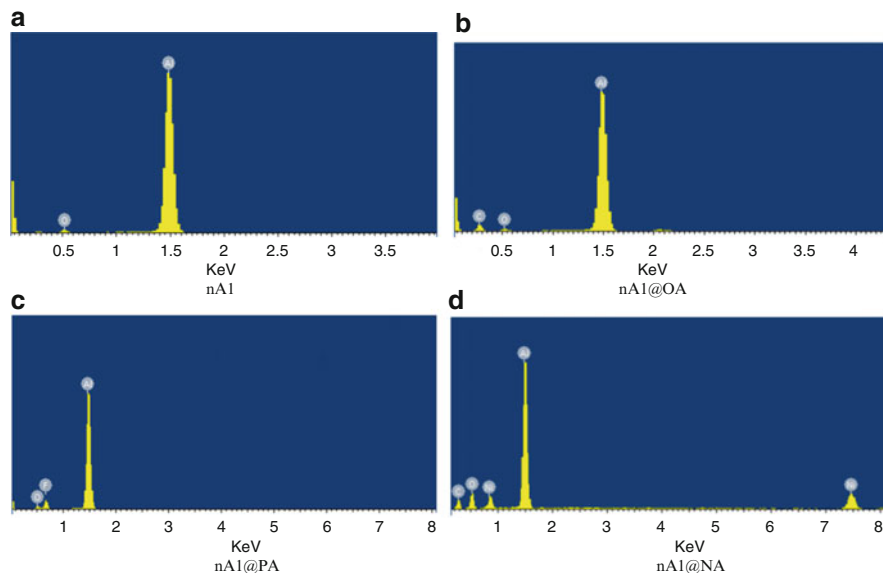
Fig. 4 EDS spectra of different aluminum nanopowders: (**a**) nAl, (**b**) nAl@OA, (**c**) nAl@PA, (**d**) nAl@NA

Figure 4 shows EDS spectra of different aluminum nanopowders. The appearance of C, O, F, Al, and Ni elements from Fig. 4 revealed that the oleic acid, perfluorotetradecanoic acid, and nickel acetylacetonate were existed on the surface of aluminum nanopowder.

3.2 XRD Analysis

Figure 5 exhibits the XRD patterns of nAl, nAl@OA, nAl@PA, and nAl@NA. Five characteristic diffraction peaks appearing at 2θ values, 38.42°, 44.66°, 65.02°, 78.10°, and 82.44°, can be readily indexed to (111), (200), (220), (311), and (222) crystal plane of face-centered cubic (fcc) lattice of Al (JCPDF: 04–0787), respectively [28–31]. The primary crystallite size of the obtained sample, estimated from the Al (111) diffraction peak broadening with the Scherrer formula, is found to be ~28 nm. Due to the organic coatings on the surface of nAl, the patterns of both nAl@OA and nAl@PA show a broadening peak at 15–20° [32].

3.3 FTIR Analysis

The FTIR spectra of oleic acid and nAl@OA are shown in Fig. 6. The spectrum of oleic acid that exhibits the characteristic absorption peaks appeared at 3006 cm^{-1}

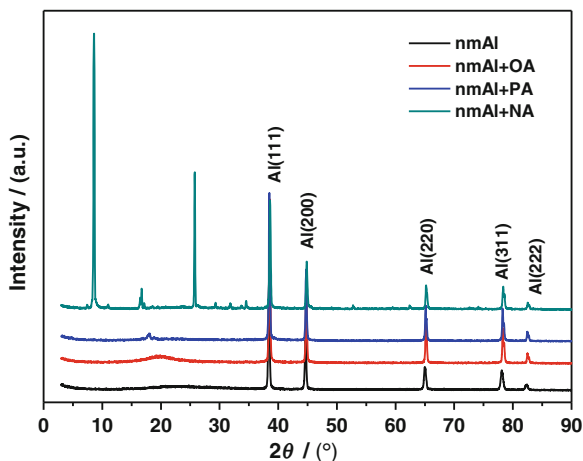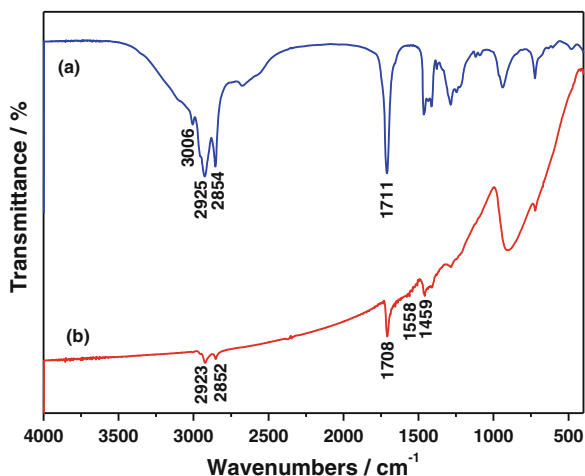**Fig. 5** XRD patterns of different aluminum nanopowders

Fig. 6 FTIR spectra of oleic acid (**a**) and nAl@OA (**b**)

(stretching vibration of O–H), 2925 cm^{-1} (symmetric stretching vibration of C–H) and 2854 cm^{-1} (asymmetric stretching vibration of C–H), and 1711 cm^{-1} (stretching vibration of C $=$ O) [33–36]. The FTIR spectrum of nAl@OA shows similar characteristic absorption peaks with oleic acid, which indicated that the oleic acid molecules are coated on the surface of nAl by physical adsorption.

The FTIR spectra of perfluorotetradecanoic acid (PA) and nAl@PA are shown in Fig. 7. Absorption peaks of PA at 3443 cm^{-1} and 3552 cm^{-1} (stretching vibration of O–H), 1703 cm^{-1} (stretching vibration of C $=$ O), and 1153 cm^{-1} and 1201 cm^{-1} (stretching vibration of C–F) were observed. In the FTIR spectrum of nAl@PA, the stretching vibration peaks of C–F still appeared at 1147 cm^{-1} and 1201 cm^{-1}, but the characteristic absorption peaks of C $=$ O at 1703 cm^{-1} and O–H at

Fig. 7 FTIR spectra of perfluorotetradecanoic acid (**a**) and nAl@PA (**b**)
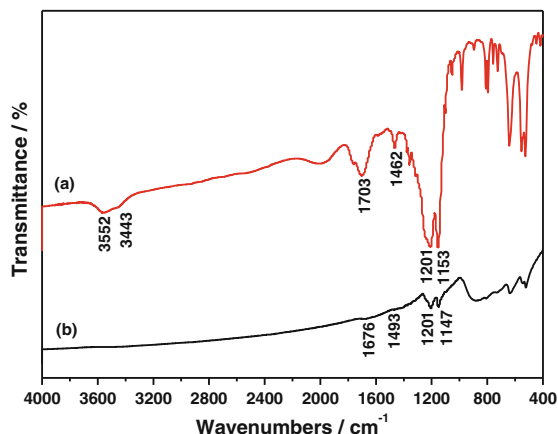
$3443\ cm^{-1}$ and $3552\ cm^{-1}$ disappeared. The weak characteristic absorption peak appeared at $1493\ cm^{-1}$, and $1676\ cm^{-1}$ was assigned to C=O of carboxylate, which indicated that the band of O–H in carboxylic acid was broken due to the reaction between carboxylic acid and the aluminum on the surface of aluminum nanopowders. The separation of absorption peak between the symmetrical and asymmetrical stretching vibration of C=O can be used to characterize the bonding geometry of the carboxylate species with the metal surface [37–39]. Deacon et al. [38] assigned the bonding geometry from a survey of compounds formed between the carboxylate species and metals. Frequency differences of $\sim$200 cm^{-1} are attributed to a bridging geometry, while differences of $\leq$80 cm^{-1} are attributed to a bidentate bonding arrangement, and differences of $\sim$300 cm^{-1} are associated with a monodentate bonding geometry. The frequency difference of $183\ cm^{-1}$ between the symmetrical and antisymmetrical stretching vibration of C=O observed in Fig. 7 for the nAl@PA indicates that the carboxylate species that is formed is bridge bonded to two aluminum atoms.

Figure 8 is the FTIR spectra of nickel acetylacetonate and nAl@NA. As can be seen from Fig. 8, there is a broad and strong absorption peak at $3410\ cm^{-1}$, which is the stretching vibration specific absorption of O–H at crystal water of nickel acetylacetonate. The methyl group absorption peaks are observed at $2990\ cm^{-1}$ (symmetric stretching vibration of C–H), $2920\ cm^{-1}$ (antisymmetric valence vibration of C–H), and $1400\ cm^{-1}$ (deformable vibration of C–H). The maximum specific absorption does not appeared at $1700\ cm^{-1}$ (stretching vibration of C = O) [40] but at $1600\ cm^{-1}$ (stretching vibration of C=O) and $1520\ cm^{-1}$ (stretching vibration of C=C). This is mainly because of the coordination between acetylacetone in the form of enolate anion and nickel ions. As shown in Fig. 8, the specific absorption peaks of nickel acetylacetonate still exist at $2930\ cm^{-1}$, $2850\ cm^{-1}$, $1570\ cm^{-1}$, $1520\ cm^{-1}$, and $1360\ cm^{-1}$ from the FTIR spectrum of nAl@NA. This indicates that the nickel acetylacetonate is attached to the surface of aluminum nanopowder in the form of physical adsorption [41–44].

Fig. 8 FTIR patterns of
nickel acetylacetonate (**a**) and
nAl@NA (**b**)
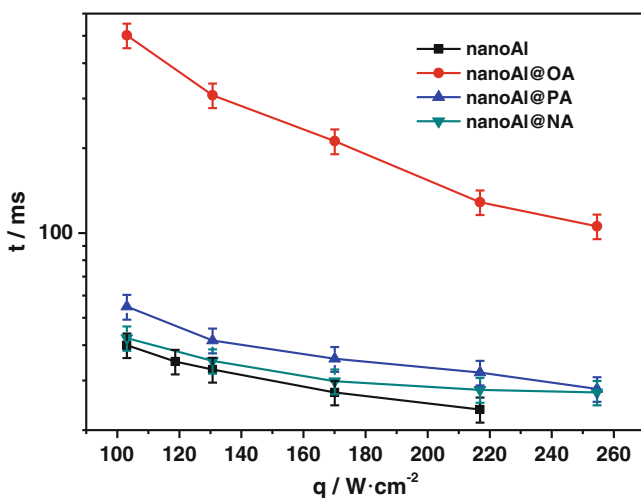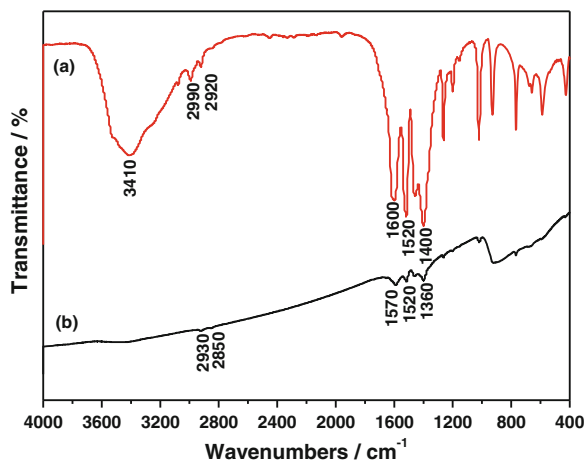
Fig. 9 Ignition delay times of different aluminum nanopowders at different heat flow density

3.4 Laser Ignition Characteristics

3.4.1 Ignition Studies of Different Aluminum Nanopowders Under Different Heat Flux

The ignition delay time of nAl, nAl@OA, nAl@PA, and nAl@NA under different heat flux densities is shown in Fig. 9. The energy density range of laser for these experiments varies from 100 to 260 W/cm^2, and the diameter of laser spot is 5.0 mm, and the diameter of samples is 4.0 mm. As can be seen in Fig. 9, there is a threshold

in the ignition process of aluminum nanopowders. The ignition delay time of nAl decreases sharply along with an increase in heat flux density in the low heat flux density. When the heat flux density is less than 120 W/cm^2, the ignition delay time of coated aluminum nanopowders is shorter than uncoated aluminum nanopowders, while when it arrives at a certain threshold, the ignition delay time is longer. This is due to the competition between the absorption rate and dissipation rate of laser radiant energy on the sample. When the laser power is sufficiently high (i.e., the heat flux density is high enough), the thermal diffusion rate is far below the heat absorption rate. This leads to the rapid energy accumulation, making the ignition occurring before energy dissipation. On the other hand, the energy transfer through the radiant point to ambience may reduce the energy accumulation rate; once heat diffusion rate is greater than that of heat accumulation rate, ignition cannot happen no matter how long the laser radiation. So the critical power existed in the laser ignition process. Under the critical power, ignition cannot happen; while above the critical power, it is helpful for the ignition because the heat diffusion rate is lower than heat accumulation rate. The ignition critical power mainly depends on the chemical decomposition react kinetics, thermal and optical properties of components, and so on [45].

Because the thermal conductivity of aluminum is higher than the oleic acid, perfluorotetradecanoic acid, and nickel acetylacetonate, the ignition delay times of nAl are shorter than that of the nAl@OA, nAl@PA, and nAl@NA. The longest ignition delay time was the nAl@OA because the oleic acid is a fixed oil, which has a high ignition temperature, and it can dissipate the energy of laser. Due to the combustion catalysis of nickel acetylacetonate, its ignition delay time is shorter than that of the nAl@OA and nAl@PA, because of the strong oxidizing fluorine of perfluorotetradecanoic acid.

3.4.2 Laser Ignition Process of Different Aluminum Nanopowders

The laser ignition process of different aluminum nanopowders under the same heat flux density of 170 W/cm^2 is shown in Figs. 10, 11, 12, and 13. As can be seen from Figs. 10, 11, 12, and 13, the ignition processes of uncoated aluminum nanopowders and coated aluminum nanopowder are different. For the nAl, the combustion process
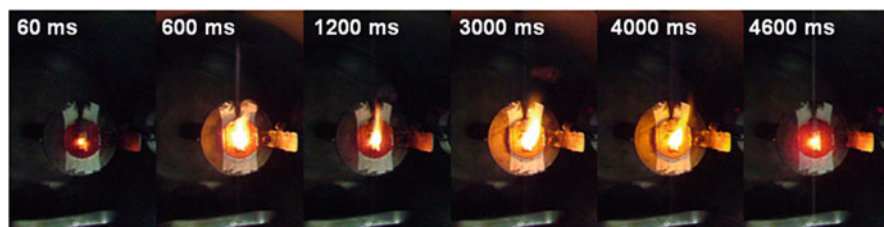
Fig. 10 Laser ignition process of nAl
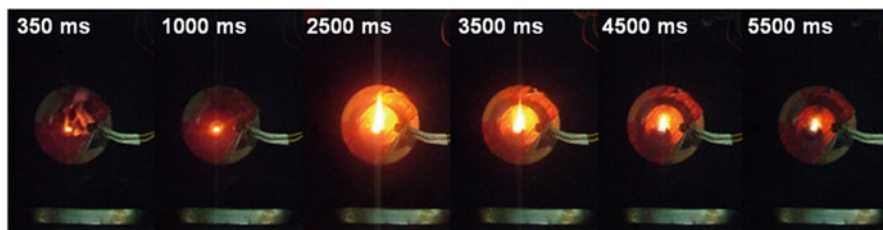
Fig. 11 Laser ignition process of nAl@OA
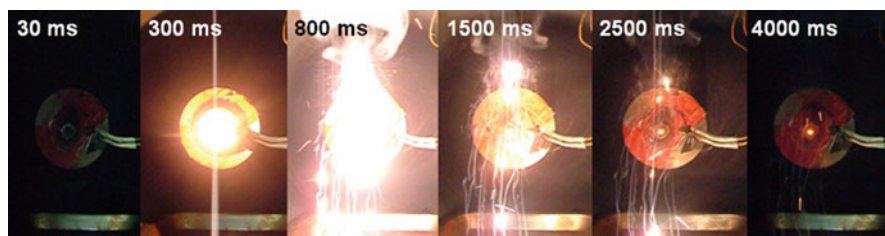
Fig. 12 Laser ignition process of nAl@PA
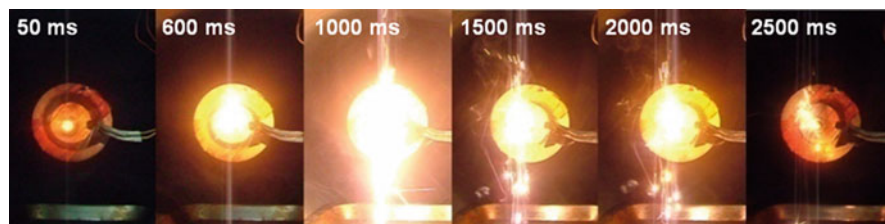
Fig. 13 Laser ignition process of nAl@NA

began from the surface of the aluminum particles and then gradually spread to the center, eventually causing internal combustion (Fig. 10). To the nAl@OA, the contact between aluminum and air was cut off by the oleic acid. So the oleic acid can be ignited at first, and the ignition delay time of nAl@OA is a little long, as shown in Fig. 11. From Fig. 12, it can be seen that the combustion process of nAl@PA is a very rapid process, which can be attributed to the intense reaction that takes place between the aluminum and the thermal decomposed production of perfluorotetradecanoic acid. Similar to the ignition process of nAl@OA, the combustion reaction was also very fast due to the combustion catalysis of nickel acetylacetonate (Fig. 13).

3.5 Combustion Process of Different Aluminum Nanopowders

Figures 14, 15, 16, and 17 show the combustion flame images of different aluminum nanopowders. As shown in Fig. 14, for the nAl, some aluminum nanopowders leave the combustion flame center with the stream of gases. The nAl@OA, on the other hand, shows shorter flame and lower burning rate due to the poorer combustion properties of oleic acid (Fig. 15). For the nAl@PA, as shown in Fig. 16, it burns intensively from the flame profile, which may be attributed
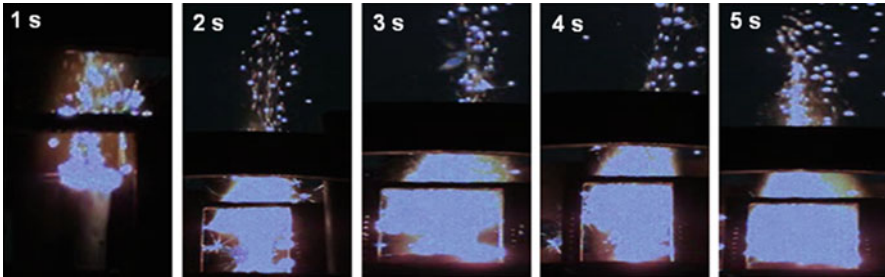
Fig. 14 Flame shape of nAl
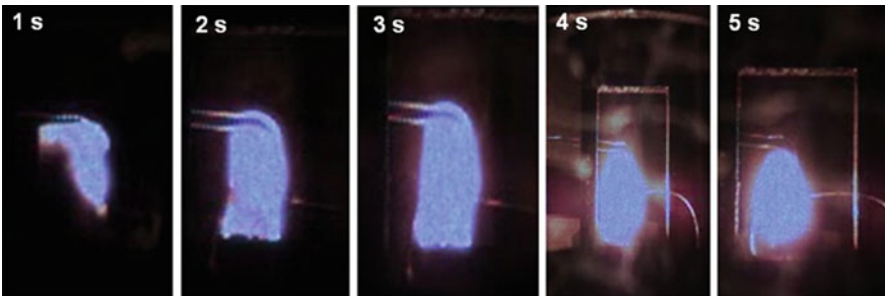
Fig. 15 Flame shape of nAl@OA
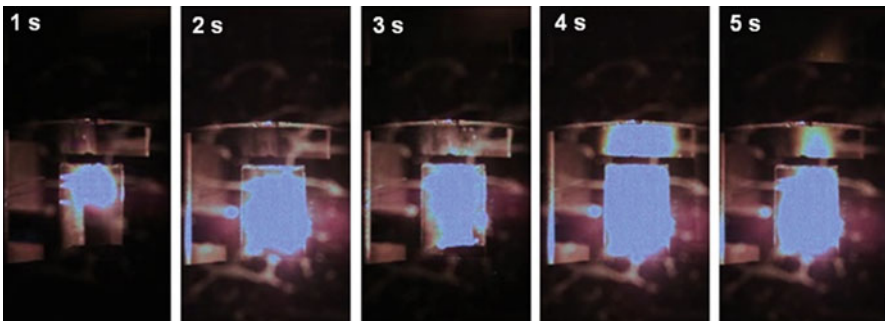
Fig. 16 Flame shape of nAl@PA
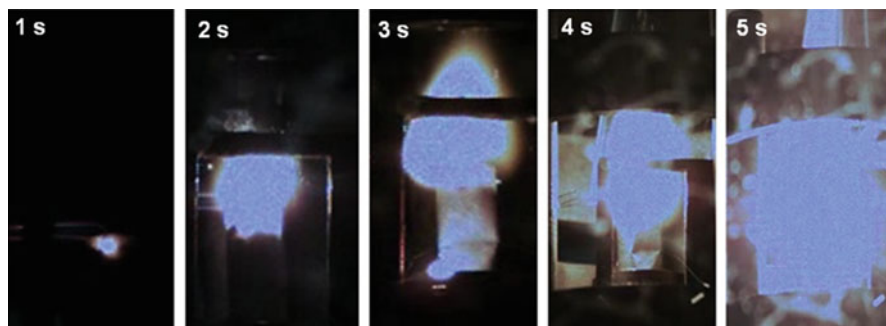
Fig. 17 Flame shape of nAl@NA

Fig. 18 Burning rates of the propellants containing aluminum powder at different pressures
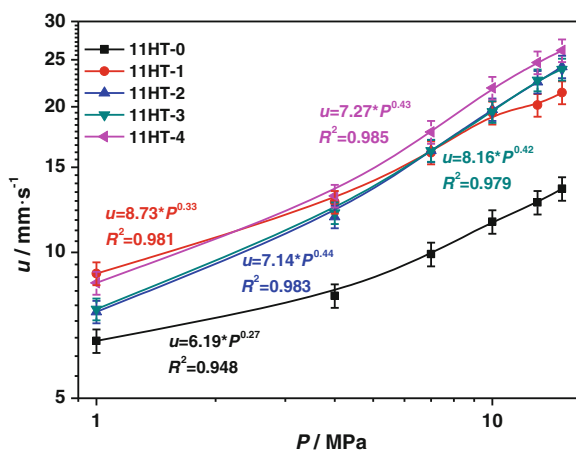
to the decomposition of perfluorotetradecanoic acid at high temperature and the exothermic redox reaction between its fluorine-containing product and aluminum. Interestingly, during the initial stage of the burning of nAl@NA, its flame is regular (Fig. 17), and then the combustion flame becomes more intense which is due to the decomposition of nickel acetylacetonate and its catalytic effect on the combustion of nanopowders.

3.6   Burning Rate and Pressure Exponent of Propellant

Figure 18 is the burning rate (u)–pressure (P) curves of different composite solid propellants containing different aluminum powders. The strand burn rate experiments were conducted in the nitrogen pressure range of 1–15 MPa. The reference formulation (11HT-0) exhibited a burning rate in the order of 6.57–13.55 mm·s^{-1}. All kinds of aluminum nanopowder lead to the increase in the

burning rate of the propellant as compared with the 11HT-0. The burning rate of 11HT-4 sample, which contains nAl@NA, is the highest at different pressure, and the maximum burning rate is up to 26.13 mm·s^{-1} at 15 MPa. The burning rates of 11HT-2 and 11HT-3 samples are almost the same at different pressures, and both are higher than those of the 11HT-1 only at the pressure range of 10–15 MPa. The burning rate decrease trends at the pressure of 15 MPa are as follows: 11HT-4 > 11HT-2 > 11HT-3 > 11HT-1 > 11HT-0.

The burning rate increase degree (Δ) of propellants containing different aluminum powders at different pressures was shown in Table 2. According to Table 2, the Δ of 11HT-4 is the highest at the pressure of 13 MPa, which can be up to 94.4 %. This was attributed to the better coating effect of nickel acetylacetonate, which can protect the aluminum particles against oxidation and make the aluminum content of aluminum nanopowders be higher. Meanwhile, another important reason is the effective combustion catalysis of nickel acetylacetonate at high pressure. The Δ is higher than those of 11HT-1 at different pressure except 4 MPa for both 11HT-2 and 11HT-3 formulations. This was owing to the oleic acid, and perfluorotetradecanoic acid was easily decomposed at low pressure. The decomposition was an endothermic process, which decreases the burning surface temperature and burning rates. As a whole, the burning rates of propellant containing nAl@OA and nAl@PA are higher than that of the propellant containing untreated aluminum nanopowder.

The burning rate pressure exponents of different propellants at different pressure range were shown in Table 3. The burning rate pressure exponent of 11HT-1 is the lowest at the pressure range of 10–13 MPa. The pressure exponents increased in the addition of different aluminum nanopowders to the propellant formulations, and the pressure exponents of propellants containing coated aluminum nanopowders were higher than those of the untreated aluminum nanopowders at the pressure range

Table 2 Δ of different propellants containing different aluminum powders at pressure of 4–15 MPa

Samples	Δ/%				
	4 MPa	7 MPa	10 MPa	13 MPa	15 MPa
11HT-0	–	–	–	–	–
11HT-1	56.1	62.1	67.8	58.9	57.9
11HT-2	45.6	63.6	70.5	77.3	78.5
11HT-3	48.3	63.6	68.7	78.8	76.3
11HT-4	60.8	78.7	88.9	94.4	92.8

Table 3 Burning rate pressure exponent at different pressure range

Samples	Pressure exponent (n) at different pressure range			
	4–7 MPa	7–10 MPa	10–13 MPa	13–15 MPa
11HT-0	0.35	0.42	0.36	0.46
11HT-1	0.42	0.53	0.14	0.42
11HT-2	0.56	0.55	0.50	0.51
11HT-3	0.52	0.52	0.57	0.36
11HT-4	0.54	0.59	0.46	0.40

of 4–7 MPa. Whereas it is a bit different at 13–15 MPa. The pressure exponent of 11HT-3 can be decreased to 0.36, which is lower than that of the 11HT-1 formulation (0.42). The pressure exponent of 11HT-4 can also be decreased to 0.40 for the combustion catalysis of nickel acetylacetonate and the exothermic reaction of the aluminum and fluorine at high pressure [46–49].

3.7 Combustion Flame Profiles of Propellant

Flame profile is an important indicator for the combustion mechanism of the propellant. The length and intensity of the flame, the dark zone and its thickness, and the morphology of the burning surface can be observed from the flame picture. Figure 19 shows the combustion flame photographs of four typical composite solid propellants containing different coated aluminum nanopowders at pressures of 1 MPa and 4 MPa. The splash of aluminum particles is not observed, and the propellant combusts stably. The flame is continuous and there are no large granular lumps in the combustion flame, which indicate that the propellant can be combusted completely. It also can be seen from Fig. 19 that the dark zone of the samples is eliminated almost completely and the luminous flame approaches the burning surface.
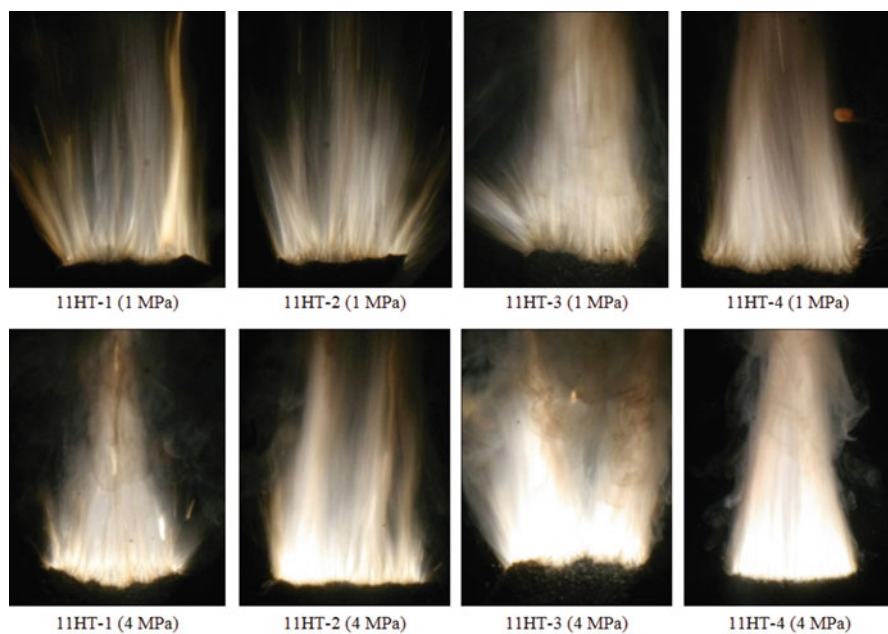
Fig. 19 Flame photographs of four typical composite solid propellants containing different coated aluminum nanopowders at pressures of 1 MPa and 4 MPa

As shown in Fig. 19, the flame shape of different propellants exhibits large difference. Compared with other samples, the combustion flame structure of 11HT-1 and 11HT-2 samples showed radialized at the pressure of 1 MPa. On the one hand, the gas-phase zone is far from the burning surface at low pressure; the heat feedback to the burning surface decreased. It makes the burning rate not uniform at different surface districts. On the other hand, the diameter of aluminum powder used in the propellant is nanosized. It is easy to agglomerate for high specific surface area and difficult to disperse uniformly in the propellant, so the flame profile is different. The combustion flame structure of 11HT-3 and 11HT-4 samples is relatively concentrated and approximately cylindrical cone, and the length of combustion flame is relatively longer. This is mainly because the combustion efficiency of aluminum particles increased and propellant combustion was fully in this two samples. The combustion flame profile of the propellant at the pressures of 4 MPa is significantly different at the 1 MPa. The flame zone is closer to the propellant burning surface at the pressure of 4 MPa. The flame length is longer and burning surface is more uniform.

3.8   Combustion Wave Structure and Flame Temperature Distribution of Propellant

The temperature distribution in heating zone and combustion wave of a typical solid propellant is shown in Fig. 20 [50]. It is shown from Fig. 20 that the combustion wave structure consists of three main zones: condensed-phase zone

Fig. 20   Schematic representation of the combustion wave structure of a typical solid propellant

(zone I), condensed-phase reaction zone (zone II), and gas-phase zone (zone III) which can be divided into gas-phase diffusion reaction zone and luminous flame zone. In heating zone I, no chemical reactions occur and the temperature increases from the in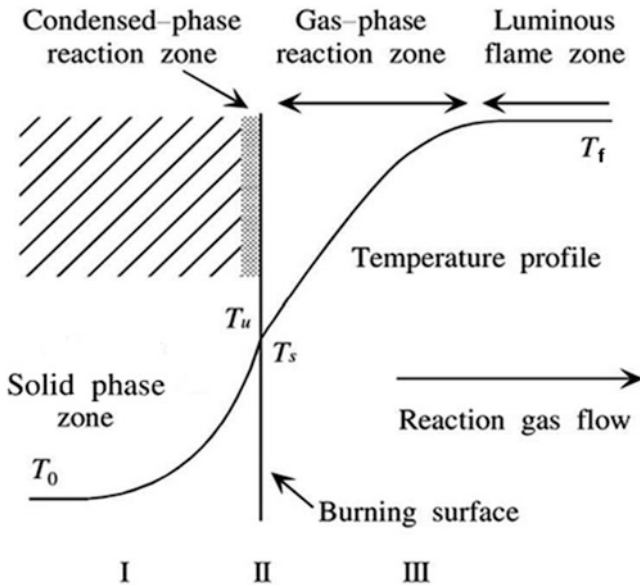itial temperature (T_0) to the decomposition temperature (T_u), through conductive heat feedback from the burning surface. In zone II, in which there is a phase change from solid to liquid and/or to gas and reactive gaseous species are formed in endothermic or exothermic reactions, the temperature increases from T_u to the burning surface temperature (T_s). Since the condensed-phase reaction zone is very thin (<0.1 mm) [26], T_s is approximately equal to T_u. In gas-phase diffusion reaction zone, in which exothermic gas-phase reactions occur, and the temperature increases rapidly from T_s to the maximum combustion flame temperature (T_f). In luminous flame zone, the exothermic reaction terminates and the final combustion products are formed, and the temperature reaches the maximum.

Temperature profiles in condensed zone and combustion wave of four different propellants at the pressures of 4 MPa and 7 MPa were shown in Fig. 21. According to Fig. 21, the temperature in the solid-phase zone increases rapidly from T_0 to T_s. The AP and HTPB directly change from solid phase to gas phase by the thermal decomposition or sublimation. On the burning surface, the AP and HTPB do not premixed, but escape from the burning surface as a kind of "airbag." Then the decomposition products of AP take exothermic reaction in the gas phase near the burning surface, forming the AP premixed flame and oxygen-enriched air flow. In the gas phase far away from the burning surface, the gas decomposition products of AP and HTPB took place diffusion combustion with aluminum, generated the final combustion products, and released a lot of heat.

Table 4 has shown the combustion wave structure parameters of four different propellants at the pressure of 4 MPa and 7 MPa, where δ is the thickness of the gas-phase diffusion reaction zone.

It can be seen from Table 4 that the maximum combustion temperature (T_f) of four different propellants at the pressure of 4 MPa and 7 MPa is almost the same, indicating that the surface coating of aluminum nanopowders has little effect on the combustion flame temperature of solid propellant. The burning surface temperature (T_s) increases with the pressure increasing besides 11HT-4. This is due to the flame zones closer to the burning surface of the solid propellant under high pressure. The heat feedback from the flame zone to the burning surface increases, so that the burning surface temperature increases. For the 11HT-4, the nickel acetylacetonate has some catalytic decomposition for the propellant. This makes decomposition reaction of propellant take place under relative low T_s.

The thickness of the diffusion reaction zone (δ) has no significant change at different pressures. But the δ of samples containing different coated aluminum nanopowders is less than the samples contained with untreated aluminum powders. To the 11HT-3 sample, the δ under different pressures is minimal with the decomposition of perfluorotetradecanoic acid on the surface of aluminum nanopowders at about 600 °C [51]. The decomposition products are fluorinated compounds, which may react with the aluminum. Because the oxidative ability of fluorine is stronger, the reaction of aluminum and fluorinated compounds is easier and the reaction
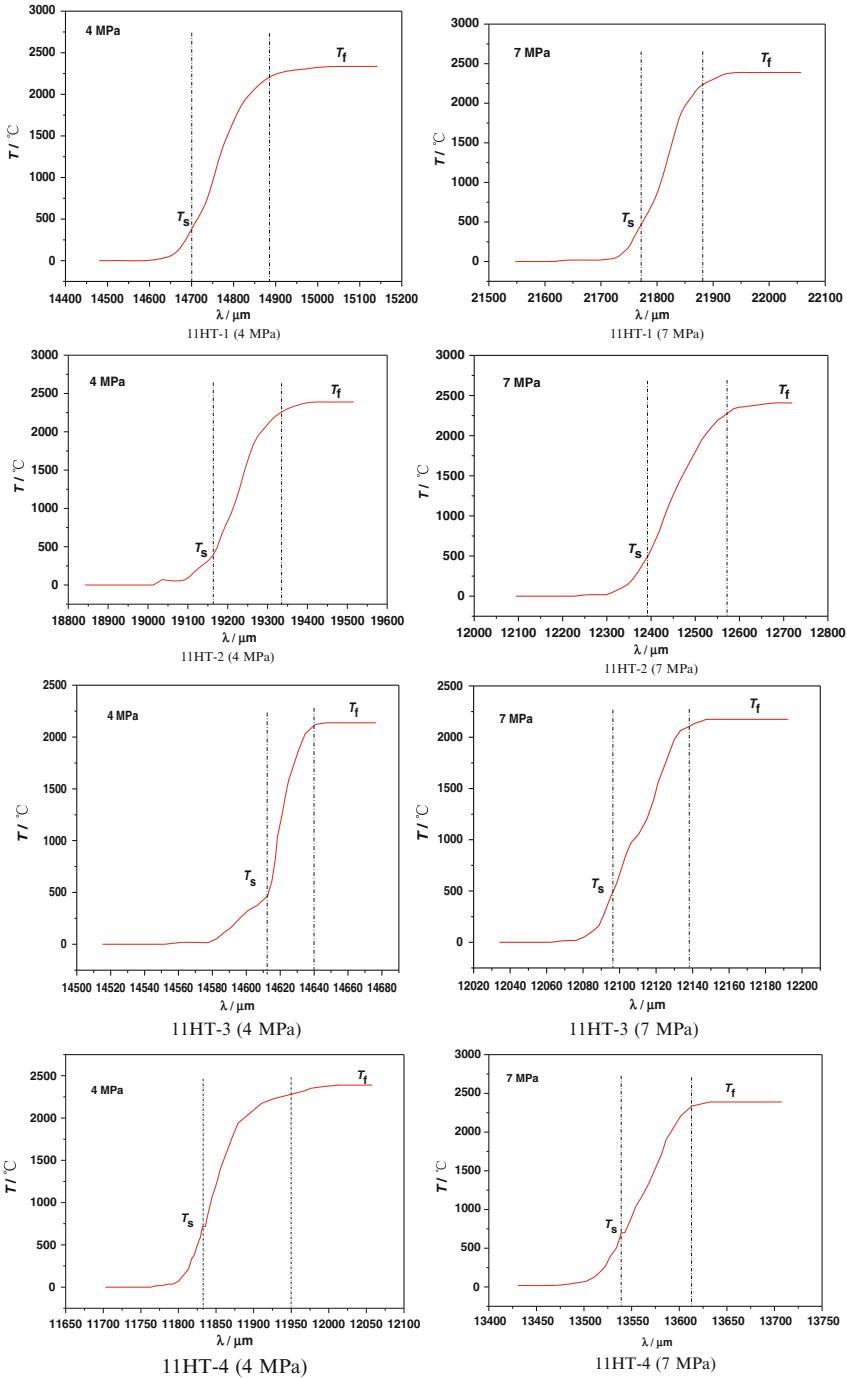
Fig. 21 Temperature profiles of condensed zone and combustion wave of tested propellants at the pressures of 4 MPa and 7 MPa

Table 4 The thickness and temperature of gas-phase reaction zone of four different propellants at the pressure of 4 MPa and 7 MPa

Samples	$\delta/\mu m$		$T_s/°C$		$T_f/°C$	
	4 MPa	7 MPa	4 MPa	7 MPa	4 MPa	7 MPa
11HT-1	185.6	109.6	370	463	2335	2389
11HT-2	170.9	179.6	392	490	2389	2407
11HT-3	27.7	41.9	460	485	2137	2173
11HT-4	117.5	84.1	718	697	2389	2385

time is shorter, increasing the diffusion reaction zone thickness. It is interesting to note that the pressure has an obvious influence on the δ of 11HT-4 sample which contained aluminum nanopowders coated by nickel acetylacetonate. The possible reason was that the nickel acetylacetonate has catalytic effect to the HTPB propellant. The nickel acetylacetonate was closer to the burning surface at high pressure. This may increase the catalytic activity and accelerate the decomposition of propellant.

It is essential that maximal measured temperature of burning surface at all studied pressures. It can be seen from Table 4 to Fig. 18 that there is a general trend, but a little discrepancy. 11HT-3 has the highest burning surface temperature, but its burning rate is nearly same with 11HT-2 at the pressure of 4 MPa. It appears that burning rates are dependent on many phenomena, maybe because the reaction of aluminum and fluorine was far away from the burning surface, but the active aluminum content of nAl@OA was higher than the nAl@PA and finally causes higher exothermic value of nAl@OA.

4   Conclusions

1. The perfluorotetradecanoic acid can react with the aluminum and form chemical bonds, but the nickel acetylacetonate only adsorbed on the aluminum nanopowder surface by physical adsorption inducing the coating was incomplete. The coating effect of perfluorotetradecanoic acid is better than the nickel acetylacetonate.
2. The ignition and combustion characteristics of different aluminum nanopowders were studied using the laser ignition system. The results show that there is a critical power of laser heat flux density in the ignition process of the coated aluminum nanopowders. The ignition delay time of nAl@NA is shorter than the nAl@PA and nAl@OA because of the combustion catalysis of nickel acetylacetonate.
3. The burning rates of propellant sample containing nAl@NA are the highest at different pressures, and the maximum burning rate is up to 26.13 mm·s^{-1} at 15 MPa. The burning rates of propellant samples containing oleic acid and perfluorotetradecanoic acid are almost the same at different pressures and higher

than the propellant samples containing untreated aluminum nanopowders only at the pressure range of 10–15 MPa.

4. The aluminum nanopowders coated with different materials have little effect on the combustion flame temperatures of solid propellants.

References

1. Brousseau P, Anderson CJ (2002) Nanometric aluminum in explosives. Propellants Explos Pyrotechnics 27(5):300–306
2. Gromov A, Strokova Y, Kabardin A, Vorozhtsov A, Teipel U (2009) Experimental study of the effect of metal nanopowders on the decomposition of HMX, AP and AN. Propellants Explos Pyrotechnics 34(6):506–512
3. Muravyev N, Frolov Y, Pivkina A, Monogarov K, Ivanov D, Meerov D, Fomenkov I (2009) Combustion of energetic systems based on HMX and aluminum: influence of particle size and mixing technology. Cent Eur J Energy Mater 6(2):195–210
4. Armstrong RW, Baschung B, Booth DW, Samirant M (2003) Enhanced propellant combustion with nanoparticles. Nano Lett 3(2):253–255
5. Ivanov YF, Osmonoliev MN, Sedoi VS, Arkhipov VA, Bondarchuk SS, Vorozhtsov AB, Korotkikh AG, Kuznetsov VT (2003) Productions of ultra-fine powders and their use in high energetic compositions. Propellants Explos Pyrotechnics 28(6):319–333
6. Baschung B, Grune D, Licht HH, Samirant M (2002) Combustion phenomena of a solid propellant based on aluminium powder. Int J Energy Mater Chem Propuls 5(1–6):219–225
7. Babuk VA, Dolotkazin I, Gamsov A, Glebov A, DeLuca LT, Galfetti L (2009) Nanoaluminum as a solid propellant fuel. J Propuls Power 25(2):482–489
8. Pantoya ML, Granier JJ (2005) Combustion behavior of highly energetic thermites: nano versus micron composites. Propellants Explos Pyrotechnics 30(1):53–62
9. Sullivan K, Young G, Zachariah MR (2009) Enhanced reactivity of nano-B/Al/CuO MIC's. Combust Flame 156(2):302–309
10. Chowdhury S, Sullivan K, Piekiel N, Zhou L, Zachariah MR (2010) Diffusive vs explosive reaction at the nanoscale. J Phys Chem C 114(20):9191–9195
11. Pivkina A, Ulyanova P, Frolov Y, Zavyalov S, Schoonman J (2004) Nanomaterials for heterogeneous combustion. Propellants Explos Pyrotechnics 29(1):39–48
12. Tepper F, Ivanov GV (1997) 'Activated' aluminum as a stored energy source for propellants. Int J Energy Mater Chem Propuls 4(1–6):636–645
13. Aumann CE, Skofronick GL, Martin JA (1995) Oxidation behavior of aluminum nanopowders. J Vac Sci Technol B 13(3):1178–1183
14. Trunov MA, Schoenitz M, Zhu X, Dreizin EL (2005) Effect of polymorphic phase transformations in Al_2O_3 film on oxidation kinetics of aluminum powders. Combust Flame 140(4):310–318
15. Sun J, Pantoya ML, Simon SL (2006) Dependence of size and size distribution on reactivity of aluminum nanoparticles in reactions with oxygen and MoO_3. Thermochem Acta 444(2):117–127
16. Morgan AB, Wolf JD, Guliants EA, Fernando KAS, Lewis WK (2009) Heat release measurements on micron and nano-scale aluminum powders. Thermochem Acta 488(1–2):1–9

17. Jouet RJ, Warren AD, Rosenberg DM, Bellitto VJ, Park K, Zachariah MR (2005) Surface passivation of bare aluminum nanoparticles using perfluoroalkyl carboxylic acids. Chem Mater 17(11):2987–2996

18. Brousseau P, Côté S, Ouellet N, Lessard P (2000) Preliminary testing of energetic materials containing aluminum nano-powders. In: 25th TTCP WPN/TP-4 meeting, energetic materials and propulsion technology technical workshop, Salisbury, South Australia, 6–7 April, 2000.

19. Jones DEG, Brousseau P, Fouchard RC, Turcotte AM, Kwok QSM (2000) Thermal characterization of passivated nanometer size aluminium powders. J Therm Anal Calorim 61(3):805–818

20. Yao E-G, Zhao F-Q, Gao H-X, Xu S-Y, Hu R-Z, Hao H-X, An T, Pei Q, Xiao L-B (2012) Thermal behavior and non-isothermal decomposition reaction kinetics of aluminum nanopowders coated with an oleic acid/hexogen composite system. Acta Phys-Chim Sin 28(4):781–786

21. Mattew C, Fred T, Vladimir L (2001) Ageing Characteristics of Alex® Nanosize Aluminium. Paper presented at the 37th AIAA/ASME/SAE/ASEE JPC conference & exhibit, Salt Lake City, Utah, 8–11 July, 2001

22. Kwon Y-S, Gromov AA, Strokova JI (2007) Passivation of the surface of aluminum nanopowders by protective coatings of the different chemical origin. Appl Surf Sci 253(12):5558–5564

23. Jouet RJ, Granholm RH, Sandusky HW, Warren AD (2006) Preparation and shock reactivity analysis of novel perfluoroalkyl-coated aluminum nanocomposites. AIP Conf Proc 845(1):1527–1530

24. Foley TJ, Johnson CE, Higa KT (2005) Inhibition of oxide formation on aluminum nanoparticles by transition metal coating. Chem Mater 17(16):4086–4091

25. Yao E-G, Zhao F-Q, Xu S-Y, Hu R-Z, Xu H-X, H-X H (2014) Combustion characteristics of composite solid propellants containing different coated aluminum nanopowders. Adv Mater Res 92(4):200–211

26. Yan Q-L, Li X-J, Wang Y, Zhang W-H, Zhao F-Q (2009) Combustion mechanism of double-base propellant containing nitrogen heterocyclic nitroamines (I): the effect of heat and mass transfer to the burning characteristics. Combust Flame 156(3):633–641

27. Yan Q-L, Song Z-W, Shi X-B, Yang Z-Y, Zhang X-H (2009) Combustion mechanism of double-base propellant containing nitrogen heterocyclic nitroamines (II): the temperature distribution of the flame and its chemical structure. Acta Astronaut 64(5–6):602–614

28. Chen L, Song W-L, Guo L-G, Xie C-S (2009) Thermal property and microstructure of Al nanopowders produced by two evaporation routes. Trans Nonferrous Met Soc China 19(1):187–191

29. Ramaswamy AL, Kaste P, Trevino SF (2004) A "Micro-Vision" of the physio-chemical phenomena occurring in nanoparticles of aluminum. J Energy Mater 22(1):1–24

30. Kassaee MZ, Buazar F (2009) Al nanoparticles: impact of media and current on the Arc fabrication. J Manuf Process 11(1):31–37

31. Olgun U (2010) Rapid microwave-assisted deposition of microwire patterns of nanoaluminum and nanosilver from colloids. ACS Appl Mater Interfaces 2(1):28–34

32. Fernando KAS, Smith MJ, Harruff BA, Lewis WK, Guliants EA, Bunker CE (2009) Sonochemically assisted thermal decomposition of alane N, N-dimethylethylamine with titanium (Iv) isopropoxide in the presence of oleic acid to yield air-stable and size-selective aluminum core−shell nanoparticles. J Phys Chem C 113(2):500–503

33. Jain TK, Morales MA, Sahoo SK, Leslie-Pelecky DL, Labhasetwar V (2005) Iron oxide nanoparticles for sustained delivery of anticancer agents. Mol Pharm 2(3):194–205

34. Bunker CE, Karnes JJ (2004) Low-temperature stability and high-temperature reactivity of iron-based core−shell nanoparticles. J Am Chem Soc 126(35):10852–10853

35. Jia Z, Xia Y (2011) Hydrothermal synthesis, characterization, and tribological behavior of oleic acid-capped lanthanum borate with different morphologies. Tribol Lett 41(2):425–434

36. Lewis WK, Rosenberger AT, Gord JR, Crouse CA, Harruff BA, Fernando KAS, Smith MJ, Phelps DK, Spowart JE, Guliants EA, Bunker CE (2010) Multispectroscopic (FTIR, XPS, and TOFMS−TPD) investigation of the core−shell bonding in sonochemically prepared aluminum nanoparticles capped with oleic acid. J Phys Chem C 114(14):6377–6380

37. Crowell JE, Chen JG, Yates JT (1986) A vibrational study of the adsorption and decomposition of formic acid and surface formate on Al(111). J Chem Phys 85(5):3111–3122
38. Deacon GB, Phillips RJ (1980) Relationships between the carbon-oxygen stretching frequencies of carboxylate complexes and the type of carboxylate coordination. Coord Chem Rev 33(3):227–250
39. Crowell JE, Chen JG, Yates JT Jr (1986) The adsorption and decomposition of carboxylic acids on Al (111). J Electron Spectrosc Relat Phenom 39:97–106
40. Wu H-X, Xu L-X, Xin C-Y, Yu X-B, Wang Z-M (2005) Synthesis and photoluminescence properties of Tb^{3+}-acetylacetone ternary complexes doped with La^{3+} or Y^{3+}. Spectrosc Spectr Anal 25(1):69–72
41. Bu C-H (2009) Preparation and characterization of magnetic nanoparticles comprised of nickel and cobalt. China University of Petroleum, Dongying
42. Zhao J-Q, Zheng Y, Lu J-G, Han J-P, Ge F-Y (2004) Study on the preparation of sol-gel entrapped Ni(acac)2•2H_2O complex and its catalytic properties on epoxidation of cyclohexene by oxygen. J Mol Catal (China) 18(4):266–270
43. Zhao D, Duan H-C, Jiang H, Gong H (2007) Solid synthesis of nickel acetylacetonate at the room temperature. Chem Ind Times 21(2):8–10
44. Mu L (2009) Study on preparation and application of chromium acetylacetonate. Southwest University of Science and Technology, Mianyang
45. Hao H-X, Pei Q, Nan B-J, Zhang H, Xiao L-B, Zhao F-Q (2001) Laser ignition characteristics of RDX-CMDB propellants. Chin J Energy Mater 19(3):276–281
46. Osborne DT, Pantoya ML (2007) Effect of Al particle size on the thermal degradation of Al/teflon mixtures. Combust Sci Technol 179(8):1467–1480
47. Yarrington CD, Son SF, Foley TJ (2010) Combustion of silicon/Teflon/viton and aluminum/teflon/viton energetic composites. J Propuls Power 26(4):734–743. doi:10.2514/1.46182
48. Watson KW, Pantoya ML, Levitas VI (2008) Fast reactions with nano- and micrometer aluminum: a study on oxidation versus fluorination. Combust Flame 155(4):619–634
49. Kappagantula K, Pantoya ML (2012) Experimentally measured thermal transport properties of aluminum–polytetrafluoroethylene nanocomposites with graphene and carbon nanotube additives. Int J Heat Mass Transfer 55(4):817–824
50. Kubota N (2007) Propellants and explosives: thermochemical aspects of combustion, 2nd edn. Wiley-VCH Verlag GmbH & Co. KGaA, Weinheim, Germany
51. Sossi A, Duranti E, Manzoni M, Paravan C, DeLuca LT, Vorozhtsov AB, Lerner MI, Rodkevich NG, Gromov AA, Savin N (2012) Combustion of HTPB-based solid fuels loaded with coated nanoaluminum. Combust Sci Technol 185(1):17–36

Experimental Investigation of an Aluminized Gel Fuel Ramjet Combustor

Gilad Gafni, Alexander Kuznetsov, and Benveniste Natan

Abstract The goal of the present study is to investigate experimentally the performance of a ramjet combustor that uses a kerosene-based gel fuel combined with aluminum powder. Gel fuels combine the benefits of both liquid and solid fuels in terms of safety and performance and allow addition of metal particles without sedimentation. A lab-scale ramjet combustor was designed and built and a parametric investigation was conducted. The test facility included also an air heater to simulate flight conditions. More than 250 valid tests were conducted, varying the gel fuel type, motor length, air bypass ratio, and more. Paraffin wax and aluminum tristearate were used as gellants to create a stable gel and provide fine droplet atomization. Mass flow rates, pressure, and thrust were measured to calculate the experimental combustion temperature. Combustion temperatures varied in the range 1500–2000 K, depending on fuel type and fuel-to-air ratio, allowing the aluminum particles to ignite. Specific impulse was found to be about 1400 s for non-aluminized fuels and 1200 s for 9 % aluminum gel fuel. Optimal aluminum loading was estimated at 9 % mass and a top combustion efficiency of 90 % was achieved.

Nomenclature

Acronyms

ATS	Aluminum tristearate
BR	Bypass ratio
GFRJ	Gel fuel ramjet
HTPB	Hydroxyl-terminated polybutadiene
VAH	Vitiated air heater

G. Gafni • A. Kuznetsov • B. Natan (✉)

Faculty of Aerospace Engineering, Technion-Israel Institute of Technology, Haifa 32000, Israel

e-mail: aerben@technion.ac.il

Symbols

c*	Characteristic velocity
f	Fuel-to-air ratio
I_s	Specific impulse
$\dot{m}$	Mass flow rate
p	Pressure
T	Temperature
Δh_f^0	Standard heat of formation
η_{c*}	c* efficiency
ρ	Density
φ	Equivalence ratio

Subscripts

a	Air
c	Combustor
main	Main flow through the injector
total	Total flow, i.e., main+bypass

1 Introduction

Ramjet engines are attractive mainly because of their significantly high specific impulse in comparison to rockets of any kind [1, 2]. The main disadvantage of the ramjet engine is that it requires a rocket motor or other means to boost it to supersonic Mach numbers. Yet, in the last decade, the interest for ramjet systems for various applications is constantly increasing worldwide. These systems focus on ducted rockets [3], such as the pan-European air-to-air missile Meteor (MBDA missile systems) and air-to-surface antiradar missile ARMIGER (Germany).

Ducted rockets require the addition of a certain amount of oxidizer for the combustion of the solid fuel-rich propellant; therefore their specific impulse is lower than that of a liquid ramjet motor.

Liquid ramjets can provide better specific impulse with fuel controllability according to the mission, but like liquid rockets, their operation system is more complex. In addition, in case of accidental tank damage, fuel leak can occur, a fact that makes the system less safe.

Natan and Rahimi [4] indicate that the use of a gel fuel provides an answer to the safety issue, since gels leak at a significantly lower rate and in most cases, a crust forms that prevents further flow. Moreover, the non-Newtonian character of the gelled fuel and the existence of a yield stress allow suspension of metal particles (aluminum, boron, magnesium, etc.) in the gel.
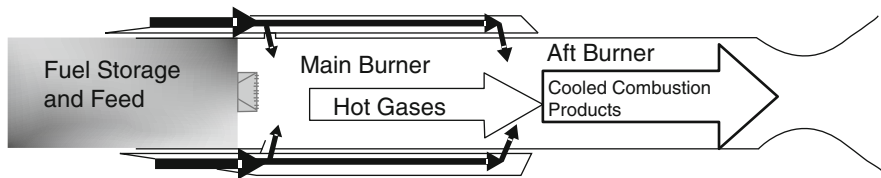
Fig. 1 A two-step combustor ramjet engine (From Haddad et al. [5])

The addition of metals to the fuel can provide even better energetic performance, especially in volume-limited systems. However, gel fuels are more difficult to atomize and burn and the gel technology has not been fully developed.

Aluminum has lower heat of combustion per unit mass than hydrocarbon fuels (∼70 %); however, because of its high density, its heat of combustion per unit volume is twice as much as hydrocarbons. Aluminum burns at high temperatures (>2300 K), and its boiling point is 2740 K; therefore the best environment for obtaining high combustion efficiency is a rocket engine, where the temperatures are high.

Ramjet engines operate at lower combustion chamber temperatures, about 2500 K. In addition, they can operate at low fuel-to-air ratios (equivalence ratio $\varphi \sim 0.4$) producing high thrust because of the high inlet air mass flow rate.

In order to achieve one of its end goals which is complete combustion of boron particles, the combustor chamber was designed to achieve combustion in two stages as indicated by Haddad et al. [5] and shown in Fig. 1.

Liquid fuels cannot carry metal particles; however, if the fuel is gelled, particle sedimentation can be avoided. The high specific impulse of the ramjet engine, combined with the ability of a gel to carry metal particles, makes the gel fuel ramjet (GFRJ) the most adequate solution for a mid-high range sustainer. In a basic theoretical feasibility study, Haddad et al. [5] indicate that a 1500 kg, air-to-surface missile, carrying a 500 kg payload and powered by a GFRJ, can reach a range of 1000 km within 17 min.

No doubt, boron seems to be the best additive in a ramjet engine. The goal of our long-term research is to verify experimentally the feasibility of such a concept. Yet, aluminum, which requires high temperatures (>2300 K) for burning completely, can be used in a lab-scale motor to study whether metalized gels can be atomized and burned, even though not efficiently, in such a motor.

A test facility and a lab-scale GFRJ have been developed to investigate atomization, ignition, and firing processes of a gel hydrocarbon fuel, with and without metal additives, as well as to check the ramjet operation as a whole.

In the present research an experimental motor has been designed and built and tests have been conducted using kerosene as the basic fuel. Kerosene was used in both liquid and gelled forms and also with addition of aluminum particles. The paper presents the experimental system in detail and the experimental results.

2 Experimental System

The test facility for the GFRJ motor, shown in Fig. 2, consists of three parts:

- A hot air supply system that includes a vitiated air heater
- Additional systems that ensure ramjet operation, such as the gel fuel supply system, fuel filling system, flushing system with pressurization system, purging system, and ignition system
- A ramjet combustor mounted on the same moving platform with the air heater

2.1 Hot Air Supply System

The hot air supply system consists of the air heater, piping, and control units.

The hot air is fed into two zones of the combustor: Part of the air (primary) is delivered into the main combustion chamber through the injection head to ensure burning of gel fuel at fuel/air ratios higher than stoichiometric. The rest of the air bypasses the main combustion chamber and is delivered to aft-mixing chamber through to assure lean fuel/air ratios. The hot air supply system is shown schematically in Fig. 3.
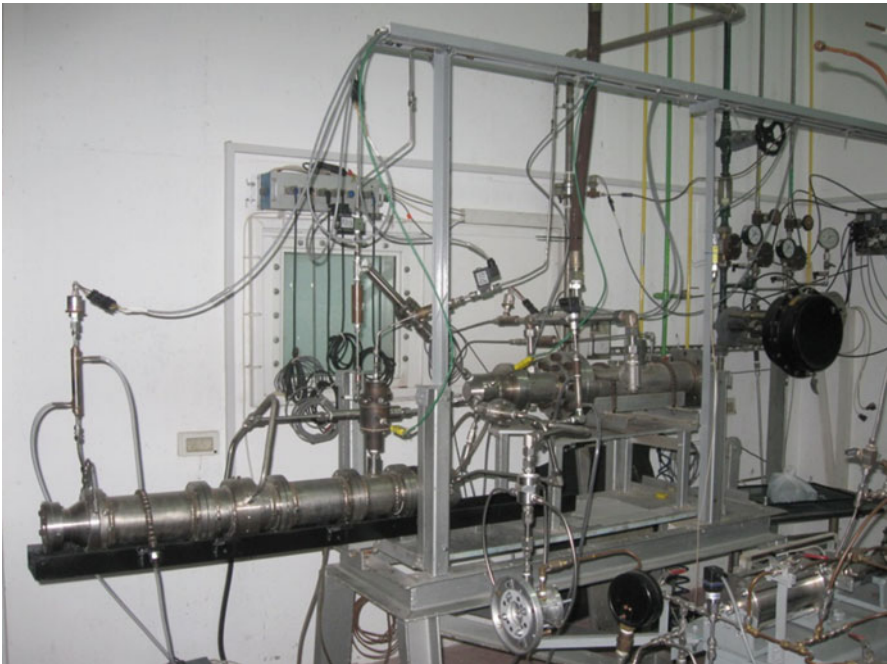
Fig. 2 General view of the test facility
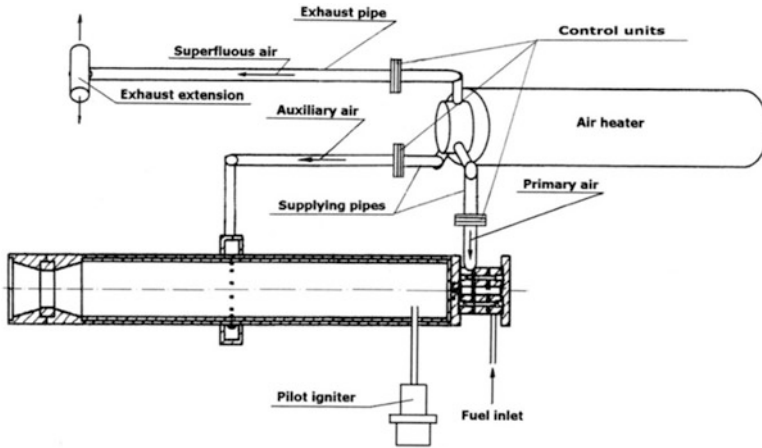
Fig. 3 Schematic of the hot air supply system

Compressed air is provided to the air heater from high pressure tanks via a flexible conduit and from opposite sides, perpendicular to the motor axis. In order to keep the oxygen by mole fraction of the vitiated air as in that of natural air (0.209), oxygen is introduced to the flow prior to entering the heater thus avoiding hazards relating to adding oxygen into hot flow. The regeneratively cooled vitiated air heater burns hydrogen with the oxygen-enriched air in order to achieve inlet total temperature of up to 1500 K, at pressures of up to 50 bar, and mass flow rates of up to 0.5 kg/s to simulate inlet stagnation conditions. The hydrogen-burning vitiated air heater (VAH) was designed by Cohen-Zur and Natan [6] and constructed to stand the demanding goals of very high pressure and temperature as was laid out by the research parameters. The air heater is located on a moving platform, which rests against a thrust transducer located on the test stand.

The drawing of the vitiated air heater is presented in Fig. 4. All lines are made from stainless-steel 316 L pipe of $0.05''$ diameter. The design was based on constructing the VAH almost entirely from stainless steel and on a regenerative cooling/heating configuration, separating the pressure mechanical load-carrying element from the thermal loading.

The VAH is constructed from three major components: outer shell, inner combustion chamber, and nozzle adapter. The outer shell is capable of carrying more than 50 bar gas and is thermally protected by the cold air entering the VAH on the downstream end and moving in the cooling duct backwards, to the upstream end of the VAH. The air enters the VAH perpendicular to its axis to attain a true thrust reading and from opposite sides to cancel side forces.

The entrance pipes are offset from the VAH center to provide the flow with tangential momentum in order to ensure air cooling around thecomplete outer shell
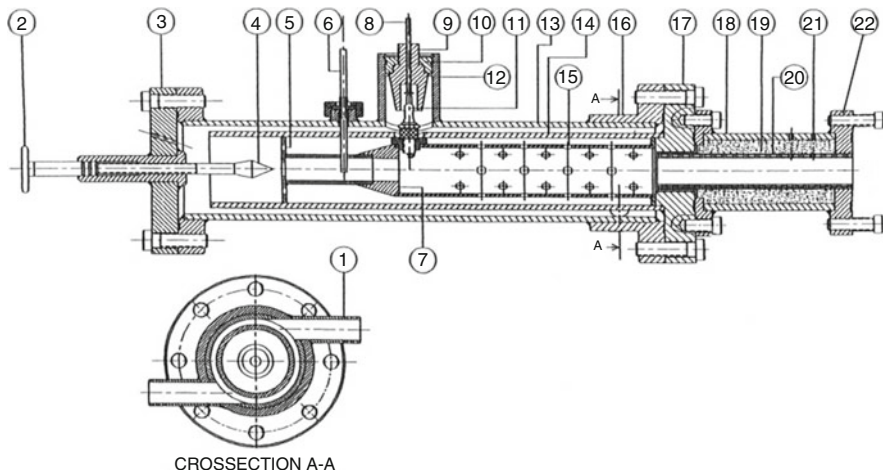
Fig. 4 Schematic of the vitiated air heater

circumference. The inner combustion chamber resembles the classical design, i.e., the air flow is divided into a central and a peripheral flow. Hydrogen is impinged into the central air flow to create a close to stoichiometric mixture and the peripheral air flow joins the combustion products through equally distributed holes on the inner liner.

2.2 Gel Fuel Supply System

The fuel supply system consists of a cylinder with a piston, which moves by an electromechanical driver. It was designed to deliver gel fuel mass flow rates between 5 and 20 g/s to the combustor.

2.3 Ignition System

The fuel/air mixture is ignited using a pilot igniter located on the motor case. The pilot is using air and ethylene to produce a high temperature gaseous flame. It consists of three parts – the injection head, a mixing chamber, and an exit tube joined together by screws. The inner surface of the igniter is protected from the high temperature combustion products by a heat-resistant ceramic material.

2.4 Data Acquisition System

For the ramjet test facility, a modular USB Data Acquisition System of National Instruments Corporation based on NI CompactDAQ is used. This system also is used for test facility control.

2.5 Lab-Scale Ramjet Motor

The lab-scale ramjet combustor is a connected-pipe type and it is designed for the investigation of the combustion process of boron and hydrocarbon gel fuel. The combustor consists of the injection head, the igniter, the combustion chamber, and the nozzle.

The combustion chamber has a 103 mm internal diameter and it is designed to allow variation of its length. The inner surface of the combustor is coated by a special heat-resistant ceramic insulation made by a thermal plasma spray method to protect the outer stainless-steel body from the high temperature combustion products. This ceramic coating allows operating temperatures up to 2000 °C.

The exhaust nozzle has a conventional design with a replaceable nozzle insert, manufactured from various materials. The throat insert has an inlet cone angle of a 60°, a short cylindrical throat, and an exit cone angle of 30°.

An injection head has been designed with internal mixing of air and fuel and is shown in Fig. 5. The mixing of the fuel and the air takes place in a special industrial air atomizing nozzle. The injection head exhibited good atomization with the gel fuel.

In the air bypass ring, located between the case and the nozzle, there are holes for superfluous air blowing up into the combustion chamber.

2.6 Gel Fuels

Several gel fuels were used based on kerosene. The gelling agent used was paraffin which was also used as fuel. Aluminum powder was added at different mass fractions. Another type of gel was investigated using aluminum tristearate (ATS – $C_{54}H_{105}O_6Al$) with some minor addition of HTPB (hydroxyl-terminated polybutadiene – $HO(C_4H_6)_{50}OH$) as gellant; however, this type of gel proves to be unstable and could only last for a couple of days. In some formulations, nickel-coated aluminum (Ni-Al) was used. The aluminum particle size was 20–25 μm. In general the formulations that were used are presented in Table 1.

Fig. 5 Injection head
drawing *1* case, *2* fuel inlet, *3*
bypass air ring, and *4* air
atomizing nozzle
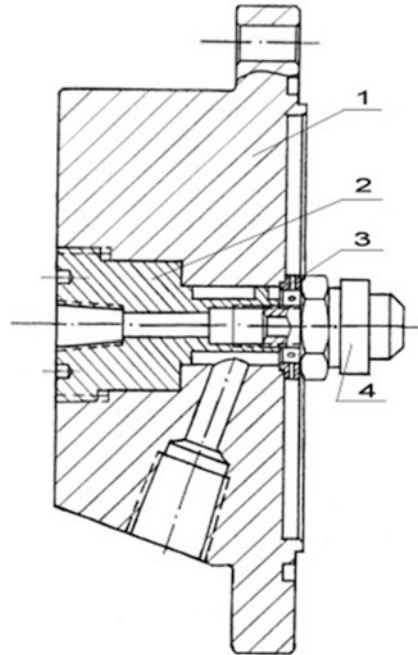
Table 1 Gel types

Mass fraction %	A0	A1	A3	A4	A5	A7	A9	ρ [kg/m³]	Δh_f^0 [MJ/kmol]
Kerosene	94.8	71.4	89.5	84.7	68	65	55	800	−7513
ATS	3.8		3.6	3.4				1070	−3280
HTPB	1.4		1.3	1.3				930	1.17
Paraffin		28.5			27.2	26	22	900	−713
Ni-Al			5.6	10.6		9		2700	0
Al					4.8		23	2700	0

3   Results and Discussion

More than 200 valid firing tests were conducted at various conditions to verify
satisfactory operation of the motor using liquid, gel, and aluminized kerosene gel
as fuels. In 120 tests, aluminum powder was added to the gel fuel. During the
tests, the following parameters were measured: main and bypass air mass flow
rates, fuel mass flow rate, air temperature at the heater exit, motor pressure, and
thrust.
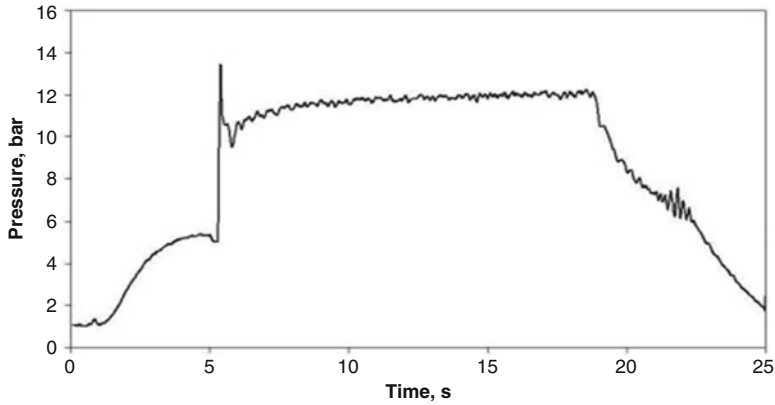
Fig. 6 Pressure time trace
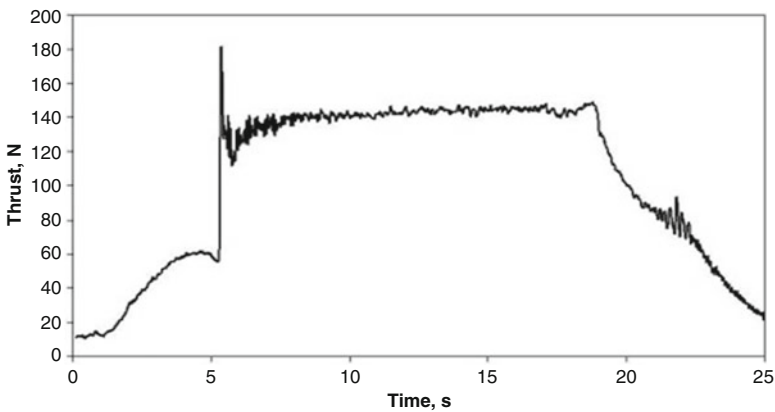
Fig. 7 Thrust time trace

Based on these parameters, the combustor temperature, the fuel-to-air ratio, the equivalence ratios, and the c* efficiency were calculated. The theoretical combustor temperature was calculated using the NASA- Gordon and McBride [7] – CEA thermochemical code.

The pressure and thrust time traces of one of the tests are shown in Figs. 6 and 7, respectively.

3.1 Non-metalized Fuels

The experimental results are presented in Table 2. The table presents for each experiment, the fuel type, the total mass flow rate, $\dot{m}_{total}$, the bypass ratio, BR,

Table 2 Experimental results for non-metalized gel fuel

Test no.	Fuel	$\dot{m}_{total}$ [g/s]	BR	T_a [K]	T_c [K]	p_c [bar]	φ	η_{C*}
L-29	Liquid kerosene	72.2	0.72	930	2230	9.8	1.089	0.919
L-31	Liquid kerosene	72.0	0.72	920	2233	9.8	1.045	0.920
L-32	Liquid kerosene	68.5	0.71	979	2417	9.7	1.078	0.952
L-33	Liquid kerosene	69.1	0.72	972	2390	9.7	1.087	0.948
L-34	Liquid kerosene	68.5	0.71	1011	2400	9.7	1.018	0.951
L-35	Liquid kerosene	68.6	0.72	1043	2365	9.6	1.012	0.945
L-36	Liquid kerosene	68.7	0.71	1100	2311	9.3	0.952	0.930
L-38	Liquid kerosene	68.2	0.71	1056	2272	9.2	0.887	0.931
G-1	Gel-A0	69.1	0.72	836	2101	9.1	1.046	0.899
G-2	Gel-A0	68.7	0.71	885	2059	8.9	1.031	0.890
G-9	Gel-A0	119.7	2.16	907	1418	12.6	0.590	0.838
G-10	Gel-A0	119.7	2.16	893	1416	12.6	0.614	0.833
G-12	Gel-A0	121.4	2.16	825	1353	12.5	0.550	0.834
G-13	Gel-A0	121.6	2.16	854	1347	12.4	0.552	0.832
G-14	Gel-A0	131.4	2.16	847	1283	13.1	0.520	0.833
G-15	Gel-A0	136.5	2.16	861	1325	13.8	0.500	0.850
G-16	Gel-A0	141.6	2.16	852	1316	14.2	0.458	0.873
G-17	Gel-A0	146.6	2.16	838	1280	14.5	0.465	0.855
G-24	Gel-A0	123.6	2.16	809	1252	12.1	0.488	0.824
G-26	Gel-A0	123.9	2.16	830	1250	12.1	0.485	0.829
G-27	Gel-A0	123.6	2.16	861	1291	12.3	0.478	0.842
G-28	Gel-A0	124.2	2.16	899	1527	13.6	0.615	0.865
G-29	Gel-A0	114.1	2.16	836	1503	12.4	0.662	0.829
G-30	Gel-A0	114.1	2.16	909	1648	13.0	0.741	0.846
G-31	Gel-A0	114.0	2.16	934	1750	13.5	0.771	0.870
G-32	Gel-A0	113.7	2.16	976	1879	14.0	0.798	0.894
G-33	Gel-A0	102.1	2.17	943	2017	13.1	0.912	0.895
G-34	Gel-A0	90.3	2.16	908	2010	11.6	1.067	0.872

the inlet and bypass air temperature, T_a, the experimental combustion chamber temperature, T_c, the combustion chamber pressure, p_c, the equivalence ratio, φ, and the c* combustion efficiency, η_{C*}.

The experimental combustion chamber temperature, T_c, was calculated based on the measured combustion chamber pressure, p_c.

The c* efficiency, η_{C*}, vs. the equivalence ratio of the liquid kerosene tests is presented in Fig. 8. It can be seen that the combustion efficiency values are quite high, between 92 and 95 %.

The combustion chamber temperature vs. the equivalence ratio for the gelled kerosene (both A0 and A1 gels) is presented in Fig. 9. The temperature varied between 1300 K at the fuel lean side to 2100 K near stoichiometric conditions. The combustion temperature for both gels was found to be lower than for liquid kerosene.
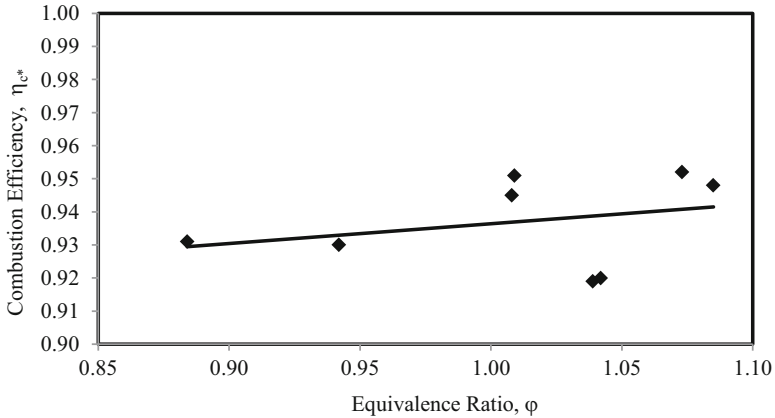
Fig. 8 The combustion efficiency of liquid kerosene for various equivalence ratios
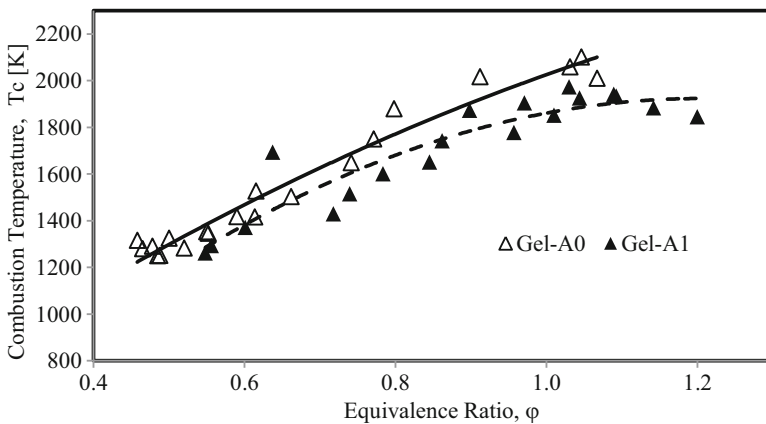
Fig. 9 The combustion temperature of gelled kerosene for various equivalence ratios

The c* efficiency vs. the equivalence ratios of the gelled kerosene tests is presented in Fig. 10. It can be seen that the combustion efficiency values are much lower in comparison to liquid kerosene, varying between 83 and 90 %, resulting from the lower combustion temperatures. It seems that gels do not perform as well as liquid fuels; however, this result can be improved by choosing adequate gellants, obtaining better atomizers, and optimizing the combustor geometry.

3.2 Aluminized Fuels

The experimental results of the aluminizedgel fuels are presented in Table 3.

The average and maximum values of the experimental combustion temperature and c* efficiency of all tests are shown in Table 4.
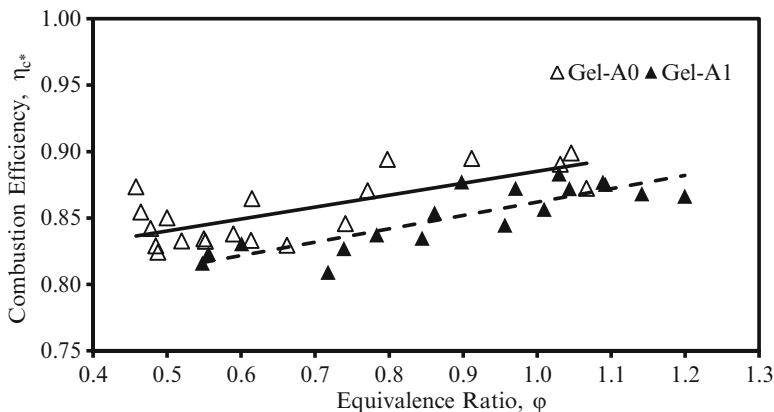
Fig. 10 The combustion efficiency of gelled kerosene for various equivalence ratios

Table 3 Experimental results for aluminized gel fuels A3, A4, A5, A7, and A9

Test no.	Fuel	$\dot{m}_{total}$ [g/s]	BR	T_a [K]	T_c [K]	p_c [bar]	φ	η_{C^*}
G-81	Gel-A3	110.2	2.16	732	1412	6.4	0.637	0.816
G-82	Gel-A3	110.6	2.16	737	1305	6.2	0.697	0.767
G-83	Gel-A3	110.4	2.17	752	1503	6.5	0.750	0.809
G-84	Gel-A3	110.5	2.16	772	1465	6.8	0.814	0.786
G-85	Gel-A3	110.7	2.17	761	1571	6.9	0.866	0.802
G-86	Gel-A3	110.6	2.16	770	1665	7.2	0.935	0.815
G-87	Gel-A3	111.2	2.17	741	1683	7.3	1.000	0.813
G-88	Gel-A3	111.5	2.16	759	1800	7.6	1.008	0.841
G-89	Gel-A4	111.7	2.17	712	1115	5.8	0.649	0.717
G-90	Gel-A4	112.0	2.16	732	1228	6.2	0.721	0.734
G-91	Gel-A4	111.8	2.16	751	1311	6.5	0.790	0.743
G-92	Gel-A4	111.9	2.16	765	1405	6.7	0.856	0.756
G-93	Gel-A4	111.8	2.16	775	1487	6.9	0.890	0.763
G-94	Gel-A4	112.7	2.16	745	1545	7.1	0.974	0.774
G-95	Gel-A4	112.3	2.16	770	1611	8.3	1.017	0.791
G-96	Gel-A5	93.3	0.6	780	1538	5.6	0.742	0.814
G-97	Gel-A5	92.6	0.6	804	1586	5.6	0.863	0.803
G-98	Gel-A5	89.6	0.6	506	1737	5.7	0.980	0.847
G-99	Gel-A5	93.1	0.6	779	1642	5.8	0.920	0.808
G-100	Gel-A5	93.2	0.6	825	1724	6.0	1.009	0.819
G-101	Gel-A5	93.1	0.6	822	1678	5.9	0.976	0.811
G-102	Gel-A5	93.8	0.6	880	1812	6.2	1.155	0.842
G-117	Gel-A7	93.9	0.59	931	1820	11.4	0.759	0.879
G-118	Gel-A7	93.9	0.59	909	1495	10.4	0.842	0.779

(continued)

Table 3 (continued)

Test no.	Fuel	$\dot{m}_{total}$ [g/s]	BR	T_a [K]	T_c [K]	p_c [bar]	φ	η_{C*}
G-119	Gel-A7	93.8	0.61	934	1576	10.7	0.890	0.791
G-120	Gel-A7	93.6	0.61	861	1653	11.0	0.983	0.799
G-121	Gel-A7	93.6	0.59	889	1717	11.3	1.017	0.812
G-122	Gel-A7	93.6	0.59	832	1784	11.5	1.121	0.827
G-123	Gel-A7	93.7	0.59	899	1849	11.9	1.157	0.843
G-124	Gel-A7	102.9	0.61	880	1869	13.1	1.162	0.848
G-126	Gel-A7	113.1	0.59	831	1826	14.1	1.095	0.836
G-127	Gel-A7	91.0	0.59	884	1368	9.6	0.815	0.750
G-128	Gel-A7	91.2	0.59	920	1735	11.1	1.119	0.815
G-129	Gel-A7	91.2	0.59	900	1818	11.5	1.247	0.844
G-130	Gel-A7	90.7	0.59	929	1753	11.6	1.363	0.842
G-131	Gel-A7	90.2	0.59	944	1832	11.6	1.439	0.870
G-132	Gel-A7	101.2	0.59	875	1786	12.7	1.339	0.847
G-133	Gel-A7	100.4	0.59	899	1805	12.8	1.427	0.862
G-134	Gel-A7	110.5	0.59	915	1972	14.5	1.261	0.880
G-135	Gel-A7	120.0	0.59	896	1990	15.7	1.130	0.873
G-136	Gel-A7	121.4	0.59	787	1939	15.8	1.240	0.881
G-137	Gel-A7	121.2	0.59	829	1961	15.9	1.270	0.889
G-139	Gel-A7	56.9	0	870	1624	6.8	1.055	0.788
G-140	Gel-A7	56.9	0	899	1708	7.1	1.284	0.822
G-141	Gel-A7	57.0	0	897	2188	8.0	1.175	0.919
G-142	Gel-A7	56.4	0	903	1688	7.0	1.305	0.819
G-143	Gel-A7	56.3	0	923	1691	7.1	1.605	0.855
G-144	Gel-A7	56.4	0	892	1674	7.0	1.432	0.831
G-145	Gel-A7	56.2	0	918	1660	7.1	1.526	0.839
G-146	Gel-A7	56.4	0	936	1603	7.0	1.567	0.830
G-147	Gel-A7	56.1	0	953	1554	6.9	1.741	0.836
G-148	Gel-A7	75.7	0	958	1755	9.6	1.261	0.831
G-149	Gel-A7	76.0	0	957	1743	9.6	1.301	0.832
G-150	Gel-A7	82.6	0	864	1841	10.4	1.070	0.839
G-151	Gel-A7	82.7	0	872	1771	10.2	1.042	0.823
G-152	Gel-A7	83.0	0	877	1525	9.6	0.943	0.771
G-153	Gel-A7	112.7	0.61	918	1249	11.3	0.632	0.632
G-154	Gel-A7	112.8	0.59	932	1255	11.4	0.739	0.739
G-155	Gel-A7	112.8	0.59	923	1359	11.9	0.771	0.771
G-156	Gel-A7	112.8	0.59	931	1394	12.2	0.964	0.964
G-157	Gel-A7	112.8	0.59	951	1498	12.6	0.927	0.927
G-159	Gel-A7	114.8	0.59	865	1741	13.9	0.991	0.991
G-160	Gel-A7	114.9	0.59	870	1586	13.5	1.098	1.098
G-161	Gel-A7	114.4	0.59	919	1712	13.9	1.197	1.197
G-162	Gel-A7	114.1	0.61	895	1726	14.1	1.349	1.349

(continued)

Table 3 (continued)

Test no.	Fuel	$\dot{m}_{total}$ [g/s]	BR	T_a [K]	T_c [K]	p_c [bar]	φ	η_{C*}
G-163	Gel-A7	114.8	0.59	906	1800	14.5	1.406	1.406
G-164	Gel-A7	114.8	0.59	941	1718	14.4	1.632	1.632
G-165	Gel-A7	114.8	0.59	943	1674	14.2	1.635	1.635
G-166	Gel-A7	103.2	0.33	1015	1587	12.2	1.288	0.777
G-167	Gel-A7	103.2	0.33	1016	1606	12.3	1.312	0.785
G-168	Gel-A7	103.3	0.33	1055	1642	12.5	1.418	0.805
G-169	Gel-A7	103.2	0.33	1072	1716	12.7	1.292	0.806
G-170	Gel-A7	103.8	0.45	955	1706	12.7	1.268	0.803
G-171	Gel-A7	103.8	0.45	964	1730	12.8	1.287	0.810
G-172	Gel-A7	103.8	0.45	991	1771	13.0	1.289	0.820
G-173	Gel-A7	103.7	0.45	1003	1772	13.0	1.387	0.830
G-174	Gel-A7	105.2	0.79	877	1813	13.4	1.431	0.846
G-175	Gel-A7	105.1	0.79	900	1885	13.5	1.250	0.842
G-176	Gel-A7	105.4	0.79	918	1876	13.7	1.516	0.870
G-177	Gel-A7	105.1	0.79	928	1939	13.9	1.541	0.887
G-178	Gel-A7	98.4	1	782	1692	12.1	1.431	0.817
G-179	Gel-A7	98.4	1	815	1690	12.1	1.423	0.817
G-180	Gel-A7	97.8	1	857	1780	12.3	1.382	0.833
G-181	Gel-A7	98.0	1	865	1715	12.3	1.613	0.844
G-235	Gel-A9	123.9	0.6	846	1879	15.3	0.745	0.888
G-236	Gel-A9	123.3	0.6	808	1419	12.9	0.570	0.828
G-237	Gel-A9	122.1	0.6	755	1373	12.7	0.642	0.782
G-238	Gel-A9	121.9	0.6	754	1239	12.1	0.680	0.732
G-239	Gel-A9	122.2	0.6	737	1306	12.4	0.726	0.745
G-240	Gel-A9	121.3	0.6	765	1399	12.9	0.810	0.751
G-241	Gel-A9	121.9	0.6	776	1406	13.3	0.879	0.742
G-242	Gel-A9	121.9	0.6	758	1408	13.4	0.926	0.734
G-243	Gel-A9	122.6	0.6	751	1430	13.7	0.990	0.734
G-244	Gel-A9	122.7	0.6	767	1467	14.0	1.101	0.739
G-245	Gel-A9	123.0	0.6	790	1563	14.6	1.199	0.764
G-246	Gel-A9	123.4	0.6	796	1626	15.0	1.190	0.780
G-247	Gel-A9	123.5	0.6	814	1668	15.3	1.279	0.795
G-248	Gel-A9	123.6	0.6	779	1659	15.4	1.358	0.802
G-249	Gel-A9	123.9	0.6	799	1730	15.8	1.403	0.822
G-250	Gel-A9	123.5	0.6	816	1755	16.0	1.471	0.834
G-251	Gel-A9	123.6	0.6	765	1255	12.1	0.573	0.789
G-252	Gel-A9	123.9	0.6	784	1378	12.9	0.758	0.772
G-253	Gel-A9	123.6	0.6	789	1359	12.8	0.849	0.754

Table 4 Average and maximum values of the combustion temperature and efficiency

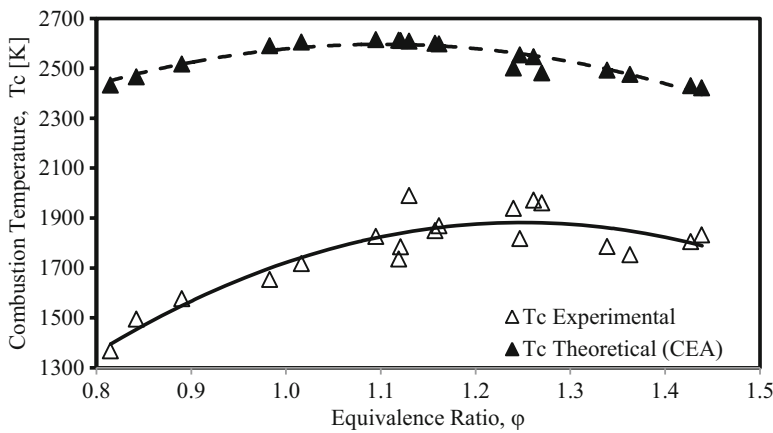| Fuel type	Tc [K]		η_{c*} [%]		Number of tests
	Max	Average	Max	Average	
Liquid kerosene	2394	2342	95	95	8
Gel-A0	2114	1788	90	86	18
Gel-A1	1904	1708	88	85	19
Gel-A3	1800	1550	84	81	8
Gel-A4	1611	1386	79	75	7
Gel-A5	1813	1673	85	82	7
Gel-A7	1972	1775	89	84	19
Gel-A9	1754	1471	83	77	19

Fig. 11 Theoretical and experimental combustion temperatures vs. equivalence ratio for Gel-A7

The combustion efficiency of the aluminized gels was found to be lower in comparison to non-metalized gel fuels. The reason for this lies in the lower combustion temperature because of incomplete combustion. The theoretical and experimental combustion chamber temperatures for Gel-A7 are presented in Fig. 11.

In general, the tests presented in the various figures were chosen from the much larger number of experimental data on the basis of similar test parameters, such as bypass ratio, air mass flow rate, inlet temperature, etc.

The c* efficiencies vs. the equivalence ratio of the aluminized gelled kerosene are presented in Fig. 12 for fuels Gel-A3, Gel-A4, Gel-A5, and Gel-A7. It can be seen that the combustion efficiency values are much lower in comparison to non-metalized kerosene, liquid and gelled, varying between 72 and 85 %. It is quite obvious that increasing the aluminum content results in decreasing the combustion efficiency, because of incomplete combustion of the particles.

It has to be noted that increasing the pressure in the combustion chamber resulted (done by decreasing the nozzle throat diameter) in increasing the combustion
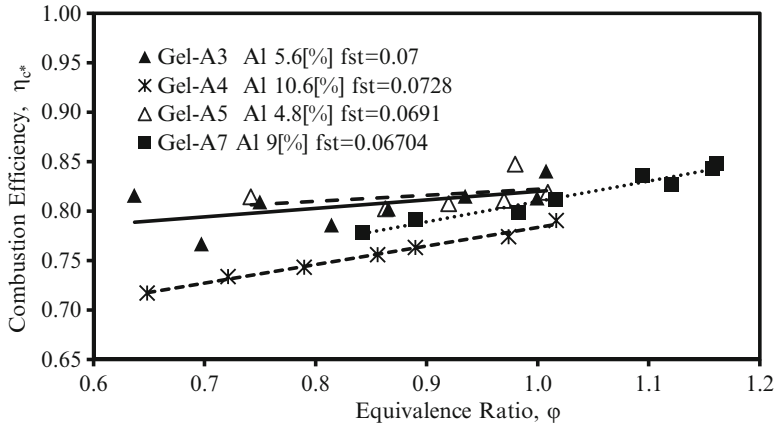
Fig. 12 The combustion efficiency of gels A3, A4, A5, and A7 for various fuel-to-air ratios

Fig. 13 Motor picture during a firing test

efficiency. For a constant mass flow rate, the pressure increase resulted in decreasing the flow velocity, which allowed an increase in the particle residence time. Consequently, this resulted in the increase in combustion efficiency.

Some tests were conducted using a longer combustion chamber. In principle the combustion efficiency should have been increased; however, in reality the opposite phenomenon was observed. The reason is that though the residence time increases, the heat losses to the walls and the environment also increase. In a real motor the insulation should be modified.

From all the aluminized gel fuels, Gel-A7 exhibited the highest combustion temperature and efficiency; however, we have to take into account that the pressure was higher.

In the frame of the parametric investigation the effect of bypass ratio for different gel types was evaluated. It seems that combustion becomes more intense after the bypass air injection as shown in the motor photograph during firing in Fig. 13. The intensity of the flame can be identified by the red color in the different motor parts.

The optimal bypass ratio value was found to be approximately 0.7 for almost all gels. The combustion efficiency as a function of bypass ratio, BR, for Gel-A7 is presented in Fig. 14.
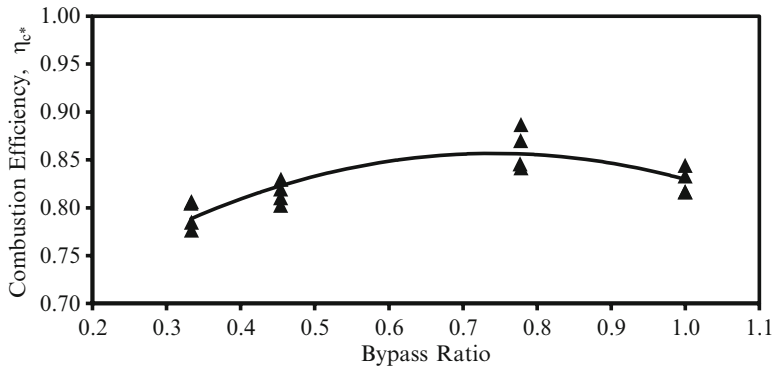
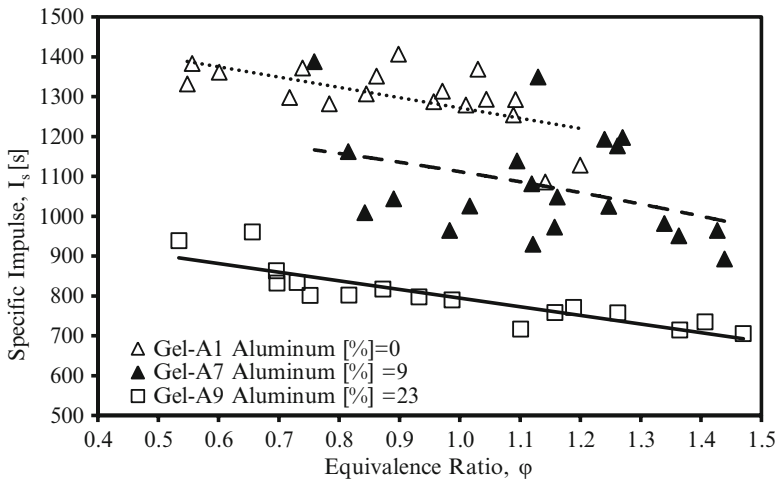**Fig. 14** Combustion efficiency vs. bypass ratio for Gel-A7

Fig. 15 Specific impulse of a ramjet missile using various gel fuel types

Based on the experimental results, the specific impulse, I_s, and the density-specific impulse, $\rho \cdot I_s$, of a ramjet missile flying at sea level at $M_a = 2.6$ for an expansion ratio $A_e/A_t = 3.37$ were estimated for the hydrocarbon gel fuel, Gel-A1, and the aluminized gel fuels, Gel-A7 and Gel-A9. The I_s and the $\rho \cdot I_s$ results are shown in Figs. 15 and 16, respectively.

These results indicate that the use of aluminum is not always beneficial. In some cases, especially if the residence times, thus combustion efficiency, are high, the density impulse may be high; however, specific impulse decreases with increasing the aluminum content.
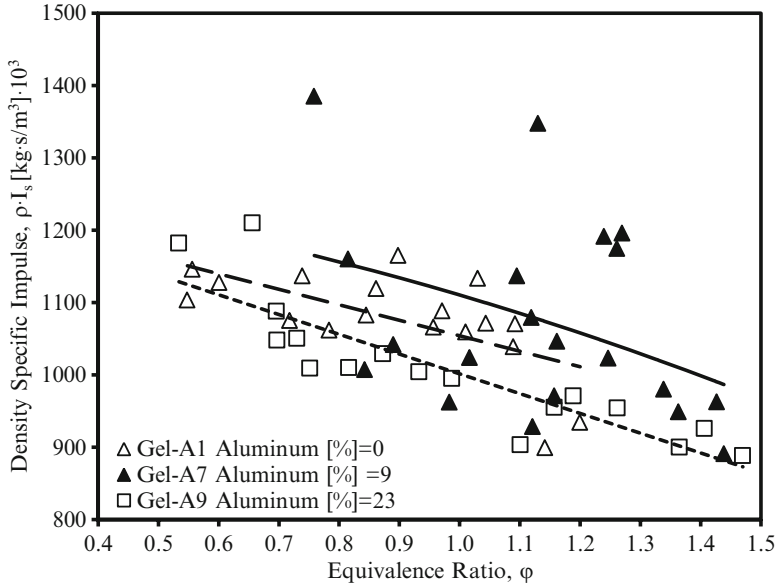
Fig. 16 Density impulse of a ramjet missile using various gel fuel types

4   Conclusion

The feasibility of an aluminized gel fuel ramjet has been examined using a lab-scale motor. A test facility and a motor have been designed and built to investigate atomization, ignition, and combustion processes of a gel hydrocarbon fuel, with and without aluminum-based additives, as well as to check the ramjet operation and performance. Gel-A7 was chosen in order to investigate various parameters in the combustor operation. Maximum combustion temperature and efficiency of 2000 K and 90 %, respectively, were achieved at $\varphi \approx 1.175$ using Gel-A7, with nickel-coated aluminum. In general, the use of aluminum as an additive did not promote the engine performance. The adequate bypass ratio for Gel-A7 was found to be $\sim$0.7. Elongating the engine does not necessarily have a positive influence on combustion efficiency, apparently due to heat losses.

References

1. Fry RS (2004) A century of ramjet propulsion technology evolution. J Propuls Power 20(1): 27–58
2. Hewitt PW (2008) Status of ramjet programs in the United States. AIAA paper 2008–5265
3. Besser H (2008) History of ducted rocket development at Bayern-Chemie. AIAA paper 2008–5261

4. Natan B, Rahimi S (2002) The status of gel propellants in year 2000. Int J Energetic Mater Chem Propuls 5(1–6):172–194
5. Haddad A et al (2011) The performance of a boron loaded gel fuel ramjet. In: Deluca LT et al (eds) Progress in propulsion physics, vol 2, EUCASS advances in aerospace sciences book series. Torus Press, Moscow, pp 549–568
6. Cohen-Zur A, Natan B (1998) Experimental investigation of a supersonic combustion solid fuel ramjet. J Propuls Power 14(6):880–889
7. Gordon S, McBride BJ (1996) Computer program for calculation of complex chemical equilibrium compositions and applications (CEA), NASA RP-1311. Glenn Research Center, Cleveland

Part IV
Solid Rocket Propulsion

Formulation Factors and Properties of Condensed Combustion Products

Valery A. Babuk

Abstract A review of state-of-the-art experimental results concerning the influence of various formulation factors on the properties of the condensed combustion products (agglomerates and smoke oxide particles) formed at the burning propellant surface is provided. The influence of the properties of binder, oxidizer, and metal fuel is investigated. Analysis is carried out with reference to the following components: active and inactive binder, ammonium perchlorate, ammonium nitrate (pure and phase stabilized), ammonium dinitramide, cyclotrimethylenetetranitramine, micro-sized and nano-sized aluminum, aluminum with a polymeric, and refractory covering. The proposed analysis is based on the formulated general physical picture of the formation of the condensed products. It is shown that the properties of the condensed products (in terms of size, chemical composition, and internal structure) depend on properties of the burning propellant surface layer, which in turn depend on the properties of the propellant components. The importance of formation of a surface layer and the properties of such structures as a skeleton layer is underlined. The results of these research activities open the possibility to take reasonable formulation decisions when creating new solid propellants.

Nomenclature

ADN	Ammonium dinitramide
AN	Ammonium nitrate
AP	Ammonium perchlorate
APPRET	$Cl_2Si[OCH_2(CF_2\text{-}CF_2)_2H_2]_2$
CCP	Condensed combustion products
CL-20	Hexanitrohexaazaisowurtzitane
CS	Carbonaceous skeleton
FCOS	Fluorine-containing organic substance
HMX	Cyclotrimethylenetetranitramine

V.A. Babuk (✉)
Baltic State Technical University (BSTU), St.-Petersburg 190005, Russia
e-mail: babuk@peterlink.ru

319

HNF	Hydrazinium nitroformate
P	Pressure
PMFA	Polymethylfluoroacrylate
SL	Skeleton layer
SOP	Smoke oxide particles

1 Introduction

Metal additives (normally, aluminum) are an indispensable component of *high-energy* solid propellants. A consequence of the usage of this component is the formation of *condensed combustion products* (CCP). The properties of these products have a critical impact on the quality of propellants, i.e., on the ability of propellants to efficiently optimize their functions in the motor. They define the rate of slag formation in the chamber, the rate of interaction of combustion products with motor elements, and also the level of losses of specific impulse. Sometimes the properties of CCP prevent the possibility of use of possible propellant compositions.

The formation of CCP at the surface of burning propellants is one of the features of the burning process. It is obvious that the propellant composition makes a defining impact on the properties of these products. A number of experimental studies, which are devoted to the study of the interrelation of formulation factors of propellant and the characteristics of CCP, have been carried out.

It is possible to quote results by Yury. V. Frolov [1–3, etc.], O. Glotov [4–7, etc.], E. Price [8–12], Luigi T. DeLuca [13–16]. Similar works were carried out in BSTU [17–27]. The distinctive features of these works were the following:

1. The analysis of all the set of the particles delivered from a surface of burning propellant in a range of the sizes from tens of nanometers to that of a thousand micrometers.
2. Definition not only of the size of particles but also their quantity in a flow of combustion products and also the chemical composition and structure parameters.

Researches were based on the following assumption: all condensed products consist of agglomerates and smoke oxide particles (SOP). Agglomerates are products of the merger of the condensed products in the surface layer of propellant. The size of agglomerates can reach hundreds and even thousands of micrometers. Smoke oxide particles are products of the combustion of metal in the surface layer of the propellant and in the gas phase at a burning surface. As a rule, the size of these particles is less than 1 μm. It is considered that agglomerates are particles with the size exceeding the maximum size of the initial particles of metal.

For quantitative description of CCP the following characteristics were used:

- $f_m(D)$ – mass function of agglomerate size distribution density
- $f_m(d)$ – mass function of smoke oxide particle size distribution density
- D_{43} – mass average diameter of agglomerates

- d_{43} – mass average diameter of smoke oxide particles
- $Z_m{}^a$ – fraction of original metal in the propellant used to form the agglomerates as a whole
- Z_m – fraction of unburned metal in agglomerates relative to original metal in propellant
- $Z_m{}^{ox}$ – fraction of original metal in the propellant used to form oxide in the agglomerates
- η – mass fraction of oxide in agglomerates
- $Z_m{}^{sop}$ – fraction of original metal in the propellant used to form smoke oxide particles

As qualitative information, we used information obtained by analyzing the photographs of collected agglomerates, their microsections, films of burning, as well as combustion residues on the bases.

The present work is a devoted *generalization* of the experimental material obtained in BSTU for the definition of character of influence formulation factors on the process of the formation CCP at a surface of burning propellant.

Let's consider a physical picture of CCP formation at a surface of the burning propellant formulated by now.

2 Physical Picture of Formation of CCP at the Surface of the Burning Propellant

It is expedient to consider separately the physical nature of the formation of agglomerates and SOP.

2.1 Formation of Agglomerates

It is shown that a necessary condition for the agglomeration process is the formation of a skeleton layer (SL) [17, 18].

The skeleton layer is a gas-permeable three-dimensional structure consisting mainly of the metal and its oxide, as well as thermostable carbonic elements, and comprising the top portion of the surface layer (Fig. 1). The specified structure arises, as a rule, on propellant burning. It provides coherence of particles of initial metal and the possibility of a delay of agglomerating particles in a surface layer, i.e., possibility of *realization of agglomeration process*. It is shown that a necessary condition of SL formation is the formation of a carbonaceous skeleton (CS) [18, 21]. Formation of this structure, in turn, is connected with the conditions of decomposition of the polymeric binder.

The completeness of transformations at decomposition increases, i.e., the probability of formation CS falls, if the concentration of oxidizing substances in the field
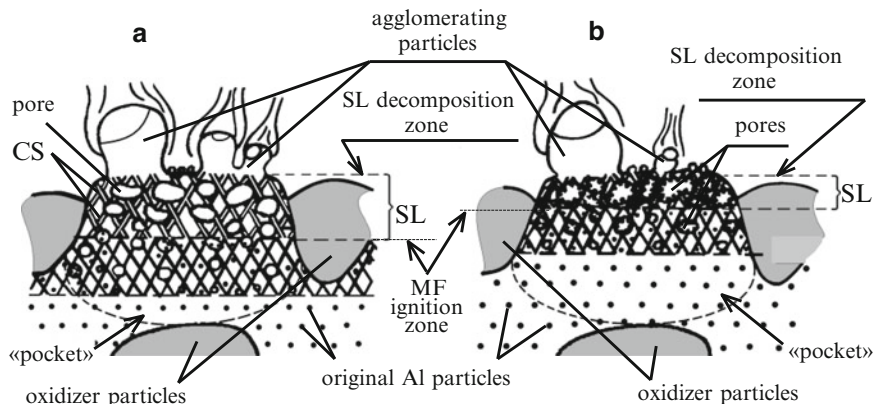
Fig. 1 Sketch of skeleton layer in combustion of propellants of classes *A* (**a**) and *B* (**b**) (*SL* skeleton layer, *CS* carbon skeleton, *MF* metal fuel) [18]

of decomposition increases. These substances can form part of the binder (active binder) and to appear owing to diffusion from the area of particles decomposition of the coarse fraction of the oxidizer. Thus, it is possible to specify the factors promoting disappearance at burning carbonaceous skeleton and, hence, a skeleton layer: presence of an active binder or pseudo-active binder (the presence in the binder of fine oxidizer fractions) and also decomposition of narrow layers of binder between large oxidizer particles.

Such a concept as "inter-pocket bridge" – binder layers between oxidizer particles within which limits of SL are not formed – has been introduced. If oxidizer particles in the surface layer lose their individuality, for example, owing to rather early fusion, the specified layers cease to be "inter-pocket bridges."

The properties of SL define the properties of the formed agglomerates. These properties depend on the behavior character of the metal fuel and the carbonaceous elements in the surface layer. Two classes of propellants exist depending on the difference between the temperature of metal ignition (T_{igm}) and the temperature of decomposition of carbonaceous elements (T_{dc}) have been introduced: **A** and **B**. Condition $T_{igm} < T_{dc}$ is for propellants class **A** and for propellants class **B** – $T_{igm} > T_{dc}$. For propellants of **A** class, the upper SL is the carbonaceous skeleton, with pore-filled liquid by metal and its oxide (Fig. 2). For propellants of **B** class, the upper SL is the metal skeleton consisting of initial particles of metal (Fig. 3) (Photos in Figs. 2 and 3 are obtained by studying combustion residues of propellant using special collecting bases.) It is obvious that the properties of agglomerates of burning propellants in the specified classes vary. For propellants in **A** class, the fraction of the metal, which is burning down in a heterogeneous mode, increases such that it increases the oxide in agglomerates. Besides, the level of the adhesive forces keeping agglomerating particles in the upper SL increases, a consequence of that, as a rule, produces growth of the size of agglomerates.
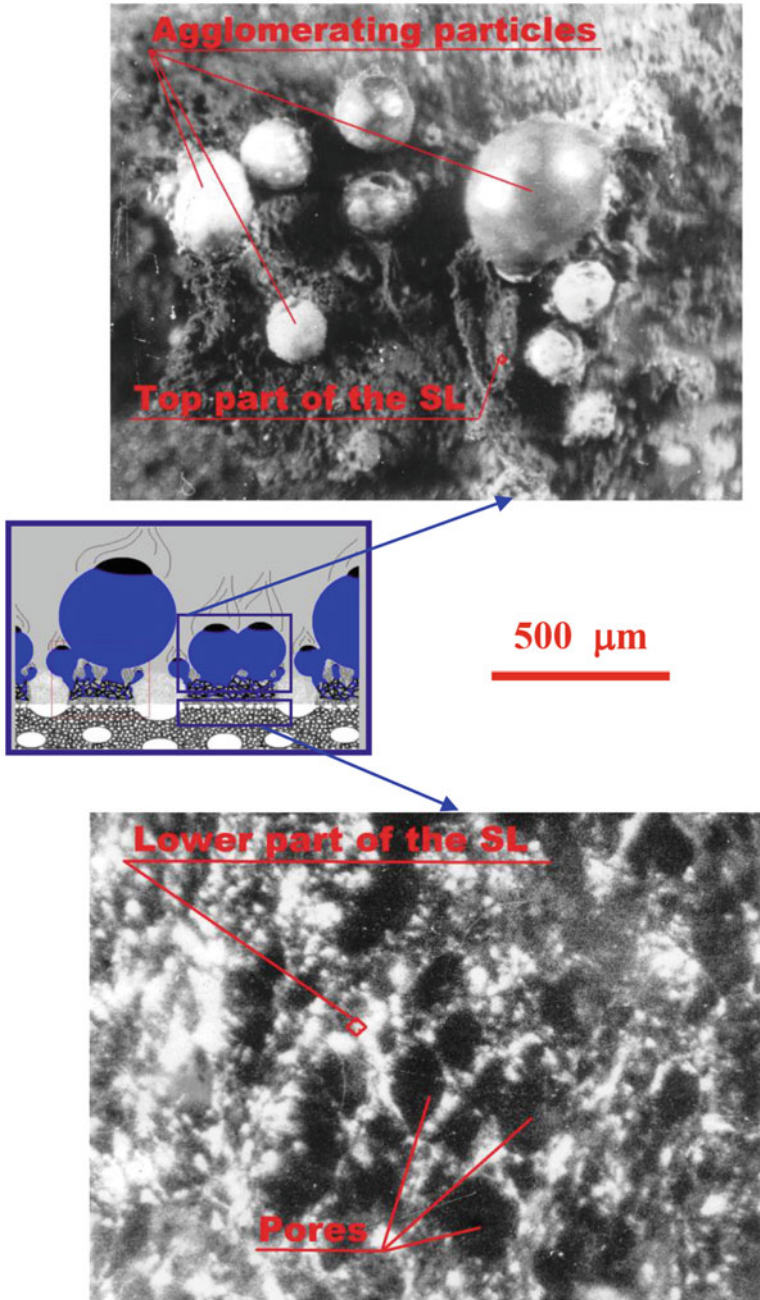
Fig. 2 *Top* and *bottom* of the SL of propellant **A** class (AN -based propellant, $P = 6.0$ MPa [20])
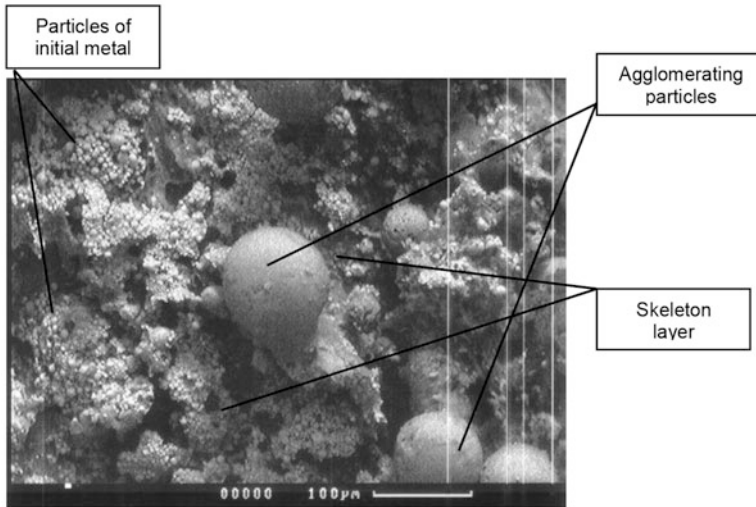
Fig. 3 *Top* of the SL of propellant **B** class (active binder – based propellant, $P = 0.8$ MPa [21])
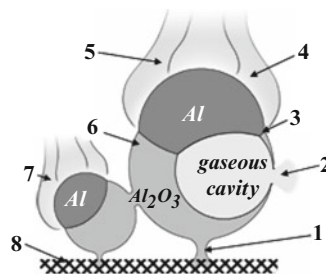

Fig. 4 Scheme of evolution process of agglomerating particles on propellant surface (*1* connection with SL, *2* collapsing of cavity, *3* chemical interaction between *Al* and Al_2O_3, *4* burning of *Al* in gas phase, *5* "tail" of SOP, *6* internal structure, *7* merging of particles, *8* upper part of SL)

The separation of a particle from the top surface of skeleton layer is defined by the behavior laws of drops on a surface under the conditions of action of external forces [28]. Each formed agglomerate is a result of the merging of the condensed products within one "pocket", if the "pocket" mechanism of agglomeration is realized. If the "inter-pocket" mechanism of agglomeration is realized, then each agglomerate is a result of the merging of the condensed products of several "pockets." On the contrary, at conditions mechanism "pre-pocket", each "pocket" is a source for the formation of several agglomerates. Laws of change size of agglomerates of depending on pressure at realization of these mechanisms are various [18].

One of the processes influencing the characteristics of agglomerates is the evolution of agglomerating particles on the top surface of a surface layer. Examining the phenomena comprising the evolution process (Fig. 4) [29].
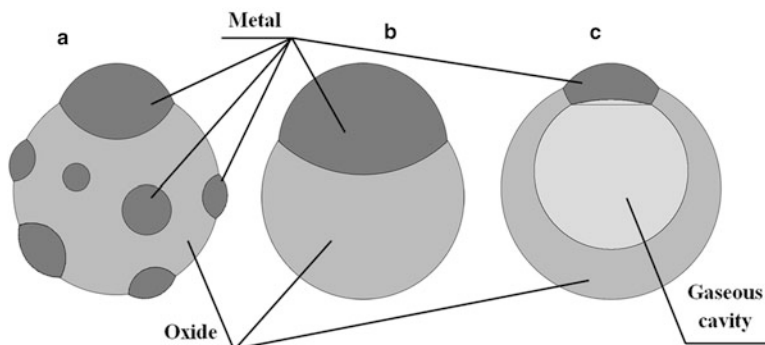
Fig. 5 Schematic illustration of observed agglomerate types: (**a**) "matrix" agglomerate, (**b**) agglomerate with "cap" oxide, (**c**) "hollow" agglomerate

(A) *Gas-phase combustion of metal*

Combustion in that mode results in formation of SOP and reduction of metal content in agglomerating particles and later on in agglomerates.

(B) *Chemical interaction condensed of Al and Al$_2$O$_3$*

A chemical interaction of condensed metal and oxide with formation of gaseous products is possible. Realization of that process and its rate depend on particle temperature which in its turn depends on relation between heat release in burning and heat loss from the particle into environment. Realization of this interaction can lead to formation of gas bubbles and removal of gaseous products of interaction.

(C) *Change of particle structure*

Changes in particle structure are connected with changes in size and fraction of metal and oxide drops, as well as gas bubble.

(D) *Feeding and merging of agglomerating particles*

Connection of agglomerating particle with the SL leads to enlargement of the particles at the expense of taking up SL "substance" and the merging of adjacent particles. Obviously the particle enlargement depends on the duration of the evolution process.

Evolution process makes essential impact on the structure of agglomerates. The basic types of structure most often fixed by this time are shown on Fig. 5.

2.2 Formation of Smoke Oxide Particles

Two mechanisms of SOP formation exist [23].

First, SOP formation is carried out at evolution of agglomerating particles (Fig. 6). The size of these particles depends on the rate of the processes of condensation and coagulation, which depend in turn on the size of the agglomerating

Fig. 6 Burning metal of agglomerating particles in gas-phase mode on a surface of the skeleton layer (AN – based propellant, $P = 3.0$ MPa [24])
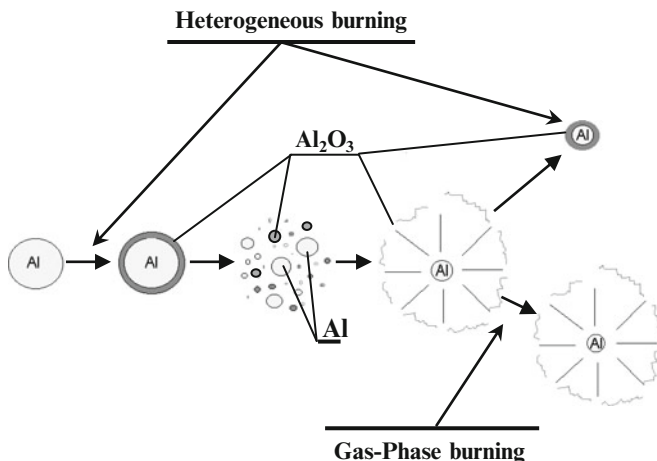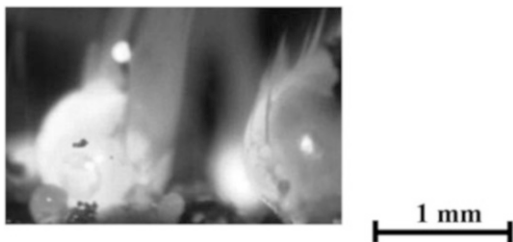

Fig. 7 Scheme of combustion non-agglomerating metal

particles and properties of a flowing round gas flow. The size of SOP increases with the increase in the size of agglomerating particles and the reduction of the speed of a gas flow and vice versa. The SOP quantity is formed in a similar way as SOP depends on the fraction of metal participating in agglomeration and the time of that evolution process.

Secondly, the formation of SOP is carried out on the combustion of the metal fuel not participating in the agglomeration (Fig. 7).

It is quite obvious that the first stage of combustion process for any particle, including the particles of rather small size, is heterogeneous burning. A feature of this mode is the diffusion of oxidizing gases to the surface of metal particles and interaction with the formation of condensed oxide. The metal particle is covered by a continuous liquid oxide film at the last stage of heterogeneous burning. This film is broken by metal steams when the particle temperature reaches boiling temperatures.

Heterogeneous burning of the non-agglomerating metal particles results in their fragmentation in most cases. This process produces many oxide and metal particles. The size of the non-agglomerating particles and of the droplets produced in their fragmentation is so small that the effect of particle size on the chemical potential

of metal and consequently on its boiling point is critical. Therefore the droplets after the fragmentation should be superheated. This leads to intensive evaporation of the metal from droplets and interaction of the vapor with oxidizing gases in the environment, i.e., gas-phase burning of the droplets goes on in nonequilibrium mode. We assume also that, with a high degree of nonequilibrium, fast evaporation of the droplets can lead to a drop in its temperature and, as consequence, a return to the heterogeneous mode of burning.

Thus, the SOP formation in the combustion of non-agglomerating metal is possible in two modes: heterogeneous and gas phase.

It is obvious that the characteristics of SOP depend on the properties of a surface layer. In reality, the size of these particles depends on the fraction of the metal participating in agglomeration, the size of agglomerating particles, and the ignition temperature of non-agglomerating metal particles, i.e., parameters which are connected with the properties of the surface layer.

3 Influence of Various Factors on Properties of CCP

Let's consider the influence on CCP, characteristics of the properties of the basic components of solid propellants: the oxidizer, binder, and metal fuel.

3.1 *Kind and Size of Oxidizer*

The required basic definition of the character of the oxidizer includes the retained or lost individuality of the oxidizer particles in the surface layer. Loss of individuality of oxidizer particles means formation of *the continuous fused layer* of oxidizer. If oxidizer particles lose their individuality then the layers between oxidizer particles lose the properties of "inter-pocket bridges," i.e., formation SL is possible within these layers.

3.1.1 Oxidizer Particles Keep Individuality

It is possible to state that the following oxidizers retain their individuality in a surface layer: ammonium perchlorate (AP), ammonium dinitramide (ADN), nitramines (HMX), and phase-stabilized ammonium nitrate with the use of a thermodynamic stabilization method (PSAN-2).

If these oxidizers are used and formation of a skeleton layer takes place, the fraction of "inter-pocket bridges" defines the degree of an involvement of the metal fuel in agglomeration process, i.e., parameter $Z_m{}^a$ (Fig. 8). The size of "pockets" makes it possible to estimate the size of agglomerates [18, 30].

Fig. 8 Dependence of Z_m^a
on mass-medium diameter of
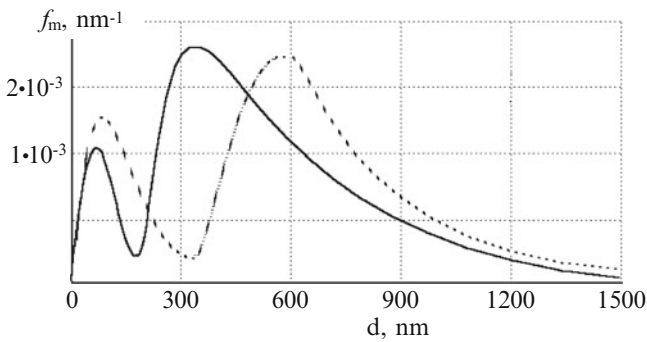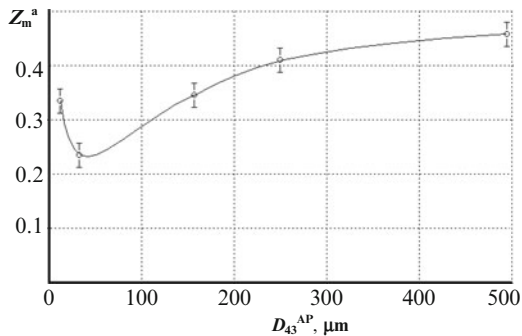AP particles [18]

Fig. 9 Functions $f_m(d)$ for two AP-based propellants at 6.0 MPa [18]

The mass-average diameter of smoke oxide particles at low intensity of the
agglomeration process (as an intensity measure parameter Z_m^a can be chosen) is
in a narrow enough range of 350–450 nm, and at high levels – of a wider range of
450–800 nm. The mass function of the size distribution density of smoke oxide
particles generally is bimodal (Fig. 9). The quantity of the particles forming a
mode in the domain of the larger sizes prevails. It is possible to assume that the
basic mechanism of the formation SOP is the fragmentation of oxide formed in
the heterogeneous combustion of the non-agglomerating metal. This assumption
is based on the analysis of a functions $f_m(d)$. The first mode on this function
is defined by particles which are formed on gas-phase burning and the second
basically heterogeneous burning. Heterogeneous burning ends with a fragmentation
of particles that have a significant impact on the final size distribution.

3.1.2 Particles of an Oxidizer Do Not Retain Individuality

It is possible to state that the following oxidizers lose individuality in a surface layer:
ammonium nitrate (AN) and phase-stabilized ammonium nitrate produced using a
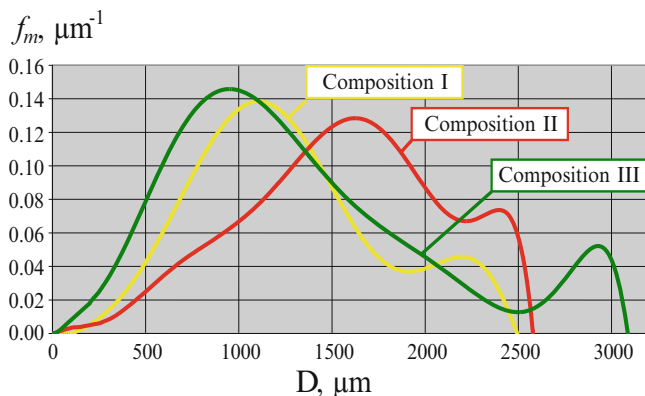kinetic method (PSAN-1) [20, 22].

Fig. 10 Functions $f_m(D)$ for three AN-based propellants at 6.0 MPa [20]. (Differences in formulation of propellants are resulted in Table 1)

Table 1 Formulation of the three AN-based propellant compositions

Substance	Composition I %	Composition II %	Composition III %
AN coarse[a]	46.2 (c/f = 2.33)	19.8 (c/f = 0.43)	33 (c/f = 1.0)
AN fine[b]	19.8	46.2	33
Al regular[c]	22	22	22
Isoprene rubber	2.4	2.4	2.4
Oil ($C_{19}H_{35}$)	9	9	9
Additives	0.6	0.6	0.6

[a]Size of particles: 250–350 μm
[b]Size of particles: 40–70 μm
[c]Mass-mean diameter of particles: 10.5 μm

Use of similar oxidizers has following consequences:

– Almost full involvement of metal fuel into agglomeration ($Z_m{}^a \sim 80$ %).
– The considerable role of the process of evolution of agglomerating particles.
– The critical content of oxide in agglomerates ($\eta \sim 85$ %).
– Considerable degree of merging of particles (Fig. 10).
– Rather high size of SOP. The mass-medium size of these particles is in a range of 700–1,200 nm.

3.2 Type of Binder

Use of the active binder has the greatest consequences for CCP properties.

The laws of formation of SL and, hence, of CCP for propellants containing active binder depend on the pressure value. In the domain of low pressure, a skeleton layer
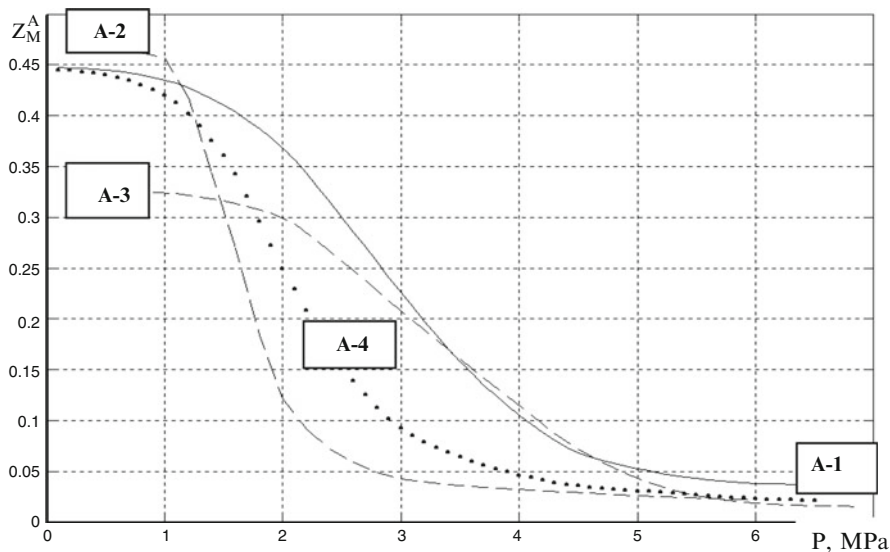
Fig. 11 Dependences $Z_m{}^a$(P) for four propellants on the basis of the active binder (A-1–A-4). All compositions contained AP, HMX, Al, and active binder. They differ in ratio of fine and coarse fractions of HMX [21]

is formed, but the SL practically disappears on transition to high pressures, which leads to a sharp falling of the mass fraction of agglomerates in CCP composition (Fig. 11).

The specified laws are connected with the combustion features of the active binder.

These binders make it possible to burn without CS formation and consequently SL formation as well. The realization of such possibility appears to depend on the relation of gasification rates of any active plasticizer (r_{pl}) and the polymer itself (r_{pol}) ($\varepsilon = r_{pl}/ r_{pol}$). If this parameter $\varepsilon <1$, then CS formation is more probable and vice versa.

The experimental data give grounds to assume that in the low pressure domain a situation arises which is connected with the realization of condition $\varepsilon <1$ and with formation of CS and SL, and in the high pressure domain – $\varepsilon \geq 1$ and formation of CS (SL) does not take place. It should be noted that the results which are related to the character of the skeleton layer formation depending on pressure have been obtained for propellant based on ultra-fine AP (characteristics of similar propellant are given in work [17]). Thus, it is possible to discuss some common laws for the burning of propellants whose properties make them close to homogeneous.

A procedure providing the delimitation of domains of high and low pressure for the type of propellants under consideration is not yet available. However, it is possible to state that the domain of high pressures is found above 5.0 MPa for all
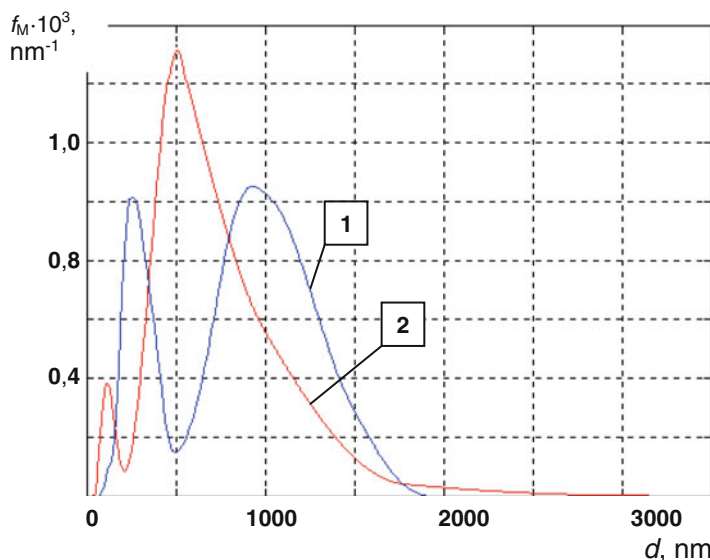
Fig. 12 Functions f_m(d) for propellants on the basis of the inactive (*1*) and active (*2*) binder [21]

propellants of this type. Parameter Z_m^a does not exceed a value of 2–4 % in this domain that allows the practical exclusion of the consideration of agglomerates.

The mass-medium size of SOP is 700–800 nm. The mass function of the size distribution density of smoke oxide particles is close to uni-modal (Fig. 12). It is supposed that the increase in the size of SOP is a consequence of the reduction of the ignition temperature of non-agglomerating metal [23].

3.3   Kind and Size of Metal Particles

Various properties of metal fuel are connected with use of nano-sized aluminum and modification of aluminum particles.

3.3.1   Use of Nano-Sized Aluminum

The laws of formation SL for nano-sized aluminum-based propellants depend on whether they retain the initial particles of metal in the propellant, that is their individuality, or form connected structures.

Contact presence between initial particles of metal in a surface layer has a basic value for formation of agglomerates and, hence, all of the set of condensed products. In reality the formation of agglomerates occurs only in the presence of contact by

particles. The formation of a skeleton layer is accompanied by the formation of the connected structures from initial particles of metal (Fig. 1). If the connected structures of metal particles in the composition of initial propellant are formed, they provide a basis for SL formation without dependence on features of the burning process, i.e., preconditions for formation of SL arise at the stage of manufacturing the propellant.

Generally, the situation caused by the presence of connected structures is undesirable for propellant properties since the value of the specific surface of metal particles falls with their presence. The probability of its occurrence is considerably increased for nano-sized aluminum-based propellants. This is connected with a sharp increase in the quantity of initial particles of metal in unit of volume of propellant. Special processing methods are used for elimination of the formation of similar structures [31].

At their absence, it is possible to state that formation connected structures is an objective reality for similar propellants. Thus, two situations are possible for considered class propellants, connected with the preconditions of SL formations: either in the course of burning or at the stage of propellant manufacture.

It was proposed to allocate depending on realization of two specified situations two types nano-sized aluminum based propellants and to name them propellants type Nano1 and Nano2 [24, 26].

Properties of SL of propellants type Nano1 are similar to the properties of skeleton layer **A** class propellants, i.e., it is possible to speak about a decrease in the ignition temperature of the metal.

If the surface layer allows retention of oxidizer particle individuality, then the fraction of the metal fuel forming SL depends on the quantity and the size of oxidizer particles. Thus, the basic agglomeration mechanisms are "pocket" and "inter-pocket", and the type of agglomerates corresponds to "matrix" agglomerates and agglomerates with "cap" oxide (Fig. 5), i.e., laws of propellants burning an **A** class are realized [17, 18].

The SL properties of propellant type Nano2 are close to properties of SL propellants of **B** class. The formation of SL is connected neither with the propellant structure nor with the conditions of its burning. It has only made it possible to draw a conclusion that the properties similar to SL are defined by manufacturing techniques. Experimental data testify to a rather considerable fraction of metal participating in its formation. Parameter $Z_m{}^a$ has high value ($\sim$0.9–0.95) which practically does not depend on pressure.

Features of agglomerates at burning propellants type Nano2 are:

- Rather small sizes of agglomerates ($\sim$ several tens micron) (this size almost ten times less the size of agglomerates for propellants type Nano1);
- Possibility of formation of agglomerates which represent a metal particle covered with rather thick cover of oxide (Fig. 13).

The mass functions of agglomerate size distribution density for propellant types Nano1 and Nano2, which illustrate essential difference at a size of agglomerates, are resulted on Figs. 14 and 15.

Fig. 13 Scheme of
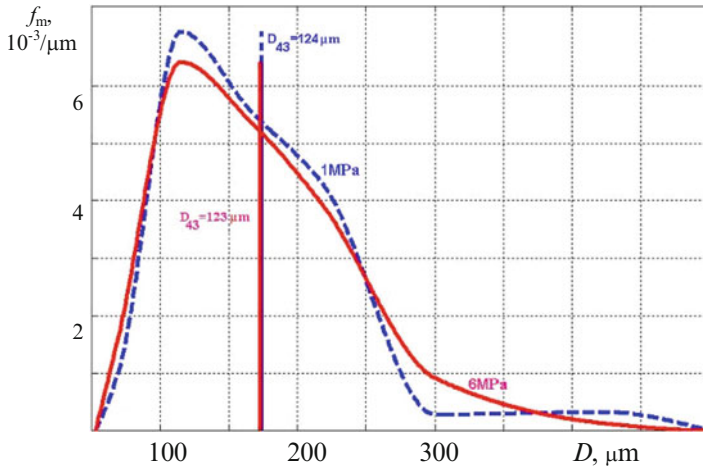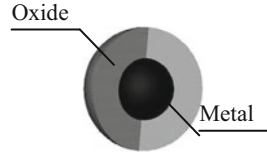agglomerate structure of
propellants type Nano2

Oxide

Metal

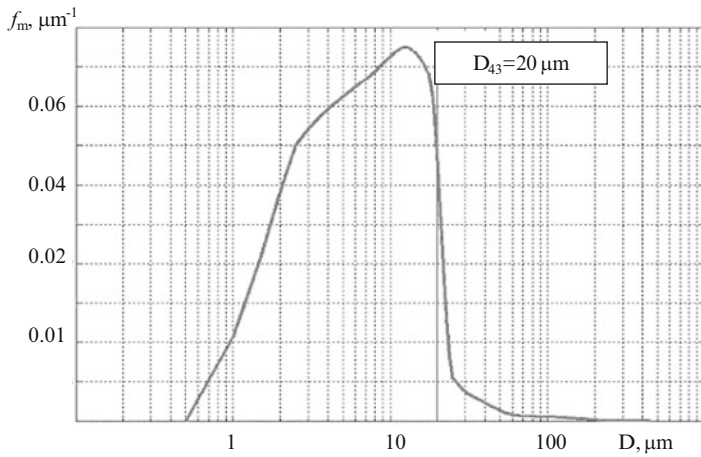**Fig. 14** Functions $f_m(D)$ for propellant Nano1 [24]

Fig. 15 Functions $f_m(D)$ for propellant Nano2 [24]

Fig. 16 Functions f_m(d) for number propellants with initial metal of the various size (compositions: NA1– AN + nano-sized Al + inactive binder, NA2– AN + regular Al + inactive binder, N4 – AP + nano-sized Al + inactive binder) [26]
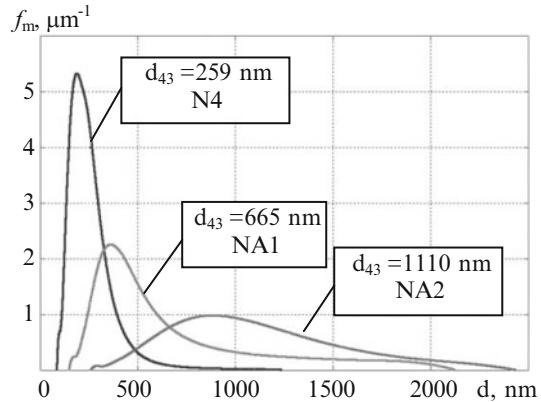

Table 2 Propellant compositions for CSP-F1, CSP-F2, CSP-F3, CSP-F4, and CSP-F5 (percentages)

Propellant	Aluminum powder		Coating	Oxidizer	Binder
	$d_{43}{}^* = 10.5\,\mu m$	$d_{43}{}^* = 22\,\mu m$			
CSP-F1	–	24	–	64	12
CSP-F2	–	24	Ni	64	12
CSP-F3	24	–	–	64	12
CSP-F4	24	–	APPRET	64	12
CSP-F5	24	–	PMFA	64	12

[*]Mass-average diameter of original metal particles

The use of nano-sized aluminum, as a rule, leads to an essential reduction of the size of SOP (Fig. 16). Further this character influence is a consequence both of the reduction of the size of agglomerating particles and the natural reduction of the size of particles on combustion of non-agglomerating metal.

3.3.2 Use of Modified Aluminum

Normally the modification of metal fuel consists of a coating of metal particles of refractory metals and fluorine-containing organic polymers. The composition of five investigated propellants [19] is given in Table 2.

Experimental data on studying of agglomeration process at two levels of pressure ($P = 1.5$ MPa and $P = 6.0$ MPa) are presented in Tables 3 and 4.

Generally, the presence of a coating on metal fuel particles may have the following consequences for the process of the formation of CCP:

- Changes in ignition temperature of metal and, as a result, as properties of SL, and consequently, of the characteristics of agglomerates, and the character of combustion of non-agglomerating metal;

Table 3 Experimental data at low pressure

Propellant	Coating	Z_m	Z_m^{ox}	Z_m^a	η	D_{43}, μm
CSP-F1	–	0.259	0.065	0.324	0.320	223
		±0.026	±0.006	±0.032	±0.030	±20
CSP-F2	Ni	0.307	0.090	0.397	0.356	138
		±0.030	±0.008	±0.038	±0.035	±13
CSP-F3	–	0.333	0.114	0.447	0.393	210
		±0.035	±0.013	±0.048	±0.038	±20
CSP-F4	APPRET	0.321	0.059	0.380	0.255	185
		±0.032	±0.005	±0.037	±0.025	±20
CSP-F5	PMFA	0.356	0.073	0.429	0.279	150
		±0.034	±0.009	±0.043	±0.027	±15

Table 4 Experimental data at high pressure

Propellant	Coating	Z_m	Z_m^{ox}	Z_m^a	η	D_{43}, μm
CSP-F1	–	0.155	0.080	0.235	0.494	213
		±0.016	±0.007	±0.023	±0.050	±20
CSP-F2	Ni	0.197	0.058	0.255	0.359	104
		±0.020	±0.005	±0.025	±0.035	±10
CSP-F3	–	0.133	0.060	0.193	0.460	126
		±0.013	±0.006	±0.019	±0.050	±14
CSP-F4	APPRET	0.126	0.033	0.159	0.334	138
		±0.011	±0.004	±0.015	±0.035	±15
CSP-F5	PMFA	0.110	0.041	0.151	0.414	133
		±0.010	±0.004	±0.014	±0.040	±12

- Changes in the surface properties of agglomerate "substance", which inevitably affect the value of adhesion force.

Results from experimental investigations made it possible to reach the following conclusions [19].

The use of nickel-containing coating leads to a change of surface properties of agglomerate "substance." A consequence of this circumstance is a reduction of the adhesive force operating on particles and a reduction of the fraction of the large fraction of agglomerates and, hence, reduction on the average the size of agglomerates (Tables 3 and 4, Fig. 17).

Use the fluorine-containing organic coatings leads to rise in ignition temperature of the metal. This circumstance has following consequences.

The fraction of the metal, which is burning down in a heterogeneous mode in SL and, hence, content of oxide in agglomerates decreases.

Properties of SL that lead to the transformation mass function of agglomerate size distribution density which produces a reduction of quantity of the largest agglomerates and a reduction of the average size of agglomerates (Tables 3 and 4, Fig. 18).

Fig. 17 Agglomerate size
distribution for propellants
CSP-F1 and CSP-F2
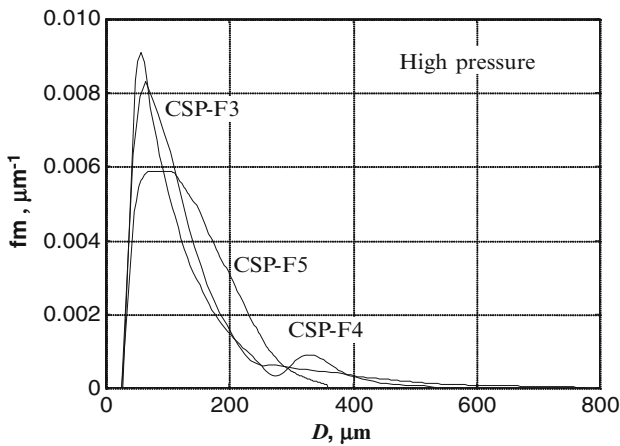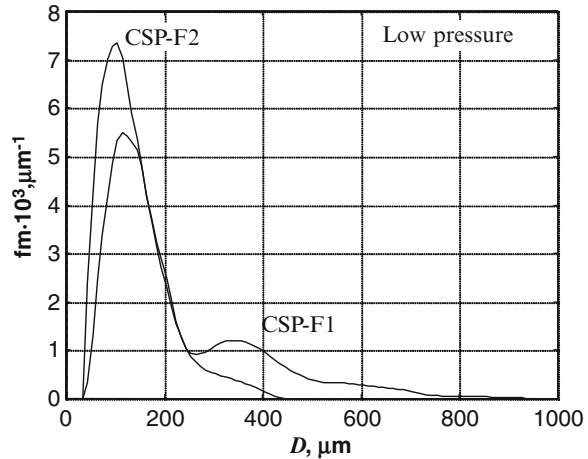
Fig. 18 Agglomerate size distribution for propellants CSP-F3, CSP-F4, and CSP-F5

The diagram illustrating the character of metal fuel modification effects on the agglomeration process of CCP formation is given in Fig. 19.

The increase in the ignition temperature of metal has a consequent reduction of the burning time in a heterogeneous mode that leads to reduction of the SOP size.

Of course, in order to resolve the practical problems of modified metal fuel applications, it will be necessary to carry out additional experiments to determine the various aspects of the modification effects on the combustion process (effect on the law of propellant burning rate, optimum coating substance content, etc.).

Fig. 19 Scheme of influence of metal modification on the process of the formation of CCP
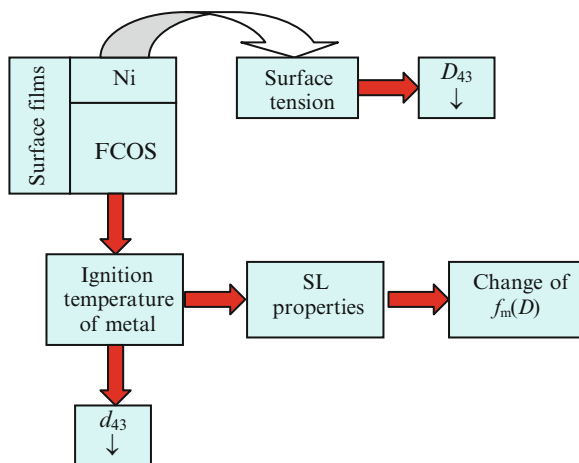
4   Summary

This analysis emphasizes the variety of burning process mechanisms and, hence, the CCP formation process. These displays are connected with influence formulation decisions on considered process. It is possible to state that the character of influence is in full conformity with the formulated physical picture of CCP formation at the surface of burning propellant. This circumstance is important. It is possible to state that the consequences of basic formulation design decisions for the process of CCP formation are established. Thus, the prediction of the impact of these decisions on the properties of CCP is possible.

The results obtained make it possible to regard the creation of propellant of optimum composition with optimism. Of course, it is necessary to continue researches at use of new components: aluminum hydride, HNF, CL-20, and others.

References

1. Pokhil PM, Belyaev AF, Frolov YV et al (1974) Gorenie porohsobraznykh metallov v activnykh sredakh (combustion of powdered materials in active media). Nauka, Moscow
2. Gladun VD, Frolov YV, Kashporov LY (1977) Aglomeraziya porohsobraznogo metalla pri gorenii smesevykh kondensirovannykh sistem (agglomeration of powdered metal at burning of composite condensed systems). OIKhPh AN SSSR, Chernogolovka
3. Frolov YV, Pokhil PF, Logachev VS (1972) Ignition and combustion of powdered aluminum in high-temperature gaseous media and in a composition of heterogeneous condensed systems. Combust Explosion Shock Waves 8(2):38–45
4. Glotov OG, Zyryanov VY (1995) Condensed combustion products of aluminized propellants. 1. A technique for investigating the evolution of disperse-phase particles. Combust Explosion Shock Waves 31(1):72–78

5. Glotov OG, Yagodnikov DA, Vorob'ev VS et al (2007) Ignition, combustion, and agglomeration of encapsulated aluminum particles in a composite solid propellant. II. Experimental studies of agglomeration. Combust Explosion Shock Waves 43(3):320–333

6. Glotov OG (2007) Condensed combustion products of aluminized propellants. IV. Effect of the nature of nitramines on aluminum agglomeration and combustion efficiency. Combust Explosion Shock Waves 42(4):436–449

7. Glotov OG, Zarko VE, Beckstead MW (2000) Agglomerated and oxide particle generated in combustion of ALEX containing solid propellants. In: Proceedings of the 31st international annual conference of ICT, June 2000, paper 130

8. Price EW, Pack CJ, Sigman RK, Sambamurthi (1981) The nature and combustion of agglomerates. In: Proceedings of the 18th JANNAF combustion meeting, V. III, Chemical Propulsion Information Agency. Laurel, p 121–145

9. Price EW (1984) Combustion of metallized propellant. Progress in astronautics and aeronautics. In: Kuo K, Summerfield M (eds) Fundamentals of solid propellant combustion, vol 90. AIAA, New York, pp 478–513

10. Price EW, Sigman RK (2000) Chapter 2.18: Combustion of aluminized solid propellants. In: Yang V, Brill TB, Ren WZ (eds) Progress in astronautics and aeronautics, vol 185. American Institute of Aeronautics and Astronautics, Reston, pp 663–687

11. Dokhan A, Seitzman JM, Price EW, Sigman RK (2001) The effects of Al particle size on the burning rate and residual oxide in aluminized propellants. In: AIAA Paper 2001–3581, 37th AIAA/ASME/SAE/ASEE joint propulsion conference and exhibit. Salt Lake City, 8–11 July 2001

12. Dokhan A, Price EW, Sigman RK, Seitzman JM (2002) Combustion mechanism of bimodal and ultra-fine aluminum in AP solid propellant. In: AIAA Paper 2002–4173, 38th AIAA/ASME/SAE/ASEE joint propulsion conference and exhibit. Indianapolis, 7–10 July 2002

13. DeLuca LT (2007) Burning of aluminized solid rocket propellants: from micrometric to nanometric fuel size. In: Ping H, Yajun W, Shengcai LI (eds) Theory and practice of energetic materials, Vol. VII, proceedings of the 2007 international autumn seminar on propellants, explosives and pyrotechnics, supported by National Natural Science Foundation of China (NSFC). Science Press, Beijing, pp 277–289

14. DeLuca LT, Galfetti L (2008) Burning of metallized composite solid rocket propellants: from micrometric to nanometric aluminum size. In: Book of proceedings 3rd Asian Joint Conference on Propulsion and Power (AJCPP) 2008 – Gyeongju. 06–08 Mar 2008

15. DeLuca LT, Galfetti L, Maggi F et al (2008) Burning of metallized composite solid rocket propellants: toward nanometric fuel size. In: ESA space propulsion 2008 – book of proceedings. Heraclion. 05–09 May 2008

16. Cerri S, Galfetti L, DeLuca LT et al (2008) Experimental investigation of the condensed combustion products of micro aluminized solid rocket propellants. AIAA Paper 07-5766, 08-11 July 07

17. Babuk VA, Vasilyev VA, Malakhov MS (1999) Condensed combustion products at the burning surface of aluminized solid propellant. J Propuls Power 15(6):783–794

18. Babuk VA, Vasilyev VA, Sviridov VV (2000) Chapter 2.21: Formation of condensed combustion products at the burning surface of solid rocket propellant. In: Yang V, Brill TB, Ren WZ (eds) Solid propellant chemistry, combustion, and motor interior ballistics, vol 185, Progress in astronautics and aeronautics. American Institute of Aeronautics and Astronautics, Reston, pp 749–776

19. Babuk VA, Vasilyev VA, Sviridov VV (2001) Propellant formulation factors and metal agglomeration in combustion of aluminized solid rocket propellant. Combust Sci Technol 163:261–289

20. Babuk VA, Vasilyev VA, Glebov AA et al (2004) Combustion mechanisms of AN-based aluminized solid rocket propellants. In: DeLuca LT, Galfetti L, Pesce-Rodriguez RA (eds) Novel energetic materials and applications. Grafiche GSS, Bergamo, pp 44–1–44–20, Dec. 2004, paper 44

21. Babuk VA, Dolotkazin Ildar N, Glebov Andrey A (2005) Burning mechanism of aluminized solid rocket propellants based on energetic binders. Propellants Explos Pyrotechnics 30(4):281–290
22. Babuk VA, Glebov A, Arkhipov VA et al (2005) Dual-oxidizer solid rocket propellants for low-cost access to space. In: DeLuca LT, Sackheim RL, Palaszewski BA (eds) In-space propulsion. Grafiche GSS, Italy, pp 15–1–15–20, Nov. 2005, paper 15
23. Babuk VA (2007) Problems in studying formation of smoke oxide particles in combustion of aluminized solid propellants. Combust Explosion Shock Waves 43(1):38–45
24. Babuk VA, Glebov A, Dolotkazin I et al (2009) Condensed combustion products from burning of nanoaluminum-based propellants: properties and formation mechanism. In: EUCASS advances in aerospace sciences. vol 1 – Propulsion physics, EUCASS, Torus Press, EDP Sciences, Paris, 2009, pp 3–16
25. Babuk VA, Vasil'ev VA, Potekhin AN (2009) Experimental investigation of agglomeration during combustion of aluminized solid propellants in an acceleration field. Combust Explosion Shock Waves 45(1):32–39
26. Babuk VA, Dolotkazin I, Gamsov A, Glebov A, DeLuca LT, Galfetti L (2009) Nanoaluminum as a solid propellant fuel. J Propuls Power 25(2):482–489
27. Babuk VA (2009) Properties of the surface layer and combustion behavior of metalized solid propellants. Combust Explosion Shock Waves 45(4):486–494
28. Babuk VA, Dolotkazin IN, Sviridov VV (2003) Simulation of agglomerate dispersion in combustion of aluminized solid propellants. Combust Explosion Shock Waves 39(2):195–203
29. Babuk VA, Dolotkazin Ildar N, Nizyaev Alexander A (2013) Analysis and synthesis of solutions for the agglomeration process modeling. In: EUCASS book series advances in aerospace sciences. vol 4 – Progress in propulsion physics, EUCASS, Torus Press, EDP Sciences, Paris, 2013, pp 33–58
30. Babuk VA, Nizyaev AA (2014) Modelirovanie structury smesevykh tverdykh topliv i problema opisaniya prozessa aglmerazii (Modeling of composite solid propellant structure and problem of the description of agglomeration process). Khimicheskaya Phizika I Mesoskopiya 16(1):31–42
31. Meleshko VY, Pavloves GY, Sarabiev VI, Mikaskin DA (2012) Sposoby kapsulyazii nanorazmernykh komponentov energeticheskikh kondensirovannykh system (ways of protection nano-sized components of the energy condensed systems). Izvestia RARAN 3:22–26

Energy and Combustion Characteristics of Propellants Based on BAMO-GAP Copolymer

Jiangfeng Pei, Fengqi Zhao, Ying Wang, Siyu Xu, Xiuduo Song, and Xueli Chen

Abstract The energy characteristics of propellants based on BAMO-GAP copolymers (the copolymer of 3,3-bis(azidomethyl) oxetane (BAMO) and glycidyl azide polymer (GAP), p(BAMO-GAP)) were theoretically calculated by "Energy Calculation Star (ECS)" software based on the principle of minimum free energy. The effects of plasticizers, oxidants, and high energy fuels on the energetic properties of propellants were discussed, and some useful suggestions were provided for high energetic propellant based on p(BAMO-GAP). The formulations of low signature propellants without AP (ammonium perchlorate) were designed, and the samples were prepared, respectively. The burning rates, combustion flame structures, and combustion wave structures of these samples were tested. The effects of oxidants and catalysts on the combustion characteristics of propellants based on p(BAMO-GAP) were investigated. The results show that there is an optimum ratio between AP and RDX (HMX or CL-20). However, the ideal energetic properties of propellants can be improved linearly when AP is replaced by ADN. When AlH_3 is added to the formulations instead of Al, the energetic properties of propellants are improved much. With the mass fraction of RDX increasing in the propellants, the burning rates at low pressure remain almost the same, but decrease observably at high pressure. With the tri-component catalysts added to the formulation, the burning rates at low pressure are improved significantly, and the burning rate pressure exponents decrease. There is no obvious dark zone in the flame of uncatalyzed propellant, and the combustion flame consists of soft orange flame and bright lines. With the catalysts added to the propellant formulation, the burning rates can be improved, and the combustion surface temperature increases.

J. Pei • F. Zhao (✉) • Y. Wang • S. Xu • X. Song • X. Chen
Xi'an Modern Chemistry Research Institute, Xi'an 710065, Shaanxi, China
e-mail: pjfpmt@163.com; npecc@163.com; lwm9924@126.com; xusy99@163.com;
song_xd@126.com; dahai99-2005@163.com

1   Introduction

High energetic polymer binder is one of the most important components for the solid high energy formulations such as propellants or explosives. It gives the certain shape and structural integrity to the formulations. The energetic thermoplastic elastomers (ETPEs) are profoundly interested as suitable candidates for binder applications because of their advantages which the traditional binders do not have [1–4], such as high energetic properties, easy to nondestructive demilitarization, and reusage [5–11]. As one kind of ETPEs, the BAMO-GAP copolymer (copolymer of 3,3′-bis(azidomethyl) oxetane (BAMO) and glycidyl azide polymer (GAP), p(BAMO-GAP)) has been centered in the search for new energetic binder of solid gun and rocket propellants [12, 13]. The propellants based on p(BAMO-GAP) always have excellent properties, such as low flame temperature, high mass impulse, good mechanical properties, and stable combustion [14, 15]. It has become one of the most potential energetic binders for the application of solid propulsions.

Currently, synthesis and characterization of p(BAMO-GAP) have been widely studied and reported [16–20]. And the combustion characteristics of propellant formulas have been reported only a little [21, 22]. However, the energetic characteristics of propellant-based p(BAMO-GAP) binder were rarely reported. In the present work, as the most important characteristics of propellants, the energetic and combustion characteristics of propellants based on p(BAMO-GAP) were studied. Placing emphasis on the investigation of the energy and combustion properties of p(BAMO-GAP)-based solid propellants with and without aluminum can be used for solid rocket motor applications.

2   Experimental

2.1   Materials and Specimen

BAMO-GAP copolymer is prepared by Xi'an Modern Chemistry Research Institute. The structural formula is showed in Fig. 1, and the characterization is as follows: FT-IR $\nu(cm^{-1})$, 3325 (ν_{OH}), 2873 ($\nu_s CH_2$), 2092 ($\nu_{as}N_3$), 1442 ($\nu_s CH_2$), 1278 (ν_sC-O-C), and 1095 (ν_{as}C-O-C). ^{13}C NMR: δ (ppm, $CDCl_3$) 45.3 ppm (quaternary carbon atom of poly-BAMO units), 49.5–50.8 ppm and 51.1–52.4 ppm (CH_2N_3 of poly-BAMO units and GAP units), 69.6–70.8 ppm (CH_2O of BAMO and GAP units), and 76.7–78.7 ppm (CHO of GAP units). Relative average molecular weight (by GPC): $M_n = 7515$, $M_w = 25{,}212$, and PD = 3.35. Elemental (CHN) analysis: C, 40.88 %; H, 5.24 %; and N, 37.71 %. Molar ratio of monomers in the copolymer: BAMO-GAP = 1/1.

Fig. 1 Structural formula of
BAMO-GAP copolymer
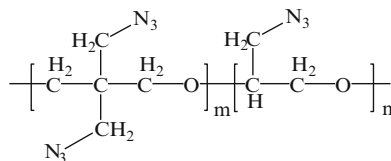
Hexogen (RDX, >98 %) and aluminum (Al,>99 %) are from industrial products.

The propellant samples are prepared by solventless extrusion technology, which includes mixing, rolling, extrusion, and cutting.

2.2 Equipment and Experimentation

The ideal properties of propellants based on p(BAMO-GAP) are calculated by means of "Energy Calculation Star (ECS)" software (5.0 edition) [23], which is developed by Xi'an Modern Chemistry Research Institute, based on the principle of minimum free energy. The operating conditions are as follows: the operating pressure is 7.0 MPa in the combustion chamber and 0.1 MPa at the exit of nozzle. The initial temperature is 298 K. The combustion products of the compositions get balance instantly in expanding process, which is equilibrium flow hypothesis [24–27].

The burning rate is measured by a chimney-type strand burner system. The propellant samples are cut to strands as $\varphi 5 \times 150$ mm and coated by polyvinyl alcohol and aired for six times. A fine metal wire is threaded through the top of the samples to ignite the propellant by a voltage at the initial temperature of 20 °C in a chamber, which is filled with nitrogen atmosphere. In order to get the burning rate, two other low-melting-point fine fuse wires are threaded through the strand at a separate distance of 100 mm which record the start and end time signal of combustion. The real-time data are recorded by a computer which processed and calculated the burning rate. Five replicate experiments are conducted at each test pressure, and the average experimental results are obtained with a standard deviation of 0.13–0.25.

The combustion flame structures are recorded by the single color frame amplification photography technology. The propellant samples are cut to strands as $1.5 \times 4 \times 25$ mm and fixed in the combustion chamber with the nitrogen atmosphere. The pressure in the burner is maintained to the set value by the automatic nitrogen gas supplier as the burning rate test system. In order to make the photos of flame vivid, nitrogen gas is purged from the bottom of the burner and exhausted from the top to the air. The photos are recorded by the camera from the observation windows.

The temperature distribution of combustion waves of propellants is studied by the Π mode miniature thermocouples which are embedded in the propellant strands. The profile of propellant strands is coated by polyvinyl alcohol and aired twice.

Table 1 Physicochemical parameters of the components [28]

	Components	Chemical formula	$\rho/\mathrm{g \cdot cm^{-3}}$	$\Delta_f H_m^\theta/\mathrm{kJ \cdot mol^{-1}}$
Binder	p(BAMO-GAP)[a]	–	1.21	85.1
Plasticizers	Diazidopentane (DIANP)	$C_4H_8N_8O_2$	1.33	539.7
	Glycidyl azide polymer (GAP)	$(C_3H_5N_3O)_n$	1.30	141.0
	Butyl nitrooxy ethyl nitramine (BuNENA)	$C_6H_{13}N_3O_5$	1.21	459.0
	Nitroglycerin (NG)	$C_3H_5N_3O_9$	1.59	−372.4
Oxidants	Ammonium perchlorate (AP)	NH_4ClO_4	1.95	−294.1
	Hexogen (RDX)	$C_3H_6N_6O_6$	1.81	70.3
	Octogen (HMX)	$C_4H_8N_8O_8$	1.90	75.0
	Hexanitrohexaazaisowurtzitane (CL-20)	$C_6H_6N_{12}O_{12}$	1.98	415.5
	Ammonium dinitramide (ADN)	$H_4N_4O_4$	1.81	−133.0
Fuels	Aluminum (Al)	Al	2.70	0
	Aluminum trihydride (AlH₃)	AlH_3	1.43	−11.6

[a]The enthalpy of formation of copolymer is calculated according to the results of combustion calorimetry experiment based on the polymer empirical formula of $C_{3.40}H_{5.20}O_1N_{2.69}$, which is obtained from the data of elemental analysis

The samples are settled and ignited in the burner which is pressurized to the desired pressure with nitrogen gas. The signals from the thermocouples are recorded by the computer at different times during the samples' burning.

3 The Energetic Properties of Series Propellants Based on p(BAMO-GAP)

In order to investigate the effects of plasticizers, oxidants, and high energetic fuels on the energetic properties of propellants, several energetic materials are chosen. Their physicochemical properties are listed in Table 1.

3.1 Energetic Performance of Different Materials

The energetic characteristics of monopropellant containing single oxidant at 7.0 MPa are calculated and listed in Table 2.

The data in Table 2 show that the values of I_s, C^*, and T_C for different oxidants are increasing in the order of CL-20>RDX>HMX>ADN>AP. The ideal property of CL-20 monopropellant is the highest among the others. Moreover, the relative molecular mass of gaseous products of CL-20 is higher than the others, whereas for the oxygen coefficient, the increasing order is AP>ADN>CL-20>RDX (HMX).

Table 2 Energetic performance of monopropellants

| Oxidants | Property parameter | | | | |
	$I_S/\text{N·s·kg}^{-1}$	$C^*/\text{m·s}^{-1}$	φ	M_C	T_C/K
AP	1561.24	1013.32	2.67	28.92	1443.98
RDX	2616.04	1647.50	0.67	24.68	3281.48
HMX	2604.10	1642.02	0.67	24.28	3269.36
CL-20	2678.89	1651.26	0.80	29.19	3599.42
ADN	2275.23	1440.40	2.00	24.81	2587.81

I_s is ideal specific impulse, C^* is characteristic velocity, φ is oxygen coefficient, M_C is relative molecular mass of gaseous products, and T_C is adiabatic flame temperature

Table 3 Energetic performance of monopropellants

| Plasticizers | Property parameter | | | | |
	$I_s/\text{N·s·kg}^{-1}$	$C^*/\text{m·s}^{-1}$	φ	M_C	T_C/K
BuNENA	2522.62	1592.50	0.15	14.23	2401.74
NG	2439.41	1551.11	0.22	16.27	2372.22
DIANP	2433.33	1532.52	0.17	14.59	2362.13
GAP	2328.32	1464.37	0.11	13.96	2173.53

3.2 Energetic Performance of Propellants Containing Different Energetic Plasticizers

In order to investigate the effects of different plasticizers on the energetic performance of p(BAMO-GAP)-based propellants, the energetic properties of the propellants containing different energetic plasticizers are calculated at 7 MPa. The mass ratio of binder and plasticizer is designed as75:25. The results are shown in Table 3.

The calculated results show that the ideal data of I_s, C^*, and T_C increase in the order of BuNENA>NG>DIANP>GAP. The order is different from that of the enthalpy of formation. Although the enthalpy of formation of DIANP is the biggest among the materials, I_s of propellant is not the largest one, which may be attributed to the low adiabatic flame temperature and low oxygen coefficient.

3.3 Effect of Single Oxidant on the Energetic Characteristics of Propellants

In order to investigate the effects of the different oxidants on the energetic performance of propellants, a series of propellant formulas containing single oxidant are designed. The binder (p(BAMO-GAP)) and plasticizer (GAP) are replaced gradually by different oxidants. The energetic characteristics of these propellants are calculated by ECS at 7 MPa. The calculated results are shown in Fig. 2.
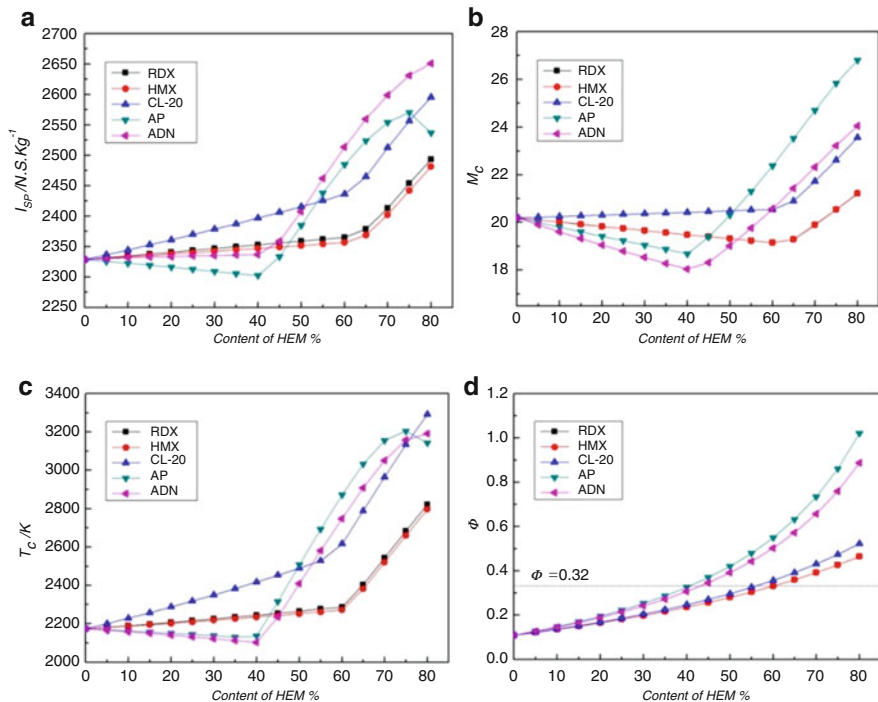
Fig. 2 The energetic characteristics of aluminized propellants containing different oxidants (**a**) Effects on the I_s (**b**) Effects on the M_c (**c**) Effects on T_C (**d**) Effects on φ

The calculated results show that there is a big difference between propellants containing various oxidants. The maximum I_s increases in the order of ADN>CL-20>AP>RDX>HMX. For the propellants containing AP, the values of I_s, M_C, and T_C decrease with an increase on the mass fraction of AP from 0 % to 40 % in the formulation, and these values increase rapidly and verge to the maximum point with the mass fraction of AP increasing from 40 to 75 %. However, there is a maximum point of I_s for AP-based propellant. For the propellants containing ADN, the I_s increases slowly when the mass fraction of oxidant is lower than 40 %. However, the I_s increases rapidly when the mass fraction of ADN increases from 40 % in the formulation, with a similar condition to that of propellants containing AP. For the propellants containing RDX, HMX, and CL-20, with the oxidants increasing from 0 % to 60 %, the values of I_s increase a little, but the values increase significantly when the mass fraction of oxidants increases from 60 % point.

To sum up, when the binder and plasticizer are replaced gradually by oxidants, the energetic properties of propellants increase. There is a turning point for each kind of oxidant. When the mass fractions of oxidants are higher than those of the turning point, the energetic data of propellants improve significantly. The influenced factors of energetic properties of propellants are not only the T_C and M_C but also

the oxygen coefficient (φ). Authoritative dotted line is painted in the curves of φ to connect each spurting point approximately, and the corresponding value of φ is 0.32. Therefore, the oxygen coefficient of propellants based on p(BAMO-GAP) with single oxidant should be larger than 0.32 in order to get higher performance.

3.4   Effect of Dual Oxidants on the Energetic Characteristics of Propellants

As a widely used oxidant in the solid propellants, AP is more effective for improving the oxygen coefficient and combustion performance of propellant. However, AP increases the signature of propellants because the hydrogen chloride is formed in the gaseous products. Therefore, other oxidants without chlorine are always added to the propellant formulations. In order to investigate the influences of the category and content of energetic materials on the energetic performance of p(BAMO-GAP)-based propellants, the formulas containing dual oxidants (which include aluminized and aluminum-free formulas) are designed, and the energetic characteristics of propellants are calculated by ECS at 7 MPa. The aluminum-free propellants are designed based on the formula as p(BAMO-GAP) 15 %, GAP 5 %, and AP80 %. And AP in the formula is replaced gradually by other oxidants. The calculated results are shown in Fig. 3.

The results in Fig. 3 show that when AP is replaced by RDX, HMX, or CL-20, the values of I_s increased at first and then decreased when the proportion of AP and other oxidant reaches a certain value. When the mass fraction of oxidants increases beyond the inflection points, the values of I_s for RDX and HMX decrease rapidly, but decrease slowly for CL-20, because the combustion temperatures of propellants containing CL-20 are much higher than those of RDX and HMX, although M_c of the former is higher. The values of I_s show the sustainable improvement for the propellants containing ADN. The curves are crossing with the others, which means that when the mass fraction of ADN is lower than the crossing points, the contribution of ADN for the energetic properties is smaller than those of the others, but they are higher when the mass fraction is higher than the points.

The results in Fig. 3b show that M_c of propellants decreases linearly when AP is replaced by other oxidants. The order of the decreasing gradient is RDX/HMX>CL-20>ADN. Figure 3 indicates that the values of T_c take on a similar trend with I_s of propellants containing different oxidants. There are crossing points between ADN and RDX or HMX. The values of ADN are lower than those of RDX or HMX when the mass fraction is below 35 %, but it is higher when the mass fraction is beyond 40 %. The values of CL-20 always are the highest one among the others.

Figure 3d shows that the values of φ drop consecutively with AP is replaced. The decreasing order is as follows: ADN>CL-20>RDX/HMX; also the decreasing gradient of ADN is much lower than the others.
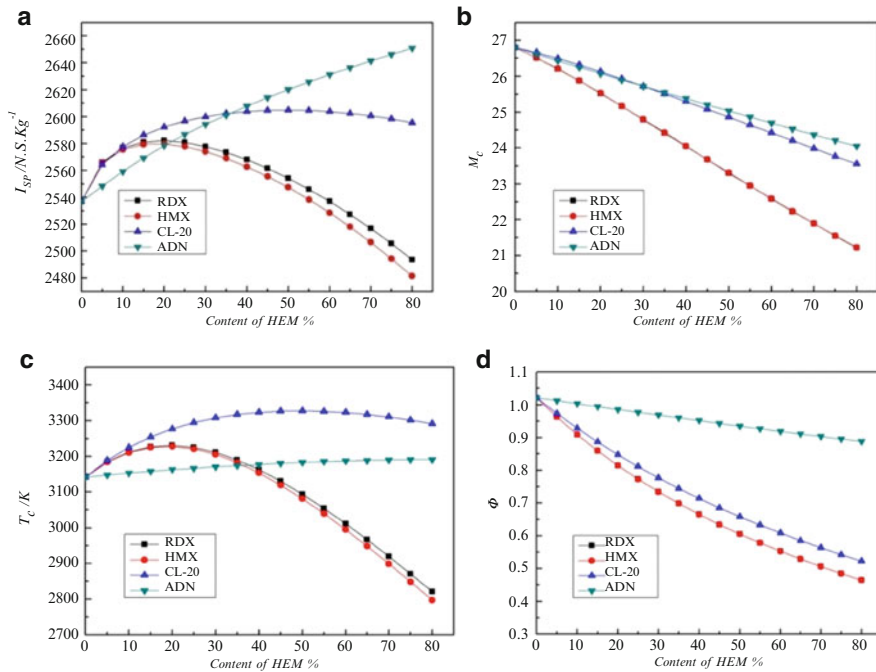
Fig. 3 The energetic characteristics of aluminum-free propellants containing different oxidants. (**a**) Effects on the I_s (**b**) Effects on the M_c (**c**) Effects on T_C (**d**) Effects on φ

Besides, the aluminized propellants containing dual oxidants are designed. The formulas are designed as p(BAMO-GAP) 15 %, GAP 5 %, AP 70 %, and Al 10 %, and AP is replaced gradually by other oxidants. The energetic characteristics of propellants are calculated by ECS at 7 MPa, and the results are shown in Fig. 4.

The calculated results (Fig. 4a) show that when AP is replaced by RDX or HMX gradually, the values of I_s increase at first then decrease when the proportion of AP and other oxidant exceeds a certain value. However, the degressive gradient is lower than those of aluminum-free propellants, and the inflection points are different with those of the propellants without Al. The values of I_s show the linear improvement for the propellants containing ADN. This variant's regular pattern is the same with that of aluminum-free propellants. The values of CL-20 increase continually when AP is replaced gradually but decrease a little when all of AP is replaced.

The results in Fig. 4b show that M_c of propellants is higher in comparison with the data in Fig. 3. However, the variant regularities are similar with that of aluminum-free propellants. The values decrease linearly whenAP is replaced
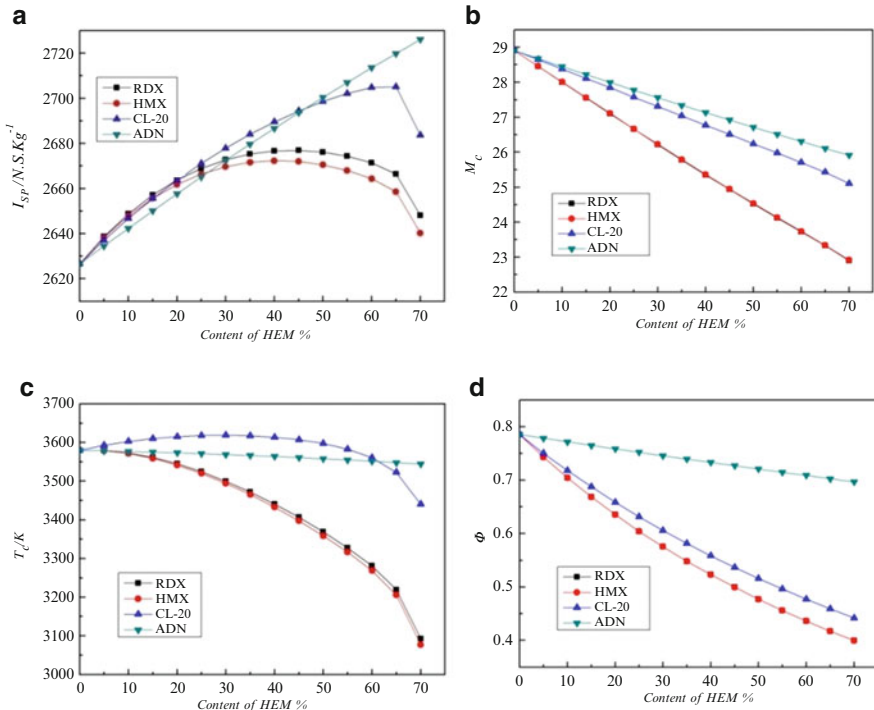
Fig. 4 The energetic characteristics of aluminized propellants containing different oxidants. (**a**) Effects on the I_s (**b**) Effects on the M_c (**c**) Effects on T_C (**d**) Effects on φ

by other oxidants. The order of the decreasing gradient is [RDX]/[HMX]>[CL-20]>[ADN], and the increasing order of M_c is in the order of [ADN]>[CL-20]>[RDX]/[HMX].

Figure 4c shows that T_c of propellants is higher in comparison with those of aluminum-free propellants (data in Fig. 3). With AP replaced by different oxidants, the values of T_c take on different variation trends. The values of [RDX] and [HMX] decrease rapidly with AP replaced gradually. However, the value of [ADN] decreases only a little. The order of T_c is [CL-20]>[ADN]>[RDX]>[HMX] when AP is replaced from 0 % to 60 %; on the contrary, the order is [ADN]>[CL-20]>[RDX]>[HMX] in the mass fraction range of 60–70 %.

Figure 4d shows that the values of φ drop consecutively with AP replaced. The higher rank is in the order of [ADN]>[CL-20]>[RDX]/[HMX], and the decreasing gradient of [ADN] is much lower than the others, which are similar with those of aluminum-free propellants. Moreover, the values of oxygen coefficient are lower than that of aluminum-free propellants.

3.5 High Energy Propellants Based on p(BAMO-GAP)

As a high energy fuel, Al is always added to the formulas to enhance the energy of propellants. However, the oxygen coefficient of the propellants will be decreased when more mass fraction of Al is added, which decreases the energy of propellants. Therefore, in order to investigate the effects of the mass fraction of Al on the energy performance of propellants, a series of propellants are designed as p(BAMO-GAP) 15 %, GAP 5 %, and oxidant 70 %. The oxidants are replaced gradually by Al in a certain proportion. The energy characteristics of these propellants are calculated by ECS at 7 MPa, and the results are shown in Fig. 5.

The calculated results in Fig. 5 show that the energetic values of each kind of oxidants are different. For the propellant containing RDX, HMX, or CL-20, when the oxidants are replaced by Al, I_s of propellants rises at first then reduces when the mass fraction of Al is beyond a certain value. There is one optimum value for the amount of Al in the propellant formulations containing different oxidants.
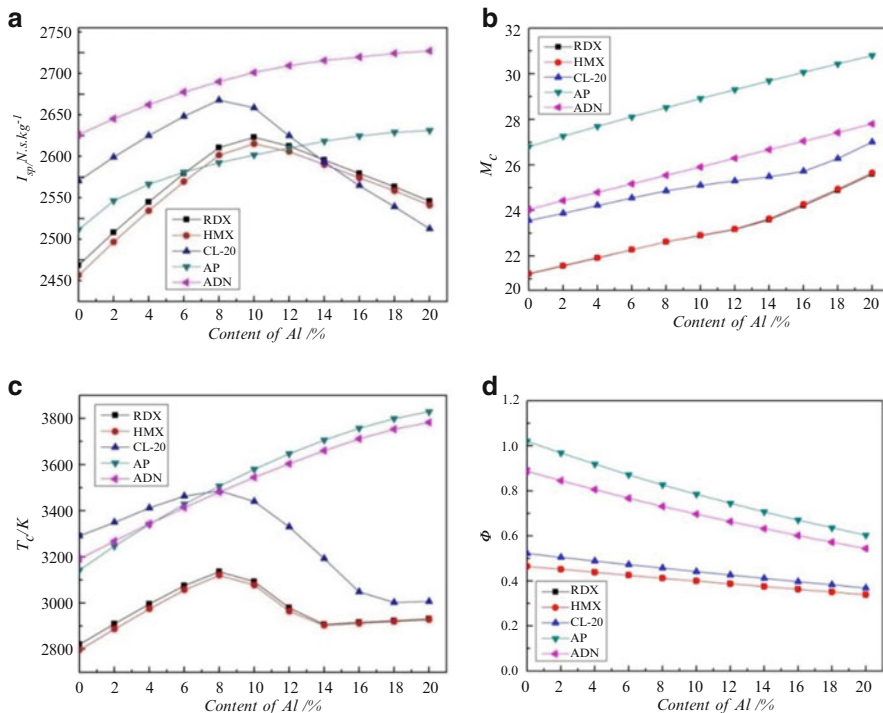
Fig. 5 The energetic characteristics of aluminized propellants containing different oxidants. (**a**) Effects on the I_s (**b**) Effects on the M_c (**c**) Effects on T_C (**d**) Effects on φ

Table 4 Optimum energy characteristic values of oxidant/Al/p(BAMO-GAP)

Samples	Oxidants/%	Al/%	I_s/N·s·kg^{-1}	T_C/K	M_C	φ
ADN	60	20	2752.3	3782.6	27.8	0.54
CL-20	72	8	2692.8	3486.5	24.9	0.46
AP	60	20	2656.4	3829.6	30.8	0.60
RDX	70	10	2648.1	3092.6	22.9	0.40
HMX	70	10	2640.2	3077.4	22.9	0.40

The optimum values are 8 % and 10 % for the propellants containing CL-20 and RDX/HMX, respectively, which may be due to the decreasing oxygen coefficients of propellants. The values of φ corresponding to the optimum values are 0.40 and 0.45 for [RDX]/[HMX] and [CL-20], respectively. It means that the values of φ should be designed to be bigger than 0.40 and 0.45 for the propellants based on p(BAMO-GAP)/RDX/Al, p(BAMO-GAP)/HMX/Al, and p(BAMO-GAP)/CL-20/Al. The value of T_C shows the same trend with that of I_s when the mass fraction of Al increases in the propellant formulations. However, for the propellants containing ADN or AP, the values of I_s increase strictly when the mass fraction of oxidants increases. This may be attributed to the high oxygen content of ADN and AP. Even when the oxygen coefficients of the metalized propellants containing ADN or AP reduce, the values go higher than 0.5 for the propellant. For the propellants containing different oxidants, the maximum increasing values of I_s are in the order of [ADN]>[CL-20]>[AP]>[RDX]>[HMX]. The optimum energetic characteristic values and the compositions of these propellants are shown in Table 4.

In order to heighten the energy of propellants greatly, besides the higher energetic materials being synthesized and applied, the metal hydride is the other choice to replace the metal fuels. The most effective one is AlH_3 among the different metal hydrides. The energy characteristics of these propellants are calculated by ECS at 7 MPa, and the results are shown in Fig. 6.

According to the calculated results in Fig. 6, the values of the energetic characteristics change linearly when the mass ratio of AlH_3 increased. The values of I_s increase in different rates for the propellants containing different oxidants. With Al replaced gradually by AlH_3, I_s is improved significantly for AP- and ADN-based propellants, but a little change occurred for RDX-, HMX-, and CL-20-based propellants. There is a crossing point between CL-20 and AP, which means that the propellants containing AP show higher energy than that of CL-20-based propellant when the mass fraction of AlH_3 is higher than the point. For the other oxidants, the increasing order of I_s is [ADN]>[CL-20] or [AP]>[RDX]>[HMX]. Other parameters (M_C, T_C or φ) all reduce in the similar gradient approximately. The all-increasing order of M_C, T_C, or φ is [AP]>[AND]>[CL-20]>[RDX/HMX] (the values of propellants containing RDX or HMX are very close).
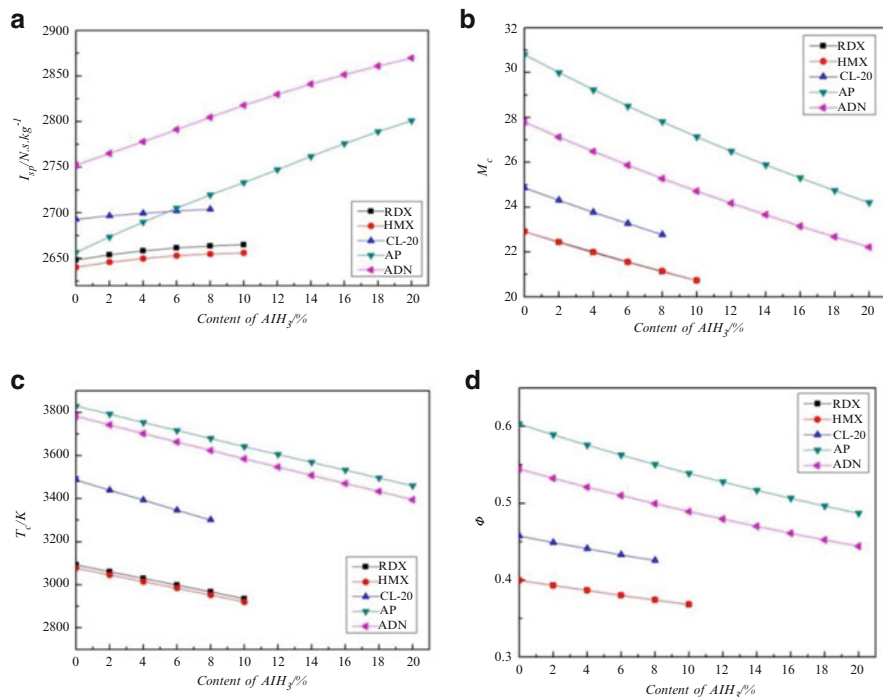
Fig. 6 The energetic characteristics of aluminized propellants containing different oxidants. (**a**) Effects on the I_s (**b**) Effects on the M_c (**c**) Effects on T_C (**d**) Effects on φ

4 Combustion Characteristics of p(BAMO-GAP)/RDX/Al Propellants

4.1 Burning Rate and Pressure Exponent

In order to investigate the effect of RDX and Al content on the burning rate and pressure exponent, a series of low signature propellants (without AP) composed of p(BAMO-GAP), RDX, and Al are designed (shown in Table 5) and prepared. The burning rates and the pressure exponents of these samples are tested and calculated. The results are discussed.

4.1.1 Effect of RDX

To illustrate the effect of mass fraction of RDX in the propellants on combustion properties, Fig. 7 shows the burning rate curves versus pressures of BGR-1 to BGR-4 formulations. It can be seen from Fig. 7 that with the pressure increasing from 1 to 20 MPa, the burning rates of four samples increase from almost 2 mm·s^{-1} to over

Table 5 Formulations of propellant samples

Samples	Binders and plasticizers/%	RDX/%	Al/%	Burning catalysts/(1–3 %)	Additives/%
BGR-1	35	62.5	–	–	2.5
BGR-2	30	67.5	–	–	2.5
BGR-3	25	72.5	–	–	2.5
BGR-4	20	77.5	–	–	2.5
BGR-5	20	72.5	5	–	2.5
BGR-6	20	67	10	–	2.5
BGR-7	20	62	15	–	2.5
BGR-8	20	72.5	5	C1	2.5
BGR-9	20	72.5	5	C2	2.5
BGR-10	20	72.5	5	C1 + C2	2.5
BGR-11	20	72.5	5	C1 + C2 + C3	2.5
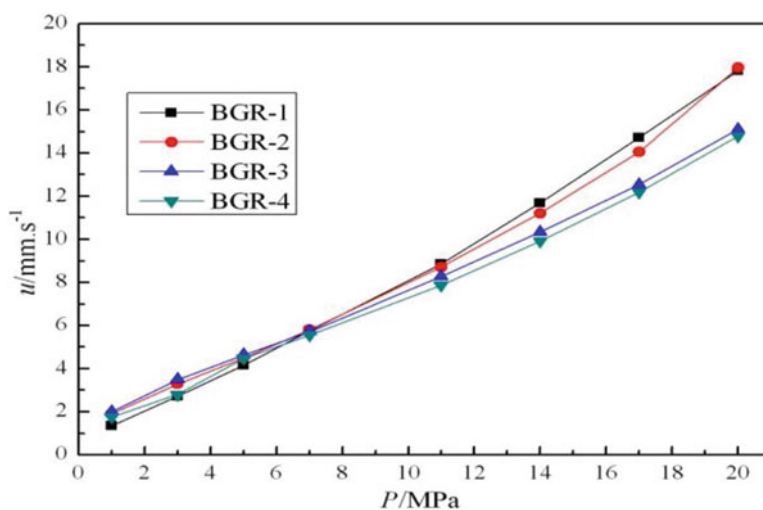
Fig. 7 Burning rates of p(BAMO-GAP)/RDX propellants

14 mm·s^{-1}. The four curves almost overlapped in the pressure range of 1–7 MPa, but are different over the higher pressure range (11–20 MPa). With the mass fraction of RDX in propellants increasing, the burning rates over high pressure range (higher than 7 MPa) drop observably, and the lower burning rate pressure exponents of the propellants are obtained correspondingly. The pressure exponents of propellants are calculated between 1 and 20 MPa and listed in Table 6.

Table 6 shows that the burning rate pressure exponents of p(BAMO-GAP)/RDX propellants are higher than 0.9 over the high pressure range(7–20 MPa) but relatively lower than 0.8 over the low pressure range (1–7 MPa). With the mass fraction of RDX in propellants increasing, the pressure exponents decrease at first then increase, and the pressure exponents get to the minimum point for BGR-3 sample.

Table 6 Burning rate pressure exponents of p(BAMO-GAP)/RDX propellants

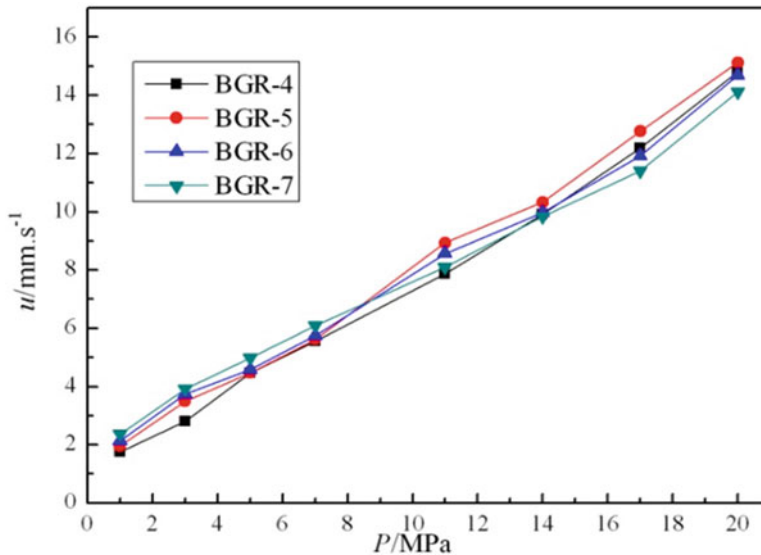| Samples	Burning rate pressure exponents		
	1–7 MPa	7–20 MPa	1–20 MPa
BGR-1	0.737	1.080	0.874
BGR-2	0.563	1.057	0.744
BGR-3	0.537	0.916	0.673
BGR-4	0.552	0.927	0.680

Fig. 8 Burning rates of p(BAMO-GAP)/RDX/Al propellants

4.1.2 Effect of Al

To illustrate the effects of mass fraction of Al in the propellants on combustion properties, Fig. 8 shows the burning rates' curves versus pressures of BGR-4 to BGR-7 formulations. It can be seen from Fig. 8 that with the mass fraction of Al increasing, the burning rates of propellants in low pressure range increase but decrease in the high pressure range except for BGR-5 sample. The burning rate pressure exponents of the propellants are decreased with an increase on the mass fraction of Al in the formulations. The exponents of propellants are calculated between 1 and 20 MPa and listed in Table 7.

Table 7 shows that the burning rate pressure exponents of p(BAMO-GAP)/RDX/Al propellants are higher than 0.7 in the high pressure range (7–20 MPa) but relatively lower than 0.6 in the low pressure range (1–7 MPa). With the mass fraction of Al in propellants increasing, the exponents are cut down as a whole. Especially, the pressure exponents reduce observably when the mass fraction of Al is more than 5 % (BGR-5).

Table 7 Burning rate
pressure exponents of
p(BAMO-GAP)/RDX/Al
propellants

Samples	Burning rate pressure exponents		
	1–7 MPa	7–20 MPa	1–20 MPa
BGR-4	0.592	0.927	0.720
BGR-5	0.531	0.923	0.686
BGR-6	0.489	0.752	0.635
BGR-7	0.479	0.779	0.582
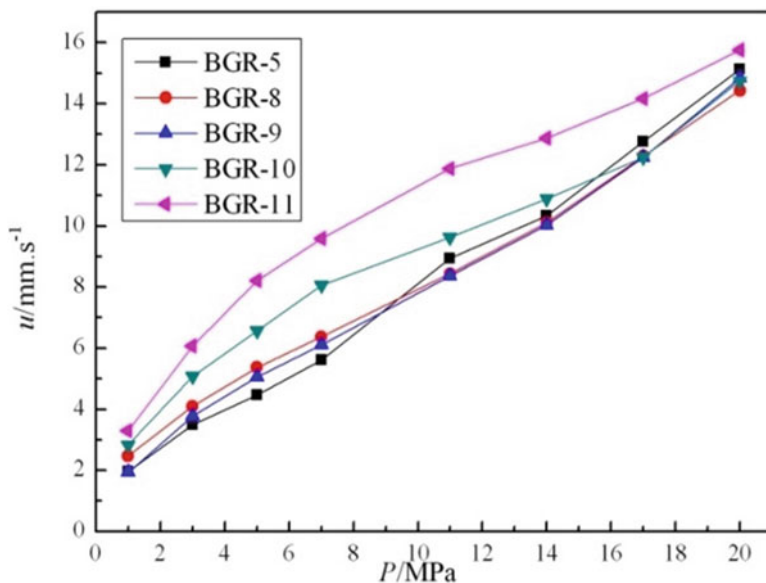
Fig. 9 Burning rates of p(BAMO-GAP)/RDX /Al/Ct propellants

4.1.3 Effect of Catalysts

To illustrate the effects of different catalysts in the propellants on combustion properties, Fig. 9 shows the curves of burning rates vs. pressures of BGR-5 and from BGR-8 to BGR-11 formulations. It can be seen from Fig. 9 that C1 and C2 increase the burning rates of propellants slightly over the pressure range from 1 to 7 MPa and reduce in the pressure range of 11–20 MPa in comparison with the uncatalyzed propellant (BGR-5). The dual-component catalysts (BGR-10) and tri-component catalysts (BGR-11) make the burning rates increase significantly. Especially for the tri-component catalysts, they make the burning rate of propellant at 5 MPa increase from 4.47 to 8.22 mm·s^{-1}. The pressure exponents are calculated and listed in Table 8.

Table 8 shows that all catalysts make the burning rate pressure exponents change over different pressure ranges. In the low pressure range (1–7 MPa), the results show that C1, as a most effective catalyst, reduces the pressure exponent from 0.531 to 0.484. However, it decreases the pressure exponent insignificantly over

Table 8 Burning rate pressure exponents of p(BAMO-GAP)/RDX/Al/Ct propellants

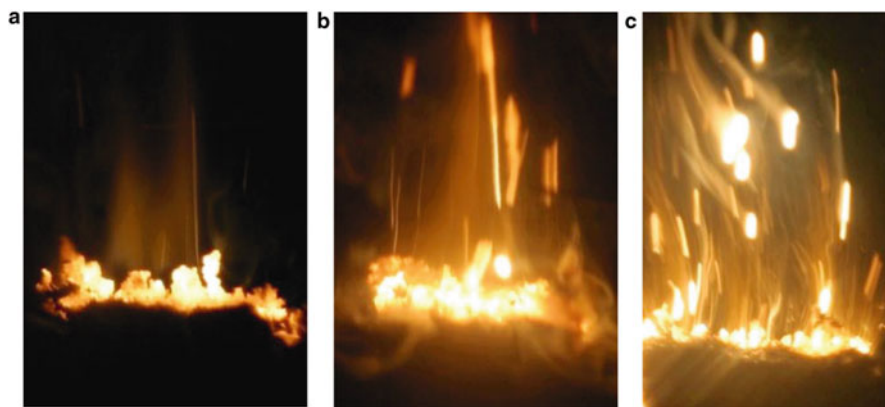| Samples	Burning rate pressure exponents		
	1–7 MPa	7–20 MPa	1–20 MPa
BGR-5	0.531	0.923	0.686
BGR-8	0.484	0.772	0.578
BGR-9	0.590	0.831	0.659
BGR-10	0.533	0.546	0.526
BGR-11	0.555	0.457	0.512

Fig. 10 Combustion flame structure photos of BGR-5. (**a**) 2MPa (**b**) 4MPa (**c**) 6MPa

a pressure range from 7 to 20 MPa. Over the high pressure range (from 7 to 14 MPa), the tri-component catalyst shows the most efficient catalysis on reducing the pressure exponent, which decreases from 0.927 to 0.457. Over the pressure range from 1 to 20 MPa, the tri-component catalysts reduced the pressure exponent from 0.686 to 0.512, which is the lowest among the propellant formulations. Therefore, the tri-component catalyst is more efficient for the combustion of p(BAMO-GAP)/RDX/Al/Ct propellants.

4.2 Combustion Flame Structures of p(BAMO-GAP)/RDX/Al/Ct Propellants

In order to investigate the effects of burning catalysts on the combustion flame structures of p(BAMO-GAP)/RDX/Al/Ct propellants, the combustion flame structures' photos of uncatalyzed (BGR-5) and propellants containing different catalysts (from BGR-8 to BGR-11) under different pressures are recorded by single color frame amplification photography technology and shown in Figs. 10, 11, 12, 13, and 14.

Figure 10 shows the combustion flame structure of uncatalyzed propellant. At the combustion surface of BGR-5 sample, the components (binders and RDX) of
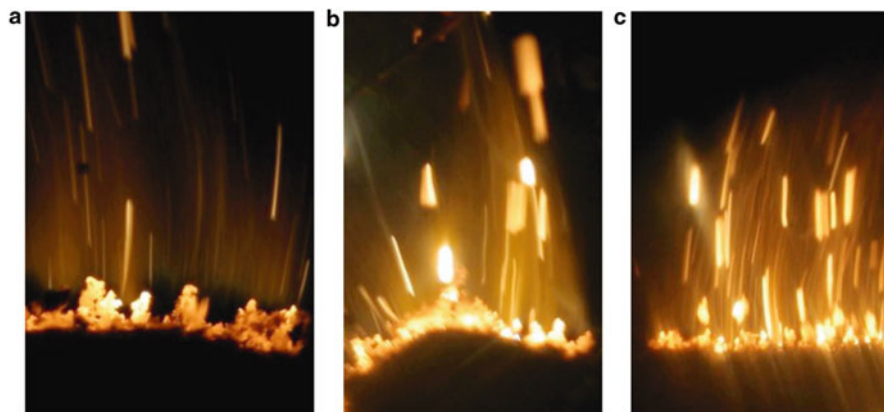
Fig. 11 Combustion flame structure photos of BGR-8. (**a**) 2MPa (**b**) 4MPa (**c**) 6MPa
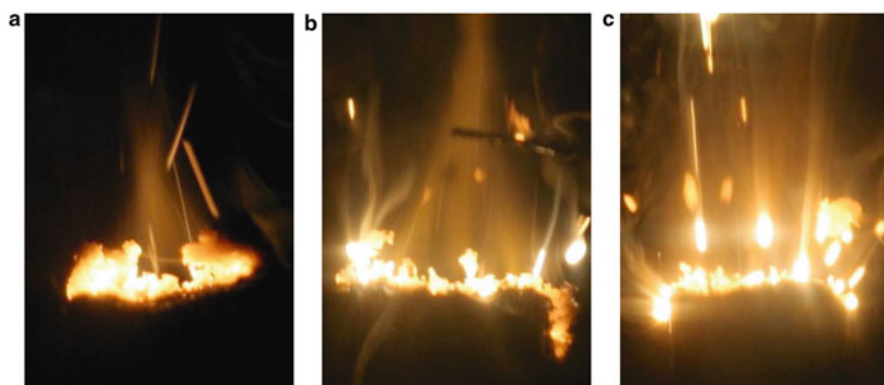

Fig. 12 Combustion flame structure photos of BGR-9. (**a**) 2MPa (**b**) 4MPa (**c**) 6MPa

propellants burn fiercely, and the irregular and lava-shaped combustion surfaces are formed. In the flame zone, the flame consists of soft orange flame and bright lines, which are yielded by binders and RDX, respectively. With the pressure increasing, the combustion surface becomes brighter, and the lava-shaped layer becomes thinner. Meanwhile, shining balls formed by the aluminum combustion and a little of them are ejected from the surface to the flame zone. With the pressure increasing further, the amount of shining balls in the flame zone increases (Fig. 10c). There is no obvious dark zone among the flame structures.

Figure 11 shows the combustion flame structure of propellant containing the catalyst, C1. Compared with the flame photos of Fig. 10 at the low pressure (Fig. 10a), there is an obvious dark zone that appeared between the flame zone and the combustion surface. The amount of bright lines in the flame zone increases significantly with C1 added (Fig. 11a). This may be attributed to the improvement of the combustion of RDX by C1. At the combustion surface, RDX is catalyzed
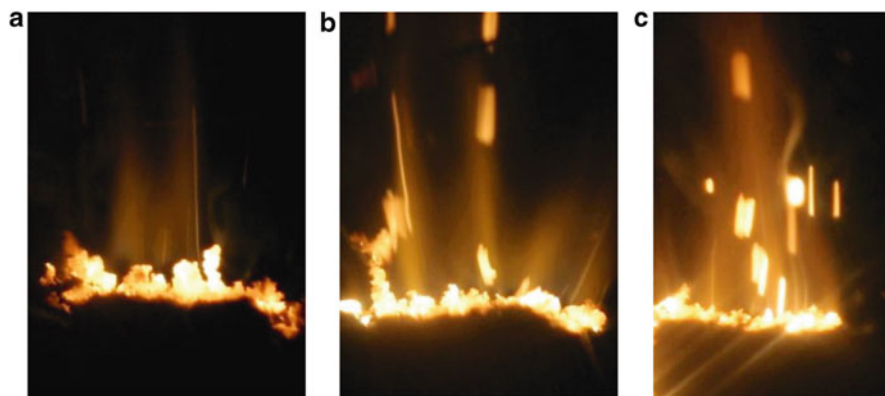
Fig. 13 Combustion flame structure photos of BGR-10 (**a**) 2MPa (**b**) 4MPa (**c**) 6MPa
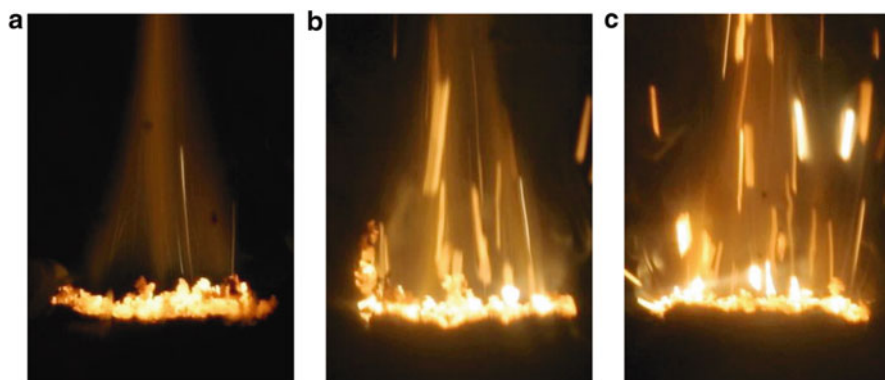

Fig. 14 Combustion flame structure photos of BGR-11. (**a**) 2MPa (**b**) 4MPa (**c**) 6MPa

to be decomposed, and the decomposition products are ejected to the combustion flame and reacted with the decomposition products of binders, which make the dark zone be formed. With the pressure increasing, the dark zone disappears, but more bright lines and shining balls are ejected because of the transported heat increasing between these two zones and the combustion of some airflows during the thermal decomposition [29, 30].

Compared with the flame photos of Fig. 10, the combustion flame structures of propellant containing catalyst C2 are similar with that of uncatalyzed propellants (Fig. 12). It indicates that the catalyst C2 is not effective for the combustion of the propellants.

Figure 13 shows the combustion flame structures of propellant containing dual catalysts (C1 and C2). The combustion flame structures of BGR-10 (Fig. 13) are similar with those of BGR-9. However, the amount of bright lines and shining balls

has decreased in comparison with those in Figs. 10 and 11. This illustrates that the reactions at the combustion surface are enhanced, which makes the burning rate higher.

With the tri-component catalysts added to the formulation, the combustion of propellant becomes fiercer (Fig. 14). The combustion surface becomes more regular and brighter in comparison with those of the formulation mentioned before. And the dark zone appears at low pressure and disappears with the pressure increasing. The decomposition and combustion of RDX are intensified. The catalysts make the reaction to mostly happen at combustion surface. The bright lines and shining balls are relatively reduced in the flame (compared with Fig. 10), which makes the burning rate higher.

4.3 Adiabatic Flame Temperatures of p(BAMO-GAP)/RDX/Al Propellants

In order to investigate the effects of catalysts on the adiabatic flame temperatures of propellants based on p(BAMO-GAP), the adiabatic flame temperature distribution at 4 MPa is tested and shown in Fig. 15. The differential curves are also shown in the figures in order to obtain the bounder temperature between two combustion zones because the changing rates of temperature versus distance on the bounder of zones are higher theoretically.

Two peak temperatures are obtained from differential curves. They divide the combustion flame into three combustion zones, which are solid reaction zone, mixed dark zone, and gas reaction zone. And the combustion surface temperature (T_s), dark zone temperature (T_d), and flame zone temperature (T_{max}) are obtained. These combustion flame structures are similar with those of propellants based on GAP [31]. However, it is inconsistent with the combustion flame structure photos of propellants, because the mixed dark zones are not observed in the photos at 4 MPa. This may be because the bright luminous flame jets from the combustion surface and the mixed dark zones are covered, which could not be observed by visual method. The analyzed data are shown in Table 9.

The results in Table 9 show that T_s increases in the order of [BGR-5]<[BGR-9]<[BGR-8]<[BGR-10]<[BGR-11], which is the same with the order of burning rates of propellants. This is because that the catalysts make the decomposition and combustion of RDX on the combustion surface improved, and there is more heat released. With the catalysts added to the formulations and the burning rate improved, the adiabatic flame temperature of mixed dark zone was enhanced as a whole, although the data are a little fluctuant. And the temperatures of flame zone fluctuate without rhyme because of the complex airflow in the gas reaction zone and the experiment error.
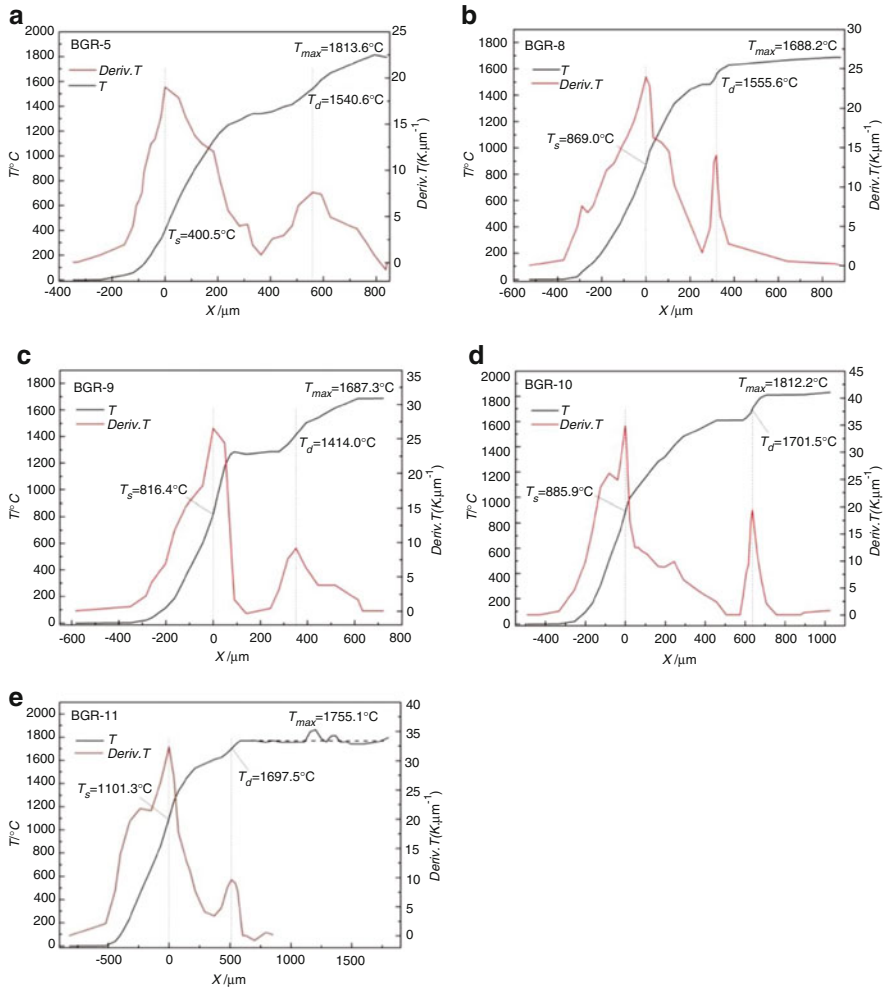
Fig. 15 Combustion wave distribution curves of propellants at 4 MPa. (**a**) BGR-5 (**b**) BGR-8 (**c**) BGR-9 (**d**) BGR-10 (**e**) BGR-11

Table 9 Combustion wave distribution data of propellants at 4 MPa

Samples	$T_s/°C$	$T_d/°C$	$T_{max}/°C$
BGR-5	400.5	1540.6	1813.6
BGR-8	869.0	1555.6	1688.2
BGR-9	816.4	1414.0	1687.3
BGR-10	885.9	1701.5	1812.2
BGR-11	1101.3	1697.5	1755.1

5 Conclusions

1. The energy properties of propellants increase when the binder and plasticizer are replaced gradually by oxidants. When AP is replaced by RDX, HMX, or CL-20, the energetic properties of propellants can be improved at first and then decreased. There is an optimum ratio between AP and other oxidants. However, the ideal energetic properties of propellants can be improved linearly when AP is replaced by ADN. When AlH_3 is added to the formulation instead of Al, the energetic properties of propellants would improve much.
2. With the mass fraction of RDX increasing in the propellants, the burning rates at low pressure remain almost the same but decrease observably at high pressure. With the mass fraction of Al increasing in the propellants, the burning rates of propellants can be improved over low pressure range but decreased over the high pressure on the whole. With the tri-component catalysts added to the formulation, the burning rates at low pressure are enhanced significantly, and the burning rate pressure exponent decreases.
3. There is no obvious dark zone in the flame of uncatalyzed propellant, and the combustion flame structure consists of soft orange flame and bright lines. When the tri-component catalysts are added to the formulation, the combustion of propellant becomes fiercer. And the dark zone appears at low pressure but disappears with the pressure increasing. The reactions of decomposition and combustion for RDX on combustion surface are intensified by the catalysts.
4. With the catalysts added to the propellant formulation, the burning rate can be improved, and the combustion surface temperature increases. The increasing order is similar with the order of burning rates of propellants. The combustion flame temperature of mixed dark zone is increasing as a whole, although the data are a little fluctuant.

References

1. Sikder AK, Reddy S (2013) Review on energetic thermoplastic elastomers(ETPEs) for military science. Propellants Explos Pyrotechnics 38:14–28
2. Miller RS (1996) Research on new energetic materials. Mater Res Soc Symp Proc 418:3–14
3. Beaupre F, Ampleman G, Ampleman G, Brousseau P, Thiboutot S (2002) Insensitive melt-cast explosive compositions containing energetic thermoplastic elastomers. Euro Patent. EP 1167324 B1
4. Nicole C (2003). Insensitive propellant formulations containing energetic thermoplastic elastomers. US Patent 608894 B1
5. Song XD, Zhao FQ, Wang JN, Gan XX, Xie B (2008) Thermal behaviors of BAMO-AMMO and its compatibility with some energetic materials. Chin J Explos Propellants 3(31):75–78

6. Gan XX, Li N, Lu XM, Han T, Xing Y, Liu Q (2008) Synthesis and properties of ETPE based on BAMO/AMMO. Chin J Explos Propellants 2(31):81–86

7. Zhang ZG, Lu XM, Gan XX, Han T, Xing Y (2007) Synthesis of BBMO and BAMO by phase transfer catalysis method. Chin J Explos Propellants 5(30):32–36

8. Song XD, Zhao FQ, Wang JN, Tian J, Zhang LY, Gan XX (2011) Thermal decomposition mechanism and non-isothermal pyrolysis kinetic analysis of BAMO-AMMO copolymer. Acta ArmamentarII 11(32):1320–1325

9. Song XD, Zheng W, Pei JF, Zhang J, Wang JN, Zhao FQ (2014) Effect of RDX content on mechanical properties of BAMO-AMMO base propellants. Acta ArmamentarII 6(35):828–834

10. Pei JF, Zhao FQ, Jiao JS, Li M, Xu SY, Chen JB (2014) Energetic characteristics of p(BAMO-AMMO) based propellants containing different metal hydride. Explos Mater 4:1–15

11. Li M, Zhao FQ, Xu SY, Yao EG, Hao HX, Li X (2013) Energetic characteristics and signature of composite propellant containing different oxidizer. J Propuls Technol 8(34):1134–1139

12. Sanghavi RR, Asthana SN, Karir JS, Singh H (2001) Studies on thermoplastic elastomers based RDX-propellant composition. J Energ Mater 19:79–95

13. Oyumi Y, Inokami K, Yamazaki K (1994) Burning rate augmentation of BAMO based propellants. Propellants Explos Pyrotechnics 19:180–186

14. Aparecida MK, Milton FD, Lucia LV, Marta FT, Thomas K, Horst K, Kaus M, Paul BK (2010) Synthesis and characterization of GAP/BAMO copolymers applied at high energetic composite propellants. J Aerosp Technol Manag 2(3):307–322

15. Thomas K, Roberto M (2009) Preliminary characterization of propellants based on p(GA/BAMO) and pAMMO binders. Propellants Explos Pyrotechnics 34:427–435

16. Keicher T, Dorich M, Foerter-Barth U, Grunfelder C, Krause H, Schaller U, Steinert S (2012) Preparation and properties of energetic thermoplastic elastomers from GAP and poly-BAMO. In: 43rd international annual conference of ICT: 8/1-8/10

17. Kawamoto AM, Oliveira JI, Dutra RC, Rezende LC, Keicher T (2009) Synthesis and characterization of energetic thermoplastic elastomers for propellant formulations. J Aerosp Technol Manag 1(1):35–42

18. Barbieri U, Keicher T, Massimi R, Polacco G (2008) Preliminary characterization of propellants based on GA/BAMO binders. In: 39th international annual conference of ICT:130/1-130/10

19. Ge Z, Luo YJ, Guo K, Lv Y, Jiu YB (2009) Review on synthesis of BAMO homopolymer and copolymers. Chin J Energ Mater 6(17):745–750

20. Zhao YB, Luo YJ, Li XM (2012) Synthesis and characterization of BAMO-r-GAP copolymer. Polym Mater Sci Eng 9(28):1–4

21. Menke K, Kempa PB, Keicher T, Kawamoto A, Holanda JA (2007) High energetic composite propellants based on AP and GAP/BAMO copolymers. In: 38th international annual conference of ICT: 82/1-82/10

22. Paletsky AA, Volkoy EN, Korobeinichev OP, Tereshchenko AG (2007) Flame structure of composite pseudo-propellants based on nitramines and azide polymers at high pressure. Proc Combust Inst 31(2):2079–2087

23. Li M, Zhao FQ, Xu SY, Gao HX, Yi JH, Pei Q, Tan Y, Li N, Li X (2013) Comparison of three kinds of energy calculation programs in formulation design of solid propellants. Chin J Explos Propellants 36(3):73–77

24. Chenoweth JD, Brinckman KW, York JJ, Feldman G, Dash SM (2007) Progress in modeling missile fuel venting and plume contrail formation. AIAA paper 2007-1012

25. Gordon S, McBride BJ (1994) I analysis: computer program for calculation chemical equilibrium compositions and applications. NASA RP-1311

26. McBride BJ, Gordon S (1996) II User's manual and program description: computer program for calculation of chemical equilibrium compositions and applications. NASA RP-1311

27. Hamilton RS, Mancini VE, Sanderson AJ (2004) ETPE ManTech program. 2004 insensitive munitions and energetic materials technology symposium

28. Tian DY, Zhao FQ, Liu JH (2011) Handbook of energetic materials and the related compounds. National Defense Industry Press, Beijing

29. Zhao FQ, Shan WG, Wang Y, Li SW, Li SF, He DQ (2000) Quenched surface characteristics and flame structure of RDX-CMDB propellants containing catalyst. Energ Mater 2(8):67–71
30. DeLuca LT, Cozzi F, Germiniasi G, Ley I, Zenin AA (1999) Combustion mechanism of an RDX-based composite propellant. Combust Flame 118:248–261
31. Zhao XB, Zhang XP, Hou LF (1999) Study of combustion wave temperature distribution of GAP/AN propellant. J Propuls Technol 20:92–95

Synergistic Effect of Ammonium Perchlorate on HMX: From Thermal Analysis to Combustion

Alla N. Pivkina, Nikita V. Muravyev, Konstantin A. Monogarov, Valery G. Ostrovsky, Igor V. Fomenkov, Yury M. Milyokhin, and Nickolay I. Shishov

Abstract The thermal decomposition and combustion of binary mixture of octahydro-1,3,5,7-tetranitro-1,3,5,7-tetrazocine (HMX) and ammonium perchlorate (AP) are investigated at various concentrations. Thermal stability was investigated by thermal analysis techniques, i.e., DSC/TGA, combined with FTIR spectrometry, and accelerating rate calorimetry (ARC). Twofold HMX/AP interaction result is observed: ammonium perchlorate as synergistic additive effectively (in 60 °C) reduces the onset decomposition temperature of HMX, whereas gaseous products of the HMX thermolysis, in turn, catalyze the AP decomposition. Burning rate of mechanical mixtures exceeds the HMX level at 4 MPa, when HMX content lies in the range close to above synergistic effect at thermolysis, and AP particle size is fine (10 μm). Addition of large AP particles to HMX does not enhance the burning rate. Comparative analysis of the combustion parameters of the mechanical mixtures and large HMX crystals covered with AP layer revealed that the direct contact between components is not a necessary condition for the HMX/AP interaction for compositions without binder, proving the gas-phase character of this effect. However, for compositions with active binder, the direct contact between components is important. Finally, the synergistic effect changes the decomposition pathway for mixtures with HMX content above 40 % and below 90 % and noticeably increases the burning rate of HMX-based compositions with active binder. Formulations with active binder and coated HMX provide higher

A.N. Pivkina (✉) • N.V. Muravyev • K.A. Monogarov
Semenov Institute of Chemical Physics, 119991 Moscow, Russia
e-mail: a7777@center.chph.ras.ru

V.G. Ostrovsky
PLC Central Scientific Design Bureau, 129110 Moscow, Russia
e-mail: ostrovskiy.valery@mail.ru

I.V. Fomenkov
Zelinsky Institute of Organic Chemistry, 119991 Moscow, Russia

Yu.M. Milyokhin • N.I. Shishov
Soyuz Federal Center for Dual-Use Technologies, Dzerzhinskii 140090, Russia
e-mail: fcdt@mail.ru

burning rate than those ones with mechanical mixtures of HMX with fine AP. It means the possibility to use the considerably less amount of ammonium perchlorate to achieve the same level of the burning rate.

Nomenclature

AFM	atomic force microscopy
AP	ammonium perchlorate
ARC	accelerating rate calorimetry
DSC	differential scanning calorimetry
FTIR	Fourier transform infrared spectrometry
HMX	octahydro-1,3,5,7-tetranitro-1,3,5,7-tetrazocine
NIST	National Institute of Standards and Technology
SEM	scanning electron microscopy
TGA	thermogravimetric analysis

1   Introduction

Octahydro-1,3,5,7-tetranitro-1,3,5,7-tetrazocine (HMX) and ammonium perchlorate (AP) are the most used components in modern solid propellants. Both compounds have very different monopropellant flame temperatures, i.e., 3200 K for HMX versus 1400 K for AP, but quite close burning rates (1.1 cm/s and 0.8 cm/s, respectively, at 68 atm) [1]. Addition of AP to HMX formulations is known to increase the burning rate and decrease the pressure exponent and the fume formation. Although the regularities of thermolysis and combustion of these two components are of very high practical importance, the systematic study of interaction between them is still to be done.

It is known that compounds with melting point below the HMX decomposition onset decrease the temperature of HMX thermolysis. Thus, ammonium nitrate addition leads to the exothermic peak temperature decrease down to 247 °C; NH_4NO_3 melts at 169 °C [2]. The addition of 10 % of $LiClO_4$ results in the onset temperature reduction to 200 °C, which is caused by the eutectic melt formation. The hydrophilic lithium perchlorate forms under air monohydrate with melting temperature $T_m = 149$ °C and trihydrate with $T_m = 95.1$ °C. Eutectic $LiClO_4 \cdot H_2O$-$LiClO_4$ melts at 146 °C. Magnesium perchlorate forms three congruently melting hydrates and decreases the HMX onset temperature down to 177 °C. Nitroguanidine melts at 230 °C, which results in onset temperature reduction to 227 °C [3].

The same effect has the addition of the metal salts of propionitrile nitramine, which melt and decompose below 200 °C, thus decreasing the HMX decomposition temperature in 60–70 °C. Authors propose that the reason of this result is formation of the highly reactive anion radicals during the salt decomposition, which in turn interact with the HMX molecule [4].

The addition of HMX to AP-based composite propellants with inert binder resulted in a marked reduction in the ignition times due to the lowering of nitramine's exothermic reaction onset [5]. Neat HMX decomposes at 280 °C, whereas the heating of HMX particles covered by AP leads to the considerable decomposition temperature decrease down to 200–225 °C with the corresponding burning rate increase [3].

During heating of the formulations active binder/HMX/AP/Al, when the ratio between AP and HMX is equal to 14/86, the DSC curve reveals three exothermic peaks. But with increasing of AP content to 35 %AP/65 %HMX, the DSC signal shows one exo peak only [6]. Thus, the literature data reveal the influence of AP on the thermal stability of HMX-containing compositions with both inert and active binder.

According to thermal analysis data, ammonium perchlorate does not melt and decompose below the phase transition temperature (240 °C); thus the reason of the considerable (up to 60 °C) decrease of the HMX onset thermolysis temperature during heating of the mixture HMX/AP is not clear. The aim of this article is to shed the light on the mechanism of the HMX thermal stability decrease in presence of ammonium perchlorate. We have focused on the systematic investigation of the HMX/AP decomposition and combustion processes by thermal analysis and burning rate measurements in the wide range of AP concentrations. The role of the contact between both components was investigated too by comparative analysis of the HMX crystals covered with AP and HMX/AP mixtures with the same components concentration. Understanding of the HMX/AP interaction is important, in particular, for the HMX-based formulations with active binder, because the search of the HMX combustion modifier, which is compatible with the active binder, is still an open unsolved problem. Understanding of the mechanism of HMX/AP interaction will enable to increase the combustion efficiency of HMX-based formulations.

2 Materials and Methods

2.1 Materials

The feedstock materials used in this work included two HMX powders with the average particle sizes of 50 and 200 μm, as well as three ammonium perchlorate powders with the average particle sizes of 230, 40, and 10 μm. AP powders were dried at 333 K during 6 h in an oven prior to use to eliminate moisture.

For thermal analysis and combustion experiments, two types of binary systems were used. First one was mechanically mixed HMX and AP powders with Turbula® mixer. The second types were HMX crystals coated with AP layer of different thickness, thus having different HMX/AP ratio.

2.2 Microstructure

To study the microstructure of the as-received powders and HMX crystals covered with ammonium perchlorate, scanning electron microscope Versa 3D DualBeam™ instrument (FEI) was used. To evaluate the uniformity and the thickness of the AP layer on the HMX crystals, X-ray 3D-tomograph Xradia VersaXRM-500 (FEI) was applied.

2.3 Thermal Analysis

Simultaneous DSC/TGA thermal analysis was performed with STA 449 F3 thermal analyzer (Netzsch). The sample with mass ≈ 1 mg was placed in closed alumina pan with a pinhole lid and heated to 500 °C with the heating rate 10 K/min under argon flow (70 ml/min).

Evolved gas products during DSC/TGA analysis were detected online with FTIR spectrometer (Alpha, Bruker) with the resolution of 4 cm^{-1}.

Accelerating rate calorimetry (MMC 274 Nexus, Netzsch) was performed on AP samples ≈ 300 mg in heat-wait-search mode.

2.4 Combustion Experiments

To obtain the burning rate parameters, HMX/AP mixtures or HMX crystals covered with AP were pressed at 350 MPa in 3 min into cylinders with diameter 8 mm and then coated on the lateral surface with epoxy adhesive Poxipol™ to provide the linear propagation of the combustion front. Measurements were performed using a constant pressure bomb (volume 1.5 l) under nitrogen. In addition to the pressure-time recording, high-speed video with 1200 fps (Casio EX-F1) was used to measure the burning rate. The resulting accuracy of the burning rate measurements was ± 5 %.

3 Results and Discussion

3.1 Microstructure

Two types of the HMX/AP mixtures were investigated, i.e., the mechanical mixture of the particles, where $d_{HMX} = 50$ µm and $d_{AP} = 40$ µm, and HMX crystals ($d = 200$ µm) covered with AP, which were produced with the ammonium perchlorate content 5–30 mass %, with the corresponding AP layer thickness variation
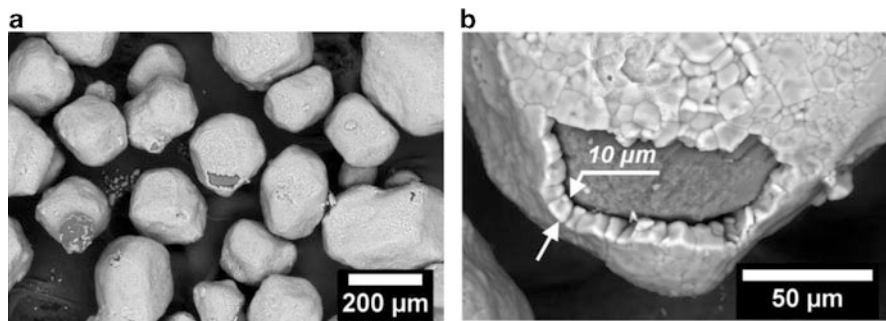
Fig. 1 SEM images of HMX crystals covered with ammonium perchlorate: general view (**a**), and the detailed microstructure of the particle edge showing AP layer thickness (**b**)

3–10 μm. Continuous uniform AP layer formation on the HMX crystals was achieved. The local partial absence of the coating on HMX crystal edge allows observation of the microstructure of the coating layer and the estimation of the layer thickness, as presented in Fig. 1. The AP coating consists of one layer of the closely packed grains with the relatively constant thickness. SEM images in Fig. 1 are obtained in the backscattered electron registration regime, thus providing the compositional contrast – AP particles are brighter than HMX. X-ray 3D tomography confirms the estimated layer thickness. The AP content for the particular sample presented in Fig. 1 is 30 mass %, whereas the layer thickness is 10 μm.

3.2   Thermal Analysis

3.2.1   General Remarks

The DSC and TGA curves obtained for neat HMX, AP powders, and HMX/AP mixture (mass ratio of HMX to AP is 1:1) at the heating rate of 10 K/min are shown in Figs. 2 and 3. Obtained dependencies for the HMX particles coated with AP were almost identical to HMX/AP mixtures with equivalent HMX content.

The first endothermic peak at DSC curve for HMX at 180–190 °C corresponds to the phase transition, where the β-polymorph converts into δ-HMX. The small endothermic peak at 280 °C is caused by the HMX melting followed by the subsequent exothermic decomposition.

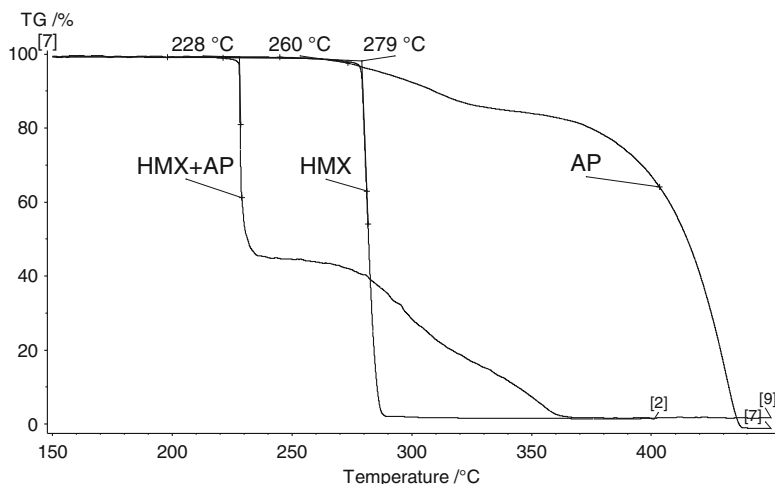According to Brill [7], the global decomposition branches for HMX are represented by the following reactions:

$$\text{HMX} \rightarrow 4\,(\text{NO}_2 + \text{HCN} + \text{H}) \tag{1}$$

$$\text{HMX} \rightarrow 4\,(\text{N}_2\text{O} + \text{CH}_2\text{O}) \tag{2}$$
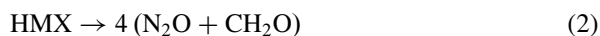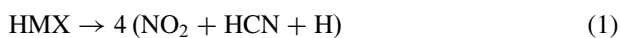
Fig. 2 TGA curves for HMX, AP, and HMX/AP (1:1) decomposition. Onset decomposition temperatures are indicated on the plot
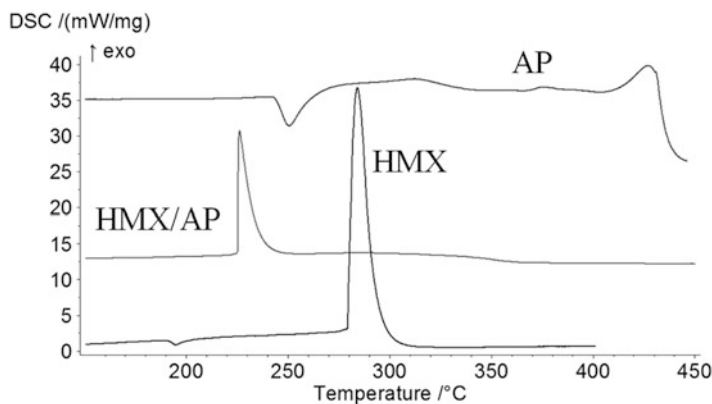

Fig. 3 DSC dependencies of AP, and HMX/AP (1:1) and HMX samples (not in one scale for visibility)

N_2O and NO_2 appear before CH_2O and HCN, which are formed from the residue left by elimination of N_2O and NO_2. This residue is a mixture of products like hydroxymethylformamide and acetamide [8, 9].

The thermal effect of HMX decomposition, as determined by DSC experiments, is equal to 1500 ± 150 J/g (average on three experiments).

Three thermal events are observed at DSC curve for AP: an endothermic peak near 240 °C and two exothermic peaks around 300 and 450 °C. The endothermic peak near 240 °C is attributed to the phase transition of AP from the orthorhombic to cubic form with the density decrease in 9.7 % (from 1950 to 1760 kg/m^3 [10]),

resulting in micro-cracks formation inside AP crystals [11]. Two exothermic peaks of AP decomposition are assigned to low- and high-temperature decomposition. According to [12], the brutto formula of AP decomposition could be presented as:

$$NH_4ClO_4 \rightarrow \alpha \, (NH_3 + HClO_4) + (1-\alpha) \left(\frac{7}{2}O_2 + \frac{1}{2}N_2 + \frac{5}{2}H_2O + \frac{1}{2}Cl_2 + \frac{2}{3}HCl \right)$$

(3)
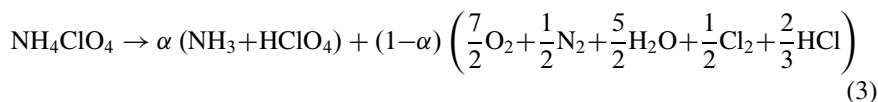
where α is the amount of sublimated substance at low-temperature decomposition, which in turn depends on the free volume.

Two main differences appear when HMX/AP (1:1) mixture decomposes: the onset decomposition point is considerably shifted to the lower temperature with the corresponding shift of DSC peak, and decomposition terminates considerably earlier than that for neat AP.

Brill [13] investigated the influence of gaseous environment on HMX decomposition in H_2, CO, O_2, or NO environments. No changes in the composition of the primary thermolysis products were revealed, but variations in secondary reactions only. In NH_3 environment the HMX decomposition starts considerably earlier than that in other investigated gases. Significant changes in the primary decomposition species were observed: the amount of CH_2O, HCN, and NO_2 quickly drops, whereas N_2O one increases probably due to reaction $NH_x + NO_x$. Ammonia acts as a hydrogen donor for HMX.

Results presented in Fig. 2 reveal that AP decomposition in the mixture HMX/AP is terminated at 360 °C, which is in ~90 °C lower than that for the neat AP. This indicates that the thermal decomposition of AP is catalyzed by HMX too. Similar effect of AP decomposition catalysis by RDX was found recently [14].

Thus, twofold HMX/AP interaction result is observed: AP decreases the onset of HMX thermolysis, whereas decomposition of nitramine, in turn, catalyzes the AP degradation.

3.2.2 Two "Scenarios" of HMX/AP Mixture Decomposition

Analysis of thermograms obtained at various component concentrations revealed that, depending on the HMX content in the HMX/AP binary mixture, thermolysis follows to one of two different "scenarios," i.e., "independent" (several exo peaks) and synergistic (one pronounced exo peak) decomposition of components.

"Independent" regime (Fig. 4) was observed for two ranges of HMX concentration: $0 < C_{HMX} < 40$ % and $90 < C_{HMX} < 100$ %. Decomposition starts with sharp DSC peak at 220–230 °C. The shape of first exo peak, the amount of heat release, and the mass loss at this stage correspond to the HMX concentration in the mixture, whereas the subsequent DSC peaks and the mass loss are ascribed to ammonium perchlorate decomposition.

"Synergistic" decomposition (Fig. 5) was founded for the HMX concentration lying in the range 40 % $\leq C_{HMX} \leq 90$ %. DSC curve has only one pronounced DSC peak around onset temperature of 225 °C, indicating both component thermolysis
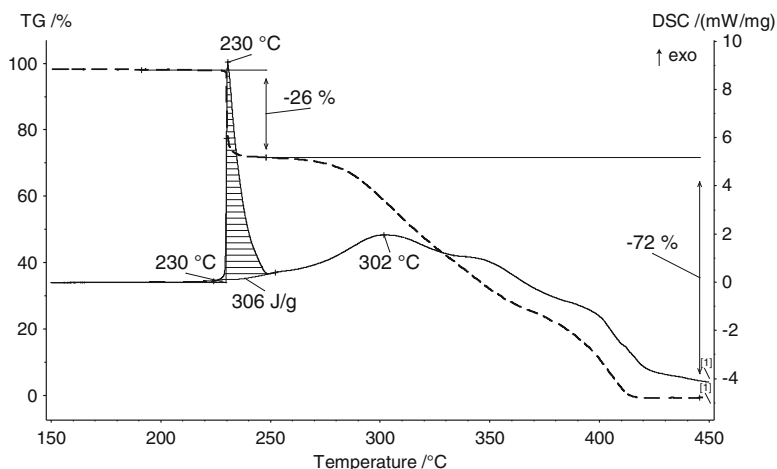
Fig. 4 TGA (*dotted line*) and DSC (*solid line*) dependencies of 20 % HMX/80 % AP mixture thermolysis
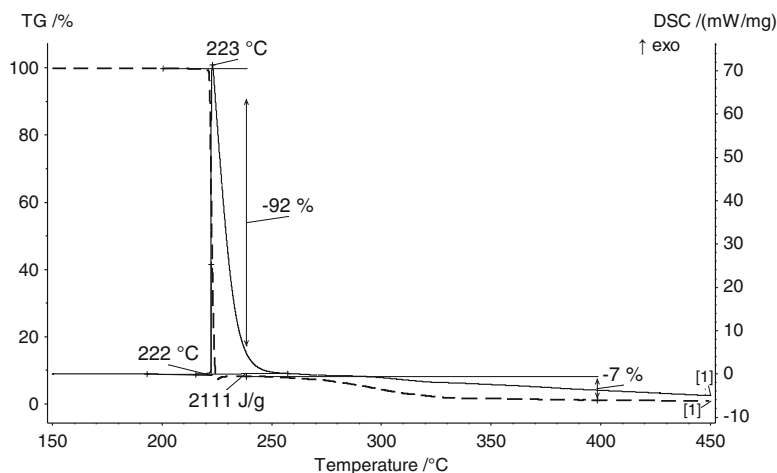
Fig. 5 TGA (*dotted line*) and DSC (*solid line*) dependencies of 75 % HMX/25 % AP mixture thermolysis

at this temperature. The maximum of the heat release rate is achieved at 230 °C, whereas the heat release of 2100 J/g exceeds this value for the neat HMX (1500 J/g at 280 °C) at the same experimental conditions. The catalytic effect of the HMX gaseous products on the AP decomposition is also the most pronounced within indicated HMX concentration range.

Figure 6 presents diagram of DSC signals (in one scale) as a function of HMX concentration in the binary mixture HMX/AP.

Fig. 6 DSC signals for HMX/AP mixtures as a function of the HMX content. DSC curves are presented in one scale; the HMX content is indicated on the plot

The position of the HMX exo peak strongly depends on the HMX/AP ratio. Below 40 % in mixture, nitramine decomposes at 225 °C with the heat release corresponding to its mass, wherein ammonium perchlorate reacts mostly at temperature slightly below the neat AP, as prese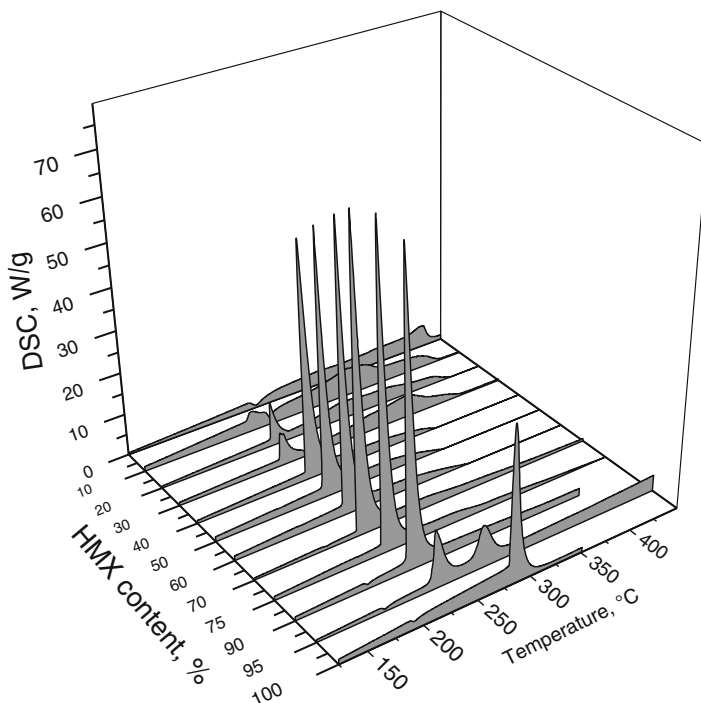nted in Fig. 4. Increasing of the HMX content to 40 % $\leq$ C$_{HMX}$ $\leq$90 % results in synergistic decomposition of both components starting at temperature 216$\leq$ T_0 $\leq$232 °C, where one sharp exo peak with higher heat release is observed. Complete mass loss of the mixture occurs in about 90 °C earlier than that for pure AP. The increase of the HMX content above 90 % leads to splitting of sharp exo peak into several peaks: part of the nitramine decomposes at temperature 225 °C, whereas the rest of HMX – at its "own" temperature 280 °C.

3.2.3   Onset Decomposition Temperature

Figure 7 represents the T_0 dependency on the HMX concentration (C$_{HMX}$) within the mixture and reveals T_0 to be practically independent on C$_{HMX}$, except 0 and 100 % points. The observed decrease of the onset decomposition temperature and
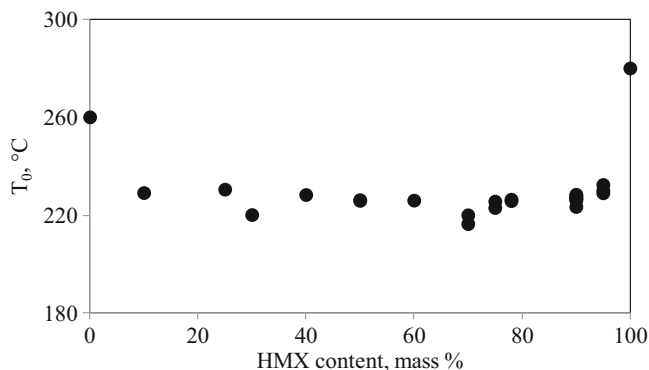
Fig. 7 Onset decomposition temperature (T_0) for the binary mixtures HMX/AP as a function of HMX content

its independency on the component concentration are very probably caused by the phase transition phenomena of HMX and/or AP, occurring in the same range.

3.2.4 HMX Phase Transition

Thermal decomposition process of HMX, AP, and HMX/AP mixture was monitored by in situ FTIR measurements at heating in DSC-TGA thermal analyzer. Resulting IR spectra at temperatures just prior and at the onset point of synergistic decomposition, i.e., 150–230 °C, are presented in Fig. 8. No gas-phase products were observed in this temperature range for ammonium perchlorate, whereas for HMX two volatile decomposition products, i.e., N_2O and HCN (not indicated in Fig. 8), were identified, accompanied by the small mass loss of 0.03 % within the temperature range from just phase transition point 187 °C till 230 °C.

It is known that $\beta \rightarrow \delta$ phase transformation is accompanied by the density decrease from 1900 to 1780 kg/m^3 with the correspondent increase of the crystal volume in 7 %, which in turn results in the crystal fracturing [15]. Increase of the chemical reactivity of HMX during or just after its polymorph transformation is initiated by the high mobility of the moving parts of the crystal lattice during its rearrangement, analogous to Hedvall effect – a significant change in the reactivity near the temperature of the phase transition [16]. It is known that the primary decomposition products react with the parent molecule and can therefore increase the sensitivity of the material and catalyze further decomposition. Both thermal decomposition and the phase transition are concerned with disruption of intermolecular forces (since the conformational change associated with β-δ has low activation energy).

Weeks et al. [17] used atomic force microscopy (AFM) to monitor the crystal surface during phase transition. They observed an increase in surface roughness by a factor of four and the opening up of voids.
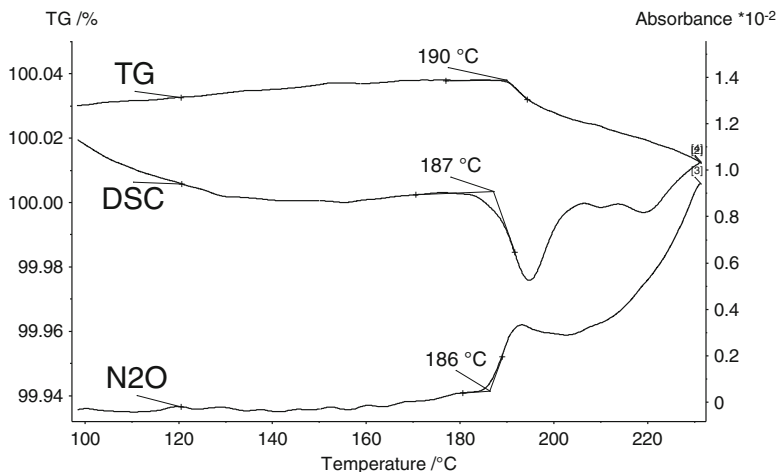
Fig. 8 HMX heating: FTIR absorbance intensity of N_2O versus temperature along with TGA and DSC (in arbitrary units) dependencies, sample mass 250 mg

Our observation of N_2O and HCN just after the phase transition is in line with Behrens data [9] on isothermal HMX decomposition at 195 °C. These products were the first ones observed; moreover, the influence of the morphology changes on the decomposition was also noticed.

3.2.5 AP Phase Transition

The phase transition of ammonium perchlorate starts under the crystal surface [18] and proceeds in two steps [10, 18–20]. The orthorhombic to cubic transformation at 240 °C follows to the transition of AP into metastable phase (order-disorder phase transition) at about 200 °C with formation of not-oriented grains of the cubic phase, as it was found experimentally by measuring the ultrasonic velocity within AP crystals [19]. This transformation proceeds without heat effect and can't be observed on DSC curves. The same phase transitions are known for other ammonium salts [20, 21]. At T >240 °C the polymorph phase transition goes via formation and abrupt increase of the needle-shaped nucleus, which is the first-order phase transition with the energy cost 11.3 kJ/mol [22]. The mass loss due to low-temperature decomposition starts just after this phase transition.

Destabilization of AP crystal during phase transformation effectively facilitates the partial conversion from the ionic state to neutral *NH₃* and *HClO₄* molecules, which are the primary products of AP decomposition at 200–250 °C, as a result of proton transfer from NH_4^+ to ClO_4^-. Ammonia is released into the gas phase, whereas perchloric acid is predominantly accumulated at the crystal surface [11, 18, 23].
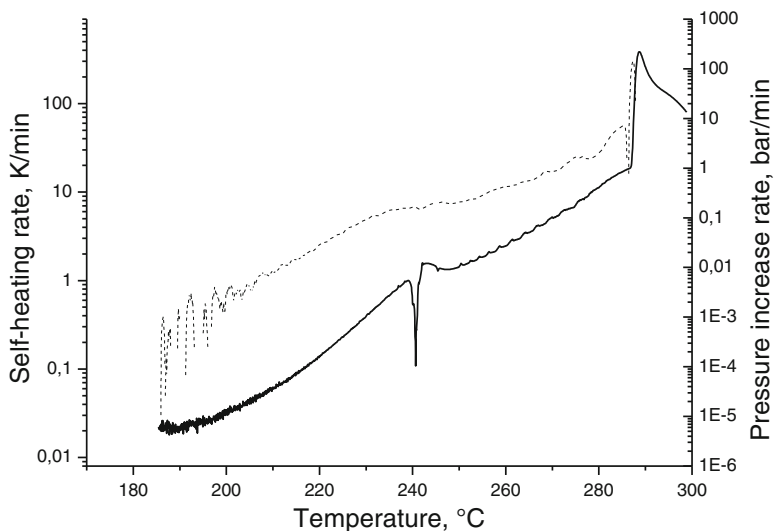
Fig. 9 Adiabatic self-heating rate (*solid line*) and pressure increase rate (*dotted line*) of ammonium perchlorate

Our FTIR experiments did not show gas-phase decomposition products after the metastable phase formation (200 °C) prior to endothermic phase transformation at 240 °C.

We use accelerating rate calorimetry to study the thermolysis of AP with enhanced sensitivity due to the increased sample mass. Figure 9 shows the self-heating and pressure increase rates as function of temperature in a pseudo-adiabatic environment. Decomposition of AP starts with the strong acceleration at 185 ± 5 °C, below the crystal phase change at 240 °C. The same result has been published by Bohn [24].

3.2.6 Gaseous Products at Maximum Decomposition Rate

The FTIR of gaseous products of AP, HMX, and HMX/AP (1:1) mixtures are presented in Fig. 10 at temperature corresponding to the maximum rate of the heat release (230 °C). Practically no gaseous products of AP at this temperature were detected, excepting CO_2, which is most likely originated from background.

N_2O and HCN peaks were identified for neat HMX. Addition of AP to HMX in proportion 1:1 results in NO_2 peak appearance, indicating the N-N bond homolysis in HMX molecules, thus proving the nitramine decomposition at this temperature.

Some bands in the range of 2778–2896 cm^{-1} (I, Fig. 10) and 1715–1788 cm^{-1} (II, Fig. 10) were not identified using the NIST Standard Reference Data [25], although authors [14] contradictorily interpreted these peaks as HCl and CH_2O, respectively. Note that these peaks are observed also in HMX spectra at 230 °C, but with much lower intensity.
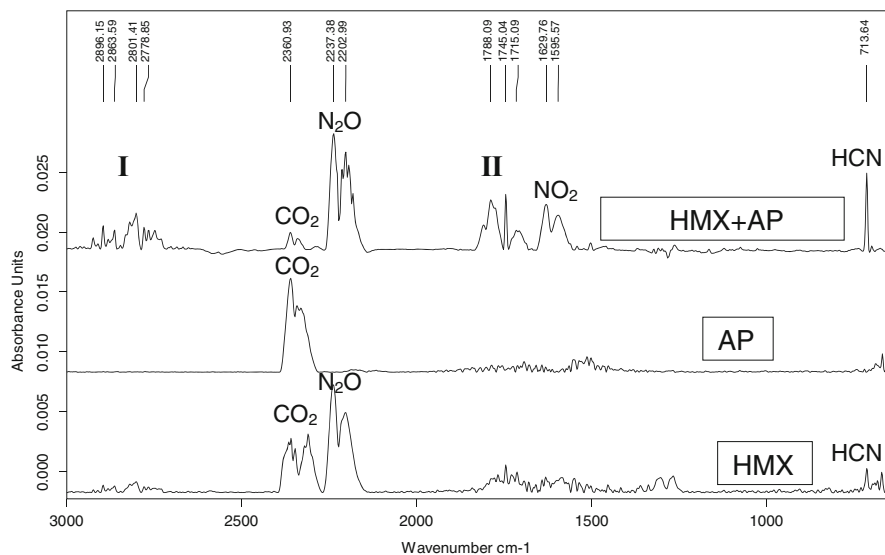
Fig. 10 FTIR curves of AP, HMX, and HMX/AP (1:1) mixtures decomposition products at a heating rate of 10 °C min^{-1} at the maximum of DSC signal, corresponding to maximum rate of the heat release (230 °C)

Thus, before the onset decomposition temperature of HMX/AP (1:1) mixture, both components undergo the phase transition. According to the literature data, AP converts into metastable phase with the crystal structure rearrangement starting from 200 °C with the subsequent gas products release. ARC experiments also prove this statement. Our experiments reveal HMX begins to decompose simultaneously with the phase transition with release of N_2O and HCN. Significant change of the reactivity of both components near the phase transition points (Hedvall effect) results in intensive interaction of the decomposition gas products with thus destabilized molecules.

3.3   Combustion Parameters

The burning rate of pressed samples, consisting of the HMX particles ($d = 200\,\mu$m) coated with different amount of AP, i.e., having a layer of different thickness, was measured under nitrogen pressure 4 MPa. Increasing of the AP content to 30 mass % results in the burning rate growth, as presented in Fig. 11.

To compare obtained U(C_{HMX}) dependency with one for the mechanical mixture of components, identical samples were fabricated with HMX ($d = 200\,\mu$m) and AP ($d = 10\,\mu$m) particles. The size of ammonium perchlorate powder was selected to be equivalent to AP layer thickness on coated HMX particles. The evolution of the
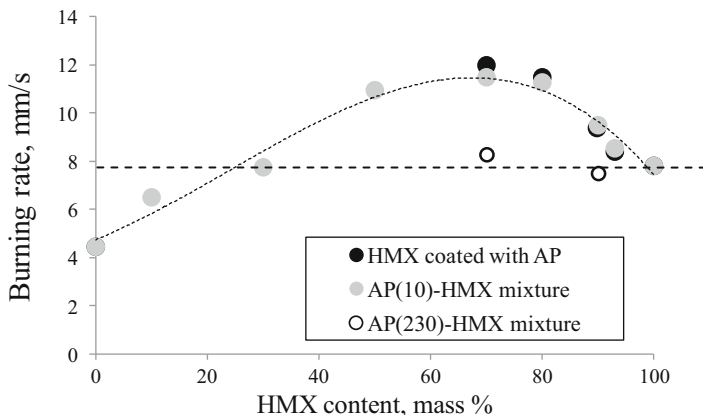
Fig. 11 Burning rate dependency on the AP content under nitrogen pressure 4 MPa for two types of HMX/AP compositions: ◔-pressed mixtures of HMX with AP ($d = 10$ μm), ◯-pressed mixtures of HMX with AP ($d = 230$ μm), and ●-HMX particles covered with AP (layer thickness 10 μm). HMX particle size is equal to 200 μm for these experiments

burning rate of this mixture with C_{HMX} shows that (i) in the range 30< C_{HMX} <93 %, close to the region of the synergistic effect appearance, U values exceed the HMX-monopropellant level at this pressure and (ii) burning rate of HMX crystals coated with AP coincides with this value for the mechanical mixture when AP particle size is close to the layer thickness. Thus, the contact between components is not a necessary condition for the HMX/AP interaction for composition without binder, proving the gas-phase character of this effect.

The use of large AP particles ($d = 230$ μm) for HMX/AP mixtures leads to the burning rate insensitivity to the AP content, confirming the key role of the AP specific surface for the synergistic effect implementation.

Results of the burning rate dependency on pressure for formulations HMX/AP/active binder revealed that the burning rate of the base composition HMX/active binder is increased with addition of HMX/AP mixtures, identically to U growth for formulations with HMX particles covered by ammonium perchlorate. The most important is that to get the same U(P) dependency for formulations with coated HMX as for compositions with AP and HMX as powdered ingredients, we can use much less amount of AP.

4 Summary

Experimental results on the HMX and AP interaction during constant rate heating and combustion have been presented. Thermal stability study revealed twofold HMX/AP interaction: from the one hand, ammonium perchlorate as synergistic

additive effectively (i.e., from 280 to 225 °C) reduces the onset decomposition temperature of HMX; from the other hand, gaseous products of the HMX thermolysis catalyze the AP decomposition.

Depending on the HMX concentration in the HMX/AP binary mixture, thermolysis follows to one of two different "scenarios," i.e., "independent" (several exo peaks) and synergistic (one pronounced exo peak) decomposition of components for mixtures with HMX content above 40 % and below 90 %.

Onset decomposition point does not depend on the HMX concentration (C_{HMX}) within the HMX/AP mixture, excepting 0 and 100 % points. The observed decrease of the onset decomposition temperature and its independency on the component concentration are very probably caused by the phase transition phenomena of both components.

Our experiments revealed that before the onset decomposition temperature of HMX/AP mixture, both components undergo the phase transition conversion. AP starts to decompose at temperature far below the phase transition point 240 °C, i.e., at 185 °C with the gas products release. HMX begins to decompose simultaneously with the phase transition at 187 °C with the release of N_2O and HCN. Significant change of the reactivity of both components near the phase transition points results in intense interaction of destabilized molecules with the decomposition gas products.

To study the role of the contact between components, large HMX crystals were covered with AP layer. HMX content from 70 % to 95 % for thus modified HMX particles was achieved by varying of the AP layer thickness. The burning rate dependency on the HMX content showed that in the HMX concentration range $30 < C_{HMX} < 93$ %, close to the region of the synergistic effect appearance, burning rate of mechanical mixtures exceeds the HMX level at pressure 4 MPa. Specific surface of ammonium perchlorate plays a key role for the synergistic effect manifestation in combustion: addition of large AP particles to HMX does not enhance the burning rate.

Comparative analysis of the combustion parameters of the mechanical mixtures and covered crystals revealed that the direct contact between components is not a necessary condition for the HMX/AP interaction for compositions without binder, proving the gas-phase character of this effect. However, for compositions with active binder, the direct contact between components is important. Thus, formulations with active binder and coated HMX provide higher burning rate than those ones with mechanical mixtures of HMX with fine AP. It means the possibility to use the considerably less amount of ammonium perchlorate to achieve the same level of the burning rate.

Obtained results need further investigations to get deeper insight into the nature of observed synergistic interaction between HMX and ammonium perchlorate.

References

1. Beckstead MW, Overview of combustion mechanisms and flame structures for advanced solid propellants. In: Yang V, Brill T., Wu-Zhen Ren (ed.) Solid propellant chemistry, combustion, and motor ballistics. Progress in astronautics and aeronautics. Washington, DC, USA. volume 185; AIAA, 2000.

2. Oxley JC, Smith JL, Wang W (1994) Compatibility of ammonium nitrate with monomolecular explosives. J Phys Chem 98:3893–3900

3. Fifer RA (1984) Chemistry of nitrate esters and nitramine propellants Fifer R.A. In: Kuo KK, Summerfield M (eds) Fundamentals of solid propellants combustion, vol 90, Progress in astronautics and aeronautics: chemistry of nitrate esters and nitramine propellants. AIAA, New York, pp 177–237, Chap. 4

4. Sokolov EV, Popenko EM, Sergyenko AV et al (2007) Influence of nitraminopropionitrile and its salts on the HMX thermal decomposition, Polsunovsky Vestnik № 3, pp 130–139, in Russian

5. Saito T, Shimoda M, Yamaya T et al (1991) Ignition of AP-based composite solid propellants containing nitramines exposed to CO_2 laser radiation at subatmospheric pressures. Combust Flame 85:68–76

6. Fang C, Li S (2002) Synergistic interaction between AP and HMX. J Energetic Mater 20:329–344

7. Brill TB (1995) Multiphase chemistry consideration at the surface of burning nitramine monopropellants. J Propuls Power 11(4):740–751

8. Karpowicz RJ, Gelfand LS, Brill TB (1982) Application of solid-phase transition kinetics to the properties of HMX. AIAA J 21(2):310–312

9. Behrens R (1990) Thermal decomposition of energetic materials: temporal behaviors of the rates of formation of the gaseous pyrolysis products from condensed-phase decomposition of octahydro-1,3,5,7-tetranitro-1,3,5,7-tetrazocine. J Phys Chem 94(17):6706–6718

10. Keenan AG, Siegmund RF (1969) Thermal decomposition of ammonium perchlorate. Q Rev Chem Soc London 23(3):435–452

11. Koroban VA et al (1981) Mechanism of the ammonium perchlorate thermal decomposition. In: Manelis GB (ed) Thermal decomposition of ammonium perchlorate. Semenov Institute of Chemical Physics, Chernogolovka, pp 5–29

12. Guirao C, William FA (1971) A model for ammonium perchlorate deflagration between 20 and 100 atmospheres. AIAA J 9:1345–1356

13. Palopoli SF, Brill TB (1991) Thermal decomposition of energetic materials 52. On the foam zone and surface chemistry of rapidly decomposing HMX. Combust Flame 87:45–60

14. Qing-Jie Jiao et al (2014) Thermal decomposition of RDX/AP by TG-DSC-MS-FTIR. J Therm Anal Calorim 1(3), Published online. doi:10.1007/s10973-013-3621-2

15. Henson BF et al (1999) Dynamic measurement of the HMX β-δ phase transition by second harmonic generation. Phys Rev Lett 82(6):1213–1216

16. Hedvall JA (1966) Solid state chemistry – whence, where and whither. Elsevier Publishing Company. Amsterdam/London/New York, p 100

17. Weeks BL, Ruddle CM, Zaug JM, Cook DJ (2002) Monitoring High-temperature Solid-solid Phase Transitions of HMX with Atomic Force Microscopy. Ultramicroscopy 93:19–23

18. Boldyrev VV (2006) Thermal decomposition of ammonium perchlorate. Thermochim Acta 443:1–36

19. Tesleva EP (2006) Investigation of polymorphic transformations of ion-molecular insulator by physical acoustics and thermophysical techniques. Dissertation, Barnaul, in Russian

20. Slater JC (1939) Introduction to chemical physics. McGraw-Hill Book Co., New York, p 293

21. Cheselske FJ (1965) Aerojet-general rept. 0372-01F, AD 458854, AF 49(638)–851, 15 March 1965

22. Evans MW, Beyer RB, McCulley L (1964) Initiation of deflagration waves at surfaces of ammonium perchlorate–copper chromite–carbon pellets. J Chem Phys 40(9):2431–2438

23. Pellet GL, Cofer WR (1969) Thermal decomposition of ammonium perchlorate by rapid heating, seventh AIAA aerospace science meeting. N Y 20:141
24. Bohn MA, Pontius H (2012) Thermal behaviour of energetic materials in adiabatic selfheating determined by ARC^{TM}. In: Proceedings of the 43rd international annual conference of ICT, pp 57-1–57-39
25. NIST Chemistry WebBook, NIST Standard Reference Database Number 69. In: Linstrom PJ, Mallard WG (eds) National Institute of Standards and Technology, Gaithersburg MD, 20899, http://webbook.nist.gov. Retrieved 2 Dec 2014

Combustion of Solid Propellants with Energetic Binders

Sergey A. Rashkovskiy, Yury M. Milyokhin, and Alexander V. Fedorychev

Abstract A dependence of the burning rate of solid energetic materials on the burning surface curvature is investigated. The model predicts an existence of a limiting value of curvature above which self-sustained combustion is impossible. This result is used for explaining the critical conditions of combustion of homogeneous condensed energetic materials. The critical combustion diameters of several homogeneous energetic materials are calculated and compared with experimental data. A combustion model for mixtures of energetic binders with inert and active fillers which takes into account the curvature of the burning surface of the binder layers and ignition delay of the filler is developed. A parametric study of the proposed model was performed over a wide range of particle sizes of the filler, its concentration in the mixture, and burning rates of the binder. The results of the model were compared with experimental data for mixtures of energetic binders with SiO_2, HMX, AP, and CL-20. A unified dependence of the ignition delay of HMX, AP, and CL-20 particles on their size, the burning rate of the mixture, and the thickness of the binder layers is proposed. The model is used for calculation of temperature sensitivity of the burning rate of propellants based on energetic binders.

Nomenclature

b	coefficient that takes into account the spatial geometry of the burning surface of the binder layer
D	particle diameter
D'	difference between burning surface of the binder and particle
d_{cr}	critical grain diameter
h	thickness of the binder layer between the particles of the filler

S.A. Rashkovskiy (✉)
Ishlinskii Institute for Problems in Mechanics of the Russian Academy of Sciences,
Moscow 119526, Russia
e-mail: rash@hotbox.ru

Yu.M. Milyokhin • A.V. Fedorychev
Soyuz Federal Center for Dual-Use Technologies, Dzerzhinskii 140090, Russia
e-mail: fcdt@mail.ru

K	burning surface curvature, dimensionless mean curvature of the burning surface
$k = \beta(T_s - T_0)$	nondimensional parameter
$k_0 = 16bk$	nondimensional parameter
K_0	dimensionless mean curvature of the burning surface at the burning rate $u_N^0(p)$
Mi	Michelson–Markstein criterion
p	pressure
R	curvature radius
R_1 and R_2	principal radii of curvature of the burning surface
T_0	initial grain temperature
T_0'	effective initial temperature connected with a curvature of burning surface
T_s	burning surface temperature
ΔT_0	effective change of the initial temperature connected with a curvature of burning surface
t_{ign}	ignition delay of the particles in propellant
t_{ign}^∞	ignition delay of the single particle in binder
u	burning rate
u_b	burning rate of the binder with planar burning surface
u_p	burning rate of the particle
u^0	steady-state burning rate
$u_N^0(p)$	dependence of the burning rate on pressure at a certain nominal initial temperature
$Z = \dfrac{u}{u_N^0}$	nondimensional burning rate

Greek Symbols

α	volume concentration of the filler particles in the mixture
$\alpha_{\max}, \delta, \tau_{ign}, \eta$	nondimensional parameters
β	temperature sensitivity of the burning rate or $\beta = u_b/u_p$
β_{ign}	temperature sensitivity of ignition delay
β_T	temperature sensitivity of the propellant burning rate
κ	thermal diffusivity of the condensed phase
$\xi = \dfrac{uR}{\kappa}, \xi_i = \dfrac{uR_i}{\kappa}$	nondimensional radii of curvature of the burning surface
τ_{ign}^∞	nondimensional ignition delay of the single particle binder
τ_0^∞, γ_0 and n	constants
ν	pressure exponent
σ and χ	factors of order unity which depends on the shape of the particles
ϕ	temperature gradient in the c-phase near the burning surface

Acronyms

AFB   nitroglycerine urethane binders
AGS   polyurethane rubber and a plasticizer which is a mixture of nitrate esters
CEM   condensed energetic material
c-phase   condensed phase

Subscripts and Superscripts

cr   critical parameter
b   binder
p   filler particle

1   Introduction

Progress in the field of energetic materials is now mainly associated with the use of mixtures based on energetic binders capable of self-sustained combustion. HMX and ammonium perchlorate (AP) are often used as fillers in such mixtures. Experimental data on the combustion of mixtures of energetic binders with HMX show that this process differs radically from combustion of mixtures of AP with inactive binders, and the mechanisms and models underlying the explanation of the combustion of AP with inactive binders cannot always be used to explain the combustion behavior of mixtures of energetic binders with active or inert fillers.

For example, in some mixtures based on fast-burning energetic binders, the HMX and SiO_2 particles of the same size have the same effect on the burning rate of the mixture [1]. For mixtures based on nitroglycerine or powder A as a binder with fine (20 and 40 μm) particles of HMX, the burning rate is lower than the burning rate of the pure binder, but the dependence of the burning rate on the filler concentration is nonmonotonic: at low concentrations of HMX particles in the mixture (up to 40 % for mixtures based on powder A and up to 60 % for mixtures based on nitroglycerine), the burning rate decreases with increasing particle concentration, whereas at high particle concentrations, it increases with increasing HMX concentration.

The goal of this work is to describe the model of combustion of binary mixtures based on the energetic binder and to explain the experimental data on combustion of binary mixtures of energetic binder with different fillers.

A unified combustion mechanism for mixtures based on energetic binders capable to self-sustained combustion with inert and active dispersed fillers was proposed in [2, 3]. It was shown that the role of particles of different natures and

different sizes reduces to curving the burning surface of the binder layers, which results in a change in the burning rate of the layers.

2 Effect of Curvature of Burning Surface on Burning Rate

Combustion of condensed energetic materials with a curved burning surface differs essentially from combustion of those with a flat surface, e.g., the surface curvature can play a key role in formation of the limiting conditions of combustion of energetic materials.

By an example of the nitroglycerine ballistite powder (powder NB), it was found [4] that combustion ceased if the inhomogeneity on the surface had a large curvature. To quantify this phenomenon, Marshakov and Istratov [4] used the Michelson–Markstein criterion $Mi = Ru/\kappa$, where u is the burning rate, R is the curvature radius of inhomogeneities on the burning surface, and κ is the thermal diffusivity of the condensed phase (c-phase) of the condensed energetic material (CEM). Combustion of the inhomogeneity on the powder surface ceased at $Mi < Mi_{cr} = 10\text{--}13$ [4].

It is well known from the theory of combustion of premixed gases that the velocity of normal propagation of the flame front depends on its curvature (Markstein effect). Taking into account the general analogy between the reaction zones in the c-phase of a homogeneous CEM and in premixed gases, we can expect that the burning rate of the CEM with a curved surface will also differ from the burning rate of this CEM with a flat surface.

This dependence can be obtained within the framework of the theory of combustion of homogeneous CEMs in a general form based on the phenomenological theory of unsteady combustion [2, 3], which offers a general method for calculating the instantaneous burning rate of CEMs.

In accordance with the phenomenological theory of unsteady combustion [5, 6] (ZN theory), the burning rate is a single-valued function of the pressure p and temperature gradient φ in the c-phase near the burning surface: $u = u(p, \varphi)$. Necessary to note, that ZN theory is applicable only to homogeneous energetic materials such as double-based propellants, energetic binders, and individual energetic materials (explosives). At the same time, ZN theory is not applicable for composite propellants. In this paper, we used ZN theory only as applied to individual homogeneous energetic components inside the composite propellants.

If the burning surface becomes curved during CEM combustion for some reasons, the temperature gradient φ differs from the corresponding value for CEM combustion under identical conditions, but with a flat surface, and depends on the burning surface curvature $K = R^{-1}$, where R is the curvature radius.

Temperature field in condensed phase of energetic material is described by equation of thermal conductivity. The solution of this equation for cylindrical and spherical shape of burning surface can be found analytically. By using this solution, the temperature gradient in the c-phase near the CEM burning surface is determined by the expression [2]:

$$\varphi = \frac{u}{\kappa} \left(T_s - T_0' \right)$$

where T_s is the burning surface temperature;

$$T_0' = T_0 + \Delta T_0$$

is the effective initial temperature connected with a curvature of burning surface;

$$\Delta T_0 = - \left(T_s - T_0 \right) \left(\frac{\exp \left(-\xi \right)}{\xi \int\limits_{\xi}^{\infty} \frac{1}{\xi} \exp \left(-\xi \right) d\xi} - 1 \right)$$

for cylindrical shape of the burning surface; and

$$\Delta T_0 = - \left(T_s - T_0 \right) \left(\frac{\exp \left(-\xi \right)}{\xi^2 \int\limits_{\xi}^{\infty} \frac{1}{\xi^2} \exp \left(-\xi \right) d\xi} - 1 \right)$$

for spherical shape of the burning surface;

$$\xi = uR/\kappa$$

For a weakly curved burning surface ($\xi = uR/\kappa \gg 1$), this dependence takes the form

$$\Delta T_0 = - \left(T_s - T_0 \right) \frac{1}{\xi} \tag{1}$$

for cylindrical shape of the burning surface and

$$\Delta T_0 = - \left(T_s - T_0 \right) \frac{2}{\xi} \tag{2}$$

for spherical shape of the burning surface.

Dependences (1) and (2) can be readily generalized to the case where two principal curvatures of the burning surface are finite and different:

$$\Delta T_0 = - \left(T_s - T_0 \right) \left(\frac{1}{\xi_1} + \frac{1}{\xi_2} \right) \tag{3}$$

where $\xi_1 = \frac{uR_i}{k}, i = 1, 2$, R_1 and R_2 are the principal radii of curvature of the burning surface.

Introducing a dimensionless mean curvature of the burning surface

$$K = \frac{1}{2}\left(\frac{1}{\xi_1} + \frac{1}{\xi_2}\right) \tag{4}$$

one can rewrite Eq. 3 in the form

$$\Delta T_0 = -2K\left(T_s - T_0\right). \tag{5}$$

Analysis of the expressions above shows that the curvature of the burning surface induces the same change in the burning rate as a change in the initial temperature of the CEM (with a plane combustion front) by the value determined by Eqs. 4 and 5.

Because of this, to determine the effect of the curvature of the burning surface on the burning rate, we can use the dependence of the burning rate on initial temperature T_0:

$$u = u^0\left(p, T_0 + \Delta T_0\left(\xi\right)\right).$$

In practice, the dependence

$$u^0\left(p, T_0\right) = u_N^0(p)\exp\left(\beta\Delta T_0\right) \tag{6}$$

or its linear approximation are often used, where $u_N^0(p)$ determines the dependence of the burning rate on pressure at a certain nominal initial temperature.

Taking into account Eqs. 5 and 6, one obtains the expression for the burning rate of the grain with a curved surface

$$Z = \exp\left(-\frac{2kK_0}{Z}\right) \tag{7}$$

where $Z = u/u_N^0$ and K_0 is the dimensionless mean curvature of the burning surface at the burning rate $u_N^0(p)$ which is determined by Eq. 4 with $\xi_i = u_N^0R_i/\kappa$.

$$k = \left(T_s - T_0\right)\frac{\partial\ln u^0}{\partial T_0} = \beta\left(T_s - T_0\right)$$

is the dimensionless temperature sensitivity of the burning rate in the ZN theory of unsteady combustion [5, 6].

For linear dependence

$$u^0\left(p, T_0\right) = u_0^0(p)\left(1 + \beta\Delta T_0\right) \tag{8}$$

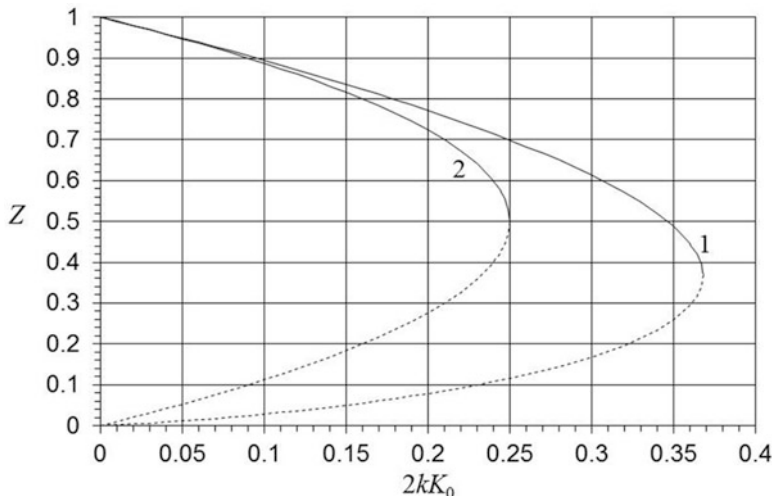The equation for burning rate is as follows:

Fig. 1 Burning rate of the condensed energetic material with the curved burning surface convex toward the c-phase versus the parameter $2kK_0$: solutions for exponential (*curve 1*) and linear (*curve 2*) dependences of steady-state burning rate on initial temperature. K_0 – nondimensional curvature of burning surface

$$Z = 1 - \frac{2kK_0}{Z}$$

and has the simple solution

$$Z = 0.5 \pm \sqrt{0.25 - 2kK_0} \qquad (9)$$

The dependences (7) and (9) of the burning rate on curvature of the burning surface are shown in Fig. 1.

It demonstrates that there is a limiting value of curvature above which a self-sustained combustion is impossible. The limiting value of the surface curvature depends on the nondimensional temperature sensitivity of the burning rate k.

The limiting value of the parameter $2kK_0$ for exponential law (6) is equal to $1/e$; the corresponding limiting value of the relative burning rate is $Z_{cr} = 1/e$ [2]. This means that combustion of the CEM with a curved surface at $2kK_0 > 1/e \approx 0.368$ is impossible. Thus, for each CEM, there is a critical value of the dimensionless curvature $(K_0)_{cr} \approx 0.18/k$, and combustion with a curved surface is possible only as long as the dimensionless curvature of the burning surface does not exceed this critical value. For linear law (8), the limiting value of the parameter kK_0 is equal to one-eight, and the critical curvature of the burning surface is equal to $(K_0)_{cr} \approx 0.125/k$. We see that critical curvature depends on the temperature sensitivity of the burning rate k and has different values for different CEMs.

Table 1 Parameters of different energetic materials and their critical diameter of combustion

Energetic material	k	u_0	Theory	Experiment
Powder N	$k = 2.4p^{-0.1}$	$u_N^0 = 0.047p^{0.67}$	$d_{cr} = 7.7p^{-0.77}$	$d_{cr} = 7p^{-0.74}$
Powder A	$k = 2.4p^{-0.1}$	$u_N^0 = 0.1p^{0.64}$	$d_{cr} = 3.6p^{-0.75}$	$d_{cr} = 6p^{-0.75}$
Powder NB	$k = 2.4p^{-0.1}$	$u_N^0 = 0.09p^{0.65}$	$d_{cr} = 4p^{-0.75}$	$d_{cr} = 6.8p^{-0.76}$
RDX	$k \approx 2.3$	$u_N^0 = 0.037p^{0.82}$	$d_{cr} = 9.3p^{-0.82}$	$d_{cr} = 9.26p^{-0.88}$

3 Critical Diameter of Combustion

The results obtained allow explaining the critical value of the Michelson–Markstein criterion, which was found experimentally in [4].

By using the results above, one can write the critical value of the Michelson–Markstein criterion $Mi_{cr} = 2ke$ which depends on the dimensionless temperature sensitivity of the burning rate k and has different values for different CEMs.

For example, for powder N ($k = 2$–2.5 at $p = 1$–5 atm [7]), we have $Mi_{cr} = 10.8$–13.5, which coincides with the estimations of Mi_{cr} obtained in [4] for powder N.

This theory can be used for explaining the critical diameter of combustion if we suppose that combustion ceasing with decreasing the grain diameter is related to supercritical curvature of the burning surface. By using the condition $R_{cr} = d_{cr}/2$, where d is the CEM sample diameter, which follows from experimental observations [4, 12], one obtains the critical grain diameter

$$d_{cr}(p) = \frac{4\kappa ek(p)}{u_N^0(p)}$$

or, taking $\kappa = 1.5 \cdot 10^{-3}$ cm²/s, one obtains

$$d_{cr} = 0.15k/u_N^0. \tag{10}$$

Hereinafter, u_N^0 is measured in centimeters per second, d_{cr} is measured in millimeters, and p is measured in atm.

Results of calculation of critical diameters by using Eq. 10 for different energetic materials and comparison with experimental data are shown in Table 1.

Thermal sensitivity of burning rate for these energetic materials has been taken from [7–11]; experimental data for critical diameters has been taken from [4, 10, 12].

One sees that the hypothesis of existence of the limiting curvature of the burning surface allows explaining the critical conditions of combustion of homogeneous condensed energetic materials.
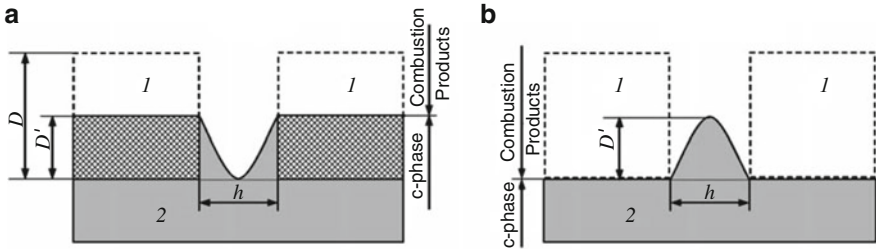
Fig. 2 Diagram of burnup of the components in a mixture of a binder and a dispersed filler capable of self-sustained combustion: (*1*) filler particles; (*2*) binder. The dashed line shows the initial particle, and the shaded region is the remainder of the particle at the time considered. (**a**) The binder burns faster than the particle; (**b**) the binder burns slower than the particles

4 Combustion Model for Binary Mixtures with Energetic Binder

A combustion model for mixtures of binders capable of self-sustained combustion with inert fillers and active fillers can be developed within the limits of the theory considered above. This model takes into account the curvature of the burning surface of the binder layers and the resulting change in the binder burning rate.

The basic assumptions of the model are as follows:

1. The burning rate of the mixture is determined by the burnup of binder layers between filler particles.
2. The burning rate of the binder in the layers between filler particles differs from the burning rate of the pure binder.
3. Change in the burning rate of binder layers between filler particles is mainly due to the curvature of the burning surface of the binder (7).
4. The burning rate of particles of the dispersed components is equal to the stationary burning rate of these components as individual substances.
5. Ignition delay of the filler particles plays an important role in formation of the burning rate of binary mixtures with energetic binder.

The diagram of burnup of the components in a binary mixture of energetic components is shown in Fig. 2.

The equations which describe this model are as follows [3]:

$$\delta = \frac{D'}{D}, \tau_{ign} = \frac{u_b t_{ign}}{D}, \eta = \frac{u_b h}{\kappa}, \xi = \frac{u_b D}{\kappa}, \beta = u_b/u_p$$

$$\delta = \begin{cases} 1, & Z_b \tau_{ign} \geq 1 \\ 1 + (Z_b \tau_{ign} - 1) \frac{1}{\beta Z_b}, & (1 - \beta Z_b) < Z_b \tau_{ign} < 1 \\ -(1 - \beta Z_b) + Z_b \tau_{ign}, & Z_b \tau_{ign} \leq (1 - \beta Z_b) \end{cases}$$

where t_{ign} is the ignition delay of the particles; u_p is their burning rate; u_b is the burning rate of the binder with planar burning surface (i.e., without taking into account curvature of its burning surface in mixture); D is the diameter of the particles; and D' is the difference between burning surface of the binder and particle.

The curvature of the burning surface of binder is determined by the expression

$$K = \pm 8bD'/h^2$$

where the plus sign is used if the burning surface is convex toward the c-phase and the minus sign is used if the surface is convex toward the combustion products; $0.5 \leq b \leq 1$ b is a coefficient that takes into account the spatial geometry of the burning surface of the binder layer: $b = 0.5$ corresponds to a cylindrical surface and $b = 1$ to a spherical surface.

We assume that the burning rate of mixtures based on binders capable of self-sustained combustion is equal to the burning rate of the binder layers between the filler particles with taking into account the curvature of its burning surface:

$$Z \equiv \frac{u}{u_b} = Z_b$$

Taking into account Eq. 7, one obtains the equation for burning rate of the binary mixtures:

$$Z_b = \exp\left(-\frac{k_0 \delta \xi}{\eta^2 Z_b}\right) \tag{11}$$

where $k_0 = 16bk$.

Ignition delay for particles of the filler depends on the pressure and parameters of the combustion of binder.

For calculation of ignition delay, we use the expressions

$$\tau_{ign}(\eta) = \tau_{ign}^{\infty}(1 - \exp(-\gamma_0 Z_b \eta))$$

$$\eta = \left(\frac{\sigma}{\alpha^{1/3}} - \chi\right)\xi$$

$$\tau_{ign}^{\infty} = \tau_0^{\infty} \frac{\xi^n}{Z_b}$$

obtained by comparison of results of simulation with well-known experimental data
[1, 13, 14], where $\gamma_0 = 1.2$ for all binders and fillers, while the constants τ_0^∞ and n
are different for different energetic materials; σ and χ are the factors of order unity
which depends on the shape of the particles; and α is the volume concentration of
filler particles in the mixture.

For HMX with different energetic binders [3]:

$$\tau_0^\infty = 1, n = -0.4$$

For AP with different energetic binders [3]

$$\tau_0^\infty = 0.15, n = 0.7$$

In this case, the empirical dependence of the burning rate of AP particles on their
diameter

$$u_p = 3.8 p^{0.45} / D^{0.15}$$

was taken into account.

For CL-20 with different energetic binders [3]

$$\tau_0^\infty = 1.57, n = -0.63$$

For inert particles (e.g., SiO$_2$), $\tau_0^\infty = \infty$.

A parametric study of the proposed model was performed over a wide range of
particle sizes of the filler, its concentration in the mixture, and burning rates of the
binder.

The results of calculations within developed model for several energetic binders
and three different fillers (HMX, AP, and CL-20) are shown in Figs. 3, 4, and 5. The
markers in Figs. 3, 4, and 5 show the experimental data [1, 13, 14], and the lines
correspond to calculation.

The combustion properties of different energetic binders and individual energetic
materials used in calculations are shown in Table 2.

The results of the model were compared with experimental data of different
authors for mixtures of active binders with SiO$_2$ and HMX, for mixtures of the
nitroglycerine urethane binder with CL-20, and for mixtures of the binder AGS with
AP [1, 13, 14]. The entire set of available experimental data can be described using
the proposed model; the burning rate of the mixtures coincides with the burning
rate of binder layers between filler particles, taking into account the curvature of the
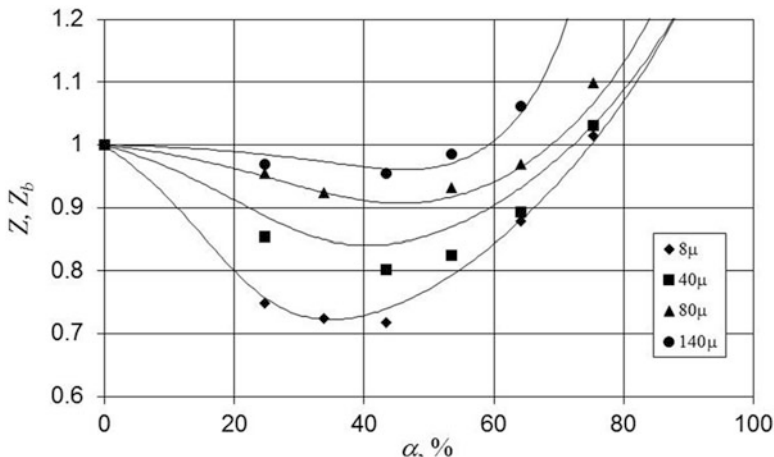burning surface of the binder layers.

Fig. 3 Calculated (*curves*) and experimental (*markers*) dependences of the burning rate of binary mixtures of HMX and energetic binder AFB3 on the volume concentration of HMX for different sizes of HMX particles at $p = 10$ MPa

Fig. 4 Calculated (*curves*) and experimental (*markers*) dependences of the burning rate of mixtures of energetic binder AGS with AP on the pressure at the volume concentration of AP in the mixture $\alpha = 29$ %; different solid lines correspond to different sizes of AP particles in the binary mixtures: 1—10 μm; 2—30 μm; 3—200 μm; dashed curves correspond to combustion of the pure binder or individual AP particles of different sizes
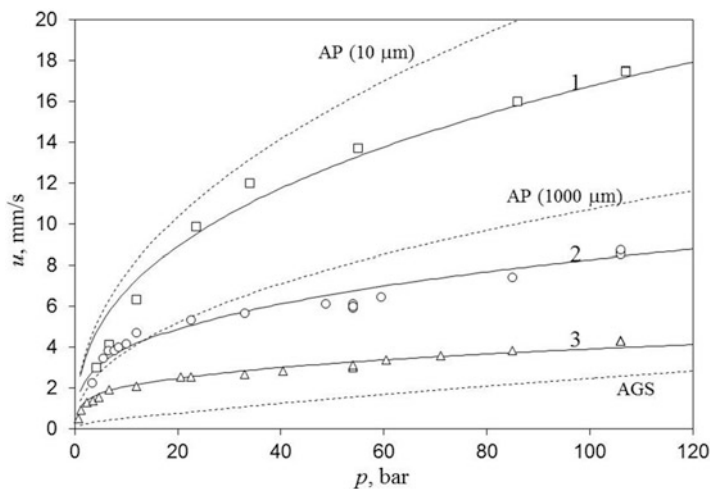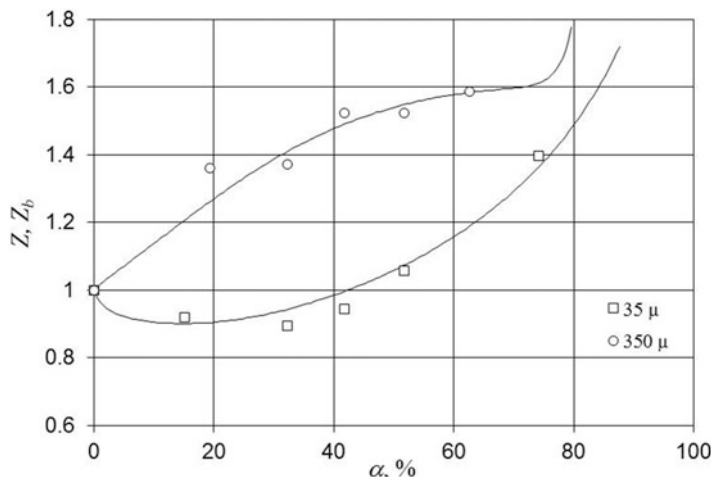
Fig. 5 Calculated (*curves*) and experimental (*markers*) dependences of the burning rate of binary mixtures of energetic binder AFB1 with CL-20 on the volume concentration of the CL-20 for different sizes of CL-20 particles at $p = 10$ MPa

Table 2 Parameters of binders and individual energetic materials used in calculations

Binder composition		
Energetic material	u_b, mm/s	Binder density, g/cm^3
AFB3	7.3 ($p = 4$ MPa)	1.520
	13.2 ($p = 10$ MPa)	
AGS [13]	$0.159p^{0.513}$ ($p \leq 21.5$ atm)	1.360
	$0.0784p^{0.748}$ ($p \geq 21.5$ atm)	
AFB1 [14]	16.9 ($p = 10$ MPa)	1.460
HMX	8.0 ($p = 4$ MPa)	1.960
	14.7 ($p = 8$ MPa)	
	17.7 ($p = 10$ MPa)	
AP particles [15]	$3.8p^{0.45}/D^{0.15}$ (p – in atm. D – in μm)	1.950
CL-20	30.5 ($p = 10$ MPa)	2.04

AFB is the abbreviation for nitroglycerine urethane binders, and AGS for polyurethane rubber and a plasticizer which is a mixture of nitrate esters

5 Temperature Sensitivity of Propellant Burning Rate

The developed model allows calculating the pressure exponent $\nu = \frac{\partial \ln u}{\partial \ln p}$ and the temperature sensitivity $\beta = \frac{\partial \ln u}{\partial T_0}$ of burning rate of binary mixtures with energetic binder.

For mixtures of energetic binder with inert filler (e.g., SiO$_2$), the relative burning rate Z_b can depend on pressure and initial temperature only through the dependences of u_b (which is included in parameter ξ) and k on p and T_0. No other parameters

of such mixtures theoretically depend on the initial temperature and pressure. Therefore, for such propellants, the burning rate pressure exponent and temperature sensitivity are defined most simply, if the dependence $u_b(p, T_0)$ is known.

In this case, it is easy to obtain

$$\nu = \nu_b \left(1 + \frac{\partial \ln Z_b}{\partial \ln \xi} \right) + \frac{\partial \ln Z_b}{\partial \ln k} \frac{\partial \ln k}{\partial \ln p} \tag{12}$$

$$\beta = \beta_b \left(1 + \frac{\partial \ln Z_b}{\partial \ln \xi} \right) + \frac{\partial \ln Z_b}{\partial \ln k} \frac{\partial \ln k}{\partial T_0} \tag{13}$$

where

$$\nu_b = \frac{\partial \ln u_b}{\partial \ln p} \tag{14}$$

$$\beta_b = \frac{\partial \ln u_b}{\partial T_0} \tag{15}$$

Parameters $\frac{\partial \ln Z_b}{\partial \ln \xi}$ and $\frac{\partial \ln Z_b}{\partial \ln k}$ can be easily calculated analytically or numerically by using the developed model.

For active particles which are capable to self-sustained combustion (HMX, AP, CL-20, etc.), it is necessary to take into account the dependences of burning rate of particles of filler u_p and their ignition delay t_{ign}^{∞} on pressure and initial temperature.

As an example, we consider the calculation of the temperature sensitivity of burning rate of propellant (binary mixtures).

Changing in initial temperature T_0 (other conditions being equal) results in changing in burning rate of binder $u_b(T_0)$, in burning rate of particles of filler $u_p(T_0)$, in dimensionless temperature sensitivity of burning rate of binder $k(T_0)$, and in ignition delay of particles of filler $t_{ign}^{\infty}(T_0)$. No other parameters of the model depend on the initial temperature.

At small variations of initial temperature, these dependences can be approximated by linear functions:

$$u_b(T_0) = u_b^N (1 + \beta_b (T_0 - T_N)) \tag{16}$$

$$u_p(T_0) = u_p^N (1 + \beta_p (T_0 - T_N)) \tag{17}$$

$$k(T_0) = k_N (1 + \beta_k (T_0 - T_N)) \tag{18}$$

$$t_{ign}^{\infty}(T_0) = t_{ign}^{\infty N} (1 + \beta_{ign} (T_0 - T_N)) \tag{19}$$

where $u_b^N, u_p^N, t_{ign}^{\infty N}, k_N$ are values of corresponding parameters calculated at some nominal initial temperature T_N; $\beta_b, \beta_p, \beta_{ign}, \beta_k$ are the constant characteristics of components of the mixture.

In what follows we assume that the parameter n does not depend on the initial temperature, so the dependence (19) is equivalent to the dependence

$$\tau_0^\infty (T_0) = \tau_0^{\infty N} \left(1 + \beta_{ign} (T_0 - T_N)\right) \tag{20}$$

with the same parameter β_{ign}.

In accordance with the results above, $\tau_0^{\infty N} \approx 1$ for HMX, and $\tau_0^{\infty N} = 0.15$ for AP.

The parameters β_b and β_p are assumed to be equal to the temperature sensitivity of burning rate of corresponding individual components. Parameter β_k can also be considered as a known characteristic of the binder, if we know the dependences β_b (T_0) and T_s (T_0). Parameter β_{ign} is considered as a fitting parameter and selected on the basis of comparison of results of calculations with experimental data. In this paper, we calculate the temperature sensitivity for different values of parameter β_{ign} in order to investigate its effect on temperature sensitivity of the burning rate of binary mixtures as a whole.

The calculations were performed for two values of β_{ign}:

1. $\beta_{ign} = -0.005 \ 1/K$; in this case the ignition delay decreases as the initial temperature increases.
2. $\beta_{ign} = 0 \ 1/K$; in this case the ignition delay does not depend on initial temperature.

The case $\beta_{ign} > 0$ is of no interest, since it corresponds to an increase in the ignition delay with increasing the initial temperature, which contradicts the representations about the ignition process.

The calculation is as follows. For a given mixture and a given pressure, two values of the initial temperature $T_0 = T_N$ and $T_0 = T_N + \triangle T_0$ are considered.

The burning rate (16) and (17), the dimensionless temperature sensitivity of the binder burning rate (18), and the ignition delay (20) are calculated for each value of the initial temperature. Then, the burning rate of propellant is calculated for each initial temperature by using the developed combustion model at the fixed values of γ_0, σ, n, and α_{max}.

Temperature sensitivity of the burning rate of propellant is determined by the expression

$$\beta_T = \frac{1}{\Delta T_0} \left(\frac{u_b (T_N + \Delta T_0) \, Z_b (T_N + \Delta T_0)}{u_b (T_N) \, Z_b (T_N)} - 1 \right).$$

Taking into account expression (16), one can write

$$\beta_T = \frac{1}{\Delta T_0} \left(\frac{Z_b (T_N + \Delta T_0)}{Z_b (T_N)} (1 + \beta_b \Delta T_0)) - 1 \right)$$
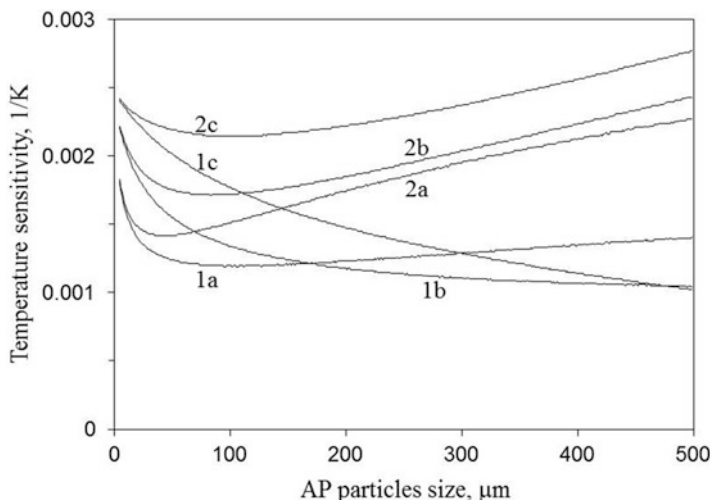
Fig. 6 Dependences of temperature sensitivity of burning rate of binary mixtures of AP with energetic binder AGS on AP particle sizes for different volume concentrations of AP at $p = 2.0$ МПа. $1 - \beta_{ign} = 0$ K^{-1}. $2 - \beta_{ign} = -0.005$ K^{-1}. Volume concentrations of AP: (**a**) $\alpha = 15$ %; (**b**) $\alpha = 29$ %; (**c**) $\alpha = 45$ %. The parameters $\beta_b = 0.0021$ K^{-1} [13]; $\beta_p = 0.0025$ K^{-1} [10]; $\sigma = 0.75$; $\alpha_{\max} = 0.75$, $k_0 = 1.2$ [3] were used for all variants of calculations

In particular, at $\Delta T_0 \to 0$, one obtains

$$\beta_T = \beta_b + \frac{1}{\Delta T_0} \left(\frac{Z_b \left(T_N + \Delta T_0 \right)}{Z_b \left(T_N \right)} - 1 \right) \tag{21}$$

It is this expression that was used for calculations of temperature sensitivity of burning rate of binary mixtures.

In this paper, we assume $\beta_k = 0$; this means that the temperature sensitivity of the burning rate of binder does not depend on the initial temperature.

Results of calculation for mixtures of energetic binder AGS with AP are shown in Fig. 6. It can be seen that at $= \beta_{ign} -0.005$, the dependences of the temperature sensitivity of propellant burning rate on AP particle sizes are nonmonotonic and have a minimum approximately at $D = 90$ μm. At the same time, for value $\beta_{ign} = 0$, this dependence is monotonically decreasing.

Figure 7 shows the results of calculations of the temperature sensitivity of the burning rate of binary mixtures of HMX and energetic binder AFB3 at $p = 4$ MPa for different volume concentrations of HMX and different sizes of HMX particles. It is seen that the dependence of β_T on the particle size for this mixture is more complicated than that for mixtures of energetic binder AGS with AP and essentially depends on β_{ign}. At small α, this dependence has a peak that increases in amplitude and shifted in the direction of smaller HMX particles with decrease of β_{ign}.
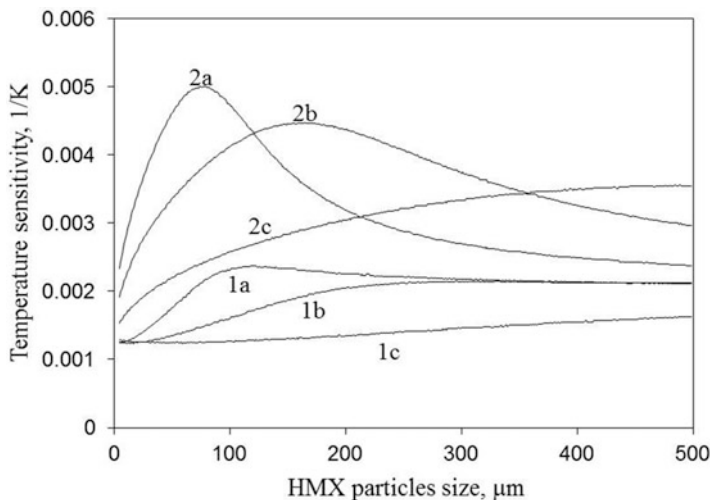
Fig. 7 Dependences of temperature sensitivity of burning rate of binary mixtures of HMX and energetic binder AFB3 on HMX particle sizes for different volume concentrations of HMX at $p = 4.0$ MΠa. $1 - \beta_{ign} = 0$ K^{-1}. $2 - \beta_{ign} = -0.005$ K^{-1}; volume concentrations of HMX: (**a**) $\alpha = 20$ %; (**b**) $\alpha = 40$ %; (**c**) $\alpha = 60$ %. The parameters $\beta_b = 0.0021$ K^{-1}; $\beta_p = 0.0013$ K^{-1} [11]; $\sigma = 0.9$; $\alpha_{max} = 0.75$, $k_0 = 1.0$ [3] were used for all variants of calculations

The analysis carried out has shown that, depending on the values of β_{ign}, the behavior of the temperature sensitivity of the burning rate of the binary mixtures with energetic binder as a function of filler particle size can be complicated and nonmonotonic; it essentially depends on parameter β_{ign} and a kind of filler. An important result of this analysis is that β_T for the binary mixtures as a whole may have an extremum at certain particle sizes.

6   Conclusion

We have described the model of combustion of homogeneous condensed energetic materials with a curved burning surface developed within the framework of the phenomenological ZN approach. We found the dependence of the burning rate on the burning surface curvature and demonstrated that there exists a limiting curvature value above which a self-sustained combustion is impossible. The limiting value of the surface curvature depends on the temperature sensitivity of the burning rate. It is shown that the hypothesis of existence of the limiting curvature of the burning surface offers an explanation for the critical conditions of combustion of homogeneous CEMs. Based on this hypothesis, the critical diameters of combustion of several homogeneous CEMs are calculated. These calculated results are in good agreement with available experimental data.

A unified combustion mechanism for mixtures based on binders capable of self-sustained combustion with inert and active dispersed fillers is proposed which involves combustion propagation of binder layers between particles. It is shown that the role of particles of different natures and different sizes reduces to curving the burning surface of the binder layers, which leads to a change in the burning rate of the layers.

A combustion model for mixtures of binders capable of self-sustained combustion with inert fillers and active fillers was developed which takes into account the curvature of the burning surface of the binder layers and the resulting change in the binder burning rate.

The model results were compared with experimental data of different authors for mixtures of active binders AFB3 with HMX, for mixtures of the nitroglycerine urethane binder with CL-20, and for mixtures of the binder AGS with AP. The entire set of available experimental data can be described using the proposed model; the burning rate of the mixtures coincides with the burning rate of binder layers between filler particles, taking into account the curvature of the burning surface of the binder layers.

A unified dependence of the ignition delay of HMX, AP, and CL-20 particles on their size, the burning rate of the mixture, and the thickness of the binder layers which is the same for all mixtures considered was proposed which takes into account collective effects on the burning surface. It was shown that the ignition delay of HMX, AP, and CL-20 particles in mixtures with binders capable of self-sustained combustion plays a crucial role in the burning rate of the mixtures.

The model considered allows direct calculating of the temperature sensitivity and the pressure exponent of the burning rate of binary mixtures based on energetic binder for a wide range of binders, fillers, concentrations of the filler in the mixture, and filler particle sizes.

References

1. Denisyuk AP, Shabalin VS, Shepelev YG (1998) Combustion of condensed systems consisting of HMX and a binder capable of self-sustained combustion. Combust Explosion Shock Waves 34(5):534–542
2. Rashkovskii SA (2011) Effect of the curvature of the burning surface of condensed energetic materials on the burning rate. Combust Explosion Shock Waves 47(6):687–696
3. Rashkovskii SA, Milekhin YM, Klyuchnikov AN, Fedorychev AV (2012) Combustion mechanism of mixtures of binders capable of self-sustained combustion with inert and active fillers. Combust Explosion Shock Waves 48(2):177–190
4. Marshakov VN, Istratov AG (2007) Critical diameter and transverse waves of powder combustion. Combust Explosion Shock Waves 43(2):188–193
5. Novozhilov BV (1973) Unsteady combustion of solid propellants [in Russian]. Nauka, Moscow
6. Zel'dovich YB, Leipunskii OI, Librovich VB (1975) Theory of unsteady combustion of gunpowder [in Russian]. Nauka, Moscow

7. Marshakov VN (2009) Structure of the combustion wave of nitroglycerin-based powders. Khim Fiz 28(12):61–65
8. Zenin AA, Leipunskii OI, Margolin AD et al (1966) Temperature field near the surface of the burning powder and stability of combustion. Dokl Akad Nauk SSSR 169(9):619–621, No. 3
9. Zenin AA (1966) Structure of temperature distribution in steady-state burning of a ballistite powder. Combust Explosion Shock Waves 2(3):40–45
10. Glazkova AP (1976) Catalysis of combustion of explosives. Nauka, Moscow [in Russian]
11. Atwood AI, Boggs TL, Curran PO et al (1999) Burning rate of solid propellant ingredients. Part 2: Determination of burning rate temperature sensitivity. J Propuls Power 15(6):748–752
12. Vishnivetskii Y, Denisyuk AP, Fogel'zang AE (1979) Critical conditions of ballistic powder combustion. Combust Explosion Shock Waves 15(1):8–13
13. Serushkin VV, Sinditskii VP, Filatov SA (2010) Combustion mechanism and temperature sensitivity of the burning rate of a solid rocket propellant based on an active binder. In: Denisyuk AP, Sinditskii VP (eds) Advances in special chemistry and chemical technology, all-Russia scientific and engineering conference dedicated to the 70th anniversary of the chemical engineering Department of Mendeleyev University of Chemical Technology of Russia (Mendeleyev University of Chemical Technology of Russia) pp 292–299
14. Sinditskii VP, Egorshev VY, Berezin MV, Levshenkov AI, Serushkin VV, Filatov SA, Chernyi AN (2010). The combustion mechanism of energetic nitro ester binders with nitramines. In: Denisyuk AP, Sinditskii VP (eds) Advances in special chemistry and chemical technology, all-Russia scientific and engineering conference dedicated to the 70th Anniversary of the Chemical Engineering Department of Mendeleev University of Chemical Technology (Mendeleev University of Chemical Technology, University of Chemical Technology) pp 285–291
15. Gusachenko LK, Zarko VE, Zyryanov VH, Bobryshev VP (1985) Modeling combustion of solid fuels. Nauka, Novosibirsk [in Russian]

Effects of Dual Oxidizers on the Properties of Composite Solid Rocket Propellants

Wei Qiang Pang, Luigi T. DeLuca, Hui Xiang Xu, Xue Zhong Fan, Feng Qi Zhao, and Wu Xi Xie

Abstract The microstructures and granular distribution of different oxidizers (AP, HMX, CL-20, GUDN, and ADN) were investigated. Several industrial and research types of hydroxyl-terminated polybutadiene (HTPB)-based composite solid rocket propellants containing different dual oxidizers (with a fraction of AP in the reference formulation replaced by HMX, CL-20, GUDN, or ADN), but featuring the same nominal composition, were prepared. The energetic properties and hazardous properties of the corresponding solid propellants were analyzed. The effects of the kind of dual oxidizers on the strand burning rate and pressure exponent of propellants were investigated. Thermal decomposition and the mechanical properties of propellants were also analyzed. It was shown that AP and prilled ADN particles are approximately ball shaped and more uniform than that of the others, while CL-20 is the most irregular one. The application of different oxidizers to composite solid propellants was revealed as feasible, and samples could be cast in vacuum and cured safely. Compositions with ADN or CL-20 filler show higher performance in terms of specific impulse, heat of explosion, burning rate, and density, but are more sensitive to impact and friction. The mechanical properties of mono-oxidizer AP-based composition (reference composition) are superior to those of the others.

W.Q. Pang (✉)
Xi'an Modern Chemistry Research Institute, Xi'an 710065, Shaanxi, China

Space Propulsion Laboratory (SPLab), Department of Aerospace Science and Technology, Politecnico di Milano, 10256 Milan, Italy
e-mail: pangwq204@gmail.com

L.T. DeLuca
Space Propulsion Laboratory (SPLab), Department of Aerospace Science and Technology, Politecnico di Milano, 10256 Milan, Italy
e-mail: luigi.deluca@polimi.it

H.X. Xu • X.Z. Fan • F.Q. Zhao • W.X. Xie
Xi'an Modern Chemistry Research Institute, Xi'an 710065, Shaanxi, China
e-mail: xhx204@163.com; xuezhongfan@126.com; zhaofqi@163.com; nwpu_pwq@126.com

Nomenclature

Acronyms

ADN	Ammonium dinitramide
AP	Ammonium perchlorate
cAP	Coarse ammonium perchlorate
CL-20	2,4,6,8,10,12-Hexanitro-2,4,6,8,10,12-hexaazaisowurtzitane
CP	Composite propellant
fAP	Fine ammonium perchlorate
GFP	Catocene
GUDN	N-Guanylurea-dinitramide
HMX	Cyclotetramethylenetetranitramine
HTPB	Hydroxyl-terminated polybutadiene
RDX	Cyclotrimethylenetrinitramine
SEM	Scanning electron microscopy
TATB	1,3,5-Triamino-2,4,6-trinitrobenzene
TDI	2,4-Toluene diisocyanate

Roman Symbols

$\overline{M}$	Mean molecular mass
a	Pre-exponential factor of steady burning rate law
d_{10}	Particle diameter corresponding to 10 % of cumulative undersize distribution μm
d_{50}	Mean particle diameter μm
d_{90}	Particle diameter corresponding to 90 % of cumulative undersize distribution μm
E	Elastic modulus MPa
I_s	Gravimetric specific impulse
n	Pressure exponent of steady burning rate law
p	Pressure MPa
Q_v	Heat of explosion
r_b	Steady burning rate mm·s^{-1}
Span	Extent of particle size distribution defined as $(d_{90}-d_{10})/d_{50}$
T_c	Combustion temperature
T_p	Peak temperature
T_{peak}	Exothermic peak temperature

Greek Symbols

$\triangle I_s$	Specific impulse variation with respect to the reference formulation
ε_m	Elongation at maximum tensile strength %
η	Viscosity Pa·s
ρ	Density g·cm^{-3}
σ_m	Maximum tensile strength MPa
τ	Yield stress MPa

1 Introduction

Solid rocket propellant containing high-energy materials is one of the highest potential developments for rocket motors [1–3]. The gravimetric specific impulse and/or density specific impulse of propellants can be increased by the inclusion of energetic materials such as 2,4,6,8,10,12-hexanitro-2,4,6,8,10,12-hexaazaisowurtzitane (HNIW, CL-20), octahydro-1,3,5,7-tetranitro-1,3,5,7-tetrazocine (HMX), ammonium dinitramide (ADN), and some other oxidizers. On the other hand, high energetic oxidizers could significantly influence the properties and performance of composite propellants (e.g., combustion behavior, sensitivity, and specific impulse) [4–6]. Among the oxidizers, CL-20 was synthesized in the 1980s and is one of the most powerful energetic compounds used in solid propellant formulations [7]. Compared to ammonium perchlorate (AP), CL-20 has a higher molecular mass, density, heat of formation, and number of NO$_2$ groups [8], and hence it can meet stringent requirements, such as minimum combustion signature. Moreover, its energy content is superior to that of ammonium perchlorate (AP), the oxidizer commonly used in current HTPB-based composite propellants. HMX is also a high explosive used in many plastic-bonded explosives (PBX), double-base propellants, and composite propellants because of its high calorific potential, high density, and smokeless burning [9]. The characteristics of HMX have been the subject of extensive studies for many years, and its complex dependence on the experimental conditions, physical state, temperature, pressure, etc., is well known [10–12]. On the other hand, N-guanylurea-dinitramide (GUDN) is a novel energetic material with a detonation velocity of 8210 m·s^{-1}, and its sensitivity and thermal stability of GUDN are superior to those of RDX, while its energy content is higher than that of TATB. Therefore, GUDN can be used both as a propellant and insensitive munition (IM) explosive [13–15]. In addition, ADN, a new kind of high energetic material with high density, has been widely studied and used in the field of solid propellants and high explosives [16–18]. Advantages of ADN over AP are clean combustion products and higher heat of formation [19,20]. Though the development of ADN-based solid propellants has faced a number of challenges, such as compatibility, coating, application to energetic materials, and more, research activities continue motivated by its high potential performance.

In order to compare the effects of different fillers especially on combustion properties, six different composite solid propellants containing different mono or dual oxidizers were prepared (by replacing part of the AP in the reference formulations by HMX, CL-20, GUDN, or ADN). This paper will show how the tested oxidizers affect the hazardous and mechanical properties of the corresponding composite propellants, but emphasis will be placed on the combustion properties (burning rate and pressure exponent) which are the key factors for design of solid rocket motors.

2　Experimental

2.1　Ingredients and Formulations

The binder system is composed of hydroxyl-terminated polybutadiene (HTPB), plasticized with di-2-ethylhexyl sebacate (DOS), and cured by 2,4-toluene diisocyanate (TDI). Micron-sized aluminum powder (Al, 30 μm, $\geq$99.8 %), GFP (a combustion catalyst for composite propellants), HMX, CL-20, GUDN, and ADN were used as components of the solid propellants. All of these ingredients are of industrial and commercial type. ADN particles were coated by polyurethane binder in Xi'an Modern Chemistry Research Institute. Bimodal AP was utilized in all propellant formulations. The coarse fraction consisted of research grade AP (>99 % pure) with an average particle size of 115–174 μm. The fine fraction was obtained by grinding the previous coarse AP to an average particle size of around 1–5 μm. Except where otherwise stated, all propellants were manufactured, processed, and tested at Xi'an Modern Chemistry Research Institute under identical experimental conditions and processing procedures.

The precise compositions of the six tested propellant formulations are reported, in terms of ingredient mass fractions, in Table 1. Notice that for practical reasons two AP-based reference formulations were used: CP-AP-1 (2 % additives) and CP-AP-2 (5 % additives). Particle size distributions of the tested oxidizers will be discussed in Table 2.

Table 1　Main propellant ingredients (mass fractions)

Samples	HTPB, %	Al, %	AP, %	Oxidizer, %	GFP, %	Additives, %
CP-AP-1	12	18	65	–	3	2
CP-HMX	12	18	50	15 [HMX]	3	2
CP-CL-20	12	18	50	15 [CL-20]	3	2
CP-GUDN	12	18	50	15 [GUDN]	3	2
CP-AP-2	13	18	64	–	–	5
CP-ADN	13	18	49	15 [ADN]	–	5

Table 2 Characteristics of AP, HMX, CL-20, GUDN, and ADN pure oxidizer particles

Items	Unit	AP (coarse)	HMX	CL-20	GUDN	ADN
d_{10}	μm	112	3	41	49	6
d_{50}	μm	156	13	92	195	23
d_{90}	μm	218	34	218	394	54
Span	–		0.686	2.465	1.925	1.775	2.120
Density	kg·m^{-3}, ×10^3	1.94	1.88	2.04	1.75	1.82
Vol. weighted mean	μm	161.2	15.9	116.3	213.4	27.0
Specific surface area	m^2·g^{-1}	0.04	1.13	0.09	0.11	0.70
Oxygen balance [15]	%	+34.04	−21.6	−10.95	−19.13	+25.79

2.2 Preparation of Propellants

All propellant formulations were mixed in 500 g batches using a vertical planetary mixer of 2 dm^3 capacity. Batches were mixed and cast under vacuum by a slurry cast technique. Propellant was cured at 50 °C for 72 h in a water jacketed oven.

2.3 Characterization Methods of Ingredients and Propellants

2.3.1 SEM and Particle Size Distribution Experiments

Particle sizes and their distributions were measured by a Mastersizer instrument. The morphologies of oxidizers were examined by a scanning electron microscope (SEM). The reported specific surface area values refer to the particle size distribution as determined by the Malvern Mastersizer.

2.3.2 Heat of Explosion Test

Heat of explosion values were measured by means of an isothermal method. A defined mass of propellant sample was put into a calorimetric oxygen bomb, which was surrounded by a fixed mass of water. The propellant was ignited in the bomb, and the sample heat of explosion was calculated according to Eq. 1 after measuring the water temperature increase:

$$Q_v = (C\Delta T - q_1)/m \qquad (1)$$

where Q_v is the heat of explosion, J·g^{-1}; C is the thermal capacity of the calorimeter, J·K^{-1}; ΔT is the water temperature increase, K; q_1 is the heat of explosion of the ignition wire, J; and m is the mass of sample, g.

2.3.3   Density Test

The density measurements of oxidizers were carried out with a Model AG 104 METTLER TOLEDO balance sing rectangular shaped samples of $30 \times 30 \times 10$ mm, which were steeped in a liquid paraffin medium at the temperature of 20 ± 2 °C.

2.3.4   Hazard Property Test

The hazard properties of the tested propellant compositions when subject to impact stimuli were determined by applying the fall hammer method (2 kg drop weight) in a Bruceton staircase apparatus [21], and results are given in terms of statistically obtained 50 % probability of explosion (H_{50}). Friction sensitivity was measured on a Julius Peter apparatus [22] by incrementally increasing the load from 0.2 to 36 kg, until no ignition was noted in five consecutive test samples.

2.3.5   Burning Rate Test

Figure 1 shows the chimney-type strand burner apparatus with observation windows used to measure steady burning rates. The measuring apparatus is fully described in references [23–25]. Propellant samples were placed vertically on the combustion rack in the sealed chamber which was then filled with a nitrogen atmosphere. A metal fine wire (0.1 mm in diameter) was threaded through the top of the strand with
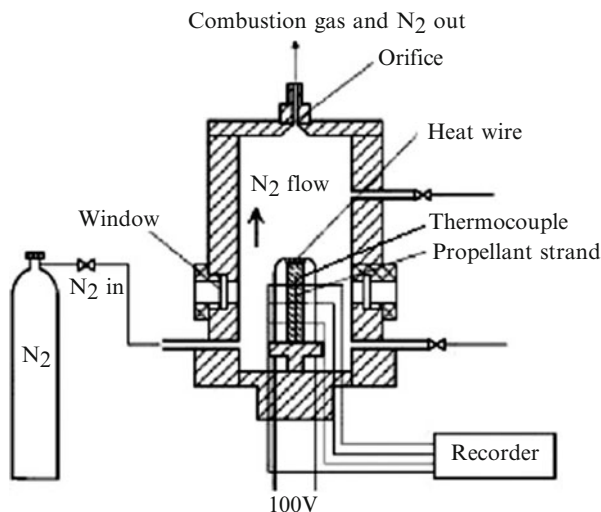

Fig. 1 The chimney-type strand burner apparatus with observation windows [23,24]

an alternating voltage of 100 V to ignite the propellant strands (5–6 mm diameter, 140 mm length) at the initial temperature of 20 °C.

Steady burning rate measurements of propellant samples were performed as follows. When a propellant strand ignites under the nitrogen gas purge flow, the pressure in the strand burner increases due to the release of gaseous products. However, the pressure valve attached to the nitrogen gas supplier is regulated automatically to reduce the nitrogen gas flow rate in order to maintain the pressure constant. Thus, the pressure in the burner is maintained at the desired combustion pressure. Burning rate is measured by determining the instant of melting of each of five low-melting-point fuse wires of lead metal, 0.1 mm in diameter, threaded through the strand at accurately known separation distances (140 mm). These five fuse wires, each in series with a resistor, form five parallel arms of an electrical circuit, whose output voltage changes discontinuously as soon as a fuse wire melts. The temperature of the strand is measured by a calibrated copper-constantan thermocouple threaded through the strand with the thermocouple bead placed at the center of the strand. Real-time data are recorded and processed by a computer which calculates the burning rates. Five experiments are replicated at each test pressure, and the average experimental results are obtained with a standard deviation of 0.13–0.25 [23,24].

2.3.6 Thermal Decomposition Analysis

Thermal analyses (TG-DTG experiments) of the tested propellant compositions were carried out on a TA instrument at a heating rate of 10 K·min^{-1} under N_2 atmosphere and with a sample mass of about 2.0 mg.

2.3.7 Mechanical Properties

Mechanical characteristics of the tested propellant compositions were determined by an Instron 4505 tensile tester. Cured propellants were cut into slices, from which JANNAF dog bone samples were stamped. Tests were carried out at 20 °C ambient temperature with 100 mm·min^{-1} crosshead speed.

3 Results and Discussion

3.1 *Microstructures and Granular Distribution Characteristics of Tested Oxidizers*

The five types of oxidizer particles were well dried in a vacuum oven at 50 °C for 3 days and then examined: their molecular structures are shown in Fig. 2, while their microstructures and granular distribution characteristics are shown in Fig. 3 and Table 2, respectively.

It can be seen from Fig. 3 to Table 2 that the microstructures of AP and prilled ADN particles are approximately ball shaped with a round surface, whereas other particles – especially CL-20 particles – present an irregular shape. Also AP particles appear more uniform than the others. The median diameter d_{50} of AP particles (155.83 µm) is much larger than those of HMX (12.76 µm), CL-20 (92.01 µm), and ADN (22.99 µm), but is smaller than that of GUDN (194.83 µm). The particle size distribution curve of AP is smoother than that of other oxidizers due to a much
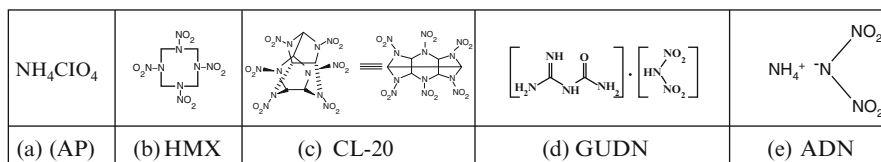
NH$_4$ClO$_4$	NO$_2$ structure	CL-20 structure	GUDN structure	ADN structure
(a) (AP)	(b) HMX	(c) CL-20	(d) GUDN	(e) ADN

Fig. 2 Molecular structures of tested oxidizers: AP, HMX, CL-20, GUDN, and ADN

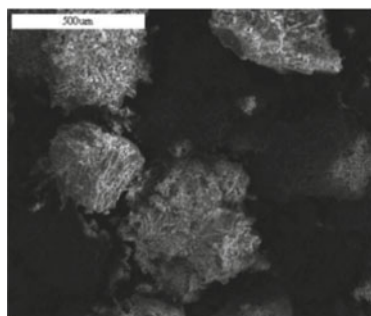**(a)** AP (coarse)

(b) HMX
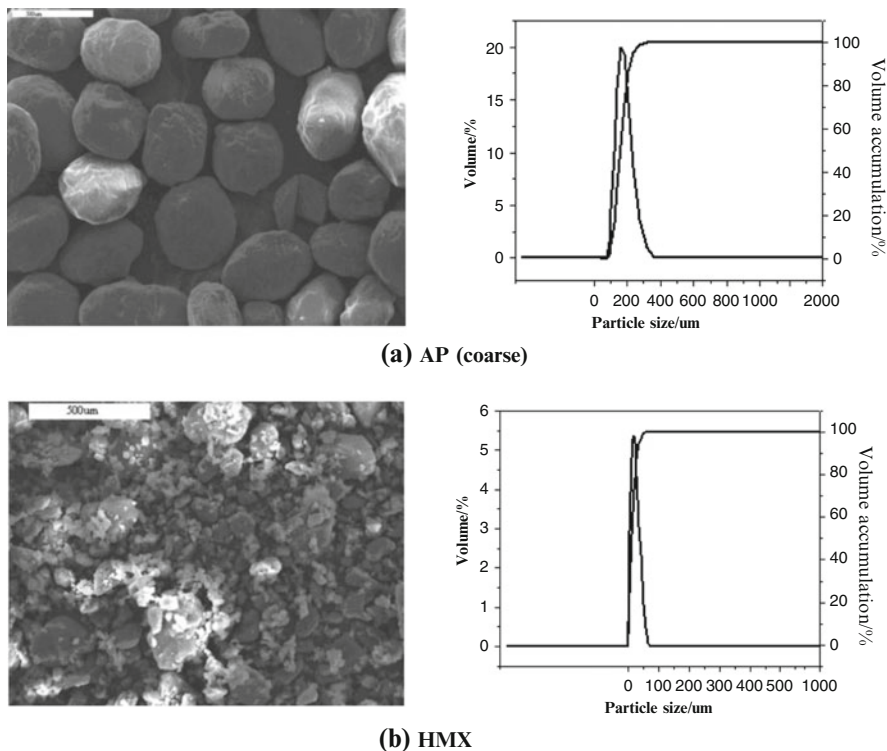
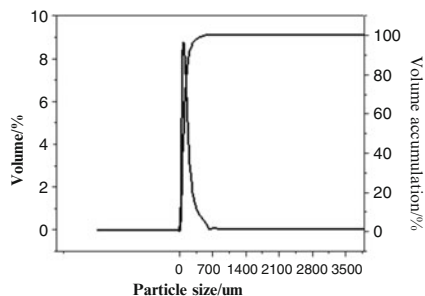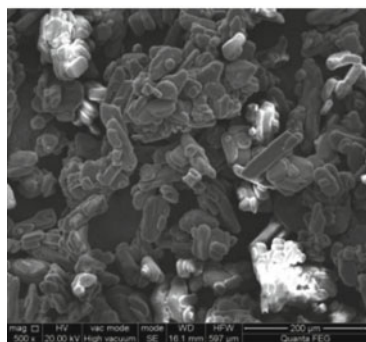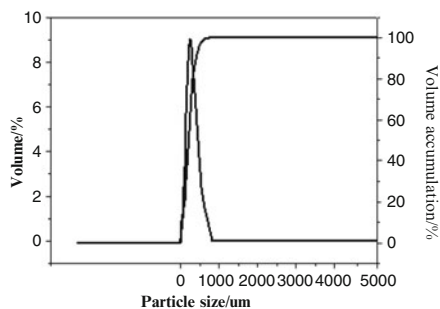**Fig. 3** SEM photographs and grain-size distributions of tested oxidizers (×500)
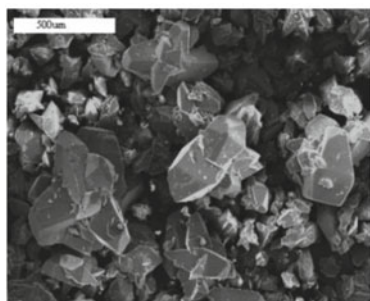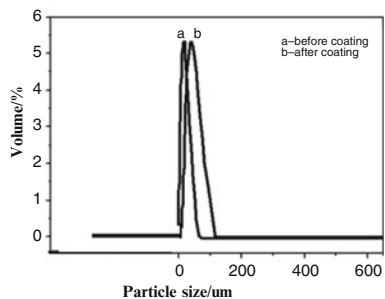
(c) CL-20

(d) GUDN

(e) ADN

Fig. 3 (continued)

lower span (0.686), compared with others (ranging from 1.775 to 2.465). Finally, the specific surface area of AP particles (0.04 $m^2 \cdot g^{-1}$) is much lower than those of the other particles, especially GUDN (0.11 $m^2 \cdot g^{-1}$), probably due to irregularities of GUDN particles.

Table 3 Calculated ideal properties of tested dual-oxidizer composite propellants

Samples	Q_v, kJ·kg^{-1}	ρ, kg·cm^{-3}	T_c, °C	$\overline{M}$, g·mol^{-1}	I_s, s	$\triangle I_s$, %
CP-AP-1	6219	1.73	3210	35.6	263.8	0
CP-HMX	5953	1.71	2993	37.2	259.9	−1.48
CP-CL-20	6223	1.75	3302	36.2	265.6	0.68
CP-GUDN	5775	1.69	3152	34.7	259.0	−1.82

$p = 7.0$ MPa, exit pressure 0.1 MPa, $T = 25$ °C

Table 4 Calculated ideal properties of tested ADN dual-oxidizer composite propellants

Samples	T_c, °C	C*, m·s^{-1}	ρ, kg·cm^{-3}	I_s, s	$\triangle I_s$, %
CP-AP-2	2866	1518.5	1.718	257.1	0
CP-ADN	2895	1537.4	1.681	259.6	0.97

($p = 7.0$ MPa, exit pressure 0.1 MPa, $T = 25$ °C) [17]

3.2 Thermochemical and Hazard Properties of Tested Propellants

3.2.1 Calculated Ideal Properties

The energetic properties of the examined dual-oxidizer composite solid propellants were calculated by means of the "Energy Calculation Star (ECS)" software [12], which was developed by Xi'an Modern Chemistry Research Institute based on the fundamental thermodynamics principle of minimum free energy. Note that density plays an important role in developing high-energy materials. For example, density is directly related to the detonation velocity of the formulation. Therefore, density and heat of explosion were evaluated for each propellant under scrutiny. The data overall obtained are listed in Table 3 (HMX, CL-20, GUDN) and Table 4 (ADN).

The calculated ideal results in Table 3 indicate that the heat of explosion of the reference AP-based mono-oxidizer propellant is 6219 J·g^{-1}, higher than those of HMX (5953 J·g^{-1}) and GUDN-based propellants (5775 J·g^{-1}) and lower than that of CL-20-based propellant (6223 J·g^{-1}). The measured densities of dual-oxidizer propellants are 1.69 g·cm^{-3} for [CP-GUDN], 1.71 g·cm^{-3} for [CP-HMX], and 1.75 g·cm^{-3} for [CP-CL-20] with respect to 1.73 g·cm^{-3} of the reference AP-based mono-oxidizer propellant. This grading is due to the partial replacement of AP by oxidizers of different density and finer grain size. Moreover, better powder packing during manufacturing leads to a higher propellant density. The adiabatic flame temperature (T_c), gravimetric specific impulse (I_s), and density (ρ) of the [CP-CL-20] composite solid propellant are higher than those of the other dual-oxidizer propellants, which may be attributed to the higher-energy performance of CL-20. The enthalpy of formation (−355 kJ·mol^{-1}) and density (1.75 g·cm^{-3}) of pure GUDN are lower than those of pure AP (−295.8 kJ·mol^{-1} and 1.95 g·cm^{-3}), resulting in lower heat of explosion and density of the corresponding propellants. Specific impulse, heat of explosion, and density of propellants with different dual

oxidizers decrease in the following order, [CP-CL-20]>[CP-AP]>[CP-HMX]>[CP-GUDN], while the adiabatic flame temperature (T_c) decreases in the order: [CP-CL-20]>[CP-AP]>[CP-GUDN]>[CP-HMX].

When 15 % AP is replaced by ADN, the thermochemical data obtained are shown in Table 4.

From the results in Table 4, it can be seen that propellants [CP-AP-2] and [CP-ADN] are quite different. The calculated ideal gravimetric specific impulse and adiabatic flame temperature increase when ADN replaces AP. But [CP-ADN] propellant density decreases, being ADN density (1.81 g·cm^{-3}) much lower than that of AP (1.95 g·cm^{-3}).

3.2.2   Hazard Properties

In addition to high density and energy, other primary considerations in developing energetic materials concern the hazard properties. Again, it is important to distinguish between the sensitivity of individual ingredients (see Table 5) and that of the final, tailored formulation. Hazard properties of the tested dual-oxidizer propellant compositions were investigated, and the results overall obtained are shown in Table 6 (HMX, CL-20, and GUDN) and Table 7 (ADN). Hazard properties of pure RDX and HMX are similar (see Table 5), but only HMX was tested in a dual-oxidizer composite propellant (Table 6).

It can be seen from the results in Table 6 that all the tested formulations are sensitive to impact and friction except [CP-GUDN], which appears less sensitive. Particularly for HMX and CL-20, this sensitivity may be attributed to the active N-NO$_2$ groups present on the oxidizer surface, in contrast with GUDN. On the opposite, the collected data reveal that incorporating GUDN leads to a significant

Table 5 Hazard properties of tested pure oxidizers [26,27]

Samples	RDX	HMX	CL-20	GUDN	ADN
Drop height (cm)	38	38	4	>159	31
Friction (N·m)	120	120	54	>350	>350

Table 6 Hazard properties of tested dual-oxidizer composite propellants

Samples	Friction (P, %)	Confidence level of 95 % believe level	Impact (H_{50}, cm)	Standard deviation S (logarithmic value)	Static E_{50}, mJ
CP-AP-1	96.0	(80 %, 100 %)	37.2	0.10	186.97
CP-HMX	96.0	(80 %, 100 %)	33.8	0.07	198.94
CP-CL-20	100	(86 %, 100 %)	25.4	0.15	215.61
CP-GUDN	60.0	(39 %, 79 %)	64.6	0.04	205.12

Table 7 Hazard properties of tested ADN dual-oxidizer composite propellants [17]

Samples	Friction sensitivity (P, %)	Impact sensitivity (H_{50}, cm)
CP-AP-2	36	112.2
CP-ADN	52	67.7

decrease in friction and impact sensitivity of the corresponding propellants, and therefore application to propellants is feasible and safe.

It can be seen from the results in Table 7 that the propellant formulation containing ADN is more sensitive to impact and friction than the reference AP-based mono-oxidizer propellant. The sensitivity may be attributed to compatibility and interfacial problems of ADN with the propellant ingredients. The data reveal that incorporating coated ADN particles of granulated and approximate spherical shape in composite propellants leads to a major increase in friction and impact sensitivity, so suitable work must be done to decrease the mechanical sensitivity of ADN-based composite propellants.

3.3 Thermal Analysis of Oxidizers and Propellants

The DSC and TG-DTG techniques were used to study the thermal decomposition of different pure oxidizers and AP mixtures with HMX, CL-20, and GUDN at 0.1 MPa. Figures 4 and 5 show the DSC and TG-DTG curves of the tested pure oxidizers under the heating rate of 10 °C·min^{-1}, respectively; the corresponding parameters are summarized in Table 8.

It can be seen that the DSC curve for pure AP shows several events (Fig. 4a):

- The first stage of AP decomposition is a topochemical reaction at crystal defects; the endothermic DSC peak at 250 °C points to AP transition from orthorhombic to cubic.
- The residue after the first stage is pure AP; the exothermic events at 348.7 °C and 453.1 °C are due to the proper decomposition of the AP crystal in ammonia and perchloric acid, followed by the formation of chloridric acid and oxygen (decomposition of $HClO_4$).

Similar results are reported in the literature [29,30]. The DSC curve of HMX also shows three peaks. At first, there is a weak endothermic peak observed at about 185–200 °C, due to the polymorphic transformation ($\beta \rightarrow \delta$) [31]. The exact transition temperature obviously depends on the heating rate. Usually the polymorphic transformations are reversible, and therefore it is tempting to say that the irreversibility in HMX is due to the different conformational structure of HMX molecules in the respective crystal structures [32,33]. After a transformation step, a sharp endothermic peak was shown at 274–281 °C which corresponds to the onset of melting. This peak is followed immediately by a strong exothermic peak, which

(a) AP

(b) ADN

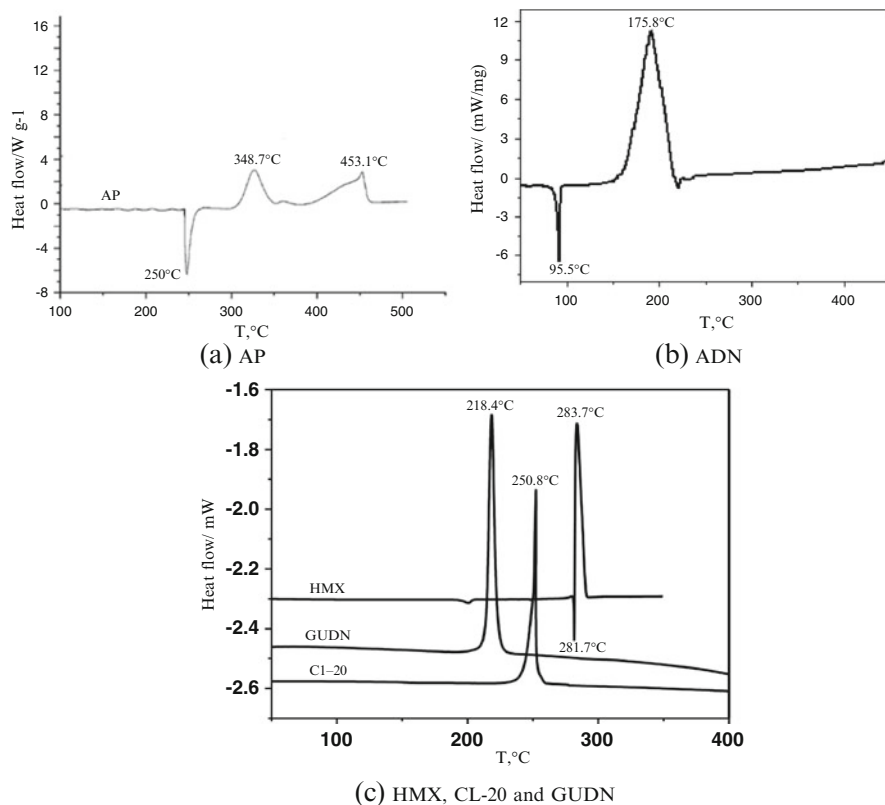(c) HMX, CL-20 and GUDN

Fig. 4 DSC curves of tested pure oxidizers under the heating rate of 10 °C·min^{-1}

is due to the self-decomposition of HMX [34–36]. On the contrary, there is only one exothermal peak at 218.54 °C for the GUDN-based sample. Seeing details in Fig. 4c, a solid–solid phase transition is detected at about 160 °C, followed by the thermal decomposition of CL-20 starting around 210 °C [36].

It can be seen from the curves in Fig. 5a that the TG curves of AP have two mass loss stages. At first, we observe a weak mass loss at about 319.2–335.2 °C, accompanied by about 25.4 % mass loss, which may be due to the crystalline transition and volatilization of ammonia, and the exact transition temperature for each particle size depends on the rate of heating. After the first step, a greater mass loss showed at 358.8–420.1 °C, which is the second mass loss stage, accompanied by 67.2 % mass loss. Corresponding to AP, there is one large mass loss stage for HMX and CL-20 particles. There is 90 ± 2 % mass loss of CL-20 particles when heated to 257 °C in a pinhole pan [37].

Figure 6 shows the TG-DTG curves of the tested dual-oxidizer composite propellants.

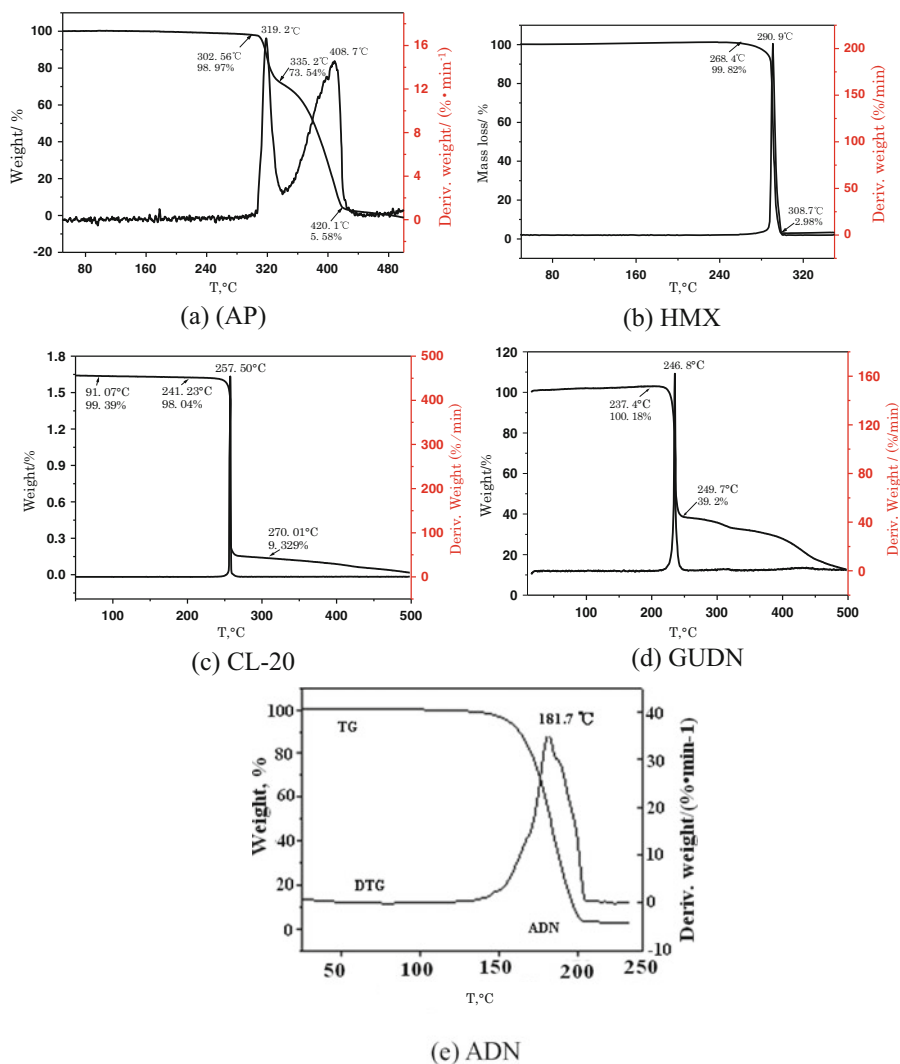Fig. 5 TG-DTG curves of tested pure oxidizers under the heating rate of 10 °C·min^{-1}

It can be seen that the TG-DTG pattern of dual-oxidizer composite propellants (Fig. 6) suggests that the AP/CL-20 formulation gave an exothermic reduction in T_{peak} values and a marginal change for HMX as compared to the reference composition. An increase of mass loss is observed for AP/CL-20 formulation. Also, its decomposition process indicates that the gaseous products formed during decomposition exert a higher heat feedback to the deflagrating propellant surface, which can increase the burning rate as confirmed by the burning rate measurements. On the contrary, the incorporation of GUDN to the formulation leads to decrease in T_{peak} which may be due to its low melting point and heat of combustion. In

Table 8 Data of thermal analysis for pure oxidizers

Oxidizer samples	DSC data	TG-DTG data	
	Max. temp. of oxidizers T_p, °C	T, °C	Mass loss, %
AP	Endothermal: 250.0	319.2	25.43
	Exothermal: 348.7, 453.1 [28]	408.7	63.22
HMX	283.7	290.9	96.84
CL-20	250.8	257.5	88.72
GUDN	218.4	246.8	60.98
ADN	175.8	181.7	34.78

(a) CP-AP-1

(b) CP-HMX

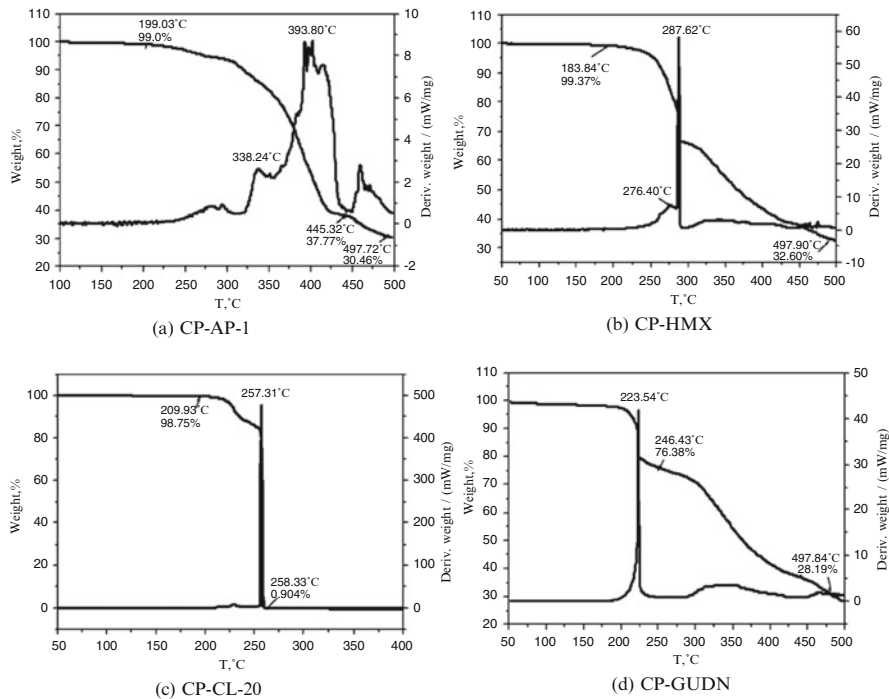(c) CP-CL-20

(d) CP-GUDN

Fig. 6 TG-DTG curves of tested dual-oxidizer composite solid propellants

view of the optimum I_s level of 265.6 s which is superior to AP, HMX, and GUDN compositions, the composition with CL-20 deserves further studies.

## 3.4 Burning Rate and Pressure Exponent

Propellant burning rates reflect the rate of gas generation, which determines the pressure inside the combustion chamber and the overall motor thrust. Burning rates herein are obtained experimentally by burning small propellant strands and

Table 9 Burning rate and pressure exponent of tested dual-oxidizer composite propellants

Samples	Burning rate, mm·s^{-1}					
	1 MPa	4 MPa	7 MPa	10 MPa	12 MPa	15 MPa
CP-AP-1	11.04	21.55	28.42	34.56	36.94	40.70
CP-HMX	10.10	19.45	25.80	32.25	33.46	36.14
CP-CL-20	12.18	23.22	30.34	36.59	39.06	42.87
CP-GUDN	9.15	18.71	24.35	30.30	31.93	34.82
	Pressure exponents, n					
	1–4 MPa	4–7 MPa	7–10 MPa	10–12 MPa	12–15 MPa	1–15 MPa
CP-AP-1	0.482	0.494	0.548	0.365	0.434	0.486
CP-HMX	0.473	0.505	0.626	0.202	0.345	0.482
CP-CL-20	0.465	0.478	0.525	0.358	0.417	0.469
CP-GUDN	0.516	0.471	0.613	0.287	0.388	0.503

Table 10 Burning rate and pressure exponent of tested AP/ADN composite propellants [17]

Samples	Burning rate, mm·s^{-1}				
	1 MPa	4 MPa	7 MPa	10 MPa	15 MPa
CP-AP-2	2.25	5.44	7.17	8.21	9.36
CP-ADN	2.57	6.58	9.51	12.40	16.01
	Pressure exponents, n				
	1–4 MPa	4–7 MPa	7–10 MPa	10–15 MPa	1–15 MPa
CP-AP-2	0.48	0.51	0.38	0.35	0.41
CP-ADN	0.61	0.78	0.74	0.63	0.68
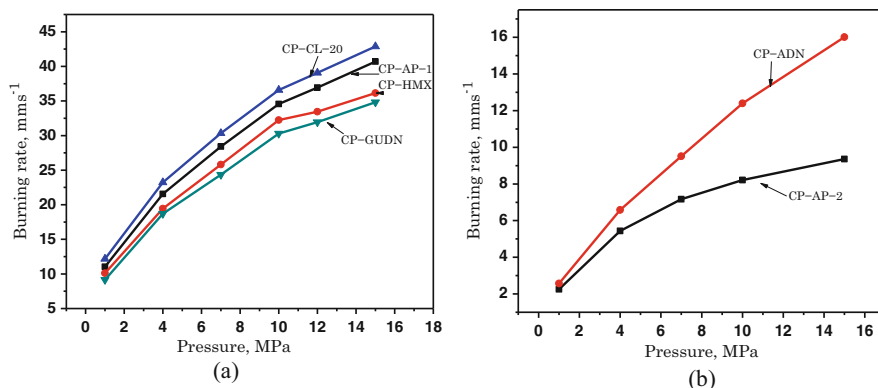
Fig. 7 Effects of tested dual oxidizers on the measured steady burning rate. (**a**) [CP-AP-1], [CP-HMX], [CP-CL-20], and [CP-GUDN] formulations; (**b**) [CP-AP-2] and [CP-ADN] formulations

measuring the surface regression versus time. Tables 9 and 10 show the measured ballistic properties (burning rate and pressure exponent n) of the tested composite propellants. Figure 7 illustrates the effects of different dual oxidizers on the burning rates of composite propellants.

For the burning rate experiments conducted over the pressure range 1.0–15.0 MPa, the reference composition containing AP mono-oxidizer exhibits a burning rate in the order of 11.04–40.70 mm·s^{-1} (Table 9). Dual-oxidizer compositions AP/HMX and AP/GUDN result in a burning rate decrease of 12.3 and 14.5 %, respectively. The negative oxygen balance of HMX and GUDN (shown in Table 2) may cause a partial oxidation of the HTPB binder. Hence, less energy is released in the combustion process occurring near the burning surface, and this causes lower burning rates. The dual-oxidizer composition obtained by incorporating CL-20 particles is relatively more effective and generates higher burning rates in the order 12.18–42.87 mm·s^{-1}. Composition AP/CL-20 offers higher burning rates and lower-pressure exponent values as compared to other propellants. Thus, CL-20 appears a relatively superior oxidizer in terms of burning rates. Overall, for the tested dual-oxidizer composite propellants shown in Table 9, steady burning rates are, in increasing order, [CP-GUDN]<[CP-HMX]<[CP-AP-1]<[CP-CL-20]. Also, their pressure exponents are all very close and appear slightly decreasing with increasing pressure (see Fig. 7a).

Regarding CP-ADN compositions (see Table 10), ADN oxidizer can increase not only the gravimetric specific impulse but also steady burning rates. Replacing 15 % mass fraction of AP by ADN may boost the burning rate much above that of the reference AP-based mono-oxidizer propellant. Also the pressure exponent increases from 0.41 to 0.68 over the 1–15 MPa range. In agreement with the literature [17], steady burning rate and pressure exponent increase with increasing ADN mass fraction in the propellant formulation (see Fig. 7b).

Lastly, the combustion performance of dual-oxidizer composite solid propellants depends on the various physicochemical parameters such as particle size, oxidizer ratio in the mixture, particle size of catalysts, and the interface between catalyst and oxidizers [28,38]. As reported in the literature [5] concerning ADN grain-size effects on the combustion properties of GAP/ADN (30/70) propellant, samples containing raw ADN show the highest pressure exponent (0.79), whereas samples with smaller ADN particle size (from 40 to 212 μm) show a smaller pressure exponent (0.52–0.61). Thus, increasing ADN prill size implies a direct increase of the pressure exponent (and therefore, indirectly, also of the burning rate). Therefore, as for all composite energetic materials, controlling the grain-size distribution is a recommended approach to achieve suitable ballistic properties. Understanding the influence on ballistic properties of additives and, possibly, also of ADN particle size should be an important objective for future research.

3.5 Mechanical Properties of Dual-Oxidizer Propellants

Four different series of propellant compositions based on mono-oxidizers and dual oxidizers were tested and the results are shown in Table 11. The composition included 15.0 % of HMX, CL-20, and GUDN oxidizers replacing AP by using slurry

Table 11 Mechanical properties of tested dual-oxidizer composite propellants

Samples	Mechanical properties (20 °C)		
	E, MPa	σ_{m}, MPa	ε_{m}, %
CP-AP-1	7.23	1.14	38.8
CP-HMX	6.81	1.03	36.3
CP-CL-20	5.44	0.62	30.2
CP-GUDN	6.20	0.95	35.1

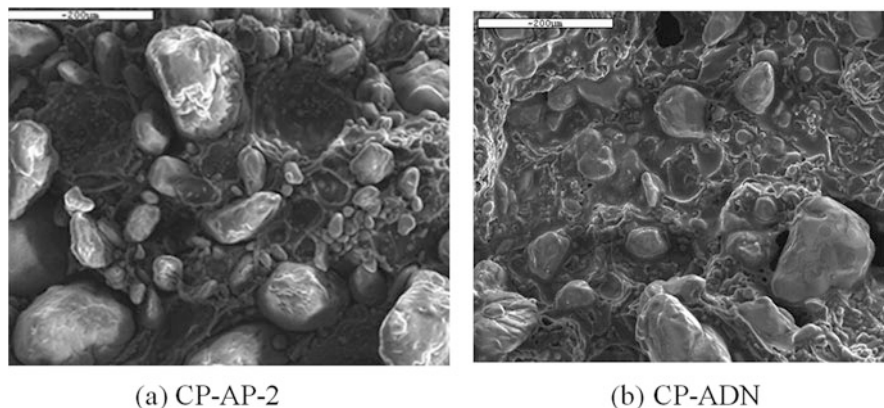(a) CP-AP-2   (b) CP-ADN

Fig. 8 Microstructures of composite propellants with and without ADN particles [17]

cast techniques. The reference composition with 67.0 % AP was also processed simultaneously. Mechanical properties were tested according to the GJB 772A-1997, 413.1 standards.

The maximum tensile strength, elongation, and elastic modulus of AP-based mono-oxidizer composition (1.14 MPa, 38.8 %, and 7.23 MPa, respectively) are higher than those of the dual oxidizers, which are in the range of 0.62–1.03 MPa, 30.2–36.3 %, and 5.44–6.81 MPa, respectively.

SEM observation of the propellant surface is one of the most important means to study the physical structures of dual-oxidizer composite propellants. SEM micrographs obtained for ADN partially replacing AP are shown in Fig. 8 (the corresponding data of Table 11 are not available).

From Fig. 8, it can be seen that there are obviously many approximate spherical and granular particles on the surface of cured solid propellants. The ADN particles are compatible with the propellant ingredients, and the granular particles with smaller diameters fill the spaces between the bigger grains well. The plain regions correspond to the linked networks of binder systems, consisting of HTPB and TDI. This indicates that AP particles are compatible with the propellant ingredients. The foam regions are due to the holes generated by the hygroscopic ADN particles at atmospheric pressure or the unlinked binder systems. All of these facts prompt for more research needs to be carried out before application of ADN to solid rocket propulsion.

4   Conclusions

1. AP and prilled ADN particles are approximately ball shaped with a round surface; HMX, GUDN, and especially CL-20 particles present irregular shapes. The median diameter d_{50} of AP particles (155.83 µm) is much larger than that of HMX (12.76 µm), CL-20 (92.01 µm), and ADN (22.99 µm), but is smaller than that of GUDN (194.83 µm). The span of AP particles (0.686) is much lower than those of the remaining oxidizers, ranging from 1.775 to 2.465. Likewise, the specific surface area of AP particles (0.04 $m^2 \cdot g^{-1}$) is much lower than that of the other particles, especially GUDN (0.11 $m^2 \cdot g^{-1}$).

2. AP-based dual-oxidizer composite solid propellants can be prepared and cured by vacuum cast techniques. All of the tested dual-oxidizer composite solid propellants burn steadily.

3. The burning response is similar for all tested dual-oxidizer formulations (see Fig. 7a), except AP/ADN (see Fig. 7b) for which a substantial increase of both burning rate and pressure sensitivity is observed. The pressure exponent of AP/ADN increases from 0.41 to 0.68 over 1–15 MPa when ADN replaces 15 % mass fraction of AP. Moreover, the pressure exponent is larger for larger ADN particle size.

4. AP/ADN dual-oxidizer formulations feature increasing calculated ideal gravimetric specific impulse but decreasing density with increasing ADN mass fraction replacing AP in the reference mono-oxidizer composition CP-AP-2. Finally, the impact and friction sensitivities increase with increasing ADN mass fraction.

5. AP/HMX and AP/GUDN dual-oxidizer formulations result in heat of explosion and density decrease and also burning rate decrease of 12.3–14.5 % compared with that of the reference mono-oxidizer composition CP-AP-1. Moreover, the mechanical properties of these dual-oxidizer compositions are lower than those of the AP-based mono-oxidizer propellant.

6. The calculated adiabatic flame temperature (T_c), ideal gravimetric specific impulse (I_s), and density (ρ) of the CL-20/AP dual-oxidizer solid propellant are higher than those of the reference mono-oxidizer composition CP-AP-1. Compared with the other oxidizers, AP/CL-20 dual-oxidizer formulation increases the propellant burning rate effectively, whereas the pressure exponent decreases. But the mechanical properties of AP/CL-20 composition are the lowest among all the tested formulations.

References

1. DeLuca LT, Maggi F, Dossi S, Weiser V, Franzin A, Gettwert V, Heintz T (2013) New energetic ingredients for solid rocket propulsion. Chin J Explos Propellants 36(6):1–14
2. DeLuca LT, Palmucci I, Franzin A, Weiser V, Gettwert V, Wingborg N, Sjöblom M (2014) New energetic ingredients for solid rocket propulsion. HEMCE-2014, 13–15 Feb, Trivandrum, India
3. Zhou G, Wang J, He W-D, Wong N-B, Tian A, Li W-K (2002) Theoretical investigation of four conformations of HNIW by B3LYP method. J Mol Struct (Theochem) 589–590:273–280
4. Babuk VA, Glebov A, Arkhipov VA, Vorozhtsov AB, Klyakin GF, Severini F, Galfetti L, DeLuca LT (2005) Dual – oxidizer solid rocket propellants for low – cost access to space, 10-IWCP. In: DeLuca LT, Sackheim RL, and Palaszeweski BA (eds) Space propulsion. Grafiche GSS, Bergamo, paper 15
5. Teipel U (2005) Energetic materials, particle processing and characterization. WILEY-VCH Verlag GmbH & Co., KGaA, Weinheim
6. DeLuca LT, Galfetti L, Signoriello D, Levi, Cianfanelli S, Babuk VA, Sinditskii VP, Klyakin GF, Vorozhtsov AB (2006) Dual – oxidizer solid rocket propellants for green access to space. The 57th International Astronautical Congress (IAC), 2006, At Valencia, Spain, 02–06 Oct 06, Volume: ISBN: 9781605600390, pp. 1–13, IAC-06-C4.3.2.
7. Wardle RB, Hinshaw JC, Braithwaite P, Rose M, Johnson G, Jones R, Poush K (1996) Synthesis of the caged nitramine HNIW (CL-20). In: Proceedings of 27th national annual conference of ICT. 27.1–27.10. Karlsruhe, June 25–28
8. Turcotte R, Vachon M, Kwok QSM, Wang R, Jones DEG (2005) Thermal study of HNIW (CL-20). Thermochem Acta 433:105–115
9. Schroeder M (1981) Thermal decomposition of HMX, vol III. In: Proceedings of the 18th JANNAF combustion meeting, Pasadena, CA, October 19–23
10. Pinheiro GFM, Lourenco VL, Iha K (2002) Influence of the heating rate in the thermal decomposition of HMX. J Therm Anal 67:445
11. Herrmann M, Engel W, Eisenreich N (1992) Thermal expansion, transitions, sensitivities, and burning rates of HMX. Prop Explos Pyrotech 17:190
12. Tian DY (2013) The optimization and design of solid propellant formulations. Defense Industry Press, Beijing
13. Lei YongPeng, Yang ShiQing, Xu SongLin, Zhang Tong (2007) Progress in insensitive high energetic materials N-Guanylurea dinitramide. Chin J Energetic Mater 15(3):289–293
14. Talawar MB, Sivabalan R, Anniyappan M, Gore GM, Asthana SN, Gandhe BR (2007) Emerging trends in advanced high energy materials. Combust Explosion Shock Waves 43(1):62–72
15. Wang BoZhou, Liu Qian, Zhang ZhiZhong et al (2004) Study on properties of FOX-12. Chin J Energetic Mater 12(1):38–39
16. WeiQiang Pang, HuiXiang Xu, YangLi, XiaoBing Shi (2012) Characteristics of NEPE Propellant with Ammonium Dinitramide (ADN). Adv Mater Res 399–401:279–283
17. WeiQiangPang, XueZhongFan, WeiZhang, HuiXiangXu, ShuxXinWu, FangLiLiu, WuXiXie, NingYan (2013) Effect of Ammonium Dinitramide (ADN) on the characteristics of Hydroxyl Terminated Polybutadiene (HTPB) based composite solid propellant. J Chem Sci Technol 2(2):53–60
18. Menke K, Heintz T, Schweikert W, Keicher T, Krause H (2009) Formulation and properties of ADN/GAP propellants. Prop Explos Pyrotech 34:218–230
19. HuiXiang Xu, LinQuan Liao, Qian Liu, YongHong Li, XiuLun Ran, FengQi Zhao (2008) Properties of prilled Ammonium Dinitramide (ADN) coated by polyurethane binders. Chin J Energetic Mater 16(6):525. (in Chinese)
20. Johansson M, de Flon J, Petterson A, Wanhatalo M, Wingborg N (2006) Spray prilling of ADN and testing of ADN-based solid propellants. In: 3rd international conference on green propellant for space propulsion and 9th international hydrogen peroxide propulsion conference

21. Mallory DH (ed) (1960) Development of sensitivity tests at the explosive research laboratory, Report no. 4236. NAVORD, Bruceton
22. Rinford JH (1981) Technical review to advance techniques in acoustical, electrical and mechanical measurements, Bruel and Kjaer, DK-2850 NAERUM, Denmark, vol 2, p 3
23. Maggi F, Bandera A, DeLuca LT (2011) Agglomeration in solid rocket propellants: novel experimental and modeling methods. Prop Explos Pyrotech 2:81–98
24. Nair UR, Asthana SN, Subhananda Rao A, Gandhe BR (2010) Advances in high energy materials. Def Sci J 60(2):137–151
25. QiLong Yan, XiaoJiang Li, YingWang, WeiHua Zhang, FengQi Zhao (2009) Combustion mechanism of double – base propellant containing nitrogen heterocyclic nitroamines (I): the effect of heat and mass transfer to the burning characteristics. Combust Flame 156:633–641
26. Hong WL, Tian DY, Liu JH, Wang F (2001) Study on the energy characteristic of propellant containing dinitroazofuroxan. J Solid Rocket Technol 24(2):41–53. (in Chinese)
27. Bazaki H, Kubota N (2000) Effect of binders on the burning rate of AP composite propellants. Prop Explos Pyrotech 25:312
28. Chan ML, Turner AD (2007) Insensitive high energy booster propellant suitable for high pressure operation. In: Kuo KK, De Dios Rivera J (eds) Advancements in energetic materials and chemical propulsion. Begell House, ISBN-13: 978-1-56700-239-3, ISBN-10: 1-56700-239-0
29. Goncalves RFB, Rocco JAFF, Iha K (2013) Thermal decomposition kinetics of aged solid propellant based on ammonium perchlorate-AP/HTPB binder, chapter 14[C], http://dx.doi.org/10.5772/52109//. Applications of calorimetry in a wide context-differential scanning calorimetry, isothermal titration calorimetry and microcalorimetry, Amal Ali Elkordy. InTech, pp 325–342. ISBN 978-953-51-0947
30. Xiao-Bin Z, Lin-Fa H, Xiao-Ping Z (2000) Thermal decomposition and combustion of GAP/NA/nitrate ester propellants. In: Progress in astronautics and aeronautics, AIAA, vol 185, pp 413
31. Wingborg N (2014) Status of ADN-based solid propellant development, Paper 07-01; Calabro M Evaluation of the interest of new ADN solid propellants for the vega launch vehicle. Paper 02-03; Weiser W, Franzin A, DeLuca LT, Fischer S, Gettwert V, Kelzenberg S, Knapp S, Raab A, Roth E Burning behavior of ADN solid propellants filled with aluminum and alane, Paper 07-02; Pang WQ Effects of ADN on the properties of nitrate ester plasticized polyether (NEPE) solid rocket propellants, Paper 07-03. Proceedings of 12-IWCP, Politecnico di Milan, Milan, 9–10 June. Milan, Italy
32. Kuo KK, Achirya R (2012) Fundamentals of turbulent and multiphase combustion. Wiley, Hoboken
33. Babuk VA, Vasilyev VA, Sviridov VV (2000) Formation of condensed combustion products at the burning surface of solid rocket propellant. In: Yang V, Brill TB, Ren WZ (eds) Solid propellant chemistry, combustion, and motor interior ballistics, progress in aeronautics and astronautics. AIAA, Reston, pp 749–776
34. Kubota N (2002) Propellants and explosives: thermochemical aspects of combustion. Wiley-VCH Verlag GmbH & Co. KGaA, ISBNs: 3-527-30210-7 (Hardback); 3-527-60050-7 (Electronic)
35. HeMiaoXiao, RongJieYang, QingPan (2005) Study on thermal decomposition of HNIW by In-situ FTIR Spectroscopy. Chin Energetic Mater 13(2):84–89. (in Chinese), China
36. Patil DG, Brill TB (1993) Characterization of residue of hexanitrohexaazaisowurtzitane. Combust Flame 92:456–458
37. Williams GK, Palopoli SF, Brill TB (1994) Thermal decomposition of energetic material 65. Conversation of insensitive explosives (NTO, ANTA) and related compounds to polymeric melone – like cyclic azine burn – rate suppressants. Combust Flame 98(3):197
38. Nedelko VV, Chukanov NV, Korsounskii BL (2000) Comparative investigation of thermal decomposition of various modifications of Hexanitrohexaazaisowurtzitane (CL-20). Prop Explos Pyrotech 25:255–259

Part V
Liquid and Gel Rocket Propulsion

Russian Engine Technologies

Dietrich Haeseler and Oskar J. Haidn

Abstract The paper summarises peculiarities of Russian rockets, their engines and components which have been developed over the last 50 years. Particular emphasis is put on the Russian moon race explaining in some detail the competing concepts, namely, the N1, the UR-700 and the R-56. Interestingly, derivatives and upgrades of some of the engines developed for these launchers are still in use today, i.e. the RD-107 in the Soyuz launcher and the RD-275 of Proton. Some Russian technologies which are the only ones of their kind in the world are explained in detail: the first full-flow cycle engines running with storable propellants (RD-270), the oxygen-rich LOx/kerosene staged combustion engine with the highest thrust (RD-170), the liquid oxygen/liquid hydrogen staged combustion engine employing both propellants in its cooling channels (RD-57), the only high-pressure oxygen-rich LOx/kerosene staged combustion engine without baffles and cavities (NK-33) or the power head of fuel-rich LOx/LH2 staged combustion engine (RD-0120) with a single pre-burner which feeds a two-stage turbine to drive a three-stage hydrogen pump and two connected oxygen pumps in series. The twin-spool LOx boost pump of the NK-33 engine has two concentric shafts, one inside the other enabling it to drive the two pump impellers at different rotational speeds. The injection systems of the pre-burners of the NK-33 or the RD-170 and the main injection systems of the RD-0120 or the RD-253 engines are worth mentioning.

1 Launch Systems

It has to be mentioned that the desire of the military for intercontinental ballistic missiles (ICMBs) was the main driver for ongoing technological developments and improvements. A typical example is the R-7 ICBM which with some modifications was transformed into the Vostok and Voskhod to Molniya and finally into different

D. Haeseler (✉)
Airbus Safran Launchers GmbH, 81663 Munich, Germany
e-mail: Dietrich.Haeseler@airbusafran-launchers.com

O.J. Haidn
Technical University Munich, 85748 Garching, Germany
e-mail: haidn@lfa.mw.tum.de

Soyuz versions which transported the first satellite (Sputnik) and the first man (Y. Gagarin) into space and is still very busy today flying from the European spaceport Kourou and transporting cargo and astronauts to the ISS. Obviously, the engines (RD-107, RD-108) of these launch vehicles have been improved over the years, but its major features are still the same and will be described in more detail later [1–3].

2 The Russian Moon Race

In the late 1950s and early 1960s, the following three different people were proposing different concepts for a launcher capable of reaching the moon:

- Sergei P. Korolev, head of OKB-1 in Podlipki in the Moscow region (today named to OAO RKK Energia), the main brain behind the Vostok programme which brought the first man (Y. Gagarin) into space
- Mikhail K. Yangel, director of OKB-586 in Dnepropetrovsk (today named Yuzhnoye State Design Office), a design bureau which worked on the development of ballistic (R14, R16) and intercontinental ballistic missiles (R-36)
- Vladimir N. Chelomei, head of OKB-52 in Reutov in the Moscow region (today named JSC MIC Mashinostroyenia)

After a lengthy debate and political struggles, only Chelomei's UR-500 and Korolev's N-1 designs were accepted. Nevertheless, Yangel continued to work on design studies of his R-56 concept at least on system level. Later into this race to the moon and beyond (1965), he proposed a joint effort to his competitors where he would be responsible for the design and manufacture of the launch vehicle; Korolev would be responsible for the manned spacecraft, while Chelomei should take over responsibility for the unmanned spacecraft. However, neither of the other chief designers agreed to this proposal and the R-56 was stopped.

2.1 Korolev's N-1 Rocket

Korolev originally proposed the N-I rocket as a launch vehicle for military space stations and manned missions with a payload capability of up to 80,000 kg. The first three stages of this five-stage rocket were dedicated to put the upper two stages into orbit which carried the payload as well as the propulsion systems for the mission-specific destinations. With the first stage removed, the rocket, called N-II, would have a payload capability of roughly 25,000 kg and thus become a competitor to Chelomei's proposed UR-200. The N-III consisted of the original N-I's three upper stages and would still have a payload capability of 5000 kg and thus become a replacement of the old R-7 rocket. One of the many variants of N-1 which were studied was designed for an ICBM with a capability of launching 17 multimegaton warheads. Another variant, the N-1M, was designed for a lift-

off thrust of 43,260 kN and a total mass of 2770 tons with a diameter of 10 m and a height of 104 m. Korolev did not agree with Valentin P. Glushko, the main designer of large liquid propellant rocket engines in Russia at that time, about the propellant combination for the moon rocket. Korolev planned to use LOx-kerosene, while Glushko opposed, based on his experience with these propellants, favouring storable propellants instead. Korolev then approached Nikolai D. Kuznetsov, who had a strong background in aero engines but no experience with rocket engines, and thus smaller LOx/kerosene engines were developed.

In the first stage, N-1 Block A, Korolev foresaw 30 engines, NK-15, which burned oxygen and kerosene to provide the necessary thrust. The stage was designed to have a structural index of about 6 % and a total mass of 2070 tons. The second stage, N-1 Block B, had a total mass of 620 tons with a structural index of roughly 9 %, featuring eight NK-15V engines which were basically NK-15s with longer expansion nozzles which increased the vacuum specific I_s from of 318 to 325 s and delivered a thrust of 1648 kN. The foreseen burn time of the stage was 120 s. The third stage, N-1 Block V, had a total mass of 210 tons with a structural index of 6.5 % and featured four NK-9 engines, each capable of providing 441 kN of thrust at an I_s of 353 s, and was designed for a burn time of 370 s. The fourth stage, N-1 Block G, featured a single NK-21 engine which burned again LOx/kerosene with a thrust of 402 kN and a total burn time of 365 s. The fifth stage, N-1 Block D, was equipped with an RD-58 engine which was designed by Korolev's design bureau for multiple ignitions and had a thrust of 83.4 kN and an I_s of 353 s. The total burn time was 680 s. In addition, the stage was equipped with small storable propellant thrusters to ensure control during coast phases.

The ultimate flight version of the N-1, the N-1F, had upgrades of engines of all stages: In the first stage, the 30 NK-15 engines would be replaced by the more powerful NK-33 with a sea level I_s of 297 s and a thrust of 1470 kN resulting from a chamber pressure of 146 bar. In the second stage, the eight NK-15 V engines would be replaced by the eight NK-43 with a vacuum I_s of 346 s, a thrust of 1755 kN and a chamber pressure of 146 bar. In the third stage, the four NK-9 engines would be replaced by four NK-39 engines with a vacuum I_s of 352 s, a thrust of 402 kN and a chamber pressure of 98 bar. In the fourth stage, the NK-21 was replaced by an NK-19, while the fifth stage remained unchanged (Fig. 1).

Interestingly, it was never planned to hot fire test the first stage on ground because the managers considered the cost too high and instead foresaw five test flights with the N-1 and the ultimate flight version N-1F which again should be tested only during flight. Each of the four flight tests 3L, 5L, 6L and 7L ended disastrously with 5L destroying the entire launch pad and delaying the program for almost two years. Two years after the 7L failure in 1972, Glushko took over control of the Korolev design bureau when the former chief Vasily P. Mishin was dismissed and stopped the N-1 programme.

It is worth mentioning that during the 1960s, an upgrade of the fourth stage, N-1 Block S, was studied and designed with a structural index of 14 % and a total mass of 58 tons which featured one D-57 engine, a staged combustion LOx/LH2 engine with a vacuum thrust of 392 kN, an I_s of 440 s and a burn time of 540 s. Furthermore,

Fig. 1 N-1 on its way to the launch pad

the foreseen upgrade of the fifth stage, N1 Block R, was designed with a structural index of 19 % and a total mass of 23 tons and featured one RD-56 engine, a staged combustion LOx/LH2 engine with vacuum thrust of 74.6 kN, an I_s of 441 s and a burn time of 1080 s. Some of the specific features of those two cryogenic engines will be discussed later.

2.2 *Chelomei's Universal Rocket Concept UR-500 and UR-700*

As mentioned previously, Chelomei followed a design concept which based on a family approach, and in addition he wanted all major components to be transportable on rails from the manufacturing site in the Moscow region to the launch site in Baikonur. The most notable launch vehicles are the UR-500, which today is still flying as the well-known Proton, and the UR-700. While the first received the go for development in 1962, the UR-700 was not selected although Glushko received the go for the RD-270 engine development which was a key element of the UR-700. Interestingly, the propulsion systems of all these launchers and stages featured the storable propellant combination of UDMH and N_2O_4. Here we only briefly describe the main features of the UR-500 and refer to the literature for more details about the Proton and focus on the UR-700 vehicle.

2.2.1   UR-500

The UR-500 polyblock was designed for a payload capacity of 12 tons into a 200 km orbit. In its first stage, which had a structural index of 7.1 %, a total mass of 379 tons and a burn time of 119 s, it featured originally four fixed 11D43s, each with a sea level thrust of 1524 kN and an I_s of 280 s from Glushko's design bureau and four gimballed 8D43 from Kosberg's design bureau with a sea level of 502 kN and an I_s of 280 s which were later replaced by six RD-253 staged combustion engines from Glushko, each with a sea level thrust of 1475 kN. The propulsion system of the second stage, having a structural index of 11.7 %, a total mass of 138 tons and a burn time of 230 s, consisted of a four-RD-0210/0211-engine arrangement with a total vacuum thrust of 2328 kN. The final third stage, with a structural index of 9.1 % and a total mass of 23.9 tons, featured one RD-0212 engine with a thrust of 613 kN and a burn time of 230 s.

2.2.2   UR-700

The UR-700 was designed for a payload capability of 151 tons into a 200 km orbit or 50 tons into a translunar trajectory with a gross lift-off mass of 4823 tons and a total thrust at lift-off of almost 56,480 kN.

The first stage had a total mass of 3210 tons, a structural index of 6.9 % and a sea level thrust of 37,650 kN, which works in parallel with the engines of the core stage, which had a total mass of 1072 tons, a structural index of 7 % and a sea level thrust of 18,830 kN. This first stage, consists of six boosters each equipped with one RD-270 engine, would operate for 151 s. The three RD-270 engines of the core stage would be fed until stage separation from tanks of the first stage, thus ensuring that the core stage tanks would be full after separation. The total burn time of the core stage was designed to be 306 s. Those RD-270 engines used the storable and hypergolic propellant combination of N_2O_4 and UDMH and were the first full-flow

cycle rocket engines with a fuel-rich and an oxidizer-rich pre-burner. They had a sea level thrust of 6275 kN (6713 kN vac.), a combustion chamber pressure of 261 bar and an incomparable thrust-to-weight ratio of 1.5 kN/kg. Specific features of the RD-253 and the RD-270 are discussed later. The third stage with a gross mass of 400 tons and a very low structural index of 6.5 % was propelled by three RD-254 engines, high altitude versions of the RD-253 with an I_s of 328 s and a burn time of 225 s. The final fourth stage, with a gross mass of 33.5 tons, had an incomparable low structural index of 5.6 % and was propelled by one gas generator 11D423 engine from Izotov with a vacuum thrust level of 194 kN and 326 s of I_s (Fig. 2).

It is worth mentioning that Chelomei foresaw a change of the storable propellant combination to LOx/kerosene and a thrust level of almost 12,000 kN for a later design study, the UR-700M. Here a staged combustion cycle, using an oxygen-rich pre-burner and a four-chamber RLA-120 engine from Glushko, which one may consider as the origin of the RD-170 for the Buran booster, was planned.

2.3   Yangel's R-56

Yangel aimed at a payload capacity of 40 tons into a 200 km polar orbit, equivalent to 6 tons into GEO. Similar to Chelomei, Yangel too considered transport issues in the design of the launch vehicle. In his case this would be a waterway transportation from the manufacturing site to all Russian launch sites, Plesetsk, Kapustin Yar and Baikonur, and resulted in a monoblock design with the advantage that major design tools from the R-36 ICBM could be used. The final vehicle was a four-stage rocket with a length of 68 m, a gross lift-off mass of 1421 tons and, in order to accommodate all 16 RD-253 engines, a diameter of 6.5 m. Interestingly the engines of all three stages were using storable propellants (Fig. 3).

The first stage, R-56 Block A, was designed with a gross lift-off mass of 1162 tons and a structural index of 14 % and featured 16 of Glushko's RD-253 engines with a burn time of 120 s and a total sea level thrust of 23,593 kN. The second stage, R-56 Block B, had a total mass of 213 tons and a structural index of 5.6 % and featured one RD-254 with a vacuum thrust of 1716 kN, an I_s of 325 s and a burn time of 370 s. The third stage, R-56 Block O, had a gross mass of 32 tons and a structural index of 6.3 % and was propelled by one RD-0213 engine, with a vacuum thrust of 582 kN, an I_s of 326.5 s and a burn time of 190 s. The final fourth stage, R-56 Block K, had a gross mass of 9.4 tons and a structural index of 7.4 % and was propelled by one RD-280 with a thrust of 118 kN, an I_s of 350 s and a burn time of 350 s. This engine operated with an N_2O_4/Aerozine-50 propellant mixture.

Later in the space race to the moon and beyond, Yangel proposed larger versions of the R-56 which aimed at applying nine of Glushko's newly developed RD-270 engines.

Since almost all of the Russian launch vehicles of the time were driven by their military application, there are a considerable number of vehicles which were developed during the moon race and remained even after the failure of the concepts

Fig. 2 Sketch of the UR-700 vehicle © Mark Wade, http://www.astronautix.com/
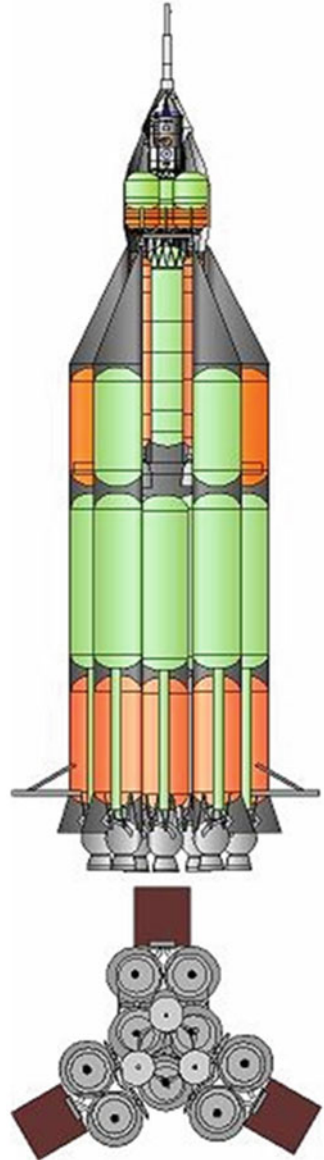
described previously. The most notable ones are the Soyuz (successor of R-7) and Proton (successor of UR-500) which in upgraded versions are still flying civil missions today. Military missiles which have been developed and manufactured in large numbers in this period were the SS-11 (UR-100) and derivatives and the SS-18 (R-36M).

Fig. 3 Model of the R-56
launch vehicle
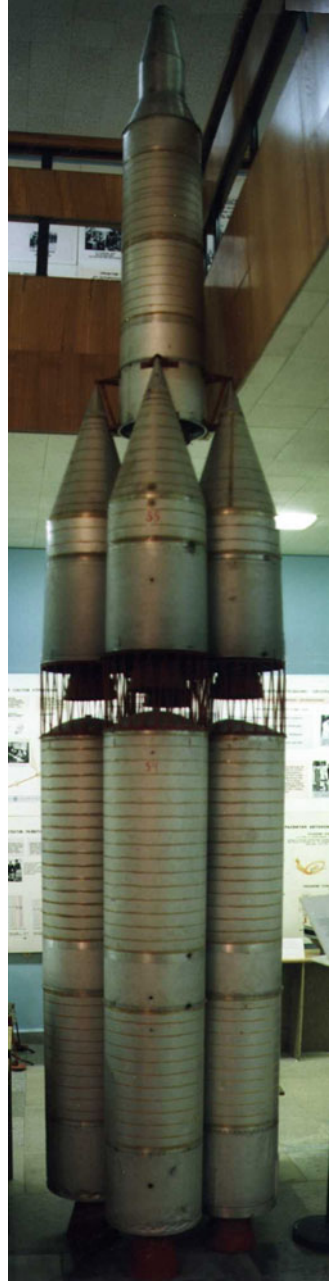
3   Energiya/Buran

With the R-56 and the UR-700 abandoned and the N1 cancelled after its failures, Russia had no launch vehicle able to lift in excess of 50 tons into a low Earth orbit. The military requested a man-rated launch vehicle which could send astronauts for satellite repair or capture, a plan designed to counter the usage of a military shuttle by the US Air Force. However Glushko was pushing for a new concept called RLA which in different studies had engines capable of generating a vacuum thrust of almost 1200 tons. This led to various heavy launch vehicle designs, among them the Energiya and the Vulkan with the latter having a gross lift-off mass of almost 4800 tons. Finally, the military insisted that a launch vehicle similar to the US shuttle should use cryogenic propellants, too. The final design of the Energiya launch vehicle consisted of one stage with four boosters, each carrying an RD-170 engine and a core stage with four RD-0120 engines. It is interesting to mention that a derivative of the RD-170 but equipped with a two-plane gimballing system, the RD-171, has been developed in parallel for the Zenit vehicle. Figure 4 provides a look at the aft of the Energiya/Buran assembly with four boosters each equipped with four-chamber RD-170 engines and the core stage with four RD-0120 engines.

4   Rocket Engines

In the course of the decades-long development of Russian liquid rocket engines, some generic technologies have been established, which are used in various engines. A considerable outcome of the internal competition between the different design bureaus was a number of rocket engines which were unprecedented at that time. Among them are Glushko's remarkable storable propellant full-flow staged combustion cycle engine RD-270 and the fuel-rich staged combustion cycle engine RD-253; the successor of the latter, the RD-276, still operates in the Proton-M launcher today. The first cryogenic staged combustion engines were Alexei M. Isayev's RD-56, which was sold to India and flew in a modified version on the GSLV, and Arkhip M. Lyulka's D-57. Both were supposed to fly on upper stages of the upgraded N-1 launcher. Furthermore Nikolai D. Kuznetsov's NK-33 engine, until recently, was foreseen to power in a tandem arrangement the Antares spacecraft. Additionally, due to their unique hydrogen peroxide-based gas generation, the RD-107 (see Fig. 5) designed by Glushko will be discussed here in more detail. All these engines were equipped with technologies which were developed and improved over time with ongoing experience. Examples of such generic technologies are given from the most important past engines or current operational engines.
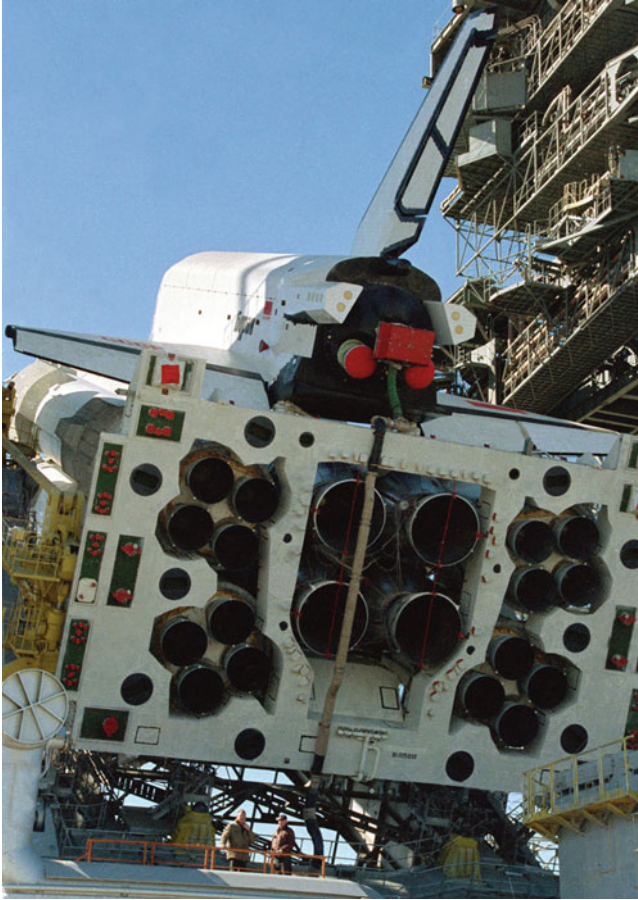
Fig. 4 View of the rear of Energiya/Buran with nozzles of RD-0120 (*centre*) and RD-170 engines

4.1 Engine System

Quite early the Russians established the closed staged combustion cycle for their engines in order to achieve high chamber pressures for high engine performance. The RD-107 and RD-108 engines of the R-7 and its successors are a considerable exception being open cycle engines since they were developed based on what was learned from the German A4 engine. For large high-thrust engines, the thrust was distributed to several chambers, fed by a common turbopump set for both propellants. This principle results also in a more compact dimension of the whole engine, using the wide diameter of the stage while keeping the height of the engine low, thus saving height and mass for the engine bay; this is even more important for intermediate stages to second and third stages. The resulting size of the chambers
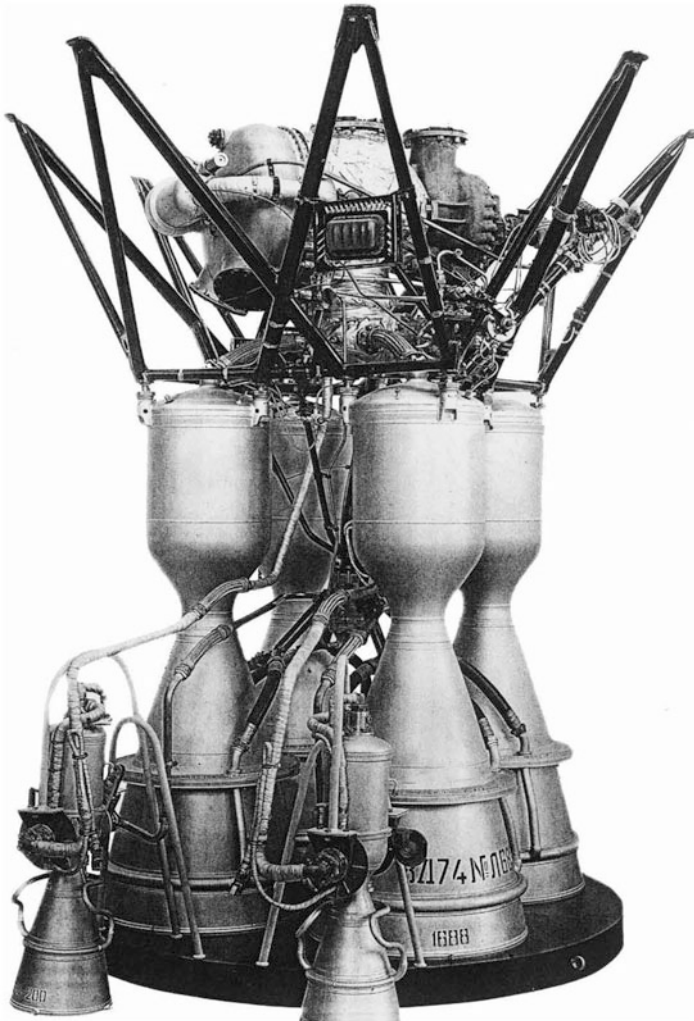
Fig. 5 RD-107 engine

was such that existing hardware from previous developments could be used as prototypes. The development risks could be limited by avoiding extrapolations of the available experience to a never-before tested larger size. The multiple chambers are all mounted with a gimbal, but mostly each chamber gimbals in only one plane. With all chambers together, full thrust vector control is obtained. The gimbal actuators are mostly driven by high-pressure fuel, tapped off downstream of the main pump.

The turbopumps for the propellants are usually mounted on a common shaft. While this imposes some restrictions in the choice of the optimum speed, it

automatically synchronises the two pumps which helps to control the start-up and shut-down transient operations. Pre-pumps are added to allow a low inlet pressure, and thus making lower tank pressures possible. These pre-pumps are often not rotational pumps but jet-pumps driven by high-pressure propellant from the main pump. Most engines have their own helium supply for valves operation and purging. Helium is also used for tank pressurisation after passing through a heat exchanger in the engine system.

One considerable exception from this multiple chamber approach was that of Kuznetsov who from the very beginning favoured single chamber designs even for high-pressure and high-thrust engines (see NK-9, NK-15, NK-19 and NK-33 engines), and the latter will be described in more detail since it was used on the Antares launcher (see Fig. 6). The NK-33 has a thrust of 1470 kN/1640 kN (sea level/vacuum) and was designed for a burn time of 300 s with a mixture ratio of 2.7.
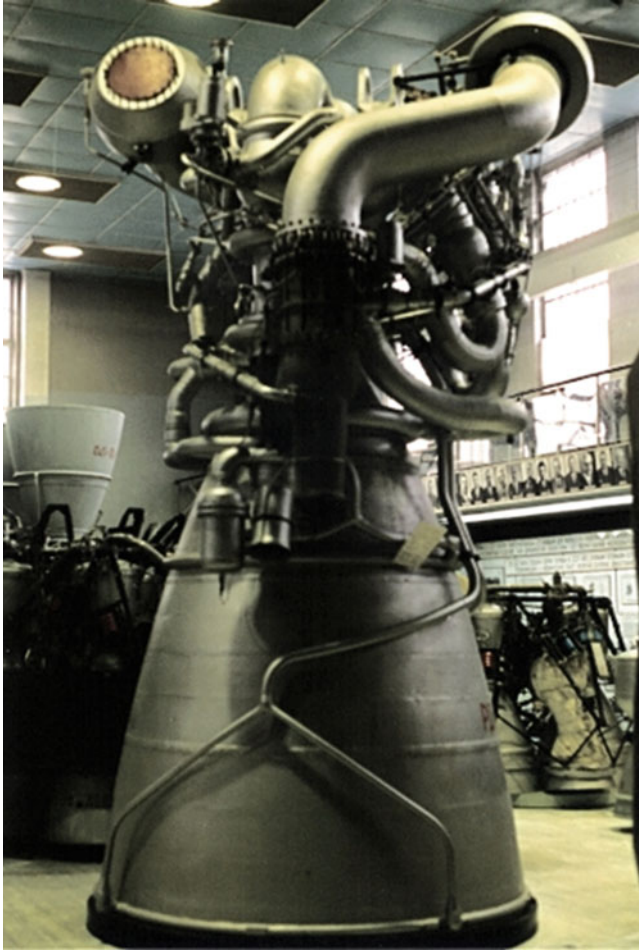
Fig. 6 NK-33 engine
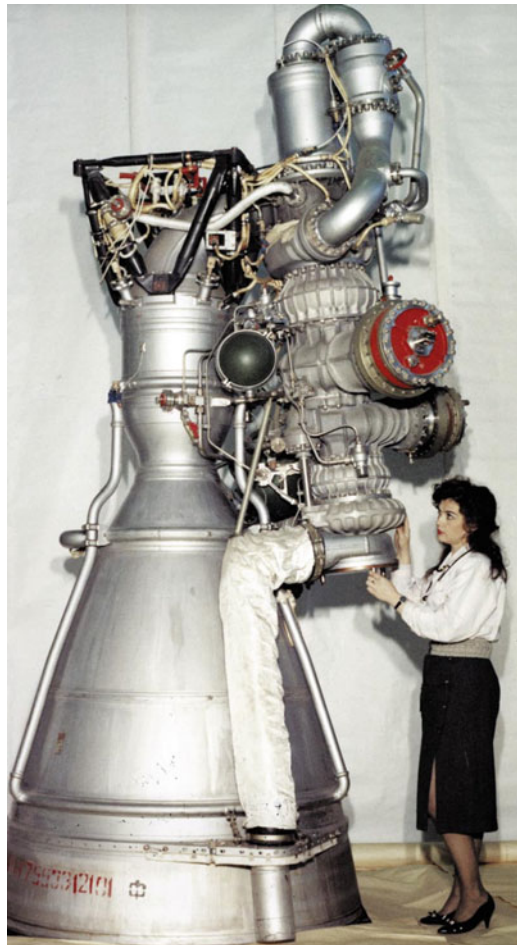
Fig. 7 Mock-up of RD-270 engine in the Energomash museum (© Haeseler)

The chamber pressure of 146 bar and the expansion ratio of 27 resulted in a sea level I_s of 297 s. The entire engine design was driven by the desire to increase as much as possible the thrust-to-weight ratio which resulted finally in a value of 1340 N/kg for the flight engine.

One masterpiece of Russian rocketry surely would have been the RD-270 shown in Fig. 7 although it never made into flight. This engine was operated with NTO and UDMH at a combustion chamber pressure of 261 bar, a mixture ratio of 2.67 which generated out of more than 2100 kg/s of propellant, a sea level thrust of 6275 kN and a vacuum thrust of 6710 kN. More than 20 engines have been built and 40 tests were performed, but until the end of the programme, not all problems could be solved and no test was fully successful. The extremely high combustion chamber pressure of 261 bar allowed for expansion ratios which enabled I_s levels of 301 s (sl) / 322 s (vac).

The currently operating masterpiece of Russian rocketry is the RD-170 LOx/kerosene engine (see Fig. 9). It employs four thrust chambers, fed by a common turbopump driven by oxidizer-rich pre-burner gases. The staged combustion cycle achieves a very high chamber pressure of about 245 bar in a compact engine system. The turbines are driven by two gas generators. The engine was designed for reusability of ten thermal cycles and has a throttling range down to 50 %. The engine is capable to generate a sea level thrust of 7251 kN and a vacuum thrust of 7903 kN, out of a total mass flow rate of 2390 kg/s. Each of the two pre-burner operates at a mixture ratio of 54.3 with a mass flow rate of 836 kg/s at a combustion pressure of 535 bar.

The Russian equivalent to the Space Shuttle Main Engine (SSME) is the cryogenic staged combustion engine of the Energiya core stage, the RD-0120 engine from Semen A. Kosberg's design bureau (see Fig. 8). This engine was able to generate a sea level thrust of 1547 kN (I_s 359 s) and 1961 kN (I_s 455 s), in vacuum, applying a chamber pressure of 218 bar and, to reach with a nozzle expansion ratio of 85.7, a thrust-to-weight ratio of almost 568 N/kg.

Fig. 8 Cryogenic high-pressure staged combustion engine RD-0120

4.2 Thrust Chamber Cooling

The thrust chamber of the RD-170 engine demonstrates the typical technologies used for Russian thrust chambers. The hot-gas wall is a copper-alloy wall for the subsonic and initial supersonic part, in regions with a high heat flux from the hot gas to the wall and coolant, while a steel alloy is used for the nozzle extension with lower heat flux. The outer liner closing the coolant channels is brazed onto the coolant channel fins. Manufacturing process developments have shown in destructive tests that a sufficient fraction of the total brazing surface obtains a firm connection. The manifolds are welded to the chamber body.

The cooling channels are milled into the copper and steel liners. For an optimisation of the coolant heating and resulting pressure to drop in the cooling channels, the coolant flow is split into different circuits for some chamber sections (see Fig. 9).

In case of very high heat flux but limited cooling capacity of the coolant, such as with kerosene, the regenerative cooling is supported by film cooling of the chamber wall with introduction of slots at up to three axial locations. Figure 10 shows the typical design for directing the regenerative coolant along the channel from one manufactured section (pos. 1) into the next one (pos. 3) via flow path 2. In addition the film cooling is split from the main coolant flow and injected into the chamber through small orifices [4].
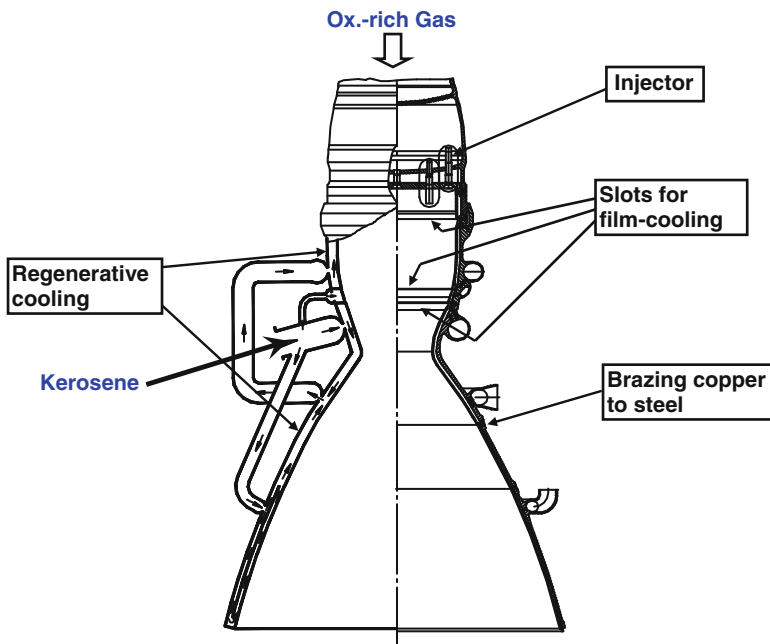

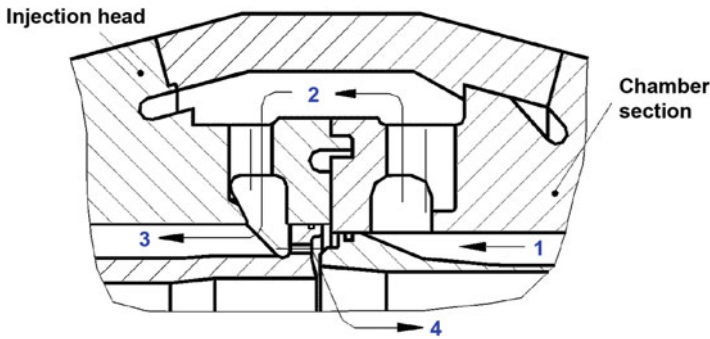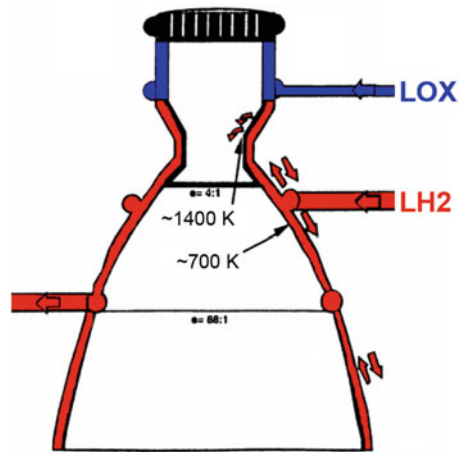**Fig. 9** RD-170 main chamber features [4]

Fig. 10 RD-170 main chamber film cooling inlet design [5]

Fig. 11 Schematic of RD-57 chamber coolants routing (Based on [6])

Further heat protection is usually provided by a thermal barrier layer composed of up to 1000 μm nickel and with up to 500 μm chromium on top.

The RD-57 combustion chamber cooling scheme is shown in Fig. 11. The chamber hot-gas wall is a copper alloy with integrally milled coolant channels closed by a brazed steel outer wall. Both propellants are used in the regenerative cooling; liquid oxygen cools the cylindrical chamber subsonic section, while the chamber throat and divergent supersonic sections are cooled by hydrogen. The chamber is protected in addition by a zirconium-oxide layer from the injector to the throat section up to an area ratio of 4:1; additionally the throat section is cooled by a hydrogen film cooling supplied at two locations upstream of the throat. This results in a wall temperature of about 1400 K on top of the thermal protection coating, while the unprotected copper wall sees a temperature of only about 700 K. This engine was developed in the 1970s, but never used on a Russian launcher.

A different approach has been followed during the development of the RD-107 engine. The coolant channels are inclined against the longitudinal axis of the
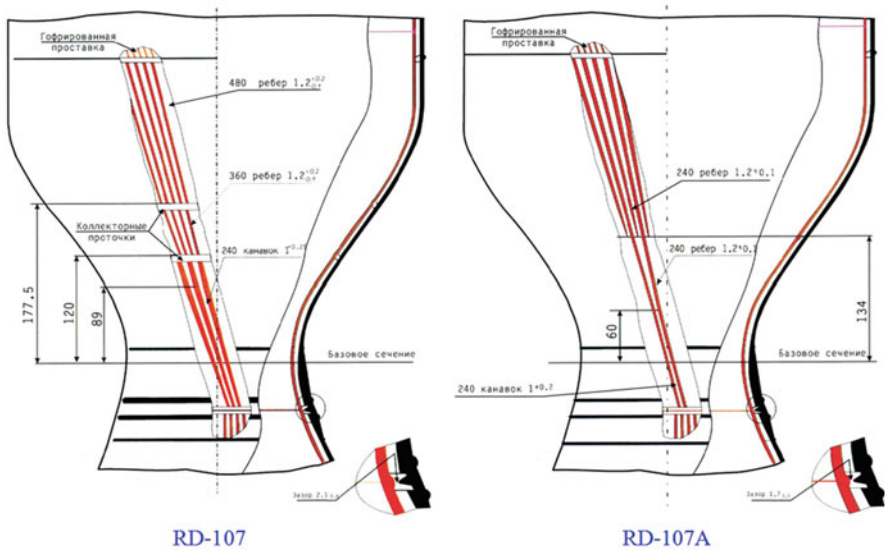
Гофрированная проставка

480 ребер 1.2

360 ребер 1.2

Коллекторные проточки

240 канавок 1

177,5

120

89

Базовое сечение

Зазор 2.1

RD-107

Гофрированная проставка

240 ребер 1.2*0.1

240 ребер 1.2*0.1

60

240 канавок 1*0.2

134

Базовое сечение

Зазор 1.7

RD-107A

Fig. 12 Coolant channel layout for the RD-107 and its improvement for RD-107A [7]

chamber to obtain an equalisation of circumferential variations of the heat flux; this avoids hot spots. This inclined orientation of the coolant channels is shown in Fig. 12 for the RD-107 engine (left). The number of the channels is changed at four axial positions with a circumferential groove. The coolant flows from the channels into that groove and is then redistributed to the next channel's sections. The homogeneous distribution to all channels is affected by the pressure drops in the channels. The optimised version RD-107A (right) has lesser channel changes, and no groove is needed since two neighbouring channels are joined by flaring the land between them to zero. The smaller channels lead to a higher flow velocity with better heat transfer characteristics.

The thrust chamber liner is classically made from a copper alloy, in the case of the RD-0120 chamber Cu-Cr-Zr-Ti, supplied with a Ni-Cr coating, while the actively cooled part of the nozzle is made from steel. The integrally machined coolant channels on the outside of the liners are closed with brazed outer walls. The hydrogen pressure in the cooling channels reaches 420 bar. Figure 13 shows a typical Russian design solution of this difficult interface between the combustion chamber and the nozzle realised by an example of the chamber RD-0120. An annular gap is provided between the outer walls of the thrust chamber and the nozzle extension in order to have access to the junction of the two inner liners for welding it. A ring split into two halves is then welded into the gap to close the coolant channels. The liner and walls may be locally enlarged in order to provide sufficient material strength for welding.

Fig. 13 Connection between chamber and nozzle as designed for, for example, the RD-0120
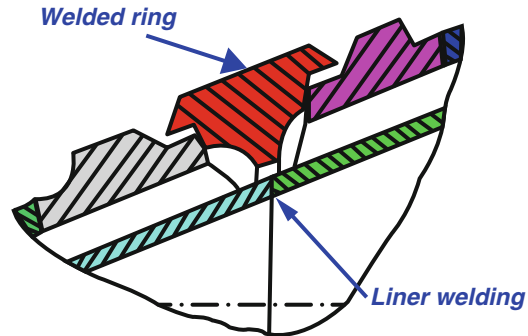
The RD-0146 is an expander cycle engine which has been developed to be applied as the upper stage for the Angara launch vehicle or as a replacement for the American RL-10 engine. This engine comes in two versions with 98 kN or 69 kN of vacuum thrust with specific impulse I_s of 463 s and 470 s, respectively. Both propellant lines are equipped with boost pumps in order to avoid cavitation issues and allow for the high combustion pressure of 80 bar. In order to increase the heat transfer in the Russian expander cycle engine RD-0146, longitudinal ribs are manufactured on the inner surface in the chamber; see section B-B in Fig. 14. These ribs are present in the cylindrical part of the chamber only. They increase the surface area for heat flux from hot gas to the coolant fluid. In addition, the inner surface of the cooling channel was artificially roughened for a further increase of the heat transfer to the coolant.

4.3 Injection

The injection head often contains several types of injection elements with propellant flow rates and mixture ratios differing by up to 10 %. This is done to spread the combustion zone and thus to have the energy release of the combustion less concentrated, which improves the combustion stability. In case of the LOx/kerosene RD-170 engine which operates with an oxygen-rich pre-burner, three groups of injection elements are present in the injector (refer to Fig. 15), plus a further variant for the elements near the chamber wall with reduced fuel flow, called injector trimming, to reduce the heat flux to the chamber wall.

Another feature of the injection head design aimed at an improvement of the margin against the onset of combustion instability is the additional baffle elements protruding into the combustion zone (for details see Figs. 16 and 17). The fuel in the annulus is flowing through channels in the double wall of each baffle element for cooling before entering the chamber.

The injection head of the NK-33 LOx/kerosene staged combustion engine, based on the NK-15 developed for the N1 launcher, features 183 coaxial injection elements

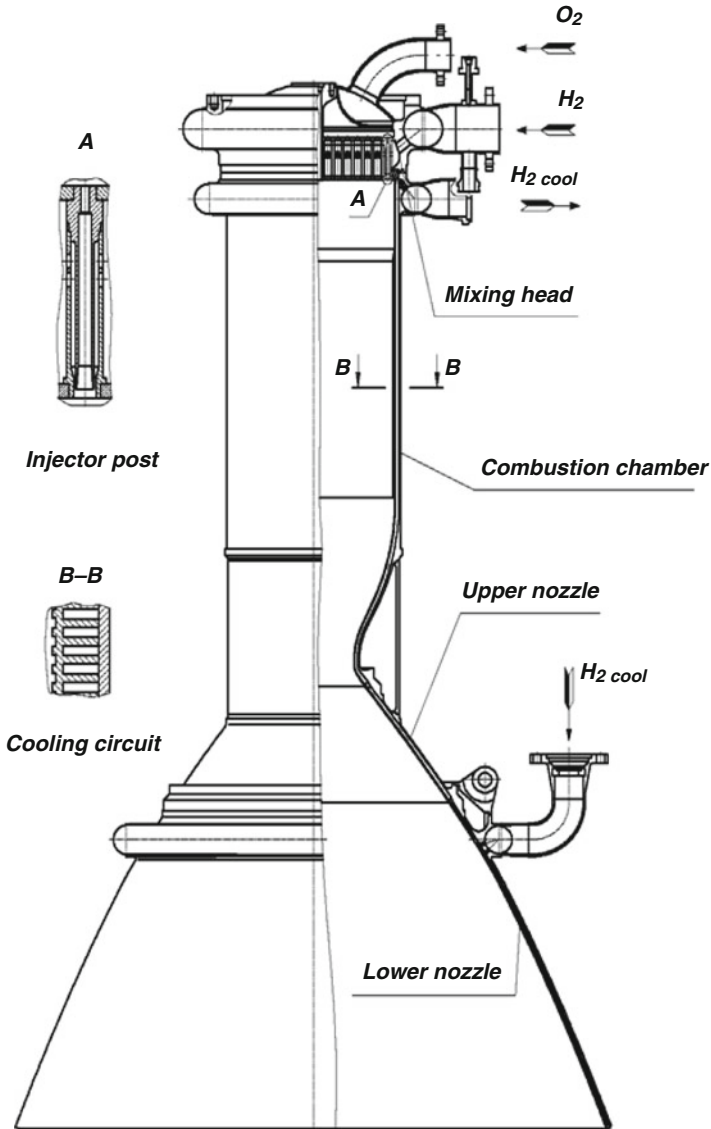**Fig. 14** Combustion chamber of the RD-0146 with a ribbed inner surface (detail B-B) [8]

with kerosene swirl (see Fig. 18). The chamber is not equipped with resonators nor cavities nor baffles to cope with combustion instabilities. Stable combustion is supported by the high temperature of the precombusted, ox-rich turbine exhaust gas of about 580 K. No instance of combustion instability occurred since the NK-15 development.
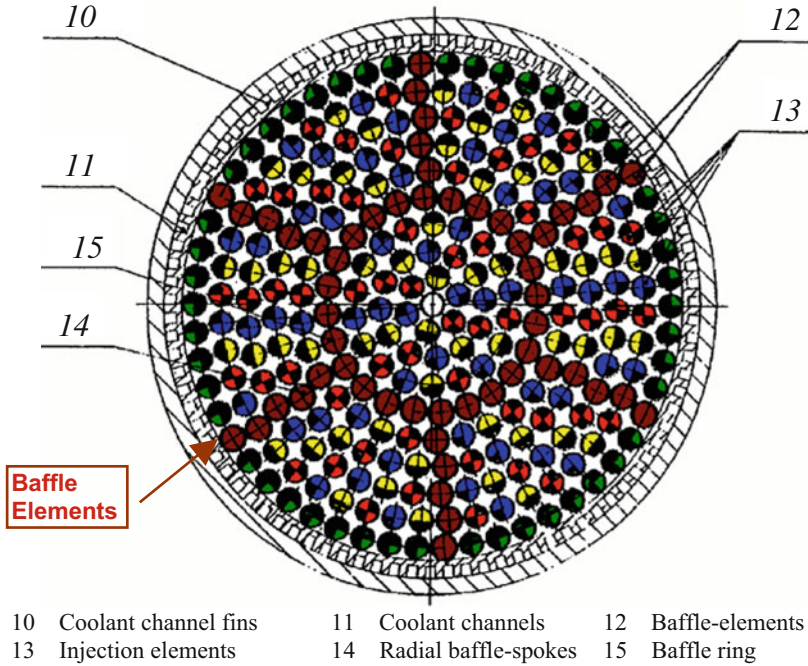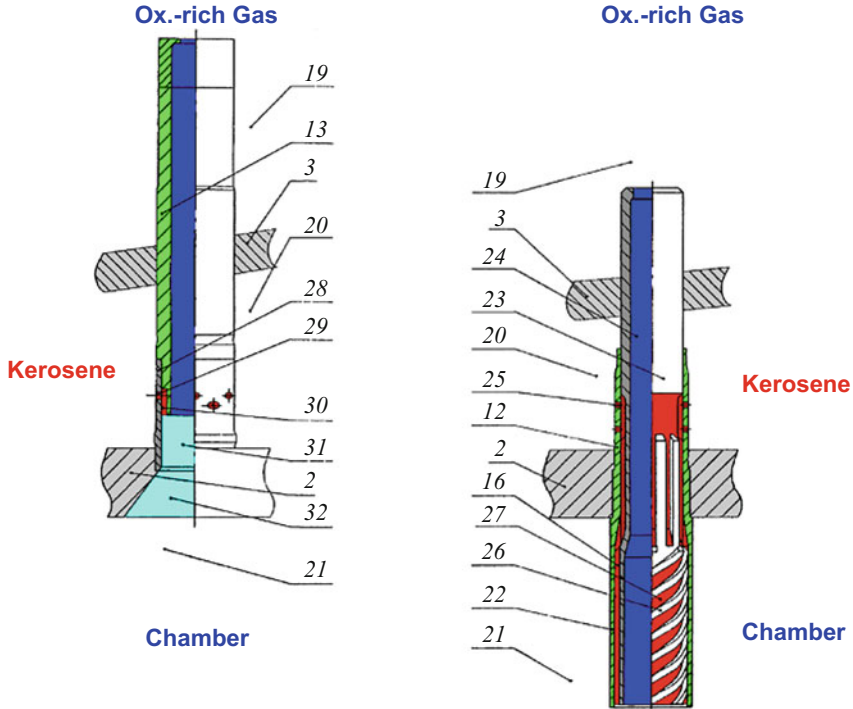
10   Coolant channel fins   11   Coolant channels   12   Baffle-elements
13   Injection elements   14   Radial baffle-spokes 15   Baffle ring

Fig. 15 Injection head pattern of RD-170 (Based on [9])

A cryogenic injection element of the cryogenic staged combustion upper stage engine RD-57 is shown in Fig. 19 where a total of 90 coaxial elements are used in the chamber. The injection head feeds the elements with hydrogen-rich exhaust gas from the turbine from the top and liquid oxygen from the interim volume. The liquid is fed tangentially into the LOx post centrally positioned in each element; this tangential injection creates a swirl flow typical for Russian engines. After many tests a displacer element was introduced into the centre of the LOx post to improve the stability margins of the chamber.

The injection head and an injection element of the cryogenic staged combustion booster engine RD-0120 are shown together in Fig. 20 where a total of 444 coaxial injection elements are used in the chamber. The resulting mass flow per element of this engine is just short of 1 kg/s while that of the SSME is just shy of 0.8 kg/s. The fuel-rich turbine gas is fed from the top to the elements. Liquid oxygen is fed into the top of three interim volumes and from there radially into the central post of each element, like with the D-57 elements. The coolant hydrogen enters the injection head in a volume between the faceplate and an interim plate. A small part of it cools the faceplate in a transpiration cooling way with 18,828 holes of 0.2 mm diameter each and through additional holes near the combustion chamber wall to build a film and reduce the near wall mixture ratio while the larger part flows upwards into the

Fig. 16 RD-170 injection elements, standard elements (*left*), baffle elements (*right*), ox-rich gas is shown in *blue*, kerosene is shown in *red*, and precombusted gas is shown in *light blue* (Based on [9])

2	Faceplate	3	Baseplate	12	Baffle element
13	Injection element	16	Sleeve	19	Ox.-rich gas
20	Kerosene	21	Chamber	22	Sleeve
23	Ox.-post	24	Ox.-gas flow	25	Kerosene entrance
26	Spiral ribs	27	Kerosene-channel	28	Kerosene sleeve
29	Tangential bore	30	Kerosene annulus	31	Element pre-mix zone
32	Faceplate taper				

central interim volume where it is mixed with the hydrogen-rich turbine exhaust gas. This mixture finally enters the annulus of the injection elements. The fine holes in the faceplate are produced by an electro-beam perforation process.

The mixture of the turbine gas with the liquid UDMH in the injection head of the engine RD-253 (used in Proton's first stage) is shown in Fig. 21. The gas comes from the top via a perforated flow distribution equaliser plate and flows straight through cylindrical elements into the main chamber. The liquid fuel UDMH is injected into the gas through a few lateral holes of each cylinder and mixes already in the element with the gas. Small fuel elements are positioned between the larger mixing elements.

Fig. 17 Baffle arrangement inside an RD-170 chamber
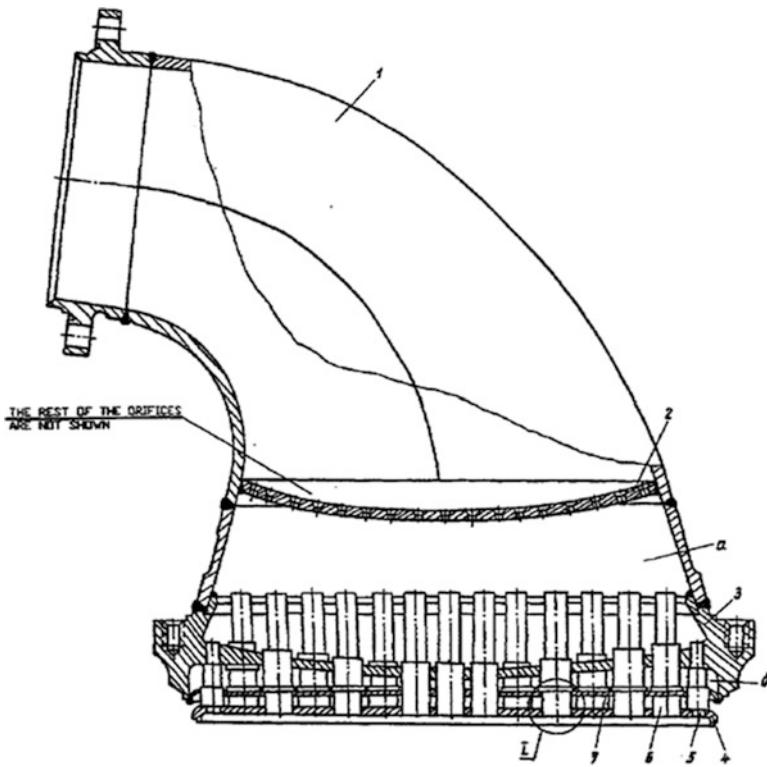
Fig. 18 NK-33 injector head [10]
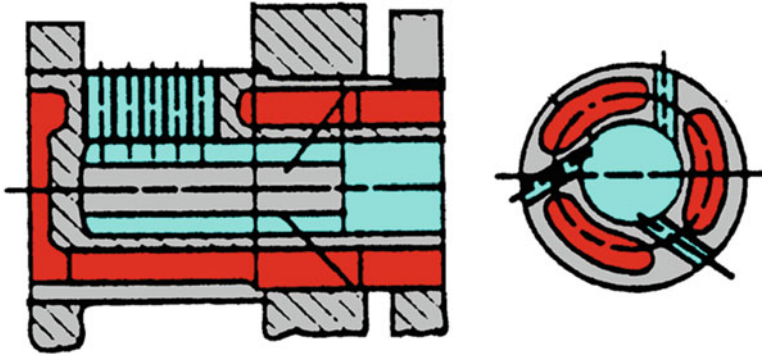
Fig. 19 RD-57 LOx/LH2 injection element [11]
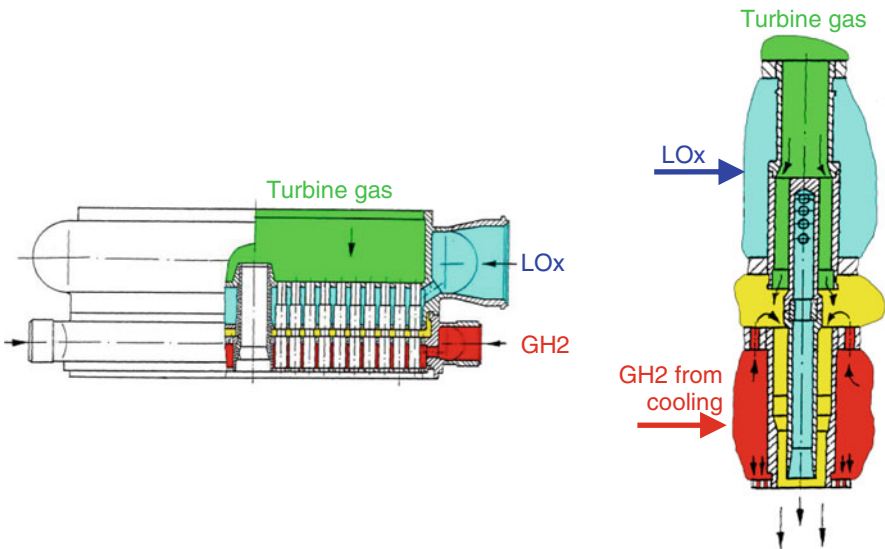
Fig. 20 RD-0120 injection head (*left*) and injection element (*right*), liquid oxygen is shown in blue, turbine gas is shown in *green*, hydrogen is shown in *red*, and mixture of gas and hydrogen is shown in *yellow* (Based on description of the prototype engine 11D122)

4.4 Ignition

Rocket engine ignition is a very complex process where absolute reliability and exact timing are of utmost importance. Furthermore, depending on the engine cycle, i.e. expander, gas generator or staged combustion cycle, the engine start-up sequence necessitates exactly timed ignitions of the main combustion chamber as well as of gas generators or pre-burners.

Fig. 21 RD-253 injection head (*left*) and injection element (*right*), turbine gas is shown in *blue*, fuel UDMH is shown in *red* (© Haeseler)

The ignition of the propellants in Russian LOx/kerosene engines is often accomplished with a hypergolic fluid which is stored under pressure in closed ampoules with bursting discs in the fuel flow path in order to supply the fluid to the combustion chamber in due time. These discs rupture by the pressure coming from fuel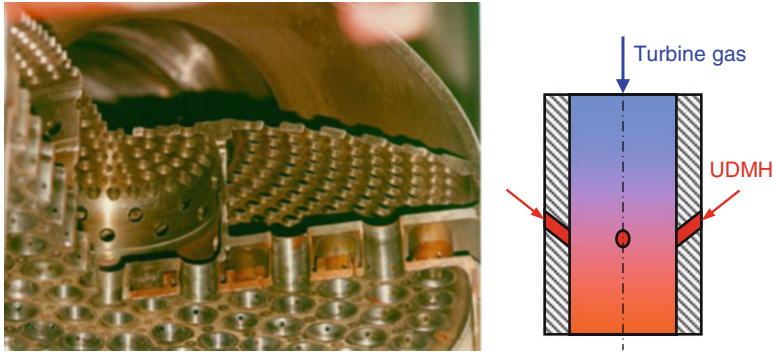 out of dedicated start tanks. The hypergolic fluid applied is usually a mixture—quite often 50/50 of triethyl-aluminium (TEA) and triethyl-borane (TEB)—which decomposes instantaneously when it gets into contact with air, oxygen or even water. This technique is used within the RD-170 rocket engine family including the RD-180 and RD-191 and the RD-120, as well as for the RD-107A/108A upgraded engines. A specific feature of the NK-33 is the application of the TEA/TEB mixture to ignite the pre-burner while classical solid pyrotechnical charges [3] ignite the main chamber. The main chamber igniters and the solid propellant charges for the turbopump starter cartridge are ignited by simple squib initiators.

Some of the older LOx/kerosene engines such as RD-107 and RD-108 were using pyrotechnical ignition systems, but the RD-107A and RD-108A engines on the current Soyuz ST have been modified towards a hypergolic ignition system [12]. All necessary component and qualification tests have been performed for an implementation of the hypergolic ignition systems for these engines, which is now in use also for launches of Soyuz from Kourou.

The cryogenic staged combustion engine RD-0120 used in the Energiya core stage and the newly developed reignitable cryogenic RD-0146 apply electric ignition systems. However, a laser-based ignition system is currently under development for the RD-0146 according to KBKhA.

4.5 Gas Generators

A typical Russian gas generator is shown in Fig. 22 from engine RD-170. A large flow of oxygen is combusted with a tiny amount of kerosene at very high pressure. Consequently, the propellants are provided at even higher pressure; this high pressure is best contained in a spherical vessel. The wall of the combustion zone is cooled by a small part of the liquid oxygen, which is injected into the hot gas at the end of the exit flange towards the turbine.
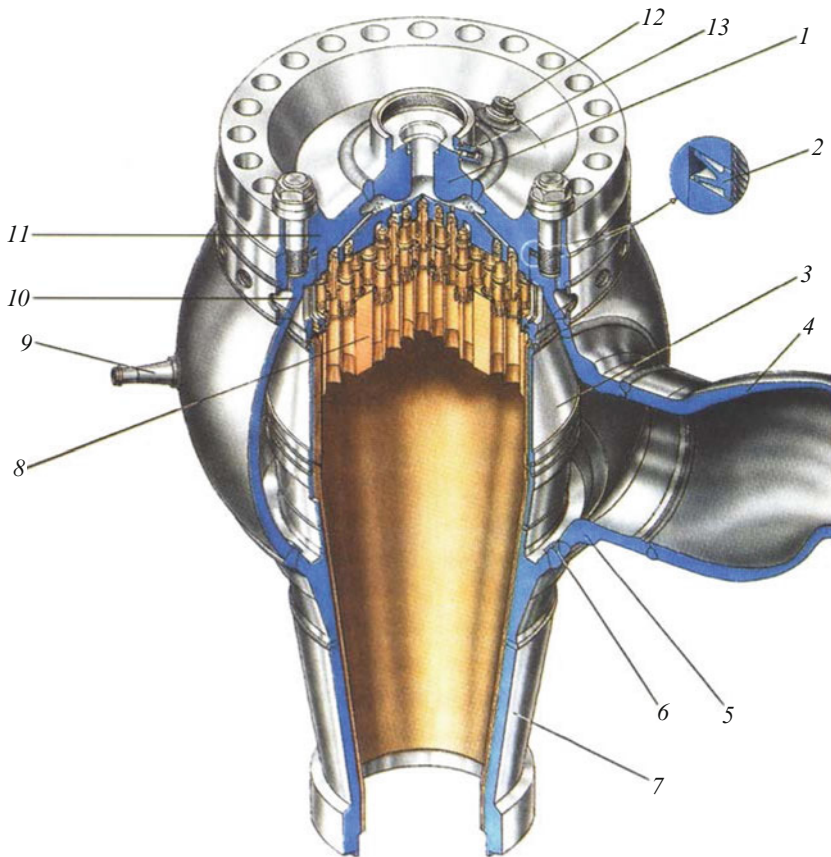
1	Fuel inlet	2	Seal	3	Chamber wall
4	Oxygen inlet	5	Interface	6	Spherical manifold
7	Turbine feed line	8	Face plate	9	Sensor connector
10	Ring	11	Body	12	Sensor connector
13	Sensor connector				

Fig. 22 Ox-rich gas generator of RD-170 engine [13]

1 Basebody   2 Kerosene metering orifices   3 Faceplate
4 Second mixing zone   5 LOx cavity   6 LOx post
7 Kerosene cavity   8 Kerosene flow path   9 Tangential holes for kerosene
10 LOx annulus   11 Tangential holes for oxygen 12 First mixing zone
13 Longitudinal grooves for LOx   14 Tapered flowpath into the gas generator
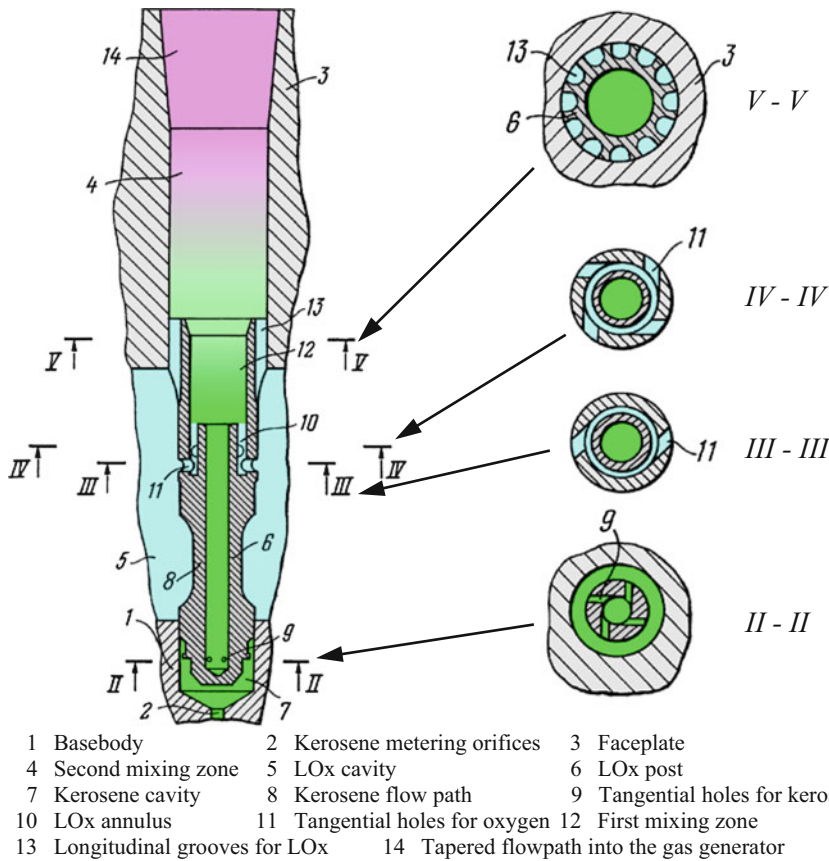
Fig. 23 Ox-rich injection element of the gas generator of RD-170 engine (Based on [14])

Since it is difficult to achieve a reliable ignition and combustion at very high mixture ratios of 30 and higher, the injection elements provide for a two-staged combustion (see Fig. 23). The complete but small kerosene mass flow rate enters the injector elements (8) through metering orifices (7) via tangential holes (7) which create a swirling flow. About 25 % of the oxygen enters an annulus (10) via tangential holes (11). Both flows are then mixed and combusted in a first zone (12) at temperatures above 2000 °C. Practically all remaining oxygen (except the small flow which cools the chamber wall) is added via axial grooves (13) which are situated between the element (6) and the faceplate (3), to the gas from the first zone (12). Both fluids are mixed in the second zone, which cools down the gas to a temperature of about 500 °C. This design assures a reliable ignition and initial combustion at sufficiently high combustion temperature while creating a gas with a temperature acceptably low for the turbine.

Fig. 24 Gas generator of
NK-33 engine (© Haeseler)

The complete propellant thus reacts inside the mixing zone of each injector separately, which prevents the energy of the complete propellant from being released commonly in one volume, thus improving the stability of the gas generator by limiting self-oscillating processes.

Another genuine method for dilution of the remaining part of the propellant into the hot gas from the initial combustion in the gas generator was developed for the NK-33 engine. The pre-burner operates at a combustion chamber pressure of 320 bar with a mass flow rate of 366 kg/s and a mixture ratio of 58.2 and generates hot gases at a temperature of 630 K to drive the turbine. The entire kerosene mass flow enters from the inlet at the right side as shown in Fig. 24 and is completely injected via a number of fuel injectors. A smaller part of the oxygen mass flow is distributed to a number of oxidizer injectors which are located between the fuel injectors in the gas generator injection plate. The main part of the oxygen is directed into a central distributor with 24 lateral fingers. Each of these fingers has some holes on the side pointing upstream towards the primary injectors. The oxygen is sprayed into the hot gas coming from the primary combustion zone for a homogeneous distribution and dilution into that main hot gas flow, resulting in a combusted gas at homogeneous moderate temperature acceptable for the turbine blade material. Finally, another small portion of the oxygen is flowing from the injector through the double wall of the gas generator to provide for sufficient cooling of the device and is then mixed with the main pre-burner gas at the end of the cylindrical section prior to the entrance into the turbine.

4.6   Turbopumps

As already mentioned previously, almost all Russian engines feature excellent turbopumps (TP) which have very specific features. Older engines such as the RD-253 were using ejector pumps to raise the suction pressure. This is necessary to avoid cavitation at the entrance into the fast turning main pumps; the speed of them is given by the optimisation of their effectivity for the huge pressure raise. Nowadays inducers and boost pumps are implemented instead. Gear boxes are used rather seldom. There is a worldwide unique feature in the cryogenic RD-0120, a two-stage oxygen boost pump having two concentric shafts, and in the LOx/kerosene engine NK-33 with two concentric shafts for the main pump (see below). Main data for several Russian turbopumps are given in Table 1.

The propellant's four-chamber RD-107 engine is fed by a TP arrangement which uses a single turbine driven by catalytically decomposed hydrogen peroxide. This two-stage turbine has a single shaft to drive both the kerosene and the oxygen pumps; two small pumps are connected additionally through a gear box in order to bring the hydrogen peroxide and liquid nitrogen up to the desired pressure level. The liquid nitrogen is pumped through the heat exchanger built into the turbine exhaust gas assembly to be vaporised so that it can be used to pressurise the main propellant tanks. The hydrogen peroxide is fed to the catalyst. To use catalytically decomposed hydrogen peroxide as a third propellant for the turbine drive, this technology stems from the Peenemünde developments, which were studied in detail and rebuilt by Russian engineers after 1945. With a concentration of only 82 %, the peroxide handling is rather safe.

The NK-33 TP arrangement (see Fig. 25) consists of a main shaft for the main turbine and the high-pressure kerosene and LOx pumps, plus two coaxial units, one for the low-pressure kerosene pump driven by a gear box from the main shaft and one for the low-pressure LOx-pump, which rotates around the main shaft and is driven by a hydraulic stage implemented into the high-pressure pump between its inducer and centrifugal stage. Both main pumps are centrifugal. The fuel boost pump is gear driven by the main fuel pump. The shafts of the centrifugal oxygen and fuel pumps are mechanically connected by a spline which allows for certain axial movement. A start turbine operated for a couple of seconds by the exhaust gas of a solid charge initiates the rotation of the two main pumps. Figure 26 shows the schematic of this TP with some operational data.

The highest operational power level of a TP is that of the staged combustion LOx/kerosene RD-170 with almost 190 MW. Such an increase was possible only due to new bearings which were capable of withstanding higher loads at a very high speed. Since propellant density and mixture ratio are not too different, the pumps can be on the same shaft with only a minor loss in performance.

The RD-180 flow schematic is shown in Fig. 27 (two-chamber version of RD-170 with the same TP routing). The entire RD-170 turbopump assembly, shown in Fig. 28, has a single stage axial flow turbine sitting on the same shaft with the main

Table 1 Operational data of selected turbopumps for Russian gas generator cycle rocket engine (Ref. 16–23 and others)

Engine	Year of development	Thrust (s-l/vac) [t]	Propellants	TP mass (dry/wet) [kg]	Power [MW]	Rotation speed [rpm]	Turbine gas temperature [K]	Ox. pressure [bar]	Fuel pressure [bar]	Gas flow rate [kg/s]
Gas generator cycle engines										
RD-100	1946–1950	26/31	LOx – ethanol	155/188	0.40	3900	653	20	23	2.2
RD-101	1947–1951	37/41	LOx – ethanol	155/188	0.74	5000	773	25	34	3.2
RD-103	1952–1955	44/50	LOx – ethanol	155/190	1.10	5450	783	34	40	3.65
RD-107	1954–1959	83/102	LOx – kerosene	237/270	3.82	8300	833	78	92.7	8.8
RD-111	1959–1962	144/166	LOx – kerosene	414.6/490	8.46	8500	1073	112	135	16.6
RD-213	1956–1957	70/76.4	AK27I – TM-185	182/214	2.16	8000	793	65	75.7	5.8
RD-214	1955–1959	64.8/74.5	AK27I – TM-185	185/218	1.88	8000	783	59	73	5
RD-216 (2 TP)	1958–1960	151.7/177.4	AK27I – UDMH	187/215	3.31	9300	1103	88	104	5.25
RD-218 (3 TP)	1958–1961	226/266	AK27I – UDMH	192/221	3.27	9300	1103	88	104	5.26
RD-251 (3 TP)	1962–1966	241/270	N_2O_4 – UDMH	188.5/215	3.99	9900	1143	98	133	6.65
RD-0110	1963–1964	–/30.4	LOx – kerosene			18,400	1050	98.1	143.2	3.97
RD-861 K	2006–	–/7.9	N_2O_4 – UDMH		0.69	34,000	1153	141	147	

Table 1 (continued)

Engine	Year of development	Thrust (s-l/vac) [t]	Propellants	TP mass (dry/wet) [kg]	Power [MW]	Rotation speed [rpm]	Turbine gas temperature [K]	Ox. pressure [bar]	Fuel pressure [bar]	Gas flow rate [kg/s]
Closed cycle engines (staged combustion cycle and expander cycle)										
RD-253	1962–1966	150/166	N₂O₄ – UDMH	32 /364	19.10	13,850	793	276.4	245.9	401.2
RD-270 (2 TP)	1962–1969	640/685	N₂O₄ – UDMH	1,58 /1955	142.6	14,500/17,000[a]	723/1043[a]	509.9	454.0	1500 / 410[a]
RD-120	1976–1986	–/85	LOx – kerosene	247.5/–	12.94	19,230	735	339.8	350.7	176.6
RD-170	1976–1988	740/806	LOx – kerosene	1706/1891	189.3	13,870	773	602.1	506.0	1757.8
RD-180	1994–1999	390/424	LOx – kerosene	950/–	103.5	16,811	785	606.6	575.2	911.6
RD-191	1999–2003	196/213	LOx – kerosene	420/–	50.06	22,810	829	585,3	564.3	462.2
RD-0124	1994–1995	–/30.0	LOx – kerosene	50	4.48	39,000	727	332.8	365.6/426.6	59.85
RD-0120	1976–1988	156/200	LOx – LH2	680	69.5	33,185	840	304 / 535	448	80.2
RD-56 (KVD-1)	1965–1976	–/7.1	LOx – LH2			42,000				
D-57	1960–1975	–/40	LOx – LH2	117	7.09	36,000	795	~250	~170	~18.1
RD-0146	Since 1999	–/10	LOx – LH2	–/16.5[a]		123,000/38,000[a]			265	
NK-33	1968–1974	154/172	LOx – kerosene		25.4	17,435	628	377.6	307	376

s-l/vac sea level/vacuum, *dry/wet* empty TP/filled TP, *AK27I* nitric acid 73 % with dinitrogen tetroxide 27 % + additive iodine, *TM-185* hydrocarbon fuel kerosene/gasoline mixture, *UDMH* unsymmetric dimethylhydrazine
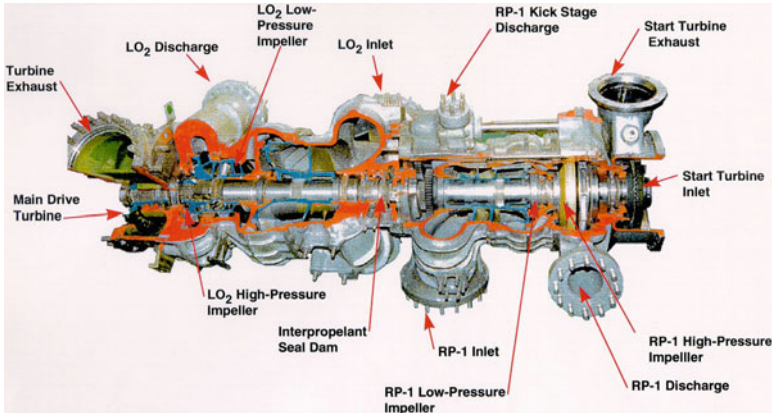
[a] Ox-TP/fuel-TP

Fig. 25 Nk-33 turbopump [10]
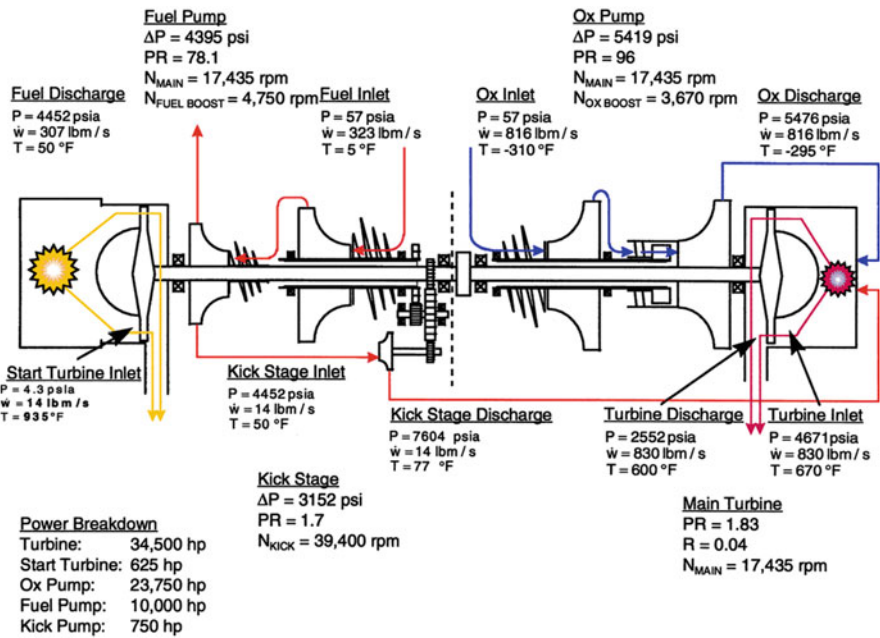
Fig. 26 NK-33 turbopump schematic [10]

oxygen and kerosene pumps. Additionally, a small kerosene pump is mounted on the same shaft which feeds the high-pressure oxygen-rich pre-burner.

Fuel and oxidizer supply lines are equipped with boost pumps, and while the oxygen pump is driven by a small portion of the turbine exhaust after it has passed the heat exchanger where it vaporises a small amount of liquid oxygen needed for tank pressurisation, the kerosene boost pump is driven by a small amount of high-
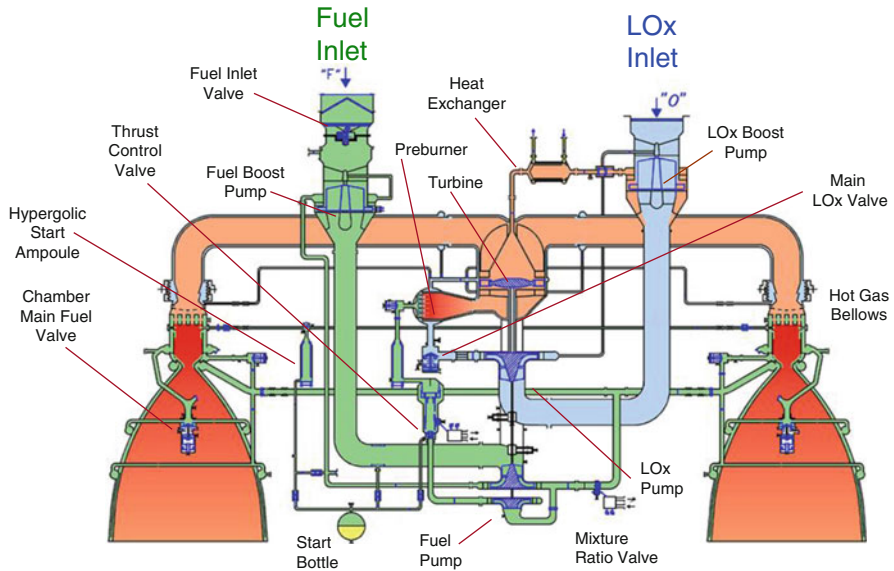
Fig. 27 RD-180 flow routing schematic (Energomash)
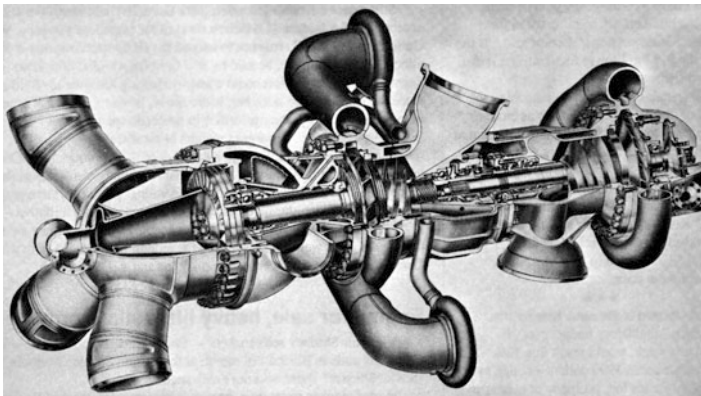
Fig. 28 View into the RD-170 turbopump

pressure fuel tapped off from the self-contained hydraulic system of the engine which operates with high-pressure kerosene.

The TP package of the RD-0120 engine is rather unique. A schematic of the flow routing is shown in Fig. 29. A single pre-burner feeds a two-stage turbine which drives the main three-stage hydrogen pump, the main oxygen pump and additional high-pressure oxygen pump which are all centrifugal ones. The output of this additional pump is split into two parts: one drives the turbine of the oxygen boost pump and its output is fed into the low-pressure oxygen flow, while the other

Fig. 29 Flow schematic of RD-0120 [15]

Fig. 30 Dual-shaft LOx
boost pump of RD-0120 [15]
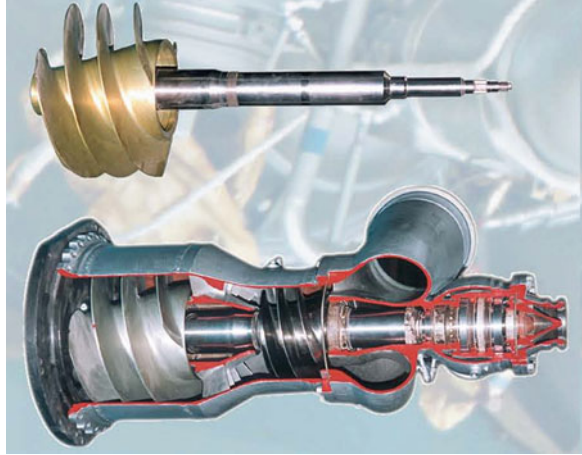
Fig. 31 RD-0120, main turbopump [15]

part goes to the fuel-rich pre-burner. This twin-spool boost pump (see Fig. 30) has
a specific feature, and it has two concentric shafts: one inside the other, which are
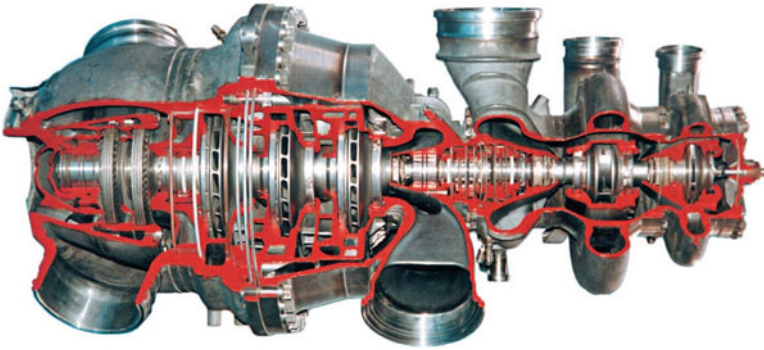able to drive the two pump impellers at different rotational speeds. The advantage of
this arrangement is that the pressure rise in the lower speed pump part reduces size
and weight of the second stage and obviously allows for a reduced rotational speed
of the main oxygen pump.

The cryogenic hydrogen from the tank goes through a single stage boost pump
which is driven by a single stage turbine fed with warm hydrogen gas from the
exhaust of the main chamber cooling channels; this turbine exhaust is then fed into
the injectors of the main combustion chamber. The hydrogen leaving the fuel boost
pump is fed to a three-stage centrifugal pump which turns at supercritical speed
(about 32,500 rpm), for the pump (see Fig. 31) and for its rotor and impellers (see
Fig. 32). The high-pressure output is split into two parts. The main portion goes to

Fig. 32 RD-0120 rotor and impellers [15]

the high-pressure fuel-rich pre-burner and the smaller part is used to cool first the main combustion chamber and then the nozzle prior to driving the fuel boost pump and being injected into the main chamber.

References

1. Isakovitz SJ, Hopkins JB, Hopkins JP (2004) International reference guide to space launch systems, 4th Edition, ISBN 1-56347-591-X, American Institute for Aeronautics an Astronautics, Reston, VA, USA
2. Moshkin Ye K (1973) Development of Russian rocket engine technology, NASA TT F-15408, translation of Razvitiye Otechestennogo Raketnogo Dvigatelestroyeniya. Mashinostroyeniye Press, Moscow
3. Lardier C, Barensky S (2013) The soyuz launch vehicle: the two lives of an engineering triumph. Springer Verlag, New York. ISBN 978-1-4614-5458-8
4. Chelkis F (2003) LOx kerosene oxygen-rich staged combustion rocket engine design and life issues. In: The 5th international symposium on liquid space propulsion, Chattanooga, USA
5. Chelkis F, The chamber cooling system of RD-170 engine family: design, parameters, and hardware investigation data, AIAA-2006-4363
6. Andreyev A, Chepkin V, Fanciullo T, Investigation of oxygen/hydrogen combustion stability in staged combustion rocket engine, AIAA-94
7. Ganin AA, Kamensky SD, Katorgin BI, Fatuev IY, Chvanov VK (2003) Process stability increase and power characteristics of liquid jet engine RD-107, RD-108 by a new injector head; Вестник СамГУ Естественнонаучная серия. Второй спец. Выпуск, pp 209–219. (in Russian)
8. Dukina NA, Lobov SD, Orlov VA, Rachuk VS, Rubinsky VR, Design and development of advanced combustion chamber for the RD-0146 expander cycle engine. In: 4th international conference on launcher technology "Space Launcher Liquid Propulsion"
9. Patent RU2158841C2 Liquid propellant thrust chamber and its casing
10. NK-33 staged combustion cycle oxygen/kerosene engine, Aerojet, AIAA Professional Development Course 1998
11. Andreyev A, Chepkin V, Fanciullo T, The development of the D-57 advance staged combustion engine for upper stages, AIAA-94
12. Fatuev IY, Ganin AA, New propellant ignition system in LV "Soyuz" rocket engine chambers, 55th international astronautical congress 2004, IAC-04-S.2.06
13. Dobrovolski MV (2005) Liquid-propellant rocket engines. Bauman MSTU, Moscow. (in Russian)
14. Patent RU2159349C1 Gas generator module
15. ЖРД РД-0120 (11Д122) http://www.lpre.de/kbkha/RD-0120/index.htm, 2014
16. Hulka J, Forde JS, Werling RE, Anisimov VS, Kozlov VA, Kositin IP (1998) Modification and verification testing of a Russian, NK-33 rocket engine for reusable and restartable applications, AIAA-98-3361, Cleveland, American Institute for Aeronautics an Astronautics, Reston, VA, USA

17. Sutton GP (2003) History of liquid-propellant rocket engines in Russia, formerly the Soviet Union. J Propuls Power 19(6):978–1007
18. KBKhA web information, http://www.kbkha.ru/?lang=ru, 2015
19. Иванов ВК, Кашкаров АМ, Ромасенко ЕН, Толстиков ЛА., *Турбонасосные агрегаты ЖРД конструкции НПО Энергомаш*, in *Конверсия в машиностроении* – 2006. № 1
20. Demyanenko Y, Dmitrenko A, Ivanov A, Pershin V, Turbopumps for gas generator and staged combustion cycle rocket engines, AIAA 2005-3946
21. Дмитренко АИ, Иванов АВ, Кравченко АГ, Момотов ВИ, Савин АА, Глебов ВА, *Разработка турбонасосных агрегатов для современных кислородно-керосиновых двигателей с дожиганием окислительного генераторного газа*, Международный научный журнал «Космонавтика» № 1-2/2012
22. Bouley SA, Grabowski Jr. RC, Rachuk VS, Dmitrenko AI, Ivanov AV, Unified low-risk single-shaft turbopump, AIAA 2010-7130
23. Demyanenko Y, Dmitrenko A, Rachuk V, Shostak A, Minick A, Bracken R, Buser M, Single-shaft turbopumps in liquid rocket engines, AIAA 2006-4377

The Status of the Research and Development of LNG Rocket Engines in Japan

Hiroya Asakawa, Hideaki Nanri, Kenji Aoki, Isao Kubota, Hatsuo Mori, Yasuhiro Ishikawa, Kenichi Kimoto, Shinji Ishihara, and Shinichiro Ishizaki

Abstract This chapter reports the status of research and development which have been carried out to realize a liquefied natural gas (LNG) rocket engine with higher performance in Japan. As a fuel of rocket engine, LNG has better characteristics, i.e., longer storage, lower cost, and nontoxic; hence, LNG rocket engines have been investigated among many countries. However, LNG rocket engines have never been used for actual flight application in Japan, even in the world. The reason is that the performance and characteristics of the current LNG rocket engines do not have enough advantages compared with other liquid rocket engines. For example, if it would apply to a future reusable liquid rocket booster, the specific impulse (I_s) of LNG rocket engine should be higher than 360 s in order to get more advantages than other liquid rocket engines. The I_s of the current LNG rocket engines in Japan is between 310 and 350 s, falling short of the target level of 360 s. Therefore, continuous research and development have been conducted for the purpose of extending the advantages and promoting the practical use of LNG rocket engines in Japan.

1 Japanese LNG Engines

The research and development of LNG engines have been carried out in Japan, and several engines have been designed, manufactured, and tested. Figure 1 shows the history of development of LNG engines in Japan.

A 100 kN-class LNG rocket engine, named LE-8, had been developed by Japan Aerospace Exploration Agency (JAXA) and IHI Aerospace Co., Ltd. (IA) till 2009 as the second stage engine of GX rocket and successfully completed more than

H. Asakawa (✉) • H. Nanri • K. Aoki • I. Kubota
Japan Aerospace Exploration Agency (JAXA), Tsukuba 305-8505, Japan
e-mail: hiroya_asakawa@ihi.co.jp

H. Mori • Y. Ishikawa • K. Kimoto
Space Development Department, IHI Corporation, Nishitama 190-1297, Japan

S. Ishihara • S. Ishizaki
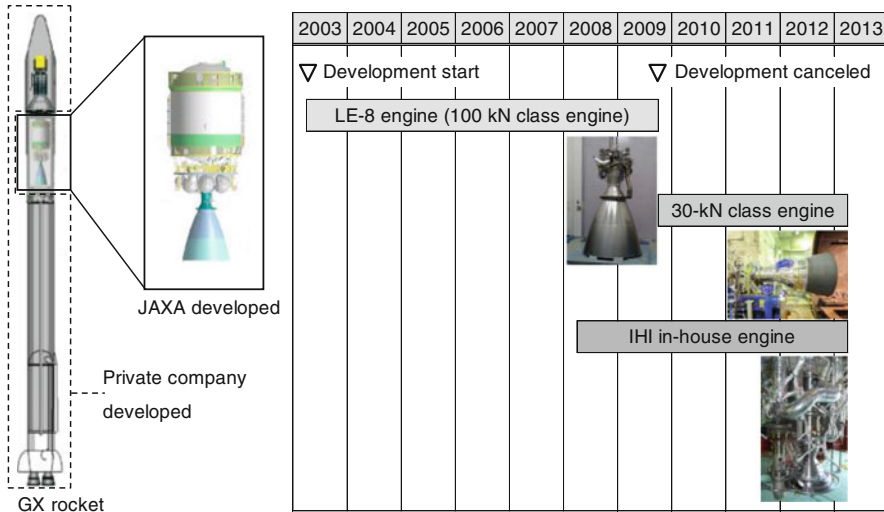Space Systems Department, IHI AEROSPACE Co., Ltd., Tomioka 370-2398, Japan

Fig. 1 History of the development on LNG engines in Japan

2000 s of its firing tests. Through the development of LE-8, the knowledge for the design of LNG rocket engines was accumulated, and the feasibility of LNG rocket engines was confirmed.

Although almost all the technical issues of LE-8 engine had been checked and solved during the development period, the performance of LNG engine was not confirmed under a flight condition, i.e., vacuum condition. After the development of LE-8, JAXA and IA started a research of LNG engine for the purpose of obtaining performance data with a high altitude test stand (HATS). The thrust level was selected to 30 kN for an experimental engine in the research because a 30 kN-class engine was considered useful for various future spacecrafts, and its small size engine was suitable for the HATS. Five firing tests with a total of 122 s were carried out, and the functions and performance of the engine were confirmed under a high altitude condition.

The LE-8 and the 30 kN-class engine consist of an ablative chamber and a liquid-liquid impinging type injector, making the engine system simpler and reducing the cost. Although the value of I_s has increased as a result of the improvement on the design of chamber and injector, it seems to have reached close to the upper limit. Aimed at improving the combustion efficiency drastically, another LNG engine which has a regenerative cooling chamber was designed and demonstrated in a ground test facility in parallel with the HATS test. The activity had been carried out by IHI Corporation (IHI) as in-house research program. The test series of the engine was successfully completed and its I_s reached to approximately 350 s.

Table 1 shows the specifications of existing Japanese LNG engines. The outline of each engine is described in the following sections.

Table 1 Specifications of Japanese LNG engines [1–5]

	LE-8 engine	30 kN-class engine	IHI in-house engine
Thrust (vacuum) (kN)	107	30	98.0
I_s (vacuum) (s)	314	335	354
Combustion chamber pressure (Pc) (MPa)	1.2	1.2	5.2
Mixture ratio (thrust chamber)	3.2	3.0	3.5
Chamber cooling	Ablative	Ablative	Regenerative
Nozzle expansion ratio	42	49	150

1.1 LE-8 Engine (100 kN-Class Engine)

The 100 kN-class LNG rocket engine, named LE-8 [1], was developed for the second stage engine of GX rocket from 2003 to 2009 [6]. The engine had about 600 s life time and completed life cycle firing tests without any trouble. The engine was checked for other functions and performance, reaching more than 2200 s of the accumulated firing duration. The vacuum specific impulse (I_s) was estimated 314–316 s based on the test results, achieving the requirements of the rocket system.

1.1.1 Engine Specification

The LE-8 engine featured gas generator (GG) cycle and an ablative-cooled thrust chamber. Figure 2a shows the engine system schematic diagram, and Table 2 shows the engine specification. The engine has two turbopumps and turbine exhaust gas flow into the nozzle extension for the thrust gain. Both igniters for the thrust chamber and the gas generator operated with oxygen and methane gases. The photographic view of the engine fabrication is shown in Fig. 2b.

1.1.2 Component Design

Like-on-like impinging elements were applied to a main injector operating with liquid/liquid propellants. The injector had baffles, which were cooled by the convective flow of propellant, to suppress combustion instability caused by acoustic
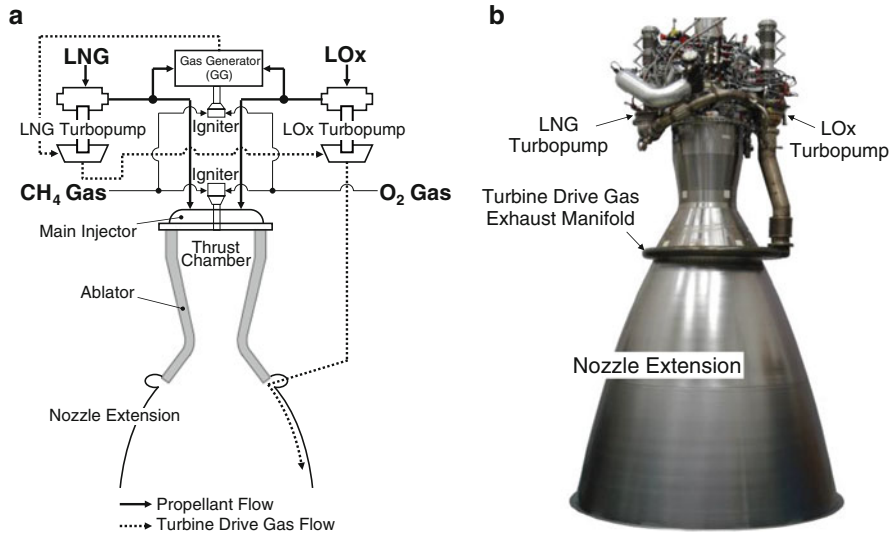
Fig. 2 (**a**) LE-8 engine system schematic diagram, (**b**) LE-8 engine fabrication

Table 2 LE-8 engine specification

Specification	
Propellant	LOx/LNG
Cycle	GG cycle
Thrust (vacuum) (kN)	107
I_s (vacuum) (s)	314
Mixture ratio (thrust chamber)	3.2
Pc (MPa)	1.2
Nozzle expansion ratio	42
Chamber cooling	Ablative

resonance as shown in Fig. 3. The injector also supplies 3 % of fuel for chamber wall film cooling. The thrust chamber consisted of silica fiber-reinforced resin and a metal jacket. A gas generator also operated with liquid/liquid propellants, and like-on-like impinging elements were adopted in the same manner as the main injector. In order to enhance the propellant mixing, a turbulence ring was installed in the GG chamber as shown in Fig. 4. The LE-8 engine had liquid oxygen (LOx) and LNG turbopumps, which were modified from LE-5B engine's LOx and liquid hydrogen (LH2) turbopumps [7], respectively. The film cooling effect of turbine exhaust gas enabled the nozzle extension to be made of cobalt-base alloy L-605 [8] instead of expensive refractory materials such as niobium (columbium).
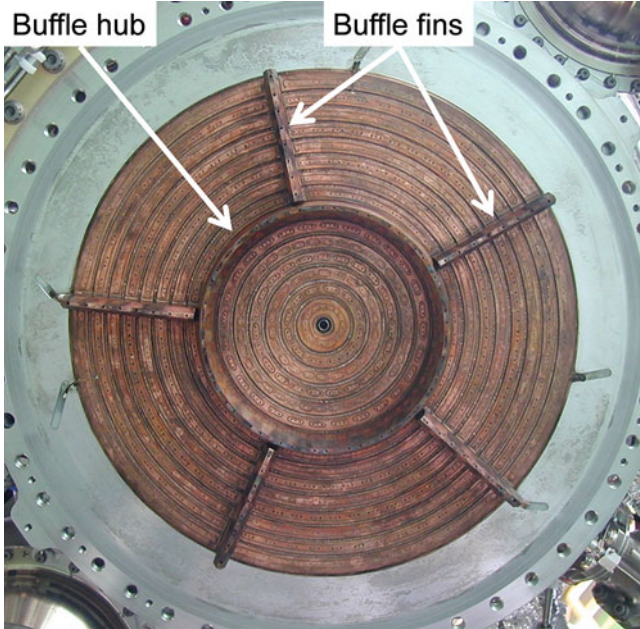
Fig. 3 Photo of the main injector surface of LE-8 engine which was taken after two times firing tests

Fig. 4 Schematic view of GG structure
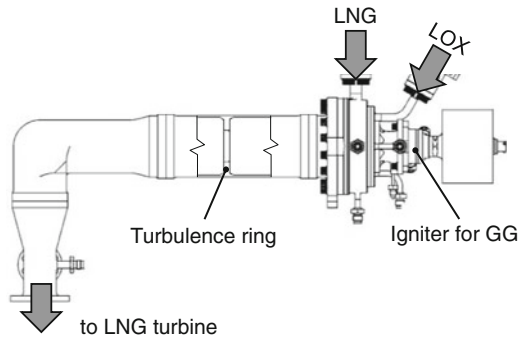
1.1.2.1 Firing Test Results

Firing tests were conducted in summer 2009. Photographic views of the engine setting and firing are shown in Figs. 5 and 6. Since the tests were conducted under sea level condition, the nozzle extension was replaced by a short nozzle of which expansion ratio was eight. In addition, the short nozzle extension was
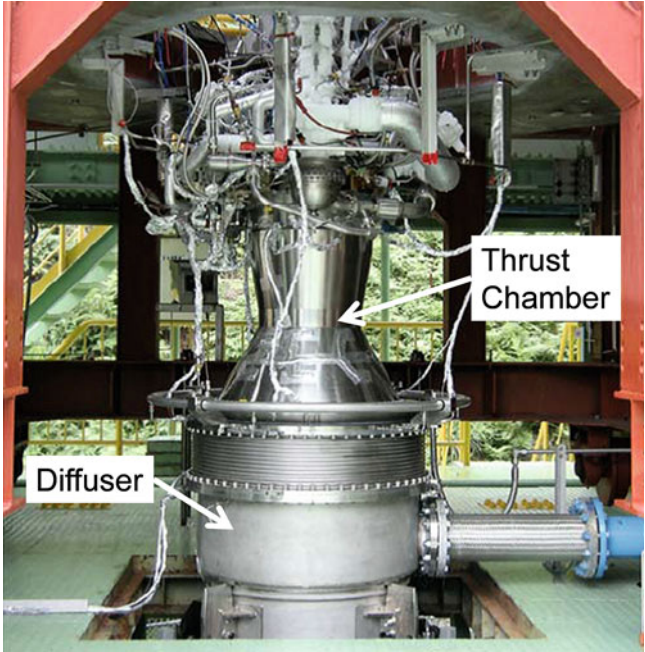
Fig. 5 Photo of engine setting connected to diffuser

Fig. 6 Photo of engine firing test of LE-8 at Aioi test facility

Table 3 Summary of firing test results

Test#	Pc (MPa)	MR^a (O/F)	Duration (s)	Remarks
001	0.68	3.136	5	Engine ignition test#1
002	1.20	2.916	60	Short-duration firing test#1
003	1.20	2.968	500	Full-duration firing #1
004	0.15	–	2	Engine ignition test#2
005	1.23	3.033	60	Short-duration firing test#2
006	1.24	3.086	500	Full-duration firing #2 at high Pc and high MR
007	1.23	2.990	600	Over full-duration firing
008	1.18	3.062	120	At low Pc and high MR
009	1.24	2.845	120	At high Pc and low MR
010	1.15	2.797	120	At low Pc and low MR
011	1.22	2.987	120	Duplicate 007 test configuration and condition

^{a}Thrust chamber mixture ratio

Fig. 7 Typical time history of combustion pressure of LE-8 engine (test# 003)
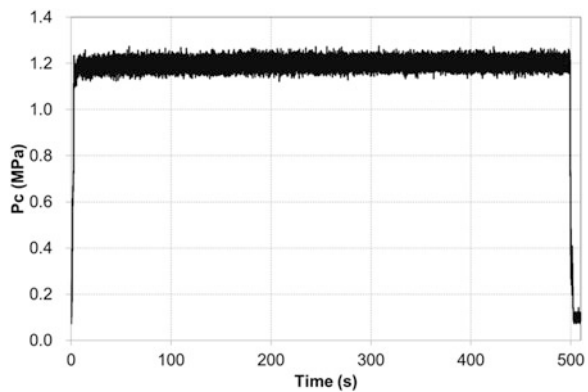
joined with a diffuser to depressurize nozzle ambient pressure. The firing test results are summarized in Table 3. The number of firings was 11 including two full-duration and one over full-duration tests. In order to obtain the ablator char depth data after each long-duration firing, four chambers were prepared for this test series.

Accumulated firing time reached 2207 s. Typical time history of combustion pressure is presented in Fig. 7. The combustion pressure was very stable in every full-duration firing. The LE-8 engine was disassembled and inspected after the test series, and each engine component was confirmed to be in good shape.

1.2 30 kN-Class Engine

Although almost all the technical issues of LE-8 engine had been checked and solved during the development, the performance of LE-8 engine had never been demonstrated under a high altitude condition. In addition, the performance (I_s) of LE-8 engine was not so high compared to the other LNG engines. Even after the cancelation of LE-8 program, we then continued the research for the purpose of increasing I_s and obtaining the data in a high altitude test stand (HATS).

Thirty kilonewton was selected for a thrust level of the experimental engine because the thrust level of LE-8 engine was too big for the other future spacecrafts. 30 kN-class engine was evaluated to be proper for the usage of various missions, and in addition, the smaller size was suitable for the HATS. We carried out five firing tests and validated the functions and performance under a high altitude condition [3, 4]. The I_s of the engine was found to be 335 s, obtaining the better performance than that of LE-8 engine.
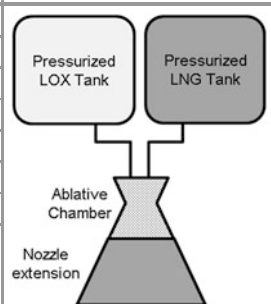
1.2.1 Engine Specification

The engine featured a tank pressure fed system and an ablative cooling thrust chamber. Table 4 shows the engine specification and the engine system schematic diagram.

1.2.2 Component Design

To achieve higher combustion performance, we had researched to improve the injector orifice design based on the technology of LE-8. Figure 8 shows the comparison of injectors of LE-8 and the 30 kN-class engine. The baffles against tangential and radial acoustic oscillations were removed to reduce the amount of

Table 4 The 30 kN-class engine specification

Specification		
Propellant	LOx/LNG	
Fed system	Tank fed	
Thrust (vacuum) (kN)	30	
I_s (vacuum) (s)	335	
Mixture ratio	3.0	
Pc (MPa)	1.2	
Nozzle expansion ratio	49	
Chamber cooling	Ablative	
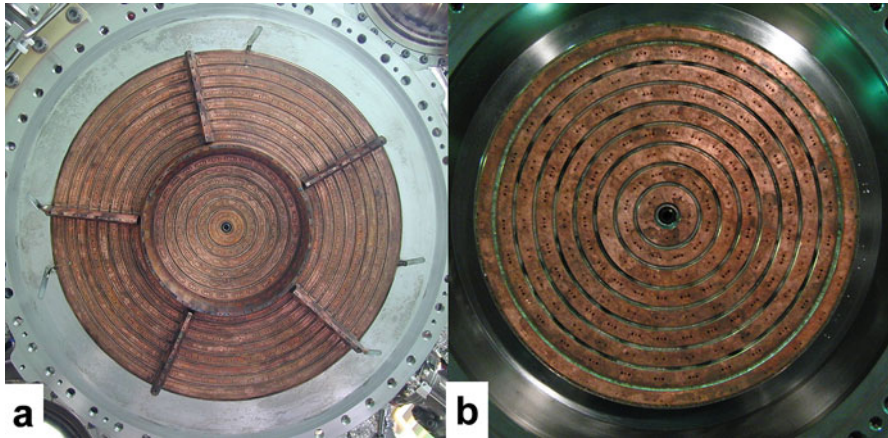
Fig. 8 Comparison of LE-8 and the 30 kN-class engine injectors. (**a**) Injector surface of LE-8 (after two times firing tests). (**b**) Injector surface of the 30 kN-class engine (after 14 times preliminary firing tests)

ineffectual propellant for the device cooling. As a result, more amount of propellant was fed to combustion chamber and could increase the combustion performance. In addition, element orifice geometry and orientation were modified to make mixing better than the former injector. Fine mixture should cause good combustion efficiency. Instead of the baffles, acoustic cavities were used as a combustion stabilization device.

An ablative cooling type was applied for the combustion chamber of the engine. And to obtain the value of the heat flux to chamber wall, water cooling chamber was used for the firing test. The upstream part of the nozzle extension was made of steel which had enough thickness to withstand severe heat condition. The downstream part was made of cobalt-base alloy L-605. The expansion ratio is 49:1, and the nozzle contour shape was designed as a truncated perfect nozzle.

1.2.3 Firing Test Results

Firing tests of the 30 kN-class LOx/LNG engine were conducted at the HATS, in the Kakuda Space Center (KSPC) of JAXA. The number of firings was five including two high altitude tests and the accumulated run time was 122 s. The summary of the test results is shown in Table 5, the photographic views of the sea level test and the high altitude test are shown in Figs. 9 and 10, respectively.

Figure 11 shows time history of combustion pressure (Pc) of the high altitude firing test (test number 5). The engine operated stably for the entire duration of firings. Characteristic exhaust velocity efficiencies were estimated to be between 95

Table 5 Summary of test results

No.	#1	#2	#3	#4	#5
Pc (MPa)	Ignition test	1.2	1.0	1.0	1.0
MR (O/F)	–	3.04	2.96	2.99	2.93
$\eta_C^{*(\%)}$	–	95.2	95.4	95.3	96.1
I_s (s)	–	234	234	335	335
Duration (s)	1.0	10.0	25.0	30.0	55.7
Nozzle expansion ratio (−)	1.6	1.6	1.6	49	49
Chamber type	Water cooling	Water cooling	Water cooling	Ablative	Ablative
Test condition	Sea level	Sea level	Sea level	High altitude	High altitude

Fig. 9 Photo of the sea level firing test at JAXA KSPC
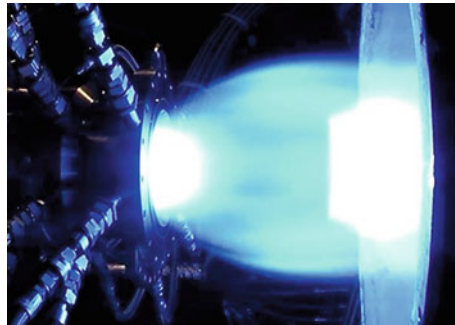
Fig. 10 Photo of the high altitude firing tests at JAXA KSPC

Fig. 11 Typical time history of combustion pressure of the 30 kN-class engine
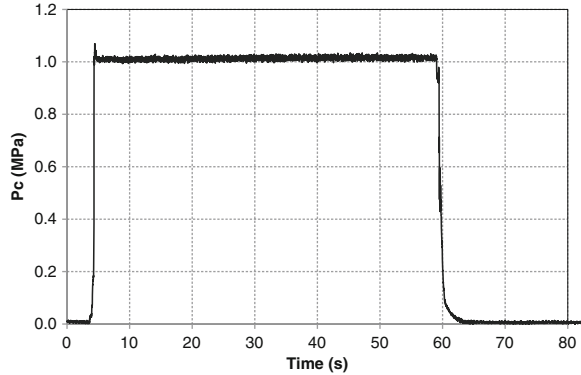
and 96 %. The average vacuum specific impulse (I_s) was 335 s. The 30 kN-class engine was improved markedly in the combustion performance from the 100 kN-class engine, LE-8.

1.3 100 kN-Class Regenerative Cooling Engine (IHI In-House Engine)

An ablative cooling chamber can reduce the production cost and the manufacturing lead time because the design is simpler than that of a regenerative cooling chamber. That was the reason why we adopted the design to LE-8 engine and the 30 kN-class engine though the design of injector was limited to a liquid-liquid impinging type which had lower combustion efficiency than a gas-liquid coaxial type. We had taken many efforts to increase the performance of ablative cooling chamber with LE-8 and the 30 kN-class engine, but it seemed facing the upper limit of efficiency.

In order to improve the combustion efficiency drastically, we changed the design of chamber from an ablative cooling type to a regenerative cooling one and adopted a gas-liquid coaxial injector. The new injector and chamber were designed for a 100 kN-class engine, and the assembled engine was developed from 2008 to 2013 [4, 5]. We carried out analyses and tests on the regenerative cooling engine and finally confirmed the feasibility of the design through 27 times with total 1650 s of firing tests. The I_s of the engine was estimated to be 356 s.

1.3.1 Engine Specification

The 100 kN-class engine consisted of a regenerative cooling chamber, an injector, turbopumps, a gas generator, propellant valves, and igniters. Figure 12 shows engine system diagram and Table 6 shows the engine specification.
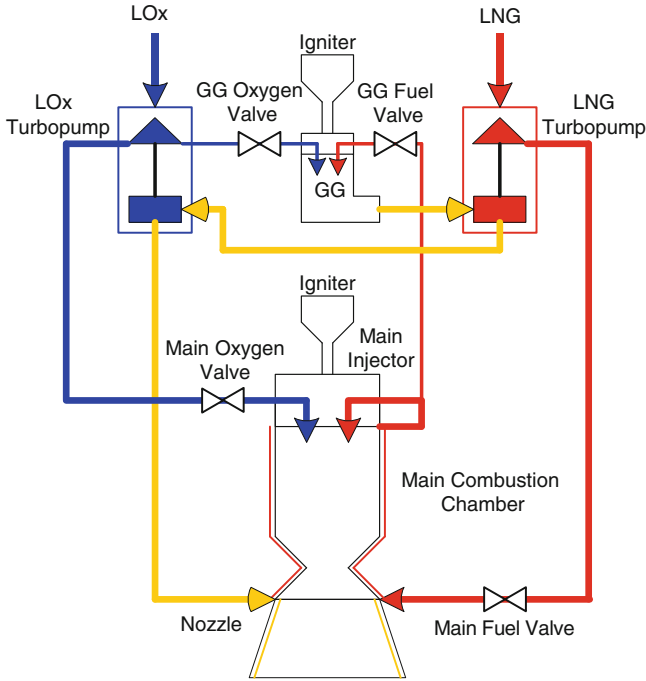
Fig. 12 Engine system schematic diagram

Table 6 Engine specification

Specification	
Propellant	LOx/LNG
Cycle	GG cycle
Thrust (vacuum) (kN)	98.0
I_s (vacuum) (s)	356.1
Mixture ratio (thrust chamber)	3.5
Pc (MPa)	5.2
Nozzle expansion ratio	150
Restart	Capable
Chamber cooling	Regenerative

1.3.2 Component Design

The injector was equipped with coaxial elements. The element's final design was fixed with results of preliminary single element firing tests [9]. The injector had acoustic cavities for combustion stabilizing device and was also prepared to install baffles in case of unexpected combustion instability.

Figure 13 shows the combustion chamber of the engine. The chamber consisted of a Cr-Zr copper alloy inner liner and a nickel electroformed outer shell [10]. The

Fig. 13 Schematic view of
the combustion chamber of
the engine

Outer shell :
Nickel electroforming

Coolant channels

Inner liner :
Cr-Zr Copper Alloy
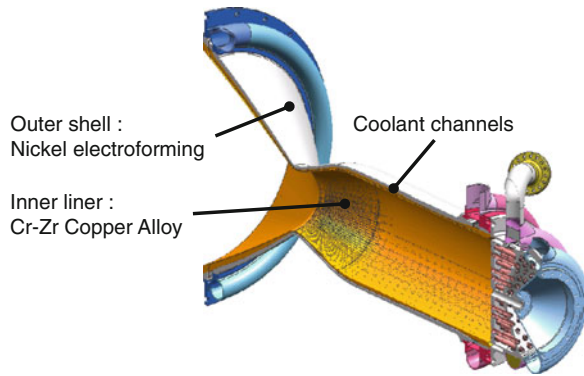
distance from the throat plane to the injector face is about 530 mm, which is longer than the case of typical LOx/LH2 engine chamber. This length of cooling passage is required to obtain proper temperature rise of CH_4 fuel, to realize stabilized combustion with high efficiency.

Oxygen turbopump (OTP) and fuel turbopump (FTP) were installed in the engine. The pumps underwent only small modification from existing pumps which are LE-5B engine's LOx and liquid hydrogen (LH2) turbopumps [7], respectively. It largely saved the development cost and time of the engine. GG injector was designed in step with the main injector. To reduce the development risk, GG injector elements were adopted coaxial type and which were designed based on the data obtained from the preliminary single element firing test.

1.3.3 Firing Test Results

After the completion of component-level testing, a demonstrator engine was assembled using developed units of engine components. Demonstrator engine firing tests were performed to obtain the system's characteristics and engineering data for flight unit design. Three series of engine tests was completed.

In the first series of tests in December 2010–January 2011, the turbopumps were driven by hydrogen gas instead of gas generator exhaust (cold drive). The tests were focused on obtaining regenerative cooling chamber characteristics.

In the second series of tests in July–August 2011, gas generator was installed to drive the turbopumps (hot drive). The purpose of the test was to verify complete GG cycle engine operation. Throughout the tests, the engine started well in every test and there were no hard start phenomena.

In the third series of tests in January–March 2013, the engine system hot firing was conducted in IHI Aerospace Aioi test facility. For the tests, the regenerative cooling chamber was modified as the result of the first chamber manufacturing and former firing tests. Both cold and hot drives were tested in series. In cold drive test, flow control valves were installed among turbine bypass lines. Using these

Fig. 14 Photo of the engine setup

control valves, thrust and mixture ratio were controlled to obtain a wide operational range of engine system within a single hot-firing duration. In hot drive test, several repeatability measurements and long-duration firing were conducted to verify the stability of the engine. The tested engine is shown in Fig. 14. In the series of the tests, a total of 11 runs were carried. The longest duration time was 300 s.

The typical test results are shown in Table 7 and the operating conditions of all firing tests through 27 tests are plotted in Fig. 15. Since 2011, 27 firing runs were carried out and the summed test time was more than 1650 s. The longest duration was achieved in SRx027 (300 s). Neither start failure caused by engine nor hard start was observed. The photo of the engine in the firing test is shown in Fig. 16. Figure 17 shows the combustion characteristics in 300 s firing test (SRx027). The combustion was stable in terms of combustion pressure (Pc).

2 Next Step of the Research

Although we have been carrying out the R&D activities on LNG engines, any Japanese LNG engines have not achieved the target I_s (360 s) as mentioned at the beginning of the section. In addition, there are no engines which could achieve the target I_s even though R&D activities on LNG engines are being promoted in the world as shown in Table 8. Therefore, we decided to improve the performance of Japanese LNG engine drastically and are planning to apply the engine to future

Table 7 Typical firing test results

Test type	Test number	Time (s)	Pc (MPa)	MR (O/F)	$\eta_{C*}(\%)$
Cold	SRx007	30.0	5.35	4.01	98.5
	SRx017	30.0	5.24	2.17	95.4
	SRx018	100.0	5.01	2.51	94.9
	SRx023	65.6	5.00	2.31	96.2
	SRx024	89.6	5.16	2.39	95.8
	SRx025	57.2	5.33	2.90	95.9
Hot	SRx015	120.0	4.78	2.77	93.6
	SRx016	120.0	5.18	2.80	93.8
	SRx019	32.7	4.90	2.70	94.7
	SRx021	120.0	5.05	2.75	94.5
	SRx022	120.0	5.10	2.75	94.5
	SRx026	120.0	5.12	3.40	95.8
	SRx027	300.0	5.15	3.12	94.8

Fig. 15 Typical operating conditions of the firing tests
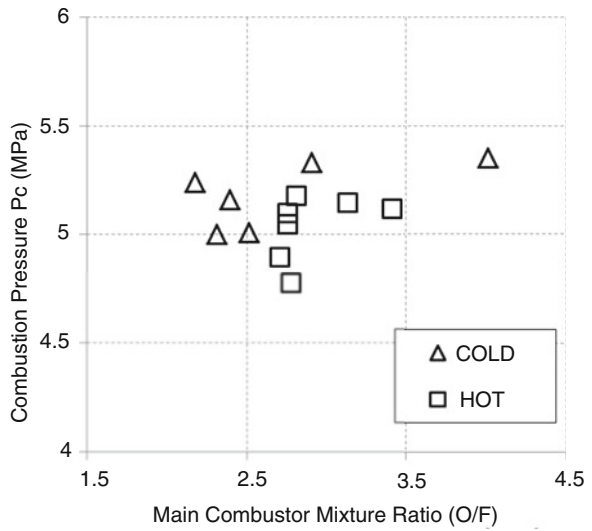
Fig. 16 Photo of the engine in the firing test (SRx027)
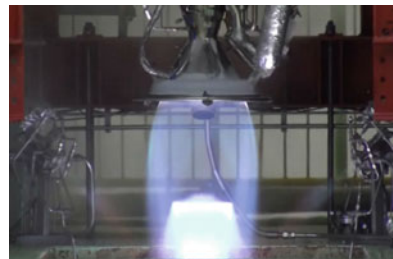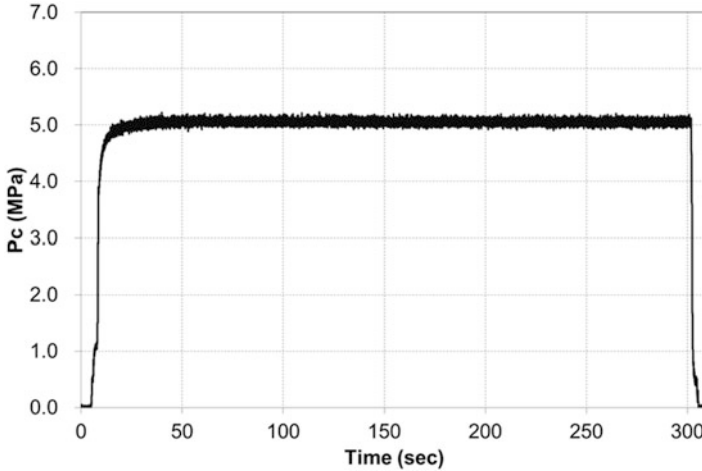
Fig. 17 Typical time history of combustion pressure of the engine

space transportation systems (e.g., a reusable liquid rocket booster and an orbital transfer vehicle). To achieve a higher performance, we started a R&D activity on LNG engine focusing on a regenerative cooling type chamber. The summary of research and development on LNG rocket engine in Japan shows in Fig. 18.

3 R&D Plan for LNG Engines in Japan

3.1 Approach of the R&D

We adopted a step-by-step approach in the past R&D and had been solving issues found in the previous development. For example, we increased the I_s in each development and modified the design which caused troubles. Consequently, the I_s and reliability of LNG engines have been gradually improved. In order to drastically improve the performance, we changed the approach of R&D from a step by step to a top down. At first, we defined a target performance of LNG engines and then clarified necessary works in order to achieve the performance. The new approach consists of four steps as shown in Fig. 19.

3.2 Setting a Target Performance (I_s) for the R&D Activity

There are two purposes in our R&D activity. One is to enhance the applicability of Japanese LNG engine for space transportation propulsion systems, and the other is to improve the international competitiveness of Japanese LNG engines. For

Table 8 Summary of LNG engines in the world [11–19]

	France-Russia	Italy-Russia	USA	USA	USA	Korea	Japan	Japan	Japan
Company/Agency	SNECMA/KBKhM	Avio/KBKhM	Aerojet	NASA	Blue Origin	DARMA Technology Inc.	IA/JAXA	IA/JAXA	IHI
Name	Volga	MIRA	–	HD4-A-LT	BE-4	CHASE-10	LE-8	–	–
Pc (MPa)	–	–	–	–	–	7.2	1.2	1.2	5.2
Thrust (kN)	2000	98.1	24.5	24.2	2450	107	107	30	98
I_s (s)	350 (plan)	364 (plan)	345 (result)	–	–	321 (plan)	314 (result)	335 (result)	356*(result)
Engine cycle	Staged combustion cycle	Full expander cycle	Pressure fed	Pressure fed	Staged combustion cycle	Gas generator cycle	Gas generator cycle	Pressure fed	Gas generator cycle
Cooling system	Regenerative	Regenerative	Ablative	Film cooling	Regenerative	Regenerative	Ablative	Ablative	Regenerative
Accumulated firing duration (s)	–	Total 100	Total 956	Total 2087	–	– (Over 180 firing tests from 10 to 200 s burn time)	Total 2207	Total 122	Total 1650

*This value was estimated under nozzle expansion ratio 150 based on test result [2]
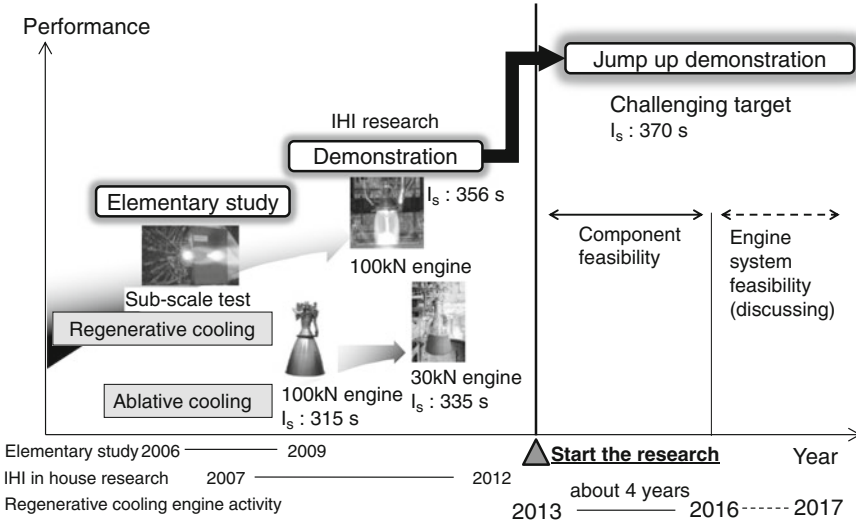
Fig. 18 Road map of the R&D activity for LNG engines in Japan

Fig. 19 Steps of R&D approach
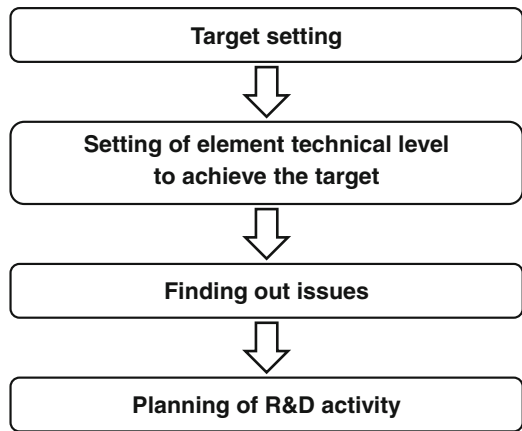
the former purpose, we set a target performance (I_s) at higher than the value of 360 s. For the latter purpose, we selected a value of the world's highest level as the target performance (I_s). Figure 20 shows the performances of hydrocarbon engines including LNG engines in the world and the target performances. The target performances of 350–370 s are higher than the fitted curve of the world's hydrocarbon engines.

An engine thrust level is also an important factor in R&D activity on rocket engine. Since we do not have any concrete missions to apply a LNG engine, we selected three target thrust levels: 30 kN, 100 kN, and 2000 kN for this R&D activity. The applications of each thrust level engines are supposed as follows: 30 kN thrust engine for an orbital transfer vehicle, 100 kN thrust engine for an experimental
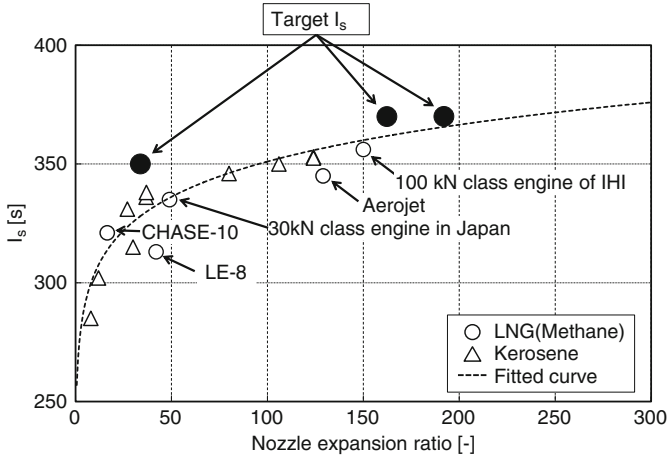
Fig. 20 Trend of performance of hydrocarbon engines in the world
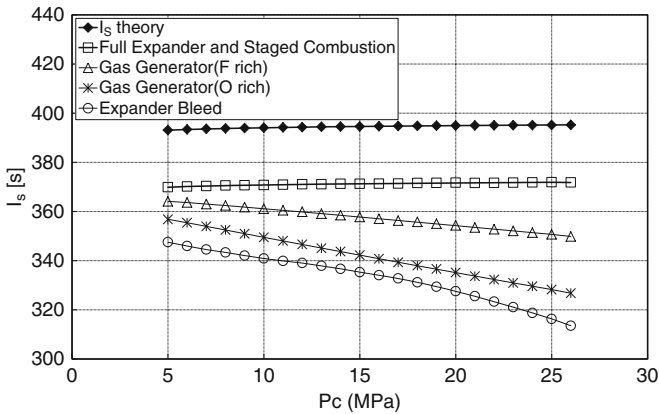
Fig. 21 Calculated I_s of each engine cycle under the condition of 150 of nozzle expansion ratio

reusable rocket and an expendable launch vehicle, 2000 kN thrust engine for a booster stage. The range of the engine thrust from 30 to 2000 kN can cover future space applications broadly.

3.3 Setting of Element Technical Level to Achieve the Target

3.3.1 Selecting the Engine Cycle

Secondary, we constructed analytical models of LNG engines with different engine cycles and then estimated operating conditions of engines which satisfied the target performance. The nozzle expansion ratio of every engine was assumed to 150 and the calculation results are shown in Fig. 21. There are only two solutions of engine

cycles: "full expander (FE) cycle" and "staged combustion (SC) cycle." We selected these cycles for further investigation.

An SC cycle engine and an FE cycle engine have disadvantages. For example, an SC cycle engine has much more components like a pre-burner and its accessories and has hot sections not only in the chamber but also in the pipe, meaning relatively expensive and breakable. On the other hand, it is difficult to get a huge thrust of an FE cycle engine because it uses not so high temperature gas for driving turbopumps and cannot generate enough power of turbopumps for the huge thrust. Taking these disadvantages into account, we selected an SC cycle for 100 kN- and 2000 kN thrust engines and an FE cycle for 30 kN and 100 kN.

3.3.2 Determine Operating Conditions

Once an engine cycle is selected, the operating conditions of main components (i.e., combustion chamber, nozzle, pre-burner, etc.) can be calculated with analytical models, and the results are shown in Table 9. And then, we assessed the technological risks and set their priorities based on the differences of the calculated operating conditions to the past experimental results. As a result, we focused on the risks for main components, such as the combustion chamber, nozzle, and pre-burner. On the other hand, we omitted the risks of turbopump and valve from our R&D activity plan.

Figure 22 shows the calculated operating conditions of mixture ratio and combustion pressure. The calculated combustion pressures are around 8–9.7 MPa, higher than the past experimental results which were approximately 5 MPa.

Table 9 Results of engine-cycle simulation

		Thrust (kN)	30	100	100	2000
		Engine cycle	FE	FE	SC	SC
Target performance		I_s (s)	370 >	370 >	370 >	350 >
Main combustion chamber		Combustion pressure Pc (MPa)	8.5	8.0	8.0	9.7
		MR	3.5	3.4	3.4	3.1
		Coolant inlet pressure (MPa)	21	19	19	21
		Coolant outlet pressure (MPa)	21	18	19	20
		Coolant inlet temperature (K)	134	132	131	125
		Coolant outlet temperature (K)	468	378	381	245
		Coolant flow rate (kg/s)	1.5	5.0	4.1	102
Pre-burner (GG)		Combustion pressure (MPa)	–	–	16	17
Nozzle		Expansion ratio	192	162	162	34
		Coolant outlet temperature (K)	618	530	374	219
		Coolant flow rate (kg/s)	0.4	1.3	2.2	39.7
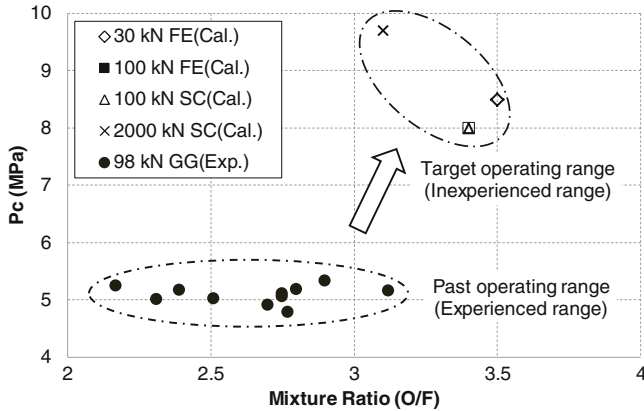
Fig. 22 Main combustion chamber pressure Pc
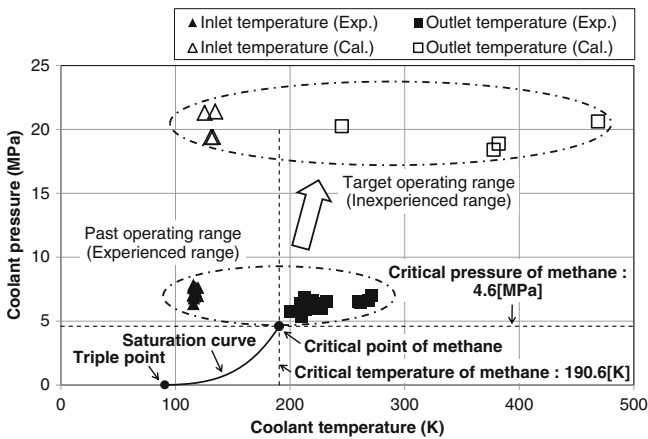
Fig. 23 Pressure and temperature of coolant

Figure 23 shows the calculated inlet/outlet temperature of chamber coolant passage and the past experimental results. The calculated inlet/outlet pressures of coolant passage are around 18–21 MPa, higher than the past experimental results which were approximately 5–8 MPa. The calculated outlet temperatures of coolant passage are around 480 K, higher than the past experimental results which were approximately 280 K. The operating conditions of main components derived from the simulation are higher than the experienced conditions, and thus we did not design and test the components under the conditions. Therefore, we need to verify the feasibility of the target engines under the operating condition derived from the simulation.

On the other hand, the operating conditions of the main components for each thrust level engine are not greatly different as shown in Figs. 22 and 23. For example,

the pressures of coolant are distributed 18–21 MPa in Fig. 23 but they are within the range of 15 % even though the thrust level varies between 30 and 2000 kN. Because the range of operating conditions are not so large, we can evaluate a design of an engine in the target operating conditions for the different thrust level engines by testing fewer test specimens.

3.4 Finding Out the Task, Research Plan Outline

There are mainly two subjects to be carried out in order to confirm the feasibility of less risk development of LNG engines which have operational conditions shown in Table 9. One is to verify the assumptions, for example, heat transfer coefficient and combustion efficiency which were used in the engine-cycle analysis. Although the assumptions were based on the results of Japanese R&D activities and many published papers, they should be verified by experiments. If the assumptions are wrong, the value of calculated performance (I_s) would be changed. The other is to check if any harmful phenomenon happens or not, for example, a combustion instability or worse ignition performance would be revealed in a development. Such harmful phenomena might disappear or problems might be solved by improving the design; however, we should pay much attention to them because we would be forced to change the design drastically if they happen. From the viewpoint of the two subjects, necessary fundamental tests and analysis were selected, and the research activities of LNG engine were planned.

3.4.1   Find a Best Design of Injection Element

There are only a few experimental results of LNG engines under high combustion pressure (8–9.7 MPa) in the world and no data in Japan. We are planning to carry out simulations and experiments of high pressure combustion on many types of injection element which has different design. The best design can be then selected based on the results.

3.4.2   Verification of Heat Exchange Performance

As shown in Fig. 23, the calculated inlet and outlet pressures in coolant passage are higher than those of past experiments. The difference between the pressures and the critical pressure is larger. Although the estimated value of heat transfer analysis becomes to have good agreement with the one of the experimental results when the difference is larger, we are planning to conduct an experiment and verify the analytical method in order to enhance the reliability. Although it is general to apply the Bartz's [20] experimental equation for the estimation of heat transfer of rocket engine, we should use other estimation method and verify it because we had experimental data that did not matched to the results of Bartz's equation.

3.4.3 Survey a Better Ignition Condition of Pre-burner

LNG has the narrow range of mixture ratio for keeping combustion compared to hydrogen and has little experimental data to ensure an ignition in a lower mixture ratio. Since a pre-burner, which is used for a staged combustion cycle engine, operates in a low mixture ratio, we are planning to find a better design of injection element of the pre-burner based on the results of analysis and experiments that will be carried out.

3.4.4 Influence of Soot of Combustion Gas

As the operational condition of targeted LNG engine varies from the existing Japanese LNG engines, we will try to estimate the amount and the deposited area of soot inside the main chamber and pre-burner. We will try to find an injection element design which generates less amount of soot.

3.5 Improvement on Design Method

The design of LNG engine has been checked with many experiments because the design tools were not so reliable for the certification of the engine specification. For example, when we started a development of LNG engine with different thrust level, we needed to design, manufacture, and test many prototype engines, resulting in the rise of the development cost. For the sake of realizing an efficient development, we are planning to change the design method of current "experimental-based way" to "analytical-based way". Figure 24 shows the diagram of the strategy
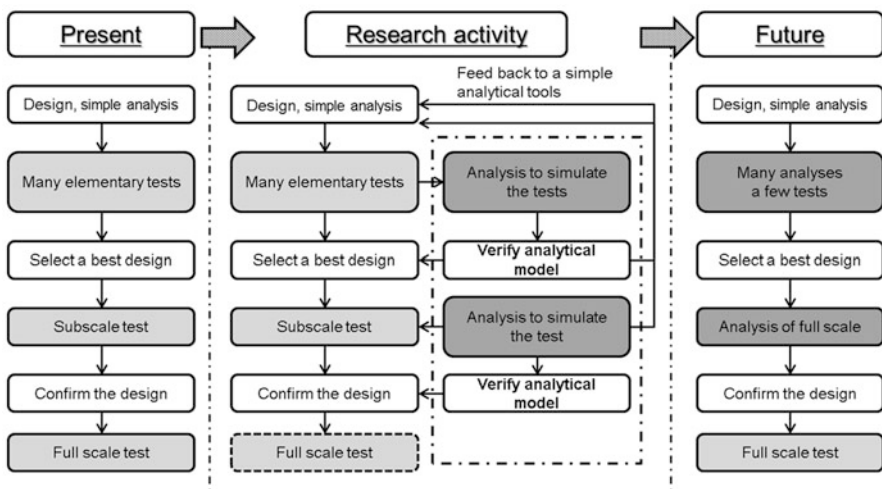

Fig. 24 Flowchart of improvement on design method through the research activity

for improvement on the design method through the research activity. Firstly, the analytical tools will be verified and matured in the research activity within 3–5 years, for which we will invest resources in making analytical tools and accumulating experimental data. After the research period, we will become able to confirm a feasibility of development with fewer resources of experiment and analysis in a shorter period.

4   Summary

The current status of research and development on LNG rocket engine in Japan is reported. Aimed at jumping up to a higher technical level, we are planning to change the design of engine system and continue the research activity to obtain the analysis results based on design methods.

References

 1. Masahiro I et al (2010) Full duration firing test results of 100 kN LOx/LNG engine. In: Paper presented at the Space Propulsion 2010, San Sebastian, 3–6 May 2010
 2. Kubota I et al (2012) Current development status of LNG propulsion system. In: Paper presented at the 53th conference on aerospace propulsion and power, Geibunkan, 4–5 Mar 2012
 3. Kano Y et al (2012) Overview of LNG propulsion system development. In: Paper presented at the 63rd international astronautical congress, Naples, 1–5 Oct 2012
 4. Taya K et al (2013) Development and test of the LOx/LNG regenerative cooled rocket engine (2nd report). In: Paper presented at the 29th international symposium on space technology and science, Nagoya congress center, Nagoya, 2–9 June 2013
 5. Taya K et al (2014) Development and test of the LOx/Methane regenerative cooled rocket engine. In: Paper presented at space propulsion 2014, Cologne, 19–22 May 2014
 6. Sato K et al (2005) Overview of GX launch services by GALEX. In: Paper presented at the 56th international astronautical congresses, Fukuoka convention center, Fukuoka, 16–21 Oct 2005
 7. Fukushima Y et al (2002) Development status of LE-7A and LE-5B engines for H-IIA family. In: Paper presented at Acta Astronautica 50(5):275–284
 8. Motogi T et al (2010) Development of L-605 Nozzle Extension. In: Paper presented at the Asian joint conference on propulsion and power 2010, Miyazaki, 4–6 Mar 2010
 9. Y Noguchi et al (2011) The result of the single element firing tests of the supercritical LOx/methane coaxial injector. In; Paper presented at 28th international symposium on space technology and Science, Okinawa, 5–12 June 2011
10. Sakaguchi H (2008) Advanced nickel electroforming technology for the regenerative thrust chamber of the rocket engine. In: Paper presented at the Asian joint conference on propulsion and power 2008, Gyeongju, 6–8 Mar 2008
11. Souchier A et al (2004) Snecma high thrust cryogenic engines for the next 20 years. In: Paper presented at the 40th AIAA/ASME/SAE/ASEE joint propulsion conference and exhibit, Fort Lauderdale, 11–14 July 2004
12. Astorg JM et al (2006) Oural: a cooperation between Europe and Russia to prepare future launcher. In: Paper presented at the 57th international astronautical congress, Valencia, 2–6 Oct 2006

13. Arione L (2013) The status on the development of LM10-MIRA LOx-LNG expander cycle engine in the frame of LYRA program. In: Paper presented at the 5th European conference for aeronautics and space sciences (EUCASS), Munich, 1–5 July 2013
14. Agenzia spaziale italiana (2015) Title of MIRA, completata la prima fase di test http://www.asi.it/it/news/mira_completata_la_prima_fase_di_test. Accessed 26 Feb 2015
15. Kyoung-Ho K et al (2006) Development of 'CHASE-10' liquid rocket engine having 10tf thrust using LOx & LNG (Methane). In: Paper presented at the 42nd AIAA/ASME/SAE/ASEE joint propulsion conference & exhibit, Sacramento, 9–12 July 2006
16. DARMA Technology Inc. (2015) Title of CHASE-10 (Methane Rocket Engine) http://www.darmatechnology.com/chase-10-methane-rocket-engine.html. Accessed 26 Feb 2015
17. Timothy D et al (2010) Propulsion risk reduction activities for nontoxic cryogenic propulsion. In: Paper presented at 46th AIAA SPACE 2010 conference & exposition, Anaheim, 30 Aug–2 Sept 2010
18. Melcher JC, Morehead RL (2014) Propulsion risk reduction activities for nontoxic cryogenic propulsion. In: Paper presented at 50th AIAA/ASME/SAE/ASEE joint propulsion conference, Cleveland, 28–30 July 2014
19. Blue Origin (2015) Title of BE-4 Fact Sheet. https://d1ljm9hc65qhyd.cloudfront.net/press-releases/2014-09-17/BE-4-Fact-Sheet.pdf. Accessed 26 Feb 2015
20. Bartz DR (1957) A simple equation for rapid estimation of rocket nozzle heat transfer coefficients. J Jet Propuls 27(1):49–51

Research and Development Activities on JAXA's Spacecraft Propulsion

Go Fujii and Hirohide Ikeda

Abstract This chapter will provide recent activities and plans for spacecraft in JAXA (Japan Aerospace Exploration Agency). In these years, JAXA launched many spacecraft, such as earth observation satellites, geostationary satellites, and HTV (H-II Transfer Vehicle). The details of propulsion system of these spacecrafts are introduced.

Also several topics of research activities are introduced. Recent activities in JAXA spacecraft propulsion have been focused on improvement of the performance and reliability of propulsion systems. In this chapter, three representative topics are introduced: (1) development of long life and high-reliability 1 N and 4 N monopropellant thrusters, (2) development of new satellite composite propellant tank, and (3) research of high-performance and low-toxic propellants. These development and research activities contribute to successful spacecraft mission.

Almost all missions involving propulsion systems on spacecraft have recently succeeded. From these experiments, the world's leading technologies were developed in JAXA, such as the highest specific impulse bipropellant apogee kick engine and the longest life 1 N and 4 N thrusters. And the research and development on propulsion systems, including verification studies to support spacecraft projects and investigations on recent technologies, are now going for future novel missions.

1   History and Introduction

Japanese space development activities started in 1969, when NASDA (National Space Development Agency of Japan, later JAXA) was established. In the early era, the spacecraft's propulsion technology was mainly introduced by the United States as well as the launch vehicle technology. For example, the first Japanese flight-proven monopropellant thruster for satellite propulsion was the ETS-III's

G. Fujii (✉) • H. Ikeda
Japan Aerospace Exploration Agency (JAXA), Ibaraki 305-8505, Japan
e-mail: fujii.go@jaxa.jp

1 N thruster, which was launched in 1982. This thruster was developed by IHI (later IHI Aerospace) under the technical assistance of the US TRW Inc. in the 1970s. Since then, satellite mass and lifetime have been extended and the requirement for spacecraft propulsion system has become severe; therefore, the successive improvement of propulsion system and components had been made. Also the challenge to develop the several components by domestic company had been conducted, such as propellant valve, propellant tank, latching valve, fill and drain valve, and so on. From these activities, the spacecraft propulsion technology in Japan was progressed.

Recently, JAXA has launched many spacecrafts, such as earth observation satellites, geostationary satellites, and HTV (H-II Transfer Vehicle). All these spacecrafts mount the propulsion system for attitude and orbit control. We, at the JAXA propulsion group, contribute to the development of these spacecraft propulsion systems and also the success of their missions. Our contribution involves not only developing the spacecraft's propulsion system but also research to secure the diversity of future space activities. Recent activities in JAXA spacecraft propulsion have focused on verification to improve the reliability of propulsion systems and improve the capability for future missions.

This paper describes JAXA's recent activities in and plans for spacecraft chemical propulsion.

2   Recent Spacecraft Projects

In recent years, JAXA has launched many spacecraft, such as earth observation satellites, geostationary satellites, and HTV (H-II Transfer Vehicle).

2.1   GCOM-W (SHIZUKU)

GCOM-W (Global Change Observation Mission) is a project for the global and long-term observation of the Earth environment and is called "SHIZUKU" (meaning "drop" in Japanese). SHIZUKU (shown in Fig. 1) carries the AMSR2 (Advanced Microwave Scanning Radiometer 2), an instrument to observe water-related targets such as precipitation, water vapor, sea surface wind speed, sea surface temperature, soil moisture, and snow depth. SHIZUKU has joined the A-Train constellation led by NASA. The participation of SHIZUKU into the A-Train constellation enables the simultaneous observation with instruments mounted on other satellites and enhances the scientific research using AMSR2 data. The satellite system was designed and manufactured by NEC, launched in 2013, and is now on orbit. The propulsion system is the monopropellant hydrazine blowdown system. Figure 2 shows the schematics of the propulsion system of SHIZUKU. It consists of 12 4 N thrusters which are designed by IHI Aerospace. Eight 4 N thrusters are used for attitude

Fig. 1 GCOM-W (SHIZUKU)
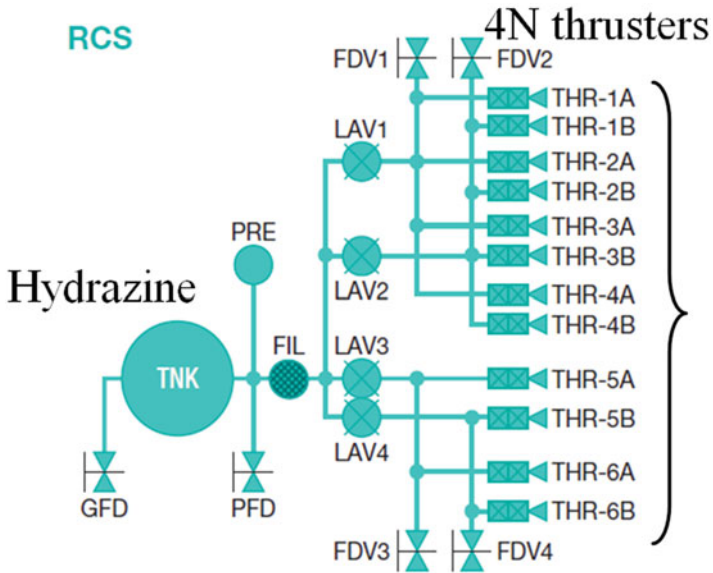
Fig. 2 Schematic of propulsion system of SHIZUKU

control (four thrusters are redundant) and four 4 N thrusters are used for orbit control. The catalyst of 4 N thruster is H-KC12GA made by Heraeus (Germany) and it was adopted to Japanese satellite for the first time. The details of 4 N thrusters are explained in section "Development of Long Life and High-Reliability 1 N and 4 N Monopropellant Thrusters." The hydrazine is supplied from channel mesh propellant tank which is designed by IHI Aerospace and pressured by helium. The fill and drain valves are designed and manufactured by domestic companies, Shimadzu and IHI Aerospace. The latch valves are also designed by domestic company Japan MOOG. They have had many flight heritages and no failure mode on orbit in the past. Other components such as filter and pressure sensor are purchased by foreign company.

2.2 ALOS-2 (DAICHI-2)

ALOS-2 (Advanced Land Observing Satellite-2 which is shown in Fig. 3) is the mission to contribute to cartography, regional observation, disaster monitoring, and resource surveys. ALOS-2 is the follow-on mission from the DAICHI and improves wide and high-resolution observation technologies. The satellite system was designed and manufactured by MELCO (Mitsubishi Electric Corporation), launched in 2014, and now on orbit. The propulsion system is the monopropellant hydrazine blowdown system designed by MELCO. Figure 4 shows the schematics of the propulsion system of DAICHI-2. It consists of eight 4 N thrusters which are

Fig. 3 ALOS-2 (DAICHI-2)
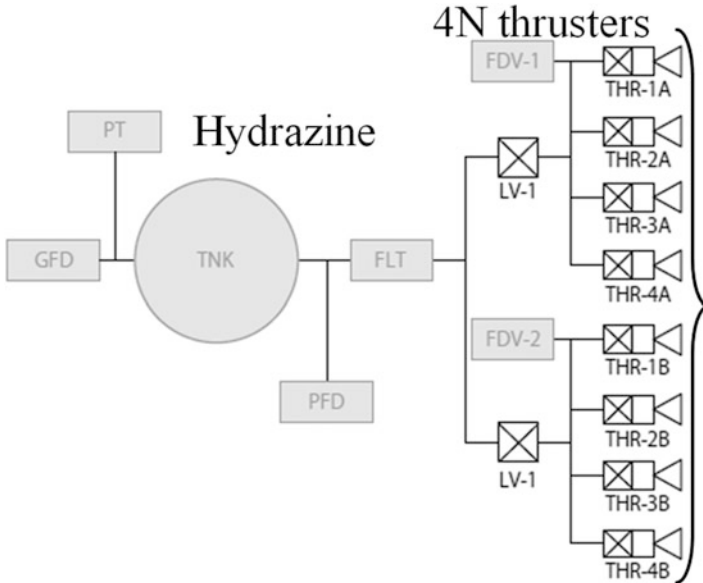
Fig. 4 Schematic of propulsion system of DAICHI-2

designed and manufactured by IHI Aerospace. The design of 4 N thrusters mounted on ALOS-2 are the same as that of GCOM-W1. They are used both for attitude and orbit control and four of them are redundant. The hydrazine is supplied from the propellant tank with surface tension device and pressured by helium.

2.3 SELENE (KAGUYA)

SELENE (SELenological and ENgineering Explorer which is shown in Fig. 5) is Japan's first large lunar explorer and is called KAGUYA. KAGUYA investigated the entire moon to obtain information on its elemental and mineralogical distribution, geography, surface and subsurface structure, the remnants of its magnetic field, and its gravity field using the observation equipment installed. The satellite system was designed and manufactured by NEC, launched in 2007, and successfully completed its mission in 2009. The propulsion system is N_2H_4/MON-3 bipropellant system designed by IHI Aerospace. Figure 6 shows the schematics of the KAGUYA dual-mode Unified Propulsion System (UPS). From the early period of development of spacecrafts in Japan, N_2H_4/MON-3 bipropellant system had been adopted for bipropellant system instead of MMH/MON-3 bipropellant system. The major reason is the high specific impulse of the N_2H_4/MON-3 bipropellant system. The KAGUYA UPS comprises a single 500-N delta V (ΔV) Orbital Maneuvering Engine (OME), 8 1-N attitude control monopropellant thrusters, 12 20-N attitude

Fig. 5 SELENE (KAGUYA)
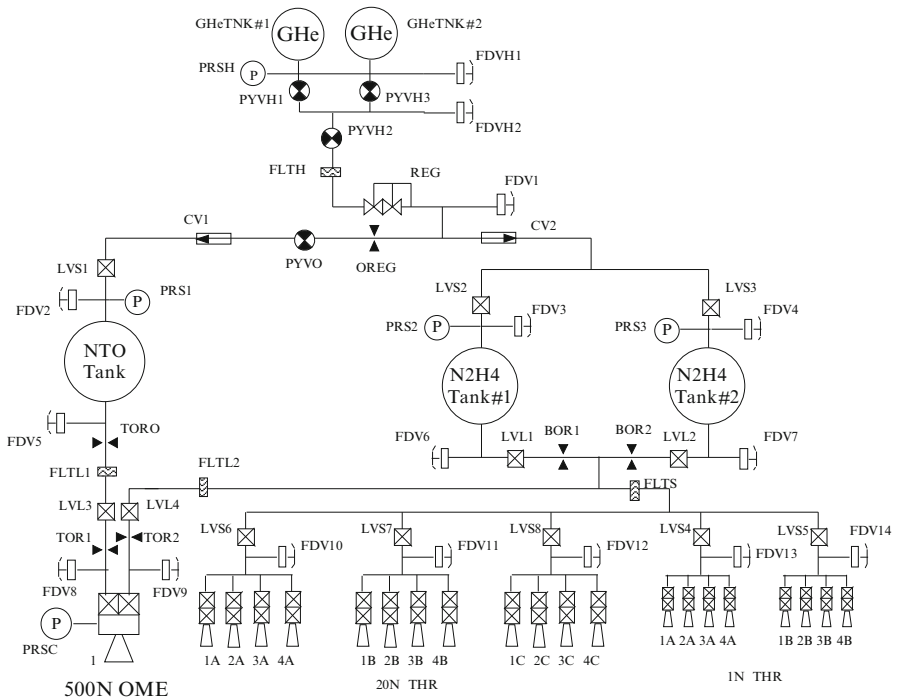
Fig. 6 Schematic of propulsion system of KAGUYA

control and ΔV monopropellant thrusters, 2 N_2H_4 (fuel) tanks, a single MON-3 (oxidizer) tank, 2 helium pressurant vessels, and components necessary to control the propellant flow and to monitor system health and performance [1]. After the qualification test campaign and the flight demonstration, the 500-N OME designed by IHI Aerospace was modified further more and achieved the world highest specific impulse 329 s at nominal condition. The engine has been adopted to many N_2H_4/MON-3 propulsion system all over the world.

2.4 HTV (KOUNOTORI)

The HTV shown in Fig. 7 is a spacecraft to carry various cargoes to the ISS in support of the ISS operation and has been launched about one per year since 2009. Figure 8 shows the schematics of HTV propulsion system. It is MMH/MON-3 bipropellant system and is equipped with 4500N engines and 28,120N thrusters to control orbit and attitude control. These products were imported from Aerojet in the beginning, but now have been replaced by domestic products which are designed by IHI Aerospace [2]. In the qualification test campaign of 500N engine, wide off nominal operating range was demonstrated by request from guidance and navigation system in order to comply to severe NASA's safety requirements. It also comprises two MMH (fuel) tanks, two MON-3 (oxidizer) tanks, four helium pressurant vessels, and components necessary to control the propellant flow and to monitor system health and performance.
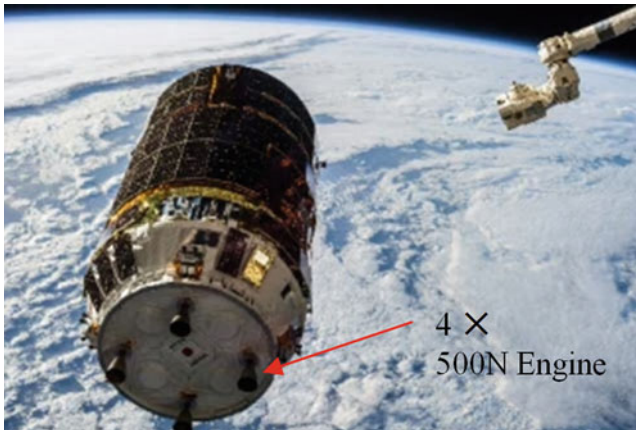
Fig. 7 HTV (KOUNOTORI)
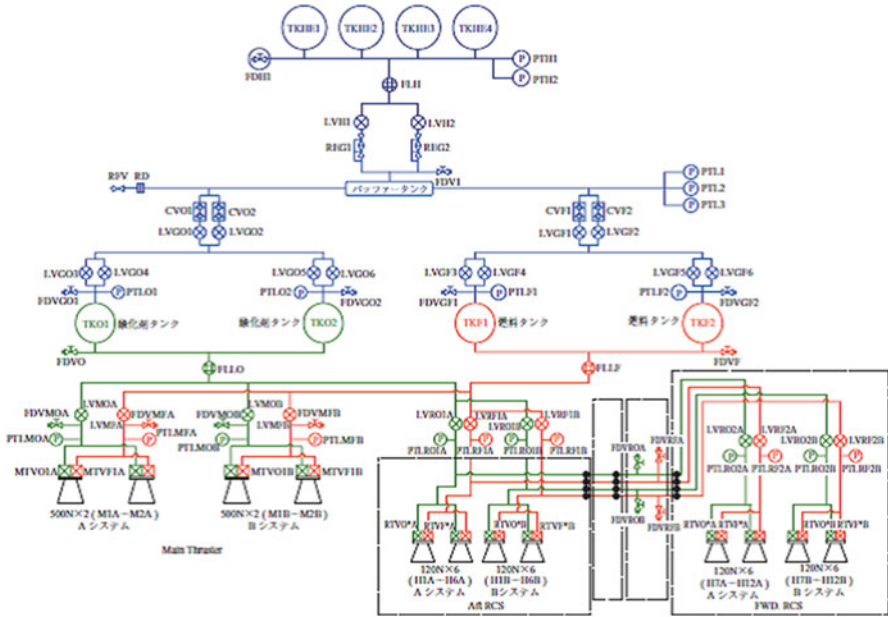
Fig. 8 The schematic of propulsion system of KOUNOTORI

2.5 Future Mission

JAXA is now developing new missions, such as SLATS (Super Low Altitude Test Satellite which is shown in Fig. 9) [3]. The purposes of SLATS include (1) test of orbit keeping with its own ion engine against high atmospheric drag at super low altitude (altitude of around 200 km) and (2) acquisition of data about atmospheric density and atomic oxygen. A satellite at super low altitude enables optical earth observation at higher resolution and lower electric power active sensing using a SAR or a LIDAR than those in use now. The orbit profile of SLATS is shown in Fig. 10. To maintain the super low altitude, it adopts an electric propulsion system using an ion engine designed and manufactured by MELCO. The monopropellant hydrazine blowdown system with four 1 N thrusters is also mounted for orbit control and also for attitude control.

3 Research and Development Activities

Recent activities in JAXA spacecraft propulsion have focused on adopting of new technology and improving the performance and reliability of propulsion systems.
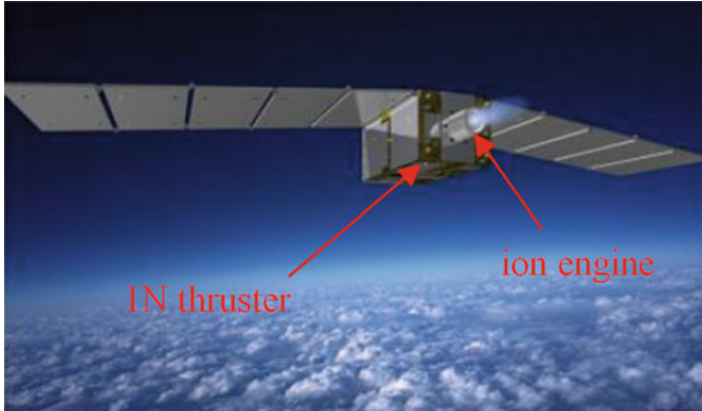
Fig. 9 SLATS
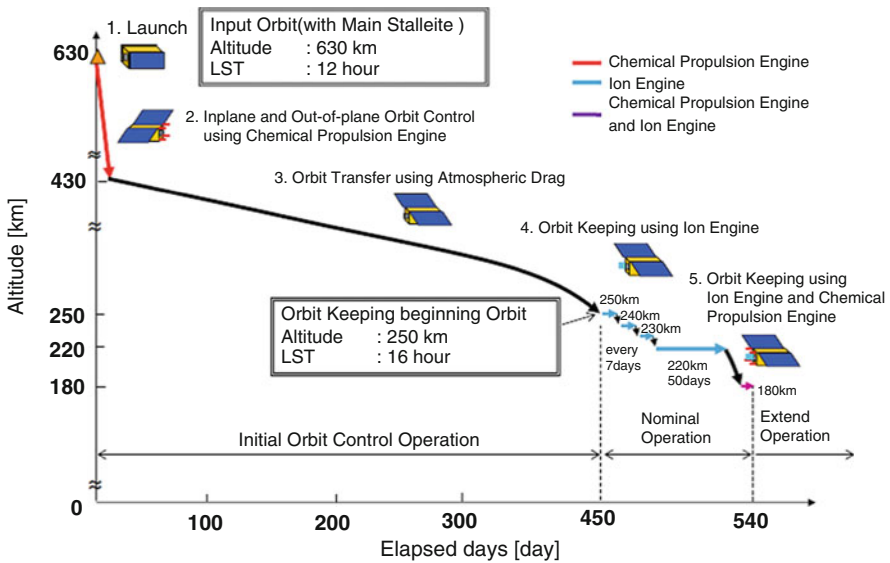
Fig. 10 Orbit profile of SLATS

3.1 Development of Long Life and High-Reliability 1 N and 4 N Monopropellant Thrusters

Monopropellant hydrazine thrusters are widely used in many satellites and propulsion systems of exploration vehicles and launch vehicle RCS due to its simplicity, high reliability, and robustness. The thrust range is mainly 1–100N, and the 1 N and 4 N thrusters are the work horses in the monopropellant thruster family, since they are suitable for attitude control or orbit control of the satellite. As 1 N and 4 N

thrusters are relatively small range of monopropellant hydrazine thrusters, they are useful for delicate control of spacecraft.

The life of the monopropellant hydrazine thruster is mainly determined by the degradation of catalyst granules. A monopropellant thruster comprises a propellant valve which controls the propellant flow and a jet motor which decomposes the liquid propellant into high temperature gas. The chamber in the jet motor is filled with catalyst granules which decompose the propellant. The catalyst is granular alumina coated with iridium. As thruster are fired, the catalyst granules in the chamber are crushed into fine particles by many factors such as thermal cycle by firing, hydrazine fluid friction, and the pressure spike in the chamber [4]. The peak of pressure spike is caused by accumulation of propellant in the void and several times larger than the design pressure. The crushed fine particles then flow downstream; some particles go out through the thruster nozzle and some are remained in the chamber and are accumulated between the catalyst granules. These are the reasons why a void in the catalyst bed is generated after firing and why the thrust degradation increases due to the pressure drop in the catalyst bed. It is difficult to quantitatively separate these effects; all these effects are alternated to the firing mode. The void of the catalyst bed causes the thruster performance degradation and the trend of it strongly depends on its firing mode. Previously, although it was known that the long cycle period and long ON time of the firing mode had a relatively severe effect on the catalyst granules, quantitative data on the relationship between the firing mode and the catalyst degradation and performance degradation trend were insufficient.

After the firing modes of thrusters are designed by a satellite system manufacturer, endurance life firing tests are often conducted to evaluate the endurance capability of the thruster life. The firing mode requirement of the thruster loaded onto the satellite is different from each satellite mission; therefore, the endurance firing tests of the mission duty cycle are needed. These firing tests increase the cost and the time required for delivery.

To eliminate these endurance firing tests in each of the satellite missions, the thruster life prediction model is considered to be helpful. To construct the life prediction model, firing tests in several single-pulse firing modes were conducted by 1 N and 4 N thrusters. These tests showed a quantitative relationship between the firing mode and the catalyst degradation or performance degradation trend. From analyzing these data, the life prediction model for 1 N and 4 N thrusters was finally constructed [4].

3.1.1 General Description of Long Life and High-Reliability 1 N Thrusters

Long life and high-reliability 1 N thrusters (see Fig. 11) were developed by the cooperative development program between JAXA and IHI Aerospace. The life of the first-generation 1 N thruster became insufficient; therefore, the design of new 1 N thruster was completely redesigned from that of the first-generation 1 N thruster. All the planned qualification tests were successfully completed in 2011 and it is
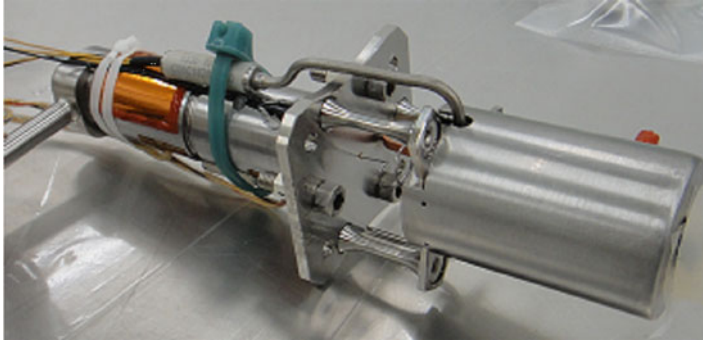
Fig. 11 Long life and high-reliability 1 N thruster
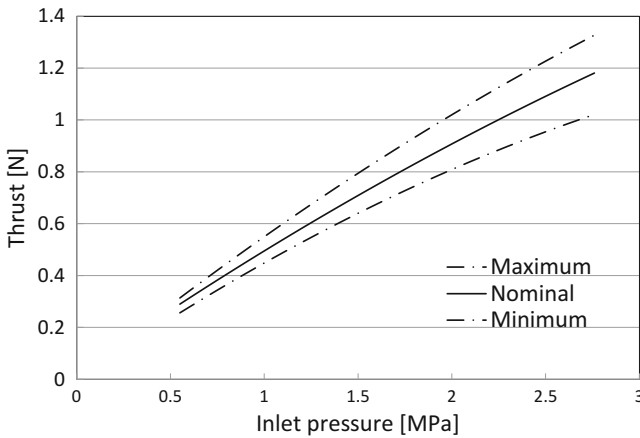
Fig. 12 Blowdown thrust profile

now ready to deliver for customers. The flight models of the second-generation 1 N thruster have been already shipped for SLATS (Super Low Altitude Test Satellite) which is the new satellite mission of JAXA and now awaiting its first flight [5].

The second-generation 1 N thruster has the following four major advantages:

1. Long life (total pulses 850,000 and total impulses 200,000 Ns were demonstrated)
2. No constraints of firing mode (no thermal problem such as thermal choke and excess heat soak back)
3. Low cost and short delivery time (competitive in the commercial market)
4. The thruster life prediction model

The detail of the thruster features and the qualification program results are described in Ref. [6, 7]. The specification of the second-generation 1 N thruster is shown in Fig. 12 and Table 1.

Table 1 Specifications and main features of the 1 N thruster

Weight	0.36 kg [thruster]
Operable pressure range	0.55–2.76 [MPa]
Thrust (BOL)	0.35–1.06 [N] (nominal at BOL(beginning of life))
I_s (BOL)	212–225 [s] (nominal at BOL)
	(Area ratio = 160)
Minimum I bit	<0.027 [Ns] at 2.41 [MPa] at 20 [ms]
Total impulse	230,208 [Ns]
	Demonstrated with H-KC12GA
Total pulses	884,274
	Demonstrated with H-KC12GA
Catalyst bed	Single layer (H-KC12GA or S405)
Power consumption	Less than 4W for catalyst bed heater
Propellant valve	Dual-seat solenoid type
	MOOG
	*Techspace Aero valves were also adopted
Minimum ON and OFF time of valves	20 ms
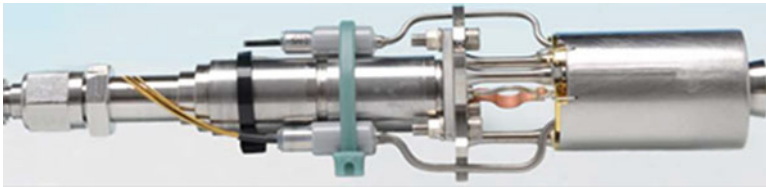
Fig. 13 Long life and high-reliability 4 N monopropellant thruster

3.1.2 General Description of Long Life and High-Reliability 4 N Thrusters

Japanese 4 N thrusters were developed by JAXA and IHI Aerospace in the 2000 s. The 4 N monopropellant thrusters are used in both Japanese LEO and GEO satellite programs, and 56 4 N thrusters were driven on orbit or are now waiting for flight. The thruster includes a two-layer catalyst bed with two sizes of catalyst granules filled into each layer. A dual-seat solenoid valve is used to control the propellant flow. Figure 13 shows the figure of the 4 N thruster designed by IHI Aerospace.

The advantage of this thruster is long life. More than 800,000 pulses at total pulses, 350,000 Ns at total impulse, and over 300 kg at hydrazine throughput at the same time were demonstrated by several thrusters.

The propellant valve and mechanical structure of the second generation of 4 N thrusters were modified from that of the first generation in 2010 to reduce their costs, shorten the delivery time, and also reduce the electric power consumption of the catalyst bed heater. The principal design of the injector and catalyst bed were unchanged from the first-generation 4 N thrusters; therefore, it was demon-

Table 2 Specifications and main features of the 4 N thruster

Weight	0.95 kg [module]
Operable pressure range	0.55–2.76 [MPa]
Thrust (BOL)	1.80–5.01 [N] (nominal at BOL)
I_s (BOL)	212–225 [s] (nominal at BOL)
Minimum I bit	<0.05 [Ns] at 2.41 [MPa] at 20 [ms]
Total impulse	572,351 [Ns]
	Demonstrated with H-KC12GA
Total pulses	970,665
	Demonstrated with H-KC12GA
Catalyst bed	Two-layer type
Power consumption	Less than 4W for catalyst bed heater
Propellant valve	Dual-seat solenoid type
	(Shimadzu Corp.) first generation
	(MOOG) second generation

strated that the performance features and specifications were not changed from the first-generation 4 N thrusters. The flight model has already been shipped and flight-proven by ASNARO in 2014. The detail of the second-generation 4 N thrusters is described in Ref. [8].

The performance specifications of the second-generation 4 N thrusters are shown in Table 2.

3.1.3   Contents of Endurance Firing Test

Endurance firing tests were conducted in the qualification test campaign of both 1 N and 4 N thrusters. The purpose of this endurance firing test was to reveal the quantitative relationship between the catalyst bed life and the firing mode. However, it was impossible to experiment with all the firing mode of thrusters which was conducted in orbit due to excessive cost and time. To collect the data effectively, 15 monopropellant thrusters of 1 N class and 19 monopropellant thrusters of 4 N class were tested. Three kinds of firing tests were planned and one thruster was fired in a single firing mode from the beginning to the end of the test.

To simulate the firing modes and estimate the catalyst bed life on orbit, we focused on the following three points:

1. Effect of the pulse firing mode
2. Effect of the propellant supplying pressure
3. Effect of the number of start cycles

To obtain these experimental data, three kinds of firing tests were planned on ground and described below:

(a) Continuous and single-pulse mode firing tests

In these tests, the effect of the continuous firing and pulse firing modes, ON time, and cycle period was investigated. Based on experience of the Japanese LEO and GEO satellite programs, three modes of the pulse firing cycle period were chosen for firing tests: short cycle period (0.2 s), middle cycle period (1 s), and long cycle period (10 s). In each cycle period, three to four different ON times were chosen. The propellant supplying pressure was fixed to 1.6 MPa which is the medium value throughout the life of the typical monopropellant blowdown system (2.41–0.69 MPa).

(b) Propellant supplying pressure tests

In these tests, to cover the supplying pressure of monopropellant blowdown systems of Japanese LEO and GEO satellite programs, two supplying pressure modes were chosen: high supplying pressure (2.41 MPa) and low supplying pressure (0.69 MPa). Together with the result of pulse mode firing tests (1.6 MPa), the result of the three levels of supplying pressure could be quantitatively unveiled.

(c) Multiple start cycle firing tests

Previous research showed that the key factor of catalyst degradation was the thermal cycle load on the catalyst bed [5]. The thermal cycle load of the catalyst bed peaks when the propellant flows into the catalyst bed, then the catalyst reaction occurs, and finally the catalyst bed temperature rises rapidly from the preheating temperature.

In this test, pulse firing started from the catalyst bed preheating temperature, until the catalyst bed temperature reached predetermined sufficiently high temperature. While the firing stopped, the catalyst bed temperature dropped to the initial temperature. Then pulse firing restarted. The temperature trend of start cycle firing test is shown in Fig. 14. This start cycle sequence was repeated over 8,000 times and the effect of the number of start cycles was evaluated (Table 3).
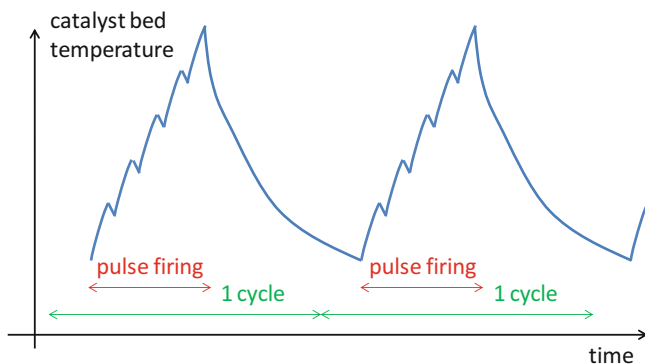
Fig. 14 Temperature trend of start cycle

Table 3 The list of 4 N thrusters and firing mode

	Firing mode		Results of firing tests			Number of cold start cycle (20 ± 10 °C)	Note
	ON time/cycle period	Supplying pressure	Total pulses	Total impulse [Ns]	Number of start cycles		
1	Continuous	1.6 MPa	11,791	356,089	214	15	Continuous firing
2	0.02 s ON / 0.2 s	1.6 MPa	809,285	69,773	201	15	Short cycle period
3	0.05 s ON / 0.2 s	1.6 MPa	809,285	153,824	201	15	Short cycle period
4	0.105 s ON / 0.2 s	1.6 MPa	810,285	302,793	266	15	Short cycle period
5	0.18 s ON / 0.2 s	1.6 MPa	809,785	520,970	194	15	Short cycle period
6	0.02 s ON / 1 s	1.6 MPa	808,306	54,843	359	15	Middle cycle period
7	0.05 s ON / 1 s	1.6 MPa	808,304	118,543	357	15	Middle cycle period
8	0.1 s ON / 1 s	1.6 MPa	808,304	304,003	357	15	Middle cycle period
9	0.25 s ON / 1 s	1.6 MPa	647,449	572,351	337	15	Middle cycle period
10	0.02 s ON / 10 s	1.6 MPa	412,352	41,789	280	15	Long cycle period
11	0.05 s ON / 10 s	1.6 MPa	417,753	70,283	313	15	Long cycle period
12	0.1 s ON / 10 s	1.6 MPa	338,019	135,964	297	15	Long cycle period
13	0.25 s ON / 10 s	1.6 MPa	255,655	228,007	251	15	Long cycle period
14	0.04 s ON / 1 s	2.41 MPa	807,296	166,620	155	15	High pressure Middle cycle period
15	0.05 s ON / 1 s	2.41 MPa	807,296	212,140	155	15	High pressure Middle cycle period
16	0.05 s ON / 1 s	0.69 MPa	807,397	88,810	158	15	Low pressure Middle cycle period
17	0.1 s ON / 1 s	0.69 MPa	807,397	170,692	158	15	Low pressure Middle cycle period
18	0.25 s ON / 1 s × 10 pulses	1.6 MPa	85,042	74,731	8134	0	Multiple start cycle
19	0.9 s ON / 1 s × 4 pulses	1.6 MPa	36,932	95,209	8148	0	Multiple start cycle
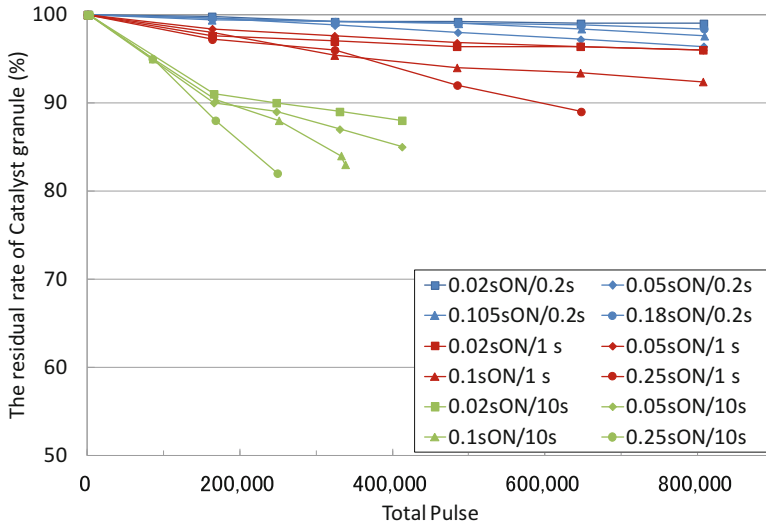
Fig. 15 Residual rate of catalyst granules of 4 N thrusters (continuous and pulse mode firing tests)

Figure 15 shows one example of the firing test results of 4 N thrusters. The degradation of catalyst granules were measured by X-ray transmission and X-ray CT photographs of catalyst bed in each phase. The figure shows that the relationship between total pulses and the catalyst degradation rate is almost linear and proportional. It is also apparent that the longer the firing pulse period and ON time are, the larger the catalyst degradation rate is. This suggests that these thermal cycle loads applied to the catalyst bed degrade the strength of the catalyst granule and cause the crush of the catalyst granule, and finally degradation of catalyst granules. The image of thermal load and firing mode is shown in Fig. 18. At the same time, performance degradation trends, such as thrust, specific impulse, impulse bit, centroid time delay, and so on, were also measured. The centroid time delay (CTD) means the time difference of the inlet time of valve driving signal and the center of occurred impulse. CTD shows the actual response time to induce the impulse bit and it is important for navigation and guidance design of spacecrafts. Figure 16 shows examples of the performance degradation trends. Since the catalyst bed degradation trend and thruster performance degradation trend were similar, a strong relationship emerges between the residual rate of the catalyst granules and the thruster performance.

The same firing test campaign was also conducted in 1 N thrusters. The quantitative catalyst bed degradation speed is different from 1 N to 4 N thrusters, but the qualitative trend is the same.
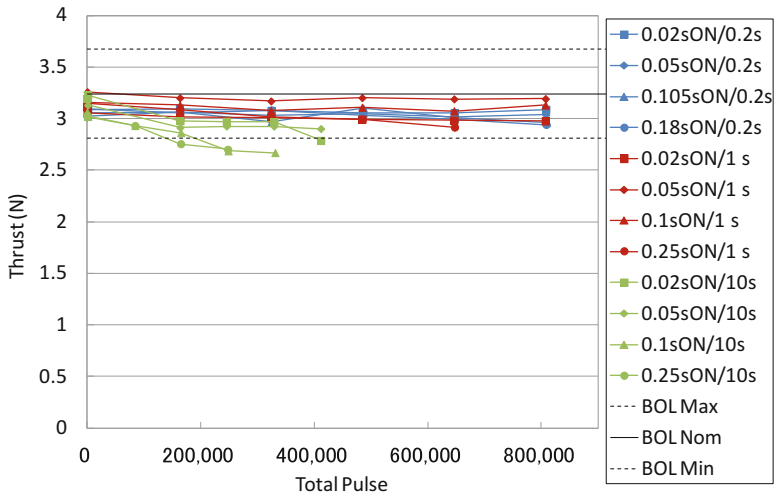
Fig. 16 Thrust trend of 4 N thrusters at1.38 MPa
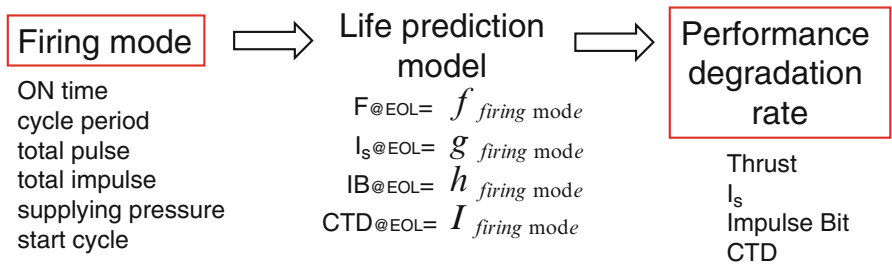
Fig. 17 The concept of the life prediction model of monopropellant thrusters

3.1.4 The Life Prediction Model of 1 N and 4 N Monopropellant Thrusters

The concept of a life prediction model is shown in Fig. 17. When users input the firing mode (pulse ON time, pulse cycle period, pulse number, supplying pressure, and so on), the performance degradation trends, such as thrust, specific impulse, impulse bit, and centroid time delay, are calculated.

As mentioned above, our major motivation to construct the life prediction model of monopropellant hydrazine thrusters is to skip the endurance firing tests of each mission duty cycle. This results in reducing the cost and the delivery time drastically for satellite system manufacturer. With the life prediction model, the satellite system manufacturer can evaluate the service life of the thrusters for each mission duty cycle from their firing mode.

Moreover, there are three major advantages to construct the life prediction model. One is the fact that these thrusters can be fired in any combination of firing modes. This advantage of any combination of firing modes can be realized by the features of no constraints of firing mode. These 1 N and 4 N thrusters are designed to avoid thermal problems such as thermal choke or excess heat soak back to propellant valves [9, 10]. To apply this advantage, one thruster can work both to orbit control which firing mode is relatively high duty mode and to attitude control which firing mode is relatively low duty mode. If one thruster works to orbit control and attitude control, the duty of thruster's firing mode becomes wide and the compatibility to the satellite system requirement is usually confirmed by the firing tests. The database of the life prediction model consists of wide range of duty cycles; therefore, the life compatibility can be predicted in the wide range of duty cycle.

The second is the fact that the dispersion of thruster performance can be minimized. Generally, the dispersion of thruster performance increases as the catalyst decreases. Using life prediction model, the catalyst degradation can be minimized and that means the dispersion of thruster performance can also be minimized. This is a key advantage for the satellite mission in which the attitude disturbance during thruster firing becomes sensitive, such as formation flight missions, telescope satellites, and so on.

The third is the fact that the life requirements of satellite systems can be extended by using the life prediction model. Though 1N and 4 N thrusters can sufficiently satisfy the thruster life requirement today, there are possibilities that it will be extended and become more severe in the future. One solution to adapt these requirements is to extend the life of thrusters more to satisfy these requirements, but it will take considerable time and cost. The other solution is to discuss the optimal firing mode of existing thrusters and extend the life of satellite system. From the thruster life prediction model, the quantitative effect of firing modes to the thruster life has been already evaluated and the severe firing mode has been known well. There is potential for users of these thrusters to discuss the firing mode with this life prediction model and can optimize the thruster life in the satellite system requirement.

3.1.5   The Process to Construct a Life Prediction Model of Monopropellant Hydrazine Thrusters

To construct the life prediction model, the quantitative effect of firing modes on thruster life was evaluated from the endurance firing test results. Before the thruster endurance firing tests, it was predicted that the performance degradation trend would be significantly influenced by the catalyst granules degradation trend.

Evaluations of firing tests revealed the following four significant points to consider for the life prediction model:

1. The performance degradation trend is similar to the catalyst granules degradation trend.

2. A linear function of the catalyst degradation rate per pulse can be induced from ON time and cycle period.
3. The catalyst degradation rate per pulse at the start of thruster firing is significantly large.
4. The effect of the supplying pressure to the catalyst degradation must also be considered.

These points were evaluated quantitatively from the thruster endurance firing test results. After it became apparent that our prediction was correct, the first step was to evaluate the relationship quantitatively between the firing mode and the degradation of catalyst granules. Subsequently, the second step was to evaluate the relationship between the trends of catalyst degradation and the thruster performance degradation. Finally, these results were combined and the life prediction model was constructed.

3.1.6 The Results of Constructing a Life Prediction Model of Monopropellant Hydrazine Thrusters

First, the experimental result of the remained catalyst bed volume, namely, the degradation of catalyst granules, is shown in Fig. 18. To construct the prediction model, the concept of "equivalent accumulative pulses" was introduced which considered the points of the evaluation results of endurance firing tests. The equivalent accumulative pulses were calculated by the function of firing mode, supplying pressure, and the number of start cycle. As the result of introducing this concept, the function of remained catalyst bed volume relative to the equivalent total pulses became almost linear in the same straight line. This means that the effect of firing mode can be defined in the one equation.
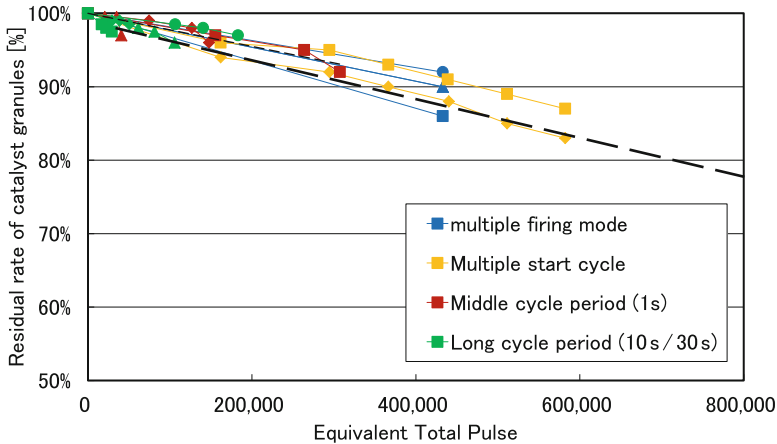
Fig. 18 Remained catalyst bed volume per "equivalent" total pulses
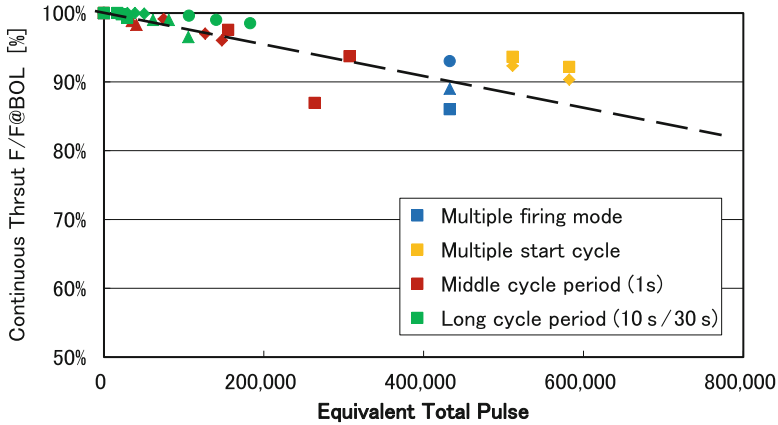
Fig. 19 Thrust degradation per "equivalent" total pulses (continuous firing at 0.69 MPa)

Second, the experimental results of performance degradation trend were evaluated. As a representative of performance, the prediction results of thrust are shown in Fig. 19. As well as the prediction of remained catalyst bed volume, the function of the thrust degradation trend became almost linear in the same straight line.

Finally, the accuracy of the prediction model was evaluated. As the results, the error of the predicted thrust degradation and experimented thrust degradation at 0.69 MPa was about 4 %. This number was considered to be low enough to evaluate the thruster life roughly and design the satellite system. Additionally, the activity to improve the prediction model and decrease the error will be continued to estimate the performance more precisely.

3.2 Development of New Satellite Composite Propellant Tank

Satellite components falling to the ground is a crucial problem, particularly titanium tanks in propulsion systems. Satellite tanks are generally made of titanium alloy because it is light and compatible with the propellants used for the system. However, it also has a high melting point, making it the least soluble material on reentry. To replace the titanium tanks, JAXA has studied tanks to prevent ground damage on reentry since 2010 [11–13] and has started the development of a new composite propellant tank since 2013. The tank structure features an aluminum liner overwrapped with carbon composite (by filament winding) which was selected as one of JAXA's strategic components. The tank is targeted not only to its demise properties but also with extended propellant storage, cost-effectiveness, and a short delivery time. In addition, the tank is estimated that its mass is as light as a titanium

tank. PDR (Preliminary Design Review) was held and the basic design was finished in 2013. In the basic design, the nominal volume and the diameter of the tank in cylindrical segment were selected at 430 L and 820 mm, respectively. Those values were determined referring to Japanese trend of satellites in low earth orbit. The volume of the new tank can be changed from 250 to 500 L by adjusting the length in a cylindrical segment. For the first step in the development, the minimum tank (Trial #1) which has the shortest length in a cylindrical segment and the volume of 250 L were manufactured to confirm the strength proof of critical portions and the adequacy of manufacturing techniques. PMD (Propellant Management Device) is also planned to manufacture to the tank shell in Trial #1. After trial #1, the nominal size of 430 L tank (Trial #2) including a PMD is planned to manufacture. This paper describes the design, trial production (Trial #1), and data acquisition tests [14, 15] in the development of the new tank [16].

3.2.1 Tank Specifications and Configuration

Table 4 shows the specification of a new composite tank. The specification was set referring to that of the earth observation satellites in Japan. The mass is aimed at the equal level to titanium tanks. Since the earth observation satellites in Japan mainly have the blowdown system with monopropellant (hydrazine) thrusters, the volume and MEOP (maximum expected operating pressure) were set at 0.43 m^3 and 2.76 MPa, respectively. The targeted life of new tank is 15 years based on the acceptable results of a propellant compatibility test. Expulsion efficiency was selected more than 99.5 %.

Figure 20 shows the configuration of the new tank. The structure features an aluminum liner overwrapped with carbon composite by filament winding. The body shell is equipped with a propellant fill/drain and a pressurization gas port, and a

Table 4 Tank specifications

Parameters	Requirements
MEOP	2.76 MPa
Proof pressure	3.45 MPa
Burst pressure	4.14 MPa
Temperature range	5–60 °C
Total volume	0.43 m^3
Propellant	Hydrazine (N_2H_4)
Other fluid	He, H_2O, IPA, N_2
External leakage	$\leq 1.013 \times 10^{-7}$ Pa $\cdot$ m^3/s at MEOP, He
Pressurization cycle	MEOP: >20, Proof pressure: >5
Expulsion efficiency	$\geq$99.5 %
Mass	$\leq$23.3 kg
On orbit life	$\geq$15 years
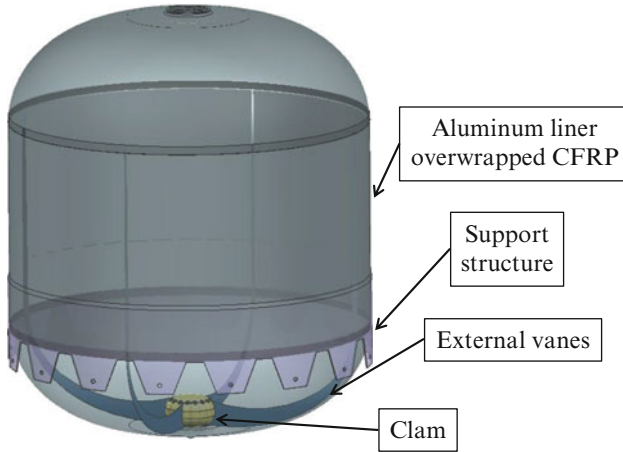
Fig. 20 Tank configuration

support structure. In the tank shell, there is PMD comprising external vanes, a clam, and internal vanes in the clam. Compared with the tank made from a titanium alloy (1538–1649 °C of melting points), the melting point of aluminum alloy is much lower (543–643 °C). If the mass and the shape are the same, an aluminum liner easily melts on reentry.

3.2.2 Development Status and Future Work

Design, data acquisition tests, and trial manufacturing are now ongoing.

For example, in order to check the propellant compatibility of a liner material, stress corrosion cracking (SCC) and elution of liner material tests were conducted using hydrazine, MMH, and MON-3. Figure 21 shows the SCC test configuration. Period of test time was corresponding 15 years accelerated by raising propellant's temperature. In SCC test, the tensile specimen with notches was subjected to the tension equivalent to 1.1 MEOP in propellants. As a result of microscope observation of the specimen after 15 years equivalent immersion, abnormalities, such as a crack from a notch section and change in color, are not seen.

PMD performance (propellant refilling, holding, and capturing) was also investigated by the free fall tower examination to realize 0G environment and obtain the design data. The free fall tower used in the tests is 50 m high and can achieve 10^{-2}–10^{-3} G for 2.5 s. The subscale PMD was installed in a fallen capsule equipped in the fall tower (Fig. 22). The tested specimen was installed on a rotating table which was able to change acceleration by change of spinning rate. There are several types of a clam to confirm the performance how it can hold propellant.
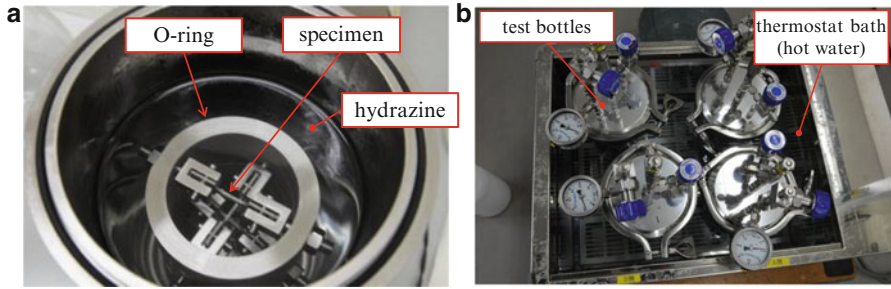
Fig. 21 SCC test configuration
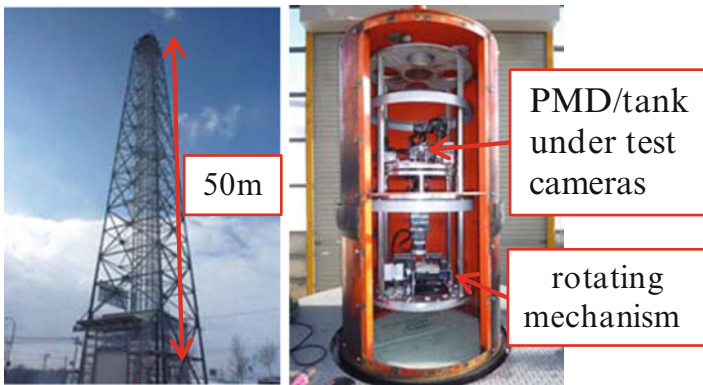
Fig. 22 Free fall tower (*left*) and test capsule (*right*)

Colored silicone oil was used to confirm the liquid movement visually. The PMD consists of vane which keeps the propellant by surface tension and clam which induce the propellant to the outlet. The tests were performed to check the influence of vane and clam configuration to the performance which holds propellant inside a clam. From these tests, the data were obtained to design PMD.

In addition, the wettability of a liner material was confirmed by the free fall tests using hydrazine. Figure 23 shows the photograph in the wettability confirmation tests. L-shaped specimens made of aluminum (same as a liner material) and titanium (Ti-6Al-4 V) were set in a glass case. Hydrazine was put in the case, 1 cm from the bottom. During the falling, the hydrazine rase along the specimens due to low gravity and surface tension. The rising speeds of hydrazine in the corner of the specimens during the falling tests were compared between aluminum and titanium materials. The test results showed that the aluminum specimen had higher wettability than that of titanium.

All the qualification tests will be finished by 2016 and ready to supply to customers.
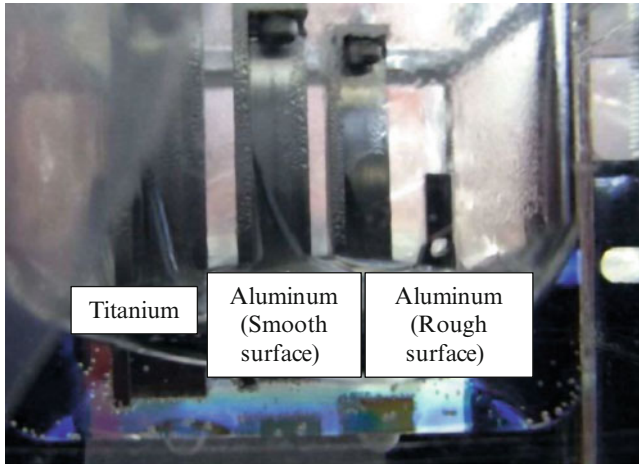
Fig. 23 Wettability confirmation tests (0.1 s after start)

3.3 Research of High-Performance and Low-Toxic Propellants

For the purpose of improving safety and reducing costs of propellant loading operations, several development programs of low-toxicity propellant or "green propellant" are being conducted in the world [17, 18]. Furthermore, hydrazine regulation by REACH law in EU is accelerating the move toward "green" propulsion systems.

JAXA has also been carrying out a research of HAN (hydroxyl ammonium nitrate)-based original mixture solution as a green propellant [19–21]. It has not only lower toxicity than hydrazine but also higher density, a lower freezing point, and higher specific impulse (I_s). Therefore, it can be a viable alternative to hydrazine and is applicable to any spacecraft such as launch vehicles, satellites, and space probes.

We introduce our research activities on HAN-based monopropellant propulsion system.

3.3.1 Evaluation of Propellants

In Japan, SHP 163 propellant has been researched. SHP163 contains 16.3 mass % methanol. Many kinds of safety evaluation were conducted with SHP163 propellant.

For example, Table 5 shows the result of the LD_{50} rat (orally) measurement for SHP163 and its comparison to hydrazine. When the GHS (Globally Harmonized System of Classification and Labelling of Chemicals) criteria for LD_{50} is applied to this result, SHP163 and ADN are categorized in category 4 (Harmful if swallowed) and hydrazine is in category 3 (Toxic if swallowed).

	LD$_{50}$rat (mg/kg)
SHP163	300–2000
AND	832
Hydrazine	60
NaCl	3750

Fig. 24 Schematics of a test tube
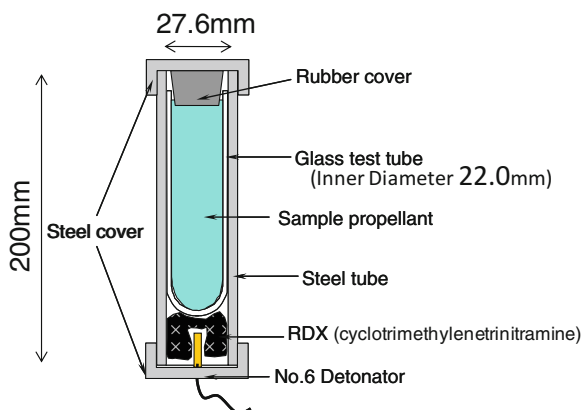
Steel tube tests were conducted to evaluate potential detonability of HAN/AN/Methanol/H$_2$O mixed solutions [22]. Schematics of a test tube are shown in Fig. 24. The detonability of the propellant was evaluated from the fragmented states of the tube in the ambient temperature. Detonability is classified into three categories: (a) "No Detonation," (b) "Partial Reaction," and (c) "Detonation," depending on the fragmented states. Figure 25 shows the detonability map (ternary diagram) with respect to the mass ratio of HAN/AN, methanol, and H$_2$O. I$_s$ (calculated) contour is also presented in the map. From this map, we can find that this solution has a potential to be higher I$_s$ than hydrazine even in No Detonation region, because No Detonation region almost corresponds to I$_s$ less than 260 s.

We also conducted UN transportation tests, material compatibility tests, a stabilization study, and so on. These test results showed that HAN solution is a viable candidate for green propellant from the viewpoint of safety.

3.3.2 Thruster Design

Firing tests using 20N class research thruster have been conducted to obtain design data of thruster and catalyst development. Figure 26 shows the basic concept of research thruster and Fig. 27 shows the picture of the thruster in vacuum chamber. The catalyst bed is preheated before firing. In these tests, the effects of each design parameters such as catalyst initial temperature and propellant mass flow to thruster performance have been evaluated [23].
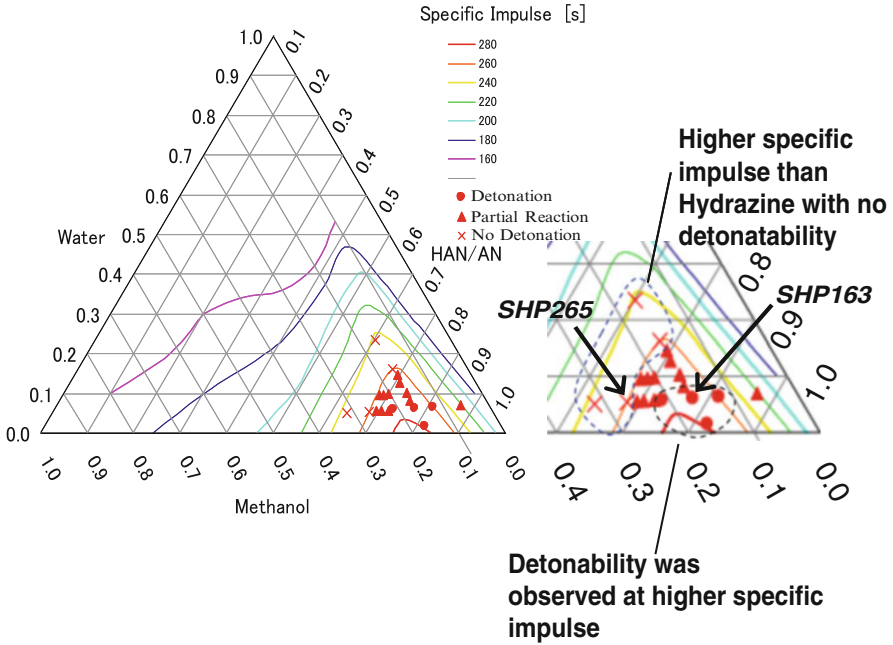
Fig. 25 Detonability map with respect to weight ratio of each solute and specific impulse contour
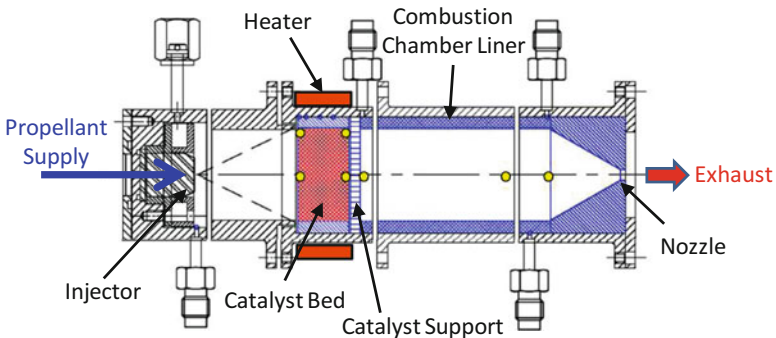
Fig. 26 Basic concept of the research thruster

3.4   System Study

One of the benefits of green propellant is cost reduction of propellant loading operation. We have been conducting a system study to simplify loading operations by taking advantage of low toxicity. Self-contained atmospheric protective ensemble (SCAPE) suits are not necessary when loading HAN-based propellant; therefore, loading operation can be shorter and simpler.

Fig. 27 Research thruster in the vacuum chamber

This system study includes the possibility of propellant loading at factory. By loading propellant at factory, operating duration at launch site will be shorter and propellant loading apparatus will be unnecessary in the launch site. We are now evaluating the cost benefit and problems of this operation.

3.5 Future Works

Many kinds of tests using HAN-based monopropellant were conducted to ensure safety, and these test results showed that HAN solution is a viable candidate for green propellant from the viewpoint of safety and performance.

In parallel with these researches, we have been making proposals for manned spacecraft missions or small satellite projects which can ride on the strength of green propulsion system. Concerning manned spacecraft mission, the green propellant propulsion system enable to approach to the spacecraft after landing as soon as possible.

4 Conclusion

JAXA's recent and near-future activities in spacecraft chemical propulsion are described. Almost all missions involving propulsion systems on spacecraft have recently succeeded. From these experiments, the world's leading technologies were

developed in JAXA, such as the highest specific impulse bipropellant apogee kick engine and the longest life 1 N and 4 N thrusters. And the research and development on propulsion systems, including verification studies to support spacecraft projects and investigations on recent technologies, are now going for future novel missions.

References

1. Goto D et al (2010) KAGUYA lunar explorer propulsion subsystem operations: orbit insertion, orbit maintenance, and maneuvered falling. Space Propulsion, Saint Sebastien
2. Takata S et al (2010) Design verification of the HTV propulsion system based on its first flight. Space Propulsion, Saint Sebastien
3. Imamura S et al Initial orbit control of SLATS using atmospheric drag. ISTS-2011, Ginowan, 5–12 June 2011, 2011-d-48
4. Fujii G et al The construction of the life prediction model of 1N and 4N monopropellant thrusters. 49th AIAA/ASME/SAE/ASEE Joint Propulsion Conference, San Jose, California, 14–17 July 2013, AIAA-2013-3855
5. Hearn HC Effect of duty cycle on catalytic thruster degradation. AIAA 81-4151
6. Goto D et al Endurance firing test results of the long life 1N hydrazine thruster. 47th AIAA/ASME/SAE/ASEE Joint Propulsion Conference, San Diego, 31 July to 3 August 2011, AIAA-2011-5772
7. Ikeda H et al (2012) Japanese new 1N monopropellant thruster qualification test results. Space Propulsion, Bordeaux
8. Fujii G et al (2014) Life evaluation test results of next generation long life 4 N hydrazine monopropellant thruster. Space Propulsion, Cologne
9. Ikeda H, Morita N et al The development result of second generation 1N and 4N monopropellant thrusters and the evaluation result of resistance to the thermal problems. ISTS-2013, Nagoya 2–9 June 2013, 2013-a-03
10. Goto D et al (2008) Research of the monopropellant thruster thermal Choke phenomena. Space Propulsion, Crete
11. Masuoka T, Masuda I, Kajiwara K, Yamada I Demise characteristics evaluation for melting promotion type tank. In: 49th AIAA/ASME/SAE/ASEE joint propulsion conference & exhibit, San Jose, 14–17 July 2013
12. Kajiwara K, Masuda I, Masuoka T, Fujii G, Saitoh N (2012) Basic design of reentry melting promotion type satellite's propellant tank. Space Propulsion, Bordeaux
13. Masuda I, Masuoka T, Kajiwara K, Yamada K (2013) Basic design and fundamental data acquisition test of reentry melting promotion type satellite's propellant tank. In: 49th AIAA/ASME/SAE/ASEE joint propulsion conference & exhibit, San Jose, 14–17 July 2013, AIAA-2013-3985
14. George C (1988) Marshall space flight center, NASA: material selection list for space hardware systems, MSFC-HDBK-527 Rev. F, Sept 30
15. Office of Mission Quality NASA: flammability, odor, and off gassing requirements and test procedures for materials in environments that support combustion, NHB 8060.1B and 1C
16. Masuda I et al (2014) Development of new satellite composite propellant tank. Space Propulsion, Cologne
17. Wuchererm EJ, Christofferson S, Reed B Assessment of high performance HAN-monopropellants. In: 36th AIAA/ASME/SAE/ASEE joint propulsion conference, Huntsville, 16–19 May 2000, AIAA 2000-3872

18. Anflo K, Crowe B In-space demonstration of an ADN-based Propulsion System. In: 47th AIAA/ASME/SAE/ASEE joint propulsion conference, San Diego, 31 July–3 August 2011, AIAA 2011-5832
19. Fukuchi A, Inamoto T et al (2008) HAN/HN-based monopropellant thrusters. In: 26th international symposium on space technology and science, Hamamatsu, 1–8 June 2008, 2008-a-34
20. Katsumi T, Kodama H et al (2009) Combustion characteristics of a hydroxylammonium nitrate based liquid propellant. Combustion mechanism and application to thrusters. Combust Explosion Shock Waves 45(4):442–453
21. Hatai K et al (2014) The research and development activities on HAN-based monopropellant thrusters in JAXA. Space Propulsion, Cologne
22. Matsuo T, Furukawa K, Nakamura T, Hori K, Sawai S, Azuma N, Shibamoto H (2010) Safety evaluation of HAN-based liquid propellant and its advantages applied to a spacecraft. IAA 50th anniversary celebration symposium in Nagoya – climate change/green systems, Nagoya, 30–31 Aug
23. Azuma N, Toshiyuki K et al (2012) Research and development of HAN (hydroxylammonium nitrate) based monopropellant thruster. Space Propulsion, Bordeaux

High Shear Rheometry of Unsymmetrical Dimethylhydrazine Gel

Mohan Varma

Abstract Gel propulsion systems promise several advantages over conventional solid, liquid, and hybrid propulsion systems and are being explored and developed for about three decades. The major focus, however, has been on monomethylhydrazine (MMH), unsymmetrical dimethylhydrazine (UDMH), and some hydrocarbon-based rocket fuels that are extensively used to prepare shear-thinning (thixotropic) gels for rocket and ramjet propulsion applications. The conversion of liquid fuel to a gelled state enables homogeneous suspension of metal powders into gel matrix. The approach improves propellant energetics on combustion and overall density specific impulse. Another important advantage is that such systems burn at a much reduced oxidizer-fuel ratio leading to reduction in net vehicle hardware weight. Gelled systems also promise considerable storage, handling, logistics, and transportation ease and do not slosh and pose engine restart problem under zero gravity conditions. The gel propellants preferred for rocket engine applications should exhibit shear-thinning behavior when injected into the combustion chamber and to assist in maintaining predictable mass flow rate. As such, these systems are delicately balanced and generally show a complex rheological and high shear flow behavior that is largely dependent on temperature, aging characteristics, etc. This paper aims to discuss key approaches for formulating UDMH-based gelled fuel systems and their mechanism of formation, their metallization using nanometer/micron-size metal powders besides explaining optimization processes. The performance characteristics, ignition, and combustion behavior have also been briefly described before giving an emphasis on low and high shear rate flow behavior of such gels.

M. Varma (✉)
Department of Space Engineering and Rocketry, Birla Institute of Technology (BIT), Ranchi-835215, Jharkhand, India
e-mail: mohanvarma@bitmesra.ac.in

Nomenclature

γ	Specific heat ratio
$\dot{\gamma}$	Shear rate
$\dot{\gamma}_c$	Corrected shear rate
$\dot{\gamma}_w$	Apparent shear rate
η_r	Reference viscosity
η_∞	Limiting viscosity
τ	Shear stress
τ_w	Apparent shear stress
τ_y	Yield stress
AA	Agar-agar (gellant)
C	Constant (Eq. 11)
ER	Equivalence ratio
F_m	Metal mass fraction in gel
g	Gravitational constant
HH	Hydrazine hydrate
I_s	Specific impulse
J	Mechanical equivalent of heat
K	Consistency index
L	Length of the capillary
M_c	Mean molecular mass of combustion products
n	Thixotropic (pseudoplastic) index
n_c	Capillary constant (Eq. 8)
P_c	Pressure in combustion chamber
P_e	Pressure at nozzle exit plane
Q	Volumetric flow rate
R	Universal gas constant
R_c	Radius of capillary
T_c	Temperature in combustion chamber
X	Oxidizer-fuel ratio
α_k	Kinetic energy correction factor
$\Delta H_{c(e)}$	Heat of combustion (experimental)
$\Delta H_{c(o)}$	Heat of combustion (theoretical assuming complete oxidation)
ΔP	Effective pressure
η_{ap}	Apparent viscosity
ρ_{fg}	Density of fuel gel
ρ_m	Density of metal
ρ_{og}	Density of oxidizer gel
ρ_p	Density of propellant

1 Introduction

The magnificent space achievements of the past four decades have used chemical propulsion systems. The major share of accomplishments were achieved using solid and liquid propulsion systems on different launch vehicles to place satellites of various categories into polar and geosynchronous orbits, onto interplanetary missions, and for a variety of missile development programs. Today, conventional chemical rockets are being successfully used to deliver thrust levels of few Newton (N) to thousands of kN. The advancements in solid, liquid, and to some extent hybrid propulsion systems meet the present-day mission requirements; however, future missions carrying larger payloads and covering greater distances pose several challenges.

The limitations of achievable specific impulse with solid and liquid rocket motors, storage and logistics of hazardous liquid bipropellant systems, geysering and slosh issues, combustion efficiency, and optimum propellant utilization led researchers to look for propulsion systems that may provide the operational benefits of conventional systems and promise a higher density specific impulse. A comprehensive project that attempted to address and assess the feasibility of a gelled propulsion system based on unsymmetrical dimethylhydrazine (UDMH) and red fuming nitric acid (RFNA) bipropellant systems was started in the late 1970s. The successful completion of this technology demonstrator with voluminous experimental data covering identification of potential gelling agents, nonintrusive transmittance measurement approach to determine gelation time, standardization of metallization process of gels, storage characteristics, performance evaluation of virgin and metallized gels, ignition and combustion characteristics, and exhaustive study on rheological behavior of un-metallized and metallized fuel systems and gelled oxidizer under a wide range of shear rate was completed [1] in 1986.

Zurawski [2] in the late 1980s and subsequently Palaszewski [3–6] at NASA Lewis Research Center conducted some important research work on assessment of launch vehicle performance using metallized, cryogenic, and gel propellants and projected significant launch mass reductions for future missions. Later on, many countries engaged in development of missiles and launch vehicle programs initiated research and development works in this emerging area of propulsion. Several important research programs in formulation and processing, theoretical and experimental performance evaluation, ignition and combustion behavior, atomization and modeling, rheological and flow characterization, and design and flight testing of rocket engines using a variety of gelled fuel systems have been conducted. Natan and Rahimi [7] and Pein [8] have reviewed the available literature. This chapter aims to give a brief background and salient developments in research work done in this fast developing technology that is close to replacing some of the existing propulsion systems in specific and challenging missions. Significant advances have been made in addressing the current problems by academic and research engineers since successful flight tests of gel propulsion systems by TRW, USA, and Bayern-Chemie in Germany.

2 Formulation of Gel Propellants

Most liquid rocket fuels and oxidizers can be converted into a gelled state by using suitable gelling agents. Gel propellants generally contain a base fuel or oxidizer, a compatible gelling agent at critical concentration level and additional additives like polar activators, surfactants, or stabilizers to tailor stability, storage, ignition, and rheological characteristics. The gelling agents commonly used can be categorized as particulate or chemical gelling agents that can further be of two types: inorganic such as silica and bentonite clays and organic gellants like a variety of cellulose derivatives, pectin, polysaccharides, etc. Inert chemicals when used as gellants in large concentrations do adversely affect the performance of parent bipropellant systems that can be compensated by adding low-molecular-mass metal powders like aluminum, magnesium, beryllium, and boron in the gels that release high energy on combustion. Efforts have also been made to synthesize gellants [9] that can work at very low concentrations.

The gelled propellants are delicately balanced systems and minor changes in quality and specifications of chemicals used; processing and storage conditions can significantly alter their overall characteristics. The optimization of processing conditions [10] has been found to be crucial to obtain gelled systems with predictable consistency in gel propellant production. Carbon dioxide present in the air may also poison the gel bonds leading to deterioration in storage stability. Some propellant gels are easy to prepare, and the two ingredients can just be mixed under ambient conditions with a laboratory stirrer, whereas in case of nonpolar fuels, high dispersion equipment and precise temperature control may be required. The physical state of gellant and particle size in case of dispersed solids normally leads to selection of roll mills, helical blade mixers, dispersers, dissolvers, and ultrasonic agitators including resonant acoustic devices.

The storable rocket monopropellants, bipropellants (fuel and oxidizers) [7, 8], and cryogenic systems [5] have been successfully gelled and reported in literature. The main interest centered on hydrazine and its derivatives [9] (Table 1) and RFNA [11] as the combination was employed in many operational propulsion systems. These propellants being highly toxic and carcinogenic, other safer fuels like 2-azido-N,N-dimethyl cyclopropanamine (ADMCPA), 2-azido-N,N-dimethylethanamine (DMAZ), etc., were also explored along with hydrocarbon mixtures like RP-1, JP-4, Jet A-1, and JP 10. It is to be noted that gellant concentration in fuel or oxidizer must be within a critical range to exhibit the desired shear-thinning behavior, i.e., the thixotropic character that is important for rocket engine application as the gel needs to flow through the feed system and injector elements to reach the combustion chamber. Oxidizer gels generally have stability, safety, and storage problems and are considered only in situations where toxic fluids have to be stored in close proximity of personnel as on naval warships, etc. Further, since metal powders are only incorporated in fuel gels, the gel of an oxidizer with an inert gellant is not desirable as it adversely affects the overall performance of propulsion system.

Table 1 Gelling ability of gellants in case of HH, MMH, and UDMH fuels

Sl. no.	Gellant	Liquid fuel		
		HH	MMH	UDMH
1	Cab-O-Sil	x	x	(5, 45)[a]
2	Pectin	(6, 10)[a]	x	x
3	12.5 % of aq. solution of PAA	(1.25, 240)	x	(0.25, 30)
4	PVA	(1.25, 120)	x	x
5	LS1MC	x	(9, 27)	(4.48, 20)
6	LS2MC	x	(11, 30)	(5, 8)
7	HSMC	x	(8, 180)	(2, 10)
8	CMC	(5, 24 h)	x	x
9	HEC	(5, 60)	(7, 45)	(7, 45)
10	HPMC100k	x	(2.75, 12)	x
11	ASPAA-II	(0.50, 1)	(1.75, 1)	x

[a]The first quantity in parentheses shows mass % of gellant, and the second one denotes gelation time at 298 K; x – no gelation occurs till 24 h using 5 mass % of gellant

The oxidizer gels of red fuming nitric acid (RFNA), IRFNA (inhibited), Russian AK 20 type oxidizer, chlorine pentafluoride, hydrogen peroxide, and liquid oxygen have been formulated in the past using sodium silicate and colloidal/fumed silica as gellants. The oxidizer gelation may have disadvantages on many counts. Gelation of hydrogen peroxide is known to accelerate its decomposition that increases the compressibility of gel and may lead to flow distortions in the gel propulsion system. Silica as gellant may react with hydrofluoric acid used as corrosion inhibitor in IRFNA that is highly undesirable. RFNA gelation is an exothermic process and generally leads to substantial loss of dissolved nitrogen tetroxide in nitric acid. The oxidizer gelation of RFNA with sodium silicate is found to reduce the optimum specific impulse of UDMH-RFNA system by nearly 5 % that is highly detrimental from performance viewpoint.

Photomicrographic and scanning electron microscopic studies are generally conducted to understand the mechanism of gel formation that largely depends on the fuel properties and physicochemical characteristics of gellant used. Cellulose and its derivatives first swell by absorbing the fuel and then either coalesce or entangle to form a three-dimensional network to imbibe the liquid fuel to form a stable gel. The gels on agitation release the imbibed liquid fuel and start flowing freely and re-gel if left undisturbed for a definite period, normally referred as regelation time that is dependent on temperature, applied shear force, diameter of the storage container, particle size of gellant used, etc. Nonintrusive techniques can be used to determine precise gelation time using visible spectrophotometers that can record percentage transmittance. The time values tend to stabilize as gelation process is completed.

Particulate gelling agents such as colloidal silica, acetylene black, finely divided carbon or charcoal, and natural and synthetic hydrophilic polymers may form gels through weak physical forces, forming a skeleton that constitutes the colloidal structure. Chemical gelling agents of inert nature have been found successful to

various gel hydrocarbon- and hydrazine-based liquid fuels [7, 8]. The gel matrix of the oxidizer like RFNA gelled with sodium silicate is achieved through an exothermic chemical reaction possibly leading to the formation of hydrosilicic acid that facilitates the formation of shining three-dimensional networks.

Metallization of fuel gels can be easily done by nanometer or micron-size metal powders of low-molecular-mass metals like Al, Mg, Be, and B, in required concentrations. The dispersion of nano-aluminum particles in fuel itself shows a gelling effect, and the requirement of chemical gellant gets significantly reduced. The heterogeneous fuel gels with different degree of metallization can be prepared by selecting a suitable methodology, dispersion equipment, operating conditions, and mixing and storage environment. The gel propellant production is influenced by processing conditions like gellant concentration, particle size, mixing time, temperature, dissolver velocity, timing, and manner of induction of powders (gellant/metal) in mixer to avoid agglomerate formation, etc., and these must be carefully optimized to produce batches with consistent quality. Innovative processing methods using resonant acoustic technology are being developed and tested to avoid complexities of internal mixing hardware such as impellers, helical or sigma blade mixers, baffles, or wipes and also to reduce wastage of material and cleaning time.

3   Performance Evaluation

The theoretical performance evaluation of gelled and metallized UDMH-RFNA system [12, 13] is reported over a wide range of oxidizer-fuel ratio to assess losses due to addition of gelling agent like methylcellulose (MC) in fuel and overall gains in specific impulse due to incorporation of metal powders like Al and Mg up to a level of 50 mass % assuming equilibrium and frozen flow conditions. Typical results for various fuel compositions and optimum O/F ratio corresponding to maximum specific impulse have been presented in Table 2. It can be observed that I_s of the gelled system gets educed in comparison with the virgin bipropellant system (Figs. 1 and 2). The I_s values are then found to increase up to 40 mass % metal loading and decrease thereafter possibly due to reduced availability of working fluid for expansion. The maximum gain of 3.1 % in I_s is achieved at aluminum concentration of 40 mass % in the fuel gel at a nominal chamber pressure of about 2.07 MPa. This appears to be fairly attractive as even 1 % increase in I_s can increase the range of an intercontinental ballistic missile (ICBM) by more than 7 %.

The variation in specific impulse with metal incorporation in gels may be explained by the equation:

$$I_s = \left[\left\{ \frac{2J}{g} \frac{(\gamma R T_c)}{(\gamma - 1)\overline{M}_c} \left[1 - \frac{P_e}{P_c} \right]^{\frac{(\gamma-1)}{\gamma}} \right\} \right]^{1/2} \tag{1}$$

Table 2 Composition of metallized UDMH-MC fuel and O/F ratio corresponding to maximum specific impulse at $\approx$ 20 atm

| Sl. no.	Oxidizer mass fraction (RFNA)	Fuel composition by mass fraction			Optimum O/F ratio (E. R.)[a]		Max. specific impulse (s)	
		UDMH	MC	Metal	Equilibrium flow	Frozen flow	Equilibrium flow	Frozen flow
1	HNO$_3$ (0.845) N$_2$O$_4$ (0.134) H$_2$O (0.020)	1.000	–	–	2.7259 (1.2)	2.4856 (1.3)	238.9	232.9
2	-do-	0.95712	0.04288	–	2.8404 (1.15)	2.4555 (1.3)	237.9	231.9
3	-do-	0.86141	0.03859	0.1 (Al)	2.4265 (1.25)	2.1246 (1.4)	239.7	233.5
4	-do-	0.76570	0.03430	0.2	1.9946 (1.4)	1.7140 (1.6)	241.2	235.5
5	-do-	0.66998	0.03002	0.3	1.3634 (1.85)	1.3225 (1.9)	243.5	237.9
6	-do-	0.57427	0.02573	0.4	0.9315 (2.45)	0.9974 (2.3)	246.3	240.5
7	-do-	0.47856	0.02144	0.5	0.9944 (2.15)	1.0197 (2.1)	246.1	238.9
8	-do-	0.86141	0.03859	0.1(Mg)	2.5097 (1.2)	2.0998 (1.4)	238.5	231.1
9	-do-	0.76570	0.03430	0.2	2.0314 (1.35)	1.6162 (1.65)	239.5	232.1
10	-do-	0.66998	0.03002	0.3	1.5383 (1.6)	1.1994 (2.0)	240.5	232.7
11	-do-	0.57427	0.02573	0.4	1.0386 (2.1)	0.9634 (2.25)	241.6	232.0
12	-do-	0.47856	0.02144	0.5	0.8938 (2.2)	0.8514 (2.3)	240.0	228.5

[a]Equivalence ratio
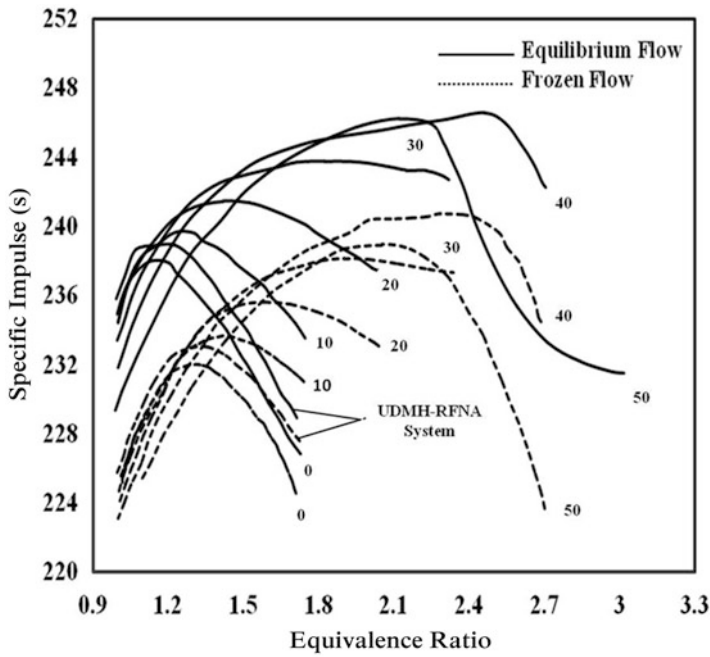
Fig. 1 Specific impulse for aluminized (UDMH-MC) gelled fuel with RFNA oxidant at different chamber pressures
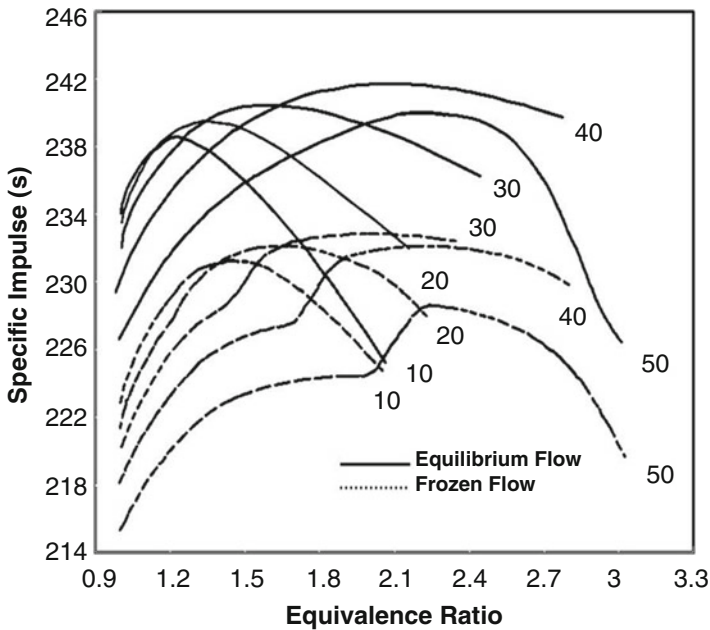

Fig. 2 Specific impulse for magnesium-containing UDMH-MC gelled fuel with RFNA

The combustion of light metals generally produces combustion temperature higher than liquid fuels because of formation of metal oxide in condensed phase which is assisted by hydrogen content of the fuel. It is further observed that the optimum ER significantly increases with metallization. An increase of 104.2 % and 75 % in case of 40 mass % of each Al- and Mg-loaded fuels, respectively, is estimated with respect to parent UDMH-RFNA system (Table 2). Beyond this point, ER decreases in case of 50 mass % aluminized gel but further increases for the same concentration for magnesium-containing gel. This is expected as the oxygen requirement for oxidation of Mg is two third of that of Al. The combustion product profiles of metallized gels show that a part of Mg goes unreacted, whereas the entire Al is found to be consumed. This significant increase in ER, i.e., drastic reduction in oxidizer requirement for metallized fuels, seems to be a very attractive feature that eventually would lead to enormous reduction in oxidizer storage tank volume and total hardware weight cutting the rocket size and rendering the propulsion system more economical.

The density specific impulse, the product of I_s and propellant bulk density ρ_p, can be calculated for different gelled and metallized systems at different oxidizer-fuel ratios. The ρ_p for metallized gelled systems can be computed using the expression:

$$\rho_p = \frac{X + 1}{\left(\frac{X}{\rho_{og}}\right) + \frac{1 - F_m}{\rho_{fg}} + \frac{F_m}{\rho_m}} \tag{2}$$

The results on computed propellant bulk density and density specific impulse corresponding to optimum O/F ratio for virgin, gelled, and metallized UDMH-RFNA systems under shifting equilibrium condition are summarized in Table 3. It is observed from the data that ρ_p increases continuously for aluminized systems

Table 3 Dependence of density specific impulse on metal loading of gelled UDMH-RFNA systems in equilibrium flow at optimum O/F ratio

Sl. no.	System	Optimum O/F ratio	Propellant bulk density (kg/m^3)	Specific impulse (s)	Density specific impulse (N.s/m^3 × 10^3)
1	UDMH	2.7259	1179.9	238.9	2764.28
2	UDMH-MC	2.8404	1190.3	237.9	2776.97
3	UDMH- MC-10 % Al	2.4265	1199.6	239.7	2819.85
4	UDMH- MC-20 % Al	1.9945	1210.5	241.2	2863.27
5	UDMH- MC-30 % Al	1.3634	1208.6	243.5	2886.04
6	UDMH- MC-40 % Al	0.9315	1227.5	246.3	2964.88
7	UDMH- MC-50 % Al	0.9944	1304.4	246.1	3148.06
8	UDMH- MC-10 % Mg	2.5097	1195.7	238.5	2796.61
9	UDMH- MC-20 % Mg	2.0314	1191.4	239.5	2798.23
10	UDMH- MC-30 % Mg	1.5383	1184.6	240.5	2793.88
11	UDMH –MC-40 % Mg	1.0386	1173.7	241.6	2780.83
12	UDMH- MC-50 % Mg	0.8938	1203.7	240.0	2833.02
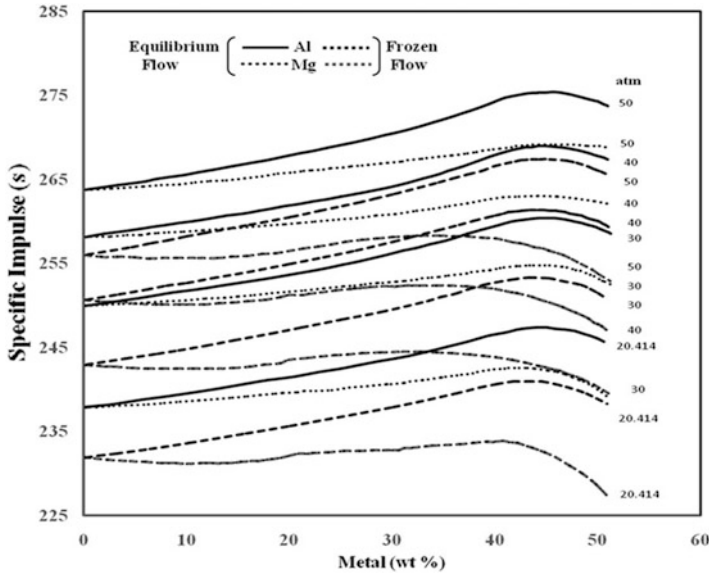
Fig. 3 Dependence of specific impulse on metal content of (UDMH-MC)-RFNA propellant as a function of chamber pressure

except at 30 mass % Al level where it marginally decreases probably because of heavy reduction (approx. 32 %) in dense oxidizer is not being compensated even by incorporation of another 10 mass % of metal.

The variation of I_s with metal (Al & Mg) loading at different chamber pressures for (UDMH-MC)-RFNA system under equilibrium and frozen flow conditions has been shown in Fig. 3. The curves exhibit a steady increase in specific impulse with chamber pressure in both the flow conditions at all gel metal loadings. It is also seen that aluminized compositions deliver higher performance in comparison with magnesium-containing gels. The increasing loading of metals in the gels is expected to increase the overall energetics of the system; however, the results indicate that the optimum performance can only be obtained around 45 mass % of metal concentration even at higher operating chamber pressures. An analysis of results reveals that a maximum gain of about 4 % in equilibrium I_s is obtained at a chamber pressure of 5.07 MPa (50 atm) corresponding to nearly 45 mass % Al loading over that of parent bipropellant system. The maximum theoretical performance may be obtained at metallization levels >40 mass %; however, processing becomes increasingly difficult and flow characteristics unacceptable for propulsion application. The correlation of propellant bulk density of metallized gelled propellants with equilibrium specific impulse is shown in Fig. 4 to have an overall assessment of performance gains for such systems.
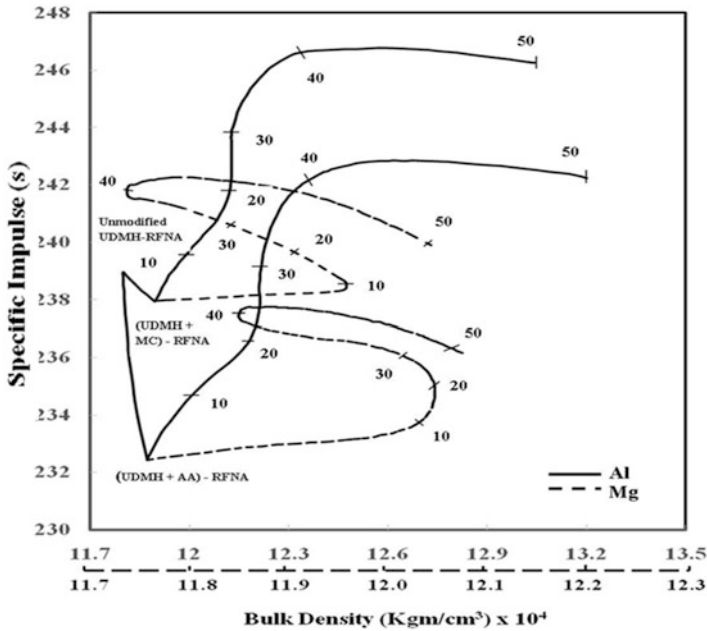
Fig. 4 Correlation of bulk density of metallized gelled propellants with equilibrium specific impulse

4 Ignition and Combustion

The spontaneous ignition and efficient combustion is highly desirable for satisfactory performance of liquid rocket engines. As the physicochemical properties of gelled and metallized non-Newtonian systems are significantly different to that of conventional liquid fuels and oxidizers, the mixing, atomization, diffusion, and chemical reaction rate are observed to be markedly different and complex. The ignition and combustion behavior of such systems have been studied [14–16] by some researchers with a view to understand the departure in involved mechanism with respect to standard bipropellant systems.

Ignition delay values of gelled and metallized systems using storable oxidizer at different O/F ratio are found to be significantly higher than corresponding virgin bipropellant system. The viscous gel resists the mixing, and subsequent chemical reactions are delayed. The gelled fuels if injected in a combustion chamber at higher pressures along with the oxidizer lead to ignition delays that are very close to parent bipropellant system. It is interesting to note [16] that minimum ignition delay for gelled system is observed at O/F ratio that corresponds to maximum specific impulse. Metallized fuels do show a significant departure, and minimum ignition delay is obtained at reduced O/F ratio with increase in metal content of the gel. The

Table 4 Heat of combustion of gelled propellants

Sl. no.	System	Heat of combustion (kJ/g)	
		Experimental, $\Delta H_{c\,(e)}$	Theoretical, $\Delta H_{c\,(o)}$
1	UDMH	32.88	32.95
2	UDMH-MC	37.30	32.88
3	UDMH-MC-10 % Al[b]	39.06	41.10
4	UDMH-MC-20 % Al	42.68	51.33
5	UDMH-MC-30 % Al	45.39	64.38
6	UDMH-MC-40 % Al	46.13	81.82
7	UDMH-MC-10 % Mg[c]	38.16	41.19
8	UDMH-MC-20 % Mg	39.37	51.27
9	UDMH-MC-30 % Mg	40.34[a]	63.88
10	UDMH-MC-40 % Mg	41.38[a]	80.29

[a] Extrapolated from available data
[b] Average particle size 20 μm; distributor MEPCO, Madurai, India
[c] Average particle size 200 μm; distributor Chemporium, Bombay, India

twin jet combustor experiments [17] have shown that spontaneous ignition can be achieved for gelled and metallized fuel systems.

The combustion behavior of gelled and metallized propellants widely varies with the nature of oxidizer, content and particle size of metal powder incorporated, and operating conditions. The oxidizer injection on the surface of semisolid gel leads to surface combustion where fuel component of the gel is spontaneously consumed; the combustion process leaves behind a large percentage of unreacted metal that increases with a degree of metallization. The results on heat of combustion (Table 4) obtained at an inert pressure of approx. 2.07 MPa using a bomb calorimeter show that a large part of metal imbedded in the matrix is consumed up to a metal loading of 20 mass %, and thereafter unreacted metal content progressively increases. The computed results on heat of combustion, assuming complete metal combustion, show significantly higher values tabulated as $\Delta H_{c\,(o)}$. Much better combustion behavior is observed at higher metal loadings when the heterogeneous gels are injected through fine injector elements in to the combustion chamber, and the fine metal particles are allowed to combust in the flame established by the parent bipropellant system. The combustion chambers with larger characteristic length facilitate enhancement of overall combustion efficiency.

The metal oxidation during the combustion process takes place by two pathways [16]: first by direct oxidation into metal oxide by oxidizing species furnished by the oxidizer itself and second by water vapors produced during reaction of the fuel and oxidizer. It has been observed that oxide formation in case of aluminum occurs mainly by water vapor-metal interaction and marginally due to direct oxidizer-metal reaction, whereas the oxidation of magnesium is predominantly affected by the oxidizer.

5 Rheological Behavior

The gelled propellants are non-Newtonian fluids and exhibit a complex flow behavior that must be understood for successful use in operational rocket engines. In addition to the factors that influence the viscosity and flow behavior of storable liquid bipropellant systems, gel propellants are susceptible to major changes in their flow properties on aging, thermal cycling, variation in storage conditions, adverse transportation conditions, etc. The rheological behavior of propellant gels must be understood in two different shear rate regions, one at low shear rates ($\leq 10^2$ s^{-1}) for characterization of gels, maintaining quality control of batches produced and assessing yield stress to ascertain stability of the gels. The fuel gels must possess adequate yield value to incorporate varied concentrations of metal powders and yet remain mechanically stable for long storage times. The metal particles imbedded in the gel formulation tend to shear the system under the influence of gravity, and this may deteriorate the homogeneity of the gel during storage. A high yield value besides preventing this problem also checks syneresis/oozing of base fuel and gel dispersion to minor accelerations.

The flow characteristics of gelled propellants under high shear rates ($\geq 10^6$ s^{-1}) that are normally encountered in propellant feed systems and injector elements are of critical importance in view of their influence on design of various elements of propulsion systems like tanks, feed system, injector design, etc. The advanced propulsion system requires high degree of combustion efficiency, and the gel propellants employed must exhibit thixotropic (shear-thinning) behavior. The shearing of the gel at high shear rates must bring the viscosity of the gel close to that of the parent fuel in order to bring desired level of atomization and mixing soon after entering the combustion chamber of the rocket engine. Once the ignition is achieved smoothly, remaining mass of gel injected in the combustor will vaporize instantly at elevated flame temperature.

Two types of viscometers – rotating spindle and cone and plate types [18–20] – have generally been used to study low shear rate regimes to characterize gels and to assess effect of gellant concentration, temperature, metal concentration, viscosity-time history during gelation process, etc. The reliable equipments need to be used for accurate results. The viscometers with stationary rotating spindles and inappropriate geometries of spindles must be avoided in study of viscous drag measurements, as these may lead to migration of low viscosity liquid in the gel close to the drag measuring element leading to erroneous results. T-bar spindles mounted on a slowly traveling viscometer present a better option as these helically moving thin bars cut the gel samples at a fresh place each time to record accurate apparent viscosity values.

High shear fluid flow measurements [10] can be done either by company-manufactured single- or double-barrel rheometers that can eject specific volume of gel through preselected die; the viscosities can be calculated at a given shear stress or shear rate using the prescribed software or by fabricating a customized
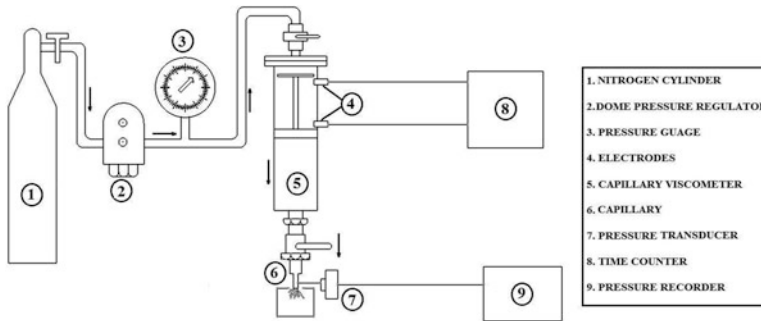
Fig. 5 Schematic representation of capillary flowmeter assembly

orifice or capillary flowmeter [21, 22] with appropriate sensors and measuring instrumentation. A typical experimental setup has been shown in Fig. 5.

5.1 Gel Characterization at Low Shear Rate

The freshly prepared gels or aged samples can be subjected to low shear rate studies in order to obtain an experimental rheogram that can indicate the rheological character based on its fluidity. Non-Newtonian flow has been dealt in various textbooks [23, 24], and relevant coverage has been given in related review articles [7, 8]. The log-log plot of shear rate versus shear stress normally gives a straight line with a slope "n," which has a value <1 for pseudoplastic fluids exhibiting a shear-thinning character. Newtonian fluids show this value to be unity; the more the departure of "n" value from unity, the higher the non-Newtonian character of the fluid. Power law can be used to determine the values of "n" and "K," for non-Newtonian apparent viscosity, η_{ap}.

$$\tau = K\dot{\gamma}^{n} \tag{3}$$

or

$$\eta_{ap} = K\dot{\gamma}^{n-1} \tag{4}$$

Tables 5 and 6 show the variation of "n" and "K" values with temperature and degree of metallization for a typical UDMH-MC gel. It can be inferred that value of "n" increases but "K" falls with rise in temperature. The gel is seen to be a highly pseudoplastic material at low temperatures, while it tends to approach Newtonian character at higher ambient temperature. The results also indicate that "n" is less sensitive to temperature than "K" which registers a severalfold decrease. Similar results are also obtained on metallization where "n" decreases and "K" increases

Table 5 Variation of pseudoplastic and consistency indices with temperature

Temperature (K)	Thixotropic index, n	Consistency index, K
273	0.655	22.682
278	0.710	18.819
283	0.854	12.231
288	0.848	9.481
293	0.878	7.365
298	0.869	3.799
303	0.897	3.072

Table 6 Dependence of pseudoplastic and consistency indices on the degree of metallization of UDMH-MC gel at 298 K

Metal	Metal (mass %)	Thixotropic index	Consistency index
Al	0	0.869	3.799
	5	0.765	10.329
	10	0.576	19.601
	20	0.560	23.474
	30	0.659	23.773
Mg	5	0.708	19.880
	10	0.744	19.595
	15	0.692	21.224
	20	0.716	22.841

substantially at a given temperature. It is also noted that "*n*" is less prone to change on metallization than "*K*." The value of "*K*" is strongly dependent on particle size of metal powder used.

The yield stress of gel propellant can be determined by using Casson's equation [25]:

$$\eta_{ap}{}^{1/2} = \eta_{\infty}{}^{1/2} + \tau_y{}^{1/2}\dot{\gamma}^{-1/2} \tag{5}$$

$$\tau^{1/2} = \tau_y{}^{1/2} + \eta_{\infty}{}^{1/2}\dot{\gamma}^{1/2} \tag{6}$$

The square roots of experimental results of variation of "*τ*" with incremental increase of '$\dot{\gamma}$' can be plotted to get straight line whose slope and intercept give the limiting high shear viscosity and yield stress values on squaring. The typical results for UDMH-MC gel at different ambient temperatures are shown in Table 7. The yield stress values for various degree of metallization for aluminized and magnesium-containing gels at 298 K are given in Table 8. It may be noticed that aluminized gels exhibit higher yield values at increased metal loading in comparison with magnesium gels. Yield stress has been found to be strongly dependent on metal particle size used in the formulation of gels.

Table 7 Effect of temperature on high shear limiting viscosity and yield stress for UDMH-MC gel

Temperature (K)	η_∞ (MPa.s)	s (in arbitrary unit)
273	7.832	3.424
278	7.566	2.272
283	7.078	0.719
288	5.290	0.634
293	4.595	0.346
298	2.440	0.139
303	2.272	0.048

Table 8 Yield stress values for UDMH-MC metallized gels at 298 K

Al (mass %)	τ_y (in arbitrary unit)	Mg (mass %)	τ_y (in arbitrary unit)
0	0.138	0	0.138
5	2.092	5	3.147
10	7.422	10	2.665
20	10.167	15	2.323
30	10.797	20	4.118

The rheological characterization of propellant gels involves the tracing of up (where shear rate is incrementally increased) and down (where shear rate is reduced in steps) curves of "η_{ap}" versus '$\dot{\gamma}$' to construct a rheogram. It may be noted that these curves do not superimpose each other, and an area is enclosed between them to form a loop known as hysteresis loop. The area encompassed within the hysteresis loop reflects the extent of thixotropic character of the gel; the larger the area, the higher is the thixotropic index and departure from the Newtonian behavior. The gels normally show reduced thixotropy at higher temperatures, but this character increases with higher degree of metallization [18].

5.2 High Shear Rheometry

The propellant gels selected for rocket propulsion are thixotropic in nature, and their viscosity will drop when subjected to high shear rates. The thixotropic fluids are time dependent in nature, i.e., the apparent viscosity is also dependent on the duration of shearing at a given shear rate. This aspect is crucial for precise design of the feed system and injector details to ascertain the desired level of atomization of propellant gel and to obtain the expected Sauter mean diameter of injected droplets. The research work done in this area is very limited, and few studies reported in literature used water gels [26, 27] that are poor substitutes to actual propellant gels. The maiden effort on rheological characterization and flow behavior of an oxidizer gel [21] at high shear rates revealed that the apparent viscosity value of the gel can be brought down from the range of several Pascal seconds (Pa.s) to few mPa.s, and a free-flowing liquid oxidizer could be collected in the receptor tank. The nominal capillary diameters in the range of 1.4–3.0 mm were selected in the study using

an effective pressure between approx. 0.2–1 MPa. Higher injection pressures and smaller diameter of injector elements are expected to reduce the apparent viscosity values to that of the parent oxidizer.

The inherent rheological behavior of the gels has strong influence on the spray characteristics and atomization process during jet impingement in the combustion chamber. As such, it all depends on the final drop in viscosity in the exit plane of injector that governs and controls the extent of atomization, droplet diameter, and rapid mixing to achieve spontaneous ignition and higher combustion efficiency. Higher viscosities of gel fragments and droplets entering the combustion chamber lead to improper mixing/diffusion and cause delayed ignition. This may eventually result in an extended characteristic length of the combustion chamber required for complete combustion of metallized gels, or else two-phase flow losses are likely to nullify the advantage expected with such systems.

The experimental study on UDMH-MC gel system was conducted using the test setup of capillary flowmeter (Fig. 5). The calibration of capillaries for actual diameter was done with the help of well-known Poiseuille equation:

$$\eta = \frac{\pi \, \Delta P \, R_c^{\,4}}{8QL} \tag{7}$$

The calibration can be done with fluids of known viscosity, and it ensures accuracy of results obtained with non-Newtonian fluids as minor variation may cause serious inaccuracies in measurement of "η_{ap}." Besides this, certain other important corrections are required to obtain accurate results. End or entrance effect correction can be equated with an increase in effective length of the capillary from L to L + ΔL where $\Delta L = n_c \, R_c$. The effective shear stress can thus be given by:

$$\frac{\Delta P \, R_c}{2 \, (L + \Delta L)} = \frac{\Delta P \, R_c}{2 \, (L + n_c \, R_c)} \tag{8}$$

The value of "n_c," a constant range between 6 and 12, and its value may approach to zero when length to diameter ratio of capillary is very high, viz., 200/1 or greater.

All applied pressure is not utilized in shearing the sample since a considerable part of it imparts kinetic energy to the fluid as it enters the capillary. The actual pressure, ΔP, can be computed by:

$$\Delta P' = \Delta P - \frac{Q^2 \rho}{\alpha_k \pi^2 R_c^{\,4}} \tag{9}$$

For non-Newtonian flow that can be represented by power law equation, kinetic energy correction factor can be determined by:

$$\alpha_k = \frac{(4n + 2) \, (5n + 3)}{\left[3(2n + 1)^2 \right]} \tag{10}$$
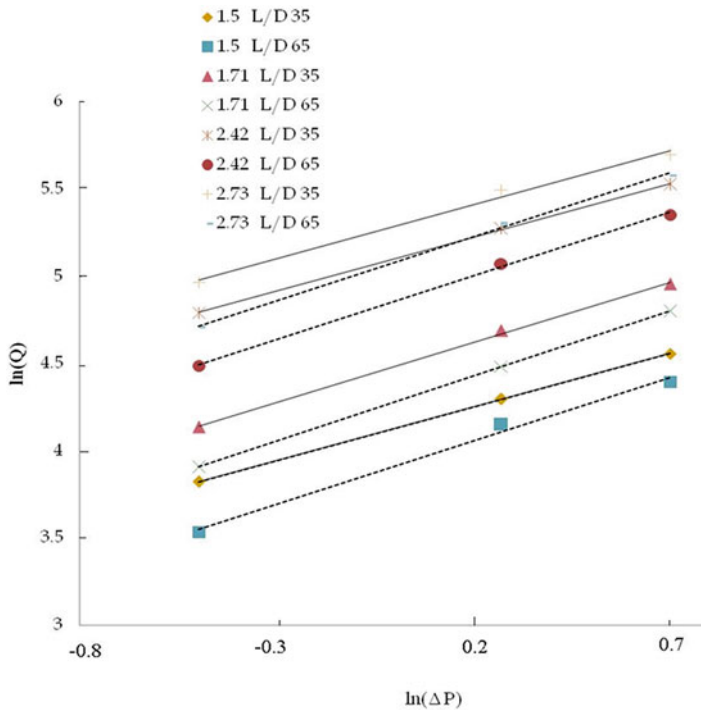
Fig. 6 Dependence of volume flow rate on effective pressure for UDMH-MC gel

The term $4Q/(\pi R_c^3)$ represents rate of shear for Newtonian flow, and a shear rate correction is done by multiplying the Newtonian value by a factor $(3+ b/4)$ where "b" is the slope of straight line obtained by plotting $\ln 4Q/ (\pi R_c^3)$ against $\ln (\Delta P' R_c /2 L)$.

The results of flow rate of UDMH-MC gel for four capillary diameters, 1.5 mm, 1.71 mm, 2.42 mm, and 2.73 mm at two L/D ratios, i.e., 35 and 65 as a function of effective pressure, are shown in Fig. 6 that reflects a linear variation according to equation:

$$\ln\ Q = n.\ln\ \Delta P + C \tag{11}$$

The calculated values of thixotropic index and constant are summarized in Table 9. The apparent shear rate, $\dot{\gamma}_w$, and apparent shear stress, τ_w, at capillary wall can be calculated from the measured flow rates and flow pressures using the following equations:

$$\dot{\gamma}_w = \frac{4Q}{\left(\pi R_c^3\right)} \tag{12}$$

$$\tau_w = \frac{\Delta P R_c}{2L} \tag{13}$$

Table 9 Dependence of constants of Eq. 11 on capillary diameter and length

Sl. no.	Capillary diameter (mm)	N	C (cm^3.s^{-1})
1	1.5 (35)[a]	0.614	15.12
2	1.71 (35)	0.687	18.23
3	2.42 (35)	0.614	39.89
4	2.73 (35)	0.618	47.76
5	1.5 (65)	0.727	9.37
6	1.71 (65)	0.746	12.95
7	2.42 (65)	0.727	24.10
8	2.73 (65)	0.733	29.76

[a]Figures in the parentheses indicate L/D ratio

Table 10 Effect of pressure on volume flow rate of UDMH-MC Gel at 298 K

Sl. no.	Capillary diameter (mm)	ΔP (MPa)	Q (cm^3.s^{-1})	τ_w (MPa)	$\dot{\gamma}_W \times 10^4$ (s^{-1})
1	1.5 (35)[a]	0.595	45.66	49.20	13.781
		1.284	73.46	92.62	22.172
		1.973	95.26	142.35	28.750
2	1.71 (35)	0.595	62.5	39.74	12.733
		1.284	108.74	85.79	22.151
		1.973	141.77	131.85	28.881
3	2.42 (35)	0.595	120.41	39.55	8.654
		1.284	194.79	85.39	14.000
		1.973	251.09	131.22	18.045
4	2.73 (35)	0.595	143.34	38.66	7.176
		1.284	243.73	83.47	12.202
		1.973	297.3	128.28	14.884
5	1.5 (65)	0.595	34.26	24.54	10.34
		1.284	63.33	52.98	19.112
		1.973	81.05	81.41	24.461
6	1.71 (65)	0.595	49.65	22.70	10.114
		1.284	88.49	49.02	18.027
		1.973	121.43	75.33	24.736
7	2.42 (65)	0.595	88.8	22.35	6.382
		1.284	159.59	48.26	11.47
		1.973	211.3	74.17	15.187
8	2.73 (65)	0.595	110.59	22.18	5.536
		1.284	200.49	47.90	10.037
		1.973	264.59	73.61	13.246

[a]Figures in the parentheses indicate L/D ratio

The results showing the effect of applied pressure on volume flow rate of UDMH-MC gel at 298 K along with the computed values of τ_w and $\dot{\gamma}_w$ are presented in Table 10. It can be observed that the flow rates increase with capillary diameter and applied pressure. Finally, the corrected shear stress and shear rate calculated are used to determine apparent viscosity of gel obtained for different capillary

Table 11 Dependence of apparent viscosity of UDMH-MC gel on shear rate

Sl. no.	Capillary diameter (mm)	Corrected shear stress τ_a (MPa)	Corrected shear rate $\dot{\gamma}_c \times 10^4$ (s^{-1})	Apparent viscosity η_{ap} (mPa. s)
1	1.5 (35)[a]	37.66	12.517	67.9
		81.67	20.139	62.0
		125.70	26.114	65.7
2	1.71 (35)	35.16	11.565	60.0
		76.27	20.12	52.9
		117.40	26.233	57.2
3	2.42 (35)	35.01	7.86	114.3
		75.95	12.716	95.9
		116.90	16.391	100.8
4	2.73 (35)	34.30	6.518	130.5
		74.42	11.083	103.5
		114.50	13.519	119.0
5	1.5 (65)	22.51	9.65	44.4
		48.96	17.837	36.9
		75.41	22.83	41.4
6	1.71 (65)	20.94	9.439	39.6
		45.56	16.825	36.0
		70.19	23.086	37.1
7	2.42 (65)	20.63	5.956	62.9
		44.89	10.705	55.9
		69.16	14.174	60.2
8	2.73 (65)	20.49	5.167	71.7
		44.58	9.368	63.2
		68.68	12.363	68.3

[a]Figures in the parentheses indicate L/D ratio

diameter and L/D ratio. The results are presented in Table 11 and show that for a given capillary diameter, η_{ap} is nearly constant irrespective of increase in shear rate which suggests that for a particular capillary, the gel has attained a near-Newtonian viscosity. The corresponding η_{ap} values at higher L/D ratio for a capillary show a significant reduction as the gels are sheared for a longer duration confirming that the propellant gel is a time-dependent thixotropic fluid.

The efforts are also made to obtain a rheogram of freshly prepared unsheared gel and a typical sheared gel sample after a capillary flow test, in low shear rate range using a Brookfield viscometer, to assess the structural breakdown of the gel. The rheograms shown in Fig. 7 reveal that the area encompassed by the hysteresis loop gets significantly reduced on shearing. It may be mentioned that a sheared sample could be studied after two hours of shearing (to remove entrapped air bubbles), and during this period the regelation process must have started to show a small hysteresis loop. Immediate measurement of rheological character after ejection of sheared gel
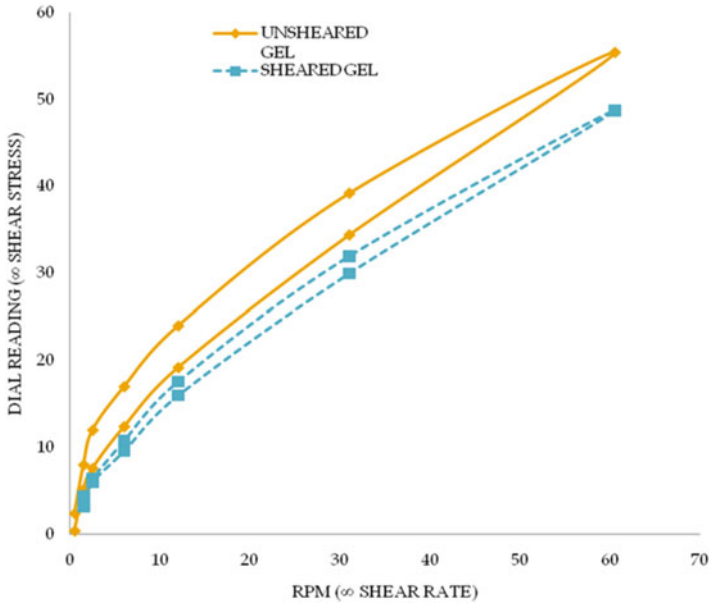
Fig. 7 Hysteresis loops showing thixotropic behavior of sheared and unsheared UDMH-MC gel

from capillary is expected to give up and down curves superimposing each other to give a linear variation of shear rate and shear stress, confirming attainment of Newtonian flow character.

Similar results have also been observed for UDMH-HSMC gelled and metallized propellant systems [17]. A comparison of η_{ap} values at low and high shear rate reveals that it drastically drops from 560 Pa.s (at 3.13×10^{-2} s^{-1}) to ~ 0.020 Pa.s (at 2.72×10^{5} s^{-1}).

6 Conclusions

The gel propulsion has attracted the attention of many researchers in Germany, India, Israel, Italy, and the USA during the past three decades and recently in China and Korea. Significant advancement has been made in various domains to have successful static and flight test of rockets using gel propulsion system. There are several areas where intensive research and development work is required to overcome the existing challenges and to realize the projected and possible high-energy gel propulsion systems with greater reliability.

Several advantages are offered by gel propellant technology that include improvement in performance by addition of low-molecular-mass metal powder in the gel, utilization of metallized gels in hybrid propulsion systems, and ease

of logistical and handling problems of reactive and toxic propellants on gelation. Gelled propellants would help in rocket engine restart under zero gravity conditions because gel will not disperse under minor accelerations. During the long-duration flights, these are expected to reduce heat transfer from warm tank walls to the low-temperature propellants. Other benefits would include safety by minimized storage and fire hazards, and such systems would be preferred if required to be stored in close proximity of personnel. Propellant leaking through cracks and minor defects in feed system components would be averted in gelled state, and this could be of great advantage in case of cryogenic propellants where boil-off losses, geysering, and cavitation problems can be effectively controlled. Density improvement with gelled liquid hydrogen may be particularly attractive in cryogenic propulsion system. Metallized liquid propellants exhibit the potential to provide an excellent approach to cut down rocket size due to improved energetic, reduced optimum O/F ratio, high propellant bulk density, and density specific impulse.

Though there are a number of possible advantages, gel propellants and propulsion system offer several challenges in their effective use. Almost all gellants used to convert liquid propellants to a gelled state lead to reduction in performance of the base bipropellant system, more so if the oxidizer is also gelled. Energetic gellants that can gel liquid propellants at low concentrations (1–2 mass %) are yet to be discovered. Most of the gels exhibit variable physicochemical characteristics with age and ambient temperature variations that are detrimental to overall system reliability. Further, total transfer and utilization of the propellant from storage tanks to combustion chamber remains an issue. The combustion and flow characteristics of gelled systems are rather complex when compared to Newtonian liquid bipropellant systems and must be closely monitored and regulated to ensure effective atomization and efficient combustion of metallized formulations.

A major problem with gelled systems has been clogging of flow channels with gelling agent and metal powder residues left after propellant vaporizes. Gelling agents having suitable melting point to address this problem may be explored. During the combustion of metallized system in a rocket motor, a part of oxidizing species are utilized in oxidation of the fuel, leaving an equivalent amount of metal un-oxidized. This incurs loss in propulsive energy, if the situation persists through the length of the combustor and nozzle. The full potential of such systems can be realized only if conditions in the combustor and nozzle permit the transfer of oxygen from water vapor (obtained from propellant combustion) to metal and absorption of generated heat by hydrogen before the combustion products are exhausted out of nozzle throat. The design of propulsion system must, therefore, consider the residence time required for completion of abovementioned process to realize maximum possible gains in propulsive energy. The research and development work should largely be directed now to mitigate operational problems and develop efficient gel propulsion systems for use in launch vehicles and missiles.

References

1. Varma M (1986) Studies on UDMH-RFNA gelled propellant systems, Ph.D. thesis, Birla Institute of Technology, Ranchi, India
2. Zurawski RL, Green JM (1987) An evaluation of metallized propellants based on vehicle performance, AIAA-87-1773, 23rd joint propulsion conference, San Diego
3. Palaszewski BA, Powell R (1991) Launch vehicle performance using metallized propellants, AIAA-91-2050, 27th joint propulsion conference, Sacramento
4. Palaszewski BA (1992) Metallized propellants for the human exploration of mars. J Propuls Power 8(6):1192–1199
5. Wong W et al (1994) Cryogenic gellant and fuel formulation for metallized gelled propellants: hydrocarbons and hydrogen with aluminum, AIAA-94-3175, 30th joint propulsion conference, Indianapolis
6. Palaszewski BA, Zakany J (1995) Metallized gelled propellants:oxygen/RP-1/aluminum rocket combustion experiments, AIAA-95-2435, 31st joint propulsion conference, San Diego
7. Natan B, Rahimi S (2002) The status of gel propellants in year 2000. Int J Energ Mat Chem Propuls 5:172–194
8. Pein R (2005) Gel propellants and gel propulsion, 5th international high energy materials conference and exhibit, DRDL, Hyderabad
9. Varma M et al (1996) Formulation & storage studies on hydrazine based gelled propellants. Def Sci J 46(5):435–442
10. Varma M, Pein R (2008) Optimization of processing conditions for gel propellant production. In: Kuo KK, Hori K (eds) Advancements in energetic materials and chemical propulsion. Begell House, New York, pp 1047–1059
11. Munjal NL et al (1985) Preparative and mechanistic studies on unsymmetrical dimethyl hydrazine-red fuming nitric acid liquid propellant gels. Prop Explos Pyrotech 10(4): 111–117
12. Munjal NL et al (1991) Performance studies on UDMH-RFNA gelled propellants. J Inst Eng (India) Aero Div 71:25–31
13. Gupta BL et al (1992) Theoretical performance of metallized unsymmetrical dimethyl hydrazine – red fuming nitric acid propellant system. Ind J Technol 30: 234–244
14. Galecki DL (1989) Ignition and combustion of metallized propellants, AIAA-89-2883, 25th joint propulsion conference, Monterey
15. Mueller DC, Turns SR (1993) Ignition and combustion characteristics of metallized propellants – phase II annual report, NASA Lewis Research Centre, NASA-CR-195107
16. Gupta BL, Varma M (1999) Ignition and combustion studies on metallized UDMH-RFNA bipropellant system. Ind J Eng Mat Sci, 6:13–21
17. Varma M, Jyoti BVS (2011) Ignition and combustion studies of heterogeneous UDMH-RFNA gel propellants. Int J Energ Mat Chem Propuls 10(3):259–275
18. Gupta BL et al (1986) Rheological studies on virgin and metallized unsymmetrical dimethyl hydrazine. Prop Explos Pyrotech 11(2):45–52
19. Jyoti BVS, Baek SW (2014) Rheological characterization of hydrogen peroxide gel propellant. Int J Aeronaut Space Sci 15(2):199–204
20. Jyoti BVS, Baek SW (2015) Formulation and comparative study of rheological properties of loaded and unloaded ethanol-based gel propellants. J Energetic Mater 33:125–139
21. Gupta BL et al (1986) Rheological characterization of fuming nitric acid gel. Prop Explos Pyrotech 11(2):85–90
22. Rahimi S, Natan B (2000) The flow of gel fuels in tapered injectors. J Propuls Power 16(3):458–471

23. Whorlow RW (1980) Rheological techniques. Wiley, New York, pp 67–74
24. Chhabra RP, Richardson JF (2008) Non-Newtonian flow and applied rheology. Elsevier, New York, pp 56–109
25. Casson N (1959) In: Mills CC (ed) Rheology of dispersed systems. Pergamon Press, New York, p 84
26. Green MJ et al (1991) Flow visualization of a rocket injector spray using gelled propellant stimulants, AIAA Paper 91-2198
27. Rahimi S, Natan B ((1998) Atomization characteristics of gel fuels, AIAA Paper 98-3830

Part VI
Hybrid Rocket Propulsion

Hybrid Propulsion Technology Development in Japan for Economic Space Launch

Toru Shimada, Saburo Yuasa, Harunori Nagata, Shigeru Aso,
Ichiro Nakagawa, Keisuke Sawada, Keiichi Hori, Masahiro Kanazaki,
Kazuhisa Chiba, Takashi Sakurai, Takakazu Morita, Koki Kitagawa,
Yutaka Wada, Daisuke Nakata, Mikiro Motoe, Yuki Funami, Kohei Ozawa,
and Tomoaki Usuki

Abstract The demand for the economic and dedicated space launchers for vast amount of lightweight, so-called nano-/microsatellites, is now growing rapidly. There is a strong rationale for the usage of the hybrid propulsion for economic space launch as suggested by the assessment conducted here. A typical concept of development of such an economic three-stage launcher, in which clustering unit hybrid rocket engines are employed, is described with a development scenario.

T. Shimada (✉) • K. Hori • K. Kitagawa • K. Ozawa • T. Usuki
Institute of Space and Astronautical Science (ISAS), Japan Aerospace Exploration
Agency (JAXA), Sagamihara 252-5210, Japan
e-mail: shimada.toru@jaxa.jp; hori.keiichi@jaxa.jp; kitagawa.koki@jaxa.jp;
kohei.ozawa@ac.jaxa.jp; usuki.tomoaki@ac.jaxa.jp

S. Yuasa • M. Kanazaki • T. Sakurai
Department of Aerospace Engineering, Graduate School of System Design, Tokyo Metropolitan
University, Hino, Japan
e-mail: syuasa2011@smail.plala.or.jp; kana@tmu.ac.jp; tsakurai@tmu.ac.jp

H. Nagata
Faculty of Engineering, Hokkaido University, Sapporo, Japan
e-mail: nagata@eng.hokudai.ac.jp

S. Aso
Faculty of Engineering, Kyushu University, Fukuoka, Japan
e-mail: aso@aero.kyushu-u.ac.jp

I. Nakagawa • T. Morita
School of Engineering, Tokai University, Hiratsuka, Japan
e-mail: nakagwa1@keyaki.cc.u-tokai.ac.jp; morita@keyaki.cc.u-tokai.ac.jp

K. Sawada
Department of Aerospace Engineering, Tohoku University, Sendai, Japan
e-mail: sawada@cfd.mech.tohoku.ac.jp

K. Chiba
Graduate School of Informatics and Engineering, The University of Electro-Communications,
Chofu, Japan
e-mail: kazchiba@uec.ac.jp

Thanks to the benefits of hybrid rocket propulsion, assuring and safe, economic launcher dedicated to lightweight satellites can be developed with a reasonable amount of quality assurance and quality control actions being taken in all aspects of development such as raw material, production, transportation, storage, and operation. By applying a multi-objective optimization technique for such a launch system, examples of possible launch systems are obtained for a typical mission scenario for the launch of lightweight satellites. Furthermore, some important technologies that contribute strongly to economic space launch by hybrid propulsion are described. They are the behavior of fuel regression rate, the swirling-oxidizer-flow-type hybrid rocket, the liquid oxygen vaporization, the multi-section swirl injection, the low-temperature melting point thermoplastic fuel, the thrust and O/F simultaneous control by altering-intensity swirl-oxidizer-flow-type (A-SOFT) hybrid, the numerical simulations of the internal ballistics, and so on.

1   Introduction

In recent years, very lightweight satellites, so-called nano-satellite (weighing 10 kg or less) or microsatellite (weighing 100 kg or less), become significantly popular for the purpose of communication, Earth observation, and many other applications. According to a survey of SpaceWorks Enterprises, Inc. [1], the number of nano-/microsatellites is expected to be 400–500 in the year of 2020. According to a different survey of Japan Space Systems and CSP Japan, Inc. [2], 394 satellites weighing less than 200 kg were launched during 2003–2013 as shown in Fig. 1. It is apparent that the fraction of nano-satellite class is growing rapidly in most recent years.

Although the demand for nano-satellite launch is growing rapidly, the launch service supply for such payloads is not enough. The 90 % of the satellites in Fig. 1 are piggyback launches and not all satellites were launched at their planned timings. In general, a piggyback launch has drawbacks of the limited launch

Y. Wada
Planetary Exploration Research Center, Chiba Institute of Technology, Narashino, Japan
e-mail: yutaka.wada@p.chibakoudai.jp

D. Nakata
Aerospace Plane Research Center, Muroran Institute of Technology, Muroran, Japan
e-mail: nakata@mmm.muroran-it.ac.jp

M. Motoe
Research and Development Directorate, Research Unit III, Japan Aerospace Exploration
Agency (JAXA), Sagamihara 252-5210, Japan
e-mail: motoe.mikiroh@jaxa.jp

Y. Funami
Faculty of Engineering, Kanagawa University, Yokohama, Japan
e-mail: funami-yuki@kanagawa-u.ac.jp

Fig. 1 Number of nano- and microsatellites (1–200 kg) launched during 11 years since 2003 (Data source: Japan Space Systems and CSP Japan, Inc. 2014 [2])
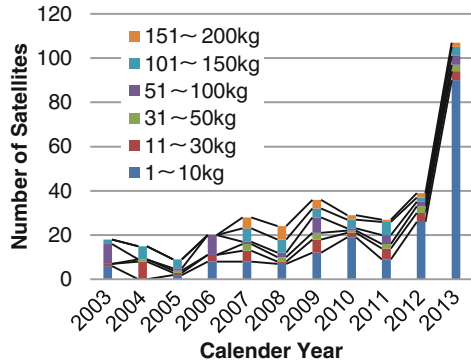
window and orbital options, as well as mission and system limitations so as not to interfere with the main payloads. Therefore, demands are growing for launching nano-/microsatellites by dedicated launch systems with high degree of freedom options concerning the launch window, orbits, and other mission and system requirements. In this context, several launch systems are being planned for 10–50 kg nano-satellites to be inserted into low Earth orbit (LEO) of 250–750 km altitudes or Sun-synchronous orbit (SSO) of 310–550 km altitudes, with target price ranges around 10 $M/launch for a 100 kg class LV [3–9].

A big interest is in question on how they manage the target price achieved to a low level. One answer to this question is utilization of nonexplosive rockets that can make economic production and operation possible. Hybrid propulsion is such a solution. In this paper, we describe why and how hybrid propulsion can make a dedicated, economic, lightweight satellite launcher possible. In the next section, assessment of conformity of chemical propulsions, such as solid, liquid, and hybrid propulsions, to an economic dedicated launcher will be described. From that we will get strong reasons why hybrid propulsion is suitable for such missions and systems. Conceptual study on such a launcher development is described in section "Conceptual study on lightweight satellite launcher using hybrid propulsion," and particular hybrid propulsion technologies that enable such launch systems are explained in section "Hybrid propulsion technologies."

2 Assessment of Conformity of Chemical Propulsions to Economic Dedicated Launcher

2.1 Mission and System Requirements and Constraints Imposed

We begin with setting the following mission requirements for the assessment of propulsion subsystem of the launcher concerned.

- The vehicle is ground-launched carrying payloads weighing 100 kg.
- Target orbit is 500 km altitude SSO or energy-equivalent transfer orbit.

Under the current social circumstances, the following constraints are appropriately imposed on the mission.

- Minimum environmental impact both on the ground and in space
- Reassuring and safe mission
- Economic development, production, and operation

As a major system requirement, we consider a three-stage launch vehicle in order to secure a variety of propulsion options to fulfill the overall mission requirements and constraints. It should be noted that, for the case of the SSO mission, the system should have a third stage propulsion system capable of two firings. We consider a three-stage launch system here, because a wider range of propulsion options is preferable.

Due to the Sun-synchronous orbit requirement, the precision of the orbit insertion has to be reasonably high. Due to the minimum environmental impact constraint, the propulsion exhaust gas has to have a minimum damage to Earth's atmosphere, and the system has to have minimum possible space debris. Due to reassurance and safety constraints, maximum safeguard consideration is made against the explosion of the propulsion system and the system has to be equipped with a flight abort system. Also, the system has to be dependable by enforcing necessary and sufficient quality assurance and quality control. And finally, the costs of development, production, transportation, storage, and operation of the system have to be kept low.

2.2 Assessment of Propulsion Subsystems

2.2.1 Performance

According to a simple evaluation using Tsiolkovsky rocket equation, the specific impulse greater than 290 s on the average is necessary to achieve the mission. In this evaluation, assumptions are made that the velocity loss is assumed 2 km/s, the Hohmann transfer is employed from 250 to 500 km altitude circular orbits, the Delta V is 8.6 km/s, the structural mass ratio is 15 %, and each stage mass ratio at the ignition is about 28:5:1 in the track of an existing three-stage launcher.

For example, in case of the combustion chamber pressure of 1 MPa, the nozzle expansion ratio of 100 and equilibrium flow, the vacuum specific impulse of representative chemical propulsion system is calculated. The combination of LO_2 and LH_2 gives the highest specific impulse of 400–460 s depending on the oxidizer to fuel ratio (O/F). The specific impulse of an ordinary composite solid propellant is 320–330 s. The specific impulse of a typical hybrid propellant, such as LO_2 and hydroxyl-terminated polybutadiene (HTPB), is 360 s, and it is comparable with that of a liquid propellant of LO_2/kerosene. When we see the density impulse, the highest is the solid propellant, the lowest is LO_2/LH_2, and the hybrid propellant lies in between.

Thrust control or throttling capability is necessary in order to satisfy the requirement of high-precision orbit insertion. Both liquid and hybrid propulsion systems are intrinsically throttleable, but solid propulsion systems are not. Throttleable solid rockets are realized only for relatively small tactical rockets.

2.2.2 Safety

The reassuring and safe mission constraints ask for lower possibility of explosion, smaller explosive safety separation distance (quantity distance), and easier abidance by the law. Solid propulsion systems have a conspicuous amount of the explosive. It is necessary to secure the quantity distance corresponding to TNT equivalence of 5 % at the launch site to be compatible with the AFMAN explosive safety standards and, at the same time, to abide by the explosive control law.

Liquid propulsion systems are also potentially at high risk of explosion because an unanticipated leakage of oxidizer and fuel can lead to vapor-phase explosion. A typical TNT equivalence is around 10–20 % and a due quantity distance is necessary. Also, in case that inflammable gas, high-pressure gas, or poisonous or deleterious substances are used, appropriate abidance by the law is necessary.

Hybrid propulsion systems are naturally very safe and at the least risk of explosion because the fuel and the oxidizer are stored in different phases and because the mechanism of combustion is governed by macroscopic turbulent diffusion flame. The static TNT equivalence is practically zero and no quantity distance is necessary. Only in the case of high-pressure gas usage, appropriate abidance by the law is necessary.

2.2.3 Environmental Impact

The characteristics of exhaust gas from propulsion systems that impact the ground environment are amounts of CO_2, HCl, metallic oxide, and toxicity. Although the exhaust gas of LO_2/LH_2 liquid rocket is very clean, the amount of CO_2 emission per unit impulse is very large due to the emission during the production of LH_2. The impact can be greatly reduced when the fuel is methane or kerosene. Hydrazine is highly toxic. Since exhaust gas from composite solid propellant combustion contains HCl and metallic oxide particles, environmental impact of solid rockets is high. Environmental impact of hybrid rocket is relatively small because the exhaust gas from the combination of LO_2 and hydrocarbon propellants basically contains only CO_2 and H_2O. Moreover, the CO_2 emission per unit impulse of hybrid propulsion during production to consumption is about ten times smaller than that of LO_2/LH_2 or composite solid propellant [10].

In order not to generate space debris, it is important that the propulsion system does not explode and does not generate metal oxide particles. In this viewpoint, hybrid rocket system is the best chemical propulsion option in terms of avoiding the generation of space debris.

2.2.4 Quality Assurance and Quality Control

The dependability of the system is the capability of achieving the mission without failures. In order to achieve necessary and sufficient dependability of the system, quality assurance and quality control (QA/QC) have to be properly conducted from the beginning of raw material selection to the final launch campaign operations. The amount of the QA/QC activities varies among the propulsion systems. In the case of liquid propulsion systems, each component has to have high quality in order to achieve the system dependability due to the large number of components. Also, in the case of solid propulsion systems, the quality of the propellant itself has to be very carefully assured because a single crack or void in the propellant can cause a catastrophic system failure. These highly demanding quality requirements in these two propulsion systems ask for large amount of the QA/QC activities. On the other hand, in the case of hybrid propulsion system, because of the relative simplicity, nonexplosive nature, and indifference of crack and void in solid fuel to the combustion and to a catastrophic failure, the amount of the QA/QC activities for the appropriate dependability of the system is relatively small and relatively easier and more efficient QA/QC is possible.

2.2.5 Cost

Because liquid rockets are complex, the production cost and the operation cost are relatively high. Although solid rockets are simple, because of the usage of explosives, the cost of safeguard actions in the processes of production, transportation, storage, and operation becomes very high for solid rockets.

On top of its relative simplicity, because of high safety and thanks to the insensitivity of the propulsion performance to fuel cracks, hybrid rockets can utilize industrial-level raw materials, production methods, and inspection methods. Also, as described in the previous subsection, QA/QC can be done efficiently, which reduces the production cost. Furthermore, because even a fully loaded launch system can be treated as "inert" and safeguard actions in launch operations can be reasonably reduced, so can be the inspection actions, both of which reduce the operational cost.

2.2.6 Summary of Assessment

The results of the conformity assessment of propulsion subsystems are summarized in Table 1 by a simple scoring rule: 3, high; 2, middle; and 1, low. Other than the aspects discussed above, "technical maturity" aspect is added. As is known well, hybrid rocket is much less matured than the other two are. The results here give the rationale for using a hybrid propulsion system to achieve the present mission and system requirements.

Table 1 Summary of results of propulsion subsystem conformity assessment

	Liquid	Solid	Hybrid
Performance	2	2	2
Safety	1	1	3
Environmental impact	2	1	3
QA and QC efficiency	1	1	3
Cost reduction potential	1	1	3
Technical maturity	3	3	1
Total	10	9	15

3   Conceptual Study on Lightweight Satellite Launcher Using Hybrid Propulsion

The keyword of the basic concept of the development is "low cost." By using hybrid rocket propulsion, a three-stage, assuring and safe, economic launcher dedicated to lightweight satellites can be developed with a reasonable amount of QA/QC actions being taken in all aspects of development such as raw material, production, transportation, storage, and operation. In this section, conceptual study examples are shown for launcher system using hybrid rockets. A multidisciplinary design optimization (MDO) with evolutionary computation has been conducted in order to obtain system design concepts optimally defined for hybrid rocket propulsion.

3.1   Conceptual Design of Three-Stage Launcher for Space Transportation

Firstly, the multidisciplinary design methodology was developed [11, 12] and demonstrated through solving the multidisciplinary design problem for a three-stage launcher which can deliver lightweight satellite to the Sun-synchronic orbit using hybrid rocket propulsion by means of the multi-objective genetic algorithm (MOGA). This study deals with the launcher, which has chambers, oxidizer tanks, pressurizing tanks, nozzles, and a payload. The evaluation of a launcher using hybrid propulsion is carried out from the empirical expression of the regression rate. Generally, the regression rate to the radial direction of the fuel, $\dot{r}_{port}(t)$, is expressed as follows.

$$\dot{r}_{port}(t) = a \cdot G_{oxi}^{n}(t) \tag{1}$$

Equation 1 is empirically defined, and the coefficient a and the index n are evaluated by experiments. The time variation of the thrust is estimated from Eq. 1 and the NASA Chemical Equilibrium with Applications (NASA-CEA) programs [13]. The chambers and the pressurizing tanks are made of the CFRP. The structural weight
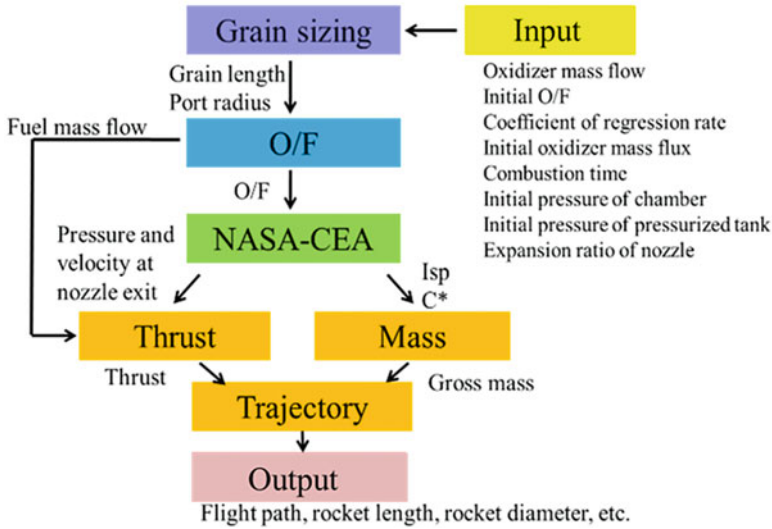
Fig. 2 Flowchart of the performance evaluation of the LV with a HRE [11, 12]

is calculated in the same manner as the M-V. The flight is simulated using the polar coordinates system. The aerodynamic performance is estimated by using the telemetry database of JAXA's solid rocket, S-520 [14]. Figure 2 shows the evaluation procedure for each stage [12]. The rocket is launched toward the south at an 89° launch angle. The second stage is immediately ignited after the combustion of the first stage is completed. The third stage coasts along the oval orbit after the combustion of the second stage is completed. After this coasting, the third stage is ignited. The coasting duration is also one of the design variables.

The design problem considers the payload and total mass ratio M_{pay}/M_{tot} maximization and the total mass M_{tot} minimization. Paraffin-based FT-0070 (melting point is 72 °C; density is 0.76 g/cm^3) is assumed as a fuel [15]. Figure 3 shows the non-dominated solutions obtained by MOGA. The results indicate that there was a trade-off between M_{tot} and M_{pay}/M_{tot}. It was also found that the maximum M_{pay}/M_{tot} was 1.17 % (identical to JAXA's solid rocket M-V) and the present LVs M_{pay} and M_{tot} for the solution were 132.2 kg and 11.3 t, respectively. Therefore, the solutions obtained in this study have capabilities comparable to those of existing solid rockets. Figure 4 shows the size of the designed rocket that can achieve the maximum M_{pay}/M_{tot} obtained via MOGA. This LV has a relatively large engine in the first stage and relatively small engines in the third stage. The design specifications of the selected solution are listed in Table 2. Such design knowledge is useful for the detail design and the development of the large-scale hybrid propulsion system for the next-generation space transportation.

Fig. 3 Non-dominated front
of the preset design problem
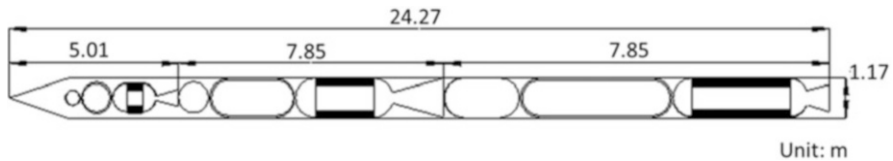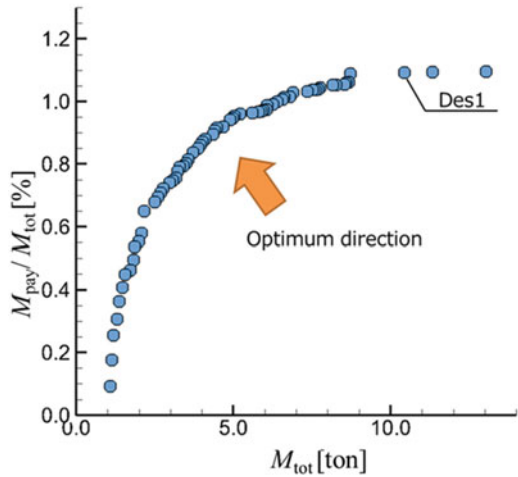obtained by MOGA for the
three-stage launcher design

Fig. 4 Specifications of Des1 obtained from non-dominated solutions

4 Hybrid Propulsion Technologies

Hybrid rocket propulsion performance depends on internal flow dynamics with heterogeneous combustion, or in other words, the boundary-layer combustion [16]. Combustion occurs in the boundary layer over a fuel surface, and the fuel regression rate is affected by the heat feedback from the flame. It is well known that hybrid rocket propulsion has some issues related to the fuel regression rate, in both meanings that it is slow and that it cannot be specified by direct design methods. For the former, a conventional approach to evade the issue is to use multi-port grain of the fuel, but this comes to a very complicated design when a high thrust is necessary so as in the first stage of a satellite launcher [17]. Because of this, more recent studies on liquefying fuel, such as paraffin fuel, are widely conducted [18, 19] because such fuels can be supplied into the flame zone threefold faster than can conventional fuels, such as HTPB, polyethylene, and so on. Another way of generating fuel gas faster than a conventional way is to utilize swirling injection of gaseous oxidizer [20–22]. Hybrid rockets using this technology are called swirling-oxidizer-flow-type or SOFT hybrid rockets. In order to secure the

Table 2 Specifications of designed launcher

	All stages in common		
Oxidizer	LO$_2$		
Baseline Fuel	Wax (FT-0070)		
Fuel mass (kg)	377		
Fuel grain length (m)	1.78		
Fuel grain outer diameter (m)	0.764		
Fuel grain inner diameter (m)	0.317		
	1st stage	2nd stage	3rd stage
AOxidizer mass flow rate (kg/s)	23.2	9.29	6.73
O/F (initial)	2.38	2.91	2.39
Regression rate magnification factor	7.3	3.4	3.4
Fuel regression rate (initial) (mm/s)	10.5	3.42	3.02
Fuel regression rate (burnout) (mm/s)	5.20	1.69	1.49
Oxidizer mass flux (initial) (kg/m^2-s)	293	117	85.1
Oxidizer mass flux (burnout) (kg/m^2-s)	48.8	19.3	13.9
Combustion pressure (initial) (MPa)	1.56	0.84	0.52
Nozzle throat diameter (m)	215	178	199
Nozzle expansion ratio	3	19	19
Thrust (initial) (kN)	74.3	29.9	27.9
Burning period (s)	33.5	104.4	118.3
Coasting time (s)		111	

effect of swirl injection, gaseous oxidizer should be injected in SOFT hybrid rockets, which necessitates the prerequisite vaporization of liquid oxidizer before injection, and some methods have been proposed and tested [23–25].

4.1 Swirling-Oxidizer-Flow-Type Hybrid Rocket and LO$_2$ Vaporization Technology

4.1.1 Features of Swirling-Oxidizer-Flow-Type Hybrid Rocket Engine

The hybrid combustion theory [16] implies that the thickness of the boundary layer over the fuel surface must be reduced to increase the fuel regression rate. To offer an innovative solution, a unique technique – a swirling-oxidizer injection at the fuel grain head, that is, a swirling-oxidizer-flow-type hybrid rocket engine [20] – was proposed. It is expected that a swirling flow field in the combustion chamber may reduce the boundary-layer thickness due to the increase in velocity by the additional tangential velocity component near the fuel surface without increasing the oxygen mass flow rate. It was shown that the overall fuel regression rates of polymethyl methacrylate (PMMA) with swirling gaseous oxygen flow could be increased up to about three times of that without swirl at the same condition of oxygen mass fluxes [21, 22].

Another big disadvantage of hybrid combustion is low combustion efficiency. The low efficiency is mainly attributed to combustion similar to a large solid fuel with a grain-length scale and to a decrease in oxidizer concentration with flow distance under extremely high flow velocity conditions, leading to an insufficient reaction time for vaporized fuel. The swirling motion has favorable effects on an increase in the intensity of turbulence in the flow field over the surface and also the mixing between the oxidizer and the vaporized fuel, causing an improvement in hybrid combustion. In fact, it was found that adding swirl to the oxygen injection clearly made the C* efficiency, equivalent to the combustion efficiency, increase by about 10 % under the same grain lengths [23].

4.1.2 Overall and Local Fuel Regression Rates

In order to put this type of engine into practical use, the fuel regression rate behavior in swirling-oxidizer flow for various engine conditions needs to be clarified in detail. The behavior of the overall and local fuel regression rates was widely examined by the swirling-oxidizer-flow-type hybrid rocket engine with the same configuration shown in Fig. 5 [21–29]. The oxidizer was GOX. The swirling-oxygen injector used in those experiments is also shown in Fig. 5, and the swirl intensity of the oxygen jet was characterized by the geometric swirl number, Sg, of the injector [30]. Sg can be defined in terms of the geometry of the injector by considering the conservation of momentum, using the following equation [21]:

$$S_g = \frac{\left(R_p - R_h\right) R_p}{n R_h^2} \tag{2}$$

where R_p is the injector port radius, R_h is the injection hole radius, and n is the number of the holes.

Various injectors with Sg up to 32.3 were used. The fuel grains were made of PMMA and polypropylene (PP). Five grain lengths were used for measuring the fuel regression rate and sometimes for observing flame appearances in the chamber.
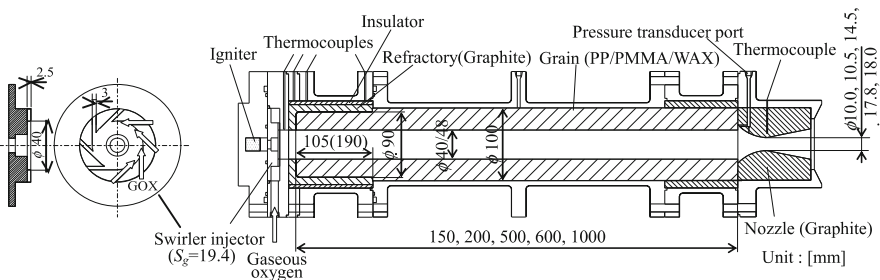

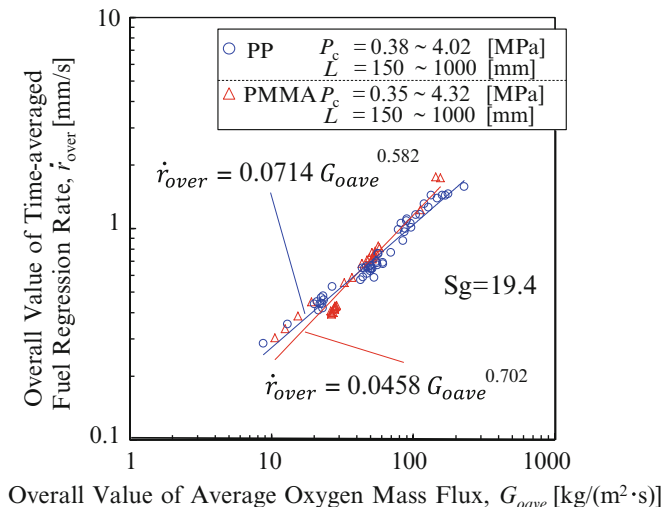**Fig. 5** Swirling-oxidizer-flow-type hybrid rocket engine

Fig. 6 Relation between overall values of time-averaged fuel regression rate and average oxygen mass flux

Burning experiments were carried out by changing the oxygen mass flow rate from about 10 to 400 g/s and the burning time, t_b, up to 27 s. The combustion chamber pressure, P_c, was varied from about 0.5–4.5 MPa.

The relation between the overall values of time-averaged fuel regression rate, $\dot{r}_{over}$, and average oxygen mass flux, G_{oave}, for various experimental conditions with swirling oxygen flow are shown in Fig. 6. It should be noted that the relations with swirling flow can be expressed by a conventional hybrid combustion regression rate formula as $\dot{r}_{over} = a\ G_{oave}{}^n$, where a and n were experimental coefficients. In these experiments, the relations were independent of the experimental parameters, in particular, pressure. The values of a and n differed according to the fuel type.

Figure 7 shows the variations of the time-averaged local fuel regression rates, $\dot{r}_{loc}$, with t_b along the distance from the grain leading edge, x, at $P_c = 1.16$–4.02 MPa [29]. For all the experiments, the values of $\dot{r}_{loc}$ up to $x = 100$–150 mm were considerably large due to the formation of impinging jet flames by the swirling oxygen flow, and they decreased sharply with x. After the rapid decrease of $\dot{r}_{loc}$, it became flattened toward the flow direction. $\dot{r}_{loc}$ of PMMA grains behaved in the same manner [28]. When P_c was kept constant, in the leading edge region up to about $x = 100$ mm, $\dot{r}_{loc}$ was independent of t_b and thus the inner port diameter during burning. However, in the downstream region from about $x = 100$ mm, $\dot{r}_{loc}$ decreased slightly with increasing t_b corresponding to an increase of the grain port area. These experimental results imply that the combustion mechanism in the leading edge region of the grain with strong oxidizer swirling motion differed from that in the rear region of the grain.
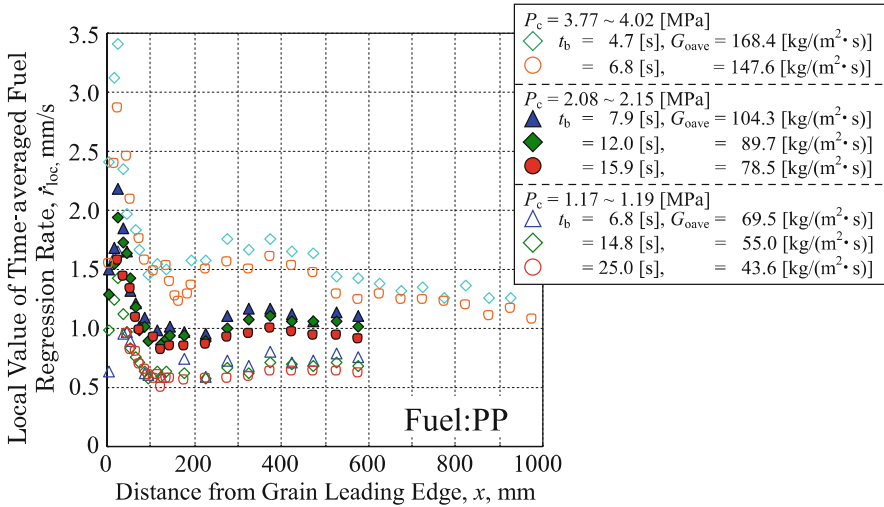
Fig. 7 Variations of local fuel regression rate of PP with burning time under various combustion chamber pressures

4.1.3 Fuel Regression Rate Controlling Parameters

The local fuel regression rates in the swirling oxygen flow were substantially independent of the grain port area in the leading edge region, but they depended on the area in the rear region. The parameters which determined the fuel regression rates were derived from the experimental findings and the consideration about the flow field in the grain and the definition of S_g. In the leading edge region, the fuel regression rates were primarily controlled by the velocity of the swirling oxygen wall jet along the grain, that is, the oxygen mass flow rate and the swirl intensity of the oxygen injector. This leads to that the controlling parameter is represented by $\left(\frac{\dot{m}_{oave}/A_{inj}}{\mu}S_g\right)$, where $\dot{m}_{oave}$ = time-averaged oxygen mass flow rate, A_{inj} = total area of oxygen injection slits, and μ = viscosity of oxygen [29]. Although the axial-averaged local value of time-averaged fuel regression rate, $\dot{r}_{locax}|_{x=0\sim100}$, obtained at various experimental conditions varied widely against the axial-averaged local value of average oxygen mass flux, $G_{olaveax}|_{x=0\sim100}$, Fig. 8a shows that $\dot{r}_{locax}|_{x=0\sim100}$ re-plotted against the parameter has one relation with the parameter, in particular, independent of P_c [29]. It is interesting to note that the experimental result with $Sg = 32.3$ was also plotted nearly on the same line, which indicates that the turbulent diffusion flames formed in the wall jet boundary layer on the grain dominate the combustion in the leading edge region. This means the fuel regression rate is independent of burning time and thus is always constant during combustion.

In the rear region, the fuel regression rate is controlled not by the oxygen wall jet velocity from the injector slits directly, but by the oxygen mass flux in the grain port section as in the conventional hybrid combustion model. The
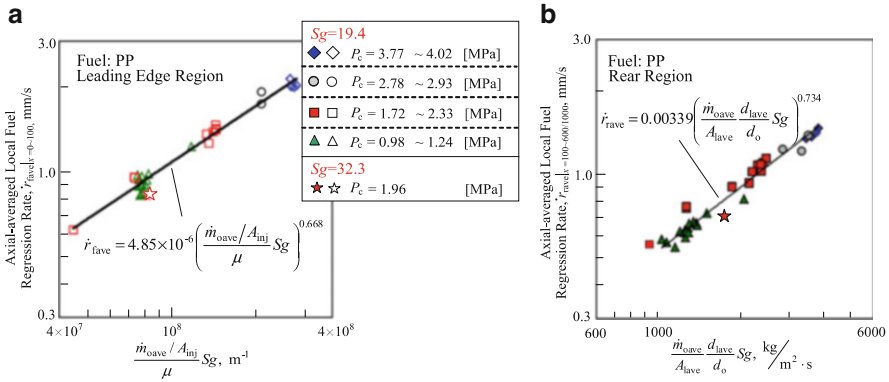
Fig. 8 Relation between axial-averaged local fuel regression rate and controlling parameters in the grain leading edge and rear regions

tangential velocity due to the swirling oxygen motion must be added to the velocity to develop the boundary layer on the grain surface, and an increase of the average diameter with t_b is also noticed. Based on this consideration, the local value of average oxygen mass flux, G_{olave}, in the rear region is approximately estimated by $G_{olave} \cong \frac{\dot{m}_{oave}}{A_{lave}} \frac{d_{lave}}{d_o} S_g$, where d_o = initial diameter of fuel grain port, d_{lave} = local value of average grain port diameter, and $A_{lave} = (\pi d_{lave}^2)/4$ [29]. Therefore, the controlling parameter to determine the fuel regression rate in the rear region would be given by $\left(\frac{\dot{m}_{oave}}{A_{lave}} \frac{d_{lave}}{d_o} S_g \Big|_{x=100\sim600/1000} \right)$. Figure 8b shows $\dot{r}_{locax}|_{x=100\sim600/1000}$ plotted against $\left(\frac{\dot{m}_{oave}}{A_{lave}} \frac{d_{lave}}{d_o} S_g \Big|_{x=100\sim600/1000} \right)$. The figure shows that the fuel regression rates obtained at various experimental conditions in the rear grain region have an almost linear relation with the parameter on a log scale. This suggests that, in the rear region, the tangential flow component played an additional role in consuming the fuel grain and is more appropriate for arranging the fuel regression rates.

4.1.4 Large Demonstration Engine

Based on these controlling parameters, the grain size of a 5 kN-thrust swirling-oxidizer-flow-type hybrid rocket engine with the similar configuration as the previous engines using the GOX/PP propellant and burning for 30 s was designed, and the engine was manufactured to examine the scale effects of the swirling-oxidizer flow on the combustion and engine performances and to demonstrate the engine technologies with swirling oxygen motion at the hybrid rocket test facility in Akiruno facility of JAXA. The burning tests have been carried out and the obtained results up to present were reported elsewhere [31–33].

4.1.5   LO$_2$ Vaporization Technology

(a) Necessity of LOx vaporization for swirling-oxidizer-flow-type hybrid rocket engine

To realize actual hybrid rocket engines, changing the oxidizer from GOX to liquid oxygen (LOx) was necessary to improve impulse density. However, for the swirling-oxidizer-flow-type hybrid rocket engine, the direct injection of the swirling LOx into the combustion chamber remarkably attenuated the angular momentum of the swirling flow, resulting in a significant reduction of engine performance when compared to that achieved when swirling GOX was injected [24]. This fact points out that vaporizing LOx before it is injected into the combustion chamber is essential to achieve the high engine performance of the swirling oxygen flow. We proposed two methods to vaporize LOx: a regenerative-cooling LOx-vaporization nozzle and a LOx-vaporization preburner. Some studies have been carried out to verify the two techniques with respect to the practicality of LOx vaporization.

(b) Regenerative-cooling LOx-vaporization nozzle

Since LOx has a lower specific heat than liquid fuels and has strong reactivity against materials, a regenerative-cooling nozzle for LOx is not common. In order to clarify the technical problems for the regenerative-cooling LOx-vaporization nozzle, we fabricated a LOx-vaporization nozzle, which could be attached to the engine shown in Fig. 5. The nozzle with 30 rectangular thin channels each with a depth of 1.0 mm was designed for a thrust of 1500 N, a LOx mass flow rate of 385 g/s, and a LOx supply pressure of 4.5 MPa. The burning tests were conducted using the experimental system with the LOx feed line shown in Fig. 9.
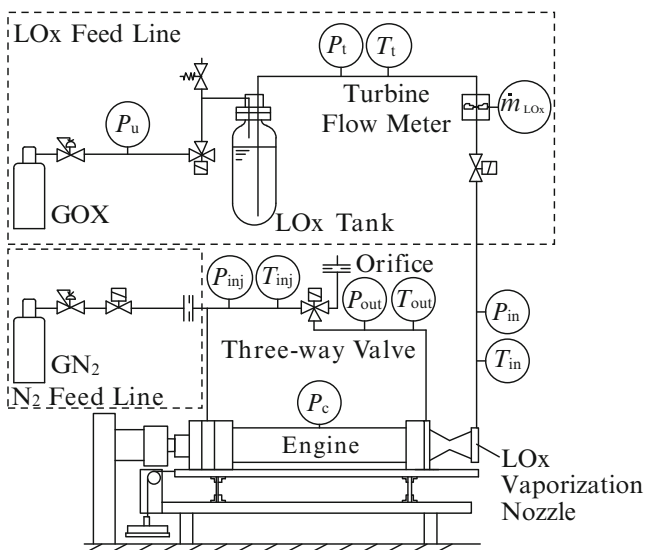

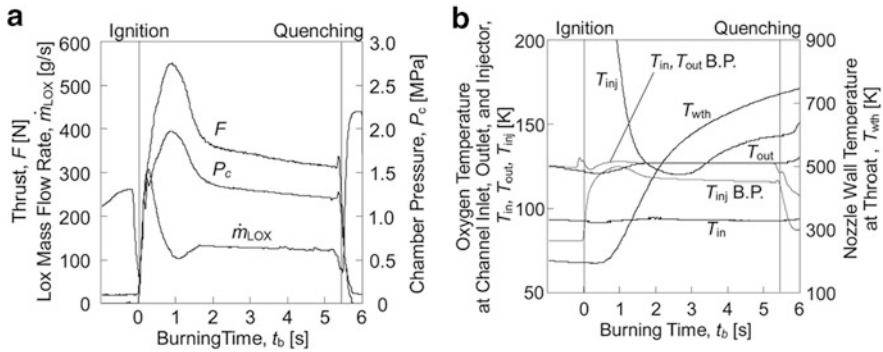**Fig. 9** Schematic of experimental system with LOx feed line

Fig. 10 Typical results of burning tests for LOx-vaporization nozzle. (**a**) Time traces of engine parameters. (**b**) Oxygen temperature records at channel inlet/outlet of nozzle and injector upstream

The experiments showed that rapid ignition and stable combustion without combustion oscillation were achieved. Typical results of the burning tests for the LOx-vaporization nozzle are shown in Fig. 10. From around 3 s after ignition, the oxygen temperature at the injector upstream, T_{inj}, was higher than the boiling temperature at the injector upstream pressure, $T_{injB.P}$, which showed that oxygen injected from the injector was completely vaporized. LOx sufficiently vaporized while passing through the nozzle. That is, we could demonstrate a self-sustained LOx-vaporization operation for the swirling-oxidizer-flow-type hybrid rocket engine. This combustion test proved that if optimal channels are designed, there was no essential problem in vaporizing LOx with a regenerative-cooling nozzle.

(c) Preburner

The concept of LOx-vaporization preburners is to utilize the heat of combustion of a small amount of solid fuel with LOx. The feasibility of the preburner using PMMA with a relatively slow and stable combustion manner as fuel was examined from the viewpoint of thermal energy. When vaporizing and heating up the required LOx mass flow rate for an engine from 90 to 300 K at 5 MPa, the burning amount of PMMA was estimated to be at about 3 % of the fuel propellant mass flow rate of the engine at an optimum performance condition [26]. This estimation indicates that the LOx-vaporization preburner is practicable in the thermal energy evaluation.

Some configurations about the LOx-vaporization preburner can be considered. One of them is the direct-burning method of PMMA in LOx, in which if stable and steady combustion of PMMA would occur in LOx, a large amount of the ambient LOx could be vaporized by directly using the PMMA flame with LOx [26]. Figure 11 shows the typical photographs of PMMA rod (φ5 mm) burning in LOx [26]. The sample was verified as having a blue flame at the lower part of the PMMA rod and a luminous flame above that. It is important to note that the PMMA rod did not break during combustion nor did explosive
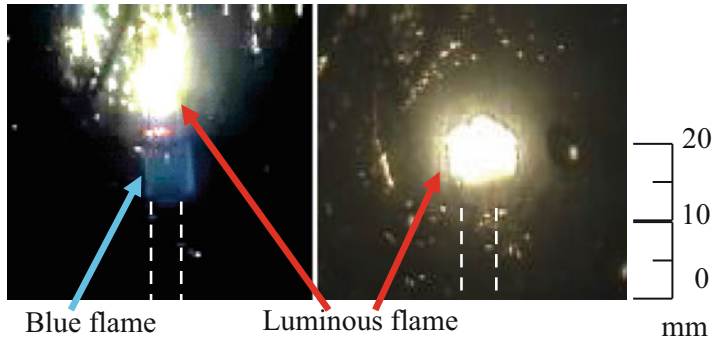
Fig. 11 Flame appearances of PMMA rod in LOx (φ5 mm)

combustion occur. The luminous flame formed intermittently, while the blue flame propagated along the PMMA rod at an almost constant velocity. These flames vaporized the ambient LOx, which generated the gaseous oxygen with an almost equal volume to the theoretical value when the complete combustion of PMMA with LOx occurred.

4.2 Multi-section Swirl Injection Method

Hybrid rocket engines have low fuel regression rate and low combustion efficiency. In order to overcome those disadvantages, a new method that can improve the fuel regression rate more than that of conventional methods is proposed. The method is multi-section swirl injection method [34–38]. The concept of multi-section swirl injection method is to provide oxidizer at multiple cross sections in order to keep strong swirl flow through the whole combustion chamber.

The schematic diagram of multi-section swirl injection method is shown in Fig. 12. High-density polyethylene fuel and paraffin fuel (FT-0070) are used for the present study. Three different grain lengths of fuel grain with inside diameter of 35 mm are tested in high-density polyethylene fuel and paraffin fuel. The diameter of the injector holes, which inject the oxidizer, is 1 or 2 mm. In the present study, four injector holes are located at four cross sections along the axis of the fuel grain. At the combustion tests, temporal combustion pressure and thrust showed steady combustion phenomena in case of multi-section swirl injection method.

The estimation of regression rate for various multi-section swirl injection methods is conducted for paraffin fuel (FT-0070). Figure 13 shows schematic diagram of grain type A through D. In order to reduce the interference of each injector port, the number of injector ports at each cross section is decreased from four (type A) to three (type B). Also, to increase turbulent combustion in grain
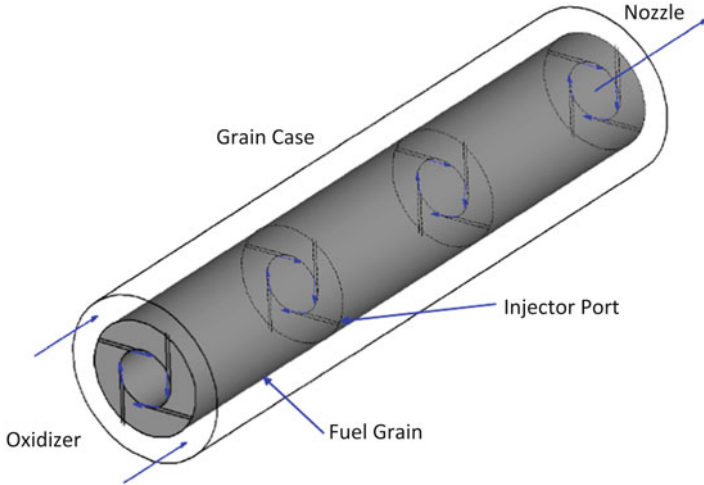
Fig. 12 Schematic diagram of multi-section swirl injection method
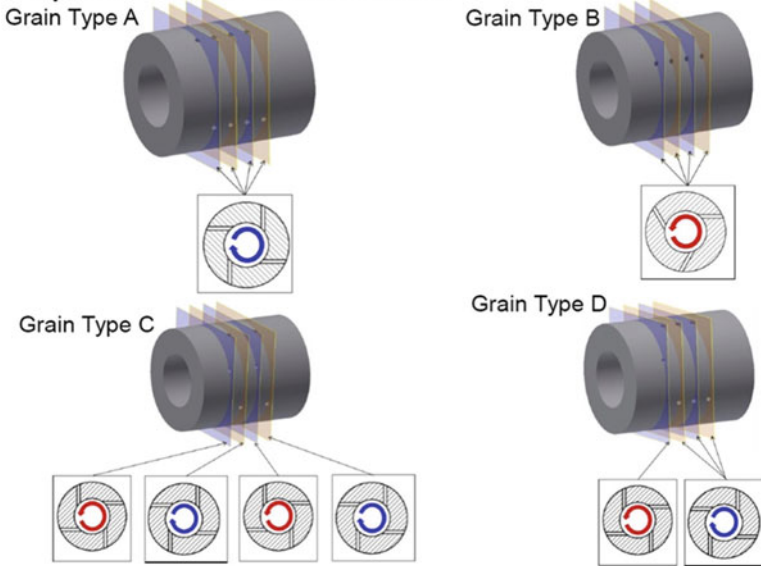
Fig. 13 Schematic diagram of grain type A through D (Fuel: paraffin fuel FT-0070)

type C, the direction of swirl is alternated between clockwise and counterclockwise as shown in the Figure. In grain type D, the direction of swirl is changed from anticlockwise direction to three clockwise directions at each cross section as shown in Fig. 13. Correlation between average regression rate and average oxidizer mass
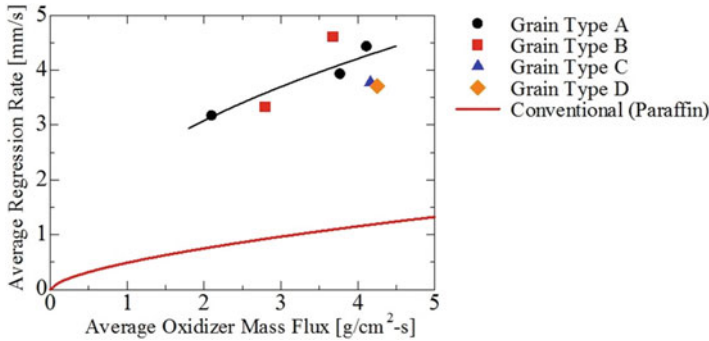
Fig. 14 Correlation between average regression rate and average oxidizer mass flux (Fuel: paraffin fuel FT-0070)

flux for testing cases is shown in Fig. 14. The results show the regression rates with multi-section swirl injection method are about 3.8 times of that of the conventional method without swirl [39]. Also, the results show type B at larger average oxidizer mass flux suggests higher average regression rate compared with that of types A, C, and D. Also the results show reduction of number of injection jets in the same cross section, and switching swirl direction of injection jets is effective to increase turbulent combustion.

4.3 Low-Melting-Point Thermoplastic Fuel (LT Fuel)

High-regression-rate hybrid rocket fuels which generate large thrust have been studied by several researchers. Thermoplastic polymers whose melting point is low such as paraffin and wax fuels exhibit high fuel regression rates. Karabeyoglu et al. investigated regression rate of paraffin and wax fuels, and they found it has another combustion mechanism [39]. These fuels have thin liquid layer on the burning surface during combustion, and the mechanical entrainment of liquid droplets occurs from liquid surface by upstream oxidizer flow. A lot of entrainment of liquid droplets is the reason of high regression rate of solid fuel, thus, the mechanism is called as the mass entrainment mechanism. Hikone et al. observed small fuel droplets of paraffin wax fuel during combustion using slab chamber under the atmospheric pressure and proved this mechanism [40]. However, these fuels need the improvements of mechanical property and adhesion with other materials such as insulation and liner to realize the use in full-scale flight rocket motors.

LT fuel, which is excellent in elongation, true stress, and its adhesive properties, has been studied. The LT fuels have been developed by Katazen Corporation, and the melting point of the fuels is approximately at 90 °C. The regression rate characteristics with gaseous oxygen were evaluated in the previous study [41].
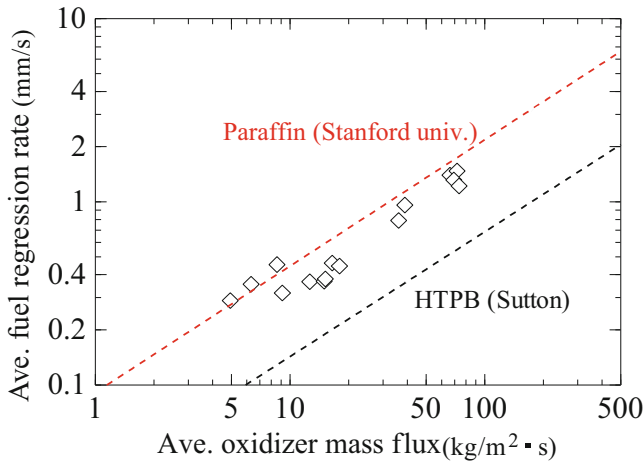
Fig. 15 Comparison of regression rates for LT fuel, HTPB, and paraffin fuel [39]

Table 3 Component and mechanical property of LT fuel samples

Component (mass %)	Sample #1	Sample #2	Sample #3	Sample #4
Styrene resin	10.2	8.7	11.3	13.1
Xylene resin	0	12.5	32.3	31.3
Stearic acid	0	4.2	3.2	6.2
Paraffin oils	89.8	74.6	53.2	49.4
Mechanical property				
Young's modulus (mN/mm^2)	22.3	37.7	267.7	617.7
Maximum stress (mN/mm^2)	0.06	0.09	0.41	0.58
Elongation (%)	437.4	378.8	344.0	300.2
Density (g/cm^3)	0.87	0.89	0.92	0.92
Temp. @ 2000 poise (°C)	Not measured	72.3	92.8	95.7
GOX regression rate @ 50 kg/m^{2}s (mm/s)	0.85	1.13	0.93	0.83

Figure 15 shows the results. The LT fuel has higher regression rate than classical fuel by three to four times because of the similar physical property with paraffin and wax fuels.

Therefore, the LT fuel looks promising for the application to large-scale motors.

The LT fuel was composed of several chemicals. Table 3 shows the compositions, mechanical properties, and the regression rate at 50 kg/m^{2}s of averaged oxygen mass flux of four samples. The paraffin oils are the main component for all LT fuels, and the styrene resin is used as the thermoplastic resin. The xylene resin is added to improve the adhesive property. Stearic acid is selected as a solubilizing agent between xylene resins to other components.

Sample #2 having highest regression rate was selected because it had the best handling properties such as viscosity at service temperatures. These regression

rates were established with averaged five experimental data points. Sample #4 was selected as fuel of large-scale motor because of its high Young's modulus and maximum stress. These LT fuels were evaluated for the adhesive property to EPDM rubber (ethylene-propylene-diene monomer rubber) using polyolefin-based adhesive and was confirmed having excellent adhesive property from the observation of cohesion failure.

Chemical Equilibrium with Applications (CEA) of NASA was used for equilibrium calculations [13, 42] in the case of the combustion chamber pressure of 5 MPa, the nozzle expansion ratio of 100, and equilibrium flow. The maximum of the vacuum specific impulse of LT/LOx is 321 s at O/F = 3, HTPB/LOx is 348 s at O/F = 2, LT/N$_2$O is 293 s at O/F = 9, and HTPB/N$_2$O is 314 s at O/F = 8. Therefore, LT #2 fuel performance is 7–8 % lower than HTPB I_s performance; however, considering the much higher regression rate of LT fuel compared with HTPB (three to four times), LT #2 fuel is better fuel than HTPB in total.

4.4 Thrust and O/F Control of Hybrid Rocket

The shift of oxidizer-fuel mass flow ratio (O/F shift) during throttling or long time burning is a unique phenomenon to hybrid rockets. This means that, in hybrid rocket combustion, optimal O/F cannot be kept constant in throttling operations or port diameter increase. These shifts can cause loss of delivered $\triangle V$. This phenomenon is caused by the nonlinear dependence of fuel regression rates on oxidizer mass flux.

O/F shifts depend on the regression exponents "n". For example, in the case of $n = 0.5$, O/F shifts due to port diameter increase do not happen. Very recently, the sensitivity analyses of O/F shifts due to port radius increase have been conducted by Karabeyoglu et al. [43]. From their results, in practical hybrid combustion, O/F shifts due to port diameter increase have slight effects on c* because the range of n is varied between 0.55 and 0.7 [44]. On the other hand, this paper also indicates practical O/F shifts due to throttling have larger effects on c*. In order to accelerate rockets effectively by reducing aerodynamic drag and the gravity loss under the restriction of maximum acceleration, thrust is preferred to be modulated. In these ways of operation, $\triangle V$ can be significantly lost by O/F shifts due to throttling.

As solutions to O/F shifts due to throttling, some techniques are proposed. All of these techniques have several branch lines in oxidizer feed system to add different effects from each other. A representative solution to this problem is altering-intensity swirl-oxidizer-flow-type (A-SOFT) hybrid rockets [45, 46]. This technique is an application of SOFT hybrid rockets [22]. Swirl injection is known as a technique to increase fuel regression rates due to circumferential velocity of oxidizer in the fuel port using headend tangential injectors. Fuel regression rates of SOFTs depend not only on oxidizer mass flux but also on the geometric swirl intensity of tangential injectors [22]. As shown in Fig. 16, the concept of A-SOFT is to alter swirl intensity of the oxidizer flow in order to control fuel regression rates. To control the swirl intensity, axial and tangential injectors are applied. An
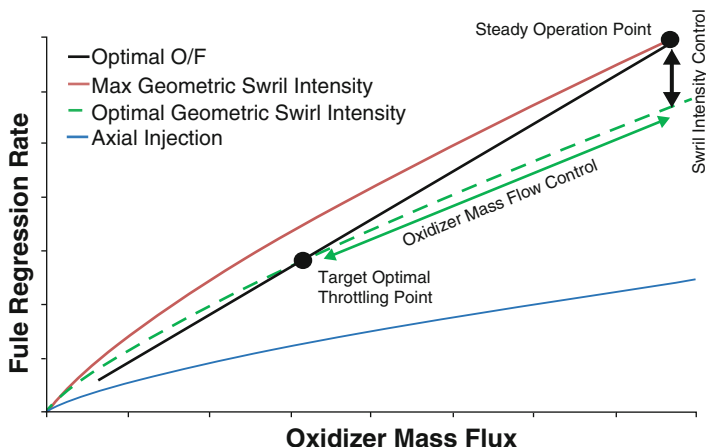
Fig. 16 Illustration of O/F control by altering oxidizer swirl intensity

oxidizer feed line splits into tangential and axial ones, and oxidizer mass flow rates can independently be changed using their control valves.

Recently, several studies on A-SOFT hybrid rockets have been started [47, 48]. First of all, it is necessary to evaluate whether there is some meaningful improvement of performance from conventional hybrid rockets with or without O/F control in practical use. This means that not only c* or I_s but also $\triangle V$ under more practical conditions should be taken into consideration. Therefore, an optimal rocket design including flight simulation is needed to study performances of both types of rockets. Secondly, fuel regression behavior of A-SOFT hybrid rockets will be studied based on theoretical and empirical approaches using one of the fuel regression data to be acquired in A-SOFT configurations besides previous studies on SOFTs. However, unsteady experimental data such as fuel regression responses to changes of oxidizer mass flow rate or geometric swirl intensity during burn do not exist in past experimental studies. Though there is a set of basic analytical studies applicable for A-SOFT hybrid rockets [49], in order to know internal ballistics in A-SOFT hybrid rockets in more detail, empirical studies such as unsteady CFD simulation and burning tests are needed. Finally, using these data and analysis, automatic throttle and O/F control system will be constructed.

4.5 Numerical Simulation of Hybrid Rocket Internal Ballistics

4.5.1 **Large-Eddy Simulation in Combustion Chamber of SOFT-HR [50]**

A sketch of a lab-scale combustion chamber of a swirling-oxidizer-flow-type hybrid rocket (SOFT-HR) motor in which oxidizer is injected tangentially from eight ports
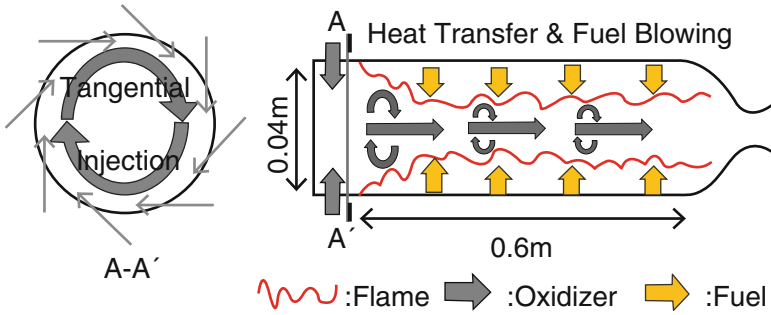
Fig. 17 Numerical setup [50]

Fig. 18 Mixture fraction at flame [50]

is shown in Fig. 17. Detailed specifications of the object under consideration and results of the experiment can be found in [51]. In the simulation, gaseous oxygen is fed into the chamber at a rate of 200 g·s^{-1} with a temperature of 300 K, while gaseous methane is injected at a rate given by local regression rate determined from the balance of surface heat flux. In this study, a high-order accurate finite volume method is chosen to conduct an implicit LES computation. As a combustion modeling, the laminar flamelet concept is employed. GRI-Mech 3.0 is used to make the flamelet table.

Figure 18 shows the iso-contours of mixture fraction at 0.2 of the stoichiometric value which approximately describes the shape of reaction zone. One can find that the shape of the reaction zone is disturbed by turbulent flow and fragments of the reaction zone present in the chamber. It is also indicated that the reaction zone stays close to the fuel grain till the middle of the chamber and then lifts up rapidly from the surface and flows toward the nozzle entrance. Figure 19 shows the iso-surface of second invariant of velocity tensor "Q-criterion" shaded by the axial
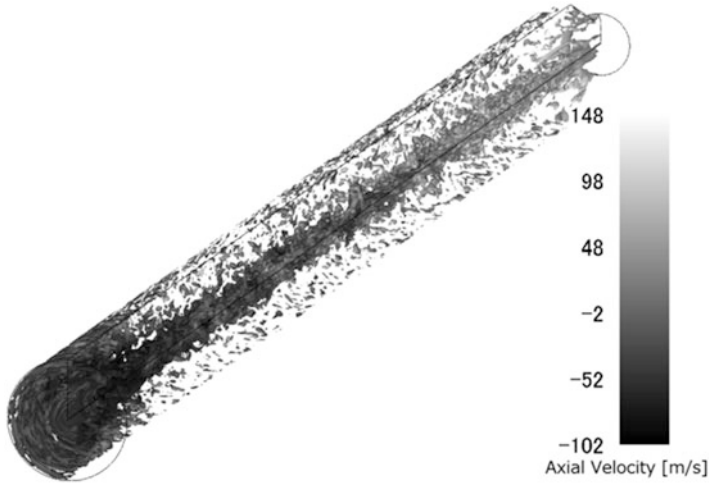
Fig. 19 Iso-surface of Q-criteria
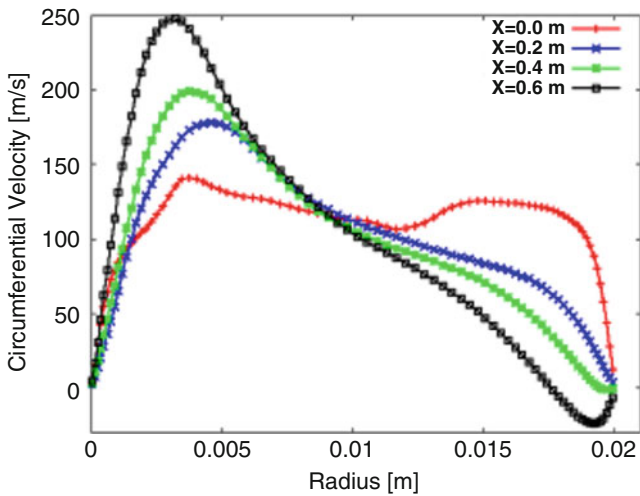
Fig. 20 Circumferential velocity distribution [50]

velocity. A large-scale longitudinal vortex is seen along the central axis. This can also be confirmed from the radial profiles of circumferential velocity at four axial positions shown in Fig. 20, where a rigid rotation appears along the axis. Toward the nozzle entrance, the peak value in the circumferential velocity becomes larger and the radius where the peak value appears becomes smaller. This phenomenon is a manifestation of angular momentum conservation and caused by contraction of flow path by the nozzle. The axial distribution of swirl number (ratio of circumferential to axial momentum of the flow) is shown in Fig. 21.
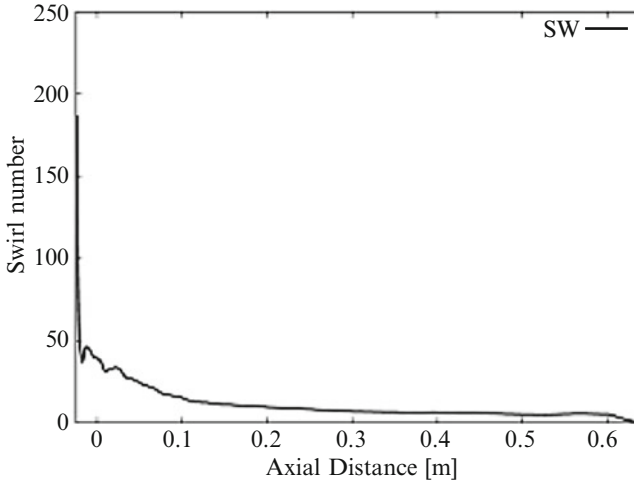
Fig. 21 Variation of swirl number as a function of axial distance

4.5.2 One-Dimensional Analysis for Hybrid Rocket Internal Ballistics [52]

The regression rate of fuel grain for a hybrid rocket engine depends not only on the combustion mechanism but also on the macroscale phenomena such as mixing of fuel gas and oxidizer in turbulent boundary layer. Owning to this dependence on macroscale phenomena, the design of hybrid rocket engine further needs to account for many parameters, such as engine geometry, engine size, injection method of oxidizer, and so on. Experiments and large-scale numerical simulation accounting for all of these parameters are extremely time consuming and high cost. Therefore, an efficient evaluation method of internal ballistics for designing a hybrid rocket engine is developed.

In the developed method, quasi one-dimensional Euler equations are employed with a conservation equation for the mixture fraction. The fuel regression rate is determined by solving the energy-flux balance equation at the solid fuel surface.

An equilibrium gas model considering nine chemical species, C_xH_y, O_2, CO_2, H_2O, CO, H_2, OH, O, and H, is chosen for the present oxygen/hydrocarbon system. The free energy minimization method based on the Lagrange method of undetermined multipliers is employed to evaluate the equilibrium chemical composition and temperature [13]. Detailed descriptions of the numerical method can be found in [52].

Using the developed method, parametric studies for hybrid rocket design parameters were conducted. In the following, an example regarding the scaling effect of chamber size is shown. A scaling factor of geometrically similar chambers is given by a dimension ratio based on the reference chamber. As shown in Fig. 22, the averaged regression rate decreases with increasing scaling factor. The present method is able to promptly and qualitatively evaluate the internal ballistics of hybrid rocket.
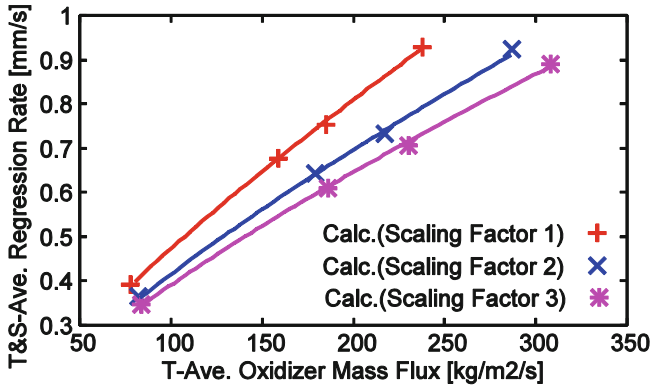
Fig. 22 Time- and space-averaged regression rates obtained by the parametric study for scaling factor

Fig. 23 Photograph of burning fuel

4.6 Diagnostic Technologies of Hybrid Rocket Combustion

4.6.1 Combustion Visualization

Combustion process of a hybrid rocket is a very complicated phenomenon, compared with that of a liquid rocket or a solid rocket, because it consists of pyrolysis, sublimation, melting, and so on, related to solid fuel regression, besides mixing and chemical reaction of gases. Combustion visualization is very useful to understand this complicated phenomenon. Some examples are shown as follows.

Karabeyoglu et al. showed that the regression rate of paraffin-based fuels is almost four times that of classic fuels such as HTPB and it is caused by the entrainment mechanism from the theoretical study. It means that materials with low surface tension and low melt-layer viscosity, such as paraffin-based fuels, generate more entrainment and increase the regression rate [39]. Nakagawa et al. tried to observe the entrainment by visualizing the combustion process [15]. Figure 23 shows the burning paraffin-based fuel in this visualizing combustion experiment. Many entrainment droplets can be observed as luminous line. Thus, the entrainment existence was proven experimentally.

This experiment was conducted under the atmospheric pressure. According to Karabeyoglu et al.'s study, the molten fuel on the solid surface is in the subcritical

Fig. 24 Flame appearance of PP grain with swirl taken from the front in the combustion chamber: $P_c = 1.0$ MPa, $G_{oave} = 12.0$ kg/(m^2•s), $\varphi = 1.62$, and exposure time $= 1/8000$ s
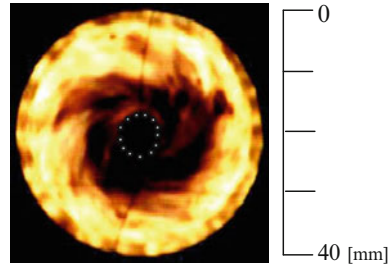
condition under the atmospheric pressure. But, paraffin waxes have low critical pressure resulting in supercritical conditions for almost all practical operating regime [53]. Therefore Wada et al. [54] and Jens et al. [55] tried to visualize combustion of liquefying fuel in the supercritical condition. The entrainment droplets were observed also at the high-pressure region up to 2 MPa.

Yuasa et al. conducted visualization of flames in combustion chamber of swirling-oxidizer-flow-type hybrid rocket engines as shown in Fig. 24. From the visualization, averaged flame zone thickness of each fuel, the effect of swirl, and some other knowledge were obtained [27].

5 Conclusion

Hybrid propulsion has potential capability for the space launch, which has never been done so far, though. One reason for why not is because fewer chances have been given for the technology development, but fundamentally it is because the propulsion is based on the boundary-layer combustion. Namely, it is because of low fuel regression rate and, more fundamentally, because the fuel mass flow rate cannot be specified directly during the combustion. On the other hand, as the assessment of propulsion subsystem in this paper shows, hybrid propulsion has a very strong rationale for economic and safe space launch systems. How can we bridge between these two opposite senses? It is the technology buildup that makes possible the economic space launch by using hybrid propulsion. Examples of multi-objective optimization for hybrid rocket propelled launch system are shown. The technology has also been applied to a launch system with engine clustering. The importance of throttling capability of hybrids should be emphasized because the capability enriches both the flexibility and the performance. One solution for the dual control of both thrust and O/F is given in which altering-intensity swirling-oxidizer-flow-type (A-SOFT) hybrid rocket plays an important role. For A-SOFT hybrid rocket, LOx must be vaporized before injection into the combustion chamber. It is necessary to develop the LO$_2$ vaporization technology.

For the future, more achievements are expected for the technology demonstration of this concept and beyond.

References

1. SpaceWorks Inc. (2014) Nano/microsatellite market assessment. http://www.sei.aero/eng/papers/uploads/archive/SpaceWorks_Nano_Microsatellite_Market_Assessment_January_2014.pdf, pp 1–18
2. Japan Space Systems and CSP Japan, Inc. private communication
3. Garvey Spacecraft Corporation (2012) Incremental evolution of a 10/250 NLV into a 20/450 NMSLV, Small Business Innovation Research 2012, 12-1 E1.02-9091. http://sbir.gsfc.nasa.gov/SBIR/abstracts/12/sbirselect/phase1/SBIR-12-1-S-E1.02-9091.html
4. Rocketdyne A (2013) Spartan nano-launch vehicle. In: 16th US Space and Missile Defense symposium. http://smdsymposium.org/wpcontent/uploads/2013/09/Kaufman-Nano-Launch-Vehicle-presentation.pdf
5. USASMDC/ARSTRAT, SWORDS. http://www.smdc.army.mil/FactSheets/SWORDS.pdf
6. Weuta PH, Jaschinski, N (2013) Preliminary, experimental studies to develop a micro satellite launch system. 7th Pico- and Nano-satellite Workshop. http://www.wepatechnologies.de/app/download/5795540964/WEPA_Technologies_FAR_PiNa2013_MicroLaunchVehicle_20130911_final.pdf
7. Nammo, Andoya Rocket Range (2013) North star. http://www.rocketrange.no/wpcontent/files/2013/01/NorthStar.pdf
8. Interorbital Systems. IOS NEPTUNE launch vehicles. http://www.interorbital.com/interorbital_03302014_012.htm
9. Generation Orbit Launch Services, Inc. GOLauncher 2. http://www.generationorbit.com/golauncher2.html
10. Fukuchi A, Aoki A, Igarashi S, Yamamoto K (2011) Environmental and cost advantages of reusable hybrid rocket engine. In: 28th International Symposium on Space Technology and Science, ISTS 2011-o-1-13v, Okinawa, Japan
11. Kosugi Y, Oyama A, Fujii K, Kanazaki M (2011) Multidisciplinary and multi-objective design exploration methodology for conceptual design of a hybrid rocket. In: Infotech@aerospace 2011, AIAA Paper 2011–1634, St. Louis, MI, USA
12. Kitagawa Y, Kitagawa K, Nakamiya M, Kanazaki M, Shimada T (2012) Multi-stage hybrid rocket conceptual design for micro-satellites launch using genetic algorithm. Trans Jpn Soc Aeronaut Space Sci 55(4):229–236
13. Gordon S, McBride BJ (1994) Computer program for calculation of complex chemical equilibrium compositions and applications I. analysis, NASA Reference Publication RP-1311, National Aeronautics and Space Administration, Lewis Research Center, Cleveland, Ohio, 44135-3191, USA. In: 26th Joint Propulsion conference, AIAA Paper 90-2762, Orlando, FL, USA
14. Flight experiment plan for 2nd sounding rocket in FY1996, ISAS/JAXA, 1996 (in Japanese)
15. Nakagawa I, Hikone S (2011) Study on the regression rate of paraffin-based hybrid rocket fuels. J Propuls Power 27(6):1276–1279
16. Marxman GA, Wooldridge CE, Muzzy RJ (1964) Fundamentals of hybrid boundary layer combustion, vol 15, Heterogeneous combustion. AIAA Progress in Astronautics and Aeronautics, Academic, New York, pp 485–521
17. Kniffen RJ, McKinney B, Estey P (1990) Hybrid rocket development at the American Rocket Company. In: 26th Joint Propulsion conference, AIAA Paper 90–2762, Orlando, FL, U.S.A.
18. Karabeyoglu MA, Altman D, Cantwell BJ (2002) Combustion of liquefying hybrid propellants: part1, general theory. J Propuls Power 18(3):610–620

19. Karabeyoglu MA, Cantwell BJ (2002) Combustion of liquefying hybrid propellants: part 2, stability of liquid films. J Propuls Power 18(3):621–630
20. Yuasa S, Shimada O, Imamura T, Tamura T, Yamamoto K (1999) A technique for improving the performance of hybrid rocket engines. In: 35th Joint Propulsion conference and Exhibit, AIAA Paper 99-2322, Los Angeles, California, U.S.A.
21. Tamura T, Yuasa S, Yamamoto K (1999) Effects of swirling oxidizer flow on fuel regression rate of hybrid rockets. In: 35th AIAA/ASME/SAE/ASEE Joint Propulsion conference & Exhibit, AIAA 99-2323, Los Angeles, California, U.S.A.
22. Yuasa S, Yamamoto K, Hachiya H, Kitagawa K, Oowada Y (2001) Development of a small sounding hybrid rocket with a swirling-oxidizer-type engine. In: 37th AIAA/ASME/SAE/ASEE Joint Propulsion Conference & Exhibit, AIAA 2001-3537, Salt Lake City, Utah, U.S.A.
23. Yuasa S, Hirata K, Shiraishi N, Sakurai T (2011) Issues for combustion characteristics of hybrid rocket engines. In: 28th international symposium on space technology and science, ISTS 2011-o-1-08, Okinawa, Japan
24. Kitagawa K, Mitsutani T, Ro T, Yuasa S (2004) Effects of swirling liquid oxygen flow on combustion of a hybrid rocket engine. In: 40th AIAA/ASME/SAE/ASEE Joint Propulsion conference and Exhibit, AIAA-2004-3479, Fort Lauderdale, Florida, U.S.A.
25. Mitsutani T, Kitagawa K, Makita M, Yuasa S (2005) Vaporization experiment of liquid oxygen cooling nozzle for hybrid rocket engine. Asian Joint conference on Propulsion and Power 2005, AJCPP 2005-22001, Kitakyusyu, Japan
26. Yuasa S, Kitagawa K, Sakurazawa T, Kumazawa I, Sakurai T (2011) LOX vaporization techniques for swirling-oxidizer-flow-type hybrid rocket engines. Int J Energ Mater Chem Propuls 10(2):155–168
27. Yuasa S, Ide T, Masugi M, Sakurai T, Shiraishi N, Shimada T (2011) Visualization and emission spectra of flames in combustion chamber of swirling-oxidizer-flow-type hybrid rocket engines. J Therm Sci Technol 6(2):268–277
28. Yuasa S, Sakamoto M, Sezaki T, Sakurai T, Shiraishi N, Shimada T (2009) Fuel regression rate behavior in swirling-oxidizer-flow-type hybrid rocket engines. In: 8th inter. sympo. on Special Topics in Chemical Propulsion, Log#143
29. Yuasa S, Shiraishi N, Hirata K (2012) Controlling parameters for fuel regression rate of swirling-oxidizer-flow-type hybrid rocket engine. In: 48th AIAA/ASME/SAE/ASEE Joint Propulsion cnference and exhibit, AIAA paper 2012-4106, Atlanta, Georgia, U.S.A.
30. Beer JM, Chigier NA (1972) Combustion aerodynamics. Applied Science Publication, London, pp 109–114
31. Ando H, Sakurai T, Yuasa S, Hatagaki S, Yui R, Takahashi S, Shiraishi N, Kitagawa K, Shimada T (2014) Development of a 5 kN-thrust swirling-oxidizer-flow-type hybrid rocket engine, In: Proc. Asian Joint conference on Propulsion and Power, AJCPP 2014-164, Jeju Island, Korea
32. Kitagawa K, Yuasa S, Sakurai T, Hatagaki S, Shiraishi N, Ando H, Yagishita T, Suzuki N, Takayama A, Yui R, Shimada T (2014) Development of test facilities for 5kN-thrust hybrid rocket engines and a swirling-oxidizer-flow-type hybrid rocket engine for technology demonstration. In: 10th inter. sympo. on Special Topics in Chemical Propulsion, Log#66
33. Sakurai T, Ando H, Yuasa S, Takahashi S, Tomizawa T, Hayashi D, Kitagawa K, Takayama A, Yui R, Shimada T (2014) Investigation of fuel regression rate characteristics of the 5 kN-thrust swirling-oxidizer-flow-type hybrid rocket engine. In; 11th international conference on flow dynamics, ICFD 2014-5363-2, Sendai, Japan
34. Hirata Y et al (2011) Improvement of regression rate and combustion efficiency of high density polyethylene fuel and paraffin fuel of hybrid rockets with multi-section swirl injection method. In: Proceedings of 47th AIAA/ASME/SAE/ASEE Joint Propulsion conference & exhibit, AIAA 2011-5907, San Diego, California, U.S.A.
35. Ohyama S et al (2012) A study of hybrid rockets with multi-section swirl injection method. In: 48th AIAA/ASME/SAE/ASEE Joint Propulsion conference & exhibit, AIAA 2012-3905
36. Ohyama S et al (2013) Effects of multi-section swirl injection method on fuel regression rate of high density polyethylene fueled hybrid rocket engine. In: 49th AIAA/ASME/SAE/ASEE

Joint Propulsion conference & exhibit and 11th international energy conversion engineering conference, AIAA-2013-4040, San Jose, California, U.S.A.

37. Araki K et al (2013) A study on performance improvement of paraffin fueled hybrid rocket engines with multi-section swirl injection method. In: 49th AIAA/ASME/SAE/ASEE Joint Propulsion conference & exhibit and 11th international energy conversion engineering conference, AIAA 2013-3634, San Jose, California, U.S.A.

38. Tada H et al (2013) Visualization of flames in combustion chamber of hybrid rocket engine with multi-section swirl injection method. In: Proceedings of 50th AIAA/ASME/SAE/ASEE Joint Propulsion conference, AIAA Paper 2014-3850, Cleveland, Ohio, U.S.A.

39. Karabeyoglu MA, Cantwell BJ, Altman D (2001) Development and testing of paraffin-based hybrid rocket fuels. In: 37th AIAA/ASME/SAE/ASEE Joint Propulsion conference and exhibit, AIAA 2001-4503

40. Hikone S, Isiguro T, Maruyama S, Nakagawa I (2010) Regression rate characteristics and burning mechanism of some hybrid rocket fuels. In: 46th AIAA/ASME/SAE/ASEE Joint Propulsion conference and exhibit, AIAA 2010-7030, Nashville, TN, U.S.A.

41. Wada Y, Jikei M, Kato R, Kato N, Hori K (2012) Application to hybrid rocket fuel of Low melting point thermoplastics. Trans Jpn Soc Aeronaut Space Sci 10(ists28):Pa_1–Pa5

42. McBride BJ, Gordon S (1996) Computer program for calculation of complex chemical equilibrium compositions and applications II. Users manual and program description, NASA Reference Publication. NASA Glenn Research Center, Cleveland, p 1311

43. Karabeyoglu MA, Toson E, Evans BJ (2014) Effect of "O/F Shift" on combustion efficiency. In: 50th AIAA/ASME/SAE/ASEE Joint Propulsion conference, AIAA 2014-3851, Cleveland, Ohio, U.S.A.

44. Karabeyoglu MA, Zilliac G (2006) Hybrid rocket fuel regression rate data and modeling. In: 42nd AIAA/ASME/SAE/ASEE Joint Propulsion conference & exhibit, AIAA 2006-4504, Sacramento, California, U.S.A.

45. Ozawa K, Shimada T (2013) Potential throttling performance and present challenges of unidirectional vortex injection hybrid rocket engines keeping optimal mixture ratio. Space Transportation symposium 2013, STCP-2013-043, 2013 (in Japanese)

46. Shimada T, Kitagawa K, Kanazaki M, Yuasa S, Sakurai T, Nakagawa I, Chiba K, Nakamiya M, Ozawa K (2014) Study of low-cost 100kg-satellite launcher using hybrid rocket engines. Paper presented at Session7 of Space Propulsion 2014, Cologne, 19–22 May 2014, DVD_SP2014/pdf/papers/session7/2980899_Shimada.pdf, 3AF, et al. www.propulsion2014.com

47. Usuki T, Ozawa K, Shimada T (2014) Flight performance estimation for swirling-oxidizer-flow-type hybrid rocket with swirling control. In: 11th International Conference on Flow Dynamics, OS8-7, Sendai, Japan

48. Ozawa K, Shimada T (2014) A theoretical study on individual and optimized control of thrust and mixture ratio of swirling-oxidizer-flow-type hybrid rocket. In: 11th international conference on flow dynamics, OS8-8

49. Ozawa K, Shimada T (2014) A linear stability analysis of unique low fre-quency mode on uni-directional vortex injection hybrid rocket engines. In: 65 international astronautical congress, IAC-14, C4,5,7, Toronto, Canada

50. Motoe M, Shimada T (2014) Numerical simulations of combustive flows in a swirling-oxidizer-flow-type hybrid rocket. In: 52nd Aerospace Sciences Meeting, AIAA SciTech, AIAA 2014-3010, National Harbor, Maryland, U.S.A.

51. Hirata K, Sezaki S, Yuasa S, Shiraishi N, Sakurai T (2011) Fuel regression rate behavior for various fuels in swirling-oxidizer-flow-type hybrid rocket engines. In: 47th AIAA/ASME/SAE/ASEE joint propulsion conference & exhibit, AIAA paper 2011-5677, San Diego, California, USA

52. Funami Y, Shimada T Combined analysis of reactive flow and heat transfer for hybrid rocket design engineering. In: 50th AIAA/ASME/SAE/ASEE Joint Propulsion conference, AIAA 2014-3456, AIAA, Cleveland, Ohio, U.S.A.

53. Karabeyoglu MA, Cantwell BJ, Stevens J (2001) Evaluation of homologous series of normal-alkanes as hybrid rocket fuels. In: 41th AIAA/ASME/SAE/ASEE Joint Propulsion conference and Exhibit, AIAA 2005-3908, Salt Lake City, Utah, U.S.A.
54. Wada Y, Kato R, Kato N, Hori K (2013) Observation of the surface regression behavior of hybrid rocket fuel using a slab motor, IAC-13, C4,2,9, x18666. In: 64th international astronautical congress, International Astronautical Federation, Beijing, China
55. Jens ET, Mechentely FS, Cantwell BJ, Hubbardx GS, Chandler AA (2014) Combustion visualization of paraffin-based hybrid rocket fuel at elevated pressures. In: 50th AIAA/ASME/SAE/ASEE Joint Propulsion conference and exhibit, AIAA paper, No. 2014-3848, Cleveland, Ohio, U.S.A.

Internal Flow Characteristics and Low-Frequency Instability in Hybrid Rocket Combustion

Kyung-Su Park, Yang Na, and Changjin Lee

Abstract The present study addressed the role of internal flow dynamics in determining regression rate and low-frequency instability in hybrid rocket. The first part was mainly devoted to examine the internal flow characteristics. Numerical simulations using large eddy simulation (LES) identified the formation of small-scale vortices by the interaction of fuel evaporation with axial flow near-surface region. Contours of instantaneous axial velocity show that the flow structure has been significantly altered and remained the isolated roughness patterns as found in several experiments. Also, the insertion of a diaphragm has been simulated with the dynamic change of turbulent coherent vortices and small vortices in the boundary layer. Results showed that small-scale vortices were not observed until a large-scale vortex shed in the downstream. Proper orthogonal decomposition analysis showed that inserting a diaphragm redistributed flow energy into lower modes 2–5, increasing the local regression rate after a diaphragm.

The second part focused on the initiation of low-frequency combustion instability (LFI) of pressure fluctuations with peak frequency of 10–20 Hz. A series of test was designed to examine the initiation of LFI. To this end, the sensitivity to instability was evaluated with parameters including volume ratio between main and post chamber, oxidizer flow rate, and solid fuel type. Results showed that the initiation of LFI was strongly related with flow dynamic change by the modification of chamber configuration. Additional studies revealed that pressure oscillations by vortex shedding in the post chamber could be closely related with the occurrence of LFI.

K.-S. Park
The 7th R&D Institute, Agency for Defense Development, Daejeon 305-152, South Korea
e-mail: parksu@add.re.kr

Y. Na
Department of Mechanical Engineering, Konkuk University, Seoul 143-701, South Korea
e-mail: yangna@konkuk.ac.kr

C. Lee (✉)
Department of Aerospace Engineering, Konkuk University, Seoul 143-701, South Korea
e-mail: cjlee@konkuk.ac.kr

577

1   Basic Features of Internal Flows

Hybrid rockets are attracting much research interests due to their well-known safety and low development cost. A recent combustion test with PMMA (polymethyl methacrylate) fuel reported a very interesting physical phenomenon produced at the fuel surface [1]. When the combustion was completed, it was found that isolated roughness spots of few millimeters in diameter are randomly distributed all over the PMMA surface. Figure 1 shows the typical shape of those cell structures captured at the end of the rocket motor. The chamber pressure was maintained at the level of about 300–400 psi. Some of the cell structures were covered with dark, unburned soot, which may be resulted from an incomplete combustion. The combustion condition was checked by the use of stoichiometric chemistry to see if the combustion occurred in a fuel-rich condition. The simple calculation of the stoichiometric reaction of PMMA with oxygen shows that the experiment was performed under an oxidizer-rich condition. The fact that dark spots were observed over the entire fuel surface even with high oxidizer-to-fuel (O/F) ratio is worthy of noting.

Figure 2 is a sequence of pictures taken with an equal interval of 1 s. It clearly displays a dramatic change of flow characteristics found on the PMMA surface. The first picture displays a typical streaky pattern of coherent vortices elongated in the main flow direction of the oxidizer. No discernible cell structure patterns are found at this time. However, these patterns (elongated in the streamwise direction) become somehow perturbed, and very tiny dark spots begin to form in the rear half of the fuel port. It should be noted, however, that the heavy concentration of dark spots in the middle of the fuel is attributed to a sudden expansion of the oxidizer flow from the pressure of 400–300 psi in the fuel port. Sometimes dark spots grow into bigger ones, and sometimes they are just washed away by the action of strong convection of the oxidizer.

Evans et al. [2] also reported similar cell structures on the fuel surface in their experiment with N_2O/HTPB (hydroxyl-terminated polybutadiene) combination.
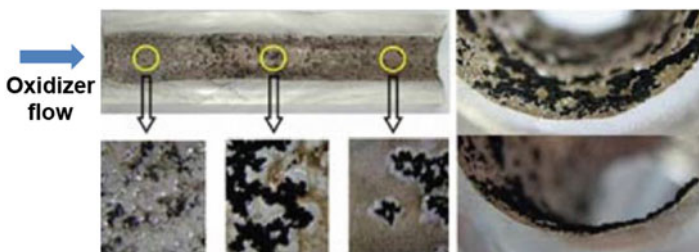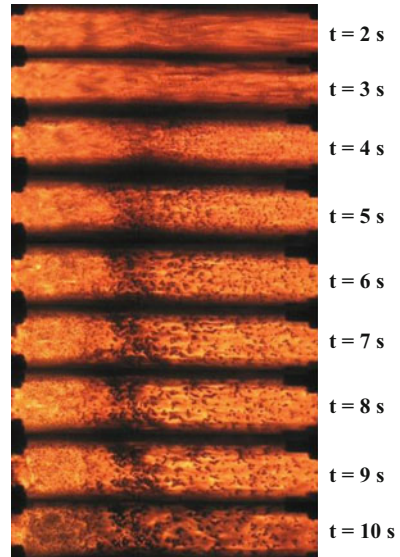

Fig. 1 Surface roughness patterns and their magnified views near the end of PMMA fuel port

Fig. 2 Sequential changes of near-surface flow patterns during PMMA combustion

A proper explanation for the formation of those roughness patterns is likely to be important to the understanding of the physics involved in the regression process of the hybrid fuel.

Meanwhile, the installation of a diaphragm draws very interesting attractions due to both its convenience for application and the effectiveness for acting as a flameholder [3, 4]. Inserting a diaphragm increases the turbulence intensity level in the chamber by enhancing the mixing of the oxidizer with the fuel vapor, which results in the increase of heat transfer to the wall. A recent work by Koo et al. [5] showed very interesting features of flow modification near the fuel surface in a cylindrical duct when a diaphragm was inserted at the front end of fuel.

An attempt of LES was made for the turbulent oxidizer flow convecting in a transpired chamber with surface mass injection in order to understand the role of turbulent structures with an objective of explaining the experimentally observed isolated cell patterns from the fluid mechanics point of view. Thus, a variation of thermodynamic properties accompanied in an actual combustion process was not taken into account here.

Also, other efforts were made to capture the flow responses near the surface when a diaphragm was inserted. Special attentions were devoted to the dynamic role of turbulent coherent vortices over the diaphragm and the active role of vertical fluctuating motions in the boundary layer, because these can determine the regression rate in the turbulent flow field. In the calculation, the Reynolds number was matched to that of the experiment [1]. Thus, up to 101 million grid points were used to resolve the essential turbulent scales involved. Also, the temperature was treated as a passive scalar with Prandtl number being 1.

2   Numerical Methodology

Considering the fact that the flow velocity inside the hybrid motor remains relatively low compared to the sonic velocity in the experiments, the flow is assumed to be incompressible. Thus, the filtered transport equation for the passive scalar in addition to continuity and momentum equations are described as follows:

$$\frac{\partial \overline{u}_i}{\partial x_i} = 0 \tag{1}$$

$$\frac{\partial \overline{u}_i}{\partial t} + \frac{\partial}{\partial x_i}\left(\overline{u}_i \overline{u}_j\right) = -\frac{\partial \overline{p}}{\partial x_i} + \frac{\partial}{\partial x_j}\left(2v\overline{S}_{ij} - \tau_{ij}\right) \tag{2}$$

$$\frac{\partial \overline{T}}{\partial t} + \frac{\partial}{\partial x_j}\left(\overline{u}_j \overline{T}\right) = \frac{\partial}{\partial x_j}\left(\alpha \frac{\partial \overline{T}}{\partial x_j} - q_j\right) \tag{3}$$

Here, the overbar denotes the grid filtering operation. In order to close the governing equations mathematically, LES models for the following residual stress tensor τ_{ij} and the residual heat flux vector q_j should be provided:

$$\tau_{ij} = \overline{u_i u_j} - \overline{u}_i \overline{u}_j, \; q_j = \overline{Tu_j} - \overline{T}\,\overline{u}_j \tag{4}$$

The following procedure was incorporated for calculation of the turbulent velocity field with a box filter in physical space:

$$\tau_{ij} - \frac{\delta_{ij}}{3}\tau_{kk} = -2v_t\overline{S}_{ij} + \left(L_{ij}^m - \frac{\delta_{ij}}{3}L_{kk}^m\right) \tag{5}$$

$$v_t = C_s\overline{\Delta}^2\overline{S}, \; L_{ij}^m = \overline{\overline{u}_i\overline{u}_j} - \overline{\overline{u}}_i\overline{\overline{u}}_j \tag{6}$$

Modified Leonard term is explicitly calculated using the filtered flow field, and the turbulent viscosity v_t is determined dynamically through the following steps using the test filtering operation denoted by tilde:

$$C_s = \frac{1}{2\overline{\Delta}^2}\frac{M_{ij}\left(L_{ij} - H_{ij}\right)}{M_{kl}M_{kl}} \tag{7}$$

$$M_{ij} = \left[\widetilde{\overline{S}\overline{S}}_{ij} - \left(\widetilde{\overline{\Delta}}/\Delta\right)\widetilde{\overline{S}}\widetilde{\overline{S}}_{ij}\right], L_{ij} = \widetilde{\overline{u}_i\overline{u}_j} - \widetilde{\overline{u}}_i\widetilde{\overline{u}}_j, H_{ij} = \widetilde{\overline{\overline{u}_i\overline{u}_j}} - \widetilde{\overline{\overline{u}}}_i\widetilde{\overline{\overline{u}}}_j \tag{8}$$

The procedure of DMM for getting the velocity field can be extended to the passive scalar in a similar manner for evaluating the residual heat flux vector q_j. As was

done for the residual stress tensor, heat flux vector consists of two terms, and the turbulent diffusivity is obtained dynamically as explained in the following:

$$q_i = -\alpha_t \frac{\partial \overline{T}}{\partial x_j} + F_j^m \tag{9}$$

$$\alpha_t = C_T \overline{\Delta}^2 \overline{S}, \quad F_j^m = \overline{\overline{T u_j}} - \overline{\overline{T}} \, \overline{\overline{u_j}} \tag{10}$$

$$C_T = \frac{1}{\overline{\Delta}^2} \frac{(F_k - G_k) H_k}{H_k H_k} \tag{11}$$

$$F_k = \widetilde{\overline{T u_k}} - \widetilde{\overline{T}} \widetilde{\overline{u_k}}, \quad G_k = \overline{\widetilde{\overline{T u_k}}} - \overline{\widetilde{\overline{T}}} \overline{\widetilde{\overline{u_k}}}, \quad H_k = \widetilde{\overline{S} \frac{\partial \overline{T}}{\partial x_k}} - \left(\widetilde{\overline{\Delta}} / \overline{\Delta}\right)^2 \widetilde{\overline{S}} \frac{\partial \widetilde{\overline{T}}}{\partial x_k} \tag{12}$$

Governing Eqs. 1–3 are integrated in time using a semi-implicit procedure. The convective term is treated by the third-order Runge-Kutta method, and the viscous term is integrated by the second-order Crank-Nicolson scheme. All spatial derivatives were conducted by the second-order central difference scheme except for the convective term of Eq. 3.

Numerical domain is shown in Fig. 3. The model rocket motor was replaced with the simple channel, and the regression process is approximated by the injection of the fluid at the wall. In order to supply the physically realistic turbulence to the region of interest with wall injection, the flow is continuously recycled in the channel placed in front of the domain.
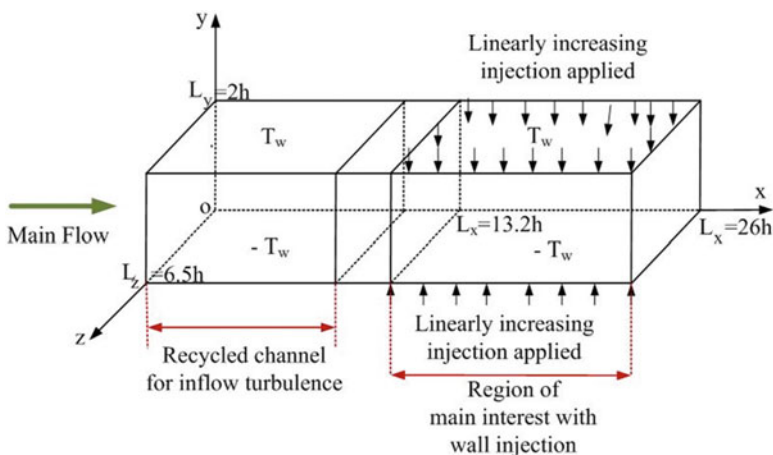

Fig. 3 Schematic of numerical domain

No-slip boundary condition was assumed along the wall except in the second half of the channel where injection is applied. The magnitude of the injected vertical velocity is assumed as a linear function from 0 to 3 % as seen in the experiment [2]. Periodic boundary condition was imposed in the spanwise direction, and the convective boundary condition was specified at the exit in order to allow turbulence structures to leave the domain with minimal distortion.

3 Results

3.1 Adjustment of Boundary Layer to Wall Blowing

The application of wall blowing brought a fundamental change in flow patterns from conventional turbulent structures which are more elongated in the streamwise direction into the isolated, round-shaped contours prevalent in the downstream of wall blowing. This is reminiscent of the surface cell structure patterns found in the experiment [1, 2] (Fig. 2). A close examination of iso-contours of coherent structures displayed in Fig. 4 reveals that the streaky structures generated upstream of wall injection are displaced away from the wall, leaving more isolated, round-shaped contours on the fuel surface as their footprints.

One of the main interests is the behavior of turbulence activity away from the wall. Figure 5 illustrates the turbulent stress and heat flux in the normal wall direction at several locations. Due to the interaction of main oxidizer flow with the wall blowing, a very strong shear layer develops away from the wall. In this shear layer, coherent structures multiply very rapidly and cause a sudden increase of turbulent heat flux in the vertical direction as well as Reynolds shear stress.

Finally, the time scale of the flow in the vicinity of the wall was investigated by inspecting the frequency spectra and autocorrelation of streamwise velocity. Note that, in the presence of wall blowing, very large negative excursion develops in the autocorrelation. For reference, it should be noted that the location of x/h = 8.1
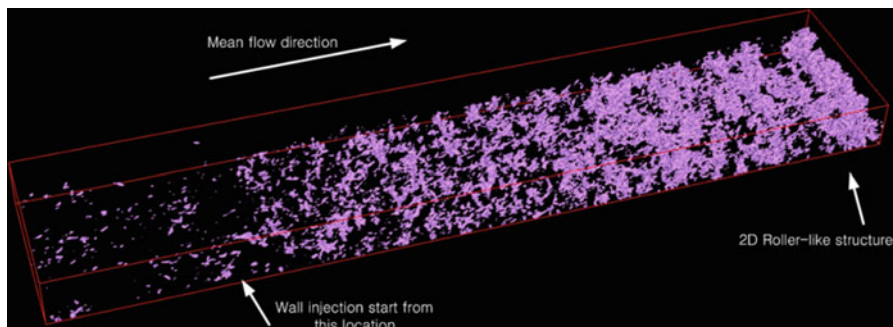
Fig. 4 Iso-contours of coherent structures in the region with wall blowing
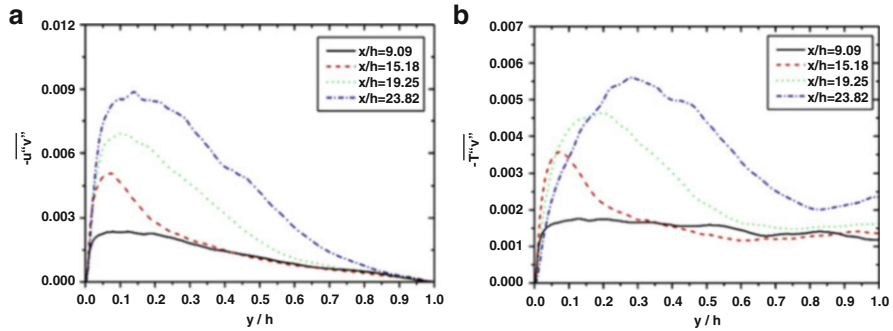
Fig. 5 Turbulent transport statistics at several locations: (**a**) Reynolds shear stress, (**b**) turbulent heat flux
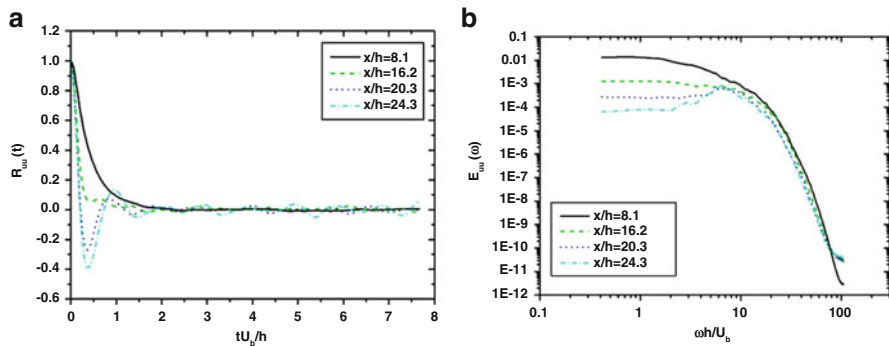
Fig. 6 Time characteristics of streamwise velocity in the vicinity of wall: (**a**) autocorrelation, (**b**) frequency spectra

corresponds to the simple change without wall injection. The presence of a large negative correlation would mean that near-wall streaky structures are not as long as in upstream, but they break down into several pieces due to the action of injection. This behavior is consistent with the appearance of isolated circular patterns in Fig. 4.

The frequency spectra in Fig. 6 also display the presence of a very distinctive peak near the nondimensional value of frequency around 8 after the application of wall injection. This characteristic frequency is much larger than that of typical vortex shedding flow configuration such as in the backward-facing step [6, 7].

3.2 Formation of Parietal Vortices

Time characteristics can be analyzed in a different way by looking at the time history of streamwise velocity component as shown in Fig. 7. This figure shows the time
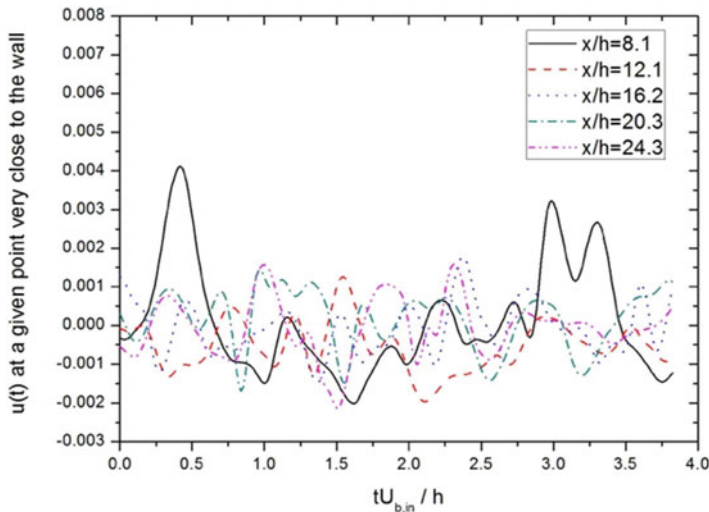
Fig. 7 Time trace of streamwise velocity in the vicinity of the wall

trace of streamwise velocity in the vicinity of the wall so that they will show how the velocity profile near the wall can be modified by the wall blowing. At all locations, instantaneous velocity can be negative for a significant time interval indicating the wall layer is vibrating forward and backwards.

The time trace of streamwise velocity includes all components of velocity contribution such as mean value, turbulent random motion, and periodic oscillating component. In order to identify the periodic oscillating components from the time trace of streamwise velocity, it is required to decompose the velocity into three components.

Figure 8 shows the instantaneous axial velocity profiles of u(y) within one cycle when wall injection is imposed. Velocity in upstream region at x/h = 9.1 shows conventional velocity profile observed in fully developed turbulent flow being characterized by sharp velocity gradient near the surface. The addition of wall blowing to the flow can modify the boundary layer by pushing flows away from the surface, and the velocity gradient diminishes gradually to zero in the downstream of the flow.

However, the velocity at x/h = 23.6 begins to experience negative fluctuations in the region very near the surface. It is believed that this negative excursion is due to the passage of roller-like vortices and is the manifestation of the periodic oscillations of surface flow. The addition of wall blowing in the upstream of the flow region does not seem to be strong enough to form roller-like vortices even though wall blowing is imposed.

Figure 9 shows the axial distribution of pressure fluctuations. Blue color represents low-pressure region, and red one corresponds to high-pressure region.
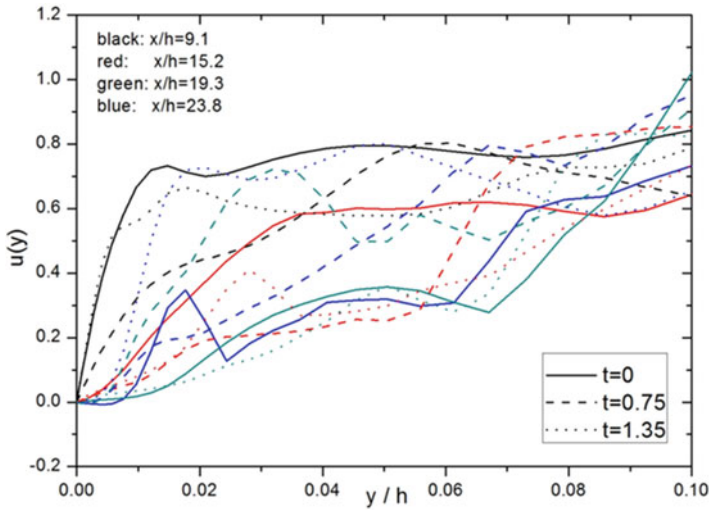
Fig. 8 Instantaneous axial velocity profile within one cycle of fluctuation
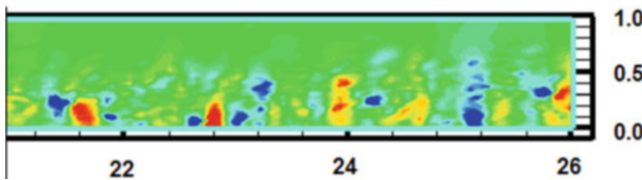
Fig. 9 The overview of the formation of pressure fluctuating spots

The periodic appearance of blue and red spots along the wall surface represents the formation of vortices caused by the interaction between main axial flow and wall blowing.

3.3 Modification of Flow Characteristics Upon Inserting a Diaphragm

Previous sections describe the fact that internal flows in hybrid rockets display very interesting features of small-scale oscillations and radial fluctuating motions due to the formation of very tiny size vortices near the wall. In experiments, inserting a diaphragm brought about the large increase in local regression rate around a diaphragm by enhancing a turbulent intensity with lumped fluctuating motions. Thus, it is very important to understand how lumped fluctuating motions could alter the already existing basic flow features near the surface and how it affects the
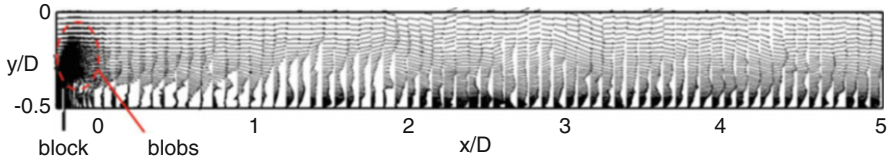
Fig. 10 Axial velocity vectors with a block
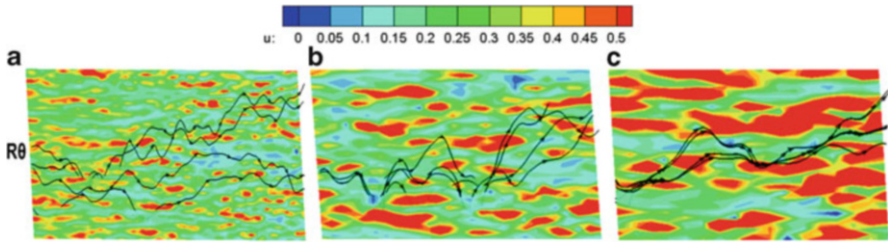
Fig. 11 Expanded view in 3D streak lines analysis on streamwise velocity in baseline (**a**) front (x/D < 5), (**b**) middle (5 < x/D < 10), and (**c**) rear section (10 < x/D < 15)
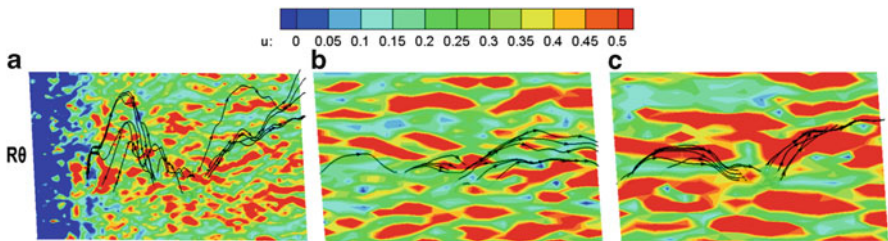
Fig. 12 Expanded view in 3D *streak lines* analysis on streamwise velocity with a block (**a**) front (x/D < 5) (**b**) middle (5 < x/D < 10), and (**c**) rear section (10 < x/D < 15)

heat transfer rate to the surface. To create a better focus on the near-wall turbulent flow with an acceptable computational cost, hybrid rocket motor was idealized by a simple pipe flow surrounded by blowing wall without considering a chemical reaction. Detail of the methodologies is well addressed in reference [5, 6].

As it is expected, thick structures of turbulent boundary layer were formed up to x/D < 5 where the flow structures broke into highly irregular ones. This can be seen in Fig. 10 as dense population of blobs is formed after a diaphragm. These blobs appeared shortly after the diaphragm, showing that the diaphragm generated irregular flow structures. But the large-scale vortex existed only in the region around a diaphragm.

Figures 11 and 12 showed magnified views of three different sections in the computational domain at a location of $y^+ = 10$. Flow rapidly moves toward the

wall in front of the positive-vorticity (defined by clockwise rotation) spot and moves away from the wall behind the spot contributing continuously squeezed and relieved motions as shown in Fig. 11.

In Fig. 12a, highly fluctuated streak lines were observed due to the dominated lumped motions just over a diaphragm. However, amplitudes of highly fluctuating streak lines decreased very quickly by dissipative cascading processes in the middle section as shown in Fig. 12b. And the new interactions began to produce small-scale vortices near surface again. Streak lines in the rear section showed very similar behaviors as ones observed in the baseline, in which small-scale vortices stimulated radial flow oscillations with continuous squeezing and relieving motions.

POD (proper orthogonal decomposition) determines a set of orthogonal functions and extracts the energetic coherent structures from the simulation data. Benefits of the method are the fact that the high-dimensional data can be divided into low-dimensional data sets with arbitrary number of data modes for one's convenience, and the divided data sets are easily reconstructed.

Figure 13 shows the comparison of the modification of allocated mode energy between the baseline and the case with a diaphragm. For baseline case, POD results clearly showed that the primary mode contains most of flow energy of about 97.5 % of total energy. Energy level allocated to mode 2–9 was less than 0.5 %, which was used to create small-scale vortices near the surface.

In the flow with a diaphragm, the primary mode energy exhibited a less energy than that in the baseline case (about 0.6 % less). The enhancement of small-scale structures in mode 2–5 seemed to be directly associated with experimentally observed local increase in regression rate after a diaphragm.
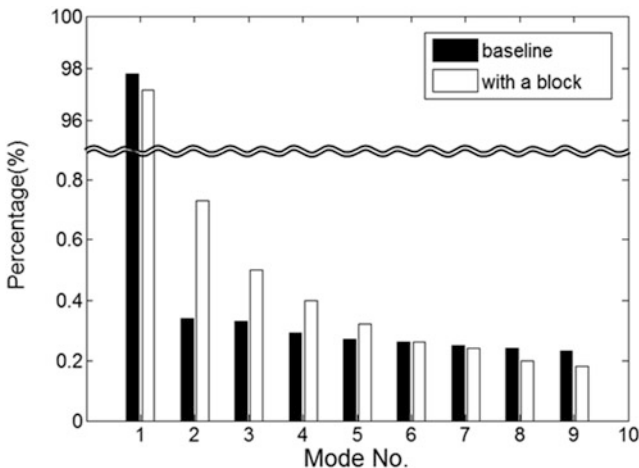

Fig. 13 Comparison of mode energy allocations between the case without a diaphragm and baseline case

4   Non-acoustic Low-Frequency Instability

Combustion in hybrid rocket motors displays relatively stable characteristics compared to other conventional chemical rockets such as solid and liquid rockets. A typical instability in the hybrid rocket combustion is a limit cycle oscillations with a peak frequency of less than 100 Hz much lower than acoustic modes. In this regard, low-frequency instability (LFI) is important to understand the nature of combustion instability in hybrid rocket because every hybrid program has reported some difficulties in handling LFI oscillations. Even though the causes of the instability are not clearly understood yet, LFI is considered as the manifestation of non-acoustic instability mode in the hybrid rocket combustion.

Many studies have been investigated on the initiating mechanisms of LFI. Especially, Karabeyoglu et al. [9] revealed that LFI was the result of complicated coupling of thermal lag of solid fuel and the boundary layer adjustment to external perturbations in hybrid rocket combustion. The results of his research yielded a good agreement with experimental data of pressure oscillations with a peak frequency up to 50 Hz. Carmicino et al. [10] performed a series of combustion tests with various injector configurations. Different injector configuration produced different types of flow pattern in combustion chambers. Results showed that combustion instability was only observed in the combustion with radial-type injectors. They claimed that unsteady heat release was possibly related with periodic formation of large-scale vortex shedding into the post chamber producing additional pressure perturbations. They proposed that a resonance of pressure perturbations by unsteady heat releases in the post chamber and acoustic excitations in the combustor can be a triggering mechanism of combustion instability.

Despite of many research efforts [9–13], no comprehensive studies are available to bridge the gap between experimental observations and physical understandings on the triggering mechanisms of LFI. A series of experimental tests was designed to investigate the triggering mechanism of LFI.

Figure 14 shows the schematic of the experimental setup. A series of hybrid rocket combustion tests was conducted with a lab scale motor of GOx and PMMA combinations as an oxidizer and solid fuel, respectively.

Table 1 reports a summary of results of all test cases. A baseline test was made as a reference case, in which combustion pressure showed stable behavior and no distinctive LFI occurred. Each test case has different configurations of main and post chamber length, whereas pre chamber length was kept unchanged. Here VR is the volume ratio between main and post chambers. The mass flow controller was used to control oxidizer mass flow from 10 to 25 g/s for providing a variety of O/F conditions.

Tests 1 and 2 were designed to investigate the effect of post chamber length on the initiation of LFI. Test 3 was the case where the main chamber length increased as twice as that of baseline. Tests 4 and 5 were attempted to examine the effect of post chamber length. Tests 6–8 were intended to investigate the effect of variation of oxidizer mass flow rate on the pressure amplifications. Tests 9–12 were
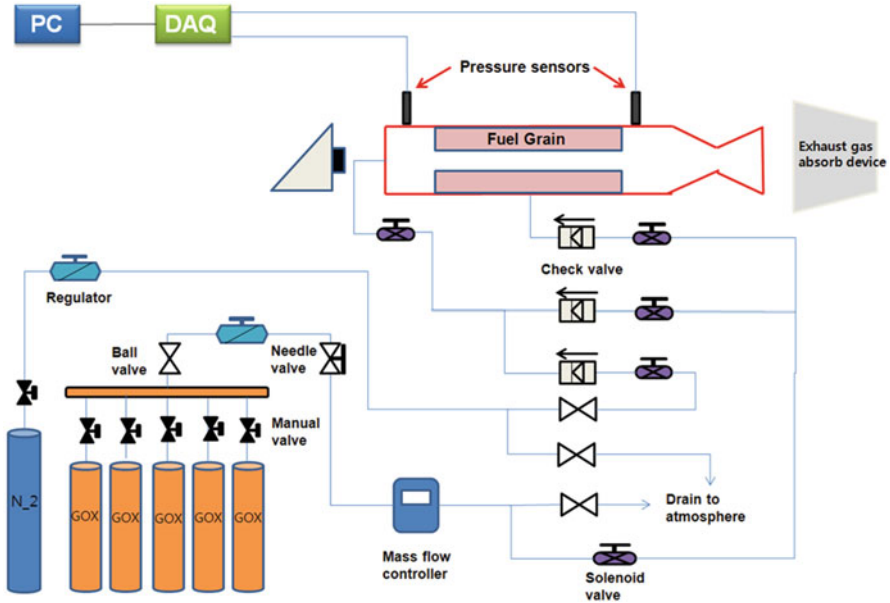
Fig. 14 Schematic of experimental setup

Table 1 Summary of combustion test results

Test no.	Solid fuel	Chamber length (mm)	Post chamber length (mm)	Oxidizer mass flow rate (g/s)	O/F ratio	LFI	Remarks	
Baseline	PMMA	200	75	20	5.20	No	Reference test	
1	PMMA	200	105	20	5.57	No	Volume ratio between main/post chamber	
2	PMMA	200	200	20	5.59	No		
3	PMMA	400	75	20	2.35	Yes		
4	PMMA	400	105	20	2.41	No		
5	PMMA	400	200	20	2.46	No		
6	PMMA	400	75	10	2.23	Yes	Oxidizer mass flow rate	
7	PMMA	400	75	15	2.29	Yes		
8	PMMA	400	75	25	2.43	Yes		
9	PMMA	400	75	20	2.31	Yes	Rear diaphragm	Vortex shedding over a backward-facing step
10	PMMA	400	75	20	2.28	Yes		

Table 1 (continued)

Test no.	Solid fuel	Chamber length (mm)	Post chamber length (mm)	Oxidizer mass flow rate (g/s)	O/F ratio	LFI	Remarks
11	PMMA	400	75	20	2.23	Yes	Cutting rear edge
12	PMMA	400	75	20	2.32	Yes	
13[a]	PMMA	400	75	20	2.43	Yes	Pressure-sensitive combustion regime
14	HTPB	200	75	20	3.78	No	Fuel type
15	HTPB	200	40	20	3.60	Yes	

[a]Nozzle throat diameter, 5.5 mm
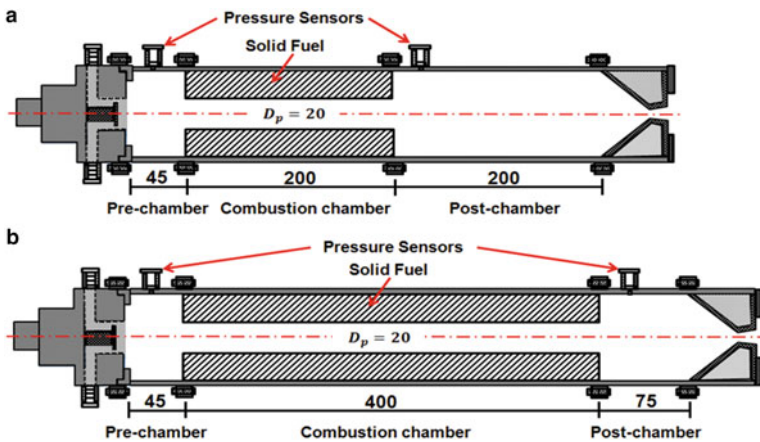
Fig. 15 Schematic of test configurations for (**a**) test 2 and (**b**) test 3

performed to examine how the formation of vortex shedding over backward-facing steps affects the initiation of LFI. Test 13 was done with a reduced throat diameter to increase a chamber pressure. In a reduced combustion pressure, the regression rate may become pressure sensitive. Test 13 was designed to investigate the effect of combustion pressure on the onset of instability. Finally, tests 14–15 were carried out to investigate the responses of combustion pressure in a different solid fuel of HTPB substituted with PMMA.

Figure 15 shows the comparison of geometrical configurations in tests 2 and 3. LFI was observed in test 3, while test 2 did not show any unstable behaviors.

4.1 Baseline Results

The baseline test was carried out in a motor with PMMA and GOx at a constant oxidizer flow rate of 20 g/s to obtain reference test data. Details of physical
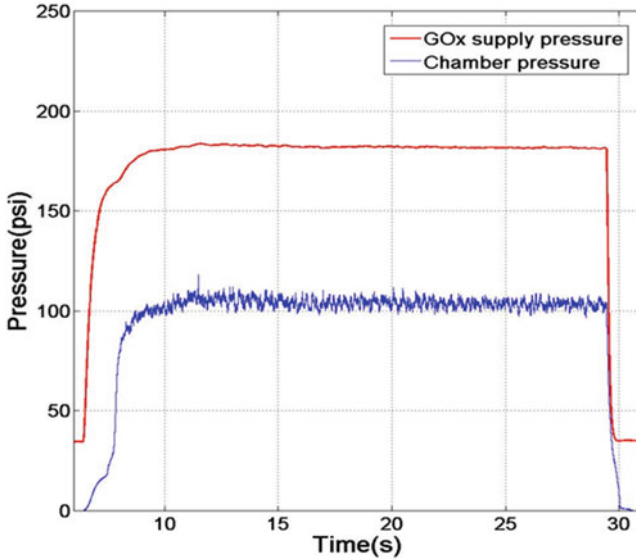
Fig. 16 Trajectory of combustion pressure of baseline
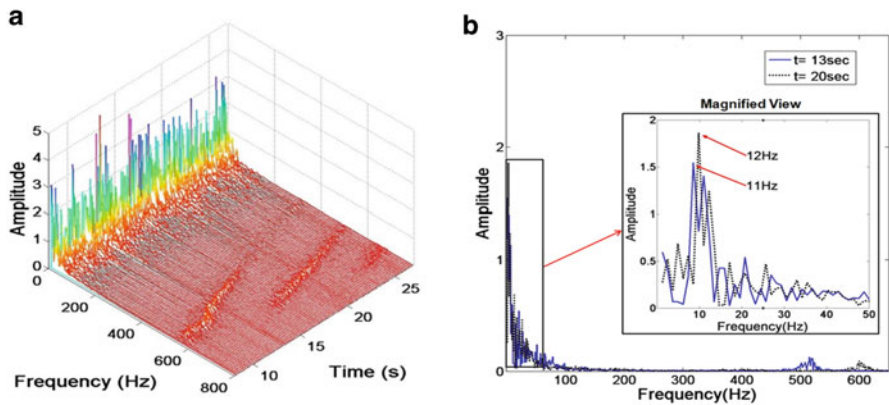
Fig. 17 (**a**) FFT Waterfall and (**b**) peak frequency for baseline

dimensions were well addressed in reference [13]. The main chamber had a length of 200 mm and the post chamber length was set to be 75 mm. Figure 16 shows a combustion pressure curve in baseline test. It displays a stable pressure trajectory of about 105 psi with moderate amplitudes of approximately 5 psi. The oxidizer supply pressure was successfully controlled at about 180 psi to maintain the constant oxidizer flow rate of 20 g/s.

Figure 17 is the FFT (fast Fourier transform) analysis of combustion pressure oscillations of baseline tests in the spectral domain of 0–800 Hz. Spectral data
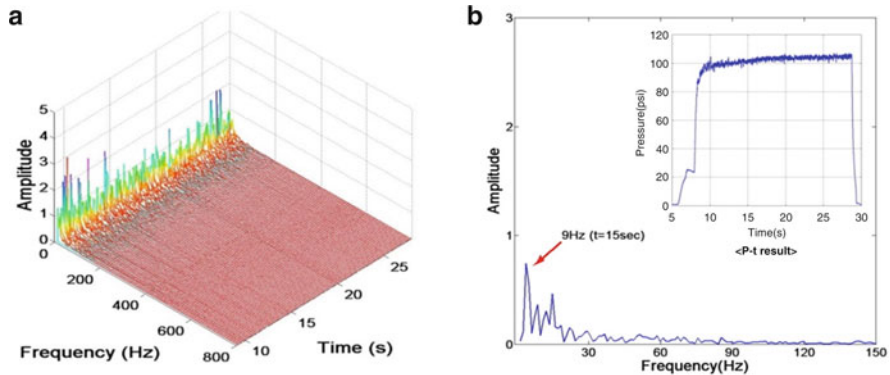
Fig. 18 (**a**) FFT Waterfall and peak frequency for test 2

showed that the dominant frequencies of combustion pressure lie in the range of 10–15 Hz, which approximately coincides with the frequency bands responsible for thermal lag oscillations in the combustion of solid fuels [9, 11]. Other frequency bands were also identified in the spectral domain as 450–550 Hz, 500–600 Hz, and 600–650 Hz, respectively, though the amplitudes of these are negligibly small.

4.2 Pressure Curves and Spectral Data in Tests 2 and 3

Test 2 was designed to examine the combustion characteristics of pressure oscillations by only increasing the post chamber length from 75 mm of baseline length to 200 mm. In this case, the combustion pressure was stably maintained at about 105 psi. Figure 18 shows the spectral analysis of pressure oscillations with peak frequency of 9–20 Hz, which is qualitatively the same range as that of the baseline case. However, oscillations with frequency peaks above 100 Hz disappeared. Since the increase in the post chamber length provides more volume, small-amplitude oscillations with peak frequency above 100 Hz were easily damped out in a larger volume.

Test 3 was attempted to investigate the effect of changes in the combustion chamber volume on the initiation of LFI by increasing the main chamber length from 200 to 400 mm, while the post chamber length was kept unchanged at 75 mm of the baseline. Figure 19 shows the trajectory of combustion pressure in test 3. The magnitude of peak-to-peak amplitudes suddenly increased from stable level up to around 30 psi at 14 s of combustion and lasted about 3 s. Spectral analysis showed that pressure oscillations with peak frequency of about 17 Hz were dominantly active in the amplification. After the end of first amplification, the second amplification with 14 Hz appeared in a row at the time of 23 s. The amplitudes of the second amplification were less than those measured at the first
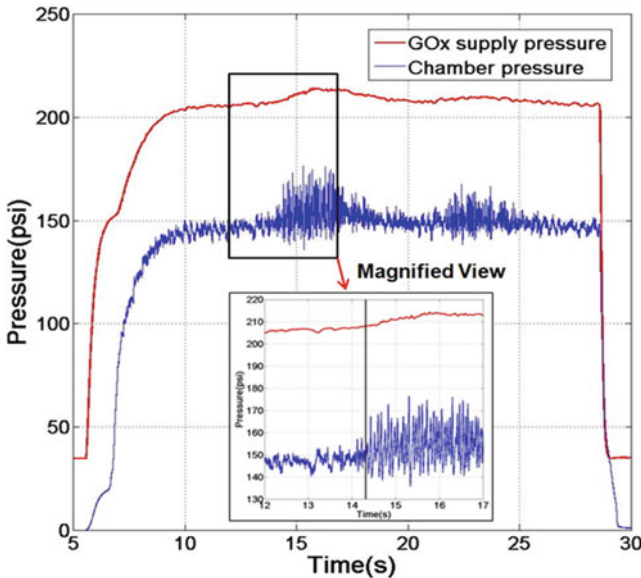
Fig. 19 Trajectory of combustion pressure and oxidizer supply pressure in test 3

one. In literature, combustion instability was defined as a case where the amplitude of pressure oscillations exceeds 5 % of an average pressure. In test 3, pressure oscillations attained amplitudes larger than 23 % and 15 % of mean pressure in each amplification, and it can be classified as the exhibition of LFI.

Note that the oxidizer flow rate in test 3 was controlled to maintain at a constant mass flow rate of 20 g/s. However, measurements showed that the oxidizer supply pressure slightly increased from the mean pressure of 210 psi at the moment of LFI, because the onset of combustion instability affected to increase the supply pressure in the upstream of injectors through the flow controller. A magnified view of pressure curve in Fig. 19 clearly showed that the first amplification was independent of an increase in the oxidizer supply pressure.

Figure 20 shows the frequency waterfall and peak frequencies of pressure curves in test 3. Pressure oscillations suddenly amplified with magnitudes three times larger than those in the baseline case. Even though the peak frequency of instability in this case (14–17 Hz) differs from one of 10–15 Hz measured in the baseline, LFI in test 3 seems to be the result of resonating two different oscillating mechanisms: pressure oscillations due to thermal lag already existed in the baseline case and the unknown source of oscillations in the combustion. In this regard, Karabeyoglu et al. [9] claimed that LFI is the result of complex coupling of thermal transients in solid fuels, known as thermal lags, and the transitional adjustment of the turbulent boundary layer to external perturbations. As mentioned, a thermal lag in the solid fuel is known as the source of typical oscillations with peak frequency of 10–30 Hz determined by the difference in thermal characteristics between solid fuel and combustion gas.
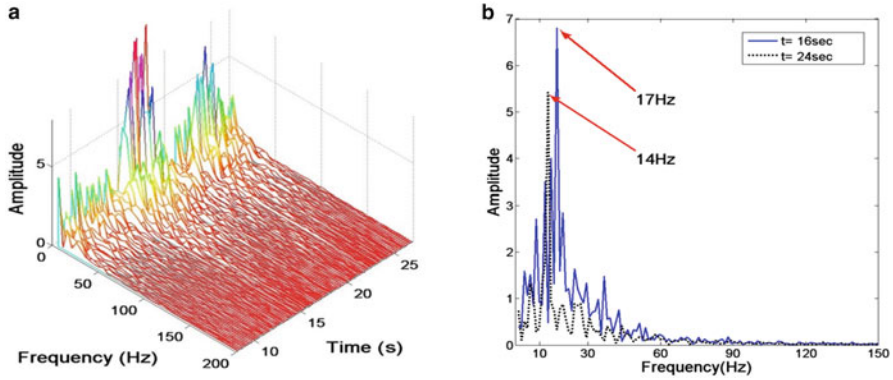
Fig. 20 (**a**) FFT Waterfall and (**b**) peak frequency in test 15
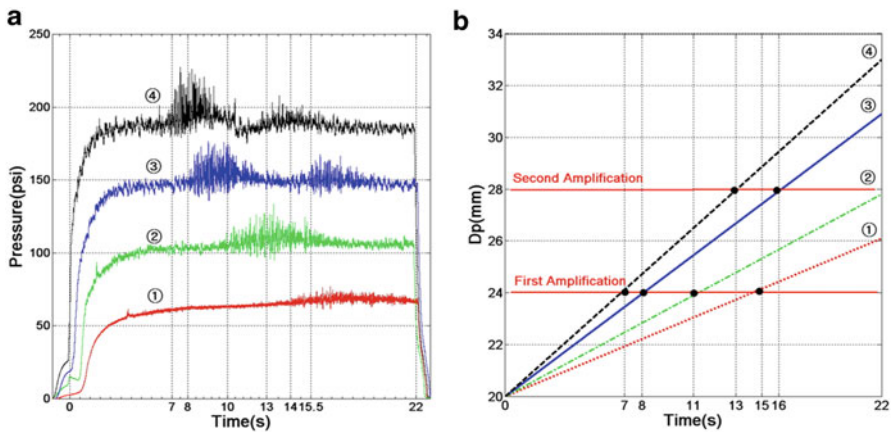
Fig. 21 (**a**) P-t results and (**b**) the variation of port diameter with different oxidizer flow rates ①
test 6 ② test 7 ③ test 3 ④ test 8

4.2.1 Controlling Oxidizer Mass Flow Rate and Solid Fuel

Tests 6–8 were designed to investigate the effect of controlling the oxidizer mass
flow rate on the initiation of LFI. In the tests, the oxidizer flow rate was controlled
to provide different O/F conditions, while other parameters were kept unchanged as
in test 3. All tests were attempted to modify flow characteristics in the fuel grain by
controlling mass flow rates.

Figure 21 depicts a summary of pressure curves with different oxidizer mass
flow rates and the variation of O/F ratio in tests 3, 6, 7, and 8 by increasing the
oxidizer flow from 10 to 25 g/s. The pressure oscillations amplified in all cases at
a certain moment of combustion. The first amplification occurred at 7, 8, 10, and
14 s of combustion depending on oxidizer flow rates. In Fig. 21a, the amplification

Fig. 22 Trajectory of combustion pressure in test 15 with HTPB
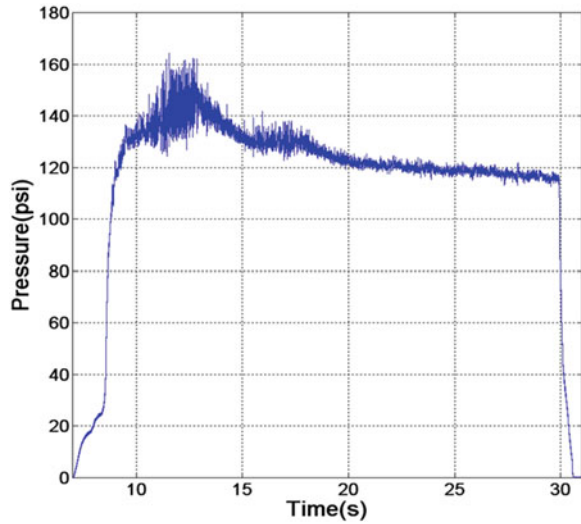
appeared at an earlier time of combustion as the oxidizer flow rate increased. Note that the second amplification was not observed in tests 6 and 7.

The time variations of fuel diameter in test 3 and 6–8 were displayed altogether in Fig. 21b based on the predictions of fuel regression rates in reference [8]. Here, the regression rate in test 3 was measured as approximately 0.25 mm/s, which showed a good agreement with the prediction of 0.27 mm/s in reference [8]. Critical fuel diameters corresponding to pressure amplification in each test were calculated by the time variation of fuel diameters in Fig. 21b. And the calculation confirmed that the critical fuel diameters in tests 6–8 were found approximately 24 and 28 mm, respectively. Note that the final fuel diameter in tests 6 and 7 did not reach to a critical diameter at which the second amplification occurred. This can explain the reason why the second oscillation was not observed in tests 6 and 7.

Next, tests 14–15 were carried out with different solid fuels by substituting PMMA with HTPB. Figure 22 shows a combustion pressure trajectory in test 15. The oscillations were amplified immediately after the ignition developing into LFI more quickly than test 3 with PMMA. The lower density and easy evaporating characteristic of HTPB are responsible for the earlier appearance of LFI than in PMMA. Generally, HTPB regressed very quickly than PMMA approaching its critical diameter where instability can be initiated.

Figure 23 exhibits a frequency waterfall and peak frequency of pressure oscillations in test 15. The peak frequency in test 15 was shifted to slightly higher one of 20–30 Hz than those in test 3. Note that the dominant frequency of oscillations in stable combustion of HTPB was mainly determined by its thermal characteristic. The frequency response of thermal lag in HTPB combustion was estimated as about 15–25 Hz [6, 10]. Therefore, the occurrence of LFI in test 15 can be considered as the result of resonating with thermal lag oscillations of HTPB.
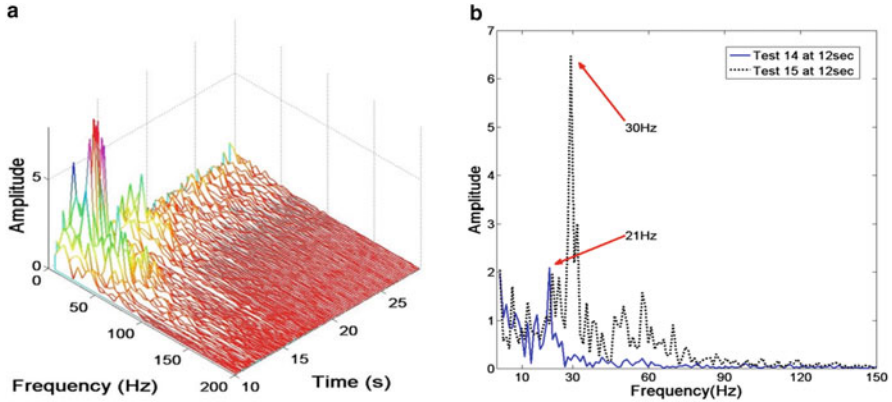
Fig. 23 (**a**) FFT Waterfall and (**b**) peak frequency in test 15

Also, LFI in tests 3 and 6–8 seems independent of either the material property, composition of solid fuels, or oxidizer mass flow.

4.2.2 Fuel Regression vs. LFI Initiation

Reviewing the results of tests 3 and 6–8, LFI occurred at a certain time of combustion or at a certain fuel diameter. In general, the inner diameter of solid fuels gradually increases as combustion proceeds. Test 8 was repeated to measure the critical fuel diameter by stopping oxidizer supply at which LFI initiated. Figure 24 shows both the entire pressure curve in test 8 and a part of pressure curve obtained by terminating at the instant of LFI. Critical diameters corresponding to the first and second amplification were calculated as about 24 and 28 mm by averaging several measurements, respectively. As seen in the previous section, the critical diameter corresponding to the first amplification in tests 3, 6, and 7 was also estimated as about 24 mm by calculating the data from Fig. 25. This result suggests that the time variation of fuel diameter takes a very important role in determining the occurrence of LFI during the combustion through the unknown coupling mechanism of pressure perturbations.

Since the diameter difference between fuel grain and post chamber composes backward-facing step height, the time variation of fuel diameters brought into a continuous reduction in step height and consequently weakened vortex strength in the post chamber. If the initiation of LFI would be associated with the formation of vortex flow in the post chamber, the installation of a diaphragm with fixed diameter of 24 mm could artificially sustain additional pressure perturbations, which could supposedly lead to LFI during the combustion. This is one of the possible scenarios that can explain the initiation of LFI in the combustion.

In order to assess the sensitivity of the time variation of fuel diameters to the initiation of LFI, tests 9 and 10 were done equipped with different rear diaphragms.
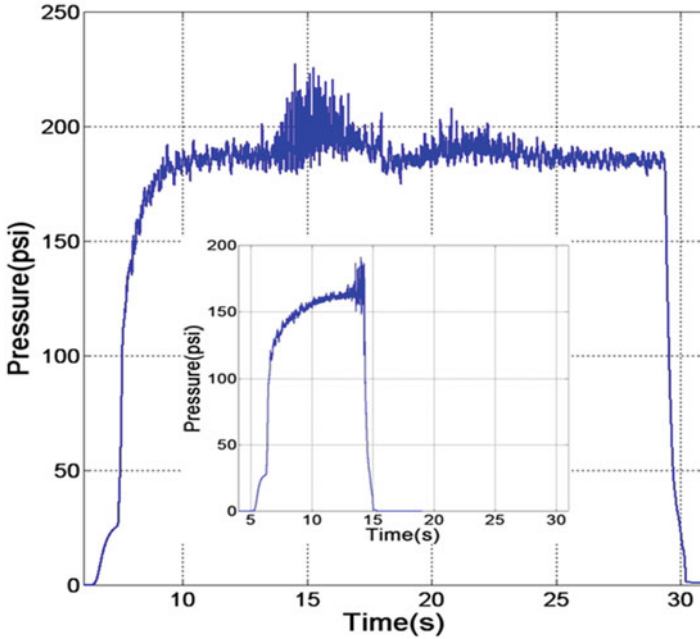
Fig. 24 Trajectory of combustion pressure in test 8

Fig. 25 Schematic of post chamber equipped with rear diaphragm
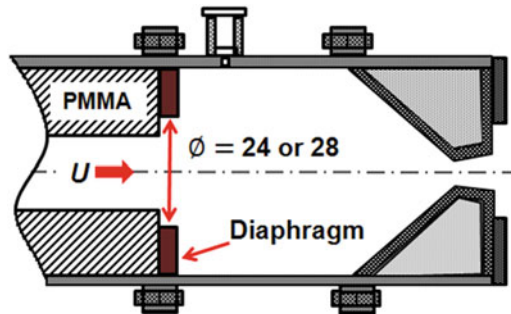
Each diaphragm has different inner diameters of 24 and 28 mm, which are the same diameters as ones measured at LFI in test 8. Figure 25 shows a schematic of post chamber configuration installed with rear diaphragms of diameters of 24 and 28 mm, respectively. Each test was done at the same test condition as in test 3.

Figure 26 depicts a summary of pressure traces in each test with two different rear diaphragms. The amplification abruptly occurred at the instant where fuel diameters regressed toward the diaphragm diameter of 24 mm. Unlike the pressure curve in test 3, LFI sustained to oscillate without any damping until the end of the test. In test 10 with a diaphragm of 28 mm diameter, the pressure amplification similarly occurred again with less amplitude. Based on the results in test 10, the initiation
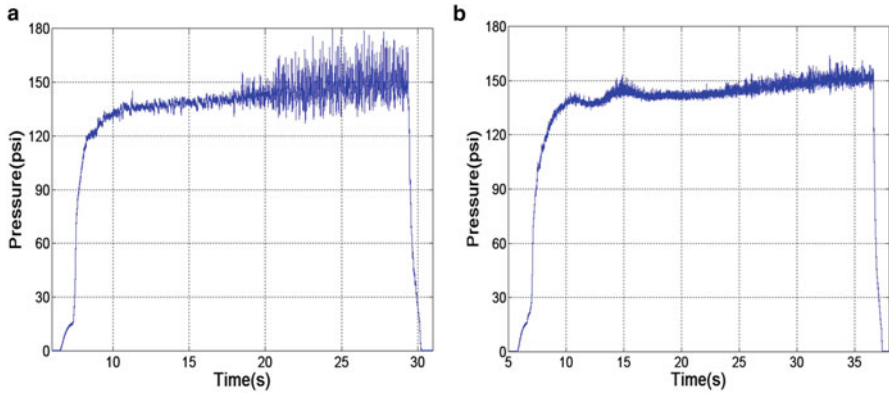
Fig. 26 Pressure trajectories with a rear diaphragm: (**a**) test 9 ($\phi = 24$ mm) and (**b**) test 10 ($\phi = 28$ mm)
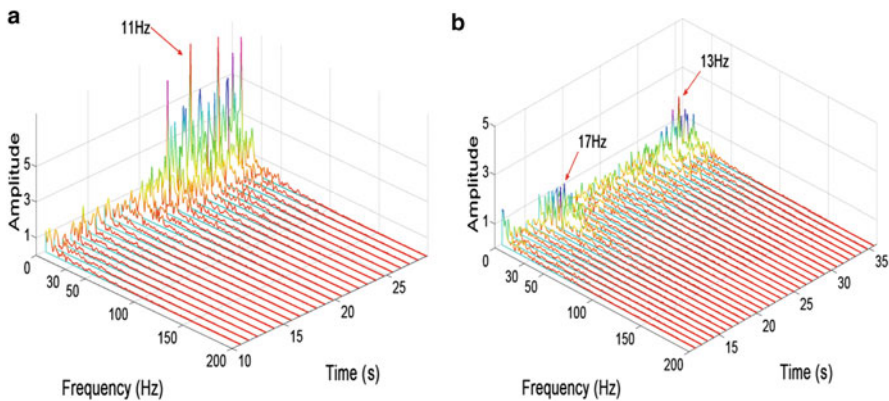
Fig. 27 Peak frequency in LFI with rear diaphragms: (**a**) test 9 ($\phi = 24$ mm) and (**b**) test 10 ($\phi = 28$ mm)

of LFI was directly related to the time variation of fuel diameters or somehow the change in combustion chamber volume due to the fuel regression.

Figure 27 displays the frequency peaks of pressure curves in each test case (a) and (b) in Fig. 26. Peak frequencies in both cases lied in the frequency range of 11–17 Hz. This range is the same one as previously identified in test 3.

4.2.3 Vortex Shedding Over Backward-Facing Step

Results from tests 9 and 10 revealed that LFI suddenly occurred at certain fuel diameters during the combustion. It is natural to suspect the time variation of geometrical shape of backward-facing step in the post chamber to be a critical

Fig. 28 Variation of edge cutting angle at rear end: (**a**) test 11 (60°) and (**b**) test 12 (30°)
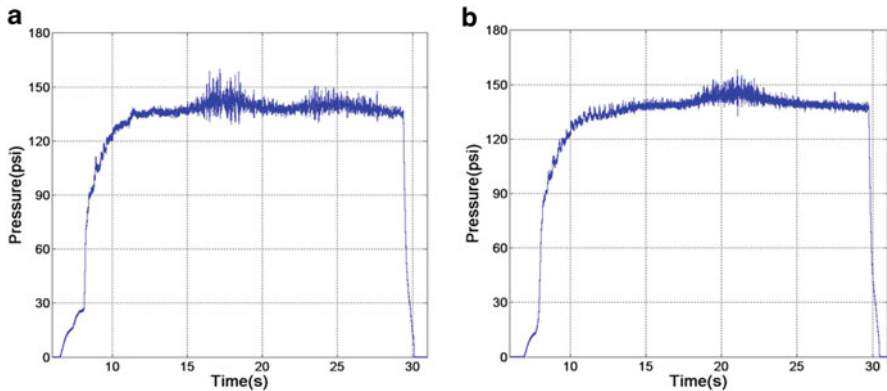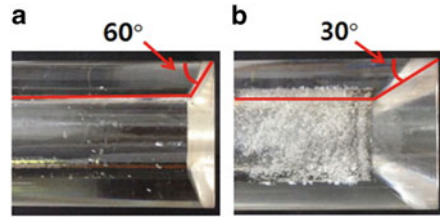
Fig. 29 P-t results with cutting of backward step: (**a**) test 11 (60°) and (**b**) test 12 (30°)

parameter in triggering LFI. And the regression of solid fuels continuously reduces step height and affects the inflow patterns of combustion gas into the post chamber including the strength of vortex shedding. To estimate the effect of vortex shedding on the initiation of LFI, additional tests were designed with fuel grains having different rear edge angles of 30 and 60°. Test conditions were maintained as the same one as used in test 3. Figure 28 shows a schematic of rear edges with different cutting angles of 30 and 60°, respectively.

Figure 29 shows the trajectories of combustion pressure of tests with different cutting angles. For the test with 60-degree edge angle, the overall pattern of pressure oscillations was very similar to the oscillations already observed in test 3, showing two consecutive pressure amplifications. However, pressure curves with the 30-degree cutting angle exhibited a relatively stable combustion without second amplification.

Figure 30 displays the spectral analysis of peak frequency of pressure oscillations of each case with different edge angles. The peak frequency in both cases was dominantly active in the range of 14–18 Hz, which is a similar range of frequency as one of 15–20 Hz identified in test 3.

In summary, the variation of rear edge cutting angles did not completely turn off the occurrence of LFI even though the cutting rear edge of fuel grain contributed to slightly reduce the oscillation amplitudes. Therefore, the scenario that the vortex formation in the post chamber is critically responsible for the initiation of LFI
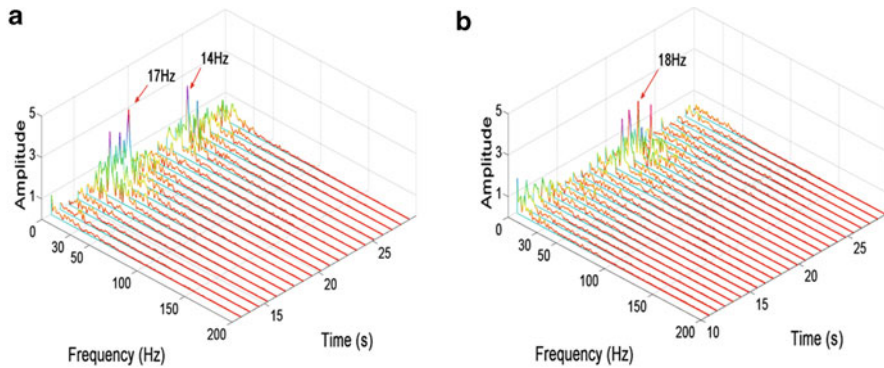
Fig. 30 Peak frequency results with cutting of backward step: (**a**) test 11 (60°) and (**b**) test 12 (30°)

has to be reviewed again. In this regard, a hypothesis can be suggested regarding the critical role of vortex shedding in the post chamber. If the vortex shedding containing unburned mixtures in the pockets would flow into the post chamber, it could generate unsteady heat releases and additional low-frequency pressure perturbations as a result of continuous combustion in the post chamber as well. Pressure oscillations would be suddenly amplified, leading to LFI in the case of the resonance with existing oscillations by the thermal lag of solid fuels.

4.2.4 Effect of Combustion Pressure

Wooldridge et al. [12] investigated that LFI could possibly occur if the combustion pressure was maintained below a critical pressure where the regression rate was dependent on the chamber pressure. In this combustion condition, fuel combustion was very sensitive to the change in combustion pressure. And the pressure perturbations could lead to the development of LFI. Therefore, test 13 was additionally designed to see what would happen if the combustion pressure of 150 psi in test 3 increases. To this end, the test was done with an increased chamber pressure of about 190 psi by reducing the nozzle throat diameter from 6.5 to 5.5 mm, at which solid combustion may not be pressure sensitive anymore. And, other test conditions were kept the same as in test 3.

Figure 31 shows the trajectories of combustion pressure oscillations in test 13. Pressure oscillations were amplified immediately after the ignition producing two consecutive occurrence of instability. The overall pattern of pressure oscillations seemed very similar to those in test 3 in which two consecutive pressure peaks occurred.

Figure 32 is the spectral analysis of pressure oscillations with peak frequency of 14–16 Hz in test 13, the similar range of peak frequency as observed in test 3. If LFI in test 3 would be initiated by the pressure sensitiveness of fuel
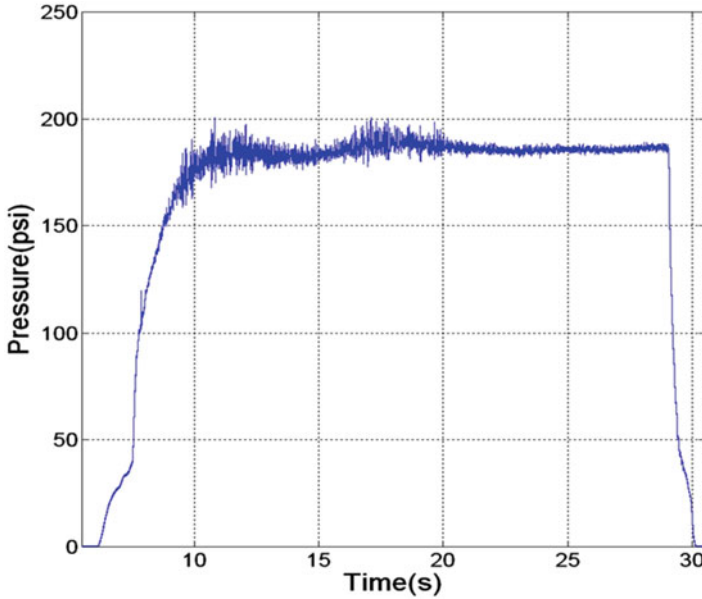
Fig. 31 Trajectory of combustion pressure in test 13
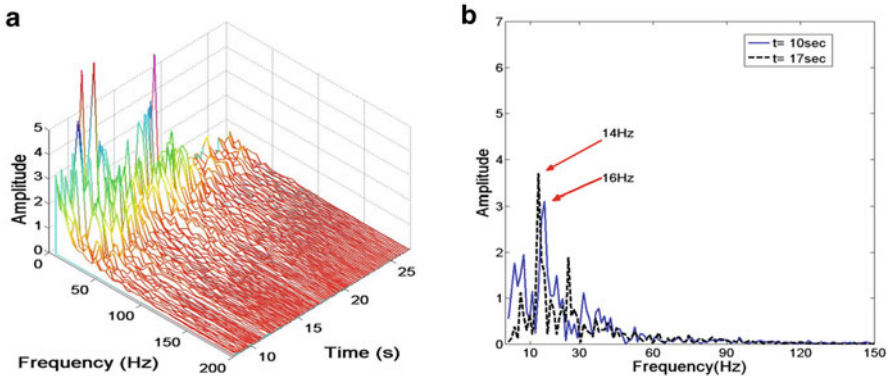
Fig. 32 (**a**) FFT Waterfall and (**b**) peak frequency in test 13

regression, the increase in combustion pressure could shift combustion dynamics rather toward stable combustion because the fuel regression was not dependent on the combustion pressure anymore. However, the pressure trajectory in test 13 shows very similar oscillation behaviors as those in test 3 in two ways. The first one is the persistent occurrence of LFI. And the other is the consecutive appearance of two amplifications. Thus, LFI in test 3 was surely not the pressure amplification coupled with fuel regression behaviors in the pressure sensitive regime.

5 Conclusions

Various realizations of instantaneous flow fields clearly show that the structural feature of turbulent vortices was significantly altered by the application of wall injection. Several turbulent statistics and correlations also support the fact that the wall injection drastically changes the characteristics of the near-wall turbulence. Unlike the typical streaky vortices found in the region without wall injection, which are mainly elongated in the streamwise direction, modified coherent structures in the tilted configuration by the action of wall injection are likely to leave isolated, round-shaped footprints of themselves on the fuel surface. Therefore, the sequential change of the patterns observed in the experiment (Fig. 2) can be strongly related to the change in kinematical configuration of near-wall structures caused by the wall blowing.

Upon inserting a diaphragm, numerical results showed that a large-scale vortex formed over a diaphragm interferes with existing vortices near the surface and limits the vortex size until the large-scale vortex starts to shed away. Highly fluctuating streak lines were observed due to the dominated lump motions over a diaphragm. In addition, POD analysis revealed that inserting a diaphragm altered the primary mode energy, reducing its energy contents slightly less than that of the baseline case. The decreased energy was mostly reallocated to raise the flow energy of lower modes 2–5. This change seemed to be directly associated with the experimentally observed local increase in the regression rate after the diaphragm.

As for the initiation mechanism of LFI in hybrid rocket combustions, combustion in baseline case showed very stable pressure oscillations with the predominant peak frequency range of 10–15 Hz. However, pressure oscillations suddenly jumped into unstable mode, leading to LFI with a peak frequency of 14–17 Hz when combustion chamber length increased from 200 to 400 mm. The dominant peak frequency of 14–17 Hz in this case was interestingly the same frequency range as those observed in the stable combustion. Interestingly, LFI suddenly initiated at the moment where the fuel diameter regressed approaching to a certain diameter of 24 and 28 mm respectively. This may be the interesting evidence that the initiation of LFI is strongly related to the change in flow dynamics induced by the modification of chamber configuration including main and post chamber volume and length.

Reviewing all available test results, vortex shedding into the post chamber with partially burned mixtures can act as unsteady heat sources through continuous combustion and produce additional low-frequency pressure perturbations in the post chamber.

References

1. Na Y, Lee C (2008) Intrinsic flow oscillation in channel flow with wall blowing, AIAA paper 2008–5019
2. Evans B, Favorito NA, Kuo KK (2006) Oxidizer-type and aluminum particle addition effects on solid fuel burning behavior, AIAA Paper 2006–4676
3. Grosse M (2009) Effect of a diaphragm on performance and regression of a laboratory scale hybrid rocket motor using nitrous oxide and paraffin, AIAA Paper 2009–5113
4. Kumar CP, Kumar A (2013) Effect of diaphragms on regression rate in hybrid rocket motors. J Propuls Power 29(3):559–572
5. Koo H, Mon KO, Lee C (2013) Effect of a block on flow oscillations near evaporating solid fuel surface. Int J Aerosp Sci Technol 30(1):269–277
6. Lee C, Na Y (2009) Large eddy simulation of flow development in a chamber with surface mass injection. J Propuls Power 25(1):51–55
7. Kim B, Na Y, Shin KH, Lee C (2012) Nonlinear combustion and fluid mechanics in a hybrid rocket. J Propuls Power 28(6):1351–1358
8. Na Y, Lee C (2013) Large eddy simulations and experiments of nonlinear flow interactions in hybrid rocket combustion. Prog Propuls Phys 4:113–132
9. Karabeyglu A, De Zilwa S, Cantwell C, Zilliac G (2005) Modeling of hybrid rocket Low frequency instabilities. J Propuls Power 21:1107–1116
10. Carmicino C (2009) Acoustic, vortex shedding, and low-frequency dynamics interaction in an unstable hybrid rocket. J Propuls Power 25(6):1322–1335
11. Lee C (2002) The application of ZN analysis to the transient combustion of hybrid rocket. In: 40th AIAA aerospace sciences meeting & exhibit, Reno, 14–17 January 2002
12. Wooldridge CE, Marxman GA, Kier RJ (1969) Investigation of combustion instability in hybrid rocket, NASA CR-66812
13. Park K, Lee C (2014) Low frequency instability in lab-scale hybrid rocket motors, AIAA paper 2014–3454

Performance Analysis of Paraffin Fuels for Hybrid Rocket Engines

Songqi Hu, Wu Guanjie, and Noor Fatima Rashid

Abstract The paraffin-based fuel has high regression rate and power, which is an ideal energy source for hybrid rocket engine. The research findings showed that: the energy characteristics of paraffin fuel and HTPB fuel with different oxidizers are similar; the specific impulse of paraffin fuel and HTPB fuel with LOx is the highest about 3194.3 N·s/kg and 3259 N·s/kg, respectively; the paraffin-based fuel/LOx propellant has low optimum oxygen to fuel ratio and high specific impulse, which is suitable for large hybrid rocket engine; the decomposition temperature of pretreated paraffin is higher than that of the unprocessed paraffin, but lower than that of HTPB; the chemical kinetics parameters of pretreated paraffin-based fuel has been calculated in oxygen atmosphere, and "E" is 101.72 KJ/mol, and pre-exponential factor "A" is 4.53382×10^{11}; the melting characteristics of paraffin-based fuel and HTPB fuel have been verified by the solid fuel melting experiment; the regression rate of paraffin-based fuel is higher than the common HTPB fuel under the same conditions; with the increase of oxidizer mass flow rate, the regression rate of solid fuel increases accordingly for the same fuel formulation; the vortex formation occurs at the front section of the hybrid engine and the afterburner section in the numerical simulation, while the main exothermic reactions take place at the section above the fuel surface and after burning chamber.

1 Introduction

The hybrid engine has combined advantages of both the solid and liquid rockets. It has thrust adjustability and can be powered off easily and switched on repeatedly; moreover, it has better controllability, very low cost, high safety, reliability, reusability, and non-pollution properties, which are among the development goals for power systems of the future aircraft industry [1–3]. Paraffin-based solid fuels are new hybrid rocket engine fuels, having nearly the same density as HTPB fuel and the combustion heat little higher than HTPB, while its regression rate is three to four

S. Hu (✉) • W. Guanjie • N.F. Rashid
School of Astronautics, Northwestern Polytechnical University, Xi'an 710072, Shaanxi, China
e-mail: pinecore@nwpu.edu.cn; wuguanjie@mail.nwpu.edu.cn; noordogar@hotmail.com

605

times that of HTPB fuel [4]. Paraffin-based fuel has gained extensive attention in recent years as an ideal hybrid engine fuel and has been used widely in the research and testing of the hybrid engine.

Stanford University has developed the paraffin-based fuel successfully and done the ground test over 300 times. In 1999, the paraffin-based fuel hybrid rocket was launched to the height of 1829 m by Stanford University [5]. The paraffin-based fuel hybrid sounding rocket which has a 3-in. outside diameter was designed and made in 2004, and it could reach an altitude of 2871 m [6]. China also carried out the research in hybrid rocket engine technology [7, 8]. Beihang University designed and developed the sounding rocket of "Beihang Series," among which "Beihang II" used N_2O as the oxidizer and HTPB as the fuel, which was launched successfully in December 2008. It was the first time of the launch and recovery of hybrid engine-powered sounding rocket in China. In addition, hydrogen peroxide was used for the first time as the oxidizer in the hybrid engine for "Beihang III," the engine has variable thrust and can work for a longer duration, and its fight test was done successfully in April 2012. In October 2010, "Chengda I" hybrid rocket, having 3.6 m length and an outer diameter of 16 cm, was launched to the height of 8 km by National Cheng Kung University. The hybrid engine used N_2O as the oxidizer, and the fuel contained 50 % paraffin and 50 % artificial rubber. The university also launched two small hybrid rockets to the height of 1.5 km in March 2014. So far, the hybrid rocket engine has used a lot of oxidizers, which mainly include N_2O, liquid oxygen (LOx), H_2O_2, and HNO_3. San Fanli [9] in Tsinghua University designed and developed the principle prototype of N_2O/HTPB hybrid rocket engine. By the analysis and evaluation of engine performance, he got the conclusion that low oxygen-fuel ratio had a great effect on the engine energy. So it was necessary to accelerate the flow rate of N_2O. Beihang University Li Xintian [10] used H_2O_2/HTPB propellant in hybrid engine experiment, and he found that the catalytic ignition gives higher regression rate and keeps pressure longer than that of igniter ignition. Northwestern Polytechnical University Wang Pengfei [11] used a rectangular hybrid engine to test the regression rate of paraffin fuel and HTPB fuel, and he found that the regression rate of paraffin fuel is 1.58–1.74 times greater than that of HTPB fuel under the same condition. The thermal degradation characteristics of HTPB/AP composite system were analyzed by the methods of PDSC, TG-DTG, and DSC-FTIR by Shi Zhenhao [12], and the results showed that the increase of pressure and addition of Al powder both could improve the propellant's thermal decomposition. By using the coupled simulation on gas-phase combustion and heat transfer in solid fuel, Yang Yuxin [13] developed a numerical method indicated by the instantaneous regression rate of solid fuel in hybrid engine and concluded that with the working of the engine, the surface temperature and the regression rate of the solid fuel decreased, while the temperatures and the regression rates of every point on the pyrolysis surface of the fuel along the axial direction of the engine differed from each other, even at the same time.

Here, the energy performance calculations for paraffin-based fuel and HTPB fuel with different oxidizers have been performed to see the effect of these bipropellant combinations. The thermal decomposition characteristics of different fuels are

obtained by the thermal decomposition experiments, and the experimental data has been used to calculate the kinetic parameters of pretreated paraffin in oxygen atmosphere. The melting characteristics of paraffin fuel and HTPB fuel have been found by using a device employing solid rocket motor which produces high-temperature and high-pressure conditions. The rectangular solid-gas hybrid engine with end face combustion has been used to measure the regression rate of paraffin-based fuel in hybrid engine, and the relationship between the regression rate and the oxidizer mass flow rate has been studied. The combustion characteristics of paraffin-based fuel in hybrid engine have been analyzed by the numerical simulation.

2   Energy Performance Calculations

In this paper, the solid fuel for hybrid rocket engine is mainly composed of HTPB and paraffin and metal powders. The main products of the fuel and oxidizer reaction are CO_2, H_2O, N_2, etc. The Gibbs free energy minimization method is used for calculation of energy performance characteristics of different propellant formulations on engine performance.

2.1   The Calculation Scheme

The thermodynamic calculation for combustion chamber and exhaust nozzle were performed by Gibbs free energy minimization method [14, 15], and some parameters of energy characteristics of the fuel were obtained. The energy characteristic calculations were performed at these conditions: initial temperature of 300 K, combustion chamber working pressure of 3.4 MPa, and nozzle expansion ratio of $A_e/A_t = 70$, and the oxidizers included are H_2O_2, LOx, N_2O, and HNO_3. The fuel formulations are shown in Table 1.

2.2   Calculation Results and Analysis

The effect on specific impulse by using different oxidizers with paraffin-based fuel and HTPB fuel is shown in Fig. 1:

Table 1 The paraffin-based fuel formulation

Sample	HTPB (%)	Paraffin (with $-OH$) (%)	Al(%)	Mg(%)	C (%)
1#	15	35	15	25	10
2#	50	0	15	25	10
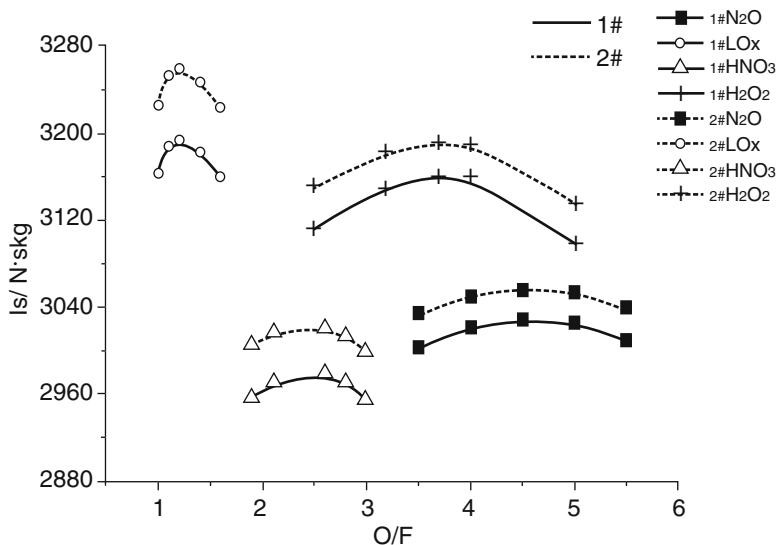
Fig. 1 The effect of O/F on Is with 1# and 2# using different oxidizers

By analyzing curves in Fig. 1, the following conclusions can be drawn: the optimal oxygen-fuel ratios of paraffin-based fuel with N_2O, LOx, HNO_3, and H_2O_2 were 4.6, 1.2, 2.5, and 3.8, respectively, while that of HTPB were 4.6, 1.2, 2.4, and 3.8, respectively. Among them, the paraffin-based fuel and liquid oxygen-specific impulse were the highest with 3194.3 N·s/kg, while that of HTPB were 3259.2 N·s/kg. For paraffin-based fuel and HTPB fuel using same oxidizer combination at the same oxidizer to fuel ratio, the specific impulse for HTPB fuel is slightly higher than the paraffin fuel that may be due to the pretreatment (make it with –OH).

2.3 The Application Prospect Analysis of Paraffin with Different Oxidizer Combinations

The currently used hybrid rocket propellant combinations are mainly N_2O/HTPB, H_2O_2/HTPB, N_2O/paraffin, and HNO_3/paraffin. Due to inherent property of paraffin (alkane), the regression rate is about two and three times than that of HTPB; therefore, a lot of researches are being carried out on various wax types for the hybrid engine.

The boiling point of liquid oxygen is 90 K, which requires a special storage device. If the liquid oxygen is used in hybrid rocket engines, it will increase the negative quality of the engine and decrease the combination property of hybrid

rocket. Based on the analysis of Fig. 1, the group of paraffin-based fuel and liquid oxygen fuel gives the highest specific impulse value of 3194.3 N·s/kg at optimum oxygen to fuel ratio of 1.2. If the design of hybrid rocket engine has high specific impulse requirements, the paraffin-based fuel and liquid oxygen as oxidizer is the best choice of propellant combination. LOx/paraffin propellant combination not only gives a very high specific impulse, but also the oxidizer consumption is very small, so it can be considered for application in large boosters.

N_2O is a kind of liquefiable gas, and it exists in liquid and had a density of 754 kg/cm^3 under the circumstance of 5.2 MPa and 20 °C. Paraffin-based fuel and N_2O reaction not only consume a lot of oxidizing agent but also results in lower specific impulse. Although N_2O has some disadvantages in the choice of properties as the propellant combination and the production and transportation costs are relatively high, considering the practical situation, without the need to reduce the temperature, N_2O can be liquefied at room temperature and easy to carry into the rocket engine, which also has good controllability as an oxidizer. Therefore, it has broad application prospect in the hybrid rocket engine. Many domestic and foreign research institutions are carrying out technical researches in hybrid engine, mostly using N_2O as oxidizer.

Nitric acid is corrosive acid and strong oxidizer. Its production is convenient and transportation is safety. If it has to be used as hybrid engine oxidizer, the storage tank, pipeline, and other allied equipment are needed to be made of anticorrosion material; at the same time, the pump will also increase the undesirable load in engine. Compared to the paraffin/HNO_3 combination and other combinations, the specific impulse of the former is not higher than others. However, considering hybrid engine's comprehensive properties which make it easy to take the liquid HNO_3 into the rocket, HNO_3 can be used as a suitable oxidizing agent in sounding rockets and some large hybrid rocket boosters.

H_2O_2 is a kind of easy oxidizing agent, whose production is nontoxic and cannot pollute the environment. After entering the combustion chamber, hydrogen peroxide and the fuel are needed at the catalytic decomposition for chemical reaction, but the effective catalytic device is difficult to achieve. The specific impulse of paraffin/H_2O_2 is little lower than that of paraffin/LOx. H_2O_2 is liquid, even without external pressure or cooling, which is safe and suitable for a variety of small hybrid rocket engines, especially sounding rockets near the earth space.

3   Thermal Characteristic Experiment

The thermal decomposition characteristics of pretreated paraffin (with –OH), pure paraffin, and HTPB were tested by differential scanning calorimetry (DSC) and thermogravimetric analyzer (TGA), under different pressure and at different heating rates.

3.1 The Experimental Scheme

In this paper, paraffin, pretreated paraffin, and HTPB are chosen as samples, named P1, P2, and P3; thermal analysis carried out by TG and DSC techniques under air and nitrogen atmosphere. The measurements are made in dynamic atmosphere with gas flow rate of 30 ml/min. For TG and DSC analysis, the temperature changed from room temperature to 950 °C [16].

3.2 TG Experimental Analysis

The TG experiments of paraffin, pretreated paraffin, and HTPB samples were conducted at the heating rate of 20 °C/min under nitrogen atmosphere. In Fig. 2, the curves P1, P2, and P3 stand for paraffin, pretreated paraffin, and HTPB in TGA, respectively.

Figure 2 shows that paraffin and pretreated paraffin began to decompose at 182 °C and 230 °C, respectively. The initial decomposition temperature of pretreated paraffin is higher than that of the untreated paraffin, which indicates that the pretreated paraffin is useful, and the characteristics of pretreated paraffin are different from the one untreated.
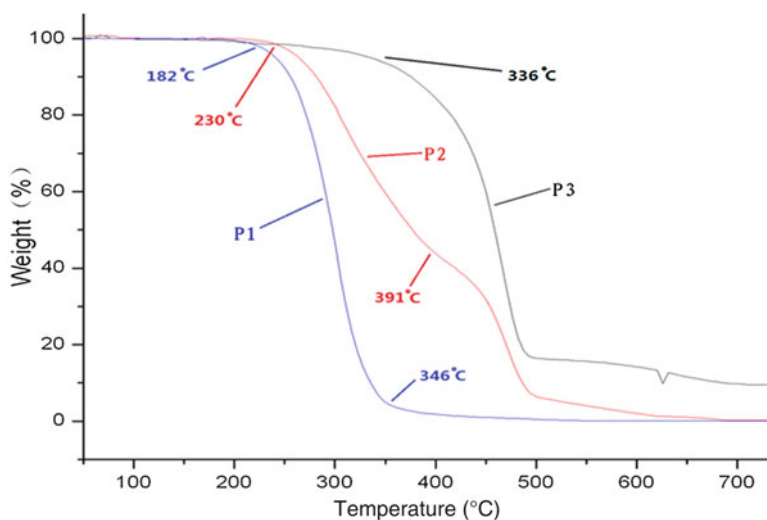
Fig. 2 The TG curves of paraffin, pretreated paraffin, and HTPB in N_2
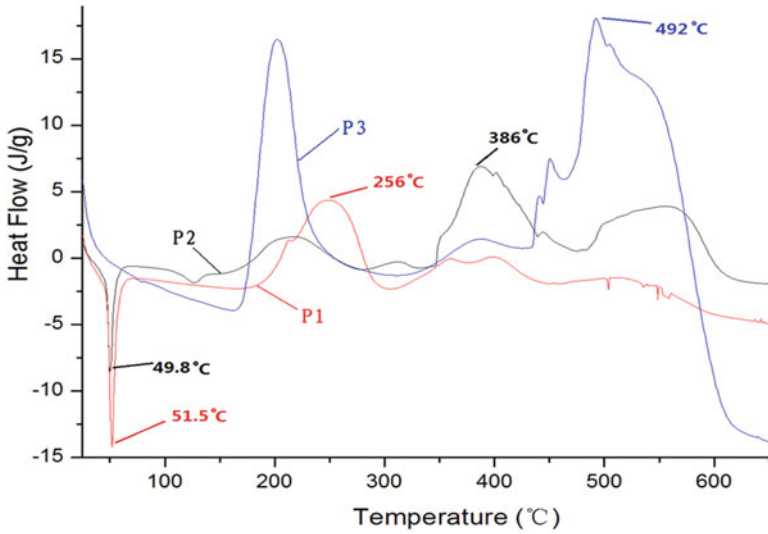
Fig. 3 The DSC curves of paraffin, pretreated paraffin, and HTPB in air

3.3 DSC Experimental Analysis

The DSC experiments of paraffin, pretreated paraffin, and HTPB samples were conducted at the heating rate of 20 °C/min under normal pressure and air atmosphere. In Fig. 3, the curves P1, P2, and P3 stand for paraffin, pretreated paraffin, and HTPB in DSC experiment, respectively.

Figure 3 shows that the exothermic peak temperatures of paraffin, pretreated paraffin, and HTPB were 256 °C, 386 °C and 492 °C, respectively, in air. Pretreated paraffin's melting temperature was 49.8 °C, and heat absorption was 149.10 J/g, which was lower than that of untreated paraffin (278.42 J/g). It showed that pretreatment could reduce paraffin's melting heat absorption.

3.4 DSC Thermal Analysis of Pretreated Paraffin Under Different Heating Rates

The DSC thermal analysis for pretreated paraffin was made under different heating rates and oxygen atmosphere. In Fig. 4, curves 1, 2, 3, and 4 stand for the DSC curves of pretreated paraffin in O_2 atmosphere under the heating rate of 5 °C/min, 10 °C/min, 15 °C/min, and 20 °C/min, respectively.
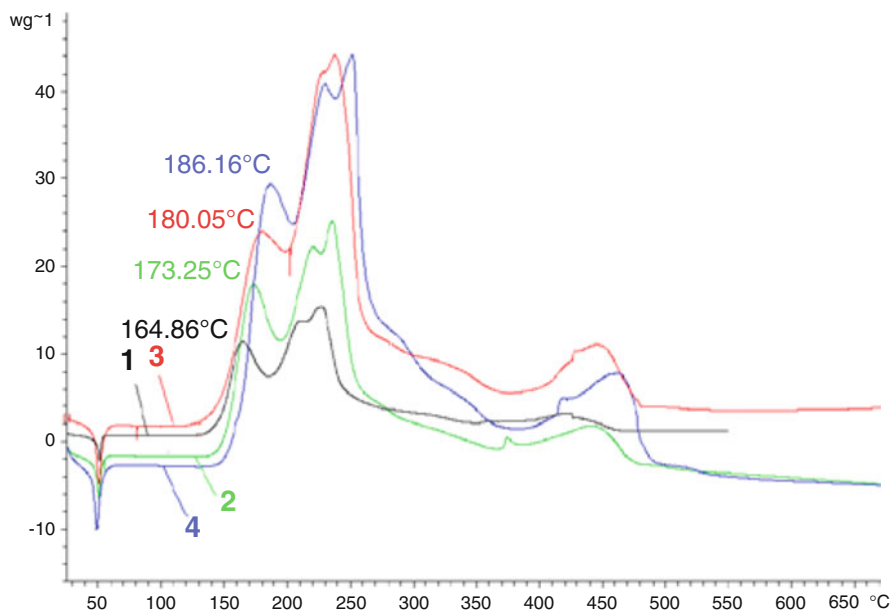
Fig. 4 The DSC curves of pretreated paraffin in oxygen with different heating rate

Table 2 The DSC results for pretreated paraffin in O_2

$\beta(°C/min)$	$T_p(K)$	$1/T_p$	$lg\beta$	$ln(\beta/T_p^2)$
5	438	0.002283	0.699	−10.5549
10	446	0.002240	1.000	−9.8998
15	453	0.002207	1.176	−9.5246
20	459	0.002177	1.301	−9.2637

Table 3 Thermal reaction kinetic parameters of pretreated paraffin in O_2

Method	E(kJ/mol)	A	r
Kissinger's	101.72	4.53382×10^{11}	0.99
Ozawa's	108.39	–	0.99

E activity energy, *KJ/mol*, *A* pre-exponential factor, *r* the correlation coefficient

By the thermal analysis experiments, the kinetic parameters of pretreated paraffin in oxygen atmosphere were calculated, and the quantitative relation of reaction rate constant and reaction temperature was obtained. Table 2 shows the DSC character value of pretreated paraffin with different heating rate in air.

The relationship between $\ln(\beta/T_p^2)$ and $1/T_p$ obtained by Kissinger method [17] can be expressed as the curve equation: Y = 17.43–12233X. The relationship between $lg\beta$ and $1/T_p$ obtained by Ozawa method [18] can be expressed as the curve equation: Y = 14.31–5955X. By the slope and intercept of the equations above, the activation energy for the reaction and pre-exponential factor and the correlation coefficient can be calculated. The values are shown in Table 3.

Table 3 shows that the values of activation energy obtained by Kissinger method and Ozawa method are in the same order of magnitude, and the correlation coefficients are both 0.99. By Kissinger method, "E" is 101.72 KJ/mol, and pre-exponential factor "A" is 4.53382×10^{11}, while by Ozawa method, "E" is 108.39 KJ/mol.

4 Fuel Melting Characteristic Experiment

The melting characteristics of paraffin-based fuel and HTPB fuel have been measured by using solid fuel melting characteristic testing device. The motor fired in the experiment used a composite propellant which produced high pressure and high temperature in the chamber to simulate actual hybrid engine environment. The fuels are subjected to these conditions and are checked for their structural integrity and melting performance. At the same condition of temperature and pressure, the paraffin-based fuel and HTPB fuel are compared before and after the test. The melting characteristics are verified by measuring the weights and the inspection of the fuel grains.

4.1 The Experimental Scheme

In solid rocket motor, a propellant is placed at fore-end of the motor. The melting characteristics of the fuel samples are measured by firing the motor, which produced a high-temperature (3100 K) and high-pressure (3 MPa) environment.

4.2 Experimental Result Analysis

The working pressure and time of motor for paraffin and HTPB fuel melting characteristic tests are shown as below (Table 4, Figs. 5, 6, and 7).

Through the above table, we can draw the following conclusions:

1. At high-temperature and high-pressure environment, the paraffin-based fuel and HTPB fuel retained their shape and did not melt. The prepared paraffin-based fuel

Table 4 The quality comparison between before and after test

Sample	Quality before test (g)	Quality after test (g)	Experimental lost Δr (%)
1# paraffin-based fuel	168.25	132.67	21.1
2# HTPB fuel	166.80	144.65	13.2

formulation can adapt to the environment of high temperature and high pressure, which lay a good foundation for future application in hybrid engine.
2. The motor's working time remains 3 s. As the carbonization reaction, the solid fuel loss weight at its surface. The weight loss in motor test fire for paraffin-based fuel is 21.1 %, while HTPB fuel lost 13.2 % after the motor test. Therefore, the paraffin-based fuel is relatively more conducive to burning than HTPB fuel, and it can greatly improve the regression rate of fuel.

5 Fuel Regression Rate Experiment

The firing tests of 1# paraffin-based fuel and 2# HTPB fuel were conducted by using solid-gas rectangular hybrid engine. The fuel working time was determined by the "pressure-time" curve, and the average regression rate in current working condition was obtained by the ratio of fuel sample thickness and working time.
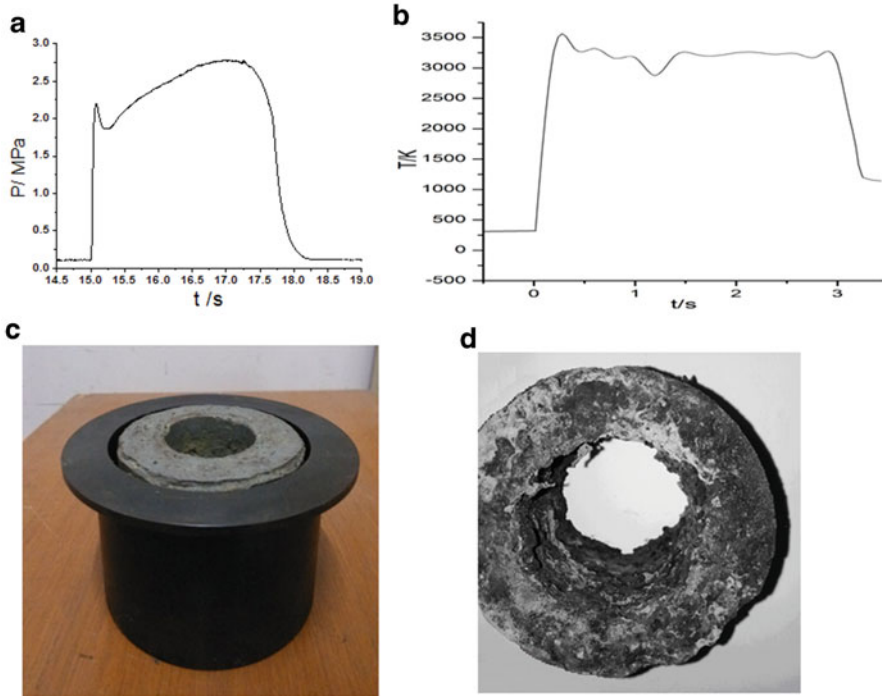
Fig. 6 The melting experiment of paraffin fuel: (**a**) the "P-s" curve, (**b**) the "T-s" curve, (**c**) the paraffin fuel before test, (**d**) the paraffin fuel after test

5.1 Experimental Scheme

In this experiment, the 1# sample and 2# sample as shown in Table 1 were used as the fuel formulations and the working pressure remained 1–2 MPa. The experimental system and the hybrid engine working process are shown as below (Figs. 8 and 9).

5.2 Experimental Result Analysis

5.2.1 Experimental Reproducibility Analysis

The test fire experiment was repeated for the same paraffin-based fuels to check the regression rate, under the oxygen mass flow rate of 40 g/s and the nozzle throat diameter of 10 mm. The test fire "pressure-time" curves are shown in Fig. 10.

There was any significant fluctuation in the "pressure-time" curve at the stable phase. The experiments were repeated three times at each working condition. The
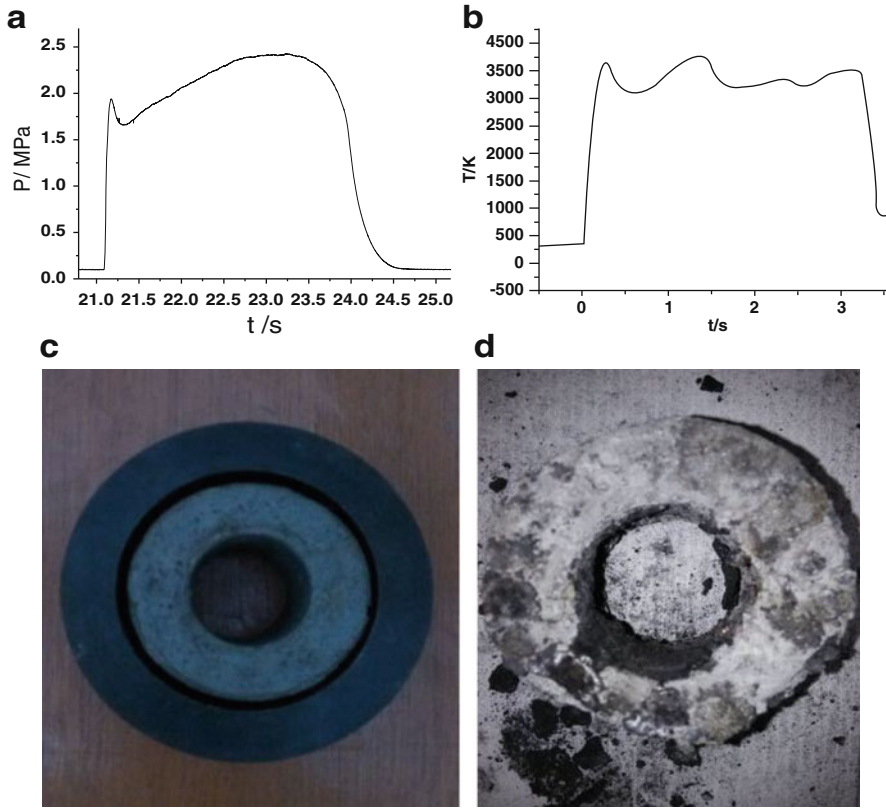
Fig. 7 The melting experiment of HTPB fuel: (**a**) the "P-s" curve, (**b**) the "T-s" curve, (**c**) the HTPB fuel before test, (**d**) the HTPB fuel after test

average value of three regression rates was 1.11 mm/s, and the relative error of regression rate are 2.70 %, 1.80 %, and 4.50 %, respectively. Therefore, it can be said that the experimental results have good reproducibility, stability, and reliability.

5.2.2 Oxygen Mass Flow Rate Impact on Fuel's Regression Rate

Four test fire experiments were conducted for sample 1# and 2# fuels, respectively, at different oxygen mass flow rate, and then the average value of the tests was evaluated. The difference in the regression rate of sample 1# and 2# fuels is shown in Table 5.

Table 5 shows:

1. The regression rate of 1# fuel increased by 63.24 %, 58.73 %, 70.37 %, and 68.09 %, respectively, when compared with the regression rate of 2# fuel, at the
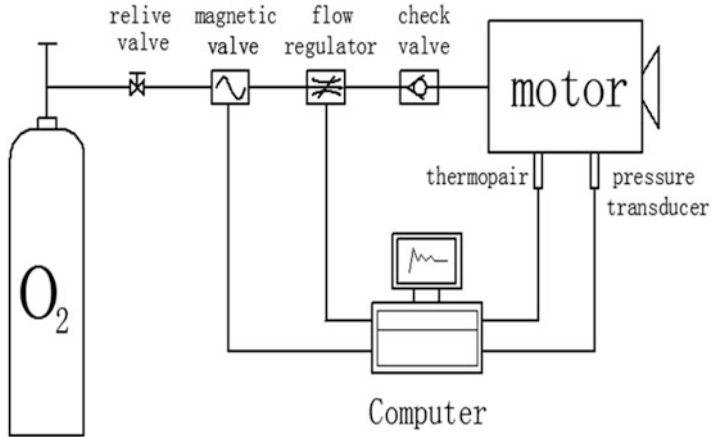
Fig. 8 The experimental system
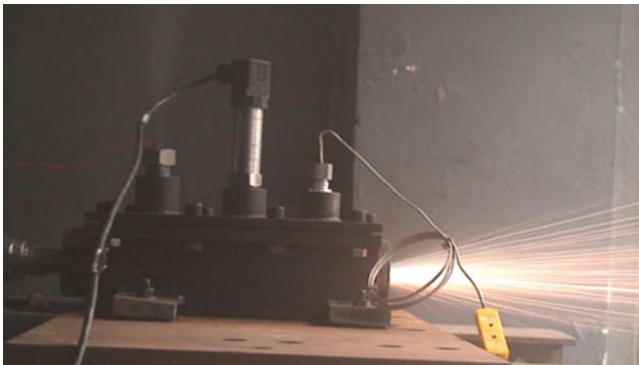
Fig. 9 The working process of hybrid engine
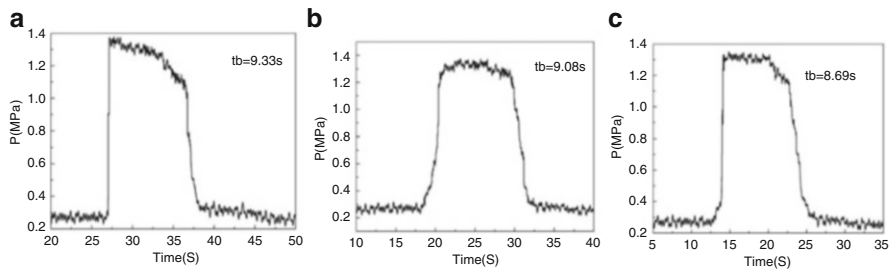
Fig. 10 The "P-t" curve for repeated experiments of paraffin-based fuel: (**a**) first "P-t" curve, (**b**) second "P-t" curve, (**c**) third "P-t" curve

Table 5 The contrast of fuel regression rate r in different formulation

$\dot{m}$ (g/s)	25	30	35	40
1# r(mm/s)	0.79	0.92	1.00	1.11
2# r(mm/s)	0.47	0.54	0.63	0.68

r = regression rate, mm/s, $\dot{m}$ = oxygen mass flow rate, g/s

Table 6 The relationship between the fuel regression rate and G_o

$\dot{m}$ (g/s)	G_o (g/(cm^2·s))	ln G_o(g/(cm^2·s))	1# ln r (cm/s)	2# ln r (cm/s)
25	0.4464	−0.8065	−2.5383	−3.0576
30	0.5357	−0.6242	−2.3860	−2.9188
35	0.6250	−0.4700	−2.3026	−2.7646
40	0.7143	−0.3365	−2.1982	−2.6883

G_o the oxidizer mass flow density, g/(cm^2·s)

oxygen mass flow rate of 40 g/s, 35 g/s, 30 g/s, and 25 g/s. It can be seen that the regression rate of paraffin-based fuel is higher than that of HTPB fuel under the same oxygen mass flow rate.

2. When the oxidizer mass flow rate is 25 g/s, 30 g/s, 35 g/s, and 40 g/s, the regression rate of 1# fuel is increased by 16.46 %, 8.70 %, and 11 %, respectively, with the increasing oxidizer mass flow, and the regression rate of 2# fuel is increased by 14.89 %, 16.67 %, and 7.94 % with the increase of oxidizer mass flow. It can be seen that, with the increase of oxidizer mass flow rate, the combustion gas velocity at the fuel surface improved, and the diffusion of solid fuel surface has been enhanced, which led to the increase in solid fuel surface temperature, and the rate of heat transfer increased which increased the combustion reaction, and the regression rate increased accordingly.

5.2.3 The Relationship Between Oxygen Mass Flow Rate and Fuel's Regression Rate

Previous researches [19, 20] show that the regression rate generally has been less affected by the combustion chamber pressure in solid-liquid hybrid rocket engine, but greatly affected by the fuel composition, combustion chamber structure, and oxidizer mass flow density. The relationship [21] between regression rate and oxidizer mass flow density is:

$$r = aG_o{}^n, \quad Go = \dot{m}/A_p$$

In the equation, a and n are the empirical parameters obtained by experiments, A_p is the grain port area, and $A_p = 56$ cm^2 in this text.

According to the experimental data above, the regression rate of 1# paraffin-based fuel and 2# HTPB fuel are shown in Table 6.

Through fitting the ln G_o and ln r, we got the relationship between oxygen mass flow rate and fuel's regression rate:

$$r_{1\#} = 0.2491G_o^{0.7103}\text{mm/s}, \quad r_{2\#} = 0.1323G_o^{0.7822}\text{mm/s}$$

It can be seen that the regression rate of fuel increased proportionately with increasing oxidizer mass flow rate; the regression rate of paraffin-based fuel is significantly higher than that of the HTPB fuel.

During the working of the engine, the oxygen was sprayed into the combustion chamber uniformly by the spray plate and oxygen reacted with the solid fuel to generate a lot of heat so that the fuel surface was melted into a thin layer of liquid film. Under the action of gas flow on the liquid film surface, the surface of paraffin-based fuel became unstable and was atomized into tiny droplets and entered into the gas phase [18]. While the liquid film was also generated during the combustion of HTPB fuel, the fuel could not be atomized effectively because of the high viscosity [22]. The paraffin droplets atomization greatly enhanced fuel's mass transport; hence, the regression rate of fuel surface was improved greatly. The high regression rate is a natural property of the paraffin-based fuel itself.

6 The Internal Flow Field Numerical Simulation of Hybrid Rocket Engine

A hybrid rocket engine has been designed using CFD numerical simulation software for paraffin-based fuel ignition, to simulate the situation of paraffin-based fuel working in hybrid engine. The result analysis gives the internal flow field distribution regularity of hybrid rocket engine.

6.1 The Simulation Model

Figure 11 shows the 3D structure diagram of a designed hybrid engine (diameter 74 mm, length 340 mm) including an injector at the front of engine for air intake (diameter 12 mm), paraffin-based fuel grain (outside diameter 86 mm, inner diameter 40 mm, length 120 mm), and nozzle (throat diameter 10 mm); the graphite heat-insulating layer is installed in the chamber and the cylindrical section of engine is provided with openings for pressure transducer and temperature sensor.

6.2 The Simulation Scheme

The solid- and gas-phase transition, gas diffusion effects, and other complex factors are taken into account in combustion of the hybrid engine, but to simplify the
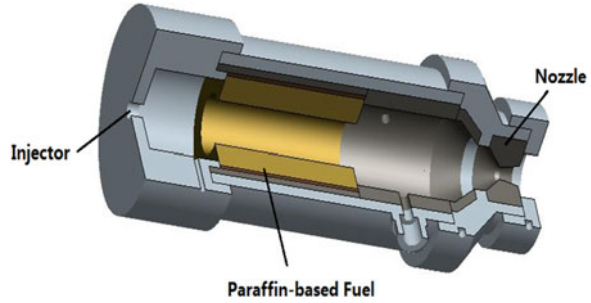
combustion model for this paper, the chemical reaction of gas-phase process is merely considered. Calculation use the incompressible Navier-Stokes (N-S) equations in the numerical simulation, and the standard wall function method is used near wall. Realizable k-epsilon turbulence model is selected, the pressure-velocity coupling uses the SIMPLE method, and diffusion is based on the second-order upwind difference scheme and the non-premixed combustion reaction model. Then the concentration of each component can be deduced from the predicted mixture fraction distribution in the generic scalar transport equation, and the appropriate simulation of turbulent diffusion flame is obtained. In the simulation of hybrid engine, boundary conditions were set as follows:

1. Inlet boundary conditions: The first inlet boundary is the injector section at the front of hybrid engine. With the inlet mass flow rate of N_2O, the mass flow rate is 120 g/s, the total pressure 5 MPa, and temperature 300 K. The second inner boundary is the surface of paraffin-based fuel. With the inlet mass flow rate, the mass flow rate is 30 g/s, the total pressure 5 MPa, temperature 300 K and paraffin-based fuel (in mass 35 % paraffin, 20 % HTPB, 25 % Mg, 15 % Al, 5 % C). The fuel gas is treated as an ideal gas in flow field calculation.
2. The outlet boundary conditions: the outlet boundary is the nozzle exit section. With the pressure outlet, the pressure is 0.1 MPa.
3. The wall boundary condition: no-slip boundary and no heat loss.

6.3   The Simulation Results and Analysis

In the internal flow field numerical simulation of hybrid rocket engine, the heat loss isn't considered through the engine casing assuming adiabatic isentropic condition. The engine internal flow field simulation results is shown below (Figs. 12, 13, 14, 15, 16, and 17).

From the above graphs, we can draw the following conclusions:

1. In the given hybrid engine, the nozzle throat diameter of 10 mm with N_2O and paraffin-based fuel mass flow rates are 120 g/s and 30 g/s, respectively; the
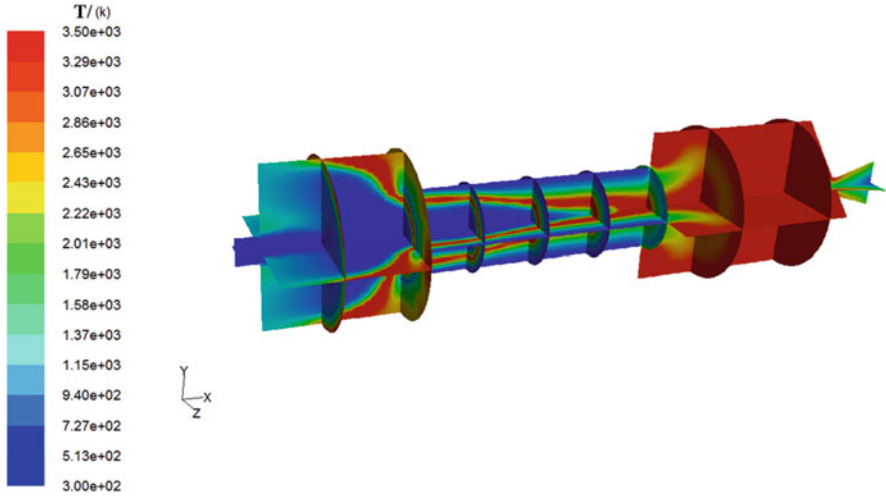
Fig. 12 The temperature distribution of hybrid engine with steady calculation

Fig. 13 The pressure distribution of hybrid engine with steady calculation

working pressure of engine is 2.5 MPa, temperature is 3500 K; and the exhaust velocity is up to 1.6×10^3 m/s.

2. In the flow field analysis, it can be seen that the vortex formation occurs at the front section of the engine and in the afterburner section. At the front of engine, the vortex formation is mainly due to high mass flow rate of N_2O which is hindered by the end face of paraffin fuel grain, and in the afterburner, the vortex formation is due to the flow of combustion gases of N_2O and paraffin fuel reaction which is hindered by the engine convergent section.
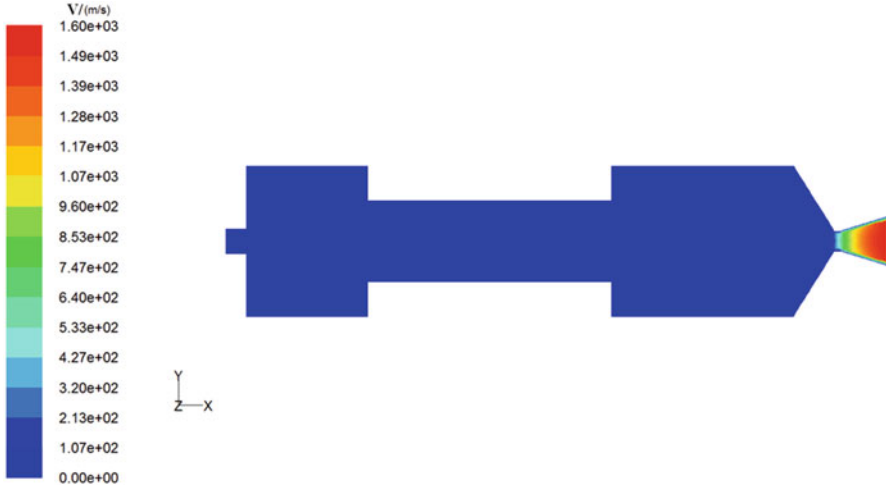
Fig. 14 The velocity magnitude distribution of hybrid engine with steady calculation
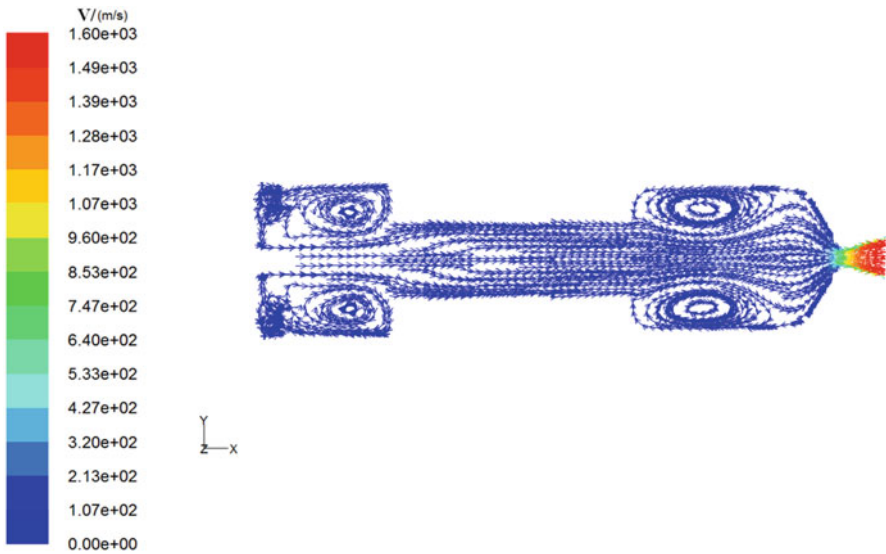
Fig. 15 Velocity vector distribution within the hybrid rocket motor with steady calculation

3. During the engine operation, the chemical reaction between the fuel and oxidizer on the surface of the fuel is not vigorous; the main exothermic reaction is above the surface of paraffin fuel and at the rear of the chamber. The analysis indicates that paraffin fuel and N_2O could not mix thoroughly and uniformly on the surface of the fuel, instead, it is near the axis and at the rear section that they mix completely and generate a lot of reaction heat.
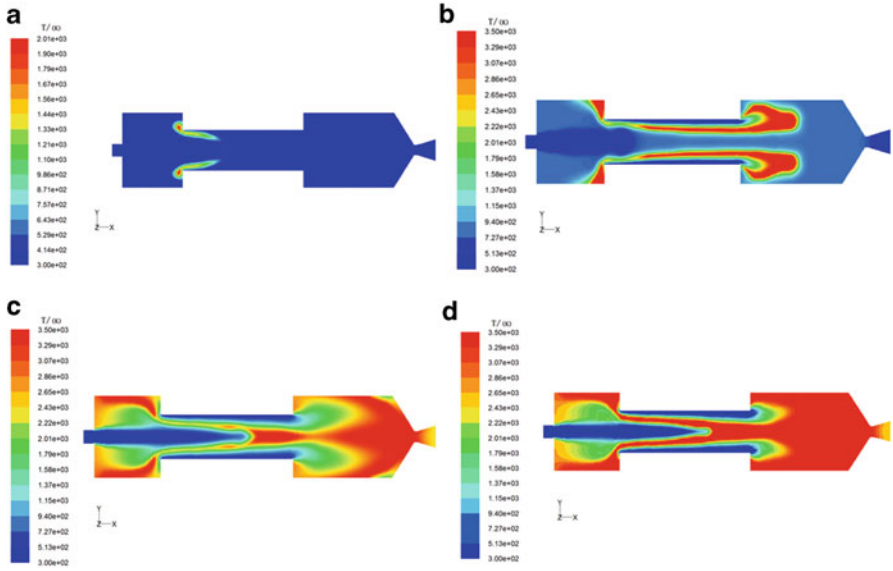
Fig. 16 The temperature distribution of hybrid engine with unsteady calculation: (**a**) $t = 0.006$ s, (**b**) $t = 0.05$ s, (**c**) $t = 0.07$ s, (**d**) $t = 0.1$ s
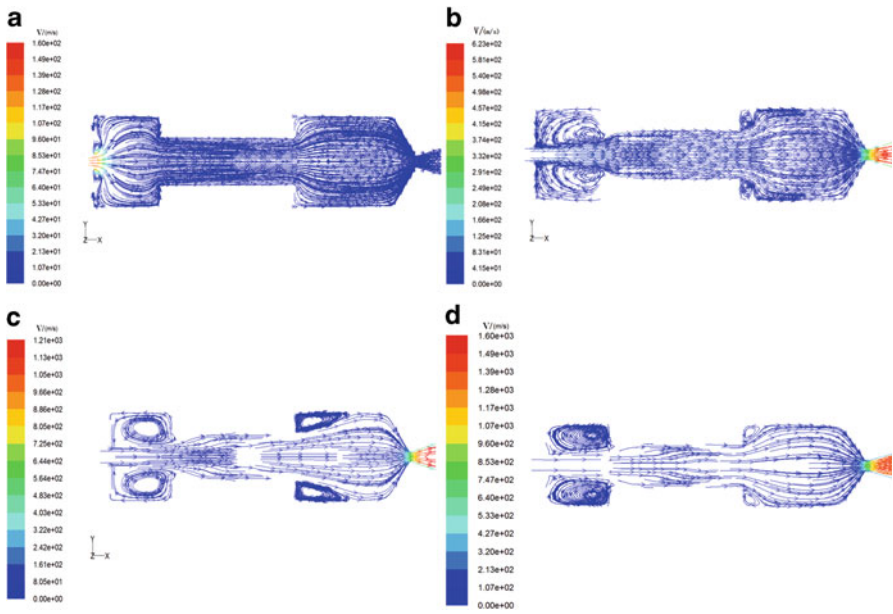
Fig. 17 Velocity vector distribution within the hybrid rocket motor with unsteady calculation: (**a**) $t = 0.001$ s, (**b**) $t = 0.01$ s, (**c**) $t = 0.05$ s, (**d**) $t = 0.1$ s

7 Conclusion

1. The optimum oxygen to fuel ratio of paraffin-based fuel and HTPB fuel with different oxidizers is nearly the same, the specific impulse of HTPB fuel is slightly higher than that of paraffin-based fuel, and the specific impulse of HTPB/LOx is 64.7 N·s/kg higher than that of paraffin-based fuel. Overall, there's little difference in paraffin-based fuel and HTPB fuel energy characteristics.
2. The initial decomposition temperatures of paraffin, pretreated paraffin, and HTPB are 182 °C, 230 °C and 336 °C, respectively, in the nitrogen atmosphere. The initial decomposition temperature of pretreated paraffin is higher than that of the untreated paraffin, which indicates that the characteristics of pretreated paraffin have changed, and the treatment technology for pretreated paraffin is useful.
3. The kinetic parameters of pretreated paraffin and paraffin-based fuel in oxygen atmosphere under different heating rates can be calculated. By Kissinger method, the pretreated paraffin activation energy "E" is 101.72 KJ/mol, and pre-exponential factor "A" is 4.53382×10^{11}; by Ozawa method, the pretreated paraffin activation energy "E" is 108.39 KJ/mol.
4. After subjecting the paraffin-based fuel and HTPB fuel to high-temperature and high-pressure environment, the paraffin-based fuel and HTPB fuel shape is not changed and also it didn't melt. Under the same conditions, the weight loss for paraffin-based fuel is higher than that of HTPB fuel. Therefore, using paraffin-based fuel in hybrid engine, the regression rate can be greatly improved.
5. The regression rate of paraffin-based fuel is increased by 68.09 %, 70.37 %, 58.73 %, and 63.24 %, respectively, as compared with the regression rate of HTPB fuel, at the oxygen mass flow rate of 25 g/s, 30 g/s, 35 g/s, and 40 g/s. It can be seen that the regression rate of paraffin-based fuel is higher than that of HTPB fuel under the same oxygen mass flow rate.
6. The vortex formation occurs at the front section of the engine and in the afterburner section; the chemical reaction between the fuel and oxidizer on the surface of the fuel is not vigorous; the main exothermic reaction is above the surface of paraffin fuel and at the rear of chamber.

References

1. Tsohas J et al (2009) Development and launch of the Purdue hybrid rocket technology demonstrator. AIAA paper 2009-4842
2. Dyer J et al (2007) Design and development of a 100 km nitrous oxide paraffin hybrid rocket vehicle. AIAA paper 2007-5362

3. Howard RD et al (2011) Dream chaser commercial crewed spacecraft overview. AIAA paper 2011-2245
4. Karabeyoglu et al (2001) Development and testing of paraffin-based hybrid rocket fuels. AIAA paper 2001-4503
5. Karabeyoglu A et al (2003) Development of high-burning-rate hybrid-rocket-fuel flight demonstrations. AIAA paper 2003–5196
6. Van Pelt D et al (2004) Overview of a 4-inch OD paraffin-based hybrid sounding rocket program. AIAA paper 2004-3822
7. Guobiao C et al (2009) Hybrid rocket motor technology. Manned Spaceflight 7(1):15–18
8. Guobiao C (2012) Development and application of hybrid rocket motor technology: overview and prospect. J Propuls Technol 33(6):831–839
9. Fanli S et al (2008) Experiments and simulations of a N_2O/HTPB hybrid rocket motor. J Tsinghua Univ 48(2):285–288
10. Xintian L et al (2009) Experimental study on burning rate of sub-scale H_2O_2/HTPB hybrid rocket motor grain. J Solid Rocket Technol 34(4):457–461
11. Wang Pengfei (2013) Research on combustion properties of paraffin-contained fuel. Northwestern Polytechnical University Master degree thesis, pp 40–60
12. Zhenhao S et al (2007) Thermal decomposition of HTPB/AP and HTPB/AP/Al studied by DSC-FTIR. Chin J Energetic Mater 15(2):105–108
13. Yang Y et al (2008) Study of instantaneous regression rate in hybrid rocket motor. J Propuls Technol 29(5):533–538
14. Zhu Chuanzheng, Xu Haihan (2000) Physical chemistry, pp 163–290
15. Nichita DV et al (2002) Multiphase equilibria calculation by direct minimization of gibbs free energy with a global optimization method. Comput Chem Eng 26(3):1703–1724
16. Guan Peng (2010) Study on paraffin-based fuel. Northwestern Polytechnical University Master degree thesis, pp 20–30
17. Kissinger HE (1957) Reaction kinetics in differential thermal analysis. Anal Chem 29(11):1702–1706
18. Ozawa T et al (1965) A new method of analyzing thermogravimetric data. Bull Chem Soc Jpn 38(11):1881–1886
19. Karabeyoglu MA et al (2002) Combustion of liquefying hybrid propellants: part 1, general theory. J Propuls Power 18(3):610–620
20. Evans B et al (2004) Characterization of nano-sized energetic particle enhancement of solid-fuel burning rates in an X-Ray transparent hybrid rocket engine. AIAA paper 2004-3821
21. Marxman GA et al (1963) Fundamentals of hybrid boundary layer combustion. AIAA paper 1963-505
22. Yufei L et al (2005) Advances in hybrid rocket: paraffin based fuel. J Rocket Propuls 31(4):36–40

Hybrid Combustion Studies on Regression Rate Enhancement and Transient Ballistic Response

Luciano Galfetti, Matteo Boiocchi, Christian Paravan, Elena Toson, Andrea Sossi, Filippo Maggi, Giovanni Colombo, and Luigi T. DeLuca

Abstract The ballistic response of hydroxyl-terminated polybutadiene (HTPB)- and paraffin-based fuel formulations burning under quasi-steady and transient operating conditions is analyzed by different diagnostics developed at the Space Propulsion Laboratory (SPLab) of Politecnico di Milano. The analysis of different fuel formulations under quasi-steady operating conditions focused on the regression rate (r_f) enhancement. HTPB loaded with coated nano-sized aluminum showed promising performance in terms of oxidizer mass flux sensitivity reduction and r_f increases in the order of 40 % over the baseline. The solid wax fuels exhibited higher r_f increases ($\sim$200 % for microcrystalline waxes) but poor mechanical properties. Due to this the possible mechanical properties enhancement by blending the solid waxes with thermoplastic polymers was investigated. The developed strategy appears promising, possibly enabling significant r_f increases over polymeric fuels thanks to the entrainment. The ballistic response of HTPB to forced transient conditions was investigated considering throttling down events. Under the tested conditions, the solid fuel exhibited a non-monotonic behavior for linear oxidizer mass flow decrease. The observed, faint r_f oscillations are probably due to thermal delay of the condensed phase.

Nomenclature

a_D	coefficient in Eq. 1 (Sect. 4.1.1)
C	specific heat, kJ/(kg K)
D_i	space-averaged diameters, mm
D_0	initial nominal value of the sample diameter, mm
E_a	activation energy, kJ/mole

L. Galfetti (✉) • M. Boiocchi • C. Paravan • E. Toson • A. Sossi • F. Maggi • G. Colombo
L.T. DeLuca
Space Propulsion Laboratory (SPLab), Department of Aerospace Science and Technology, Politecnico di Milano, 20156 Milan, Italy
e-mail: luciano.galfetti@polimi.it; matteo.boiocchi@polimi.it; christian.paravan@polimi.it; elena.toson@polimi.it; andrea.sossi@polimi.it; giovanni.colombo@polimi.it; filippo.maggi@polimi.it; luigi.deluca@polimi.it

G'   storage modulus, Pa
G_{ox} oxidizer mass flux, kg/(m^2 s)
H   enthalpy, J/kg
K   thermal diffusivity, m^2/s
$\dot{m}_{ox}$ mass flow rate, kg/s
n_D coefficient in Eq. 1 (Sec. 4.1.1)
p_c pressure chamber, bar
r_f regression rate, mm/s
t_{ign} ignition time, s
t   time, s
t_0 time at which the ignition stimulus initiates, s
T   temperature, °C
V   voltage, V
ρ   density, kg/m^3
τ   characteristic time, s

Subscripts

dec   decomposition
fin   final
g   gas
m   melting
s   solid
stor   storage

Abbreviations

ALEX   nano-Aluminum powder
CB   Carbon Black
DOA   Di-Octyl Adipate
DSC   Differential Scanning Calorimetry
EEW   Electrical Explosion of Wire
FO   Fiber Optics
GW   reference paraffin used in this work
HREs   Hybrid Rocket Engines
HTPB   Hydroxyl-Terminated PolyButadiene
IPDI   IsoPhorone Di-Isocyanate
SEBS-MA   Styrene-Ethylene-Butylene-Styrene grafted with Maleic Anydride
SL   quasi-Steady Leg (Sec. 4.2)
TL   Transient Leg (Sec. 4.2)
TMD   Theoretical Maximum Density
TOT   Thickness Over Time
VF-ALEX   nano-Aluminum powder coated by Fluorel

1 Introduction

Hybrid rocket engines (HREs) offer attractive features over the mature liquid propellant engines and solid rocket motors (high specific impulse, enhanced safety and operating flexibility). On the other hand, the exploitation of HREs is nowadays limited by the low regression rates (r_f), the poor combustion efficiencies, and the intrinsic performance shift during the burning.

2 State of the Art

The combustion of hybrid propellants is ruled by the diffusion of the gasifying solid reactant (typically, the fuel) in the turbulent boundary layer generated by the fluid component flow (usually, the oxidizer) [1–3]. A detailed survey of studies about the solid fuel regression process is given by Chiaverini et al. [4]. The key factors for an effective exploitation of HREs features can be identified as increased r_f (for applications requiring high thrust levels), combustion efficiency enhancement, and better understanding of the solid fuel ballistic response to forced transients (thrust throttling).

Techniques for r_f enhancement include solid fuel loading with energetic additives [5], entrainment of melted fuel droplets [6, 7], and nonconventional oxidizer flow injections [8, 9]. Solid fuel grain r_f can be enhanced resorting to fuel formulations loaded with energetic additives as metal or oxidizer powders and hydrides [5, 10–20, 33]. From this point of view, the most promising additives in terms of r_f enhancement are the innovative micron-sized composite/activated powders [10, 19, 20] and the nano-sized energetic materials [10, 11]. Entrainment-producing fuels offer significant r_f increases [16–18], but their possible applications are nowadays limited by their poor mechanical properties [21]. The r_f enhancement techniques based on nonconventional oxidizer injection are highly effective in promoting high r_f values [8, 9]. Nevertheless their practical applications are limited to relatively small scales.

In spite of the importance of HREs throttleability and stop/restart capability, only few studies on the ballistics of hybrid systems under forced transient conditions are available in the open literature [22–25]. In particular, Karabeyoglu [24] conducted a theoretical study on transient effects during solid fuel throttling events on polymethyl methacrylate (PMMA)- and hydroxyl-terminated polybutadiene (HTPB)-based fuels. The coupling between convective heat transfer and boundary layer transients is included in this study that shows the possible overshooting/undershooting of r_f during the throttling events.

Space Propulsion Laboratory (SPLab) of Politecnico di Milano has developed test rigs and diagnostic techniques to investigate hybrid combustion. The aim of SPLab experimental activity is the identification of a solid fuel formulation with high enough r_f as well as a suitable set of properties for industrial, large-scale applications (performance, safety, and costs).

3 Ingredients Characterization

The HTPB- and the paraffin-based fuel formulations considered in this study are manufactured at lab-scale level. The HTPB binder formulation is based on HTPB R45 HTLO resin (79.2 mass %), dioctyl adipate (DOA, 13.1 mass %), and isophorone di-isocyanate (IPDI, 7.7 mass %). The binder curing level ($-$NCO/$-$OH) is 1.04. Dibutyltin diacetate is used as curing catalyst (and is added in excess to the formulation <0.01 mass %).

The relative ballistic grading of the HTPB-based fuel formulations is performed considering nano-sized Al (nAl) as energetic additive. Two nAl powders produced by electrical explosion of wire (EEW) and passivated by air are considered [26]. The first powder is non-coated (ALEX), and the second (VF-ALEX) is coated by Fluorel™ [27] and ester from esterification of 1H,1H-perfluoro-1-undecanol with furan-2,5-dione (with final filtration and fast heating of the suspension) [10, 28]. The coating procedure of the VF-ALEX is done at lab-scale level. A detailed characterization of the tested powders is reported in [10, 28].

The characterization of the paraffin-based fuel formulations is articulated in two steps. In each of these two steps, pre-burning analyses and combustion tests are combined. In a first step, different commercially available solid waxes are characterized. An overview of the tested solid paraffin waxes considered in this study is presented in Table 1.

Wax1, Wax2, Wax3, and Wax4 are macrocrystalline paraffin waxes, while WaxMix is a paraffin wax-based formulation including additives for mechanical properties' improvement. Micro1 is a ductile microcrystalline paraffin wax. The microcrystalline paraffin waxes are characterized by branched molecules and long chain lengths. These characteristics yield higher densities, melting point temperatures, and liquid-phase viscosities with respect to the macrocrystalline waxes [29, 30, 45].

The materials presented in Table 1 are used for the manufacturing of paraffin-based formulations composed by 88 mass % of wax, 10 mass % of stearic acid, and

Table 1 Tested solid paraffin wax properties as provided by the manufacturers [29, 30]

Wax ID	Congealing point[a], °C	Oil content[b], mass %	Penetration[c] at 25 °C, 1/10 mm	Kinematic viscosity, mm^2/s
Wax1	58–60	–	–	–
Wax2	60–62	0–0.5	17–20	–
WaxMix	64–68	–	8–13	880–920[d]
Wax3	66–70	0–1	16–20	6–8[d]
Wax4	66–70	0–1	10–14	–
Micro1	83–94	0–2	4–10	8.5–12.5[e]

[a]Method ASTM D 938
[b]Method ASTM D 72
[c]Method ASTM D 1321
[d]Data evaluated at 100 °C by method ASTM D 156
[e]Data evaluated at 120 °C by method ASTM D 445

Table 2 Composition and theoretical maximum density (TMD) of pure paraffinic materials and SEBS-based blends

Fuel ID	Composition	TMD, g/cm^3
GW	Paraffin wax	0.870
SEBS-MA	Styrene 30 %, maleic anhydride 2 %	0.910
S05G	SEBS 5 %, GW 94 %, CB 1 %	0.883
S10G	SEBS 10 %, GW 89 %, CB 1 %	0.885

2 mass % of graphite. The addition of stearic acid enhances the mechanical properties of the mixture [31], while the addition of graphite increases the absorptivity of radiation and can consequently prevent the possibility of sloughing of the internally heated fuel [6]. The solid wax formulations are identified by the wax ID presented in Table 1, followed by the label BL.

In the second step, different blends of solid wax and thermoplastic polymers are investigated with the aim of overcoming the main limitation of entrainment-producing paraffinic fuels: the poor mechanical properties of the solid grain. The selected paraffin wax was a commercial paraffin supplied by an Italian Company, hereafter named GW. Paraffin was mixed with SEBS-MA, which is a styrene-ethylene-butylene-styrene block copolymer, grafted with maleic anhydride (hereafter named SEBS), and supplied by Sigma-Aldrich. Different compositions were manufactured and characterized, according to the list and the nomenclature of Table 2. The mixing between SEBS and wax is obtained firstly by melting a 50/50 % mixture under stirring at 120 °C; when the mixture becomes homogeneous, the last part of paraffin has to be added reducing the temperature at 90 °C. The last ingredient to be added is carbon black. For paraffin-based mixtures, it is generally true that the higher temperature of the melt is, the stronger the shrinkage effect of the mixture into the mold during the cooling.

3.1   Thermal Characterization

The thermal characterizations of the solid wax formulations were performed by differential scanning calorimetry (DSC). The DSC tests were performed with a heating rate of 10 °C/min, in a N$_2$ environment. Two cycles from 0 up to 200 °C were executed. A clean cycle was executed before every experimental campaign, in order to avoid errors due to residual material left from previous tests.

The DSC traces of the tests performed on solid paraffin-based formulations are reported in Fig. 1. The mixtures based on macrocrystalline paraffins, Wax1BL, Wax4BL, WaxMixBL, Wax2BL, and Wax3BL, show a main distinctive melting peak in the range 62.6–72.1 °C. Wax1BL shows also another distinctive melting peak, before the main one. The mixture based on microcrystalline paraffin wax, Micro1BL, shows a different behavior. This mixture presents a wider phase transi-
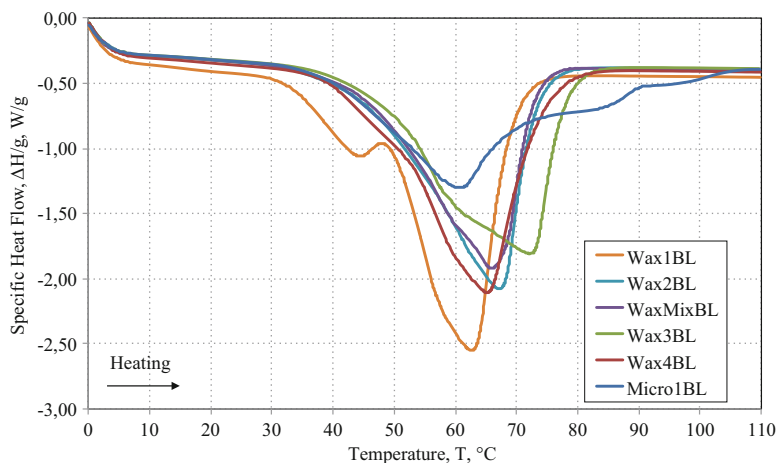
Fig. 1 DSC traces for the melting behaviors of the paraffin-based mixtures
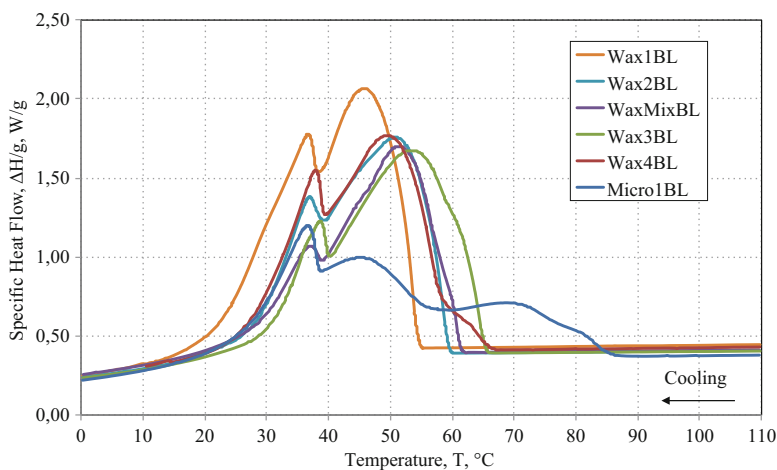
Fig. 2 DSC traces for the congealing behaviors of the paraffin-based mixtures

tion interval, with a relatively low specific heat flow. This behavior is affected by the relatively high content of isoparaffin, which results in a gradual heat release. In general, microcrystalline paraffin waxes often exhibit additional peaks, interpreted as evidences of similar solid-solid transitions [32].

Figure 2 shows the DSC traces of the congealing behavior. The macro-paraffin-based mixtures show two main distinctive peaks, differently from Micro1BL, which, as in the melting phase, shows a wider phase transition temperature interval without well-marked peaks. A common peak occurs in the range between 36.8 and 38.7 °C, not associated to the paraffin content of the mixture.

Table 3 Summary of the thermal characterization data for the solid paraffin-based fuels

	Melting			Enthalpy, h_{melt}, J/g	Congealing			
	Peak temp., T_{melt}, °C				Peak temp., T_{freeze}, °C			
Fuel ID	1st	2nd	3rd		1st	2nd	3rd	4th
Wax1BL	44.5	62.6	–	183.3	45.9	36.8	–	–
Wax2BL	67.2		–	168.9	50.7	37.0	–	–
WaxMixBL	65.9	–	–	147.0	51.4	37.1	–	–
Wax3BL	72.1	–	–	170.2	53.5	38.7	–	–
Wax4BL	65.3	–	–	179.1	50.1	37.5	–	–
Micro1BL	60.8	84.7	93.7	137.7	80.8	70.2	46.05	36.9

Table 4 Parameters obtained from DSC measurements for paraffinic waxes (temperature, T; specific enthalpy, ΔH; for melting, m; and decomposition, dec)

Fuel ID	$T_{m,p1}$, °C	$T_{m,p2}$, °C	ΔH_m, J/g	T_{dec}, °C	ΔH_{dec}, J/g
GW	36.8	56.0	206.2	275.4	185.4
S05G	36.7	55.3	198.3	273.2	154.9
S10G	37.4	55.2	188.6	278.2	92.1

A summary of the thermal characterization results of the solid wax-based fuels is given in Table 3.

The DSC scan of the GW paraffin and its blends used throughout this study span between −10 and 350 °C. As a typical macro-paraffin, the GW endothermic thermograph is composed by two well-defined peaks. The high-temperature endothermic peaks, occurring between 190 and 300 °C, are due to the gasification/decomposition processes. Considering the SEBS-based blends shown in Table 4, and in particular the third and fourth column, a minimum thermal shift of the main endothermic peaks is noticed. A similar behavior was observed by Seno [44] performing blends with SEBS-MA and Polyamide12. The measured melting point of GW was 56.0 °C. The addition of the thermoplastic polymer was related with a small variation of the temperature of the main peak (55.3 °C and 55.2 °C for S05G and S10G, respectively). This trend is due to the amorphous nature of the polymer or to its very low grade of crystallinity. When the GW content in the considered blends decreases, ΔH_{dec} also decreases for all the formulations. The decrease could be explained considering the lesser amount of paraffin and also a retention effect of the soft segments of the polymer on the paraffinic molecules. The retention effect could explain a formation of a compound which needs a higher temperature to be decomposed, so the DSC apparatus cannot detect the whole decomposition process.

3.2   Rheological Characterization

The rheological characterization was performed in terms of the storage modulus (G′). The rheological tests were performed using a parallel plate configuration, with plate diameters of 25 mm. The initial sample gap was between 2.3 and 2.6 mm. The applied constant strain was set at 1 %. The shear rate sweep ranged between 0.5 and 50 Hz. The investigated temperature range was from 21 °C up to the melting temperature, with temperature steps of 3 °C. Figure 3 shows the storage modulus comparison in a logarithmic scale plot. Up to 42 °C, all the tested mixtures show nearly the same storage modulus. From the temperature of 42 °C, different storage modulus behaviors can be identified. The Wax1BL storage modulus falls down rapidly at 42 °C, followed by that of Wax3BL at 45 °C. The storage components of both Wax2BL and Wax4BL fall at 48 °C, while at the temperature of 51 °C, the Micro1BL transition is observed. The mixture based on microcrystalline paraffin wax keeps its elastic energy up to higher temperatures, due to its peculiar thermal behavior. WaxMixBL shows a complete different trend: the storage modulus slowly decreases for increasing temperature (below 60 °C) and rapidly falls at 60 °C, probably due to the additives added for mechanical properties enhancement.

Table 5 shows viscosity results obtained on the paraffin-polymer blends by using a Couette test apparatus at a temperature ranging between 70 and 160 °C. As temperature increases, viscosity decreases from 0.5 to 0.046 Pa*s for the formulations S05G, and from 1.694 to 0.011 Pa*s for those S10G. At the same temperature, for instance, 100 °C, the viscosity value of S05G is roughly 3.4 times lower than that of S10G.
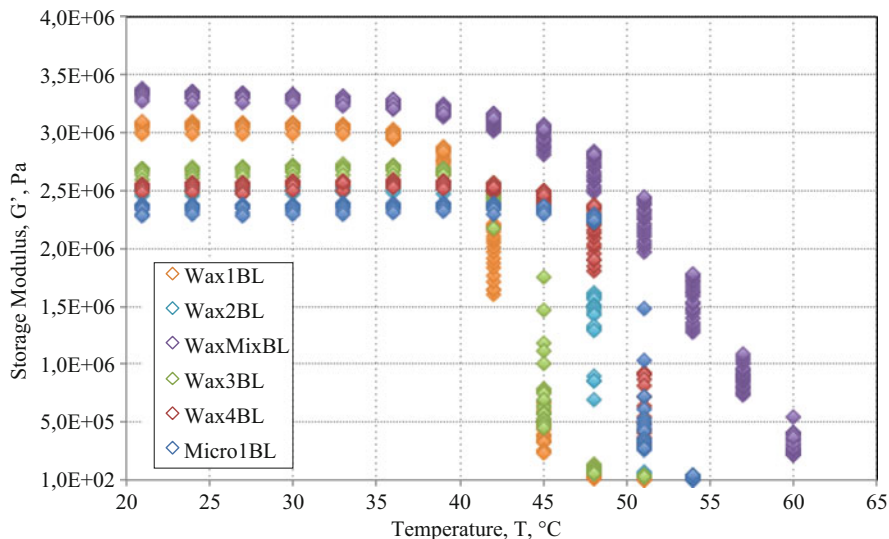
Fig. 3 Storage modulus as a function of temperature in linear scales. The investigated shear rates range from 0.5 to 50 Hz

Table 5 Viscosity values obtained with Couette rheometer tests at 400 s^{-1}

Material	Viscosity [Pa*s]					
T [°C]	70	80	100	120	140	160
S05G	0.50	0.123	0.046	–	–	–
S10G	–	1.694	0.157	0.044	0.023	0.011
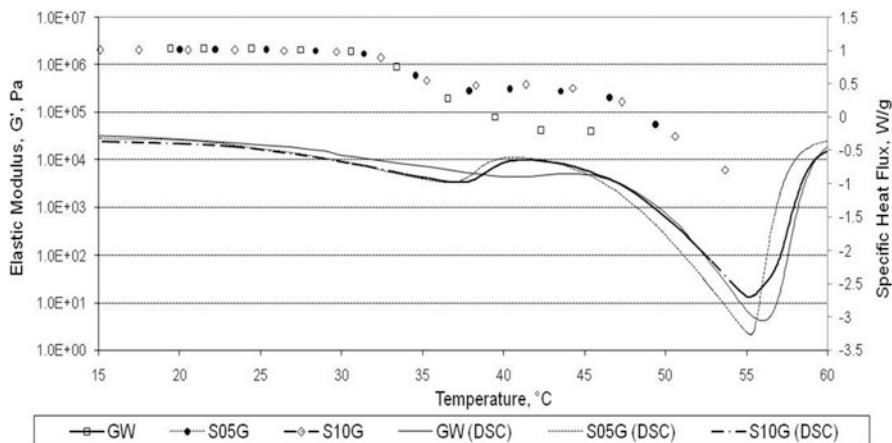
Fig. 4 Trend of the elastic modulus (G′) for GW and its blends, compared with the respective DSC thermographs between 20 and 60 °C

Figure 4 shows the trend of the elastic modulus (G′) for GW and its blends compared with the respective DSC thermographs in the range between 15 and 60 °C. A value of percentage strain of 1 % was selected as a good trade-off between the needed stress/strain linearity and the sensitivity of the test bench. The overlapping with DSC traces allows an interpretation of the softening behavior of a typical macrocrystalline paraffin.

Two critical temperatures define the G′ trace into three main areas. The first one finishes as the solid/solid transition occurs, which is 31 °C, due to the clear decrease of the G′ values for all the tested formulations. The second can be identified between the solid/solid and the solid/liquid transition of the paraffin: from 31 to 43 °C concerning GW and from 31 to 37 °C considering the blends. The last one can be associated to the temperature range between the solid/liquid transition and a limit temperature (T_{lim}) defined as the temperature at which the rheometer cannot perform the measure. DSC tests point out that the peak where GW melting occurs is at 54 °C but the temperature limit for the GW sample tested in the rheometer was 46 °C. As the polymer concentration increases, the difference between T_{lim} and T_{mp} decreases: 5 °C and 1 °C for S05G and S10G, respectively. The decrease of the elastic modulus of pure SEBS-MA starts at 80 °C [46]. Investigations to study structural morphologies [47–50] and viscoelastic and thermal properties of styrene-based thermoplastic elastomers and their blends with different polymers and fillers [51–53] were performed. The results show that gels rheological and mechanical

Table 6 Young modulus obtained with tensile tests at −19 °C, 8 °C, and 0.5, 50 mm/min for SEBS containing formulations

Rate – $T_{stor,}$ mm/min – °C	Young modulus/standard deviation, MPa		
	GW	S05G	S10G
0.5/8	119 ± 17	123 ± 8	127 ± 1
0.5/−19	–	143 ± 18	141 ± 16
50/8	–	246 ± 24	252 ± 19
50/−19	–	334 ± 14	327 ± 36

properties are affected by block copolymer concentration, molar mass, end-block ratio, and chemical compatibility with the filler. SEBS-MA have been studied both from a ballistic and rheological point of view obtaining a clear response indicating the maleated formulation as the best choice.

3.3 Mechanical Characterization

Pure GW shows a strong influence of the temperature on the maximum load (from 0.54 to 0.2 MPa) and on the value of elongation at break (which increases from 0.7 to 2.7 %). The strong sensitivity to the temperature is linked to the softening of the material starting at 15 °C. Considering SEBS-based samples, as shown in Table 6, the higher the polymer fraction is, the higher the Young modulus. The most representative result obtained by the introduction of the thermoplastic polymer into the paraffinic matrix can be appreciated comparing the behavior of the tested materials at low temperatures and high elongation rate values. The brittleness typical of macrocrystalline paraffinic materials has been decreased with the compositions S05G and S10G.

4 Experimental Results and Discussions

In this section, ballistic results are discussed. The relative grading of different HTPB- and paraffin-based formulations under quasi-steady operating conditions is introduced first, before discussing the forced transient ballistic response. The presentation of the quasi-steady ballistic results is divided into three subsections. Each subsection presents the results obtained by a specific SPLab diagnostics.

4.1   Ballistics Under Quasi-steady Conditions

4.1.1   The 2D Radial Microburner and the Time-Resolved r_f

The 2D radial microburner is a facility designed to provide the relative grading of different fuel formulations burning under controlled operating conditions. Figure 5 shows a schematic view of the facility, while the injector head of the burner is presented in Fig. 6.

A detailed discussion of the 2D radial microburner features is reported in [10, 34]. The original design of this test rig enables the visualization of the strand head-end during the combustion process. The injector head enables both standard and swirl oxidizer injections (see Fig. 6). Thanks to the head-end visualization, the
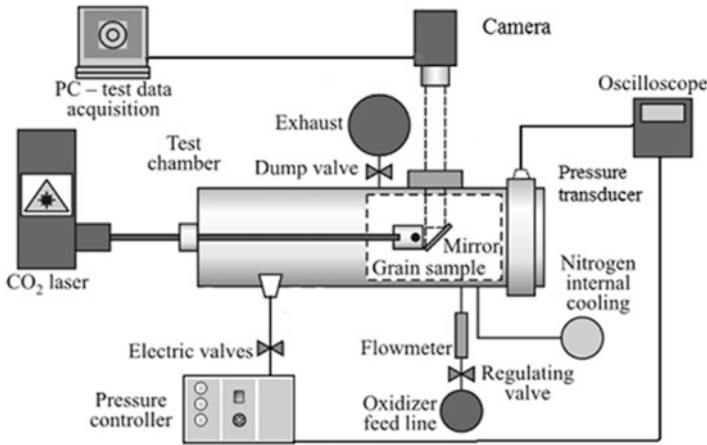
Fig. 5 Schematics of the 2D radial microburner [10, 34]. Note the 45° mirror that, together with the injector implementation, enables sample head-end visualization

Fig. 6 Details of injector system: (*1*) oxidizer inlet, (*2*) preinjection chamber, (*3*) sealing flanges (with optical access for the strand visualization), (*4*) injector head with screws for oxidizer injection control (standard/swirl flow), and (*5*) injector terminal for sample lodging [34]
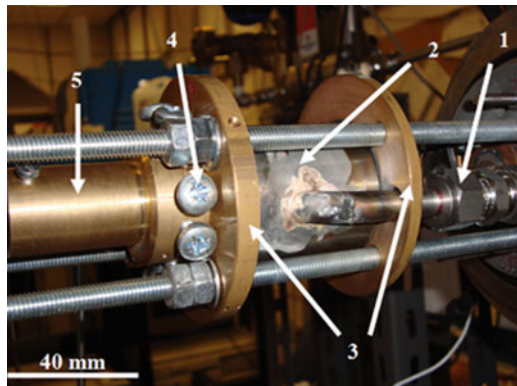
solid fuel r_f can be evaluated by a continuous tracking of the regressing surface during the burning run. In particular, a time-resolved data reduction technique for the r_f was implemented [10, 34]. In this procedure, the central port diameter of the strand is sampled in time along different radial directions. The diameter sampling frequency is typically 10 Hz (depending on the visualization quality). The space-averaged sampled diameters $(\overline{D}_i)$ series is then fitted by a power law, yielding to the definition of diameter evolution in time with respect to the initial nominal value (D_0) as

$$\overline{D}(t) - D_0 = a_D \cdot (t - t_0)^{n_D}, \quad t \geq t_{ign} > t_0 \tag{1}$$

In Eq. 1, the power law is valid starting from the ignition time $t_{ign}s$ (being t_0 the time the ignition stimulus initiates at). This parameter is ad hoc defined as the one maximizing the data fitting of Eq. 1 [10, 34]. The $(t_{ign} - t_0)$ values result in agreement with open literature models for the ignition delay evaluation [36]. The $r_f(t)$ can be evaluated by the time derivative of Eq. 1 as

$$r_f(t) = \frac{1}{2} \frac{d\left[\overline{D}(t) - D_0\right]}{dt} = \frac{1}{2} a_D n_D (t - t_0)^{n_D - 1}, \quad t \geq t_{ign} > t_0 \tag{2}$$

Similar equations can be derived for all of the ballistic parameters of interest, as the oxidizer mass flux (G_{ox}) and the oxidizer to fuel ratio (O/F). With the time-resolved approach, a single run can provide a r_f definition over a wide G_{ox} range. The time-resolved ballistics derived from Eq. 1 is subjected to consistency checks with the corresponding thickness over time (TOT) data evaluated between following sampled diameters and over the whole burning [10, 34].

The single combustion runs of a fuel formulation under given operating conditions can be collapsed in a time-resolved ensemble average. This is done by an overall interpolation of the $\overline{D}(t) - D_0$ of the single runs. The latter is of the kind of Eq. 1 [10]. From this, the ensemble time-resolved r_f can be defined. This ensemble average curve enables error bars definition. In order to evaluate the error bars, the definition of a proper t (or G_{ox}) interval is required. The latter is determined considering the limits where the $\overline{D}(t)$ $\left[\text{or } r_f(G_{ox})\right]$ curves of all the performed single tests are defined. Within this range, the error bars are evaluated by 95 % accuracy for confidence intervals centered on the average $\overline{D}$ (or r_f) resulting from the single runs. Finally, the ensemble average $r_f(G_{ox})$ is interpolated by a proper power law as

$$r_f(G_{ox}) = a_r \cdot G_{ox}(t)^{n_r}, \quad t \geq t_{ign} > t_0 \tag{3}$$

Details on the operating steps of the time-resolved r_f data reduction are available in Refs. [10, 34]. The relative grading of HTPB- and paraffin-based fuel formulations is hereby reported considering the corresponding ensemble average and taking cured HTPB as the baseline. Combustion runs are performed in gaseous oxygen (GOX) with combustion chamber pressure, p_c, of 10 bar or 16 bar. The nAl-loaded formulations contain 10 mass % additive.
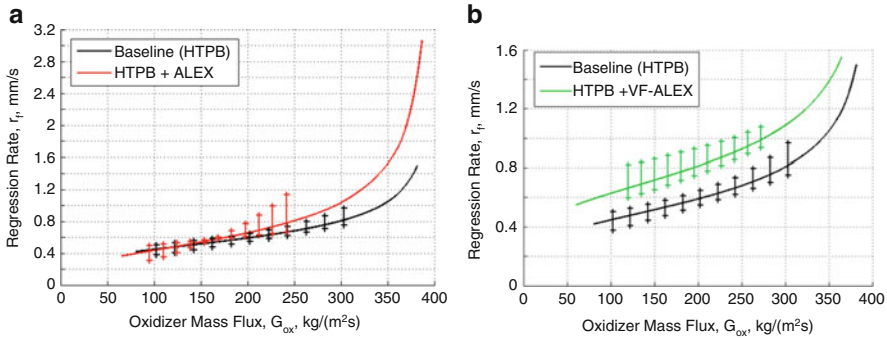
Fig. 7 Combustion of HTPB-based fuels. (**a**) HTPB + ALEX exhibits a strong G_{ox} sensitivity, testified by $n_r = 0.959 \pm 0.022$ (see Eq. 3). (**b**) HTPB + VF-ALEX provides a reduced dependence from G_{ox} changes with $n_r = 0.535 \pm 0.010$ (see Eq. 3). The ballistics of HTPB + ALEX is defined in the range 375–70 kg/(m^{2}s), while the VF-ALEX data extends from 364 to 60 kg/(m^{2}s)

Under the investigated conditions, HTPB + ALEX exhibits a marked initial r_f enhancement with respect to the baseline (see Fig. 7a). The percent r_f increase over the baseline is 54 % at 370 kg/(m^{2}s). As G_{ox} decreases the percent r_f enhancement diminishes from 42 % at 350 kg/(m^{2}s) down to 6 % at 150 kg/(m^{2}s). Experimental evidences from Refs. [10, 35, 37] suggest that this behavior can be due to aggregation/agglomeration phenomena in the condensed phase. HTPB + VF-ALEX (see Fig. 7b) presents a different behavior. This fuel formulation provides a percent r_f increase over the baseline of 30 % at 350 kg/(m^{2}s). Unlike the ALEX-fuel case, the HTPB + VF-ALEX ballistic response is enhanced as G_{ox} decreases, reaching a 44 % increase at 100 kg/(m^{2}s); see Table 7. This behavior can be partially justified by evidences from powder non-isothermal oxidation in air (10 °C/min), where the VF-ALEX exhibits a reduced reactivity (higher oxidation onset, lower enthalpy release for T < 660 °C) with respect to ALEX [28]. This can cause the absence of marked initial r_f values in the ballistic response of HTPB + VF-ALEX, and on the other hand, it can limit the aggregation/agglomeration reactions in the condensed phase probably affecting the HTPB + ALEX combustion [10, 34]. Finally, under the high heating rates of the combustion process, the coating decomposition products of VF-ALEX can provide fluorinated species participating to the fuel oxidation. Further, detailed investigations are required in order to clarify these effects.

The ballistic characterization of the paraffin-based formulations tested on the 2D radial setup was done for $p_c = 16$ bar. The HTPB baseline used for the relative grading was tested under $p_c = 19$ bar. In order to capture possible anisotropy effects, the central port sampling was performed along four radial directions.

As testified by the data presented in Table 7, all of the paraffin-based formulations exhibit significantly higher r_f than the baseline. Under the investigated conditions, a percent r_f enhancement of all the solid wax fuels is observed; the enhancement is lower for WaxMixB. This is mainly due to the entrainment mass transfer. The

Table 7 Percent r_f enhancement with respect to the baseline for HTPB- and solid paraffin-based formulations tested by the 2D radial microburner

G_{ox}, kg/(m²s)	Fuel				
	Percent r_f increase with respect to the baseline, %				
	150	200	250	300	350
HTPB + ALEX	6	12	19	22	42
HTPB + VF-ALEX	41	39	37	34	30
Wax1BL	202	204	205	NA	NA
Wax3BL	168	166	164	NA	NA
Wax2BL	200	207	215	NA	NA
WaxMixBL	32	8	6	NA	NA
Micro1BL	145	134	123	NA	NA
Wax4BL	198	196	195	NA	NA

different behavior of WaxMixBL is linked to its rheological properties (see Fig. 3); the WaxMix ballistic response is influenced by the additives used for the mechanical properties enhancement, limiting the entrainment of the fuel.

4.1.2 The Lab-Scale Hybrid Test Facility and the Fiber Optic Sensors

Fiber optic sensors represent one of the most innovative techniques to measure very high-speed events, such as velocity of detonation in explosives. Firing tests were carried out using a lab-scale hybrid test facility designed and developed at SPLab.

Commercial fiber optic combined with relatively inexpensive commercial electronic instruments can be used to measure the regression rate of hybrid fuels. The free head-end of each optical fiber of the used ribbon is opportunely sealed with a ceramic material and leaned to the fuel inside the combustion chamber. An electronic analyzer, consisting in an array of 16 photodiodes, was used to turn a luminous signal into an electrical signal. Finally, a plot reporting the trend of the light intensity of 12 luminous signals versus time was used to calculate the regression rate value. Each fiber in this experimental configuration could be treated as a luminous switch: on/off. As the luminous combustion surface approaches the fiber optic head-end, the respective photodiode turns from dark to light identifying the time value needed to obtain the fuel regression rate. Results of the fiber optic technique implementation, used to obtain a local, quasi-continuous measure of the fuel regression rate, are shown in Fig. 8.

Table 8 points out that regression rates measured using fiber optics FO are higher than those measured using a "consumed mass" technique (Δm); the first one is a local and quasi-continuous technique, while the second one is a technique averaged both in space and time. Firing tests have been performed using gaseous oxygen; as the G_{OX} values increase, the gap between regression rate values calculated by FO and Δm techniques decreases. The effect on the regression rate of the increase of
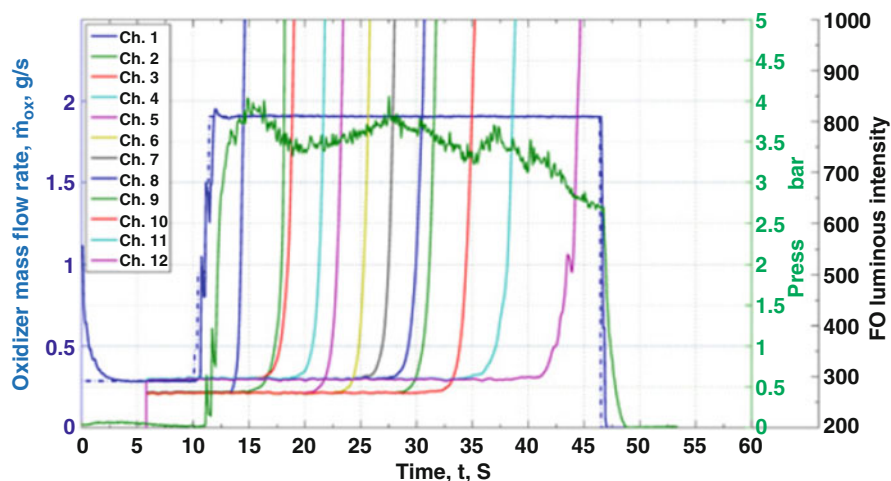
Fig. 8 Luminous signals collected by the fiber optic sensor

Table 8 Regression rate measured by using a fiber optic sensor and by considering the mass variation before and after the firing test

Fuel ID	r_f (FO), mm/s	r_f (Δm), mm/s	O/F	G_{ox}, kg/m^{2}s
	2.70	1.54	1.96	72.4
S05G	2.66	1.72	2.32	90.5
	2.31	1.98	2.34	108.6
S10G	2.28	1.38	2.21	72.4
	2.32	1.44	2.74	90.5

the polymer content is linked with the increase of the viscosity and, at least, with the decrease of the regression rate.

It can be observed that, according to results obtained using FO technique, the regression rate of the fuel containing a small fraction of polymer decreases when the oxidizer flux increases, which is in contrast with a well-known trend. This behavior was deeply investigated, compared with other studies aimed to characterize the entrainment effects and compared with the trend observed at higher polymer mass fraction, as shown in Table 8 for a polymer mass fraction of 10 % (composition S10G). If the polymer content is below 10 %, the behavior of the blend is close to that typical of a pure paraffin wax; in this case, the reliability and precision of the FO technique are questionable. The explanation is linked with the thickness of the melted layer and the oscillatory movement of the wave into the liquid on the solid fuel surface. If the melted layer is deep enough to contain more than three or four FO head-ends, a wave of low-viscosity liquid fuel can cover/discover fiber optics with an order different than that expected, causing very noisy, irregular FO signals. This phenomenon doesn't occur when, in a fuel blend containing a high mass fraction of polymer, the liquid layer contains only one or two FO head-ends. Blends with a low

content of polymer usually burn with very high regression rate, but, on the other hand, interesting mixtures for rocket applications are probably those containing a higher polymer mass fraction. For these compositions, the FO method to measure the local and quasi-instantaneous regression rate could be considered one of the more efficient and precise methods.

4.1.3 Swirl Injection and r_f Sensor

Swirl injection effects were investigated by a dedicated setup [40]. The test rig enables the combustion of cylindrical strands with single, central port perforation. The r_f of the tested fuel formulations is evaluated by a nonintrusive optical technique [10, 34] and by an innovative r_f sensor developed at SPLab [41]. This device is based on the wire cut principle and is characterized by an original implementation of the electric resistor bridge connections [41]. The SPLab wire cut sensor was developed and tested at lab scale, but validation tests were performed also in hybrid rocket firing runs performed for the FP7 SPARTAN project [42].

In wire cut sensors, a set of wires is embedded in the solid propellant/fuel strand. Each wire is connected to a resistor. The wires are parallel to the regressing surface and are broken as they reach it [40]. In this array the resistors are connected in parallel each other, and the whole block is connected to a power source by a known resistance (probing resistance). The voltage across the probing resistance is monitored in time and provides an indication of the gasifying surface regression, as shown in Fig. 9.
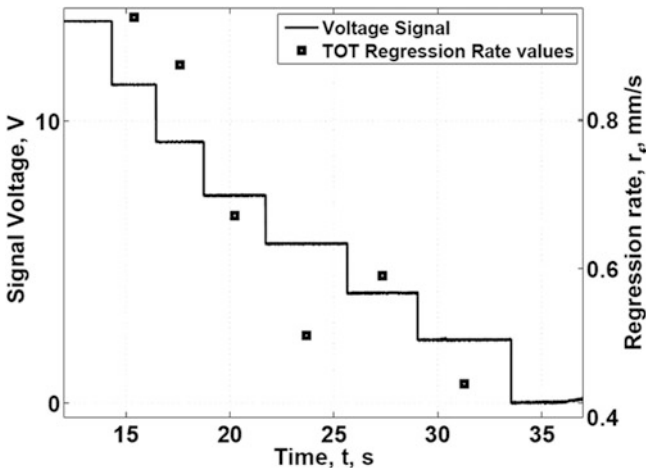
Fig. 9 Voltage across the probing resistance of a wire cut sensor. The signal steps correspond to the wire cut due to the regressing surface passage at the wire position. These steps are used for the r_f evaluation by TOT

The wire cut sensor signal is evaluated by a TOT approach. Considering two following steps in the voltage signal on the probing resistance (corresponding to t_{i+1} and t_i), Eq. 6 can be applied, since the wire positions in the solid grain ($\overline{D}_{i+1}$ and $\overline{D}_i$) are known by the sensor geometry and accommodation in the strand. A typical output for an HTPB fuel burning in GOX is shown in Fig. 9. The r_f and the corresponding G_{ox} evaluated by the sensor TOT data can be related by a power law interpolation of $r_f(G_{ox})$ yielding

$$r_f = 0.237 \ G_{ox}^{0.360} \tag{4}$$

Under the investigated conditions (inducer geometrical swirl number 4.75 [43], $\dot{m}_{ox} = 5 \cdot 10^{-3} \text{kg/s}, p_c \sim 1.5$ bar), the swirl flow yields a relatively low G_{ox} sensitivity of the r_f.

4.2 Ballistics Under Forced Transient Conditions

The investigation of solid fuel ballistic response under forced transient conditions is performed on the 2D radial microburner [10, 34]. The hereby presented data refer to a dedicated implementation of the facility. In particular, the injection condition was changed promoting a swirl flow (see Fig. 6). Thanks to this the combustion visualization quality was increased. On the other hand, this change in the nature of the inlet flow influenced the quasi-steady r_f value [34]. The forced transient ballistic tests were performed on HTPB burning in gaseous oxygen.

The presented results focus on throttling down events. The typical operating profile showing the quasi-steady leg (SL) followed by the transient leg (TL) is shown in Fig. 10.

Under the investigated conditions, the SL is characterized by $p_c = 16$ bar and $\dot{m}_{ox} = 5 \cdot 10^{-3}$ kg/s. The TL conventionally starts at the time the $\dot{m}_{ox}$ decreases below 99 % of the SL value and finishes when $\dot{m}_{ox} = 0$ kg/s. The transient leg duration is $\left(t_{TL,fin} - t_{TL,in}\right) = 47$ ms, thus yielding $d\dot{m}_{ox}/dt = -11 \cdot 10^{-2}$ kg/s^2.

With the new injector implementation, the SL r_f of HTPB results higher than the corresponding value for quasi-steady runs by 25 % on average [34]. This was due to the swirl flow realized by the injector. The power law approximation of r_f versus G_{ox} (Eq. 3) for the SL ensemble average yields

$$r_f = (0.028 \pm 0.001) \, G_{ox}^{(0.640 \pm 0.001)}, \quad R^2 = 0.96 \tag{5}$$

The result shown in Eq. 5 is mainly due to swirl effects induced by the new injector configuration (see also Eq. 4, in spite of the operating condition differences), augmenting the r_f values over the whole investigated range (a_r effect) and limiting the G_{ox} sensitivity of the ballistic response (n_r effect). The SL ensemble average is used for the definition of the characteristic times of the hybrid combustion process (see Table 9). Under the investigated conditions, the characteristic times of the
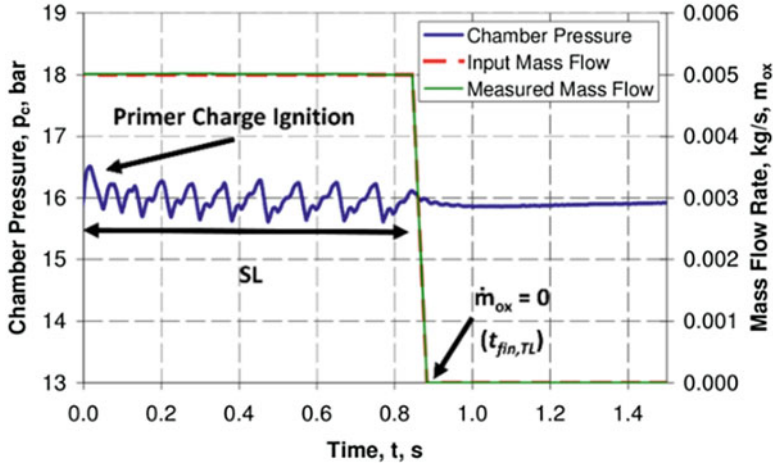
Fig. 10 Time history of operating parameters for a throttling test. The combustion chamber pressure is not affected by the $\dot{m}_{ox}$ decrease, due to the electro-valves acting on the exhaust line (Fig. 6)

Table 9 Characteristic times for transient combustion. Data are evaluated for SL ensemble average at $t_{fin,SL}$ [34]

$\tau_c = \frac{\kappa_s}{r_f^2}$, s	$\tau_s \cong \frac{R_u T_s}{E_a} \tau_c$, s	$\tau_g \cong \frac{\rho_g k_g C_s}{\rho_s k_s C_{p,g}} \tau_c$, s	$\tau_{bl} = c' \frac{L_p}{u_e}$, s
$20 \cdot 10^{-2a}$	$25 \cdot 10^{-3} - 5 \cdot 10^{-3b}$	$75 \cdot 10^{-5}$	$33 \cdot 10^{-4c}$

[a]$\kappa_s = 1 \cdot 10^{-7} \mathrm{m^2/s}$ [24, 38]
[b]$E_a = 50$–250 kJ/mol [24]
[c]See Ref. [39]

surface (τ_s) and gas phase (τ_g) reactions result shorter than the $(t_{TL,fin} - t_{TL,in})$. The same holds for the boundary layer characteristic time (τ_{bl}) but not for the one of the condensed phase reactions (τ_c). Therefore, during the investigated throttling down events, the condensed phase undergoes transient phenomena whose impact on the solid fuel ballistic response has to be investigated in order to evaluate their possible effects on hybrid combustion stability.

The forced transient test data reduction was based on the central port diameter sampling in time previously described [10, 34]. The SL time-resolved r_f is evaluated by Eq. 1, while the TL data requires a dedicated procedure. During the throttling down event, the $\overline{D}(t)$ and the $r_f(t)$ can present a non-monotonic behavior that cannot be captured by Eq. 1. Therefore, the $\overline{D}_l$ and the corresponding t_i are used in a TOT-based approach. Sampling frequencies up to 100–200 Hz were realized in TLs, depending on combustion visualization quality. In order to lessen data scattering due to the use of TOT over small time intervals, a smoothing procedure (moving average) is applied to the TL $\overline{D}_l$ and t_i [34]. The moving average step depends on the number of the TL $\overline{D}_l$ (and t_i) and must grant that
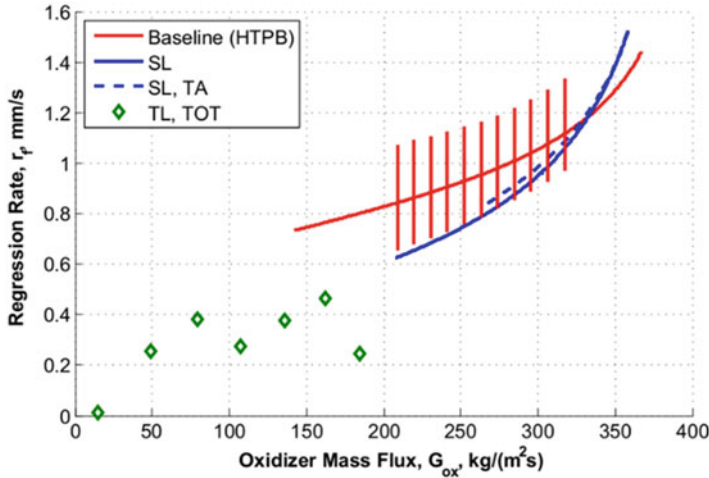
Fig. 11 Ballistic response of Test No. 1T. The moving average step for the TL is 7. The TL is characterized by a marked initial r_f decrease followed by faint oscillations. Error bars for TOT data not reported to improve readability [34]

$$r_{f,i+\frac{1}{2}} = \frac{1}{2} \frac{\overline{D}_{i+1} - \overline{D}_i}{t_{i+1} - t_i} \geq 0 \qquad (6)$$

Clearly the oxidizer mass flux at the time $t_{(i+\frac{1}{2})}$ can be expressed considering the measured $\dot{m}_{ox}$ as

$$G_{ox,i+\frac{1}{2}} = \dot{m}_{ox}\left(t = t_{i+\frac{1}{2}}\right) \Big/ \left[\frac{\pi}{4}\left(\overline{D}_{i,t_{i+\frac{1}{2}}}\right)^2\right] \qquad (7)$$

The r_f history in G_{ox} of the Test No. 1T is presented in Fig. 11. In this figure the SL ensemble average of the four performed transient runs is presented as a baseline. The SL of the Test No. 1T presents a monotonic r_f decrease. In spite of the linear $\dot{m}_{ox}$ decrease (see Fig. 11), test No. 1T presents a non-monotonic decreasing behavior of the r_f in the TL. Under the investigated conditions, the observed, faint r_f oscillations may be due to thermal lag effects in the condensed phase. The oxidizer mass flow throttling is exerted in a shorter time span. Due to finite thermal diffusivity, the thermal profile of the solid phase cannot be instantaneously modified as the operating condition changes. Moreover, $\dot{m}_{ox}$ reduction induces convective heat transfer decrease. Under these circumstances an increase in the convective heat transfer blockage is likely. This could yield r_f decrease. In turn, the r_f fall can hinder the blockage effect, thus originating the faint oscillations captured by the optical technique.

The ballistic response behavior of Test No. 1T is the most commonly observed under the investigated conditions [34]. On the other hand, some different r_f (G_{ox})
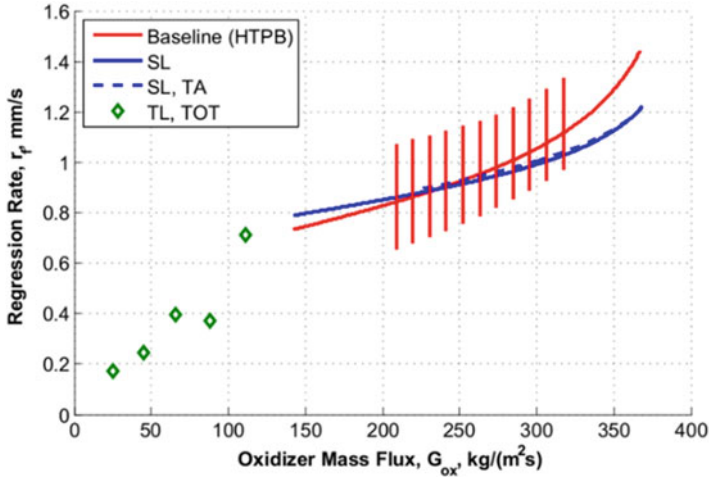
Fig. 12 Ballistic response of Test No. 2T. The moving average step for the TL is 5. The TL is characterized by faint r_f oscillations. *Error bars* for TOT data not reported to improve readability [34]

was observed in Test No. 2T (see Fig. 12). Test No. 2T exhibits no definite r_f decrease during the earlier phases of the TL, though an oscillating behavior is still recognizable. The TL of Test No. 2T is affected by a poor quality of the visualization possibly influencing the data reduction. Visualization of Test No. 2T was performed with a lower video recording rate and image spatial resolution with respect to the other performed tests. The latter conditions were tested in order to evaluate the possibility of tracking the regressing surface after the shutdown transient in a second forced transient with $\dot{m}_{ox}$ throttling up. The video recording frame rate reduction was due to hardware limitations (fast camera internal memory). Indeed, $\dot{m}_{ox}$ throttling up was performed in all of the runs, though only part of the transient can be recorded due to the hardware limitations. Moreover, two other factors hindered the analyses of the throttling up transients. First, the digital flow meter operating on the oxidizer feed line had its operating parameters optimized for throttling down events, and thus the $\dot{m}_{ox}$ increase resulted too slow (requiring more than 1 s). Second, the overall quality of the combustion visualization resulted too low during the throttling up event. As a consequence, only qualitative observations are possible for the throttling up transient.

In this respect, the most interesting observation is related to the ability of the solid fuel grain to undergo reignition after $\dot{m}_{ox}$ extinction, as shown in Fig. 13. In the investigated operating profile, $\dot{m}_{ox} = 0$ kg/s for 5–6 s from $t_{fin,TL}$. During this time interval, the temperature of the fuel subsurface is increased by thermal diffusion [23]. As a result, the condensed phase is preheated. After $\dot{m}_{ox}$ throttling up is started, hot spots trigger the restart of the combustion process. In the restart phase, solid fuel fragments detaching from the head-end of the grain (and likely from the whole
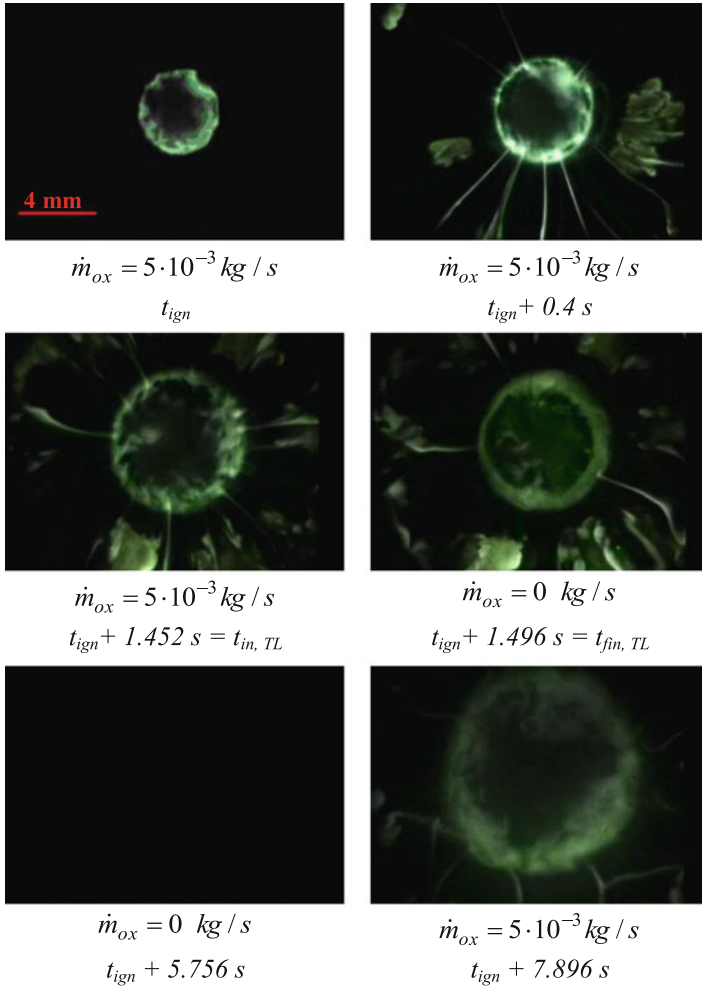
Fig. 13 Test No. 2T. Under the investigated operating conditions, the solid fuel restart is triggered by hot spots and throttling from 0 up to $5 \cdot 10^{-3}$ kg/s [34]

regressing surface) were noticed. In spite of this, under the investigated conditions, ballistic response to throttling up shows (apparently) little dynamic effects [34].

5 Conclusions and Future Developments

This paper focuses on the quasi-steady and the forced transient burning of solid fuel formulations for hybrid rocket propulsion. The quasi-steady burning data deals with the relative grading of HTPB- and paraffin-based fuel formulations. The combustion

test runs are performed on different setups enabling the use of various diagnostics for the data reduction. The transient burning tests focused on oxidizer mass flow rate throttling down.

The ballistics of HTPB-based fuels loaded with nAl and of unloaded paraffin waxes are evaluated by an optical time-resolved technique enabled by the continuous tracking of the regressing surface [10, 34]. The HTPB + ALEX formulation exhibits a marked initial r_f value yielding a percent increase over the baseline of 54 % at 370 kg/(m^{2}s). This performance enhancement is strongly dependent on the G_{ox} and disappears around 100 kg/(m^{2}s). An opposite behavior is exhibited by the HTPB + VF-ALEX formulation. This fluoropolymer-coated additive yields a ballistic response characterized by a reduced G_{ox} sensitivity (see Fig. 7b). On the one hand, the coating reduces the additive reactivity at high G_{ox}, limiting the initial r_f enhancement over the baseline with respect to the uncoated ALEX. On the other hand, the oxidizing species release from the coating decomposition can promote the solid fuel ballistic response for decreasing oxidizer mass fluxes. From this point of view, the use of coating on air-passivated nAl appears as a promising path for performance tailoring.

The thermal, rheological, and ballistic characterization of the six different paraffin-based fuels enabled the identification of peculiar behaviors of the commercially available products. One identified trend is associated to the mixtures based on macro-paraffin-based waxes, except the particular WaxMixBL mixture: these mixtures are characterized by low melting points, softening point temperatures which range from 42 to 48 °C, and high regression rates. A second trend is related to the micro-paraffin-based mixture Micro1BL, which shows a higher melting temperature, preserves its elastic modulus up to 51 °C, and shows a regression rate between the fast macro-paraffin mixtures and the slow, not-loaded HTPB. A third behavior refers to the particular mixture WaxMixBL; it presents a low melting temperature with a storage modulus that slowly falls down due to its high elasticity and a comparable regression rate with respect to the HTPB.

For the strengthening of paraffin waxes, a styrene-based thermoplastic elastomer (polystyrene-*block*-poly(ethylene-*ran*-butylene)-*block*-polystyrene grafted with maleic anhydride, SEBS-MA) was considered. An investigation of the thermal, rheological, mechanical, and ballistic behavior of these blends was performed in order to reach a good trade-off between mechanical and ballistic properties. The overlapping of DSC thermographs (SEBS-MA cannot be detected by DSC, being an amorphous polymer) and elastic modulus traces confirms the presence of critical temperature values which explain the rheological behavior of paraffin wax blended with different mass fraction values of SEBS-MA. The tested polymer improves paraffin mechanical properties, thus allowing the use of blends for propulsive applications.

A SPLab-developed r_f sensor showed promising performance both at lab level and at the test bench due to its original, innovative design [41, 42].

The investigation of the ballistic response to the oxidizer mass flow throttling down was performed on an HTPB fuel burning in gaseous oxygen [34]. The

throttling down was performed with $\dot{m}_{ox}/dt = -11 \cdot 10^{-2}\text{kg/s}^2$. The ballistic data were reduced by a modified TOT approach. Under the investigated conditions, condensed phase thermal delay effects produced faint r_f oscillations. A detailed analysis of the possible $\dot{m}_{ox}/dt$ influences on the observed solid fuel behavior is recommended for the future analyses.

References

1. Marxman GA, Gilbert M (1963) Turbulent boundary layer combustion in the hybrid rocket. In: 9th international symposium on combustion. Academic, New York, pp 371–383
2. Marxman GA (1967) Boundary layer combustion in propulsion. In: Proceedings of the 11th symposium (international) on combustion. The Combustion Institute. Pittsburgh, pp 269–289
3. Marxman GA, Wooldridge CE (1968) Research on the combustion mechanism of hybrid rockets. In: Advances in tactical rocket propulsion, AGARD conference proceedings no. 1, pp 421–477
4. Chiaverini MJ (2007) Chapter 2: Review of solid fuel regression rate behavior in classical and nonclassical hybrid rocket motors. In: Chiaverini MJ, Kuo KK (eds) Fundamentals of hybrid rocket combustion and propulsion, vol 218, AIAA Progress in Astronautics and Aeronautics. AIAA, Reston, pp 37–125
5. Risha G, Evans BJ, Boyer E, Kuo KK (2007) Chapter 10: Metals, energetic additives and special binders used in solid fuels for hybrid rockets. In: Chiaverini MJ, Kuo KK (eds) Fundamentals of hybrid rocket combustion and propulsion, vol 218, AIAA Progress in Astronautics and Aeronautics. AIAA, Reston, pp 413–456
6. Karabeyoglu MA, Altman D, Cantwell BJ (2002) Combustion of liquefying hybrid propellants: part 1, general theory. J Propuls Power 18:610–620. doi:10.2514/2.5975
7. Karabeyoglu MA, Cantwell BJ (2002) Combustion of liquefying hybrid propellants: part 2, stability of liquid films. J Propuls Power 18:621–630. doi:10.2514/2.5976
8. Knuth WH, Chiaverini MJ, Sauer JA, Gramer DJ (2002) Solid-fuel regression rate behavior of vortex hybrid rocket engines. J Propuls Power 18:600–609. doi:10.2514/2.5974
9. Takashi T, Yuasa S, Yamamoto K (1999) Effects of swirling oxidizer flow on fuel regression rate of hybrid rockets. Am Inst Aeronaut Astronaut. doi:10.2514/6.1999-2323
10. Paravan C (2012) Ballistics of innovative solid fuel formulations for hybrid rocket engines. PhD dissertation, Politecnico di Milano
11. Sossi A, Duranti E, Manzoni M, Paravan C, DeLuca LT, Vorozhtsov AB, Lerner MI, Rodkevich NG, Gromov AA, Savin N (2013) Combustion of HTPB-based solid fuels loaded with coated nanoaluminum. Combust Sci Technol 185:17–36
12. George P, Krishnan S, Varkey PM, Ravindran M, Ramachandran L (2001) Fuel regression rate in hydroxyl terminated polybutadiene/gaseous oxygen hybrid rocket motors. J Propuls Power 17(1):35–42
13. Frederick RA Jr, Whitehead JJ, Knox LR, Moser MD (2007) Regression rates study of mixed hybrid propellants. J Propuls Power 23:175–180. doi:10.2514/1.14327
14. Maggi F, Gariani G, Galfetti L, DeLuca LT (2012) Theoretical analysis of hydrides in solid and hybrid rocket propulsion. Int J Hydrog Energy, 10th international conference on clean energy 2010, 37:1760–1769. doi:10.1016/j.ijhydene.2011.10.018
15. Karabeyoglu AM, Arkun U (2014) Evaluation of fuel additives for hybrid rockets and SFRJ systems. Am Inst Aeronaut Astronaut. doi:10.2514/6.2014-3647
16. Larson D, Boyer E, Wachs T, Kuo K, DeSain J, Curtiss T, Brady B (2011) Characterization of the performance of paraffin/LiAlH4 solid fuels in a hybrid rocket system. Am Inst Aeronaut Astronaut. doi:10.2514/6.2011-5822

17. DeSain J, Curtiss T, Metzler K, Brady B (2010) Testing hypergolic ignition of paraffin Wax/LiAlH4 mixtures. Am Inst Aeronaut Astronaut. doi:10.2514/6.2010-6636

18. Galfetti L, Merotto L, Boiocchi M, Maggi F, DeLuca LT (2011) Ballistic and rheological characterization of paraffin-based fuels for hybrid rocket propulsion. Am Inst Aeronaut Astronaut. doi:10.2514/6.2011-5680

19. Hahma A, Gany A, Palovuori K (2006) Combustion of activated aluminum. Combust Flame 145:464–480. doi:10.1016/j.combustflame.2006.01.003

20. Maggi F, Dossi S, Paravan C, DeLuca LT, Liljedahl M (2015) Activated aluminum powders for space propulsion. Powder Technol 270(Part A):46–52. doi:10.1016/j.powtec.2014.09.048

21. Kim S, Lee J, Moon H, Sung H, Kim J, Cho J (2010) Effect of paraffin-LDPE blended fuel on the hybrid rocket motor. Am Inst Aeronaut Astronaut. doi:10.2514/6.2010-7031

22. Williams FA (1965) Grain design and throttling of hybrid rocket motors. Chem Eng Prog Ser 62(61):86–94

23. Saraniero MA, Caveny LH, Summerfield M (1973) Restart transients of hybrid rocket engines. J Spacecr Rocket 10(3):215–217

24. Karabeyoglu MA (2007) Chapter 9: Combustion instability and transient behavior in hybrid rocket motors. In: Chiaverini MJ, Kuo KK (eds) Fundamentals of hybrid rocket combustion and propulsion, vol 218, AIAA Progress in Astronautics and Aeronautics. AIAA, Reston, pp 351–411

25. Lee C, Lee JW, Byun DY (2003) Transient analysis on hybrid rocket combustion by the Zeldovich-Novozhilov method. KSME Int J 17(10):1572–1582

26. Advanced Powder Technology LLC, Tomsk. www.nanosized-powders.com

27. 3M material safety data sheet fc-2175 fluorel brand fluoroelastomer. www.machichemicals.com/pdf/3M_FC-2175.pdf

28. Sossi A, Duranti E, Paravan C, DeLuca LT, Vorozhtsov AB, Gromov AA, Pautova YI, Lerner MI, Rodkevich NG (2013) Non-isothermal oxidation of aluminum nanopowder coated by hydrocarbons and fluorohydrocarbons. Appl Surf Sci 271:337–343

29. Carlo Erba Reagenti Srl, Cornaredo. www.carloerbareagents.com

30. Sasol wax GmbH hot melt adhesives brochure. www.sasolwax.com

31. Paravan C, Viscardi M, DeLuca LT, Kazakov A (2009) Regression rates and anisotropy effects in hybrid rockets microburner. 3rd EUCASS (European Conference for Aerospace Sciences) conference, Versailles, 04–07 July 2009

32. Meyer G, Matthai M, Auge J, Lindow H (2005) Crystallization processes and hardness of paraffin waxes characterized by DSC, ultrasonic, x-ray and needle penetration measurements. SOFW-J 37:131–138

33. DeLuca LT, Galfetti L, Maggi F, Colombo G, Paravan C, Reina A, Dossi S, Fassina M, Sossi A (2014) Chapter 12: Characterization and combustion of aluminum nanopowders in energetic systems. In: Gromov AA, Teipel U (eds) Metal nanopowders: production, characterization, and energetic applications. Wiley, Weinheim, pp 301–400

34. DeLuca LT, Maggi F, Dossi S, Fassina M, Paravan C, Sossi A (2016) Prospects of aluminum modifications as energetic fuels in chemical rocket propulsion. In: DeLuca LT, Shimada T, Sinditskii VP, Calabro M (eds) Chemical rocket propulsion: a comprehensive survey of energetic materials. Springer, Cham

35. Paravan C, Manzoni M, Rambaldi G, DeLuca LT (2013) Analysis of quasi-steady and transient burning of hybrid fuels in a laboratory-scale burner by an optical technique. Int J Energy Mater Chem Propuls 12:385–410. doi:10.1615/IntJ.EnergeticMaterialsChemProp.2013005756

36. Ohlemiller TJ, Summerfield M (1968) A critical analysis of arc image ignition of solid propellants. AIAA J 6(5):878–886

37. DeLuca LT, Paravan C, Reina A, Spreafico M, Marchesi E, Maggi F, Bandera A, Colombo G, Kosowski BM (2010) Aggregation and incipient agglomeration in metallized solid propellants and solid fuels for rocket propulsion. Am Inst Aeronaut Astronaut. doi:10.2514/6.2010-6752

38. Lengellé G (2007) Chapter 3: Solid fuel pyrolysis phenomena and regression rate, part 1: mechanism. In: Chiaverini MJ, Kuo KK (eds) Fundamentals of hybrid rocket combustion and propulsion, vol 218, AIAA Progress in Astronautics and Aeronautics. AIAA, Reston, pp 127–165

39. Schlichting H, Gersten K (2003) Chapter 21: Unsteady turbulent boundary layers. In: Boundary layer theory. Springer Verlag, Berlin, pp 645–649
40. Tadini P, Paravan C, Maggi F, Boiocchi M, Colombo G, DeLuca LT (2013) Regression rate measurements in lab-scale hybrid burners. Presented at the 5th EUCASS, 20–27 July, Munich
41. Galfetti L, Maggi F, Colombo G (2013) Regression sensor for solid material. Italian patent DAST.13.011.A-MI2013A 002122072013
42. SPARTAN project homepage. http://www.spartanproject.eu. Available 26 Nov 2014
43. Beer JM, Chigier NA (1972) Combustion aerodynamics. Applied Science Publishers, London
44. Seno J, Selvin TP (2006) Thermal and crystallisation behaviours of blends of polyamide 12 with styrene–ethylene/butylene styrene rubbers. Polymer 47:6328–6336
45. Boiocchi M, Milova P, Galfetti L, Di Landro L, Golovko AK (2013) In: Haidn OJ, Zinner W, Calabro M (eds) A wide characterization of paraffin-based fuels mixed with styrene-based thermoplastic polymers for hybrid propulsion. In; 5th European conference for Aerospace Sciences (EUCASS). ISBN: 9788494153105, pp 1–14
46. Reynders K, Mishenko N, Mortensen K (1995) Stretching-induced correlations in triblock copolymer gels as observed by small-angle scattering. Macromolecules 28:8699
47. Laurer JH, Bukovnik R, Spontak RJ (1996) Morphological characteristics of SEBS thermoplastic elastomer gels. Macromolecules 29:5760
48. Wilkinson AN, Laugel ML, Clemens VM, Harding VM, Marin M (1999) Phase structure in polypropylene/PA6/SEBS blends. Polymer 40:4971–4975
49. Asthana S, Kennedy JP (2002) Novel polyisobutylene stars. XXIII. Thermal, mechanical and processing characteristics of poly(phenylene ether)/polydivinylbenzene (polyisobutylene-b-polystyrene)$_{37}$. Blends J Appl Polym Sci 86:2866–2872
50. Laurer JH, Mulling J, Khan SA, Spontak R, Bukovnik R (1998) Thermoplastic elastomer gels. I. Effects of composition and processing on morphology and gel behavior. J Polym Sci Part B: Polym Phys 36:2379
51. Laurer JH, Mulling J, Khan SA, Spontak R, Bukovnik R (1998) Thermoplastic elastomer gels. I. Effects of composition and temperature on morphology and gel rheology. J Polym Sci Part B: Polym Phys 36:2513
52. Wang J, Calhoun MD, Severtson SJ (2008) Dynamic rheological study of paraffin Wax and its organoclay nanocomposites. J Appl Polym Sci 108:2564–2570
53. Benterou J, Udd E (2007) Measurements using fiber-optic bragg grating sensors. EuroPyro. In; 34th international pyrotechnics seminar, Beaune

Part VII
New Concepts in Chemical Propulsion

In-Space Chemical Propulsion System Roadmap

Bryan A. Palaszewski, Michael L. Meyer, Les Johnson, Dan M. Goebel, Harold White, and David J. Coote

Abstract In-space propulsion begins where the launch vehicle upper stage leaves off, performing the functions of primary propulsion, reaction control, station keeping, precision pointing, and orbital maneuvering. The main engines used in space provide the primary propulsive force for orbit transfer, planetary trajectories, and extraplanetary landing and ascent. The reaction control and orbital maneuvering systems provide the propulsive force for orbit maintenance, position control, station keeping, and spacecraft attitude control.

Advanced in-space propulsion technologies will enable much more effective exploration of our solar system and will permit mission designers to plan missions to "fly anytime, anywhere, and complete a host of science objectives at the destinations" with greater reliability and safety. With wide range of possible missions and candidate propulsion technologies, the question of which technologies are "best" for future missions is a difficult one. A portfolio of propulsion technologies should be developed to provide optimum solutions for a diverse set of missions and destinations. A large fraction of the rocket engines in use today are chemical rockets;

B.A. Palaszewski (✉) • M.L. Meyer
NASA Glenn Research Center, MS 5-10, Cleveland, OH 44135, USA
e-mail: bryan.a.palaszewski@nasa.gov; michael.l.meyer@nasa.gov

L. Johnson
NASA Marshall Space Flight Center, Huntsville, AL 35811, USA
e-mail: les.johnson@nasa.gov

D.M. Goebel
Jet Propulsion Laboratory, Pasadena, CA 91109, USA
e-mail: dan.m.goebel@nasa.gov

H. White
NASA Johnson Space Center, Houston, TX 77058, USA
e-mail: harold.white-1@nasa.gov

D.J. Coote
NASA Stennis Space Center, Stennis Space Center, MS 39529, USA
e-mail: david.j.coote@nasa.gov

that is, they obtain the energy needed to generate thrust by chemical reactions to create a hot gas that is expanded to produce thrust. A significant limitation of chemical propulsion is that it has a relatively low specific impulse (I_s or thrust per mass flow rate of propellant).

A significant improvement (>30 %) in I_s can be obtained by using cryogenic propellants, such as liquid oxygen and liquid hydrogen, for example. Historically, these propellants have not been applied beyond upper stages.

Nomenclature

AF315E	Liquid monopropellant under study at Edwards Air Force Base
AHMS	Advanced Health Management System
AMPM	Agency Mission Planning Model
ARC	Ames Research Center
ATP	Authority to proceed
CFM	Cryogenic fluid management
ClF_3	Chlorine trifluoride
ClF_5	Chlorine pentafluoride
DRA	Design Reference Architecture
DRM	Design Reference Mission
ECLS	Environmental Control and Life Support
EHS	Environmental Health System
GRC	Glenn Research Center
GTO	Geostationary transfer orbit
HEDM	High-energy density materials
HEFT	Human Exploration Framework Team
HmNT	Hydrazine milli-Newton thruster
HTPB	Hydroxyl-terminated polybutadiene
IMLEO	Initial mass in low Earth orbit
ISHM	Integrated System Health Management
ISPSTA	In-space propulsion system technology area
ISRU	In situ resource utilization
ISS	International Space Station
JAXA	Japanese Aerospace Exploration Agency
JSC	Johnson Space Center
KSC	Kennedy Space Center
LST	Life Support Technologies
MMH	Monomethylhydrazine
MMOD	Micrometeoroid/orbital debris
MSFC	Marshall Space Flight Center
NOFB	Nitrous oxide fuel blend monopropellants
NTO	Nitrogen tetroxide, N_2O_4
OF_2	Oxygen difluoride

ProSEDS	Propulsive Small Expendable Deployer System
RCS	Reaction control system
SDI	Strategic Defense Initiative
SMD	Science Mission Directorate
SOA	State-of-art
TA	Technology area
TABS	Technology Area Breakdown Structure
TRL	Technology Readiness Level
XLR-132	Advanced NTO/MMH pump-fed engine technology
ZBO	Zero boil-off

1 Introduction

Space exploration is about getting somewhere (reduced transit times), getting a lot of mass there (increased payload mass), and getting there cheaply (lower cost). The simple act of "getting" there requires the employment of an in-space propulsion system, and the other metrics are modifiers to this fundamental action.

Development of technologies within this technology area (TA) will result in technical solutions with improvements in thrust levels, I_s, power, specific mass (or specific power), volume, system mass, system complexity, operational complexity, commonality with other spacecraft systems, manufacturability, durability, and, of course, cost. These types of improvements will yield decreased transit times, increased payload mass, safer spacecraft, and decreased costs (Refs. [1–6]). In some instances, development of technologies within this TA will result in mission-enabling breakthroughs that will revolutionize space exploration. There is no single propulsion technology that will benefit all missions or mission types. The requirements for in-space propulsion vary widely due according to their intended application. The technologies described herein will support everything from small satellites and robotic deep space exploration to space stations and human missions to Mars. Furthermore, numerous concepts for advanced propulsion technologies, such as electric propulsion, are commonly used for station keeping on commercial communication satellites and for prime propulsion on some scientific missions because they have significantly higher values of specific impulse.

However, they generally have very small values of thrust and therefore must be operated for long durations to provide the total impulse required by a mission. Several of these technologies offer performance that is significantly better than that achievable with chemical propulsion. This roadmap describes the portfolio of in-space propulsion technologies that could meet future space science and exploration needs. In-space propulsion represents technologies that can significantly improve a number of critical metrics.

Figure 1 is a graphical representation of the in-space propulsion technology area breakdown structure (TABS). The TABS is divided into four basic groups: (1) chemical propulsion, (2) nonchemical propulsion, (3) advanced propulsion tech-
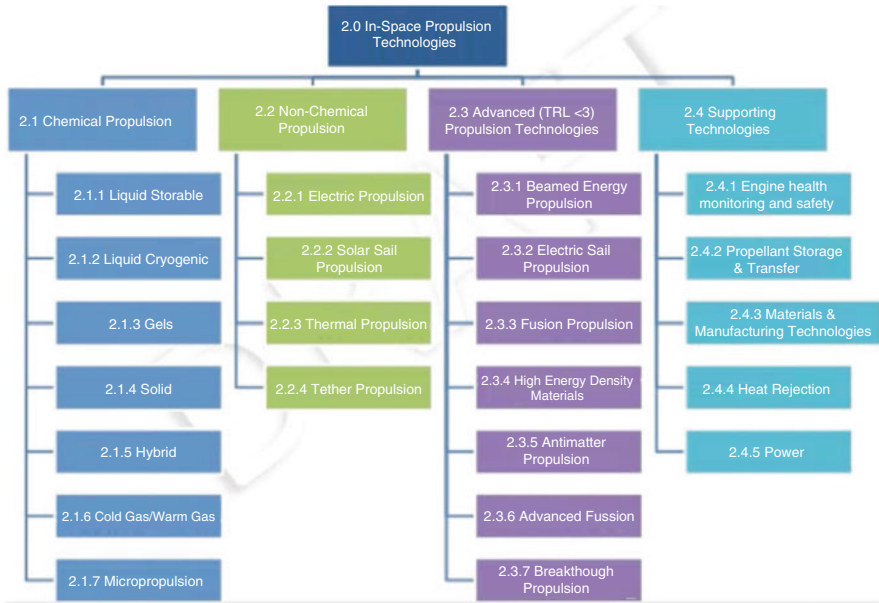
Fig. 1 In-space population technology area breakdown structure

nologies, and (4) supporting technologies, based on the physics of the propulsion system and how it derives thrust as well as its technical maturity. There may be credible meritorious in-space propulsion concepts not foreseen or captured in this document that may be shown to be beneficial to future mission applications. Care should be taken when implementing future investment strategies to provide a conduit through which these concepts can be competitively engaged to encourage continued innovation.

Figure 2 is the roadmap for the development of advanced in-space propulsion technologies showing their traceability to potential future missions. The roadmap makes use of the following set of definitions and ground rules. The term "mission pull" defines a technology or a performance characteristic necessary to meet a planned NASA mission requirement. Any other relationship between a technology and a mission (an alternate propulsion system, for example) is categorized as "technology push." Also, a distinction is drawn between an in-space demonstration of a technology versus an in-space validation. A space demonstration refers to the spaceflight of a scaled version of a particular technology or of a critical technology subsystem; a space validation would serve as a qualification flight for future mission implementation. A successful validation flight would not require any additional space testing of a particular technology before it can be adopted for a science or exploration mission. The graphical roadmap provides suggested technology pursuits within the four basic categories and ties these efforts to the portfolio of known and potential future NASA or non-NASA missions.
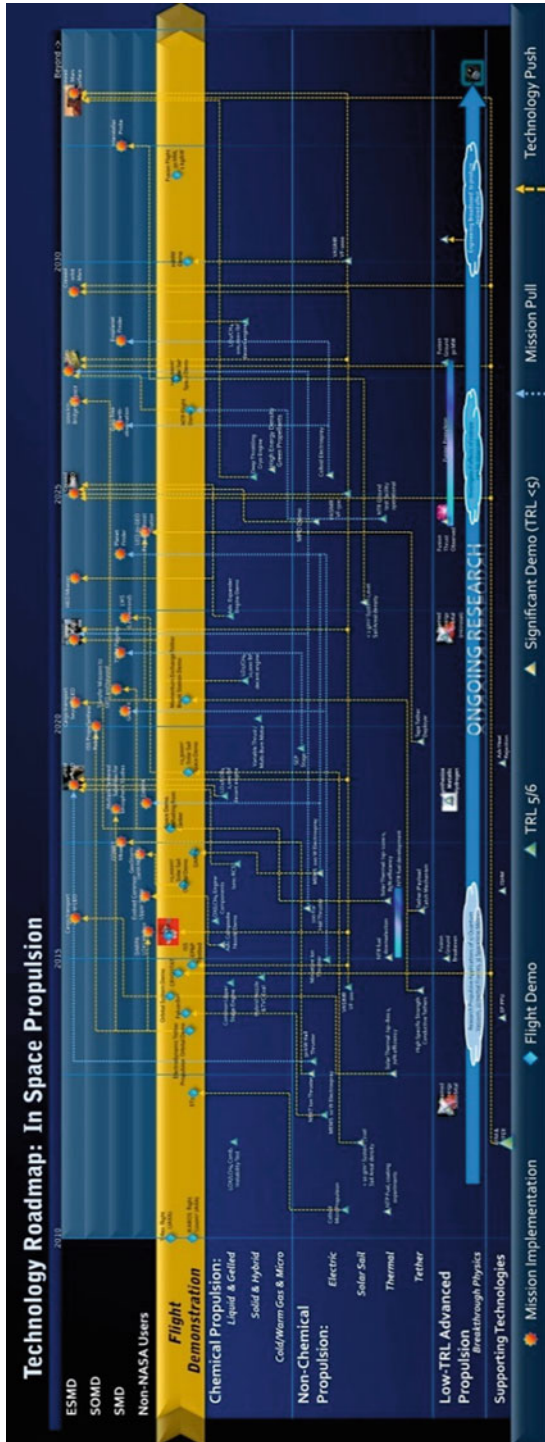
Fig. 2 TA02 technology roadmap

2 General Overview

2.1 Technical Approach

For both human and robotic exploration, traversing the solar system is a struggle against time and distance. The most distant planets are 4.5–6 billion kilometers from the Sun, and to reach them in any reasonable time requires much more capable propulsion systems than conventional chemical rockets. Rapid inner solar system missions with flexible launch dates are difficult, requiring propulsion systems that are beyond today's current state of the art. The logistics, and therefore the total system mass required to support sustained human exploration beyond Earth to destinations such as the Moon, Mars, or near-Earth objects, are daunting unless more efficient in-space propulsion technologies are developed and fielded. With the exception of electric propulsion systems used for commercial communication satellite orbit positioning and station keeping and a handful of lunar and deep space science missions, all of the rocket engines in use today are chemical rockets; that is, they obtain the energy needed to generate thrust by combining reactive chemicals to create a hot gas that is expanded to produce thrust. A significant limitation of chemical propulsion is that it has a relatively low specific impulse (thrust per unit of mass flow rate of propellant). Numerous concepts for advanced in-space propulsion technologies have been developed over the past 50 years. While generally providing significantly higher specific impulse compared to chemical engines, they typically generate much lower values of thrust. Thrust to weight ratios greater than unity are required to launch from the surface of the Earth, and chemical propulsion is currently the only propulsion technology capable of producing the magnitude of thrust necessary to overcome Earth's gravity. However, once in space, more efficient propulsion systems can be used to reduce total mission propellant mass requirements.

Advanced in-space propulsion technologies will enable much more effective exploration of our solar system and will permit mission designers to plan missions to fly anytime, anywhere, and complete a host of science objectives at their destinations. A wide range of possible missions and candidate chemical and advanced in-space propulsion technologies with diverse characteristics offers the opportunity to better match propulsion systems for future missions. Developing a portfolio of in-space propulsion technologies will allow optimized propulsion solutions for a diverse set of missions and destinations. The portfolio of concepts and technologies described in this roadmap is designed to address these future space science and exploration needs.

2.2 Benefits

In-space propulsion is a category of technology where developments can benefit a number of critical figures of merit (metrics) for space exploration. Space exploration

is about getting somewhere safely (mission enabling), getting there quickly (reduced transit times), getting a lot of mass there (increased payload mass), and getting there cheaply (lower cost). The simple act of "getting" there requires the employment of an in-space propulsion system, and the other metrics are modifiers to this fundamental action. Simply put, without a propulsion system, there would be no mission. Development of technologies within this TA will result in technical solutions with improvements in thrust levels, specific impulse (I_s), power, specific mass (or specific power), volume, system mass, system complexity, operational complexity, commonality with other spacecraft systems, manufacturability, durability, and of course, cost. These types of improvements will yield decreased transit times, increased payload mass, safer spacecraft, and decreased costs. In some instances, development of technologies within this technology area (TA) will result in mission-enabling breakthroughs that will revolutionize space exploration.

2.3 Applicability/Traceability to NASA Strategic Goals, AMPM, DRMs, and DRAs

The in-space propulsion roadmap team used the NASA strategic goals and missions detailed in the following reference materials in the development of this report: Human Exploration Framework Team products to extract reference missions with dates, Science Mission Directorate (SMD) Decadal Surveys, past Design Reference Missions (DRMs), Design Reference Architectures (DRAs), historical mission studies, in-space propulsion technology concept studies, and internal ISS utilization studies. The references identify missions used for categorizing pull and push technology designations.

2.4 Top Technical Challenges

The major technical challenges for in-space propulsion system technology area (ISPSTA) were identified and prioritized through team consensus based on perceived mission need or potential impact on future in-space transportation systems. These challenges were then categorized into near- (present to 2016), mid- (2017–2022), and far-term (2023–2028) time frames, representing the point at which TRL 6 is expected to be achieved. It is likely that support of these technologies would need to begin well before the listed time horizon. TRL-6 readiness dates were determined by considering stated mission pull (e.g., Human Exploration Framework Team (HEFT), Decadal Surveys stating mission need dates, etc.), the state of the art for specific technologies that could be matured to the point of quickly enabling missions of interest to potential users (technology push), and the need for a breadth of technology-enabled capabilities across all time frames.

3   Detailed Portfolio Discussion

The roadmap for this technical area is divided into four basic groups:

- (1) Chemical propulsion
- (2) Nonchemical propulsion
- (3) Advanced propulsion technologies
- (4) Supporting technologies

The first two categories are grouped according to the governing physics. Chemical propulsion includes propulsion systems that operate through chemical reactions to heat and expand a propellant (or use a fluid dynamic expansion, as in a cold gas) to provide thrust. Propulsion systems that use electrostatic, electromagnetic, field interactions, photon interactions, or externally supplied energy to accelerate a spacecraft are grouped together under the section titled "Nonchemical Propulsion." The third section, "Advanced Propulsion Technologies," is meant to capture technologies and physics concepts that are at a lower TRL level (< TRL3). The fourth section, "Supporting Technologies," identifies the pertinent technical areas that are strongly coupled to, but are not part of, in-space propulsion, such that focused research within these related areas will allow significant improvements in performance for some in-space propulsion technical areas. In addition, development of some advanced forms of chemical propulsion will have modeling challenges to better understand and predict dynamic instability during combustion, and electric propulsion technologies require the enhancement and validation of complicated life models to shorten life qualification testing.

Development of technologies within this TA will result in technical solutions with improvements in thrust levels, specific impulse, power, specific mass, system complexity, operational complexity, commonality with other spacecraft systems, manufacturability, and durability. The benefits to be derived from each technology in the TABS will be identified with one of the icons as described in the list of technologies.

Within each section of the technology descriptions, there are three elements. The first element provides a summary description of a particular technology, explaining its governing physics and method of operation. The second element identifies at a high level the technical challenges that must be overcome to raise its maturity. The third element for sections "Chemical Propulsion," "High-Energy Oxidizers," and "Advanced (TRL <3) Propulsion Technologies" describes the significant milestones to be reached for a given technology to attain TRL 6. In Section "Liquid Cryogenic Propellants," this element describes the milestones required for attaining TRL >3. This roadmap makes use of the following set of definitions and ground rules. The term "mission pull" defines a technology or a performance characteristic necessary to meet a planned NASA mission requirement. Any other relationship between a technology and a mission (e.g., an alternate propulsion system) is categorized as "technology push." Also, a distinction is drawn between an in-space demonstration

Fig. 3 TA02 technology roadmap

of a technology versus an in-space validation. A space demonstration refers to the space flight of a scaled version of a particular technology or of a critical technology subsystem; a space validation would serve as a qualification flight for future mission implementation. A successful validation flight would not require any additional space testing of a particular technology before it can be adopted for a science or exploration mission. The graphical roadmap representation (Fig. 3) provides suggested technology pursuits within the four basic categories and ties these efforts to the portfolio of known and potential future NASA/non-NASA missions. Most of the near-term content on the graphic is based on actual plans, while the out years can be considered to have larger uncertainty bars on the placement of items within the timeline. Tables 1 and 2 provide the final ranking on all of the in-space propulsion technologies and their linkages to related supporting technology areas.

Table 1 Technology rankings and priorities

Rank	Description	Priority
1	Power processing units (PPUs) for ion, Hall, and other electric propulsion systems	Near
2	Long-term in-space cryogenic propellant storage and transfer	Mid
3	High-power (e.g., 50–300 kW) class solar electric propulsion	Mid
4	Advanced in-space cryogenic engines and supporting components	Mid
5	Developing and demonstrating MEMS-fabricated electrospray thrusters	Near
6	Demonstrating large (over 1000 m^2) solar sail-equipped vehicle in space	Near
7	Nuclear thermal propulsion (NTP) components and systems	Far
8	Advanced space storable propellants	Mid
9	Long-life (>1 year) electrodynamic tether propulsion system in LEO	Near
10	Advanced in-space propulsion technologies (TRL <3) to enable a robust technology portfolio for future missions	Far

3.1 Chemical Propulsion

Chemical propulsion involves the chemical reaction of propellants to move or control a spacecraft. Chemical propulsion system functions include primary propulsion, reaction control, station keeping, precision pointing, and orbital maneuvering. The main engines provide the primary propulsive force for orbit transfer, planetary trajectories, and extraplanetary landing and ascent. The reaction control and orbital maneuvering systems provide the propulsive force for orbit maintenance, position control, station keeping, and spacecraft attitude control.

3.1.1 Monopropellants

3.1.1.1 State of the Art

Hydrazine thrusters use a catalytic decomposition reaction to generate high-temperature gas for thrust. Hydrazine is SOA. Spacecraft reaction control system (RCS) performance is near $I_s = 228$ s. Lander engines have higher I_s (238 s). Freezing point is 3 °C.

3.1.1.2 Challenges

Catalyst life, inability for cold starts, increased thrust and I_s performance with pumped systems, reduction of freezing point from 3 °C needed without compromising the performance.

Table 2 TA02 relationships to other technology areas

Relationship with TA2: In-Space Propulsion	TA1	TA2	TA4	TA5	TA6	TA7	TA8	TA9	TA10	TA11	TA12	TA13	TA14	TA15
	S	F	F					T	S		F	T	F	

TA1 LAUNCH PROPULSION SYSTEMS
TA2 SPACE POWER AND ENERGY STORAGE SYSTEMS
TA4 ROBOTICS, TELE-ROBOTICS, AND AUTONOMOUS SYSTEMS
TA5 COMMUNICATION AND NAVIGATION SYSTEMS
TA6 HUMAN HEALTH, LIFE SUPPORT AND HABITATION SYSTEMS
TA7 HUMAN EXPLORATION DESTINATION SYSTEMS
TA8 SCIENTIFIC INSTRUMENTS, OBSERVATORIES, AND SENSOR SYSTEMS
TA9 ENTRY, DESCENT, AND LANDING SYSTEMS
TA10 NANOTECHNOLOGY
TA11 MODELING, SIMULATION, INFORMATION TECH, AND PROCESSING
TA12 MATERIALS, STRUCTURAL AND MECH, SYSTEMS, AND MANUFACTURING
TA13 GROUND AND LAUNCH PROCESSING
TA14 THERMAL MANAGEMENT SYSTEMS
TA15 AERONAUTICS

	Extensive		Close synergy in tasks	S
	Limited		Technologies from TA2 to related TA	T
			Technologies from related TA to TA2	F

3.1.1.3 Milestones to TRL 6

Evaluate alternate propellants such as NOFB and AF315E. Develop thrusters to operate in pulse and continuous operation with new propellant. Qualify propellants and components (valves, filters, regulators, etc.).

3.1.2 Bipropellants

3.1.2.1 State of the Art

Bipropellant thrusters use the chemical reaction, typically hypergolic, to generate high-temperature gas that is expanded to generate thrust. Nitrogen tetroxide (NTO)/hydrazine (N_2H_4) is SOA with $I_s = 326$ s for fixed thrust (450 N) planetary main engine.

3.1.2.2 Challenges

Increased thrust with improved packaging for landers and orbit insertionThrottle capability for planetary landers Pumped systems desirable for planetary spacecraft vs. pressure-fed systems Mixture-ratio control and propellant gauging to reduce residuals and improve performance.

3.1.2.3 Milestones to TRL 6

Develop and qualify pumped bipropellant system.
Develop and qualify throttleable bipropellant valve/system.
Recapture XLR-132 NTO/MMH pump-fed engine technology.

3.2 High-Energy Oxidizers

High-energy oxidizers such as fluorinated compounds include chlorine trifluoride (ClF_3), chlorine pentafluoride (ClF_5), and oxygen difluoride (OF_2). These oxidizers have a long history of testing with most recent testing in the 1980s under the Strategic Defense Initiative (SDI). Stages for interceptors were created for flight testing using hydrazine/ClF_5.

3.2.1 Challenges

Fluorinated propellants have safety issues (high reactivity), but the upper stage processing methods to isolate ground support personnel from the oxidizers have been developed. These processing methods have not been exercised since the 1980s.

3.2.2 Milestones to TRL 6

The stage development for this technology was designed for Strategic Defense Initiative (SDI), etc. Recapturing the handling and upper stage ground processing methods is needed.

3.3 Liquid Cryogenic Propellants

3.3.1 Oxygen/Methane Propulsion

SOA is MMH/NTO at TRL 9 for reaction control system (RCS) and orbital maneuvering propulsion, which are integrated. LOx/methane is proposed to enable higher performance, space storability, pressure-fed and pump-fed options, common LO_2 and LCH_4 components (lower cost), application to in situ resource utilization (ISRU) for Mars, and higher density for improved packaging. LOx/methane is TRL 4–5 in that cryogenic fluid management (CFM), feed systems, RCS, main engine, and components have been tested in vacuum environments.

3.3.2 Challenges

System-level integration and test of the component technologies are needed.

Improvement in the main engine injector performance and stability. Development of flight-weight compact exciter and demonstrating the ability to deliver the correct quality of propellant for repeatable engine performance are needed.

3.3.3 Milestones to TRL 6

Perform system-level integration and test of the component technologies.

Some component improvements are required such as to improve the main engine injector performance and stability.

Test a regeneratively cooled main engine.

3.4 Advanced (TRL <3) Propulsion Technologies

3.4.1 Metallic Hydrogen

Metallic hydrogen is a theoretically dense energetic material (not yet produced on Earth). The TRL level is not at level 1 as the characteristics are based on theoretical calculations. The estimated density at ambient conditions is 7 g/cc, ten times LH_2. Above a critical temperature, possibly 1000 K, metallic hydrogen will become unstable and recombine to the molecular phase, releasing the energy of recombination, 216 MJ/kg (for reference: $H_2 + O_2$ in the SSME releases 10 MJ/kg,

LO_2/RP_1 releases 6 MJ/kg). Ongoing experiments are using diamond anvil cells and short-pulse laser technologies to follow the hydrogen melt line toward the conditions for the metallic state. Expected I_s values are in the 500–2000 s range.

3.4.2 Challenges

Upgrading existing experimental equipment is required for synthesis and characterization of small quantities of metallic hydrogen. Scaling up production by many orders of magnitude is required. Engine components must be developed that are compatible with metallic hydrogen. Test engines must be developed to verify expected operations and performance with a variety of diluents and mixture ratios. There is a potential need for tankage that operates at millions of psi.

3.4.3 TRL Maturation Plan

Demonstrate synthesis of metallic hydrogen in laboratory.
Evaluate characteristics of metallic hydrogen in laboratory.
Develop production scaling techniques.
Develop engine components and test various diluents.
Perform propellant tankage development.
Perform tests of various engine sizes and diluents.

3.4.4 Atomic Boron/Carbon/Hydrogen

Atoms trapped in solid cryogens (neon, etc.) at 0.2–2 mass %. Atomic hydrogen, boron, and carbon fuels are very high-energy density, free-radical propellants. Atomic hydrogen may deliver an I_s of 600–1500 s. There has been great progress in the improvement of atom storage density over the last several decades. Lab studies have demonstrated 0.2 and 2 % weight atomic hydrogen in a solid hydrogen matrix. If the atom storage were to reach 10–15 %, which would produce an I_s of 600–750 s.

3.4.5 Challenges

Storage of atoms at 10, 15, or 50 mass % is needed for effective propulsion.

3.4.6 TRL Maturation Plan

Formulate atom storage methods for high density.
Develop engine designs for recombining propellants without immediate deflagration.
Perform testing and validation of engine designs.

3.4.7 High-Nitrogen Compounds (N4, N5+)

These are the most powerful explosives created in history. Work was conducted under the high-energy density materials (HEDM) program. Gram quantities formulated in laboratory (1999). Theoretical studies have shown that these materials may have in-space propulsion applications.

3.4.8 Challenges

The propellants are highly shock sensitive. Challenges include fabrication, transportation, ground processing, and personnel safety to name a few. Presently, there are no integrated vehicle designs that can make use of this possible propellant.

3.4.9 TRL Maturation Plan

Perform inhibitor research to facilitate safe scaling.
Develop high-speed deflagration/detonation engine technology.
Perform testing and validation of engine technology

4 Dawn of Space Commercialization

While the technologies described above have many applications, the most recent space commercialization vehicles may be their first users. With the retirement of the Space Shuttle in the USA, new directions for space exploration have begun. While NASA is now more focused on planetary exploration with robots and humans, NASA has begun fostering commercial companies to provide the more near-Earth cargo and personnel deliveries to the International Space Station (ISS). Several companies, SpaceX, Orbital, and Boeing, are providing space vehicles that can deliver cargo or people or both to the ISS. SpaceX is even hoping to build a large launcher that can deliver sizable 1 metric ton payloads to Mars, with a modification of their Dragon capsule (see Fig. 4). In addition, several companies such as Virgin Galactic (a venture with Great Britain and the USA) are planning for short flights in microgravity for space tourism. All of these applications can benefit from more advanced chemical propulsion: improved propellants with higher specific impulse (I_s) for space tourism, as well as higher density propellants for first-stage applications.

Space tourism vehicles, such as Virgin Galactic's SpaceShipTwo, use hybrid propulsion: a solid fuel and a liquid/gaseous oxidizer. While it is touted as a safer rocket motor over a pure solid rocket motor, the issues of reliability over long periods of time may lead the designers to higher I_s liquid rocket engines. Multiple flights per day were planned for the SpaceShipTwo vehicle. Replenishing
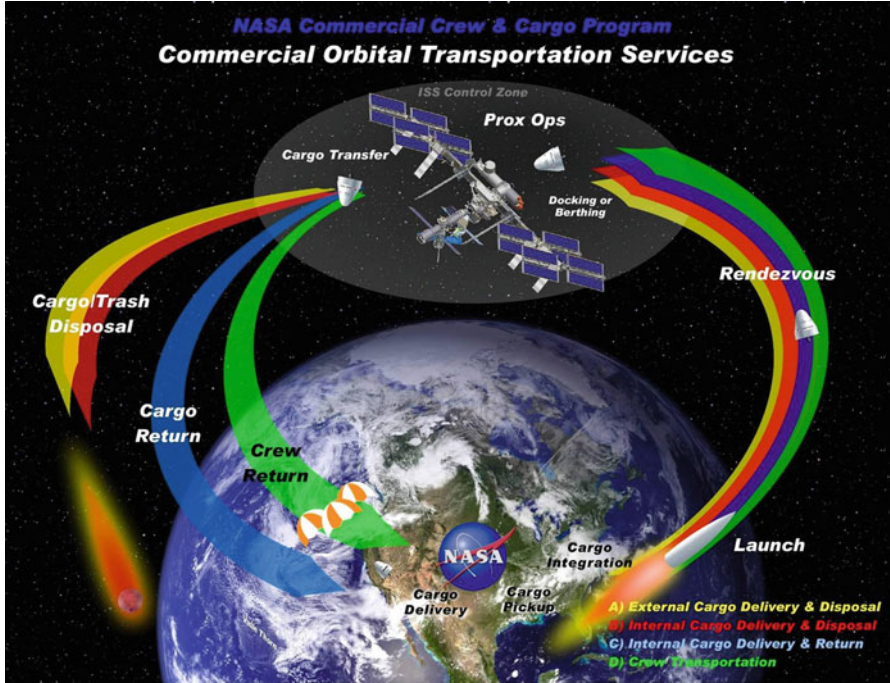
Fig. 4 Commercial orbital transportation systems

the liquid/gaseous oxidizer and refitting a new solid fuel grain on the vehicle may limit its flight rate. An all liquid rocket engine may simplify the refueling logistics and eliminate any need for solid fuel grain replacements.

In the SpaceX Falcon launch vehicle planning, the first stage is to be reused. The stage is to use its rocket engines to land softly on a robotic recovery ship. Carrying this additional retropropulsion and landing propellant will lead to a reduction in the total payload mass to orbit. A higher I_s rocket engine would reduce or potentially alleviate this payload mass penalty.

For its Mars landing option, the SpaceX Dragon capsule would use its integrated launch abort system rocket thrusters to effect the final landing. Based on preliminary studies, these thrusters could allow a Mars landing using only supersonic retro-propulsion and eliminate the need for a parachute landing system. The deceleration during landing would be very high, so such a landing mode would accommodate only robotic missions and would be too great of a stress on human astronauts. Higher I_s rocket engines would allow higher payloads to be landed on Mars. Also, if the liquid engines could be throttled over a wider range, the capsule would be more likely to accommodate human astronauts.

References

1. Frisbee RH (2003) Advanced space propulsion for the 21st century. J Propuls Power 19(6), Jet Propulsion Laboratory
2. Hoffman SJ, Kaplan DI (eds) (1997) NASA Special Publication 6107, Human exploration of mars: the reference mission of the NASA Mars exploration study team. Lyndon B. Johnson Space Center, Houston. Human Exploration of Mars Design Reference Architecture 5.0, NASA SP—2009–566, July 2009
3. Human Exploration Framework Team (HEFT) DRM review – phase 1 closeout, Steering Council. http://www.nasawatch.com/archives/2010/09/human-explorati.html. 2 Sept 2010
4. Johnson L, Farris B, Eberle B, Woodcock G, Negast B (2002) Integrated in-space transportation plan. NASA/CR-2002–212050, October 2002
5. "NASA Exploration Team (NEXT), Design Reference Missions Summary," FOR INTERNAL NASA USE ONLY, National Aeronautics and Space Administration, Draft, July 11, 2002
6. Balint TS Design reference mission set for RPS enabled missions in support of NASA's SSE roadmap. Jet Propulsion Laboratory, California Institute of Technology, IEEE Aerospace Conference (IEEEAC) Paper #1461, Version 2, updated December 5, 2006

Mapping of Aluminum Particle Dispersion in Solid Rocket Fuel Formulations

Arezoo Zare, Tres A. Harriman, Don A. Lucca, Silvia Roncalli, Bernard M. Kosowski, Christian Paravan, and Luigi T. DeLuca

Abstract Composite specimens consisting of two different kinds of hydroxyl-terminated polybutadiene (HTPB) loaded with either micron- or nanometer-sized Al powders were synthesized. The spatial distribution of the particles was investigated with a combination of Raman spectroscopy, atomic force microscopy (AFM), and scanning electron microscopy (SEM). The tested specimens were prepared by different manufacturing procedures to inhibit particle clustering. Although the dispersion of nano-sized Al particles was the primary interest, micron-sized Al was also used as a reference. Some specimens were prepared by ultrasonic-assisted mixing, others by a simple mechanical mixing procedure, and further specimens by a mechanical mixing process with the addition of dispersing agents (used commercially in pigment and coating applications to reduce inter-particulate attraction forces between particles). Spatial mapping of the C=O Raman mode associated with the HTPB was used to quantify the dispersion of the micron-sized Al particles. Tapping mode AFM and SEM measurements were used to identify the dispersion of both the micron- and nano-sized Al particles. The presence of clusters composed of many nano-sized particles was also identified and their size measured. The results obtained show the potential of these characterization techniques in evaluating the effectiveness of the manufacturing processes of the tested solid fuels and of the examined dispersion processes.

A. Zare • T.A. Harriman • D.A. Lucca (✉)
Oklahoma State University, School of Mechanical and Aerospace Engineering, Stillwater, OK 74078, USA
e-mail: arezoo.zare@okstate.edu; tres.harriman@okstate.edu; lucca@okstate.edu

S. Roncalli
Space Propulsion Laboratory (SPLab), Department of Aerospace Science and Technology, Politecnico di Milano, 20156 Milan, Italy

MACH I, Inc., King of Prussia, PA 19406, USA
e-mail: silvia@machichemicals.com; silvia.roncalli@mail.polimi.it

B.M. Kosowski
MACH I, Inc., King of Prussia, PA 19406, USA
e-mail: bernie@machichemicals.com

C. Paravan • L.T. DeLuca
Space Propulsion Laboratory (SPLab), Department of Aerospace Science and Technology, Politecnico di Milano, 20156 Milan, Italy
e-mail: christian.paravan@polimi.it; luigi.deluca@polimi.it

Nomenclature

AFM	Atomic force microscopy
ALEX	Aluminum exploded
C_{Al}	Active Al content
DOA	Dioctyl adipate
HTPB	Hydroxyl-terminated polybutadiene
HTPB-45M	MACH I® propulsion grade™ HTPB
HTPB-R45HTLO	Commercial Poly bd® HTPB
IPDI	Isophorone diisocyanate
nAl	Nano-sized Al particle
SEM	Scanning electron microscopy
S_{sp}	Specific surface m^2/g
TEM	Transmission electron microcopy
μAl	Micron-sized Al particle

1 Introduction

Metal powders are commonly used as fuel in energetic systems including rocket propulsion [1–5]. During the combustion process, metallic powders release considerable energy due to their high enthalpy of combustion. Aluminum powders have been one of the most commonly used metal fuels because of their high oxidation enthalpy, high density, low price, good availability, and low oxygen demand. Micron-sized aluminum (μAl) powders have been used for decades in solid propellants to increase the formulation specific impulse and the resistance to high-frequency acoustic instabilities. The former effect results from the augmented adiabatic flame temperature whose increase exceeds that of the combustion products' average molar mass induced by the metal presence. In principle, the ratio of the adiabatic flame temperature to the average molar mass of combustion products is the key parameter for the specific impulse determination of chemical rocket propellants. However, the aggregation of μAl particles prior to ignition may intensify the well-known agglomeration phenomena of melting and coalescence, leading to specific impulse losses due to incomplete metal combustion and two-phase flow effects [6–12]. In hybrid rocket fuels, μAl has been used to augment the radiative heat feedback from the flame zone to the gasifying surface, with the aim of increasing the regression rate, which is currently one of the limiting factors of these propulsive systems.

However, the use of the conventional μAl powders has been ineffective in enhancing either the burning rate of solid propellants or regression rate of solid fuels in hybrid propellants. Thus, propellant formulators have directed their attention to nano-sized aluminum (nAl) powders, which offer the potential for improved combustion properties and in particular faster propagation rates. While μAl particles mainly affect the radiative heat feedback, decreasing the Al particle size to the nano

range leads to a decrease in ignition temperature and an increase in the burning rates (in solid propellants) or regression rates (in solid fuels) of the corresponding metallized formulations [1–4, 8–16]. For example, Meda et al. showed that by reducing the size of Al particles from 3 μm to 30 nm, the solid propellant burning rate increased while the ignition time and temperature were reduced by a factor of two [3]. Risha et al. tested several solid fuels loaded with additives in the nano-sized range, achieving significant regression rate enhancements while burning hydroxyl-terminated polybutadiene (HTPB) loaded with 100–150 nm Al [11]. As a result, there has been considerable interest in using nAl, instead of μAl, in solid rocket fuels.

Conventional μAl is generally characterized by a specific surface area (S_{sp}) lower than 1 m^2/g and a metal content (C_{Al}) higher than 98 mass %. On the other hand, nAl features a much higher S_{sp} ($\sim$10 m^2/g) with a C_{Al} less than 90 mass % [1]. The C_{Al} of nAl is highly dependent on the powder passivation technique utilized. Air passivation leads to the formation of an amorphous Al_2O_3 shell around the Al core and a relatively high C_{Al} [17, 18]. Air-passivated nAl can be further coated by different materials (e.g., hydrocarbons or fluorohydrocarbons) in order to improve the aging behavior of the material or the quality of the powder-binder system [17, 19, 20]. However, the coating of an air-passivated powder leads to further reduction in C_{Al} and the possible formation of particle clusters [17, 20, 21].

To fully exploit the benefits of nAl, proper dispersion of the nano-sized particles is necessary. Due to their high S_{sp}, nAl particles exhibit a marked tendency to cluster. These clusters effectively behave as large particles and diminish the nAl reactivity. As a result, creating a well-dispersed HTPB composite containing nAl is a topic of interest in the field of both solid and hybrid rocket propulsion. A variety of approaches to mitigate the clustering of particles have been reported [22–27]. The effects of the mechanical mixing parameters (i.e., mixing time and intensity) are discussed by Payne [23]. Stuvyen et al. [26] reported that the joint action of hydrodynamic and magnetic forces yields clustering mitigation for aqueous suspension of γ-Al_2O_3. Steric and electrostatic stabilization are the basic mechanisms exploited when using dispersing agents to improve the nano-sized filler dispersion. The first mechanism relies on a strong adsorption on the particle surface of the anchoring group of polymer chains. This adsorbed layer forms a diffusion barrier maintaining the dispersed particles in a stable non-flocculant state. The second mechanism is based on the electrostatic repulsion that is due to the overlap of the electric double layer of different particles [27]. The most explored technique for the dispersion of nano-sized particles in a matrix is through the use of ultrasound [28–30]. In this technique, an ultrasonic source causes localized stresses that break apart clusters and thus any remaining clusters are reduced in size. Ultrasound frequencies in the range of 5 kHz to 1 MHz have been reported [2], and the effects of the ultrasound treatment duration are discussed in detail elsewhere [30].

Atomic force microscopy (AFM) and scanning electron microscopy (SEM) have been used as powerful techniques to study the morphology and phase distribution of composites containing nanoparticles [31–33]. AFM has the advantage of requiring minimum sample preparation (especially for nonconductive composites) compared to SEM and is capable of revealing fine details about the distribution

of nanoparticles. On the other hand, SEM is capable of scanning a larger area and providing more general information about the overall particle distribution. For example, Russell and Chartoff [31] used AFM and SEM to determine the morphology and phase distribution of dispersed rubber particles in a rubber-modified epoxy resin. It was reported that some nanoparticles, that were not visible in SEM images, could be observed using AFM.

The objective of the present study is to map the dispersion of Al particles embedded within a HTPB matrix. The effects of Al particle size (μAl vs. nAl), nAl surface treatment (simple air passivation, coating by catechol or stearic acid), and manufacturing procedures (mechanical mixing with and without ultrasonic vibration and the use of different dispersing agents) on fuel powder dispersion were investigated with SEM, AFM, and Raman spectroscopy.

2 Fuel Formulations and Manufacturing

The fuel formulations used in this investigation are based on a HTPB binder that was composed of HTPB (79.2 mass %), dioctyl adipate (DOA, 13.1 mass %), and isophorone diisocyanate (IPDI, 7.7 mass %). The binder could be either the commercial Poly bd® HTPB or MACH I® Propulsion Grade™ HTPB. The curing process was catalyzed by the excess addition of dibutyltin diacetate (0.05 % of the HTPB + IPDI mass), and the curing ratio ($-NCO/-OH$) of the binder formulation was 1.04. The Al powder content of all the fuel formulations was 10 mass %. Four types of Al powders with different particle size, active metal content, and surface characteristics were considered in this study. The C_{Al} of each powder was evaluated by a volumetric technique based on the $Al + H_2O$ reaction [16]. Spherically shaped μAl powder was considered as a reference for the analysis, and it had a mean mass diameter (D_{43}) of 19.8 μm (evaluated by laser diffraction) with a C_{Al} of (99.5 ± 0.4) mass %. Three variants of air-passivated nAl were investigated. The nano-sized powders were produced by APT LLC (Tomsk, Russia) exploiting the electrical explosion of wires (EEW) [16]. The smallest of the tested nAl was an air-passivated Al exploded (ALEX) powder. The nominal particle size of this powder was 50 nm (ALEX50). The S_{sp} of the ALEX50 was 19.0 m²/g (as evaluated by nitrogen adsorption isotherm), while its C_{Al} was (91 ± 1) mass % [34]. Based on the S_{sp} and a density of 2.70 g/cm³, the average particle diameter of spherical, nonporous ALEX50 would be 116 nm. The second nAl was an air-passivated ALEX with a nominal particle size of 100 nm, coated with 0.2 mass % catechol (ALEX100) [24]. The average diameter of the ALEX100 was estimated to be 210 nm based on the S_{sp} from nitrogen adsorption (10.7 m²/g), while its C_{Al} was (88.0 ± 0.5) mass %. The last nAl powder was the same air-passivated ALEX used for the ALEX100 but was instead coated with stearic acid (L-ALEX). The coating fraction was 5–10 % of the total nAl powder mass [16] and the C_{Al} was (82.8 ± 2.1) mass %.

The tested fuel formulations were manufactured by different techniques. An overview of the fuel compositions and manufacturing techniques used to create the specimens is presented in Table 1. The implemented dispersion procedures differ

Table 1 Overview of the prepared fuel formulations. Specimens A–D were manufactured with HTPB-R45HTLO, while Specimens E–H were based on MACH I® Propulsion Grade™ HTPB-45M

	Fuel composition	Notes
Specimen A	HTPB + μAl	Mechanical mixing only
Specimen B	HTPB + ALEX100	Mechanical mixing only
Specimen C	HTPB + ALEX100	Mechanical mixing with ultrasonic vibration during mixing (24 kHz) and before casting (38 kHz)
Specimen D	HTPB + L-ALEX	Mechanical mixing with ultrasonic vibration during mixing (24 kHz) and before casting (38 kHz)
Specimen E	HTPB + ALEX50	Mechanical mixing only
Specimen F	HTPB + ALEX50 + acid dispersing agent	Mechanical mixing only
Specimen G	HTPB + ALEX50 + amine dispersing agent	Mechanical mixing only
Specimen H	HTPB + ALEX50 +base dispersing agent	Mechanical mixing only

mainly by the application of a dispersion protocol based on ultrasonic vibration or by the use of dispersants. "Specimen A," "Specimen B," and "Specimen E" were manufactured without implementing any dispersion procedure and were considered as reference formulations for the analyses. In the nAl dispersion procedure implemented by ultrasound vibration ("Specimen C" and "Specimen D"), the fuel formulation was sonicated during mechanical mixing with a frequency of 24 kHz. At the end of the mixing process, the composition was sonicated with a frequency of 38 kHz. In the formulations exploiting dispersing agents ("Specimen E," "Specimen F," "Specimen G," and "Specimen H"), a two-step mechanical mixing procedure (without ultrasound vibration) was used. In the first step, the HTPB was mixed with the dispersing agent and ALEX50 using a Waring Laboratory Science blender, while the mixture was heated to approximately 40 °C. In the second step, the curing agent, DOA, and IPDI were added and mixing was performed without heating. The dispersing agents used in "Specimen F" and "Specimen G" were characterized by having acid and amine anchoring groups, respectively, while the dispersing agent used in "Specimen H" was a base with 60 % active content in mineral oil. The dispersant content in each fuel formulation was 4 % of the overall mass.

3 Experimental Setup

The shape, core-shell structure, and clustering of the as-prepared nAl powders (ALEX50, ALEX100, and L-ALEX) were studied by SEM (JEOL JSM-7600F) and TEM (JEOL JEM-2010). After the fuel formulations were prepared, the specimens were cut with a sharp blade, and segments from the cross section near the center

of the specimens were used to investigate the morphology of the Al powders within the HTPB binder. Initially, a Hitachi S-4800 m FE SEM in secondary electron mode was used to study the clustering and dispersion of the Al powders. An accelerating voltage of ≤ 1.0 kV was used for the SEM experiments to avoid charge buildup. Although the SEM images provided valuable information about the overall dispersion of the powders, fine details about the nature of the clusters were not visible. Therefore, a commercial Bruker AFM was used to more closely examine the clustering of the Al powders. The AFM experiments were performed in tapping mode where phase-contrast images were obtained over different scan sizes. The differences between the adhesion forces and viscoelastic properties of the Al powder and HTPB binder led to a change in phase lag between the AFM cantilever movement and the external force acting on it and thus created a contrast in the recorded AFM images [35]. In addition to SEM and AFM, Raman spectroscopy experiments were also performed on the specimens using a commercial confocal microscope. A frequency doubled Nd:YAG laser with a wavelength of 532 nm was used as the excitation source. A 100x/0.9NA microscope objective was used to focus the excitation light onto the specimens with a spot size of roughly 0.5 μm. The same objective then collected the scattered light and focused it onto a 100 μm optical fiber that acted as a confocal pinhole. A piezoelectrically driven stage allowed spatial scans to be performed by scanning the laser spot across the surface of the specimen.

4 Experimental Results and Discussion

Figures 1 and 2 present the TEM and SEM images, respectively, of the investigated ALEX powders. Both transmission and scanning micrographs show spherically shaped particles. The TEM image of the ALEX100 shows the double-shell structure of the particles where the Al core is surrounded first by an alumina layer and then by an outer catechol coating. A similar double-shell structure can also be observed in the TEM image of L-ALEX powder shown in Fig. 3. The clustering behavior of the particles can be observed for all of the tested nAl (Figs. 1, 2, and 3).

"Specimen A" was prepared using μAl powder and was mechanically mixed without ultrasonic vibration. Figure 4a, b shows typical SEM images of this

Fig. 1 Air-passivated ALEX50: TEM image showing spherical and clustered particles [34]

86 nm
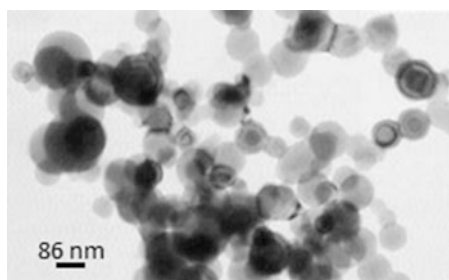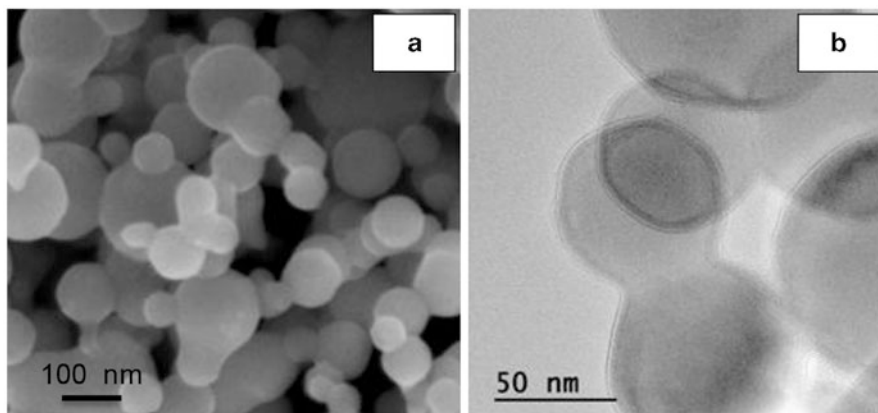
Fig. 2 Air-passivated, catechol-coated ALEX100: (**a**) SEM and (**b**) TEM images. Note the double-shell (Al_2O_3 + catechol) structure in (**b**)

Fig. 3 Stearic acid coated, air-passivated L-ALEX: TEM image showing (*1*) the Al_2O_3 shell and (*2*) the coating layer
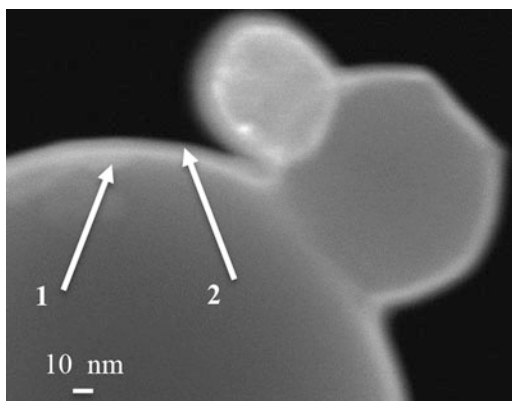
specimen at different magnifications. Most of the μAl particles had diameters in the range of 6–14 μm; however, particles as large as 35 μm were also observed. Overall, the μAl particles were found to be highly dispersed and exhibited little to no clustering. Figure 4c shows a typical phase-contrast AFM image of "Specimen A" over a scan area of 40×40 μm. Circular features with diameters of about 9 μm were observed in the AFM images, which is consistent with the shape and size of the μAl particles shown in Fig. 4a. This indicates that phase-contrast AFM is sensitive to detecting the presence of Al particles and distinguishing them from the HTPB binder, which allows for the measurement of the particle size.

There were a number of Raman modes observed between 250 and 3500 cm^{-1} from the HTPB as shown in Fig. 4d. Spatial maps of the Raman response were created for each area scan using the integrated intensity of the 1660 cm^{-1} peak, related to C=O vibrations, since it was the most intense and isolated single peak. Since Al is not Raman active, it was expected that the presence of Al particles on
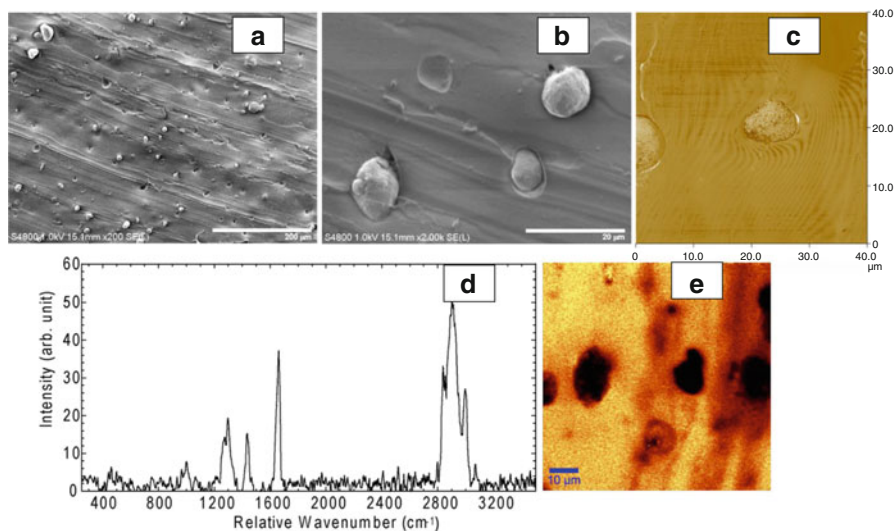
Fig. 4 The morphology and distribution of μAl particles in "Specimen A" obtained by SEM (**a**, **b**) and AFM (**c**). Along with a Raman spectrum of HTPB (**d**) and a map of the spatial variation in the intensity of the 1660 cm^{-1} Raman peak for "Specimen A" (**e**)

or near the surface would attenuate the 1660 cm^{-1} peak originating from C=O in the HTPB binder. A typical Raman scan of "Specimen A" over a scan area of 80×80 μm is shown in Fig. 4e and is the result of 102,400 individually collected spectra. Distinct circular regions with diameters of 8–10 μm were observed where there was no evidence of a 1660 cm^{-1} peak. A comparison between Fig. 4b, c, e confirms that these circular features observed in the Raman images are the μAl particles. Smaller regions were also observed where the 1660 cm^{-1} peak was still observable, but its intensity was reduced compared to the rest of the specimen. Two potential sources for these features include the presence of an Al particle just below the surface or geometric effects from impressions left on the surface from where a particle resided prior to cutting the specimen.

"Specimen B," "Specimen C," and "Specimen D" were prepared using nAl particles (ALEX100). Figure 5 shows typical SEM images obtained from these specimens at two different magnifications. All SEM images show the presence of circular features on the surface which are either individual nAl particles or clusters of multiple nAl particles. The overall dispersion of the particles can also be observed from the SEM images. "Specimen B" appears to have not only more clusters of nAl particles but also larger clusters than either of the other two specimens containing nAl. This suggests that the ultrasonic vibration used in "Specimen C" and "Specimen D" helps to reduce the occurrence of clustering. Comparing "Specimen C" containing ALEX with "Specimen D" containing L-ALEX, it appears that the coating does not have a significant effect on the clustering of nAl particles in the final fuel.
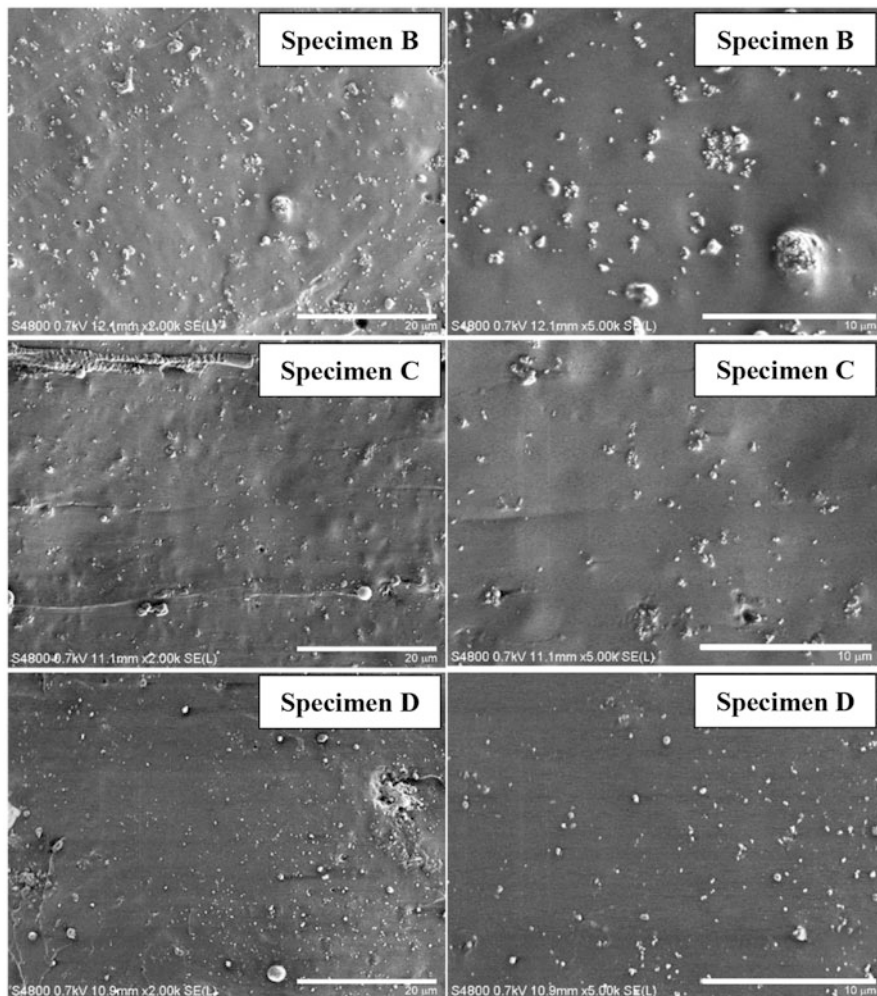
Fig. 5 Typical SEM images of the specimens containing ALEX100 nAl particles

In order to study the details and nature of the clustering of the nAl in HTPB, the surfaces of "Specimens B," "Specimen C," and "Specimen D" were examined by AFM using two different scan sizes. Typical phase-contrast images over a scan area of 10×10 μm are shown in Fig. 6. In addition to individual nAl particles, multiple clusters with dimensions smaller than 5 μm are observed on the surface of all the specimens. A comparison between the AFM images shown in Fig. 6 shows the presence of larger clusters on the surface of "Specimen B" compared to the other two. This observation is in agreement with our findings from the SEM images.

A series of AFM scans over smaller scan areas (2×2 μm) were also performed with the purpose of investigating the interactions between the individual nAl

Fig. 6 Typical AFM phase-contrast images of the specimens containing ALEX100 nAl particles over a scan area of $10 \times 10 \, \mu m$

particles. The obtained phase-contrast images are shown in Fig. 7. A comparison between these images reveals a slightly different nature of the clusters, where individual particles in the clusters of "Specimen B" exhibit a much tighter spacing compared to those in "Specimen C" and "Specimen D" which were created with the assistance of ultrasonic vibration. The AFM images of clusters in the specimens fabricated with ultrasonic vibration show a higher dispersion than those fabricated without ultrasonic vibration. This further supports the notion that ultrasonic vibration helps to diminish the tendency of nAl particles to cluster.

Raman spectroscopy scans of the specimens containing nAl did not exhibit any regions with noticeable reductions in the 1660 cm^{-1} peak intensity. The observed Raman response for "Specimen B," "Specimen C," and "Specimen D" (not shown here) is consistent with the limited spatial resolution of the technique. The focused
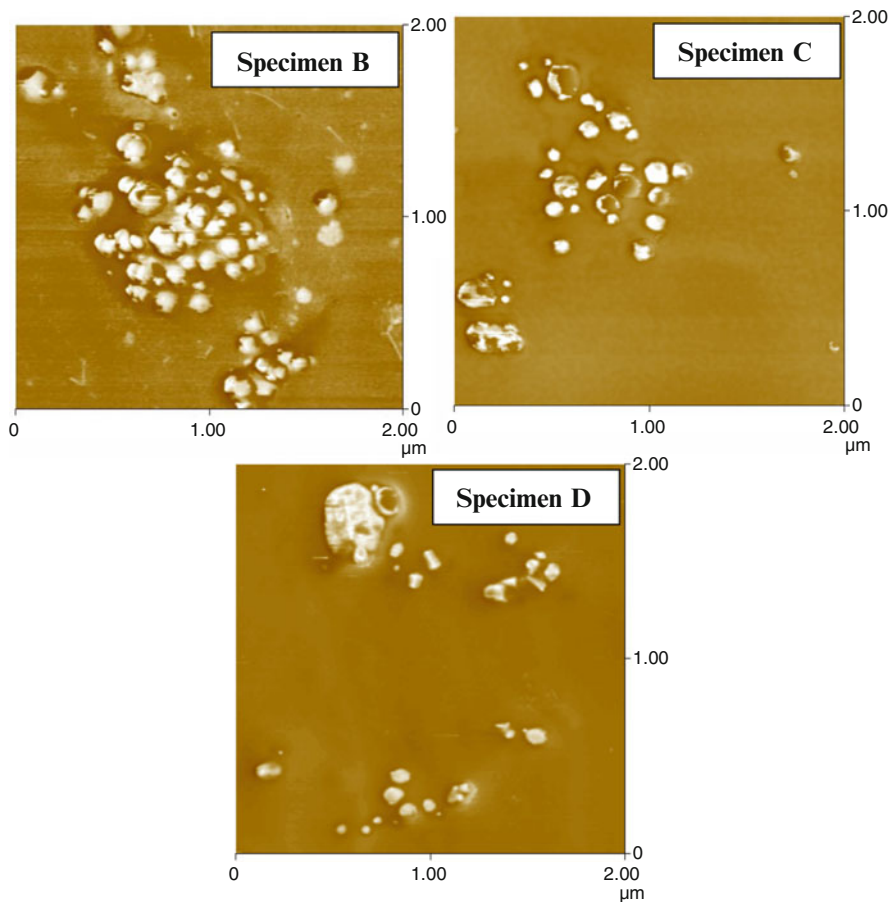
Fig. 7 Typical AFM phase-contrast images of the specimens containing ALEX100 nAl particles over a scan area of 2×2 μm

laser spot size was approximately 0.5 μm making Raman spectroscopy better suited for mapping μAl rather than nAl.

To investigate the effect of different chemical dispersing agents on the distribution of nAl particles (ALEX50) within HTPB, "Specimen E," "Specimen F," "Specimen G," and "Specimen H" were created using only mechanical mixing. "Specimen E" was a reference specimen prepared using no dispersing agent. "Specimen F," "Specimen G," and "Specimen H" were prepared using dispersing agents that were characterized as having an acid anchoring group, an amine anchoring group, or a base mixed with mineral oil, respectively. AFM scans were performed over 10×10 μm areas and 2×2 μm areas, and the results are shown in Figs. 8 and 9, respectively. As expected for nAl particles without a dispersing agent, "Specimen E" exhibited a considerable amount of clustering, and the size
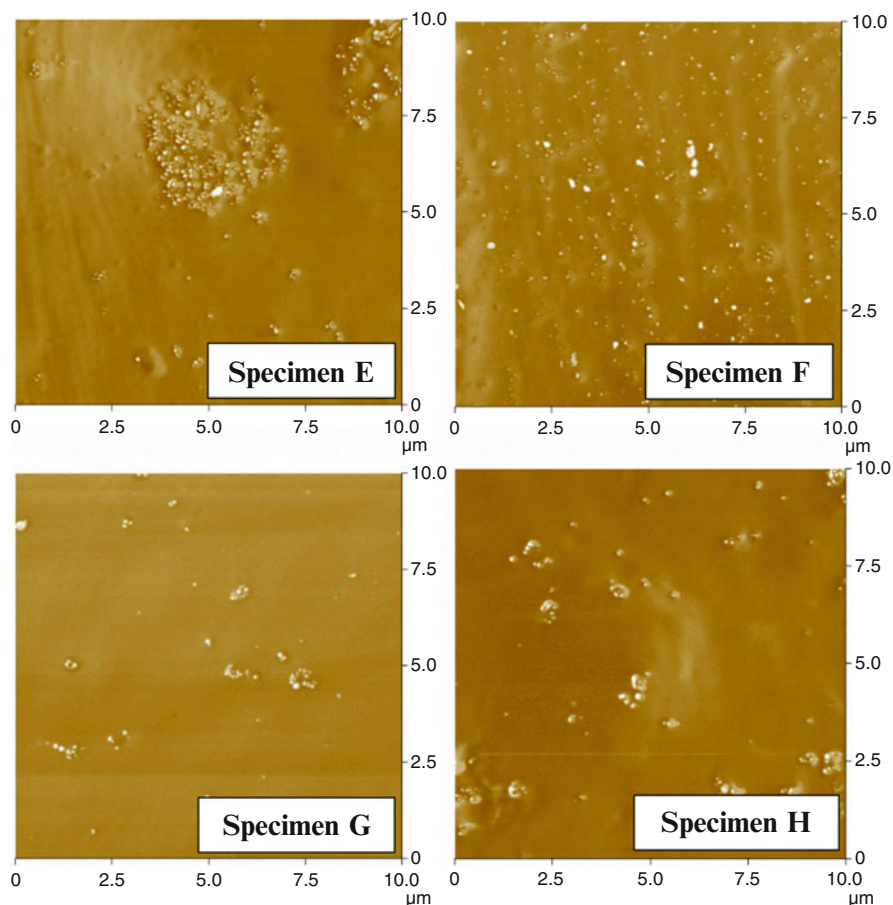
Fig. 8 Typical AFM phase-contrast images of the specimens containing ALEX50 nAl particles over a scan area of $10 \times 10\ \mu m$

of the clusters that were present was frequently as large as 5 μm in diameter. All of the specimens with a dispersing agent showed far less clustering than that of the reference specimen. The dispersant with an acid anchoring group resulted in the formation of very few clusters and those that were present were very small, consisting of only a few individual particles. The dispersing agents containing amine anchoring groups or a base in mineral oil both had similar amounts and sizes of clusters, with the majority of clusters being smaller than 1 μm in diameter. Both of these dispersing agents led to better dispersion than was achieved in the reference specimen but not as good as that with dispersing agent containing acid anchoring groups.

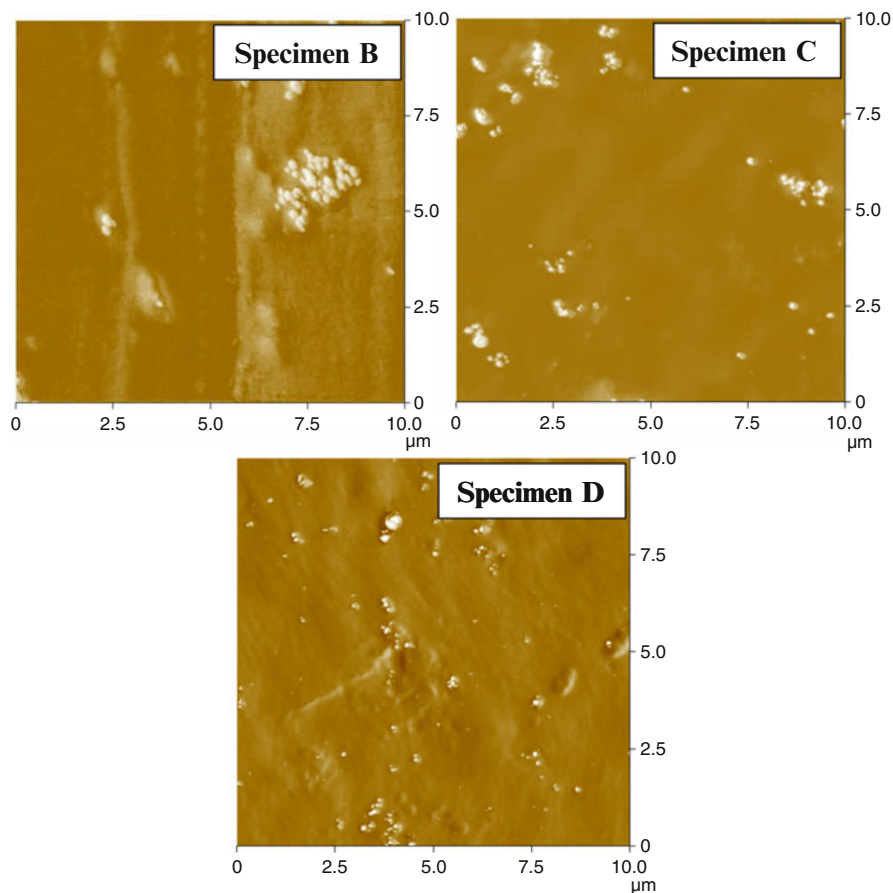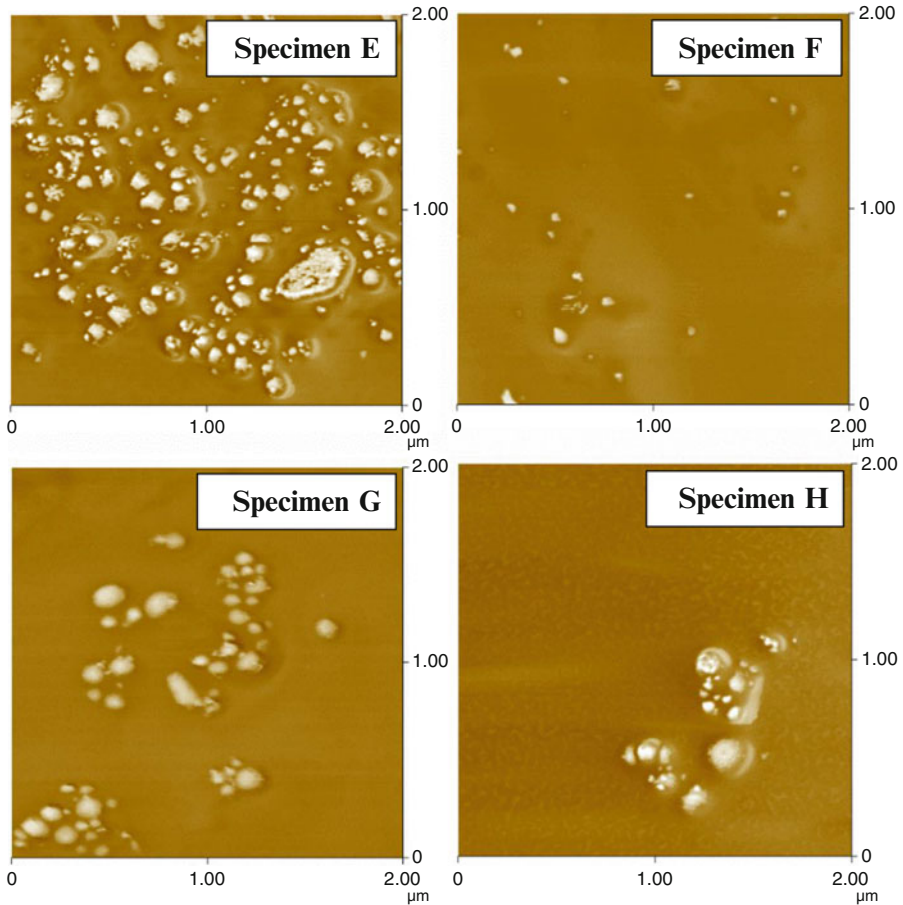**Fig. 9** Typical AFM phase-contrast images of the specimens containing ALEX50 nAl particles over a scan area of 2×2 µm

5 Conclusions and Future Developments

The morphology and distribution of Al particles within a HTPB binder were studied by SEM, AFM, and Raman spectroscopy. Although only mechanical mixing was used for the preparation of the specimen containing µAl powder, "Specimen A," the results revealed little to no clustering. This is mainly due to the low tendency of µAl particles to cluster as a result of their relatively small specific surface area. Furthermore, a comparison between the AFM images, SEM micrographs, and Raman spectroscopy results for "Specimen A" showed the ability of phase-contrast AFM imaging to distinguish the Al particles from the HTPB binder.

The effect of an ultrasonic vibration-assisted fabrication procedure on the formation of clusters was studied through a comparison between "Specimen B" and "Specimen C" both of which contained air-passivated, catechol-coated nAl powders (ALEX100). Both the SEM and AFM images revealed a more uniform dispersion of nAl particles, the formation of smaller clusters, and a higher occurrence of individual particles when ultrasound was used in conjunction with mechanical mixing. The results show the efficiency of the ultrasonic-assisted mechanical mixing procedure in mitigating the clustering of nAl particles. To study the effect of coated nAl particles on clustering, "Specimen D" was prepared with ultrasonic vibration-assisted mechanical mixing of air-passivated nAl particles that were coated with stearic acid (L-ALEX). The SEM and AFM results showed the presence of clusters with similar dimensions for both the ALEX and L-ALEX. This indicates that the coating has a minimum influence on the dispersion of nAl particles.

The effect of three different dispersing agents on the dispersion of nAl powders (ALEX50) was studied in specimens that were created with only high-shear mechanical mixing. As a reference, "Specimen E" did not contain a dispersing agent and was found to have many clusters that were often as large as 5 μm in diameter. "Specimen F," "Specimen G," and "Specimen H" used dispersing agents that had an acid anchoring group, an amine anchoring group, or a base mixed with mineral oil, respectively. The dispersing agent with the amine anchoring group and the dispersing agent with the base in mineral oil resulted in similar dispersions of the nAl, which exhibited a much better dispersion than the reference specimen. Fewer clusters were observed and the clusters that were present were typically less than 1 μm in diameter. The dispersing agent with the acid anchoring group led to the best overall dispersion with little to no clustering. The few clusters that were observed typically consisted of only a few individual particles.

Overall, our findings on the specimens containing nAl particles showed that AFM phase-contrast imaging is a technique capable of creating dispersion maps for metal nanoparticles used in solid fuel formulations.

Future developments of the present work could include further characterizing nAl-loaded fuels with AFM and SEM. Additional measurements and further analysis of the size of the resulting clusters would allow for a quantitative measure of the particle dispersion. This information, in conjunction with the ballistic response of the same solid fuel formulations obtained from combustion testing, would open the door for developing a better understanding of the effects that specific dispersing agents and manufacturing procedures have on the combustion process. Such an understanding could have profound impacts in identifying how to effectively use energetic nano-sized materials in propulsion systems.

References

1. DeLuca LT, Maggi F, Dossi S, Fassina M, Paravan C, Sossi A (2016) Prospects of aluminum modifications as energetic fuels in chemical rocket propulsion. In: DeLuca LT, Shimada T, Sinditskii VP, Calabro M (eds) Chemical rocket propulsion: a comprehensive survey of energetic materials. Springer, Cham

2. DeLuca LT, Galfetti L, Maggi F, Colombo G, Paravan C, Reina, A, Dossi, S, Fassina, M, Sossi A (2014) Chapter 12: Characterization and combustion of aluminum nanopowders in energetic systems. In: Gromov AA, Teipel U (eds) Metal nanopowders: production, characterization, and energetic applications, Wiley, Weinheim, Germany, pp 301–400

3. Meda L, Marra G, Galfetti L, Severini F, DeLuca LT (2007) Nano-aluminum as energetic material for rocket propellants. Mater Sci Eng C 27(5):1393–1396

4. Liu H, Ye H (2008) Synthesis and property of poly (trimethylolpropane triacrylate)/Al nanocomposite particle by in situ solution polymerization. Appl Surf Sci 254(15):4432–4438

5. Sippel TR (2009) Characterization of nanoscale aluminum and ice solid propellants, Doctoral dissertation, Purdue University

6. Sippel TR, Son SF, Groven LJ (2014) Aluminum agglomeration reduction in a composite propellant using tailored Al/PTFE particles. Combust Flame 161(1):311–321

7. Babuk VA, Dolotkazin I, Gamsov A, Glebov A, DeLuca LT, Galfetti L (2009) Nanoaluminum as a solid propellant fuel. J Propuls Power 25(2):482–489. doi:10.2514/1.36841

8. Sippel TR, Son SF, Groven LJ, Zhang S, Dreizin EL (2015) Exploring mechanisms for agglomerate reduction in composite solid propellants with polyethylene inclusion modified aluminum. Combust Flame 162(3):846–854

9. Galfetti L, DeLuca LT, Severini F, Colombo G, Meda L, Marra G (2007) Pre and post-burning analysis of nano-aluminized solid rocket propellants. Aerosp Sci Technol 11(1):26–32

10. DeLuca LT, Galfetti L, Colombo G, Maggi F, Bandera A, Babuk VA, Sinditskii VP (2010) Microstructure effects in aluminized solid rocket propellants. J Propuls Power 26(4):724–732

11. Risha GA, Evans BJ, Boyer E, Kuo KK (2007) Metals, energetic additives and special binders used in solid fuels for hybrid rockets. In: Chiaverini MJ, Kuo KK (eds) Fundamentals of hybrid rocket combustion and propulsion, AIAA Progress in Aeronautics and Astronautics, vol. 218, American Institute of Aeronautic & Astronautics, Reston, VA, pp 413–456

12. Paravan C (2012) Ballistics of innovative solid fuel formulations for hybrid rocket propulsion, Doctoral dissertation, Science and Technology Dept., Politecnico di Milano

13. Dokhan A, Price EW, Sigman RK, Seitzman JM (2001) The effects of Al particle size on the burning rate and residual oxide in aluminized propellants, AIAA Paper 2001-3581, doi:10.2514/6.2001-3581

14. Fanton L, Paravan C, DeLuca LT (2012) Testing and modeling fuel regression rate in a miniature hybrid burner. Int J Aerosp Eng 2012:673838, doi:10.1155/2012/673838

15. Sossi A, Duranti E, Manzoni M, Paravan C, DeLuca LT, Vorozhtsov AB, Lerner MI, Rodkevich NG, Gromov AA, Savin N (2013) Combustion of HTPB-based solid fuels loaded with coated nanoaluminum. Combust Sci Technol 185(1):17–36. doi:10.1080/00102202.2012.707261

16. Fedorov SG, Guseinov SL, Storozhenko PA (2010) Nanodispersed metal powders in high-energy condensed systems. Nanotechnol Russ 5(9–10):565–582

17. Sossi A, Duranti E, Paravan C, DeLuca LT, Vorozhtsov AB, Gromov AA, Pautova YI, Lerner MI, Rodkevich NG (2013) Non-isothermal oxidation of aluminum nanopowders coated by hydrocarbons and fluorohydrocarbons. Appl Surf Sci 271:337–343

18. Gromov AA, Il'in AP, Föerter -Barth U, Teipel U (2006) Effect of the passivating coating type, particle size, and storage time on oxidation and nitridation of aluminum powders. Combust Explos Shock Waves 42(2):177–184. doi:10.1007/s10573-006-0036-4

19. Mary B, Dubois C, Carreau PJ, Brousseau P (2006) Rheological properties of suspensions of polyethylene-coated aluminum nanoparticles. Rheol Acta 45(5):561–573

20. Paravan C, Reina A, Frosi A, DeLuca LT (2013) Nanosized aluminum for regression rate enhancement. Proceedings of the Fifth European Conference for Aerospace Sciences (EUCASS), Munich, Germany, 01–05 Jul 13, Torus Press, Moscow, Russia. ISBN: 9788494153105

21. Mench MM, Kuo KK, Yeh CL, Lu YC (1998) Comparison of thermal behavior of regular and ultra-fine aluminum powders (Alex) made from plasma explosion process. Combust Sci Technol 135(1–6):269–292. doi:10.1080/00102209808924161

22. Napper DH (1977) Steric stabilization. J Colloid Interface Sci 58(2):390–407

23. Payne AR (1965) Effect of dispersion on the dynamic properties of filler-loaded rubbers. J Appl Polym Sci 9(6):2273–2284

24. Reina A (2013) Nano-metal fuels for hybrid and solid Propulsion, Doctoral dissertation, Science and Technology Dept., Politecnico di Milano

25. Wang Q, Xia H, Zhang C (2001) Preparation of polymer/inorganic nanoparticles composites through ultrasonic irradiation. J Appl Polym Sci 80(9):1478–1488

26. Stuyven B, Chen Q, Van de Moortel W, Lipkens H, Caerts B, Aerts A, Giebeler L, Van Eerdenbrugh B, Augustijns P, Van den Mooter G, Van Humbeeck J, Vanacken J, Moshchalkov VV, Vermant J, Martens JA (2008) Magnetic field assisted nanoparticle dispersion. Chem Commun 1:47–49. doi:10.1039/B816171B

27. Hunter RJ (1987) Foundations of colloidal science, vol 1. Oxford University Press, Oxford, pp 588–589, 129

28. Lee EC, Mielewski DF (2005) Method for producing a well-exfoliated and dispersed polymer silicate nanocomposite by ultrasonication, US Patent US 2005/0122834 A1

29. Risha GA, Evans BJ, Boyer E, Wehrman RB, Kuo KK (2003) Nano-sized aluminum- and boron-based solid-fuel characterization in a hybrid rocket engine, AIAA Paper 2003-4593

30. Gedanken A (2007) Doping nanoparticles into polymers and ceramics using ultrasound radiation. Ultrason Sonochem 14(4):418–430

31. Russell B, Chartoff R (2005) The influence of cure conditions on the morphology and phase distribution in a rubber-modified epoxy resin using scanning electron microscopy and atomic force microscopy. Polymer 46(3):785–798

32. Wetzel B, Haupert F, Zhang MQ (2003) Epoxy nanocomposites with high mechanical and tribological performance. Compos Sci Technol 63(14):2055–2067

33. Zou H, Wu S, Shen J (2008) Polymer/silica nanocomposites: preparation, characterization, properties, and applications. Chem Rev 108(9):3893–3957

34. Advanced Powder Technology LLC (2015) http://www.nanosized-powders.com. Accessed 31 Mar 2015

35. Tamayo J, Garcia R (1996) Deformation, contact time, and phase contrast in tapping mode scanning force microscopy. Langmuir 12(18):4430–4435

New Concept of Laser-Augmented Chemical Propulsion

Ruiqi Shen, Lizhi Wu, Zhao Qin, Xiaoyong Wang, and Nianbai He

Abstract The applications of laser propulsions to explore space have been discussed for long time. The laser ablation or laser plasma propulsions by high-power laser are discussed in terms of launching, orbit keeping, and attitude controlling for microsatellites and vehicles. The advantage of laser ablation propulsion is higher specific impulse than other conventional propulsions, but a lightweight and high-power laser is required. A new concept of laser-augmented chemical propulsion (LACP) is proposed to control variable thrust and to turn on/off thrust easily by a low-power laser. The principle of laser-augmented chemical propulsion is based on the solid propellant combustion under thermal radiation, in which the burning rate of solid propellant depends linearly on the radiation strength of a continuous wave (CW) laser. Some photosensitive and lower energetic propellants are used for the laser-augmented chemical thrusts, such as ammonium nitrate (AN), guanidine nitrate (GN), carbamide, and 5-aminotetrazole (5-ATZ), in which the propellants can burn under laser radiation, but flame off when turning off laser radiation. The propulsion energy comes from chemical reaction heat and laser energy. The feasibility and ballistics of laser-augmented chemical propulsion are discussed in experimental and theoretical analysis in the paper. The specific impulse and the thrust depend on the irradiation strength. The specific impulse equation $I_s \propto 1/\sqrt{\rho b A_r q}$ shows that the specific impulse will decrease with increase of radiant flux (q) and radiation sensitivity coefficient (b), but the thrust $F_{cp} \propto \sqrt{\rho b A_r q}$ will increase with the increase of radiant flux and radiation sensitivity coefficient.

1 Principle of Laser-Augmented Chemical Propulsion

The ablated gaseous products and thermal energy induced and transferred by a high-power CW laser or a pulsed laser are used in conventional laser propulsions to push small-space vehicles. The laser ablation propulsion concepts, such as the

R. Shen (✉) • L. Wu • Z. Qin • X. Wang • N. He
School of Chemical Engineering, Nanjing University of Science and Technology,
Nanjing 210094, Jiangsu, China
e-mail: rqshen@njust.edu.cn; wulizhi82@163.com; qzhao87@163.com; 549960482@qq.com;
425066037@qq.com

CW CO_2 laser propulsion for launch, the pulsed laser propulsion, and the laser-electric hybrid [1] for attitude transfer or orbit control, were reviewed as well [2]. One of the advantages of laser ablation propulsions is its high specific impulse, but the bottleneck technology is in light, miniaturized, and high-power laser. If a ground-based laser is used to launch vehicles, the problems of size, weight, and power for laser system are easy to overcome, but a small-size, lightweight, and high-power laser is required in space-based laser propulsion and onboard laser propulsion. Laser-augmented chemical propulsion (LACP) is a new concept to overcome the disadvantage of laser ablation propulsion. LACP takes the principle of laser-controlled combustion, not the principle of laser ablation, whose propulsion energies come from chemical energy and laser energy, so that LACP does not require a high-power laser and can easily vary thrust. The fundamentals of the concept, the burning of propellant under external irradiation [3], were researched by a CW CO_2 laser as long as 40 years ago [4–7], and it was found that the burning rate of double-base (DB) propellants depends on radiant flux in a piecewise linear function. The dependence between burning rate and radiant flux was analyzed theoretically well on the base of Fourier equation [8, 9]. In the early, the researches on the burning of solid propellants under external irradiation were focused on a ignition and unstable combustion, but the results can be applied to variable thrust and turn on/off thrust of rocket motor by laser controlling the combustion of propellant.

The burning of propellants is effected by radiation of laser; their burning rate depends linearly on the radiant flux, shown in Figs. 1 and 2. The effects of irradiation are in a two broken linear relationships between burning rate and radiant flux, a piecewise function for double-base propellants, but only a linear dependence for HTPB.

Fig. 1 Burning rate of propellants 1040 and 1041 at 1.49 MPa. The experimental points [10] are approximated by a piecewise function

$$1 - u = 3.91 + 2.055\, q$$
$$2 - u = 4.92 + 1.308\, q$$
$$3 - u = 1.98 + 2.037\, q$$
$$4 - u = 3.06 + 1.134\, q$$
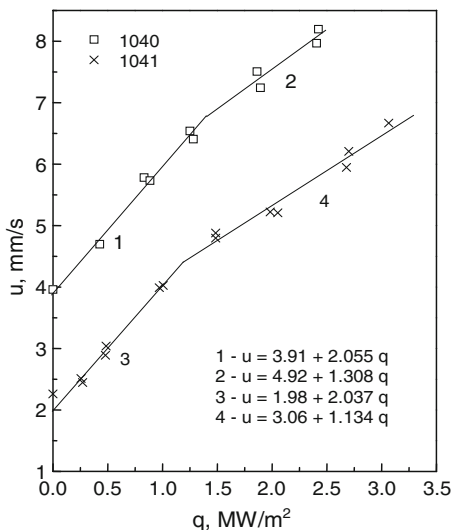
Fig. 2 Regression rate of
HTPB at a slight positive
pressure over 0.1 MPa [11]
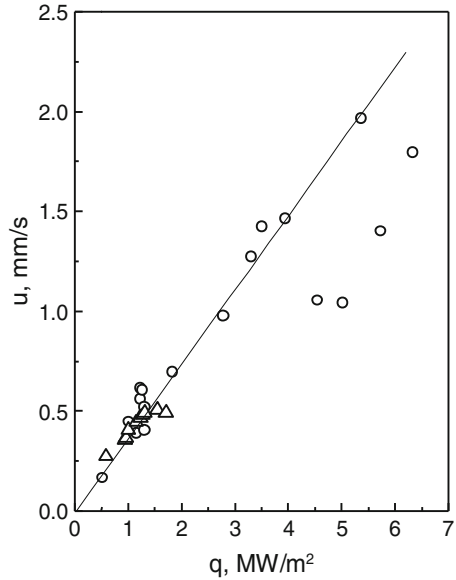
The dependence of burning rate on radiant flux is shown in Eq. 1. The function
consists of the burning rate under radiation-free and the burning rate under radiation.

$$u = a + bq \tag{1}$$

Where u is the burning rate of propellant (mm/s), a is the burning rate under
radiation-free (mm/s), b is the radiation sensitivity coefficient ((mm/s) / (MW/m^2)),
and q is the radiant flux (MW/m^2).

The function $u = u(a, b, q)$ is approximated by the straight line and is accordant
with the experimental results very well. The results are easy to treat by using a
simple expression, a simplified solution of the Fourier equation,

$$m\left[c\left(T_s - T_0\right) - Q_s\right] = q_g + q \tag{2}$$

or

$$u = a + bq \tag{3}$$

$$a = \frac{q_g}{\rho\left[c\left(T_s - T_0\right) - Q_s\right]} \text{ and } b = \frac{1}{\rho\left[c\left(T_s - T_0\right) - Q_s\right]} \tag{4}$$

$$q_g = \frac{a}{b} \tag{5}$$

Table 1 Factors of piecewise function for propellants

Propellant	Line 1		Line 2		Pressure (MPa)	Ref.
	a	b	a	b		
HTPB	0	0.34	–	–	0.1	[11]
RDX	0.38	0.63	–	–	0.1	[12], [13]
HMX	0.40	1.20	0.65	0.46	0.1	[14]
N5 DB	0.56	3.35	–	–	0.1	[15]
1040 DB	3.91	2.06	4.92	1.31	1.5	[10]
1041 DB	1.98	2.04	3.06	1.13	1.5	[10]
SQ-2 DB	1.11	0.98	2.45	0.19	0.1	[16]
AP/HTPB (50/50)	0.31	0.75	–	–	0.1	[17]
	0.42	0.97	–	–	0.3	[17]
	0.32	1.02	–	–	0.5	[17]

Units of parameters: a (mm/s), b (mm/s/MW/m^2)

Table 2 Properties of rich nitrogen compounds

Compound	Oxygen balance (%)	Nitrogen content (%)	Combustion heat (kJ/kg)	Explosion heat (kJ/kg)	$I_{s,vac}$ (s)	T_f (K)
AN	+20.0	35	−2631.25	1601	185	1243
GN	−26.2	46	−7179.70	2709	248	1933
Carbamide	−80.0	47	−10,519.15	None	–	–
5-ATZ	−30.7	54	−8493.56	3724	253	1297

Where m is the mass burning rate ($m = \rho u$), c is the mean specific heat in the temperature region of T_0 to T_s, q is the external radiant flux, q_g is the flux of heat in the condensed phase at the expense of gas phase reactions, T_s is the surface temperature, T_0 is the initial temperature, and Q_s is the reaction heat of the condensed phase.

The experimental factors of piecewise function for different propellants are listed in Table 1. The higher radiation sensitivity coefficient is beneficial for LACP.

The clear combustion products are required for laser propulsion. The possible compounds of LACP propellant are nitrogen-enriched compounds, such as ammonium nitrate (AN), guanidine nitrate (GN), carbamide, and 5-aminotetrazole (5-ATZ), to protect the laser window installed on the laser-augmented chemical propulsion motor (LACPM). Their molecular structures and properties are shown in Table 2. Vacuum theoretic specific impulses ($I_{s, vac}$) and adiabatic flame temperatures (T_f) were calculated by NASA-CEA code at $A_e/A_t = 40$ and 0.5 MPa chamber pressure.

AN

GN
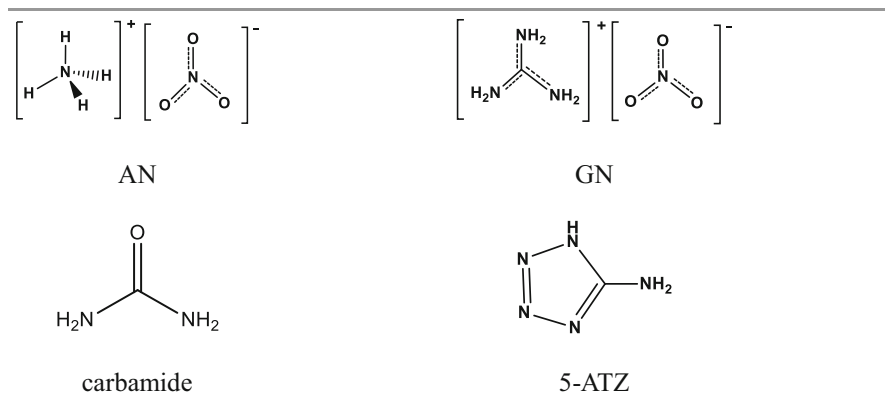
carbamide

5-ATZ

The possible propellant formula is AN/Fuel + carbon (1–2 %), in which carbamide, 5-ATZ, or GN can be selected as fuel and carbon is a radiation absorber.

2 Ballistics of Laser-Augmented Chemical Propulsion Motor

There are many modes of laser-augmented chemical propulsion in LACPM, as shown in Fig. 3. Two arrows show the directions of laser beam and gasification flow in LACPM, for example, a laser beam radiates to the surface of propellant and the gaseous products by gasification or burning will flow out from the nozzle in the vertical direction of laser beam, shown in Fig. 3b. The structure of LACPM in mode (b) is shown in Fig. 4 and the experimental set of mode (b) LACPM is shown in Fig. 5.

The ballistics of LACPM are similar to the conventional solid rocket motor (SRM), except that the burning rate or regression rate of propellant depends on the radiant flux of the laser.
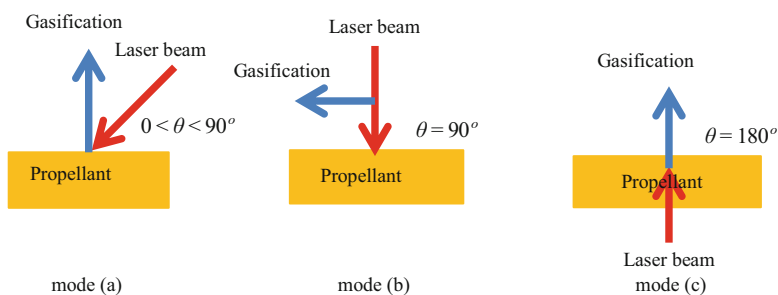
Fig. 3 Ballistic modes of laser-augmented chemical propulsion in LACPM

Fig. 4 Schematic diagram of LACPM structure in mode (b)
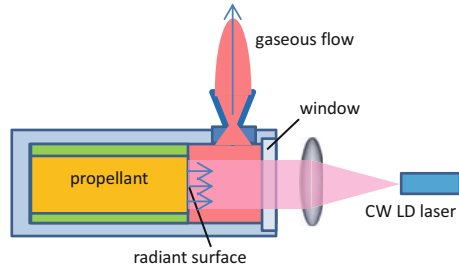
Fig. 5 Experimental set of LACPM in mode (b)
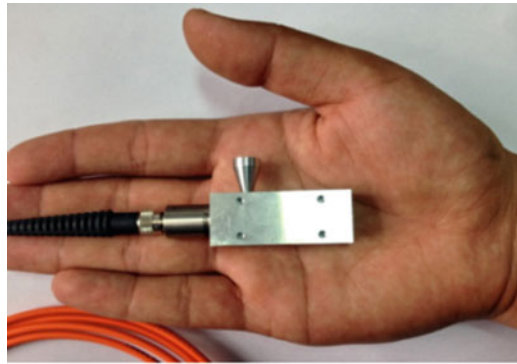
4.5cm X 2cm X 2cm

The mass rate of gaseous products and its energy in burning or gasification can be calculated in Eqs. 6 and 7, respectively:

$$\dot{m}_g = \rho \left(a + bq \right) A_r \tag{6}$$

$$H_g = \rho \left(a + bq \right) A_r q_c + A_r q \tag{7}$$

where $\dot{m}_g$ is the mass rate at the radiant surface by radiation, A_r is the area of radiated surface, H_g is the sum of energy from chemical reaction and radiation, q is the radiant flux or the intensity of radiation, and q_c is the heat of chemical reaction.

On the basis of classical interior ballistics of SRM, the thrust and theoretic specific impulse can be calculated in Eqs. 8 and 9, respectively:

$$F_{cp} = I_s \dot{m}_g \text{ or } F_{cp} = I_s \rho A_r \left(a + bq \right) \tag{8}$$

$$I_s = \left[\left(\frac{2k}{k-1} \right) \left(R^0 / \dot{m}_g \right) T_c \left(1 - \left(\frac{P_e}{P_c} \right)^{\frac{k-1}{k}} \right) \right]^{0.5} \tag{9}$$

$$T_c = \frac{H_g}{\bar{c} \dot{m}_g} + T_0 \tag{10}$$

where p_c is the pressure of chamber, p_e is the environment pressure, T_c is the temperature of chamber, and R^0 is the universal gas constant. $\overline{c}$ is the mean specific heat in the temperature region of T_0 to T_c.

LACPM is usually applied in a space environment, so that the temperature of chamber depends on the radiant flux and the environment pressure is about zero, or $p_e = 0$. If propellants do not burn without irradiation, then $a = 0$. The calculation of the thrust and the specific impulse are simplified in Eqs. 11 and 12 at $p_c \gg 0$.

$$F_{cp} = I_s \rho b A_r q \tag{11}$$

$$I_s = \left[\left(\tfrac{2k}{k-1} \right) \left(R^0 / \dot{m}_g \right) T_c \right]^{0.5} \text{ or } I_s = \left[\left(\tfrac{2k}{k-1} \right) \tfrac{R^0 T_c}{\rho b A_r q} \right]^{0.5} \tag{12}$$

$$T_c = \left(\frac{q_c}{\overline{c}} + \frac{1}{\overline{c}\rho b} + T_0 \right) \tag{13}$$

3 Conclusion

The thrust and the specific impulse of LACPM depend on the radiant flux and the radiation sensitivity coefficient. The specific impulse equation $I_s \propto 1/\sqrt{\rho b A_r q}$ shows that the specific impulse will decrease with increase of radiant flux and radiation sensitivity coefficient, but the thrust $F_{cp} \propto \sqrt{\rho b A_r q}$ depends on the increase of radiant flux and radiation sensitivity.

The high radiation sensitivity coefficient (b) will let specific impulse decrease, but increase thrust. The higher specific impulse is pursued for rocket motor and propellant, but the controlling ability (turn on/turn off) of thrust is more important than the efficiency for attitude and orbit control, so the high radiation sensitivity coefficient is required for LACPM.

The clear propellants or fuels and correct optical design are required for laser propulsion to prevent fouling of the window. Nitrogen-rich compounds will be selected as the component of propellant, in which AN and 5-ATZ are useful components. Mode (a) and mode (c) may be good designs, but their structures are more complex than mode (b).

References

1. Horisawa H, Shinohara T, Tei K (2010) Development of compact high-power laser system for laser-electric hybrid propulsion system. 46th AIAA/ASME/SAE/ASEE joint propulsion conference and exhibit, 25–18 July 2010, Nashville: AIAA 2010-6937
2. Phipps C, Birkan M, Bohn W (2010) Review: laser-ablation propulsion. J Propuls Power 26(4):610–637

3. Zarko VE, Simonenko VN, Kiskin AB (1992) Study of solid propellant combustion under external radiation. Def Sci J 42(3):183–189
4. Kondrikov BN, Summerfield M, Ohlemiller T (1970) Ignition and gasification of a double-base propellant induced by CO_2 laser radiation. In: Thirteenth international symposium on combustion, Salt Lake City, 23–29 Aug
5. Kondrikov BN, Ohlemiller T, Summerfield M (1974) Ignition and gasification of double-base propellant subjected to radiation of CO_2 laser. Voprosy teorii vzryvchatykh vestchestv (Problems of theory of explosives). Proc Mendeleev Inst Chem Technol Moscow 83:67–78
6. DeLuca LT, Caveny LH, Ohlemiller TJ, Summerfield M (1974) Radiative ignition of double-base propellants: I. Some formulation effects. AIAA J 14(7):940–946
7. DeLuca LT, Caveny LH, Ohlemiller TJ, Summerfield M (1976) Radiative ignition of double-base propellants: II. Pre-ignition events and source effects. AIAA J 14(81976):1111–1117
8. Kondrikov BN, DeLuca LT, Cristoforetti S (2000) Induced gasification of solid propellants under thermal radiation. Space solid propulsion conference, Rome, 21–24 Nov
9. Shen R, Kondrikov BN (2005) Thermophysical and chemical processes of burning of double-base solid propellants under external irradiation. Propell Explos Pyrot 30(4):256–263
10. Caveny LH, Ohlemiller TJ, Summerfield M (1975) Influence of thermal radiation on solid propellant burning rate. AIAA J 13:202–205
11. Esker DR, Brewster MQ (1966) Laser pyrolisis of hydroxyl-terminated polybutadiene. J Propuls Power 12(2):296–301
12. Zenin A (1995) HMX and RDX: combustion mechanism and influence on modern double-base propellant combustion. J Propuls Power 11:752–758
13. DeLuca LT, Cozzi F, Germinasi G, Ley I, Zenin AA (1999) Combustion mechanism of an RDX-based composite propellant. Combust Flame 118:248–261
14. Simonenko VN, Zarko VE, Kiskin AB (1998) Characterization of self-sustaining combustion of cyclic nitramines, energetic materials: production, processing and characterization. In: 29th annual conference of ICT, Karlsruhe
15. Konev EV, Khlevnoi SS (1966) Burning of a powder in the presence of luminous radiation. Fiz Goreniya Vzryva 2(4):33–41
16. Qin Z, Shen R, Du J Al (2011) Combustion characteristics of solid propellant under laser irradiation. International autumn seminar of propellants, explosives and pyrotechnics, pp 731–735
17. Qin Z, Wu J, Shen R, Ye Y, Wu L (2014) Laser-controlled combustion of solid propellant. Adv Mater Res 884–885:87–90

Catalytic Aspects in the Synthesis of a Promising Energetic Material

Irina L. Simakova and Valentin N. Parmon

Abstract Synthesis of a promising energetic material CL-20 requires the two-step catalytic re-functionalization of N-bonded benzyl groups (CH_2-C_6H_5) of hexaben-zylhexaazaisowurtzitane (HBIW) into acetyl (-CO-CH_3) or formyl groups (-CHO) over Pd/C catalyst before its direct nitrolysis into final CL-20 product. Utilization of an expensive palladium-based catalyst deactivated fast during reaction contributes substantially to a high CL-20 cost being a significant hurdle limiting wide application of CL-20 in a propellant formulation. In this work a careful systematic study was performed to improve efficiency, resistance to deactivation, and life-time of Pd/C catalysts as well as to elucidate the optimal hydrodebenzylation reaction conditions. The catalyst activity decrease for Pd/C was found to be caused mainly by agglomeration of metal nanoparticles, Pd re-deposition on inaccessible inner areas of the carbon support, and blocking of the metallic palladium with by-products of intermediates destruction. Different ways to enhance Pd/C catalytic activity through an improvement of Pd dispersion and resistance of Pd particles to agglomeration and re-oxidation as well as through an increase of Pd accessibility for large HBIW molecules were proposed. The two-step HBIW debenzylation with a separately repeated use of the catalyst in each catalytic stage was considered as a promising way to increase catalyst productivity and to diminish CL-20 production costs.

Nomenclature

AcCl	Acetyl chloride
Ac_2O	Acetic acid anhydryd
AcOH	Acetic acid
CCD	Central composite design
CL-20	2,4,6,8,10,12-hexanitro-2,4,6,8,10,12-hexaazatetracyclo [5.5.0.0^{3,11}.0^{5,9}] dodecane
CFC	Catalytic filamentous carbon

I.L. Simakova • V.N. Parmon (✉)
Boreskov Institute of Catalysis SB RAS, Novosibirsk State University,
Novosibirsk 630090, Russia
e-mail: simakova@catalysis.ru; parmon@catalysis.ru

EXAFS	Extended X-Ray Absorption Fine Structure
DMA	Dimethyl acetamide
$D_{pore\,av}$	Average pore size, nm
DMF	Dimethyl formamide
GC	Gas chromatography
GC/MS	Gas chromatography–mass spectrometry
HBIW	Hexabenzylhexaazaisowurtzitane
HEM	High energetic material
HNIW	2,4,6,8,10,12-hexanitro-2,4,6,8,10,12-hexaazatetracyclo [5.5.0.0^{3,11}.0^{5,9}] dodecane
HPLC	High-performance liquid chromatography
HRTEM	High Resolution Transmission Electron Microscopy
I_s	Specific impulse
Pd(OAc)$_2$	Palladium acetate
PhBr	Phenyl bromide
(PhCO)$_2$O	Benzoic anhydride
S_{sp}	Specific surface area, m^2 g^{-1}
TADBIW	4,10-dibenzyl-2,6,8,12-tetraacetyl-2,4,6,8,10, 12-hexaazaisowurtzitane
TADFIW	4,10-diformyl-2,6,8,12-tetraacetyl-2,4,6,8,10, 12-hexaazaisowurtzitane
TADEIW	Tetraacetyldiethylhexaazaisowurtzitane
TAIW	Tetraacetylhexaazaisowurtzitane
TADNIW	Tetraacetyldinitrosohexaazaisowurtzitane
TEM	Transmission Electron Microscopy
V	Porous volume, mL g^{-1}
XANES	X-ray Absorption Near Edge Structure
XPS	X-ray Photoelectron Spectroscopy

1 Introduction

Catalysis, which significantly changed the face of the chemical science in the twenty-first century, nowadays is playing a leading role in increasing efficiency of modern chemical processes. A cutting edge of modern synthetic methods is introduction of functional groups and more complex structural units into organic molecules with a high control over the course of chemical transformation [1].

In the area of energetic materials the major focus is currently on the development of advanced solid propellants having higher energy (I_s), environment friendly combustion products and insensitivity to detonation [2]. The polyazapolycyclic caged polynitramine 2,4,6,8,10,12-hexanitro-2,4,6,8,10,12-hexaazatetracyclo [5.5.0.0^{3,11}.0^{5,9}] dodecane (also referred to as CL-20 or HNIW, 2,4,6,8,10,12-hexanitro-2,4,6,8,10,12-hexaazaisowurtzitane ($C_6H_6N_{12}O_{12}$)) is a relatively new high energetic material (HEM) which has not being utilized so far in any military

production. Originally synthesized in 1986 by Arnold Neilsen at the Naval Surface Weapons Center at China Lake, California (hence the CL- designator), CL-20 is the highest energy compound as well as the highest density compound known among organic chemicals albeit some concerns about its susceptibility to impact and friction [3, 4]. It is manufactured in the dense epsilon crystal phase in batches of about 100 kg by Thiokol (USA) and the French company SNPE, now SAFRAN-HERAKLES [5].

The concept of a caged nitramine based on amine/glyoxal chemistry was proposed in 1970s resulting later in development of a number of alternative routes for synthesis of CL-20 [6]. Methods of synthesis and properties of HNIW are carefully analyzed and surveyed in a comprehensive review written by Singh and co-workers [7]. These topics were as well reported by Sakovich and co-workers [8, 9]. All known methods of producing CL-20 are based on the same starting material, hexabenzylhexaazaisowurtzitane (HBIW). Conversion of HBIW directly to CL-20 is one of the major challenges. Direct nitration of HBIW to CL-20 by nitrolysis was unsuccessful because of competing nitration of the phenyl rings [10] thereby necessitating debenzylation by catalytic hydrogenation prior to nitration. Hexaazaisowurtzitane itself is unstable in the reaction medium, and thus its hydrogenation in the absence of a reactive acetylation agent leads to a collapse of the cage structure. Reductive debenzylation of HBIW under a wide variety of hydrogenation conditions in the presence of a palladium catalyst was reported by Bellamy [11]. Hydrogenation in the presence of acetic anhydride excess results in formation of the 4,10-dibenzyl-2,6,8,12-tetraacetyl-2,4,6,8,10,12-hexaazaisowurtzitane (TADBIW) derivative as was also reported by Nielsen et al. [12–14]. According to the seminal work of Nielsen et al. [10, 12–14] HNIW can be obtained readily in three reaction steps with isolation of two intermediates (**3** and **4**, Fig. 1). First, benzylamine (**1**) is condensed with glyoxal (**2**) under acidic and dehydrating conditions giving the first intermediate HBIW (**3**). Four benzyl groups can selectively undergo hydrogenolysis using a palladium on carbon catalyst and hydrogen. The amino groups are then acetylated during the same step using acetic anhydride yielding TADBIW (**4**). Finally, compound **4** is reacted with N_2O_4, HNO_3/H_2SO_4, nitronium tetrafluoroborate (NO_2BF_4), or nitrosonium tetrafluoroborate ($NOBF_4$) resulting in maximum 52 % of HNIW for the latter oxidizing agents [15].

A rather low yield of HNIW and high costs of NO_2BF_4 and $NOBF_4$ have motivated further improvements of HNIW synthesis method (Fig. 2). A catalytic re-functionalization of residual benzyl groups of TADBIW (**4**, Fig. 2) into formyl groups was proposed leading to 4,10-diformyl-2,6,8,12-tetraacetyl-2,4,6,8,10,12-hexaazaisowurtzitane (TADFIW) (**5**, Fig. 2). Thereafter TADFIW was directly nitrated with a mixture of nitric and sulfuric acids [7] or with concentrated nitric acid (98 %) at a higher temperature (125 °C) to produce CL-20 with a 90–97 % yield [7].

The benzyl groups of TADBIW can also be removed or changed by other groups, with the formation of tetraacetyldiethylhexaazaisowurtzitane (TADEIW), tetraacetylhexaazaisowurtzitane (TAIW), or tetraacetyldinitrosohexaazaisowurtzi-
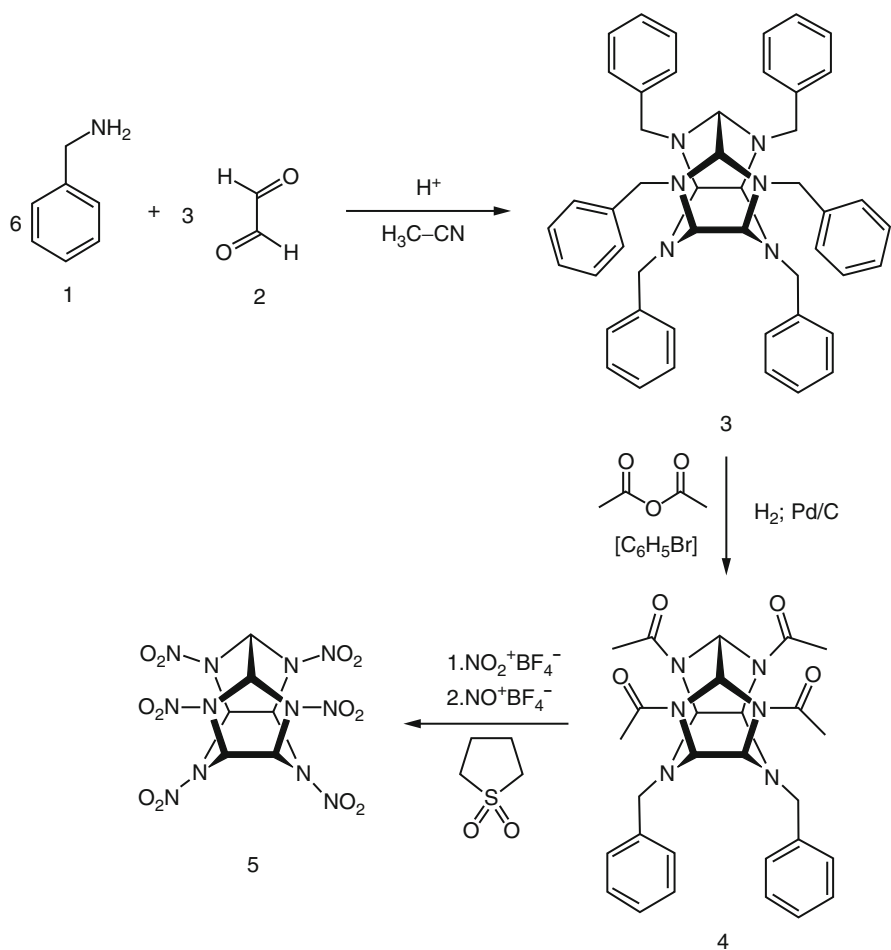
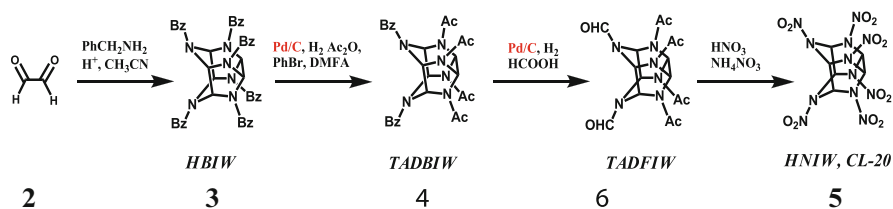**Fig. 1** Scheme of HNIW synthesis via transformation HBIW->TADBIW->HNIW

Fig. 2 Scheme of HNIW synthesis via HBIW->TADBIW->TADFIW->HNIW

tane (TADNIW). TADBIW conversion to TADNIW by adding N_2O_4 or $NOBF_4$ followed by TADNIW nitration with NO_2BF_4 to CL-20 leading to 90 % yield is reported in much detail [12, 16]. Other attempts to synthesize CL-20 by nitrating TADBIW (obtained by reductive debenzylation–acetylation of HBIW) with a $NOBF_4$-NO_2BF_4 mixture as a nitrating agent were also made [17]. One-pot synthesis reported by Wang et al. [15] is a modified approach of CL-20 preparation from TADBIW through TADNIW with a yield up to 82 % and purity up to 98 %. Subsequent attempts were made to apply synthesis approaches [7] involving TAIW nitration by 95–99 % nitric acid. TAIW direct nitration with a mixture of nitric and sulfuric acids at 85 °C with 99 % conversion within 10 min was described [7, 18]. Kawabe et al. [19] claimed that the mixed acid nitration of TAIW at 60 °C for 24 h yielded 98 % of CL-20. Recently TAIW nitration was reported to be made using N_2O_5/HNO_3 as the nitrating agent with CL-20 yield of 86 % and 99 % purity [20]. Chung et al. [21] made an attempt to synthesize pentaacetylhexaazaisowurtzitane or pentaacetylformylhexaazaisowurtzitane as a precursor to HNIW. The reaction parameters were optimized allowing 85 % yield of CL-20.

Nowadays a practical implementation of HNIW instead of HMX meets difficulties because of a higher cost (US$1,300/kg) of the former compared to HMX (US$100/kg) [5] which would be expected to fall by a factor of perhaps 5 or 10 when production is scaled up. Nevertheless economic analysis shows that the cost of the palladium catalyst consumed inevitably during hydrodebenzylation can run up to 35–40 % of HNIW net cost being almost the main pricing factor [1, 22].

Currently a catalyst-free two-stage CL-20 synthesis was reported starting from allylamine and glyoxal to form hexaallylisowurtzitane followed by a direct nitration with NO_2BF_4 or sulfuric/nitric acids without application of any catalyst [23]. Attempts to realize heavy-metal-free synthesis of CL-20 via hexa(1-propenyl)hexaazaisowurtzitane also failed giving the yield of the desired CL-20 of only 11–55 % [24].

In view of high costs of $NOBF_4$ and NO_2BF_4 a scheme involving two consecutive catalytic steps HBIW->TADBIW->TADFIW over Pd/C can be considered as the most efficient known method of CL-20 synthesis.

Analysis of scientific literature shows that majority of the studies on CL-20 focuses on the process development, namely formulation of the synthesis, e.g. process conditions [25, 26], separation of CL-20 as well as preparation of its required polymorphic crystal phase [27, 28] and composites on its basis. However, hardly any attention is paid to the catalytic aspects of HNIW synthesis and palladium on carbon catalyst is just added as one of the reagents [29]. Recently registered patents [30, 31] described a modified catalyst $Pd(OH)_2/Al_2O_3$-C. While first debenzylation–acylation reactions were carried out preferably over Pearlman's 20 mass % $Pd(OH)_2/C$ catalyst [12, 32], the inventors of the patents [30, 31]

proposed to carry out reductive debenzylation over $Pd(OH)_2/Al_2O_3$-C catalyst using as a carrier granules of α-alumina coated successively with γ-alumina (5–15 mass %) and pyrocarbon (1–5 mass %) with deposited palladium hydroxide (2–20 mass % metal loading). The two-step catalytic reductive debenzylation–acylation of HBIW into TADFIW was carried out under hydrogen pressure 5–20 bar at temperature 20–35 °C at the beginning of the process with a subsequent increase up to 45–60 °C. The authors claimed that $Pd(OH)_2/Al_2O_3$-C catalyst was subjected to less abrasion noticeably decreasing a loss of the active component during the reaction and filtration providing a higher yield of the desired product. It could be assumed that the active component of the catalyst is metallic Pd generated in-situ by reduction of $Pd(OH)_2$ under high hydrogen pressure. However, the authors did not provide any details at all on the catalyst preparation, possibility of recycling and characterization of both fresh and spent catalysts. Thus there was no systematical study of catalytic steps so far. Several works of Parmon and co-workers devoted to the two-stage catalytic reductive debenzylation–acylation of HBIW (**3**, Fig. 2) into TADFIW (**6**, Fig. 2) attempted to study the effect of the method of catalyst synthesis as well as reaction conditions on its catalytic activity [33–36].

It would be expected that a careful selection of the catalytic system Pd/C required for two-step reductive debenzylation (*HBIW→TADBIW→TADFIW*) during HNIW synthesis reduces the HNIW production cost and promotes its wider application.

This article considers development of different approaches to design more efficient heterogeneous catalytic systems for the synthesis of HNIW precursor. First a study of the Pd/C catalyst deactivation was carried out. The influence of Pd/C preparation modes [37] on catalytic activity in the reductive debenzylation of HBIW and a possibility of catalyst recycling were investigated. Physico-chemical methods such as low-temperature nitrogen adsorption, chemisorption of CO, XPS, EXAFS and XANES were applied to understand the formation of the active Pd component in the presence of a reducing modifier and to determine the composition of the most active phase. The nature of the carbonaceous material and its pretreatment were varied as well as the methods employed for palladium adsorption and reduction. Therefore the following aspects were studied to improve Pd/C activity and resistance to deactivation:

- Influence of the carbonaceous support
- Study of the Pd/C catalyst deactivation
- Effect of the Pd precursor reduction mode
- Identification of debenzylation step mainly responsible for Pd/C deactivation
- Effect of the solvent nature and metal loading
- Effect of reaction temperature on the Pd/C activity and selectivity
- Scaling up TADFIW catalytic synthesis

2 Influence of the Carbonaceous Material Nature and Catalyst Preparation Method on the Pd/C Catalyst Activity and Stability

The porous structures of starting carbonaceous material, dispersion of the catalytically active metal as well as its location in the porous media and its environment are important characteristics of palladium-based catalysts. The prepared catalysts differed by the type of the carbon carrier (Norit-SX, Sibunit, CFC) and the method of its preliminary treatment (33 mass % H_2O_2 aqueous solution, 5 or 10 mass % HNO_3 aqueous solution, etc.) as well as by the method of the catalyst reduction (by HCOONa, N_2H_4, H_2 in solution and H_2 in flow).

The palladium-based catalysts were prepared by adsorption of $PdCl_2$ in HCl solution on a carbonaceous material followed by neutralization with the 1 mol L^{-1} aqueous solution of sodium carbonate and the subsequent reduction of the catalyst [38]. The nature of the carbonaceous material and its pretreatment were varied as well as the methods employed for palladium adsorption and reduction (see Table 1). The following carbonaceous materials were used: two types of

Table 1 HBIW hydrodebenzylation over palladium-based catalyst samples [33]

Catalyst	Carrier		Metal		Rate of H_2 uptake, (mol H_2/mol HBIW·h)	TADBIW yield[b], mass %
	Type	Pretreatment[a]	Pd, mass %	Reduction		
Pd/C (Degussa)	–	–	10	–	1.5	61
Pd/C (ICT-3-23)	Sibunit I	–	6	–	1.0	56
K-I	Sibunit I	–	4	HCOONa	0.9 (3.0)[c]	0 (74)[c]
K-II	Sibunit I	HNO_3 (5 %)	4	HCOONa	1.0 (3.1)[c]	0 (76)[c]
K-III	Sibunit II	–	6	HCOONa	1.1	80
K-IVa	Sibunit II	HNO_3 (5 %)	6	HCOONa	1.2	82
K-IVb	Sibunit II	HNO_3 (10 %)	6	HCOONa	0.9	60
K-Va	Sibunit II	H_2O_2 (33 %)	6	HCOONa	1.6	81
K-Vb	Sibunit II	H_2O_2 (33 %)	6	H_2, in sol.	1.5	80
K-Vc	Sibunit II	H_2O_2 (33 %)	6	H_2, in flow	1.4	78
K-Vd	Sibunit II	H_2O_2 (33 %)	6	N_2H_4	1.5	79
K-VI	CFC	–	6	HCOONa	0.9	84
K-VII	CFC	HNO_3 (5 %)	6	HCOONa	1.0	80
K-VIII	Sibunit II	H_2O_2 (33 %)	10	HCOONa	1.8	86
K-IX	Norit-SX	–	6	HCOONa	0.2	0

[a]Carbonaceous material (10 g) was slurred with 10 ml of the oxidizing agent. The suspension was sustained during 1 day thereafter the carbonaceous material was separated over a glass porous filter, washed by distillate water and dried in air
[b]Catalytic activity is tested accordingly to a standard technique [40] with the following reagent loading: 3.4 g HBIW, 5 mL Ac_2O, 0.6 mL PhBr (10 % DMF solution), 10 mL DMF. The catalyst: substrate mass ratio was 1:10 and at 25 °C under hydrogen pressure 4 bar
[c]Catalyst: substrate mass ratio = 1:5

mesoporous carbon Sibunit (Sibunit I – specific surface area $S_{sp} = 280$ m^2 g^{-1}, porous volume $V = 0.66$ mL g^{-1}, and Sibunit II – $S_{sp} = 320$ m^2 g^{-1}, $V = 0.80$ mL g^{-1}, both with the maximum of the pore size distribution at 4 nm and grain size <50 µm), "catalytic filamentous carbon" (CFC, prepared by methane decomposition at 625 °C over Fe$_{62}$Ni$_8$-Al$_2$O$_3$, $S_{sp} = 150$ m^2 g^{-1}, $V = 0.66$ mL g^{-1}, with the maximum of the pore size distribution at 17.5 nm (K-VI, K-VII)), and commercially available Norit-SX (Degussa). To increase hydrophilicity of the carbon surface, some carbon samples were pretreated by various oxidizers. To reduce the catalyst, aqueous solutions of HCOONa (1 mol L^{-1}) or N$_2$H$_4$ (1 mol L^{-1}) were added dropwise in the molar ratio 2.5/1 or alternatively gaseous hydrogen was bubbled until decoloration of the catalyst suspension in water. The catalyst was further separated with the glass porous filter and dried in air. Humidity of the prepared catalysts was about 50 % from their weight. One sample of the Pd/Sibunit catalyst was prepared by reduction of adsorbed Pd(OH)$_2$ in a hydrogen flow (K-Vc). For comparison, two commercially available catalysts, 10 mass % Pd/C (Degussa) and 6 mass % Pd/C (ICT-3-23), were also tested.

Some data on the catalytic runs with the prepared palladium-based catalysts are shown in Table 1. Earlier it was reported that Pd/C catalyst gives the best activity when generated by reduction of palladium hydroxide on carbon (Pearlman's catalyst) and used in a ratio of about one-fourth the weight of HBIW. Dry palladium on charcoal (3–20 %) may also be used but gives lower yields (40–50 %) [39].

However Pd(OH)$_2$/Sibunit which was not pre-reduced did not provide any HBIW hydrodebenzylation activity. It was observed that HBIW hydrodebenzylation over 6 mass % Pd on microporous carbonaceous material Norit-SX did not give the target product TADBIW and only a small quantity of hydrogen was consumed during the reaction. The absence of any activity seems to be a result of the catalyst active centers location in the micropores which are not accessible for large HBIW molecules. It was suggested that the use of a carrier with wider transport pores provides a better access to metallic palladium. Sibunit is one of the most known synthetic mesoporous carbonaceous materials of a broad use in catalytic organic chemistry [41]. This carbonaceous material possesses a well developed transport porous system and a low content of contaminants [42, 43]. Besides, there is an opportunity to tune the concentration of the adsorption sites on the carbon surface by oxidizing agents.

A high rate of hydrogen consumption and a sufficient TADBIW yield are reached over 6 mass % Pd/Sibunit catalyst prepared from pre-oxidized Sibunit by hydrogen peroxide (33 %) with the subsequent reduction of the sample by sodium formate (sample K-Va). The catalytic activity of this sample is higher than that for the early reported prototypes [40] at the same conditions (at 25 °C under hydrogen pressure 4 bar). According to the TEM data (Fig. 3), the Pd particle size in the K-Va sample is lower than that for the industrial ICT-3-23 catalyst. It indicates that the specific surface area of the active metal in K-Va is larger than for the industrial catalyst which explains its higher catalytic activity.
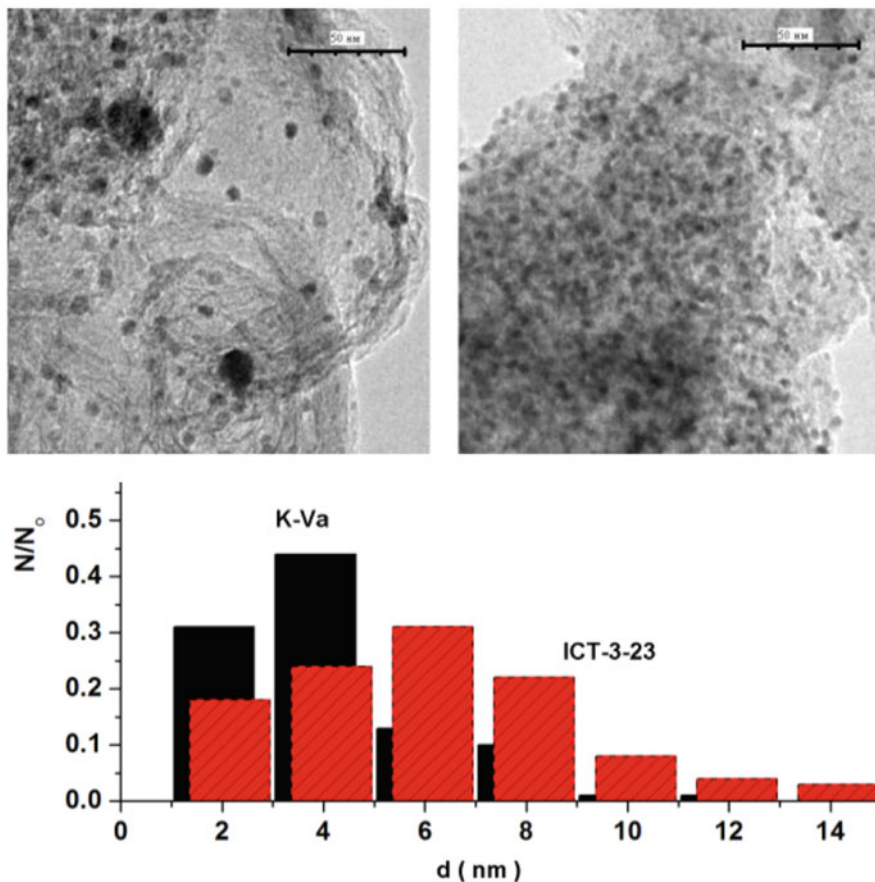
Fig. 3 TEM images of ICT-3-20 (*left top*) and K-Va (*right top*) and histograms of the particle size distribution (*bottom*) (N/N_o is the relative quantity of particles, d is the average diameter of Pd particles, *nm*)

As a consequence it is possible to use K-Va (6 mass % Pd/Sibunit) catalyst with a sufficiently smaller content of the noble metal than in the commercially available prototype 10 mass % Pd/C (Degussa) at the same catalyst: substrate weight ratio (1:10). The yields of the target product over these catalysts are 82 % and 61 %, respectively. The K-VIII sample (10 mass % Pd/Sibunit) allows achieving the highest yield of TADBIW (86 %) that turned out not to be proportional to the increase of metal loading. Samples K-I – K-V exhibited high activity, however, deactivated quickly during a two-stage cycle of the HBIW hydrodebenzylation similar to prototypes Pd/C (Degussa) and ICT-3-23 [33].

Another kind of mesoporous carbonaceous materials is CFC ("catalytic filamentous carbon") which represents the dense interlacing of the carbon nanofibres generated by catalytic pyrolysis of methane over Fe–Ni alumina supported catalysts. The samples of Pd/CFC (6 mass % Pd on CFC, K-VI) and Pd/CFC-ox (6 mass % Pd on CFC preliminary treated by HNO_3 (10 mass %), K-VII) have been prepared by a standard technique [37]. We have shown that despite an essential decrease of the hydrogenation rate (in comparison with K-Va sample) it is possible to synthesize the target product TADBIW with a higher yield (84 %). The decrease of the hydrogenation rate seems to be due to a much lower (in comparison with Sibunit) specific surface area of the carbonaceous carrier. However, hydrodebenzylation over Pd/CFC-ox catalyst prepared on the basis of the preliminary oxidizing carbon support gives a smaller yield of TADBIW (80 %). The latter seems to result from a partial destruction of the carbon nanofibers by the oxidizing pretreatment. In spite of its high catalytic activity, Pd/CFC is also quickly deactivated during the two-stage process of hydrodebenzylation–acylation.

It is worth to note that deactivation of Pd/C catalysts during the hydrodebenzylation stage does not depend on the method of catalyst preparation.

As a result, the optimal catalyst was found to be 6 mass % Pd supported on mesoporous Sibunit pretreated before deposition by an aqueous solution of 5 mass % HNO_3 or 33 mass % H_2O_2 with sodium formate or gaseous hydrogen acting as reducing agent. An attempt was made to improve operational parameters of 6 mass % Pd/Sibunit (analog of K-Va catalyst, Table 1) and to increase activity and resistance to deactivation by changing textural properties of the applied carbon support Sibunit II [44]. In that study the samples of mesoporous carbon support Sibunit selected for Pd catalyst preparation varied in the specific surface area from 300 to 375 m^2 g^{-1}, total pore volume from 0.37 to 0.71 cm^3 g^{-1}, and in the range of pore sizes from 4.84 to 7.34 nm (Table 2).

According to the obtained results the samples S3-1, S3-2 and S3-3 with the highest specific surface area and the largest pore size displayed the highest catalytic activity. It is important to note that the sample S3-2 is the most stable and enables

Table 2 Catalytic properties of 6 mass % Pd/Sibunit (analog of K-Va catalyst, Table 1) with different support fractional composition and textural characteristics

Sibunit	S_{BET}[a], m^2 g^{-1}	Pore volume, V_Σ cm^3 g^{-1}	$D_{pore av}$[b], nm	Grain size range, μm	TADBIW yield, mass % on each cycle
S1-1	315	0.43	5.46	<40	82, 65
S1-2	318	0.38	4.84	40–70	53, 22
S1-3	301	0.37	4.90	70–100	65
S3-1	388	0.71	7.34	<40	83, 63
S3-2	369	0.61	6.61	40–70	79, 79, 61, 44, 6
S3-3	375	0.62	6.65	70–100	81, 74, 65

[a]S_{sp} specific surface area of carbon support
[b]$D_{pore av}$ the average pore diameter
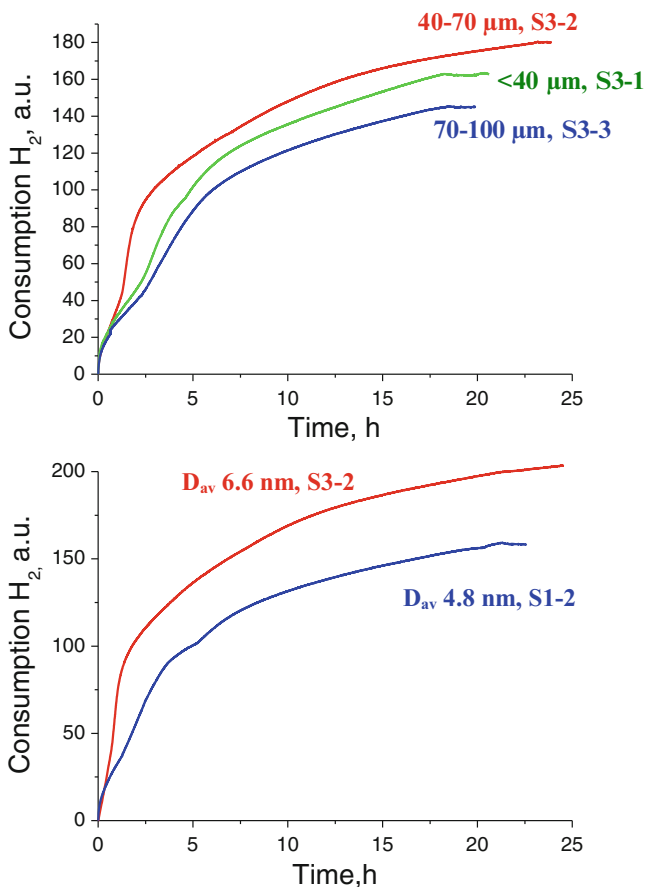
Fig. 4 HBIW hydrodebenzylation over the Pd/Sibunit catalyst: effect of Sibunit fractional composition (D$_{pore\ av}$ 6.6–7.3 nm) (*top*), effect of Sibunit pore size (fractional composition 40–70 μm) (*bottom*). Reaction conditions (3.4 g HBIW, 0.34 g catalyst, 10 mL DMF, 5 mL Ac$_2$O, 0.06 mL PhBr, hydrogen pressure 4 bar and reaction temperature 25 °C)

four to five reaction cycles without addition of a fresh catalyst (Fig. 4). In general, catalysts in S1 series are significantly inferior in the catalytic activity compared to S3 series.

Thus, as a result an impact of fractional composition and textural characteristics of carbon support on the catalytic activity and stability of the supported Pd/C catalyst was found in the HBIW hydrodebenzylation–acylation indicating that the catalytic properties may be modified by variation of the carbon support parameters and thereby leading to the optimum parameters for Sibunit.

3   Study of the Pd/C Catalyst Deactivation

A better understanding of deactivation processes is essential for improving and optimizing the process conditions and catalysts and for circumventing premature catalyst degradation minimizing additional costs [45].

While studying HBIW debenzylation it was found that the weight of the washed spent Pd/C samples is larger than for the initial catalysts. Furthermore, it was shown that it is impossible to regenerate the deactivated catalyst (6 mass % Pd/C, K-Va) by extraction of Pd from the carbon pores by aqua regia followed by re-adsorption on a fresh carrier. XRF revealed that the catalyst obtained in such way contains a significantly lower quantity of palladium than the initial one (2.5 mass % instead of 6.0 mass %). This indicated that the metallic palladium cannot be extracted completely from the spent catalyst. A comparative study of the fresh and spent samples of K-Va by low-temperature (77 K) nitrogen adsorption has shown that the specific surface area and the porous volume in the spent catalyst are substantially lower than those in the fresh one (229 and 324 m^2 g^{-1}, 0.67 and 0.83 mL g^{-1}, respectively). The low specific surface area and the palladium inaccessibility can be explained by blocking a part of the carbon carrier pores and the metal inside them by irreversibly adsorbed organic compounds.

A set of experiments with different time in HBIW to TADBIW hydrodebenzylation over K-Va catalyst has been performed to study the dynamics of blocking the catalytically active centers. Hydrodebenzylation was stopped at various levels of hydrogen consumption (54, 74, 94, 110, 120 and 150 % compared to stoichiometry). Pd/Sibunit (K-Va) was separated from the reaction mixture, washed with formic acid and dried in vacuum. The highest yield of TADBIW was reached at the hydrogen consumption above 120 %. A study of the porous structure of the obtained catalyst samples has shown that the specific carbon surface area (S_{sp}) decreased as the hydrogen consumption increased [33]. An essential change of the specific carbon surface area starts at hydrogen uptake above 110 % from the stoichiometry (Fig. 5). However, the catalytic activity of Pd/C catalyst at hydrogen consumption lower than 110 % is the same as for the same catalyst samples at larger hydrogen consumption. All catalyst samples exhibited a low catalytic activity in the HBIW to TADBIW hydrodebenzylation recycling experiments.

TEM was used for investigating changes in the morphology of the carbon supported palladium particles during hydrodebenzylation. A clear agglomeration of palladium particles in the spent catalyst was found leading to a decrease in the active metal surface area. Thus, a relative amount of large Pd particles with sizes over 5 nm substantially increased, while the amount of small particles (<10 nm) decreased (Fig. 6).

The above-stated observations allow an assumption that the agglomeration of palladium particles is the main reason of the Pd/C activity loss. At present, it is not completely clear which kind of processes can lead to agglomeration of palladium particles during hydrodebenzylation at low temperature. Probably this agglomeration could proceed via dissolution of heterogeneous palladium into the
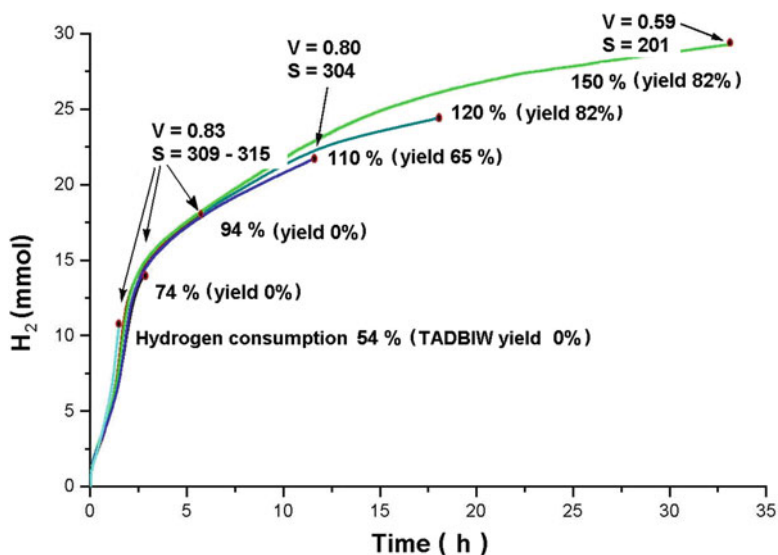
Fig. 5 Hydrodebenzylation recycle over the K-Va catalyst (3.4 g HBIW, 0.34 g K-Va catalyst, 10 mL DMF, 5 mL Ac$_2$O, 0.06 mL PhBr, hydrogen pressure 4 bar, reaction temperature 25 °C) (Taken from reference [33])
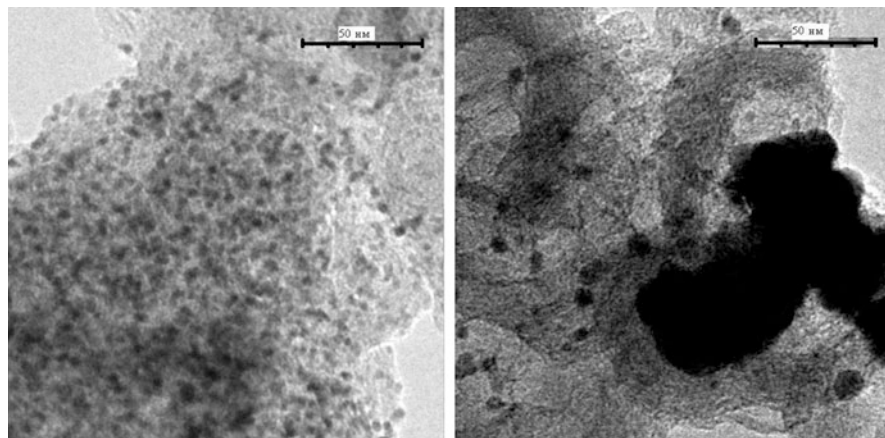
Fig. 6 Pd/Sibunit catalyst K-Va before (*left*) and after (*right*) two-stage catalytic process HBIW->TADBIW->TADFIW

reaction solution with the subsequent re-adsorption of the metal in the form of large agglomerates[1]. This is in line with the observations showing that a homogeneous catalyst Pd(OAc)$_2$ or palladium complexes do not catalyze HBIW transformations

---

[1]The suggested "agglomeration" mechanism of Pd particles in catalysis is quite different from that occurring for Al particles in propellant burning.

into TADBIW [46]. Therefore, it could be assumed that a substantial decrease in the catalytic activity results from blocking of the active palladium particles by oligomerization products inside the carbon pores as well as from agglomeration of the metal particles.

A HRTEM study of Pd/Sibunit samples before and after HBIW->TADBIW hydrodebenzylation confirmed that the amount of Pd nanoparticles on the outer surface of Sibunit decreased while it increased on the inner surface of the support. Thus, along with an enlargement of Pd nanoparticles, deactivation of Pd catalysts could be caused by migration of Pd nanoparticles from the Sibunit outer surface into the micropores inaccessible for large HBIW molecule (Fig. 7).

A TEM study of the catalyst samples demonstrated that in the repeated use of the catalyst, palladium particle size increased considerably and, hence, the active metal surface area decreases. The growth of palladium particles in both first HBIW->TADBIW and second TADBIW ->TADFIW debenzylation steps occurs from one cycle to another attaining a certain critical value after which the catalyst completely loses its activity. These values are considerably different for the first and second debenzylation steps (Fig. 8). It was found that for the first step of HBIW debenzylation, an optimal average palladium particle size of the catalyst is 2.3–2.8 nm and the catalyst completely lost its activity for the average particle size above 4 nm. For the second step, the catalyst exhibited high activity even when for Pd particle size of 4–6 nm and became inactive as the average particle diameter has increased to 10–11 nm [1].

An increase in the metal dispersion in Pd/C catalyst was found to substantially enhance the catalytic activity, which makes it possible to perform the process under mild conditions at room temperature.

4 Effect of Pd Precursor Reduction Mode on Catalytic Activity

The procedure of the deposition of palladium compounds on carbon support is typically considered as "know-how" [47, 48]. Traditionally preparation of palladium catalysts supported on porous carbon with a controlled Pd particle size involves adsorption of mono- and polynuclear Pd(II) hydroxo complexes followed by reduction of the adsorbed compounds to the metallic state [49]. Thus one of the catalysts K-Vc (Table 1) was prepared by reduction in hydrogen flow. Influence of the reduction modes of polynuclear Pd (II) hydroxide deposited on the carbon support Sibunit on the catalytic activity in the reductive debenzylation and a possibility of recycling the catalysts were studied [35]. It was found that in the presence of molecular hydrogen the optimum conditions of nanosized metallic palladium particle formation on the surface of the carbon support are reduction of polynuclear Pd (II) hydroxides up to 250 °C with a temperature ramp 1.5°K/min providing the largest activity and stability in hydrodebenzylation–acylation reaction (Table 3).
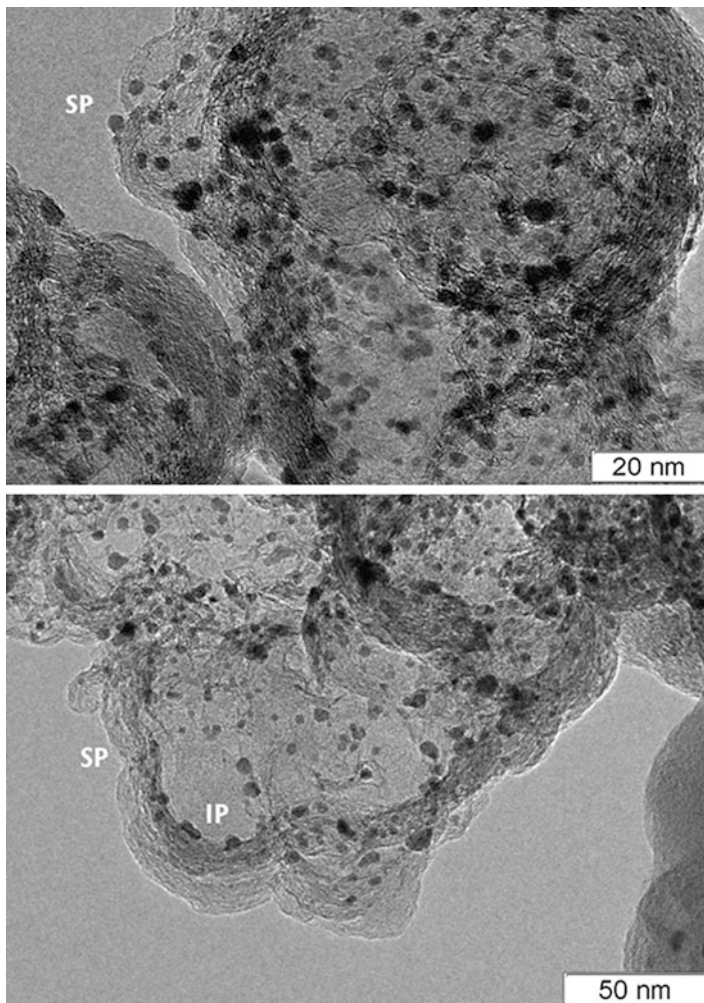
Fig. 7 HRTEM micrographs of Pd/Sibunit (K-Va) catalyst before (*top*) and after hydrodebenzylation HBIW->TADBIW (*bottom*). Reaction conditions: 3.4 g HBIW, 0.34 g catalyst, 10 mL DMF, 5 mL Ac$_2$O, 0.06 mL PhBr, hydrogen pressure 4 bar and reaction temperature 25°C. *SP* – Pd nanoparticles on the Sibunit surface, *IP* – Pd inside Sibunit globules

A possibility to stabilize the active sites of Pd during Pd (II) reduction by a "wet method" through introduction of III, IV, and V groups elements, coming from the corresponding reducing agents such as hydrazine hydrate, sodium formate and sodium tetrahydroborate, was investigated after Pd (II) deposition on Sibunit II designated as PdN, PdC, PdB correspondingly [35]. Physico-chemical methods of low-temperature nitrogen adsorption, CO chemisorption, XPS, EXAFS and XANES were applied to study the formation of the active Pd component in the

Fig. 8 Pd particle size after repeated use of Pd/Sibunit in catalytic stages: HBIW->TADBIW (*white*), TADBIW ->TADFIW (*gray*), d_{Pd} the average diameter of Pd particles (Adapted from [1])
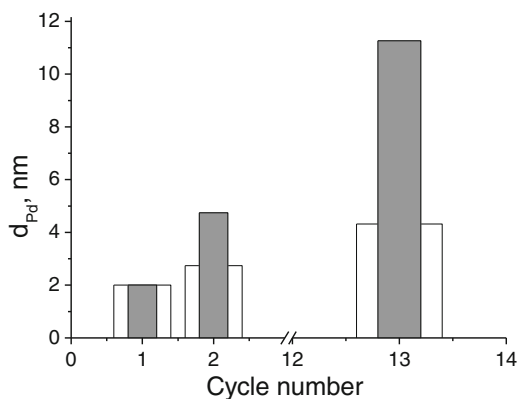
Table 3 Catalytic properties of 6 mass % Pd/Sibunit (analog of K-Vc, Table 1) depending on the reduction mode in hydrodebenzylation HBIW->TADBIW

Sample	$T_{red.}$ [a]	Temperature ramp, K min^{-1}	d_{Pd} [b], nm	S_{BET} [c], m^2 g^{-1}	Pore volume, cm^3 g^{-1}	TADBIW yield in cycles[d], mass %
PdH-1	250	1.5	4.1	401	0.7	75, 73, 44, 53, 21
PdH-2	350	1.5	4.2	399	0.8	81, 71
PdH-3	450	1.5	6.9	402	0.8	0
PdH-4	250	10.0	4.1	401	0.9	82, 42
PdH-5	350	10.0	4.1	403	0.7	0
PdH-6	150	1.5	4.1	401	0.7	81, 40
PdH-7	350	5.0	4.2	400	0.8	63, 52, 29

[a]$T_{red.}$ the final reduction temperature
[b]d_{Pd} the average diameter of Pd particles
[c]S_{sp} specific surface area of carbon support
[d]Reaction conditions: 3.4 g HBIW, 0.34 g catalyst, 10 mL DMF, 5 mL Ac$_2$O, 0.06 mL PhBr, hydrogen pressure 4 bar and reaction temperature 25°C

presence of a reducing modifier and to determine the composition of the most active phase. It was shown by EXAFS and XANES that as a result of the heteroatom introduction the order in crystallinity decreases in the row: PdN> PdC> PdB as Pd coordination number changed in the row 7.8>6.6>5.8 correspondingly while the coordination number for Pd foil is 11.9. Interestingly the catalyst stability in HBIW hydrodebenzylation increased in the opposite way PdN< PdC< PdB. At the same time according to XPS the chemical nature of the reducing agent influenced the oxidation state of Pd (Fig. 9). Thus PdN contains 86 % Pd(0) and 14 % Pd(2+), PdC has approximately equal ratio of Pd(0) and Pd(2+), 51 % and 49 %, respectively, while PdB consists of 58 % Pd in the oxidation state between 0 and +2 which can be assigned to Pd bound with boron typical for amorphous metal glasses. It was stated [35] that, namely PdB compositions, representing presumably metallic palladium glasses (Fig. 9), are the most stable catalysts for the synthesis of 4,10-dibenzyl-2,6,8,12-tetraacetyl-2,4,6,8,10,12-hexaazaisowurtzitane.

Fig. 9 XPS of polynuclear Pd(II) hydroxo complexes adsorbed on Sibunit after reduction by hydrazine hydrate (*PdN*), sodium formate (*PdC*) and sodium tetrahydroborate (*PdB*)
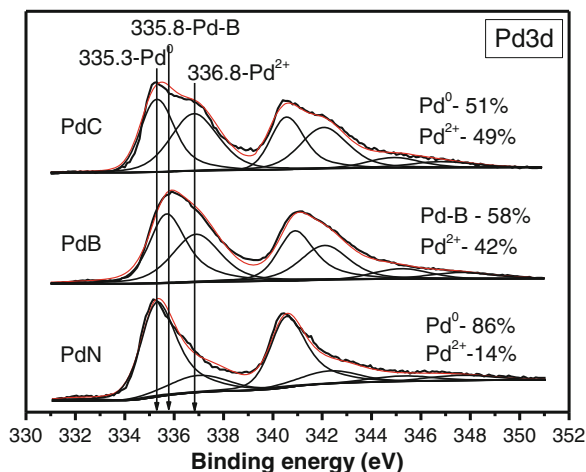
A known method for increasing the stability of palladium metal particles in the Pd/C catalysts is introduction of a stabilizing metal into the catalytic system [1]. Stabilization can be attained due to both the electronic effect (change in the electronegativity of the active metal) and modification of the carbon support surface. The causes of synergistic effects for various catalytic systems differ significantly and cannot always be generalized, because they depend on the specific character of a particular catalytic system (catalyst and the reaction it catalyzes). A patent [36] describes a series of bimetallic systems which were tested in the two-step hydrodebenzylation reaction (HBIW->TADBIW->TADFIW). A particular attention was paid to a possibility of conducting the second hydrodebenzylation cycle (recycle) with the spent catalysts. According to the obtained results, an addition of the stabilizing metal ions during the catalyst preparation resulted, in some cases, in increase of the catalyst productivity for the target product due to enhanced catalyst stability. However, the overall yield of TADFIW per gram of the catalyst should be still improved.

5 Identification of Debenzylation Step Mainly Responsible for Pd/C Deactivation

When HBIW (**3**) (Fig. 2) was dissolved in acetic anhydride (or heated in DMF), the solution darkened rapidly. The ^{1}H NMR analysis of the obtained mixture indicated a decrease in the intensity of signals at δ 3.5–4.5 corresponding to the signals of the CH groups of the hexaazaisowurtzitane framework. This process is accelerated upon addition of Pd/C catalyst to the solution; however, the mixture remains colorless, because the colored products of HBIW destruction are adsorbed on the carbon supported catalyst. The catalyst stored in a mixture of HBIW with acetic anhydride and DMF for 1 day deactivated completely.

Table 4 HBIW hydrodebenzylation over K-IVa (Table 1) [34]

	Product yield, %		
Reaction	Fresh	First	Second
HBIW->TADBIW[a]	82	0	–
TADBIW->TADFIW[b]	85	77	75
HBIW->TADBIW->TADFIW[c]	69	0	–

[a]Reactant loading: 3.4 g HBIW (**3**), 0.34 g of Pd(6 %)/Sibunit (K-IVa), 5 mL Ac$_2$O, 0.06 mL PhBr, and 10 mL DMF, hydrogen pressure 4 bar, temperature 25 °C
[b]Reactant loading: 1.97 g TADBIW, 0.34 g Pd(6 %)/Sibunit (K-IVa), and 9.8 mL of HCOOH (88 %); hydrogen pressure 4 bar, temperature 25 °C
[c]Yield of TADFIW (**6**) synthesized in the two-step cycle of hydrodebenzylation with respect to compound HBIW (**3**)

The reactions **3**->**4** and **4**->**6** (Fig. 2) were carried out separately with two samples of the same Pd/C catalyst (K-IVa). It turned out that hydrogenation of compound **4** to compound **6** on the same catalyst can be carried out at least three times, whereas hydrogenation of compound **3** to compound **4** cannot be repeated (Table 4). Therefore, the main contribution to the catalyst deactivation happened during the first debenzylation step. In the second debenzylation step, the destruction of the hexaazaisowurtzitane framework occurs less intensively, because compound **4** is substantially more stable than compound **3**. In fact, a higher stability of compound **4** framework makes it possible to use more drastic reaction conditions for the replacement of the benzyl groups by the formyl groups and even to carry out the synthesis of CL-20 by the nitrozative debenzylation of compound **3** as shown in [12].

According to GC/MS the composition of the liquid phase of the reaction mixture after the first hydrodebenzylation step includes benzylacetamide and several non-identified nitrogen-containing compounds in addition to the residual peaks of the reactants and the group of peaks of the expected debenzylation products (toluene, benzene, and acetic acid). Benzylacetamide is formed because of the hexaazaisowurtzitane framework opening followed by acylation of the destruction products [11]. It is known that benzylacetamide can form stable complexes with palladium and the essential role of this compound in the deactivation of the palladium catalysts was repeatedly pointed out in the literature [50]. A preliminary treatment of the Pd/C catalyst with benzylacetamide (synthesized by the retro synthesis) resulted, indeed, in a complete catalyst deactivation. Nevertheless, when performing hydrodebenzylation from **3** to **4**, no correlation was observed between the amount of benzylacetamide in the reaction mixture (determined by GC/MS) and the degree of deactivation of the catalyst. It is most likely that benzylacetamide is not the single and strongest catalytic poison for Pd/C catalyst formed in the reaction mixture. In an earlier work [11] more than five different nitrous residues of the hexaazaisowurtzitane framework formed by hydrogenolysis have been identified. Each of the residues can deactivate Pd/C to a different extent. Generally the ease of N-debenzylation is influenced by substitution on the nitrogen atom [51],

namely the quaternary and tertiary amines can easily be debenzylated already at atmospheric pressure and room temperature, while the same reaction for secondary or primary amines requires higher pressure (>4 bar) and temperature (>40 °C). The hydrogenolysis products are strong basic amines which can deactivate the supported precious metal catalysts due to their poisoning effects [52–54]; therefore a higher catalyst amount or addition of acids is necessary to complete the reaction. At the same time, Pd could be poisoned by CO formed during decarbonylation of acetic or formic acids during debenzylation over Pd/C which was not considered at all [55–57].

6 Effect of the Solvent Nature and Metal Loading

The HBIW catalytic debenzylation was proved to proceed stepwise according to the analysis of the reaction mixture with HPLC and GC. Bromobenzene (PhBr) added to the reaction mixture accelerates the first debenzylation step being a source of hydrogen bromide. The latter is a co-catalyst of the C–N bond hydrogenolysis. Kinetic curves of hydrogen consumption by the reaction mixture over Pd/C catalysts with different amounts of the active metal are shown in Fig. 10.

The acceleration of the process in the initial debenzylation step is presumably related to the accumulation of acids in the reaction mixture. As well known, the acids, namely HBr and AcOH, promote hydrogenolysis of the C-heteroatom bond [58]. Then the rate of hydrogen uptake and, hence the hydrogenolysis rate decreases, because solubility of HBIW intermediates decreases with the substitution of the benzyl groups for the acetyl groups in hexaazaisowurtzitane. In addition Pd/C catalyst is gradually deactivated.

Fig. 10 Hydrogen consumption by the reaction mixture during the process on the K-Va (6 %) (*1*) and K-VIII (10 %) (*2*) catalysts under a hydrogen pressure 4 bar and a temperature 25 °C. Composition of the mixture: 3.4 g HBIW, 0.34 g catalyst, 10 mL DMF, 5 mL Ac_2O, 0.06 mL PhBr (Reproduced from [34])
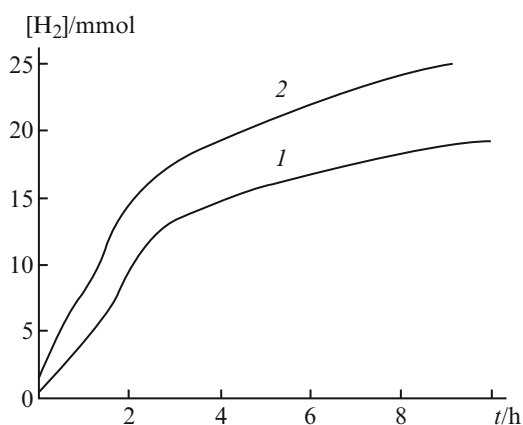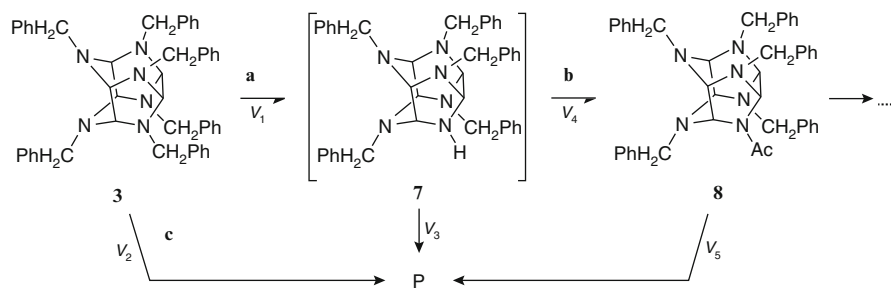
Fig. 11 A tentative scheme of consecutive hydrodebenzylation. Reagents: *a* Pd/C, H_2, PhBr, DMF; *b* Ac_2O, DMF; *c* Ac_2O, acids, H_2O. *P* – destruction products of the HBIW polycyclic framework, v_1, v_2, v_3, v_4, v_5 – corresponding reaction rates (Adapted from [34])

Hydrogen can be consumed by the reaction mixture via several paths: hydrogenation of acetic anhydride and bromobenzene, hydrogenolysis of internal and external C–N bonds of the hexaazaisowurtzitane framework, and hydrogenation of residues of the framework. The consideration in Fig. 11 demonstrated that an increase in the rate v_1 of the target hydrogenolysis reaction should increase the v_1/v_2 ratio as well as v_4/v_3 and, therefore, should decrease the amount of the destruction products, which formation is a reason for catalyst deactivation. The authors of this review have experimentally studied the influence of the concentrations of the substrate, the acylation agent and hydrogen pressure on the course of the process and the yield of the target product [34]. It was found that the effect of the acetic anhydride concentration is twofold: on the one hand, an excess of the acylating agent accelerates side processes and, on the other hand, its deficiency results in a decrease in the acylation rate of the unstable amine v_4 [50], which is also unacceptable. Replacement of acetic anhydride (Ac_2O) with acetyl chloride (AcCl) resulted in the formation of resins, while the use of benzoic anhydride (($PhCO)_2O$) did not lead to any advantages in debenzylation. The most productive was the use of solvents containing the amide groups. Application of such solvents as DMF (TADBIW yield on K-IVa catalyst was 82 %), DMA (80 %), and *N*-methylpyrrolidone (50 %) accelerated the acylation reaction due to basicity of the amide nitrogen atom. When ethers and hydrocarbons are used, the yield of the target precursor of CL-20 was substantially lower. The results obtained with Pd/Sibunit catalyst confirmed the literature data, showing that PhBr is the optimum source of HBr and its optimum amount is 1/8 molar fraction with respect to the substrate [12]. Absence of bromobenzene substantially retards hydrogenolysis of the C–N bond and prevents this reaction to occur at a room temperature. In addition the Pd/C catalyst is gradually deactivated.

It was shown by means of the three-dimensional response surface method that hydrogen pressure did not have a significant effect on the debenzylation HBIW-> TADBIW [26]. Nevertheless from the viewpoint of the final product yield and the reaction rate, hydrogen pressure of 4 bar seems to be optimal for debenzylation. A decrease in the hydrogen pressure considerably decreases the rate of debenzylation
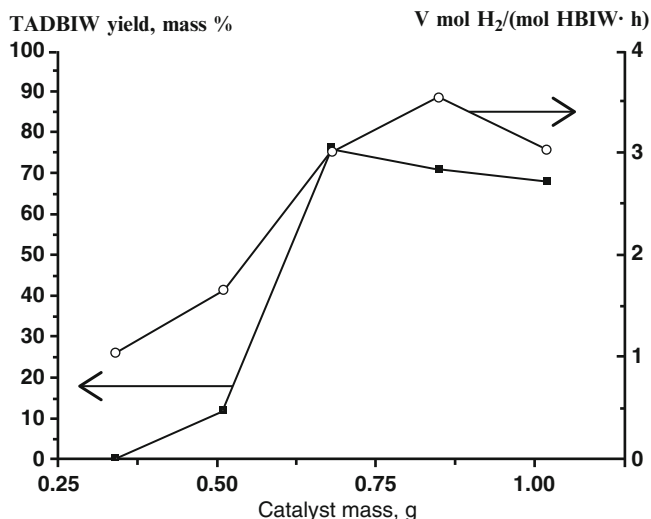
Fig. 12 Effect of the mass of the loaded 4 mass % Pd/Sibunit (K-II) catalyst on the rate of hydrogen uptake (V) and the yield TADBIW under reaction conditions PH$_2$ 4 bar, 25 °C, 3.4 g HBIW, 10 mL DMF, 5 mL Ac$_2$O, and 0.06 mL PhBr

v_1. An increase in the hydrogen pressure increases the contribution of the side reactions resulting in the absence of TADBIW in the reaction products.

A series of experiments were carried out varying amounts of 4 mass % Pd/Sibunit (K-II) keeping the same concentrations of the reactants and the co-catalyst, hydrogen pressure, and stirring efficiency [34] (Fig. 12). The rate of hydrogen uptake by the reaction mixture increased with an increase in the catalyst load. The highest rate of hydrogen uptake was observed when the weight ratio catalyst/substrate = 1/4 was used; however, HBIW yield decreased, being 71 %. For the purpose of the highest target product yield, the catalyst/substrate loading with the weight ratio 1/5 was found to be optimum. With loading larger than 1/5 an acceleration of the C–N bond hydrogenolysis is accompanied by an increase in the rates of the side reactions. A series of the hydrogenation catalysts of different nature was tested in HBIW debenzylation (Table 5) with an aim to find a more stable catalytic system for TADBIW debenzylation.

The catalyst screening did not reveal any system comparable in catalytic activity with Pd/Sibunit catalyst. Samples with a high content of the noble metal should be used to accelerate debenzylation by Pd/Sibunit. The use of K-II catalyst (loading of the catalyst/substrate with the weight ratio 1/10) did not allow obtaining the target precursor of CL-20 in the stepwise reaction. In this case, due to deactivation, the moment, when the debenzylation rates v_1, v_4 become lower than the rate of irreversible side processes v_2, v_3, v_5 associated with opening of the framework of HBIW, preceded the step of TADBIW formation.

The ^{1}H NMR study of the reaction mixture indicated that the process ceases at the step of diacetyl hexaazaisowurtzitane product formation [34].

Table 5 TADBIW yield in HBIW debenzylation depending on reaction temperature

Catalyst	$d_{Pd}{}^a$, nm	V^a, mole H_2/(mole HBIW·h)		TADBIW yield[b], mass %	
		25 °C	50 °C	25 °C	50 °C
ICT-3-23[c]	5.0	1.0	3.2	56	80
6 mass % Pd/Sibunit					
E101 NE/W[c]	6.0	1.5	3.3	61	80
10 mass % Pd/C					
K-IVa	3.0	1.5	3.7	82	0
K-VIII	1.8	–	3.8	86	0

[a]Average size of palladium particles

[b]Reaction conditions: 3.4 g HBIW, 0.34 g catalyst, 5 mL Ac_2O, 0.06 mL PhBr, 10 mL DMF, PH_2 4 bar, V – the rate of hydrogen uptake

[c]Commercially available catalyst

7　Effect of Reaction Temperature on the Pd/C Activity and Selectivity

Unlike the earlier known prototypes of the catalysts, namely, Pd (10 %)/C (E101 NE/W, Degussa), Pd (20 %) $(OH)_2$/C (Pearlman's catalyst), and Pd (6 %)/C (ICT-3-23), debenzylation on the Pd (4–10 %)/Sibunit catalyst prepared by Koskin et al. [34] should be carried out at room temperature. Even an insignificant rise of the reaction temperature to 40–50 °C resulted in a substantial decrease in the selectivity of C–N bond hydrogenolysis and the yield of the target product. At the same time, activity of the mentioned catalysts is insufficient for debenzylation to occur at room temperature. Presumably the difference observed in the properties of the catalysts resulted from the differences in the sizes of the metal Pd clusters in the self-prepared catalyst samples compared to the known prototypes. According to TEM data, metal particles of 3 nm are predominant in Pd (6 %)/Sibunit catalyst, whereas 6-nm particles prevail in Pd (10 %)/C (Degussa) (Table 5). The activity of the Pd/C catalysts increases with a decrease in the average particle size and, hence, with an increase in the active surface area; however, their selectivity in C–N bond hydrogenolysis decreases. A possibility to perform the process at lower (room) temperature has several advantages, the main of which is a partial suppression of the hexaazaisowurtzitane framework destruction which occurs at elevated temperatures.

Analysis of the literature data and the own experimental work of the authors indicate that the catalyst/HBIW ratio, Pd dispersion, temperature, H_2 pressure, Ac_2O/HBIW, and Ac_2O/BrPh ratios are the key factors influencing the TADBIW yield. Recently Bayat et al. [26] (Fig. 13) applied a central composite design (CCD) to optimize four parameters, the catalyst to HBIW percent, Ac_2O/HBIW molar ratio, temperature and hydrogen pressure in HBIW->TADBIW reaction over 12.5 % Pd$(OH)_2$/C. The values of parameters deviated around the experimental data reported by Parmon and co-workers [33]. Increasing the reaction temperature up to 48 °C resulted in an increase in the reaction efficiency, but further enhancement of
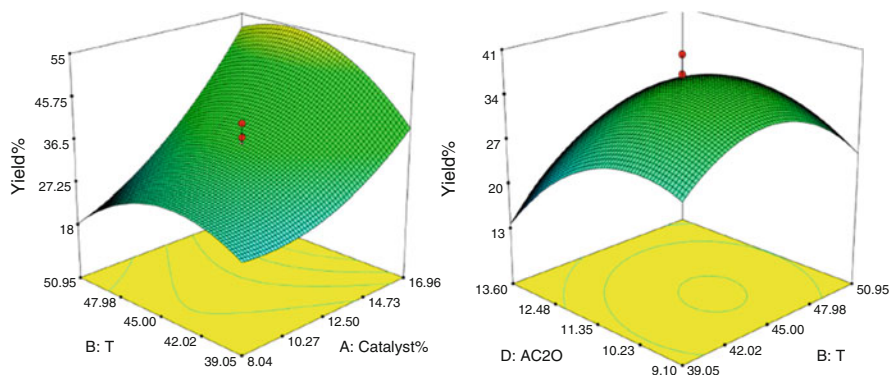
Fig. 13 Three-dimensional response surface for TADBIW yield as a function of catalyst/HBIW percent (**a**) and temperature (**b**) (Ac$_2$O/HBIW = 11.4) (*left*); temperature (**b**) Ac$_2$O/HBIW (D) (catalyst/HBIW percent = 12.5) (*right*) [26]

the reaction temperature caused slight damage of HBIW or activated other reaction pathways. Catalyst percent was found to be the most significant factor, that was not surprising since much more active sites for the substrate appeared and, therefore, the probability of the reaction proceeding enhanced (Fig. 13).

8   Upscaling TADFIW Catalytic Synthesis

Industrial production processes of HNIW with a capacity of 5–100 ton per year are required for solving important practical problems [1]. With respect to implementation of the HNIW industrial production, Sysolyatin and co-workers considered the scope and limitations of the HBIW catalytic process. Although the repeated use of the palladium catalyst in two steps of HBIW debenzylation–acylation has been patented [40], a lot of results obtained indicated that the Pd/C catalyst is deactivated very fast during the first step of the debenzylation process. Thus, in the second catalyst cycle, the TADBIW yield considerably decreases approaching subsequently zero. A suggested method for increasing stability of palladium metal particles in Pd/C via introduction of a stabilizing element into the catalytic system [33] or application of bimetallic systems [36] allowed to increase the resistance of the catalyst to deactivation and prolong the catalyst life. Such approaches might require adaptation in the case of scaling-up. Assuming that the use of the catalyst only in one debenzylation step stabilizes the catalyst operation, a process scheme with a separate use of the Pd/Sibunit catalyst was proposed (Fig. 14) [1, 59].

Optimal reaction conditions provide a possibility of a repeated use of the catalyst containing ∼6 % palladium in the first debenzylation step (HBIW ->TADBIW) (Fig. 15) [1]. The second debenzylation step is less sensitive to palladium dispersion
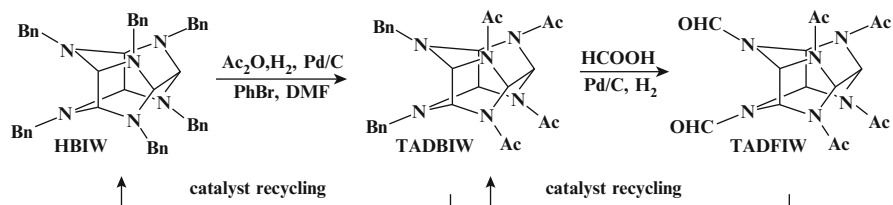
Fig. 14 Scheme of TADFIW synthesis with repeated use of Pd/C catalyst separately on stage 1 (HBIW->TADBIW) and stage 2 (TADBIW->TADFIW) (Adapted from [1])
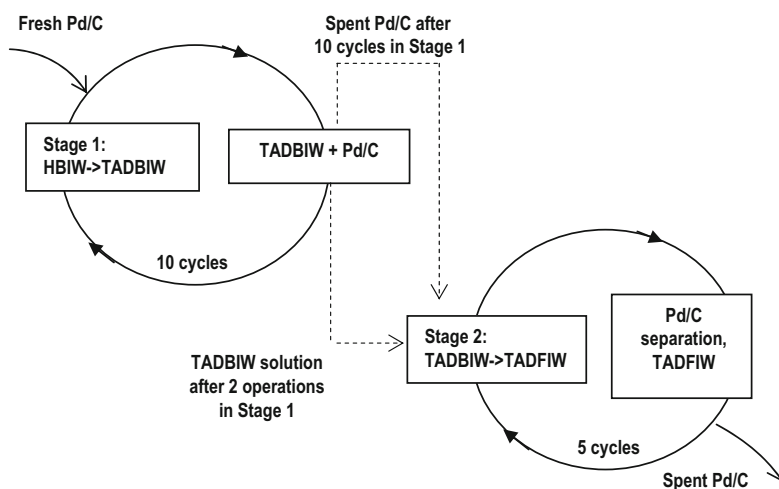
Fig. 15 Scheme of TADFIW synthesis with a repeated use of Pd/C catalyst in stage 1 HBIW->TADBIW and stage 2 TADBIW->TADFIW: (stage 1) Pd/C catalyst was regenerated by washing before recycling, TADBIW was diluted in a mixture of formic and acetic acids, and (stage 2) TADFIW was isolated (Adapted from [1])

[34]. When the process employed the reused catalyst, the TADFIW yield decreased noticeably only in the 14th cycle [1]. Moreover the catalyst that has already served for ten cycles in the first step was able to perform seven more cycles in the second step giving TADFIW with yields 84–85 %. In order to eliminate the step of crystalline TADBIW isolation from the acetic acid solution the second debenzylation step was proposed to be carried out in a mixture of formic and acetic acids [60]. Two-step HBIW debenzylation with a separately repeated use of the catalyst in each catalytic stage was proposed (Fig. 15) [1]. The average product yields in steps 1 and 2 were 80 % and 84 %, respectively, yielding 16.6 g TADFIW/g of catalyst, which is much larger than the values reported by Ananikov et al. [1].

9 Conclusions

As a result of the significant economic relevance of palladium-based catalysts for conversion of HBIW into CL-20 many studies have been performed to elucidate the physico-chemical properties of these materials in more detail and to reveal the various reasons for the loss of activity or selectivity under unfavorable or irregular operation conditions. Using modern methods of analysis, the optimal dispersion of Pd catalyst was established for HBIW debenzylation. It was shown that in the two-step catalytic debenzylation the decrease in the Pd/C activity occurs mainly due to agglomeration of metal particles, Pd re-deposition on inaccessible inner areas of the carbon support and blocking of the metallic palladium with by-products of intermediates destruction. This article shows a possibility to enhance Pd/C catalytic activity through an improvement of Pd dispersion, resistance to re-dissolution–deposition as well as to oxidation, increasing accessibility of the active sites for large HBIW molecules. Based on the current extensive research the two-step HBIW debenzylation with a separately repeated use of the catalyst in each catalytic stage was considered as a promising way to increase catalyst productivity and to reduce CL-20 production costs. However, novel synthetic routes to CL-20 significantly reducing the production costs are of great interest.

References

1. Ananikov VP, Khemchyan LL, Ivanova YV, Bukhtiyarov VI, Sorokin AM, Prosvirin IP, Vatsadze SZ, Medved'ko AV, Nuriev VN, Dilman AD, Levin VV, Koptyug IV, Kovtunov KV, Zhivonitko VV, Likholobov VA, Romanenko AV, Simonov PA, Nenajdenko VG, Shmatova OI, Muzalevskiy VM, Nechaev MS, Asachenko AF, Morozov OS, Dzhevakov PB, Osipov SN, Vorobyeva DV, Topchiy MA, Zotova MA, Ponomarenko SA, Borshchev OV, Luponosov YN, Rempel AA, Valeeva AA, Stakheev AY, Turova OV, Mashkovsky IS, Sysolyatin SV, Malykhin VV, Bukhtiyarova GA, Terent'ev AO, Krylov IB (2014) Development of new methods in modern selective organic synthesis: preparation of functionalized molecules with atomic precision. Russ Chem Rev 83:885–985. doi:10.1070/RC2014v83n10ABEH004471
2. Singh H (2005) Current trend of R&D in the field of high energy materials (HEMs): an overview. Explosion 15:120–132
3. Simpson RL, Urtiew PA, Ornellas DL, Moody GL, Scribner KJ, Hoffman DM (1997) CL-20 performance exceeds that of HMX and its sensitivity is moderate. Propellants Explos Pyrotechnics 22:249–255. doi:10.1002/prep.19970220502
4. Bumpus JA (2012) A theoretical investigation of the ring strain energy, destabilization energy, and heat of formation of CL-20. Adv Phys Chem. doi:10.1155/2012/175146, Article ID 175146, 7 pages
5. http://www.gizmag.com/cl-20-high-power-military-explosive/24059/
6. Willer RL (2013) The early history of CL-20 (HNIW). New trends in research of energetic materials, Czech Republic, pp 384–397
7. Nair UR, Sivabalan R, Gore GM, Geetha M, Asthana SN, Singh H (2005) Hexanitrohexaaza-isowurtzitane (CL-20) and CL-20-based formulations: a review. Combus Explo Shock Waves 41:121–132. doi:10.1007/s10573-005-0014-2

8. Sysolyatin SV, Lobanova AA, Chernikova YT, Sakovich GV (2005) Methods of synthesis and properties of hexanitrohexaazaisowurtzitane. Russ Chem Rev 74:757–764. doi:10.1070/RC2005v074n08ABEH001179

9. Sysolyatin SV, Sakovich GV, Surmachev VN (2007) Methods for the synthesis of polycyclic nitramines. Russ Chem Rev 76:673–680. doi:10.1070/RC2007v076n07ABEH003716

10. Nielsen AT (1997) Caged polynitramine compound. US Patent 5,693,794, 2 Dec 1997

11. Bellamy AJ (1995) Reductive debenzylation of hexabenzylhexaazaisowurtzitane. Tetrahedron Lett 51:4711–4722. doi:10.1016/0040-4020(95)00155-2

12. Nielsen AT, Chafin AP, Christian SL, Moore DW, Nadler MP, Nissan RA, Vanderah DJ (1998) Synthesis of polyazapolycyclic caged polynitramines. Tetrahedron 54:11793–11812. doi:10.1016/S0040-4020(98)83040-8

13. Nielsen AT, Nissan RA, Vanderah DJ, Coon CL, Gilardi RD, George CF, Flippen-Andersen JL (1990) Polyazapolycyclics by condensation of aldehydes with amines. Formation of 2,4,6,8,10,12-hexabenzyl-2,4,6,8,10,12-[5.5.0.0$^{3.11}$.0$^{5.9}$]dodecanes from glyoxal and benzylamines. J Org Chem 55:1459–1466. doi:10.1021/jo00292a015

14. Nielsen AT, Nissan RA, Chafin AP, Gilardi RD, George CF (1992) Polyazapolycyclics by condensation of aldehydes with amines. 3. Formation of 2,4,6,8-tetrabenzyl-2,4,6,8-tetraazabicyclo[3.3.0]octanes from formaldehyde, glyoxal, and benzyl amine. J Org Chem 57:6756–6759. doi:10.1021/jo00051a016

15. Wang C, Ou Y, Chen B (2000) One-pot synthesis of hexanitrohexaazaisowurtzitane. Beijing Ligong Daxue Xuebao Trans Beijing Inst Technol 20:521–523

16. Latypov NV, Wellmar U, Goede P, Bellamy AJ (2000) Synthesis and scale-up of 2,4,6,8,10,12-hexanitro-2,4,6,8,10,12-hexaazaisowurtzitane from 2,6,8,12-tetraacetyl-4,10-dibenzyl-2,4,6,8,10,12-hexaazaisowurtzitane (HNIW, CL-20). J Org Process Res Dev 4:156–158. doi:10.1021/op990097d

17. Geetha M, Nair UR, Sarwade DB, Gore GM, Asthana SN, Singh H (2003) Studies on CL-20: the most powerful high energy material. J Therm Anal Calorim 73:913–922. doi:10.1023/A:1025859203860

18. Sanderson AJ, Wardle RB, Warner KF (2000) Process for making 2,4,6, 8,10,12- hexanitro-2,4,6,8,10, 12- hexaazatetracyclo [5.5.0.0$^{5.9}$·0$^{3.11}$]-dodecane. WO2000052011 8 Sep 2000

19. Kawabe S, Miya H, Kodama T, Miyake N (1998) Process for the preparation of hexanitrohexaazaisowurtzitanes. PCT Int. Appl. WO 9805666 12 Feb 1998

20. Zhenhua M, Hua Q, Lü C (2013) Nitration of TAIW to synthesize CL-20 using N_2O_5/HNO_3 as nitrating agent. Rasayan J Chem 6:29–33

21. Chung HY, Kil HS, Choi IY, Chu CK, Lee IM (2009) New precursors for hexanitrohexaazaisowurtzitane (HNIW, CL-20). J Heterocycl Chem 37:1647–1649. doi:10.1002/jhet.5570370640

22. Chen JP, Penquite CR, Thakur DS (2001) Precious metal catalyst for debenzylation. US Patent 6,992,037, 31 Jan 2006

23. Cagnon G, Eck G, Herve G, Jacob G (2007) Process for the 2-stage synthesis of hexanitrohexaazaisowurtzitane starting from a primary amine. US Patent 7,279,572, 9 Oct 2007

24. Chapman RD, Hollins RA (2008) Benzylamine-free, heavy-metal-free synthesis of CL-20 via hexa(1-propenyl)hexaazaisowurtzitane. J Energetic Mater 26:246–273. doi:10.1080/07370650802182385

25. Mandal K, Pant CS, Kasar SM, Soman T (2009) Process optimization for synthesis of CL-20. J Energetic Mater 27:231–246. doi:10.1080/07370650902732956

26. Bayat Y, Ebrahimi H, Fotouhi-Far F (2012) Optimization of reductive debenzylation of hexabenzylhexaazaisowurtzitane (the key step for synthesis of HNIW) using response surface methodology. Org Process Res Dev 16:1733–1738. doi:10.1021/op300162d

27. Aldoshin SM, Aliev ZG, Goncharov TK, Korchagin DV, Milekhin YM, Shishov NI (2011) New conformer of 2,4,6,8,10,12-hexanitro-2,4,6,8,10,12-hexaazaisowurtzitane (CL-20). Crystal and molecular structures of the CL-20 solvate with glyceryl triacetate. Russ Chem Bull 60:1394–1400. doi:10.1007/s11172-011-0209-5

28. Lapina YT, Lobanova AA, Savitskii SA, Zolotuxina II, Kireeva AV (2012) Method of synthesis of gamma-polymorphous modification 2,4,6, 8,10,12- hexanitro- 2,4,6,8,10,12-hexaazatetracyclo [5.5.0.0$^{5.9.}$0$^{3.11}$]-dodecane. RU Patent 2,447,075, 10 Apr 2012
29. Kodama T, Ishihara N, Minoura H, Miyake N, Yamamatsu S (2002) Method of acylating of hexakis(phenylmethyl)hexaazaizowurtzitane. WO 99/19328. RU Patent 2,182,151, 10 May 2002
30. Kozlov AI, Zbarskii VL, Ignatov AV, Pinchuk YA, Kuznetsov LA, Merkin AA, Komarov AA, Rybin VE, Mikhailov YM, Mizgunova EN, Vidyaeva TI (2012) Method of preparation of substituted hexaazaizowurtzitane. RU Patent 2,451,020, 20 Apr 2012
31. Kozlov AI, Zbarskii VL, Grunskii VN, Yudin NV, Kuznetsov LA, Merkin AA, Komarov AA, Kozlov IA, Rybin VE., Mikhailov YM, Mizgunova EN, Vidyaeva TI (2012) Method of debenzylation of 2,6,8,12-tetraacetyl-2,4,6,8,10,12-hexaazaisowurtzitane. RU Patent 2,448,110, 20 May 2012
32. Bernotas RC, Cube RV (1990) The use of Pearlman's catalyst for selective N-debenzylation in the presence of benzyl ethers. Synth Commun 20:1209–1212
33. Koskin AP, Simakova IL, Parmon VN (2007) Study of the palladium catalyst deactivation in synthesis of 4,10-diformyl-2,6,8,12-tetraacetyl-2,4,6,8,10,12-hexaazaisowurtzitane. React Kinet Cat Lett 92:293–302. doi:10.1007/s11144-007-5203-4
34. Koskin AP, Simakova IL, Parmon VN (2007) Reductive debenzylation of hexabenzylhexaaza-isowurtzitane – the key step of the synthesis of polycyclic nitramine hexanitrohexaazaisowurtz-itane. Russ Chem Bull 56:2370–2375. doi:10.1007/s11172-007-0377-5
35. Simakova IL, Prosvirin IP, Kriventsov VV, Parmon VN (2012) The effect of preparation conditions on the catalytic and physical-chemical properties of Pd/C in reductive debenzylation of hexabenzylhexaazaisowurtzitane. J Siber Fed Univ Chem 3:238–245 (Rus, abstr. Engl.)
36. Koskin AP, Simakova IL, Troitskii SY, Parmon VN (2009). The catalyst, its preparation and process for preparing tetraacetyldiformylhexaazaisowurtzitane. RU Patent 2,359,753, 27 June 2009
37. Toebes ML, van Dillen JA, de Jong KP (2001) Synthesis of supported palladium catalysts. J Mol Cat A Chem 173:75–98. doi:10.1016/S1381-1169(01)00146-7
38. Kent R, Evans R (1972) Carbon supported palladium catalyst. US Patent 3,804,779, 16 Apr 1974
39. Norris WP, Nielsen AT (1994) Calalitic synthesis of caged polynitramine compounds. US Patent 8,017,768, 1 Sep 2011
40. Wardle RB, Edwards WW (1995) Rapidly adding hydrogen immediately upon adding acetic anhydride and palladium catalyst to reaction mixture of hexabenzylhexaazaisowurtzitane (HBIW), cosolvent, and bromine source; by-product inhibition, simplification. US Patent 5,739,325, 14 Apr 1998
41. Simakova OA, Simonov PA, Romanenko AV, Simakova IL (2008) Preparation of Pd/C catalysts via deposition of palladium hydroxide onto sibunit carbon and their application to partial hydrogenation of rapeseed oil. React Kinet Catal Lett 95:3–12. doi:10.1007/s11144-008-5373-8
42. Semikolenov VA, Lavrenko SP, Zaikovskii VI (1994) Development of supported palladium particles in Pd/C catalysts. Kinet Catal 35:573–576
43. Maki-Arvela P, Kuusisto J, Sevilla EM, Simakova IL, Mikkola J-P, Myllyoja J, Salmi T, Murzin DY (2008) Catalytic hydrogenation of linoleic acid to stearic acid over different Pd- and Ru-supported catalysts. Appl Catal A Gen 345:201–212. doi:10.1016/j.apcata.2008.04.042
44. Simakova IL, Parmon VN (2013) Synthesis of 4,10-diformyl-2,6,8,12-tetraacetyl-2,4,6,8,10,12-hexaazaisowurtzitane over palladium on carbon. In: Abstracts of the 10th congress on catalysis applied to fine chemicals, Abo Akademi University, Turku/Abo, June 16–19, p 68
45. Albers P, Pietsch J, Parker SF (2001) Poisoning and deactivation of palladium catalysts. J Mol Catal A Chem 173:275–286. doi:10.1016/S1381-1169(01)00154-6

46. Simakova IL, Prosvirin IP, Parmon VN (2013) The insight on 4,10-diformyl-2,6,8,12-tetraacetyl-2,4,6,8,10,12-hexaazaisowurtzitane synthesis over colloidal Pd/C. In: Abstracts of the 9th high energy materials workshop, Institute of space and astronautical science/Japan aerospace exploration agency, October 7–9, O-61, pp 138–139

47. Blaser H-U, Indolese A, Schnyder A, Steiner H, Studer M (2001) Supported palladium catalysts for fine chemicals synthesis. J Mol Catal A Chem 173:3–18. doi:10.1016/S1381-1169(01)00143-1

48. Gurrath M, Kuretzky T, Boehm HP, Okhlopkova LB, Lisitsyn AS, Likholobov VA (2000) Palladium catalysts on activated carbon supports: influence of reduction temperature, origin of the support and pretreatments of the carbon surface. Carbon 38:1241–1255. doi:10.1016/S0008-6223(00)00026-9

49. Simonov PA, Troitskii SY, Likholobov VA (2000) Preparation of the Pd/C Catalysts: a molecular-level study of active site formation. Kinet Catal 41:255–269. doi:10.1007/BF02771428

50. Wardle RB, Hinshaw JC (1992) Method for making new polycyclic polyamides as precursors for energetic polycyclic polynitramine oxidizers. US Patent 6,147,209, 14 Nov 2000

51. Kovács E, Thurner A, Farkas F, Faigl F, Hegedűs L (2014) Hydrogenolysis of N- and O-protected hydroxyazetidines over palladium: efficient and selective methods for ring opening and deprotecting reactions. J Mol Catal A Chem 395:217–224. doi:10.1016/j.molcata.2014.08.027

52. Maxted EB, Biggs MS (1957) 764. The catalytic toxicity of nitrogen compounds. Part I. Toxicity of ammonia and of amines. J Chem Soc 3844–3847. doi:10.1039/JR9570003844

53. Hegedűs L, Máthé T (2002) Hydrogenation of pyrrole derivatives. Part V. Poisoning effect of nitrogen on precious metal on carbon catalysts. Appl Catal A Gen 226:319–322. doi:10.1016/S0926-860X(01)00898-5

54. Studer M, Blaser H-U (1996) Influence of catalyst type, solvent, acid and base on the selectivity and rate in the catalytic debenzylation of 4-chloro-N, N-dibenzylaniline with Pd/C and H2. J Mol Catal A Chem 112:437–445. doi:10.1016/1381-1169(96)00151-3

55. Simakova IL, Rozmysłowicz B, Simakova O, Mäki-Arvela P, Simakov A, Murzin DY (2011) Catalytic deoxygenation of C18 fatty acids over mesoporous Pd/C catalyst for synthesis of biofuels. Top Catal 54:460–466. doi:10.1007/s11244-011-9608-y

56. Snåre M, Mäki-Arvela P, Simakova IL, Myllyoja J, Murzin DY (2009) Overview of the catalytic methods of next generation biodiesel production from natural oils and fats. Russ J Phys Chem B 3:17–25. doi:10.1134/S1990793109070021

57. Madsen AT, Rozmyszowicz B, Simakova IL, Kilpio T, Leino A-R, Kordás K, Eränen K, Mäki-Arvela P, Murzin DY (2011) Step changes and deactivation behavior in the continuous decarboxylation of stearic acid. Ind Eng Chem Res 50:11049–11058. doi:10.1021/ie201273n

58. Nishimura S (2001) Handbook of heterogeneous catalytic hydrogenation for organic synthesis. Wiley, New York

59. Sysolyatin SV, Kalashnikov AI, Malykhin VV, Surmacheva IA, Sakovich GV (2010) Reductive debenzylation of 2,4,6,8,10,12-hexaazaisqwurtzitane. Int J Energ Mater Chem Propuls 9:365–375. doi:10.1615/IntJEnergeticMaterialsChemProp.v9.i4.60

60. Kalashnikov AI, Sysolyatin SV, Sakovich GV, Surmacheva IA, Surmachev VN, Lapina YT (2009) Debenzylation of 2,6,8,12-tetraacetyl-4,10-dibenzyl-2,4,6,8,10,12-hexaazatetracyclo[5.5.0.0^{3,11}0^{5,9}]dodecane. Russ Chem Bull 58:2164–2168. doi:10.1007/s11172-009-0295-9

Part VIII
Life-Cycle Management of Energetic Materials

Ageing, Hazards, Impact, Disposal, and Remediation

Environmental Aspects of Energetic Materials Use and Disposal

Adam S. Cumming

Abstract Management of the environment is an important part of the legal frameworks in most nations. Defense and space are not exempt from the impact of this. Therefore, work is in progress on greener technology for all aspects involving explosives and propellants.

The problem of minimizing environmental impact is often defined with reference to new materials; new ingredients that appear to offer a way to reduce the impact of a system and provide ways of making a greener munition. However, new materials are less well understood, and therefore, the risks they may pose may in reality be greater than those of existing materials and they can therefore offer an illusion of compliance. Toxicity estimation is therefore a significant requirement to manage such risks.

Further, any attempt to manage the impact requires an understanding of the whole life of the system, which is a part of Whole Life Assessment (WLA). Life Cycle Analysis (LCA) is therefore a critical part of future approaches to environmental management. However, much of that data is missing though may be intelligently estimated, though any estimation needs to be critically reviewed and updated.

This understanding complements on that performance and vulnerability and contributes to the development of a true whole life cost approach. The lines of research and the present state of the art for environmental management are outlined.

1 Introduction

Over the last 20 years, there has been increasing concern over the environment and the impact human activities are having on it. Munitions are not exempt from this with major concerns over energetics use and the residues left from activities [1–5]. These activities include:

1. Manufacture of the ingredients and components
2. Storage and transport of the complete system throughout its life

A.S. Cumming (✉)
School of Chemistry, University of Edinburgh, Edinburgh EH9 3FJ, UK
e-mail: adam.cumming@btinternet.com

3. Warfare – use in active engagement
4. Training – the controlled use of materials on ranges
5. Disposal – effective dismantling and disposal at the end of life or of residues after use

Legislation, both national and international [6], is increasing the pressure on government ministries to demonstrate a responsible attitude and policy over the environment. The North Atlantic Treaty Organization (NATO) and others are attempting to develop an understanding of the problems and seeking to provide tools for their assessment and management.

One of the approaches is to seek ways of producing greener systems such as "green munitions." Green munitions are those that have a minimal impact on the environment which includes manufacture through life use and disposal. This is therefore a part of the system management through Whole Life Assessment (WLA). It is not limited to energetics but covers all aspects of the energetic system. This requires that contamination by energetic materials be understood and managed. It does include the ability to recycle materials, including energetic materials.

2   Risks and Approaches

One example of risk concerns smoke from rocket motor exhausts – all smoke must be assumed to be a potential threat, but the questions remains of how much of a threat does it pose? It is often acidic (e.g., hydrogen chloride), whose damage is visible but can also include other species equally damaging even though invisible. Examples of these include potentially toxic hydrocarbons and nitrogenous species, and examples are shown in Figs. 1 and 2.

Fig. 1 Example of smoke from shoulder-launched missile

Fig. 2 Example of smoke from vehicle-launched missile

Fig. 3 Experimental firings. The motor firing on the left is a typical composite motor, while that on the right is an experimental composition of the same performance, but smokeless. This was part of a multinational program involving the United Kingdom, France, Germany, and the United States [7]

Smoke reduction is one research priority, though not normally for environmental reasons. Toxicity and contamination is considered particularly for large motors such as boosters, though examples such as that above may produce more immediate human risks.

One example of research output is shown in Fig. 3 with a visual comparison of an experimental sustain composite motor and a typical service composite motor. It involved joint studies on the formulation and testing of a smokeless propellant for tactical systems. The aim was proof of principle, but environmental issues did not play a major part in the study. It has interesting aspects, however, as elimination of acid smoke has been a first target for environmental improvement for the United States and other environmental agencies.

The experimental composition was intended to demonstrate the possible performance and vulnerability of new materials while also producing smokeless performance. This was the totality of the environmental assessment undertaken and was considered adequate at the time. Figure 4 illustrates that the visible smoke is
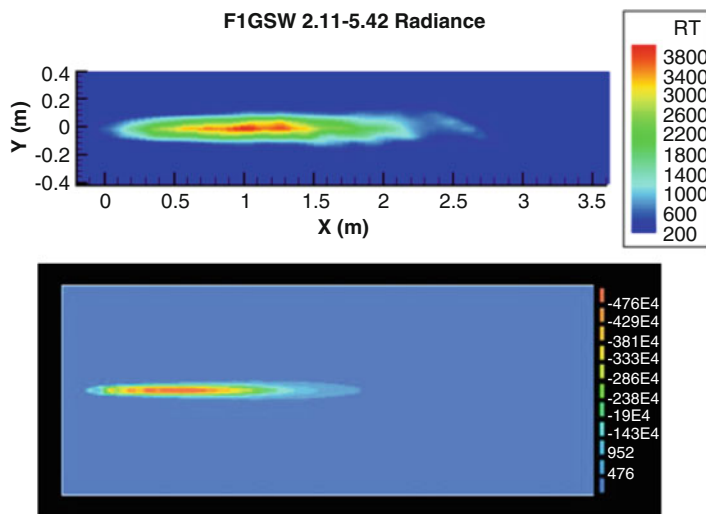
Fig. 4 Measured and predicted short-wave IR emissions indicating that smoke is merely one characteristic of performance

Table 1 Experimental smokeless composition

Energetic solid	Ammonium nitrate, CL20, GZT 24
Binder	PolyGLYN
Plasticiser	TMETN/BTTN

only part of the emission. The composition assessed in the program is given in Table 1. Interestingly, even though it contained CL20, it was, at the time, classed as UN 1.3. Most CL20-containing systems have been classed as UN 1.1.

This performance demonstrates some improvement in many ways, but there will be other products which may be just as hazardous as the eliminated smoke. In some ways, an invisible product (e.g., HCN) can be more hazardous. Therefore, there is a need for clear demonstration of safety and proven ways of assessing true impact. This needs examination and experimental proof.

The conclusion from these types of assessments is that simple answers, such as assessment of smoke content as a measure of environmental impact can be incomplete, and it is clear that assumptions need testing before acceptance. These are the constraints that must be addressed, and while some methods do exist this is an area which requires work.

3 Legislative Impact and Greener Energetic Systems

The activities of the US Environmental Protection Agency and the European Union [6] have focussed on minimizing environmental impact. In the EU, legislation for the control of chemicals is being introduced. Therefore, changing public perception

and new legislation means that the environmental impact of munitions and their ingredients cannot be ignored. We require understanding of the problems if they are to be dealt with simply:

1. What is the impact of manufacturing processes as presently used and how may they be improved? Are there alternatives available or likely to become available?
2. What is the effect of use – on humans and on the environment?
   What are the toxicity effects in handling and use?
   What are the effects on land and managing contamination?
3. Are there disposal techniques available using safe methods?
4. Can improved disposal methods be devised?

Research is therefore in progress to understand the impact and behavior of materials and to look for both new materials made safely and new versions of existing materials with reduced environmental impact. These are "Greener Energetics."

A further requirement is for tools to assess and deal with human and environmental damage. Test ranges are often contaminated with "hotspots" corresponding to areas of intense activity. These can often contain unexpected materials deposited over many years and include historical species no longer acceptable. Understanding of the persistence of materials, their decomposition pathways, and metabolic impact on plants, animals, and insects is needed in order to assess the position and manage it.

It is clear from examining the published literature that no one nation has all the answers and that no one nation has unique problems. While legal requirements do vary, there are common themes affecting all.

There is active research and development ongoing in the United States under the Strategic Environmental R&D Program, SERDP, a joint approach between Dept. of Defense, Dept. of Energy, and the Environmental Protection Agency. The European Defence Agency (EDA) and NATO (within the Science and Technology Organization) have also sponsored research.

4   NATO Studies on Energetics and the Environment

Several activities have been completed or are in progress. Some have been openly reported (8), but others may be available and/or subject to approval.

AVT 115 – Environmental Impact of Munition and Propellant Disposal – Study completed in 2009 and reported as an open document [8]

AVT 177 – Symposium in Edinburgh 2011 – Munition and Propellant Disposal and its Impact on the Environment

AVT 179 – Design for Disposal of Present and Future Munitions and Application of Greener Munition Technology (Completed 2013)

AVT 197 – Munitions Related Contamination – Source Characterization, Fate, and Transport (2012–2014)

The study which was reviewed and discussed widely produced the following conclusions [8]:

- Open Burning Open Demolition (OB/OD) is not generally acceptable, though there are dissenting opinions and the use of amelioration technology is possible.
- Forensic studies have shown that residues do remain after detonation – these are used as court evidence. Whether these are meaningful in contamination terms needs discussion and examination.
- Technology exists for most current problems – current systems can generally be dealt with, though accidental failures or articles later discovered may need special treatment, and pyrotechnics can pose significant problems.
- Technology and needs are separated in many cases – e.g., the United States has technology/information and it is needed in, for example, parts of Asia.
- Availability of surplus systems must be considered as a target for terrorists as an easy source of materials.

There are therefore good safety and security reasons for dealing promptly with disposal. It should be added that next-generation compositions, while being intrinsically safer to handle, appear to pose disposal problems since existing tools fail to deal with them as effectively as would have been expected [9–14]. This is an area only now developing with detailed assessments being undertaken of new less sensitive energetics.

4.1 Studies on Greener Munitions and Motors

One of the areas identified for further immediate action within NATO was that of Greener Munitions. This formed the basis of a further study. Parts of the report are available and have been published. At the outset of this study, the group identified several key issues that appeared to need examination:

1. Ingredients
2. Manufacturing
3. Use
4. Whole Life Cycle Management
5. Disposal
6. Impact on Environment

It became clear during the early stages of the study that the concept of greener munitions is far from simple. Not only are the individual aspects more complex, but their interactions are important and equally complex.

As a result, it must be treated as a systems concept. Unfortunately, in attempting to use life cycle analysis tools, it was apparent that a considerable amount of necessary data was unavailable. Collection and verification of these data is essential to allow development of reasonable tools for management of the risks and to provide methods for the proper assessment of new or even existing materials.

Fig. 5 The LCA phases based on ISO 14040, 2006. A systematic approach to LCA indicating the links between topics
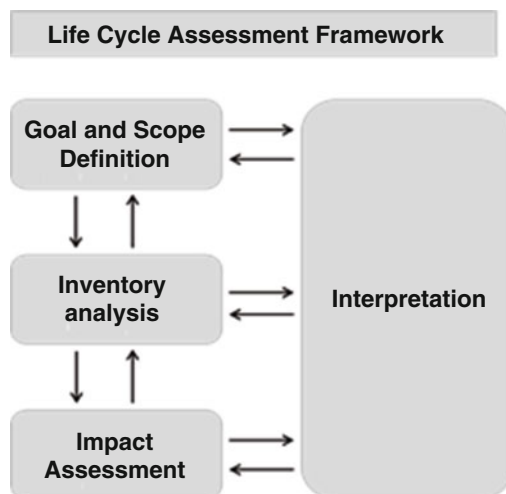
There is a general approach to Life Cycle Analysis (LCA) [15, 16], as shown in Fig. 5.

The areas that are considered during an LCA study include those listed in Fig. 6, drawn from the NATO Study of Greener Munitions.

The diagram (Fig. 7) below outlines the approach that has been developed in Canada as part of their program attempting a systematic approach to management of the whole area. The recently completed Revolutionary Insensitive, Green and Healthier Training Technology with Reduced Adverse Contamination Technical Demonstrator Program (TDP) RIGHTTRAC [17] included new materials, assessment, and range management. As Canada has worked on range contamination and management, often in partnership with the United States, it was a logical next step to move to examining a systems approach, looking at improved materials and assessing their environmental impact in use. As part of the program, a protocol was developed and is shown below. This attempted to capture the whole range of effects to ensure that a complete picture was obtained.

This is coupled to a risk-based approach as outlined below where the past, present, and future use is considered in the management plan (Fig. 8):

Toxicity testing takes time and effort and produces delays and expense in approving new materials for use. Failure to do this can have significant health impact, and so ways of approaching this are being worked on. The simple approach is by analogy, and databases are used to attempt this. However, there are uncertainties in this approach and modeling is being investigated to assist in rapid assessment [11, 15].

Modeling tools are being developed, partially by the pharmaceutical industry, in the use of Quantity Structure–Property Relationships (QPSR) approaches in order to predict properties [18]. These can be used to indicate bioactivity and hence estimate toxicity. Any such indication should reduce the testing and hence delays in introducing materials into use. It is important that they are used intelligently.

Activities – Mine and Process iron ore and copper, manufacture and process steel, and copper, transport steel, forging, machining, x-ray, manufacture and process zinc, assembly, manufacture explosives, seal ammo boxes **Aspects** – Use of energies and fuels, other material e.g. wood. Use of water etc.	**Activities** – Storage, transportation, Shell impacts with targets, Movement of OME teams, Movement of materials, Movement and disposal of packaging. **Aspects** – Fuel use, electricity, human effort, packaging, explosives.	**Activities** – Loading and unloading and transport, storage, incineration, landfill, burning, treating waste water, processing explosive slurry, recycling. **Aspects** – Fuel, electricity, chemical, oil, water, oil lubricant.
Manufacturing	**In-service**	**Disposal**
Activities – Mine and Process iron ore and copper, manufacture and process steel, and copper, transport steel, forging, machining, x-ray, manufacture and process zinc, assembly, manufacture explosives, seal ammo boxes, heat explosives **Aspects** – Emissions to air, explosive residue, noise, vibration, dust, waste water, emissions to air, heat, x-rays.	**Activities** – Storage, transportation, Shell impacts with targets, Movement of OME teams, Movement of materials, Movement and disposal of packaging. **Aspects** – Emissions to air, waste to landfill, damage to local terrain, noise, pressure, vibration, particulate left in ground.	**Activities** – loading and unloading and transport, storage, incineration, landfill, burning, treating waste water, processing explosive slurry, recycling, hot water wash-out. **Aspects** – Emissions to air, noise, hazardous and no-hazardous waste, contaminated water, vibration.

Fig. 6 Areas for consideration and management for LCA approach for a generic munition which covers both production and use (Courtesy NATO Study)

5   Land Contamination Management

Land gets contaminated by use [9, 10]. There is deposition from trials and tests as well as from impact and accidents. Often the use of ranges is poorly documented, and this is likely to be even more the case for battlefields. This is a prime source of contamination by hazardous materials, especially with incomplete functioning of the system.

As reactive chemicals, energetic materials will have an effect on biology. This can be useful with nitrate esters being used to manage heart conditions, but on ranges, it means that they can be bioavailable and therefore pose risks to health. For example, perchlorate (used as ammonium perchlorate in propulsion) is widely found and reported, particularly in the United States, and as a bioactive material has provoked a series of programs to understand its behavior. Naturally, this has

Fig. 7 Schematic of approach to the management of the environmental impact of energetic formulations, courtesy of Defence Research and Development Canada (DRDC)
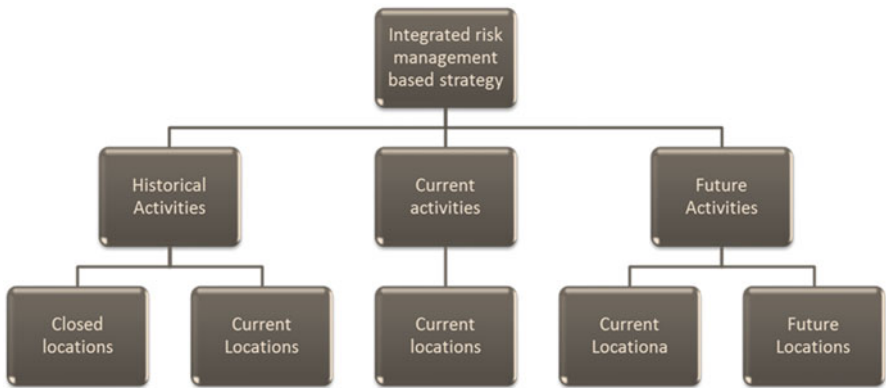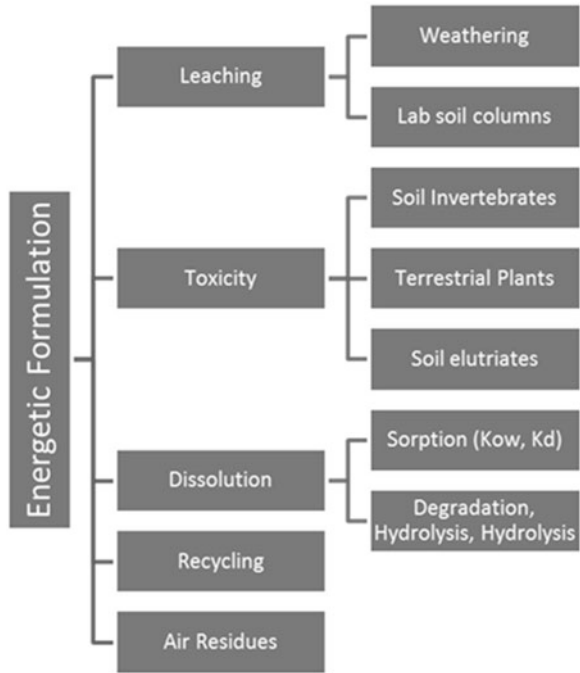
Fig. 8 Schematic for systematic planning, courtesy of DRDC

been extended to other energetic materials, with studies on behavior and retention in soil and water. The behavior depends on many factors including hydrogeology, soil structure, climate, and exposure. They all need consideration as do methods of assessing and managing any contamination.

Methods for destroying contamination include bacteria and plants [19, 20] as well as more traditional chemical methods. Programs on understanding the metabolism of energetics have been fairly successful and reported, with plants

engineered to digest energetics. This is a developing and important area, though it has been observed that energetics are not the preferred feedstock (other than ammonium nitrate) for bacteria as energetics have less energy than more normal feedstock. Therefore, there is an opportunity to the application of biotechnology for the improved biodisposal of contaminants.

As is mentioned elsewhere, new materials produce new problems as their behavior is not identical to those with which we have experience. The work on 2,4-dinitroanisole (DNAN) derivatives reported recently illustrates this [12–14].

As part of another multinational program, there was a detailed study of eco-toxicology and land contamination. This work, involving the United Kingdom, the United States, Canada, and Australia, was published as shown below in Fig. 9

Fig. 9 Illustration of published ecotoxicology text

[21, 22]. This publication marked the state of the art at the time, but requires updating on a regular basis to provide a measure of current understanding. However, the approach remains appropriate and the assessments and methods provide a sound basis for the necessary approach.

Recently, the final report for the study was declassified to assist others in their approach to range contamination management [21]. This provides a protocol for management of environmental impact. The report will be available on an open website (http://www.em-guidelines.org/docs.htm) along with earlier work.

6 Recycling

Recycling is often seen as a way of covering the costs of disposal. However, experience has shown that at best, it can be a disposal cost offset. Metal parts can be recycled once certified free of explosives and the recovered energetics can possibly be reused for civil and military applications.

Techniques such as supercritical fluid extraction or liquid ammonia extraction can produce recovered material which may be acceptable for use. However, a major drawback is the need to satisfy authorities of the consistency and safety of the recovered materials. These need to be demonstrated to be safe and that no contaminants remain which will prevent safe use. This adds significantly to the cost. However, not all nations see this as an issue. It is likely to become more common, especially with rare or expensive ingredients. It will require processes capable of producing a consistent product, or of making a consistent product from variable ingredients and hard evidence will be required to validate any such claims.

7 Design for Life

This probably offers the greatest possibilities for changing the environmental impact of an energetic system. It is the logical extension of the Canadian RIGHTTRAC approach [17]. However, it does demand that there is sufficient understanding of the various components and how they interact. Only with that understanding can a true system be designed.

It also allows for the proper design for optimum performance. It has been suggested that newer materials, designed for reduced sensitivity, do not deliver performance to the same level as more conventional systems [11–13]. It should be observed that this may be partially, if not completely, caused by failure to optimize the design for the new materials within the system. Assumptions that there is a "drop-in" replacement are naïve and require to be tested. This is one of the advantages of proper design, not just for disposal but for all aspects of the system life.

It will be necessary to ensure that the data and tools exist to:

1. Plan the use of specific materials, including choosing the best to meet the requirements. This means making choices among competing requirements and reaching an intelligent conclusion. It may also move to using the understanding to design materials to meet the requirement. Co-crystals may offer this option. Processing must be a part of this design [23].
2. Plan shelf life – optimizing this to meet the real requirements. Early destruction costs money and also reduces the likely impact on the environment. Delayed or overextended life introduces additional risks including those of environmental contamination.
3. Plan to open motors for disposal after removal from service – if this is difficult, then costs and risks rise. It is therefore important to plan and document this initially. Naturally, problems will arise, but these can be minimized with preparation.

These requirements all mean that it is necessary to plan the end of the system's life in the design phase. It also requires that systems planning for the future is essential, including ensuring that technical developments and options are reviewed. Promising options need assessment and investment. This will not be purely to meet environmental needs but also for other reasons and advantages. These will include performance, life, vulnerability, and power density.

It also means that changes in legislative and perception requirements also require review in order to prepare for changes that may be imposed and to grasp new opportunities.

8   Future Directions

Several directions are being actively pursued at present. Some will naturally prove to be more effective than others.

Research will continue on new or improved materials, but as has been shown, there are risks associated with that, so the tools are required for their assessment including prediction of toxicology as discussed above.

Methods for the handling of contamination will continue to develop including the use of biological systems for enhanced natural attenuation.

New methods for more efficient manufacture are being investigated [23, 24]. These are aimed at cost reduction through more efficient approaches which will also lessen the environmental impact. They can also offer routes to new forms of materials. One of these, Resonant Acoustic Mixing (RAM), appears to offer some major advantages for mixing: control of effluent and the ability to make new ingredients such as co-crystals effectively. A schematic of the mixing process is shown below (Fig. 10) and illustrates that novel approaches are being taken to provide new options. The level of publication is increasing, but there are several

Fig. 10 Schematic illustration of Resonant Acoustic Mixing technology
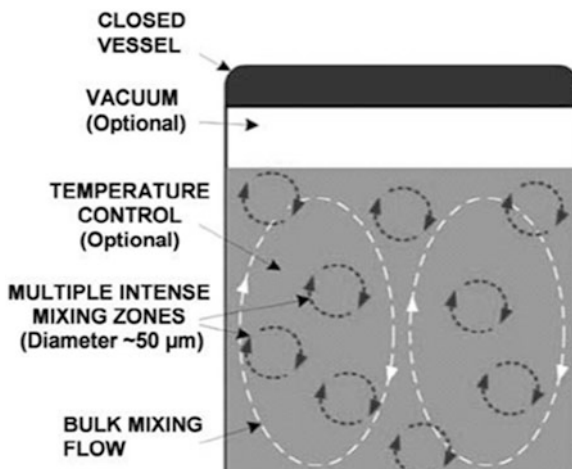
areas where research is needed to understand the process. These include temperature management and scalability.

It must be observed that this investment is not purely for environmental reasons but that it forms part of the perceived possible advantages of the technique. Any method that offers a range of advantages is more likely to be exploited and this is likely to be true for many of the options. It will be rare for environmental requirements to monopolize the approach.

9 Conclusions

Finally, it is clear that there are several ways to manage the potential environmental impact of energetic systems. Firstly, while it is not merely a matter of using new materials, they do offer sound options. However, they need to be understood well enough to deliver all the requirements placed upon them. This requires an understanding of likely toxicology and environmental and human impact as well as performance, aging, and vulnerability. Since value for money also needs consideration, it may be that better specified and understood versions of existing materials will be more rapidly and effectively employed.

New processes can reduce manufacturing impact. Many existing methods were designed when there was less understanding of the effects and new approaches can be more efficient with reduced cost.

One such novel approach is the use of RAM as outlined above, which seems to offer new options for manufacturing. Others such as twin screw extrusion also exist, allowing for the redesign of processes and for the development of new methods and materials for more effective use and management.

New range management methods avoid damage and remove old damage. This is not limited to test ranges but also for manufacturing plants and storage facilities.

Therefore, systems designed for life minimizes overall impact.

All activities described require the understanding of what is needed and also of the materials that we use! This means an intelligent assessment of the options with strengths and weaknesses. It also requires an understanding of what can be done within the constraints imposed. It is intelligent risk management, not risk avoidance. Risks will always exist but, if understood and gaged properly, can be accepted and managed properly.

Finally, environmental issues are increasing in importance and this is not likely to change. The direction and emphasis may alter and the materials may also change, but the constraint will remain. For example, reclamation and recycling may increase in importance.

While munitions and energetics are a very small part of environmental management, they cannot be ignored, and "Duty of Care" (good stewardship) requires that they are managed properly.

These constraints and requirements should be considered a major drive for research and a scientific and engineering challenge. They require:

1. New methods for analysis
2. New or re-engineered and well-characterized materials for use
3. New methods for disposal

This should be regarded as an opportunity and not a threat!

References

1. Proceedings of the NATO ARW on conversion concepts for commercial applications and disposal technologies of energetic systems, Moscow, May 1994
2. Cumming AS, Mostak P, Volk F (2001) Influence of sampling methodology and natural attenuation of analysis of explosives content in contaminated sites. 7th international symposium on the analysis and detection explosives, Edinburgh, July 2001
3. Branco PC, Schubert H, Campos J (2004) Defense industries: science and technology related to security – impact of conventional munitions on environment and population. NATO Science Series IV Earth and Environmental Sciences, vol 44, Kluwer (ARW in 2001)
4. Cumming AS (2008) Recent and current NATO RTO work on munitions disposal; new trends in research of energetic materials. In: Proceedings of 11th seminar pardubice, Czech Republic, Apr 2008
5. Ruppert WH et al. A history of environmentally sustainable energetics, 2010 insensitive munitions & energetic technology symposium, Munich
6. Regulation (EC) No 1907/2006 of the European Parliament and of the Council of 18 December 2006 concerning the Registration, Evaluation, Authorisation and Restriction of Chemicals (REACH), establishing a European Chemicals Agency. European Union, 2006
7. Cumming AS, et al (2007) Performance tests of next generation solid missile propellants; NDIA 2007 insensitive munitions and energetic materials technology symposium, Miami Oct 2007

8. RTO-TR-AVT-115 – environmental impact of munition and propellant disposal NATO RTO, open publication, 2010
9. Jenkins TF, Grant CL, Walsh ME, Thorne PG, Thiboutot S, Ampleman G, Ranney TA (1999) Coping with spatial heterogeneity effects on sampling and analysis at an HMX – contaminated antitank firing range. Field Anal Chem Technol 3(1):19–28
10. Thiboutot S. Characterisation of residues from the detonation of insensitive munitions, SERDP ER-2219. Available at www.serdp-estcp.org/Program-Areas/ Environmental-Restoration/Contaminants-on-Ranges/Characterizing-Fate-and-Transport/ER-2219/ER-2219
11. Lima DR, Bezerra ML, Neves EB, Moreira FR (2011) Impact of ammunition and military explosives on human health and the environment. Rev Environ Health 26(2):101–110
12. Walsh MR, Walsh ME, Taylor S, Ramsey CA, Ringelberg DA, Zufelt JE, Thiboutot S, Ampleman G, Diaz E (2013) Characterization of PAX-21 insensitive munition detonation residues. Propellants Explos Pyrotech 38:399–409
13. Walsh MR, Walsh ME, Ramsey CA, Thiboutot S, Ampleman G, Diaz E, Zufelt JE (2014) Energetic residues from the detonation of IMX-104 insensitive munitions. Propellants Explos Pyrotech 39:243–250
14. Walsh MR, Walsh ME, Poulin I, Taylor S, Douglas TA (2011) Energetic residues from the detonation of common US ordnance. Int J Energetic Mater Chem Propuls 10(2):169–186
15. Rosenbaum K, Bachmann M, Gold S, Huijbregts J, Jolliet O, Juraske R, Koehler A, Larsen F, MacLeod M, Margni M, McKone T, Payet J, Schuhmacher M, Meent D, Hauschild Z (2008) USEtox – the UNEP-SETAC toxicity model: recommended characterization factors for human toxicity and freshwater ecotoxicity in life-cycle impact assessment. Int J Life-Cycle Assess 13:532–546
16. Ferreira C, Ribeiro J, Mendes R, Freire F (2013) Life cycle assessment of ammunition demilitarisation in a static kiln. Propellants Explos Pyrotech 38:296–302
17. Brousseau P, Brochu S, Brassard M, Ampleman G, Thiboutot S, Côté F, Lussier L-S, Diaz E, Tanguay V, Poulin I (2010) RIGHTTRAC technology demonstration program: preliminary IM tests, 2010 insensitive munitions & energetic materials technical symposium, Munich, 11–14 Oct 2010
18. Schultz TW, Cronin MTD, Netzeva TI (2003) The present status of QSAR in toxicology. J Mol Struct (THEOCHEM) 622(1–2):23–38
19. Bruce NC (2011) Plant and microbial transformations of explosives, human and environmental toxicology of munitions-related compounds – from Cradle to Grave, TNO, Netherlands, 2011 Apr, Amsterdam
20. French CE, Binks PR, Bruce N, Clayton J, Cumming AS, Nicklin S (1998) Biodegradation of explosives by the bacterium Enerobacter Cloacae PB2 Proc of the 6th international symposium on analysis and detection of explosives Prague, July 1998
21. Brochu S, Williams LR, Johnson MS, Hawari J, Monteil-Rivera F, Sunahara G, Simini M, Kuperman RG, Eck WS, Checkai RT, Cumming AS, Doust E, Provatas A (2013) Assessing the potential environmental and human health consequences of energetic materials: a phased approach, TTCP WPN TP-4 CP 4-42, Final report, TTCP TR-WPN-TP04-15-2014, Dec 2013, DRDC Valcartier SL 2013-626
22. Sunahara G (2009) Ecotoxicology of explosives. Taylor & Francis, Boca Raton
23. am Ende DJ, Anderson SR, Salan JS (2014) Development and scale-up of cocrystals using resonant acoustic mixing. Org. Process R&D
24. (1901) Synthesis of highly loaded gelled propellants; Scott L. Coguill Resodyn Corporation, South Franklin, Butte MT (406) 723-2222 scoguill@resodyn.com

Overview and Appraisal of Analytical Techniques for Aging of Solid Rocket Propellants

Ruth Tunnell

Abstract There are many solid rocket propellant compositions used in military and civilian applications. For all classes of propellant though, aging, which is essentially deterioration and the change in chemical, physical, and mechanical properties, limits the time in which they can be stored safely or used.

The assessment of the degree of degradation and therefore the remaining in-service time of the propellant involves the use of more than one analytical technique. A number of parameters need to be understood, including the chemical composition and the mechanical properties; these are connected with the decomposition reactions as a function of time, temperature, and environmental conditions.

Many of the techniques for following the aging behavior of propellants are well established. For example, chemical decomposition can be determined through the use of gas chromatography (GC). In addition, the thermal decomposition of propellants at high temperatures may be monitored through the application of differential scanning calorimetry (DSC). Finally, the mechanical properties can be measured by tensile testing. There are also other techniques that are less frequently used to characterize aged propellant samples but still provide a valuable insight into aging behavior, and these include nuclear magnetic resonance (NMR).

An overview of the chemical, mechanical, and thermal analytical techniques which are used to determine the decomposition behavior of propellants is given. The more established methods will be briefly described and information also provided on some of the techniques that are less widely used but can still provide an insight into the degree of aging of such materials.

Nomenclature

ADN	Ammonium dinitramide
Al	Aluminum
AP	Ammonium perchlorate

R. Tunnell (✉)
Energetics Performance, QinetiQ, Fort Halstead, Kent TN14 7BP, UK
e-mail: rtunnell@qinetiq.com

CTPB	Carboxy-terminated polybutadiene
DMA	Dynamic mechanical analysis
DSC	Differential scanning calorimetry
DVS	Dynamic vapor sorption
EDX	Energy dispersive x-ray
FT-IR	Fourier-transform infrared
GAP	Glycidyl azide polymer
GC	Gas chromatography
GPC	Gel permeation chromatography
HFC	Heat flow calorimetry
HPLC	High-performance liquid chromatography
HTPB	Hydroxy-terminated polybutadiene
IC	Ion chromatography
IR	Infrared
LC/MS	Liquid chromatography/mass spectrometry
MS	Mass spectrometry
NC	Nitrocellulose
NEPE	Nitrate ester plasticized polyether
NG	Nitroglycerine
NMR	Nuclear magnetic resonance
PEG	Polyethylene glycol
RH	Relative humidity
SEM	Scanning electron microscopy
TGA	Thermogravimetric analysis

1 Introduction

Solid rocket propellant compositions used in military and civilian applications can initially be broadly described in terms of two types. The first are composite propellants, which typically contain 60–72 % ammonium perchlorate (AP) as the oxidizer, up to 22 % aluminum (Al) powder as a fuel and between 8 % and 16 % of a rubber-like binder such as hydroxyl-terminated polybutadiene (HTPB), which also incorporates a plasticizer, for example, dioctyl adipate [1]. Suggested tests for characterizing composite propellants both before and after aging are provided in STANAG 4581 [2].

The other major class of solid propellants is known as double base, and these usually contain nitrocellulose (NC) and nitroglycerine (NG), along with smaller amounts of other additives including stabilizers which are added to slow down the degradation of the nitrate esters.

Because of the sheer number of different compositions, there are various ways that rocket propellants can be classified. Further information regarding this can be found in Davenas [3] who described propellants in terms of six "families" with three of these being different combinations of composite and double base.

For all classes of propellants, aging limits the time in which they can be stored safely or used in the proper property range, and the degradation behavior will clearly depend upon the composition of the material. When new compounds, such as ammonium dinitramide (ADN), are introduced into propellants, it is particularly important to determine their chemical compatibility with the other components in the formulation not only at manufacture but also over the time that the material is expected to be in service [4, 5]. If there are compounds within the propellant which are incompatible with each other, then undesirable chemical reactions may occur which ultimately increase the rate of decomposition, and so the in-service time of the material is shortened.

In general, the characteristics of the propellant will be determined as soon as possible after manufacture. This provides baseline data to which all future samples will be compared. It is important to note that at this point, the stability of the material is being assessed and there is a distinction between determining the stability of propellant compositions and defining its aging behavior.

Stability tests are typically conducted for one test temperature and one defined test time period, and so they have lower or very selected time-temperature loads compared with aging studies. Also, they are used to determine the state of the material at that time under particular conditions, whereas aging can be used to predict the behavior of the propellant over extended times and temperatures [6]. Commonly employed stability methods, which are not generally used for aging studies, include the suite of hazard tests that assess the material's response to external stimuli such as impact and friction [7], the Bergmann-Junk-Siebert test [8], vacuum stability test [9], and the Dutch mass loss test [10].

Once the stability of the material has been defined, it can then be subjected to an aging regime. This essentially involves heating the propellant for a known period of time and is usually carried out at a number of different temperatures. The form of the propellant might be as a rocket motor with a liner present in between the propellant and case. Following aging, the propellant can be nondestructively evaluated using a technique such as x-ray computer tomography [11] to look for physical changes. In some cases, small pieces of the propellant from particular areas of the rocket motor might be analyzed for parameters such as thermal stability or the entire motor can undergo sectioning for full chemical, mechanical, and physical analysis including assessing the bond strength between the propellant and liner interface [12]. In some cases, the propellant might not be cast into a rocket motor but will be aged as slabs [13] or cut up into small pieces. The assessment of the aging processes on the various forms of material may involve different techniques as some methods of analysis will be more applicable for whole motors, such as the use of penetrometers [14], compared with small chunks of material.

If the propellant is not being aged as a whole motor, then the form of the material and the environmental conditions are important. As discussed by Judge [15], the amount of oxygen surrounding the propellant during aging needs to be taken into account, and in some cases, experiments may also be conducted under different levels of relative humidity (RH). A study by Wilker et al. [16] looked at the effect of the atmosphere on the aging of single-, double-, and triple-base propellants, and among their conclusions was the fact that the amount of oxygen around the

propellant affected the stabilizer depletion rate and that the concentration of water present also influences decomposition pathways.

It is therefore important to consider whether propellant samples should be aged wrapped in foil, in tubes, or in jars, and the headspace around the material needs to be carefully controlled. For certain compositions, such as composite propellants, inhomogeneous aging is common where the exposed surfaces age more rapidly than in the bulk, and so the form of material and atmosphere are crucial to understanding the results of the experiments [17].

Aging of the propellant may be conducted to determine different properties. For example, a specific parameter regarding the material, such as stabilizer depletion [18, 19] or the change in mechanical properties with temperature [20], might need to be measured.

It is possible for a propellant to be mechanically stable but the chemical decomposition might have reached an unacceptable level which limits the in-service time of the material. However, the opposite situation, where the material has degraded mechanically but still contains significant levels of stabilizer or antioxidant, often applies.

The ballistic properties of the propellant with aging also need to be determined. This can be achieved in a number of ways including by burning coated strands from cast propellant blocks in an instrumented, temperature-controlled pressure chamber. Alternatively, whole motors may be fired and the chamber pressure versus time data can be collected [21]..

The ultimate aim of aging is to enable predictions to be made about the safe in-service time of the propellant at in-service temperatures [22, 23]. Increasingly, experimental data are being incorporated into computer models such as finite element analysis in order to do this [12, 24].

The kinetics of the decomposition of solid propellants can be described in principle by Eq. 1 [25]:

$$\frac{d\alpha}{dt} = k(T)f(\alpha) \tag{1}$$

where α represents the extent of the reaction or conversion ($0 \leq \alpha \leq 1$), t is time, $k(T)$ is the rate constant, and $f(\alpha)$ is the reaction model, which describes the dependence of the reaction rate on the extent of the reaction.

In some cases, the temperature dependence of $k(T)$ can be described by the Arrhenius equation, whose substitution into Eq. 1 gives Eq. 2:

$$\frac{d\alpha}{dt} = A \exp\left(\frac{-E}{RT}\right) f(\alpha) \tag{2}$$

where:

A – Pre-exponential factor
E – Activation energy (KJ mol^{-1})
R – Gas constant (J K^{-1} mol^{-1})
T – Absolute temperature (K)

However, it should be noted that Eq. 2 only applies in situations where simple reactions are occurring. In reality, the decomposition of energetic materials is much more complex, and $f(\alpha)$ is an involved function comprising of a number of reaction constants which may have to describe processes such as evaporation, decomposition, and autocatalysis taking place in parallel.

Accelerated aging tests are generally carried out over at least three different temperatures, and the activation energy for the process is then calculated. This can then be used to calculate the rate of reaction at different temperatures. However, a limitation of this approach is that reactions which take place during the artificial aging experiments may not occur at lower temperatures, and for some materials, there may be a change in the activation energy at lower temperatures [26]. There are numerous papers in the literature which discuss the different mathematical treatments for describing the aging behavior of rocket motor propellants and the various limitations of these [27–29].

A final consideration with regard to aging is selecting the analytical techniques which are to be used to study the processes. Before any aging is conducted, thought should be given to the likely failure mode of the material. For double-base propellants, this might be stabilizer consumption or significant changes to the mechanical properties. Composite propellants exhibit different aging mechanisms to double-base materials as degradation occurs by the oxidation of the binder matrix and loss of plasticizer by migration and evaporation. These materials may also exhibit dewetting where the solid particles separate from the binder as well as failure in the binder itself [23]. For more complex formulations, which are a mixture of composite and double-base compositions, there may be different modes of failure than those exhibited in either predecessor type of propellant. It has also been found that traditional analytical techniques and test methods do not always detect the degradation of some high energy compositions, and so alternative ways of following the aging processes need to be devised [30].

Figure 1 (reproduced from reference [31]) describes the principles of aging. This diagram is for a composite propellant, but the general methodology can be applied to other propellant compositions.

An overview of the chemical, thermal, mechanical, and physical analytical techniques which are used to determine the decomposition behavior of propellants will be discussed in the following sections. The more established analytical methods will be described briefly, and information will also be provided on some of the methods that are less widely used.

There are many analytical techniques which can be used to determine the characteristics of propellants, and these include x-ray diffraction (XRD) [32], thermomechanical analysis (TMA) [33], and chemiluminescence [34] which may be oxides of nitrogen or oxygen based. However, only those which have been reported in the literature as being used in aging studies for rocket motor propellants are discussed.
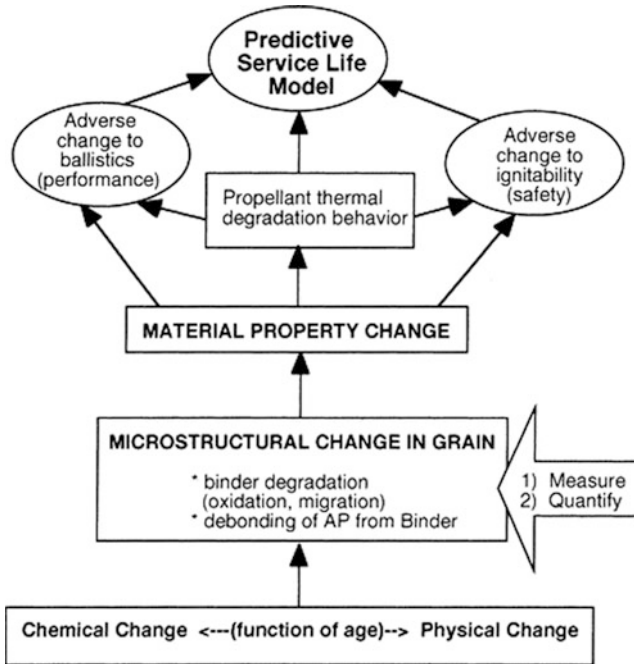
Fig. 1 Understanding the critical aging processes and the correlation of the process to the safety and performance of a composite propellant (Reproduced from Celina, Minier et al. [31])

2 Chemical and Thermal Analysis Techniques

There are a wide range of analytical techniques which can be used to assess the chemical and thermal properties of rocket motor propellants. Some of these, such as gas chromatography (GC), have been well established for decades now, whereas others, like heat flow microcalorimetry (HFMC), are being used increasingly.

2.1 Chromatographic Techniques

Chromatographic methods are used to study compounds in a mixture. The propellant is extracted in a solvent which is then injected into a chromatography instrument where it passes down a column. The compounds in the extract interact to different extents with the mobile and the stationary phases and so become separated by the time they reach the detector. Irrespective of the detector type, the resultant output is a chromatogram which is a plot of the detector's signal as a function of time [35]. The individual peaks in chromatograms can then be integrated and used alongside standard samples containing known amounts of the analytes of interest

to quantify the concentration of different compounds in the mixture or in the case of gel permeation chromatography (GPC), to ascertain the molecular mass of the polymer chains in the material.

Gas chromatography and liquid chromatography – high-performance liquid chromatography (HPLC) and liquid chromatography/mass spectrometry (LC/MS) – are frequently used to determine the concentration of stabilizers in propellant samples. These techniques may also be used for measuring the amount of antioxidants in composite propellants.

In 1986, Haberman [36] reported an HPLC method to monitor the stabilizer content of propellants containing diphenylamine derivatives as they were subjected to aging. To do this, the propellant samples were extracted in methanol, and then HPLC was used to quantify the concentration of diphenylamine and its associated degradation products such as 2-nitrodiphenylamine. As technology has improved, enhanced detectors have become available which have enabled the improved quantification of stabilizers more rapidly [37].

If aging of propellants is conducted at a number of temperatures, it is possible to measure the rate of stabilizer or antioxidant consumption as a function of temperature. Fengqi et al. [38] carried out research to determine the safe in-service storage time of a range of propellants at 30 °C by applying both the Berthelot and Semenov equations to the experimental data. While they used a titrimetric, as opposed to a chromatographic method, for their research it is still possible to adopt this mathematical approach using chromatographic techniques for rocket motor propellants.

Ion exchange chromatography (IC) [39] works on the same principles as GC and HPLC and is another method for analyzing compounds in a mixture. It is specifically performed for the identification and quantification of ionic species such as ammonium, chloride, chlorate, and nitrate. Klassen et al. [40] reported the use of this technique to quantify the concentration of chloride ions in an AP-based composite propellant as it underwent decomposition. They noted that it is important to measure the concentration of chloride ions in the unaged propellant as well as they can be present in the AP as a contaminant in the first place.

An analytical technique which is becoming increasingly employed for studying the aging of propellants is GPC [41]. This can be used to ascertain the molecular mass of polymers such as NC, HTPB, and polyethyleneglycol (PEG) in the material, and this links to the mechanical properties of the propellant.

Matečic-Mušanić et al. [42] used GPC to study the reduction in the mean molecular mass of NC during a double-base propellant aging study. In addition to this, they followed the depletion of stabilizer during the same study via HPLC, as it was found that there were significant changes in the mean molecular mass of NC after 60 days at 90 °C. In addition, there were also a great range of molecular masses of NC present in the mixture.

The rate of breakdown of NC into smaller molecular masses was also followed and this is illustrated in Fig. 2. These results demonstrate that the breakdown of NC becomes faster at elevated temperatures.
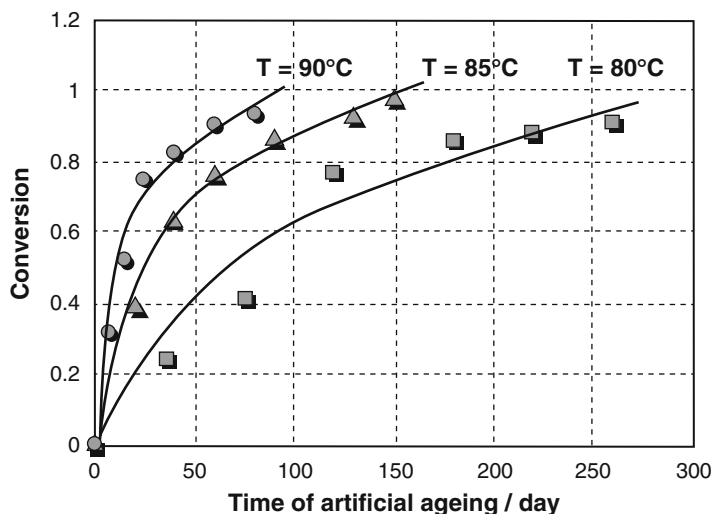
Fig. 2 Degree of conversion degree (α) of Mn of NC versus time of accelerated aging of DB rocket propellant samples at different temperatures, i.e., 80, 85, and 90 °C (Reproduced from [42])

Finally, Matečić-Mušanić et al. were able to use the data, and Eqs. 1 and 2 to calculate the activation energy for the decomposition of NC. They determined this to be 145 kJmol-1 which was reported to be consistent with previous values detailed in the literature.

2.2 Spectroscopic Methods

The spectroscopic methods for studying the aging behavior of propellants include nuclear magnetic resonance (NMR) and infrared (IR). NMR is a technique that uses radio waves to enable the structural identification and quantification of compounds. A detailed explanation of the theory behind NMR analysis can be found in Günther [43], while Griffiths and Haseth [44] provide some further background on IR.

However, like IR, NMR is not readily used for rocket propellant aging studies. It is frequently employed for characterizing certain compounds within a propellant matrix such as stabilizer degradation products [45] or for studying one aspect of the propellant in detail like the diffusion coefficient of plasticizers within the binder matrix [46], but there are few examples in the literature where NMR has been used as part of a complete aging study on propellant samples.

In 1998, Tod et al. [47] reported the use of NMR to assess aged propellants that contained a PEG-based binder. The propellants were extracted in solvent and the amount of free or uncross-linked PEG was quantified. This showed that when the material underwent aging, there was an increase in the amount of uncross-linked PEG. The NMR results correlated with the mechanical analysis data which showed

that the shear modulus of the propellant decreased with aging illustrating that the material had softened, and this was thought to be due to the hydrolysis of the PEG binder which caused it to be broken down into smaller fragments.

Tunnell et al. [48] also followed the aging behavior of compositions with a PEG-based binder. It was demonstrated that following aging at 80 °C, virtually all of the PEG had become uncross-linked in one composition which had resulted in the sample turning from a rubbery solid into a viscous liquid. NMR also showed that for this composition, there was also an increase in the amount of 1,2-dinitroglycerin present in the sample illustrating that the NG had also degraded and had undergone acid hydrolysis.

As is the case for NMR, IR is often used for compositional analysis of propellants [49] but is less frequently employed for rocket propellant aging studies. Torry and Cunliffe [50] reported the use of Fourier-transform infrared (FT-IR) spectroscopy to follow the degradation behavior of a HTPB/AP propellant as it was heated. The propellant samples were aged in the form of blocks and then sliced into cross sections, which were approximately 30 μm thick, using a microtome. The AP was extracted using solvent and the subsequent sample was subjected to FT-IR mapping. The data were used to obtain oxidation profiles, and it was found there was a correlation between cross-link density and the concentration of carbonyl end groups present which reflects the degree of oxidation. The research of Torry and Cunliffe showed that the heterogeneous aging across the propellant block depends strongly on the concentration of minor components present.

2.3 Acidity Analysis

McDonald [51] has reported a method for measuring the change in pH levels of propellants based on nitrate esters as they undergo aging. This involves extracting propellant in distilled water for 48 h and measuring the pH of the water at the start and the end of the process. His research demonstrated that there was a greater fall in the pH of propellant samples when they had been aged at elevated relative humidity (RH). A fall in the pH of propellant samples is indicative of degradation and suggests that nitrate esters, such as NC and NG, have undergone acid hydrolysis. For nitrate ester-based compositions, if the acid content increases with aging, there may be other indicators of degradation such as increased heat flow from the sample, breakdown of the binder matrix and enhanced stabilizer consumption [48].

2.4 Oxygen Consumption Measurements

While nitrate ester-based propellants may suffer from acid-driven decomposition processes, composite propellants may undergo oxidative degradation. One of the ways to understand if this is an issue is to measure the rate of oxygen consumption as

propellants age using a coulometric oxygen sensor [52]. Celina et al. [31] measured the rate of oxidation of aged propellant samples and from the data; they calculated the activation energy for the process at low and high temperatures in order to predict the rate of oxidation at a range of temperatures in future years. Their data also suggested that the processes responsible for mechanical failure were closely related to total oxidation.

2.5   Sol/Gel Determination

Oxidative aging of composite propellants can be investigated by measuring the concentration of extractable, or soluble, polymer content as this provides a means of assessing the degree of cross-linking or chain scission [13, 53]. Once the soluble content is known, the cross-link density of the binder can be estimated [2, 54].

Cunliffe et al. [54] used sol/gel analysis to understand the aging behavior of HTPB-based composite propellants. While some researchers [55] thought the source of the oxygen was from the AP within the propellant, the experiments by Cunliffe et al. showed that the aging decomposition mechanisms were largely driven by atmospheric oxygen. Sol/gel measurements for a composition containing a transition metal showed that there were very little changes in the extractable binder in the propellant which had been protected from the atmosphere. However, there was extensive cross-linking at the exposed surface, meaning the sol/gel content had decreased. Furthermore, as time progressed, the cross-linking processes started to take place in the bulk of the propellant and became extensive at the surface. If the source of oxygen driving degradation was AP, then the propellant would be expected to age in a homogeneous manner and it was demonstrated that this was not the case.

Bohn et al. [53] also employed sol/gel analysis in order to investigate the aging behavior of four HTPB-based propellant formulations. This, in conjunction with the data from GPC and DMA, illustrated that there were two competing processes occurring upon aging: chain scission and chain recombination with cross-linking.

2.6   Thermal Methods

Among the well-established thermal methods used to study the aging behavior of propellants are differential scanning calorimetry (DSC) and thermogravimetric analysis (TGA).

The technique of heat flow calorimetry (HFC) is being used increasingly. It is a very sensitive technique, with a detection limit which is just 1 μW, and so it is employed to measure the heat evolution from compositions.

Another technique which falls in to this category is dynamic vapor sorption (DVS). This can be used to follow the effect of moisture on the aging behavior of propellants as they are heated at the temperature of interest.

DSC is used to understand the thermal properties of samples. It can be employed to follow a wide range of processes occurring within materials such as decomposition, curing, oxidation, and melting. It is also identified in STANAG 4147 [56] as a method for investigating the compatibility of energetic materials. Along with TGA, it might be coupled to other techniques such as MS or IR in order to identify the compounds which are causing the peaks in the thermogram as the material undergoes reactions [57].

The technique of DSC needs to be employed with care when it comes to analyzing propellants. First of all, the sample size is very small, often of the order of just a few milligrams, and so if the material is heterogeneous, the DSC response will not be representative of the material as a whole. Secondly, upon aging, shifts in the temperature of events may be observed, but it can be difficult to understand when these become significant and what the implications are for the safe in-service time of the material. Thirdly, the sensitivity of DSC is not sufficient to be able to detect decomposition reactions at typical in-service temperatures of 50–90 °C. Finally, the sample will react differently at different heating rates, and so it is important that the heating rate is defined, and all of the aged samples are treated in the same manner.

There are a number of methods which employ DSC- or TGA-derived data to understand the kinetics of propellant degradation including those defined by Kissinger [58], Ozawa [59] and Flynn [60]. The Ozawa method is one of the most popular methods for estimating activation energies and is a so-called isoconversional method where no knowledge of the kinetics of the reaction is required as the time taken for a particular event to occur (such as degree of mass loss, amount of conversion of reactants to products) is measured at different heating rates. While DSC and TGA cannot be used to understand the complete mechanism of thermal degradation of propellants, it is often employed as it provides information on the frequency factor (A), activation energy (E), and the overall reaction order [61]. Such data is useful for slow cook-off experiments, but care must be taken as it is only applicable for the temperature range where substantial conversion of the reactants into products has taken place.

In a study by Trache and Khimeche [62] on double-base propellants, it was demonstrated that decomposition occurs with both artificial and natural aging and that degradation also increases with heating rate. The authors conducted their experiments at five different heating rates, and they were then able to calculate the activation energy for the decomposition process using the decomposition peak temperature and heating rate. Furthermore, they illustrated that the activation energy for the decomposition process fell with aging.

With some instruments it is possible to collect DSC data as the sample is undergoing TGA [63]. This technique records the weight of a sample as it is heated or cooled, and the result is a thermogram which illustrates the dependence of this parameter with temperature. This can be further analyzed to provide information such as the approximate amounts of the compounds in the composition, their thermal stability, and if any products are formed on heating. Like with DSC, TGA can be carried out on unaged and aged propellant samples at different heating rates in order to assess if the activation energy for the decomposition processes changes

with aging. Oyumi [57] used TGA in conjunction with DSC and gas analysis to study the thermal decomposition of a composite propellant containing HMX. It was found that there were two stages to the thermal degradation process, but neither of these was significantly affected by aging.

HFC can be used to determine the stability of propellants [64] as well as the compatibility of such materials with nonexplosive components [56]. In the most commonly used form of the test, a small amount of material – typically 2–3 g – is placed into a sealed glass ampoule. This is then placed in the HFC instrument at a particular temperature, and the heat evolved or taken in by the sample is recorded. Because the instrument can be run at a particular temperature for long periods of time, it is possible to carry out aging studies in this way, or propellant samples can be aged in another environment before being transferred to the HFC for thermal analysis. Often it is possible to correlate the peaks in the heat flow with other events occurring in the propellant such as stabilizer depletion as measured by HPLC or binder breakdown which is evident by GPC or NMR [48]. This is illustrated in Fig. 3.

One of the initial uses of HFC was to monitor decomposition in NC-based propellants. It should be noted that the sentencing criteria detailed in STANAG 4582 [64] for this method are only applicable to these materials. Increasingly though,

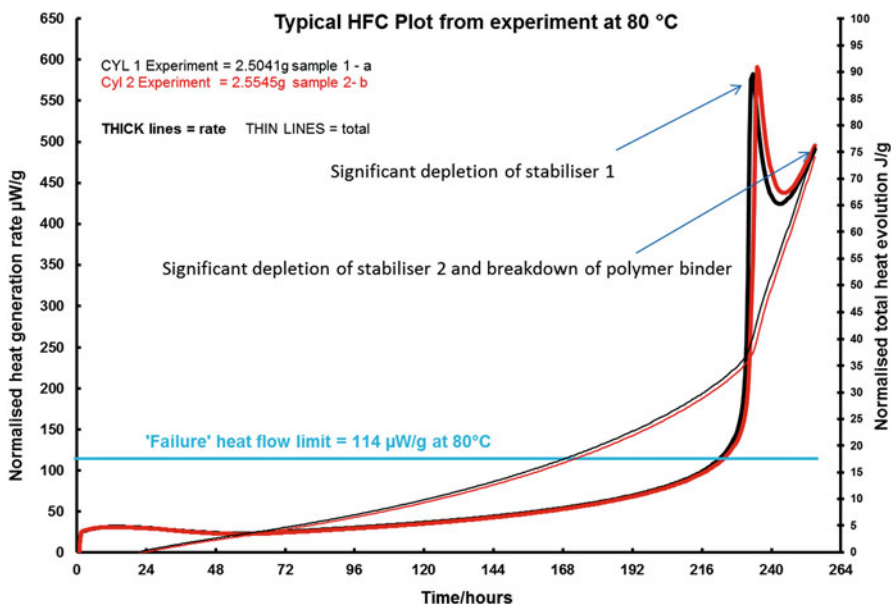**Fig. 3** Typical HFC plot from a sample undergoing significant decomposition at 80 °C. HPLC and GPC analysis carried out on samples in parallel in separate aging experiments at 80 °C indicate that the peaks in the heat flow are due to stabilizer degradation and breakdown of binder. The failure heat flow criterion as defined in reference [64] is also shown (Figure reproduced from reference [65])

this technique is being applied to measure the degradation in other propellant compositions and their constituent components [66]. While the technique provides an insight into the decomposition processes, care needs to be taken when analyzing the data. For example, just because the sample gives a very low heat flow over the course of the experiment, it does not mean it is not undergoing decomposition.

DVS is a technique which can be used to study the effect of humidity on propellants as they are held at a particular temperature. The instrument is similar to a TGA in that the mass loss or gain by the sample is recorded, but the humidity can also be carefully controlled at the same time. In general, the amounts of material which can be tested are also significantly larger than for TGA and can be up to several hundred milligrams in mass. Liebens and Neviere [67] carried out DVS measurements on a HTBP-based propellant. From this, they were able to calculate the diffusion coefficients for the uptake of water by the material. They combined this with the mechanical properties of the propellant when it was aged under different humidities and temperatures in order to create an aging law to predict the characteristics of the propellant.

3   Mechanical and Physical Analysis Techniques

In order to fully describe the degradation processes occurring as propellant samples are aged, it is not only necessary to investigate the chemical decomposition mechanisms but it is also important to understand how the mechanical and physical properties of the propellant change. It is possible for the propellant to contain sufficient concentrations of stabilizer to be considered chemically stable, but it may have undergone significant changes in the mechanical properties such that the rocket motor would be considered unsafe for service use.

3.1   *Dynamic Mechanical Analysis (DMA)*

One of the most commonly employed methods for understanding the mechanical properties of aged propellant samples across a wide temperature range is to use DMA [17, 53, 68–73].

Results are usually indicated on a graph by plotting three parameters against measurement temperature. These are the storage or elastic modulus, G', the loss or viscous modulus, G'', and the tangent of the loss angle, $\tan \delta = G''/G'$, which is the called the loss factor. G' is the component of the modulus that is in phase with the applied strain. It represents the stored elastic energy. G'' is the part of the modulus that is out of phase with the applied strain and it is a measure of the energy lost during deformation. Tan δ represents the ratio of loss modulus to storage modulus or the ratio of viscous modulus to elastic modulus. Typical DMA data from a rocket motor propellant which softens with aging are shown in Figs. 4, 5 and 6.
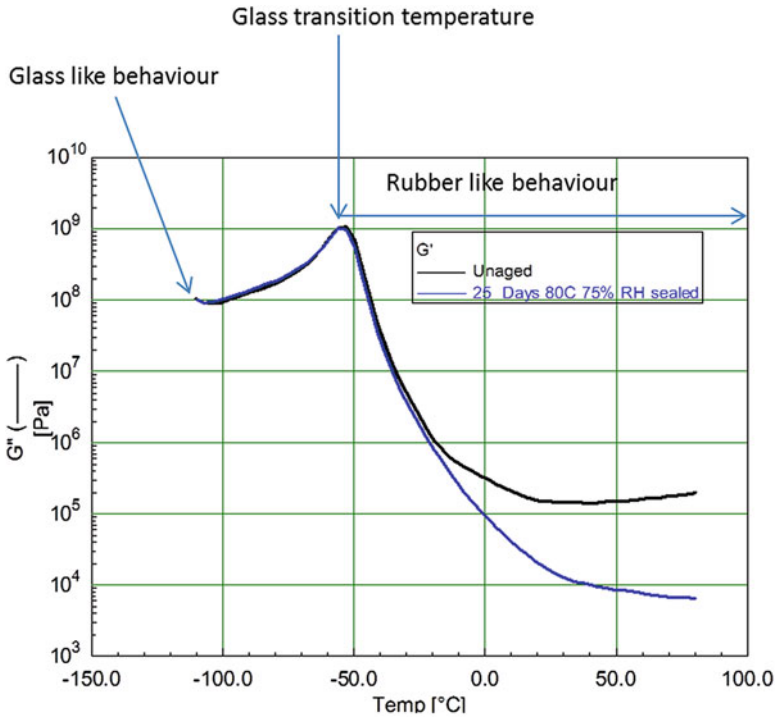
Fig. 4 Typical G′ trace obtained by torsion DMA comparing aged and unaged samples (Figure reproduced from Ref. [65])
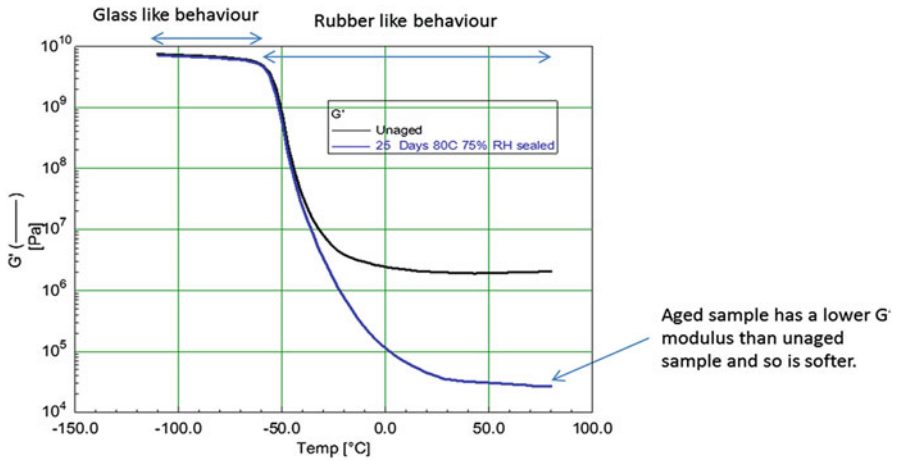
Fig. 5 Typical G″ trace comparing aged and unaged samples (Figure reproduced from Ref. [65])
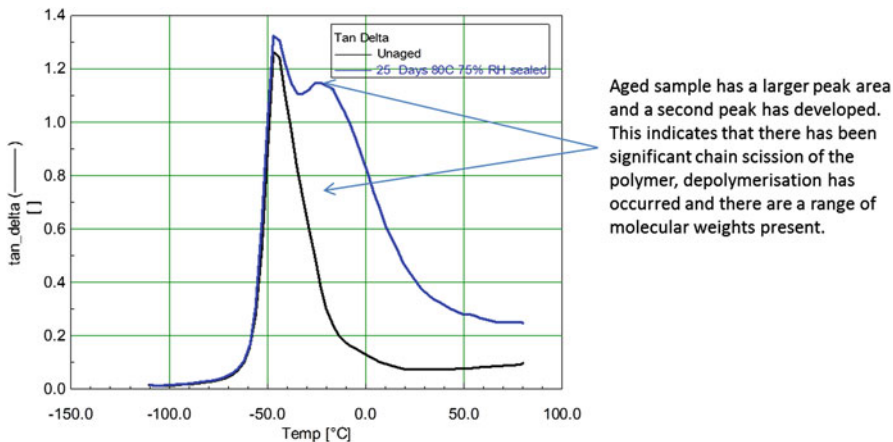
Fig. 6 Typical loss factor trace (tan δ) comparing aged and unaged samples (Figure reproduced from Ref. [65])

Cerri et al. investigated the aging of a HTPB/Al/AP rocket propellant formulation using DMA in torsion mode [27]. For these materials, they measured the area under the tan delta curves which represents the ability of the propellant samples to dissipate energy during molecular rearrangement. Upon aging, the area under the curve decreases which is likely to be due to an increase in material stiffness which is probably as a result of oxidative aging.

DMA testing can also be used to assess the change in mechanical properties of double-base propellants as a result of plasticizer migration. Torry et al. [17] reported the application of DMA to study the aging behavior of two propellants with slightly different compositions which are used as boost and sustain propellants inside a rocket motor. The two compositions were wrapped in contact with each other and heated at 50 °C, 60 °C and 70 °C. DMA revealed that the moduli of the boost propellant doubled, while those of the sustain propellant halved. This was thought to be due to the migration of the NG from the boost to the sustain propellant. The correlation between the mechanical and chemical data for this research is illustrated in Fig. 7. This migration could ultimately result in stresses and strains in a rocket motor which could have an impact upon in-service time.

3.2 Tensile Testing

In order to measure the mechanical properties of a sample of propellant when it is deformed, compression and tensile testing can be carried out. Both tests provide an assessment of the strength of the sample, but the sample geometry for the two methods is different [74, 75].
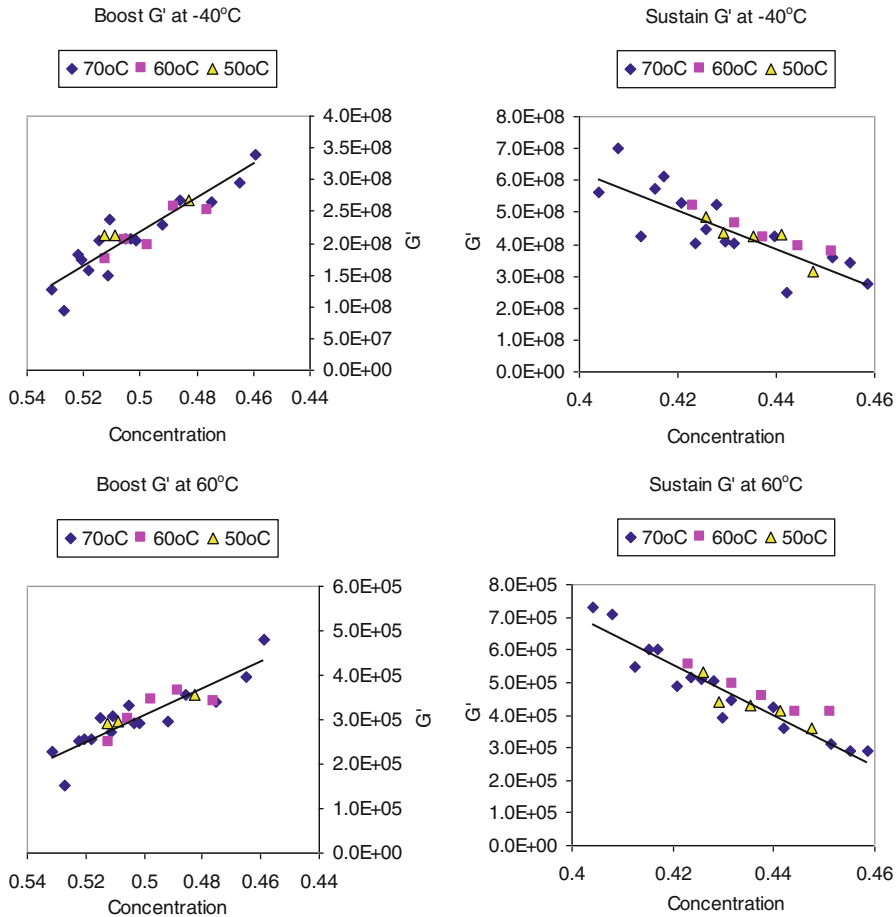
Fig. 7 Shear modulus of propellant versus fraction concentration of plasticizers measured at −40 °C and 60 °C (Reproduced from [17])

For compression testing, the samples are usually milled into cylinders, while tensile testing is carried out on dog-bone-shaped samples. Figures 8 and 9 illustrate typical tensile and compression data for a rocket motor propellant composition which softens with aging. The variation in the strain at breaking point is variable which is typical for highly filled propellant compositions.

Jeremic [76] used tensile testing to determine the elasticity modulus, maximum stress, and maximum strain of a carboxy-terminated polybutadiene (CTPB)-based composite rocket motor propellant. Experiments were conducted over a range of temperatures from 193 to 293 K. From this, Jeremic was able to produce master curves to describe the temperature dependence of the tensile parameters, enabling predictions to be made of the mechanical properties of the propellant at temperatures outside of the experimental range.
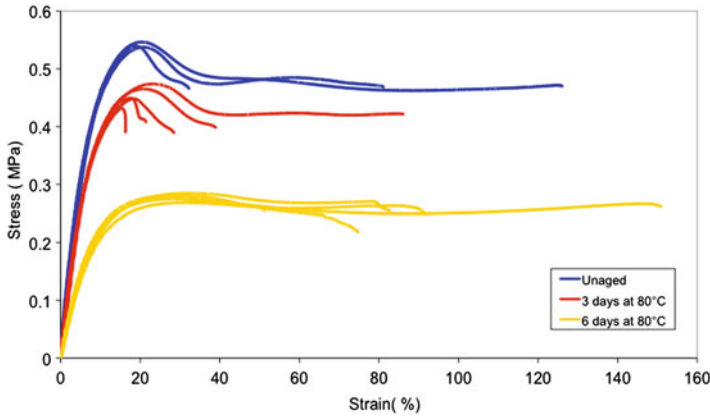
Fig. 8 Typical tensile test data (Figure reproduced from Ref. [65])
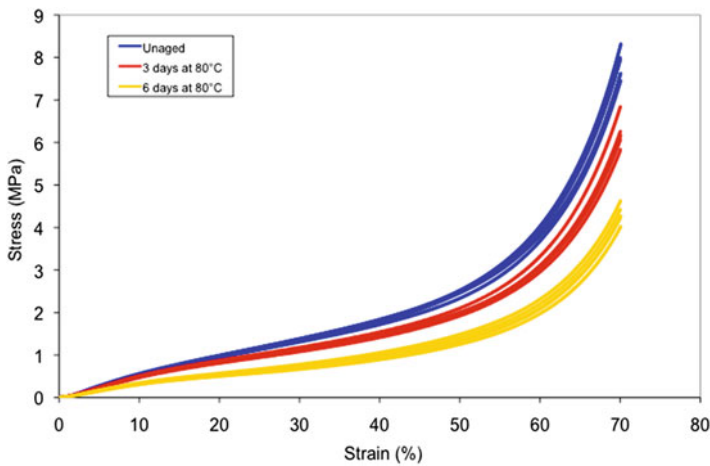
Fig. 9 Typical compression test data (Figure reproduced from Ref. [65])

Other researchers who have used the results of tensile testing to make predictions regarding the in-service time of rocket propellants include Wang et al. [22]. They aged nitrate ester plasticized polyether (NEPE) propellants at four elevated temperatures and then determined the strength limit of the materials. It was shown that this varies during the aging process but falls quickly with prolonged aging. By applying the Berthelot equation, the authors used the tensile test data to predict the in-service time of NEPE propellants.

Instruments that measure the tensile properties of propellants can also be employed to determine the same parameters but in compression mode. Suceska et al. [77] used compression testing to understand the mechanical properties of naturally aged double-base rocket propellant samples which had been stored for up to 35 years

at ambient temperatures. They measured the maximum stress and deformation which were obtained from stress-strain curves. Their research demonstrated that for the propellant studied, the compressive stress at maximum load increased slightly. This was thought to be due to a decrease in the amount of NG which acts as a plasticizer, and as the concentration of this falls, the mobility of the NC molecules also reduces which results in the stiffening of the propellant.

It is important to note that the NG loss would be considered a change to the chemical composition of the material, but it is one that affects the mechanical properties. This highlights the fact that when studying aging, more than one parameter should be measured and that analytical techniques should not be used in isolation.

3.3 Creep and Stress Relaxation

The physical aging properties of rocket motor propellants can also be understood by measuring the material's likelihood to deform under mechanical stress. This is known as creep testing and a load (stress) is applied to a bar of material and the subsequent flow is monitored. Further details regarding the apparatus for such tests can be found in reference [78].

Greidanus and Struik [79] used creep testing as a way of assessing the mechanical properties of double-base rocket propellants as a function of aging. Their research showed that for their materials, the creep rates decreased significantly upon aging, indicating that the propellant had stiffened. The creep tests were conducted for short periods of time, and the researchers concluded that a strong contribution to stiffening was as a result of physical aging processes which could be reversed if the propellant was heated and so softened again.

Stress relaxation, meanwhile, involves applying a strain to a material which causes it to deform. The force necessary to maintain this strain is not constant but decreases with time [80].

Kadiresh and Sridhar [81] carried out stress relaxation tests on aged propellant samples. This involved applying a 5 % strain to the samples and recording the stress in the material over a period of 180 min. Their research showed that with aging, the relaxation load increased by as much as 50 %, and they stated that this demonstrated that the propellant samples had hardened with heating due to a loss of plasticizer.

3.4 Dilatation Testing

One of the methods for understanding the interactions between the particles and binder in highly filled propellants as aging takes place is to carry out dilatation testing. When such materials are put under tension, the particles begin to separate

from the binder in a process called dewetting and vacuoles begin to form. By applying mathematical treatment, it is possible to determine the number of vacuoles formed and the rate of development from the strain of the material [82].

Dilatation testing is often carried out in a Farris gas dilatometer [83]. This essentially measures the pressure differential between the sample and reference chambers via a pressure transducer. As the sample is extended, the sample chamber volume may change due to dewetting, and this is then compared with the reference chamber.

Davis [13] used dilatation testing to understand the aging behavior of a HTPB-based composite propellant containing AP and Al. The results indicated that overall, the changes in the dilatation were due to changes in the polymer network only and were not as a result of the binder/filler interactions. The author thought that the data suggested that aging in the presence of humidity does not affect the dilatation behavior which again illustrates that moisture does not directly affect the binder/filler interactions.

3.5 Hardness Testing

Measuring the hardness is a quick and simple way of assessing the mechanical properties of propellants [84]. It is important to understand how this property changes with aging as an increase in hardness can lead to the cracking of the propellant grain. There are five major hardness scales [85], but the most commonly employed method for propellants is to use a durometer with a Shore A digital scale. Testing is usually conducted in accordance with the procedure ASTM 2240-05 [86], and the technique measures the depth of indentation of the sample which is then converted to give hardness.

Hocaoğlu et al. [87] manufactured composite propellant samples which were HTPB and AP based, and these were then heated at 65 °C. Their research illustrated that during the initial stages of aging, there was a sharp increase in the hardness of the materials, but later on during the aging process, there were only slight changes. They attributed to this to that fact that once there was a very high cross-link density present, the propellant showed a lower tendency to deform.

Hardness testing can also be used to understand how composite HTPB-based propellant samples, which are bonded to an insulant and are affected by the diffusion of plasticizer during aging at room temperature and 80 °C. Libardi et al. [88] carried out tests on different regions of aged propellant. They demonstrated that for both the room temperature and elevated temperature samples, there was softening in the first 3 mm of the propellant. Overall, the propellant samples aged at room temperature hardened which was thought to be due to the diffusion of plasticizer or oxidation of the polymer matrix. However, the samples aged at elevated temperatures showed the opposite effect which could be due to changes in the morphology of the polymer and solid particles or possibly as a result of the presence of moisture.

A similar device to a hardness tester is a penetrometer. This also involves an indenter, which is pressed into a material, and from this the modulus, strength, and strain can be determined. This method is used to follow the aging of rocket motors and is nondestructive so the motors do not need to be disposed of after testing [14].

3.6 Microscopy

In order to investigate the physical structure of propellants as a consequence of aging, the samples can be subjected to microscopy. If a more detailed investigation of the tomography of the material is required, then scanning electron microscopy (SEM) is often used, and this is sometimes coupled with energy dispersive x-ray (EDX) which provides information regarding the composition of the sample [89].

SEM is often used in conjunction with other analytical techniques to understand what has happened to the propellant structure visually as a result of the aging conditions. Libardi and Morais [88] were studying a HTPB-based rocket motor propellant, and they employed SEM to look at the changes in the superficial morphology of the propellant as it was aged in contact with a liner material. Typical images from their research are shown in Figs. 10 and 11. Figure 10 shows the interfacial layer between the propellant and liner after 20 days at room temperature, while Fig. 11 illustrates the interfacial layer after 54 days both at room temperature and at 80 °C.
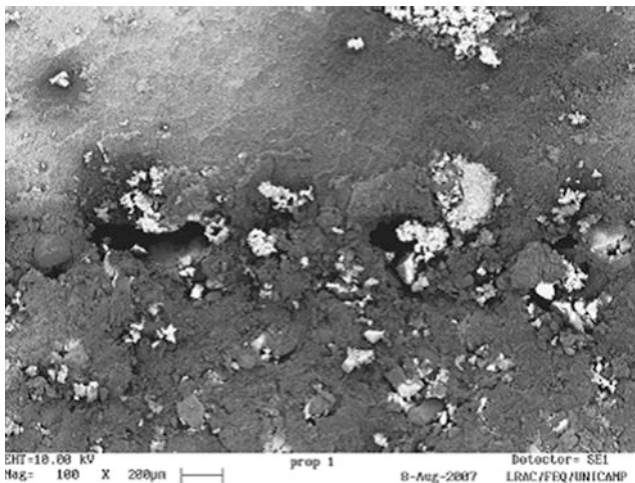
Fig. 10 SEM micrograph (100×) of the interfacial layer between propellant and liner obtained 20 days after the cure period at room temperature (Image reproduced from [88] (Authors: Libardi, J., Morais. Journal: Polimeros))
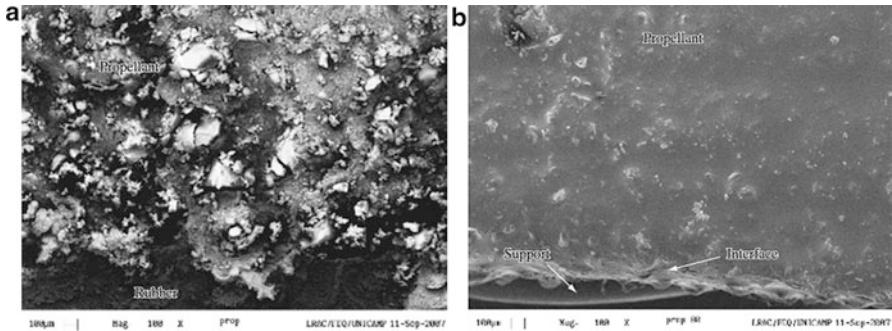
Fig. 11 SEM micrographs (100×) of the interfacial layer of the propellant sample obtained 54 days after the end of the cure period, aged at: (**a**) room temperature and (**b**) 80 °C (Image reproduced from [88] (Authors: Libardi, J., Morais. Journal: Polimeros))

Figure 10 illustrates that the aluminum particles tend to sit on the surface and that they can undergo oxidation to form aluminum oxide which is a white compound. By comparing the images in Figs. 10 and 11, Libardi and Morais were able to demonstrate that there are changes in the surface morphology of the propellant samples, both compared with the initial state and following aging. It was demonstrated that after aging at 80 °C, there were significant changes to the surface topography with the solid particles appearing to be embedded in the polymer matrix. This was attributed to an increase in the diffusion process of plasticizers at elevated temperatures which caused structural changes to the polymer and an increase in the interaction between the solid particles and the matrix. Finally, it was also concluded that there was a correlation between the SEM images and tomography of the propellant and the hardness testing results (section "Hardness Testing").

McDonald et al. [90] used microscopy and SEM to look at the effect of moisture on the aging behavior of an AP-/Al-based HTPB propellant. They subjected the samples to different relative humidities (0 %, 27.8 %, 75.1 % and 100 %) for 10 days at 70 °C before drying the samples to equal moisture content and then examining them using microscopy and SEM. The images from microscopy at 30 times magnification showed that there were no differences in the samples aged up to 75 % RH. However, at 100 % RH, there was recrystallisation of AP which formed rod-like features (Fig. 12).

SEM was then used to obtain images of the surface tomography of the propellant samples from 40 times magnification up to 3000 times magnification. The results for the samples aged at the lower RH were inconclusive, but SEM revealed that for the propellant aged at 100 %, there were significant changes as there were areas where there were no particles on the surface, but instead there were web-like structures which were consistent with the images obtained using optical microscopy (Fig. 13).
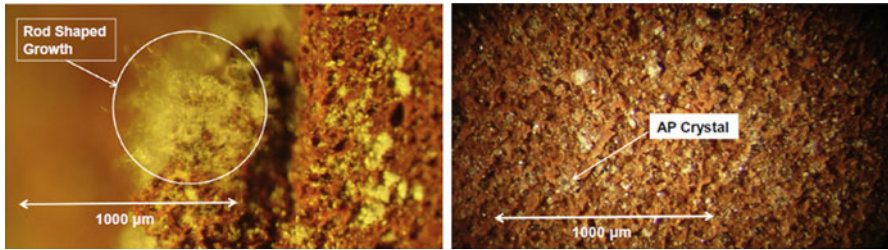
Fig. 12 Optical microscope images (30×) of unaged propellant (*right*) and propellant aged at 70 °C for 10 days in the presence of 100 % RH (*below*) (Images reproduced from [90])
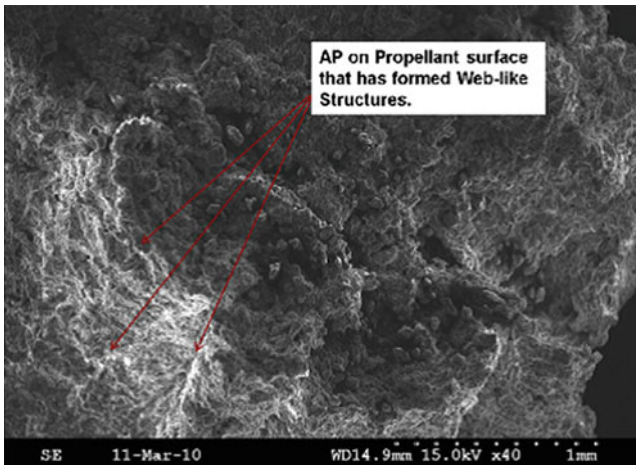
Fig. 13 SEM micrograph (40×) of propellant aged in the presence of 100 % RH (Images reproduced from [90])

3.7 Assessment of Ballistic Properties

Aging can also affect the ballistic properties of solid rocket propellants. The changes in the burn rate can be used to judge the storage stability of the material [91].

For example, Prasad et al. [92] found that for an AP-based propellant, the burning rate increased with aging. They also stated that it was possible to correlate mechanical properties with the ballistic properties. It was demonstrated that there was a linear relationship between ultimate compressive strength and the burn rate.

Judge et al. [21] measured the ballistic properties of a glycidyl azide polymer (GAP)-based propellant upon aging. This research also demonstrated that the material burned faster and reached a higher chamber pressure upon aging.

However, the burning rate does not always change upon aging. Kadiresh and Sridhar [93] demonstrated that for an AP-based propellant with an HTPB binder, the burning rate at low pressures did not particularly differ with aging, but there were significant changes in the mechanical properties.

4 Conclusions

Aging of rocket motor solid propellants can be conducted on different forms of material in order to determine a range of properties. The ultimate aim is to be able to make predictions about the in-service time of the propellant at in-service life temperatures. In order to do this successfully, it is important to measure the chemical, thermal, mechanical, and physical properties of the material rather than relying on isolated results from one or two methods. It has been demonstrated that there are a vast range of analytical techniques at the disposal of those conducting aging experiments on rocket motor solid propellants irrespective of the material's composition.

References

1. Sutton GP, Biblarz O (2001) Rocket propulsion elements. Wiley, Canada
2. NATO (2006) STANAG 4581 (Edition 1) – Explosives, assessment of ageing characteristics of composite propellants containing an inert binder. North Atlantic Treaty Organisation, Brussels
3. Davenas A (2003) Development of modern solid propellants. J Propuls Power 19(6): 1108–1128
4. De Klerk W, Schrader M, Van de Steen A (1999) Chemical compatibility of energetic materials, which technique? J Therm Anal Calorim 56(3):1123–1131
5. Myburgh A (2006) Standardization on STANAG test methods for ease of compatibility and thermal studies. J Therm Anal Calorim 85(1):135–139
6. Bohn MA (2007) NC based energetic materials – stability, decomposition and ageing. In: Nitrocellulose – supply, ageing and characterisation, Atomic Weapons Establishment (AWE), England, 24–27th Apr 2007
7. Lee P (1998) Hazard assessment of explosives and propellants. In: Jonas A, William Walters P (eds) Explosive effects and applications. Springer, New York, pp 259–339
8. Meyer R, Köhler J, Lomburg A (2008) In: Explosives, Philomena Ryan-Bugler and Helen Goltz, Germany, Wiley, pp 32–33
9. Wang L, Liu Z-R, Zhang L-Y, He S-R, Yue P, Han F, Zhang L-J (2010) Compatibility of double base propellant with priming composition. Chin J Energetic Mater 18(1):47–50
10. Bohn MA (2003) Thermal ageing of rocket propellant formulations containing ε-HNIW (ε-CL20) investigated by heat generation rate and mass loss. Thermochem Acta 40(1):27–41
11. Youngberg J, Burstein P (1995) Three dimensional computed tomography for rocket motor inspection. Proc SPIE 2455:291–298
12. Yildirim H, Özüpek S (2011) Structural assessment of a solid propellant rocket motor: effects of ageing and damage. Aerosp Sci Technol 15(8):635–641
13. Davis D (2001) Use of dilatation in understanding composite propellant aging. In: 37th American Institute of Aeronautics and Astronautics, Society of Automative Engineers and American Society of Mechanical Engineers joint propulsion conference and exhibition, Salt Lake City, US, 8–11 July 2001
14. Faulkner G, Thompson A, Buswell H (1996) The penetrometer: non-destructive testing of composite propellant rocket motor grains to determine ageing characteristics. In: AGARD PEP

symposium on service life of propellant systems, Athenes, North Atlantic Treaty Organisation, Brussels, 10–14 May 1996

15. Judge M (2003) An investigation of composite propellant accelerated ageing mechanisms and kinetics. Propellants Explos Pyrotechnics 28(3):114–119

16. Wilker S, Ticmanin U, Stottmeister L (2001) Influence of atmospheric conditions on the ageing of single, double and triple base propellants, In: 12th symposium on chemical problems connected with the stability of explosives, Karlsborgs Fästoring, Karlsborg, Sweden, 2001

17. Torry S, Earl J, Cunliffe A, Tod D (2006) Effect of plasticiser diffusion on the mechanical properties of double base propellants. In: Insensitive munitions & energetic materials technology symposium, Atomic Weapons Establishment (AWE), Reading, Bristol, 2006

18. Asthana S, Divekar C, Singh H (1989) Studies on thermal stability, autoignition and stabilizer depletion for shelf life of CDMB propellants. J Hazard Mater 21:35–46

19. NATO (2008) AOP 48 – explosives, nitrocellulose-based propellants, stability test procedures and requirements using stabilizer depletion. North Atlantic Treaty Organisation, Brussels

20. Herder G, Weterings F, de Klerk W (2003) Mechanical analysis on rocket propellants. J Therm Anal Calorim 72:921–929

21. Judge M, Lessard P (2007) An advanced GAP/AN/TAGN propellant. Part I: ballistic properties. Propellants Explos Pyrotechnics 32(2):175–181

22. Wang N, Qian W, Sui X, Xiong Y (2014) Life predictions of NEPE propellants. Propellants Explos Pyrotechnics 39(1):102–107

23. Bunyan P, Cunliffe A, Davis A, Kirby F (1993) The degradation and stabilisation of solid rocket propellants. Polym Degrad Stab 40:239–250

24. Niu R-M, Zhou Q-C, Xiong C, Yu-Tao J, Zhen W, Zheng J (2014) Experimental and numerical analysis of mode II fracture between propellant and insulation. Int J Adhes Adhes 52:1–10

25. Sell T, Vyazovkin S, Wight C (1999) Thermal decomposition kinetics of PBAN-binder and composite solid rocket propellants. Combust Flame 119:174–181

26. Bunyan P (2003) Activation energy measurements on a double base propellant by microcalorimetry over the temperature range 40°C–90°C, paper no. D1. In: 4th international heat flow calorimetry symposium on energetic materials, Trevor Griffiths QinetiQ, Ted Charsley University of Huddersfield, Leeds, 2003

27. Cerri S, Bohn MA, Menke K, Galtetti L (2009) Ageing behaviour of HTPB based rocket propellant formulations. Cent Eur J Energetic Mater 2:149–165

28. Bohn MA (2012) Generic formulation of performance assessment quantities for stability, compatibility and ageing of energetic materials. In: 43rd international conference of the ICT, Fraunhofer ICT, Karlsruhe, Germany, 2012

29. Smirnov L (2004) Chemical physics of decomposition of energetic materials problems and prospects. Russ Chem Rev 73(11):1121–1141

30. Bunyan P (2001) Accelerating rate calorimetry studies on experimental hybrid compositions. In: 12th symposium on the chemical problems connected with the stability of explosives, pp 31–43, Karlsborgs Fästoring, Karlsborg, Karlsborg 2001

31. Celina M, Minier L, Assink R (2002) Development and application of tools to characterize the oxidative degradation of AP/HPTB/Al propellants in a propellant reliability study. Thermochem Acta 384:343–349

32. Chaturvedi S, Pragnesh D, Patel N (2014) Thermal decomposition of Al/HTPB based propellants in presence of Zn alloys. In: Applied nanoscience, Available via http://link.springer.com/article/10.1007/s13204-014-0296-3. Accessed 7th Nov 2014

33. Eringen A, Liebowitz H, Koh S, Crowley J (1967) Mechanics and chemistry of solid propellants. Pergamon Press, Oxford

34. Wallace I, Powell R (1980) Application of a chemiluminescence nitric oxides analyser to stability testing. In: Annual international conference of the ICT energetic materials, Fraunhofer ICT, Karlsruhe, pp 195–217, Germany, 1980

35. Harvey D (2000) Modern analytical chemistry. McGraw-Hill Higher Education, New York

36. Haberman J (1986) High performance liquid chromatography of propellants part 1 – analysis of M1, M6 and M10 propellants, technical report ARAED-TR-86017, US Army Armament research and development center, Dover

37. Oehrle S (1997) Analysis of stabiliser degradation products using HPLC and photodiode array (PDA) detection. J Energetic Mater 15(1):21–23
38. Fengqi Z, Shuyun H, Rongzu H, Hongxu G, Fang H (2007) A study of kinetic behaviours of the effective centralite/stabilizer consumption reaction of propellants using a multi-temperature artificial accelerated ageing test. J Hazard Mater 145:45–50
39. TOSOH, http://www.separations.us.tosohbioscience.com/ServiceSupport/TechSupport/ResourceCenter/PrinciplesofChromatography/IonExchange. Accessed 10th Nov 2014
40. Klassen S, Massis T, Boesplug E, Montoya B, Reif J (2002) Ion chromatography of energetic materials at Sandia national laboratories. Thermochem Acta 384:329–341
41. Waters (2014) http://www.waters.com/waters/en_GB/GPC--Gel-Permeation-Chromatography/nav.htm?cid=10167568&locale=en_GB. Accessed 10th Nov 2014
42. Matečić-Mušanić S, Sućeska M, Ćuljak R (2013) The applicability of chromatographic methods in the investigation of ageing processes in double base rocket propellants. Cent Eur J Energetic Mater 10(2):245–262
43. Günther H (1995) NMR spectroscopy, 2nd edn. Wiley, India
44. Griffiths P, de Hasseth JA (2007) Fourier transform infrared spectrometry, 2nd edn. Wiley-Blackwell, Hoboken
45. Lussier L-S, Bergeron E, Gagnon H (2006) Study of the daughter products of Akardite-II propellants. Explosives 31:253–262
46. Grythe K, Hansen F, Walderburg H (2004) NMR self-diffusion and viscosity of polyurethane formulations for rocket propellants. J Phys Chem B 108(33):12404–12412
47. Cunliffe A, Dodds J, Tod D (1998) A screening approach to propellant ageing assessment. In: Symposium on stability of explosives, Hemmeslövs Herrgord, Bastad, Sweden, 1998
48. Tunnell R, Ashcroft M, Dale R, Tod D, Proud W (2014) Ammonium perchlorate, friend or foe? Propellants Explos Pyrotechnics 39(5):707–713
49. Pristera F (1953) Analysis of propellants by infra-red spectroscopy. Anal Chem 25(6):844–856
50. Torry S, Cunliffe A (2003) The inhomogeneous ageing of composite propellants. In: 34th international annual conference of ICT, Fraunhofer ICT, June 24–June 27, 2003
51. McDonald B (2011) Effect of humidity and temperature induced aging on the rheology of a nitrate ester plasticized/poly (glycoladipate)/solids loaded propellant, p 44. In: 43rd international conference of the Fraunhofer ICT, Karlruhe, June 28–July 1 2011
52. ASTM Standard D3985-81, Oxygen gas transmission rate through plastic film and sheeting using a coulometric sensor
53. Cerri S, Bohn MA, Menke K, Galfetti L (2010) Ageing of HTPB/Al/AP/rocket propellant formulations investigated by DMA measurements, sol-gel and GPC analysis, vol 42, In: 42nd international conference of the Fraunhofer ICT, Karlruhe, Fraunhofer ICT 2010
54. Cunliffe AV, Davis A, Tod D (1996) Life prediction of composite propellant motors, AGARD. In: 87th PEP symposium, service life of propellant systems, North Atlantic Treaty Organisation, Brussels, Athens, May 1996
55. Christiansen AG, Layton LH, Carpenter RL (1980) HTPB propellant ageing and service life. In: AIAA-80-1273, American Institute of Aeronautics and Astronautics, Society of Automotive Engineers and American Society of Mechanical Engineers, 16th joint propulsion conference,Hartford, USA, July 1980
56. NATO (2001) STANAG 4147 – chemical compatibility of ammunition components with explosives (non-nuclear applications), Edition 2
57. Oyumi Y (1993) Thermal decomposition of BAMO/HMX propellants. Propellants Explos Pyrotechnics 18:62–68
58. Kissinger H (1957) Reaction kinetics in a differential thermal analysis. Anal Chem 29:1702
59. Ozawa T, Isozaki H, Negishi A (1970) A new type of quantitative differential analysis. Thermochem Acta 1:545–553
60. Flynn J (1966) A quick, direct method for the determination of activation energy from thermogravimetric data. Thermochem Acta 4:323
61. Goncalves R, Rocco J, Iha K (2013) Thermal decomposition kinetics of aged solid propellant based on ammonium perchlorate – AP/HTPB binder, applications of calorimetry in a wide context – differential scanning calorimetry, isothermal titration calorimetry and

microcalorimetry. Dr. Amal Ali Elkordy (ed), Available from: http://www.intechopen.com/books/applications-of-calorimetry-in-a-wide-context-differential-scanning-calorimetry-isothermal-titration-calorimetry-and-microcalorimetry/thermal-decomposition-kinetics-of-aged-solid-propellant-based-on-ammonium-perchlorate-ap-htpb-binder. Accessed 5th Nov 2014

62. Trache D, Khimeche K (2013) Study on the influence of ageing on thermal decomposition of double-base propellants and prediction of their in-use time. Fire Mater 37:328–336

63. Blažek A (1973) Thermal analysis. Van Nostrand Reinhold Company Ltd, New York

64. NATO (2007) STANAG 4582: explosives nitrocellulose based propellants stability test procedure and requirements using HFC, Edition 2. North Atlantic Treaty Organisation, Brussels

65. Tunnell R (2013) Degradation of complex hybrid propellants, PhD thesis

66. Bohn MA (2012) Generic formulation of performance assessment quantities for stability, compatibility and ageing of energetic materials, Paper no. 59. In: International conference of the ICT, Energetic Materials, Fraunhofer ICT, Germany, 2012

67. Liebens E, Neviere R, Chevalier S (2004) Ageing simulation of solid propellant grains. In 13th Jan Hannson symposium chemical problems, Sunbyberg, Sektionen, Sweden, 6–10th June, 2004

68. Husband M (1992) Use of dynamic mechanical measurements to determine the aging behavior of solid propellant. Propellants Explos Pyrotechnics 17(4):196–201

69. de la Fuente J, Rodríguez O (2003) Dynamic mechanical study on the thermal aging of a hydroxy-terminated polybutadiene based energetic composite. J Polym Sci 87(14):2397–2405

70. Liebens E, Neviere R, Chevalier S (2005) Ageing simulation methodology of solid propellant grains. In: NIMIC-MSIAC workshop, North Atlantic Treaty Organisation, Brussels, Helsinki, 22–27 May, 2005

71. Sućeska M, Matečić- Mušanić S (2009) Artificial ageing of double base rocket propellant effect on dynamic mechanical properties. J Therm Anal Calorim 96(2):523–529

72. Sui X, Wang N, Wan Q, Bi S (2010) Effects of relaxed modulus on the structure integrity of NEPE propellant grains during high temperature ageing. Propellants Explos Pyrotechnics 35:535–539

73. NATO (2002) STANAG 4540 – explosives, procedures for dynamic mechanical analysis (DMA) and determination of glass transition temperature, Edition 1. North Atlantic Treaty Organisation, Brussels

74. ASM International (2004) Introduction to tensile testing, http://www.asminternational.org/documents/10192/3465262/05105G_Chapter_1.pdf/e13396e8-a327-490a-a414-9bd1d2bc2bb8. Accessed 10th Nov 2014

75. Instron, http://www.instron.co.uk/wa/applications/test_types/compression.aspx. Accessed 10th Nov 2014

76. Jeremic R (1999) Some aspects of time-temperature superposition principle applied for predicting mechanical properties of solid rocket propellants. Propellants Explos Pyrotechnics 24:221–223

77. Sućeska M, Fiamengo I, Matečić-Mušanić (2010) Study of mechanical properties of naturally aged double base rocket propellants. Cent Eur J Energetic Mater 7(1):47–60

78. van der Waal C, Drent R (1968) A torsional creep apparatus. Rheol Acta 7(3):265–271

79. Greidanus P, Struik L (1980) Physical aging of double-base propellants. In: American Institute of Aeronautics and Astronautics, Society of Automative Engineers and American Society of Mechanical Engineers 16th joint propulsion conference, American Institute of Aeronautics and Astronautics, Connecticut, June 30–July 2, 1980

80. Spetz G (1999) Stress relaxation tests, technical report, 98/1, 2nd edition http://www.axelproducts.com/downloads/Relax.pdf. Accessed 8 Oct 2014

81. Kadiresh PN, Sridhar B (2008) Experimental evaluation and simulation on aging characteristics of aluminised AP HTPB composite solid propellant. Mater Sci Technol 24(4):406–412

82. Yilmazer Y, Farris RJ (1983) Mechanical behaviour and dilatation of particulate filled thermosets in the rubbery state. J Appl Polym Sci 28:3386

83. Farris RJ (1964) Dilatation of granular filled elastomers under high rates of strain. J Appl Polym Sci 1964(8):25
84. Davenas A (1979) Solid rocket propulsion technology. Pergamon Press, New York
85. Instron, (http://www.instron.co.uk/wa/glossary/Hardness-Test.aspx). Accessed 6 Nov 2014
86. American Society for testing and materials (2005) ASTM D 2240-05: standard test method for rubber property: durometer hardness
87. Hocaoğlu Ö, Özbelge T, Pekel F, Özar S (2001) Aging of HTPB/AP-based composite solid propellants, depending on the NCO/OH and triol/diol ratios. J Appl Polym Sci 79:959–964
88. Libardi J, Morais (2010) Diffusion of plasticizer in a solid propellant based on hydroxy-terminated polybutadiene. Polimeros 20(4):241–245
89. Goldstein J, Newbury DE, Joy DC, Lyman CE, Echlin P, Lifshin E, Sawyer L, Michael JR (2003) Scanning electron microscopy and X-Ray microanalysis, 3rd edn. Springer, Berlin, New York
90. McDonald B, Rice J, Kirkham M (2014) Humidity induced burning rate degradation of an iron oxide catalyzed ammonium perchlorate/HTPB composite propellant. Combust Flame 161:363–369
91. Kishore K, Verneker VR, Prasad G (1978) Storage stability of solid rocket fuels. 2. Effect of oxidizer loadings. Fuel 57(1):22–24
92. Prasad G, Kishore K, Verneker V (1980) Effect of ageing on ballistic and mechanical properties of propellants having various oxidiser loadings. Combust Flame 37:197–199
93. Kadiresh P, Sridhar B (2007) Mechanical and ballistic property variations of a solid propellant during accelerated ageing. J Des Manuf Technol 1(1):71–73

Aging Behavior of ADN Solid Rocket Propellants and Their Glass-Rubber Transition Characteristics

Manfred A. Bohn and Sara Cerri

Abstract Solid rocket propellants (SRPs) using ammonium dinitramide (ADN) as oxidizer are of interest because they belong to the classes of "green propellants" and signature-reduced propellants. The present study investigated several ADN-based rocket propellant formulations containing different prepolymers (glycidyl azide polymer (GAP); Desmophen® D2200), curing agents (bis-propargyl succinate (BPS); Desmodur® N3400), and filler types (aluminum (Al); octogen (HMX)). Ammonium perchlorate (AP)-based formulations have also been manufactured to make comparisons. SRP formulations have been investigated using dynamic mechanical analyses (DMA), mass loss, and tensile strength measurements. The accelerated aging program was between 60 and 85 °C with aging times adjusted to a thermal equivalent load of 15 years at 25 °C. The dynamic mechanical behavior of the ADN formulations differs from the hydroxyl-terminated polybutadiene (HTPB)-based materials: results show only one obvious peak in the loss factor curve instead of two. Fuel fillers, oxidizers, and curing agents have influences on the glass-rubber transition temperature (T_g) and the peak broadness. The loss factor peak of the GAP formulations is broader than the one of the Desmophen® formulations. Lowering of T_g by using AP instead of ADN was found. DMA investigations revealed distinct changes in the shape of the loss factor curves. Their detailed analyses with exponentially modified Gaussian (EMG) functions showed that the loss factor curves have two parts with different molecular mobilities during the transition of the material from energy-elastic (glassy) to the entropy-elastic (rubbery) state. Aging acts strongly on the part with restricted mobility.

M.A. Bohn (✉)
Fraunhofer-Institut für Chemische Technologie (ICT), Energetic Materials, 76318 Pfinztal, Germany
e-mail: Manfred.Bohn@ict.fraunhofer.de

S. Cerri
SC Consulting, 28060 Curoggio, NO, Italy
e-mail: Cerri.Sara@gmail.com

Nomenclature

ADN	Ammonium dinitramide
Al	Aluminum
AN	Ammonium nitrate
AP	Ammonium perchlorate, sometimes also named APC
BLC	Baseline correction
BPS	Bis-propargyl succinate, a non-isocyanate curing agent, applicable with GAP; curing based on the Huisgen reaction between the ethine groups of BPS and organic azides of GAP
CRP	Composite rocket propellant
D2200	Polyester polyol type, Desmophen® D2200, inert binder
DMA	Dynamic mechanical analysis
DSC	Differential scanning calorimeter
E_a	Activation energy, [kJ·mol^{-1}]
EMG	Exponential modified Gauss function
G'	Storage shear modulus, determined by torsion DMA, [Pa]
G''	Loss shear modulus, determined by torsion DMA, [Pa]
GAP	Glycidyl azide polymer, energetic binder, polyether type
GvH	Generalized van't Hoff rule
HCl	Hydrogen chloride
HDI	Hexane diisocyanate, curing agent
HEC	High explosive charge
HMX	Octogen, energetic filler
HNF	Hydrazinium nitroformate
HTPB	Hydroxyl terminated polybutadiene, inert binder, butadiene based
HX-880	Bonding agent, N,N-bis (2-hydroxyethyl) glycol amide, referred as BHEGA, delivered from MACH I company (HX-880 may act also as a cross-linker)
ICT	Fraunhofer Institute of Chemical Technology
IPDI	Isophorone diisocyanate, curing agent to produce PUR elastomers
I_s	Gravimetric or mass specific impulse, [s], [Ns kg^{-1}]
JANNAF	Joint Army, Navy, NASA, Air Force Interagency Propulsion Committee
ML	Mass loss
N100	Polyisocyanate curing agent, HDI-based, Desmodur® N100, to produce PUR elastomers
N3400	Polyisocyanate curing agent, HDI-based, Desmodur® N3400, to produce PUR elastomers
nAl	Nanometer sized Al powder
NCO	Isocyanate group, also a functional group in PUR formation
OH	Hydroxyl group, also a functional group in isocyanate curing
PUR	Polyurethane

Req	Equivalent ratio between two reactive sites, here mostly between OH groups and NCO groups to form polyurethane elastomers taking into account the molecular conditions of the substances carrying these functional groups, [−]
RP	Rocket propellant
SEM	Scanning electron microscopy
SRP	Solid rocket propellant
tan δ	Loss factor, $\tan\delta = G''/G' = E''/E'$, [−]
TEL	Thermal equivalent load
$T_{g,DMA,f}$	Glass-to-rubber transition temperature determined by DMA, [°C]; full information includes also the used excitation frequency f, $T_{g,DMA,\,xxHz}$
$T_{g,DSC,h}$	Glass-to-rubber transition temperature determined by DSC, [°C]; full information includes also the used heat rate h, $T_{g,DSC,\,xx°C/min}$
TMETN	Trimethylolethyltrinitrate, liquid energetic filler, in part acting as plasticizer
μAl	Micrometer sized Al powder
–C≡C	Ethine group, also a functional group in azide curing
–N=N=N	Azide group, also a functional group in BPS curing (1,3 dipolar cycloaddition)

1   Introduction

Current Western composite rocket propellants (CRPs) are ammonium perchlorate (AP) based, because AP is still the most effective oxidizer, providing high performance with high specific gravimetric and volumetric impulses. But during the combustion process, high amounts of hydrogen chloride are produced causing signature of the exhausted gases and severe corrosion problems at the launch platforms. Furthermore, AP produces increasing problems by contaminating drinking water, which can affect the thyroid gland function because the perchlorate anion competes with the iodide anion in the thyroid tissue. This problem could increase in importance with the replacement of the propellant materials having reached or being near the end of their designed in-service time [1].

Thus, several efforts have the aim to develop solid rocket propellants (SRPs), which are smokeless, have low signature, are environmentally friendly, or are with reduced pollution [2–10]. In addition, they should have ballistic, mechanical, and aging characteristics similar to the current HTPB/AP/Al-based systems. The search is now for oxidizers, which could replace AP. The demands for them are chlorine-free, as low toxic as possible, thermally stable, compatible with used propellant ingredients, and an overall good aging behavior during in-service time.

Oxidizers which are presently in selection are hydrazinium nitroformate (HNF), ammonium nitrate (AN), and ammonium dinitramide (ADN). HNF was ruled out already [11] because of compatibility problems with ingredients and not stabilizable decomposition behavior [12]. Trials of SRPs have shown in the burning rate very

high-pressure exponents near one, and when the reduction was successful, a severe incompatibility was observed [13, 14]. The stabilizability is no problem with ADN, because the intermediate products, which foster decomposition, are relatively long living [15], and their effect is suppressable by applying some stabilizers [16]. AN alone does not have satisfying burning characteristics for rocket propellants and its changes in crystallographic phases in the range of in-service temperatures are always a matter of concern, even when phase stabilized.

From these facts, ADN seems the best candidate. It has good values with regard to oxygen balance, 25.8 %; mass density, 1.812 g·ml^{-1}; and the enthalpy of formation, −149.8 kJ·mol^{-1} is less negative than the one of AP with −295.8 kJ·mol^{-1} [17]. It is chlorine-free and allows to obtain propellants with mass specific impulse (I_s) higher than 280 s [18], and it shows a highly exothermic combustion reactions near the surface, which improves the heat feedback to the burning surface causing increase of the burning rate.

Therefore, a study was performed on ADN propellant formulations using tensile test, mass loss (ML), and dynamical mechanical analysis (DMA) to obtain a detailed characterization of the propellants' behavior with respect to mechanical and thermal properties and their change with aging. In principle, the ADN-based composite propellants show the same aging effects as the AP-based ones. However, a severe additional aging can be caused by the aggressive oxidizing ability of ADN. The low-symmetry structure of the dinitramide anion (Fig. 1a) is one of the reasons for the reactivity and the instability of ADN. Instead, ammonium perchlorate (Fig. 1b) is nearly not reactive due to the high symmetry and low energy of the tetrahedral structure of the perchlorate anion. Thus, a different reaction and compatibility behavior of these two substances with the other formulation ingredients should be expected.

From the present knowledge, it was decided not to use HTPB-based binders with ADN particles, because the double bonds are immediately attacked by ADN causing chain cleavage and porosity around the oxidizer particles. Therefore, the use of polyether- and polyester-based binder systems was chosen to create the rubbery
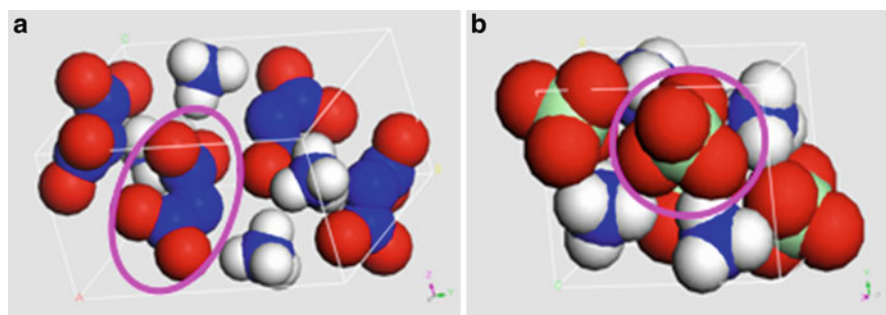
Fig. 1 a Crystal structure of ADN: see the detail of the dinitramide anion (*ellipse*). **b** Crystal structure of AP: see the detail of the perchlorate anion (*circle*)

polyurethane network. In the present paper glycidyl azide polymer (GAP)- and Desmophen®-based binders are investigated. Comparisons with "state-of-the-art" formulations, represented by HTPB/AP/Al-based propellant formulations, are also included.

2 Design of Formulations

Tables 1 and 2 display the compositions of the investigated ADN-based formulations. The binders are polyether and polyester based. The analogous formulations, using AP instead of ADN, were also included for comparison, in order to elucidate and to find out the behavior caused by ADN. The investigated propellants have a lower solid load than the standard AP/HTPB-based formulations; typical values are about 65 m.% and 85 m.%, respectively. This was due to a technical limitation. ADN is available in crystalline state with needle shape of the crystals. Therefore, the morphology must be improved. Prilling techniques have been developed to convert the ADN crystals to spherical particles either in suspension in an inert fluid or in a gas stream. The ADN prills used (uncoated and unstabilized) were processed at Fraunhofer ICT (details of the prilling process can be found elsewhere [19]) and had an average particle size of 60–120 μm. Propellant ballistic properties are influenced to a greater degree by the oxidizer type and the particle distribution than by the metal fuel content, which increases the flame temperature [20]. Recent results [21] have shown that it is possible to produce ADN particles with an adequate particle size by combining the micro-reaction technique and the ADN emulsion crystallization process. Because at the time of this study multimodal ADN distributions were not available, the multipacking density approach could not be used, and the only possibility to achieve higher solid load, density, and performance of the propellants was obtained by adding another filler, such as HMX or Al. Table 1 shows the compositions of several GAP-bonded samples with different curing agents: bis-propargyl succinate (BPS) or Desmodur® N100 (N100).

In a second set of formulations (Table 2), a polyester diol-based polyurethane binder was employed in contrast to the energetic polyether polyol-based GAP binder. The polyester diol used was Desmophen® D2200 (D2200), and the curing agent was Desmodur® N3400 (N3400), a hexane diisocyanate (HDI)-based condensation product.

The aim of the broad diversity of formulations was to break up the formulation complexity in order to study the individual effects given by different components:

- Influence of fuel filler type – Al versus HMX
- Influence of binder types – GAP/BPS versus D2200/N3400
- Effectiveness of the bonding agent HX-880 for ADN
- Change in oxidizer – replacement of ADN with AP

Table 1 Compositions in mass % of the ADN-GAPxx formulations – BPS cured, in comparison with AP analogues

Component		ADN-V127	ADN-V128	ADN-V129	AP-13	AP-14
ADN prills, 106 μm	(m.%)	56	56	56	–	–
AP 200 μm/AP 45 μm	(m.%)	–	–	–	37.34/18.66	37.34/18.66
HMX, 5 μm	(m.%)	–	–	10	10	10
μAl, 8 μm	(m.%)	10	5	–	–	–
nAl, 100–200 nm	(m.%)	–	5	–	–	–
GAP diol/triol	(m.%)	18.58/3.625	18.58/3.625	18.58/3.625	16.37/3.20	18.68
BDNPF-A	(m.%)	8.1	8.1	8.1	–	–
TMETN	(m.%)	–	–	–	10.8	10.8
Stabilizers	(m.%)	1.6	1.6	1.6	1.6	1.6
BPS	(m.%)	2.095	2.095	2.095	2.03	–
Desmodur® N100	(m.%)	–	–	–	–	2.92
Solid load	(m.%)	66	66	66	66	66
Req (C≡C/"OH")	–	1.00	1.00	1.00	1.10	–
Req NCO/OH	–	–	–	–	–	1.00

μAl micro-sized Al powder, *nAl* nano-sized Al powder, *BDNPF-A* bis(2,2-dinitropropyl) formal/bis(2,2-dinitropropyl) acetate, *TMETN* trimethylol ethyl trinitrate

Req equivalent ratio between two reactive sites, here mostly between hydroxyl groups (OH) and isocyanate groups (NCO) to form polyurethane elastomer taking into account the molecular conditions of the substances carrying these functional groups

"*OH*" pseudo OH group. During the curing process the triple bonds (C≡C) of BPS react in 1,3 dipolar cycloaddition (Huisgen reaction) with the azido groups of GAP to form cross-links via triazoles. This type of curing is named triazole curing. Therefore, a pseudo OH group, named "OH," was considered in the equivalent ratio Req

Table 2 Compositions in mass % of the D2200xx formulations. AP-12 corresponds to ADN-V142, and both formulations contain HMX; AP-11 corresponds to ADN-V144, and both formulations contain μAl

Component		ADN-V142	ADN-V144	AP-11	AP-12
ADN prills, 106 μm	(m.%)	56	56	–	–
AP, 45 μm/200 μm	(m.%)	–/–	–/–	18.66/37.34	18.66/37.34
HMX, 5 μm	(m.%)	10	–	–	10
μAl, 8 μm	(m.%)	–	10	10	–
Desmophen® D2200	(m.%)	17.42	17.42	17.42	17.42
TMETN+0.5%NDPA	(m.%)	10.8	10.8	10.8	10.8
HX-880	(m.%)	0.14	0.14	0.14	0.14
Stabilizers	(m.%)	1.6	1.6	1.6	1.6
Desmodur® N3400	(m.%)	4.04	4.04	4.04	4.04
Solid load	(m.%)	66	66	66	66
Req (NCO/OH)	–	1.00	1.00	0.99	0.99

To simplify the reading, the formulations will be called in the following way:

– GAPxx – GAP-based formulations
– D2200xx – Desmophen®-based formulations

Depending on the oxidizer considered, the prefix ADN or AP will be added.

3 Aging Plan

Accelerated aging conditions (temperature and time) were chosen simulating an in-service time of up to 15 years of natural aging at 25 °C. Samples were aged from 65 to 85 °C in air, with relative humidity (RH) below 10 %, and in load-free conditions; this means no effect of stress and/or strain caused by the motor case occurred. The aging performed considers the worst case situation in order to get in acceptable times the effect of aging. With real propellants in sealed motors, their aging state can be found out by comparison with the extent of the aging effect. The aging conditions were determined using the thermal equivalent load (TEL) principle to exert at each condition the same thermal load. The correlation between the conditions was achieved by the generalized van't Hoff (GvH) rule [22] with a scaling factor of 2.9 per 10 °C temperature change. The value of the F factor depends on the activation energy range of the aging process, e.g. with values of the activation energies of about 80–120 kJ·mol^{-1}, and a temperature range between 20 and 90 °C the scaling factor is about 3. The principles and handling of the extrapolation by the GvH and the choice of the appropriate F value are explained in [22]. The higher the activation energy, the higher the F factor and the shorter the aging times. Considering that the activation energies in the ADN systems can be higher than with the HTPB-based formulations [23], a value of F moderately higher than the one used for the AP/HTPB-formulations investigated in a previous study with $F = 2.5$ [24] was used, in order to not shorten too much the accelerated aging times. The study focused on the accelerated aging of the surface layer of SRPs, which means that no "in-core" analysis was considered.

The calculation of the test times (t_T) for the chosen aging temperatures (T_T) to reach preset in-service times (t_E) at certain in-service temperature (T_E) conditions is shown in Eq. 1:

$$t_T [d] = 365.25 \cdot t_E [a] \cdot F^{-(T_T - T_E)/\Delta T_F} \tag{1}$$

1 year = 365.25 days (averaged with leap years)
1 month = 365.25/12 = 30.44 days
t_E = in-service time in years at temperature T_E
t_T = test time in days at test or aging temperature T_T
T_T = test or aging temperature
T_E = in-service temperature
F = acceleration or deceleration factor per 10 °C temperature change
ΔT_F = temperature interval assigned to actual value of factor F, here 10 °C

Table 3 Applied accelerated aging conditions (time and temperature) to simulate an in-service time period of up to 15 years at 25 °C

Natural aging or in-service time periods (in years)			
In-service temperature T_E (°C)	In-service time t_E (a)		
25	5	10	15
TEL-determined accelerated aging conditions from preset in-service times using GvH rule with $F = 2.9$			
Aging temperature T_T (°C)	Aging time t_t^a (d)		
85	4	8	12
80	6	12.5	20
70	15	30	45
65	23.5	47	70.5

[a]The given aging times are rounded up

The aging plan is shown in Table 3. The upper part presets the in-service time periods at 25 °C. To reach the corresponding TEL values by accelerated aging, the defined storage times at given aging temperatures have to be applied to the samples. These are compiled in the lower part of Table 3. The scaling from in-service times to accelerated aging conditions was made by GvH. This ensures longer aging times than an Arrhenius-based scaling.

4   Applied Investigation Methods

4.1   Tensile Tests

The mechanical behavior was characterized with a tensile test machine of type UPM 1476, manufactured by company Zwick Roell, D-89079 Ulm, Germany. JANNAF "dogbone" samples (125 mm length, 25 mm width, 10–12 mm thickness) were used in uniaxial tensile tests at room temperature and atmospheric pressure at one strain rate of 0.0167 s^{-1}. The applied force and the elongation of the gauge length were recorded by a load cell and an extensometer, respectively.

4.2   Dynamic Mechanical Analysis (DMA)

Dynamic mechanical measurements were carried out in torsion mode using a DMA instrument of type ARES™ (Advanced Rheometric Expansion System) manufactured by former Rheology Unit of Rheometric Scientific Inc., Piscataway, NJ, USA (now belonging to Waters, Inc., BU TA Instruments, New Castle, DE, USA). A liquid nitrogen cooling accessory was used for the low- and high-temperature operations. Samples were rectangular bars of 10 mm width, 4–5 mm thickness

and 30 mm length. The temperature range was −80 °C to +80 °C, with stepwise heating by 1 Kmin^{-1} and a soak time (equilibration time) of 28 s. Specimens were tested at four deformation frequency values: 0.1, 1.0, 10.0, and 30.0 Hz. The ADN propellants are softer than the HTPB/AP/Al-based ones investigated in a previous study [24] due to the lower solid load. A strain control equal to 0.0012 was too low for getting good data, especially at temperature values above 25 °C. Therefore, two strain controls were used: 0.00237 from −80 °C up to +15 °C and 0.01 from +16 to +80 °C. Measurement reproducibility is very high, and only one sample was used. In case of anomalous behavior, a second measurement was performed.

4.3 Mass Loss Measurements

Samples were stored at different isothermal temperature values in glass vials with glass stoppers loosely inserted. Samples were cut in small pieces of about 2 mm cubes. For each chosen aging temperature, two samples were considered. Stoppers were not fixed by clamping and not sealed with grease, so gas exchange could take place. The weighing was done offline with an analytical balance from company Mettler Toledo in appropriate time intervals, at least twice a week.

5 Results

5.1 Tensile Properties

The maximum corrected stress (σ_{corr}) (Eq. 2) and the maximum natural or logarithmic strain, also called Hencky strain (ε_{log}) (Eq. 3), have been determined for the several types of propellant formulations including the present standard, HTPB-isophorone diisocyanate (IPDI)-based CRP with AP and Al, and are shown in Fig. 2. The corrected quantities are calculated directly from the measured (engineering) quantities, linear strain ε_{lin} and nominal or engineering stress σ_{en}:

$$\sigma_{corr} = \sigma_{true} = \sigma_{en} \cdot (1 + \varepsilon_{lin}) \tag{2}$$

$$\varepsilon_{log} = \varepsilon_{true} = ln\,(1 + \varepsilon_{lin}) \tag{3}$$

Clearly, the propellants with GAP-BPS binder have the lowest strength and a medium strain capability. The propellants with D2200-N3400 have medium strength but low strain capability. Both development propellant types are quite far away from the values of the HTPB-IPDI propellants.
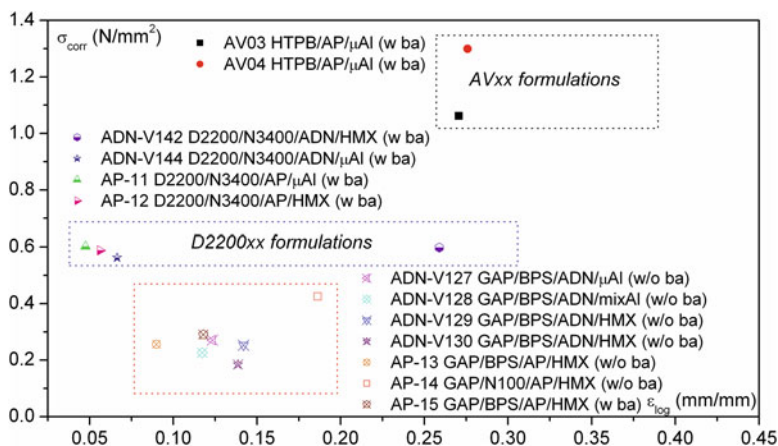
Fig. 2 Maximum corrected stress versus maximum natural strain of three types of CRPs, with bonding agents (w ba) and without bonding agent (w/o ba) (Reproduced from Cerri et al. [8])

5.2 Chemical Stability Determined by Mass Loss

Many methods can be applied to investigate the so-called chemical stability of energetic substances. The reasons for the appearance of self-decomposing reactions in substances are reactive sites in molecules, low activation energy barriers, and finally the lower values of thermodynamic potentials for the reaction products. The reactions are driven mostly by redox and sometimes by acid-base situations in the energetic molecules themselves or in mixtures of oxidizing and reducing substances. All applied methods use any property of the substance in consideration, which changes during the course of the decomposition reactions. This can be mass loss (ML) or gas generation, heat generation, and generally the evolution of the decomposition products or the consumption of substances.

To follow the stability of ADN prills and of the formulations, the method of determining the mass loss was considered. Figures 3 and 4 show the mass loss evolution with aging time at 85 °C storage temperature for formulations containing HMX and μAl.

All ADN propellants show a beginning increase of mass loss after about 10 days. However, the formulations called AP-11 and AP-12, which are analogous to ADN-V144 and ADN-V142, respectively, have only a slight mass loss at the beginning of the storage, and then it stays constant. These differences in mass loss evolution show clearly that ADN is the cause for the higher and even accelerating mass loss of the ADN formulations. This behavior was also observed at lower temperatures [8].

The compatibility between components of a formulation is an essential criterion for the long-term stability and the aging behavior. The substance HX-880, N,N-bis (2-hydroxyethyl) glycolamide, referred as BHEGA, was introduced as bonding in high explosives containing RDX and HMX. The bonding agent acts as "bond
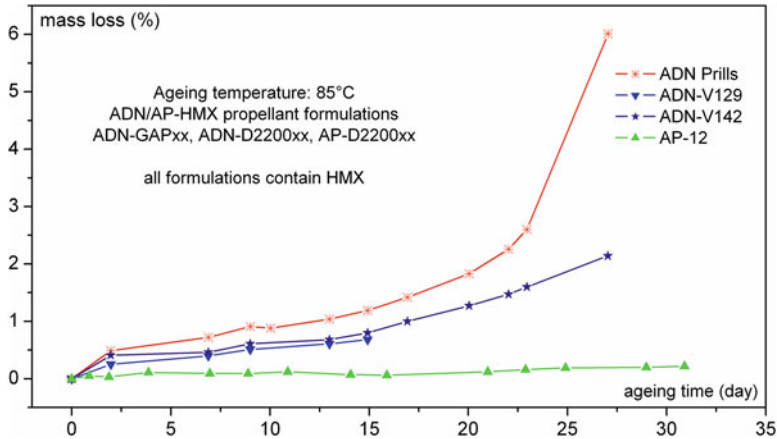
Fig. 3 Mass loss of ADN prills, ADN-based propellants, and AP-12 formulation. All formulations contain HMX (Reproduced from Cerri et al. [8])
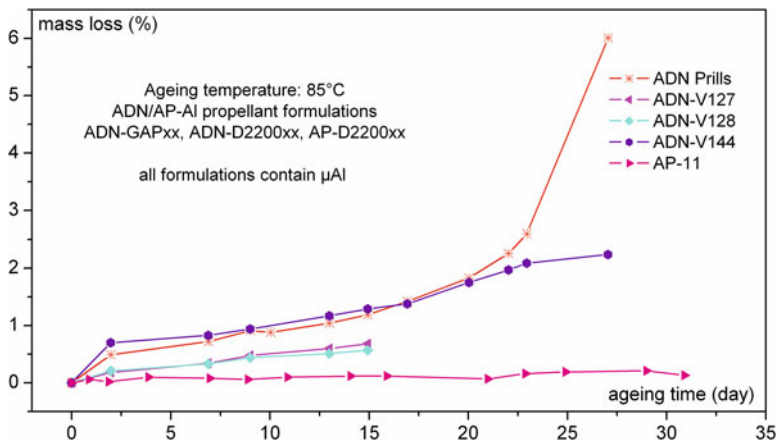
Fig. 4 Mass loss of ADN prills, ADN-based propellants, and AP-11 formulation. All formulations contain µAl (Reproduced from Cerri et al. [8])

bridge" between crystalline particles and the elastomer binder. For AP the type HX 878 is used successfully. It could be also useful as bonding agent for ADN. But HX-880 has three OH-groups and may act as cross-linker in polyurethane systems; therefore, a reduction of strain capability can result. Here the question arose about its compatibility with ADN. The chemical compatibility testing can be done with the same methods used for determining the chemical stability. Mass loss as function of time at 80 °C was considered. In order to quantitatively determine the compatibility, the two components alone and the mixture itself must be measured.

In the ideal case, no reaction occurs between the components, and then the subtraction of the data of the components from the ones of the mixture should
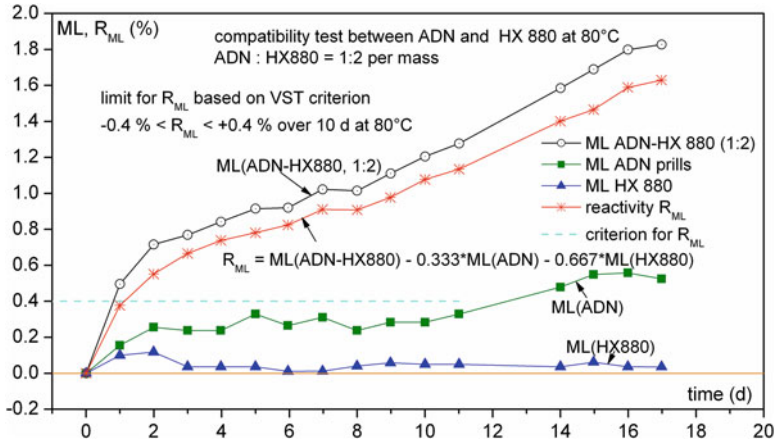
Fig. 5 Chemical compatibility of ADN with HX-880 determined by mass loss. According to the criterion for the mass loss compatibility function (R_{ML}) [25], the values of R_{ML} are already from 2 days on higher than the limit value of +0.4 %. The assessment is that ADN is incompatible with HX-880

give zero, regarding the relative weight of the components in the mixture. With a 1:1 per mass mixture, the relative weights are equal to one [25]. Figure 5 shows the compatibility measurement of ADN with HX-880. The compatibility function $R_{ML}(t)$ was calculated from the individual mass loss data as shown in Fig. 5. To assess the data, criteria must be established. This was done in an earlier publication [25]. According to the criterion for the mass loss compatibility function R_{ML}, the values of R_{ML} are already from 2 days on higher than the limit value of +0.4 %. Compatibility would be stated, if this limit value would not be exceeded for at least 10 days at 80 °C. The assessment is that ADN is incompatible with HX-880. The analogous data for AP are shown in Fig. 6. The values of R_{ML} are up to 15 days not beyond the limit value of +0.4 %. The assessment is that AP is compatible with HX-880.

5.3   DMA Measurements and Use of Loss Factor

The typical DMA curves from torsion mode, storage shear modulus (G') and the loss shear modulus (G''), of a high explosive charge (HEC) with HTPB-IPDI-bonded RDX particles are shown in Fig. 7 as function of the temperature and three different deformation frequencies. By increasing frequency, the curves shift systematically to higher temperature values because of the so-called strain rate hardening of the material. More information on this HEC can be found in [26].

The loss factor curves $\tan\delta = G''/G'$ corresponding to the material of Fig. 7 are shown in Fig. 8. The loss factor can be seen as the loss modulus normalized with the storage modulus. It is proportional to the energy consumed by the sample during
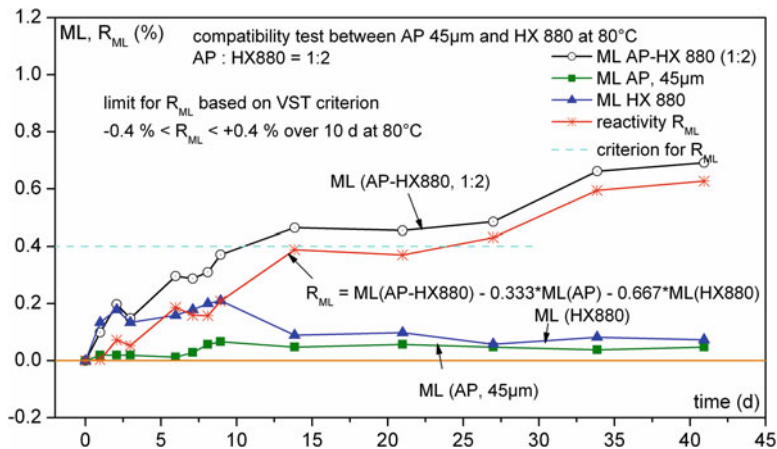
Fig. 6 Chemical compatibility of AP with HX-880 determined by mass loss. According to the criterion for the mass loss compatibility function (R_{ML}), the values of R_{ML} are up to 15 days not beyond the limit value of $+0.4\%$. The assessment is that AP is compatible with HX-880
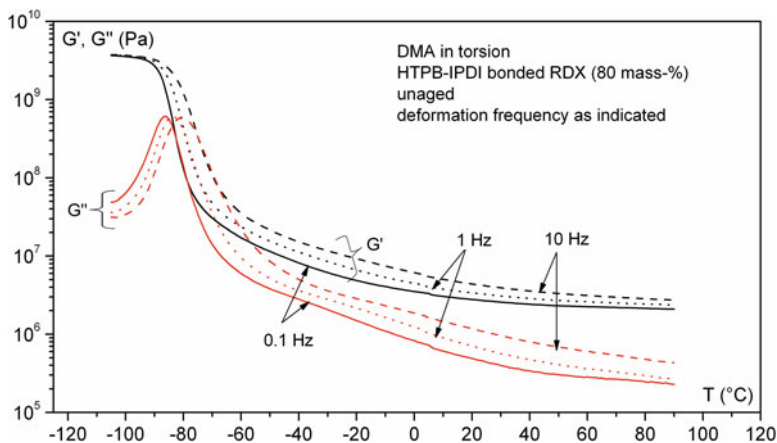
Fig. 7 Storage shear modulus (G') and loss shear modulus (G'') of the high explosive charge (HEC) HX1 as function of measurement temperature at three deformation frequencies (Reproduced from Bohn [26])

its mechanical excitation in the DMA measurement (excitation loss). The structure of the loss factor curves shown in Fig. 8 is typical for the HTPB-IPDI binders with an equivalent ratio Req between 0.8 and 1.0. It is independent from the type of HTPB. Both of the most used Sartomer types HTPB R45 M and HTPB R45 HTLO have the same structure in loss factor, and also HTPB types from other producers show the same behavior. Further, the structure of loss factor is independent from the DMA measurement mode. The loss factor curve has apparently two peaks: a tall and narrow one at low temperature side and a broad and less high one on
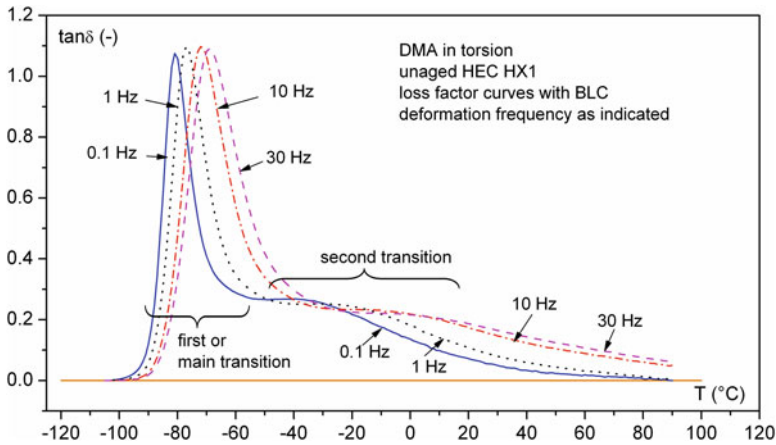
Fig. 8 Loss factor tanδ = G''/G' of HEC HX1 as function of measurement temperature at four deformation frequencies. Apparent are two peaks caused by the binder HTPB-IPDI (Reproduced from Bohn et al. [30])

the high temperature side. One recognizes the small, near zero values on the low temperature side of the curves; this is due to no or very low loss of excitation energy in the glassy or energy-elastic state. On the high temperature side, there remains an intensity of the loss factor, which means that part of the excitation energy is dissipated inside the sample. The interpretation of these phenomena is the loss of excitation energy by friction between binder and solid filler particles in the filled elastomer. From this point of view, it becomes clear that for a quantitative use and interpretation of the loss factor as indicator for transition in the molecular arrangements from the glassy to the rubbery state, such dissipative parts should be removed. This is described and discussed in section "Methodology to Quantify DMA Loss Factor Curves." The basic interpretations of the structure of the loss factor curve of filled HTPB elastomers are the following: (1) the main tall peak at lower temperature values represents the mobility of the, by fillers, unrestricted binder part. The less the restrictions by the fillers, the larger the area and the height of the peak. The temperature of the maximum of the first peak does not change much, because this part behaves like the pure binder (which means without fillers). (2) The second transition, at higher temperature values, is caused by chains or part of chains restricted in mobility. These parts are in interaction with the fillers, but also the chain parts around the curing agent are subjected to mobility restriction. Some interpretations of this second peak assume reptation movements of not cross-linked HTPB molecules. Reptation [27] is a snake-like movement of polymer molecules through the bulk and was found in the melts of thermoplastic polymers. Reptation is seen not as dominant mechanism with the formulations investigated here.

The glass-rubber transition temperature (T_g) is defined as the temperature at the maximum of the loss factor (tanδ) and is named $T_{g,DMA}$. It is dependent on the applied deformation frequency. Therefore, it is recommended to add the information

of the applied deformation frequency in the parameter, for example, $T_{g,DMA,0.1Hz}$. With differential scanning calorimetry (DSC), the probing of the glass-rubber transition is by the change in specific heat c_P of the sample, which increases in going from energy to entropy elasticity. It is dependent on the used heating rate. This is a different probing compared to DMA, but both responses originate from the same processes inside the material. These processes are the molecular rearrangements due to the increase of free volume with temperature and the reduction of intermolecular interaction energies between the binder molecules. DSC-determined glass-rubber transition temperatures $T_{g,DSC}$ at 10 °C/min have approximately the same values as DMA-determined $T_{g,DMA}$ at about 0.001 Hz deformation frequency.

Because the basic molecular reorientation processes inside the material are, in principle, independent from the deformation mode applied in DMA, the loss factor curves should not be influenced by the mode, which means $\tan\delta = G''/G' = E''/E'$. The measurement modes often used are torsion, tensile, three-/point bending, and cantilever. By comparing torsion and tensile measurements, there may arise a difference, because measurements in tension need a pre-straining, which orients the elastomer molecules, especially during the glass-rubber transition and in the rubbery state. This can have an observable effect, and differences between these two measurement modes can occur, especially, if one uses higher pre-straining values.

The loss factor is a composed distribution function (nonnormalized density function) describing the distributions of the glass-rubber transitions of the structural elements of the polymer network in the formulations. If the transitions are deformation frequency (rate) dependent, they are so-named relaxation transitions, which shift to higher temperature with increasing deformation frequency [28, 29]. The relaxation meant here is the molecular reorientation process in going from lower to higher temperature values, which means to reach the condition for the minimal free enthalpy, and the system "relaxes" to the new equilibrium condition [30]. The same holds vice versa, when going from the rubbery to the glassy state,

5.4 DMA Measurements on ADN Propellant Formulations

ADN-based and AP-based GAPxx and D2200xx propellants show different thermo-viscoelastic behavior in comparison with the AP/HTPB-based ones and any filled HTPB binder [24], please refer to Fig. 9 in comparison with Fig. 8. The loss factors of the GAPxx formulations show one apparent peak, which has a tailing toward the higher temperature measurement side. Moreover, the investigated formulations show significant higher glass-rubber transition temperature values. They are 40 to 50 °C higher than the ones of the HTPB/AP/Al-based propellants [24, 31]. The BPS cured GAP-ADN-propellants have a quite high glass-rubber transition of about −25 °C at 0.1 Hz deformation frequency. From the comparison of the two AP formulations AP-13 and AP-14, one can conclude that the curing of GAP with N100 improves the T_g value, which means a shift to lower temperature values. Because both energetic liquid fillers BDNPF-A and TMETN are polar and have
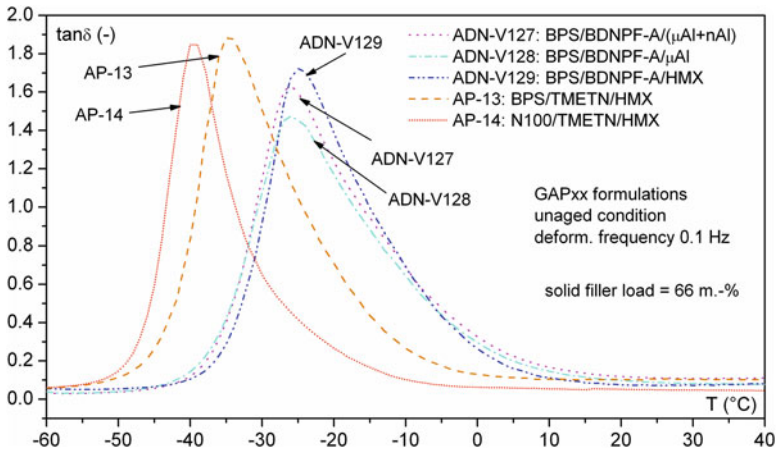
Fig. 9 Loss factor curves of several ADN propellant formulations using GAP-BPS binder and comparisons with AP analogues (Reproduced from Cerri et al. [8])
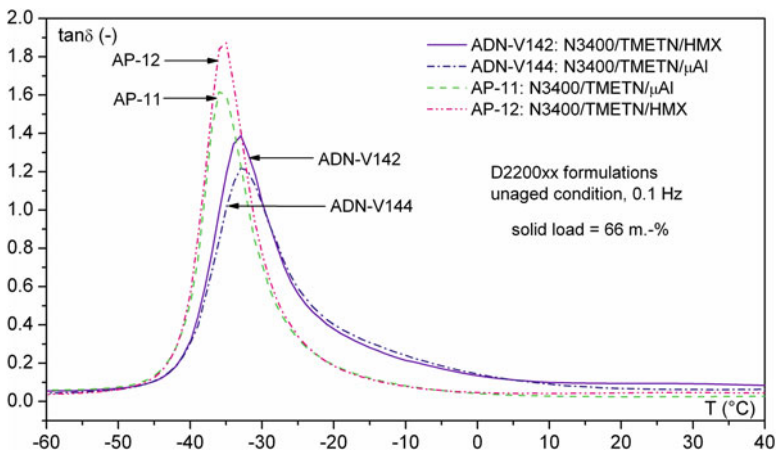
Fig. 10 Loss factor curves of two ADN propellant formulations with D2200-N3400-based binder in comparison with their AP analogues (Reproduced from Cerri et al. [8])

about the same plasticizing capability, one can conclude that AP exerts less mobility hindrance than ADN, resulting in lower T_g and a higher maximum in loss factor. This interpretation is based on the behavior of ADN-V-129 and AP-13 (Fig. 9).

The loss factors of the four discussed D2200-N3400 formulations, namely, pair AP-11, ADN-V144 and pair AP-12, ADN-V142, are shown in Fig. 10. Clearly, the AP-based formulations have lower T_g and less broad peaks than the corresponding ADN-based formulations. Furthermore, the peak heights of the loss factors of the AP-based formulations are greater than the ones of the ADN-based formulations. The conclusion is that the binder is less hindered in the AP-based formulations than
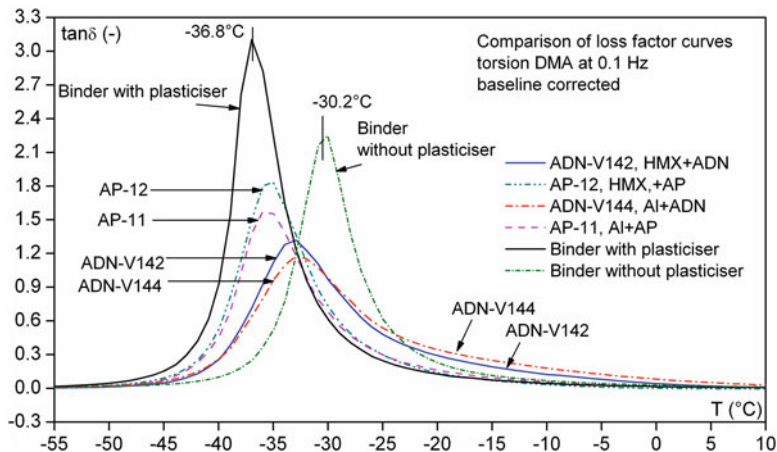
Fig. 11 Comparison of the loss factor of the D2200-N3400-binder based propellant formulations (two with ADN and two with AP) with the binder with and without plasticizer (better called energetic liquid filler) TMETN (Reproduced from Cerri et al. [32])

in the ADN formulations. The reason is the dipolar interaction between binder and filler, which is caused by the lower symmetry of the dinitramide anion compared to the perchlorate anion (see Fig. 1).

Figure 11 shows the loss factors of the four D2200-N3400-binder based formulations and also the ones of the pure binder with and without plasticizer TMETN. The plasticizer content with regard to the binder is the same as in the formulations. Therefore, Fig. 11 is a good example of the effect of a plasticizer: it must lower the glass-rubber transition temperature and increase the transition intensity; only then the effect is as wished, namely, to increase the free volume or the mobility of the binder chains. Further on, the plasticizer should increase strain capability. A special observation must be highlighted: the maxima of the AP-xx formulations are nearly at the same position as the maximum of loss factor of pure binder with plasticizer; but the ones of the ADN-based formulations are clearly situated at higher temperature values. This again supports the interpretation that ADN hinders more the binder mobility by dipolar interaction than AP does.

Whereas the loss factors of the two AP-based materials change only marginally by aging, the ADN-based ones show significant variations [32]. The positions of the main peak are slightly influenced; but the intensity on the high temperature side of the loss factor curves increases, see Figs. 12 and 13.

Figure 14 shows the trend of the loss factor curve of ADN-V144 and of the storage modulus G′ with aging: the width of the loss factor curve becomes larger, and the height of the right side part of it increases. Moreover, the storage modulus decreases with aging. This is a completely different behavior with respect to the HTPB/AP/Al-based propellants [24], see Fig. 15.
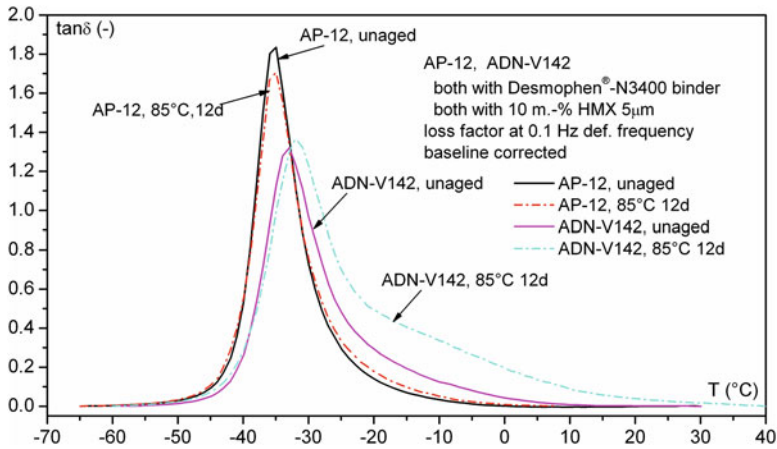
Fig. 12 Comparison of the loss factor of unaged and aged AP-12 and ADN-V142, the two analogous formulations. The loss factor of AP-12 changes only marginally, but the one of ADN-V142 shows strong increase of intensity on the high temperature side (Reproduced from Cerri et al. [32])
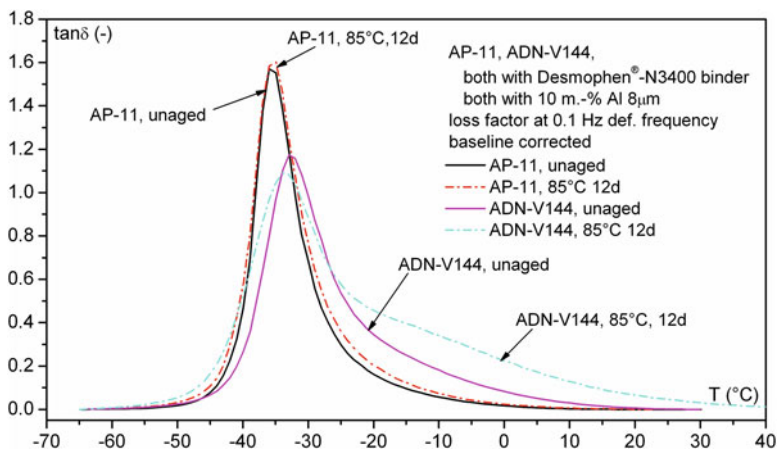
Fig. 13 Comparison of the loss factor of unaged and aged AP-11 and ADN-V144, the two analogous formulations. The loss factor of AP-11 changes only marginally, but the one of ADN-V144 shows strong increase of intensity on the high temperature side

For the ADN-D2200-N3400 propellants, these trends can be explained as chain scission [33] and/or de-wetting phenomena [34], and the cause can be attributed to the presence of ADN instead of AP. ADN causes, by chemical decomposition, an attack on the binder, and the scission of the chains is induced in the binder shell. The prills de-wet from the binder, resulting in less mobility restriction in the binder shell, which leads to an increase in transition intensity from this part of the binder,
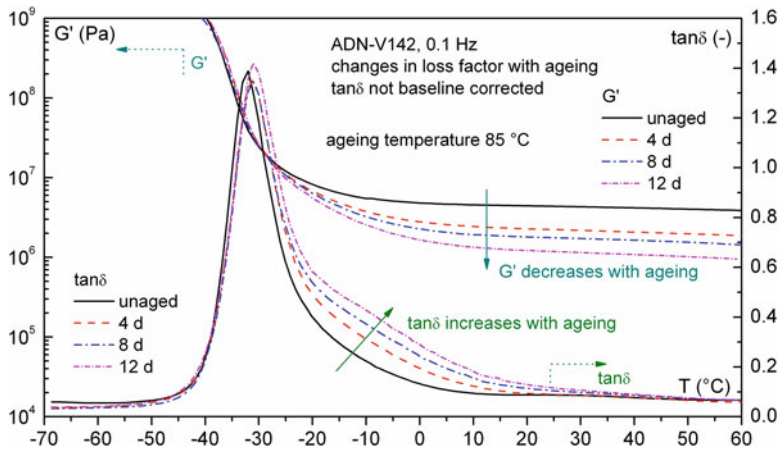
Fig. 14 Comparison of the loss factor of unaged and aged ADN-V142 in comparison with the storage modulus G′. In the range of loss factor increase, one finds a decrease in G′, which means the material becomes softer (Reproduced from Cerri et al. [32])
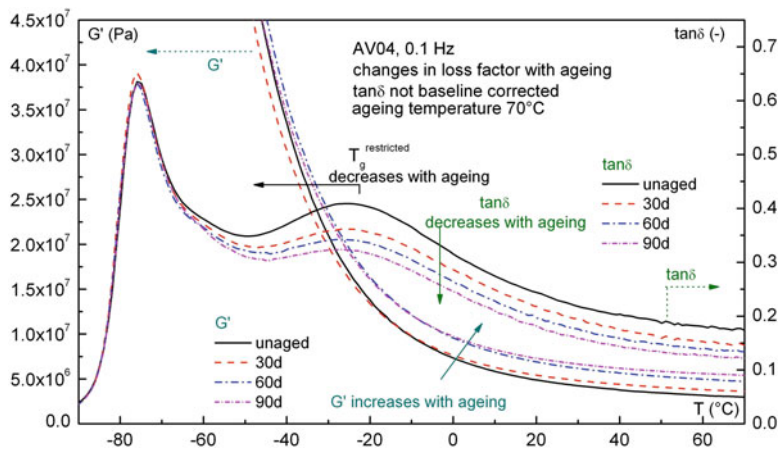
Fig. 15 Comparison of the loss factor of unaged and aged HTPB/AP/Al-based propellant formulation AV04 in comparison with the storage modulus G′. In the range of loss factor decrease, one finds an increase in G′, which means the material becomes harder by aging (Reproduced from Cerri et al. [24])

which is also called bound rubber. A further mechanism, which could interfere, is a slight solubility of ADN in the binder. The HTPB/Al/AP propellants harden in the binder shell, which means that additional cross-linking happens, which reduces mobility and causes the decrease of intensity in loss factor curve in the range of the second transition. Consequently, the storage modulus increases here, as shown in Fig. 15.

5.5   Methodology to Quantify DMA Loss Factor Curves

The excitation energy applied to the sample during the DMA measurements is in part transmitted loss free from the donor to the acceptor of the specimen holder, and in part, it is used by the sample itself. This second part has two different components: a purely dissipative one in which the energy is transformed to heat by frictional effects inside the sample and a component used for the molecular rearrangements of the binder network. The rearrangement energy is taken up to separate the molecular chains in the energy-elastic state to allow multiple configurations in the entropy determined state and, on the other side, to overcome diffusion barriers in the entropy-elastic state to reach the optimal arrangements for the energy determined state. Outside the glass transition regions, only dissipative consumptions occur, which are usually small, particularly in the energy-elastic state. For filled elastomers, these dissipative effects can become significant in the entropy-elastic state [35]. They are visually recognizable by the baseline offset between the start and the end of the tanδ curve distribution, see Fig. 16.

   In order to extract the information concerning the interpretation of the loss factor by molecular rearrangements of the binder molecules, these dissipative frictional effects must be separated from the non-dissipative part. This can be done by applying a suitable baseline correction (BLC) function (Eq. 4). An adjustment of the baseline weights along the loss factor curve is achieved with a cumulative partition function α(T) formed from the tanδ curve itself (see Eq. 5). In this way, the start and the end of the baseline are adapted to the course of the loss factor data in the right manner, which means here to enter the plateau values on both sides. The procedure is shown in Fig. 16 and is applied in a loop until a certain difference limit between two successive corrected loss factor curves is reached.
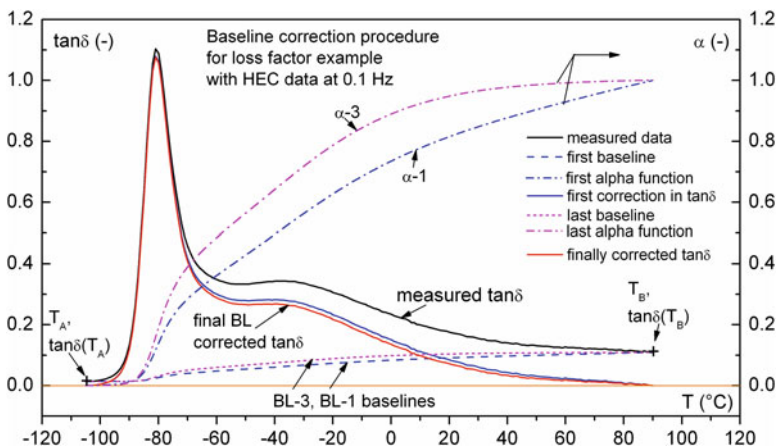
Fig. 16 Procedure of baseline correction (BLC) of the loss factor curves. Here shown with a formulation based on HTPB-IPDI binder (Reproduced from Bohn [26])

$$BL_\alpha(T) = (1 - \alpha(T)) \cdot \tan \delta \left(T_A\right) + \alpha(T) \cdot \tan \delta \left(T_B\right) \tag{4}$$

$$\alpha(T) = \frac{\displaystyle\int_{T_A}^{T} \tan \delta(T) \cdot dT}{\displaystyle\int_{T_A}^{T_B} \tan \delta(T) \cdot dT} \tag{5}$$

$BL_\alpha(T)$ = baseline correction function based on $\alpha(T)$ between T_A and T_B $(-)$
$\alpha(T)$ = normalized cumulative partition function of $\tan\delta(T)$ $(-)$
T_A = lower selected temperature for baseline (°C)
T_B = upper selected temperature for baseline (°C)

After the baseline correction, the loss factor curve has to be analyzed in order to describe the experimental data and to identify and to separate the loss factor parts, which are caused by changes in the molecular structure at different temperature ranges. As clearly visible in Figs. 9 to 13, the shapes of the loss factor curves are not symmetrical like a Gauss distribution, meaning that some dissipative parts are still present in the experimental data, which have to be separated from the parts caused by the molecular rearrangement processes. In principle, the loss factor curves can be represented by Gauss distributions because of the randomly underlying process in the material, see also Fig. 19 later on. The dissipative effects can be considered with relaxation curves, which are mostly represented by exponentially decreasing functions. A combination of Gauss distribution and exponential function is given by the exponentially modified Gauss (EMG) distribution, a convolution between Gauss distribution (Eq. 6) and exponential decay function (Eq. 7), and used earlier to describe the loss factor functions [36]. Such EMG functions have been already used successfully for characterization of the HTPB/AP/Al formulations [24]. The Eq. 8, which represents a sum of EMG functions, was used to model the data. A previous study analyzed several types of distribution functions [37]. Finally the EMG turned out to be most suitable.

$$f_G(T) = \frac{A}{w\sqrt{2\pi}} \cdot \exp\left[-0.5 \cdot \left(\frac{T - Tc}{w}\right)^2\right] \tag{6}$$

$$f_E(T) = \exp\left(-\frac{T}{To}\right) \tag{7}$$

$$\tan \delta_{BLC} = td_0 + \sum_{i=1}^{N} \frac{A_i}{2 \cdot To_i} \exp\left[0.5 \cdot \left(\frac{w_i}{To_i}\right)^2 - \frac{T - Tc_i}{To_i}\right]$$
$$\cdot \left\{1 - erf\left[-\frac{1}{\sqrt{2}}\left(\frac{T - Tc_i}{w_i} - \frac{w_i}{To_i}\right)\right]\right\} \tag{8}$$
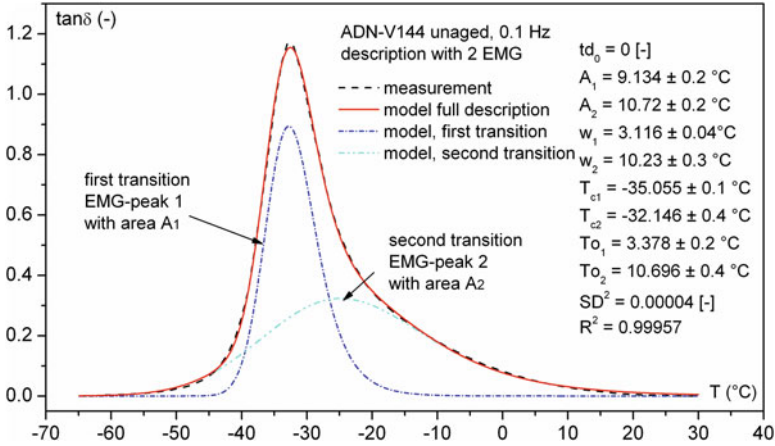
Fig. 17 Application of EMG functions with the baseline corrected loss factor curve of formulation ADN-V144. Already two EMG functions give a very well description of the experimental data (Reproduced from Cerri et al. [32])

T = measurement temperature (°C)

$\tan\delta_{BLC}$ = value of the loss factor after the baseline correction (BLC), a function of temperature (−)

A_i = peak area of the ith EMG peak, equal to the area of the ith Gauss peak (°C)

w_i = half peak width at half height of the ith Gaussian part of the EMG (°C)

Tc_i = temperature at peak maximum of the ith Gaussian part of EMG (not the peak maximum of EMG) (°C)

To_i = relaxation parameter in the ith exponential part of the EMG (°C)

td_0 = offset in tanδ data (−), for the evaluations made here, td_0 was set 0;

N = number of EMG fitting functions

erf = the error function; it is an odd function, which means −erf(−x) = erf(x)

Figure 17 shows an example of the modeling of the loss factor curves of the ADN-V144 propellant formulation. The modeling of the baseline corrected loss factor data was complete already with two EMG functions. The description of the experimental data is also very well expressed in the high value of the correlation coefficient R^2. The dissipative parts during the rearrangement processes are considered by the exponential relaxation function and are characteristic for the molecular structure of the propellant formulation. They can be qualitatively visualized by plotting the formal Gauss peaks of each EMG and the EMG peaks of the molecular transition regions, see Fig. 18. The maximum of the EMG peak lies always on the corresponding Gaussian curve. Depending on the relative weight of the dissipative part, the EMG functions are moving from the maximum of the Gauss curves (which means no dissipative part) to their base on the left, whereby the EMG peak broadness and its skewness increase and therewith the dissipative part in the transition. Surely, a quantitative way to assess the dissipative part is via
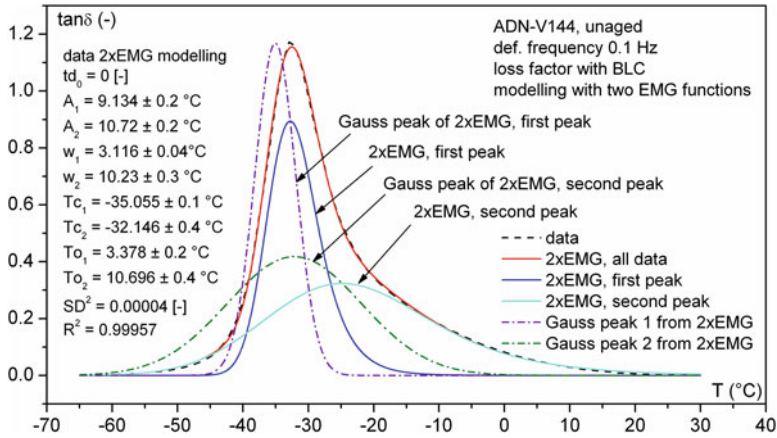
Fig. 18 Illustration of the two EMG peaks and their corresponding Gauss peaks with the analysis of loss factor of ADN-V144. The EMG peak maxima lie always on their corresponding Gauss peak shapes. The maxima of the EMG-Gauss peaks are always at lower temperature values than the ones of the EMG peaks
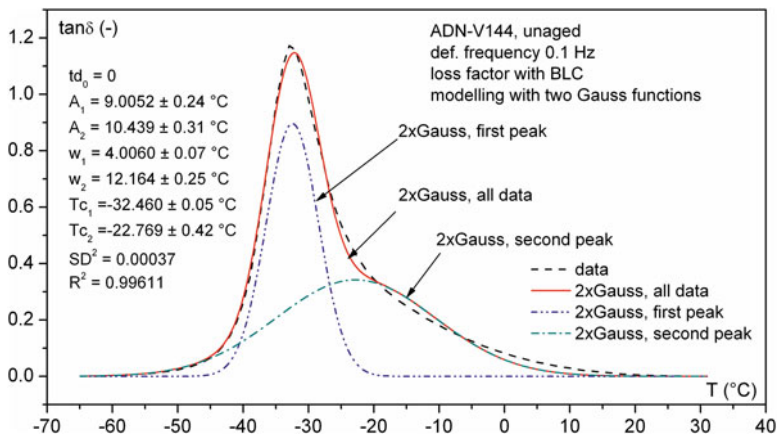
Fig. 19 Modeling of the baseline corrected loss factor of ADN-V144 with two Gauss functions. Already qualitatively good description of the data is achievable. This confirms that the underlying processes in the material are random and of Gauss type

the relaxation parameter To_i of the exponential part in the EMG. If To_i is zero, then a pure Gauss distribution results. In Fig. 19 the modeling of the ADN-V144 loss factor with only two pure Gauss functions is shown. Qualitatively the description is already good. This confirms that the underlying molecular processes are random and of Gaussian type.

In comparison with HTPB-IPDI/Al/AP propellant formulations, D2200-N3400-based propellants and GAP-BPS-based ones have only two sub-peaks in the loss

factor curve instead of three. Peak 1 represents the main prepolymer transition peak (GAP or polyester polyurethane), and peak 2 is the peak related to the mobility-restricted polymer shell around the ADN particles and shows changes with aging caused by chain scission and/or de-wetting phenomena.

5.6   Evaluation of DMA Loss Factor Curves by EMG Functions

The loss factor curves of the aged samples have been modeled with the EMG description. The first peak named A_1 in Fig. 17 seems to be not dependent on aging, whereas the transition called A_2 evidences an aging behavior. Peak 1 represents the main transition peak of the elastomeric polyester polyurethane, while peak 2 is related to the restricted polymer shell around the ADN particles. It shows changes caused by chain scission and/or de-wetting phenomena. Previous mass loss investigations compared the aging behavior of ADN prills with the aging of the ADN/Desmophen®- and AP/Desmophen®- based formulations. The role of ADN in the decomposition process of the material was evident. Measurements of mass loss revealed an acceleratory behavior, which is in part caused also by autocatalysis. Mass loss values were below of the pure ADN ones due to a less ADN content in the formulations. In conclusion, ADN decomposes and shrinks in diameter during aging [8]; therefore, also de-wetting occurs. This phenomenon questions also the usefulness of coating of ADN prills.

The areas of the two transitions were plotted as function of the aging time, Fig. 20. The area A_1 of the first transition stays constant with aging time, whereas
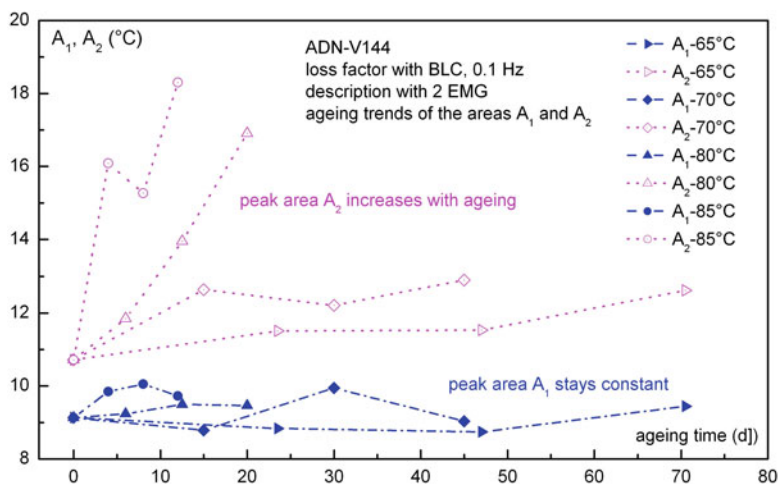
Fig. 20   Result of the evaluation of the areas A_1 and A_2 of the two peaks of the loss factor of the aged formulation ADN-V144. The area of peak 1 stays constant but the area of peak 2 increases with aging (Reproduced from Cerri et al. [32])

area A_2 tends to increase. An increase in loss factor intensity means an increase in binder mobility around the ADN particles (in the binder shell): the molecular mechanisms assumed here are de-wetting and binder chain scissions.

The change rates of the areas A_2 can be described by a formal rate equation of zero order (Eq. 9):

$$\left(\frac{d\left(A_2\left(t, T\right) \right)}{dt} \right)\Bigg|_{T} = S \cdot k_{A2}(T) \tag{9}$$

$k_{A2}(T)$ = change rate constant for area A_2 ($°C \cdot d^{-1}$)
S = sign factor; $S = -1$ for decreasing area with time; $S = +1$ for increasing area with time

The integration of Eq. 9 gives the Eq. 10:

$$A_2\left(t, T\right) = A_2(0) + S \cdot k_{A2}(T) \cdot t \tag{10}$$

A linear dependence of k_{A2} with aging time was observed at all aging temperature values. By plotting the natural logarithm of the change rate constants, $\ln(k_{A2})$, versus $1/T$ (temperature is in K) (Eq. 11), the values of the activation energy (E_a) and the pre-exponential factor (Z) are obtained for each formulation and are compiled in Table 4.

Because the areas $A_2(t,T)$ have the unit $°C$, the decrease rate of not normalized k_{A2} has the unit $°C \cdot time^{-1}$, here given in $°C \cdot d^{-1}$.

$$\ln\left(k_{A2}(T) \right) = \ln\left(Z\left(A_2\right) \right) - \frac{E_a\left(A_2\right)}{R} \cdot \frac{1}{T} \tag{11}$$

In comparison to the activation energies found with the HTPB/Al/AP propellants for the change rate in the corresponding transitions, about 70–85 $kJ \cdot mol^{-1}$ [24], the values found here are significantly greater. An interpretation of these high activation energy values can be referred to the higher intermolecular interaction energies between ADN and binder, which has polar groups in contrast to HTPB. The outer parts of ADN particles establish dipole-dipole interactions with the carboxyl groups of Desmophen® D2200. Additional induced dipolar interactions occur due to ion charges. Furthermore, the decomposition reactions of ADN can have E_a-values in this range [38, 39].

Some considerations can be made also for the change of the glass-rubber transition temperature values with the aging time using the Gauss peak maxima

Table 4 Arrhenius parameters for the change rate of the peak areas A_2 for the formulations ADN-V142 and ADN-V144 obtained by the aging investigation. Log means decadic logarithm

Propellant	Fuel	$A_2(0)$ ($°C$)	$E_a(A_2)$ ($kJ \cdot mol^{-1}$)	$Log(Z(A_2))$ ($°C \cdot d^{-1}$))	$R^2(A_2)$
ADN-V142	HMX	10.99	171.4 ± 20.5	24.706 ± 3.082	0.9721
ADN-V144	μAl	10.72	162.2 ± 2.0	23.446 ± 0.308	0.9997
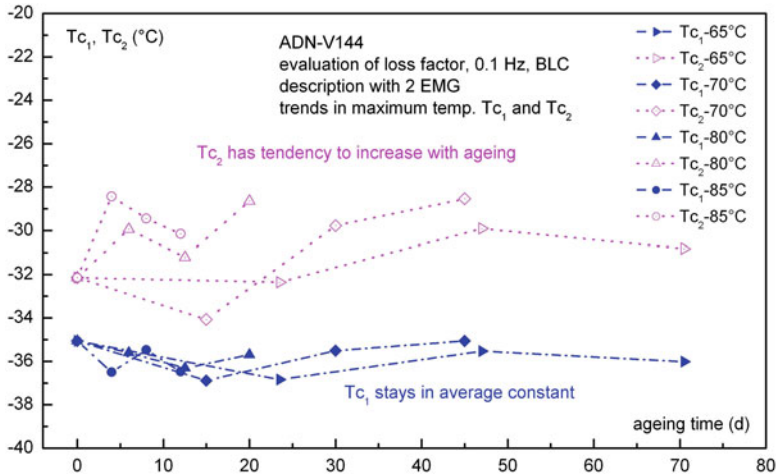
Fig. 21 Result of the evaluation by EMG functions of the aged formulation ADN-V144 by using the Gauss part. The maximum temperature of peak 1 stays constant, but the one of peak 2 increases as seen in trend. This can be interpreted as originating from cross-linking between binder chains in the outer polymer shell. (Reproduced from Cerri et al. [32])

temperature values. The peak temperatures characterizing the first transition (Tc_1) stay constant with aging, whereas Tc_2 increases with aging time, see Fig. 21.

In Fig. 22 the result of the evaluation by EMG functions of the aged formulation ADN-V144 by using the relaxation parameter of the exponential part can be seen. The relaxation parameter of peak 1 stays constant, but the one of peak 2 increases, here visible only for the two higher aging temperatures. By increasing aging time at lower temperatures, the same behavior will result. During the first stages of aging, the relaxation parameter of peak 2 stays constant also. From this, one can conclude that there are two mechanistic effects of the aging. In the first part ADN decomposes slowly by itself and shrinks and de-wetting occurs. With increasing aging, ADN oxidizes increasingly the binder environment, and the resulting decomposition of the binder causes increasing dissipative loss on mechanical excitation of the sample. The oxidation of the binder by ADN results mainly in chain scission in the neighborhood of ADN prills indicated by reduction in G'. But in small part also radical induced chain recombination occurs in the outer polymer shell causing the small shift of the Tc_1 values to higher temperatures.

6 Conclusions

The so-called state-of-development formulations GAPxx cured with BPS containing AP or ADN show low strength and low strain capability. The formulations with Desmophen® D2200 cured with Desmodur® N3400 have low strain capabilities but higher strength values than the formulations GAPxx cured with BPS. There is only
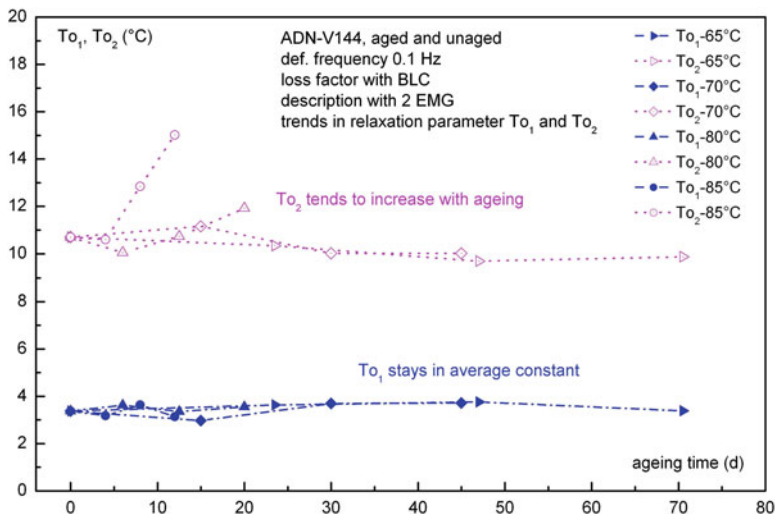
Fig. 22 Result of the evaluation by EMG functions of the aged formulation ADN-V144 by using the relaxation parameter of the exponential part. The relaxation parameter of peak 1 stays constant, but the one of peak 2 increases, here visible only for the two higher aging temperatures

a negligible effect of the used bonding agent HX-880 on the mechanical properties; results have shown that it is incompatible with ADN. All ADN propellant formulations show autocatalytic decomposition behavior, which can be well observed with isothermal mass loss determinations.

The dynamic mechanical behavior of the state-of-development formulations is different with respect to the HTPB-based propellants. Only one apparent peak in the torsion DMA loss factor curve ($\tan\delta = G''/G'$) was found. The fact that systematically the glass-rubber transition temperature is lower with the AP formulations compared to the ADN formulations can be explained with a stronger interaction between ADN and binder chains resulting in more mobility restrictions.

The Desmophen®-based propellant formulations were subjected to an extensive aging program. The aging temperature range was between 60 and 85 °C with aging times adjusted to a thermal equivalent load of 15 years at 25 °C. Whereas the AP-based materials do not change by aging, the ADN-based ones show significant degradation effects.

The loss factor curves were modeled with exponentially modified Gauss distribution functions after a suitable baseline correction. The modeling revealed a second smaller peak hidden in the tailing of the total loss factor curve. The first peak represents the main binder prepolymer transition peak (from GAP or polyester diol D2200), and the hidden one is the peak related to the binder shell around ADN prills, where chain scission of the binder and/or de-wetting phenomena between ADN and binder happen with aging. The area of the first peak does not change with aging, whereas the area of the second peak increases. By plotting the logarithmic change

rate constants of the areas of the "hidden" peaks in tanδ as function of reciprocal temperature, the activation energies of the processes were obtained. The values are between 160 and 180 kJ·mol^{-1}. The decisive effect to prove aging of composite rocket propellants of any kind is the change of loss factor curve with aging.

Considering the found incompatibility between the bonding agent HX-880 and ADN, it is still an issue to find a suitable bonding agent for ADN. The demands for such a substance are high, because of the high oxidative-reactive activity of ADN, which is not the case for AP or RDX. The possible failure of bonding is the decomposition of ADN in its outer particle ranges, and thereby any bonding can be destroyed. This is also the case in using a full coating of ADN particles. Even if the coating material is not decomposed, the shrinking of the ADN particles inside the coating will cause problems.

References

1. Cumming A (2008) Recent and current NATO RTO work on munitions disposal. In: Proceedings of the 11th international seminar on new trends and research in energetic materials, University of Pardubice, Czech Republic, 9–11 April 2008
2. United States Environmental Protection Agency (2005) Perchlorate treatment technology update, May 2005, http://www.epa.gov/tio/download/remed/542-r-05-015.pdf. Accessed 15 Apr 2015
3. High Performance Solid Propellants for In-Space Propulsion (HISP), FP7 project, reference n. 262099, http://www.foi.se/en/Customer--Partners/Projects/HISP/HISP/ and www.hisp-fp7.eu. Accessed 15 Apr 2015
4. Johansson M, De Flon J, Petterson A, Wanhatalo M, Wingborg N (2006) Spray prilling of ADN and testing of ADN-based solid propellants. In: Proceedings of the 3rd international conference on green propellants for space propulsion, Poitiers, France, 17–20 September 2006
5. Nagamachi MY, Oliveira JIS, Kawamoto AM, Dutra RL (2009) ADN – the new oxidizer around the corner for an environmentally friendly smokeless propellant. J Aerosp Technol Manag 1(2):153–160
6. Larsson A, Wingborg N (2011) Green propellants based on ammonium dinitramide (ADN). In: Hall J (ed) Advances in spacecraft technologies, Web-based access: InTech, doi:10.5772/13640
7. Jones DEG, Kwok QSM, Vachon M et al (2005) Characterization of ADN and ADN-based propellants. Propellants Explos Pyrotech 30(2):140–147
8. Cerri S, Bohn MA, Menke K et al (2014) Characterization of ADN/GAP-based and ADN/desmophen®-based propellant formulations and comparison with AP analogues. Propellants Explos Pyrotech 39(2):192–204
9. Landsem E, Jensen TL, Hansen FK et al (2012) Mechanical properties of smokeless composite rocket propellants based on prilled ammonium dinitramide. Propellants Explos Pyrotech 37(6):691–698
10. Menke K, Heintz T, Schweikert W et al (2009) Formulation and properties of ADN/GAP propellants. Propellants Explos Pyrotech 34(3):218–230

11. Bohn MA (2007) Thermal stability of hydrazinium nitroformate (HNF) assessed by heat generation rate and heat generation and mass loss. J Pyrotech 26:65–94
12. Bohn MA (2015) Review of some peculiarities of the stability and decomposition of HNF and ADN. In: Proceedings of the 18th seminar New Trends in Research of Energetic Materials (NTREM), University of Pardubice, Czech Republic, 15–17 April 2015, NTREM-18:4–25
13. Tummers MJ, van der Heijden AEDM, van Veen EH (2012) Selection of burning rate modifiers for hydrazinium nitroformate. Combust Flame 159:882–886
14. Welland WHM, van der Heijden AEDM, Cianfanelli S et al (2007) Improvement of HNF and propellant characteristics of HNF based composite propellants. In: Proceedings of the 43rd AIAA/ASME/SAE/ASEE joint propulsion conference & exhibit, Cincinnati, Ohio, USA, 8–11 July 2007, AIAA 2007-5764
15. Bohn MA, Grillo ME (2006) Quantum mechanical calculations used to reveal decomposition ways of ammonium dinitramide (ADN). In: Proceedings of 37th int. annual conference of ICT, Karlsruhe, Germany, 27–30 June 2006
16. Bohn MA (2003) Stabilization of the new oxidizer ammonium dinitramide in solid phase. In: Proceedings of the 8th int. seminar EuroPyro 2003 combined with the 30th international pyrotechnics seminar, Saint Malo, France, 23–27 June 2003, pp 274–291
17. Bohn MA, Aniol J, Pontius H et al (2006) Stability and stabilization of ADN-water solutions suitable as oxidizer investigated by heat generation rate. In: Proceedings of the 33rd international pyrotechnics seminar, Fort Collins, Colorado, USA, 16–21 July 2006
18. Talawar MB, Sivabalan R, Mukundan T et al (2009) Environmentally compatible next generation green energetic materials (GEMs). J Hazard Mater 16:589–607
19. Teipel U, Heintz T, Krause H (2000) Spherical ammonium dinitramide (ADN) particles. Propellants Explos Pyrotech 25(2):81–85
20. Boyars C, Klager K (1969) Propellants manufacture, hazards, and testing. In: Gould RF (ed) American Chemical Society Advances in chemistry series 88. Washington, DC
21. Heintz T, Fuchs A (2010) Continuous production of spherical ammonium dinitramide particles (ADN-prills) by microreaction technology. In: Proceedings of the 41st international annual conference of ICT, Karlsruhe, Germany, 29 June–2 July 2010
22. Bohn MA (2009) Prediction of equivalent time-temperature loads for accelerated ageing to simulate preset in-storage ageing and time-temperature profile loads. In: Proceedings of the 40th international annual conference of Fraunhofer ICT, Karlsruhe, Germany, 23–26 June 2009
23. Celina M, Gillen KT, Assink RA (2005) Accelerated aging and lifetime prediction: review of non-Arrhenius behaviour due to two competing processes. Polym Degrad Stab 90:395–404
24. Cerri S, Bohn MA, Menke K et al (2013) Aging of HTPB/Al/AP rocket propellant formulations investigated by DMA measurements. Propellants Explos Pyrotech 38(2):190–198
25. Bohn MA (2012) Generic formulation of performance assessment quantities for stability, compatibility and ageing of energetic materials. In: Proceedings of the 43rd international annual conference of ICT, Karlsruhe, Germany, 26–29 June 2012
26. Bohn MA (2012) Impacts on the loss factor curve and quantification of molecular rearrangement regions from it in elastomer bonded energetic formulations. In: Armstrong RW, Short JM, Kavetsky RA, Anand DK (eds) Energetics science and technology in central Europe. CALCE EPSC Press, University of Maryland, College Park, pp 195–235
27. de Gennes PG (1971) Reptation of a polymer chain in the presence of fixed obstacles. J Chem Phys 55:57. doi:10.1063/1.1675789
28. Ehrenstein GW, Riedel G, Trawiel P (2003) Praxis der Thermischen Analyse von Kunstoffen. Carl Hanser Verlag, Munich
29. Widmann G, Shawe J, Riesen R (2002) Interpreting DMA curves, Part 1.Thermal Analysis UserCom 15, Mettler Toledo, 1–6 Jan 2002
30. Bohn MA, Mussbach G, Cerri S (2012) Influences on the loss factor of elastomer binder and its modeling. In: Proceedings of the 43rd int. annual conference of ICT, Karlsruhe, Germany, 26–29 June 2012

31. Cerri S, Bohn MA, Menke K et al (2009) Ageing behaviour of HTPB based rocket propellant formulation. Cent Eur J Energ Mater 6:149–165
32. Cerri S, Bohn MA, Menke K et al (2014) Aging of ADN-rocket propellant formulations with desmophen®-based elastomer binder. Propellants Explos Pyrotech 39(4):526–537
33. Kumar A, Commereuc A, Verney V (2006) Ageing of elastomers: a molecular approach based on rheological characterization. Polym Degrad Stab 85:751–757
34. Lepie A, Adicoff A (1972) Dynamic mechanical behavior of highly filled polymers: dewetting effect. J Appl Polym Sci 16:1155–1166
35. Cerri S, Bohn MA, Menke K et al (2010) Ageing of HTPB/Al/AP rocket propellant formulations investigated by DMA measurements, Sol-Gel and GPC analysis. In: Proceedings of the 41st international annual conference of ICT, Karlsruhe, Germany, 29 June- 2 July 2010
36. Tsagaropoulos G, Eisenberg A (1995) Dynamical mechanical study of the factors affecting the two glass transition behavior of filled polymers. Similarities and differences with random ionomers. Macromolecules 28:6067–6077
37. Cerri S, Bohn MA, Menke K et al (2009) Ageing behavior of composite rocket propellant formulations. In: Proceedings of the 3rd European conference for aerospace science (EUCASS), Versailles, France, 6–9 July 2009
38. Bohn MA, Aniol J, Pontius H et al (2007) Thermal stability and stabilization of ADN-water gels. In: Proceedings of 38th international annual conference of ICT, Karlsruhe, Germany, 26–29 June 2007
39. Bohn MA, Gerber P (2007) Stabilization of solid ADN and liquid (melted) ADN-aluminium mixtures – suitable stabilizing substances investigated by heat generation rate, mass loss and product analyses. In: Proceedings of the 9th international seminar EuroPyro 2007 combined with the 34th international pyrotechnics seminar, Beaune, France, 8–11 October 2007, p 153
40. Cerri S (2011) Characterisation of the ageing of advanced solid rocket propellants and first step design of green propellants. PhD Thesis, Politecnico di Milano, Dipartimento di Energia, Dottorato di Ricerca in Energetica, XXII ciclo

Lessons Learned in the Thruster Tests of HAN

Keiichi Hori

Abstract Since 2000, the Institute of Space and Astronautical Science (ISAS)/Japan Aerospace Exploration Agency (JAXA) is involved in the research and development (R&D) of a hydroxyl ammonium nitrate (HAN)-based liquid propellant, SHP163 which is composed of HAN, ammonium nitrate (AN), methanol, and water. The thruster initially employed in the tests was 3 N type but was later expanded to 20 N type in 2004. In this series of tests, there have been four failures so far. The first two were very simple; however, the latter two were not small and the last one is rather complicated. The first one is due to the lack of control of the catalyst bed temperature, and the second one could be attributed to the well-known "heat soak back" effect. The third one could have been avoided using a vertical test thruster setting, and the last one was due to the lack of knowledge about the chemical reaction of HAN/AN. The reasons and the countermeasures of the four failures are presented in this article; in particular, the latter two are explained in detail.

It is likely that several accidents occur during the R&D of all propulsion system; however, most of these are not presented and published elsewhere. Therefore, the knowledge gained from failures in the thruster tests, presented here, would be useful for understanding the potential hazards in R&D task using high energetic materials and for minimizing the predictable failures in the testing systems.

1 Introduction

The high demand for green propellants has been recognized over the last two decades, especially, recently in the application of the EU regulations known as REACH [1], and the replacement of hydrazine by green propellants is the main concern in the field of liquid propellants for thruster applications. Several chemical compounds have been identified as suitable candidates for propellants,

K. Hori (✉)
Department of Space Flight Systems, Institute of Space and Astronautical Science (ISAS),
Japan Aerospace Exploration Agency (JAXA), Sagamihara 252-5210, Japan
e-mail: hori.keiichi@jaxa.jp

of which ammonium dinitramide (ADN) and hydroxyl ammonium nitrate (HAN) have been widely studied for many years. The ADN-based liquid propellant LP-103S developed by ECAPS, Sweden – which is composed of ADN, methanol, ammonia, and water – already has the "one-year flight-proven" experience at the Prisma satellite project and will be used in the Skybox project from 2015. Further evaluation of this propellant is underway at NASA, USA [2–5]. The HAN-based propellant AF-M315E developed by US AFRL (Air Force Research Laboratory), USA – which is composed of HAN, hydroxyethylhydrazine (HEH), and water – will be used in the Green Propellant Infusion Mission (GPIM) project in 2015 [6–8]. SHP-163, which is composed (in mass) of 73.6 % of HAN, 3.9 % of AN, 16.3 % of methanol, and 6.2 % of water, was developed in 2000 in Japan and is being currently researched for application in thrusters [9–12]. In this propellant, methanol is chosen as a fuel because it is the most effective stabilizer among alcoholic fuels to reduce gas-phase instability. AN is added to minimize the water content to avoid the very high burning rate characteristics often observed in HAN-based liquid propellants and also to lower the freezing point of the propellant in order to eliminate heaters from the propellant tanks of satellites.

HAN was discovered in the 1960s in the USA. HAN is a crystalline solid as shown in Fig. 1; thus, this material was initially used as a solid oxidizer in composite propellants. However, the HAN-oxidized solid propellant exhibited unstable combustion [13], and subsequently HAN was used in liquid propellant for thruster partly because it is highly hygroscopic.

HAN-based liquid propellants often exhibit very high burning rate characteristics even at low-pressure range, which hampered the use of those solutions for thruster. Therefore, controlling the burning rate through variation of composition is necessary. Further, catalytic modification is also required. HAN can be decomposed with the same catalysts as those for hydrazine such as Ir and Pt. However, they are not suitable to realize a good pulse mode response at a relatively low temperature. Catalysts with higher low-temperature activity and heat resistance are required for achieving long and highly reliable service life of thrusters.

Fig. 1 HAN crystal

Since 2000, ISAS/JAXA has conducted burning tests using SHP-163 solution and a variety of catalyst material with test thrusters. The test initially employed 3 N-type thruster. However, it was difficult to conduct several measurements with this small thruster; therefore, we decided to increase the scale of the test thruster to 20 N type. The first failure occurred with the 3 N thruster and the rest with the 20 N thruster. This paper describes the four failures, in particular, latter two in detail.

2 Four Failures and Countermeasures

2.1 First and Second Failures

First failure happened with the 3 N test thruster, which was used for hydrazine. Initially, S-405 catalyst – which is typically used for hydrazine thrusters – composed of granular and 30 mass % of Ir supported on alumina particles was used for SHP-163 test because it is effective for HAN decomposition (active temperature against HAN is approximately 70 °C). In this test thruster, the initial temperature of the catalyst bed was controlled using heaters attached to the outer surface of the chamber. In the burning tests for hydrazine, the catalyst bed was usually heated up to 200 °C at the beginning. The same procedure was employed for SHP163; however, attention was not paid to the temperature distribution within the catalyst bed. The burning test was initiated when the solution was injected into the catalyst bed, and an explosion sound was heard from the video camera monitor. The catalyst bed was damaged immediately after the injection of the propellant, and the test was stopped. On further inspection later, it was found that while the temperature at the downstream end of the catalyst bed was maintained at 200 °C before the test, the upstream inlet temperature of the catalyst bed was approximately 150 °C. The injection of HAN solution into the bed likely lowered the temperature to not well above the active temperature. This temperature reduction induced the accumulation of unreacted SHP163 in the catalyst bed, which finally initiated the decomposition reaction at the downstream of the bed that still maintained a sufficiently high temperature. To avoid this failure, we decided to monitor the both ends of the catalyst bed and maintain its inlet temperature considerably higher than the activation temperature even after the injection of liquid propellant into the bed. Further, we also decided to monitor the temperatures at several places for the understanding the phenomena occurring inside the chamber. Therefore, the larger test thruster, 20 N class, was employed because it is very difficult to handle multiple sensors with a smaller thruster.

The second failure happened in the testing using 20 N class test thruster, and the failure was also due to a simple error. The "heat soak back" effect was not considered thoroughly. Initially, in the burning tests using a new 20 N thruster, a short burning time was used because these tests were conducted for checking of the testing system. Later, burning time was prolonged to several tens of seconds, and the failure happened.
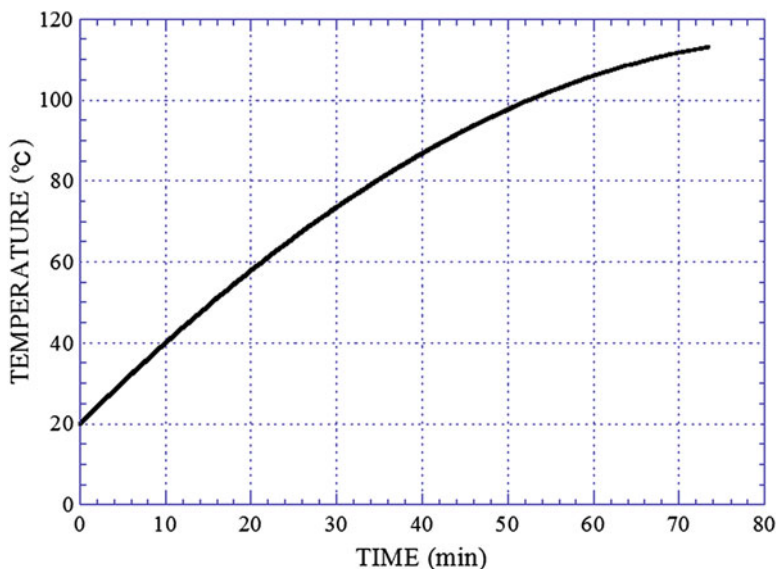
Fig. 2 Temperature history of propellant valve

At the end of a series of tests, a loud sound was heard through the monitor coupled with the video image, and the propellant valve was damaged. The thermocouple attached to the outer surface of the valve showed the temperature at approximately 110 °C at the moment of the valve fracture (Fig. 2). Temperature was approximately 95 °C at the end of the burning tests on that day and then increased to 110 °C owing to heat soak back. The inner temperature of the valve and, thus, the propellant temperature must be higher and equal to the decomposition temperature of SHP163.

Figure 3 shows the DTA and TG curves of SHP163 at 0.5 MPa. This graph shows the decomposition temperature is 177.7 °C at 0.5 MPa, which is 22 °C lower than that at 0.1 MPa. In the case of this failure, propellant was subjected to a pressure slightly higher than 0.5 MPa; thus, the decomposition started below 177.7 °C. After this accident, Teflon sheet and later an EPDM rubber sheet reinforced by Aramid fibers, which have low heat conductivity and high heat resistance, were set between propellant valve and the injector. Further, an automatic shutdown system was introduced that operated when any of the thermocouples attached to the testing setup showed a temperature higher than 150 °C. After this countermeasure, such a failure never happened.

2.2 Third Failure

Third failure was the most serious one in terms of accident severity. At the time of the failure when the 20 N class test thruster was in use, the propellant flow rate,
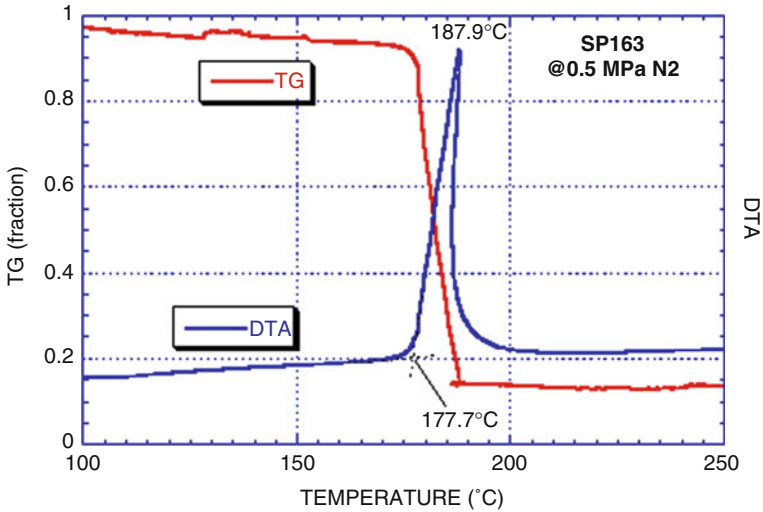
Fig. 3 TG & DTA curves of SHP163 at 0.5 MPa

catalyst type, and catalyst bed configuration were chosen as parameters, and their effects on the thruster performance, temperature distribution in the catalyst bed, and chamber temperatures were investigated thoroughly. In one series of experiments, tests with very high propellant flow rates were conducted to observe their effects on combustion efficiency for the given catalyst bed. The test thruster was set horizontally, and we observed from video images that the unreacted propellant solution flew out of the chamber in the tests prior to this series of experiments; thus, all of the unreacted propellant was considered to flow out of the chamber through the nozzle.

When the propellant flow rate was increased more than 50 % greater than the nominal value, an explosion occurred after 7.8 s from the start time. The test thruster dropped from the test stand but retained its shape, and the propellant tank exploded. The recorded traces of pressure, temperature, and piston location showed the followings as a most likely scenario took place:

 (i) Pressure suddenly increased in the thruster chamber.
 (ii) Piston was pushed back to the original position.
(iii) Propellant tank exploded.

Figure 4 shows the chamber pressure curve during the failure. Pressure trace was not stable probably due to the excess flow rate and showed irregular peaks twice at 4.5 s and 7.6 s. The first peak had no effect whatsoever, but the second one triggered an explosion at 7.8 s. Pressure sensor was out of order at this moment and the pressure trace thereafter had no meaning.

Figure 5 shows the inlet temperature of the catalyst bed. The catalyst temperature was set at 473 K before the start of the firing test, and it was kept stable at
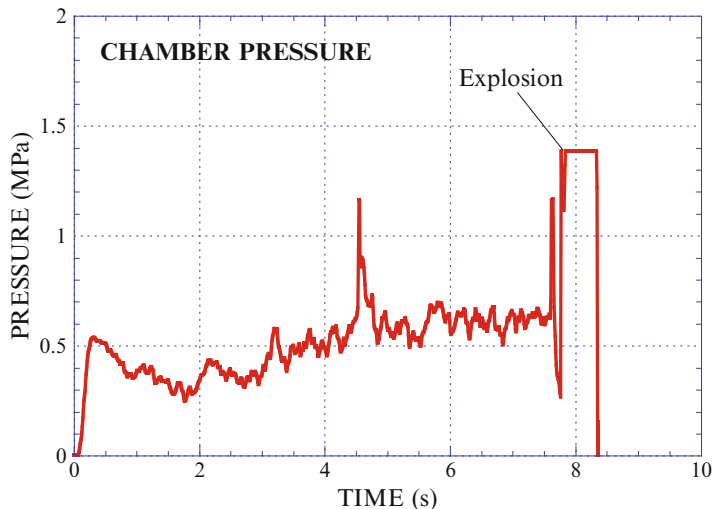
Fig. 4 Pressure curve at the third failure
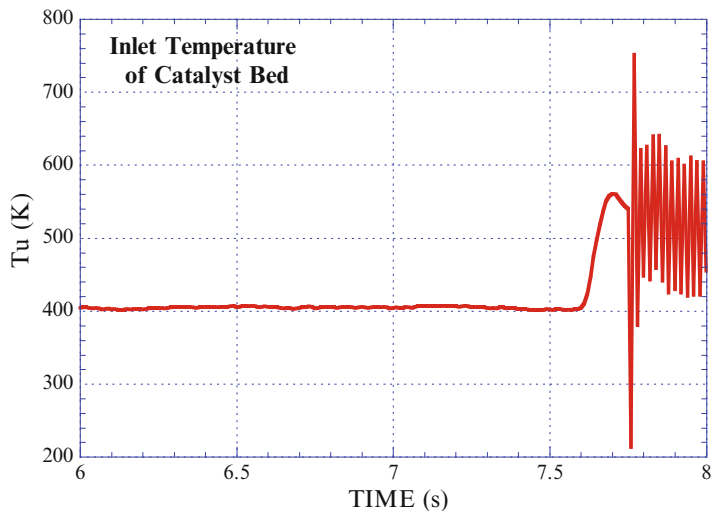
Fig. 5 Catalyst bed temperature at inlet

approximately 400 K which is well above the activation temperature of S-405 catalyst. At 7.6 s, the temperature started to increase, which means that the flow rate of SHP163 decreased due to the pressure increase of the thruster chamber. Finally, continuity of the thermocouple was lost just before 7.8 s.

Figure 6 shows the position of the piston of the propellant tank. In our experiments, propellant flow rate is measured in two ways: (1) by using a Coriolis flowmeter, which is suitable for the flow measurement at constant and long-period
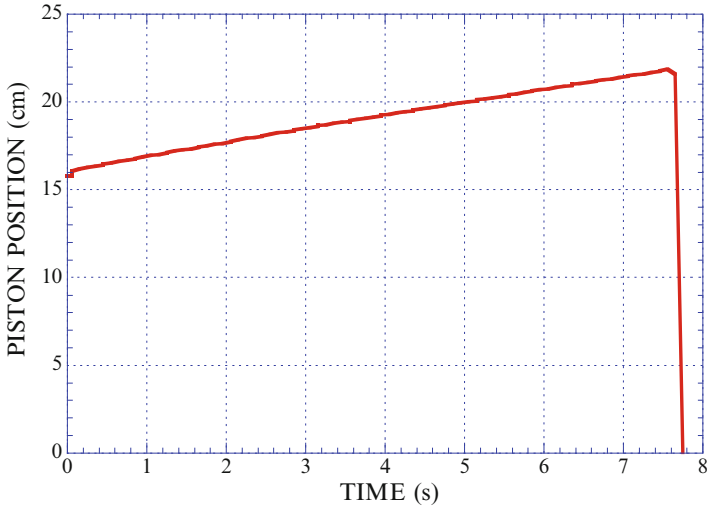
Fig. 6 Piston position

Fig. 7 Destroyed tank

testings, and (2) by measuring the piston position by a laser displacement meter, which is used for the short-period testings. Figure 6 shows the piston position placed approximately 16 cm from the original position, and it moved (propellant pushed from the tank) up to 22 cm at 7.6 s, after which suddenly dropped to zero before 7.8 s. This shows that the propellant in the line was pushed back to the tank, and, then, the hot gas from the thruster chamber ignited it. The amount of the propellant at that moment was estimated at approximately 400 cc, which is sufficient to destroy the tank and the pipings in nearby regions. Figure 7 is a photograph of the destroyed tank.

Figure 8 shows the probable schematic of the failure. The propellant mass flow was too high for the catalyst bed processability, and the unreacted propellant was

S-405 Catalyst Bed
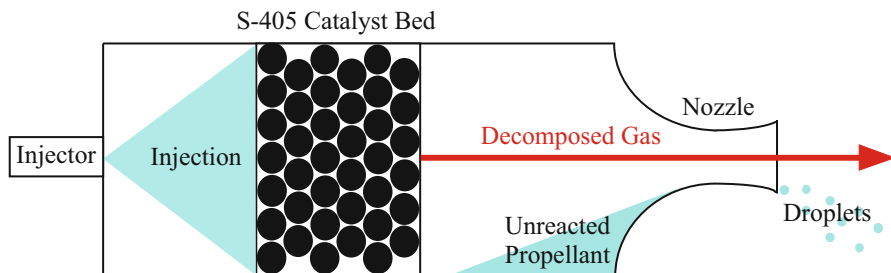
Fig. 8 Probable schematic at the failure

Fig. 9 Horizontal test setup
before third failure
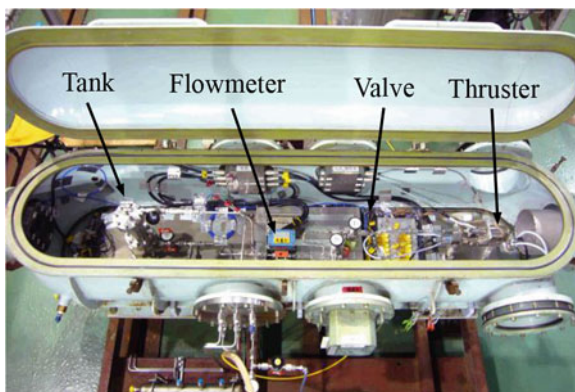
stored at the downstream of the bed. A part of them flowed out through nozzle
as droplets, and the rest was accumulated in the thruster chamber as shown in
Fig. 8. Finally, this accumulated propellant came in contact with the catalyst bed
whose temperature was sufficiently high to activate the unreacted propellant. This
decomposition reaction of the accumulated propellant led to the sudden increase of
the pressure at 7.6 s and led to the scenario above.

The main countermeasure for this failure is very simple. The reason of the
propellant accumulation in the chamber was, of course, very high propellant mass
flow rate, and another reason was the horizontal setup of the thruster. Thus, we
decided to change the setup direction of the test apparatus from horizontal to
vertical. Figures 9 and 10 are the test setups before and after the third failure.

2.3 Fourth Failure

All of the last three failures occurred during the firing tests, but the fourth failure
occurred during the preparation process. After the third failure, we conducted about
30 days of safe testings using the vertical setup shown in Fig. 10. The fourth
failure occurred during the preparation process "leak check," which was conducted

Fig. 10 Vertical test setup
after third failure
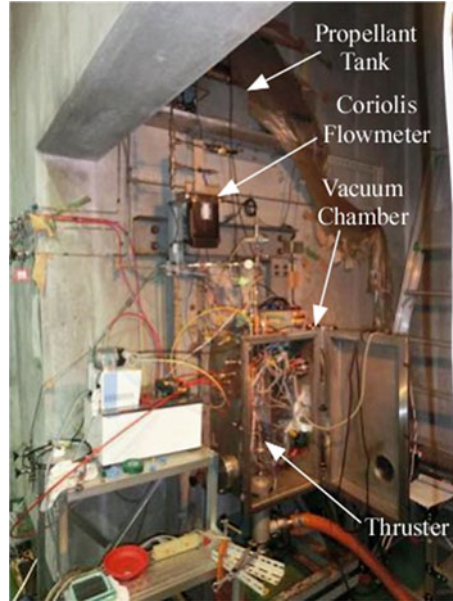
at 0.5 MPa nitrogen gas. Unfortunately, the failure affected the eardrums of two employees. Figure 11 shows the schematic of the test line. Propellant tank was pressurized with nitrogen gas, propellant flowed along the main line, and the flow meter, cut valve, filter, check valve, filter again, and finally the propellant valve were set in this order in the upstream direction of the thruster. The area surrounded by dotted line is the vacuum chamber that was typically operated at 10 Torr during the testings. Further, there were two other lines; one was the nitrogen purge line that is used at the cleaning process after the end of burning tests, and the other one was for the supply of the liquid propellant into the tank or introduction of water during the cleaning process.

For the fourth failure, we intended to use a 1 N flight model thruster provided by a private company, and so we were not familiar with it. Further, the propellant valve attached to this thruster was also flight type one, and its operation voltage was 29 V; accordingly, we changed the operation voltage of our original devices from 24 to 29 V. At that time, it was impossible to change the operation voltage of each device independently.

As described in section "First and second failures," we set the critical temperature when we stop the propellant injection at 150 °C, and we did not predict any temperature, especially the cut valve temperature, would exceed 150 °C at 29 V operation. Thus, we started the preparation of the test with this voltage setting.

First, we ensured that there was no gas leak in the main streamline at 0.5 MPa, which is the typical burning pressure level. The upstream of the propellant valve was pressurized at 0.5 MPa, and the cut valve was turned on then. This process took approximately 20 min. The next process was the leak check of the entire line
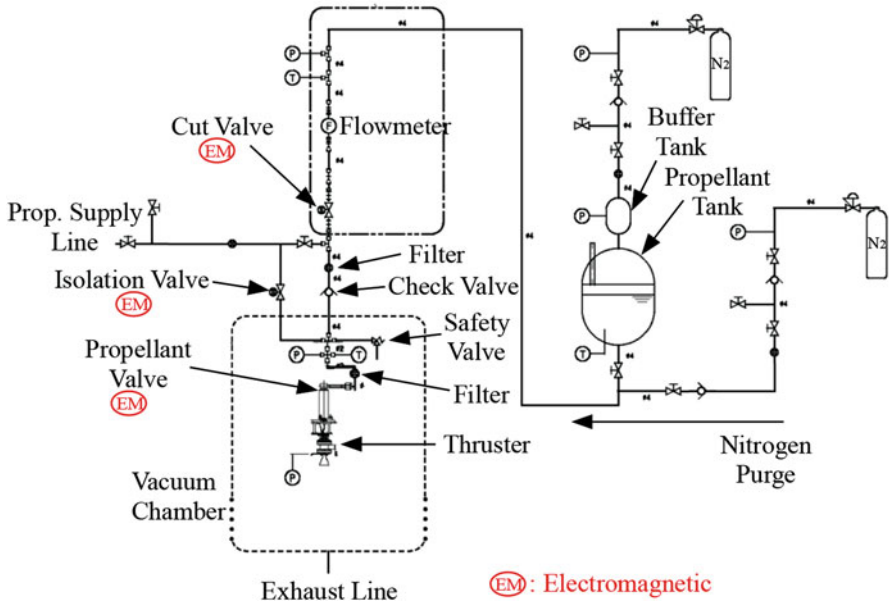
Fig. 11 Schematic of test line

Fig. 12 Broken tubing
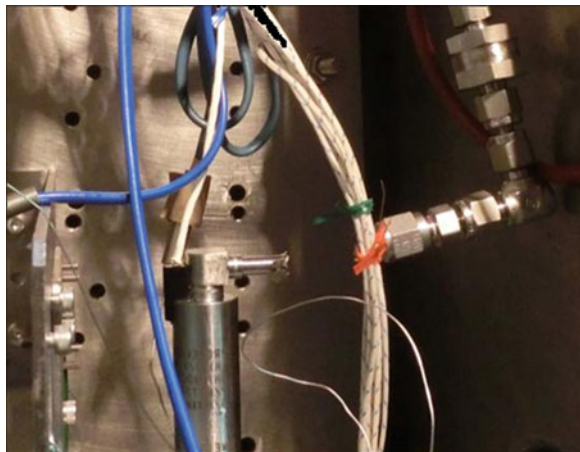
up to the exit of the nozzle of the thruster. The propellant valve was turned on and nitrogen gas was filled to the end. After 10 min, an explosion occurred.

Four major damages occurred of this explosion. The first damage was of the upstream tube of the propellant valve, as shown in Fig. 12. Approximately 40 mm of the SUS304 tube, which was 0.25 in. in diameter and 0.35 mm in thickness, was lost. The second damage was the isolation valve between propellant supply line and vacuum chamber. Figure 13 shows the distorted line and the valve blown off and
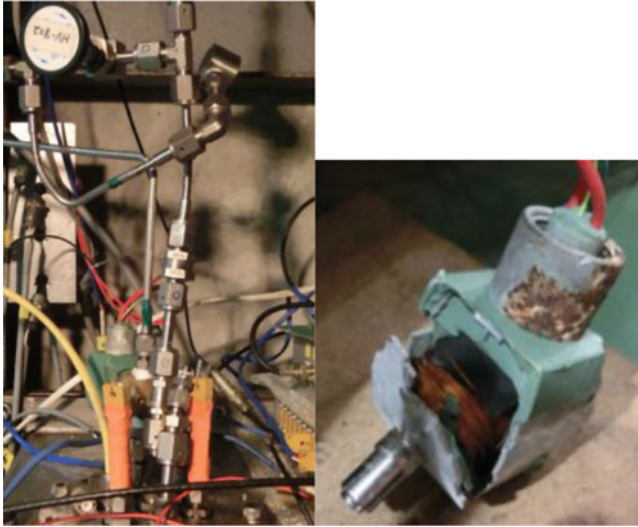
Fig. 13 Distorted line and blown off valve

found on the floor. The third and fourth damages are of the tube to the pressure measurement line and the connection to the check valve. The tube expanded, and the connection part was seriously distorted.

A detailed fault tree analysis (FTA) was conducted, but owing to space constrains, only the main stream part of the FTA is presented here in this report.

The following conclusions were drawn from the FTA:

1. The explosion was triggered by the exothermic chemical reaction within the cut valve, which was operated at a higher voltage than usual.
2. The chemical reaction propagated along inner wall of the tubing.
3. Finally, the explosion occurred at the tube connected to the safety valve.

We identify three important factors that cause these three events. The first factor is due to poor cleaning after tests. At the end of the test day, after the burning tests have been completed, we separate thruster from the experimental line and clean both of the thruster and the propellant lines; however, we found that this cleaning procedure was not adequate. This first factor plays a part in causing all the three events. The cleaning process was as follows. First, fill water in the line to dissolve the propellant remaining on the wall of the line. Then, purge the water to the outside using nitrogen gas. Finally, evacuate the line to remove the water stuck to the inner wall surface of the line. The last step is useful for eliminating water and methanol; however, it may promote the accumulation of HAN and AN crystals on the inner wall surface of the line.

The next factor we discuss is the temperature increase due to cut valve, being operated at a higher operation voltage than usual. The temperature inside the cut valve, Marotta MV100 model, at 24 V and 29 V was measured. As shown in Fig. 14,
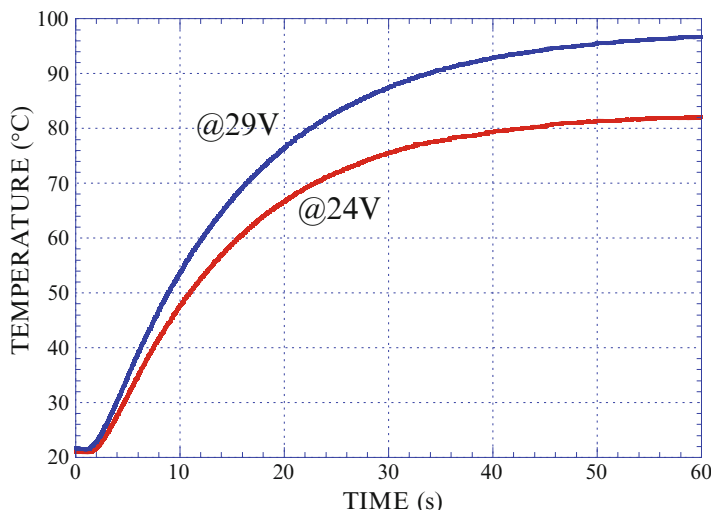
Fig. 14 Temperature histories within the cut valve

at the usual operation voltage of 24 V, the temperature approached 82 °C after 1 h, and at 29 V, the temperature approached 97 °C. Thus, the temperature was increased to approximately 100 °C at the failure, which is still much lower than the critical temperature of 150 °C, and the reaction commencement temperature of 177.7 °C at 0.5 MPa of nitrogen. We considered there must be a lack of knowledge regarding propellant chemistry, and hence, we decided to evaluate the chemical characteristics of the propellant at a constant temperature in the range of 100 °C by referring to the temperature history results within the cut valve at 29 V.

Figure 15 shows the setup for the reactivity test at constant temperatures for longer time. 0.6 cc of the sample was heated at the predetermined temperature and kept under nitrogen atmosphere because the explosion occurred in the nitrogen gas environment at the leak check. The pressure and temperature of the sample cell were monitored, and the exothermic reaction was detected through the change of both the pressure and cell temperature. Experiments were conducted at different pressures and temperatures, and Fig. 16 shows the result of these experiments for (i) SHP163 and (ii) HAN 95 mass % aqueous solution to observe the characteristics of HAN itself.

As shown in Fig. 16a, SHP163 at 0.1 MPa of nitrogen shows an exothermic reaction quickly at 135 °C; however, it takes about 45 min for the reaction to take place at 125 °C. The open symbols indicate "no change" or "no reaction"; therefore, the symbol at 120 °C at 0.1 MPa indicates that no reaction occurred for 3 h. However, at high pressures, this tendency shifts to lower temperatures. At 0.9 MPa, SHP163 shows a reaction after 110 min at 105 °C, and no reaction occurs for 3 h at 100 °C. Therefore, we may infer that operation under 120 °C and 100 °C at 0.1 MPa and 0.9 MPa of nitrogen, respectively, is considered to be safe. Figure 16b
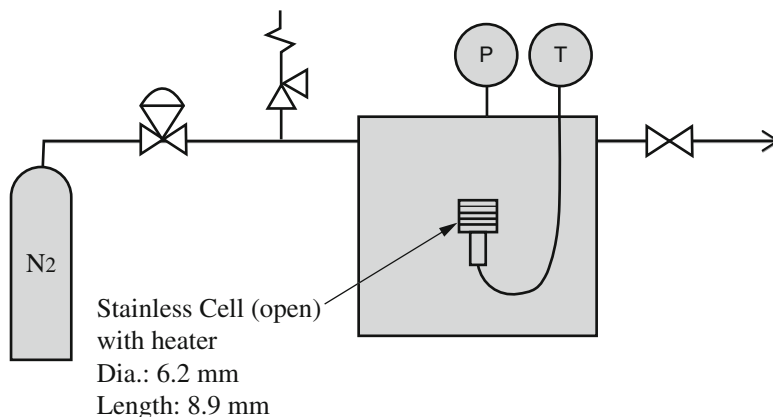
Fig. 15 Reactivity test setup
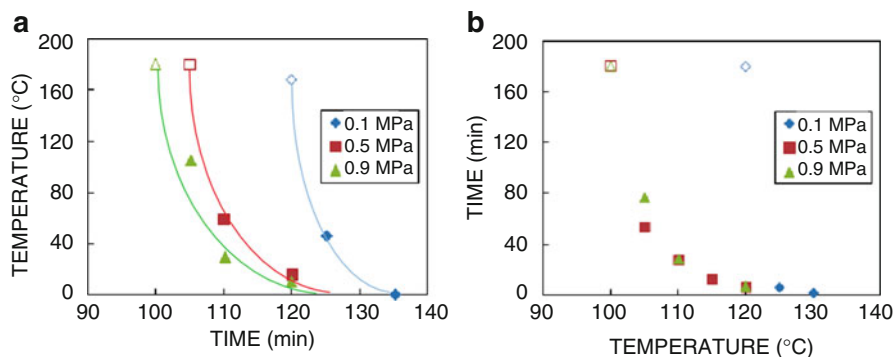
Fig. 16 Results of (**a**) SHP163 and (**b**) HAN 95 mass % aq. solution

shows the results for HAN 95 mass % aq. solution. The results are similar to those of SHP163; thus, these characteristics can be representative of HAN.

Further, the effects of various contaminations were also investigated. Many kinds of metallic cations were tested as a function of their concentration. Among them, the cations of aluminum and iron had a considerable influence to the reactivity. The results obtained using HAN 95 mass % aq. solution at the highest cation concentration of 30 mg/l in this test are shown in Fig. 17 for (a) 0.1 MPa and (b) 0.5 MPa. Through a comparison with Fig. 16b, we observe that these cations accelerate the reaction. The effect is not so significant at 0.1 MPa; however, at 0.5 MPa, the effect is considerable, especially for Fe^{3+}. At 0.5 MPa, the safe region is reduced to 90 °C, and the time taken for the reaction to take place at 95 °C is 75 min, which shows the relevance to the situation of the accident which happened probably at 97 °C.

The last factor we discuss is the poor design of the tubing. In the experimental setup, there were two horizontal parts where propellant can be trapped even after
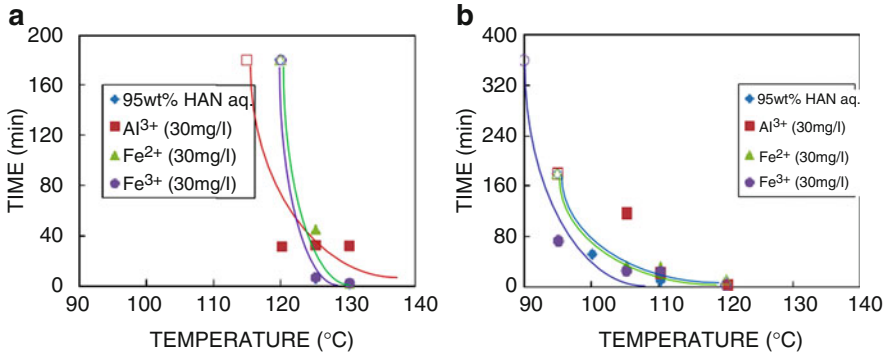
Fig. 17 Effects of contamination at (**a**) 0.1 MPa and (**b**) 0.5 MPa
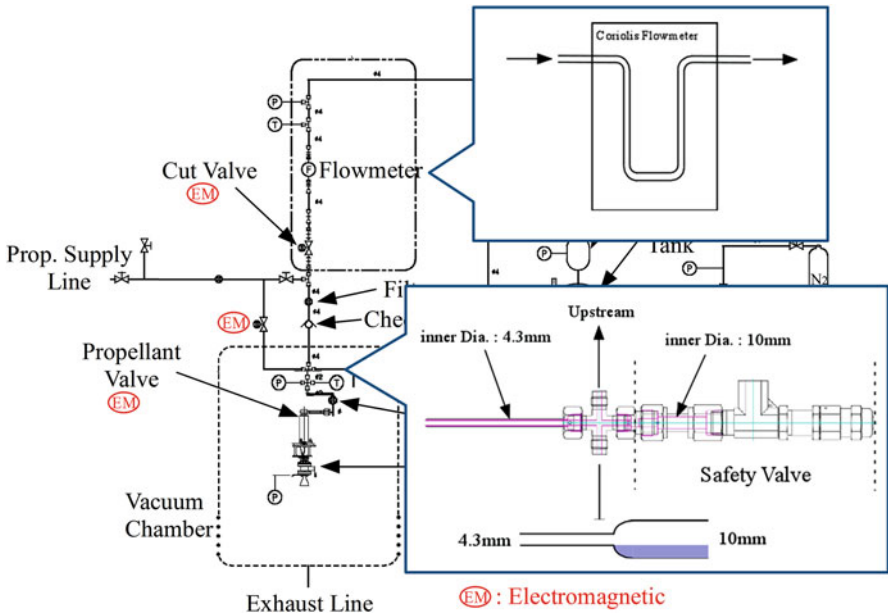
Fig. 18 Probable portions for propellant trap

the cleaning process. The first one is the inner structure of the flowmeter, which is shown in the upper pop-up view in Fig. 18. The other part is shown in the lower pop-up view. The tube diameter (10 mm) within the safety valve was larger than the other horizontal line diameter (4.3 mm), and the estimated volume of the trapped propellant is 2.7 cc; the energy of the propellant was evaluated to be sufficient to cause this explosion.

We attempted to verify the scenario obtained through the FTA by using a simulation test setup described hereafter. The verification test line setup was
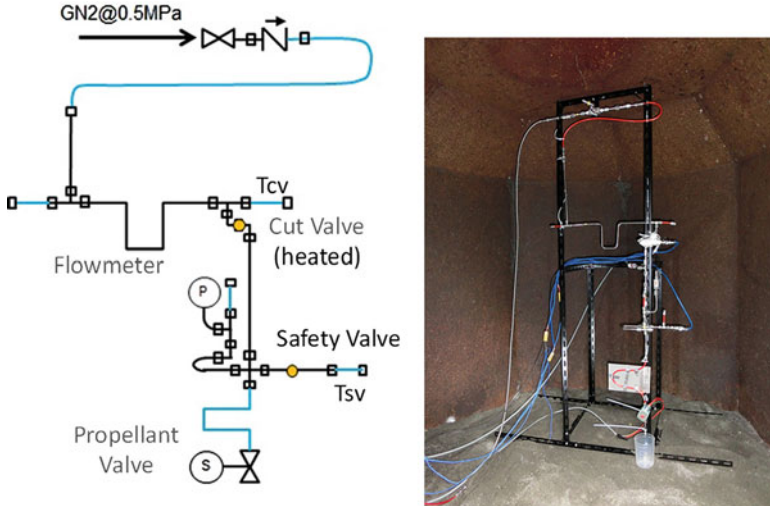
Fig. 19 Verification test setup

assembled as shown in Fig. 19, and the routine procedure at a test day was repeated for 30 times because burning tests were conducted for 30 days before the accident. The propellant solution was introduced in the line and kept for 5 h at 0.5 MPa, after which the cleaning process was carried out. This procedure was repeated 30 times, and the verification test was conducted. The three locations – flowmeter, cut valve, and propellant valve – were simply simulated by tubes, and only the safety valve was an actual valve. Pressure was measured near the safety valve (denoted by "P" in Fig. 19), and the temperatures at the cut valve location, Tcv, and at the safety valve, Tsv, were measured.

Figure 20 shows the history of Tcv from the verification test. The history curve was controlled to adjust the temperature history at 29 V in Fig. 14. First, we predicted something would happen at approximately 100 °C; however, nothing happened, and thus, we continued to increase the temperature further. Finally, an explosion occurred at approximately 110 °C, as seen in Fig. 20. The safety valve was seriously destroyed, but the location of flowmeter was safe. This is probably because (i) the flowmeter is easier to clean than safety valve because the flowmeter is located upstream (nitrogen purge takes place from upstream side) and (ii) the structure of safety valve facilitates trapping of the propellant.

Figure 21 shows the Tcv, Tsv, and pressure data from the explosion. Tcv started to increase from 110 to 140 °C, and approximately 1.6 s later, the pressure started to increase very rapidly and no meaningful signal after that. Both of Tcv and Tsv started to rise slightly later than the pressure probably because of the difference in the time responses between pressure sensor and thermocouples.

Data of the verification test are not consistent with the prediction. In the actual failure, explosion occurred approximately 30 min after the cut valve was turned
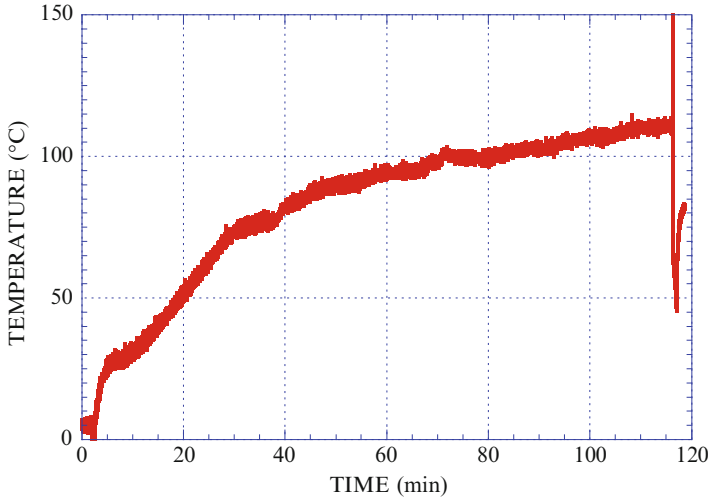
Fig. 20 Time history of *Tcv* at the verification test
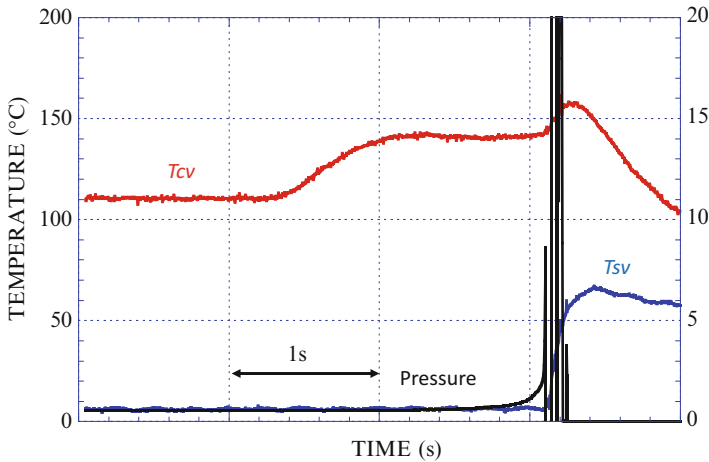
Fig. 21 *Tcv*, *Tsv*, and pressure traces at the explosion

on; however, the time taken in the verification test was much longer. Further, the chemical reaction was predicted to occur at a temperature between 90 and 100 °C based on the measured temperature inside the cut valve at 29 V and the data of the reactivity test; however, the reaction took place at 110 °C at this verification test. These results are contradictory, and the FTA conclusion seems not verified; however, it should be emphasized that this phenomena is the "topochemistry." Such a condensed-phase process may develop differently owing to the interactions with the crystalline field, and the dissociation barriers may be affected by irregular

structures, defects in crystals, shear strain, surfaces condition (charged or excited), and other imperfections and contaminations. Therefore, we judge those differences in time and temperature are acceptable, and the FTA conclusion can be verified.

The countermeasures for this failure are as follows.

1. Eliminate the structures that trap the propellant. Eliminate horizontal line and replace safety valve with a rapture disk or resin pipe, which can be destroyed more easily. Make the branch part in welding structure and minimize the number of joints.
2. Improve the cleaning process. We eliminated the evacuation step from the original cleaning process and conducted the same test as the verification test with this cleaning procedure repeated twice. We repeated this procedure 30 times and conducted the same test. We recognized the temperature increase at the heated location at the cut valve, but there was no explosion at the safety valve. Considering this result, we decided to repeat this cleaning procedure three times at every cleaning opportunity.
3. Eliminate the heat source. Replace the electromagnetic valve with a latch valve or pneumatic valve.

With these three countermeasures, we have conducted firing tests in safe for 2 years, thus far.

3 Summary

Four failures that took place in the preparation process or firing testings of HAN thruster, as well as the countermeasures against them, are summarized. Only the last failure is rather complicated to explain; the reasons for the other three failures are simple, and these failures can be avoidable with extra care. It is often said that the research and development of propulsion system using high energetic materials is always accompanied with accidents; however, we hope these lessons learned through the four failures in the HAN thruster study will be useful for other research and development using other high energetic materials.

References

1. http://ec.europa.eu/enterprise/sectors/chemicals/reach/index_en.htm
2. Wingborg N, Eldsäter, Skifs H (2004) Formulation and characterization of ADN-based liquid monopropellants. In: Proceedings of 2nd international conference on green propellants for space propulsion, Chia Laguna, Sardinia, Italy
3. Wingborg N, de Flon J (2010) Characterization of the ADN-based liquid monopropellant FLP-106. In: Proceedings of space propulsion, San Sebastian
4. Anflo K, Moore S, King P (2009) Expanding the ADN-based monopropellant Thruster Family. In: 23rd annual AIAA/USU conference on small satellites, SSC09-II-4

5. http://www.sscspace.com/nasa-to-test-and-evaluate-ecaps-green-propulsion-technology
6. Spores RA, Masse R, Kimbrel S, McLean C (2014) GPIM AF-M315E propulsion system. AIAA Paper, 20140012587
7. Spores RA, Masse R, Kimbrel S, McLean C (2013) GPIM AF-M315E propulsion system. AIAA Paper 2013-3849
8. Masse RA, Overly JA, Allen MY, Spores RA (2012) A new state-of-the-art in AF-M315E Thruster Technologies. AIAA 2012-4335
9. Katsumi T, Kodama H, Matsuo T, Nakatsuka J, Hasegawa K, Kobayashi K, Ogawa H, Tsuboi N, Sawai S, Hori K (2009) Combustion characteristics of HAN-based liquid monopropellant – combustion mechanism and application to thruster. Combust Explos Shock Waves 45(4):442–453
10. Katsumi T, Kodama H, Shibamoto H, Nakatsuka J, Hasegawa K, Kobayashi K, Ogawa H, Tsuboi N, Sawai S, Hori K (2009) Combustion characteristics of HAN-based liquid monopropellant. Sci Technol Energetic Mater 70(2):27–32
11. Katsumi T, Matsuda R, Inoue T, Tsuboi N, Ogawa H, Sawai S, Hori K (2010) Combustion characteristics of hydroxylammonium nitrate aqueous solutions. Int J Energetic Mater Chem Propuls 9(3):219–231
12. Katsumi T, Inoue T, Hori K (2013) Mechanism of high burning rate of HAN-based solutions. Sci Technol Energetic Mat 74(1):1–5
13. Private communication. Dr. Woddward Waesche

Physical Mechanisms of Upper Atmosphere Optical Phenomena Associated with Rocket Engine Operation

Yulii V. Platov and Sergey Sh. Nikolayshvili

Abstract With the development of rocket and space technology and intensive study of near-Earth space, optical phenomena associated with the technical impact on the environment became increasingly observed. One can divide several basic types of such phenomena: rocket engine torch plumes, observed during the launch of missiles and maneuvers of spacecraft, the phenomenon observed at reentry of spacecraft into denser layers of the atmosphere, the gas and dust clouds formed with rocket engines operation, phenomena developing in the process of an interaction of the combustion products with atmospheric components, and shock waves generated by rocket engines in the upper atmosphere. Phenomena associated with the launches of solid-fuel missiles have a number of features related to the specifics of the operation of such engines and fuel composition. Optical phenomena connected with rocket engine operations are a good tool for the investigation of physical conditions and processes in the upper atmosphere. Also systematic observations of these phenomena assist in making an environmental impact assessment of missile launches on the upper atmosphere.

1 Introduction

Natural optical phenomena in the upper atmosphere which are available to visual observations are relatively not numerous. These include the aurora, meteor phenomena, noctilucent clouds, and, probably, quite rare phenomena associated with electrical discharges, such as the electric jets in the ionosphere (see Fig. 1a–d).

Mainly "poorness" of these phenomena is determined by the low density of the atmosphere at high altitudes and, as a consequence, by low brightness optical

Y.V. Platov (✉)
Pushkov Institute of Terrestrial Magnetism, Ionosphere and Radio Wave Propagation RAS,
Troitsk, Moscow 142190, Russia
e-mail: yplatov@mail.ru

S.Sh. Nikolayshvili
Fedorov Institute of Applied Geophysics, Moscow 129128, Russia
e-mail: ser58ge@gmail.com
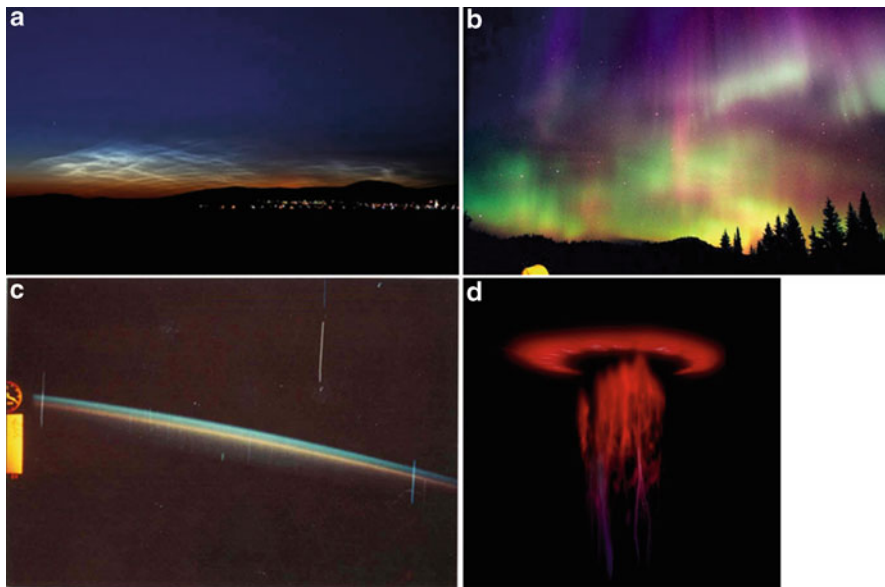
Fig. 1 Some natural optical phenomena developing in the upper atmosphere. (**a**) Noctilucent clouds localized at heights ∼90 km; (**b**) aurora; (**c**) emission layers – oxygen (*top*) and sodium (*lower*) – recording on the space station "Salut 7" 1982; (**d**) ionosphere jets red Elf

phenomena. Of course, in the upper atmosphere, there is a vast class of phenomena, like airglow, developing due to physical and chemical processes. There are, in particular, so-called emission layers of the upper atmosphere, which, however, can be recorded only with the help of highly sensitive equipment.

Since the middle of the last century, optical phenomena associated with the technical activities, namely, with the power rocket launches, have been observed in the upper atmosphere. In the upper atmosphere, optical phenomena have been observed associated with the technical activities, namely, with the power rocket launches.

These phenomena are quite unique because they do not have natural analogues. Probably it is the reason that for a long time they were perceived by witnesses as something abnormal, up to contacts with extraterrestrial civilizations – the UFO.

The whole complex of optical phenomena associated with missile activities can be divided into several categories: rocket plumes and rocket traces in the atmosphere, phenomena connected with reentry rocket and satellite fragments, luminosity of gas–dust clouds of combustion products in the upper atmosphere, and optical emissions determined by the interaction of rocket combustion products with atmosphere components.

2   Rocket Plumes and Rocket Traces in the Atmosphere

Observations of missile plumes and missile trails in the atmosphere are probably the most trivial phenomenon and, as a rule, do not cause ambiguities in their interpretation. Figure 2 illustrates some examples of such phenomena. Obviously, the brightest part of the plume corresponds to the high-temperature region in the vicinity of the engine nozzle. It is easy to estimate that the power of such light source in the optical range may exceed 1 MW, and its brightness is about $3 \cdot 10^4$ sb. Taking into account the fact that these objects may be at high altitudes, it is not surprising that they can be observed visually from distances up to 1000 km.

Probably this is the only "rocket optical phenomenon" which has some natural analogue. It is the entry of spacecraft or its fragments into the dense layers of the atmosphere, which is similar to meteor phenomena (see Fig. 3).

The basic physical mechanism of gas–dust cloud luminosity is the scattering of sunlight by dispersed particles of combustion products. One of the first instrumental observations of such events was carried out at the Observatory Haleakalā, Hawaiian Islands, during Saturn IV launcher engine operation in the Apollo 8 program on 21 December 1968 (see Fig. 4).

Kung et al. [1] were the first to assume the presence of a condensed phase in combustion products for an explanation of the optical phenomena observed during rocket engine operation. The intensity of optical phenomena, developing in the upper atmosphere, was compared with the much lower much less intensity of phenomena localized in troposphere. It is because the density of the atmosphere at altitudes of 100–300 km is 10^7–10^{12} times less than the density of the air near the Earth's surface.

However, the scale of the phenomena at high altitudes may be many times greater than the characteristic sizes of the troposphere or stratosphere phenomena and can make up hundreds of kilometers.

Since the intensity I of scattered light very strongly depends on the size (d) of particles $I \sim I_0 \, \underline{\boldsymbol{d^6}}$ (Rayleigh scattering), it is obvious that the presence of large dispersed particles in the exhaust jet is an important factor for the possibility of observation of these formations in twilight conditions.

Virtually, the only mechanism of the formation of artificial gas–dust clouds in the upper atmosphere is the injection of combustion products during missile launches or maneuvering space vehicles. Phenomena associated with the operating of rocket engines in the upper atmosphere are observed in twilight conditions and, depending on the type of engines and their operation mode, vary in the duration of their development, dynamics, sizes, and geometric characteristics [2–4]. The combustion products of solid-fuel engines always contain dispersed particles (soot, Al, Al_2O_3), which composition is determined by the components of the fuel. During the operation of liquid rocket engines, dispersed particles can be formed only in the process of the condensation of water vapor and carbon dioxide in the exhaust jet as a result of sharp fall of combustion product temperature at their extension. The presence of condensed phase in combustion products is confirmed by numerous

Fig. 2 Rocket plumes and traces: (**a**) the plume of "Proton" launcher in the troposphere, (**b**) the trace of Ariane-5ECA, (**c**) the launch of "Minuteman," (**d**) rocket trace in the stratosphere diffused by winds

observations of the optical effects associated with the launching of missiles. In Fig. 5, one can see the cloud condensed particles formed during the operation of different launchers and spacecrafts.

The modeling of these effects requires solving two main tasks. They are the investigation of the condensation process of combustion products in the exhaust jet

Fig. 3 Reentry space craft (SC) "Jules Verne" 03 September 2008 (**a**) and the without slit spectrum of this phenomenon (**b**). The intense glow in the blue region of the spectrum shows a very high temperature in the head part of this object. Cheljabinsk meteorite, 15 February 2013, Russia (**c**)

Fig. 4 Apollo 8 translunar injection burn observed in twilight, 1968
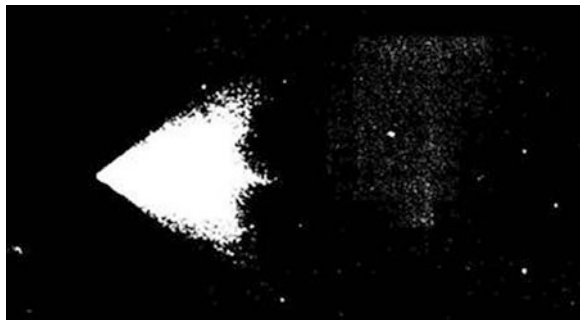
and dynamics of gas–dust clouds. Condensation of combustion products can take a place when the partial pressure of water vapor or carbon dioxide in the exhaust jet exceeds its saturation pressure. Comparison of the partial pressures of water vapor and carbon dioxide in the combustion products for different engines and saturated vapor pressures of these gases as a function of distance from the nozzle are shown in Figs. 6 and 7.

It follows from these figures that the conditions necessary for the condensation of water vapor in exhaust jets of the final stages of "Proton," "Molnija," and "Start" launchers are started at the distances from the nozzle of $\sim$100, $\sim$150, and $\sim$120 m, respectively.
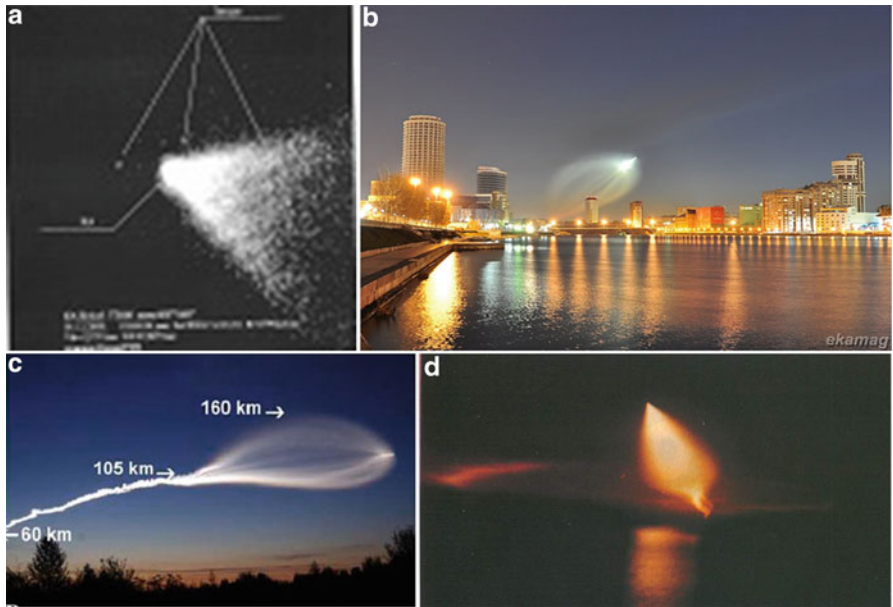
Fig. 5 Gas–dust clouds formed during operation of different rocket objects: (**a**) SC "Sirius 3" height ∼18,000 km, (**b**, **c**) launchers "Molnija," (**d**) launch of navel solid-fuel (SF) missile. Canary Islands
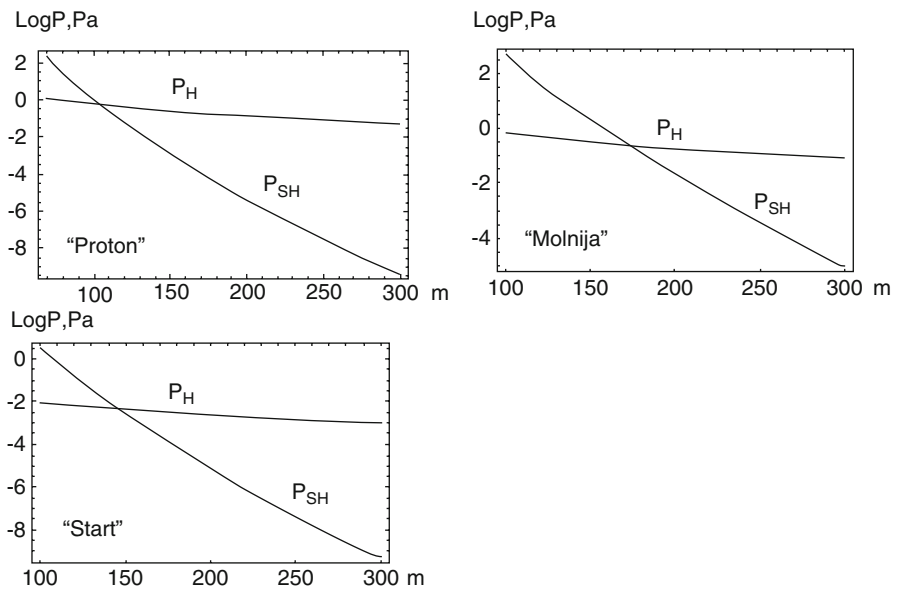
Fig. 6 The dependence of water vapor partial (P_H) and saturation (PS_H) pressures corresponding to the local value of the combustion product temperature on a distance from a nozzle to a central stream for "Proton," "Molnija," and "Start" launchers
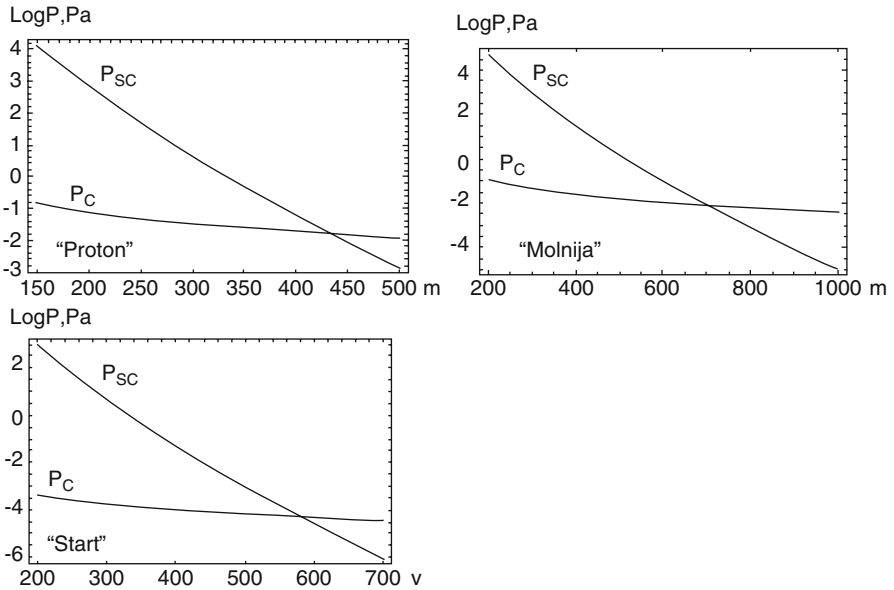
Fig. 7 The dependence of carbon dioxide partial (P_C) and saturation (P_{SC}) pressures corresponding to the local value of the combustion product temperature on a distance from a nozzle to a central stream tube for "Proton," "Molnija," and "Start" launchers

The condensation of carbon dioxide in plumes of these engines can occur at distances greater than ∼450, ∼650, and ∼600 m. It is obvious that the larger distance from the nozzle for carbon dioxide condensation region in comparison with the zone of water vapor condensation is determined mainly by the fact that the temperature of carbon dioxide condensation ($-78.5°$ C) is much less than the temperature of condensation of water vapor ($0°$ C). One of the main tasks of modeling the process of condensation in rarefied environment is the definition of the mechanism of dissipation energy released in the process of condensation.

This process can be described by the equation of balance of energy and equation of a size change of condensed particles [5, 6].

The following designations are accepted in this article:

W, energy; $l(t)$, distance from a rocket nozzle to condensation region; t, time of combustion products motion at a distance l from nozzle; $T_v(t)$, water vapor temperature in exhausts; T_p, temperature of condensed particles; r, characteristic size (radius) of condensed particles; ρ, particle density; $q(T_p)$, heat capacity; Q_{con}, latent heat of condensation; α, adaptation factor of water molecular to a condensate surface; $P_S(T_p)$, saturated vapor pressure over particle surface; $P_v(t)$, partial water vapor pressure in rocket exhaust; $P(t)$, combustion product pressure in rocket exhaust; k, Boltzmann's constant; σ, Stefan–Boltzmann's constant; $\chi(r, \lambda)$, water absorption factor; $B(\lambda,T)$, Planck function; $F_S(\lambda)$, energy flux of

sunlight outside the terrestrial atmosphere; S_N, area of engine nozzle; Q_{col}, factor of heat collisional transmission; μ, water molecule mass

$$dW_p = Q_{con}dm + dW_{Sun} + dW_{Noz} + dW_{rad} - dW_{col}$$

$$dr = f(P, T, \rho)\, dt$$

Here

$Q_{con}dm = 4\pi r^2 Q_{con}\alpha \left[\left(P_v(t) - P_S\left(T_p\right)\right)\right]\sqrt{\mu/2\pi kT_v}dt$ – energy released by condensation.

$dW_p = 4/3\pi r3\, q\left(T_p\right)dT$ – change of particle energy

$$dW_{Noz} = \pi r^2 \frac{S_N}{2\pi l^2(t)}\int \chi(r, \lambda)\, B(T_N, \lambda)d\lambda$$

$$dW_{Sun} = \pi r^2 \int \chi(r, \lambda)\, F_S(\lambda)\, d\lambda$$

– energy of solar radiation and radiation of the engine nozzle absorbed by the particle, respectively.

$dW_{rad} = 4\pi r^2 \gamma\sigma T^4$ – energy losses in the heat radiation ($\gamma \approx 0.92$ is emissivity of water)

$$dW_{col} = 4\pi r^2 \varepsilon\left(T_p - T_v\right)\, P(t)/P_0$$

– energy losses in the heat transfer to the surrounding gas ($\varepsilon \approx 10{,}500$ W/m^{2}K – transfer coefficient condensing steam at atmospheric pressure P_0).

These equations have been analyzed in detail in [5, 6]. The results of the numerical solution of these equations are shown in Fig. 8.

3 Dynamics of Gas–Dust Clouds

The spreading of combustion products in the direction perpendicular to the motion of a rocket is determined by the development of a strong shock wave in the atmosphere under rocket engine operation. Indeed, the typical value of combustion product pressure at the nozzle exit section, working in the upper atmosphere, is about 0.005 MPa; therefore, an under-expansion factor (ratio of gas pressure at the nozzle exit and external pressure P_p/P_∞) exceeds 10^7. Such a ratio of gas pressures should lead to the phenomena comparable to a strong explosion in perpendicular to the rocket motion direction and gas expansion with the velocities up to 3–5 km/s.
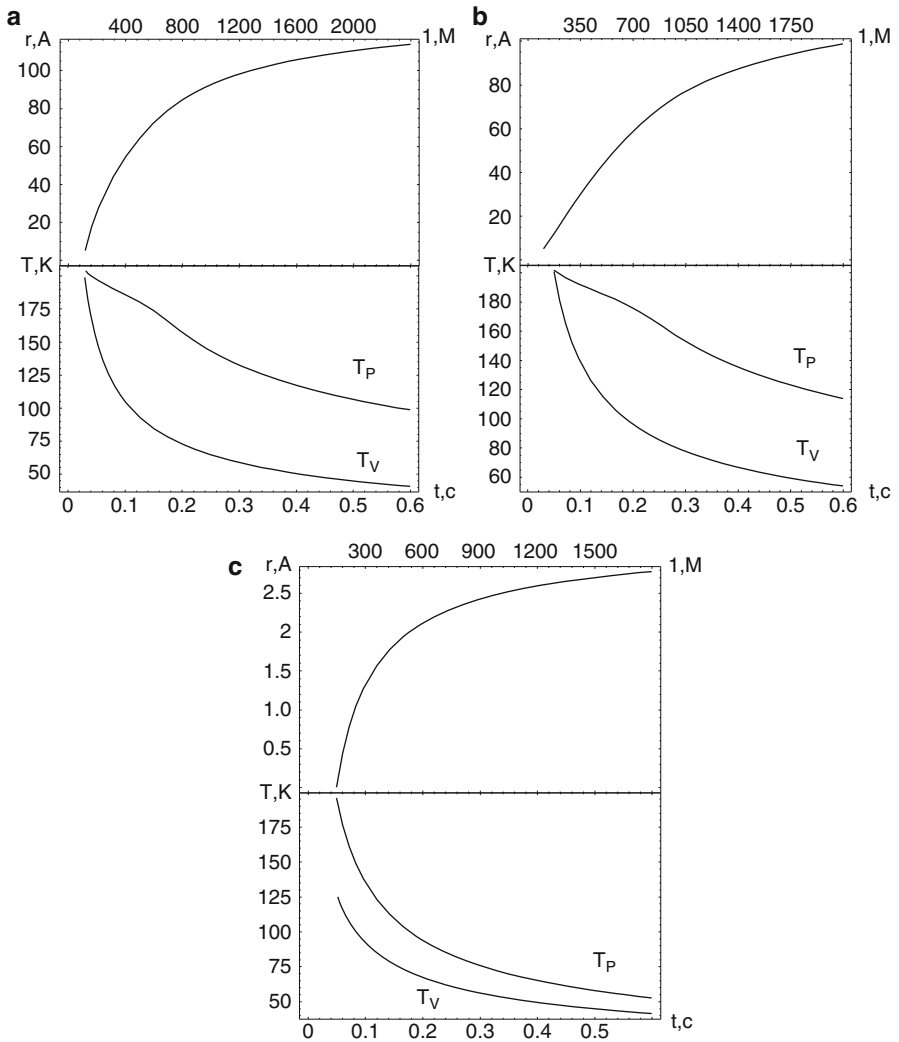
Fig. 8 Changing the thickness of the condensed layer (r, E) and a temperature of condensed particles (T_P) for water vapor in the exhaust jet engines: (**a**) "Proton," (**b**) "Molnija," (**c**) "Start" on the time (the distance from a nozzle). For comparison, the figures show also the change in temperature of the combustion products (T_V)

A rocket plume may be schematically divided into three regions (see Fig. 9). Region (1) is nearest to the rocket region with a complex structure of the shock waves. This region may extend to several kilometers.

Region (2) may be called a region of a cylindrically symmetric explosion where the pressure of combustion products is still much higher than the ambient
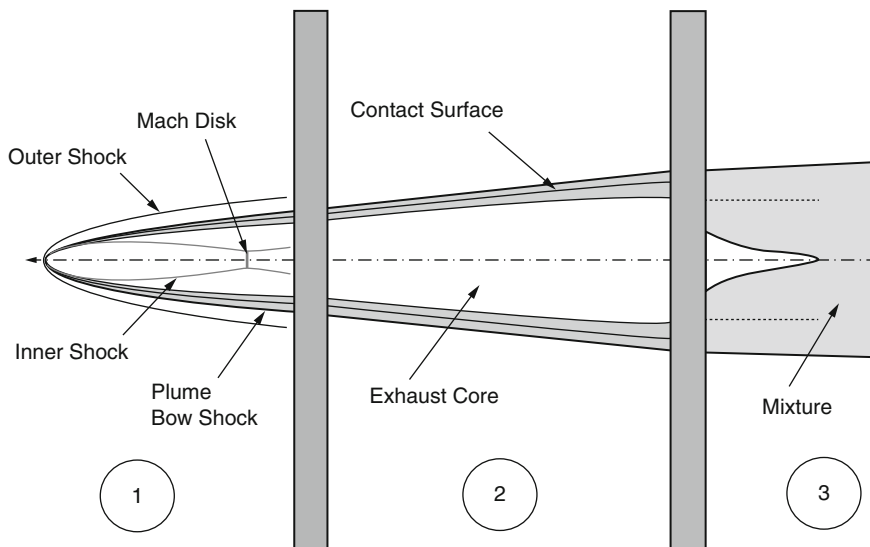
Fig. 9 Structure of a rocket plume in the upper atmosphere: *1* rocket nearest region, *2* region of a cylindrically symmetric explosion, ($P_p \gg P_\infty$), *3* region of the sound perturbations and a diffusive mixing with ambient gas ($P_p \approx P_\infty$)

gas pressure – $P_p \gg P_\infty$. It is characterized by almost a free gas expansion in a transversal direction and may occupy from tens to hundreds kilometers.

In region (3), where the pressure of combustion products becomes comparable with the ambient pressure, $P_p \approx P_\infty$, the diffusive processes prevail. This region may extend up to thousand kilometers.

The first area was studied in detail in [7–9]. The investigation of a rocket plume structure in region (2) was carried out in works [10, 11]. A radial expansion of a plume, in this region, was described [10] with the help of the self-similar self-consistent solutions for a cylindrically symmetric point-like explosion. It should, however, be noted that the self-similar solutions are not suitable for an accurate description of large central parts of a plume and large parts of the space where the ambient medium pressure is to be taken into account. We, therefore, had to undertake the numerical calculations based on 3T 1D gas dynamic equations in a cylindrically symmetric geometry in order to describe in detail the motion of combustion products.

In order to estimate the fields of applicability of a self-similar solution, we compare it with a numerical calculation of a transversal rocket plume expansion in a cylindrical geometry. It was assumed, in the numerical calculations, that the exhaust plume is concentrated, initially, in a cylinder of the nozzle radius r, the density being determined from the exit gas velocity V_e, and the known value of the fuel consumption rate. Figure 11 demonstrates the calculation results of a position and velocity of a contact surface motion for the Saturn IVB rocket exhaust plume at
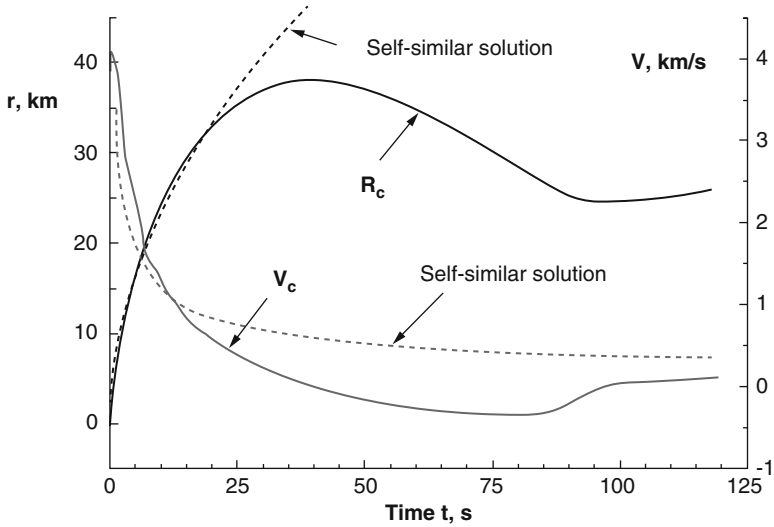
Fig. 10 Temporal dependence of the contact surface velocity V_c and coordinate R_c at the altitude 200 km. A self-similar approximation is plotted by *dots*

the altitude of 250 km. A composition of the combustion products was 30 % H_2, 70 % H_2O with an initial concentration 2.10^{-2} kg/m^3, and temperature 1400 K. Density and temperature of ambient atmosphere were, respectively, 10^{-10} kg/m^3 and 1000 K.

Figure 10 demonstrates the calculation results for the density and velocity transverse profiles of the exhaust plume and ambient gas motion for the abovementioned initial conditions. It is seen that about 10 s after a rocket transit moment, near the rocket's trajectory axis, a specific region with a decreased gas concentration is formed. This region may be called a gasdynamic hole. This gasdynamic hole exists during a few minutes.

The cross section of a gasdynamic hole increases with altitude and may achieve about one hundred kilometers.

From calculations, it follows that condensed particles can be accelerated to speeds of 2–3 km/s in transversal movement only in the first seconds. Superposition of movement of a rocket with a speed of ∼6 km/s and expansion of particles lead to the formation of the characteristic cone-shaped "clouds," which are observed in twilight conditions as a result of sunlight scattering on a disperse component of combustion products. It is obvious that a corner at a cone point is defined by the relation of the speed of a rocket movement and the radial speed of the dispersed components.

Phenomena associated with the launches of solid and liquid propellant missiles are in many respects similar. However, there is number of features related to the specifics of the operation of solid-fuel engines.
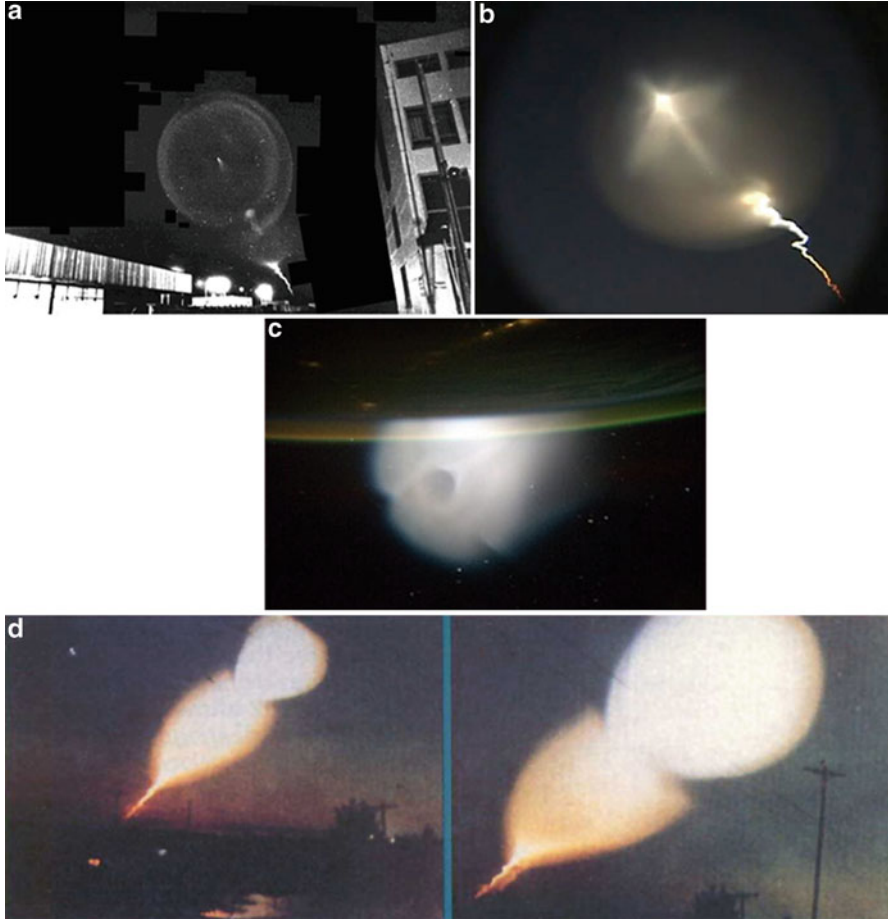
Fig. 11 (**a**) The of "bagel hole" gas–dust cloud formed under separation stages of solid-fuel rockets. There is in the bagel center the plume of the last stage; (**b**) the initial phase of the development of the gas–dust cloud; (**c**) missile launch creates weird light in the sky (The photo was obtained on the International Space Station); (**e**) development of "spherical" clouds during launch of navel SF missile. Canary Islands [12]

For example, the shutdown process of solid-propellant rocket engines is often accompanied by the development of large-scale dynamic formations with a torus shape in the image plane (see Fig. 11).

The evolution of the dust clouds created under rocket launches and during active experiments in the upper atmosphere (see Fig. 12) has been considered in the work [13].

This process is connected with a sharp drop of pressure in the combustion chamber during a cutoff thrust, which leads to an almost instantaneous injection of a large amount of fuel components and combustion products into the atmosphere. The quantity of the injected matter for powerful rockets can reach of hundreds
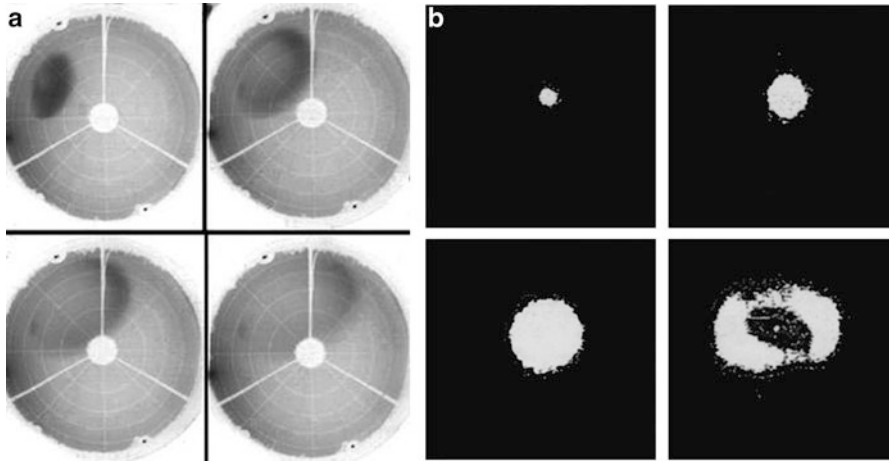
Fig. 12 (**a**) The example of the development gas–dust cloud after separation of stages solid-fuel missiles. Images obtained by chambers of patrol recording of the Aurora (negative image); (**b**) evolution of a cloud of monomethyl hydrazine injected at a height of ∼250 km. The sequence of the photographs corresponds to 1, 5, 20, and 60 s after injection. There is in the center of last frame the image of empty canister

kilograms; a considerable part of this matter is in a dispersive state due to the specific composition of fuel and incomplete combustion of fuel. The mass of an injected matter into the atmosphere is determined by the pressure in the combustion chamber P, chamber volume W, temperature T, and the average molar mass of combustion products μ: $M = \mu PV/RT$. For the characteristic values $P \approx 10$ MPa, $W \approx 20$ m^3, $T \approx 2800$ K, and $\mu \approx 0.35$, the mass of injected substance can be 300–400 kg. An expansion velocity of such "clouds" is ∼2 km/s, and their transverse size can reach ∼1000 km [4]. In some cases, fragments of such formations can rise up to heights of ∼700 km. This indicates that their initial vertical velocity is ∼4 km/s which is a vector sum of the vertical velocity of a rocket at the instant of cloud formation (6–7 km/s) and the velocity of the cloud itself relative to the rocket. The development time of such phenomena is mainly determined by the time of rise and sedimentation of ejected substance under the gravity action to ∼100 km, i.e., to the boundary of the turbopause.

The development of these phenomena can be modeled by the approximation of a strong explosion in a rare gaseous medium. Since the pressure in the combustion chamber of a rocket (∼10 MPa) considerably exceeds the pressure of the surrounding gas (∼5 10^{-4} Pa), the condition for the applicability of an automodel solution is satisfied. In this approximation, the dependences of radius r and velocity V and temperature of the shock wave on time for a spherically symmetric case have the form

$$r = (E/\rho)^{1/5}t^{2/5}, V = (E/\rho)^{1/5}t^{3/5},$$

$$T = \frac{2(\gamma - 1)}{R(\gamma + 1)^2}c^2 = \frac{2(\gamma - 1)}{R(\gamma + 1)^2}\frac{4E}{25\rho r^3}$$

where E is the energy released during the explosion and ρ is the initial gas density. Supposing that $E \sim 2\ 10^8$ J (for P $\approx$ 10 MPa, $W \approx 20$ m^3, and $\rho \sim 10^{-10}$ kg/m^3), it is easy to find that the characteristic shock wave velocity is $\sim$2 10^3 t$^{-3/5}$ m/s. The obtained value agrees well with the measurement results for the expansion velocities.

4 Turquoise (Blue–Green) Luminescence

The second class of specific phenomena is connected with the chemical composition of the fuel. It produces regions with intense turquoise (blue–green) luminescence that are observed under twilight conditions. Figure 13 illustrates some photographs of such formations.

Spectral observations show that this effect is caused by the emission of molecules monoxide aluminum AlO. During the combustion process, Al normally oxidizes to Al_2O_3 and AlO not contained in the combustion products.
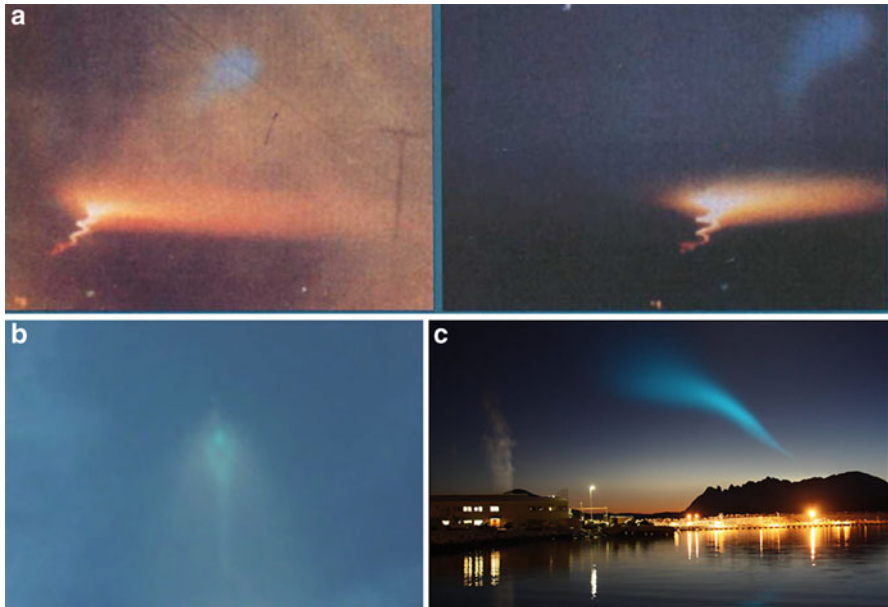
Fig. 13 (**a**) The blue–green cloud formed during launch of navel SF rocket (Canary Islands). (**b**) The launch of "Topol M." (**c**) Unique photo turquoise glow during the launch of the "Bulava" (Norway)
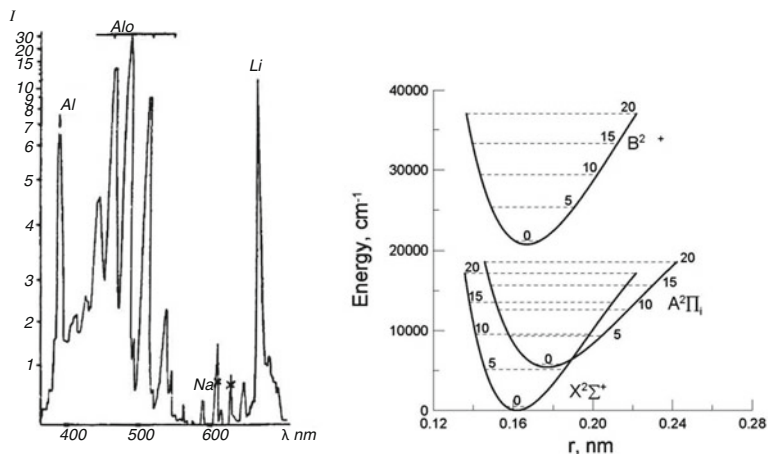
Fig. 14 Spectrum of a "turquoise" cloud and a structure of electron levels of AlO molecular. The luminescence intensity is presented in relative units because absolute calibration was not carried out

The aluminum monoxide *AlO* is a very interesting molecule. An example of the spectrum of blue-green luminescence and structure of the electronic levels of the molecule AlO is shown in Fig. 14. Unlike other oxides of aluminum, the formation reaction of its formation is endothermic, i.e., it is going on with absorption energy ($\sim$67 KJ/mol) under a sufficiently high temperature (about 3000 K).

It has been detected in the gas phase after the explosion of aluminized grenades in the upper atmosphere and in stellar absorption spectra in particular in the spectra of sunspots (T $\sim$ 4000 K) [14].

Simple estimates are made for the approximation of self-similar solutions and show that the temperature at the front of a shock wave, formed during stage separation of solid-fuel missiles, could reach 4000–5000 K at a distance of $\sim$10 km from the rocket. Therefore, the formation of aluminum monoxide is quite possible at this stage of expansion of the rocket exhaust jet.

The most likely reactions of formation *AlO* are $Al+O_2$ (k $\sim 10^{-10}$), $Al+H_2O$ (k $\sim$ 1–7 10^{-11}), and $Al+CO_2$ (k $\sim$ 3 10^{-12} – 2 10^{-11}).

AlO can also be formed as a result of the addition of aluminum molecules to aluminum oxide Al_2O_3 at high temperatures (above 1300 K).

Under the conditions of illumination of artificial formations by solar light, the excitation mechanism for *AlO* emissions is the resonance scattering of solar radiation $AlO + h\nu \rightarrow AlO^* \rightarrow AlO + h\nu$ in the wavelength range from 4374 Å to 5424 Å. The "long afterglow" of a turquoise cloud during more than an hour after a rocket's flight is determined by a comparatively small coefficient of diffusion of rather heavy (relative to the surrounding gas) *AlO* molecules.

The intensity of the recording glow of *AlO* permits an estimation of the concentration of these molecules in the atmosphere. The uncertainty of such

estimates is very large, but it can be assumed that for observed effects, it is likely that <1 % of the total number of aluminum contained in the mixed fuel exist as *AlO*.

Will investigations of such phenomena accompanying the operation rocket engines in the upper atmosphere be applied in addition to a simple understanding of the mechanisms of their development? Probably in this plan, it is possible to allocate two basic aspects.

First, optical phenomena are a good tool for the investigation of physical conditions and processes in the upper atmosphere.

And, probably the most important reason, systematic observations of these phenomena assist in making an environmental impact assessment of missile launches on the upper atmosphere.

References

1. Kung RV, Cianciolo L, Myer JA (1975) Solar scattering from condensation in Apollo translunar injection plume. AIAA J 13(4):432–437
2. Wu BJC (1975) Possible water vapor condensation in rocket exhaust plumes. AIAA J 13(5):797–802
3. Simmons FS (2000) Rocket exhaust plume phenomenology. Aerospace Press 2350 El Segundo, California
4. Platov YV, Chernouss SA, Kosch VJ (2004) Classification of gas-dust formations from rocket exhaust in the upper atmosphere. J Spacecr Rocket 41(4):667–670
5. Platov YV (2014) Condensation of water vapor and carbon dioxide in the jet exhausts of rocket engines. Geomagn Aeron (Russ) 54(1):111–115
6. Platov Yu, DeLuca LT. Heterogeneous condensation of water vapor and carbon dioxide in rocket engine plumes, operated in the upper atmosphere. In: 5th EuCASS conference, propulsion physics, Munich, Germany, 1–5 July 2013
7. Draper JS, Sutton EA (1973) Nomogram for high-altitude plume structures. J Spacecr 10:682
8. Draper JS, Bien F, Huffman RE, Paulsen DE (1975) Rocket plumes in the thermosphere. AIAA J 13:825
9. Boynton FP (1967) Highly underexpanded jet structure: exact and approximate calculations. AIAA J 5:1703
10. Ivlev LS, Romanova VI (1993) Model of a gas-dust cloud in high-altitude rocket plumes. Opt Atmos Ocean (Russ) 6:458
11. Molchanov AG, Platov YV (2010) Gas dynamics of a rocket plume in the upper atmosphere. J Russ Laser Res 31(5):410–414
12. Ballester Olmos V-J. http://www.anomalia.org/bibliog1.pdf
13. Belikov YE, Nikolaishvili SS, Peradze RK (1993) Model of solar light scattering by and artificial spherical dispersed gas cloud in the Earth's upper atmosphere. Kosm Issled 31(1):135–142
14. Sriramachandran S, Viswanathan B, Shanmugavel R (2013) Occurrence of AlO molecular lines in sunspot umbral, spectra. Sol Phys 286:315–326

Green Technologies for the Safe Disposal of Energetic Materials in the Environment

Shalini Anand and S. Mary Celin

Abstract The processes involved in the large-scale manufacturing and processing of energetics, the testing of explosives, and firing training and evaluation activities, together with the destruction of ammunition stocks, have led to accumulation of energetic compounds in the environment. This can result in the contamination of soil and water resources. In the recent past, an increased environmental awareness of the harmful effects of explosives in the defense sector has compelled agencies to evaluate the impacts of military activities on the quality of soil, ground, and surface water in order to employ various strategies for the effective management and cleaning of the environment. The physical and chemical methods currently used for remediation of contaminated sites are expensive and can sometimes result in the formation of toxic by-products. The limitations faced by these treatment technologies may be overcome by biotreatment, which offers highly efficient, cost-effective, environment friendly, and economically feasible way of cleaning the environment using plants and native microbes.

Plants possess the ability for metabolism and degradation of many recalcitrant xenobiotics and are considered as "green livers," acting as an important sink for environmentally damaging chemicals. Microbes are known to possess highly versatile effective metabolism systems/catabolic mechanisms capable of degrading and utilizing various toxic compounds, as an energy resource for growth. Thus in the near future, present explosive waste management strategies will experience a global shift toward usage of highly efficient green technologies, promising for improving the environmental quality of water and soils/sites contaminated with energetic materials.

S. Anand (✉) • S.M. Celin
Centre for Fire Explosive and Environment Safety (CFEES), Defence Research Development Organization (DRDO), Timarpur, Delhi 110054, India
e-mail: sdk_anand@yahoo.com; celinkumaran@yahoo.com

Nomenclature

2-ADNT, 4-ADNT	Aminodinitrotoluenes
2,4-DANT	Diaminonitrotoluenes
2,4-DAT	2,4-diaminotoluene
2-ADNT	2-amino-4,6-dinitrotoluene
4-ADNT	4-amino-2,6-dinitrotoluene
2,4 DA-4-NT	2,4-diamino-4-nitrotoluene
2,4 DA-6-NT	2,4-diamino-6-nitrotoluene
2-A-4-NT	2-amino-4-nitrotoluene
4-A-2-NT	4-amino-2-nitrotoluene
2,6-AMNT	2,6-aminonitrotoluenes
2,4-DAMNT	2,4-diaminonitrotoluenes
BTEX	Benzene, toluene, ethylbenzene, and xylene
DOE's	Department of Energy's
GABA	Gamma-aminobutyric acid
GEM	Green energetic materials
HADNT	Hydroxylaminodinitrotoluene
HE	High Energy
HMX	Octahydro-1,3,5,7-tetranitro-1,3,5,7-tetrazocine
IAAP	Iowa Army Ammunition Plant
LDNR, lead	Lead dinitroresorcinate
LMNR	Azotetrazole, lead monoresorcinate
MAAP	McAlester Army Ammunition Plant
NACs	Nitroaromatic compounds
NC	Nitrocellulose
NG	Nitroglycerin
PBR	Previously bioremediated hydrocarbon
PCBs	Polychlorinated biphenyls
RDX	Hexahydro-1,3,5-trinitro-1,3,5-triazine
SBR	Sequencing Batch Reactors
TNT	2,4,6-trinitrotoluene
UXO	Unexploded ordnance
VOC	Volatile organic compound

1 Part I: Treatment of Contaminated Water

Shalini Anand • S. Mary Celin

1.1 Introduction

The processes involved in the large-scale manufacturing and processing of energetics, the testing of explosives, and firing training and evaluation activities, together with the destruction of ammunition stocks, have led to the accumulation of energetic compounds such as TNT (2,4,6-trinitrotoluene), RDX (hexahydro-1,3,5-trinitro-1,3,5-triazine), HMX (octahydro-1,3,5,7-tetranitro-1,3,5,7-tetrazocine), etc. in the environment. This can result in the contamination of soil and water resources. In the recent past, an increased environmental awareness of the harmful effects of explosives in the defense sector has compelled agencies to evaluate the impacts of military activities on the quality of soil, ground, and surface water in order to employ various strategies for the effective management and cleaning of the environment. The physical and chemical methods, viz., advanced oxidation, adsorption, and incineration, currently used for remediation of contaminated sites are expensive and can sometimes result in the formation of toxic by-products. The limitations faced by these treatment technologies may be overcome by biotreatment, which offers highly efficient, cost-effective, environment friendly, and economically feasible way of cleaning the environment using plants and native microbes.

Plants possess the ability for the metabolism and degradation of many recalcitrant xenobiotics (the compounds that resist biodegradation and thereby persist in the environment) and are often considered as "green livers," acting as an important sink for environmentally damaging chemicals [1]. Microbes, which are the oldest inhabitants on Earth, are ubiquitous, the most abundant, versatile, and also adaptive to the changing environment and can provide a cost-effective measure to combat the present problem of contamination. They are known to possess highly versatile and effective metabolism systems/catabolic mechanisms [2] capable of degrading and utilizing various toxic compounds as an energy resource for growth [3]. It is reported that despite of the toxicity of nitroaromatic compounds, many microorganisms are able to degrade them and hence are used in bioremediation. Significant progress has recently been made in studies of aerobic and anaerobic biodegradation of nitroaromatic compounds [4], thus making bioremediation using explosive degrading microorganisms a feasible method for the cleaning of effluent water contaminated with these compounds.

In this part of the chapter, we will discuss in detail the fate and transport of energetic materials in water and the related toxic effects, green technologies available, and developing priority green areas to be further explored for the successful bioremediation of explosive-contaminated water sources.

1.2 Entry of the Energetic Chemicals in the Water and Its Subsequent Fate

Manufacture of nitroorganic explosives generates toxic wastes leading to contamination of soils and waters especially groundwater. Typical explosive-contaminated

sites may contain up to 100 mg/L TNT in water. Anand et al. [5] reported that the concentrations of TNT and DNT in the contaminated water samples from the TNT manufacturing facility in India were up to 107 and 162 mg/L, respectively, and the average amount of HMX estimated from effluent samples from HMX manufacturing plant was 230 mg/L. Following entry into the environment, both abiotic and biotic processes will influence the fate of explosive compounds. The degree to which the explosive chemicals remain in the soil or are transported to groundwater depends on various parameters such as chemical nature, sorption (Koc) values, Log Kow values (octanol-water partition coefficient), etc. All explosive chemicals are persistent in nature [6] and have low biodegradability and hence remain active for a long period after release into the environment. These substances, their by-products and metabolites, can be highly toxic, mutagenic, and carcinogenic, thereby threatening the environment and human health [7]. Since production of all nitroexplosives involves the nitration process using concentrated nitric acid, the wastewater generated is highly acidic in nature and contains a very high concentration of nitrates along with traces of explosives and other nitro compounds. Apart from this, during their load, assemble, and pack operations, a large amount of contaminated water is generated.

Water contamination occurs when the volume of contamination exceeds the capacity of the soil to attenuate it, for example, manufacturing plants and load-and-pack sites. The primary mechanism for the transport and dissemination of explosive compounds throughout the environment is via dissolution into water. Due to the aqueous solubility of TNT (130 mg/L), RDX (42 mg/L), HMX (5 mg/L), and PETN (43 mg/L), discrete particles resulting from various defense-related activities which are of the order of low detonation which may dissolve slowly over time result in a constant release of explosive compounds to groundwater, surface water, marine environments, or subsurface soil over extended time periods.

As a large volume of water is required, it is necessary to locate the factories near natural sources of water – mostly rivers. The environment around large rivers is usually characterized by sand-rich soil that allows easy seepage of rainwater. Nitroaromatic compounds (NACs) are therefore continually washed out from the contaminated soil and subsequently contaminate groundwater. As the sandy soil is usually not rich in humic substances, the capacity for binding of TNT and its derivatives may be limited [8, 9].

1.2.1 Toxicity of Nitroexplosives

The nitroexplosives as well as their intermediate products and metabolites are very toxic, mutagenic, and carcinogenic, thereby threatening the environment and human health. Exposure to these substances is associated with the symptoms of illness such as methemoglobinemia, kidney diseases, jaundice, etc. in humans. Therefore, it is necessary to remove these compounds from the wastewater before their disposal.

RDX is a human carcinogen. RDX induces seizures by binding to the GABA(A) receptor-convulsant site and blocking GABA receptor-mediated currents in the

amygdala [10]. The toxicity and the risk associated with nitroorganic explosives [11] necessitate the development of cost-effective bioremediation technologies for their removal.

1.3 Current Status of Green Technologies for Their Removal and Disposal

The use of energetic materials has resulted in severe contamination of the environment in some areas; strategies are now being developed to clean these substances in an economical and eco-friendly manner. Bioremediation is a natural process that uses plants (phytotransformation) and microorganisms (microbial remediation) to transform hazardous materials into more benign substances.

1.3.1 Status of Phytoremediation and Its Scope

Phytoremediation is a green technology method for remediation using plants to degrade, stabilize, and/or remove contaminants. Plants directly uptake organic and nutrient contaminant from soil and groundwater and subsequently transform them. It is an environmentally friendly, economical, and low-maintenance method. This solar-driven, green technology has two major advantages over more conventional methods: it is relatively inexpensive and associated with minimal environmental disturbance leading to adequate and efficient removal of pollutants from various matrices. For these reasons, phytoremediation has a high public acceptability.

Consortia of many wetland species and aquatic plants have been used as a vegetative filter for treating groundwater and agricultural land contamination and for wastewater treatment in engineered systems because of the large surface area, ease of culture, and high organic uptake potential [12].

1.3.1.1 Constructed Wetlands

Constructed wetlands are a complex mixture of water, substrates, plants, and dead plant material and bacteria and have a great potential for the treatment of wastewater. These systems consist of beds or channels which have been planted with helophytes (water-loving plants), which rely upon physical, chemical, and biological processes to remove contaminants from wastewater.

In a field demonstration initiated at the Milan Army Ammunition Plant near Milan, Tennessee, and Iowa, USA [13], a successful phytoremediation of TNT and RDX from contaminated water by aquatic plant species such as parrot feather (*Myriophyllum aquaticum*), sweet flag (*Acorus calamus* L.), wool grass (*Scirpus cyperinus* L. Kunth), waterweed (*Elodea canadensis* Rich. in Michx), sago

pondweed (*Potamogeton pectinatus* L.), water star grass (*Heteranthera dubia* Jacq. MacM), and curlyleaf pondweed (*Potamogeton crispus* L.) in constructed wetlands was shown. The uptake and fate of TNT and RDX in three aquatic and four wetland plants in the laboratory were also studied using mineral nutrient solutions, in explosive-contaminated groundwater originated from a local aquifer at the Milan Army Ammunition Plant water [14–16]. Biotransformation of TNT and RDX had occurred in all plant treatments after 7 days and 13 days of incubation, respectively. A small-scale 4-month study was also carried out at the Volunteer Army Ammunition Plant, Chattanooga, TN (US Army Ammunition Base), to study the tolerance of submerged and emergent plants toward explosives in a constructed wetland [17].

Jacobson et al. [18] used laboratory and field test in developing bench and field-scale pilot-testing protocols for design of aquatic plant lagoons to treat water contaminated with 2,4,6-trinitrotoluene (TNT). The results from pilot-scale testing indicated that created wetlands are ready to treat groundwater along with monitoring of by-products and optimization of plant density, residence time, and flow rate.

Vanek et al. [19] reported that emergent plants (helophytes) such as *Phragmites australis*, *Juncus glaucus*, *Carex gracilis*, and *Typha latifolia* were able to degrade TNT (2,4,6-trinitrotoluene) under in vitro conditions. The plants took up and transformed more than 90 % of TNT from the medium within 10 days of cultivation. The most efficient species was *Ph. australis* which took up 98 % of TNT. The results were verified in a pilot-constructed wetland for cleaning explosive-containing wastewaters in a producing factory area.

Flokstra et al. [20] reported that poplar (*Populus deltoides* × nigra DN34) tissue cultures removed 2,4,6-trinitrotoluene (TNT) from an aqueous solution in 5 days, reducing the toxicity of the solution from a high toxic Microtox® EC value to that of the control. Also 1,3,5-trinitro-1,3,5-triazacyclohexane (RDX) was taken up by the plant tissue cultures at a slower rate, but toxicity reduction of the solution was still evident.

Nandan et al. [21] in a lab study reported phytoremediation of 2,4,6-trinitrotoluene (TNT) from synthetic TNT solutions by using a selected macrophyte, *Azolla microphylla*, within 7 days.

In order to achieve successful, optimized phytoremediation, a more systematic approach concerning the selection of plants and optimization of remediation processes is urgently required.

1.3.2 Status of Microbial Remediation of Energetic Materials

The incredible metabolic versatility inherited by microbes results in degradation of explosives which in turn manifest in the biogeochemical cycles [22]. Several microbes catalyze mineralization and/or nonspecific transformation of explosive waste either by aerobic or anaerobic processes. In case of TNT, bacteria may degrade it under aerobic or anaerobic conditions directly (TNT is source of carbon

and/or nitrogen) or via co-metabolism where additional substrates are needed [23]. Both the free cell culture and immobilized cell culture studies for treatment of explosive-contaminated water are in progress.

Claus et al. [24] described free cells of a new isolate *Raoultella terrigena* strain HB originating from a contaminated former explosive production site, as a vehicle to remove TNT completely from contaminated waters (10 and 100 mg/L) under optimum aerobic conditions within 7 days of incubation. HPLC analysis revealed up to 10–20 % aminodinitrotoluenes (2-ADNT, 4-ADNT) and diaminonitrotoluenes (2,4-DANT) as the metabolites which remained soluble in the culture medium and up to 80–90 % water insoluble azoxy-dimers as the main products in the cell extracts. The accumulation of TNT metabolites within the bacterial cells offers the opportunity to clean up contaminated waters after separation of the biomass. Geetanjali et al. [25] showed the 100 % disappearance of TNT within 30 h by *S. typhimurium* under aerobic conditions which is very encouraging and may indicate its potential in bioremediation of TNT. Mulla et al. [26] studied the degradation of 2-nitrotoluene by cells of *Micrococcus* sp. strain SMN-1 in free cells and cells immobilized in various matrices such as polyurethane foam, sodium alginate, sodium alginate polyvinyl alcohol, agar, and polyacrylamide. Immobilized cells showed higher degradation and could be reused more than 24 cycles without losing their degradation capacity and showed more tolerance to pH and temperature changes than freely suspended cells.

Immobilized bacterial cells have a great potential for application in bioremediation. Immobilized microbes have several advantages over freely suspended cells, including their easy separation from the reaction mixture, repeated use, and avoidance of cell washout during the continuous degradation process. Immobilized cells have higher activity, higher density, and longer stability than free cells. Hence the immobilized cells have the potential to degrade the toxic chemicals at higher concentration as compared to the freely suspended cells. Tope et al. [27] studied the transformation of 2,4,6-trinitrotoluene (TNT) by immobilized and resting cells of *Arthrobacter* spp. in the aqueous phase. Immobilized microbes showed more efficient TNT transformation as compared to resting free cells. Hafiz Ullah et al. [28] reported the biodegradation of TNT from water by immobilized *Bacillus* sp. YRE1 isolated from red effluent in free state and also cells immobilized on charcoal and polystyrene. The maximum percentage reduction of TNT was found with immobilized cell to be 96 %.

These shake flask degradation studies are upgraded by the use of bioreactors. The use of slurry and packed-bed bioreactors [29, 30] has been shown to be effective for wastewater treatment containing nitroaromatic compounds.

1.3.2.1   Bioreactors

Bioreactors are an ex situ biological treatment system that can be used to treat contaminated waters. The contaminated water flows through a reactor containing microbes which will degrade the contaminants. A bioreactor provides a more ideal

Table 1 No. of days taken for degradation of nitroaromatic compounds by cultures of *Pseudomonas putida* HK-6

Parameter	Chemicals in mg/L	Number of days of incubation for degradation
1. Individual degradation	TNT (100)	04
	RDX (15)	24
	Atrazine (50)	02
	Simazine (15)	04
2. Simultaneous degradation	TNT (30)	03
	RDX (05)	12
	Atrazine (20)	01
	Simazine (05)	03

environment for the microorganisms than the subsurface, because factors such as temperature, contaminant concentration, and the addition of nutrients can be better controlled.

A bench-scale anoxic membrane bioreactor (MBR) system, consisting of a bioreactor coupled to a ceramic cross-flow ultrafiltration module, was evaluated to treat synthetic wastewater containing alkaline hydrolysis products (hydrolysates) of RDX [31].

Krauter et al. [32] have developed a wetland bioreactor with a stable ecosystem of indigenous organisms to remove perchlorate (14–27 mg/L) and nitrate (48 mg/L) from contaminated groundwater. Cho et al. [33] reported the feasibility of using cultures of *Pseudomonas putida* HK-6 for simultaneous degradation of nitroaromatic compounds TNT, RDX, atrazine, and simazine (TRAS) with the aim of microbial application in wastewater treatment in bench-scale bioreactors. The observations are enumerated below in Table 1.

Biological treatment with the employment of anaerobic fluidized-bed reactor (AFBR) for the treatment of army ammunition production waste containing perchlorate and RDX was carried out by Atikovic et al. [34]. A detail of different types of bioreactors used for the treatment of perchlorate are reviewed by Srinivasan and Thiruvankatachari [35]. Biodegradability of TNT and 2,4-DNT in an aqueous system using an anaerobic filter (AF) combined with a biological aerated filter (BAF) was evaluated in two different sets of studies [36, 37]. The removal efficiency was above 99 %, and GC-MS analysis demonstrated that TNT was reduced to 4-amino-2,6- dinitrotoluene (4-ADNT), 2-amino-4,6-dinitrotoluene (2-ADNT), 2,4-diamino-6-nitrotoluene (2,4 DA-6NT), and 2,4-diamino-6-nitrotoluene (2,4 DA-4 NT), and 2,4-DNT was mainly reduced to 2-amino-4-nitrotoluene (2-A-4-NT), 4-amino-2-nitrotoluene (4-A-2-NT), and 2,4-diaminotoluene (2,4-DAT) during the anaerobic reaction. Further research revealed that new 2, 4-DNT-resistant bacteria had been generated during the stress of TNT and 2,4-DNT for 150 days.

Montgomery et al. [38] compared the incorporation and mineralization of TNT by natural assemblages from a small estuary and stated that one fate of

aromatic organic carbon metabolized by bacteria is incorporation into bacterial macromolecules and another fate is mineralization to CO_2 and respired for energy.

Thus these studies throw light on the application of bioremediation involving combination of oxic and anoxic conditions in a bioreactor. This would provide a novel method for the degradation of explosives which is difficult to degrade by traditional biological methods in aqueous systems.

1.4 Technologies to Be Explored for High Energetic Material Effluent Disposal

1.4.1 Coupled Chemical and Biological Reactor

The Department of Energy's (DOE's) Pantex Plant, Texas, USA, and Hawthorne Army Depot's Western Area Demilitarization Facility, Nevada, disassemble nuclear weapons as it reduces the size of the stockpile and generates high-explosive (HE) waste in the process. The Pantex Plant in Amarillo, Texas, uses coupling of chemical process that removes and degrades HE using carbon with subsequent biological treatment of wastewater to render by-products nonhazardous. Flushing the carbon-filled column with heated (80 °C) alkaline water (base hydrolyses) regenerates the carbon by removing the trapped HE and transforming them into nonexplosive easily degraded hazardous carbon compounds. As the wastewater flows from carbon column to bioreactor column, ethanol and other nutrients are added to the mixture. Microbial action in the bioreactor rapidly completes the breakdown process to nonhazardous products. This coupled chemical and biological method of regenerating activated carbon laden with HE is feasible effective, safe, and efficient [39].

Thermophilic aerobic treatment of explosive wastes (pink water sludge) was also evaluated by Wujcik et al. [40]. Explosive wastes are generated by US Army facilities. These nitroaromatic compounds are relatively refractory to biological degradation. Thermophilic aerobic treatment systems offer the potential to degrade these compounds. This system is a combination of single-stage thermophilic aerobic biological treatment, sidestream chemical treatment step, and efficient solid separation. A 4-month bench test was conducted using explosive wastes from McAlester Army Ammunition Plant (MAAP) in Oklahoma. The bench test covered several different and variable loading conditions. Respirometric test procedures were used to validate whether or not waste destruction had occurred due to biological activities.

1.4.2 Consortia of Bacteria

An immobilized consortium of bacteria using several species of bacteria at once can be a viable strategy for degradation of explosive waste found in contaminated waters of producing units. Consortia methods can improve degradation results. Existing

natural consortia could be stimulated to grow in situ by adding a good source to a contaminated aquifer. If sufficient bacteria are not present originally, then they could be added in a form of spores [41].

It has also been reported that a mixed microbial population in digested sewage culture degraded 110 mg TNT/l reduced to a non-detectable amount (>99 % removal) under strict anaerobic conditions in 6 days [42]. Red color due to the electron charge of NO_2 groups becomes colorless after 6 days of incubation, while the autoclave control remained red in color. Further stepwise deamination and subsequent mineralization by ring cleavage occurred by mixed nitroreductase which is available from many of the denitrifying bacteria predominantly in sewage culture.

1.4.3   Biogranulation

Bacteria also have the ability to attach to one another and form self-immobilized granules, by a process known as biogranulation. These granules are dense, compact aggregates and consist of a consortium of different microorganisms held together in a common polymer matrix. Granule development is mediated by auto-aggregating or co-aggregating abilities of the various interacting bacteria. Formation of microbial granules from microbial flocs under aerobic conditions is currently an active area of investigation for developing new generation wastewater treatment plants [43–45]. Nearly 6000 industrial wastewater treatment plants based on anaerobic granulation technology are in operation worldwide. Nancharaiah et al. [46] reported that the aerobic granular biomass, self-immobilized microbial consortia cultured in aerobically operated bioreactors, primarily consisting of mixed of species of bacteria ensconced in an extracellular polymeric matrix of their own creation has the potential to be employed as an effective biosorbent material for recovering/removing uranium (and probably other radionuclides) from dilute nuclear wastes.

Nancharaiah et al. [46, 47] examined the development of aerobic granular sludge in the presence of a synthetic chelating agent, nitrilotriacetic acid (NTA), in sequencing batch reactors (SBR). This showed the efficient degradation of NTA by aerobic granules.

Since self-granulation capability of microbes does not require any external bio-carrier for immobilization, biogranulation technology can be explored for the disposal of explosive-contaminated waters.

1.4.4   Microbial Mats

Microbial mats under the name of *Biomat*™, a proprietary microbial consortium, are photosynthetic in nature. It uses atmospheric carbon dioxide and water to produce oxygen and is nitrogen fixing (i.e., it uses atmospheric nitrogen to make usable nitrogen compounds for its growth). It contains anoxic (without oxygen) and oxic (with oxygen) zones in close proximity, which are assumed, to simultaneously facilitate dechlorination and cleavage of aromatic carbon rings, respectively, in

difficult organic contaminants as polychlorinated biphenyls (PCBs) and chlordane. Anoxic conditions mean depletion of dissolved oxygen which will occur if the rate of oxidation of organic matter by bacteria is greater than the supply of dissolved oxygen. The *Biomat*™ tolerates chemical toxins and various pH, salinity, and temperature levels. In the laboratory, it has removed an array of heavy metals and metalloids, mineralized pesticides, PCB, solvents, oils, and explosives to carbon dioxide and removed mixed waste in a continuous flow system. In the field, it has removed manganese, zinc, and other heavy metals (e.g., silver, chromium, cadmium, copper, lead, nickel, and iron) from mine drainage and a gasoline mixture of benzene, toluene, ethylbenzene, and xylene (BTEX), from contaminated groundwater. Current research is examining the role of mats in the nitrification of nutrient-enriched effluents from aquaculture. The role of microbial mats for multiple applications in aquaculture and bioremediation has been reviewed in detail [48]. Phillips and Bender [49] showed biological remediation of mixed waste in the form of organic and metal mixtures and radionuclides and mixed metals by microbial mats.

Planteco Inc. uses engineered Microbial Mat Aquatic Treatment System (MMATS) for the passive treatment of municipal and agricultural wastewater, landfill leachate, oil spills, acid mine waste, pink water, and militarization/demilitarization wastewater. The organic and inorganic contaminants are removed including metals and the result is reusable "Green Water" and "Green Energy" [50].

Thus it is again highlighted that integrated technologies involving phytoremediation and microbial remediation, coupled with chemical treatments, may be a significant leap forward in safe disposal of energetic materials, as compared to the classical method of using independent technologies.

2 Part II: Treatment of Contaminated Soil

S. Mary Celin • Shalini Anand

2.1 Introduction

The defense sector has a major responsibility for the production and handling of energetic materials – such as propellants and explosives for various applications. These tasks and activities have strong influence on the environment, generating toxic and harmful wastes at various stages of production and use. Energetic materials contain various formulations of explosive chemicals that are characterized by dissimilar biodegradation and transport patterns in contaminated soils. They are known to behave differently in a soil environment when compared with most other organic contaminants and they pose an immediate safety hazard when present

in large quantities. Unique behavior of energetic materials in soil is due to its unique entry in to the environment. As reported by Lewis et al. [51], the vector for introducing these compounds into the environment is explosive-filled munitions. However, there are several ways that the explosives may escape into the environment from munitions, including high-order detonation, low-order detonation, and dud munitions.

Soil acts as a link between air, water, and biota, and it is essential to maintain good soil health for a sustainable environment. The quality of soil gets affected by the amounts of energetic materials being handled during various military activities which result in the use and deposition of chemicals and hazardous substances into the soil. In order to improve the deteriorated soil quality, various scientific approaches involving physical, chemical, and biological concepts are being developed and applied. It is of utmost importance to adopt appropriate green technologies which exploit the abilities of nature's own agents such as plants and microbes to ameliorate the energetic material contaminated soil ecosystem.

This part of the chapter will focus on the various green remediation technologies for treating soils contaminated with energetic materials. Issues such as process description of these technologies, environmental effectiveness, and a review of successful applications at field level are discussed.

2.2 Soil Contamination by Energetic Materials: Magnitude of the Problem

Energetic materials consist of explosive and propellants which belong to a narrow range of organic and inorganic chemical groups. The three major organic chemical compounds are nitroaromatics, nitramines, and nitrate esters. Among the nitroaromatics, TNT (2,4,6-trinitrotoluene) is widely used as an explosive, and DNT (2,4-dinitrotoluene) as a component of many single-base propellants. RDX (hexahydro-1,3,5-trinitro-1,3,5-triazine) and HMX (octahydro-1,3,5,7-tetranitro-1,3,5,7-tetreazocine) are nitramines used in various explosive formulations. NG (nitroglycerin) and NC (nitrocellulose) are nitrate esters used in gun and some rocket propellants. There are a number of inorganic compounds with explosive properties. They are commonly used as initiators. Examples of inorganic explosives include lead azide, lead styphnate, lead dinitroresorcinate (LDNR), lead azotetrazole, lead monoresorcinate (LMNR), and mercury fulminate.

Based on the susceptibility to initiation, explosives can be further classified into primary and secondary explosives. Primary explosives are highly susceptible to initiation and are often used to ignite secondary explosives; soil contamination caused by primary explosives may be very dangerous, as these substances are highly sensitive and will detonate with the slightest movement. It is utmost important to carry out soil analysis of these sites to determine the extent of contamination and

Table 2 Risk-based concentrations of common explosive chemicals in soil [54, 55]

Risk-based concentrations of common energetic chemicals in soil (ref: http://www.epa.gov/reg3hwmd/risk/index.htm)		
Analyte	Industrial (mg/kg)	Residential (mg/kg)
TNT	95	21
RDX	26	5.8
HMX	51,000	3900
NG	200	46
2,4-DNT	2000	160
2,6-DNT	1000	78

a detailed work procedure for this has been approved [52]. Secondary explosives, such as TNT, RDX, and HMX, pose the largest potential concern to the environment because they are produced and used in defense in the greatest quantities. Soils with a 12 % or greater concentration of secondary explosives, such as TNT and RDX, are capable of propagating (transmitting) a detonation if initiated by flame [53]. Soils containing more than 15 % secondary explosives by weight are susceptible to initiation by shock. In addition, chunks of bulk explosives in soils will detonate or burn if initiated, but a detonation will not move through the soil without a minimum explosive concentration of 12 %. Threshold levels for energetic compounds in soils are often evaluated on a site-by-site basis, depending on factors such as the proximity of the contaminated soils to other locations and the use of surrounding groundwater. Future use of the site is also taken into account. Risk-based concentrations of common explosive chemicals in soil are given in Table 2.

Soil contamination by energetic materials can be caused by two different sources: (1) Explosive manufacturing processes and hot water washing for demilitarization come under the first category wherein explosive chemicals present in the aqueous phase contaminate the soil profile and groundwater as a result of improper disposal of effluents. (2) Energetic material contamination by load, assemble, and pack operations, firing activities, incomplete destruction of explosives in open burn/open detonation operations, unexploded ordnance, partially detonated explosives, and underground buried explosives all come under the second category wherein the explosive chemicals are released in solid phase and persist in the environment beyond the intended time period and are known to cause soil and groundwater pollution. Apart from polluting the environment, partially detonated pieces and the unexploded ordnance pose a serious occupational threat to workers.

Energetic material contamination in soil poses a serious threat to human health and the ecosystem. For instance, soils contaminated with explosive chemicals due to emissions and disposal from various operations could damage the soil and the adjoining water and air environment. Toxic and mutagenic effects of the energetic material contamination in soil and their bioaccumulation and transformation products on human, soil invertebrates [56–58], bioaccumulation in marine ecosystem [59], and livestock have been and are being well researched and reported [60, 61].

2.3   Green Remediation Approaches for Treating Energetic Materials in Soil

The remediation of explosive-contaminated sites has been recognized as a challenging environmental problem, and several remediation strategies have been implemented with varying degree of success. Physical and chemical treatment methods used thus far (incineration, adsorption, advanced oxidations processes, chemical reduction, etc.) have not only been very expensive but also caused additional environmental problems by transferring the pollutants from one phase to the other. Environmentally compatible green disposal methods are highly recommended for different energetic materials. The disposal and recycling processes for explosives must be safe, technically feasible, environmentally safe, and economic in their operation.

Green technologies intended for remediation/disposal of energetic materials in the soil environment can be grouped into two categories, viz., ex situ and in situ technologies, which in turn are classified further. Ex situ bioremediation processes require excavation of contaminated soil or pumping of groundwater before they can be treated. Examples of ex situ technologies include composting/land farming, bioreactor, and biopiles. In situ bioremediation treats the contaminated soil or groundwater in the location in which it was found, and these include technologies such as phytoremediation, bioremediation, and bioventing.

2.3.1   Ex Situ Technologies

2.3.1.1   Composting/Land Farming

Composting takes place in aboveground piles, while land farming incorporates contaminated soil into soil that is uncontaminated within a designed treatment cell. Both composting and land farming make use of bacteria and other microbes to degrade the contaminants in soil. Greatest destruction and removal efficiencies could be achieved by these techniques for treating energetic materials in soils. Composting residues will support the growth of vegetation after treatment, unlike incineration ash or soils treated by solidification/stabilization. The final volume increase in soil is approximately 50–100 %, similar to stabilization/solidification technologies.

Composting has been demonstrated successfully in pilot- and full-scale levels for treating explosive-contaminated soils and sediments. The Umatilla Army Depot in Hermiston, Oregon, has successfully used composting to convert 15,000 tons of contaminated soil into safe soil containing humus. Cleanup goals for Umatilla were established at concentrations of less than 30 mg per kg for 2,4,6-trinitrotoluene (TNT) and Research Development Explosive (RDX) [62].

Windrow composting is one type of outdoor composting process wherein compost is placed in long piles known as windrows and periodically mixed by mechanical agitation which is provided by straddle turners and other specific mobile equipments.

Pilot- and full-scale projects have demonstrated that aerobic, thermophilic composting is able to reduce the concentration of explosives, viz., TNT, RDX, HMX, and ammonium picrate, to acceptable levels. 99.8 % destruction efficiency for soils contaminated with explosive chemicals, viz., TNT, RDX, and HMX, has been reported at Umatilla Army Depot and Naval Submarine Base, Bangor [63, 64].

Land farming was found to treat low to medium concentrations of explosives in soils. This technique was evaluated for the treatment of soil contaminated with explosives in Louisiana Army Ammunition Plant, Minden, Louisiana, and was found to have potential for degrading explosives [64, 65]. Though composting and land farming are useful in treating the explosive contaminants in soil, there are limitations to the use of composting for remediation. These include: challenges in scaling up from bench to full-scale operations, possible generation of intermediate decomposition products with even higher levels of toxicity volatilization of gases, and the resultant air pollution problem followed by the need for environmental monitoring.

2.3.1.2   Bioreactor

In a bioreactor the treatment of the contaminated media takes place in a controlled manner. The two major types of soil reactors are dry and slurry bioreactors. Dry bioreactors treat soil with no other amendments other than microbes and nutrients. Adequate moisture is maintained for microbial growth by a sprinkler system or by rainfall. Physical mixing of the soil keeps it aerated. Only soils that are contaminated at a shallow depth are practical to treat with a soil pile reactor. It also frequently results in soil/microbe pellet formation which hinders remediation by reducing the availability of pollutants to microbes. Slurry bioreactors have proven more effective and efficient against a wider range of pollutants. In a slurry reactor the soil is mixed with equal or greater amounts of water and mixed with microbes and nutrients to form soil slurry. Bioslurry/bioreactors are technically simple, and pellet formation can be avoided during dry treatment. Conditions in a slurry reactor are easier to maintain than dry reactors and result in faster treatment rates [66].

Column bioreactor studies were carried out for treating soils contaminated with TNT wherein it was found that the most efficient removal of this compound was achieved by the soil column that was operated periodically with flooding with molasses solution, followed by draining and aeration. Findings of this study were found to improve the design and operation of field-scale bioremediation systems [67]. Two ex situ bioremediation methods, viz., soil slurry reactor and land farming technique, were evaluated for the treatment of soil contaminated with explosives in Louisiana Army Ammunition Plant, Minden, Louisiana. The soil had a high concentration of 2,4,6-trinitrotoluene (TNT) of 10,000 mg/kg of soil and a medium level contamination of RDX 1900 mg/kg and HMX 900 mg/kg of soil. The results indicated that a soil slurry reactor under co-metabolic condition with molasses as co-substrate removed TNT more efficiently than the land farming method [65]. Anaerobic degradation of TNT was studied in a soil slurry reactor under sulfate- and

nitrate-reducing conditions using enrichment cultures developed from a TNT-contaminated soil from the Louisiana Army Ammunition Plant (LAAP) in Minden, USA. Sulfate-reducing conditions were found to have better degradation efficiency than nitrate-reducing conditions. The metabolic analysis showed complete mineralization of TNT with acetic acid, CO_2, and ammonia as end products [68].

The bioremediation of 2,4,6-trinitrotoluene (TNT)-contaminated soil was performed on a laboratory scale. Comparative performance of a soil slurry reactor with a soil column reactor was evaluated for the removal of TNT. Optimal conditions for the two bioremediation systems for the removal of TNT were obtained. The performance of soil slurry reactor was better than column reactor wherein, about 60 % of the 1000 mg/kg TNT-contaminated soil was degraded after 10 days, nearly complete biodegradation (>99 %) was achieved within 25 days and better growth of microorganisms was also observed. These results were found to help in determining the best bioremediation method and improve the design and operation of large-scale cleanup of contaminated sites by bioremediation systems [69].

2.3.1.3 Biopiles

Biopile treatment is a full-scale technology in which excavated soils are mixed with soil amendments, placed on a treatment area, and bioremediated using forced aeration. The contaminants are reduced to carbon dioxide and water. Developed by the Naval Facilities Engineering Service Center, the basic biopile system includes a treatment bed, an aeration system, an irrigation/nutrient system, and a leachate collection system. Moisture, heat, nutrients, oxygen, and pH are controlled to enhance biodegradation. The irrigation/nutrient system is buried under the soil to pass air and nutrients either by vacuum or positive pressure. Soil piles can be up to 20 ft high and may be covered with plastic to control runoff, evaporation, and volatilization and to promote solar heating. If volatile organic compounds (VOCs) in the soil volatilize into the airstream, the air leaving the soil may be treated to remove or destroy the VOCs before they are discharged into the atmosphere. Treatment time is typically 3–6 months [70].

2.3.2 In Situ Technologies

2.3.2.1 Phytoremediation: A Promising Green Technology Concept

Use of plant species for remediating contaminated ecosystems is a proven technology with potential for the treatment of contaminated soils and shallow aquifers. The estimated low expense of phytoremediation in comparison to that of conventional soil treatment is its most attractive feature [71]. Phytoremediation, unlike conventional treatment technologies, does not require frequent monitoring [72].

Higher forms of plants possess a pronounced ability for the metabolism and degradation of many recalcitrant xenobiotics and can be considered as "green livers"

acting as an important sink for environmentally dangerous chemicals. For instance, elemental pollutants enter the plant through normal nutrient uptake mechanism of plants. However, the degradation of endogenous toxic organics and possible sequestration in vacuoles protect plants from toxic xenobiotics [73].

A study carried out by Lamichhane and their group [74] evaluated the potential effects of molasses on the bioremediation and phytoremediation potential of Guinea grass (*Panicum maximum*) for treating energetic materials such as RDX- and HMX-contaminated soil from the open burn/open detonation area of the Makua Military Reservation, Oahu, HI (USA). The study showed that irrigating with diluted molasses is effective at enhancing RDX degradation mainly in the root zone and just below it. The long-term sustainability of active training ranges can be enhanced by bioremediation using molasses treatments to prevent RDX deposited by ongoing operations from migrating through the soil to groundwater and off-site [75].

Enzymes present in plants play a major role in breaking down the contaminants present in their metabolic systems. It is identified that nitroreductase enzyme in plants is responsible for TNT transformation and degradation in plants. The rate of TNT breakdown is directly proportional to the amount of nitroreductase in plant [76]. Enzymes such as laccase cleave the aromatic ring after TNT is reduced to triaminotoluene. Hybrid poplar (*Populus* spp.), stonewort (*Nitella* spp.), and parrot feather (*Myriophyllum aquaticum*) were found to reduce nitro groups on explosives and other aromatic compounds [77]. Phytoremediation was successfully implemented at field-scale level as a method for treating TNT and RDX using treatment wetlands at the Iowa Army Ammunition Plant (IAAP) in Middletown, Iowa [78].

2.3.2.2 Bioremediation of Energetic Materials in Soil

Bioremediation has been used at a number of sites worldwide with varying degrees of success. The control and optimization of bioremediation process is a complex system of many factors. These factors include: the existence of microbial population capable of degrading the pollutants, availability of contaminants to the microbial population and environmental factors such as type of soil, temperature, pH, presence of oxygen, and nutrients, etc. [79]. In nature diverse types of microorganisms and energy sources exist. This diversity makes it possible to break down a large number of different organic chemicals but individual microorganisms cannot mineralize most hazardous substances. At times, the target pollutant is a complex molecule or a mixture of compounds that can only be broken down by a very specific combination of microorganism called a consortium through different steps in degradation pathway. Complete mineralization can be accomplished through a sequential degradation by a consortium of microorganisms, and it involves synergism and co-metabolic actions [80].

Explosive treatment processes use two general approaches to bioremediation – biostimulation and bioaugmentation. Biostimulation relies on altering external conditions such as temperature, mixing, nutrients, pH, soil loading rates, and

oxygen transfer to favorable conditions for growth of native microbial populations. Bioaugmentation relies on these same factors to a lesser extent and also relies on the use of additional inoculants to increase the performance of the system [81]. Bioaugmentation is proven as a feasible strategy for contaminant removal and site remediation [82, 83]. With respect to biostimulation, the concentration of contaminant to be degraded and the selection and concentration of stimulant are important for effective treatment [84].

Bioremediation of TNT in soil was reported by a variety of indigenous and exogenous microbial cultures. For instance, indigenous free bacterial cell cultures such as *Delftia tsuruhatensis* [85] and *Pseudomonas aeruginosa* [86] were reported to cause biotransformation of TNT in soil. Similarly RDX was found to be degraded by the fungus *Phanerochaete chrysosporium* in soils [87]. Scientific approaches such as utilization of microbial consortia [88, 89], application of genetically engineered microorganisms [90], and adoption of integrated multiple biodegradative and biomonitoring mechanisms [91] have been successfully practiced at lab-scale and pilot level for various energetic materials.

2.4 Recent Trends in Green Technological Approaches for Treating Energetic Materials in Soil

2.4.1 Application of DARAMEND: An Organic Carbon-Rich Amendment for Treating Explosives in Soil

DARAMEND is an amendment-enhanced bioremediation technology which involves sequential anoxic and oxic reaction conditions. It was found to successfully treat TNT, DNT, and tetryl in soils. Investigations on anaerobic remediation of PETN-contaminated soil were carried out at a site near Denver, Colorado. Both granular iron and organic carbon amendments were used in the laboratory and pilot-scale tests. The laboratory results showed that, with various organic carbon amendments, PETN at initial concentrations of between 4500 and 5000 mg/kg was effectively removed within 84 days. In the field trial, after a test period of 446 days, PETN mass removal of up to 53,071 mg/kg of PETN (80 %) was achieved with an organic carbon amendment (DARAMEND) of 4 % by weight. In previous laboratory studies, granular iron has shown to be highly effective in degrading PETN. However, in this case for both the laboratory and pilot-scale tests, granular iron was proven to be ineffective. This was a consequence of the passivation of the iron surfaces caused by the very high concentrations of nitrate in the contaminated soil. This study indicated that low concentration of organic carbon was a key factor limiting bioremediation of PETN in the contaminated soil. Furthermore, the addition of organic carbon amendments such as the DARAMEND materials or brewers grain proved to be highly effective in stimulating the biodegradation of PETN and could provide the basis for full-scale remediation of PETN-contaminated sites [92].

2.4.2 Application of Previously Bioremediated Soil for Degrading TNT Chips

The potential of a previously bioremediated hydrocarbon (PBR)-contaminated soil was evaluated for degrading TNT chips in soil. Residual TNT chip analysis showed greater TNT degradation in PBR soils (70 %) and significantly higher metabolic rates (4.5-fold increase in cumulative CO_2 levels). Findings of this study on harnessing the ability of previously bioremediated soil promote sustainable reuse of waste soils extending the life span of landfill sites [93].

2.4.3 Hybrid Technologies: Microbial Assisted Phytoremediation

There has been an increased effort to enhance the efficacy of phytoremediation of contaminated environments by exploiting plant-microbe interactions. The combined use of plants and endophytic bacteria is an emerging approach for the cleanup of soil and water polluted with organic compounds. In plant-endophyte partnerships, plants provide the habitat as well as nutrients to their associated endophytic bacteria. In response, endophytic bacteria with appropriate degradation pathways and metabolic activities enhance degradation of organic pollutants and diminish phytotoxicity and evapotranspiration of organic pollutants. Moreover, endophytic bacteria possessing plant growth-promoting activities enhance the plant's adaptation and growth in soil and water contaminated with organic pollutants. Overall, the application of endophytic bacteria gives new insights into novel protocols to improve phytoremediation efficiency [94].

Combined efficiency of several bioremediation techniques such as natural attenuation, bioaugmentation with microbes, and phytoremediation was evaluated for degrading TNT in actual field conditions. The bacteria, *Pseudomonas putida* JLR11, were inoculated with plants such as maize (*Zea mays* L.) and broad beans (*Vicia faba* L.). It was found that when plants were inoculated with bacteria, TNT disappeared to an even greater extent (80–88 %) in soil [95]. The use of genetically modified plants, which combines the ability of bacterial genes to detoxify compounds with the phytoremediation benefits of plants, was found to be promising for degrading energetic materials such as TNT, RDX, and HMX in soils [96].

2.4.4 UXO Disposal by Incorporating Microbes in the Design of Explosive Formulations

Unexploded ordnance (UXO) from military operations worldwide also poses a serious environmental threat due to the release of toxic substances from the corroding ordnance, in addition to the risks associated with the potential for an accidental detonation [97]. For the safe destruction of explosive chemicals present in unexploded ordnance, underground buried explosive formulations, and partially detonated explosives, an eco-friendly approach was attempted by incorporating

microbes into the explosives without compromising the explosive quality after long-term storage [98]. Incorporation of bacterial organisms such as *Pseudomonas putida* GG04 and *Bacillus* SF into an explosive formulation to enhance bioremediation of 2,4,6-trinitrotoluene residues caused sequential reduction of TNT resulting in the formation hydroxylaminodinitrotoluene (HADNT), 4-amino-2,6-dinitrotoluenes, 2-amino-4,6-dinitrotoluenes, different azoxy compounds, 2,6-aminonitrotoluenes (2,6-AMNT), and 2,4-diaminonitrotoluenes (2,4-DAMNT), and the accumulation of dead-end metabolites such as AMDNT and DAMNT was prevented by the incorporation of guaiacol and catechol during the biotransformation process [98].

2.5 Conclusions

The incorporation of sustainable concept in every sphere of human activity offers the opportunity to integrate ecological interest in the defense mandate too. An increase in awareness is essential for the protection of our environment from contamination of our environment by energetic materials. Energetic compounds, consisting of explosives, propellants, and chemicals used in pyrotechnics, demolition, and mining, are essential for both peaceful and military purposes [99]. The entire life cycle of energetic materials right from development, manufacturing, testing, usage, and disposal has detrimental effects on various environmental components.

Concerns about the deterioration of environmental quality by residues and transformation products of energetic materials present in soil and groundwater necessitate the need for the development of green technologies which will leave the least environmental footprint. A clear understanding on uptake, transport, translocation of energetic contaminants in plants and microbes and their degradation pathway, and detoxification of contaminants and interactions between plants and microorganisms are critical in developing effective green technologies for environmental cleanup. Green treatment technologies are emerging as one of the important components of waste management for treating recalcitrant contaminants. In the near future, the present explosive waste management strategies will experience a global shift toward usage of highly efficient green technologies. Public acceptance of green technologies is generally higher than that of chemical processes. Adoption of green approaches in explosives industry will result in production of green energetic materials (GEMs) which contributes environmental conservation. It also promotes compliance with environmental regulations [100]. The successful application of green technological concepts will reduce the risk to the environment and the public by eliminating residues of energetic materials that otherwise would contaminate surface soils and groundwater.

Therefore, adoption of green chemical approaches for the manufacture of energetic materials and innovative green strategies harnessing the degradative abilities of nature's own agents can go a long way in ensuring proper life management and the resultant safe end use of energetic materials in the environment.

References

1. Schwitzguebel JP (2004) Potential of phytoremediation, an emerging green technology: European trends and outlook. Proc Indian Natl Sci Acad B70(1):131–152
2. Paul D, Pandey G, Pandey J, Jain RK (2005) Accessing microbial diversity for bioremediation and environmental restoration. Trends Biotechnol 23:135–142
3. Watanabe K (2001) Microorganisms relevant to bioremediation. Curr Opin Biotechnol 12:237–241
4. Szecsody James E, Comfort S, Herbert L, Fredrickson, Boparai HK, Devary BJ, Thompson KT, Phillips JL, Crocker FH, Girvin DC, Resch CT, Shea P, Fischer AE (n.d.) SERDP ER1376 enhancement of in situ bioremediation of energetic compounds by coupled abiotic/biotic processes: final report for 2004–2006
5. Anand S, Celin SM, Nandan Sahai S (2014) Importance of environmental site assessment for taking up waste management in contaminated defence sites. In: Proceedings of 9th International High Energy Materials Conference and Exhibits (HEMCE), 13–15 February, Thiruvananthapuram
6. Hannink N, Rosser SJ, French CE, Basran A, Murray JAH, Nicklin S, Bruce NC (2001) Phytodetoxification of TNT by transgenic plants expressing a bacterial nitroreductase. Nat Biotechnol 19:1168–1172. doi:10.1038/nbt1201-1168
7. Juhasz AL, Naidu R (2007) Explosives: fate, dynamics and ecological impact in terrestrial and marine environments. Rev Environ Contam Toxicol 191:163–215
8. Ahmad F, Hughes JB (2002) Reactivity of partially reduced arylhydroxylamine and nitrosoarene metabolites of 2,4,6-trinitrotoluene (TNT) toward biomass and humic acids. Environ Sci Technol 36:4370–4381
9. Wang CJ, Thiele S, Bollag JM (2002) Interaction of 2,4,6-trinitrotoluene (TNT) and 4- amino-2,6-dinitrotoluene with humic monomers in the presence of oxidative enzymes. Arch Environ Contam Toxicol 42:1–8
10. Williams LR, Aroniadou-Anderjaska V, Qashu F, Finne H, Pidoplichko V, Bannon DI, Braga MF (2011) RDX binds to the GABA(A) receptor-convulsant site and blocks GABA(A) receptor-mediated currents in the amygdala: a mechanism for RDX-induced seizures. Environ Health Perspect 119(3):357–363. doi:10.1289/ehp.1002588
11. Sunahara GI, Kuperman RG, Lotufo GR, Hawari J, Thiboutot S, Amplemen G (2009) Introduction. In: Sunahara GI, Lotufo GR, Kuperman RG (eds) Ecotoxicology of explosives. CRC Press, Taylor & Francis Group, Boca Raton. London, New York. ISBN 978-0-8493-2839-8
12. Behrends LL, Sikora FJ, Bader DF (2000) Phytoremediation of explosives-contaminated groundwater using constructed wetlands. In: Means JL, Hinchee RE (eds) Wetlands & remediation. Battelle Press, Columbus, pp 375–381
13. Best EPH, Zappi ME, Fredrickson HL, Larson SL, Sprecher S, Miller J (1996) Screening for removal of TNT and RDX by submerged and emergent plant species from contaminated ground water. In: Proceedings of the 1996 HSRC (Hazardous Substance Research Centre/WERC (Waste–Management and Education Research Consortium) Joint Conference on the Environment, 9p
14. Best EPH, Sprecher SL, Larson SL, Fredrickson HL, Bader DF (1999) Environmental behavior of explosives in groundwater from the Milan army ammunition plant in aquatic and wetland plant treatments. Uptake and fate of TNT and RDX in plants. Chemosphere 39:2057
15. Best EPH, Sprecher SL, Larson SL, Fredrickson HL, Darlene BF (1999) Environmental behavior of explosives in groundwater. In groundwater from the Milan army ammunition plant in aquatic and wetland plant treatments. Removal, mass balances and fate in groundwater of TNT and RDX. Chemosphere 38:3383–3396
16. Best EP, Miller JL, Larson SL (2000) Explosives removal from groundwater at the volunteer army ammunition plant, TN in small scale wetland module. In: Means JL, Hinchee RE (eds) Wetlands and remediation. Battella Press, Columbus, pp 365–373

17. Best EP, Miller JL, Larson SL (2001) Tolerance towards explosives, and explosives removal from groundwater in treatment wetland mesocosms. Water Sci Technol 44(11–12):515–521

18. Jacobson ME, Chiang SY, Gueriguian L, Westholm LR, Pierson J, Zhu G, Saunders FM (2003) Transformation kinetics of trinitrotoluene conversion in aquatic plants. In: McCutcheon SC, Schnoor JL (eds) Phytoremediation: transformation and control of contaminants. Wiley, Hoboken, New Jersey, pp 409–427

19. Vanek T, Nepovim A, Podlipna R, Hebner A, Vavrikova Z, Gerth A, Thomas H, Smrcek S (2006) Phytoremediation of explosives in toxic wastes. In: Twardowska et al (eds) Soil and water pollution monitoring, protection and remediation. Springer, Dordrecht, pp 3–23

20. Flokstra BR, Aken BV, Schnoor JL (2008) Microtox® toxicity test: detoxification of TNT and RDX contaminated solutions by poplar tissue cultures. Chemosphere 71(10):1970–1976, http://dx.doi.org/10.1016/j.chemosphere.2007.12.020

21. Nandan, Celin SM, Anand S, Bhalla R, Mittal AK (2013) Phytoremediation of 2, 4, 6-Trinitrotoluene (TNT) using selected macrophyte, *Azolla microphylla*. Int J Appl Eng Res 8(9):39–44, ISSN: 0973-4562

22. Singh B, Kaur J, Singh K (2012) Microbial remediation of explosive waste (review). Crit Rev Microbiol 38(2):152–167

23. Rylott EL, Jackson RG, Edwards J, Womack GL, Seth-Smith HMB, Rathbone DA, Stand SE, Bruce NC (2006) An explosive-degrading cytochrome P450 activity and its targeted application for the phytoremediation of RDX. Nat Biotechnol 24:216–219

24. Claus H, Bausinger T, Lehmler I, Perret N, Fels G, Dehner U, Preu J, Konig H (2007) Transformation of 2, 4, 6-trinitrotoluene (TNT) by *Raoultella terrigena*. Biodegradation 18:27–35

25. Geetanjali LM, Suresh JG, Vikram SG (2005) TNT biotransformation potential of the clinical isolate of *Salmonella typhimurium*-potential ecological implications. Indian J Occup Environ Med 9(1):29–34, ISSN: 0973-2284 EISSN:1998-3670

26. Mulla SI, Talwar MP, Bagewadi Hoskeri ZK, Ninnekar HZ (2012) Enhanced degradation of 2-nitrotoluene by immobilized cells of Micrococcus sp. strain SMN-1. Chemosphere 40:870–877, http://dx.doi.org/10.1016/j.chemosphere.2012.10.030

27. Tope AM, Jamil K, Baggi TR (1999) Transformation of 2,4,6- Trinitrotoluene(TNT) by immobilized and resting cells of *Arthrobacter* sp. J Hazard Subst Res 2(3):1

28. Ullah H, Ali Shah A, Hasan F, Hameed A (2010) Biodegradation of TNT by immobilized *Bacillus* sp. YRE. Pak J Bot 42(5):3357–3367

29. Shen J, He R, Yu H, Wang L, Zhang J, Sun X, Li J, Han W, Xu L (2009) Biodegradation of 2,4,6-trinitrophenol (picric acid) in a biological aerated filter (BAF). Bioresour Technol 100:1922–1930

30. Mulla SI, Talwar MP, Bagewadi ZK, Hoskeri RS, Ninnekar HZ (2013) Enhanced degradation of 2-nitrotolune by immobilized cells of *Micrococcus* sp. strain SMN-1. Chemosphere 90(6):1920–1924

31. Zoh KD, Stenstrom MK (2002) Application of a membrane bioreactor for treating explosives process waste water. Water Res 36:1018–1024

32. Krauter P, Daily B Jr, Dibley V, Pinkart H, Legler T (2005) Perchlorate and nitrate remediation efficiency and microbial diversity in a containerized wetland bioreactor. Int J Phytoremediation 7(2):113–128

33. Cho YS, Lee BU, Oh K (2008) Simultaneous degradation of nitroaromatic compounds TNT, RDX, atrazine, and simazine (TRAS) by *Pseudomonas putida* HK-6 in bench-scale bioreactors. J Chem Technol Biotechnol 83:1211–1217

34. Atikovic E, Suidan MT, Maloney SW (2008) Anaerobic treatment of army ammunition production waste water containing perchlorate and RDX. Chemosphere 72:1643–1648

35. Srinivasan A, Viraraghavan T (2009) Perchlorate: health effects and technologies for its removal from water resources review. Int J Environ Res Public Health 6:1418–1442. doi:10.3390/ijerph6041418, ISSN 1660-4601www.mdpi.com/journal/ijerph

36. Wang ZY, Ye ZF, Zhang MH, Bai X (2010) Degradation of 2,4,6-trinitrotoluene (TNT) by immobilized microorganism-biological filter. Process Biochem 45:993–1001

37. Wang ZY, Ye ZF, Zhang MH (2011) Bioremediation of 2, 4-dinitrotoluene (2, 4-DNT) in immobilized micro-organism biological filter. J Appl Microbiol 110(6):1476–1484. doi:10.1111/j.1365-2672.2011.04997.x, Epub

38. Montgomery MT, Coffin RB, Boyd TJ, Osburn CL (2013) Incorporation and mineralisation of TNT and other anthropogenic organics by natural microbial assemblages from a small, tropical estuary. Environ Pollut 174:257–264

39. Knezovich JP, Daniels JI, Stenstrom MK, Heilmann HM (1995) Microbial treatment of high explosives. In: Conference: Luxembourg international symposium on the rehabilitation of military sites and demilitarization of explosive ordnance, Kirchberg (Luxembourg), 14–18 November and at Joint Army-Navy NASA – Air Force safety and environmental protection subcommittee meeting, Tampa (United States), 5–8 December

40. Wujcik WJ, Kim BJ, Rozich AF (2002) Proceedings of the water environment federation. WEFTEC, Sect 61 through 70: 169–177 (9), Publisher water federation, http://dx.doi.org/10.2175/193864702784900633

41. Crawford DL, Crawford RL (1996) Bioremediation principles and application. Cambridge University Press, Cambridge, pp 1–34

42. Kwom SH (2000) A biological approach in the treatment of TNT wastewater. Toxicol Environ Chem 75(1–2):17–23

43. Nicolella C, Van Loosdrecht MC, Heijnen JJ (2000) Particle-based biofilm reactor technology. Trends Biotechnol 18:312–320

44. Morgenroth E, Sherden T, Van Loosdrecht MCM, Heijnen JJ, Wilderer PA (1997) Aerobic granular sludge in a sequencing batch reactor. Water Res 31:3191–3194

45. De Kreuk MK, Heijnen JJ, Van Loosdrecht MC (2005) Simultaneous COD, nitrogen, and phosphate removal by aerobic granular sludge. Biotechnol Bioeng 90:761–769

46. Nancharaiah YV, Joshi HM, Mohan TVK, Venugopalan VP, Narasimhan SV (2006) Aerobic granular biomass: a novel biomaterial for efficient uranium removal. Curr Sci 91(4):503–509

47. Nancharaiah YV, Joshi HM, Mohan TVK, Venugopalan VP, Narasimhan SV (2008) Formation of aerobic granules in the presence of a synthetic chelating agent. Environ Pollut 153:37–43

48. Bender J, Phillips P (2004) Microbial mats for multiple applications in aquaculture and bioremediation. Bioresour Technol 94(33):229–238

49. Phillips P, Bender J (1995) Biological remediation of mixed waste by microbial mats. Fed Facil Environ J 6(3):77–85

50. Nzengung V (2010) Innovative explosives remediation PLANTECO Environmental Consultants, LLC. Global demilitarization symposium and exhibition, 10–13 May, Tulsa, 41 slides

51. Lewis J, Marte R, Trépanier L (2009) Quantifying the transport of energetic materials in unsaturated sediments from cracked unexploded ordnance. J Environ Qual 38: 2229–2236

52. U.S. Army Corps of Engineers (2000) Ordnance and explosives response: engineering design, EP 1110-1-18

53. USEPA (2002) Draft final open burning/open detonation permitting guidelines, contract no. 68- w-99-020

54. Rosenblatt DH (1986) Contaminated soils cleanup objectives for Cornhusker Ammunition Plant. US Army Medical Bioengineering Research and Development Laboratory; Report Number 8603, Fort Detrick, Frederick, MD

55. Walsh ME, Jenkins TF, Thorne PG (1995) Laboratory and field analytical methods for explosives residues in soil. In: Proceedings of the symposium on alternatives to incineration for disposal of chemical munitions and energetics 2, pp 17

56. Kuperman RG, Checka RT, Phillips CT, Simini M, Anthony JS (2014) An emerging energetic soil contaminant, CL-20, can affect the soil invertebrate community in a sandy loam soil. Appl Soil Ecol 83:210–218

57. Best EPH, Geter KN, Tatem HE, Lane BK (2006) Effects, transfer, and fate of RDX from aged soil in plants and worms. Chemosphere 62:616–625
58. Robidoux PV, Gong P, Sarrazin M, Bardai G, Paquet L, Hawari J, Dubois C, Sunahara GI (2004) Toxicity assessment of contaminated soils from an antitank firing range. Ecotoxicol Environ Saf 58:300–313
59. Rosen G, Lotufo GR (2007) Bioaccumulation of explosive compounds in the marine mussel, *Mytilus galloprovincialis*. Ecotoxicol Environ Saf 68(2):237–245
60. Fuchs JS, Oneto ML, Casabé NB (2001) Ecotoxicological characterization of a disposal lagoon from a munition plant. Bull Environ Contam Toxicol 67:696–703
61. Pichtel J (2012) Distribution and fate of military explosives and propellants in soil: a review. Appl Environ Soil Sci 2012, Article ID 617236, 33 pages
62. Weston RF (1993) Windrow composting demonstration for explosives-contaminated soils at the Umatilla Depot Activity. Hermiston. Document No: CETHA-TS-CR-93043
63. Craig HD, Sisk WE, Nelson MD, Dana WH (1995) Bioremediation of explosives contaminated soils: a status review. In: Proceedings of tenth annual conference on hazardous waste research, Great Plains Rocky Mountain Hazardous Substance Research Center, Manhattan, pp 23–24
64. Montgomery M, Osburn C, Boyd T, Hamdan L, Walker S (2008) Biotic and biotic attenuation of nitrogenous energetic compounds (NEC) in coastal waters and sediments. U.S. Naval Research Laboratory, SERDP Project ER-1431, NRL/MR/6110–08-9139
65. Clark B, Boopathy R (2007) Evaluation of bioremediation methods for the treatment of soil contaminated with explosives in Louisiana Army Ammunition Plant, Minden, Louisiana. J Hazard Mater 143:643–648
66. Nyer EK (1993) Practical techniques for groundwater and soil remediation. Lewis Publishers, Boca Raton
67. Boopathy R, Widrig DL, Manning JF (1997) *In situ* bioremediation of explosives-contaminated soil: a soil column study. Bioresour Technol 59:169–176
68. Boopathy R (2014) Biodegradation of 2,4,6-trinitrotoluene (TNT) under sulfate and nitrate reducing conditions. Biologia 69:1264–1270, Springer Link
69. Park C, Kim TH, Kim S, Lee J, Kim SW (2003) Bioremediation of 2,4,6-trinitrotoluene contaminated soil in slurry and column reactors. J Biosci Bioeng 96:429–433
70. USAEC (2000) Biopiles of POL contaminated soils. U.S. Army Engineer Environmental Center. http://aec.army.mil/prod/usaec/et/restor/pol01.htm
71. Flathman PE, Lanza GR (1998) Phytoremediation: current views on an emerging green technology. J Soil Contam 7:415–432
72. Pivetz EB (2001) Phytoremediation of contaminated soil and ground water at hazardous waste sites national risk management research laboratory subsurface protection and remediation division Robert S. Kerr Environmental Research Center Ada, Oklahoma Superfund Technology Support Center for Ground Water Man. Tech Environmental Research Services Corporation, P. O. Box 1198, Ada, OK 74820 EPA/540/S-01/500
73. Nwoko OC (2010) Trends in phytoremediation of toxic elemental and organic pollutants – review. Afr J Biotechnol 9:6010–6016
74. Lamichhane KM, Babcock RG Jr, Turnbull ST, Schenck S (2012) Molasses enhanced phyto and bioremediation treatability study of explosives contaminated Hawaiian soils. J Hazard Mater 243:334–339
75. Ampleman G, Thiboutot S, Lavigne J, Marois A, Hawari J, Jones AJ, Rho D (1995) Synthesis of ^{14}C-labeled RDX, TNT, NC and GAP for use in assessing the biodegradation potential of these energetic chemicals. J Label Compd Radiopharm 36(6):559–577
76. Watanabe ME (1997) Phytoremediation on the brink of commercialization. Environ Sci Technol 31:182a–186a
77. Sandermann H (1994) Higher plant metabolism of xenobiotics: the green liver concept. Pharmacogenetics 4:225–241

78. McCutcheon S, Schnoor JL (2003) Overview of phytotransformation and control of waste. In: McCutcheon S, Schnoor JL (eds) Phytoremediation: transformation and control of contaminants. Wiley, New York, pp 3–58

79. Vidali (2001) Bioremediation-an overview. Pure Appl Chem 73:1163–1172

80. Singer AC, Gilbert ES, Luepromchai E, Crowley DE (2000) Bioremediation of poly chlorinated bi-phenyl contaminated soil using carvone and surfactant grown bacteria. Appl Microbiol Biotechnol 54:838–843

81. Craig HD, Sisk WE, Nelson MD, Dana WH (1995) Bioremediation of explosives contaminated soils: a status review. In: Proceedings of tenth annual conference on hazardous waste research, Great Plains Rocky Mountain Hazardous Substance Research Center, Manhattan, Kansas, pp 23–24

82. Ruberto L, Vazquez SC, Mac Cormack WP (2003) Effectiveness of the natural bacterial flora, biostimulation and bioaugmentation on the bioremediation of a hydrocarbon contaminated Antarctic soil. Int Biodeter Biodegr 52:115–125

83. Jacques RJS, Okeke BC, Bento FM, Teixeira AS, Peralba MCR, Comargo FAO (2008) Microbial consortium bioaugmentation of a polycyclic aromatic hydrocarbons contaminated soil. Bioresour Technol 99:2637–2643

84. Kulkarni M, Chaudhari A (2007) Microbial remediation of nitro-aromatic compounds: an overview. J Environ Manage 85:496–512

85. Hooda L, Celin SM, Anand S, Bhalla R, Singh SK (2013) Qualitative studies on evaluation of 2,4,6-trinitrotoluene degradation by *Delftia tsuruhatensis* isolated from contaminated site. Presented in international conference on plant biotechnology, molecular medicine & human health, New Delhi

86. Oh BT, Shea PJ, Drijber RA, Vasilyeva GK, Sarath G (2003) TNT Biotransformation and detoxification by a *Pseudomonas Aeruginosa* strain. Biodegradation 14:309–319

87. Hawari J, Halasz A, Sheremata T, Beaudet S, Groom C, Paquet L, Rhofir C, Ampleman G, Thiboutot S (2000) Characterization of metabolites during biodegradation of hexahydro-1,3,5-trinitro-1,3,5-triazine (RDX) with municipal sludge. Appl Environ Microbiol 66: 2652–2657

88. Robertson BK, Jjemba PK (2005) Enhanced bioavailability of sorbed 2,4,6-trinitrotoluene (TNT) by a bacterial consortium. Chemosphere 58:263–270

89. Zhuang L, Guj L, Gillham RW (2012) Biodegradation of pentaerythritol tetranitrate (PETN) by anaerobic consortia from a contaminated site. Chemosphere 89:810–816

90. Filonov AE, Akhmetov LI, Puntus IF, Esikova TZ, Gafarov AB, Izmalkova TYSSL, Kosheleva IA, Boronin AM (2005) The construction and monitoring of genetically tagged, plasmid containing, naphthalene degrading strains in soil. Microbiology 74: 453–458

91. Stenuit BA, Agathos SN (2010) Microbial 2,4,6-trinitrotoluene degradation: could we learn from (bio)chemistry for bioremediation and vice versa? Appl Microbiol Biotechnol 88: 1043–1064

92. Zhuang L, Gui L, Gillham WR, Landis CR (2014) Laboratory and pilot-scale bioremediation of Pentaerythritol Tetranitrate (PETN) contaminated soil. J Hazard Mater 264: 261–268

93. Erkelens M, Adetutu EM, Taha M, Aherobo LT, Antiabong J, Provatas, Ball AS (2012) Sustainable remediation the application of bioremediated soil for use in the degradation of TNT chips. J Environ Manage 110:69–76

94. Afzal M, Khan QM, Sessitsch A (2014) Endophytic bacteria: prospects and applications for the phytoremediation of organic pollutants. Chemosphere 117:232–242

95. Dillewijn VP, Caballero A, Paz JA, Gonzalez-Perez MM, Oliva JM, Ramos JL (2007) Bioremediation of 2,4,6-trinitrotoluene under field conditions. Environ Sci Technol 41: 1378–1383

96. Panz K, Miksch K (2012) Phytoremediation of explosives (TNT, RDX, HMX) by wild-type and transgenic plants. J Environ Manage 113:85–92

97. Kalderis D, Juhasz AL, Boopathy R, Comfort S (2011) Soils contaminated with explosives: environmental fate and evaluation of state-of- the-art remediation processes (IUPAC Technical Report). Pure Appl Chem 83:1407–1484

98. Nyanhongo GS, Aichernig N, Ortner M, Steiner W, Guebitz GM (2009) Incorporation of 2,4,6-trinitrotoluene transforming bacteria into explosive formulations. J Hazard Mater 165:285–290

99. Pichtel J (2012) Distribution and fate of military explosives and propellants in soil: a review. Appl Environ Soil Sci 2012: AI-617236, 33 pp

100. Talawar MB, Sivabalan R, MukundanT MH, Sikder AK, Gandhe BR, Rao AS (2009) Environmentally compatible next generation green energetic materials (GEMs). J Hazard Mater 161(2–3):589–607

Part IX
Space Launchers

Challenges in Manufacturing Large Solid Boosters

Shri M. Chandradathan

Abstract India as a spacefaring nation has been stressing on low-cost access to space as a major objective while developing propulsion modules for launch vehicles. This chapter dwells in detail the history of solid motors developed for rockets and launch vehicles by India. India's maturity in design, development and operationalising large solid boosters for launch vehicle application is also given.

The development of S200 solid booster for GSLV MK III, the new generation vehicle, has been brought out in detail. A number of challenges like realisation of long S200 motor case segments to minimise segment joints and thereby reducing the inerts, casting of 100 T propellant within the penetrometric pot life of HTPB-TDI propellant, handling and transportation of heavy S200 case segments, infrastructure build-up towards propellant processing and assembly and testing of S200 motor and flex nozzle system are discussed in detail. S200 pyrogen igniter development and propellant properties evaluation are brought out along with the demonstration of thrust differential seen in the flight performance of the two S200 strap-on motors in LVM3-X mission. Pressure oscillations seen in S200 motor are compared with large segmented motors like P-230, RSRM etc., and elimination of thrust oscillation isolation system has been validated in LVM3-X mission. Future road map envisaged for solid motor system development is addressed with a focus to reduce the inerts in solid propulsion system.

Nomenclature

Acronyms

Al	Aluminum
AP	Ammonium perchlorate
ASLV	Augmented satellite launch vehicle

S.M. Chandradathan (✉)
Vikram Sarabhai Space Centre, Indian Space Research Organisation (ISRO), Thiruvananthapuram, Kerala 695022, India
e-mail: mcdathan@yahoo.co.in

863

C/C	Carbon/carbon
CTPB	Carboxy-terminated polybutadiene
EPDM	Ethylene propylene diene monomer
FDI	Fault detection and insulation
GEO	Geosynchronous transfer orbit
GSLV	Geosynchronous satellite launch vehicle
GSLV MK III (LVM-3)	GeoSynchronous Satellite Launch Vehicle mark 3
HEF-20	High-energy fuel 20
HTPB	Hydroxyl-terminated polybutadiene
INCOSPAR	Indian National Committee for Space Research
ISRO	Indian Space Research Organisation
MEOP	Maximum expected operating pressure
PBAN	Polybutadiene acrylic acid acrylonitrile
PM	Pitch minus
PP	Pitch plus
PSLV	Polar satellite launch vehicle
PVC	Polyvinyl chloride
RSR	Rohini Sounding Rocket
SLV-3	Satellite launch vehicle 3
TDI	Toluene diisocyanate
TERLS	Thumba Equatorial Rocket Launching Station
TOIS	Thrust oscillation isolation system

Symbols

I_s	Specific impulse
kN	Kilonewton
m	Metre
MPa	Megapascals
Q	Dynamic pressure
s	Seconds
T	Ton
φ	Diameter

1 Introduction

In 1962 India started off in a modest way in the space segment with an agreement signed by the Indian National Committee for Space Research (INCOSPAR) with the National Aeronautics and Space Administration (NASA) for meteorological studies on equatorial region using sounding rockets. Initially in 1963, the US rockets with solid motors were assembled and launched as sounding rockets (Nike Apache) from Thumba Equatorial Rocket Launching Station (TERLS), Thiruvananthapuram,

situated in Kerala at the southern tip of India. Later in 1965, an agreement was signed with SUD Aviation, France, for a know-how transfer to realise and launch Centaur sounding rockets. A number of sounding rockets with Centaur rocket motors were realised, assembled and launched from TERLS. Rocket motor RH-75 indigenously developed by India for sounding rockets was launched in 1967 from TERLS. In 1968, TERLS was dedicated to the United Nations by the Prime Minister of India, and from then on, starting from 1971, M100 rockets were launched from TERLS routinely. Parallelly RH-125 and RH-200 motors were developed on indigenous propellant composition and added to Rohini sounding rockets family. This was followed by RH-300 and RH-560 rockets with solid motors. The Indian Space Programme was given a major thrust by design, development and successful launch of SLV-3, a four-stage (all-solid motors) launch vehicle which put Rohini satellite into orbit in 1980.

In 1992, this was followed by ASLV with additional strap-on solid motors for launching 150 kg class satellite. With rich experience gained in the SLV-3 and ASLV programme, Indian Space Research Organisation (ISRO) embarked on an ambitious programme to develop Polar Satellite Launch Vehicle (PSLV) to launch 1 ton class satellites in the polar orbit of 1000 km circular with a lift of mass of 292 T. PSLV envisaged a combination of solid and liquid stages with bigger solid booster, graduating from 1 m dia 10 T class of solid motors of SLV, ASLV, to 2.8 m dia 138 T solid booster. From 1994, PSLV became the workhorse vehicle of ISRO performing a number of successful and unique missions starting from polar to GTO missions. The GSLV, largely with PSLV heritage, has a lift-off mass of 412 T with combination of solid, liquid and cryogenic stages. It could place 2 T class satellite in GTO in 2002 to fulfil the communication needs of the country. The GSLV MK III, conceived as a heavy lift launch vehicle with lift-off mass of 630 T, being developed for launching 4 T class satellites in GTO has large 200 T solid motor as strap-ons. With the successful development and testing in ground as well in GSLV MK III–X mission as strap-ons, India has become the third country next to the USA and Europe (joint project Italy and France), to successfully develop and induct large solid booster with HTPB propellant for launch vehicles (Fig. 1).

2 SLV-3 All-Solid Launch Vehicle

The Rohini sounding rocket (RSR) solid motors, with polyvinyl chloride (PVC)-based plastisol propellant with lesser solid loading and comparatively lower performance in terms of energetics, were generally cast as free grains and subsequently charged into the rocket motor casing with an epoxy- or polyester-based charging resin. The development of solid motors for the SLV-3 programme called for case-bonded motors with energetic solid propellants which were in situ cast into the motor case. Figures 2 and 3 give details on the solid motors [1] of SLV-3 launch vehicle.
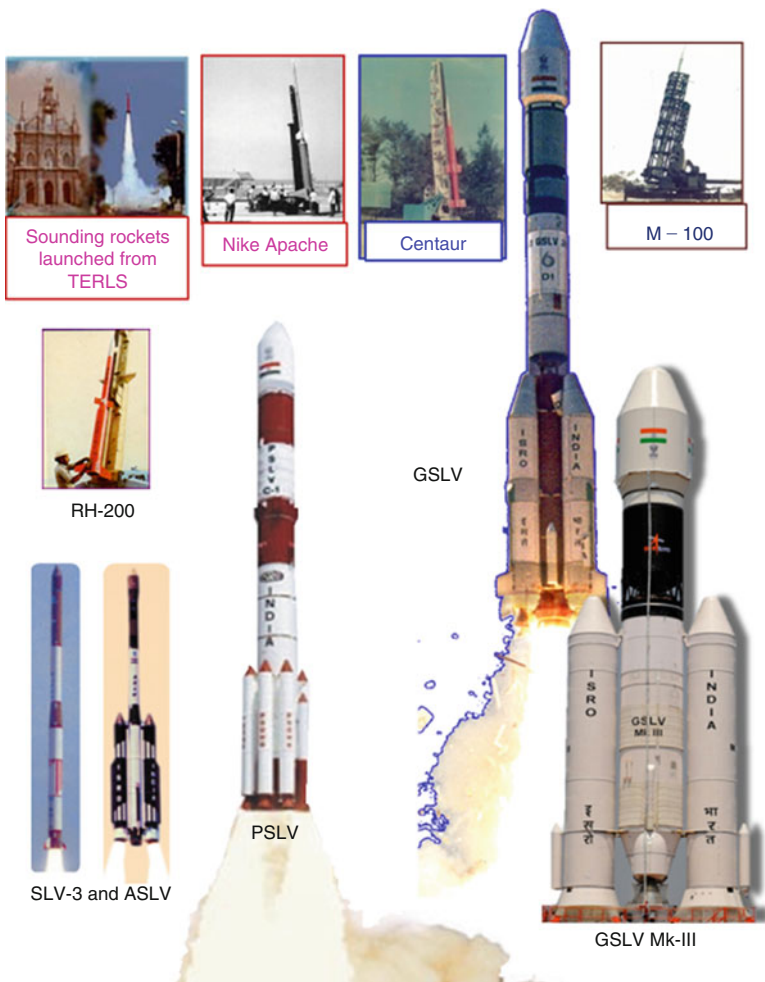
Fig. 1 History of rocketry in India

3 ASLV Motors

In the subsequent launch vehicle development, the PBAN- and CTPB-based propellant systems were replaced by hydroxyl-terminated polybutadiene (HTPB)-based propellant system which showed excellent mechanical, ballistic properties and superior performance. Table 1 on 1 m φ motor variants speaks for itself. The PS0M and PS0M-XL classes of 1 m φ motors with HTPB propellant have become the workhorse solid strap-on motors for PSLV in the operational programme, for a variety of missions with excellent track record. For the ASLV, AS0 motors with canted nozzle were realised with specific propellant formulations with faster burn rate in HE segment and slower burn rate in mid- and NE segments to modify the

- FG/EPOXY AND KEVLAR/EPOXY CASE
- MOULDED ROCASIN INSULATION
- HEF 20 PROPELLENT

All solid four stage rocket successful launched on July 19, 1980

- FG/EPOXY CASE.
- HEF-20 PROPELLANT

15CDV6 MOTOR CASE

- SEGMENTED MOTOR
- ROCASIN INSULATION DEVELOPMENT
- PBAN PROPELLANT DEVELOPMENT
- QUANTUM LEAP IN SIZE w.r.t RSR MOTORS
- 15CDV6 MOTOR CASE

Total length	Total weight	Pay load	Orbit
22 m	17T	40Kg	LEO

Fig. 2 SLV-3 all-solid launch vehicle

Motor	Dia (mm)	Length (mm)	Propellant	Propellant mass (kg)	Mass ratio	Area ratio	I_s (s)
S1	1000	10000	PBAN	8950	0.850	6.66	254.5
S2	800	6350	PBAN	3250	0.812	14.20	271.6
S3	810	2440	CTPB	2750	0.878	25.73	274.5
S4	655	1390	CTPB	320	0.889	28.56	274.5

S4

S3

S2

Fig. 3 SLV-3 solid stages description

Table 1 Variants of 1 m diameter motor – 1977–2010

	Propellant	Propellant mass, kg	Burn rate at 33ksc, mm/s	Burn time, s	I_s, s	Nos flown/tested
SI	PBAN/AP/Al	8660	4.8	45	253	6
ASO	PBAN/AP/Al	8637	4.8	45	253	7
ASO M type	HTPB/AP/Al	8520	5	45	259	7
ASI PBAN	PBAN/AP/Al	8900	5	45	259	4
ASI HTPB	HTPB/AP/Al	8915	5	45	262	2
PSOM	HTPB/AP/Al	8915	5	45	262	76
PSOM XL	HTPB/AP/Al	12400	5	50	265	8
RLV	HTPB/AP/Al	9100	3.7	90	255	1

All the motors tested at ground or flown consecutively were successful
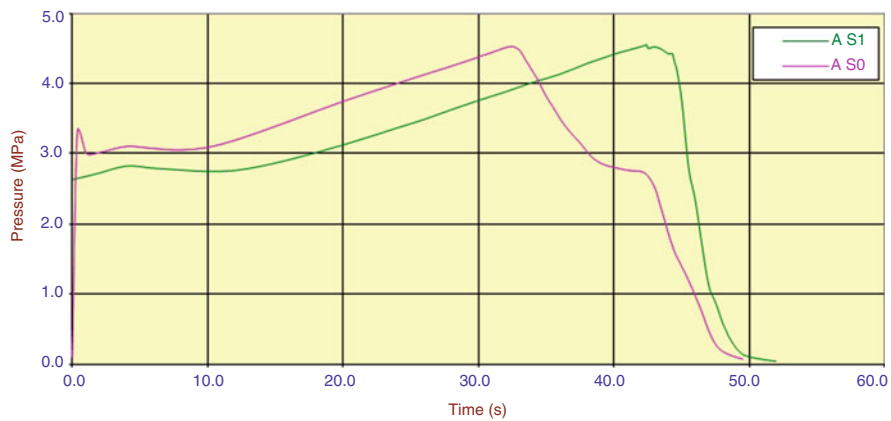
Fig. 4 Performance of AS1 and AS0 motors

thrust time profile of S1 motor. These motors were triple cast for confirming the pair motor identity for the strap-on motors for flight, by ground testing the third motor as batch motor for assuring the flight performance.

The first stage and second stage performance of ASLV was improved by replacing PBAN propellant (12 % Al) with HTPB propellant (18 % Al). Figures 4, 5, and 6 give the details of ASO and ASI motors and their performance.

Based on the experience gained in thrust shaping in ASO motor to contain the dynamic pressure (Q) during the transonic phase, the PSLV and the GSLV MK III solid boosters were designed with M-type thrust time curve by choosing a combination of star and cylindrical propellant ports for the boosters. The same approach was followed in the later improvements carried out on the PSO variant PSO-XL to enhance the propellant loading by 3 T and modifying the thrust time profile similar to M-type curve adopted in PSLV first stage motor. However, this M-type curve in PSO-XL motor is achieved by adopting cylindrical port at the head end and middle segments followed by combination of cylinder and star at the nozzle end

Fig. 5 ASLV launch vehicle

Fig. 6 Static test of AS1 motor

segment. Table 1 gives the details on 1 m dia variants developed by ISRO. Table 2 gives the comparison of PS0M and PS0M-XL motor with CASTOR-IVA-XL of the USA.

In the 1 m dia class of motors, different combinations of thrust time profiles was achieved to meet mission requirements. Though PS0M-XL and RLV SB motors adopt M-type thrust time profile, in view of Reusable Launch Vehicle (RLV) mission, HTPB propellant with retarder to give low burn rate has been chosen to meet the requirement for the RLV solid booster (RLV SB). Figure 7 gives the thrust time profile comparison of all the booster motors developed by ISRO for various missions.

Table 2 Comparison of 1m diameter motors

Sl. no.	Parameter	PSOM	PSOM-XL	Castor-IVA-XL
1	Propellant mass, kg	8915	12400	13000
2	Propellant	HTPB, 18 % Al	HTPB, 18 % Al	HTPB, 20 % Al
3	Action time, s	48.6	52.8	60
4	Vacuum I_s, s	262	264.5	269
5	Nozzle type	Canted, 9°	Canted, 9°	Canted, 11°
6	Grain configuration	6 point star	Cylindrical with 10 point star at nozzle end	Cylindrical with star at nozzle end
7	Area Ratio	6.42	7.57	15
8	Mass ratio	0.849	0.855	0.87

4 Overview of S200 Motor [2]

GSLV MK III (LVM3) is ISRO's third-generation launch vehicle capable of injecting 4 T class satellite into Geo Transfer Orbit (GTO). Paired strap-on S200 motors form the first stage of LVM3 and provide propulsive power for lift-off and ascend phase during the atmospheric regime of flight. S200 is configured as a three-segmented motor with 3.2 diameter and 22 m length. The motor has a flex nozzle and the motor ignition is achieved through a pyrogen igniter. The head end segment is 3 m long, whereas the mid- and nozzle end segments are about 8 m in length. Each S200 motor carries 207 T of HTPB propellant with a mass ratio of 0.89 and develops a peak thrust of 610 T. S200 motor delivers a specific impulse of 275 s (Fig. 8).

The head end segment has a ten-lobed star port geometry for the propellant grain, whereas mid-segment and nozzle end segments have tapered cylindrical grains. Segment ends are inhibited using castor oil-based inhibition system to prevent end burning. Silica-filled nitrile rubber-based material is used in the segments as thermal insulation. Motor case is fabricated with M250 maraging steel through roll and weld route and is designed to withstand a maximum pressure of 5.88 MPa. The three segments are assembled through tongue and groove joints.

The state-of-the-art submerged flex nozzle has an area ratio of 12. Nozzle vectoring is achieved by means of electro-hydraulic actuators powered in a blowdown mode.

4.1 Challenges in S200 Motor Development [3–5]

S200 motor has the largest motor case segment hardware manufactured in the world by roll and weld route (3.2 m Ø, 8.1 m and 8.3 m long mid- and nozzle end segments, respectively). The motor case hardware is proof pressure tested vertically with a floating piston arrangement for the nozzle end segment for simulating the throat open condition as in flight (Figs. 9, 10 and 11).
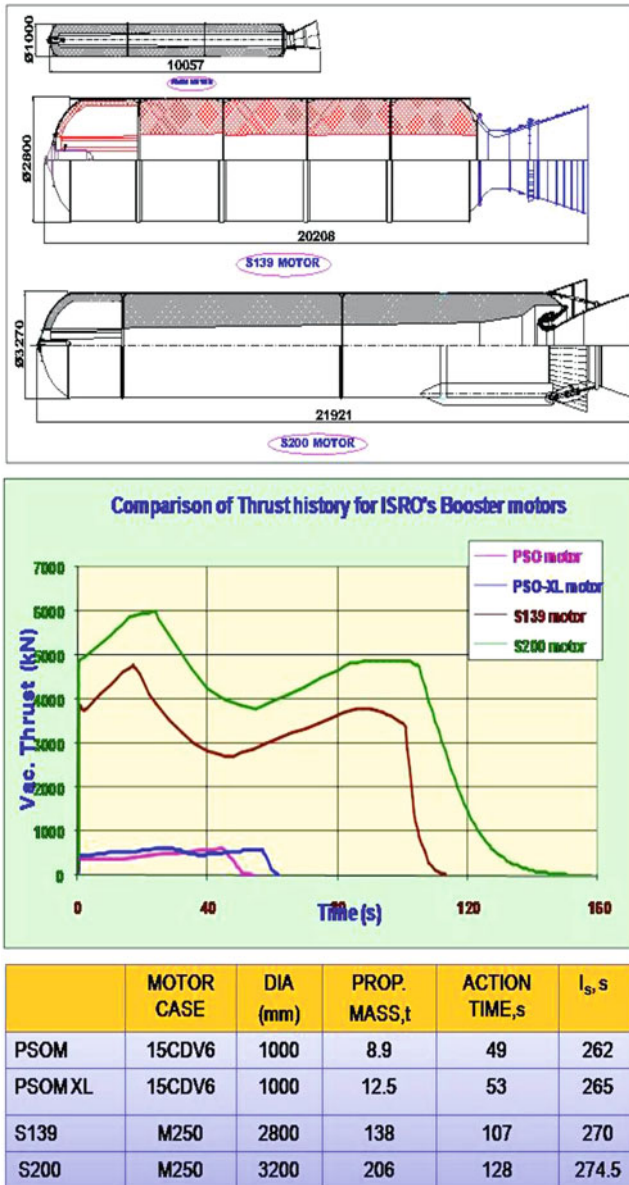
Fig. 7 Solid motors used currently as booster stage in ISRO

Processing of S200 motor involves major challenges like casting of 100 T propellant in single segment without defects, transportation and handling of segments as well as assembled motor at various facilities. Limiting the differential thrust between the strap-on S200 motors during GSLV MK III flight is achieved through

Description	Head End Segment	Middle Segment	Nozzle End Segment
Configuration	10 lobed star	Tapered cylindrical grain	Tapered cylindrical grain with counter bore at aft portion
Propellant loading	27T	97T	83T
Length	3m	8.1m	8.3m
Insulation		Silicon filled NBR	
Inhibition		Asbestos filled castor oil based	
MEOP		5.88Mpa	
Peak Thrust		610T	
Sp.Impulse I_s		275s	
Mass ratio		0.89	

Core motor Diameter	4.0 m
Strap on Diameter	3.2 m
Fairing Diameter	5.0 m
Lift-off-Weight	636 t
Overall length	43.43 m

S200 STAGE CONFIGURATION FOR GSLV MkIII

Fig. 8 GSLV MK III vehicle and S200 motor
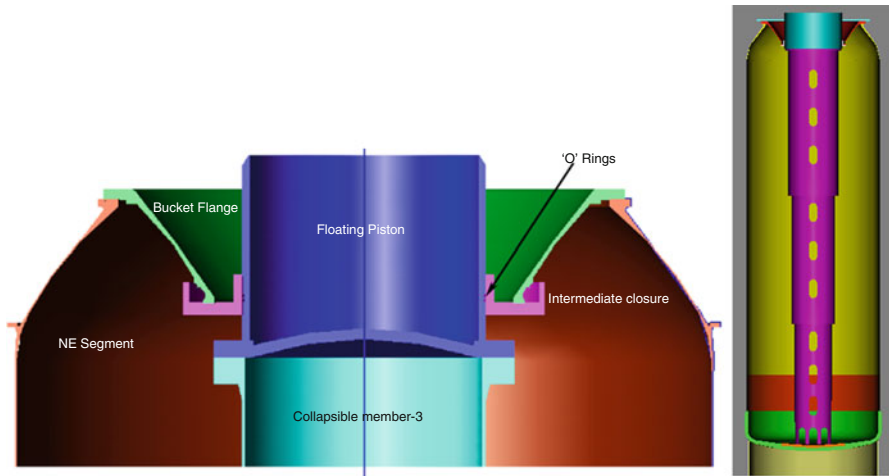
Fig. 9 Floating piston used in optimisation of motor case joints

Fig. 10 Hardware weld set-up

Fig. 11 Case PPT set-up

matched pair concept. Key propellant raw materials are chosen from the same batch for propellant processing of the strap-on motor segments. Thrust profile is shaped appropriately so as to achieve a gradual thrust fall rate during tail-off phase.

The sequence of operations, in composite propellant processing right from raw material preparation to propellant finishing operations, is given in Fig. 12.

Major facilities established for processing S200 motor include five mixing stations so as to process and cast the 100 T propellant within the penetrometric pot life of the propellant. A casting station with bowl tilting mechanism, sample
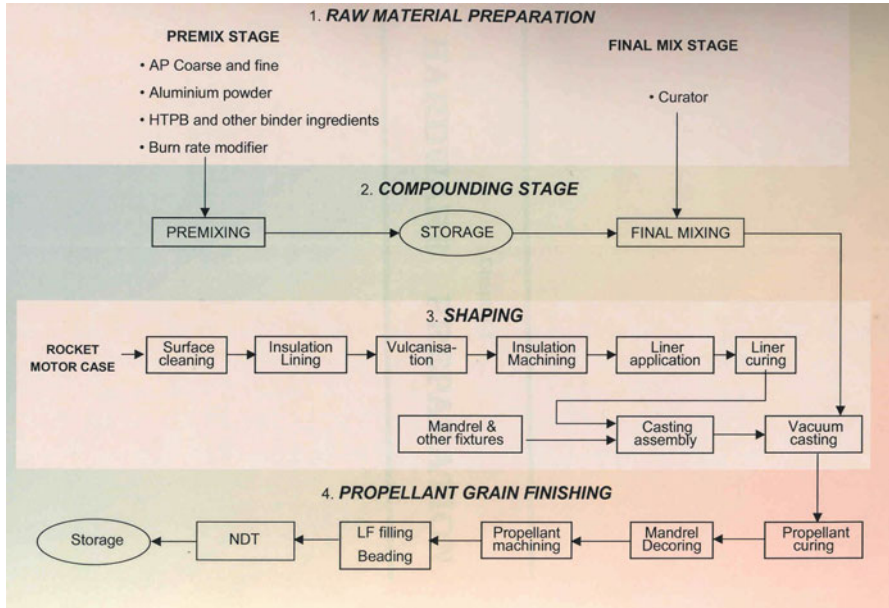
Fig. 12 Sequence of operations in propellant processing
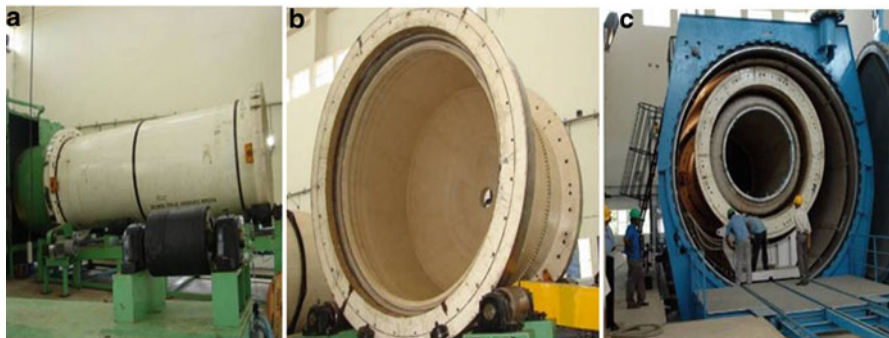
Fig. 13 a Blast cleaning machine. **b** Insulation lining on roller. **c** Insulation vulcanisation in autoclave

processing facility, curing oven, propellant machining and NDT facility were built for manufacturing the large S200 booster motor. Curator toluene diisocyanate (TDI) batching is introduced during propellant mixing to avoid manual intervention during the operation. Automated spill collection tray is provided at the mixing station to collect propellant slurry from the mixer blades. For hardware preparation and insulation lay-up, a facility for blast cleaning, degreasing and insulation lining and a 4 m diameter autoclave were installed (Figs. 13, 14, 15, 16 and 17).

Fig. 14 Spill tray collection system

Fig. 15 TDI batching

Fig. 16 2.5 T-mixer

A centralised control centre is established for synchronised propellant mixing and dispatch for casting. The earlier concept of change can converted to continuous casting by incorporating master hopper and continuous slurry transfer. Master hopper, slurry transfer systems, a feed control involving automatic control valve

Fig. 17 Control system room
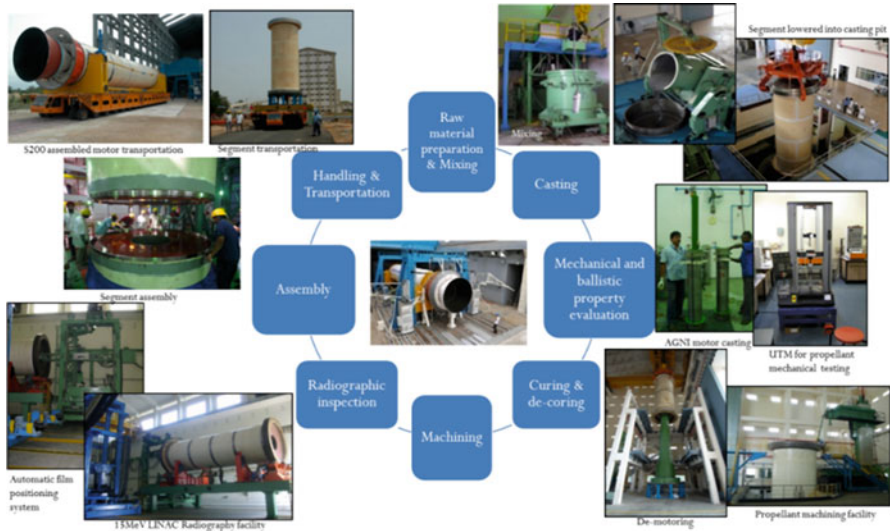
Fig. 18 Manufacturing challenges for large solid motors

and weighing systems for segment were procured for the new casting facility for realising S200 segments. Fabrication and transportation of 7 m diameter and 15 m long vacuum chamber weighing more than 130 T and producing a defect free 100 T segment with high casting rate of 4.5 T/h were some of the challenges faced during the development phase of S200 motor. Semiautomated slurry collection and bowl cleaning were established to reduce manual intervention and to adhere to safety standards. Propellant specimen preparation and sample processing facility is established with automation to reduce manual work load. During material processing, symsorting of ammonium perchlorate (AP) is introduced by identifying same batch for pair segments. Hydraulic tilting system for tilting 100 T segment and introduction of C-arm tackle or grabber for vertical handling of segment have minimised human intervention during propellant processing. Figures 18, 19, 20, 21 and 22 give details of manufacturing challenges during the development.

Fig. 19 Change can type casting

Fig. 20 Continuous casting with master hopper

Fig. 21 Vacuum chamber during transportation

New facilities for drying, classification and blending for augmenting the production of ammonium perchlorate (AP) are established. AP recovery plant is established to recover AP from the process effluent. Indigenous AP grinder is developed for producing AP fines.

Fig. 22 Segment being lowered into casting pit

Fig. 23 Flex nozzle 12 AR
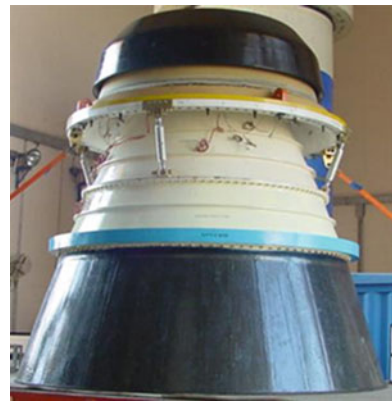
The flex nozzle is processed as five subassemblies utilising modular concept. The flex seal employed is the second largest in the world and enables vectoring of the nozzle up to 8°. The elastomer formulation has been tailored to achieve low shear modulus to bring down actuation torque. The flex seal is made through compression moulding. The nozzle liners in pair strap-on motors are parted from a single liner block to avoid differential performance. Electro-hydraulic actuators used with the flex nozzle are of 30 T capacity with fault detection and isolation (FDI) scheme inbuilt into the control electronics (Figs. 23, 24 and 25).

A thin-webbed igniter grain is made with modified technique of introduction of intermittent vibration during casting to ensure the absence of grain defects. Figures 26, 27 and 28 give the features of S200 igniter development.

After realising the S200 motor, the ballistic performance needs to be evaluated through static test. The quality of the motor is confirmed through various methods. During the initial design stage, the master stress relaxation curve and the failure boundary curve for the finalised propellant formulation are evaluated. The basic

Fig. 24 Moulded flex seal
(dia 1700)

Fig. 25 30 T
electro-hydraulic actuator

Fig. 26 S200 igniter grain
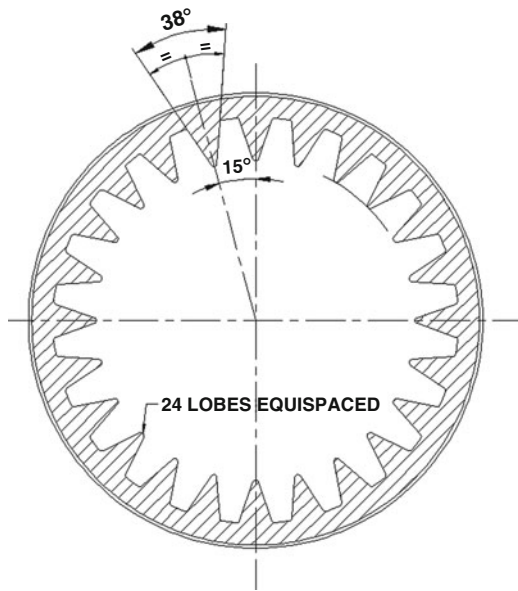
Fig. 27 S139 igniter grain
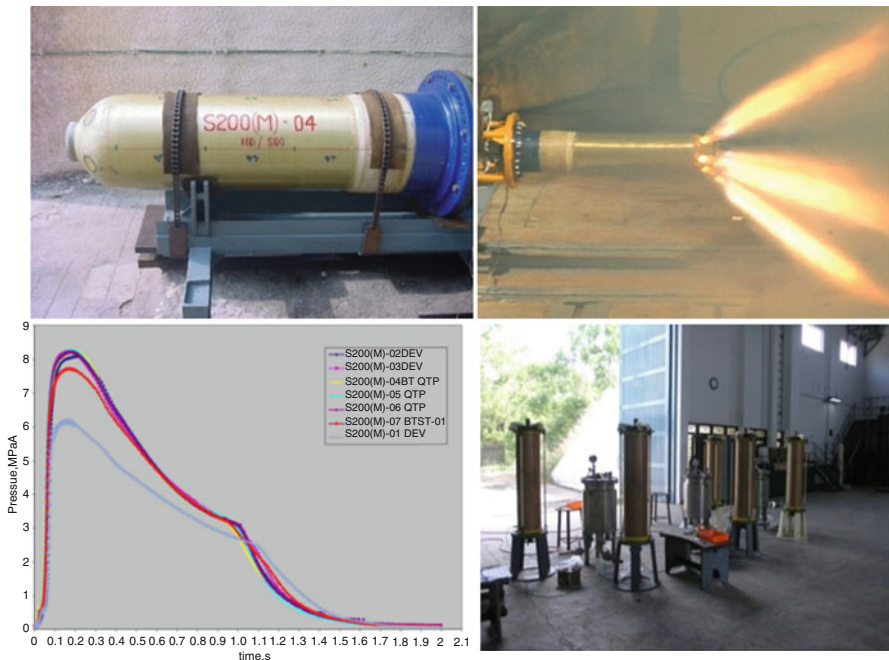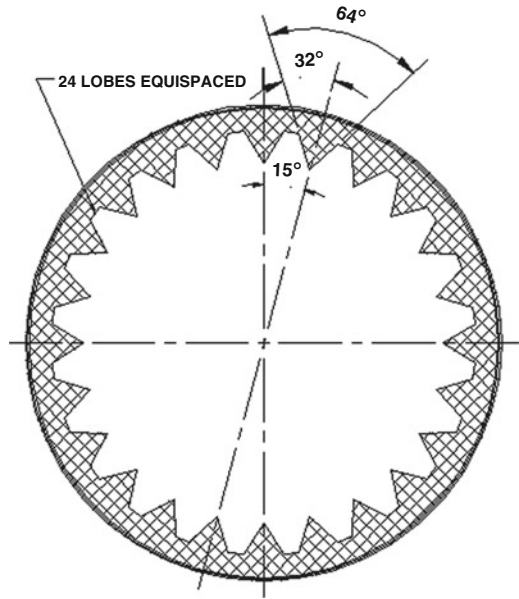
Fig. 28 S200 igniter development
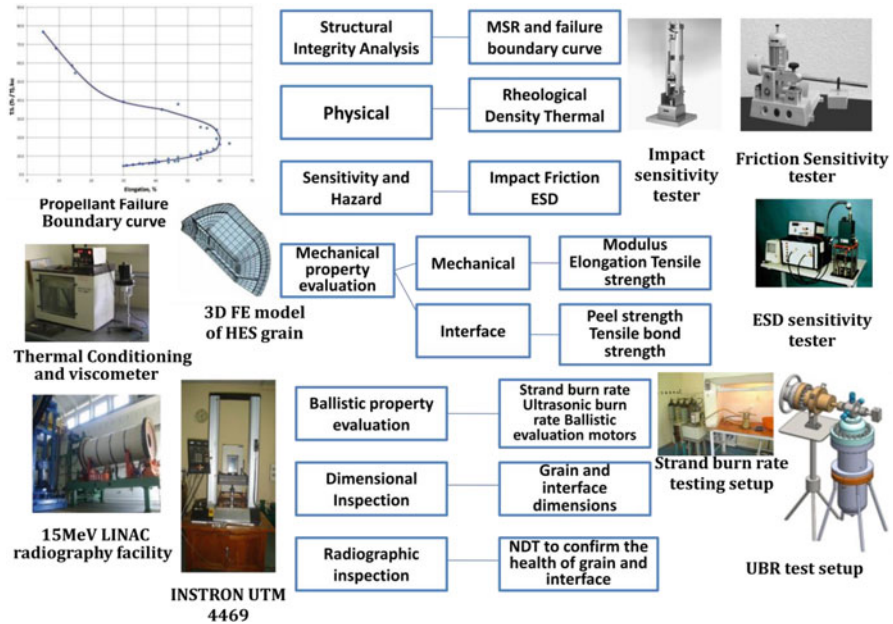
Fig. 29 Evaluation of propellant properties

physical, mechanical and interface properties of the propellant are evaluated to provide inputs for structural analysis of the grain. Then the structural analysis of the cast segments is carried out to confirm the margins on the grain and at the interfaces. The ballistic properties of the propellant are evaluated through solid strand burn rate, through ultrasonic burn rate and through ballistic evaluation motors. The dimensions of the grain at the interface and at the port are measured to confirm the interface requirement for integration as well as for ballistic performance prediction. Finally, the soundness of the grain and the interface integrity are evaluated by radiography (Fig. 29). During the propellant processing and realisation of the S200 motor, manual intervention is minimised to the maximum extent and good safety procedures are put in place to make this large solid propellant plant a safe working place.

After confirming the quality and health of the motor, the segments and the subsystems like flex nozzle and igniter need to be assembled together. New facilities for vertical integration of the motor and for trial actuation of the flex nozzle are built. Facilities for static test are augmented to meet the testing requirements of the S200 motor. Two static tests are successfully carried out demonstrating the identical performance of the two S200 motors. The recent successful GSLV MK III–X mission with two S200 solid boosters as strap-ons has demonstrated the pair motor performance and differential thrust in the flight (Figs. 30 and 31).

Table 3 gives the performance of S200 flight motors in LVM3-X mission. Table 4 gives comparison of S200 motor with contemporary boosters.
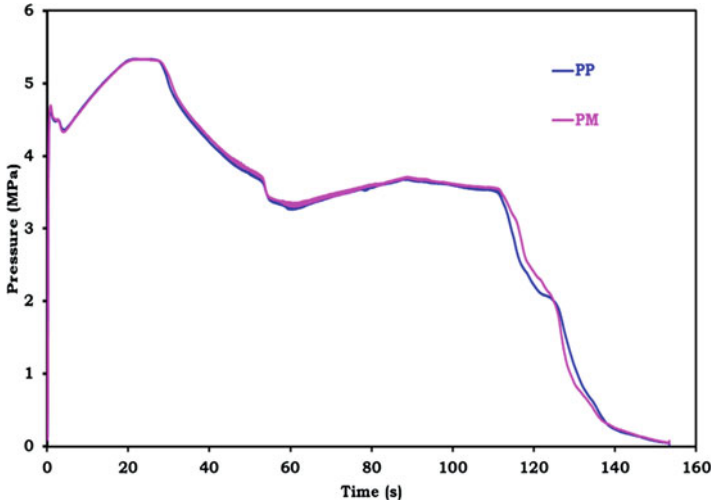
Fig. 30 Performance of S200-X-PP and PM motors
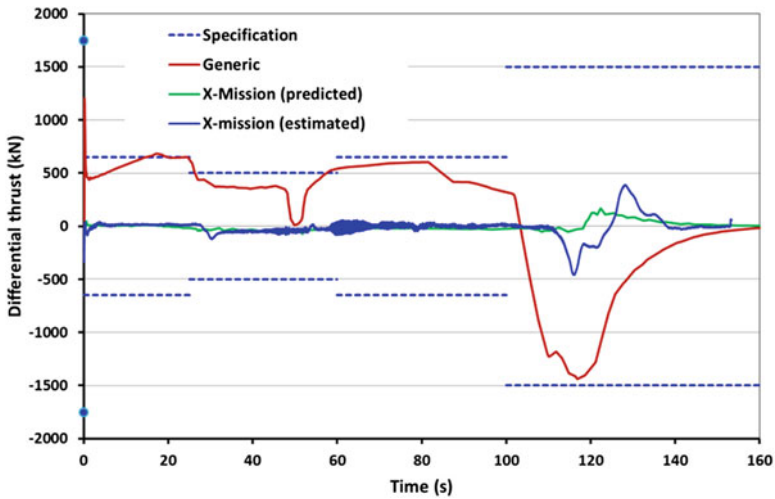
Fig. 31 Differential thrust measured during flight

5   Pressure and Thrust Oscillations [7, 8]

As observed in other contemporary motors like P230 and RSRM, pressure and thrust oscillations were observed during the two motor ground tests and in LVM3-X mission flight as well. The oscillations are mainly due to the coupling of the vortices formed due to the protrusion of the left out segment joint inhibition into the port to

Table 3 Performance summary of S200 motors in flight

Parameter	S200-X-PM	S200-X-PP
Burn time (s)	111.6	111.3
Action time (s)	134.5	135.5
Maximum pressure (MPa)	5.332	5.334
Pressure integral (MPa-s)	498.2	495.6
Maximum vacuum thrust (kN)	5770.6	5788.5
Average vacuum thrust (kN)	4138.9	4102.6
Vacuum specific impulse (s)	276.7	276.2
Total impulse (MN-s)	561.5	559.9
Max. differential thrust, kN	459	

Table 4 Comparison of S200 motor with large solid boosters [6]

	RSRM	SRMU	P230	SRB-A	S 139	S200
Motor launcher	Shuttle	Titan 4B	Ariane IV	H II A	PSLV	MK III
Diameter (m)	3.7	3.2	3.0	2.5	2.8	3.2
Motor length (m)	38	31	27	12	20	19.3
Propellant mass (tons)	503	314	240	65	138	207
Binder	PBAN	HTPB	HTPB	HTPB	HTPB	HTPB
Segment	4	3	3	1	5	3
MEOP (MPa)	7.0	8.4	6.8	11.8	5.88	5.88
Case material	D6AC	Carbon	D6AC	Carbon	Maraging Steel	Maraging Steel
Throat material	Phenolic	Phenolic	C/C	C/C	Phenolic	Phenolic
Actuation	Flex seal Hydraulic	Flex seal Hydraulic	Flex seal Hydraulic	Flex seal EMA Electromechanical actuation	Liquid Injection	Flex seal Hydraulic
Motor inert mass (tons)	68	29	29	6	18	25
Stage inert mass (tons)	88	36	36	11.5	30	30
Average thrust (MN)	11.8	6.1	5.0	1.8	3.6	3.64
Specific impulse (s)	267	284	275	280	269	275

the motor acoustic modes. The disturbances due to vortices will grow at frequencies near to the acoustic mode of the combustion chamber.

Table 5 gives the comparison of the pressure oscillation of S200 motor with the boosters elsewhere in the world.

The thrust to pressure oscillation amplitude ratio is estimated as 14 % for design purposes after removing the damping provided by the thrust measurement system. The frequency of pressure and thrust oscillations are similar even though their occurrence is not simultaneous. The pressure/thrust oscillation begins after the

Table 5 Comparison of oscillations observed in S200 motor with contemporary motors

Motor	L (m)	Dia (m)	Seg	Inhib (yes/no)	Inter-seg cavity	Burn time (s)	Acou modes	Freq (Hz)	Dp/p (%)	Time (s)
P230	25	3.05	3	Yes	Yes	129	1	18–23	0.5	60–110
							2		0.2	40–80
							3		0.1	~50
RSRM	35	3.8	4	Yes	Yes	123	1	12–15	0.48	110–115
							2	25–30		
SRMU	32	3.2	3	No	Yes	138	1	15–20	0.27	57–64
PS1	16.5	2.8	5	Yes	No	100	1	27	0.3	45–72
							2	33		72–94
S200	19.5	3.2	3	Yes	No	105	1	21–26	1.3	40–110

burnout of the HE segment and continues till the burnout of the motor. The effect of inhibition thickness on the amplitude of oscillations is demonstrated in the two ground tests. Higher thickness of the inhibition results in deeper protrusion into the flow and stronger oscillations and vice versa. Thrust oscillation isolation system (TOIS) proposed earlier was later dispensed with based on the studies conducted with the measured pressure and thrust oscillations in the S200 ground tests. LVM3-X flight has been flown successfully without TOIS.

6 Future Road Map for Solid Motors [9]

Future road map envisages performance improvement by improving the motor/stage mass ratio. Focus will be on the following aspects:

- Segmented composite motor case with higher pressure capability to be developed to reduce the inert mass of the motor case and nozzle by reducing the throat diameter as well as improve the area ratio.
- Fifteen to 20 % reduction in insulation mass when nitrile rubber is changed to ethylene propylene diene monomer (EPDM)-based rubber.
- Composite flex seal shims in place of metallic shims to reduce the mass of flex seal and to avoid thermal boot and hence reduce the torque requirement for vectoring.
- The hoop stress component on the FNC tank can be shared by the composite overwrap. This will help in reducing the mass of the gas tank to the extent of 35 %.
- As the stress on the divergent hardware is very minimal, the material of construction can be changed to aluminium alloy.
- Un-submerged flex nozzle system offers advantage of minimal spring stiffness where an electromechanical actuator is sufficient to vector the nozzle. Electromechanical actuation system has an advantage of minimum prelaunch activities and minimum movable parts as compared to electro-hydraulic system.
- High energy and green propellants are the next options for improvement in specific impulse and minimal effect on the environment.
- Extensible exit cone for upper stages to accommodate higher area ratio nozzle within the available space.

7 Conclusion

The successful development of the family of large solid boosters of ISRO for various missions has demonstrated its capability and maturity in solid motor design and solid propellant technology. The technology is totally homegrown and indigenous.

References

1. Srinivasan V (2011) Saga of solid motors. National Conference on Expanding Frontiers in Propulsion Technology, ASET 2011, 17–18 Jun 2011
2. Abraham PJ, Eswaran V, Srinivasan V et al (2010) S200 solid booster development. Proceedings of 61st International Astronomical Congress, IAC-10, C4.2.1.Prague, 27 Sep–1 Oct 2010, vol 3 of 13
3. Ariane 5 – solid rocket motor development and qualification test results, IAF-95-S-2.09
4. AIAA 26th Joint Propulsion Conference-Ariane 5 SRM Nozzle Design, AIAA 90-2083
5. ARIANE 5 SRM nozzle evolution, AIAA2002-4193
6. Ariane-5 solid booster stage development, ESA SP-293 Aug 1989
7. Thrust oscillations of the space shuttle solid rocket booster motor during static tests, AIAA 79-1138
8. Ballereau S, Godfroy F (2009) Two minutes inside the ARIANE 5's SRMs: effect of different sources of pressure oscillations during operation, IAC-09-C4.2.2
9. Eswaran V, Srinivasan V et al (2002) New frontiers in solid rocket nozzle system. Proceedings of workshop on Futuristic Propulsion Technology applicable to aerospace vehicles

Evaluating the Interest of New Propellants for the VEGA Launch Vehicle

Max Calabro

Abstract Classic hydroxyl-terminated polybutadiene (HTPB) propellants have few competitors, are relatively cheap and safe, and have low environmental impact and low burning rates. New ammonium dinitramide (ADN)/HTPB propellants appear very promising in the search for a product that will provide a 10 % increase in launcher performance. The challenges are to produce ADN at an attractive cost and to manufacture ADN-based propellants with suitable ballistic properties (burning rate and pressure exponent). In this respect, additives can be used to reduce the burning rate and/or reduce the pressure exponent. The paper will describe the methodology involved in a realistic prospective study by first defining the reference case, then replacing the current propellant with a new propellant in a motor model and estimating the performance in terms of kg payload into orbit. We illustrate this approach by replacing the propellant in the solid stages of the European Launcher VEGA, assuming the propellant mass of each stage is unchanged.

Acronyms

ADN	Ammonium dinitramide
Al	Aluminum
AP	Ammonium perchlorate
GAP	Glycidyl azide polymer
HTPB	Hydroxyl-terminated polybutadiene
EPDM	Ethylene Propylene Diene Monomer
MEOP	Maximum Expected Operating pressure
SRM	Solid Rocket Motor
MDO	Multi-Disciplinary Optimization
GSE	Ground Support Equipment
HISP	High Impulse Solid Propellant

M. Calabro (✉)
The Inner Arch, 4, rue Saint Sébastien, 78300 Poissy, France
e-mail: max.calabro@innerarch.eu

1 Introduction

Any new propellant for large solid rocket motors (SRMs) in a launch vehicle such as VEGA must be of class 1.3, with a burning rate <15 mm/s. Classic hydroxyl-terminated polybutadiene (HTPB) propellants have few competitors, are relatively cheap and safe, and have low environmental impact and low burning rates. A literature survey has suggested that ammonium dinitramide (ADN)/HTPB propellants could be feasible, with an acceptable burning rate for boost stages. In the short term, ADN combined with a conventional binder such as HTPB appears very promising in the search for a product that will provide a 10 % increase in launcher performance. The challenge will be to produce ADN at an attractive cost.

Any additive must reduce the burning rate and/or the pressure exponent. A research and development (R&D) program must now explore these additives in terms of their effects, which may differ with ADN versus ammonium perchlorate (AP). The effects of two different propellants will be estimated: the first with aluminum as fuel, the second replacing aluminum with alane, which has an improved $I_{s,vac}$ but is less dense. The product $\rho \cdot I_s$ is generally used to compare new propellants; however, this process is not particularly relevant if the effect of the specific impulse is always of primary importance. For example, for VEGA, the influence is the same in the first and the third stage (15 kg increase of payload per second of I_s). Conversely, in the first stage, the effect of the inert mass is 15 times less important, so the effect of density is of no importance. Therefore, to be relevant, any evaluation must be based on an analysis that accounts for, as much as is possible, the design of the entire launch vehicle.

The Inner Arch has developed several software packages, four of which are listed below.

- SoME: dedicated to solid propulsion projects
- PLISE: dedicated to liquid propulsion projects
- HYES: dedicated to hybrid propulsion
- PERFOL: used to design the launch vehicle and optimize its trajectory and propulsion parameters.

The paper will briefly describe the main software packages used for this study and illustrate how we used these tools to create a more realistic prospective study than a simple $\rho \cdot I_s$ evaluation. First, the design codes were used to estimate the parameters of the inert mass and of the specific motor impulse resulting from a new propellant. Second, we estimated the increase in payload from a new propellant by using the trajectory computer code or derivatives obtained using it.

2 The Computer Codes

The propulsion modeling was based on the methodology and the design described in Humble et al. [1] and Parts "Liquid and Gel Rocket Propulsion", "Hybrid Rocket Propulsion", and "New Concepts in Chemical Propulsion" in this book. First, we created a geometrical design considering the state of the art for a given dataset (propellant mass, combustion pressure, area ratio, propellant characteristics and performance, etc.). We obtained masses using polynomial formulas involving geometrical data and operating parameters; for example, tanks were dimensioned taking into account the internal pressure (maximum expected operating pressure [MEOP]) with adjustment coefficients. Masses of components are often issued using regression polynomial formulas, as in Humble et al. [1].

The three software packages modeling the propulsion systems use Microsoft® Excel, which had the following advantages in this case:

- To calibrate software on detailed projects to obtain good results. Excel, with its specific functionalities (solver, target function), is well suited
- To directly investigate the effect on the design when a parameter is changed
- To compare architecture options
- To evaluate the influence of operating parameters
- To evaluate the effects of technological options.

Therefore, an analysis can be made to estimate the effect of a modification (e.g., propellant characteristics) or a new design on the performance parameters (dead mass, $I_{s,vac}$, A_e, t_c) needed for the trajectory computation.

Nevertheless, a model based on existing motors has limitations: lack of data on the effect of several phenomena such as, for example, for solids, the throat erosion or ablation of internal insulation versus the characteristics of a new propellant (with no existing reduced modeling).

2.1 PLISE

This light software for modeling liquid propulsion systems is based on Humble et al. [1] and Huzel and Huang [2].

2.2 SoME

SoME models SRMs with fixed or movable nozzles (flexseal) with an electro-mechanical thrust vector control (TVC). The main inputs are the stage diameter, propellant mass, propellant characteristics, grain parameters, integration of the nozzle, and average area ratio associated with a set of technological hypotheses.

The Inner Arch — P65

Diameter	3.00	m
MP	65000	kg
Pmax	87	bars
Paverage	59.4	bars
SUBMERGE	0.379	
r	10.8	mm/s
Tcu	110.0	s
dm/dt average	590.9	kg/s
Thrust vaccuum	1618	kN
I_s,vac Efficiency	0.941	
I_s, vac	279.1	s
Exit Area	2.274	m2
r 7MPa	9.53	mm/s

Technologies

Flexseal 6 Degrees		
VEGA P80 Propellant		
Finocyl GRAIN		
nD C-C 2 THROAT		
Composite Case		
ΦThr Initial	0.423	m
Throat Area	0.157	m2
ΦThr.average	0.447	m
δΦ col	48.0	mm
Φ exit	1.702	m
Σ average	14.5	
Σ initial	16.2	

SoME

Masses	[kg]	
Propellant	65000	
Structure	2634	
Igniter	89	
Struct.		71
Prop.		18
Internal Ins.	889	
Therm. Ins.		826
Liner		63
Nozzle	1590	
Misc.	293	
TVC		236
Mi	5494	
Mi with EPU	5731	
Mi/Mp	0.088	
M total	70731	

Solid Motor Evaluation

Dimensions (m,m2)	
Φ Inner bore	0.60
Ext L case	7.22
ΦRear Polar Boss	1.31
ΦFwd Polar Boss	0.61
Lemerging nozzle	1.26
L nozzle	2.03
Lstage	6.49
Total Length	8.48
Exit Area	2.27
A stage	7.08
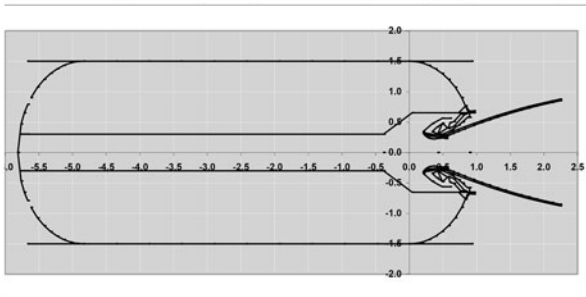
Fig. 1 Main data and output of SoME

The output includes a mass breakdown, combustion time, effective specific impulse I_s, total exit area of the nozzle, and a scheme. See Fig. 1.

One limitation of this model is the prediction of the specific impulse for fuels other than aluminum. For this, empirical formulas found in the open literature were well validated on many kinds of aluminized or not solid propellants (safety class 1.1 or class 1.3). This light software modeling system is based on Humble et al. [1], Huzel and Huang [2], and Landsbaum et al. [3].

2.3 HYES

As with SoME, HYES models the solid part with fixed or movable nozzle (flexseal). The main inputs are the stage diameter, propellant mass, integration of the nozzle, and the average area ratio associated with a set of technological hypotheses; the liquid tank can be pressurized or pressure fed. The major difference with the solid case is the assumption of a tapered grain (star or circular inner bore) and combustion with a constant oxidizer flow or regulation to maintain the optimum mixture ratio (or a constant flow and then a controlled flow) [4].
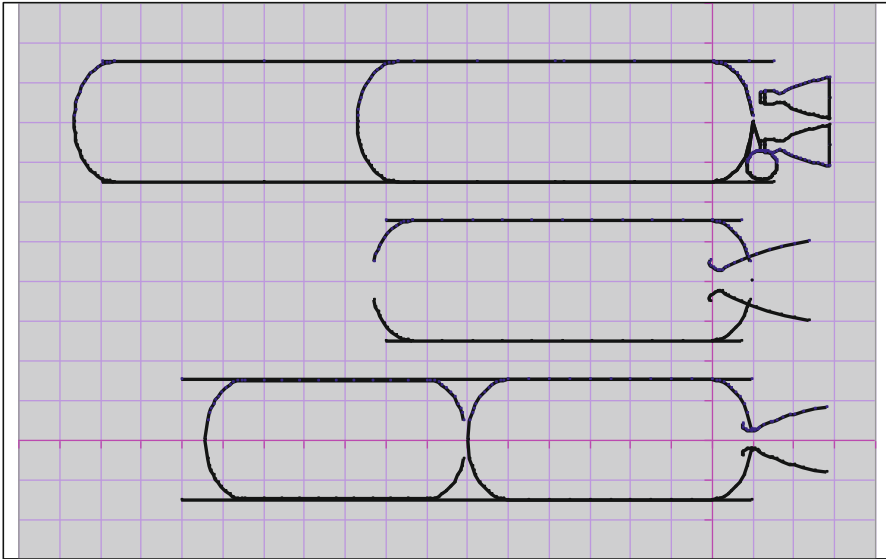
Fig. 2 Comparison of size: LOx/methane vs. SRM vs. hybrid stages (with 90 t of propellant)

A comparison of the length of three stages of 90 t of propellant is given in Fig. 2; the comparison was made using these codes.

2.4 PERFOL

This software optimizes the trajectory and the flight sequence, but with the following requirements:

- Robustness and ease of use: anybody, even someone with no skills in performance computation, may obtain an accurate result, from different launch pads and for different missions. The input is as simplified as possible.
- The computation time is short enough to be used in a multidisciplinary design optimization (MDO) software/platform.
- Microsoft environment
- Excel interface.

2.5 Coupling PERFOL, SoME, or HYES

Traditionally, influence coefficients (dpayload/dMp, dPayload/dIs, etc.) are computed using a trajectory code; these coefficients allow the intrinsic propulsion

parameters to be optimized. For simple prospective studies, the optimization can also be directly conducted by running PERFOL. This approach was used in the HISP = High Impulse Solid Propellant. HISP was a programme funded by the European Community [5].

3 New Propellants

Research on new propellants is mainly driven as follows:

- For boost stages: improved cost effectiveness coupled with a lower environmental impact (e.g., ozone layer depletion, even if negligible, vs. natural causes).
- For upper stages: a payload increase or improved cost effectiveness.

These days, operational space launchers use liquid or solid propellants. The smallest launchers use mainly solid propellants for the main stages if the country has mastered this technology.

The largest use liquid propellants with or without add-on solid boosters such as liquid oxygen (LOx)/kerosene for boost stages, and LOx/LH2 are used extensively for boost and upper stages; the only newcomer is the combined LOx/methane, which is associated with staged combustion engines and provide interesting performance effectiveness. Therefore, all new research on propellants other than liquids must be compared with these most recent propellants.

Current solid stages all use HTPB propellants with ammonium perchlorate (AP) as the oxidizer and aluminum as the fuel. Remarkably, the raw materials are not expensive, the resulting motors have no safety problems (they may be classified as class 1.3), and the burning rate can be tailored to a satisfactory range for civilian applications. Small launchers using solid propellants are cost efficient; if the specific impulses of solid propellants can be increased, they will compete with liquids for a greater number of missions.

A new composite propellant must have better performance, mainly in terms of specific impulse, so a new powerful oxidizer must be easy to produce and of good quality; it can be associated with aluminum—the more powerful non-toxic metallic fuel—or to a hydride, the best of which being aluminum hydride. The binder must, as an initial requirement, allow a high volumetric ratio for the solid loading; using an energetic binder, even with good mechanical properties, will give only a marginal gain versus HTPB, with possible safety issues.

In a short-/mid-term approach, new possibilities exist using a powerful oxidizer (ADN) and hydrides; HTPB has no real competitor as a binder that can obtain as high as possible volumetric loading of solids (to obtain good mechanical properties, the binder must be in the range of 20–27 % in volume).
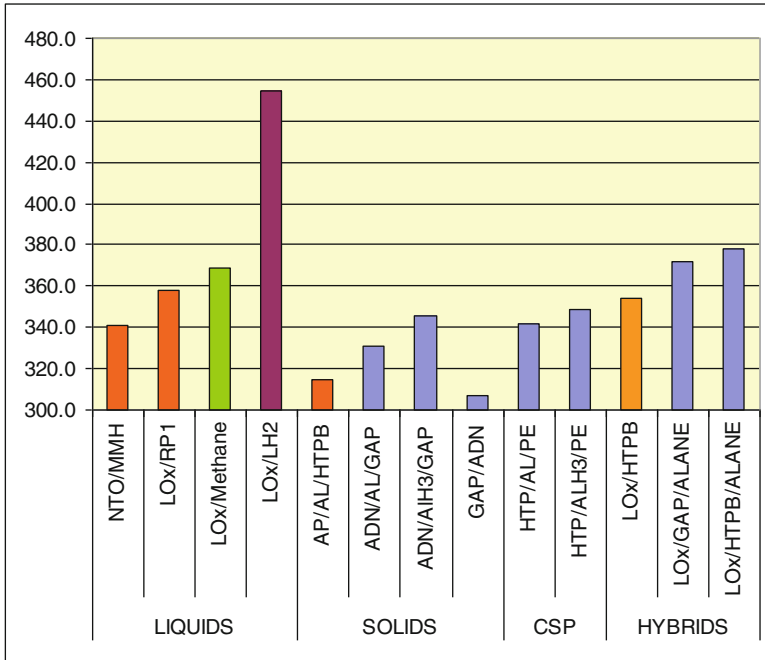
Fig. 3 Compared $I_{s,vac(40)}$ of different propellants

In the frame of the European program HISP, production of ADN was studied and appears possible at a reasonable cost. A small quantity of good-quality alane (AlH_3) was produced.

Taking into account HISP results, ADN associated with a compatible binder as HTPB could allow the realization of class 1.3 propellants.

Note:

1. The way to obtain optimized compositions would be via hybrid propulsion: a solid grain containing only the fuel as a solid load is more or less constrained by a loading volumetric ratio. Therefore, it could be a competitive potential solution versus LOx/methane.
2. Use of cold solid gelled propellant is another potential method of increasing the specific impulse of a solid. Remaining in the industrial range of cold (-18 °C/0 °C), inhibition of chemical reaction may enable the mixing, as for solids, of a fuel and a liquid oxidizer, such as hydrogen peroxide, with resulting potential self-ignition over 0 °C.

In Fig. 3, the specific impulses of potential new propellants are compared with current propellants [6]; see also Fig. 4.

Propellant		Mixture Ratio	Equivalent Density [kg/m³]	$I_{s,vac}$ Th (P_c = 7MPa, Σ=40)
Solid (AP/Al/HTPB)		68/18/14	1750	315
Hybrid (LOx / HTPB)		72/28	1060	354
Liquid Bi Propellants	NTO/MMH	2.37	1200	341
	H2O2/RP1	7.0	1320	314
	Lox/RP1	2.77	1030	358
	Lox/CH4	3.45	830	369

Fig. 4 Main current propellants

3.1 Burning Rate of Solid and Hybrid Propellants

To design a large propellant grain, hybrid or solid, with only a central bore, the propellant must regress in a range of 5–15 mm/s [7].

The first generation of hybrid propulsion sounding rockets in Europe used amines with or without a loading of hydrides (boron hydrides for the Swedish?). Onera used the combined MON-nylon/metatoluenediamine, with a regression rate of 3.5–5 mm/s, in its LEX [8]. The next generation mainly focused on the combined HTPB/LOx associated with a multi-perforated grain to be compliant with the low regression rate (around 1 mm/s). Hydrides could be part of a solution to increase the burning rate.

For solid propellants using "ADN", the burning rate is too high with glycidyle azide polymer (GAP) as the binder. While the rate is acceptable with HTPB, the pressure exponent is too high. Nevertheless, the propellant targets are based on a combination using HTPB instead of GAP [5, 9, 10]. Specifically HTPB, used as a burning rate modifier associated with a classic one, may be a way to explore, allowing a compliant pressure exponent with a relatively high increase of the specific impulse (target propellant Solid Two). The addition of alane strongly lower the pressure exponent (target propellant Solid One).

Given the results from the European HISP Programme [5], we selected the two target propellants—Solid One and Solid Two—for the evaluation, and assumed the burning rate could be tuned to the required value and the pressure exponent could be lowered to around 0.5 using ballistic additives for Solid One or alane for Solid Two.

Table 1 HTPB propellant effect of replacing AP with ADN on the burning rate (mm/s) [5,10]

Pressure (Mpa)	ADN	0	10	15	20	70	90	100
	1	2.25	2.44	2.57	2.80			2.50
	4	5.44	6.26	6.58	6.62	8.00	8.17	8.35
	7	7.17	9.35	9.51	10.38	12.80	13.20	13.59
	10	8.21	11.88	12.40	13.37	17.50	18.00	18.53
		Chinese results				Interpolation		FOI

Table 2 Payload derivative values (*) of Vega launcher

Stage	Parameter	kg%	kg/kg
1	Inert Mass	−4.35	−0.051
2	Inert Mass	−3.72	−0.145
3	Inert Mass	−9.67	−0.712

Stage	Parameter	kg%	kg/s
1	Is	46.18	16.205
2	Is	28.48	9.924
3	Is	43.34	14.772

(*): First value: derivative with respect to a parameter variation of 1 %
(*): Second value: derivative with respect to a parameter variation of 1 unit

4 Example of Application: Evaluation of the Effect of New Propellants on the VEGA Launch Vehicle

4.1 Intrinsic Sensitivity to Specific Impulse and Density

For new propellants, two performance drivers must be considered: specific impulse and density.

VEGA is a launch vehicle with four stages, here under are given the derivatives for the three first solid stages, while avum—a post-boost stage—has a derivative of mass of 1 kg/kg.

It can be seen that the effect of the propellant density will have a weak effect on the launcher payload mass, resulting in a low value of the inert mass derivatives of the two first stages (see Table 2).

Nevertheless, their intrinsic influences are not of equal importance when analyzed in a comparative design of stages with our models and then using a trajectory code (§ 2).

5 Effect of Density on VEGA Performance

The first figure shows the effect of an $I_{s,vac}$ increase in the propellant; the second shows the effect of a lower-density propellant of the VEGA launcher.

The effect of the density is evaluated running SoME to estimate the dead mass increase. The density effect is less important, mainly for the two lower stages: the specific impulse increase is a major driver.

The results are shown in Fig. 5.

5.1 Effects of Hydrides as Fuel

Hydrides are powerful fuels that can be used in all kinds of chemical propulsion, with the following limitations:

- For solid propulsion, the volumetric ratio of load limits the possibility of the alane percentage; mechanical properties require good-quality crystals (e.g., α-alane).
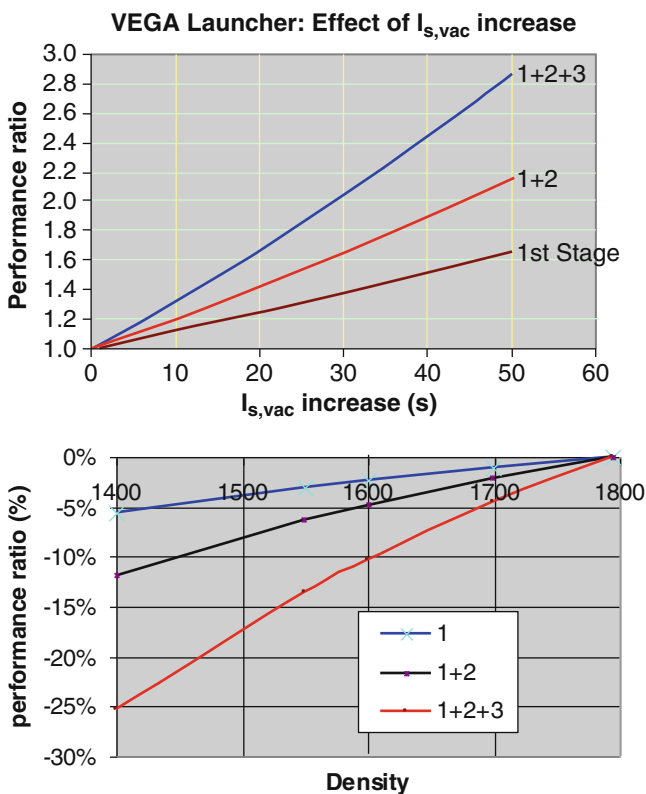
Fig. 5 Payload gain for VEGA

- Hybrid propulsion enables an optimized formulation without the manufacturing problem of the fuel grain (the amount of hydride can be high). It is the *only easy way* to realize fuel/oxidizer couples with an $I_{s,vac}$ close to 400 s (upper stages) and better than that of LOx/methane.

6 Hydrides for Hybrid Propulsion

As mentioned above, hybrid propulsion allows for an optimized formulation without the manufacturing problem of the fuel grain (the specification of the hydride may be lightened). It is the only easy way to realize fuel/oxidizer couples with an $I_{s,vac}$ close to 400 s (upper stages) or better than the $I_{s,vac}$ of LOx/methane; see Figs. 4 and 6.

As opposed to solid propellant, the addition of aluminum does not greatly increase the theoretical specific impulse (5 s max). Given the additional two-phase flow losses, the effects of HTPB loaded with aluminum versus pure HTPB, the best hydride AlH3 or alane gives 25 more $I_{s,vac}$ than pure HTPB.

Alane was formerly used as a solid propellant ingredient in Russia, and can be compatible with HTPB; if not available in Europe, other hydrides may also be considered (i.e., lithium hydride).

Moreover, hydrides have some other advantages. Since hydrides may greatly increase the regression rate, Fig. 7 [7], the grain could have a conventional star or tapered shape with a high loading volumetric ratio. It becomes easier to obtain a low level of solid residual.

The exhaust gases contain a very low percentage of water (mainly CO, hydrogen, and metallic oxide) (Table 3). Therefore, and in contrast with classic hybrids, the use of hydrides leads to non-erosive formulations and allow to use classical carbon/carbon material for the nozzle throat.
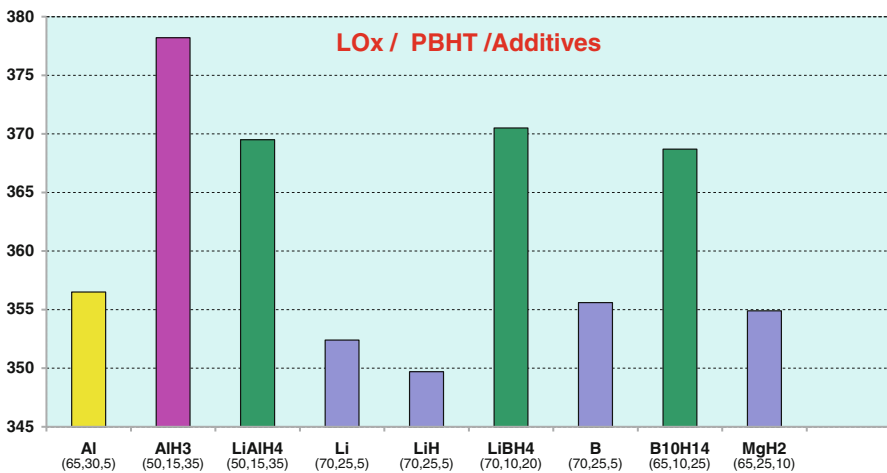
Fig. 6 Hybrid LOx/HTPB maximum $I_{s,vac(40)}$ for different additives to HTPB
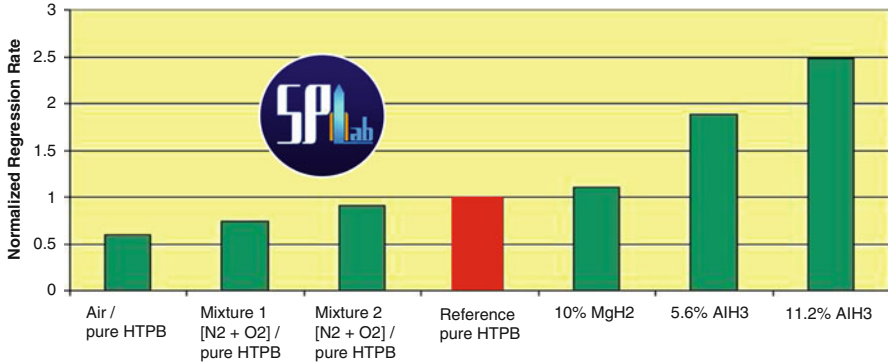
Fig. 7 Effect of additives on the burning rate of an HTPB hybrid

Table 3 Comparison of exhaust gas contents

Moles/100g	LOx-CH$_4$	VEGA	Solid 1	Solid 2	Hybrid
H	0.161	0.148	0.035	0.151	0.099
H$_2$	0.398	1.086	3.02	1.405	2.26
H$_2$O	2.112	0.413	0.003	0.026	0.261
O	0.085	0.002			
O$_2$	0.178				
CO	0.824		0.983	0.895	1.077
CO$_2$	0.562			0.021	0.022
N$_2$		0.293	0.836		
AL$_2$O$_3$		0.325	0.291	0.339	0.583
HCL		0.487		0.104	

Solid 1: HTPB/ADN/ALANE 13/57/29
Solid 2: HTPB/ADN/AP/AI 12.5/53.5/15/19
Hybrid: LOx/ HTPB/ Alane 50/15/35

6.1 Technical Choices

The propellant is an HTPB/alane 50/15/35 with a density of 1181 kg/m^3, a combustion temperature of 4024 K, and a specific impulse 40 of 377.8 s.

Solid part: Turbulence-enhancement devices (slots or others) for higher combustion efficiency and less risk of instability. Composite case, Flexseal, EPDM internal insulation, oxidizer injection by a pole, high combustion pressure, HTPB loaded with a 35 % alane.

The area ratio of the nozzle is close to 20, and the practical expected specific impulse could be >340 s.

Liquid part: Tank material: Aluminum 2219, pressure 3.5 bars, reversed common bottom (foam sandwich), helium initial pressurization then self-pressurized (inlet turbine evaporator). Turbopump: Initial speed given by Ground Support Equipment (GSE). Turbine: combustion gas bled (tap-off + LOx injection cooling), submerged LOx pump.

6.1.1 The VEGA Application

With the same set of hypotheses, the estimate was calculated only on **the first-stage replacement**.

The amount of residuals was assumed to be 2 tonnes and the $I_{s,vac}$ in the range of 330–340 s. The hybrid motor is longer (14.5 vs. 10.8 m), and the payload increase is in the range of 400–600 kg compared with a version with a performance of 1300 kg; see Figs. 8, 9 and 10.

Fig. 8 Hybrid booster

Lox Turbopump for injection

Mass Flow rate vs time

(kg/s)

(s)
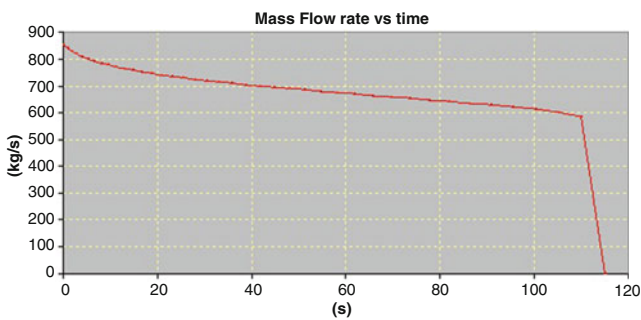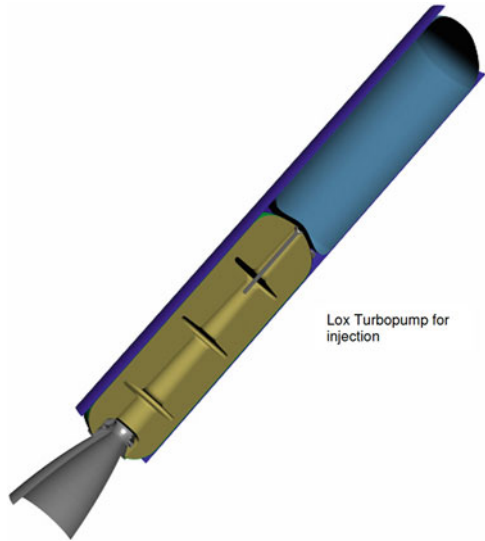
Fig. 9 Mass flow rate (kg/s) vs. time (s) of the hybrid first stage
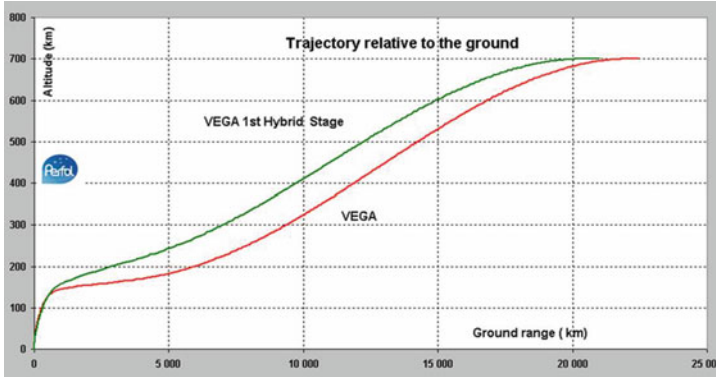
Fig. 10 New trajectory vs. nominal trajectory (in *red*)

Table 4 Propellant characteristics

Composition %	Density (kg/m3)	C* (m/s)	$I_{s,vac(40)}$ (s)	T_c (K)
Vega HTPB/AP/AL 12/69/19	1794	1582.0	317.69	3533
Solid 1 HTPB/ADN/ALANE 14/59/27	1492	1694.0	338.7	2778
Solid 2 HTPB/ADN/AP/Al 12.5/53.5/15/19	1719	1642.3	326.6	3462

7 Evaluation of the Payload Increase Using a New ADN Solid Propellant

The results of the study conducted within the framework of the HISP program [5] indicate that a potential new propellant appears feasible with a burning rate around 13 mm/s; this propellant contains AP to reduce the pressure exponent to an acceptable value (hypothesis to be verified).

Moreover, these new propellants will be less erosive for the throat (lower combustion temperature, much lower water content in the gases, and more hydrogen), leading to lower losses that are difficult to estimate at this stage. As gases, Solid One produces mainly hydrogen and nitrogen; the drawback is its low density. Solid Two is less impulsive but does not contain alane; see Table 4

7.1 New P80

The only complementary assumption is a tailoring of the burning rate and the initial inner bore shape such as to obtain the same combustion time and a thrust law compliant with requirements.

The assumption at the base of this estimation of the performance increase (Table 5) is that it will be possible to realize the same characteristics of the motor

Table 5 Characteristics of P80s and payload gain (P80 replacement only)

Propellant	M_i (kg)	$I_{s, vac}$ (s)	Total Length (m)	Payload Gain (kg)
Vega	7240 estim	280.6 estim	10.77 estim	0
Solid 1	8270	299.4	12.06	+200
Solid 2	7560	285.4	10.85	+60
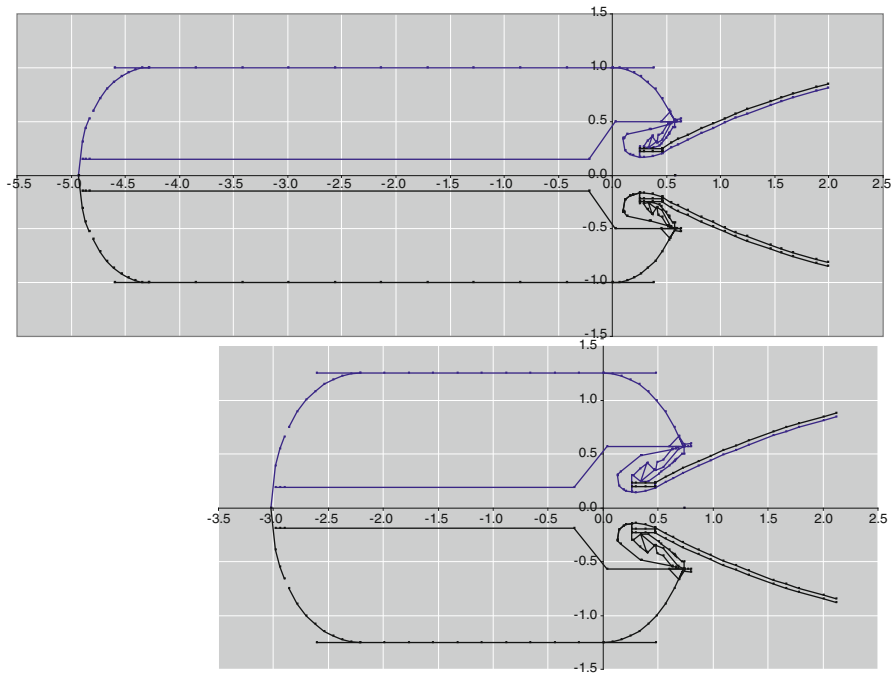
Fig. 11 Possible new version of Z23 compared with the current version

in terms of thrust law shape and combustion time. Nevertheless, this comparison shows the interest in searching to increase the specific impulse by developing both a new energetic fuel and a new energetic oxidizer (with the prerequisite of remaining in safety class 1.3).

7.2 New Z23 and New Z9

The burning rate of this new propellant is too high to retain the motors unchanged. The motor diameter must be increased and, as a result of this modification, the nozzle can be extended. Thus, a new Z23 is considered.

The drawing in Fig. 11 represents a Z23 with the same operating characteristics except the nozzle is extended from an average area ratio of 25–35, a diameter of

Table 6 Payload gain estimate (Z23 replacement only)

Propellant	M_i (kg)	$I_{s,vac}$ (s)	Total Length (m)	Payload Gain (kg)
Vega	0	0	0	0
Solid 1	+320	+19.4	+0.70	+145
Solid 2	+100	+8.4	+0.20	+70

2.5 m compliant with a burning rate at 7 MPa of 13 mm/s. Increasing the diameter of the stage is a source of potential $I_{s,vac}$ gain through the increase of the area ratio of the nozzle: this new version performs slightly better than the current version. It will be taken as a reference to evaluate the added gain resulting from the use of new propellants (as for the P80, only the characteristics of the propellant changes). Nevertheless, the design of a launcher will interact with the design of its propulsion system. If a new propellant is available, a complete redesign of the launcher will be required to obtain improved accuracy of the potentiality offered by this new propellant Table 6.

For the Z9, the only solution will be to modify the propellant grain with a head-end configuration (or partly inhibited inner bore in the aftward part), as it is not viable to increase the diameter (a composite case with no cylindrical part is not feasible).

This exercise has been conducted with AVIO [5] on the Z9 stage. Z9A needs a lower and Z9B a higher burning rate. The two versions of the stage have quite the same performance: Z9B will be taken as reference for the propellant comparison (Fig. 12).

Figure 2 shows the new version and Table 7 compares the characteristics of Z9B with the current one; Table 8 gives the estimation of the performance increase obtained by changing the propellant.

7.3 *Global Gain Resulting from Using Target Propellants*

By using derivatives, the order of magnitude of the payload increase of a propellant HTPB/ADN/Al is 220 kg; this result was verified by running the trajectory code PERFOL. By using the target propellant with Alane, the global increase could be close to 50 % of the nominal payload.

8 **Conclusions**

Easy-to-use tools allow pertinent prospective studies to be conducted efficiently and may detect potential breakthroughs such as, for example, the use of hybrid propulsion with new formulations using hydrides on new launchers with no layout
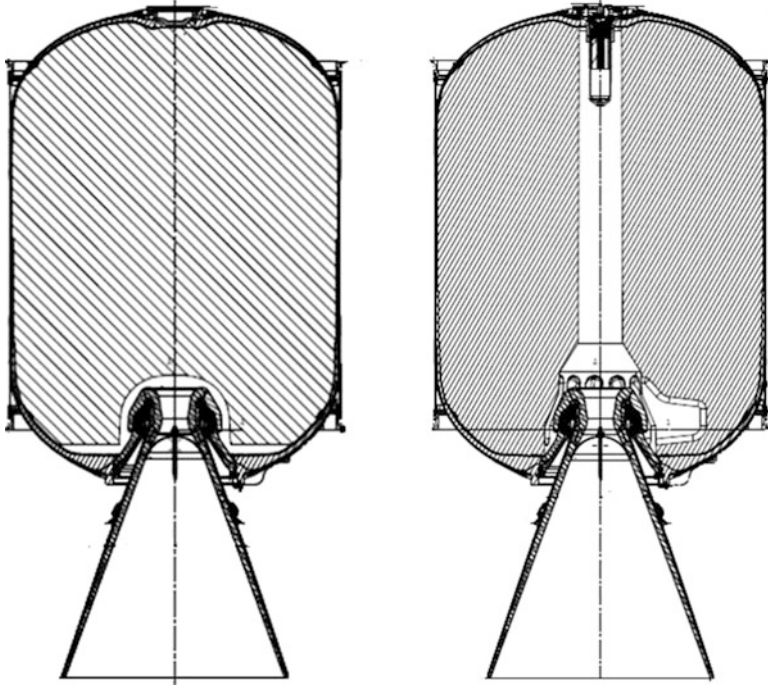
Fig. 12 Head end grain Z9B vs. nominal Z9A

Table 7 Comparative data Z9A vs. Z9B

	Z9A	Z9B	
Action time	117.1	121.1	s
Total propellant mass	10568	10596	kg
MEOP	8.59	8.59	MPa
Initial throat dia	149.5	149.5	mm
Final throat dia	196.3	190.0	mm
Exit dia	1273	1273	mm
r (7 MPa)	7	15.2	mm/s
Average area ratio Σ	52.2	56.5	
I_s on action time	295.2	296.2	s

Table 8 Characteristics of Z9B and payload gain (Z9 replacement only)

Propellant	M_i (kg)	$I_{s,vac}$ (s)	Total Length (m)	Payload Gain (kg)
Vega	0	0	0	0
Solid 1	+90	+20	+0.45	+240
Solid 2	+35	+8	+0.10	+90

constraints (however, basic assumptions are that such hybrid engines with hydrides will have a high regression rate and good combustion behavior).

New solid formulations using hydrides are also an interesting challenge leading to potential breakthroughs in terms of performance should a hydride with low manufacturing costs and high performance exist. However, a realistic intermediate step will be to partly replace AP with ADN in classic HTPB propellants, leading to a greener and more impulsive propellant with a credible target performance increase of 10–15 % for a new small launcher.

References

1. Humble RW, Henry GN, Larson WJ (1995) Space propulsion analysis and design, Space technologies series. The McGraw Hill Companies, New York
2. Huzel DK, Huang DH (1992) Modern engineering for design of liquid propellant rocket engines. AIAA Prog Astronaut Aeronaut 147
3. Landsbaum EM, Salinas MP, Leary JP (1979) AIAA 79–1359 Specific impulse prediction of SRMs. AIAA-JPC 1979 Las Vegas.
4. Altman D (2003) Highlights in hybrid rocket history, 8-IWCP "Rocket Propulsion: Present and Future". In: DeLuca LT, Grafiche GSS (eds). Bergamo, Paper No. 07
5. EC HISP programme: mission benefits using high performance solid propellants 2013
6. Calabro M (2004) LOx/HTPB/AlH$_3$ hybrid propulsion for launch vehicle boosters. AIAA Paper No. 04–3823
7. Calabro M, DeLuca LT, Galfetti L, Perut C (2007) Advanced hybrid solid fuels, IAC-07-C4.2.09, 24–27 Sep 07, Hyderabad
8. DeLuca LT, Galfetti L, Severini F, Rossettini L, Meda L, Marra G, D'Andrea B, Weiser V, Calabro M, Vorozhtsov AB, Glazunov AA, Pavlovets GJ (2007) Physical and ballistic characterization of AlH3-based space propellants. Aerosp Sci Technol 11(1):1–8, Jan 2007
9. Chan ML, Johnson CE (2003) Evaluation of AlH3 for propellant application. In: DeLuca LT, Grafiche GSS (eds) Proceedings 8-IWCP. Bergamo, Paper 33
10. Wei-qiang P et al (2013) Effect of Ammonium Dinitramide (ADN) on the Characteristics of Hydroxyl Terminated Polybutadiene (HTPB) Based Composite Solid Propellant. Mod Chem Res Inst J Chem Sci Technol 2(2):53–60

Overview of Research and Development Status of Reusable Rocket Engine

Makoto Yoshida, Toshiya Kimura, Tomoyuki Hashimoto, Shinichi Moriya, and Satoshi Takada

Abstract This paper reports the status of research and development of a reusable rocket engine in Japan. In the case of an expendable engine, in system selection, much weight must be put on performance, whereas in the case of a reusable engine, in addition to satisfactory performance required by the mission, reusability must be considered. In the system study, total design management (TDM) was employed for the LOx/ethanol engine, and the relation between performance and reusability was quantitatively evaluated. In the research on key components, the combustion chamber, bearings, and seals for turbopumps were selected as key components. To extend the lifetime of the combustion chamber, lowering the wall temperature is important, and thermal barrier coating (TBC) or film cooling (FC) becomes necessary. Turbopumps with a port for installation of a fiberscope on the bearing's inner ring and on the shaft seal's nose for direct observation were developed, and the feasibility of 100 reuses was established. A demonstration engine of the reusable sounding rocket was manufactured, and more than 100 operation cycle tests were carried out to confirm the feasibility of 100 reuses. Durability was confirmed by lifetime audit testing.

1 The Difference Between Reusable and Expendable Rocket Engines

Achievement of price reduction by the introduction of private sector vitality or by reexamination of existing technology has recently been given priority over the goal of superior performance in Japan's space transport system. To realize a drastic price reduction, a reusable space transport system is indispensable. The US Space Shuttle program has realized a reusable space transportation system, but the operating costs are extremely high and price reduction by such a system has still not been realized.

As for the design of a reusable rocket engine, ostensibly, there is not a big difference between it and the conventional expendable type of engines. However,

M. Yoshida (✉) • T. Kimura • T. Hashimoto • S. Moriya • S. Takada
Aerospace Research and Development Directorate, Japan Aerospace Exploration Agency (JAXA), Kakuda 981-1525, Japan
e-mail: yoshida.makoto@jaxa.jp

in the case of a conventional expendable rocket, the rocket engine and the vehicle generate a peak performance within a short period after which their work is finished, whereas in a reusable transport system, the design method is the same as that of the ordinary ground transportation systems or that of an aircraft. In the field of aircraft design, since the accident involving the Comet, which was a jetliner pioneer, the concepts of design, manufacture, and operation seem to have improved as follows: "The product must be designed and manufactured so as not to break. Even if there is breakage, this must not become fatal. Furthermore techniques must be established to enable restoration of troubled elements or their replacement by predicting trouble before it becomes fatal" [1]. Implementation of the first part of this concept in the expendable space transport system has been achieved, but realization of the second part is problematic.

In the case of the expendable engine, in system selection, much weight must be put on performance, whereas in the case of the reusable engine, reusability must be considered in addition to satisfactory performance required by the mission. The word "reusability" includes high operability, low cost, abortability, and robustness, in addition to a longer life span of each engine element. It is also related to engine cycle and fuel.

We have established the following guidelines to examine a reusable engine:

(A) *System pressure and temperature should be low*.
     The margin of material strength and of key component design such as that of a turbopump can be increased.
(B) *Engine configuration should be simple*.
     For example, engines with expander cycles do not have pre-burners, and the total number of components is small, which increases reliability.
(C) *Good operability*.
     Liquid propellants, such as hydrocarbon, at room temperature have better operability than cryogenic hydrogen and do not need precooling.

In this paper, we studied the following two engines by considering these conditions:

Engine with LOx/ethanol. Ethanol can be stored at room temperature and has good availability and operability. However, it has poor specific impulse (I_s) compared with LH_2, and it is not suitable for expander cycles because of its low specific heat. Gas generator (GG) cycles or staged combustion (SC) cycles are suitable. Another demerit of low specific heat is that the temperature of the inside wall of the combustor is higher than that of the LH_2 cooled engine, which results in a short lifetime. Therefore, thermal barrier coating (TBC) or film cooling (FC) of the inside of the chamber wall should be considered.

Engine with LOx/LH_2. LH_2 fuel shows good performance, and we have sufficient experience with it, but its operability is not good. From the standpoint of simple structure, expander cycles are suitable, and an expander bleed (EB) cycle is better than a full expander (FE) cycle because it has lower system pressure.

In the system study section, the flow of system study by Total Design Management (TDM [2]) was introduced using a LOx/ethanol engine. Results of the study of key components such as combustion chamber and tribological elements such as bearings and seals are presented, and finally, the design of an engine for the reusable sounding rocket and its demonstration results are discussed.

2   Engine System and Its System Performance

Generally, in the case of reusability, some aspects are contrary to high performance. In this section, the future propulsion system is reviewed, and the relation between performance and reusability is quantitatively shown. A two-stage-to-orbit (TSTO) space transportation system is assumed. A takeoff weight of 800 tons and an upper stage orbiter weight of 75 tons are assumed. The first stage has five engines, each of them having about 2500 kN of thrust. The second stage has three engines, each of them having 250 kN of thrust. Hydrocarbon fuel is assumed and ethanol is selected because of its excellent operability and its eco-friendliness. Liquid oxygen is selected as the oxidizer.

Regarding the engine system, it has an in-vacuum thrust of 250 kN, equal to or more than 320 s of in-vacuum Is, a nozzle exit diameter equal to or less than 1.8 m, as shown by simple orbit analysis of the abovementioned space transportation system and of the engine for the orbiter. It produces an in-vacuum thrust of about 2500 kN, equal to or more than 315 s of in-vacuum specific impulse, a nozzle exit diameter equal to or less than 2.2 m of the booster engine.

In the concept review stage, the system request to the engine can easily change with change in the system. To minimize the recalculation of the case, the technique of TDM was introduced. TDM is a technique of establishing a mathematical or physical model, an analysis tool for use in design. It facilitates identification of a design solution based on design variables and selection of a solution, followed by filtering of the required performance (the evaluation index) and satisfaction of a request. If these models are established, it is easy to obtain new design parameters for the engine with just the filtering processes, even if the performance request changes. By managing the mathematics, the physical model, the reliability, and the precision of the analysis tool, the transparency of the design process is secured.

2.1   Engine and Turbopump Performance

As the analysis tool to estimate engine performance, one-dimensional engine (ODE) analysis [3] was used. The design parameters employed were chamber pressure, throat diameter, C^* efficiency (η_{C^*}), mixture ratio, and expansion ratio. The solution for the engine thrust and specific impulse can be established by changing these

design parameters within the given limits and by applying ODE to a combination of all the parameters.

Design parameters of turbopumps are pump efficiency, turbine efficiency, pump flow rate, turbine flow rate, turbine pressure ratio, and turbine drive gas temperature. A solution set with the quantity of the pump boosting pressure is derived by changing each parameter in the constant within the given limits. A combination of parameters which satisfies the quantity of the boosting pressure can be chosen.

2.2 Engine Cycles

Because ethanol, which is assumed as fuel, is liquid at normal temperature, turbine drive by vaporization of fuel cannot be expected in the start-up sequence. Also, as the specific heat is smaller than those of other hydrocarbon fuels, ethanol is disadvantageous for an expander cycle engine. Therefore, the SC cycle and GG cycle were selected as subjects of this study.

2.3 Review of Flow

The chamber pressure, throat diameter, and combustion chamber propellant flow rate of the engine which satisfies the required performance can be obtained by a filtering process using the required performance of the solution set obtained in Sect. 2.1. Figure 1 shows the state of narrowing of an engine solution set by filtering as an example of the orbiter engine. The axis of each figure shows an in-vacuum thrust, an in-vacuum specific impulse, and chamber pressure. The parameter ranges are set as they are in the upper left of the figure, creating a graph in the upper left of all results of the numerical engine (thrust, specific impulse, and chamber pressure) by those combinations in the plot. The remainder of the calculated data after filtering of the nozzle exit diameter is equal to or less than the requested 1.8 m as shown in the graph in the upper right.

As for the η_{C*}, in the present situation, 0.95 is expected from the burning experiment. Therefore, it becomes the solution set in the lower left when C* does more filtering at 0.95 and becomes the solution set in the lower right with filtering in the in-vacuum thrust, which is the required performance. Because the engine reviewed here is a reusable engine, the lower the chamber pressure, the more favorable the combustion chamber lifetime, which has the biggest influence on engine life. The optimum solution set of the engine in hanging filtering of the specific impulse, which is the required performance, is established.

In the candidate engine, the chamber pressure in each case was 6, 7, and 8 MPa, the one where the specific impulse was the highest being chosen. O-1, O-2, and O-3 are the highest cases for each pressure. We assumed the SC or GG cycle for each case and reviewed the formability of the turbopump. It was found that there was sufficient formability. A performance overview of these engine candidates
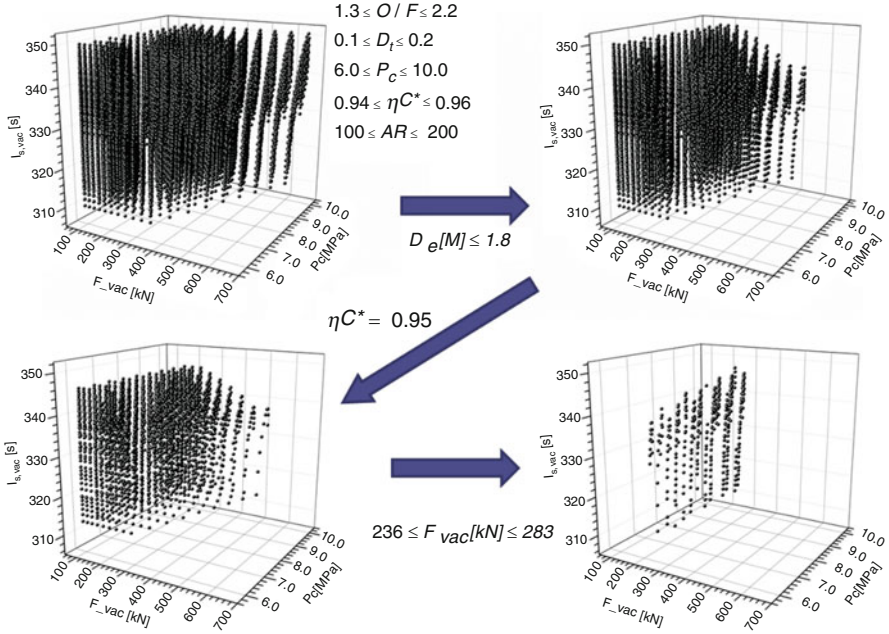
Fig. 1 Filtering process of engine solution by TDM

Table 1 Engine sample for an orbiter stage

Engine	Cycle	Pc(MPa)	Dt(m)	AR	De(m)	F_{vac}(kN)	Fcc(%)	$I_{s,vac}$(s)
O-1	SC	6.0	0.160	130	1.8	247	–	340.5
O-2		7.0	0.145	160	1.8	241	–	343.9
O-3		8.0	0.135	185	1.8	239	–	345.9
O-1	GG	6.0	0.160	130	1.8	247	3.0	330.6
O-2		7.0	0.145	160	1.8	241	3.0	333.9
O-3		8.0	0.135	185	1.8	239	3.0	335.9

is shown in Table 1, where Dt represents the throat diameter, AR represents the nozzle expansion ratio, De represents the nozzle exit diameter, F_{vac} represents the in-vacuum thrust, f_{GG} represents the ratio to the combustion chamber fuel flow rate of the turbine drive gas flow rate with the GG cycle, and $I_{s,vac}$ represents the in-vacuum specific impulse.

2.4 Estimation of the Engine Life

In the case of the reusable rocket, evaluation of lifetime becomes necessary. The main elements which determine the lifetime of the rocket engine are the combustion

chamber, the mechanical element of the turbopump, bearings and seals, and turbine blades. Turbine blades were designated as being very important items by the report on the Space Shuttle Main Engine (SSME) [4]. Turbine blades are operated under severe environmental conditions such as high temperature, high stress, and thermal shock, and they cause hydrogen embrittlement, fatigue, creep, and so on. However, as we concluded that the turbine problem may be avoided by selection of an appropriate engine cycle and operation point, we do not consider turbine problems in this paper. The lifetime of the combustion chamber determines the lifetime of the engine because the lifetime of the turbopump can be extended by replacing bearings and seals, but the combustion chamber is the main element of the engine. To increase the number of times an engine can be reused, the combustion chamber wall must be sufficiently cooled.

As a way of decreasing heat flux from the combustion gases, the use of TBC or FC is possible (see Sect. 3.1). As for the candidate engine which was reviewed in Table 1, lifetime evaluation of the combustion chamber and examination of the life-lengthening effect of using TBC and FC were conducted. Analysis of combustion chamber wall cooling was conducted by using the equation of Taylor [5] with the equation of Bartz [6]. The heat transfer percentage of coolant was estimated based on the heat transfer percentage of the combustion gases and a one-dimensional regular heat transfer equation in the direction (the combustion gases, the combustion chamber wall coolant) perpendicular to the cooling flow channel wall. Also, as for the coolant, its condition was determined based on the conservation law with the mass, momentum, and energy necessary for quasi-one-dimensional regular flow to the exit side from the entrance side. As for TBC, its material and the effect of its thickness were considered by one-dimensional heat transfer analysis at the combustion chamber wall. Also, as for FC, its heat shield effect was evaluated by the empirical formulation obtained from the film cooling test. This effect changes with the flow rate because with FC, fuel flows along the combustion chamber's internal surface. Therefore, 10, 15, and 20 % of the combustion chamber fuel flow rate were assumed. The fuel used for FC decreases the I_s because it does not contribute to the thrust. Because the heat flux in the throat part becomes the most severe, the condition of the combustion chamber determines the lifetime of the throat part. Using two-dimensional nonsteady finite element method (FEM) analysis for the combustion chamber section, the levels of fatigue damage and that of creep damage in one cycle of burning are calculated, and lifetime analysis is performed using the linear damage law. Heat transfer percentage, temperature, and pressure on the coolant side, which were obtained by the cooling analysis, are given as the boundary conditions of the FEM analysis.

2.5 Performance and Lifetime

The lifetime analysis results are shown in Fig. 2. The horizontal axis of the figure shows cooling conditions. RC means regenerative cooling, TBC means thermal barrier coating, and FC means film cooling and ratio of the main fuel flow rate
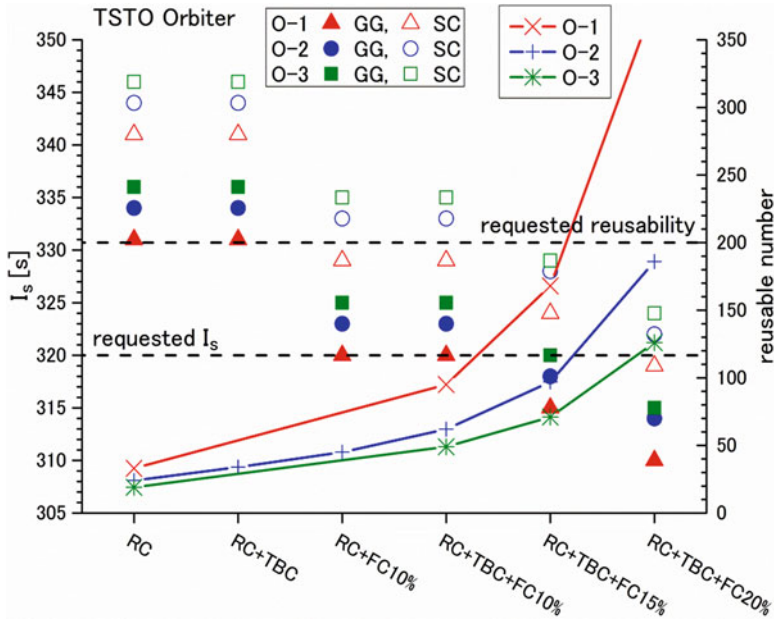
Fig. 2 Relation between engine performance (I_s) and reusability

to the coolant flow rate with film cooling. The further to the right, the higher the effect of the heat shield on the combustion chamber's internal surface. The vertical axis on the left shows the in-vacuum specific impulse, and the vertical axis on the right shows the combustion chamber lifetime (the number of reuses). The circles, triangles, and squares show the performance (I_s) in case of the GG cycle and the SC cycle for each engine candidate. Because the gas which drives the turbine in the GG cycle is discarded, the combustor and the nozzle performance discussed in Table 1 decline, and the I_s of the GG cycle is 10 s lower than that of the SC cycle. When using only TBC for the heat shield, performance is not influenced, but when the cooling flow rate of the film cooling increases, the performance declines. The performance improves to the extent that the burning pressure is high even in the same cycle because the throat area can be small for the same thrust and has a bigger expansion ratio. The combustion chamber lifetime of each engine is shown by the solid line. Even if the heat shield effect becomes large for each solid line, the estimated lifetime increases. Because the heat flux increases when the chamber pressure is high, the lifetime decreases.

From Fig. 2 it can be seen that the estimated lifetime increases concomitant with good results of the heat shield in the combustion chamber. On the other hand, as performance increases, the lifetime decreases. The level dotted line shows the number of times the engine was reused. Reusing 200 times is quite a high standard, but it is quite possible that an engine capable of 100 reuses, which exceeds the required performance by the GG cycle or the SC cycle with a chamber pressure of 6 MPa, can be achieved.

3   Key Component Technology: Combustion Chamber

The longer life of the combustion chamber of the liquid rocket engine is an important factor in reusable rockets, and much research has been done on this for many years. This research can be classified into the following four types:

1. Reduction of the heat flux
2. Elastic structure
3. Micro channel
4. Strengthening of the combustor liner (the inner liner) material

3.1   Reduction of Heat Flux

First, the most effective way to achieve longer life is to reduce the heat distortion, i.e., the reduction of heat flux. When the heat flux is high, the temperature gradient in the combustor wall section becomes high and the heat distortion which occurs in the wall increases, and as a result, the lifetime decreases. Figure 3 presents an example of the result of lifetime analysis for the LOx/LH$_2$ combustor. This analysis was done for creep fatigue using the finite element analysis code and the linear damage law. The lifetime is normalized by a heat flux of 100 MW/m^2 as 1. When heat flux decreases, the lifetime of the engine increases. To decrease heat flux, thermal barrier coating, film cooling, and transpiration cooling are possible options. Among these, thermal barrier coating and film cooling at the throat part are employed in the RD-170 engine [7]. Transpiration cooling is applied to the injector surface, and there have been some reports on the application of transpiration cooling to combustion
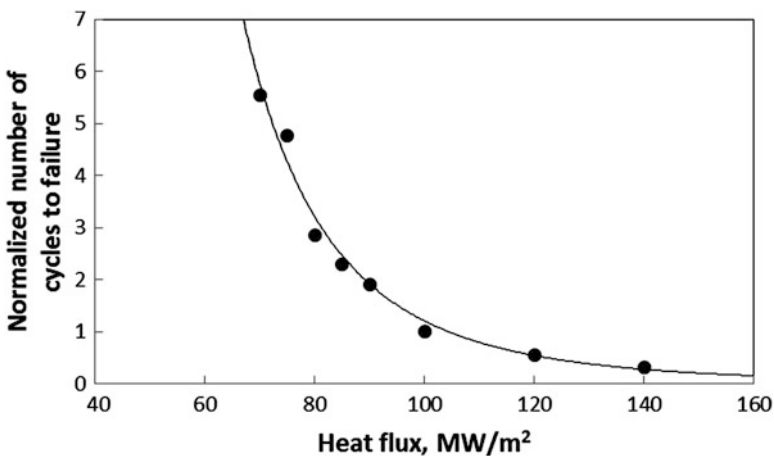
Fig. 3   Analysis results of relationship of combustor life cycle and heat flux for LOx/LH$_2$ chamber

chambers, which are still in the research phase [8–10]. The merit of transpiration cooling is that the place to be cooled can be pinpointed. On the other hand, because film cooling and transpiration cooling are accompanied by degradation, a trade-off with lifetime becomes necessary.

3.2 Thermal Barrier Coating

TBC is a typical way to increase engine lifetime. According to an experimental report by Quentmeyer et al. [11], the lifetime of a combustor liner (CuZr, Amzirc) was 393 ignitions, whereas the lifetime of the bond coat with thermal sprayed ZrO_2 coating (film thickness, 0.076 mm) and thermal sprayed NiCr (film thickness, 0.025 mm) was 1450 ignitions, about 3.7 times greater. Furthermore, when using the inside-out method for coating electroformed copper, longer life can be expected by using a heat-resistant copper alloy.

However, TBC of the combustor internal surface is exposed to the compression stress field during burning, and buckling sometimes occurs because of this compressive stress. Figure 4 shows the state of damage after a burning test of the combustor that the authors conducted, in which partially stabilized ZrO_2 (PSZ) coating was applied by the inside-out thermal spraying method. It was found that bulging occurred because of buckling of PSZ by the compression stress field. This phenomenon is problematic when using ceramic-type TBC under a high heat flux.

On the other hand, as for the engine of the RD-170, a coating of Cr and Ni is applied inside the combustor, Cr for the combustion gas side, and Ni for the copper alloy side. The heat-resistant temperature is not high compared with the temperature in each layer with the ceramics, but there are few concerns with buckling of this coating. Also, it has been reported that a vertical crack stops at the boundary with

Fig. 4 Buckling of PSZ top coat induced by compressive stress state

the Ni layer even if the vertical crack occurs in the Cr layer. Therefore, there is no problem of shieldability if the delamination in the TBC layer does not occur even if a vertical crack occurs.

3.3   Film Cooling

Cooling of the throat is necessary, and thus a jet orifice must be installed at the middle of the regenerative-cooling channel. The RD-170 engine has more than one film cooling orifice for kerosene near the chamber cylinder and the convergent section for film cooling of the combustor internal surface [7]. Though the required lifetime of RD-170 is 11 reuses, it is reported that the RD-170 engine has achieved 17 reuses and 25 reuses of demonstrated life by the abovementioned combination of Cr/Ni TBC [12].

3.4   Transpiration Cooling

It is effective for the engine if the heat flux in the throat part is especially high as in a high chamber pressure booster engine. However, no such engine for practical use has been developed. Transpiration cooling is more effective than film cooling because the part which should be cooled can be pinpointed. To realize a transpiration cooling method, the following three things must be achieved:

1. Establishment of a design technique and manufacturing technology for combining a transpiration cooling structure with the inside of the regenerative-cooling structure
2. Establishment of cleanness control technology in the plumbing to prevent blockage of the cooling structure
3. Development of technology to prevent blockage of a coolant flow channel by solid body residue formed by pyrolysis

3.5   Elastic Structure

The combustor consists of a copper alloy inner liner which has a cooling channel and a high-intensity metal outer shell of Ni base alloy or Ni closeout. Combustion gas side heat distortion increases more for heating by combustion gases, and expansion of the copper alloy combustion liner is restricted by the external cylinder. Moreover, in case of cooling by liquid hydrogen, the heat distortion of the copper alloy combustion liner further increases by cooling of the external cylinder. Therefore, the elastic structure technique is used to ease the binding force by the external cylinder

and to reduce heat distortion so as to achieve longer life of the combustion liner. The elastic structure technique is characterized as follows:

1. It reduces the stiffness of the external cylinder.
2. It creates a barrier between the combustion liner and the external cylinder and eases the binding force.
3. In this technique, a low elastic material and an insulator are inserted between the combustion liner and the external cylinder.

In a review by Kasper [13], glass fiber-reinforced plastic (GFRP) was chosen to reduce the stiffness of the external cylinder. As a specimen, GFRP was put at the periphery of the external cylinder material and subjected to analysis and evaluation by testing. Calculation showed that the heat distortion declined because the stiffness of the external cylinder declined, consequently increasing the lifetime of the combustion chamber. Results of the burning test showed that the lifetime was extended about 30 % in the chamber overlapped by GFRP as compared with the Ni closeout chamber. The cause of this result is thought to be that the contact between the overlapping GFRP and the combustion liner was insufficient because the throat diameter was small and the throat part was not restricted by the external cylinder.

Figure 5 shows the result of evaluation by analysis of the influence on the lifetime by changing the stiffness of the external cylinder. The external cylinder was made of CFRP with small heat contraction, the stiffness of the external cylinder being changed by changing the thickness. Here, the stiffness was calculated by the elastic modulus multiplied by wall thickness. Figure 5 shows that stiffness declines more
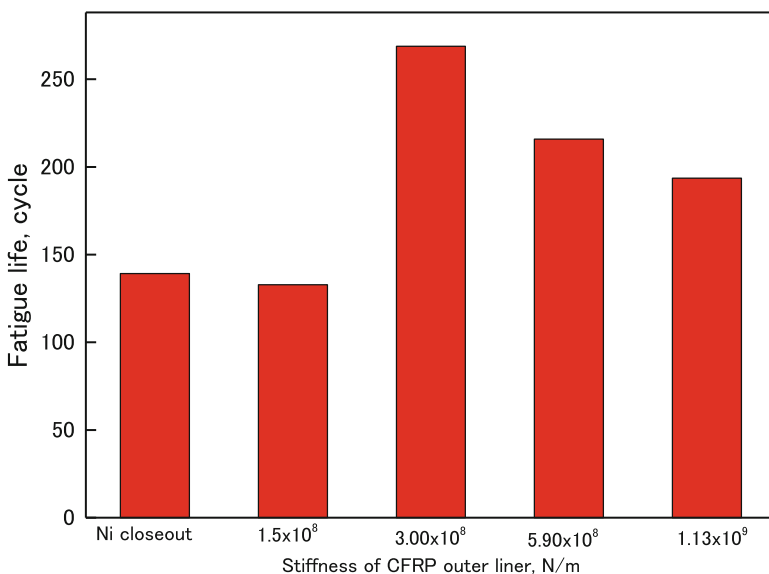
Fig. 5 Analysis results of stiffness of CFRP outer shell and fatigue life
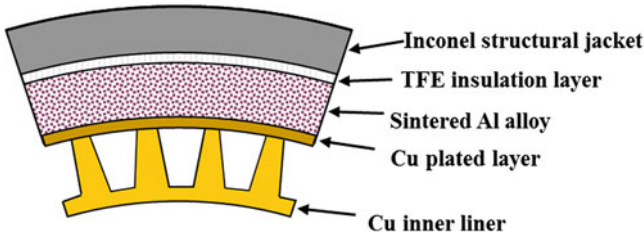
Fig. 6 Elastic structure with low stiffness sintered Al alloy layer and insulation layer

than Ni closeout and that the lifetime increases (in Fig. 5, it is equal to or more than 3.00×10^6 N/m) but that the lifetime declines if the stiffness is too small (in Fig. 5, it is 1.5×10^8 N/m). It was found that there is an optimum stiffness of the external cylinder to achieve a longer lifetime.

Popp [14] has proposed that the lifetime of an engine can be increased by three to ten times by using a structure which combines a coolant side slot and a pressurized gap.

Niino [15] has proposed the elastic structure shown in Fig. 6, which consists of a copper alloy combustion liner, a porous low stiffness sintered Al alloy layer, a Teflon insulator layer, and an Inconel external cylinder. The porous low stiffness sintered Al alloy layer eases binding force to the thermal expansion of the copper alloy combustion liner, and the Teflon insulator layer eases the increase of the heat distortion of the copper alloy combustion liner by heat contraction of the Inconel external cylinder by liquid hydrogen coolant. About a threefold increase of life-lengthening effects is obtained in Niino's analysis result.

3.6 Micro Channel

Micro channels are used to lower the combustion gas side wall temperature. The fin effect in the walls of the cooling channel is increased by the number of cooling channels by decreasing cooling channel width and by reducing hot gas wall thickness [11, 14]. However, it has been pointed out that the microstructure decreases rib width and wall thickness, and, consequently, the thermal capacity declines [14]. As a result, when burning exceeds a nominal operation point, there is a possibility of melting because thermal capacity is exceeded.

3.7 Improvement of the Copper Alloy

Five characteristics of ideal combustor liner material have been enumerated in the literature [14]:

1. Maintains high intensity of tensile strength, fatigue strength, and the creep strength at 900 K.
2. Has as much ductility as oxygen-free copper (reduction of area ≥ 50 %).
3. Has a degree of thermal conductivity which is the same as copper ($\lambda \geq 300$ W/m/K).
4. Has a low-heat expansion coefficient from 20 to 900 K (in case of liquid hydrogen coolant, the cold side is 20 K) ($\beta \leqq 15 \times 10^{-6}$ K^{-1}).
5. The crystal boundary size is small. (It is desirable to be one-third the size of the cooling channel board thickness.)

Examples of copper alloy materials employed include oxygen-free copper OFHC (HM7), CuAgZr (Vulcain, SSME), CuCrZr (RD-0120, LE-7A, LE-5B), CuCr (RD-170), and so on. Also, CuCrNb has been studied and developed in the United States as a new copper alloy material. Moreover, a fiber-reinforced copper alloy and a particle-reinforced copper alloy have also been proposed. However, a copper alloy material that extends the lifetime of a high-pressure combustor such as that of a booster engine 10 or more times has not yet been developed. It should be noted that low-cycle fatigue data on uniaxial stress gained in material testing and the cycle life test in an actual combustor do not always agree [14]. Also, as for the CuAgZr copper alloy, chemical damage by oxygen has been reported, and the influence of the atmosphere must be considered in addition to the dynamic strength [16].

4 Key Component Technology: Mechanical Elements

As for the rocket engine, it has a wide range of tribological elements in the turbopump which sends pressurized propellant into the combustion chamber, valves to control the rocket engine, gimbaling to control the direction of the thrust vector, and so on. Specifically, to realize a reusable rocket, the valves which control the thrust and bearings and the seals which are necessary for a high-speed turbopump become key components.

4.1 Bearings for the Turbopump

For high-efficiency rocket engines, a turbopump to send pressurized oxidizer and fuel into the combustor is indispensable. In the case of a highly efficient rocket with a combination of oxidizer and fuel, oil lubrication cannot be used because most high-efficiency propellants are cryogenic fluid. Therefore, a high-speed rotor is supported by polytetrafluoroethylene (PTFE) solid lubrication (Fig. 7). A retainer made from PTFE first forms a thin lubrication film on the ball surface by contacting the walls of the pocket. Moreover, by rolling contact with balls and the inner ring and balls and the outer ring, a film of PTFE solid lubrication is formed on the contact surface. In usual oil lubrication, oil has the functions of lubrication and

Fig. 7 Bearings for liquid rocket engines

Fig. 8 Mechanism of
self-lubricating bearing
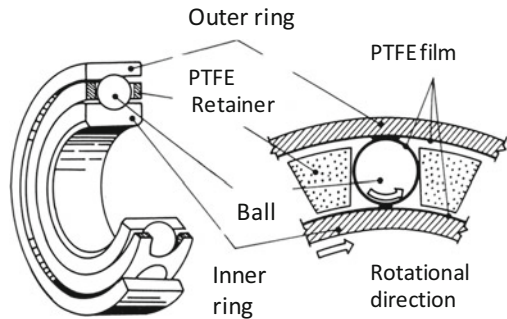
cooling, but in case of the rocket engine, the solid lubrication film is responsible for lubrication (Fig. 8), and fuel, which is the working fluid of the pump, realizes cooling. Conditions for the bearing of the cryogenic turbopump are severe, equal to or more than two digits of lifetimes lower than the case of usual industrial high-speed rotation machines.

The relation between the bearing cooling flow rate and the bearing temperature of the liquid hydrogen of the hybrid ball bearing with an inner diameter of 25 mm is shown in Fig. 9. The temperature rises with the decrease of the cooling flow rate, and the bearing exhaust temperature reaches the saturation temperature of the atmospheric pressure. Because it is assumed that cooling of a bearing is insufficient in the condition that the bearing exhaust temperature reaches the saturation temperature, an appropriate flow rate which can support high-speed rotation is required to extend the lifetime of the bearing.

It is difficult to detect severe damage which occurs during the turbopump operation and to stop an engine automatically. Therefore, research has been done on inspection methods and replacement timing of the bearing. In the present study, a turbopump with a port for installation of a fiberscope to be placed on a bearing inner ring for direct observation was developed.

Also, oil-lubricated bearings are candidates which would greatly extend engine lifetime. Normal temperature fuel (ethanol, kerosene, and so on) is used for this purpose. When using a kerosene-type fuel, a longer lifetime can be expected because
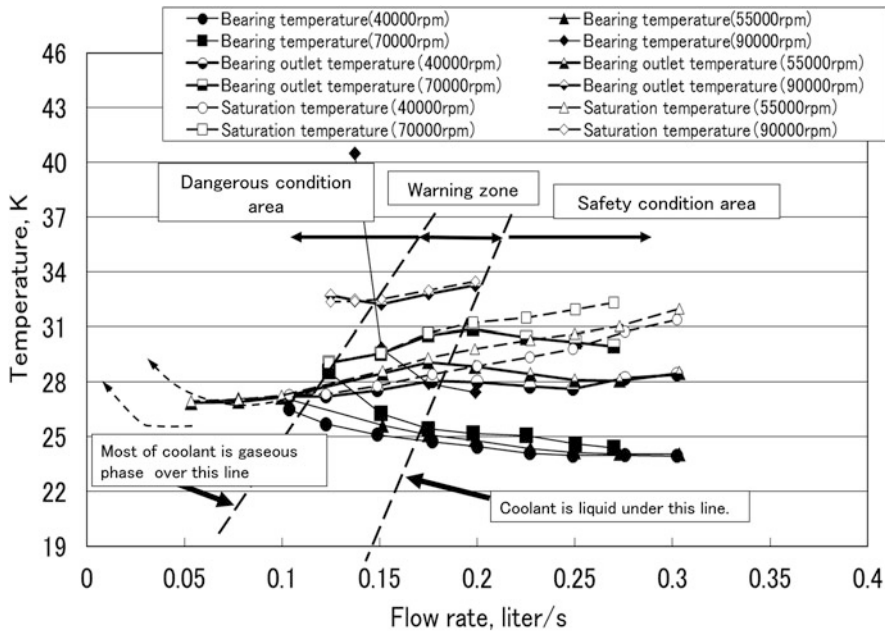
Fig. 9 The relation between the coolant flow rate and bearing temperature in liquid hydrogen

kerosene itself has a lubrication action. Bioethanol is also an environmentally friendly candidate of fuel. However, it is difficult to operate a bearing at high speed in ethanol for a long time because of its poor cooling capacity, and, what is worse, highly efficient synthetic lubricating oil dissolves in ethanol.

4.2   Shaft Seal for Turbopump

The turbopump shaft seal for the rocket engine must stop the leakage of the fluid which has a strong chemical reactivity. Shaft seals can be categorized into two groups, i.e., contact-type seals such as mechanical seals and segmented seals and noncontact-type seals such as labyrinth seals, wear-ring seals, and floating ring seals. The flow of fluid cannot be fully stopped by any type of shaft seal (Fig. 10). In other words, the shaft seal is a mechanical element for decompression.

As for the contact-type seal, there is a very low quantity of leakage and seal performance is high. However, it has a short lifetime as abrasion cannot be avoided. Moreover, according to the high heat of the strong chemical reaction and high-speed sliding, there is a danger of excessive abrasion and explosive burning. The test results of the relation between the lifetime and the leakage flow rate of the contact-type mechanical shaft seal are shown in Fig. 11. At the mechanical shaft seal, abrasion by contact increases leakage during operation. Also, because abrasion

Floating Ring Seal

Labyrinth seal

Bellows Seal
(Mechanical Seal)

Segment seal
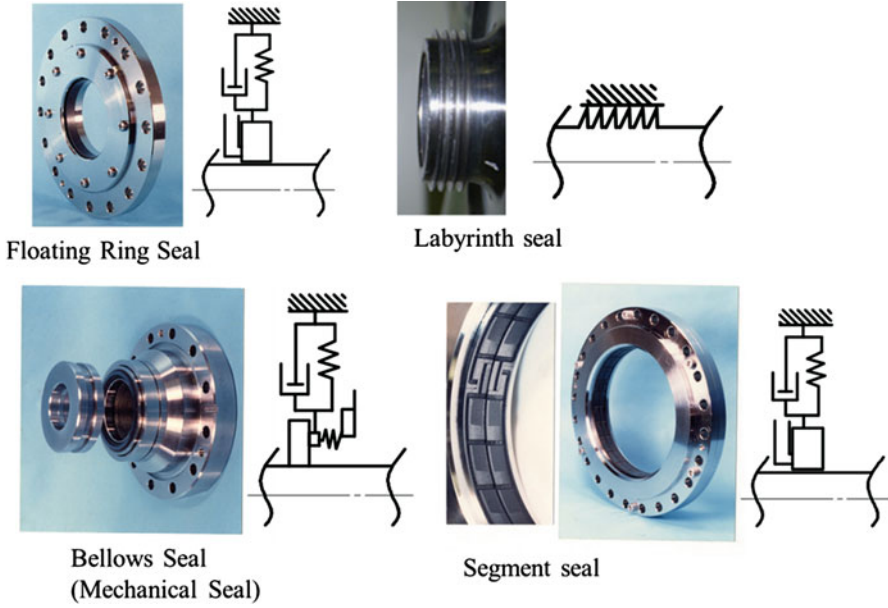
Fig. 10 Seals for reusable turbopumps

Black marks : Continuous operation
White marks : Contact surface was cleaned every 100 km
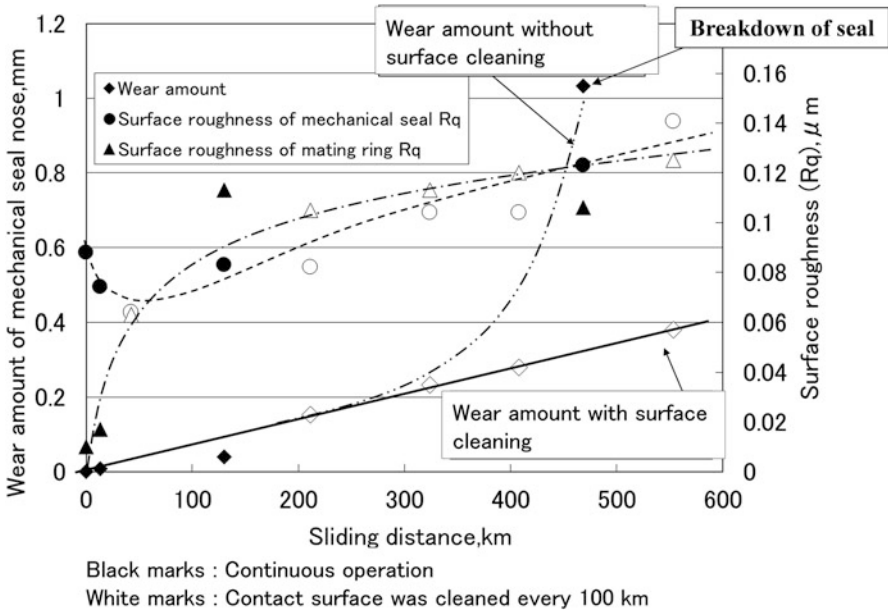
Fig. 11 Abrasion characteristics of mechanical seal nose

powder occurs, abrasion might be accelerated, but lifetime can be extended by removing the powder. When using a contact-type shaft seal in a liquid oxygen environment, liquid oxygen compatibility must be checked beforehand. When using a reusable rocket engine, it is necessary to understand shaft seal lifetime and to replace the seal regularly. Recently, efforts are being made to develop a reusable rocket engine in which replacement of the shaft seal on site is possible.

As for the noncontact seal, there is no high-speed sliding part during operation, and lifetime is quite long, but because the quantity of leakage is not small, seal performance is not high. When shaft seal leakage occurs in the turbopump in the engine precooling process of the launch preparation, there have been many engines of this structure in which the propellant has leaked outside of the engine, which is potentially dangerous. To prevent this problem, the contact-type of mechanical shaft seal is suitable, but unfortunately, it has a short lifetime and is not suitable for a reusable engine. Therefore, a combination of noncontact seals was applied to the reusable engine which required long life. As a shaft seal which satisfies the requirement of long life during operation and leakage prevention during precooling, a mechanical shaft seal which operates using the difference of the turbopump internal pressure (lift-off seal) is a practical option. As for this seal, in an engine which requires throttling, the change of pressure difference is large and the operation is not stable. A lift-off seal, which operates by pressure from outside, has been developed and is being subjected to engine tests recently. The basic structure of the lift-off seal is shown in Fig. 12. By supplying pressure in the space of the double bellows from outside or in the high-pressure part inside, leakage can be mechanically stopped.
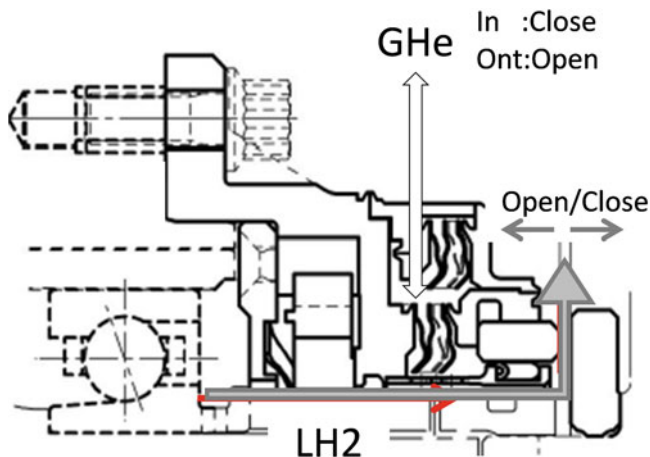
Fig. 12 Lift-off seal

4.3 Valve

Because there are many elements such as the drive mechanism and the seal mechanism, durability, such as of the valve, is an important subject, as the valve is a very important part of a reusable engine. The valve is operated under severe environmental conditions such as cryogenic temperature which controls propellant, high temperature to control turbine drive gas, and the vacuum in space. For the control valve, because the contact pressure of the drive mechanism is the element which determines the size and the weight of the valve, research on solid lubrication film in an extreme environment is being conducted. As for the valve for the reusable rocket engine, health monitoring of the valve is important. Specifically, in case of the control valve, monitoring of the valve position, the driving torque in the flight, and so on are very important for maintenance and sound operation. Also, in the case of the solenoid-controlled valve, monitoring of the temperature rise of the solenoid and the quantity of the electric current is important.

5 Technology Demonstration of the Reusable Rocket Engine

The key points for which care must be taken when designing a reusable rocket engine were explained in the previous sections. In this section, a technology demonstration of the recently developed reusable rocket engine is introduced.

5.1 Mission of the Reusable Sounding Rocket (RSR)

The Institute of Space and Astronautical Science (ISAS) of JAXA has been conducting research of the Reusable Rocket Vehicle Test Program (RVT) since 1998. The purpose of this research is to acquire operation technology for the reusable rocket which will be necessary in the future. The whole vehicle, including the fuselage and the engine, has been manufactured and subjected to flight testing. In a flight test conducted in 2002, this vehicle reached a height of 42 m, hovered for a while, and then landed vertically (Fig. 13). Technology demonstration of the reusable sounding rocket has been proceeding since 2010 to further develop the previously obtained technology. To further develop RVT technology, element technology tests and technology demonstration of the reusable sounding rocket have been conducted since 2010 (Fig. 13). The RSR is a suborbital type of reusable rocket. Figure 14 shows a vehicle image of the RSR and a typical flight operation. This vehicle lifts off vertically and goes up to more than 100 km, reenters in a nose-first position, then turns over, reignites, and lands vertically. Specifications of

Fig. 13 Flight test of RVT (*left*) and image of reusable sounding rocket (*right*)
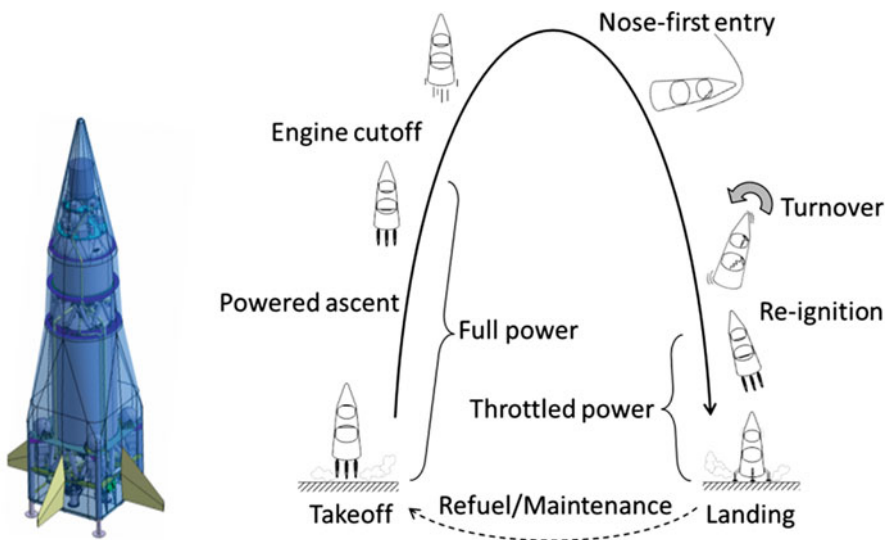
Fig. 14 Reusable sounding rocket (RSR) and its flight pattern

RSR and engine performance are shown in Table 2. So far, an expendable type of sounding rocket with a solid rocket motor has reached a height of about 300 km. Many experiments and observations in high-altitude atmosphere have been done. This project is significant in that using a sounding rocket with a stable customer is the first step toward the realization of reusable space transport system.

Table 2 Specifications of reusable sounding rocket (RSR) and engine performance

Reusable sounding rocket		Engine performance	
Payload	100 kg	Propellant	LOx/LH$_2$
Altitude	>100 km	Thrust	41 kN
Vehicle height	13.5 m	I$_s$	320 s
Vehicle diameter	3.0 m	Burning pressure	3.4 MPa
Total weight	10,750 kg	Mixture ratio	>4.7
Dry weight	3814 kg	Throttling	40–100 %
Reusability	100 times	Reignition capability	Multi
Turnaround time	24 h	Engine cycle	Expander bleed
Flight time	550 s		
Number of engines	4		
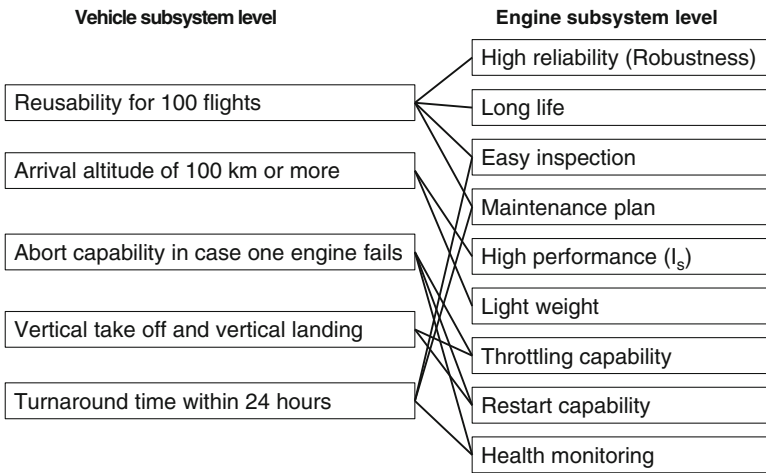
Fig. 15 Mission requirements for RSR and necessary functions for engine

5.2 Required Functions for Engine of Reusable Sounding Rocket

To achieve the mission of a RSR, a wide range of features are required of the engine which were not required in the former expendable rocket. Figure 15 shows the features which the engine should have to realize a mission request for a reusable sounding rocket. The mission demands on the whole rocket system are listed on the left. Nine kinds of requests to be met by the engine subsystem are listed on the right.

5.2.1 Vertical Takeoff and Landing

To realize vertical takeoff and landing of the space transport vehicle, the throttling performance of the engine is important. Specifically, at the time of the vertical landing, tender throttling becomes necessary according to change in the acceleration of the descent. Also, in the return phase, fuel is in an approximately empty condition except for the spare fuel, and the engine needs the ability to control the light fuselage in case of landing. That is, a wide range of throttling ability is required. In addition, a weightless environment in the coasting phase in space may be required, and all engines must be cut off. Reignition ability is necessary after that for return.

5.2.2 Reusability for 100 Flights

For the purpose of realizing 100 reuses of the engine, the engine for the reusable sounding rocket must possess good reusable operation by both enhancement of longer life of the parts and inspection and replacement of parts based on a maintenance plan. To realize the ease of inspection is an important feature.

5.2.3 Abort Capability

Not losing an engine and a fuselage even if they develop troubles is necessary to realize cost efficiency, which is the main merit of reusable transport. For this purpose, a health monitoring feature to detect signs of trouble and to avoid accidents is necessary. A reusable sounding rocket has four engines which can generate a thrust of 41 kN. When one engine breaks down, this concept makes it possible to return to the landing place with the remaining three engines.

5.2.4 Turnaround Time Within 24 Hours

To realize this, the engine for the reusable sounding rocket follows the operation procedure of aircraft, and the operation and maintenance plan for the whole engine and components is specified. The status of the engine can be confirmed by health monitoring during and after the flight. For this purpose, a check port and check jig for the engine are necessary for ease of inspection.

5.3 Engine Design of the Reusable Sounding Rocket

To achieve an engine which can realize the mission of the rocket as described in Sect. 5.2, the following features are needed for the reusable engine.

5.3.1 Long Life

Key components incapable of reuse 100 times were extracted: the wall between the cooling channel and the inner wall of the combustor (the heat flux being high near the throat) and the bearing and shaft seal used for the turbopump. Control of lifetime was found to be possible by limiting the surface temperature of the inside of the combustion chamber wall (the flue gas side). A combustor was designed that could tolerate being used 200 times by utilizing this knowledge and suppressing the combustor inside temperature to the limited value.

The upper limit with OTP number of rotations was fixed as the number of rotations possibly for 100 reuses of the contact-type mechanical seal. A bearing capable of 100 reuse times was developed based on post research results and using the ball bearing of SUS440C. Next, as for the fuel turbopump (FTP), a hybrid ceramic ball bearing which used a silicon nitride (Si_3N_4) balls was selected to realize a rapid rotation and a longer life.

5.3.2 Easy Inspection

To detect abrasion and other damage, check ports for places such as the nose part of the mechanical shaft seal of the turbopump and the inner ring tracking surface of the bearing were installed. Also, a design which facilitates the replacement of important elements such as bearings, shaft seals, and so on is important. A photograph of the turbopump bearings from the inspection port is shown in Fig. 16.

5.3.3 Lightweight

The weight of a component generally tends to increase when high efficiency is pursued. Engine weight, too, tends to increase when attempting to achieve a longer

SUS440C balls (oxygen turbopump) Si_3N_4 balls (fuel turbopump)
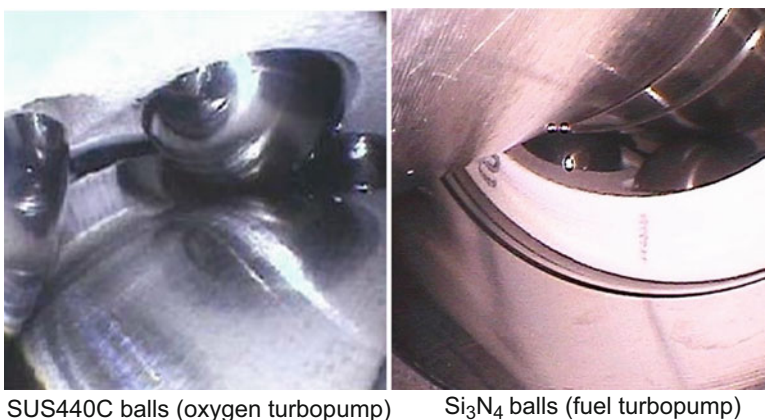
Fig. 16 Quick observation of bearing inner ring and balls by fiber scope

engine life. First, by setting burning pressure at a high level as a trade-off with superior performance, the I_s becomes high, whereas it is possible to endure high pressure, the weight of the combustor external cylinder being thick and heavy. Therefore, a burning pressure of 3.4 MPa is chosen to optimize carrying capacity and lifetime. Besides, the weight of the electric system component as part of the total engine weight compared with such weight in conventional expendable space transport is high because there are many electronic devices to support the health monitoring feature.

5.3.4 Throttling Capability

Need necessitates a low engine expansion ratio to prevent delamination in the nozzle, and low thrust occurs and specific impulse declines as a result. To prevent the decline of the specific impulse, 40 % of thrust is set as the throttling range of the engine thrust.

5.3.5 Restart Capability

With the reusable sounding rocket, reignition in the atmosphere is possible for the first time. However, blockage by ice at the surface of the injector or in the pressure port may occur. These problems are taken into consideration by thermal management at the time of coasting after burning, and the quantity of purged gas is determined.

5.3.6 Health Monitoring

Technology to improve system reliability of the space transport is very important. In comparison with conventional expendable space transport vehicles, many sensors are used in reusable space transport vehicles, thus greatly increasing the weight of the electric system. Simplification of the optimization and inspection logic of the sensor position and number are important problems for future work.

5.3.7 Robustness

When designing an engine based on these criteria, an operation point is selected that does not violate criterion after considering manufacturing and operation point errors in construction, a loose leeway above 6σ being secured on both sides of the operation point range.
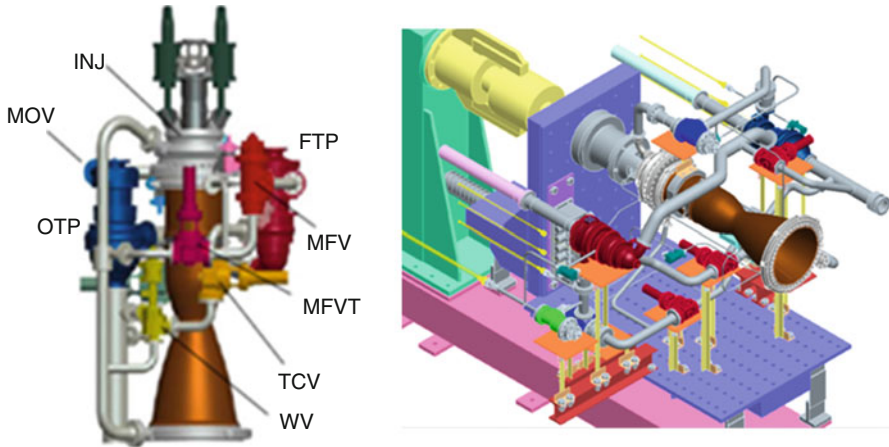
Fig. 17 RSR engine (*left*) and its BBM-type demonstration engine (*right*)

5.4 Technology Demonstration of the Engine of the RSR

Based on consideration of the factors so far described, a reusable engine for technology demonstration was designed and manufactured (Fig. 17). Schematics of this engine is shown in Fig. 18, and specification is described in Table 2. As for the engine system burning test, the purpose of the first series was to grasp the constancy ability and to confirm three design conditions of 40 %, 70 %, and 100 % of thrust by a basic performance audit test. The purpose of the second series was confirmation of the realization of various features required of engine for the reusable sounding rocket, conformation of the operation and so on, to imitate throttling response speed and reignition in various flight sequences by an advanced feature audit test. As for lifetime audit tests and engine operation cycle tests, actually more than 100 tests were carried out to confirm reusability of 100 times and durability.

Figure 19 shows the first series of tests of throttling capability with 100 % and 40 % of thrust level. There is no problem for either condition, and no flow separation occurred at the nozzle exit. Figure 20 shows the assumed throttling pattern of a real reusable sounding rocket flight. The test following this throttling pattern was successfully completed. Some other patterns were checked by simulating real flight, such as abort mode with failure of one engine during the assent phase necessitating safe landing by the other three engines. Every test went as planned, and the final repetition tests demonstrated that more than 140 reuses were possible.

Among the series, nondestructive inspection by X-ray computed tomography of the combustor was implemented, and the status of the transformation of the combustor cooling channel and the occurrence of micro-cracks were observed. In the same way as in the basic performance test and the advanced features test, measurement of the change of the nozzle throat diameter in every test as well as of
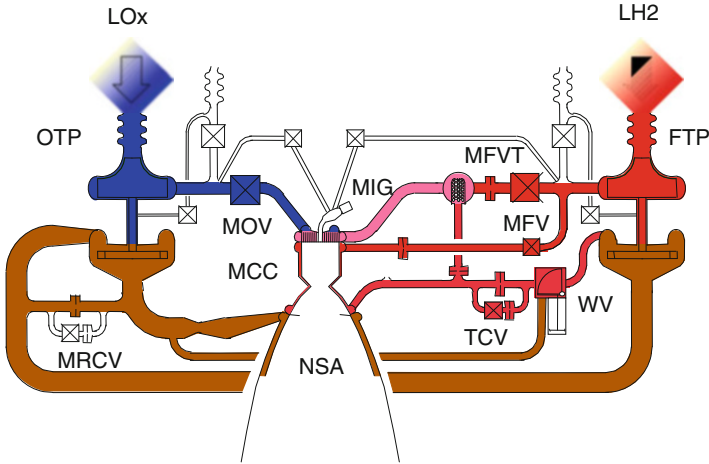
Fig. 18 Schematics of RSR engine (coolant breed cycle)
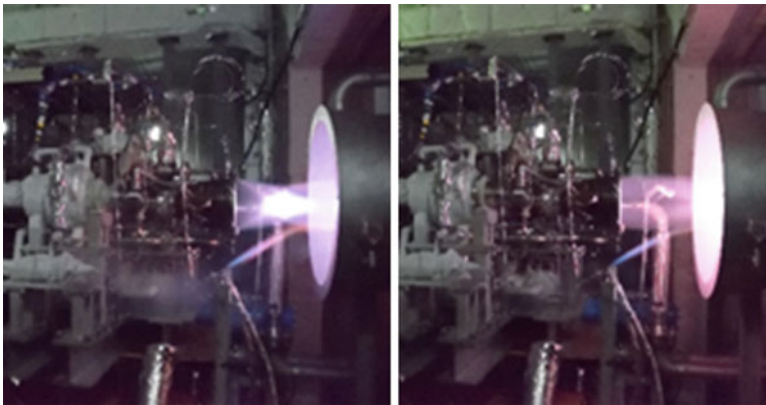
Fig. 19 RSR engine firing test (*left*, 40 % of thrust; *right*, 100 % of thrust)

the change of the cooling channel board thickness using an ultrasonic flaw defector and so on was performed, and verification data of the heat fatigue damage of the combustor were accumulated.

5.5 Future Plan for Reusable Sounding Rocket

The technology demonstration of the engine for the reusable sounding rocket was finished in January 2015. Technology demonstration of the fuselage system by 2016 is planned, as is study of factors involved in launch and operation. In the next stage,
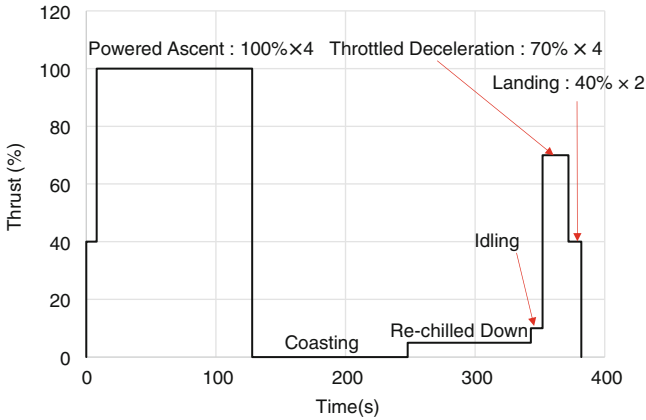
Fig. 20 Flight simulation test with real flight throttling pattern

the operability of the reusable sounding rocket with four engines in one fuselage at launch and during operation will be evaluated with a combined cluster burning test of the fuselage at various altitudes.

6   Summary

The current status of research and development of a reusable rocket engine in Japan was reported. There is still room for refinement of the technology employed for the reusable rocket engine. Parallel with development of the reusable sounding rocket, which represents a step forward in technology, we are aiming to realize a future reusable transport system.

References

1. Kobayashi S (2012) Lessons learned from aircraft accident. Kodansya, Tokyo
2. Kure H et al (2010) Study on methodology for total design management. IHI Eng Rev 43(2):77–88
3. Gordon S, McBride BJ (1971) Computer program for calculation of complex chemical equilibrium composition rocket performance, incident and reflected shocks and Chapman-Jouguet detonation, NASA-SP-273, NASA
4. MacGregor CA (1982) Reusable rocket engine maintenance study, NASA CR-165569, NASA
5. Taylor MF et al (1968) Correlation of local heat-transfer coefficients for single-phase turbulent flow of hydrogen in tubes with temperature ratios to 23, NASA TN D-4332, NASA
6. Bartz DR (1968) Survey of relationships between theory and experiment for convective heat transfer in rocket combustion gases. In: Penner SS (ed) Advances in rocket propulsion. AGARD, Manchester, UK

7. Fedorov V et al (2006) The chamber cooling system of RD-170 engine family: design, parameters, and hardware investigation data. AIAA-2006-4363, 42nd Joint Propulsion Conference, Sacramento, 9–12 July
8. Valler HV (1979) Performance of a transpiration-regenerative cooled rocket thrust chamber, Aerojet Liquid Rocket Company, NASA CR-159742, NASA Lewis Research Center, Cleveland
9. May L, Burkhardt WM (1991) Transpiration cooled throat for hydrocarbon rocket engines, Aerojet Propulsion Division, KEE6-FR, NASA Marshall Space Flight Center, Huntsville
10. Haeseler D et al (1998) Experimental investigation of transpiration-cooled hydrogen-oxygen subscale chambers. AIAA 98-3364, 34th Joint Propulsion Conference, Cleveland, 13–15 July
11. Quentmeyer RJ (1990) Rocket combustion chamber life-enhancing design concepts. AIAA-90-2116, 26th Joint Propulsion Conference, Orlando, 16–18 July
12. Katorgin BI et al (2003) LOx/Kerosene oxygen rich staged combustion rocket engine design and life issues. In: Proceedings of fifth international symposium on liquid space propulsion, Chattanooga, 27–30 October
13. Kasper HJ, Notardonato JJ (1979) Effect of low-stiffness closeout overwrap on rocket thrust-chamber life. NASA technical paper 1456, NASA Lewis Research Center, Cleveland
14. Popp M, Schmidt G (1996) Rocket engine combustion chamber design concepts for enhanced life. AIAA-96-3303, 32nd Joint Propulsion Conference, Lake Buena Vista, 1–3 July
15. Niino M et al (1985) Life prediction of CIP formed thrust chamber. Proceedings of IAF'85, IAF-85-192, 36th IAF, Stockholm, 7–12 October
16. Murphy M et al (1986) Effects of oxygen/hydrogen combustion chamber environment on copper alloys. NASA CP-2437, vol II, Advanced Earth-to-Orbit Propulsion Technology 1986, NASA Marshall Space Flight Center, Huntsville, 13–15 May

Part X
Further Applications
of Energetic Materials

Some Civilian Applications of Solid Propellants

Vladica Bozic and Boris Jankovski

Abstract The history of rocket (and thus also propellant) development is closely related to military applications. But besides military applications (bombardment), from the beginning of development, rockets with solid propellants have found a variety of civilian uses like signaling and fireworks. Modern solid propellants have evolved the field of application of rocket missiles for civil/scientific use to sounding rockets and launch vehicles. As solid propellants after ignition can generate large quantities of gas for a short time, it can also be used to produce force (i.e., mechanical work) or power. These attributes have led to the proliferation of commercial application in recent years in different safety devices with special purposes in the automotive and aviation industries, among them inflators in air bags. Other applications involved various separation mechanisms, pyrotechnic valves and actuating devices, emergency systems, and devices designed to ensure auxiliary propulsion. Three applications in the civilian sphere are reviewed in this chapter in more details: the small low-altitude sounding rockets which are used to prevent hailstone formation in turbulent atmospheric conditions and in this way damage on the crops; gas generators suited for fire suppression, called solid propellant fire extinguishers, where gas produced by controlled combustion of solid propellant is discharged directly into the fire-affected area in a non-propulsive manner and suppresses fire via a combination of different physical mechanisms like dilution, cooling, flow rate, and chemical effects; and solid propellant gas generators applied in systems for emergency surfacing of submarines, ships, or any other sinking objects.

V. Bozic (✉)
Ministry of Environment, Belgrade 11000, Serbia
e-mail: vladicabozic@gmail.com

B. Jankovski
VEDA, Skoplje 1060, Macedonia

1 General Introduction

The earliest known use of energetic propulsion materials dates from 1232 when the Chinese used arrows fastened with rocket cartridges ("fire lances" or "fire arrows") in the warfare against the Mongols. As military needs have stimulated most advances in rocket technology, the history of rocket (and thus also propellant) development is closely related to military applications. But besides military applications (bombardment), from the beginning of development, rockets with solid propellants have found a variety of civilian uses like signaling and fireworks. Due to excellent performance characteristics, reliability and safety, as well as relatively simple and economic manufacturing and usage, modern solid propellants have evolved the field of application of rocket missiles for civil/scientific use to sounding rockets and launch vehicles. A sounding rocket is a projectile that is launched into the atmosphere for different applications, mainly to study unexplored features of the upper atmosphere and near-Earth orbit such as weather, climate, and environmental observation and forecasting. A launch vehicle is a rocket-powered vehicle used to lift satellites and spacecraft into orbit around the Earth.

Besides the application in rocket motors, energetic materials – mainly different kinds of solid propellants – have found additional applications in various devices with special purposes in the automotive and aviation industries. As solid propellants after ignition can generate large quantities of gas for a short time, from the Second World War, they have been applied in gas generators, devices where gas is used to produce force (i.e., mechanical work) or power. These attributes of gas generators have led to the proliferation of commercial application in recent years in different safety devices, among them inflators in air bags. Other applications of gas generator systems involved various separation mechanisms, pyrotechnic valves and actuating devices, emergency systems, and devices designed to ensure auxiliary propulsion. Due to high combustion temperature, solid propellants also found application in the destruction of hazardous biological or chemical agents and persistent pollutants. Additionally, they can be used for enhanced oil recovery, which relies on various processes including heat to increase the amount of fuel extracted from underground reservoirs. In this chapter, several applications of solid propellants in the civilian sphere have been described in more details.

2 Anti-hail Rockets

Hail is defined as precipitation in the form of small balls or particles of ice with a diameter of at least 5 mm falling from a cloud either separately or agglomerated into irregular lumps [1]. Hailstorms are among the most devastating weather manifestations. In many areas of the world, hail causes enormous damage to agriculture, particularly fruit orchards, grain fields, and property, with the cost of hail damage amounting to billions of dollars [2]. The devastation encouraged

operational hail suppression activities which are to be undertaken in many countries. Among these activities is a cloud seeding method based on the addition of artificial ice-forming nuclei by utilizing special rockets.

2.1 Hail Formation and Suppression Techniques

Hail is usually developed in tall convective clouds, cumulonimbuses (CB), when evaporated surface water is carried aloft by warm, rising air and reaches cooler, higher altitudes, where it condenses into water droplets. Caught in strong updrafts, the droplets reach the upper portion of the cumulonimbus clouds where the temperature is below freezing, and they become supercooled. Tiny nuclei of matter like dust or pollen whipped up by surface winds also ascend in the warm air, and when supercooled water droplets collide with these particles, ice crystals are formed around these condensation nuclei. The further growth of ice crystals to hailstones is a result of the collision and coalescence of ice particles and supercooled water droplets inside a cumulonimbus cloud, which add layers of ice. When the hailstones (usually roughly spherical in shape) become too large and heavy to overcome the updrafts, they fall out of the cloud with high velocity and reach the ground (Fig. 1). One possibility for reducing hail damage is to use protective screens above the crops, but it can be only applied on small areas and have limited influence on the crop climate. Also there are problems of mounting the nets and of reduced accessibility to the crop [3].

In order to prevent or reduce the damage caused by hail on large areas, primarily in agriculture, two hail-suppression techniques are used. They are based on the concept of transformation of dangerous convective cloud so as not allow the formation of large hailstones. Classical approach is based on the use of brute force in an attempt to weaken or to destroy the formed hailstones by way of explosions, with firing of cannons and rocket explosions [4, 5]. Brute force method was not proven experimentally, as there is no evidence of effective protection against hail, but in recent years, anti-hail activities using cannons to produce loud noises have reemerged in some countries.

A modern approach is to try influencing the hail formation process by seeding the clouds with artificial ice-forming nuclei. Usually, the number of ice crystals in a cloud is small, and they then begin to rapidly grow by collecting subcooled liquid droplets to hailstones with large sizes. As a consequence, large hailstones develop which ascending air motion (convection) cannot hold, so that they fall with high velocity and reach the ground in a very short time. The addition of high concentrations of artificial ice-forming nuclei into the particular zone (supercooled parts) of cumulonimbus significantly increases ice embryo concentration so that the artificial and natural ice particles compete with each other for available liquid water. The supercooled water redistributes between all hail coagulative embryos, thus resulting in more and smaller hailstones. The smaller hailstones fall with a lower velocity through the layer of warm air below the freezing level, thus spending
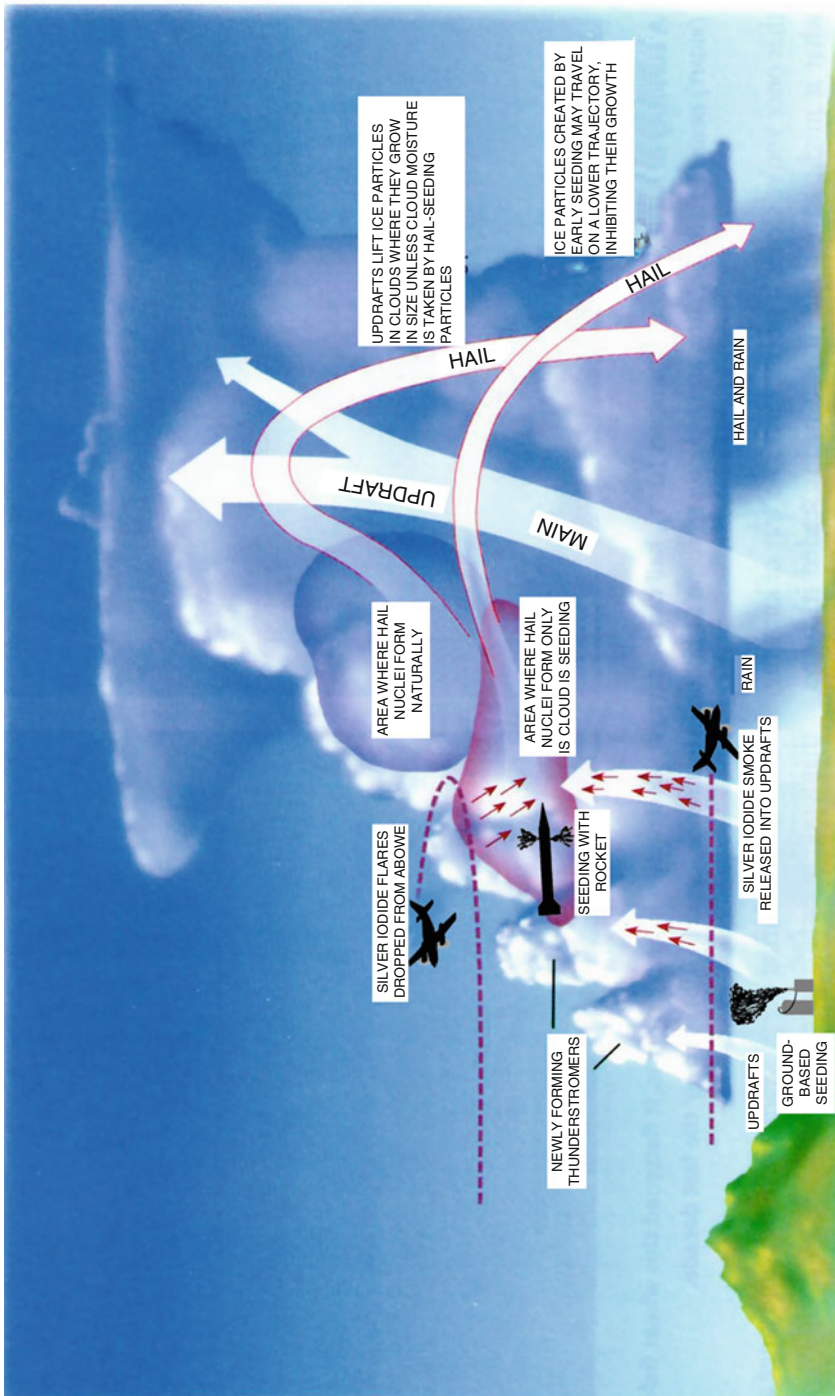
Fig. 1 The formation of hailstones and seeding methods

more time in the positive temperature domain, which further melt small stones and decrease their size. Even if they did not melt completely falling to the ground to form rain or sleet, by the time the hailstones reached the ground, they would be too small to do any serious damage – this is called beneficial competition.

2.2 Cloud-Seeding Techniques

The method of the delivery of meteorological reagents which produce artificial ice-forming nuclei in clouds is called overseeding. For overseeding to be effective, artificial particles need to be present in the thundercloud in high concentration and prior to the development of hailstones, which means that the dispersion of artificial ice-forming nuclei should be performed in the areas with high supercooled liquid water content and weak updraft at the early stage of the development of hail dangerous clouds.

For the purpose of hail suppression with cloud seeding, a variety of active reagents are used in different parts of the world. The most common chemicals include silver iodide (AgI), potassium iodide, and dry ice (solid carbon dioxide). Liquid propane, which expands into a gas, has also been used [6–8]. The activity of such a chemical is strongly affected by temperature, as the temperature affects the rate of growth and shape of the ice crystals [7]. Since in nature ice droplets form at high altitudes, at temperatures between -10 and -15 °C, it seems the best results could be obtained with the injection of the meteorological reagent which produces ice-forming nuclei in the proper seeding area, the layer where the temperatures are between -5 and -10 °C, prior to hail development. As the strong updrafts provide new quantities of supercooled liquid water and carry the ice crystals to the upper part (anvil) of the cloud, the best effect is achieved if ice-forming nuclei are introduced at regular intervals during the whole period of hail danger.

The efficiency of hail suppression system of overseeding is strongly dependent on the technical devices in use, and the way they are used. In the world there are three methods for cloud seeding with active reagents to manipulate the hail embryo formation process and thus limit the growth of hailstones: from aircrafts, ground-based sources, and rockets or artillery (Fig. 1).

Aircraft seeding is based on using specially modified planes, which fly into storms and spray a chemical into the clouds to which supercooled water droplets attach themselves and thus reduce the damage on the ground. Aircraft can fly below the clouds equipped with silver iodide flares mounted on frames extending aft of an airplane wings, which produce fine particles by burning, or above the cloud dropping AgI flares into clouds from a rack mounted underneath. In the first option, the delivery of nuclei to the upper part of the cloud is entrusted to the cumulonimbus updraft, while in the second option, good timing and having aircraft in the right area at the right altitude are crucial factors in effective cloud seeding. Hail suppression by plain seeding has been applied in the USA since the 1960s, and later in some other countries like Austria, Germany, Greece, Slovenia and its results are still uncertain [9–11].

The second method is raising the average concentration of nuclei in a limited region by generators on the ground when a menacing cloud front is approaching. This is performed by a network of generator stations with a typical mesh size of about 7 km [12, 13]. The generator consists of an air container filled with a silver iodide–acetone solution, which vaporizes and goes into the burner chimney, where it after burning and abrupt cooling forms AgI crystals of size 0.06–0.08 µm. Again the delivery of nuclei at cloud top level is entrusted to convective updrafts. As the generator will be started prior to the start of hail formation, the national weather service must be involved to deliver a local forecast of general hail probability, 4 h ahead. When such a forecast is given, a network of about a hundred local volunteer stations is alerted to start up their burners. Such surface-based seeding networks have been set up in southern France, Spain, and Hungary. In the 1990s, analysis of the French network claimed 16–30 % hail damage diminishment [14].

The injection of ice nuclei directly into the supercooled parts of clouds by means of artillery or rockets was applied first by the Soviet experimenter Sulakvelidze [15] and later was spread to other countries of Eastern Europe [16]. In the first technique a projectile explodes and disperses the nuclei, while in the second the rockets carry a container with a pyrotechnic substance impregnated with meteorological reagent (usually silver or lead iodide). It passes through the cloud while burning and inject the nuclei directly into the upper cloud region where the hail develops, typically about 1 km^3 at 5 km height. Seeding with this device must be synchronized with weather radar and weather supervision system, which are used for the identification of different kinds of clouds such as hail or potentially dangerous hail. Governmental organizations and financing are required to set up this system as radar technicians and meteorologists are needed to indicate when and where to send the nuclei, and also artillery personnel must be available to fire the rockets in a precise manner at the right time. Spectacular success in hail reduction was reported by Soviet scientists and over 50 % hail diminishment was claimed. The benefit-to-cost ratios cited ranged from 4–1 up to 17–1. Later independent tests did not produce such great success of these procedures. Around 1980 a large experiment was organized in Switzerland with French and Italian support, using Soviet-style rocket delivery, and the seeding produced only 5 % less risk [17, 18]. Later evaluations indicate that in suitable climates, the hail damage reduction might be from 15 to 20 % [19].

2.3   Basic Design of Anti-hail Suppression Rocket

The anti-hail rocket seeding operation system consists of an anti-hail sounding rocket, a launcher, a launcher–controller, and other accessories. The launch pad is steerable with positioning able to cover 360° in azimuth and 85° in altitude before the rocket is launched. Launchers can be hand operated, semiautomatically controlled by commands from the panel of wireless remote control on distance or automatically controlled by commands from the computer via wireless communication. Rockets are placed on launcher conventionally or in tube, with or without
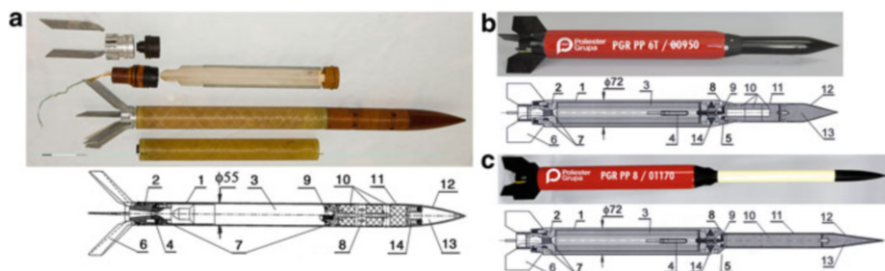
Fig. 2 Anti-hail rockets with grains made of (**a**) composite (**b**, **c**) double-base propellant

gas generator, and fired electrically. Second way of launching provides increasing of launch velocity, which enables the extension of operation range and reduction of surface wind sensitivity of the trajectory. This can be very important as the flight is realized in the rough air in the presence of the ground and ballistic winds and as these rockets usually are not supplied with the control system, which means that flight is controlled by initial orientation only.

Most of the rockets are single stage and may attain up to 8 km altitudes, but double-stage versions are also available. Meteorological reagent can be dispersed from the rocket usually as smoke from a pyrotechnic generator or much rarely in the form of the rocket exhaust plume if it is incorporated in the later/burning part of the solid propellant. As the rockets should be cheap, they are simple design with reduced grain and rocket weight, low price of each item of rocket, but safe and easy to handle even operating staff is not highly qualified. Typical anti-hail rocket consists of a motor and a container with pyrotechnic mixture (Fig. 2).

The rocket motor comprises a (1) motor case (combustion chamber), (2) nozzle, (3) propellant grain, (4) igniter, (5) connector, (6) fins, (7) and self-destruction system. The container consists of (8) spray nozzle with connection part, (9) timing system, (10) pyrotechnic generator with reagent, (11) body, (12) nose cone, (13) ballast, (14) and detonator (or safety system). The igniter is fixed inside the connecting piece of the combustion chamber, where the motor grain is placed.

Grain should have appropriate energetic performance and mechanical properties, but as operating temperature range is from −5 to +50 °C, other properties have lower requirements then in military application. In manufacturing of propellants, which should be cheap and based on low-cost ingredients, either double base or composite are used for grain production. Among composite propellants very often are used thermoplastic propellants, because in these binder systems, all ingredients are standard materials used in the chemical industry, which are commercially available and low cost.

Various forms of grains can be used in this application (Fig. 3). For example, the rocket shown in Fig. 2a used wire end-burning grain made from composite thermoplastic propellant, based on modified PVC binder with content from 25 to 31 % and ammonium perchlorate as oxidizer with content of 69–75 % mass percent.
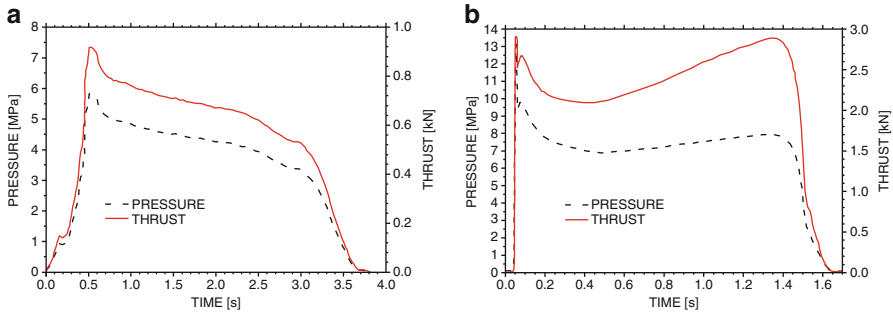
Fig. 3 Pressure-time and thrust-time curve of the grain shown on (**a**) Fig. 2a (wire end-burning free-standing grain) and (**b**) Fig. 2b, (**c**) (star free-standing grain)

Star grain made from extruded double-base propellant with around 56 % of nitrocellulose (12 % N) and 27 % of nitroglycerin is used in rockets shown in Fig. 2b, c.

When the propellant is exhausted, the container may remain attached to the rocket motor (Figs. 2a, b) or is separated due to the aerodynamic drag of the motor and then flies freely from the initial momentum (version shown in Fig. 2c). In both variants, meteorological reagent is ignited at programmed time, and the desired attitude and the artificial ice-forming nuclei begin to disperse continuously along the flying trajectory and spread to the surroundings rapidly, where in contact with the cold atmosphere, a reagent aerosol is formed. When the reagent pyro-mixture is completely dispensed in seeding area (end of active phase), a detonator is activated which disintegrates the rocket in the form of harmless particles or the safety system acts and lands the rocket which remains at low speed.

The potential seeding area is optimized according to meteorological influences on the rocket as well as the quality of the reagent. The best place to seed is in the front part of the arriving cumulonimbus cloud. Targets should be entire front-right parts of the cloud from the launcher sites located along the possible cloud path. Firing rockets in precipitation areas should be avoided.

2.4 Spreading of Reagents

According to experience, it seems that for relatively small rockets, the best seeding material is an AgI-based mixture [20]. The elevation also influences the reagent activity, as the best results are obtained with cloud-seeding between the –5° and –15 °C isotherms [21–23] which are usually at the 3–6 km altitudes [22]. To achieve this, the best elevations are between 45° and 65° at the base of the rocket ballistic properties (Fig. 4), as a result of isotherm studies. In dependence of type or rocket, the good results are obtained at the distances of 3–9 km, and the best are at 4–8 km (Fig. 5). With the assumed spreading speed of the reagent 10–20 m/s, the full volume is seeded in 1–2 min.
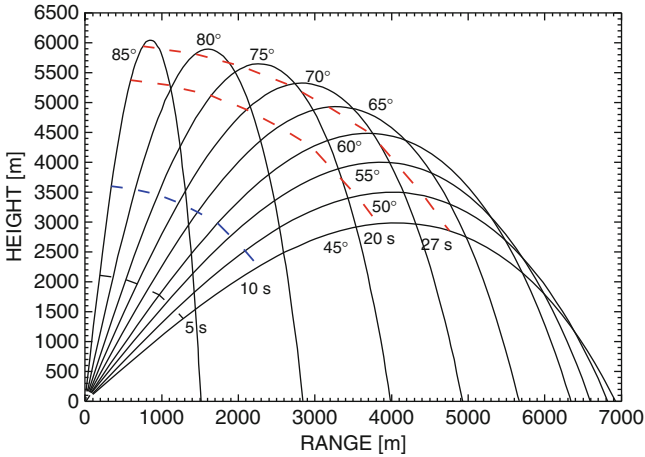
Fig. 4 Ballistic trajectories of the anti-hail rocket
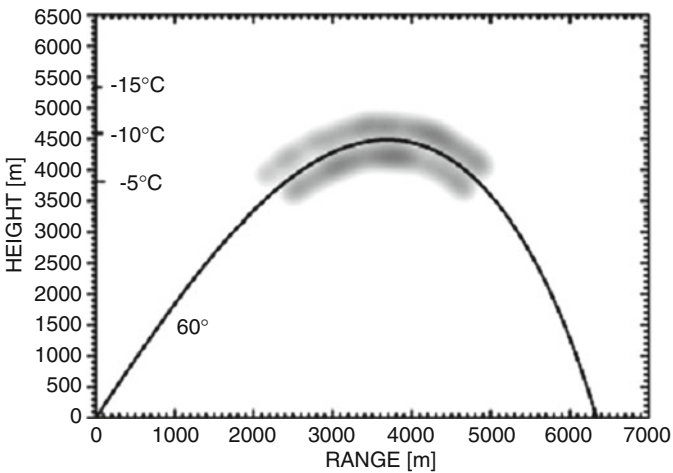
Fig. 5 Seeding area with single rocket

For the seeding of the hail-embryo growth zone, about ten active nuclei are required per 1 m³. In above rockets, the container is filled with 400 g Agl-based reagent with 12–20 % Agl. According to measurements, Agl-based mixture in rockets shown in Fig. 2b, c could release 4.1×10^{12} active nuclei per gram of mixture at $-10\,°C$, i.e., 1.6×10^{15} active nuclei per container. For emission average duration of 27 s, a mass flow rate of reagent is 15 g/s, i.e., 6×10^{13} active nuclei per second, which at an average flight speed of 200 m/s produces 3×10^{11} active nuclei per meter of path. As the seeding trace of the container is about 5.4 km long (50° elevation), a calculation shows that a container at $-10\,°C$ could seed about 16 km³. The rocket
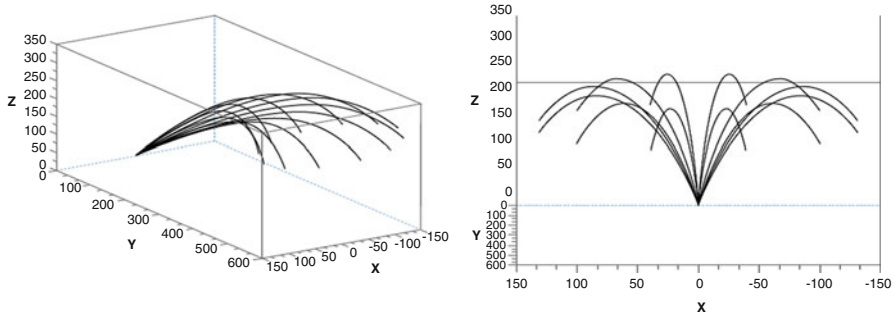
Fig. 6 Seeding possibilities of a single launching station

shown in Fig. 2a has the same flight parameters, but its reagent emitted 1×10^{13} active nuclei per gram of mixture at $-10\,°C$ (2.5 times more).

A hail suppression action is a race against time because of the great speed of hail processes in cloud systems. Although the method of delivery of active reagent – artificial ice-forming nucleus in clouds by rockets – enables the direct and continuous dispersion of reagent in seeding cloud areas, hail suppression rockets' launching time after the decision to act sometimes can be limited to 2 min. To obtain efficient seeding, anti-hail rockets can be fired simultaneously from the multiple rockets launcher in beams at different azimuths and elevations, which is shown in Fig. 6. After firing from a launching station, the distance between rockets increases with time, and as a consequence several seeding areas are formed which can be a unique space. For example, using 45–65° elevations and $-50°$ to $+50°$ azimuths beam, every launching station can seed a toroidal-shaped volume with radius from 1.5 to 10 km and 1.5–6.5 km altitude, respectively [20].

2.5 Conclusion

Modern sounding rockets intended for anti-hail suppression have been developed based on numerous studies in the interdisciplinary fields of meteorology, ballistics, and general rocket technology. Due to that, these rockets have low mass, ultimate precision, wide operation range, high launch altitude, stable performance together with easy handling, and reliability in use. Also, their hail-suppression operation systems have such characteristics as high nucleus forming rate, rapid nucleation, efficient catalyst effect, no pollution, and so on. Besides hail suppression, it can effectively perform other operations for weather modification such as increasing precipitation (rainfall/snowfall) or fog dissipation.

Hail suppression during the past period has been carried out with a better understanding of the meteorological processes as well as with the development of anti-hail seeding devices. However, further development of methodology and technology of hail suppression is required together with a better understanding of atmospheric processes.

3 Solid Propellant Fire-Extinguishing Technology

Research on efficient fire-extinguishing devices is a permanent activity of many scientific institutions and research and development teams of fire suppression system manufacturers. In addition to the necessary efficiency, today there are increasing demands for environmental compatibility of the extinguishing devices, in particular with respect to the ozone layer protection. For example, although bromofluorocarbons such as halon were widely used as fire-extinguishing agents with great success in many applications, because of their inherent ability to inhibit flames at low concentrations with no residue, they have been precluded for firefighting due to their deleterious effects on stratospheric ozone [24, 25]. The ban of halon has forced fire suppression system manufacturers to search for sustainable alternative, which led to the development of novel types of extinguishing agents and delivery mechanisms. Among those are gas generators based on solid propellants suited for fire suppression applications, called Solid Propellant Fire Extinguishers (SPFE) [26]. Solid propellant fire-extinguishing technology is based on controlled combustion of propellants, which after ignition generate large quantities of gas for a short time. This gas is discharged directly into the fire zone of protected area in a non-propulsive manner and suppresses fire via a combination of different physical mechanisms like dilution, cooling, and flow rate. Fire suppression effectiveness of SPFE systems can be increased by appropriate propellant composition, which enables during propellant combustion chemical active agents (or combustion radical scavengers) to be produced in the form of solid particles [27]. The chemical active agents are rapidly delivered directly into the fire zone by the high-pressure and high-temperature exhaust gases and act catalytically on fire combustion process. They are capable of interfering with and terminating radical processes associated with hydrocarbon combustion by removing (or "trapping") chemical radicals, such as hydroxide ions (OH•) and hydrogen ions (H•) from the combustion process. That makes SPFE an ideal platform for the creation and distribution of reactive powders, droplets, and dust and enables SPFE to have wider application than any other conventional fire extinguisher.

3.1 General System Description

Functioning of a SPFE (Fig. 7) is quite similar to that of a conventional stored pressure fire extinguisher (typically filled with nitrogen) in that both begin with electrical initiation. Upon receipt of an electrical signal, the SPFE initiator functions to ignite a booster charge. This booster, in turn, ignites the main propellant grain or pellets, which during burning causes internal pressure to increase rapidly and rupture a series of hermetic seals. The chemical reaction generates radical-trapping agents during the combustion inside the SPFE device which flows through a cooling area with granules along with the large amounts of simultaneously generated inert gases which consist mainly of CO_2, N_2, and H_2O, and then out of the openings of
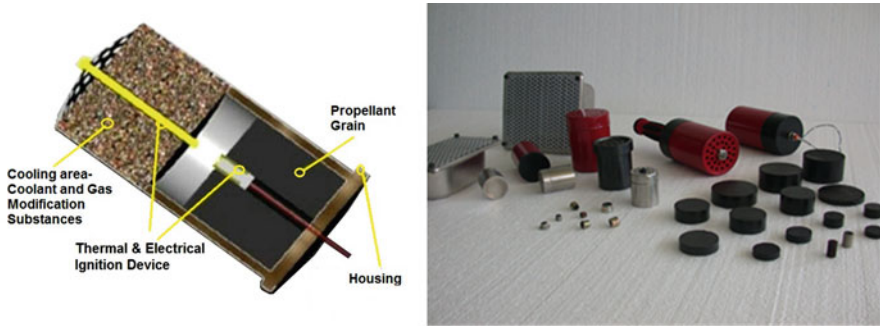
Fig. 7 Solid propellant fire extinguisher and SPFE devices and grains designed by VEDA

the extinguisher, emerging into the fire zone as a fine aerosol. Fine-grid metallic meshes and porous plates are usually used downstream of the agents to enhance the mixing between gases and agents prior to entering the distribution tube.

If SPFE and stored pressure fire extinguisher systems are compared, they both deliver large quantities of suppression agents in a rapid, mass- and volume-efficient manner. Maintaining high discharge rates requires maintaining a sufficiently high internal pressure during discharge process in either SPFE or a bottle of stored pressure fire extinguisher. Thus, internal pressure has maximum in the predischarge condition, and it decreases rapidly upon the initiation of the discharge process in both extinguisher systems. Where the solid propellant fire extinguisher differs from the stored pressure fire extinguisher is the ability to store firefighting agent at zero internal pressure and then to generate high pressures internally by the combustion of the solid propellant to form a blend of inert gases. Another difference between SPFE and stored pressure systems is the fact that the gases generated by propellant combustion are hot. Reducing the temperature of the exhaust gases would increase their fire suppression effectiveness, since they would then be capable of absorbing more heat from the fire. Additionally, cooler exhaust gases would have less impact on the structures and materials with which they contact during the agent discharge process. To achieve this, means in the form of grain (coolant) are placed in cooling area that can absorb heat when they are mixed with the hot combustion gases and in this way reduce the temperatures of exhaust.

The propellant used for fire-extinguishing application must meet requirements like reliable ignition, high yield of gas, neither toxic nor highly reactive combustion products, relatively fast gas production, adequate burning rate, low combustion temperature, chemical and thermal stability, reliable operation at low and high ambient temperatures, low costs, environmental protection, etc.

3.2 SPFE Fire Suppression Mechanism

Combustion or burning is the sequence of exothermic chemical reactions between a fuel and an oxidant accompanied by the production of heat and conversion of

chemical species. The release of heat can produce light in the form of either glowing or a flame. The chemical kinetics occurring in the flame is very complex and involves typically a large number of chemical reactions and intermediate species, most of them radicals. Flame combustion is often modeled using a one-step chemical reaction expression [28], whereby the rate of the reaction is related to the extent of collisions between fuel molecules and oxidizer molecules. This collision frequency is related to fuel concentration [fuel] and oxidizer concentration [oxide], according to

$$\text{Rate} = k \, [\text{fuel}] \, [\text{oxide}] \tag{1}$$

and the rate constant k is expressed as

$$k = A \, T_n{}^{\beta} \exp^{(-E_a/RT)} \tag{2}$$

where A is the pre-exponential factor, β is the temperature exponent, E_a is the energy of activation, R is the gas constant, and T is temperature. In general, Eqs. (1) and (2) indicate that the rate of combustion can be diminished by decreasing the concentration of the relevant species, [fuel] and/or [oxide], and decreasing the reaction temperature T.

A concise approach expressing the extinction condition in a global form was developed by Damkohler [27]. The Damkohler number D

$$D = \tau_{\text{res}} / \tau_{\text{chem}} \tag{3}$$

is given as the ratio of the residence time of combustion species in the combustion zone τ_{res} ($\tau_{\text{res}} \sim$ flame zone length/flow rate) and the characteristic chemical reaction time τ_{chem} ($\tau_{\text{chem}} \sim$ 1/reaction rate) from one-step model (Eq. 1). As ignition occurs when critical Damkohler number D_e is attained, the conditions of extinction are possible below a critical ratio, which can be achieved by decreasing τ_{res} or by increasing τ_{chem}. Shorter residence time can be achieved by increasing the flow rate through the flame zone. Cooling the mixture (see Eq. 2), diluting the reactants (see Eq. 1), flow rate effects, or chemical interference in the combustion process can produce longer chemical reaction times and influence extinguishing a fire.

Dilution or oxygen displacement is a physical effect which happens when the third gas is added to a fuel–air mixture, which leads to a reduction in chemical reaction rates. Cooling is a physical effect of reducing the flame temperatures below the point when combustion reaction can no longer be sustainable. As the rate of the combustion chemical reactions decreases rapidly with reductions in reaction temperature, quenching of combustion, or extinguishing a fire, can be achieved. Flow rate effect-flame strain is the flow of large quantities of high-rate gas which can result in the detachment of the flame from combustibles. It will reduce the residence time (high-velocity flow of products) and increase the chemical time (by direct alternating the reactant concentrations, oxygen displacement effect), resulting

in sudden extinction of flame. This effect is consistent with decreasing the residence time or flow time of fuel and oxidizer species in the combustion zone.

Hydrocarbon (e.g., various flammable fluids like oil, petrol, diesel, jet fuel, hydraulic fluids, natural gas) combustion is a process driven by reactive fragments known as chemical radicals, such as OH• and H•. Chemical effect inhibition is the addition of certain substances to combustion which can combine with, or "trap," these radical species and remove them from the combustion gases; it is possible to withdraw energy available to sustain the combustion process. These substances are called anticatalysts or inhibitors, and they can act through (1) chain-breaking (by stopping the chain reaction) and (2) "preferential oxidation" (by interruption of the oxidation process at the molecular level) [29].

3.3 Active Chemical Agents

Studies of chemical kinetics indicate that certain substances (like salts of alkali metals) can react with chemical radicals such as hydrogen or hydroxide and thus are capable of exerting an inhibiting effect on the hydrocarbon combustion reaction. The effectiveness is largely determined by the properties of alkali metals alone, increasing in the following order Li, Na, K, Rb, and Cs [29]. The effectiveness also varies depending on the radical attached to the metal and seems to be the greatest for radicals containing oxygen and for halides. The relative effects of halogen substitution on extinction properties follow the series I > Br > Cl > F. The best substances for extinguishing fires are the halides and sodium and potassium carbonates (K_2CO_3, KCl, Na_2CO_3, NaCl) due to the significant levels of their chemical activity [30]. By making suitable combinations of fuels and oxidizers in the propellant formulation of SPFE, alkali metal halides will be formed through propellant combustion process at very high temperatures in gaseous form. Later, they can condense when the temperature is decreased during exhaust, and solids which are formed tend to be of micron particle size. If these condensed by-products are directed to the fire zone (as aerosols because they are carried by other gaseous by-products of propellant combustion reactions), they will be consumed by the flame in a controlled but rapid fashion as flame temperatures would cause the thermal dissociation of these salts [31], e.g.:

$$MX \rightarrow M\bullet + X\bullet \qquad (4)$$

where M• stands for an alkali metal ion and X• stands for a halogen ion. Thermally generated atomic radicals (ions with an unpaired electron) can then combine with radical species present in the combustion process (hydroxyl and hydrogen ions) and remove them, inhibiting the homogenous gas-phase reaction and thereby terminating or quenching the combustion process.

Potassium carbonate (K_2CO_3) has shown greater efficiency than alkali halides (MX) [31], which can be explained by alkali atoms, rather than halogen atoms,

being the primary agents for chemical effectiveness. Also, the greatest activity was demonstrated by pyrotechnically generated powders of small particle size (below 30 μm) and gases of greater specific heat [32].

3.3.1 Propellant Composition

Although a number of potentially suitable binders (fuels) and oxidizers can be applied at SPFE, attention is focused on potassium nitrate (KNO_3) and potassium perchlorate ($KClO_4$), which are often used in pyrotechnic mixtures. These oxidizers upon combustion reaction with binder fuels are reduced to solids of potassium chloride and potassium carbonate (approximately 30–47 % of the effluent), the active fire suppressants, which immediately sublimate after dispersion into the atmosphere. As the chlorine atom is in a solid ingredient both before and after use, no halide containing compound can pollute the upper atmosphere. The main gaseous products are water, carbon dioxide, and nitrogen (and a small percentage of carbon monoxide in some cases although undesirable). The ozone depletion potential equals zero. The only global warming agents in the effluent are carbon dioxide (and carbon monoxide, in some), which constitute 33–40 % of the effluent. Thus, the global warming potential is 0.3–0.4, and the effluent of these propellants therefore is environmentally benign.

3.4 Experimental Techniques

Small-scale rocket motor tests are performed to evaluate burning stability and overall burning rate at different temperatures. After ballistic properties of propellants are determined, the potentialities of different compositions to suppress the live fire are tested by the direct application of SPFE (Fig. 7) in lab-scale and full-scale devices. In this way, different active agents in the exhaust can be investigated under conditions of comparable rates of applications. Also, these tests can determine the quantity required, the necessary rate of application, and the optimum methods of distribution for various fire-extinguishing propellants.

Closed tanks of different volumes are required to provide a platform where fire suppressants can be evaluated under repeatable test conditions (Fig. 8). Different fuels can be used to create fire in these tanks. The laboratory device is designed as a robust construction of stainless steel, because it must be used multiple times, but one side has a glass window intended for visual observation of fire phenomenon. Two tubes are placed on the lateral side of tanks, one to provide air inlet flow from a compressor and the other to discharge exhaust, thus creating internal airflow or venting if it is necessary during the tests. Typically, the values measured are pressure and temperature rise in the tank caused during aerosol generation or at any other place like generator case. A PC (personal computer)-based data acquisition and control system is used for collecting data during these tests. The pressure measuring

Fig. 8 Fire test tank

Fig. 9 Photograph made during the test

system consists of an externally mounted strain gage transducer, charge amplifiers, and a recording system. K-type (chromel/alumel (0–1370 °C)) exposed junction thermocouples are installed inside the container to measure the air/gas temperature in the tank. SPFE device, which is used in testing, is fixed to the appropriate position in the tank, depending on the type of the test. Grains are ignited by electricity from a remotely controlled ignition circuit. The power supply is switched to the ignition system of solid propellant fire extinguisher after a command from the personal computer.

Visual observation is very useful for analyzing the phenomena which occur during fire development and extinguishing (Fig. 9). Visual records of the fire suppression tests in tanks will show a difference between a dilution/cooling/strain extinguishment and chemical activity. The interference of the combustion reaction by the active agents in the exhaust, like the agent engulfing (or absorbing) the fire, as a function of time can be observed. In this way, the discharge time of the SPFE units can be measured together with time necessary to extinguish the fire.

Testing of chemically active SPFE technology in full-scale fire test fixtures is a representative of real fire protection applications with various flammable fluids and solids including gasoline, diesel, and natural gas as well as different types of plastic. Also, the evaluation of SPFE technology for various land vehicle applications is considered to be testing.

3.5   Results and Discussion

Testing has shown that there are many test variables that affect the amount of agent required to extinguish a fire. Typically, the fire intensity increases with the threat size, baffle-stabilized pool fires are more difficult to extinguish than spray fires, and gasoline fires generally require more agent than natural gas fires. Enclosed spaces with significant internal airflow or venting flush out fire suppressant more rapidly and are more susceptible to a fire reignition than spaces with minimal internal airflow and venting. Some spaces are more challenging as a result of their aspect ratio and other design-related features. Finally, different compositions of propellants greatly influenced aerosol reactivity as the composition and concentrations of active agents in the exhaust varied.

The direct method of testing clearly demonstrated the advantages of the addition of chemical activity to SPFE technology, as it improved the performance/weight of inert gas producing SPFEs at least two times [33]. The chemically active SPFE also outperformed the nitrogen-pressurized powder system which delivered chemically active powder and other non-halon fire suppression technologies, on a performance/agent weight basis. The most effective solid propellant composition tested is the one which delivers a mixture of an inert gas blend with potassium carbonate and potassium chlorate. Laboratory tests indicated that reducing the potassium carbonate by 50 % in aerosol exhaust results in a falloff in effectiveness, which is in light of reports from other workers [34, 35] indicating a saturation of chemically active agent effectiveness beyond some critical concentration. As a direct influence, the propellant weight of an SPFE can be decreased by 50–70 % with the addition of active additives. Additionally, incorporation of coolant compounds like $CaCO_3$ into the SPFE hardware was shown to be an effective means for reducing exhaust temperatures. Other coolant compounds can be used in conjunction with chemically active agents to increase fire suppression effectiveness of the whole exhaust. Although evaluation of relative importance of fire suppression mechanisms is very complex, it is estimated that chemically active SPFE technology extinguishes fires via a mechanism that is approximately 10 % dilution, 20 % cooling, 20 % strain, and 50 % chemical.

Test results also show the advantages of SPFE technology associated with a high velocity agent discharge. The rapid agent delivery (even 100 ms in SPFE designed for a rapid discharge) produces much higher momentum, thus augmenting the effectiveness of a chemically active agent by giving better flame front penetration

characteristics and better distribution throughout the enclosed space. As a result, the rapid agent discharge overwhelms other factors like internal airflow and venting that typically contribute to fire suppression effectiveness.

3.6 Conclusion

SPFE devices may be used as an alternative to different types of existing fire extinguishers with extinguishing agents like cartridge-operated or stored-pressure devices. They are able to produce large quantities of inert gases, such as nitrogen, carbon dioxide, and water vapor, in a very rapid fashion, thus providing dilution, cooling, and flow rate effects in fire suppression. Along with the inert gases, solid propellant fire extinguishers offer a highly effective means for delivering a chemically active agent [36]. Adding "radical traps" to the exhaust and delivering to the fire zone will provide chemical termination of the combustion process, hence increasing the overall effectiveness of the fire suppressant, due to synergistic interactions of dilution, cooling, flow rate, and chemical interference. Laboratory and full-scale testing demonstrated that SPFE delivery of chemical agents offers advantages of lightweight, small size, rapid action, and robust performance that is more efficient than is currently available in other fire suppression technologies. SPFE systems require no distribution lines and provide fire protection at volume/weight requirements comparable or better than previously used halon systems. Propellant formulations are lighter in weight than halon for comparable fire suppression effectiveness, but without the hazards associated with ozone depletion capability.

Also, SPFE systems should be employed in fire protection for a whole range of applications requiring an adequate concentration of extinguishing agent at enclosed space where fire is located (total flooding principle), such as volumes containing machines, electronic systems, and devices, like ships or process modules in the oil and gas industry, as well as vehicle engine compartments, where a small and lightweight fire protection system is desired. Additionally, the entire room's volume can be protected by a constant distribution of the extinguishing agent (aerosol), regardless of the fire location within the room (the floor or ceiling).

4 System for Emergency Surfacing of Sinking Objects by Gas Generators

To control its buoyancy, the submarine has ballast tanks and auxiliary, or trim tanks, which can be alternately filled with water or air (Fig. 10). In certain disastrous events, like uncontrolled ingression of water in the ballast tanks or even in the pressure hull with people (flooding) due to the ruptured hull, it is desirable to get

AFT TRIM TANK   MAIN BALLAST TANKS   FORWARD TRIM TANK
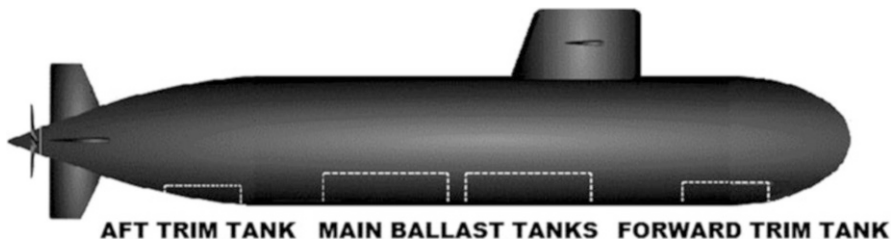
Fig. 10 Schematic representation of the ballast tanks at subsea vessel

the ship to the surface as quickly as possible. For this purpose it is necessary to establish a rescue system, which is capable of generating buoyancy whenever it is required [37]. Such submarine rescue system which ensures rapid surfacing in the case of emergence of submarine is developed based on rocket propellant-driven gas generators. Gas generators produce needed gas for blowing out the water from the tanks, thus causing the ship to become lighter (buoyancy exceeds gravity) and rise to the surface. The system can also be applied in other submarine emergency situations which are especially dangerous when the craft is submerged such as the outbreak of fire on board, failure of propulsion/maneuvering system, uncontrolled dive of the vessel due to the jamming of the hydroplanes in a diving position on account of hydraulics systems failure, or submerged collision. In these and other emergency situations which make it necessary to prevent submarine from sinking to its crush depth, the system can blow out the main ballast tanks in all diving depths and surface the submarine. Another application would be installation in the systems used for the lifting of sunken vessels, or other objects from the seabed, or for quick stabilization of capsized ships [38]. In the last case, this system can be installed on all ship types as a preventive measure, especially on cargo ships with large cargo holds and ballast tanks, e.g., tankers and bulkers, and on fishing vessels. It would allow the crew enough time to safely abandon the ship, help prevent a vessel from sinking, and as a consequence minimize the ecological threats that result from such an event (oil spills, etc.).

4.1   General System Description

The rescue system is composed of a number of propellant gas generator units and electronic components which activate the system (starter). The amount of gas that needs to be provided and thus the required number and position of gas generators for the submarine to return to the surface are directly dependent on the weight, volume and design of the sinking object, volume of the main ballast tanks, as well as the initial water depth. The gas generators are preferably located outside of the principal pressure hull of the craft, e.g., inside the ballast tanks, but not necessarily. Consequently, a sufficient number of gas generator units must be mounted inside or

around the submarine to provide rapid surfacing from depths to which submarines can dive (sometimes greater than 400 m), but the number of gas generators which will be activated depends on the actual diving depth. They will produce a hot gas that is cooled and guided by suitable gas ducts into the upper regions of the main ballast tanks of the submarine or variable tanks in the case of sinking vessels. The high-pressure gas entering the tanks rapidly evacuates the ballast water and thus creates buoyancy. Subsequently, the submarine or other object is stabilized, its attitude is restored, and it safely rises to the water surface. The gas generators in the aft or forward trim tanks stabilize the boat when surfaced.

In a gas generator which is used in rescue systems, gas can be developed from liquid or solid rocket propellants [39]: one containing hydrazine (a monopropellant system including pressurant and catalyst bed reactor) and the other being loaded with a composite propellant. The gas produced from the liquid propellant is a result of catalytic decomposition of the fuel into a hot gaseous mixture; the solid propellant produces the pressure gas by combustion. These propellants differ with respect to the amounts of gas produced by one generator, the gas temperature at the outlet of the gas duct, and the composition of the produced gas. Hydrazine reactor has the capability to develop larger quantities of gas with the lower exhaust gas temperatures at a relatively high rate in comparison with solid propellants. Due to that, the total solid propellant gas generator mass is almost double that for the hydrazine system for the same volume of produced gas, and hence hydrazine is preferred for smaller packaging.

Gas generator with liquid propellant is constructed as a container, which is protected against seawater corrosion (Fig. 11a). This container has three separated compartments: one containing a pressurant (driving gas); the second one for storage of decomposable liquid, e.g., hydrazine; and the third one containing a catalytic
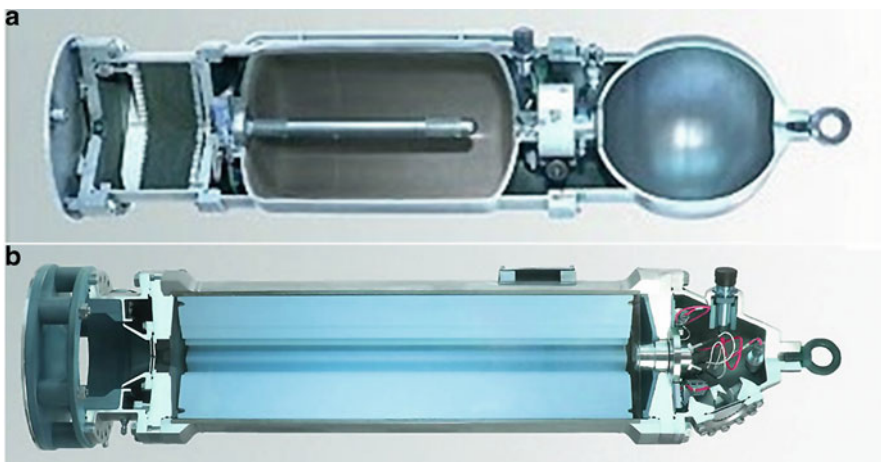
Fig. 11 Cutaway view of gas generators for emergency surfacing developed by EADS-Airbus DS with (**a**) liquid propellant and (**b**) solid propellant

reactor which converts the hydrazine into gas. From gas generator, gas is discharged into a ballast tank of the vehicle where expel water from the tank over gas duct. The three compartments are normally separated, but communicate in the emergency case so that the pressurant forces the hydrazine into the reactor, in a manner overcoming the effective gas back pressure.

The main element of the solid propellant gas generator unit is grain (Fig. 11b). Grain is placed in seawater corrosion-resistant nonmagnetic steel motor case (combustion chamber), where nozzle-ejector assembly is installed, connecting head and nozzle membrane. Gas generator unit is hermetically sealed. Burning grain produces high amount of gases, which blow out water from the tanks. Intensive cooling of combustion products is performed during blowing operation by mixing them with water, thus making the gas temperature in the tank acceptable for tanks construction.

Solid propellant for this application has a pressure exponent below 0.6, excellent chemical stability, and life cycle longer than 10 years. Also, the propellant has burning rate of around 5–6 mm/s at operating pressure between 70 and 100 bars to provide that the amount of produced gas is approximately equal to the amount of expelled water. Gas products of combustion should be nonflammable, hydrogen-free, nontoxic and environmentally clean, and insoluble or slightly soluble in water, with a low temperature of combustion. They are exhausted through the nozzle to the ejector, where water from the outside is injected as well, and produce a mixture of hot combustion gases and cold water steam with the temperature at the outlet (approximately 300 °C), which depends on the mixture ratio. The injection of water in the nozzle throat is enabled by the pressure difference between outside water and nozzle throat.

The gas generators are actuated from the control unit by an electric pulse via cable connection. Electric signal releases a pyrotechnic valve in the case with liquid fuel generation or activates an igniter in the case with solid propellant. Once the gas generators have been actuated, the development of gas by the generator does not depend on any control, but a triggered generator develops all of the gas which is capable of developing. Also, it is impossible to interrupt or reverse the process. Whole system is working independently from other power systems.

4.2 Demonstration Tests

In the second half of the 1980s, a submarine rescue system based on gas generator with solid composite propellant grain was being developed in the Laboratory for jet propulsion of the Faculty of Mechanical Engineering in Belgrade. The gas generator was loaded with free-standing grain from composite propellant of outside diameter 250 mm, in cylindrical form with concentric bore, which was inhibited from one head and laterally.

During the development of the system, a series of experiments were performed with gas generator unit with 300 mm diameter and maximum length of 1300 mm
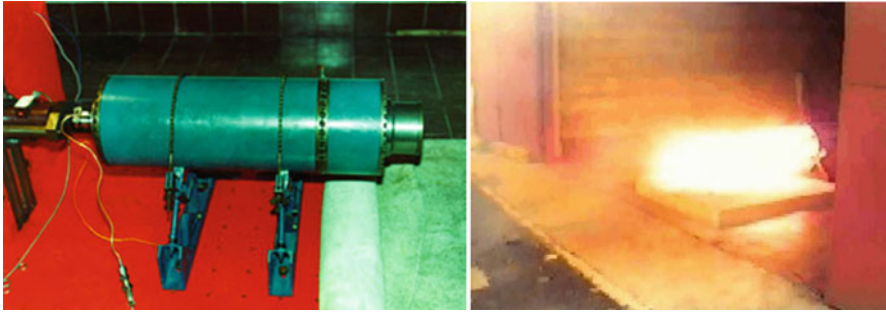
Fig. 12 Tests of gas generator at atmospheric pressure
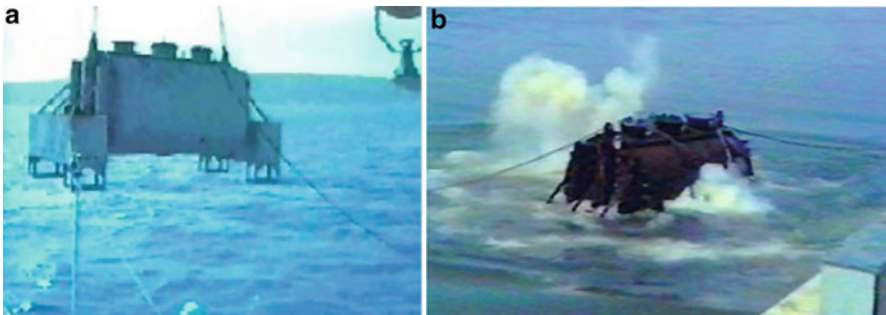
Fig. 13 Tests of gas generator unit on the open sea (**a**) immersing of tank with lift crane barge (**b**) surfacing of tank

at the ambient pressure, to check its performances and the possibility of surfacing of sinking objects. At the beginning, gas generator unit was tested at atmospheric pressure on the test stand, like any other rocket motor (Fig. 12). These tests showed that grain has uniform burning and that it can be used as gas generator charge.

4.2.1 Open Sea Tests

Gas generator unit was further tested through trials on the open sea (Fig. 13). Simulations and experiments were conducted using a tank for testing, whose construction was similar to the ballast tanks of submarine. Its volume was 15 m^3, with two scuppers with an area of 0.125 m^2 each, for water and gases releasing. It was possible to add extra weight of up to 14 tons to the tank as ballast [40]. One or two gas generator units were installed directly on the tank below the upper wall. Water valve, water level transducer, safety valve and cables for ignition, and pressure transducers were also placed into the tank.

During the tests on the open sea, the tank for testing was immersed in seawater with heavy lift crane barge and filled with water. In this way, the conditions for

venting water from the tank by means of a gas generator were similar to those in real conditions on the submarine. Initially, the tests were carried out with the tank at a shallow depth, at 5 m, to check the accuracy of measuring equipment and reliability of the whole systems. The first test was performed with the tank for testing fixed to the seabed, and as gas generators showed stable operation, the tank was released and further examinations were performed related to its surfacing. Later tests were performed at depths between 10 and 200 m, and the tank was self-raised back to the surface after gas generator activation. In the final tests cylindrical tank volume of 9.2 m^3 (dimensions $\phi 2 \times 2.95$ m), which was completely filled with water, was emerged to the surface from the depth of 300 m (Fig. 13b). These experiments have shown that the system can be successfully used for surfacing of sinking objects. During the tests the following parameters were measured: changes in buoyancy force (as a function of the mass of expelled water), overpressure, ambient temperature, and temperature in the tank and on the walls of the tank. Typical measuring results obtained during these tests are shown in Fig. 14:

Δp_{max} – maximum overpressure in the reduced tank
Δp_o – changing of ambient pressure during emerging the tank
T_{1max} – maximum temperature of gas at a distance of 1500 mm below wall of tank
T_{3max} – maximum gas temperature, near the wall of tank
t_1 – time necessary for stabilization of overpressure in tank
t_2 – time of sound effect occurrence
t_3 – time of the beginning of raising the tank
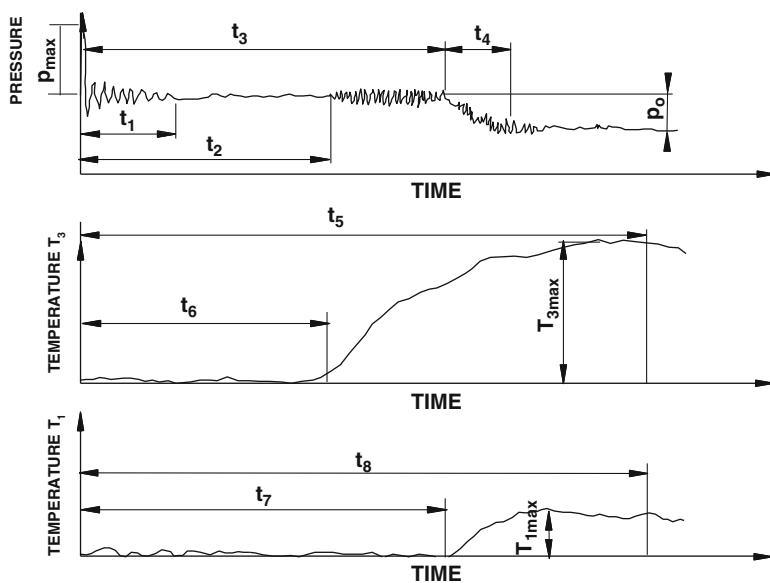
Fig. 14 Typical measuring results obtained during tests on the open sea
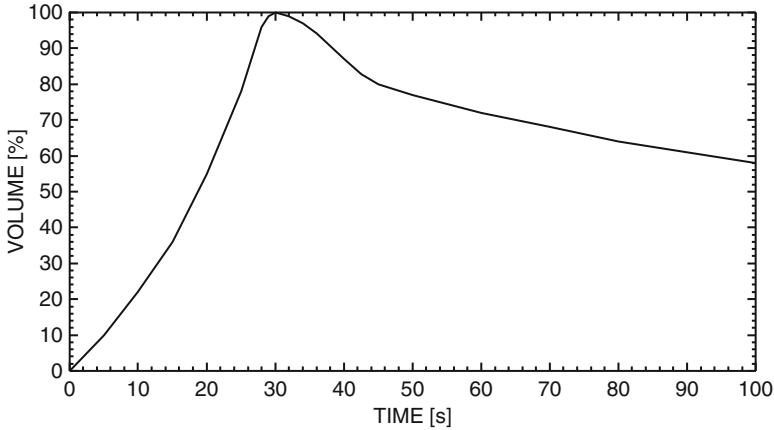
Fig. 15 Changes of volume (buoyancy) with time in tank for testing

t_4 – time necessary for raising
t_5 – start time of constant decrease T_3
t_6 – start time of significant increase T_3
t_7 – start time of significant increase T_1
t_8 – start time of constant decrease T_1

It is noted during the tests that as the gas in the tank cools down after the inflation process, its volume decreases which results in decreasing buoyancy force. This process is shown in Fig. 15, where the decrease in volume (or buoyancy) depending on time is presented. It is obvious that maximum value is around $t = 30$ s, and that around $t = 50$ s it fell to a little less than 80 % of the maximum value. Further decreasing of buoyancy to below 60 % of its maximum value will occur in the period of up to 100 s. It is explained by the condensation of water vapor at temperatures below 100 °C, whose one part is transformed into water and results in the loss of volume of gas phase.

Upon noticing this phenomenon, significant improvements in venting of tanks were carried out with better utilization of thermal energy of propellants. It was realized by the appropriate design of gas ducts, which assured that the gas products of combustion pass the shortest route to the upper regions of the tank, under stirring with a limited amount of water.

Tests on the open sea demonstrated the suitability of the gas generator system for the release of larger quantities of gas. As the solid propellant gas generator is much smaller in relation to the high-pressure air bottles for the same amount of produced gas, it is more efficient in blowing out ballast tanks than conventional compressed air systems. This is shown in Fig. 16, where it is represented as the volume of the blowout water depending on the water depth for the same mass of solid propellant gas generator and pressurized bottle system (volume 40 l, pressure 20 MPa, and
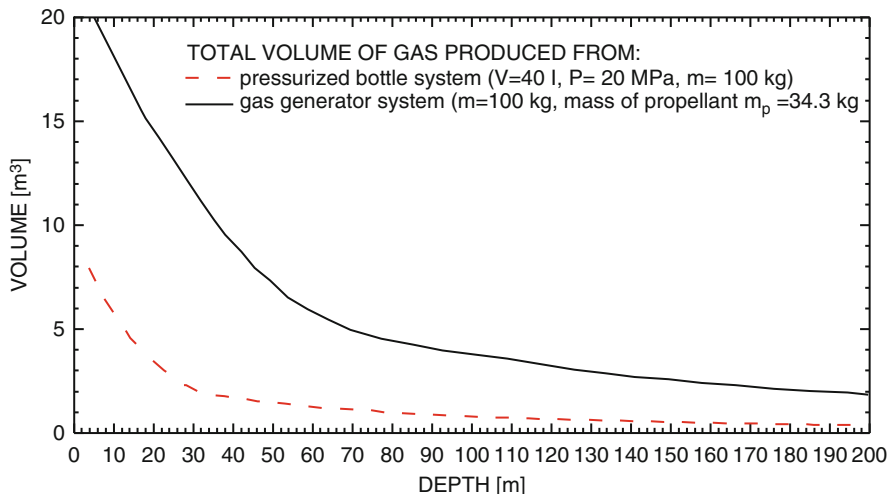
Fig. 16 Comparison between total volume of gas produced from pressurized bottle system and gas generator system with the same total mass of device

mass 100 kg). For example, 1 l of compressed air will blow out 0.013 m^3 of water, while 1 kg of propellant from gas generator will blow out 0.0625 m^3 water at depth of 200 m, which is five times more [40].

Experiments have shown that gas generator system can be successfully used for emergency surfacing of sinking objects from diving depth over 300 m. It can be expected that due to the high output pressure, the system enables surfacing from diving depths in excess of 400 m. At these diving depths, pressurized air systems are no longer effective so that the system provides the only option available for emergency surfacing. With this feature, the system can be of special interest for navies operating submarines predominantly in deep water areas.

4.3 Conclusion

Open sea tests have proven the concept of surfacing of sinking objects with solid propellant gas generator unit and provided the opportunity to carry out all necessary measurements which collect data for the design of systems on real submarines. Gas generator unit which was developed has a plain design, is compact, and without any mobile parts. Besides this, it was largely maintenance-free, low risk, and cost efficient. The unit was reusable (with a new grain and igniter), which means that after repair it can be used later for other salvaging operations. Results have shown that solid propellant grain 50 kg in weight was enough to blow out all the water from the 15 m^3 tank.

After the concept has been validated for the model, it should to be applied on a real vessel. In this case, several gas generators should be located in the main ballast tanks and forward and aft trim tanks of the submarine and by introducing gas water would be ejected and thus buoyancy would increase. Unfortunately, this has never been implemented in practice due to the suspension of further research. But similar emergency surfacing system RESUS-KILO was developed by Astra Bayer and installed on submarines operated by the navies of Germany, Italy, Greece, Turkey, India, and South Korea [41]. The system is based on gas generators positioned in the ballast tanks of the submarines and is intended to help the submarines surface from diving depths greater than 250 m.

5 Final Conclusion

The solid propellants provide wide range of applications in the civilian sphere, and three of them are reviewed in more details. The small low-altitude sounding rockets are used to prevent hailstone formation in turbulent atmospheric conditions and in this way damage on the crops from the 1960s. Despite the controversy over their effectiveness, anti-hail rockets are still used in many parts of the world, for example, Argentina, China, Croatia, Serbia, Romania, and Russia. The second application in gas generators suited for fire suppression, called Solid Propellant Fire Extinguishers, is developed since the late 1980. Solid propellant fire-extinguishing technology is based on the controlled combustion of propellants, which after ignition generate large quantities of gas for a short time. This gas is discharged directly into the fire-affected area in a non-propulsive manner and suppresses fire via a combination of different physical mechanisms like dilution, cooling, flow rate, and chemical effects. Variations in propellant composition and the design of the gas generator can provide a wide range of local fire protection applications like electromechanical systems and devices, power generation, transport, machinery, data processing, communication, and kitchens. The third application of solid propellants in systems for emergency surfacing of submarines, ships, or any other sinking objects was in use more than three decades. The system is composed of a starter and a series of solid propellant gas generator units, whose number and position are in direct dependence on the weight and design of a sinking object. Mounting a required number of gas generator units around the sinking object ensures thrust force after the activation of gas generators, which pushes the object to the surface.

References

1. World Meteorological Organization (1975) International cloud atlas, vol I. WMO No 407, pp 112
2. Changnon S (2009) Increasing major hail losses in the U.S. Clim Chang 96(1–2):161–166
3. Van Arkel P (2003) Hagelnetten ook in Nederlandse appelteelt. Fruitteelt 93(1):7–9

4. Ruby F (1953) Les nouvelles methodes de defence contre la grele. La Météorologie J 29:61–72
5. Vittori O (1960) Preliminary note on the effects of pressure waves upon hailstones. Nubila 3(1):34–52
6. Federer B, Shneider A (1981) Properties of pyrotechnic nucleants used in Grossversuch IV. J Appl Meteorol 20:997–1005
7. Fukuta N (1980) "Side-skim seeding" for convective cloud modification. Paper presented at the 3rd WMO scientific conference on weather modification, Clermont-Ferrand, France, 21–25 July 1980
8. Bahlanov AM, Gorbunov NA, Kakutkina IP et al (1982) Isledovanie dispersnosti i ledoobrazujucih aktivnosti aerosolei iodistoga serebra generirujumih pirosastavima. Izv Akad Nauk SSSR FAO 18(5):506–512
9. Schleusener RA (1968) Hailfall damage suppression by cloud seeding – a review of the evidence. J Appl Meteorol 7:1004–1011
10. Kraus TW (1999) Hail suppression. Paper presented at the 7th WMO scientific conf. on weather modification, Chiang Mai, Thailand, 17–22 February 1999: WMO Technical document No 936, WMP Report No 31, pp 33–38
11. List R (2004) Weather modification, a scenario for the future. Bull Am Meteorol Soc 85:51–63
12. Federer B (1977) Methods and results of hail suppression in Europe and in the USSR. In: Foote GB, Knight CA (eds) Hail: a review of hail science and hail suppression. Am Meteor Soc. Metrological monographs, vol 16(38), pp 215–223
13. Dessens J (1986) Hail in southwestern France, II: results of a 30-year hail prevention project with silver iodide seeding from the ground. J Clim Appl Meteorol 25:48–58
14. Dessens J (1998) A physical evaluation of a hail suppression project with silver iodide ground burners in southwestern France. J Appl Meteorol 37:1588–1599
15. Sulakvelidze GK, Bibilashvili NS, Lapacheva VF (1965) Formation of precipitation and modification of hail processes. Gidrometeoizdat, Leningrad (Translation: Jerusalem, Israel Program for Scientific Translations 1967), 208 pp
16. Abshaev MT (1999) Efficiency of Russian hail suppression technology in different regions of the world. Paper presented at the 7th WMO conf. on weather modification, Chiang Mai, Thailand, 17–22 February 1999. WMO Technical Document No 936, WMP Report No 31, pp 411–414
17. Federer B, Waldvogel A, Schmid HH et al (1986) Main results of Grossversuch IV. J Clim Appl Meteorol 25:917–957
18. Vento D, Damiani S (1987) "Grossversuch IV", valutazione di un sistema antigrandine - contributo italiano. Riv Meteor Aeron 47:215–240
19. Mesinger F, Mesinger N (1992) Has hail suppression in eastern Yugoslavia led to a reduction in the frequency of hail? J Appl Meteorol 31:104–111
20. Horvat V, Lipovscak B (1983) Cloud seeding with TG-10 rockets. J Weather Modif 15(1): 56–61
21. English M, Marwitz IP (1982) The evolution of radar echo in a seeded cloud. Atmos Ocean 20(1):28–38
22. Sedunov JS, Chernikov AA (1979) Scientific concepts of hail suppression and hail suppression experience in USSR, Scientific lecture presented at the 7th session of the Commission for Atmospheric Sciences, World Meteorological Organization, Manila, Philippines, March 1978
23. Federer BA, Waldvogel W, Schmid F et al (1978/1979) Plan for the swiss randomized hail suppression experiment. Design of Grosservsuch IV, Pageoph, vol 117. Birkhauser Verlag, Basel
24. Grosshandler WL (1995) In search of alternative fire suppressants. Paper presented at the thermal science and engineering symposium in Honor of Chancellor Chang-Lin Tien, November 1995, Berkeley, CA, pp 275–282
25. Wickham RT (2002) Status of industry efforts to replace Halon fire extinguishing agents. Report prepared for the U.S. Environmental Protection Agency, Wickham Associates, Stratham, 89 pp

26. Agafonov VV, Kopylov SN, Sychev AV et al (2004) The mechanism of fire suppression by condensed aerosols. In: Proceedings of the 2004 Halon options technical working conference, Albuquerque 24–26 May 2004, pp 984–993
27. Dricker GY (2000) New fire extinguishing agents in Russia in the 1990s. In: Proceedings of the 2000 Halon options technical working conference, Albuquerque, 2–4 May 2000, pp 424–430
28. Williams FA (1974) A unified view of fire suppression. J Fire Flammability 5:54–63
29. Fryburg G (1950) Review of literature pertinent to fire-extinguishing agents and to basic mechanisms involved in their action. NACA TN 2102
30. Ewing CT, Faith FR, Hughes JT et al (1989) Flame extinguishment properties of dry chemicals. Fire Technol J 25:134–149
31. Wierenga PH, Holland GF (1999) Developments in and implementation of gas generators for fire suppression. In: Proceedings of Halon options technical working conference, Albuquerque, pp 453–468
32. Coward HF, Hartwell FJ (1926) Extinction of methane flames by diluent gases. J Chem Soc 1:1522–1532
33. Hamins A, Cleary T, Yang J (1997) An analysis of the Wright-Patterson full-scale F-22 Engine Nacelle Fire Suppression Experiments. National Technical Information Service (NTIS). NISTIR 6193
34. Linteris GT, Knyazev V, Babushok V (2001) Premixed flame inhibition by manganese and tin compounds. In: Proceedings of the 2001 Halon options technical working conference, Albuquerque, NM, pp 72–82
35. Williams BA, Fleming JW (1999) Suppression mechanisms of Alkali metal compounds. In: Proceedings of the 1999 Halon options technical working conference, Albuquerque NM, pp 157–169
36. Vorozthsov A, Osipkov VN, Gruzdev AG et al (2013) Automatic modules of fire extinguishing-a field of effective application of pyrotechnic gas generating devices. Paper presented at the 9th International high energy materials workshop, Institute of Space and Astronautical Science, Sagamihara, Japan, 7–9 October 2013
37. Jacob P (2002) Development of a gas-generator propellant for a rescue system for submarines based on the energetic binder GAP. Paper presented at the specialists' meeting on advanced rocket performance life and disposal, Aalborg, Denmark, 23–26 September 2002
38. Ahlers R, Doyle R (2014) Stabilisation of vessels with support of balloons. Paper presented at the Transport research arena 2014 conference, Paris, France, 14–17 June 2014
39. Astrium NV (2014) RESUS – rescue system for submarines. http://cs.astrium.eads.net/sp/Trauen/resus/index.html. Accessed 3 May 2014
40. Mavra G, Sljukic M (1990) Analysis of the real test model of the unit for venting gas generators ballast tanks (on Serbian). In: Proceedings of the 18th conference of JKEM, Kupari, Yugoslavia, 23–26 May 1990, pp 572–583
41. Langer T, Korn O (2003) RESUS-KILO CLASS an emergency surfacing system for 877 EKM Project Submarines (Kilo Class). In: Maslov VN (ed) Proceedings of the 3rd international conference: Navy and shipbuilding nowadays (NSN' 2003), Krylov Shipbuilding Research Institute, St. Petersburg, Russia, 26–28 June 2003, pp 54–66

Novel Ammonium Nitrate-Based Formulations for Airbag Gas Generation

Shingo Date

Abstract In recent years, there have been researches and developments (R&D) using ammonium nitrate (AN) as an oxidizer of novel azide-free gas-generating agents in automobile airbag systems. AN theoretically generates only clean gases during decomposition, and it also has advantages of higher gas yield, less residue, and lower cost as compared to conventional oxidizers such as potassium perchlorate (KP), strontium nitrate (SrN), and basic copper nitrate (BCN). However, AN has a number of disadvantages, such as low ignitability, low burning rate, multiple crystal transitions at various temperatures, and hygroscopic property. For the AN-based mixtures to be effective as gas-generating agents in automobile airbag systems, their burning performances need to be improved.

In this review, a brief overview of the automobile airbag system, including its activation process and its history, is given, followed by reviews of the past and present ingredients used for pyro-type gas-generating agents, and some studies on the burning characteristics of AN-based gas-generating agents, including the recent studies where fuel compound in fuel compound/AN/additive mixture is one of tetrazole compound, e.g., aminoguanidinium 5,5′-azobis-1H-tetrazolate (AGAT); guanidine-derivative compound, e.g., guanidine nitrate (GN); or azo compound, e.g., azodicarbonamide (ADCA).

1 Introduction

1.1 Overview of Automobile Airbags

Automobile airbag systems are supplementary restraint systems (SRSs) for passengers inside automobile compartments, complementing the role that could not be fully covered by seatbelts, in order to reduce the risk of damage that could be inflicted on the passengers inside compartments upon collision. There are

S. Date (✉)
Department of Applied Chemistry, National Defense Academy, Yokosuka, Kanagawa 239-8686, Japan
e-mail: sdate@nda.ac.jp

963

Fig. 1 Schematic diagram of
an automobile airbag system
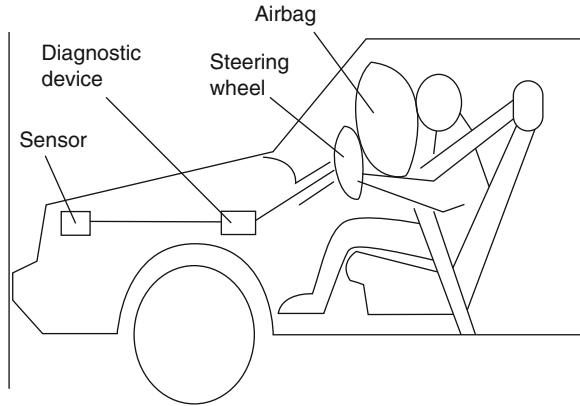
mainly three main types of airbag systems, i.e., compressed gas type which utilizes
compressed gas stored in canisters, pyro-type that utilizes burning gas products
of solid gas-generating agents that are generally categorized as low explosives, or
hybrid type which is a combination of pyro-type and compressed gas type. In this
chapter, the main focus is on the pyro-type system.

In pyro-type airbag inflators, the gas-generating agents are ignited inside a burn-
ing chamber of an inflator through a squib shortly after impact, and the gas products
generated from combustion of gas-generating agents inflate the airbag rapidly,
absorbing kinetic energy of the passenger moving inside the car compartment upon
impact, to protect passengers from crashing into the dash board, the front window,
etc.

The pyro-type airbag system consists mainly of impact sensors, a diagnostic
device, and an airbag module (consists of an inflator, an airbag, and a pad cover), as
shown in Fig. 1. When an automobile collides on a large foreign object, its built-in
sensors instantaneously sense the collision, and after diagnosis using a diagnostic
device as to whether or not collision has actually occurred, electric signal is sent to
the inflator which is shown in Fig. 2, where an igniter in a squib is ignited, which in
turn ignites a booster, which in turn ignites gas-generant pellets. The combustion of
gas-generant pellets produces gases that pass through the built-in filter in an inflator
to inflate the airbag while the airbag releases exhaust gas from its rear opening so
that the airbag absorbs kinetic energy of the passenger. The required time taken
from an impact to an opening of a pad cover and the onset of opening of the airbag
is 10 ms [2], the time taken to full inflation of the airbag is 12–50 ms [2], and the
time taken for the contraction of airbag to obtain full visibility is 80–100 ms [2].

Nowadays, cars that are sold worldwide have airbag systems for the driver's seat
and for the passenger's seat as standard features, and there are also side airbags
and curtain shield airbags as options. Meanwhile, even though the pyro-type airbag
inflators are containing explosives, when "installed in vehicles, vessels or aircrafts
or in completed components such as steering columns, door panels, seats etc. are
not subject to these Regulations", according to United Nation's Recommendations
on the Transport of Dangerous Goods [4].
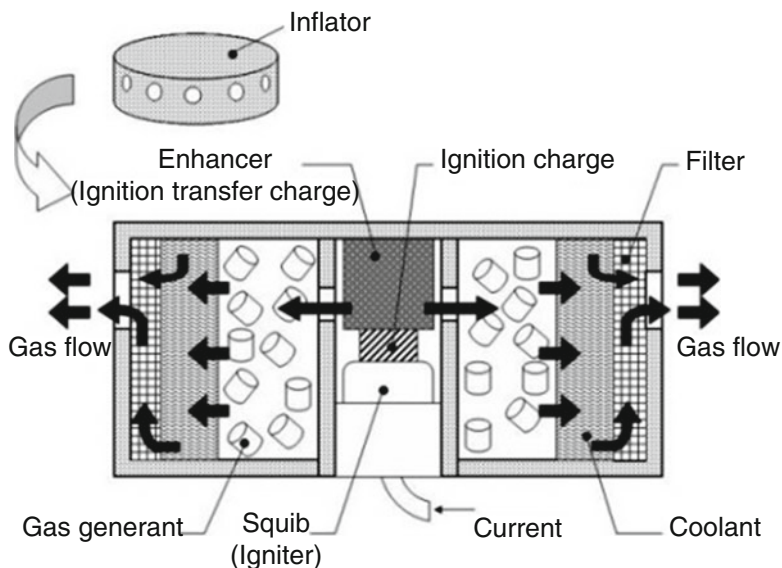
Fig. 2 Structural diagram of an inflator for driver's seat [3]

1.2 Brief History of Automobile Airbags

The origin of airbag systems dates back to the US patent (US 1331359) by Parrott and Round [5] on air cushion system, aimed especially for use on aircrafts, which was registered in 1920. Later on, patents on air cushion for automobile using compressed air were registered by Hetrick [6] in the US, and Linderer [7] in Germany, both in 1953. Major automobile companies joined in later on in R&D of airbag systems, with General Motors and Ford both starting R&D in 1957, and Daimler-Benz starting R&D in 1966. Following field tests conducted by Ford vehicles with 500 modules in 1972 [8], General Motors conducted field tests with 1000 modules in 1973 [8], and during 1974–1976, General Motors offered airbags as optional features for 10,000 modules [8]. The sales by General Motors, however, were suspended as of 1976, due to lack of demand [1]. Nevertheless, with the enactment of Federal Motor Vehicle Safety Standard (FMVSS) No. 208 [9] by the National Highway Traffic Safety Administration (NHTSA) in the United States on July 11, 1985, in which 10 % of 1987 model cars, 25 % of 1988 model cars, 40 % of 1989 model cars, and 100 % of 1990 model cars to be sold in the United States are required to be equipped with passive restraint systems, the production of airbags for cars in the United States has revived from the 1980s, and it continues until this day.

As for a brief overview of the evolution in airbag options, Daimler-Benz produced the first models in serial configuration with an airbag option in 1980 [8]. Honda released the Legend model with airbags in 1987 [1, 2, 8]. Daimler-Benz introduced the first passenger side airbag in 1988 [8]. Honda released motorcycle airbag systems in 2006 [10]. Toyota developed the world's first rear window curtain

shield airbag in 2008 that absorbs shock upon impact from the rear [11]. Recently, in 2012, Volvo has released the first model equipped with airbags on the bonnet in order to absorb impact that could be inflicted on the pedestrian upon collision [12].

The source of gas generation was originally compressed gas, but due to its low efficiency of gas generation and its relatively large volume and mass, it was replaced by pyro-type gas-generating agents using sodium azide [13–18] in the 1980s, and it was used up until the 1990s. Although sodium azide has been considered an ideal fuel component due to its relatively high thermal stability and relatively benign gas products, its use was abolished in 1999 in Japan because of the toxicity of the material; high risk of producing highly sensitive explosive azide compounds upon contact with copper or lead, i.e., copper azide or lead azide; and high risk of producing toxic hydrogen azide upon contact with water [1]. Major fuel components are currently replaced by non-azide compounds, e.g., tetrazole compounds [19–23, 34, 35], and guanidine-derivative compounds [24–33]. They are organic compounds with high-nitrogen content containing high-energy content per unit mass. There is, however, a common risk of producing harmful gas products [2], e.g., CO and nitrogen oxides (NOx).

1.3 Requirements for Gas-Generating Agents for Automobile Airbags

Yoshida and Hasegawa [2] have given the requirements for airbag gas-generating agents as listed below:

1. Moderate burning rate
   It would be possible for the airbag inflator to inflate the airbag in a short period of time if the gas-generating agents have a relatively high burning rate as well as large volume of gas product upon combustion. It is given by Ludstrom et al. [24], for example, that the linear burning rate of gas-generating agents be equal to or faster than 0.40 in s^{-1} (10.2 mm s^{-1}) at 1000 psi (6.895 MPa).
2. Exhaust gas not poisonous
   Since burning product gases of the gas-generating agent are released inside the compartment of an automobile at the same time as the inflation of an airbag, it is necessary for the exhaust gases to be nonpoisonous.
3. Less aerosol particulates
   If aerosol particulates are produced during combustion of gas-generating agents, there is a possibility to produce very fine particles that could pass through the filter inside the combustion chamber and form a mist inside the compartment that can obscure the view and also harm human the respiratory system; therefore, it is important to avoid its production.
4. Low exhaust gas temperature
   If exhaust gas temperature is high, it has the risks of damaging the inflated airbag, causing burns on the passenger, so it is important for the exhaust gas to be relatively cool, so long as the pressure rise inside the airbag is not hindered.

5. Do not release high-temperature-condensed products

   The production of high-temperature-condensed products has a risk of damaging the airbag and causing harm on the passenger, so it should therefore be avoided.

6. Large volume of product gas

   It is important for the inflator to be as small and be as light as possible. In order to achieve downsizing of inflators, it is necessary for a gas-generating agent to produce large gas volume per unit volume and unit mass.

7. Safe to handle

   As previously mentioned, pyro-type gas-generating agents use low explosives. If it is excessively sensitive, there would be a high risk of ignition during production and use, so it should be insensitive.

8. High thermal stability

   Automobile airbag systems are required to be able to use under a wide variety of temperature conditions over the years, e.g., under high temperature inside the compartment of an automobile that could reach near 100 °C in summer and under cold temperature that could reach well below freezing point in the winter. Since airbag gas-generating agents are required to be stable for 15 years [2], thermal stability tests are conducted, e.g., an inflator is put into a thermostat with temperature controlled at 380 K for 400 h, and verifying that the performance of the inflator does not deteriorate [2]. According to Yoshida and Hasegawa [2], the airbag system containing a gas-generating agent mixture which is stable up to 200 °C (473 K) during DSC test can endure the thermal stability test. According to Khandhadia and Burns [25], meanwhile, the airbag system containing a mixture with melting point at or above 388 K can endure the thermal stability test.

9. Resistant against fluctuation in environmental condition

   As mentioned in 8, it is required for the system to endure fluctuation in environment for 15 years [2], so it is important for the gas-generating agent to be less affected in gas-generating ability with the fluctuation in environmental condition.

10. Relatively cheap cost

    In order to meet the needs of increasing numbers in airbag systems inside an automobile and therefore the reduction in cost per system, the ingredients of these gas-generating agent mixtures need to be as cheap as possible.

11. Nontoxic during handling

    Other than nontoxicity of product gas as mentioned in 2, it is necessary for the mixture to be also nontoxic upon contact through the skin for the safety during production and disposal.

12. Safe to manufacture

    It is necessary to avoid substances for gas-generating mixtures that have high risk of ignition or autoignition or damaging of the skin or internal organs upon direct contact.

1.4   Overview of a History of Researches and Developments of Gas-Generating Agents

In the past, there have been researches and developments (R&D) for effective and commercially viable automobile gas-generating agents:

1. Gas-generating agents using nitrate salts as oxidizer
   There have been inventions, e.g., Shaw [22] and Gast et al. [27], where potassium nitrate (KN) is used as an oxidizer. It has been pointed out, however, that when such oxidizer is used, burning residues would contain caustic substances, i.e., potassium oxide K_2O, potassium carbonate K_2CO_3, and potassium hydroxide KOH, and because of their relatively low melting point, they have the risk to become liquid upon combustion of the mixture, so they have the risk of penetrating through the filter of the combustion chamber and then subsequently turning into solid state, damaging the airbag and passengers [3].

   Meanwhile, there have been inventions and researches using strontium nitrate (SrN) as an oxidizer: for inventions, e.g., Wardle et al. [28], Poole [29], Lund et al. [30], Gast et al. [31], and Sato et al. [32]; there are also researches by Hasue et al. [33] on 5-ATZ/SrN mixtures and by Iwakuma et al. [34] on 5,5′-azobis-tetrazole aminoguanidine (AGAT)/SrN mixtures. However, there is a problem that SrN is converted to strontium carbonate $SrCO_3$ upon combustion that would remain as a solid residue, causing low gas yield that is disadvantageous as gas-generating agents.

   There are also patents in which basic copper nitrate is used as an oxidizer for gas-generating agents, e.g., Barnes and Taylor [35], Lundstrom et al. [36], and Thibieroz et al. [37].

2. Gas-generating agents using metal oxides as oxidizer
   There have been inventions and researches using cupric oxide as an oxidizer: for inventions, e.g., Blau and Lund [38], Taylor et al. [39], and Yamato [40]; there are also researches by Abe et al. [41] on CuO-based mixtures, Date et al. [42] on guanidinium 1,5′-bis-1H-tetrazolate (G15B)/CuO mixtures, and Date et al. [43] on G15B/metal oxide mixtures. However, similar to that of SrN, there is a problem in which the metal oxide is converted to solid residues (metal, metal oxide, and/or metal nitrate), e.g., in case CuO is used as an oxidizer, Cu, Cu_2O, and $Cu(NO_3)_2$ are produced, causing low gas yield that leads to lower rate of pressure rise, which is, here also, disadvantageous as gas-generating agents.

3. Gas-generating agents using metal perchlorates as oxidizer
   There have been inventions and researches using metal perchlorates as an oxidizer; for inventions, e.g., Takahori et al. [44]; there are also researches, e.g., by Hara et al. [45] on ADCA/KClO$_4$ (KP) mixtures, Hasue et al. [46] on B/KP mixtures, Hasue et al. [47] on 5-ATZ/KP mixtures, Miyata et al. [48] on 5-ATZ/NaClO$_4$ (NaP) mixtures, and Date et al. [49] on G15B/KP mixtures. However, there are risks of the production of chlorine Cl_2 and hydrogen chloride HCl gases and high temperature of product gases [50].

2 Overview of the Researches of Ammonium Nitrate-Based Gas-Generating Mixtures

In recent years, there has been R&D on ammonium nitrate (AN)-based gas-generating agent mixtures. They have the advantage of high gas generation yield since AN does not produce solid residue upon decomposition. The production of large volume of gas is also expected because it produces gas species with small molecular weight, i.e., N_2, O_2, and H_2O. Being also an ingredient of fertilizers, AN is relatively cheap and abundant. On the whole, it is considered as an ideal oxidizer for gas-generating agents. It has been pointed out, however, of the hygroscopic characteristic of AN, poor ignitability, relatively low burning rate, and changes in crystal structures with fluctuations in ambient temperature, as shown in Fig. 3 [1] (which is a cause of caking and eventual powdering [1]).

In order to solve the problem of hygroscopic characteristic, measures have been taken, such as coating the surface of AN particles with thin impermeable polymer films through, e.g., spray drying [51, 52]. In order to solve the problem of low ignitability and low burning rate, a number of measures have been taken: (1) utilizing fuel component with high-energy content, e.g., triazole compounds [53, 54], tetrazole compounds [55, 56], guanidine-derivative compounds [57, 58], or diazo compounds [59, 60, 66]; and/or (2) adding catalysts, e.g., metal oxides [55, 59, 60, 66], metal nitrates [57, 58], activated carbon [61, 62], metal halides [61], etc. to the AN-based mixture. In order to solve the problem of multiple crystal transitions, adding anticaking agent such as ammonium sulfate $(NH_4)_2SO_4$ [63], metal nitrate, e.g., KN [56], or metal oxide, e.g., CuO [64], ZnO, [64] to AN in order to produce phase-stabilized AN particles but there is nonetheless a current issue [65].

2.1 Burning Characteristics of Some Tetrazole/Ammonium Nitrate-Based Mixtures

As mentioned above, tetrazole compound, which has high-energy content per mass, has been studied as fuel component of AN-based as generating agent mixtures [55, 56].
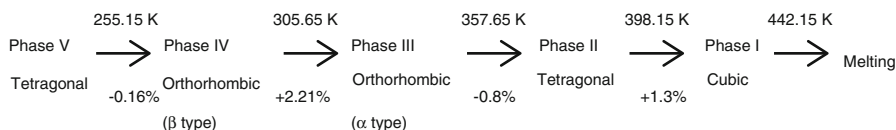
Fig. 3 Summary of changes in crystal structures of AN (*value above arrow*: temperature of change in crystal structure; *value below arrow*: change in volume percentage from phase on the left) (Based on 1)

2.1.1　Burning Characteristics of Aminoguanidinium 5,5′-Azobis-1H-Tetrazolate/Ammonium Nitrate-Based Mixtures

Miyata et al. [3, 55] selected AGAT (Fig. 4), which has high heat content per mass and which undergoes exothermic decomposition, as a fuel for the AN-based mixture.

Miyata [3] has studied the effects of additives, i.e., CuO or MnO_2 on the mass burning rate, m, of AGAT/AN-based mixtures, using chimney-type strand burner. The comparison of the measured m for AGAT/AN mixture and AGAT/AN/CuO mixture at 243, 298 or 343 K is shown in Fig. 5 and Table 1, where sample A denotes AGAT/AN mixture in which AGAT and AN are mixed at 50: 50 mass % ratio, B denotes AGAT/AN/CuO mixture in which 5 mass % CuO was added. Meanwhile, the comparison of the measured m for AGAT/AN mixture and AGAT/AN/CuO

Fig. 4 The chemical structure of bis (aminoguanidinium)5,5′-azotetrazolate (AGAT) [3]
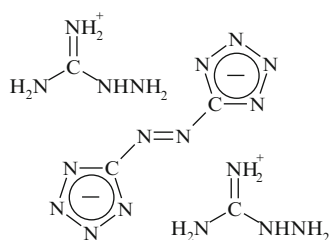
Fig. 5 Effect of CuO on mass burning rate at 243 K, 298 K, and 343 K [3]
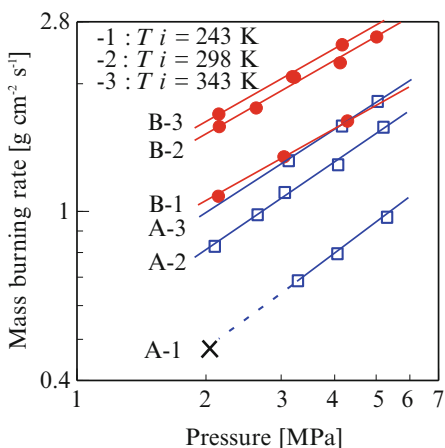
Table 1 The value of a_m and pressure sensitivity n for sample A and B [3]

Initial sample temperature [K]	a_m		n	
	Sample A	Sample B	Sample A	Sample B
243	0.292	0.696	0.719	0.588
298	0.499	1.03	0.694	0.565
343	0.612	1.10	0.672	0.563

Fig. 6 Effects of MnO$_2$ on mass burning rate at 243 K, 298 K, and 343 K [3]
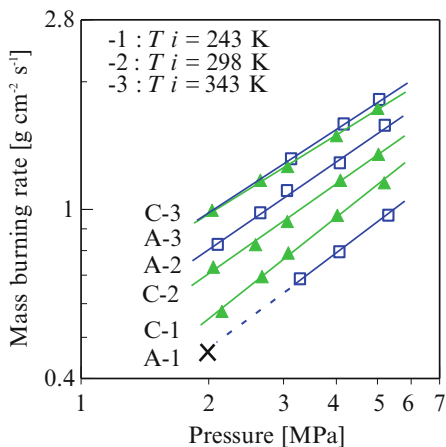
Table 2 The value of a_m and pressure sensitivity n for sample A and C [3]

Initial sample temperature [K]	a_m		n	
	Sample A	Sample C	Sample A	Sample C
243	0.292	0.318	0.719	0.792
298	0.499	0.434	0.694	0.701
343	0.612	0.643	0.672	0.611

mixture at 243, 298 or 343 K is shown in Fig. 6 and Table 2, where C denotes AGAT/AN/MnO$_2$ mixture in which 5 mass % MnO$_2$ was added, while A is the same mixture as above. It was shown from these data that m increased with P, obeying the Vieille law, which is expressed with the following Eq. 1 [3]

$$m = a \ P^n \tag{1}$$

Here, P is the average absolute pressure, a is the pre-exponential factor, and n is the pressure exponent of the burning rate. It was found from Fig. 5 and Table 1 that the addition of CuO accelerated m and also reduced n for all temperatures that were experimented, while the addition of MnO$_2$ did not significantly accelerate the mass burning rate m of AGAT/AN mixture as shown in Fig. 6 and Table 2.

In order to study on the burning mechanism of AGAT/AN-based mixtures, Miyata et al. [55] have also measured the temperature histories of AGAT/AN-based mixtures as shown in Fig. 7, where samples A and B represent AGAT/AN/CuO mixture and AGAT/AN mixture, respectively. It was found that the temperature gradient above the burning surface has increased by adding CuO, suggesting increased heat feedback from the flame to the burning surface [55].

Observations of burning flames using high-speed camera were also carried out for the combustion of AGAT/AN-based mixtures, and it was found that for AGAT/AN mixture, some AGAT particles popped out of the burning surface before
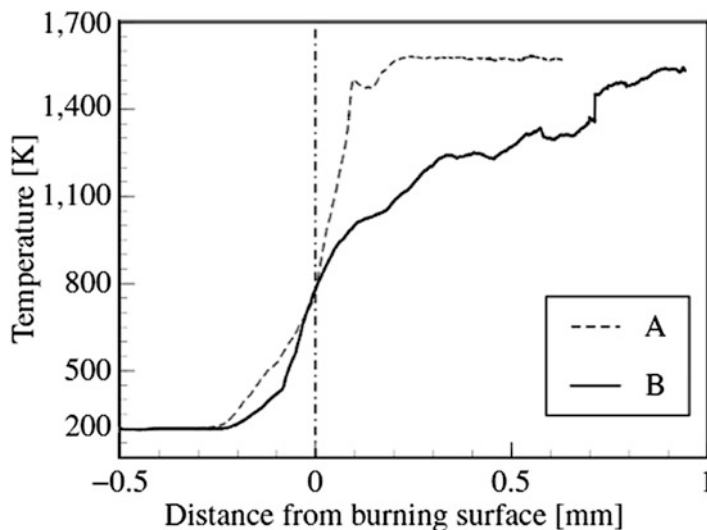
Fig. 7 Temperature profile of some AGAT/AN-based mixtures at 4 MPa [55]

their decomposition in the condensed layer, ignited in the midst of the gas layer full of gaseous AN decomposition product, forming diffusion flames to complete the burning process, while for AGAT/AN/CuO mixtures, the flames apparently came immediately out of the burning surface [3].

Miyata et al. [55] have also studied on the thermal decomposition behavior of AGAT/AN/CuO mixture through DSC and have made comparisons with those of original AGAT/AN mixture and AGAT/AN/MnO$_2$ mixture, as shown in Fig. 8, where samples A, B, and C represent the same as denoted previously in Figs. 5 and 6. It was shown that the mixture with CuO has a greater exothermic peak in the temperature range between approximately 400–440 K as compared to the AGAT/AN mixture, suggesting that the addition of CuO has accelerated exothermic decomposition of AN in the condensed layer. As for the mixture with MnO$_2$, the DSC curve of the mixture was very similar to that of the chemical stoichiometric ratio mixture up until approximately 440 K, suggesting that MnO$_2$ does not play a significant role in accelerating AN decomposition, while MnO$_2$ was suggested to accelerate exothermic decomposition of AN in the temperature range between approximately 490–550 K, it was also shown that the endothermic heat was pronounced in the temperature range between approximately 440–530 K.

In addition, Miyata [3] has found from interrupted heating during TG-DTA of AN/CuO mixture and the subsequent XRD analysis that CuO was converted to Cu$_2$(OH)$_3$NO$_3$ before exothermic decomposition, which is then converted back to CuO after exothermic decomposition, and from these results, catalytic cycle of AN through CuO was suggested, as shown in Fig. 9 [3], causing accelerated decomposition of AN. It was further suggested that such catalytic cycle has accelerated the burning characteristics of AGAT/AN mixture, as shown in Fig. 10 [3].

Fig. 8 DSC curves for AGAT/AN-based mixtures [55]
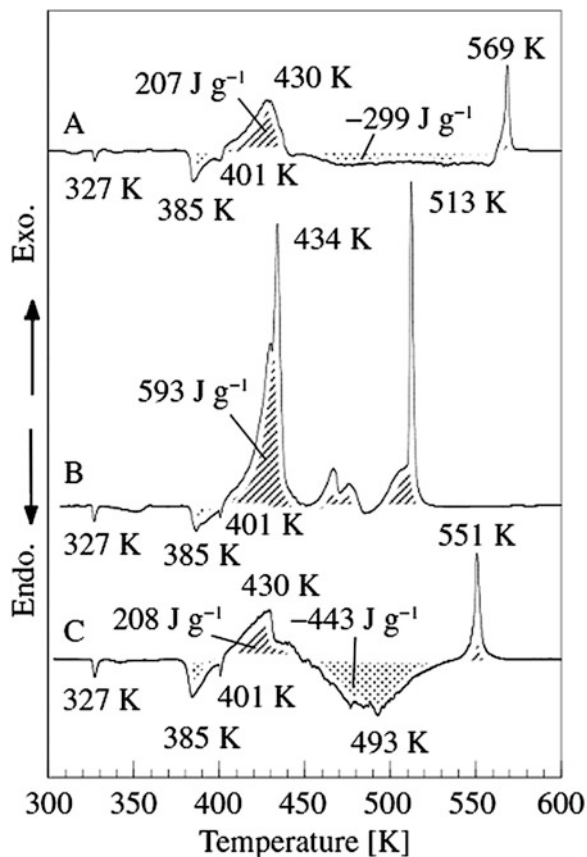
Fig. 9 Catalytic cycle of AN through CuO [3]
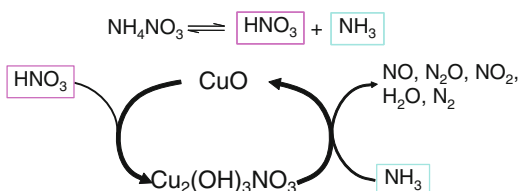
2.2 Burning Characteristics of Some Guanidine Derivative Compound/Ammonium Nitrate-Based Mixtures

Wada et al. [57] and Arai et al. [58] have studied on combustion characteristics of guanidine nitrate (GN)/AN-based mixtures in which BCN was added as a burning rate modifier. It was found from strand burner tests that adding BCN to GN/AN mixture which did not originally ignite, enabled the ignition at lower pressure from about 1 MPa. It was also found that the value of n of the linear burning rate, r, was in the range between 0.41 and 0.45 in mixtures with a high AN content or
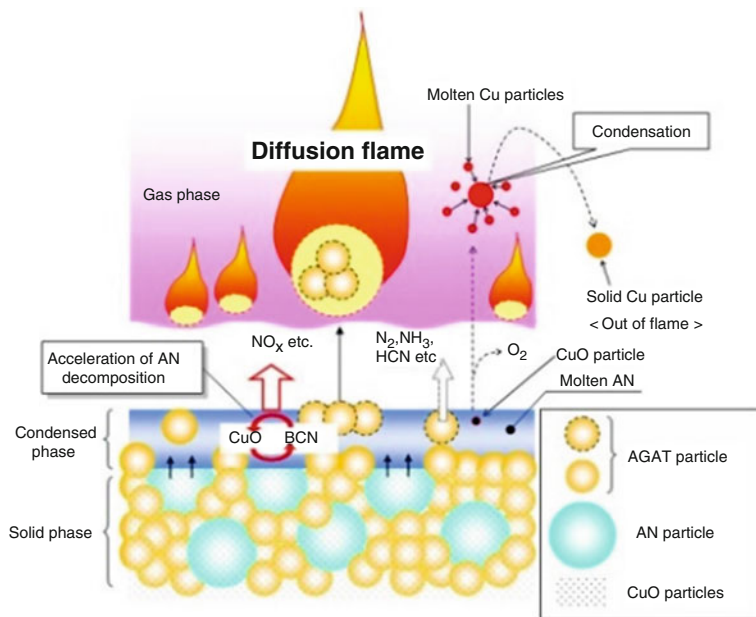
Fig. 10 Burning mechanism of AGAT/AN/CuO mixtures [3]

when the test was conducted under pressure lower than 5 MPa, but larger in value (0.67–0.77) for mixtures with a low AN content or when the test was conducted under pressure higher than 5 MPa. Meanwhile, it was also found that the nature of the combustion residues from the GN/AN/BCN mixtures varied depending on the combustion conditions and the mixing ratio of the sample mixture: the residues from samples with smaller values of n contained mainly Cu_2O powder, while the residues from samples with greater values of n contained metallic copper [57].

Wada et al. [57] have also studied on the burning mechanism of GN/AN/BCN mixture from the temperature history measurement, and it was found that the combustion wave could be divided into four regions based on the temperature and phase of the mixture: unreacted zone, condensed phase zone, preheating zone, and adiabatic combustion zone. It was also suggested that the diffusion combustion and homogeneous combustion coexist [57].

2.3 Burning Characteristics of Azodicarbonamide/Ammonium Nitrate-Based Mixtures

Linear burning rate, r, and rate of pressure rise of some azodicarbonamide (ADCA, as shown in Fig. 11) /AN/additive mixtures were measured by using closed strand burner. Additive that was added to the stoichiometric ADCA/AN mixture was one of MnO_2, Cu, CuO, or BCN.

Fig. 11 Chemical structure of azodicarbonamide (ADCA) [59]
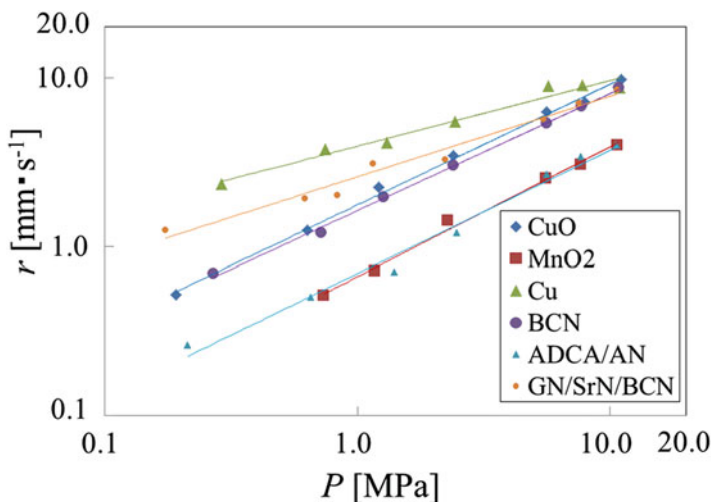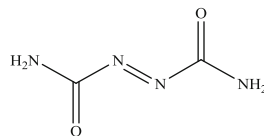
Fig. 12 Linear burning rates for ADCA/AN-based mixtures [59]

Table 3 Values of a and n of the Vieille law for ADCA/AN-based mixtures [59]

Sample	a [mm•s^{-1}·MPa^{-1}]	n [–]
ADCA/AN	0.70	0.73
ADCA/AN/CuO	1.77	0.72
ADCA/AN/MnNO$_2$	0.67	0.77
ADCA/AN/Cu	3.93	0.39
ADCA/AN/BCN	1.64	0.69
GN/SrN/BCN	2.59	0.48

2.3.1 Linear Burning Rate Characteristics

Figure 12 shows the results of log-log plot of P vs r for ADCA/AN-based mixtures [59]. Sustained burning was observed for all mixtures from a gauge pressure of 0.1 MPa, except for ADCA/AN/MnO$_2$ mixture that could not be ignited at or below 0.5 MPa. It was also shown that while the addition of Cu, CuO or BCN increased r, as compared to stoichiometric ADCA/AN mixture, there was a little difference in r for ADCA/AN/MnO$_2$ mixture.

Table 3 gives the values of a and n determined from Fig. 12. It was found that the addition of Cu-based additives (Cu, CuO, or BCN) increased the values of a while it generally reduced the values of n. This indicates also that r of the Cu added mixture
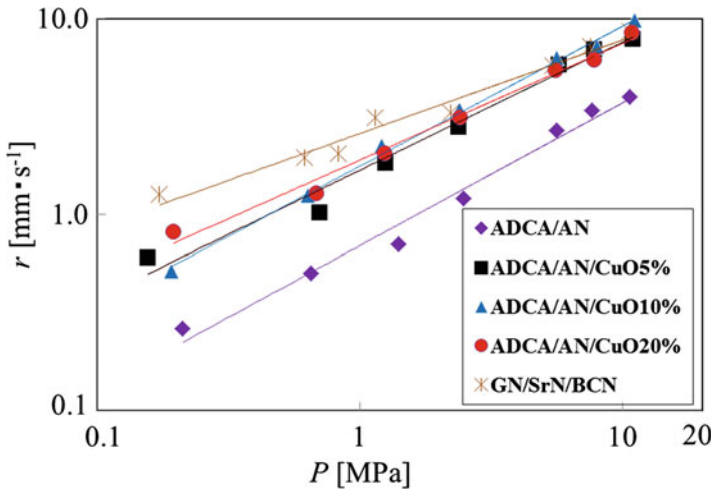
Fig. 13 Linear burning rates for ADCA/AN-based mixtures [60]

Table 4 Values of *a* and *n* of the Vieille law for ADCA/AN-based mixtures [60]

Sample	a [mm•s^{-1}•MPa^{-1}]	n [–]
ADCA/AN	0.70	0.73
ADCA/AN/CuO 5%	1.69	0.65
ADCA/AN/CuO 10%	1.78	0.72
ADCA/AN/CuO 20%	1.90	0.60
GN/SrN/BCN	2.59	0.48

was higher than that of GN/SrN/BCN mixture. It was also found that increasing the amount of CuO up to ten parts by weight have raised *r*.

As for the effect of the amount of CuO that was added, Fig. 13 shows the results of log-log plot of *P* vs *r* for ADCA/AN/CuO mixtures [60]. Sustained burning was observed for all mixtures from a gauge pressure of 0.1 MPa. It was also shown that while the addition of CuO increased *r* as compared to ADCA/AN mixture, there was little difference in *r* with the change in the amount of CuO that was added. Table 4 gives the values of *a* and *n* determined from Fig. 13. It was found that the addition of CuO increased *a* while it generally decreased *n*, except for an increase in *n* from an increase in CuO content of 5–10 mass %. This indicates also that *r* of ADCA/AN/CuO 10 % mixture was higher than that of GN/SrN/BCN at pressure over 5 MPa.

2.3.2 Rate-of-Pressure-Rise Test

Typical pressure histories during the rate-of-pressure-rise tests are shown in Figs. 14 and 15. $(\Delta P)_{av}$, $(\Delta t)_{av}$, and $(\Delta P(\Delta t)^{-1})_{av}$ from the tests are shown in both Tables 5 and 6.
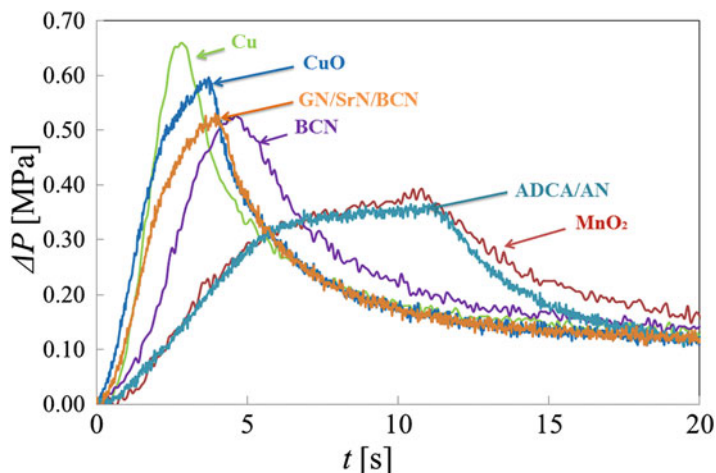
Fig. 14 Pressure time histories of ADCA/AN-based mixtures from rate-of-pressure-rise tests [59]
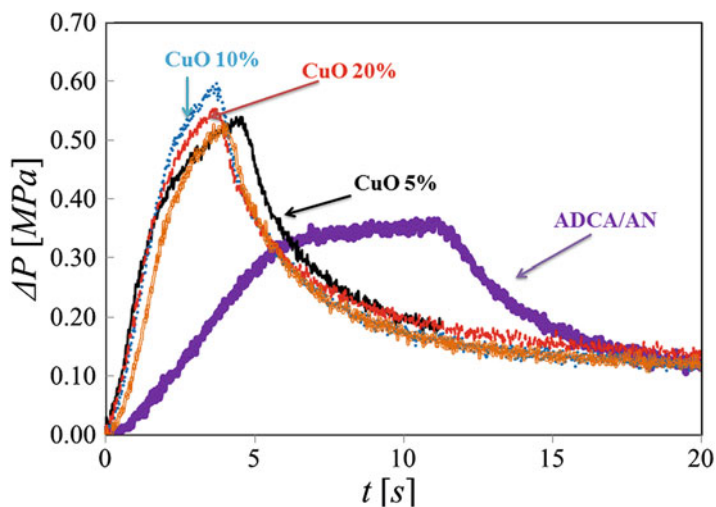
Fig. 15 Pressure time histories of ADCA/AN mixture and ADCA/AN/CuO mixtures from rate-of-pressure-rise test [60]

It was shown from Table 5 that $(\Delta P(\Delta t)^{-1})_{av}$ of ADCA/AN/Cu mixture and ADCA/AN/CuO mixture were higher than that of GN/SrN/BCN mixture, showing that both mixtures have the potential as gas-generating agents. In the case of BCN added mixture; $(\Delta P(\Delta t)^{-1})_{av}$ was close to that of GN/SrN/BCN mixture. It was also found from Table 6 that increasing the amount of CuO up to ten parts by weight increased $(\Delta P(\Delta t)^{-1})_{av}$. As for the effect of CuO content on the burning performance, it was found from Table 6 that increasing the amount of CuO up to ten

Table 5 ΔP, Δt, and $\Delta P(\Delta t)^{-1}$ of ADCA/AN-based mixtures [59]

Sample	ΔP[MPa]	Δt[s]	$\Delta P|\Delta t$ [MPa•s^{-1}]
ADCA/AN	0.36	11.06	0.033
ADCA/AN/CuO	0.59	3.52	0.168
ADCA/AN/MnO$_2$	0.40	11.27	0.035
ADCA/AN/Cu	0.67	2.80	0.239
ADCA/AN/BCN	0.54	4.60	0.118
GN/SrN/BCN	0.53	4.19	0.126

Table 6 ΔP, Δt, and $\Delta P (\Delta t)^{-1}$ of ADCA/AN mixture and ADCA/AN/CuO mixtures [60]

Sample	ΔP[MPa]	Δt[s]	$\Delta P|\Delta t$ [MPa•s^{-1}]
ADCA/AN	0.36	11.06	0.033
ADCA/AN/CuO 5%	0.54	4.38	0.123
ADCA/AN/CuO 10%	0.59	3.52	0.168
ADCA/AN/CuO 20%	0.56	3.68	0.152
GN/SrN/BCN	0.53	4.19	0.126

parts by weight increased $(\Delta P(\Delta t)^{-1})_{av}$. Compared with the data of GN/SrN/BCN mixture, it was shown that $\Delta P(\Delta t)^{-1}$ of ADCA/AN/CuO 10 % and 20 % mixtures were higher than that of GN/SrN/BCN mixture, showing that ADCA/AN/CuO mixtures have the potential as gas-generating agents.

2.3.3 Temperature History of Combustion Waves

In order to investigate how the addition of CuO affects the combustion mechanism of ADCA/AN mixtures, temperature histories in the vicinity of the burning surface were measured, and the burning surface temperatures (T_s) were determined through the temperature inflection point method by Sabadell et al. [67]. Equation 2 [67] represents the temperature history at the solid phase:

$$T - T_0 = (T_S - T_0) \exp\left(\frac{c\rho r x}{\lambda}\right) \tag{2}$$

Here, T_0 is the initial temperature, λ is the thermal conductivity of the solid phase, ρ is the sample density, c is the specific heat of the solid phase, r is the linear burning rate, and x is the distance in the direction of the combustion. Using this equation, the onset temperatures of the condensed phase were also determined, and from the positions of these two temperatures, the thickness of the condensed phase was determined.

Figure 16 shows an example of the relationship between $\ln(T-T_0)$ and x, and Figs. 17–19 are the measured results of onset temperature of condensed layer, burning surface temperature, and thickness of condensed layer, respectively, for each mixtures, where T_1 is the onset temperature of the condensed phase and x_c is the thickness of the condensed phase.
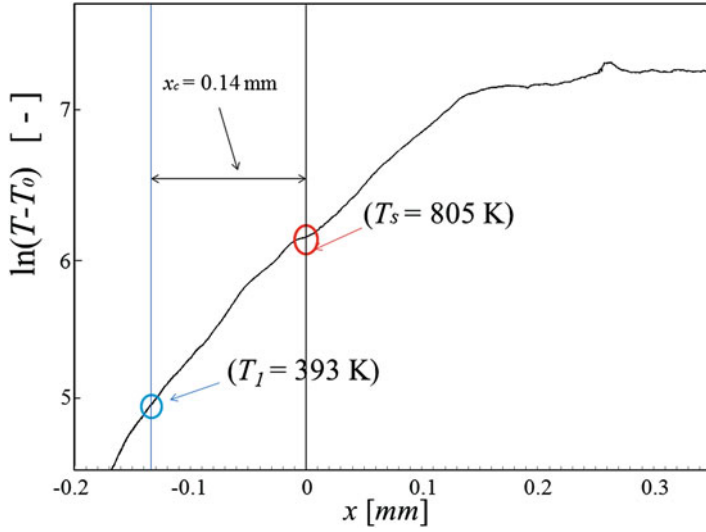
Fig. 16 An example of ln(T-T_0) vs x curve for ADCA/AN mixture at 2 MPa [60]
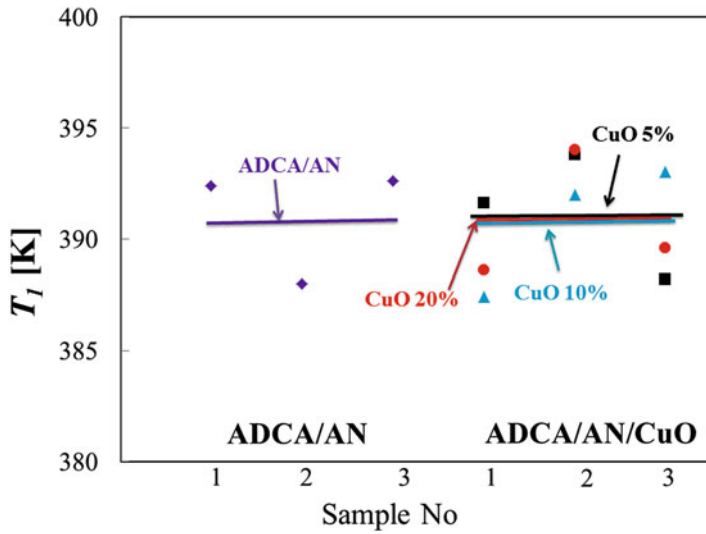
Fig. 17 Onset temperatures of the condensed phase for ADCA/AN-based mixtures [60]
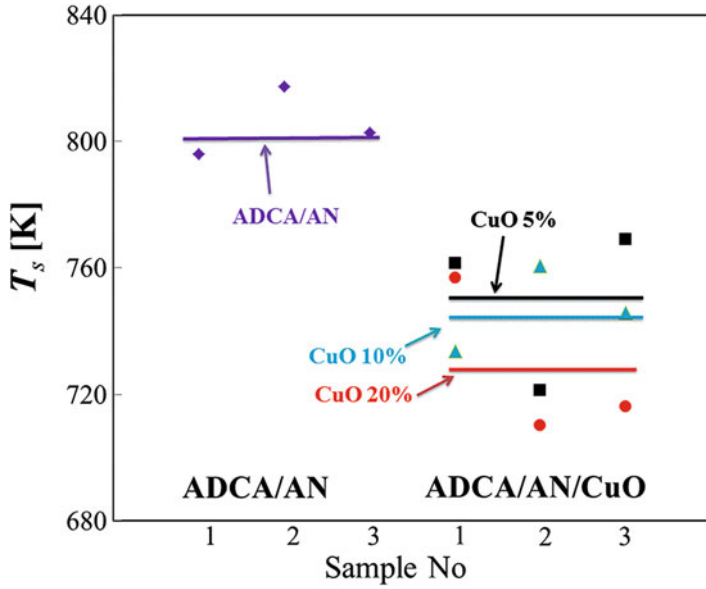
Fig. 18 Burning surface temperatures for ADCA/AN-based mixtures [60]
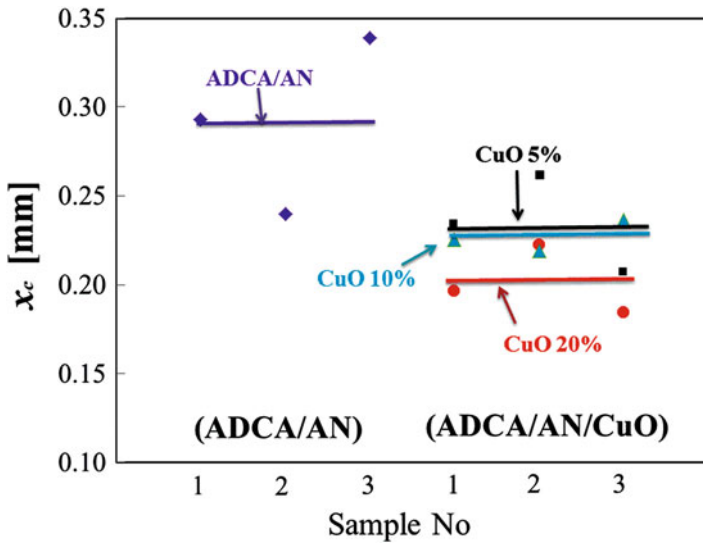
Fig. 19 Thickness of condensed phase for ADCA/AN-based mixtures [60]
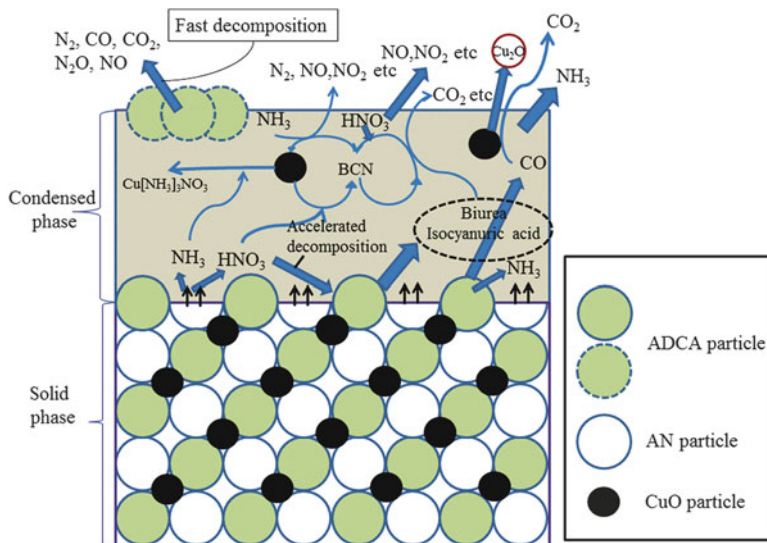
Fig. 20 Suggested burning mechanism of ADCA/AN/CuO mixtures [66]

As shown in Fig. 17, the onset of temperature of the condensed phase generally did not change. However, burning surface temperatures generally became lower with the addition of CuO as compared to the stoichiometric ratio ADCA/AN mixture, as shown in Fig. 18. In addition, burning surface temperatures also became lower by increasing the amount of CuO. Meanwhile, as shown in Fig. 19, the thicknesses of the condensed phase for ADCA/AN/CuO mixtures were also smaller than those of ADCA/AN mixture, and it was shown that the thickness became smaller with the increase in the amount of CuO that was added. Based on the experimental results, Ikeda [66] has suggested the burning mechanism of ADCA/AN/CuO mixtures as given in Fig. 20, where catalytic AN decomposition cycle involving CuO, similar to Miyata [3] (except that $Cu(NO_3)_3$ NO_3, as well as $Cu_2(OH)_3NO_3$, is also formed as intermediate) takes place inside the condensed phase, causing accelerated combustion of ADCA/AN-based mixture.

3   Conclusions

Brief overviews of the process and history of automobile airbag systems, ingredients used for pyro-type gas-generating agents, and some past studies on the combustion behaviors of AN-based gas-generating agents are given, including the recent studies, e.g., AGAT/AN/CuO mixtures, ADCA/AN/CuO mixtures, that demonstrated superior combustion characteristics as compared to conventional gas-generating agents. Past studies on the burning mechanisms of some AN-based gas-generating agents

were also given. For the additive CuO which was shown to accelerate the AN-based mixtures, catalytic cycle of the CuO in the condensed phase was suggested, causing accelerated decomposition of AN, which in turn has accelerated the burning characteristics of the AN-based mixture.

References

1. Japan Explosives Society (ed) (2010) Energetic materials handbook, 2nd edn. Maruzen, Tokyo (in Japanese)
2. Yoshida T, Hasegawa K (1996) Application of reactive chemical substance – from fireworks to airbags, space rockets. Tokyo Progress System, Tokyo (in Japanese)
3. Miyata Y (2009) Combustion characteristics of aminoguanidinium 5,5′-azobis-1H-tetrazolate/ammonium nitrate based gas generating agents, National Defense Academy Doctorate Thesis (in Japanese)
4. United Nations (2011) Recommendations on the transport of dangerous goods – model regulations volume 1 seventeenth revised edition. United Nations, New York and Geneva
5. Parrott AH, Round H (1920) US Patent, US 1331359, Air Cushion
6. Hetrick JW (1953) US Patent, US 2649311A, Safety Cushion Assembly for Automobile Vehicles
7. Linderer W (1953) German Patent DE 896312 C, Einrichtung zum Schutze von in Fahrzeugen befindlichen Personen gegen Verletzungen bei Zusammenstoessen
8. Ziegahn K-F (2006) AIRBAG 200X – how the largest technical community meeting has influenced R&D. In: Proceedings of 8th international symposium and exhibition on sophisticated car occupant safety systems, V8-1 ∼ 8-8, Karlsruhe, Germany, 4–6 Dec
9. National Highway Traffic Safety Administration (1985) Federal Motor Vehicle Safety Standard (FMVSS) No. 208
10. Iijima S (2006) Airbag System for Motorcycle, Proceedings of 8th international symposium and exhibition on sophisticated car occupant safety systems, V17-1 ∼ 17-18, Karlsruhe, Germany, 4–6 Dec
11. Toyota (2008) Toyota Media Release, (http://media.toyota.ca/curtain-shield-airbag)
12. Volvo Car Group (2012) Volvo Car Group Global Newsroom Press Release May 23 2012 (https://www.media.volvocars.com/global/en-gb/media/pressreleases/43844)
13. Kaufman MH, Davidson JS (1964) US Patent, US 3122462, Novel Pyrotechnics
14. Klager K, Dekker AO (1974) US Patent, US 3814694, Non-toxic Gas Generation
15. Sidebottom EW (1975) US Patent, US 3883373, Gas Generating Compositions
16. Pietz J F (1975) US Patent, US 3895098, Method and Composition for Generating Nitrogen Gas
17. DiValentin MA (1976) US Patents, Metal Oxide/Azide Gas Generating Compositions
18. Hasue K, Kazumi T, Iwama A (1991) Combustion aspects of sodium azide and its mixtures with potassium perchlorate and burning catalysts. Kogyo Kayaku (Sci Tech Energetic Mater) 52:190–198 (in Japanese)
19. Prior J, Siegelin W (1973) US Patent, US 3719604, Pressurizing-gas-producing Charges Containing an Aminoguanidine Tetrazole and an Oxygen-liberating or Gas-evolving Additive
20. Catanzarite VO (1975) US Patent, US 3910805, Low Temperature Gas Generating Compositions
21. Chang MS, Whitman CL, Haiss HS, Highby JH (1975) US Patent, US 3909322, 1975, Solid Gas Generating and Gun Propellant Compositions Containing a Nitroaminotetrazole Salt
22. Shaw GC (1983) US Patent, US 4369079, Solid Non-azide Nitrogen Gas Generant Compositions

23. Lund GK, Blau RJ (1996) US Patent, US 5500059, Anhydrous 5-Aminotetrazole Gas Generating Compositions and Methods of Preparation
24. Lundstrom NH, Scheffee RS, Luke DS (2000) US Patent, US 6123790, Nonazide Ammonium Nitrate Based Gas Generant Compositions that Burn at Ambient Pressure
25. Khandhadia PS, Burns SP (2001) US Patent, US 6306232B1, Thermally Stable Nonazide Automotive Airbag Propellants
26. Shaw GC (1983) US Patent, US4369079, Solid Non-azide Nitrogen Gas Generant Compositions
27. Gast E, Semmler P, Schmid B (1995) Worldwide Patent, WO 95/09825, Gas Developing Agent
28. Wardle RB, Hinshaw JC, Hajik RM (1990) US Patent, US 4993112, Gas Generating Compositions Containing Nitrotriazolone
29. Poole DR (1998) US Patent, US 5035757, Azide-free Gas Generant Compositions with Easily Filterable Combustion Products
30. Lund GK, Stevens MR, Edwards WW, Shaw III GC (1993) US Patent, US 5197758A, Nitrogen Gas Generators for Inflatable Devices or Propellants
31. Gast E, Semmler P, Schmid B (1998) German Patent, DE 19812372 C2, Propellants for Gas Generator (in German)
32. Sato E, Kubo D, Ikeda K (2002) World Patent, WO 02/30850, Gas Generating Agent Composition and Gas Generator Employing the Same
33. Hasue K, Boonyarat P, Miyata Y, Takagi J (2001) Combustion characteristics of 5-amino-1H-tetrazole and strontium nitrate mixtures. Sci Tech Energetic Mater 62:168–174
34. Iwakuma K, Miyata Y, Date S, Kohga M, Hasue K (2006) A study on the combustion of 5,5′-azobis-tetrazole aminoguanidine/strontium nitrate as a gas generating agent. Sci Tech Energetic Mater 68:95–101
35. Barnes MW, Taylor RD (1997) US Patent, US 5608183, Gas Generant Compositions Containing Amine Nitrates plus Basic Copper(II) Nitrate and/or Cobalt (III) Triamine Trinitrate
36. Lundstrom NH, Scheffee RS, Luke DS (2000) US Patent, US 6143102, Burn-rate-enhanced Basic Copper Nitrate-containing Gas Generant Compositions and Methods
37. Thibieroz B, Giraud E, Choune G (2005) French Patent, FR 2866022, Pyrotechnic Composition for the Generation of Gas to Inflate Safety Bags used in Protection Systems for Occupants of Automobile Vehicles
38. Blau RJ, Lund GK (1995) US Patent, US 5472647, Method for Preparing Anhydrous Tetrazole Gas Generant Compositions
39. Taylor RD, Deppert TM, Barnes MW (1995) US Patent, US 5467715A, Gas Generant Compositions
40. Yamato Y (2000) Japanese Patent, JP 2000-86375, Gas Generating Agents for Airbags (in Japanese)
41. Abe M, Ogura T, Miyata Y, Okamoto K, Date S, Kohga M, Hasue K (2008) Evaluation of gas generating ability of some tetrazoles and copper(II) oxide mixtures through closed vessel test and theoretical calculation. Sci Tech Energetic Mater 69:183–191
42. Date S, Itadzu N, Sugiyama T, Miyata Y, Iwakuma K, Abe M, Yoshitake K, Nishi S, Hasue K (2009) A study on the combustion of guanidinium 1,5′- bis - 1H -tetrazolate/copper (II) oxide. Sci Tech Energetic Mater 70:152–157
43. Date S, Sugiyama T, Itadzu N, Miyata Y, Iwakuma K, Abe M, Yoshitake K, Nishi S, Hasue K (2009) A study on the burning characteristics of some guanidinium 1,5′- bis - 1H - tetrazolate/metal oxide mixtures. Sci Tech Energetic Mater 70:23–26
44. Takahori K, Yamato Y, Yokoyama T (1994) Japanese Patent, JP 1994-239683, Gas Generating Agent Compositions (in Japanese)
45. Hara K, Yoshida T, Misawa T, Maekawa T, Yoshi S, Yokoyama T, Kazumi T, Hayashi M (1998) Concept and performance of a non-azide propellant for automotive airbag inflators. Propellants Explos Pyrotechnics 23:28–33
46. Hasue K, Matukawa M, Tamura H (1999) Combustion aspects of the consolidated mixtures of boron and potassium perchlorate at cryogenic temperatures. Kayaku Gakkaishi (Sci Tech Energetic Mater) 60:17–23 (in Japanese)

47. Hasue K, Akanuma T, Hodai H, Date S (1999) Combustion aspects of the consolidated mixtures of 5-amino-1H-tetrazole and potassium perchlorate. Kayaku Gakkaishi (Sci Tech Energetic Mater) 60:31–37 (in Japanese)

48. Miyata Y, Kanoh H, Date S, Hasue K (2005) Combustion characteristics of the consolidated mixtures of 5-amino-1H-tetrazole and sodium perchlorate. Sci Tech Energetic Mater 66:233–239

49. Date S, Boonyarat P, Kazumi T, Hasue K (2002) Screening test of gas-generating agents using closed strand burner. Kayaku Gakkaishi (Sci Tech Energetic Mater) 63:209–215

50. Date S, Miyata Y, Kazumi T, Hasue K (2005) Study on the reduction of possible harmful gases from gas generating agents (I): effect of addition of organic compounds. Sci Tech Energetic Mater 66:307–314

51. Fuhr I, Birke C, Leisinger K, Reinhard W, Heintz T (2006) Continuous production of spherical ammonium nitrate particles. In: Proceedings of 8th international symposium and exhibition on sophisticated car occupant safety systems, P35-1 – 35-12, Karlsruhe, Germany, 4–6 Dec

52. Nagayama S, Katoh K, Higashi E, Nakano K, Habu H (2014) Effect of polymer addition amount and type on thermal decomposition behavior of spray-dried particles comprising ammonium nitrate, potassium nitrate, and polymer. J Therm Anal Calorim 118:1221–1227

53. Kumasaki M, Miyasaka R, Kiuchi H, Wada Y, Arai M, Tamura M (2001) The properties of azole-copper complexes. Kayaku Gakkaishi (Sci Tech Energetic Mater) 62:109–116

54. Kumasaki M, Nakano M, Sasahara K, Date S, Mizutani T (2014) Study on synthesis and properties of ammonium salts of 1,2,4-triazole-3-one and 1,2,4-triazolidine-3,5-dione. Sci Tech Energetic Mater 75:157–161

55. Miyata Y, Abe M, Date S, Kohga M, Hasue K (2008) Burning characteristics of aminoguanidinium 5,5′-azobis-1H-tetrazolate/ammonium nitrate as gas generating mixtures. Sci Tech Energetic Mater 69:117–122

56. Hasue K, Yoshitake K (2013) The mixture of the phase stabilized ammonium nitrate containing potassium nitrate and 1HT as the new gas generant composition. Sci Tech Energetic Mater 74:66–72

57. Wada Y, Hori K, Arai M (2010) Combustion mechanism of mixtures of guanidine nitrate, ammonium nitrate, and basic copper nitrate. Sci Tech Energetic Mater 71:83–86

58. Arai M, Wada Y, Tomiyama S, Iwai Y, Oda S (2012) US20120261040 A1, Gas-Generating Agent Composition

59. Ikeda K, Doi A, Date S (2014) Burning characteristics of some azodicarbonamide/ammonium nitrate/additive mixtures(II). Sci Tech Energetic Mater 75:83–85

60. Ikeda K, Shiraishi Y, Date S (2014) Burning characteristics of some azodicarbonamide/ammonium nitrate/additive mixtures. Sci Tech Energetic Mater 75:59–63

61. Sinditskii VP, Egorshev VY, Levshenkov AI, Serushkin VV (2005) Ammonium nitrate: combustion mechanism and the role of additives. Propellants Explos Pyrotechnics 2005(30):269–280

62. Izato Y, Miyake A, Date S (2013) Combustion characteristics of ammonium nitrate and carbon mixtures based on a thermal decomposition mechanism. Propellants Explos Pyrotechnics 38:129–135

63. Brodhacker JW, Stengel LA, (1953) US2657977, Process for Preventing the Physical Disintegration of Ammonium Nitrate by Temperature Fluctuations

64. Menke K, Bohnlein-Mauss J, Schmid H, Bucerius K M, Engel W (1996) US5589661, Solid Propellant Containing Ammonium Nitrate Phase-stabilized with Copper or Zinc Oxide, Binder Polymer, Energy-rich Plasticizer, Burning Moderator of Vanadium/Molybdenum Oxide

65. The National Highway Traffic Safety Administration (2014) NHTSA statement on Takata air bag inflators. (http://www.safercar.gov/Vehicle+Owners/NHTSA-statement-on-takata-air-bags)

66. Ikeda K (2014) Effect of addition of CuO upon the combustion characteristics of azodicarbonamide/ammonium nitrate based gas generating agents, National Defense Academy Master Thesis (in Japanese)

67. Sabadell AJ, Summerfield M, Wenograd J (1965) Measurement of temperature profiles through solid-propellant flames using fine thermocouples. AIAA J 3:1580–1584

Comparison of Chemical Propulsion Solutions for Large Space Debris Active Removal

Pietro Tadini, Urbano Tancredi, Michele Grassi, Carmen Pardini, Luciano Anselmo, Toru Shimada, and Luigi T. DeLuca

Abstract In recent years, the development of active removal missions, to face the growing risk of catastrophic collisions and new debris generation due to the high density of orbital debris in LEO, is widely discussed in the international space community. Besides legal and political issues, active removal solutions are strongly hampered by the high costs involved. Chemical propulsion might represent the preferred way to carry out the controlled reentry of large abandoned objects, and, in the perspective of cost reduction, hybrid rocket technology is considered a valuable option, due to the potential lower fabrication and operational costs, if compared with bipropellant liquid systems. The possibility to use nontoxic propellants, besides their lower prices, reduces the complexity of handling, storability, and loading operations, decreasing the connected costs and avoiding the need of a special staff. Solid rocket technology allows for very small and compact motor units, although without throttleability and reignition capability and characterized by lower safety level than liquid and hybrid systems. This study deals with the preliminary design and mass budget of solid, liquid, and hybrid propulsion modules, as well as their comparison, to be used for active removal of large abandoned rockets in LEO.

P. Tadini (✉) • L.T. DeLuca
Space Propulsion Laboratory (SPLab), Department of Aerospace Science and Technology, Politecnico di Milano, 20156 Milan, Italy
e-mail: pietro.tadini@polimi.it; luigi.deluca@polimi.it

U. Tancredi
University of Naples "Parthenope", 80133 Naples, Italy
e-mail: urbano.tancredi@uniparthenope.it

M. Grassi
University of Naples "Federico II", 80138 Naples, Italy
e-mail: michele.grassi@unina.it

C. Pardini • L. Anselmo
Institute of Information Science and Technologies (ISTI), Consiglio Nazionale delle Ricerche (CNR), 56124 Pisa, Italy
e-mail: carmen.pardini@isti.cnr.it; luciano.anselmo@isti.cnr.it

T. Shimada
Institute of Space and Astronautical Science (ISAS), Japan Aerospace Exploration Agency (JAXA), Sagamihara 252–5210, Japan
e-mail: shimada.toru@jaxa.jp

985

Acronyms

ADR	Active Debris Removal
CCPs	Condensed Combustion Products
CEA	Chemical Equilibrium for Applications
DeoKit	De-orbiting Kit
DOF	Degrees-of-Freedom
ESA	European Space Agency
FPA	Flight Path Angle
GEO	Geostationary Orbit
GOX	Gaseous Oxygen
HPM	Hybrid Propulsion Module
HTP	High-Test Peroxide
HTPB	Hydroxyl-Terminated Polybutadiene
IADC	Inter-Agency Space Debris Coordination Committee
LEO	Low Earth Orbit
LOx	Liquid Oxygen
LPM	Liquid Propulsion Module
MMH	Monomethylhydrazine
NTO	Nitrogen Tetroxide
PB	Polybutadiene
PE	Polyethylene
PMD	Post-Mission Disposal
PMM	Polymethyl methacrylate
RAAN	Right Ascension of the Ascending Node
RCS	Reaction Control System
SPM	Solid Propulsion Module
UDMH	Unsymmetrical Dimethylhydrazine

1 Introduction

Since the 1980s, the increasing relevance of the orbital debris problem, in order to guarantee the sustainable future use of circumterrestrial space, became progressively evident [1]. In addition to the voluntary adoption of specific mitigation measures by single space agencies, the need of addressing the issue on a global basis led to the creation of the Inter-Agency Space Debris Coordination Committee (IADC), which approved in 2002 the first version of a set of recommended space debris mitigation guidelines [2]. These inspired national laws or guidelines and international standards, intended to direct the actions of government and private entities in space. Finally, in 2007, recommendations derived from the IADC guidelines were endorsed by the United Nations [3].

During the past quarter of century, the efforts were concentrated on the adoption of mitigation measures, aiming at reducing or preventing the production of new

orbital debris. These measures included the passivation of spacecraft and upper stages at the end of their operational life, in order to prevent accidental explosions; the choice of hardware and procedures to minimize the release of mission-related objects; the end-of-life removal of spacecraft from relatively crowded space regions, as the geostationary orbit (GEO) ring; the limitation of the residual orbital lifetime of abandoned spacecraft and rocket bodies in low Earth orbit (LEO), below the altitude of 2000 km; and the prevention of accidental catastrophic collisions with conjunction assessments and, if needed, avoidance maneuvers [4]. Unfortunately, notwithstanding the progresses observed over the course of the years, the global level of compliance with the mitigation recommendations, in particular those dealing with the re-orbiting of spacecraft and upper stages after mission completion, is still relatively modest, being around 2/3 in GEO [5] and short of 60 % in LEO [6].

Moreover, during the last decade, the results of some long-term simulations of the debris evolution suggested that mitigation measures alone, even if duly implemented in more than 90 % of the cases, might not be sufficient to stabilize the number of orbital debris >10 cm in the currently most crowded altitude ranges in LEO, being such objects the typical "projectiles" able to cause the catastrophic fragmentation of average spacecraft or rocket bodies at characteristic collision velocities in excess of 10 km/s [7–9]. Invoking the recourse to "remediation," by managing the existing space debris population through Active Debris Removal (ADR), became, therefore, more and more popular in recent years [10–12], and various ranking schemes were developed to prioritize the potential target objects to be removed first, in order to favor a more benign evolution of the circumterrestrial environment on the long term [10, 13–17].

Unfortunately, the ranking schemes developed so far are affected by some evident drawbacks, because very often the provided indications are either obvious or nonsensical. In fact, they try to find a deterministic order in a problem, the long-term evolution of orbital debris in LEO, which would be driven, after several decades at most, by a few tens of catastrophic collisions (over 200 years). And the latter, from the occurrence point of view, have the properties of discrete-time Markov chains [18]. In other words, the debris long-term evolution would be driven by a memoryless random process, i.e., the occurrence of catastrophic collisions, characterized by an extremely wide range of possible cumulative outcomes, in terms of debris number and distribution. In addition to that, the modeling of the long-term debris evolution is affected by large uncertainties in several critical areas [18–22], so the justification of expensive remediation actions on quite uncertain assumptions and results may still be premature.

Even though the evidence available so far is not reliable enough to support a specific remediation strategy, some basic facts cannot be disputed. Most of the cross-sectional area and mass in orbit (approximately 7000 metric tons) are concentrated in about 4750 abandoned intact objects, i.e., spacecraft and rocket bodies, plus a further 1250 operational spacecraft [23, 24]. In LEO, the abandoned objects and the associated mass are not evenly distributed but quite often concentrated in relatively narrow altitude-inclination bands, where the probability of catastrophic collision is significantly above the average. This clustering pattern frequently involves a
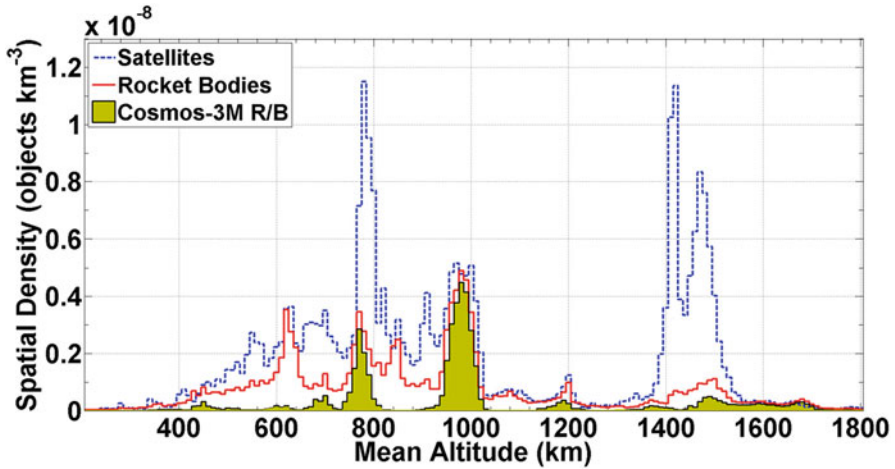
Fig. 1 Spatial density in LEO of intact satellites and rocket bodies. The spent Cosmos-3M second stages account for most of the abandoned rocket bodies in two of the most crowded altitude shells, between 750 and 1050 km

substantial number of identical objects, as upper stages of the same model. For instance, the former Soviet Union, Russia, and Ukraine have left in orbit 291 Cosmos-3M second stages, with a mass of 1400 kg; 110 Tsiklon-3 upper stages, with a mass of 1410 kg; and 22 Zenit second stages, with a mass of 8900 kg [23]. The combined mass of these three types of objects alone is around 758 metric tons, representing more than 1/4 of the mass resident in LEO [14, 25].

It seems quite reasonable that any plausible remediation scheme, if and when deemed necessary, should start considering the active removal of abandoned mass (as much and rapidly as possible) from crowded LEO regions [26], and the targeting of very similar objects in general, and of upper stages in particular, would offer a lot of advantages already discussed elsewhere [25, 27]. A very attractive target for active removal would then be represented by the Russian Cosmos-3M second stages, with diameter of 2.4 m and length of 6.5 m, mainly concentrated in four critical altitude-inclination bands: 650–850 km, $i = 74$ deg; 850–1050 km, $i = 83$ deg; 900–1000 km, $i = 74$ deg; and 900–1050 km, $i = 66$ deg (Fig. 1).

Considering the current presence of 291 stages of this kind in orbit, any developed approach, capture, and removal techniques or procedures might be used many times over several decades. The moderate size and mass of these upper stages, coupled with their simple and compact shape, would be safer for initial demonstration missions and for routine operations as well. Moreover, it could be possible to operate in at least four separate altitude-inclination critical bands, the reentry risk assessment for de-orbiting (fragmentation analysis) should be needed only for one representative object, and the de-orbiting kits might be tailored for small series production. In addition, multiple rendezvous might be feasible within a single mission, because, for any given inclination, an average of about two stages

would be present in each 5 deg bin of right ascension of the ascending node, with more favorable concentrations around specific orbit planes [14, 25]. Furthermore, the technology kit developed, once proven its feasibility, might be applied to larger abandoned rocket bodies, like Zenit second stages. Last, but not least, the choice of the Cosmos-3M second stages would offer the occasion for a broad and systematic cooperation with Russia, which would be of paramount importance for the knowledge of the rocket body itself, for the eventual availability of launchers at low cost, and to solve a number of legal issues affecting any future active removal mission.

The latter aspect cannot be ignored, because the Liability Convention [28] states that "launching states" are liable for damages procured in space or on the ground by a space object, like those targeted for active removal. Additional legal issues arise from the Outer Space Treaty [28] and the Registration Convention [28]. Moreover, specific national directives or laws often address the ground safety issues, creating a quite complex web of national and international regulations to be met. Any significant and effective remediation initiative will therefore need a substantial amount of international cooperation.

2   Active Multi-removal Mission Concept

An active debris removal mission requires a very complex functional spacecraft, capable of performing a number of challenging operations, from rendezvous to debris capture and disposal. The ADR system complexity grows if a multi-removal capability is required, since the abovementioned operations have to be repeated a certain number of times [29]. In this case, indeed, a space system must be capable of reaching, capturing, and removing several targets, typically orbiting at different altitudes and inclinations. Nowadays, it does not exist a standard mission outline, because of the presence of different target typologies located in correspondence of several orbital altitudes and inclinations. The most critical aspect of an ADR mission is the target capture, because of the important challenge represented by the docking with a large noncooperative object, whose attitude might be unknown, requiring a safe relative rotation reduction [25, 30–32]. In this respect, different technological solutions are under investigation. However, assuming the capability of target capturing, its consecutive disposal plays the main role. In regard to the body size of the considered objects, instead of their transferring to a 25-year residual lifetime orbit or to a higher graveyard orbit outside LEO, a controlled atmospheric reentry toward a non-inhabited region might become a fundamental requirement in next future [14, 25, 30, 32, 33]. In fact, the latter solution allows for the control of the impact footprint and location of the object's fragments, providing a fast disposal and significantly reducing the collision probability that affects long-term disposal approaches.

To reduce the high cost and risk related to the design and development of a such complex system, as well as its operation control, a possible solution regards

the use of the launcher's upper stage to place in orbit a certain number of deorbiting kits (DeoKits), each one removing a single large abandoned object [34]. The DeoKit shall be able to perform the rendezvous with the selected target and, being equipped with an automated device, the safe debris capture and mating, as well as the target safe de-orbiting and reentry into the Earth atmosphere, by means of a suitable primary propulsion module [14, 25, 34]. Among the space launchers owned by the European Space Agency (ESA), concerning the ADR mission concept here analyzed, the upper stage of Soyuz (Fregat) might represent the best candidate for DeoKits carrying and distribution, once verified the ADR economical feasibility. Specifically, Fregat can be restarted up to 20 times and has a total ΔV capability of about 4.7 km/s [35]. This provides the possibility of performing multiple removals with a single launch, using Fregat propulsion to deploy each DeoKit close to the debris to be removed. Of course, once the candidate targets have been identified, the removal sequence has to be optimized based on Fregat capability in terms of total velocity increment, as well as number and mass of the de-orbiting kits embarked on board. The multi-removal mission under analysis involves several steps and critical aspects. Apart from setting the best rendezvous sequence, an effective midrange rendezvous maneuver is required for each DeoKit, exploiting its primary propulsion module, to reach the selected debris, after separation from Fregat. Once in the vicinity of the target, a secondary propulsion system made by a reaction control system (RCS) must allow for close-proximity operations [14, 30], as well as object capturing. In addition, in order to perform the debris disposal, the DeoKit must be rigidly and reliably connected to the target external structure with a mechanism such as, for example, the one proposed in [14, 27, 29]. With reference to Fig. 2, the different steps of a single removal phase can be summarized as follows:
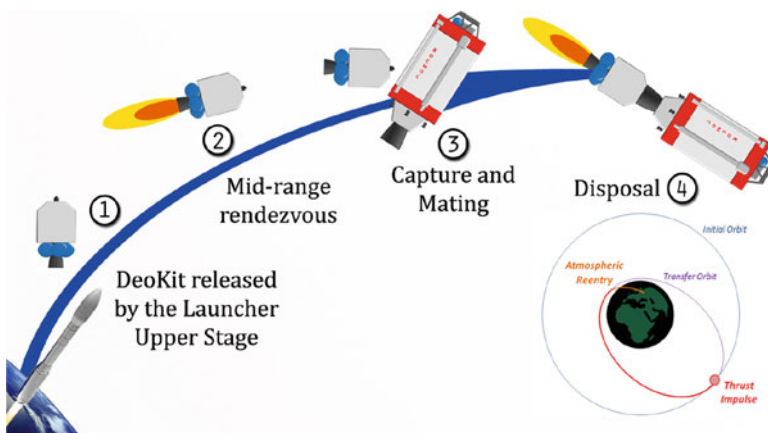
Fig. 2 ADR mission conceptual scheme: removal of a Cosmos-3M second stage

1. The DeoKit is released by the upper stage at a prefixed distance from the first target in the same orbit plane.
2. The DeoKit uses its own propulsion unit to perform terminal rendezvous.
3. Once reached the object, the DeoKit proceed with capture and mating to rigidly connect itself with the debris, by means of specific mechanisms [14, 25].
4. The propulsion module of the DeoKit is remotely ignited to perform the target disposal: target and de-orbiting kit are de-orbited in the mated configuration, after a phasing time needed to aim at the selected zone of the Pacific Ocean.

Once the first DeoKit has been released, the upper stage moves toward the next target on a different orbit, and operations from 1 to 4 are carried out by a second DeoKit. After the release of the last de-orbiting kit, Fregat is de-orbited as well. In order to perform preliminary analyses, a demonstrative two-removal mission is investigated considering the removal of two Cosmos-3M second stages, namely, Cosmos-3M 11112 and Cosmos-3M 22676, located at an average altitude of 767.62 and 777.97 km, respectively, and 74 deg inclination. To this end, it is assumed that the removal system is injected in a 700 km circular orbit in the same plane of the first target. Considering the rendezvous strategy and the assumptions introduced in [25], the two rendezvous maneuvers would require a total velocity increment of about 100 m/s. The additional ΔV needed to nullify the right ascension of the ascending node (RAAN) differences can be estimated in about 600 m/s, considering that, typically, an average of about two stages would be present in each 5-deg bin of RAAN. Thus, the total velocity increment required for each removal would be lower than 700 m/s. Considering Fregat total ΔV capacity, this would allow the removal of more than five objects within a single mission. On the contrary, if we limit the multi-removal mission to five objects, as suggested by the debris population evolution scenarios, the ΔV which could be used for each rendezvous maneuver would be slightly lower than 1000 m/s, thus allowing to nullify RAAN differences up to about 7°–8°. Nevertheless, it is worth outlining that the actual required velocity increment for each removal depends on the strategy being used for the multi-removal mission, which is not described in details, being it beyond the aim of this preliminary analysis.

2.1 De-orbiting Phase Design

Once the DeoKit has been rigidly connected to the selected debris, it is ignited to start the controlled de-orbiting and atmospheric reentry. For the disposal, both single apogee burn and multi-burn strategies could be envisaged, even though the large size of the reentering objects suggests to limit the number of burns to allow an immediate reentry, so to relax the attitude control requirements of the mated configuration. Indeed, below 300 km the atmospheric torque can significantly affect the controlled reentry maneuver [36]. On the other hand, a multi-burn approach might be considered when the abandoned object orbits at high altitudes in order to achieve a better control of the conditions for the final atmospheric reentry and

Fig. 3 De-orbiting maneuver schematic
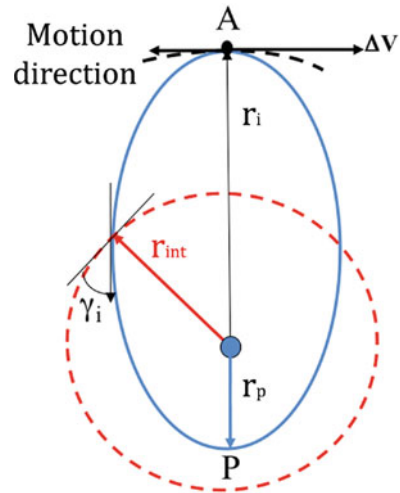
impact footprint [32]. Due to the large size and mass of the reentering objects, the destruction process in the atmosphere could be incomplete, with a high residual risk of ground impact. Hence, the reentry shall be controlled and directed to a specific location on Earth (South Pacific or Atlantic Ocean). With reference to previous studies on LEO de-orbiting strategies [36], a disposal strategy is pursued in which the mated configuration (DeoKit debris) is steered to an elliptical transfer orbit with a perigee enough low to allow for an immediate atmospheric capture. In addition, to limit the ground impact area of fragments surviving the atmospheric phase, a sufficiently steep flight path angle (FPA) is required. In particular, a preliminary, non-optimized, reentry trajectory analysis is performed in which an elliptical disposal orbit with a perigee below 60 km and FPA < -1.5 deg at 120 km is considered.

Figure 3 illustrates the de-orbiting strategy, where A is the apogee of the disposal ellipse and P is its perigee, whereas the red circle represents the reentry interface located at 120 km altitude. Under Keplerian orbit assumption, Eq. 1 relating the perigee radius r_p to the flight path angle at the reentry interface, γ_i, is found:

$$r_p = \frac{(r_i - r_{\text{int}})r_{\text{int}}\cos^2\gamma_i}{r_i - r_{\text{int}}\cos^2\gamma_i} \tag{1}$$

where r_{int} is the radius corresponding to an interface of 120 km altitude, while r_i is the radius of target's orbit. From Eq. 1, the perigee radius corresponding to a given FPA (or vice versa) is computed, and then, the ΔV needed for de-orbiting can be obtained. This study is focused on the comparison of different chemical propulsion technologies, as well as their respective motor performance and preliminary mass budget. From the point of view of multi-removal missions, small and compact propulsion modules are preferred, in order to maximize the number of DeoKits (i.e., of removed objects) carried on orbit by a single launch. Once released by

the launcher upper stage, each DeoKit is an autonomous spacecraft composed by a primary propulsion module and a service platform, here called ADR platform.

The latter includes the needed avionics, instrumentation and sensors for mission operations, the thermal system, batteries for power supply, the capture and mating mechanisms, as well as a secondary propulsion system (RCS) for the spacecraft attitude control. With the purpose of propulsion modules comparison, the same target and disposal profile are considered for all engine types. More specifically, the object to be removed is a Cosmos-3M second stage at an altitude of 770 km, requiring a ΔV of about 200 m/s. The reentry phase is simulated using a 3-deegres-of-freedom (DOF) standard dynamics model taking into account longitudinal motion only [37], spherical gravity, and US 76 Standard Atmosphere. A simplified hypersonic aerodynamic model of the Cosmos-3M mated to the DeoKit is used, based on assuming purely ballistic reentry and a Mach-independent drag coefficient, yielding a ballistic coefficient of about 100 kg/m^2.

The disposal simulation is performed by a single apogee burn, assuming a DeoKit mass of 566 kg estimated in previous work [34]; in this manner, a FPA of -1.74 deg at 120 km and a perigee altitude of about 54.7 km are achieved with a motor thrust of 4.2 kN for 90 s of combustion time (keeping the average acceleration level within 0.4 g). Figures 4 and 5 show, respectively, the average thrust and propellant mass flow rate required to satisfy the mission constraints and the FPA variation during the disposal flight of the mated configuration (DeoKit debris).
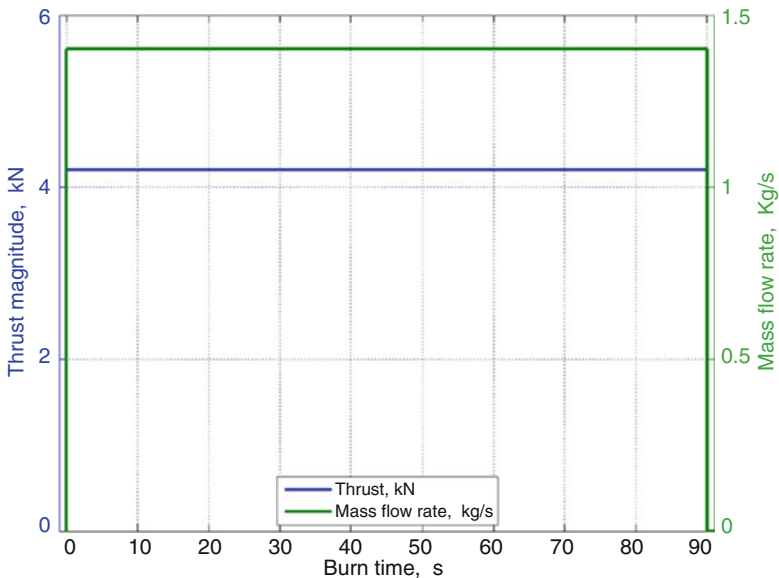
Fig. 4 Average thrust (*green*) and propellant mass flow rate (*blue*) needed to remove 1400 kg by means of a DeoKit of 566 kg, satisfying the constraints on FPA and perigee altitude
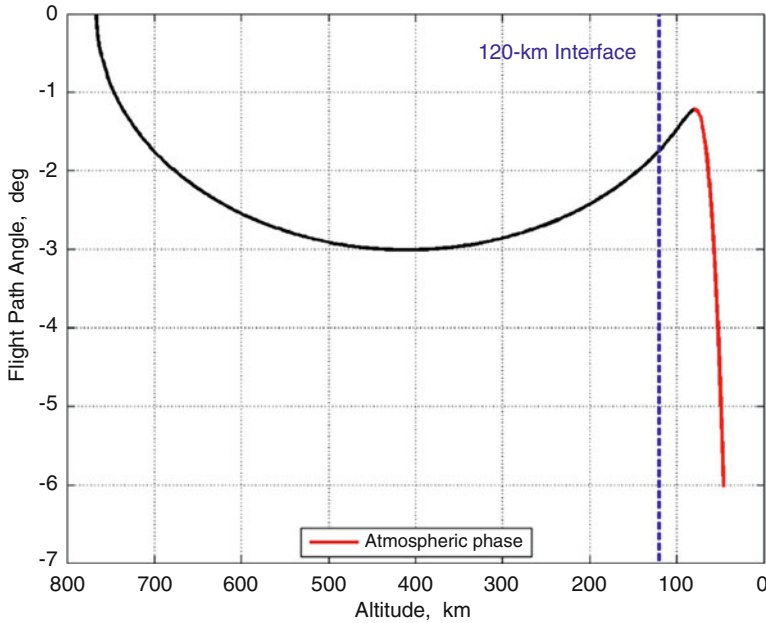
Fig. 5 Flight path angle change during the disposal maneuver
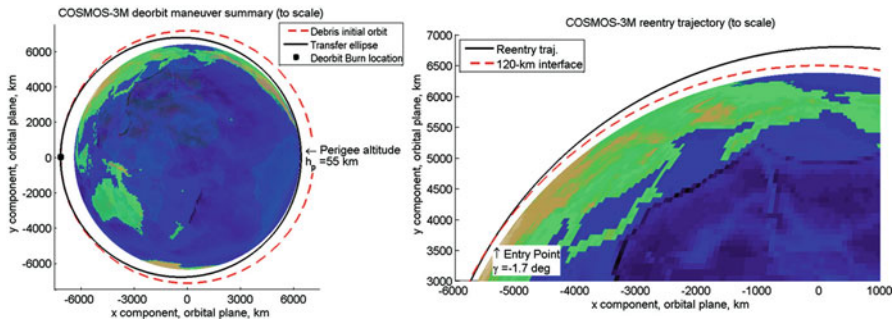
Fig. 6 Disposal trajectory summary: elliptical transfer orbit with FPA of −1.74 deg at 120 km and perigee altitude of 54.7 km

In Fig. 6, one can see the disposal trajectory. The propulsion module mass budget resulting from the preliminary design will be expressed as a percentage of total DeoKit mass (assumed as fixed value), thus identifying the amount of load, assigned to the ADR platform, which the engine can carry in addition to the target mass (1400 kg). According to this preliminary estimation, the Fregat would be able to carry 5 DeoKits (566 kg each one), for a total mass of 2830 kg, preserving about 2000 kg on the total payload capacity to LEO, confirming the Soyuz as possible candidate for a multi-removal demonstrative mission. However, the actual number

of DeoKits carried in orbit shall be checked against the volume available within the Soyuz fairing, the target orbits, and a more detailed mass budget including also the dispenser, as well as the possible presence of a satellite.

3 Propulsion Module

The target size, the disposal strategy, and the propulsion technology are important aspects with a strong impact on mass budget, system volume, and cost of the propulsion unit. Considering a large object, the capability of throttling and reignition may represent a stringent requirement for the adequate control of the rendezvous and disposal maneuvers, whereas compact design is important for easier docking to the target and for dynamic stability of the final assembly. A compact volume may request a higher average propellant density but may collide with the ΔV requirements for a controlled atmospheric reentry, needed for the LEO objects in the highest altitude. Thrust level should stem from a trade-off choice about the risk of debris fragmentation, especially for large spacecraft, and long mission duration (correlated to propellant storability and collision risk during the maneuver). In the frame of chemical propulsion, solid propellants represent a simple, reliable, and proven technology with good specific impulses but feature limited flexibility and not suitability for multi-burn missions, whereas liquid bipropellants fill the gaps left by the solid systems, but larger volumes and higher degree of complexity are requested. In fact, the walls of combustion chamber and nozzle require to be cooled to sustain the aggressive combustion environment with which they are in direct contact, so high resistance and more expensive materials are needed; also the injection and feeding systems require a complex design, thus involving a quite high level of costs for liquid propulsion technology. Furthermore, the propellants handling must be carefully considered, due to the high toxicity of typical liquid substances used for space applications (NTO, MMH, UDMH, etc.). In this respect, a great interest is oriented to hybrid rocket technology, due to the high specific impulse achievable, intrinsic safety, possibility of green propellant use, low-cost technology, and, especially, reignition and thrust throttleability. Among the latter, also owned by liquid propulsion technology, the first allows for multi-burn disposal, which is highly recommended when the target orbits at high altitudes, in order to favor a better reentry trajectory selection, while the second might represent a key aspect to avoid the risk of fragmentation for the most fragile components of a large abandoned satellite during the de-orbiting maneuver.

3.1 Hybrid Propulsion Module

A hybrid rocket motor typically features the oxidizer in the liquid or gaseous state, while the fuel is in the solid state. Its safety is guaranteed by no contact between fuel

Table 1 Conceptual comparison between different features of chemical propulsion systems

	Solid propulsion	Liquid propulsion	Hybrid propulsion
Toxicity	Reduced	High	No
Performance I_s (s)	250–310	300–500	250–340
Safety	Low	Intermediate[a]	High[b]
Complexity-cost	Low	High	Reduced
Throttleability	No	Limited	Yes[c]
Reignition	No	Yes	Yes
TRL	9	9	7

[a]Explosion hazard due to leak of both fuel and oxidizer at gaseous phase
[b]Only the oxidizer presents hazard of leaks at gaseous phase, fuel is solid and inert
[c]The effective throttleability range of hybrid rocket is still under investigation among researchers

and oxidizer, except during the combustion phase. A hybrid rocket can also be built with particular geometries, by means of tangentially oxidizer injection, resulting very compact in size and highly efficient [38, 39]. Such characteristics could be the right solution for space debris mitigation, by supplementing new satellites with this engine type in the next future. Clearly, considering long time space missions, the solid fuel selection must account for materials characterized by negligible properties shifting because of aging. This technology seems very promising even in the field of space debris remediation, making possible the active removal in LEO of large intact objects (several metric tons), both spacecraft and rocket bodies, by using a chaser vehicle equipped with a hybrid propulsion module (HPM) for the controlled reentry maneuver and several micro-thrusters, for the attitude control, spilling directly the HPM liquid oxidizer to be used as a monopropellant (dual-mode use) [27, 40].

Overall, a hybrid motor represents a solution that mediates benefits and drawbacks from both liquid and solid rocket technology. In Table 1, a conceptual comparison between the three different propulsion systems is resumed. On one side, it is bestowed the throttleability and reignition capability typical of liquids, specific impulse levels that fall in between the performance of solid and liquid propulsion, and a higher mean propellant density due to the use of a solid fuel. Nevertheless, a technological gap exists due to its late development (i.e., low technology readiness levels) and lack of in-orbit demonstration. In the simplest possible configuration, a hybrid rocket is made by a central-perforated solid fuel placed in the combustion chamber where an injector blows liquid/gaseous oxidizer. This grain configuration shows a quite high volumetric efficiency ($\sim$80 %) for fuel amounts below 800 kg, with length-to-diameter L/D smaller than 20 [41], that would be the case of ADR missions. The main drawbacks of hybrid technology are, besides low fuel regression rate, poor combustion efficiency, hence unburned products, and oxidizer-to-fuel ratio (O/F) shifting with consecutive specific impulses losses. However, different means are considered, especially for the enhancement

Fig. 7 Hybrid motor alternative geometry configuration suggested by Gibbon et al. for satellites orbital transfer [46]
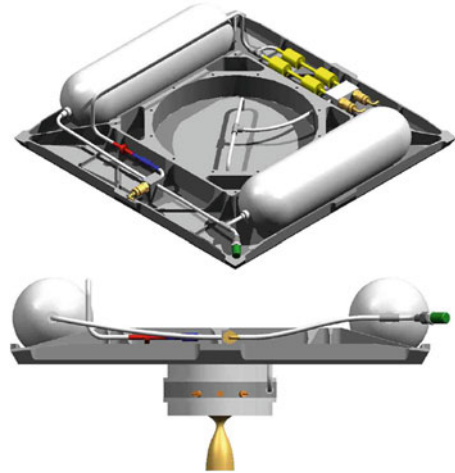
of mass burning rate, spanning from the use of advanced additives to different injection approaches (swirling oxidizer and vortex combustion) [38, 39, 42, 43]. In this respect, innovative designs of the combustion chamber, such as vortex pancake, provide higher combustion efficiency, low performance variation during combustion, and, in the case of solid metal additives, reduced emission of condensed combustion products (CCPs) thanks to the vortex combustion [38]. The vortex pancake configuration might represent a very interesting solution for post-mission disposal (PMD) maneuvers [44–46]: this small and compact hybrid rocket could be easily integrated in the design of new satellites (see Fig. 7), providing both the maneuver capability and the final disposal to a 25-year residual lifetime orbit, or a direct atmospheric reentry.

Therefore, cheap technological solutions might allow for a more easy approach to ADR by the international space community. Hybrid propulsion could help in this direction; in fact, once reached its complete maturity, the costs of hybrid motors might become very low, due to cheap propellants and construction materials, as well as technological solutions required. For example, aluminum can be used for the combustion chamber, which does not need a cooling system for walls, since they are protected by the solid fuel, which is itself an insulating material. The exhaust nozzle can be realized without a cooling system too, if the burn times are small $(90 \div 100\,s)$ [41]. Moreover, the injection system does not need a complex design, as well as the tanks and feed system, depending on the oxidizer selected. The ignition, if allowed by the oxidizer, can be performed by catalyst reaction, avoiding the need of a pyrotechnic ignition system (instead required for solid motors). Overall, this so reduced complexity could provide an important decrease in design and manufacturing costs, making hybrid motors more suitable for controlled reentry than liquid motors, in the perspective of ADR missions.

3.1.1 Propellant Selection

A great advantage of hybrid propulsion is the use of nontoxic propellants that are also significantly cheaper than common substances used in solid and liquid propulsion. Typical hybrid propellants almost do not exhibit explosion hazards since the oxidizer and the fuel remain separated during all manufacture, storage, and transport operations. This level of safety, together with their non-toxicity, reduces the overall costs of all ground operations before the mission. Different solid materials are considered as solid fuel, especially within the family of hydrocarbons [39]. During the years, the attention of research studies was mainly focused on carbon-based polymers and paraffin wax materials, depending on their costs, mechanical properties and combustion performances. In the polymers group, typical fuels are polyethylene (PE), polymethyl methacrylate (PMM), and polybutadiene (PB) with hydroxyl or carboxyl ion as chain terminators. These materials are quite cheap if compared with typically employed liquid propellants [41]. Moreover, cracks and voids in solid fuel are not so critical as in solid propellants, thus reducing the need of industrial-level high-quality control and assurance, in term of both manufacture and final product inspection. This aspect also contributes to reduce costs. The hydroxyl-terminated polybutadiene (HTPB) is the most popular and well-known solid fuel for hybrid propulsion, also due to its large use in solid propulsion as binder. It is a rubber compound very safe to handle, allowing to be easily powered with metal additives, maintaining very good mechanical properties. HTPB shows an isotropic behavior during the combustion [47], resulting very suitable for multiple burns missions. Although the regression rates provided are not so high with respect to paraffin-based fuels, HTPB is a quite energetic and very safe material, since if soaked in liquid oxygen it is not explosive [41]. Metal additives allow to reach greater regression rate levels, also providing a little increase in fuel density, which, for pure cured rubber, is about 915 kg/m^3 [41].

Compared to HTPB, PE and PMM are cheaper, but the latter, for large grains, can be subjected to cracks due to heat loads during the combustion process [41], introducing the hazard of nozzle throat obstruction. Because of this, PMM might result expensive, owing to the need of X-ray computed tomography and ultrasonic inspections for large size grains. Returning to HTPB, for example, not cured polymer can cost about 10 $/kg, depending on the supplier and purchased amount. Considering that for an ADR mission a relatively small quantity of fuel is required, due to the low ΔV involved, a solid grain charge would not have a strong impact on overall mission costs. On the other hand, paraffin wax materials are recently acquiring large interest in the research community, due to the higher regression rate provided, up to two or three times that of HTPB [47]. Nevertheless, paraffin-based fuels display anisotropic combustion and poor mechanical properties, the latter requiring the addition of polymeric additives in order to increase the elastic modulus and avoid the risk of cracks due to strong thermal and fluid dynamic stresses [39, 47]. In the frame of a multi-burn mission, the anisotropic behavior might represent a significant drawback, since the shape and conditions of the fuel perforation after the firing would not be easily predictable (as regards the oxidizer mass flux

Fig. 8 Ideal vacuum-specific impulse for HTPB with different oxidizers (chamber pressure 3.0 MPa and nozzle expansion area-ratio 50) [34]
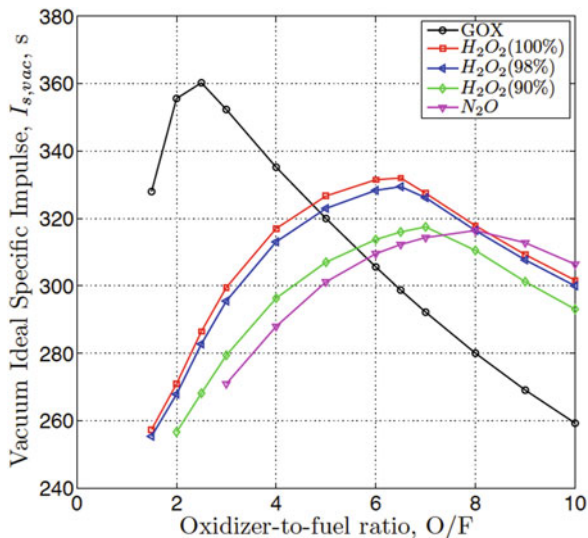
estimation for the following burn). In the light of these considerations, HTPB seems to be the most suitable choice for ADR applications, being a well-known and safe material, tested in different operating conditions, able to provide quite high performance, with ideal vacuum-specific impulses $I_{s,vac}$ close to that of paraffin wax [27]. However, paraffin materials, if fitted out with additives for mechanical properties improvement, in the case of single-burn mission might represent an interesting solution, especially for small PMD on-board engines.

The most interesting oxidizers are gaseous or liquid oxygen (GOX or LOx), nitrous oxide (N_2O), and hydrogen peroxide (H_2O_2) at high concentration, also known as high-test peroxide (HTP) [38, 39, 41, 44, 48]. Their performance, in terms of $I_{s,vac}$, is compared in Fig. 8, estimated using the Chemical Equilibrium for Applications (CEA) software [49, 50], assuming 3.0 MPa of chamber pressure, an area ratio of 50 and shifting nozzle expansion. HTPB is selected as solid fuel and introduced in the software by means of an empirical chemical formula evaluated in SPLab [34]. All these oxidizers provide ideal $I_{s,vac}$ above 300 s in correspondence of their optimal O/F, representing a valid option for rocket applications. Of course, liquid oxidizers with higher density are preferred for system volume constraints. However, before entering in contact with the fuel port, the oxidizer must be properly vaporized, in order to limit combustion inefficiencies, not regular usage at the head section of the solid grain and the annihilation of the tangential velocity component in case of swirling injection [41, 51]. Therefore, LOx requires a separated gas generator to provide hot gases in the precombustion chamber, and, being a cryogenic substance, a more complex and expensive system is necessary for its storage. These features also entail a significant addition of mass on the overall propulsion system.

On the contrary, the hydrogen peroxide can be easily vaporized by means of a catalytic decomposition, so injecting in the combustion chamber gaseous O_2

and H_2O at temperatures up to 1000 K, depending on HTP concentration and reaction efficiency. In this case costs and complexity can be strongly reduced, just requiring a catalyst system for the oxidizer injection. The temperature of the produced gaseous mixture is enough for the HTPB ignition (≈ 800 K) [27], avoiding the need of a complex ignition system. Hydrogen peroxide is a well-known substance used for different applications in commercial, aerospace, and defense industries during the last 100 years. In the 1930s, its decomposition reaction was exploited to develop the first monopropellant system [40, 48, 52]. A very low vapor pressure characterizes the hydrogen peroxide, making it easier to handle with respect to other liquid oxidizers or monopropellants, such as LOx and the toxic group made by nitrogen tetroxide (N_2O_4) or NTO, monomethylhydrazine (MMH), and unsymmetrical dimethylhydrazine (UDMH).

A toxic propellant involves higher costs, especially for handling and ground operations: specialized staff and plants are required for the safe management of toxic substances, and their price is subjected to environmental laws that will tend to become more strict in the next future (with consequent costs growth). In fact, by way of example, the average price of MMH and UDMH during the 1990s was, respectively, about 17 and 24 $/kg, but later, due to the upgrade of environmental regulation, the price of MMH jumped to 170 $/kg [53, 54]. The non-toxicity of hydrogen peroxide together with its easy handling, as well as its large diffusion, reduced the average price of HTP (with concentrations of 90–95 %) down to about 1 $/kg, during the 1990s. Although the propellant cost represents a very small portion of the economical effort required by an ADR mission, a so large difference in costs and handling, together with a less complex propellants legislation, makes the hydrogen peroxide, as well as hybrid propulsion, a very suitable option for new commercial companies that decide to deal with the development of propulsion systems for small satellites orbital transfer and post-mission disposal. For rocket applications, the high concentration of H_2O_2 is blended with water, typically at 90 %, the most common grade, but even up to 98 %. The latter provides higher mixture gas temperatures and better performance, but its price becomes greater, and the significant change in the adiabatic decomposition temperature involves a more complex design of the catalyst bed and more particular materials, with respect to typical systems used for HTP(90 %) [40]. Because of the relatively low temperatures, the catalyst system (chamber, pipes, etc.) can be implemented with stainless steel, thus keeping low the costs, while the catalyst bed is generally made by silver. The oxidizer density is about 1390 kg/m³ for HTP(90 %). The change in concentration entails the change of other properties, such as the freezing point which, for a percentage of 90 %, is about 261.77 K (-11.5°C) [52]. Therefore, speaking of missions in space, a thermal system for the control of the oxidizer temperature must be considered. Despite this, hydrogen peroxide would represent a key choice for hybrid propulsion units designed for ADR, also because of its dual-use capability. The latter consists in the possibility to use HTP as oxidizer for the primary HPM and as monopropellant for the secondary propulsion system, made by several micro-thrusters for attitude control, spilling the oxidizer directly from the main tank [25, 27, 40]. Historically, the hydrogen peroxide became famous as

a hazardous substance due to some incidents mainly happened between the 1930s and the 1960s, when the industrial practices for handling and rocket development were still immature and characterized by incidents even with other substances. In more recent years, two notable incidents, described and discussed in [55], enhanced the negative opinion about hydrogen peroxide, but they were provoked by the use of incompatible materials and system-design failures. Despite this, H_2O_2 with concentrations below 90 %, under the correct precautions, is enough stable both for what concern typical industrial uses and space missions, as demonstrated by the COMSAT spacecraft with a stored time of 17 years in vented tanks [56]. Modern industrial techniques are able to produce high hydrogen peroxide quality, with very low presence of impurities, making it safer both for handling and for storing. Research studies have been carried out with the aim to improve the propellant properties especially for space applications; for example, the natural decomposition rate of hydrogen peroxide can be significantly reduced if stored in tanks made by specific materials, thus improving its long-term stability [55]. In conclusion, with regard to active debris removal, hydrogen peroxide with concentration up to 90 % might represent a good candidate oxidizer together with HTPB solid fuel, despite the lower specific impulse achievable with respect to LOx. The latter, besides greater system complexity and costs, can unlikely be stored for long times, limiting the possibility of its employment for ADR missions that can last several months.

3.2   Preliminary Design and Mass Budget

The preliminary mass budget of a DeoKit for the active removal of a Cosmos-3M second stage is carried out. Besides the ADR platform, made by avionics, communication, measuring, and support systems, as well as the soft and hard docking mechanisms [27, 34], the principal component is the propulsion module. Different configurations can be designed depending on the rocket technology selected: solid (SPM), liquid (LPM), or HPM. In Fig. 9, one can see possible conceptual DeoKit designs with respect to various motor solutions. In case of a HPM powered by HTPB+HTP(90 %), the propellant for RCS is spilled from oxidizer tanks. Moreover, the high L/D ratio of HPM solid fuel requires arranging the engine within the ADR platform volume. On the contrary, the LPM, due to its compact combustion chamber, can be attached on the aft section of the service platform. For the SPM, a specific integration should be performed, since its size strongly depends on the solid grain geometry. Furthermore, an additional propulsion unit for the initial midrange rendezvous is required, due to the no-reignition capability. In this case, depending on the required thrust, a small solid rocket or a more powerful RCS system might be exploited.

The mass budgets of liquid and solid propulsion modules, regarding the same mission requirements and ADR platform, are finally compared with the hybrid solution. Of course, reduced motor masses (i.e., lighter DeoKits) would favor multi-removal mission strategies, performed with a single launch. The mass and size
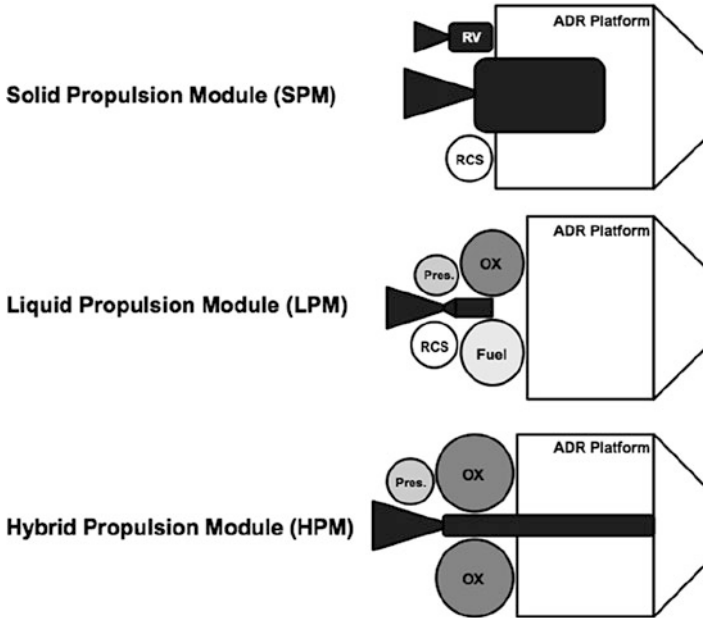
Fig. 9 Conceptual DeoKit configuration with different chemical propulsion modules

criteria of the different components assembled in the propulsion modules, here considered, are based on reference design concepts for rocket motors [41].

For the hybrid propulsion module, a more complex calculation method was carried out in order to estimate the fuel regression rate for the couple HTPB+H_2O_2, of which poor data are available in the literature survey. A computational tool was implemented for internal ballistics analysis and engine sizing based on the approach suggested by Funami and Shimada [57]. The calculation domain consists of the solid fuel cylindrical perforation and a de Laval nozzle. The flowfield is described by quasi-one-dimensional nonviscous compressible Euler equations with the addition of mixture fraction conservation. The mass release from the solid fuel surface is considered as a source term, in which the fuel mass flux is evaluated with Eq. 2, the Marxman model, assuming pure convective regime [58, 59]

$$\rho_f r_f = 0.03 G \left(\frac{G \cdot x}{\mu} \right)^{-0.2} \left(\frac{St}{St_o} \right) \left(\frac{u_e}{u_{\text{fl}}} \right) \frac{\Delta h}{\Delta H_{v,\text{eff}}} \tag{2}$$

where G is the local specific mass flux, μ is the gas-phase viscosity, x is the axial location, St/St_o is the ratio between the Stanton number with and without fuel suction, u_e is the main stream velocity, u_{fl} is the velocity at the flame, and Δh is the difference between the enthalpy at the flame and at the wall of the gas phase. $\Delta H_{v,\text{eff}}$ is the HTPB vaporization enthalpy. Oxidizer and fuel are considered at

gaseous phase, with instant mixing and reacting inside each finite volume [57]. The vaporized HTPB is represented by gaseous butadiene monomers (C_4H_6), whereas the hydrogen peroxide enters in the combustion chamber already decomposed in oxygen and steam. For the combustion, chemical equilibrium is applied to a reduced number of selected chemical species [49, 50, 57] in order to obtain thermochemical and transport properties of the gaseous mixture, required in Eq. 2. A detailed description of the computational method is available in [34, 57]. The calculated time- and space-averaged regression rate was compared with the experimental results of Shanks and Hudson [60] for the couple HTPB+GOX [34]. With this computational tool, the Marxman et al. model underestimates the regression rate of about 16 % at high mass flux and up to 50 % at low mass flux. This lack between numerical solution and experimental data can lay at both the use of a pure convective energy flux balance at the fuel surface and the effects of injector geometry on the flow path of the experimental motor [39, 61]. The second can significantly affect the flame development within the turbulent boundary layer, producing regression rate trends quite different from that predicted by the classic theory. However, despite its limitations, this numerical approach provides regression rates of realistic order of magnitude, resulting useful for propellant consumption estimation, preliminary rocket investigations, and design choices. Moreover, the underestimation of the regression rate plays a conservative role on the preliminary sizing. Motor performance is evaluated assuming Bray expansion [62], two-dimensional nozzle losses, and throat erosion rate, the latter based on numerical results of Bianchi and Nasuti for the couple HTPB+H_2O_2 with a graphite nozzle [63]. The code assumed not diluted hydrogen peroxide, so the final performance are corrected with respect to the effective H_2O_2 concentration, by means of correction factors estimated with NASA CEA software [49, 50]. For the combustion chamber an aluminum alloy is assumed, whereas phenolic material, due to its higher resistance than graphite based, is considered for the nozzle. The latter is not cooled, so short burning times ($\sim$100 s) must be considered. The liquid oxidizer is stored in four spherical aluminum tanks, pressurized, by means of a pressure-regulated system, with gaseous nitrogen loaded in a spherical titanium tank. The catalyst system for motor ignition is designed assuming the validity ranges tested for HTP(90 %) by Ventura [40], with silver-based catalyst beds.

Concerning the preliminary design of LPM, the motor performance, for the typically employed propellant couple NTO+UDMH, is evaluated with NASA CEA software (considering Bray expansion and two-dimensional nozzle losses) assuming a constant O/F of 2.2 during combustion. The mass budget of the overall system is estimated using semiempirical design relations, based on historical motors database, as suggested in [41]. With regard to an ADR mission and the strong need of cost reduction, the combustion chamber and the nozzle are assumed to be protected by an estimated amount of ablative material. The liquid propellants are stored in four spherical aluminum tanks, pressurized, by means of a pressure-regulated system, with gaseous nitrogen loaded in a spherical titanium tank. The combustion chamber and nozzle are made by columbium, typically used for these applications.

For SPM, the propellant consumption during combustion is estimated by means of an experimental burning rate law (Eq. 3), evaluated at SPLab [64] for the solid formulation AP(68 %)+HTPB(14 %)+ μAl(18 %)[1]

$$r_b = 1.08 \pm 0.03 \cdot p_c^{0.46 \pm 0.01} \qquad R^2 = 0.996 \qquad (3)$$

where p_c is the combustion pressure in bar and r_b is expressed in mm/s. This solid propellant has a theoretical density of $1.761\,kg/m^3$. The motor size and mass are estimated assuming a graphite cylindrical chamber (L/D $\sim$ 1.5) with a spherical dome and De Laval nozzle. The mass of the latter and of the other components, such as igniter and internal insulation, are evaluated with empirical relations and mass ratios based on historical solid motors database [41, 65]. Just as for LPM, motor performance evaluation is carried out with NASA CEA software.

For all designed motors, a nozzle area-expansion ratio of 80 is imposed. A chamber pressure of 8.0 MPa is assumed for SPM, while a pressure of 1.7 MPa is considered for HPM and LPM. To the latter, an increase of 40 % on the inert mass is applied, to account for structure connection elements, bosses, valves, cables, etc. Concerning the SPM, being characterized by a simpler structure without tanks and feed system, an increase of 10 % is considered [41].

Each propulsion unit is able to provide about 4.2 kN of thrust for 90 s of combustion, necessary to perform the disposal of a Cosmos-3M second stage from an altitude of 770 km, by means of a DeoKit with a total mass of 566 kg (see Sect. 2.1). Such maneuver requires a ΔV of 200 m/s, to which a 10 % is added as safety margin to account for performance losses. Further 15 m/s are assumed, for HPM and LPM, to account of the propellant mass useful for a midrange rendezvous with the target. The total velocity increment of 235 m/s (220 m/s for SPM) is provided by each motor with a single burn.In Table 2, the preliminary mass budget results are summarized. The mass percentages of propulsion module and ADR platform are evaluated with respect to the DeoKit mass (566 kg), for each motor type, and compared in Fig. 10.

Table 2 Preliminary design results for different chemical propulsion modules

	Solid propulsion	Liquid propulsion	Hybrid propulsion
M_{PM} (kg)	153.6	188.0	216.5
$\%_{deokit}^{PM}$	**27.1 %**	**33.2 %**	**38.3 %**
M_{ADRpt} (kg)	412.4	378.0	349.5
$\%_{deokit}^{ADRpt}$	**72.9 %**	**66.8 %**	**61.7 %**
M_{prop} (kg)	141.2[a]	141.1	150.2
Average $I_{s,vac}$ (s)	301.4	328.1	300.2

M_{PM} propulsion module mass, M_{ADRpt} ADR platform mass, M_{prop} propellant mass
[a]The propellant amount of SPM is based on the disposal maneuver only

[1]Aluminum powder with average diameter of 30 μm.

Fig. 10 Propulsion modules mass percentage with respect to DeoKit total mass
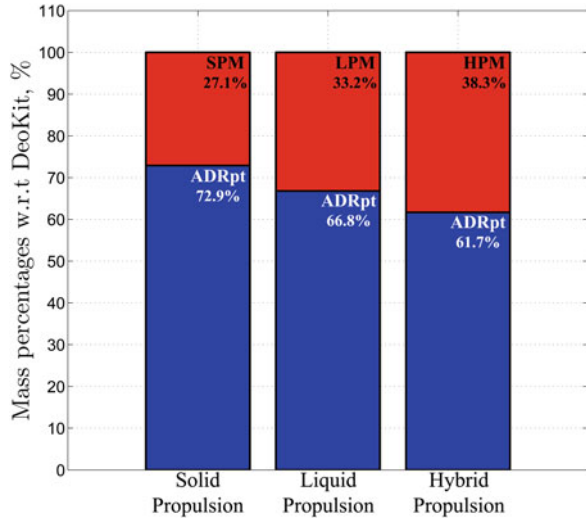
In the case of HPM, the disposal flight simulation was recalculated with motor's effective performance, since hybrids are characterized by O/F shifting (increase) and consequently not constant thrust (decrease) during the combustion. A maximum theoretical I_s of 312 s is achieved with a mixture ratio of 6.5, which, during the 90 s of combustion, grows from 5 to 9 yielding, respectively, 308 and 294 s of specific impulse. The produced thrust almost linearly decreases from 4.5 kN, at the beginning of combustion, to 4.0 kN after 90 s. The chamber pressure decreases from 1.7 to 1.3 MPa, while the gaseous mixture temperature also drops from an initial value of 2750 K. Low pressure and temperature limit the throat erosion rate, in this instance estimated as 5 mm of diameter enhancement at the end of combustion. Hydrogen peroxide allows for lower combustion temperatures with respect to gaseous or liquid oxygen, producing a lesser nozzle throat erosion [63] and related performance losses. At this chamber conditions, the inlet oxidizer mass flow rate is imposed to achieve an initial mass flux (G_{ox}) of about 600 kg/(m$^2 \cdot$ s), thus estimating a space-averaged regression rate of about 1 mm/s, which, accordingly to Marxman model, decreases with the G_{ox} drop, due to the growth of fuel port diameter during the combustion. As previously asserted, the calculated regression rate shows a certain level of underestimation, but this plays a conservative role in the HPM preliminary design. The HPM allows to achieve a FPA of -1.77 deg at an interface of 120 km and a perigee altitude of 52.3 km, satisfying the mission requirements. With regard to solid propulsion mass budget, it is important to highlight that the SPM is designed only for the disposal maneuver; hence, an additional propulsion unit (monopropellant, hybrid, or solid) must be accounted for the midrange rendezvous between the DeoKit and the target.

Despite this, solid rocket solutions can provide very compact motors, of which 92 % of their total mass is the propellant. These results suggest that solid propulsion might be exploited with a different mission approach: a chaser spacecraft could

carry few SPMs to be attached (if the feasibility will be demonstrated) to different targets. Each solid motor should be equipped with the instrumentation for the disposal control and the mating system for the joint with the target. The chaser should be a complex spacecraft able to perform multiple precise rendezvous, so loaded with a great amount of propellant, also required for its final disposal (once released all SPMs). The chaser might be powered by a liquid or hybrid rocket, or an existing launcher upper stage could be directly modified and equipped with the ADR platform, as well as a certain number of SPMs. This alternative solution should be explored, in contrast with the approach of multiple autonomous DeoKits described in Sect. 2. Besides the ADR possibility, solid motors represent a valuable option for the post-mission disposal of new satellites (boarded engine).

Focusing on liquid and hybrid systems, the HPM results heavier than LPM, of about 28.5 kg, corresponding to a difference of 5 % with respect to the DeoKit mass. At this preliminary design phase, the two technologies provide modules of comparable mass and also nearly equal width (∼90 cm). They mainly differ in combustion chamber length, which for HPM results significantly longer, with a solid fuel grain of 1.6 m. In the light of these results, the selection of the best propulsion option for ADR missions deals with the most favorable features provided by each technology. Liquid propulsion might be preferred for disposal strategies based on low thrust with one long burn times that also provide a further mass saving, according to the preliminary design approach described in this chapter: a thrust of 1.0 kN provided for 445 s could satisfy the disposal requirements with a LPM of about 177 kg (31.2 % of the total DeoKit mass). Nevertheless, this mass reduction could be counterbalanced by the addition of a more efficient and complex cooling system, required for long combustion times, as well as its correlated greater design and realization costs. Despite this, a long burn strategy with reduced thrust levels entails low accelerations imparted to the target structure, decreasing the breaking risk for the target's deployed appendages and structures [25]. On the contrary, abandoned rocket bodies, due to the aim of their use, are able to sustain strong axial accelerations and structural stresses produced by larger thrust values. At present, the orbital debris characterized by the highest removal priority are all massive rocket bodies (>4000 kg) and only one is a spacecraft (Envisat[2]) [14, 66]. Therefore, a LPM might be employed in the frame of an ad hoc mission for Envisat recovery and disposal whereas HPMs for a more continuing removal strategy of large abandoned rocket bodies. However, lower thrust levels can be provided also with a hybrid motor by implementing multi-burns disposal strategies, limiting each combustion phase below a fixed time.

Hybrid propulsion seems to be a valid alternative to liquid propulsion, in the light of its intrinsic safety and possibility of cost reduction for engine manufacturing, but also simpler ground operations such as components assembling, propellants handling, and storage, due to the use of cheap and nontoxic substances. In addition, the ADR platform mass must account of RCS for close-proximity operations

---

[2]Earth-observing satellite lost by ESA in April 2012, after 10 years of service.

(low thrust) with the target and attitude control (high thrust) during the midrange rendezvous and disposal. By selecting HTP(90 %) as monopropellant, a propellant amount of about 20 kg can be estimated assuming 2000 low-thrust impulses ($\sim$3 N) and 500 high-thrust impulses ($\sim$50 N). With respect to RCS, the use of hybrid motor represents an advantage due to the possibility of spilling the hydrogen peroxide directly from the main oxidizer tank, avoiding the need of an additional tank, with its own pressurization system, as required for SPM and LPM. Hybrid rocket technology has not been tested in space yet, but its possible implementation in the frame of active debris removal might promote its full development, as well as an effective cost reduction, strongly required to ensure that hybrid becomes a valid alternative to liquid propulsion for orbital transfers in the next future.

4   Conclusions

In recent years, the active debris removal concept is widely discussed in the international space community and, besides the technological challenge, significant obstacles are put by its economic impact and, in a more complex manner, by political and legal issues related to the implementation of specific technologies. In this work, the way to use chemical propulsion modules for the controlled reentry of large abandoned objects was discussed. This approach seems to be one of the most effective and safe, allowing for a fast removal of the selected targets from the most crowded orbital bands. The Cosmos-3M second stage represents a very interesting candidate for mission demonstration and study of multi-removal strategies, promoting the development of technologies directly applicable also to larger abandoned rocket bodies (e.g., Zenit second stages), characterized by masses above 4000 kg.

The removal mission might be performed by a de-orbiting kit, here called DeoKit, made by a primary chemical propulsion module and by an ADR platform, which includes avionics, sensors, capture mechanisms, and a secondary propulsion system (RCS) for the attitude control. With the aim of multi-removal missions, several DeoKits might be carried in orbit by a launcher upper stage able to release each de-orbiting kit in the proximity of the selected targets. The Soyuz launcher, with Fregat upper stage, which exhibits the capacity to carry several DeoKits, might represent a valid candidate for a multi-removal demonstrative mission. Nevertheless, the number of carried de-orbiting kits must be evaluated taking into account the target orbits (i.e., ΔV to be provided by Fregat), the available volume of the payload fairing and a detailed mass budget for the overall effective payload.

From the propulsion systems comparison performed assuming the same disposal mission requirements, the solid motor results in a very compact system with a lower wet mass than that of liquid and hybrid motors. However, solid propulsion technology lacks in throttleability and reignition capability, but the advantage provided by its compactness might be exploited by a different ADR mission approach: a chaser spacecraft able to perform multiple rendezvous with different

targets and to attach a SPM to each them. In this instance, the chaser could be conceived as powered by a LPM or HPM or, as alternative, made up by an existing upper stage modified and equipped with an ADR platform. On the other hand, a smaller mass difference is achieved between liquid and hybrid motors, the latter resulting 28.5 kg heavier. At this preliminary design phase, the relatively small mass difference between hybrid and liquid propulsion technology allows to mainly base the choice on their features comparison. In addition, the underestimation which affects the regression rate estimation allows for a certain margin for the improvement of HPM performance and mass budget. Hybrid motors provide several advantages with respect to liquid rockets, in particular an enhanced system safety, use of nontoxic propellants, dual-use of the oxidizer to supply also the RCS for the DeoKit attitude control, and possibility of significant overall cost reduction. The latter is one of the basic aspects, since the development of ADR entails a large economical effort and would not provide any profit to the executor agency, making impossible eventual long-term amortization. The lower cost promised by hybrid propulsion might be helpful in this direction, making available relatively cheap motor systems for ADR missions.

Future steps of this research should improve the quality of propulsion system comparison, by considering a more complete analysis of performance losses and combustion efficiency for all propulsion systems, an enhanced regression rate prediction precision for hybrid motor, as well as a more detailed mass evaluation for rocket subsystems. Furthermore, the two described ADR mission approaches should be evaluated and compared in details, focusing the attention to the mass budget of the overall ADR system and the total velocity increment required for both rendezvous and removal of multiple targets.

References

1. Secure World Foundation (2014) Space sustainability: a practical guide. Creative Commons, Mountain View
2. IADC Steering Group & Working Group 4 (2002) Space debris mitigation guide-lines. Inter-Agency Space Debris Coordination Committee (IADC), document IADC-02-01
3. United Nations (2008) Space debris mitigation guidelines of the United Nations Committee on the Peaceful Uses of Outer Space. A/62/20 (2007), endorsed by the General Assembly Resolution A/RES/62/217, United Nations, New York
4. IAA Study Group 5.1 on Space Debris Mitigation Rules for Launch Vehicles and Spacecraft (2006) Position paper on space debris mitigation: implementing zero debris creation zones. ESA SP-1301, European Space Agency, Noordwijk
5. Flohrer T, Krag H, Lemmens S et al (2014) End-of-life practices in GEO and LEO protected regions: evaluation of recent adherence from catalogue data. In: Alby F (ed) Proceedings of the 5th European workshop on satellites end of life, CNES Headquarters, Paris, 28 Jan 2014

6. Dolado-Perez JC, Morand V, Le Fevre C et al (2014b) Analysis of mitigation guidelines compliance at international level in low earth orbit. In: Proceedings of the 65th international astronautical congress, Toronto, 29 Sept–3 Oct 2014. International Astronautical Federation, paper IAC-14-A6.4.4

7. Rossi A, Anselmo L, Pardini C et al (2004) Upgrade of the semi-deterministic model to study the long term evolution of the space debris. Final report of the ESA/ESOC Contract No. 15857/01/D/HK(SC), ISTI/CNR, Pisa

8. Liou J-C, Johnson NL (2006) Risks in space from orbiting debris. Science 311:340–341

9. Liou J-C, Johnson NL (2008) Instability of the present LEO satellite populations. Adv Space Res 41:1046–1053

10. Liou J-C, Johnson NL (2009) A sensitivity study of the effectiveness of active de-bris removal in LEO. Acta Astronaut 64:236–243

11. Liou J-C, Johnson NL (2010) Controlling the growth of future LEO debris populations with active debris removal. Acta Astronaut 66:236–243

12. Liou J-C (2011) An active debris removal parametric study for LEO environment remediation. Adv Space Res 47:1865–1876

13. Utzmann J, Oswald M, Stabroth S et al (2012) Ranking and characterization of heavy debris for active removal. In: Proceedings of the 63rd international astronautical congress, Naples, 1–5 Oct 2014. International Astronautical Federation, paper IAC-12-A6.2.8

14. DeLuca LT, Lavagna M, Maggi F et al (2013b) Active removal of large massive objects by hybrid propulsion module. In: Proceedings of the 5th European conference for aero-space sciences (EUCASS), Munich, 1–5 July 2013

15. Radtke J, Flegel SK, Roth S et al (2014) Deriving the spacecraft criticality from Monte-Carlo simulations of the space debris environment. In: Proceedings of the 65th international astronautical congress, Toronto, 29 Sept–3 Oct 2014. International Astronautical Federation, paper IAC-14-A6.2.6

16. Rossi A, Valsecchi GB, Alessi EM (2014) An evaluation index for the ranking of LEO objects. In: Proceedings of the 65th international astronautical congress, Toronto, 29 Sept– 3 Oct 2014. International Astronautical Federation, pa-per IAC-14-A6.2.7

17. Anselmo L, Pardini C (2014) Compliance of the Italian satellites in low earth orbit with the end-of-life disposal guidelines for space debris mitigation. In: Proceedings of the 65th international astronautical congress, Toronto, 29 Sept–3 Oct 2014. International Astronautical Federation, paper IAC-14-A6.4.5

18. Pardini C, Anselmo L (2014) Review of the uncertainty sources affecting the long-term predictions of space debris evolutionary models. In: Bonnal C (ed) Proceedings of the 3rd european workshop on space debris modelling and remediation, CNES Headquarters, Paris, 16–18 June 2014

19. Pardini C, Anselmo L (2014) Review of past on-orbit collisions among cataloged objects and examination of the catastrophic fragmentation concept. Acta Astronaut 100:30–39

20. Dolado-Perez JC, Revelin B, Di-Costanzo R (2014a) Sensitivity analysis of the long-term evolution of the space debris population in LEO. In: Proceedings of the 65th international astronautical congress, Toronto, 29 Sept–3 Oct 2014. International Astronautical Federation, paper IAC-14-A6.2.3

21. Blake R, Lewis HG (2014) The effect of modelling assumptions on predictions of the space debris environment. In: Proceedings of the 65th international astronautical congress, Toronto, 29 Sept–3 Oct 2014. International Astronautical Federation, paper IAC-14-A6.2.4

22. Bastida Virgili B, Lemmens S, Flohrer T et al (2014) Influence of solar activity on long term propagations. In: Proceedings of the 65th international astronautical congress, Toronto, 29 Sept–3 Oct 2014. International Astronautical Federation, paper IAC-14-A6.2.5

23. Space Track Organization (2014) Satellite catalog data. https://www.space-track.org. Accessed 6 Nov 2014

24. Union of Concerned Scientists (2014). UCS satellite database 2014-07-31. http://www.ucsusa.org. Accessed 6 Nov 2014

25. Tadini P, Tancredi U, Grassi M et al (2014) Active debris multi-removal mission concept based on hybrid propulsion. Acta Astronaut 103:26–35
26. Bastida Virgili B, Krag H (2009) Strategies for active removal in LEO. In: Lacoste H (ed) Proceedings of the 5th European conference on space debris. ESA SP-672, European Space Agency, Noordwijk
27. DeLuca LT, Bernelli F, Maggi F et al (2013a) Active space debris removal by hybrid engine module. Acta Astronaut 91:20–33
28. United Nations (2014) United nations treaties and principles on outer space: related general assembly resolutions and other documents. ST/SPACE/61/Rev.1, Office for Outer Space Affairs, V.14-00496 (E), United Nations, Vienna
29. Barbee B, Alfano S, Pinon E et al (2011) Design of spacecraft missions to remove multiple orbital debris objects. In: Aerospace conference, 2011 IEEE, Montana, Mar 2011
30. Castronuovo MM (2011) Active space debris removal – a preliminary mission analysis and design. Acta Astronaut 69:848–859
31. Branz F, Francesconi A (2012) Innovative technologies for non-cooperative targets close inspection and grasping. In: Proceedings of the 63rd international astronautical congress, Naples, 1–5 Oct 2012. International Astronautical Federation, ISSN 1995–6258
32. Martin Th et al (2013) Active debris removal mission design in low earth orbit. Prog Propuls Phys 4:763–788
33. Lazare B, Bonnal C (2014) Active debris removal: Possibility of an "interim provision" rule concerning acceptability of random reentry of large debris. In: Proceedings of the 3rd European workshop on space debris modeling and remediation, Poster #P.10, CNES HQ, Paris, 16–18 June 2014
34. Tadini P (2014) Hybrid rocket propulsion for active removal of large abandoned objects. PhD thesis, Politecnico di Milano, Milano
35. Perez E (2006) Soyuz CSG User's Manual, Issue 1, Rev. 0, Arianspace, June 2006
36. Janovsky R et al (2004) End-of-life de-orbiting strategies for satellites. Sci Technol Ser 109:411–428
37. Vinh NX, Busemann A, Culp RD (1980) Hypersonic and planetary entry flight mechanics. NASA STI/Recon Technical Report A, 81, 16245
38. Gibbon DM, Haag GS (2001) Investigation of an alternative geometry hybrid rocket for small spacecraft orbit transfer. Surrey Satellite Technology LTD, Surrey, 27 July 2001. Final Report 0704–0188
39. Chiaverini MJ, Kenneth KK (2007) Fundamentals of hybrid rocket combustion and propulsion. Volume 218 of progress in astronautics and aeronautics. American Institute of Aeronautics and Astronautics, Reston
40. Ventura M, Wernimont E (2001) Advancements in high concentration hydrogen peroxide catalyst beds. In: 37th AIAA/ASME/SAE/ASEE joint propulsion conference and exhibit, Salt Lake City, 8–11 July 2001, AIAA No. 01–34049
41. Humble R, Henry G, Larson W (1995) Space propulsion analysis and design. McGraw-Hill, New York
42. Yuasa S, Shimada O, Imamura T et al (1999) A technique for improving the performance of hybrid rocket engines. In: 35th AIAA/ASME/ SAE/ASEE joint propulsion conference and exhibit, Los Angeles, 20–24 June 1999, AIAA No. 99–2322
43. Czysz P, Bruno C (2006) Future spacecraft propulsion system. Springer Praxis, Chichester, UK
44. Haag GS, Sweeting MN, Richardson G (1999) Low cost propulsion development for small satellites at the surrey space centre. Paper SSC99-XII-5
45. Micci MM, Ketsdever AD (2000) Micropropulsion for small spacecraft. Volume 187 of AIAA Progress in Astronautics and Aeronautics. American Institute of Aeronautics and Astronautics, Reston
46. Gibbon DM, Paul M, Jolley P, et al. (2001) Energetic green propulsion for small spacecraft. In: 37th AIAA/ASME/SAE/ASEE joint propulsion conference, Salt Lake City, 8–11 July 2001, AIAA No. 2001–3247
47. Paravan C, Viscardi M, DeLuca LT, Prada Lopez L (2009) Anisotropy effects in hybrid fuels burning in a micro-burner. In: XX AIDAA Congress, Milan, 29 June–3 July 2009

48. Ventura M, Mullens P (1999) The use of hydrogen peroxide for propulsion and power. In: 35th AIAA/ASME/SAE/ASEE joint propulsion conference and exhibit, Los Angeles, 20–24 June 1999, AIAA No. 99–2880
49. Gordon S, McBride BJ (1994) Computer program for calculation of complex chemical equilibrium composition and applications I. Analysis. NASA, Reference Publication 1311
50. McBride BJ, Gordon S (1996) Computer program for calculation of complex chemical equilibrium composition and applications II. Users manual and program Description. NASA, Reference Publication 1311
51. Kitagawa K, Mitsutani T, Ro T, Yuasa S (2004) Effects of swirling liquid oxygen flow on combustion of a hybrid rocket engine. In: 40th AIAA/ASME/SAE/ASEE joint propulsion conference and exhibit, Fort Lauderdale, 11–14 July 2004
52. Ventura M, Yuan S (2000) Commercial production and use of hydrogen peroxide. American Institute of Aeronautics & Astronautics, Reston, AIAA No. 00–36740
53. N2O4/MMH (2014) Propellant Combinations Database In: Encyclopedia astronautica. http://www.astronautix.com/props/n2o4mmh.htm. Accessed 9 Dec 2014
54. H2O2/UDMH (2014) Propellant combinations database In: Encyclopedia astronautica. http://www.astronautix.com/props/h2o2udmh.htm. Accessed 9 Dec 2014
55. Ventura M, Wernimont E, Heister SD, Yuan S (2007) Rocket grade hydrogen peroxide (RGHP) for use in propulsion and power devices – historical discussion of hazards. In: 43rd AIAA/ASME/SAE/ASEE joint propulsion conference and exhibit, Cincinnati, 8–11 July 2007, AIAA No. 2007–5468
56. Ventura M (2005) Long term storability of hydrogen peroxide. In: 41st AIAA/ASME/SAE/ASEE joint propulsion conference and exhibit, Tucson, 10–13 July 2005, AIAA No. 2005–4551
57. Funami Y, Shimada T (2012) Validation with experiments on simplified numerical prediction of hybrid rocket internal ballistics. AIP Conf Proc 1493:395–400
58. Marxman GA, Gilbert M (1963) Turbulent boundary layer combustion in the hybrid rocket. In: Ninth symposium (International) on combustion, at Cornell University Ithaca, New York, pp 371–383
59. Marxman GA, Wooldrige CE, Muzzy RJ (1963) Fundamentals of hybrid boundary layer combustion. In: Heterogeneous combustion, Palm Beach, 11–13 Dec 1963. AIAA No. 63–505
60. Shanks RB, Hudson MK (1994) The design and control of a labscale hybrid rocket facility for spectroscopy studies. In: 30th AIAA/SAE/ASME/ASEE joint propulsion conference and exhibit, Indianapolis, 27–29 June 1994, AIAA No. 94–3016
61. Carmicino C, Russo Sorge A (2005) Role of injection in hybrid rocket regression rate behavior. J Propuls Power 21(4):606–612
62. Bray KNC (1963) Chemical reactions in supersonic nozzle flows. Int Symp Combust 9(1):770–784
63. Bianchi D, Nasuti F (2012) Numerical analysis of nozzle material thermochemical erosion in hybrid rocket engines. In: 48th AIAA/SAE/ASME/ASEE joint propulsion conference and exhibit, Atlanta, 30 July–1 Aug 2012, AIAA No. 2012–3809
64. Dossi S, Reina A, Maggi F, DeLuca LT (2012) Innovative metal fuels for solid rocket propulsion. Int J Energ Mater Chem Propuls 11(4): 299–322
65. Carr CE, Walstrum DW (1989) Solid rocket propulsion for small-satellite applications. In: 3rd annual AIAA/Utah State University conference on small satellites, Logan, 26–28 Sept 1989
66. Envisat (2014) ESA Earth Online: https://earth.esa.int/web/guest/missions/esa-operational-eo-missions/envisat. Accessed 8 Dec 2014

Part XI
History of Solid Rocket Propulsion in Russia

Highlights of Solid Rocket Propulsion History

Luigi T. DeLuca

Abstract The history of solid rocket propulsion covers a span of more than 2000 years, starting in China with the accidental discovery of black powder (or something similar) around 220 BC ca and continuing up to the current days. It is an interesting route that the idea of black (or gun) powder traveled: moving from East China to Korea, India, Arab countries, Europe, and finally the USA. Extensive Mongolian raids and land as well as sea trade routes were the main avenues, for this slow but continuous move westward then covering the whole planet. Fireworks and military operations were the main drivers, without forgetting the first reckless attempt of space travel by a Chinese astronaut in 1500 ca. However, black powder should only be seen as a precursor of solid propellants. In spite of the previous large-scale activity, the transition toward modern solid rocket propulsion actually occurred at two quite distinct focal points in space and time: Caltech, Pasadena, CA, during the period 1936–1944 and the Institute of Chemical Physics, Moscow, Russia, during the period 1960–1980. In both cases, the interplay of great minds and the assignment of precise objectives triggered tremendous scientific progress, but without a successive well-organized strategic planning, this spark would have gone in vain.

Since the US side of the story is quite well known, chapters "Survey of Solid Rocket Propulsion in Russia" to "The Russian Missile Saga: Personal Notes from a Direct Participant" are dedicated to an historical survey mainly of the Russian developments in solid rocket propulsion. This particular contribution is included to put things in the right overall perspective.

L.T. DeLuca (✉)
Space Propulsion Laboratory (SPLab), Department of Aerospace Science and Technology, Politecnico di Milano, 20156 Milan, Italy
e-mail: luigi.deluca@polimi.it

Nomenclature

AD	Anno Domini
ADN	Ammonium DiNitramide
AFOSR	Air Force Office of Scientific Research
AP	Ammonium Perchlorate
ARC	Atlantic Research Corporation
ATK	Alliant Techsystems Inc.
BC	Before Christ
ca	circa
CalTech	CALifornia institute of TEChnology
CDB	Cast Double-Base
CL-20	2,4,6,8,10,12-hexanitro-2,4,6,8,10,12-hexaazaisowurtzitane
CMDB	Composite Modified Double-Base
CTPB	Carboxyl-Terminated PolyButadiene
DB	Double-Base
EDB	Extruded Double-Base
EMCDB	Elastomer Modified Cast Double-Base
ERL	Explosive Research Laboratory
ESD	ElectroStatic Discharge
GALCIT	Guggenheim Aeronautical Laboratory at California Institute of Technology
HDI	Hexane diisocyanate
HEDM	High-Energy Density Material
HMX	cyclotetramethylenetetranitramine, High Melting Explosive (also known as Octogen, Her Majesty's Explosive)
HTPB	Hydroxyl-Terminated PolyButadiene
HTPE	Hydroxyl-Terminated PolyEther
IASPEP	International Autumn Seminar On Propellants, Explosives and Pyrotechnics
ICBM	InterContinental Ballistic Missile
IRBM	Ballistic Missile
ICP	Institute of Chemical Physics
IM	Insensitive Munitions
JATO	Jet Assisted Intermediate Range Take Off
JPL	Jet Propulsion Laboratory
KP	Potassium Perchlorate
LRE	Liquid Rocket Engine
NASA	National Aeronautics and Space Administration
N	The first operational Russian Double-Base propellant
NC	NitroCellulose
NEPE	Nitrate Ester Plasticized polyEther (or Nitrate Ester PolyEther)
NG	NitroGlycerine
OB	Oxygen Balance
PBAA	PolyButadiene Acrylic Acid

PBAN	PolyButadiene acrylic acid AcryloNitrile
PEG	PolyoxyEthylene Glycol
PETN	PentaErythritol Tetra Nitrate
PGA	PolyGlycol Adipate
PTFE	PolyTetraFluoroEthylene
PU	Polyurethane
PVC	PolyVinyl Chloride
RDX	cyclotrimethylenetrinitramine, Research Department explosive (also known as Hexogen, Cyclonite, T4, Royal Demolition Explosive)
SP	Solid Propellant
SRB	Solid Rocket Booster
SRM	Solid Rocket Motor
USA	United States of America
USSR	Union of Soviet Socialist Republics
V2	Vergeltungswaffe 2, the German long range missile used at the end of World War 2.
XLDB	Cross-Linked Double-Base

1 Prologue

This part of the book comprises four papers. The opening paper by DeLuca underlines the highlights of the overall solid propulsion history, while the remaining three papers deal specifically with Russian developments in solid rocket propulsion. The paper by Lipanov and Zarko [1] offers a general overview, historical as well as technical, of the Russian efforts and should be considered as a continuation of previous papers published by the senior author [2, 3]. Two more papers [4, 5] are historical essays dedicated to peculiar aspects of the Russian heritage in the area of solid rocket propulsion.

In the Greek mythology, Icarus escaped from the Cretan labyrinth, with his father Daedalus, by flying on wings of wax and feathers; see Fig. 1. While Daedalus landed in Sicily, Icarus fell into sea (Island of Icaria, surrounded by the Icarian sea, in the North Aegean sea, close to Turkey) due to wax melting as he flew too near the sun. Ironically, wax is considered today a promising solid fuel for hybrid rocket propulsion. Starting from this mythological episode, highlights in the worldwide history of energetic materials' developments are succinctly summarized in Table 1, based on the indicated references.

2 Black Powder from China

Solid rocket propulsion fortuitously stems from alchemist activities in China dating as early as 220 BC ca. Drugs made from minerals and metallic substances were considered more effective than the herbal ones. Black powder, or something

Fig. 1 The dream in Greek
mythology (Courtesy of
Vallardi Editore, 1964)

similar[1], was a mixture of saltpeter (KNO_3), sulfur, and charcoal initially studied
for medical reasons (elixir, longevity, immortality). Later, some of the alchemists
noticed that the mixture would easily burn and also that a loud bang would be
originated if the powder were to be enclosed in a proper tube of thick paper or
bamboo cane. In fact, the bamboo hollow air pockets inflate and burst with a
big sound when subjected to heat. Black powder could then be used to frighten
evil spirits (fireworks) or as an incendiary solid charge carried by arrows to burn
opposing camps (flying fires).

Somebody further noticed that the presence of an incendiary solid charge would
increase the range of the arrows, which then became a guide control device; see
Fig. 2. The search for elixirs of immortality failed (being actually poisonous),
but a new weapon was instead discovered. The news reached the Roman emperor
Domitianus in 85 AD, and pyrotechnic displays were regularly given in the Roman
circus. Fireworks were held to honor emperors Carinus (282–283) and Diocletian
(284–286) [7, 8].

---

[1]There is no conclusive evidence of "black powder" in China, and probably this historical invention
was rather a mixture based on nitrates, which Chinese used in pyrotechnic devices, arrowthrowers,
and rockets. The real invention of black powder is shrouded in mystery [PengFei Li, IASPEP
Conference, Qingdao, China, 17 Sep 2015].

Table 1 Highlights in the history of energetic materials [6–14]

Date	Event
220 BC	Chinese alchemists accidentally made black powder (or something close)
85 ca	Roman emperor Domitianus alerted to the use of incendiary arrows
690	Arabs used black powder at the siege of Mecca
940	The Chinese invented the "Fire Ball" which is made of an explosive composition similar to black powder
1232	Battle of Kai-Fung-Fu: rockets or incendiary arrows repelled Mongols
1379	Battle for Isle of Chiozza: devastating powder rockets used as "rocchetta"
1500 ca	The Chinese Wàn Hǔ, during the Ming dynasty, first recorded astronaut
1792	Combustion chambers with metallic walls allowed the Indian troops of Tipu Sultan to twice defeat the British army at Seringapatam
1799	
1805	After defeats in India, the British Colonel William Congreve extended the range of powder rockets from 600 to 2000 yard (ca 550 to 1829 m)
1807	Most of Copenhagen burned by 14,000 powder rockets by Royal Navy
1812	Congreve's rockets used by Royal Navy at siege of Fort McHenry, Baltimore (rockets' red glare in "The Star Spangled Banner")
1816	The Austrian Count Frederick Von Stadion synthesized KP in Germany
1831	The French G.S. Serullas discovered AP
1846	The Italian A. Sobrero discovered liquid nitroglycerine
1863	The Swede A. Nobel manufactured nitroglycerine
1863	The Prussian F.E. Schultze prepared smokeless NC propellant
1864	The French P. Vieille prepared smokeless NC propellant
1875	Nobel mixed nitroglycerine with nitrocellulose to form a gel
1888	Nobel invented the smokeless double-base Ballistite
1889	The British F. Abel and J. Dewar patented smokeless double-base Cordite
1899	The German G.F. Henning prepared RDX for medicinal use
1938	A.F. Belyaev and Ya.B. Zel'dovich, ICP, Russia, proposed "Theory of combustion of volatile explosives" (leading reaction in the gas phase)
1942	Ya.B. Zel'dovich, ICP, Russia, published "On the theory of the combustion of powders and explosives" (transient solid propellant burning)
1942	First castable KP composite solid propellant by J. Parsons at GALCIT (later JPL), CA, USA
1943	The American W.E. Bachmann prepared HMX (first synthesized in 1930)
1948	KP first replaced by AP at Aerojet to reduce smoke
1955	Al first tested at ARC by C. Henderson and K. Rumbel
1960	First operational AP + Al + PU (Polaris A1)
1962	First operational AP + Al + NC/NG (Polaris 2)
1964	First operational AP + HMX + Al + NC (Polaris 3)
1964	Cubanes first synthesized at University of Chicago, IL, USA by Eaton and Cole
1970	Poseidon C3 first submarine launch, 2 stages CMDB
1977	Trident I C4 first launch, 3 stages XLDB-70 (70 % solids)
1971	ADN first synthesized by V.A. Tartakovsky and O.A. Luk'yanov, Zelinsky Institute of Organic Chemistry, Moscow, Russia (SRI, 1988)
1987	CL-20 first synthesized by Arnie Nielsen, China Lake, CA, USA
1990	Trident II D5 first submarine launch, 3 stages XLDB-75 (75 % solids)
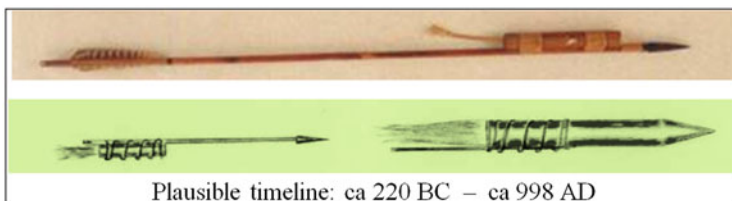
Fig. 2 From incendiary arrows (Chinese fire arrow, *top*) to primordial rocket propulsion (*bottom*) (Courtesy of NASA)
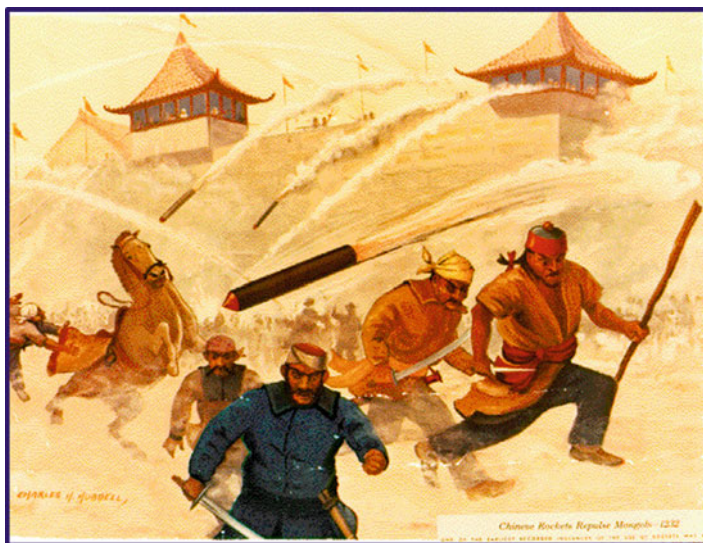
Fig. 3 Rockets used in the battle of Kai-Feng or Kai-Fung-Fu in 1232 (Courtesy of NASA)

Weapons and fireworks or firecrackers were the most common applications. Rockets, at least as incendiary powder packets tied to arrows, were used to defend the Chinese city of Kai-Feng or Kai-Fung-Fu, in 1232, against a Mongolian siege [8, 10–12]. An arrow with a tube of gunpowder produced a fearful flying fire capable of defeating the enemy (see art view in Fig. 3). The Chinese character standing for both "rocket" and "fire arrow" is shown in Fig. 4. Chinese soldiers launching multiple fire arrows are portrayed in Fig. 5. A Chinese soldier ready to operate a launch pad for flying fire arrows is shown in Fig. 6.

From China this knowledge spread to Korea, India, the Arab countries, and finally Europe, through the wide ranging raids of the Mongolian hordes led by Genghis Khan and Ögedei Khan. In 1241, Mongols used rocket weapons against Magyars in the battle of Mohi, to conquer the town of Baghdad in 1258, and to invade Japan in 1275 led by Kublai Khan [8]. First in Europe, in 1249, the English monk Roger Bacon and then in Syria, 1270–1280, the scholar Hassan al-

Fig. 4 The Chinese characters stand for both "rocket" and "fire arrow" (Courtesy of NASA)

Fig. 5 Chinese soldiers equipped with fire arrows canisters (Courtesy of NASA)

Rammah wrote detailed recipes for gunpowder and instructions for making rockets, called "Chinese arrows" [8, 12]. From Northern China rocket technology easily spread to Korea, where a wheeled fire chart, called "hwacha," was first designed in 1409 as a multiple rocket launcher (precursor of the Russian Katyusha); see Fig. 7. Under the encouragement of King Sejong the Great, a hwacha was developed which was able to fire simultaneously up to 200 "singijeon" (fire arrow rockets) and allowed his forces to defeat Japanese invaders in the battle of Haengju in 1593 [15].

Fig. 6 Chinese fire arrows and a soldier with a ready launch pad (Courtesy of NASA)

Chinese soldier launches fire-arrow

Fig. 7 Korean multiple launcher "hwacha" as displayed at the War Museum, Seoul, Korea

Black powder technology was transmitted along land trading routes and also by sea trade. In this respect, also Marco Polo (1254–1324) may have played a role. A significant contribution was made by the fleets of the "Maritime or Sea Republics" (in particular, Venice, Genoa, and Amalfi) ca 1000–1500. In the battle for Isle of Chiozza (today Chioggia), in 1379, between the then-maritime super powers of Genoa and Venice, powder rockets were used to set a defending tower on fire.

By destroying the tower, the Genovese fleet won the battle but eventually lost the war against the Venetian fleet [10–12]. The words "rocket" (English), "roquette" (French), "rakete" (German), and raketa (ракета, Russian) derive from the Italian word "rocchetta" (i.e., little fuse), a small firecracker created by the Italian artificer Muratori and used in the battle for Isle of Chiozza in 1379 [13]. The Italian engineer Giovanni De Fontana, in 1405, authored a book describing battle cars and torpedoes powered by rockets [11, 12].

In China, amusement was a main driver for black powder applications' development. The first rockets were created for elaborate firework displays, which became popular everywhere. Royal pyrotechnicians were appointed to design and execute the displays for the royal houses throughout Europe. Italians brought the art of fireworks to high levels of sophistication and provided pyrotechnicians to Europe for many decades [12].

The Chinese Wàn Hǔ, during the Ming dynasty, was the first recorded astronaut (ca. 1500); see Fig. 8. He attempted to fly to the moon seating on a large wicker chair to which were fastened 47 rockets. An equal number of assistants, each armed with torches, rushed forward to ignite the fuses. After his takeoff in a thick cloud of
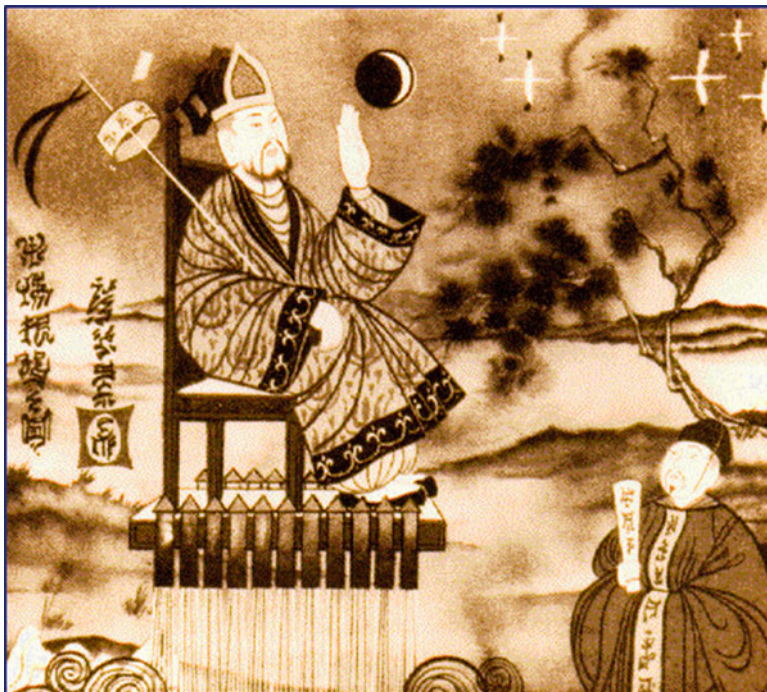

Fig. 8 The Chinese Wàn Hǔ was the first recorded astronaut (ca. 1500). In his attempt he used 47 solid propellant rockets (KNO_3 + S + charcoal in bamboo canes) (Courtesy of NASA)

smoke and accompanied by a tremendous roar, Wàn Hǔ was never seen again. The crater Wàn Hǔ, on the far side of the Moon, is named after him [11].

What would be recognizable today as solid propellant rockets, burning black powder in some rudimentary combustion chamber, were introduced by the Chinese in the early thirteenth century. One of the earliest devices recorded was a special firework (called "ground rat") used for entertainment, of the Chinese imperial family and their foreign visitors, as early as 1264. Such rockets may have been used in battle by the Chinese in 1232 against the Mongol hordes at Kai-Fung-Fu, but this is not confirmed. There are, however, hints that useful rockets were invented in 998 by Tang Fu, who was credited with a fire arrow of a new kind having an iron head [8].

One of the earliest texts to mention the use of rockets was written by the Chinese artillery officer Jiao Yu in the mid-fourteenth century. It is also mentioned the first multistage rocket, the "fire dragon issuing from the water," used by the Chinese navy [8].

An important step forward is due to Indian Sultan, Tipu, who introduced metallic combustion chambers instead of the previous multiple paper layers, cardboard, or bamboo canes. Trajectory stability was achieved by fastening the rocket to a 3 m long bamboo sticks; the warhead was a sword or a sharpened stake. The improved weapon had about 2 km range and allowed the Indian troops of Tipu Sultan to twice defeat the British army at Seringapatam. The British Colonel William Congreve learned the lesson: the Indian technology was imported to the UK and refined. His rockets were heavily used in Europe during the Napoleonic wars and against the US rebels [12].

3 Homogeneous Solid Propellants from Europe

The Chinese black powder producing a lot of deleterious smoke was used for centuries as gun powder and was replaced only much later by smokeless homogeneous solid propellants such as NC single-base (Schultze, 1863, Prussia and Vieille, 1864, France), NC/NG double-base (Ballistite by Nobel, 1888, Sweden, and Cordite by Abel and Dewar, 1889, the UK), and RDX (Henning, 1899, Germany) initially proposed for medicinal use and later as a smokeless propellant. The first widely used smokeless solid propellant for rocket motors in the world was conceived in 1925 by S.A. Brouns (Russia). This formulation was based on Pyroxylin (a highly flammable mixture of NC); in 1933, it was replaced by an energetically more efficient double-base propellant (the historical Russian powder N); for details, see [1–3].

4 First Castable Composite Solid Rocket Propellant from USA

Advances were made in the USA in the framework of the GALCIT (Guggenheim Aeronautical Laboratory at California Institute of Technology) program while working on jet-assisted takeoff (JATO) units. In response to the lack of cooperation
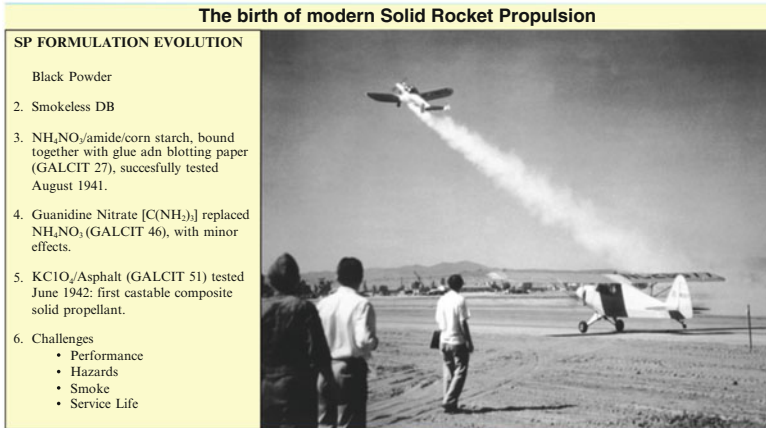
Fig. 9 An Ercoupe monoplane, fitted under the wings with 6 JATO boosters burning GALCIT 27 composite propellant, was the first rocket-assisted takeoff aircraft. US Army Air Corps, March Field, CA, USA, 12 Aug 1941 (Courtesy of NASA)

by the suspicious and secretive Goddard, active in liquid propulsion JATO for the US Navy, a project was started in 1936 to implement solid propulsion JATO for US Army Air Corps; see Fig. 9. This project was directed by Dr. Theodore Von Karman and also included Martin Summerfield, Frank Malina, and Jack (John) Parsons. In June 1942 Parsons, a self-educated and eccentric but also very imaginative chemist, combining an organic matrix (asphalt) and a crystalline inorganic oxidizer (potassium perchlorate) succeeded in making the first castable composite solid propellant [14].

The program was run by von Karman and his associates, see Fig. 10, at CalTech essentially over the years 1936–1944. During these years the GALCIT team created the Aerojet Engineering Corporation in 1942 (later sold to General Tire and Rubber Company) and finally transformed into what is today JPL in 1944. In addition to composite solid propellants, the project also covered liquid propellants [16] and the first studies of solid rocket motor interior ballistics, combustion, ignition, and related structural materials' issues. The GALCIT project was the start of modern solid propellant rocketry. Composite propellants eventually replaced double-base propellants (based on mixtures of NC and NG) in most rocket applications.

In turn, ammonium perchlorate (AP) started replacing potassium perchlorate (KP) as inorganic oxidizer, initially at Aerojet in 1948 with the purpose of reducing smoke. But the first AP-based operational vehicles are dated 1960 (Polaris A1 by Aerojet) and 1962 (Sergeant by Thiokol, Polaris A2 by Hercules, and Minuteman I by Thiokol).

Use of aluminum as high-energy fuel was first advocated by Friedrich A. Tsander, in Russia, in 1909 [17]. After many efforts and mistakes, the first aluminized propellant was successfully bench tested by Charles Henderson and Keith Rumbel at the Atlantic Research Corporation (ARC) around 1955. Disproving

Fig. 10 Theodore Von Karman (center) discussing over the Ercoupe wing with Martin Summerfield (left) and Frank Malina (right), assisted by Clark Millikan and Jack Parsons (barely visible) at the far left and pilot Homer Boushey (a former Von Karman MSc. Student) at the far right, CalTech, 1940 (Courtesy of NASA)

the thermochemical misconception at the time that at most 5 % (in mass) Al could be effective, they burned a mixture containing 21 % Al powder with particle diameter in the range about 1–20 μm, dispersed in a matrix of 59 % AP + 20 % plasticized polyvinyl chloride binder (PVC). Aerojet later verified their findings in a demonstration 100 lb (about 442 N) rocket in early 1956 [14].

5 Development of Composite Solid Rocket Propellants in USA

Following the breakthrough by Parsons in 1942, composite solid propellants (conventional, high-energy and innovative formulations) were actively developed in the USA, but along a range of directions. Asphalt as fuel binder was replaced by synthetic polymers by 1950, KP as crystalline inorganic oxidizer was replaced first by AN and then AP by 1960, and Al as high-energy fuel was added starting in 1955. For each of these "new" ingredients, many years were needed to move from lab-scale experiments to the full scale of operational systems. For example, the first tests with AP started in 1948, and Al addition was unsuccessful until Henderson and Rumbel utilized micron-sized particles in 1955.

The USA, Russia, and all other important worldwide players in rocket propulsion for years followed the liquid propulsion philosophy, based on the German V2 success. A strong impulse in favor of composite solid propellants came only in
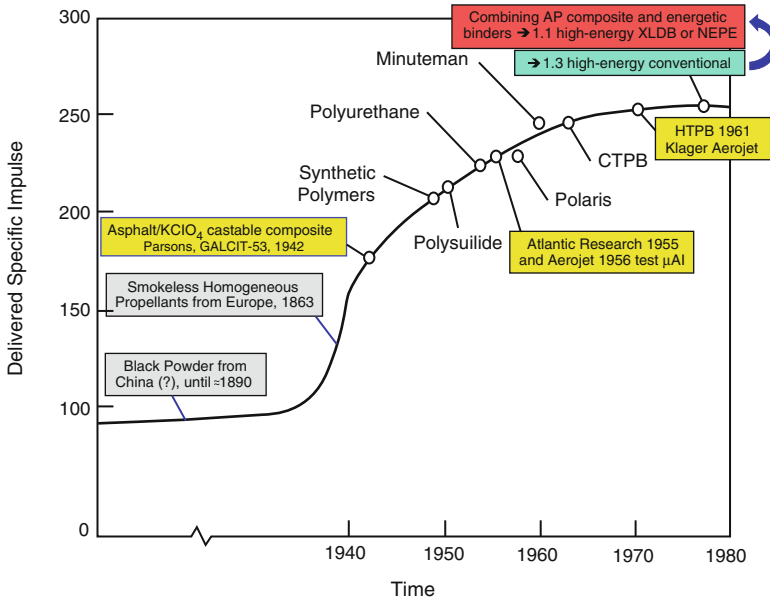
Fig. 11 Delivered I_s vs. time according to Umholtz, Aerojet [18]

1956, when the US Navy decided to design a vehicle based on a solid propellant rocket motor (Polaris) instead of another LRE to replace the Jupiter IRBM. This new project focused the major efforts in one specific direction, and finally the basic formulation AP/Al/inert binder was mastered. This reference formulation first became operational with Polaris A1 (1960, USA), Sergeant (1962, USA), and Minuteman (first stages, 1962, USA) and is still used by most solid propellant space launch components as of this writing.

As shown in Fig. 11, the gravimetric specific impulse I_s increased from about 80 to 180 s moving from black powder to the KP + organic binder composite formulation by Parson, raising to 215 s for composite formulations based on AP + synthetic binders. The introduction of micron-sized Al allowed a further increase of 15 % I_s and 3 % density, also allowed a sensible mitigation of high-frequency combustion instabilities but at the same time caused the emission of copious white smoke [19].

The next step was the introduction of energetic ingredients, such as NC/NG binder for Polaris A2 (1962, USA), HMX as an oxidizer additive (in partial replacement of AP) for Polaris A3 (1964, USA), and both NC/NG and HMX for the third stage of Minuteman (1962, USA); see Fig. 12. This allowed a further increase of I_s to 270–275 s and also of density, but at the cost of sensible primary and secondary smoke. By employing high-energy additives and reducing AP, minimum smoke composite propellants for tactical missiles are capable of $I_s = 245$–250 s [19].
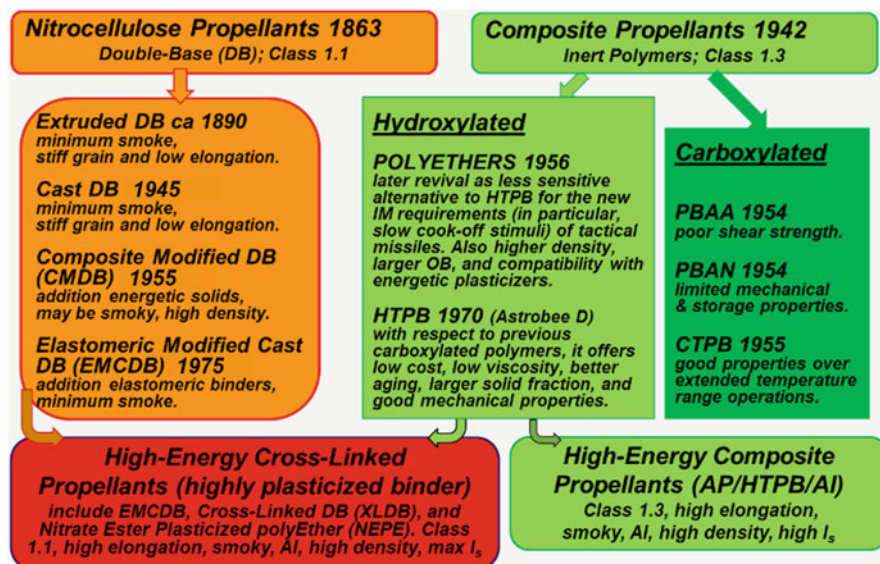
Fig. 12 Combining ingredients from composite and double-base propellants gives rise to high-energy cross-linked propellants with slightly superior performance but of class 1.1 with respect to the conventional high-energy composite propellants [21–24]

Other important improvements were brought about by the introduction of bonding agents, greatly improving not only the propellant's mechanical properties but also its resistance to aging, humidity, and temperature cycling (see Sect. 4 in Chapter "An Introduction to Energetic Materials for Propulsion"). Casting of DB for rocket propulsion was successively mastered by Hercules Powder Company after a breakthrough at the Explosive Research Laboratory (ERL) of Bruceton, PA in 1945 [20].

The study of the most suitable "inert" fuel binder continued for many years and is not yet concluded. Gradually replacing PBAA, PBAN, and CTPB, the currently most successful product is HPTB. This binder, although known [14, 19] to Klager at Aerojet as early as 1961, was first tested in flight only in 1970 (Aerobee D sounding rocket). Starting in the late 1970s, it became the material of choice for a variety of commercial applications. A "propulsion grade" HTPB is being tested in the USA as of this writing.

The need of more volume-efficient propellant for the launch of ICBMs from submarines (US Navy) and silos (US Air Force) was the strongest driver for advancing solid propellant formulations. But this push toward more and more performance seems now at its end, as shown by the flattening curve in Fig. 11 of delivered I_s over the last few decades.

6 High-Energy Composite Solid Rocket Propellants

Two main families can be distinguished essentially based on the kind of the organic binder system and this implies an important consequence in terms of classification hazards, in turn a discriminating factor for applications. Cross-linked (XLDB) propellants using energetic binders or at least plasticizers generally belong to class 1.1, while conventional composite propellants using inert binders belong to class 1.3 (see Sect. 4 in Chapter "An Introduction to Energetic Materials for Propulsion"). An instructive summary plot is shown in Fig. 13. High-energy conventional composite solid rocket formulations typically resort to highly metalized AP/HTPB/Al propellants, but performance can further be augmented by adding nitramines. High-energy XLDB solid rocket formulations achieve the max I_s by using energetic instead of inert ingredients for the binder or plasticizer and partially replacing AP with HMX. High-energy XLDB formulations in a way represent the merging of the historical class of homogeneous formulations used as gun propellants and the castable heterogeneous formulations first devised by Parsons. This type of propellant is preferably called cross-linked double-base propellants (XLDB) by Davenas [21, 22] or elastomer-modified cast double-base propellants (EMCDB) by Sutton and Biblarz [23], emphasizing in either case the importance of cross-linking and plasticizer. Yet, definitions are somewhat loosely applied and the nomenclature is confusing. Despite the different casting techniques, Klager and Zimmerman (p. 91 of 24) consider equivalent the various expressions CMDB,
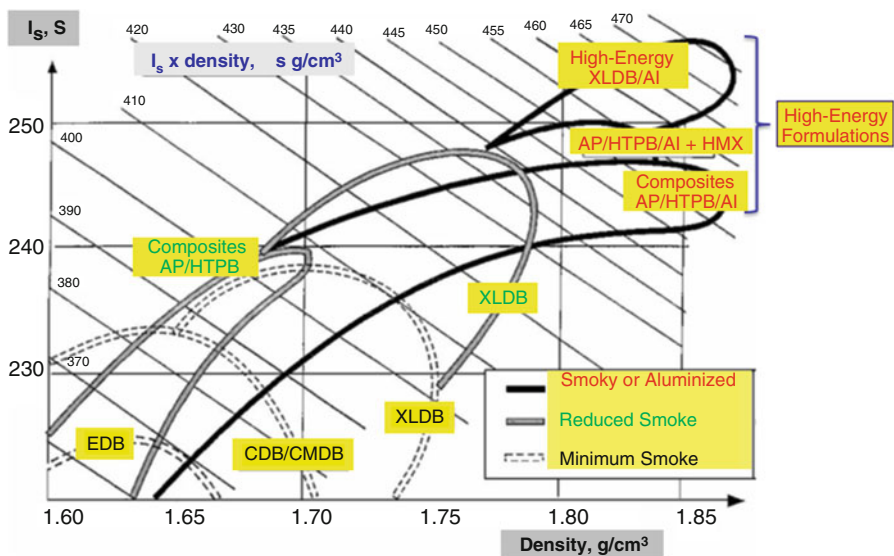
Fig. 13 Delivered I_s and densities of the main solid propellant families expanding from 7 to 0.1 MPa ($\approx$ 1000 to 14.7 psi [21–24] [Adapted from [21], Courtesy of AIAA]

XLDB, and EMCDB. Geisler [25] points out NEPE as a later evolution of the initial XLDB. Aoki and Kubota [26] also use the generic designation Composite DB. Both high-energy formulations are smoky, but can be made "reduced smoke" by eliminating/reducing Al. By eliminating/reducing AP (containing Cl) as well, "minimum smoke" formulations are obtained. Operational systems using high-energy solid rocket propellants are mainly submarine launched ICBM's, with >40 years lifetime. Prominent examples are [21]:

- Trident I C-4: XLDB-70 contains 70 % solids (AP, Al, and HMX) and is based on a polyglycol adipate (PGA) prepolymer – hexane diisocyanate (HDI) binder system, highly plasticized by nitroglycerine (NG).
- Trident II D-5: XLDB-75 (or PEG/NG-75 or the commercial trade name NEPE-75) contains 75 % solids and is based on a polyether, polyoxyethylene glycol, with a delivered I_s close to 255 s and a density >1.85 g/cc.

HTPE is primarily used as a binder for rocket propellants that contain energetic plasticizer, usually Bu-NENA, providing formulations with relatively high elongations. Propellants based on HTPE binder essentially feature mechanical properties similar to those that use HTPB, but show a less severe response to 'slow cook-off', electrostatic discharge (ESD), and bullet impact tests for IM compliance. Density for HTPE is higher than for HTPB (1.04 vs. 0.92). In addition, the oxygen balance (OB) for HTPE is larger than for HTPB (-220.5% vs. -323.8%), thus allowing more Al to be loaded and further increasing density.

7 Innovative Composite Solid Rocket Propellants from Russia

The Russians arrived late to the solid propellant arena, due to a more persistent preference for LRE, but they quickly recovered and their advances appear to have surpassed other technologies in this area [5]. According to Pak [27], a composite propellant using ADN (instead of AP), AlH_3 (instead of Al), and nitrate ester binder offers the highest ideal specific impulse among all of the currently viable solid rocket propellants. The combined use of ADN and AlH_3 in Russia dates back many years, but it still is unparalleled in the Western world. Readers might wish to read Chapter "An Introduction to Energetic Materials for Propulsion" to get a reasonable overview of the current situation and what can be expected in the near future.

8 Concluding Remarks

Starting from the initial black powder (or something similar) accidentally discovered by Chinese alchemists and used for centuries for incendiary devices and fireworks, solid propellant rockets have reached a high level of sophistication in several

countries. Homogeneous Solid Propellants were initially proposed in Western Europe, and later refined for rocket applications first in Russia and then USA. However, modern solid rocket propulsion was actually born at what is now JPL, CA, in 1942, thanks to the first castable composite propellant produced by Parsons. A continuous push toward higher and higher performance that occurred mainly in the USA, for about 20 years, has shown less benefit during the last 50 years. Basic research activities are needed to make possible further progress in many areas of solid rocket propulsion; in the area of new energetic materials, the recent (1960–1980) contribution of ICP in Russia is prominent.

References

1. Lipanov AM, Zarko VE (2016) Survey of solid rocket propulsion in Russia. In: DeLuca LT, Shimada T, Sinditskii VP, Calabro M (eds) Chemical rocket propulsion: a comprehensive survey of energetic materials. Springer, Cham
2. Lipanov AM (2002) Brief history of development of solid propellant rockets in Russia in XX century, Izhevsk, pp 84
3. Lipanov AM (2003) Historical survey of solid-propellant rocket development in Russia. J Propuls Power 19(6):1067–1088
4. Berlin AA, Frolov YV, Isaevich YG (2016) The contribution of the Semenov Institute of Chemical Physics to the Science of Combustion: a historical review. In: DeLuca LT, Shimada T, Sinditskii VP, Calabro M (eds) Chemical rocket propulsion: a comprehensive survey of energetic materials. Springer, Cham
5. Manelis GB (2016) The Russian Missile Saga: personal notes from a direct participant. In: DeLuca LT, Shimada T, Sinditskii VP, Calabro M (eds) Chemical rocket propulsion: a comprehensive survey of energetic materials. Springer, Cham
6. Akhavan J (2004) The chemistry of explosives. Royal Society of Chemistry, Cambridge
7. Encyclopedia Britannica, vol V10, p 423, 1911. Retrieved 31 May 2015
8. Rocket Encyclopedia the Free Dictionary by Farlex Inc., Article distributed under the terms of GNU Free Documentation License. Retrieved 31 May 2015
9. Solid – Encyclopedia Astronautica, www.astronautix.com/props/solid.htm. Retrieved 31 May 2015
10. NASA (1966) Space: the new frontier
11. NASA, MSFC History Office, Rockets in Ancient Times (100 BC to 17th Century). A timeline of rocket history. Retrieved 31 May 2015
12. Miller R (2008) Rockets, twenty-first century books (TFCB), a Division of Lerner Publishing Group, Inc. Minneapolis
13. Von Braun W, Ordway FI (1966) History of rocketry & space travel. Crowell, New York
14. Hunley JD. The history of solid-propellant rocketry: what we do and do not know. AIAA 99-2925
15. Lee K-B, Schultz EJ (2005) New history of Korea, 2nd edn. Harvard University Press, Cambridge, p 518. ISBN 978-0-674-61576-2
16. Caveny LH. Martin Summerfield and his Princeton University propulsion and combustion laboratory, AIAA Paper 2011–5711

17. Korneev LK (ed) (1961) Problems of flight by jet propulsion, Moscow (English translation, NASA, TTF-147, 1964)
18. Umholtz PD (1999) The history of solid rocket propulsion and aerojet. AIAA Paper 99-2927
19. Klager K (1989) Historical breakthroughs and their effect on solid rocket performance. AIAA meeting, Monterey, 10–14 July 1989. See also "Polyurethanes, the most versatile binder for solid composite propellants", AIAA 84-1239
20. Steinberger R, Drechsel PD (1969) Manufacture of Cast Double-Base Propellant. In: Boyars C, Klager K (eds) Propellants Manufacture, Hazards, and Testing. Advances in Chemistry Series Vol. 88, pp. 1–28, American Chemical Society, Washington, DC, USA
21. Davenas A (2003) The development of modern solid propellants. J Propuls Power 19(6): 1108–1128
22. Davenas A (1996) Solid rocket motor design (Chapter 4). In: Jensen GE, Netzer DW (eds) Tactical missile propulsion, Progress in Astronautics and Aeronautics, vol 170. AIAA, Reston
23. Sutton GP, Biblarz O (2010) Rocket propulsion elements, 8th edn. Wiley, New York
24. Klager K, Zimmerman GA (1992) Steady burning rates and affecting errors: experimental results (Chapter 3). In DeLuca LT, Price EW, Summerfield M (eds) Nonsteady burning and combustion stability of solid propellants, Progress in astronautics and aeronautics, vol 143. AIAA, Reston, pp 59–109
25. Geisler AA (1993) My memoirs of solid propellant development at the Air Force Rocket Propulsion Laboratory, AIAA Paper, 93-1783
26. Aoki I, Kubota N (1994) History of solid propellant development in Japan, AIAA Paper 94, 3059
27. Pak ZP (1993) Some ways to higher environmental safety of solid rocket propellant application. AIAA Paper No. 93-1755

Survey of Solid Rocket Propulsion in Russia

Alexey M. Lipanov and Vladimir E. Zarko

Abstract A short survey of development of solid propellants and solid rockets in Russia till the beginning of the twenty-first century is presented. The design solutions are considered which were used in development of ballistic missiles (field, tactical, mid-range, and intercontinental), as well as of other rockets like surface-to-air, air-to-air, sea, and antitank. The problems and accomplishments are considered concerning the justification of expediency and possibility of application of solid-propellant rockets. These works resulted in the creation of the theory of intra-chamber processes, including experimental and theoretical studies of processes of solid-propellant combustion and ablation of thermal protection coverings (insulating liners) of internal surfaces of solid motors and nozzles. Upon development of solid-propellant rockets, different automated systems have been employed: for design of elements of rocket as a whole, for processing experimental information, and for planning scientific and technological experiments. Development of novel design rockets was carried out in different Research and Development and Technological organizations of Russia. Practically all plants for production of solid propellants and manufacturing the motor cases and nozzles were established in the second half of the twentieth century. The exceptions are the plants which dealt with the volley fire rocket systems (Katyusha). Not everything could be discussed in this survey because design details of propellant charges and motors, as well as data on solid-propellant formulations, are not available in open literature.

A.M. Lipanov
M.V. Keldysh Institute of Applied Mathematics, Russian Academy of Sciences, Moscow 125047, Russia
e-mail: aml35@yandex.ru

V.E. Zarko (✉)
V.V. Voevodsky Institute of Chemical Kinetics and Combustion, Russian Academy of Sciences, Novosibirsk 630090, Russia

National Research Tomsk State University, Tomsk 634050, Russia
e-mail: zarko@kinetics.nsc.ru

Nomenclature

ADN	Ammonium dinitramide
AP	Ammonium perchlorate
AS	Academy of Sciences
ASD	Automatic systems of design
ASPEI	Automatic systems of processing experimental information
ASSDD	Automatic systems of service of design development
ASSSR	Automatic systems of service of scientific research
CPSU	Communist Party of the Soviet Union
CVEI	Copolymer of vinyl ether of ethylene glycol mononitrate and isoprene
ICBM	Intercontinental ballistic missile
ICP	Institute of Chemical Physics
k	ZN stability parameter
MAI	Ministry of Aviation Industry
MDI	Ministry of the Defense Industry
MGME	Ministry of General Mechanical Engineering
MITT	Moscow Institute of Thermal Technology
MMEI	Ministry of Mechanical Engineering Industry
QSHOD	Quasi-steady gas-phase homogeneous one-dimensional
r	ZN stability parameter
SP	Solid propellant
SRM	Solid rocket motor
USSR	Union of Soviet Socialist Republics
α	Coefficient in Beer-Lambert-Bouguer law

1 Introduction

The authors present information on different samples of military equipment from strategic rockets to antitank missiles, being at present on arms of the Russian Army. For this reason the data on design details of propellant charges and rocket motors are usually not available, as well as the data on formulation of solid propellants.

When speaking about solid-propellant rocket development in the beginning of the twenty-first century, it must be kept in mind that all this was created and designed at the turn of the twentieth century. In any case it is necessary to speak about the link of times and a continuity of developing both the technological processes and design solutions. In this regard it is necessary to make short historical excursus in order to tell about expediency of creation of solid-propellant rockets of various categories along with development liquid rocket motors, about work on ensuring the minimum dispersion of interior ballistic parameters, and about development of the theory of combustion and intra-chamber processes and development of various automated systems to design and control the production of solid motors.

To start with design and manufacture of solid-propellant rockets, the USSR Government in the beginning of the 1960s was urged to establish the new industry headed by the USSR Ministry of Mechanical Engineering Industry (MMEI), which financed and controlled works on developing the formulations and charges of solid propellants to various motors of all types of solid-propellant rockets.

The outstanding organizer of munition production, graduated from the Mechanical Department of Lomonosov Moscow State University, V.V. Bakhirev, headed this Ministry throughout nearly three decades [1]. Of course, MMEI performed only a certain part of the work. Acted as the leading organizations for developing solid-propellant rockets were the Ministry of the Defense Industry (MDI), the Ministry of General Mechanical Engineering (MGME), as well as the Ministry of Aviation Industry (MAI).

As a rule, the principal customer of solid motors was MDI, which also controlled the systems of volley fire, production of the antitank shells, and all ballistic missiles from tactical to intercontinental as well as all types of sea systems. MAI controlled the antiaircraft missiles and also the rockets of "air-to-air" and "air-to-ground" classes.

MGME generally directed works on development of liquid rockets. Solid-propellant units were used there for the auxiliary purposes mainly. However, in several cases, the MGME developed also solid-propellant rockets. As an example it can be called the first USSR intercontinental ballistic missile (ICBM) RT-2 (Fig. 1) launched from the underground silo (Chief designer Korolev S.P.). This three-stage rocket (SS-13 mod.1 Savage by NATO classification) had a flight distance of 9500 km and was exploited in the period of 1968–1994. It can be also mentioned

Fig. 1 The very first Russian ICBM RT-2 http://cannons.ru/atombomb/nositeli/ussr/RT-2.htm
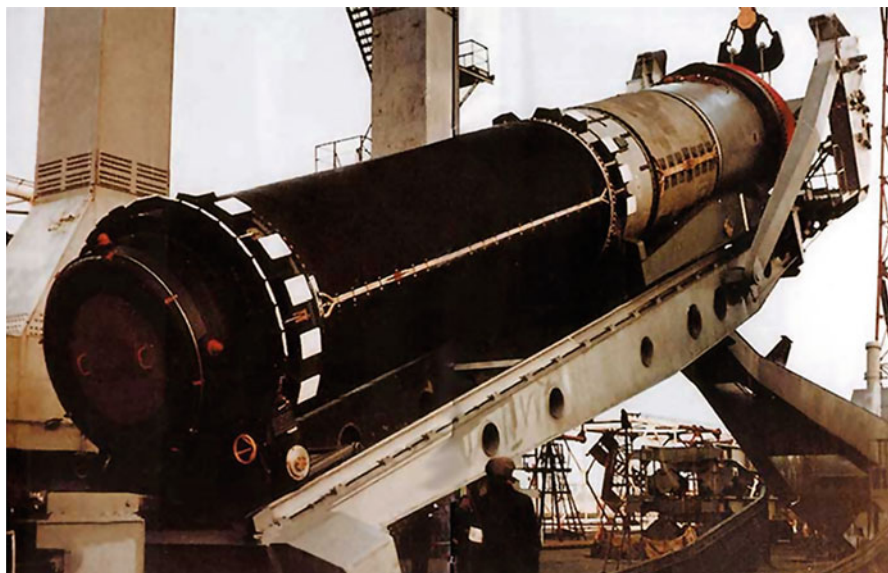
Fig. 2 Submarine rocket RSM-52 "Typhoon" http://rbase.new-factoria.ru/sites/default/files/
missile/r39/r39.jpg

the sea ICBM "Typhoon" (Fig. 2) launched from submarines (Chief designer V.P.
Makeev). But these ones were only rare examples among the set of the liquid rockets
created by the MGME organizations.

In the second half of the twentieth century, work on new solid-propellant rockets
was strongly motivated by the fierce competition for supremacy in defense and space
applications between the world superpowers.

2   History of Solid Rocket Motor Design in Russia

After World War II, the USSR started creating liquid-guided missiles for which it
was clear how to create the guiding units. The relevant design solutions for solid-
propellant rockets were not known.

Besides, when speaking about launching on the long distances, charges of big
dimensions (calibers) are required as well as motors with the mass perfection
coefficient values (ratio of dry rocket mass to total propellant mass) equal to that
of liquid rocket engines. But at that time, the USSR had only systems of volley fire
(multiple rocket launchers) with charges of all-sides burning and with the coefficient
of mass perfection exceeding unity. Consequently, the opinion existed that solid
rocket propulsion could be exploited to realize only unguided short-range missiles.

However, in 1960, under the guidance of Prof. R.E. Sorkin, at the Scientific Research Institute 125,[1] engineers A. Gorodetskaya and Alexey M. Lipanov executed systematic calculations of the mass distribution on two-, three-, and four-stage solid-propellant rockets. They took into account the values of the mass perfection coefficient and propellant-specific impulse of a missile stage that would ensure delivery of a given payload over a certain distance with the minimum launch weight.

Calculations showed that motors having a value of the mass perfection coefficient close to 0.1 would allow developing intercontinental three-stage solid-propellant rockets using USSR-produced ammonium perchlorate (AP)-based formulations. These missiles would be capable to fly up to 10,000 distance km with a payload of 1000 kg and a launch weight of 50–60 tons.

Sorkin informed about those findings the Director of the Institute B.P. Zhukov who reported later to the Secretary of the CPSU Central Committee, D.F. Ustinov, responsible for defensive issues. The latter understood the importance of this finding and informed the staff of the USSR State Committee on defensive engineering.

As a result, in the same year, 1960, the rocket Chief designer S.P. Korolev declared that it is possible to manufacture a three-stage intercontinental rocket which he called RT-2, while another Chief designer A.D. Nadiradze declared that it is possible to manufacture operational and tactical two-stage solid-propellant rockets (1000 km flight distance) with mobile start. A.D. Nadiradze called it "Temp-S."

As the Chief designers showed interest in developing solid rocket motors (SRMs), it became necessary to build the production bases for manufacturing solid rocket propellants and charges from them along with the production of the motor cases, electronics elements, and devices for control systems of flight of rockets.

The first large-size motors had four nozzles. It allowed solving a problem of executive units to guide the rocket flight on all three channels (tankage, snaking, and maneuvering) in a simpler way. The four-nozzle design of solid motor, of course, caused some overweighting but allowed to manufacture the rockets.

This was the start point to establish research and development organizations and engineering capacities to manufacture solid propellants and charges, produce motor cases, and build specialized facilities for testing rocket motors on ground under simulated vacuum conditions. In parallel, groups of scientists, designers, and technologists engaged in design of rocket flight control systems and element base for the corresponding devices were formed. These works were controlled by the Ministries of Electronic and Radio Industries of the USSR as well as the Ministry of Communication Industry.

At that time there was a need to solve the problems of stability of properties of the used materials and minimization of dispersion of parameters both at the received materials and in the manufactured motors. Sorkin in 1961 derived expressions for variations of pressure, mass flow rate, and thrust of solid motor induced by occasional deviations of construction, technology, and exploitation parameters against their nominal values. The problem was solved for quasi-steady-

---

[1]The modern name is the Federal Center for Dual-Use Technologies "Soyuz (Union)."

state motor performance and for volume-averaged parameters. Considering the random deviations as independent values with zero mathematical expectation, he obtained the formula for the maximum pressure deviations in the motor (with a given probability). It became clear that for the mid-range SRMs, the pressure exponent in the burning rate law of solid propellants has to be of low magnitude (around 0.2–0.3), and scatter in the values of solid-propellant burning rates has to come closer to the level of deviation for values of other parameters such as density of solid-propellant or design parameters of the propellant charge [2].

Serious work had to be conducted in order to elaborate the methods for even distribution of heterogeneous components in a propellant slurry and then in a propellant charge with the proper choice of components and their sizes. That was necessary to provide suitable conditions to both pilot productions of the research organizations and industrial serial conditions. Paying a great tribute to efforts of scientists-chemists and engineers-technologists including those at serial plants, it can be stated that this problem was successfully solved.

3   Studies on Solid-Propellant Combustion and Internal Ballistics in Russia

To correctly design and test SRMs, it was necessary to investigate the internal processes occurring in the motor. Therefore in the mid-1960s, Alexey M. Lipanov, at that time a PhD student of Prof. R.E. Sorkin, investigated the 1D problem of initial period of solid motor operations. The transient heating of the propellant charge, the ignition of main charge by the combustion products of igniter, and the gas flow pattern from the charge bore into the pre-nozzle space were studied. The calculation results fitted well with the experimental data. At that time, one-dimensional gas dynamic models of the combustion products motion in the channel of the solid-propellant charge were elaborated for the initial stage of SRM operation [3]. This allowed determining correctly the loads acting on the motor construction, optimizing the case design, and choosing the mass of the igniter charge. To describe the quasi-stationary period of SRM operation, an averaging hypothesis was made along with the one-dimensional model of gas flow [4–6].

Important fundamental works were performed to explore the combustion mechanism of solid propellants. For example, V.N. Vilyunov studied the mechanism of erosive (turbulent) burning of double-base solid propellants, including conditions of its arising [7, 8]. Based on these results, the designers of charges and motors avoided operating conditions which would make possible the rise of turbulent burning. Even in the later works, the SRM designers preferred to choose the parameters of charge and gas flow which mainly provided a nonturbulent gas flow in the combustion chamber.

A similar theory of turbulent combustion was not created for composite solid propellants. Therefore, in all concrete cases, the existence of turbulent combustion

was determined experimentally. Fortunately, the use of case-bonded charges of solid propellant excluded the rise of turbulent burning owing to charge designs with relatively large internal bore diameter.

Much attention was paid to research of nonstationary processes of solid-propellant combustion, including ignition and extinction under abrupt changes of external conditions. Here the ideas of Academicians N.N. Semenov and Ya.B. Zel'dovich were fruitfully developed. Note that the well-known pioneering work by Zel'dovich [9], published in 1942, appeared as a reply to urgent practical needs of solid rocket motor development. The first Russian field missile M8 (further used in a volley fire called "Katyusha" in 1940s) employed double-base propellants which experienced pronounced unstable combustion. The Zel'dovich work promoted further studies of solid-propellant combustion and for a long time served as a basis for numerous combustion investigations in Russia.

It happened that Zel'dovich's ideas became available in the West much later. Nevertheless, they made an important impact on the development of the combustion theory throughout the world. In 1942, the model of transient combustion of homogeneous solid propellants proposed by Zel'dovich was based on the following assumptions [9]:

1. The characteristic thermal relaxation time in the gas phase is much less than that in the condensed phase (i.e., the gas-phase processes are quasi-steady).
2. The temperature at the burning surface is constant at a given pressure ($T_{s0} =$ const).
3. There are no chemical reactions in the condensed phase and the burning rate is totally determined by the reactions in the gas phase.

Later on, that model was improved by Novozhilov [10] assuming that the burning surface temperature at a given pressure is a function of the surface temperature gradient. This allowed performing more detailed and objective analysis of the burning rate response to variations of environmental conditions. The improved transient combustion model received abroad the title of ZN approach [11].

There is a significant difference between the approaches developed in the 1960s in Russia (then USSR) and the USA to understand SRM internal ballistics. The USA approach put emphasis on acoustic combustion instabilities, whereas the Russian approach seems to have been broader, applying the fundamental ZN transient combustion approach to a wide variety of applications such as extinguishment, ignition, spontaneous oscillatory combustion, etc. (remark made by Beckstead in [12]). In the USA, different theories based on different flame models were applied to each specific application. The basis for the US approach to evaluate combustion instability was established by Denison and Baum [13]. An important generalization of the theoretical knowledge available at that time in the Western literature was made in 1968 by Culick [14], who reviewed and summarized the various combustion models in terms of pressure-driven frequency response function. He concluded that all QSHOD transient flame models (that assume a quasi-steady gas-phase, homogeneous condensed-phase, and one-dimensional burning) lead to a common

numerical form of such a function. A critical review of QSHOD transient flame models was presented in [15].

Few years later, in 1971, Summerfield et al. [16] published the first work in the USA based on the ZN approach. This started a debate about which approach is better. Several papers were published by J. Osborn team and other investigators comparing the results of the ZN approach and flame model methods in general [17]. A straight comparison is not an easy task, because the results are very sensitive to the influence of the initial temperature parameters. Direct comparisons between several transient flame models and the ZN approach, in terms of predicted instantaneous burning rate, show different trends not only between ZN and flame models approach but also among the different transient QSHOD flame models tested. For example, the ZN approach with respect to flame models predicts less sharp but protracted excursions from quasi-steady behavior for the pressurization comparative tests conducted in [18, 19].

However, it was also established that, within the assumption of a quasi-steady gas-phase flame (t_c approximation in the Novozhilov's terminology), the Denison and Baum and the ZN approaches are exactly equivalent in terms of intrinsic stability boundary. The first recognition of that was published by Novozhilov in his 1973 monograph [20] and later discussed in detail in [21]. According to Novozhilov, in terms of two parameters, $k = (T_{s0} - T_a) (\partial lnu / \partial T_a)_p$ and $r = (\partial T_{s0} / \partial T_a)_p$, the conditions of unstable combustion are formulated as $k > 1$ and $r < (k-1)^2 / (k+1)$. Here T is the temperature and u is the burning rate. Subscripts s stand for surface, a for ambient, 0 for stationary conditions, and p for pressure.

Exactly the same expressions can be derived within the framework of the Denison and Baum approach. The advantage of using the ZN approach is the potential possibility of determining the parameters k and r under steady-state combustion tests; however, initial temperature sensitivity data are not easy to collect and suffer low accuracy. Later, Novozhilov developed also an extended stability analysis which accounts for finite thermal inertia time in the gas phase in addition to the condensed-phase lag time [20].

Also for the problem of pressure-coupled response function of solid propellants, the ZN approach can be shown to be numerically identical to the flame model approach [12]. However, one must always remember that the ZN approach is intended exclusively to treat homogeneous solid propellants and B.V. Novozhilov never applied it for treating heterogeneous propellants combustion. An attempt to do that was made by King [22], who concluded that further work is needed to include the effects of surface heat release parameters and its dependency on combustion environmental conditions.

The stability of combustion process under finite amplitude disturbances of the combustion environment, such as time-dependent pressure, blowing gas flow, radiant flux, etc., is important for several practical application problems which have to be understood by the theory. The question arises, what are the critical values of external parameters which could induce a catastrophic decrease in the burning rate? The first estimate of the critical values was made by Zel'dovich [9, 11].

His analysis was based on the assumption of extremely high surface temperature gradients (erroneously attributed to the very low initial temperatures), which could cause the extinction of the propellant.

The Zel'dovich concept of extinction can be called "static," as it predicts a cessation of combustion immediately after reaching critical value of surface temperature gradient. A static concept is very attractive due to its great simplicity and was indeed used in several works [15, 16]. When combined with the Novozhilov's stability analysis, the concept meant that the combustion ceases at the boundary of oscillatory combustion. However, this concept was later doubted by Frost and Yumashev [23]. They discovered, through computer-aided simulation of propellant combustion under fast depressurization, that no special hypotheses are needed about critical conditions in order to characterize the extinction phenomenon. The extinction occurs due to progressive cooling of the condensed-phase surface layer and this manifests itself in the appearance of an inflection point on the temperature profile in the bulk of the propellant. They also discovered that, in the course of transient combustion, the parameters of the burning system may temporarily correspond to an unstable combustion domain, but this is not a sufficient condition for extinction.

These findings motivated the development of a "dynamic" extinction concept based on examining the dynamic behavior of burning rate. According to this concept, the extinction is determined not only by the instantaneous parameters of the system at a given instant of time but also by the previous history of heating and dynamic properties of the system (temperature sensitivity of the burning rate). Further, a significant contribution in the development of the dynamic concept was made by DeLuca [24]. Critical review and applicability limits of the phenomenological models of transient combustion of solid propellants have been presented in 2010 by Zarko and Gusachenko [25]. It is necessary to keep in mind that the t_c approximation fails for high oscillation frequencies in the gas phase or for high pressures as well as for very low magnitude of the r parameter. Under these extreme operating conditions, higher level analytical approaches or numerical simulations with the support of detailed combustion models are required.

Another problem, which is also of great importance for practice, is ignition and stability of transition to self-sustained combustion. The generalization of the results of theoretical and experimental studies on condensed system ignition conducted in Russia in 1960–1980s was made by Vilyunov and Zarko in a monograph [26]. The available models of condensed- and gas-phase ignition were discussed in detail and ignition criteria were formulated. It was experimentally established that, upon action of a short impulse of powerful igniting radiant flux, the transition to self-sustained burning does not occur. Recently, the problem was thoroughly examined theoretically and it was shown that the transition process stability dramatically depends on the steepness of the trailing edge of the energy pulse [27].

Illustrative examples of the calculated response to the action of thermal radiation pulses, for homogeneous energetic materials, are shown in Fig. 3. In the case of a rectangular form of the radiation pulse, one can analyze the ignition-to-combustion transition diagram qualitatively identical to that registered in pioneering
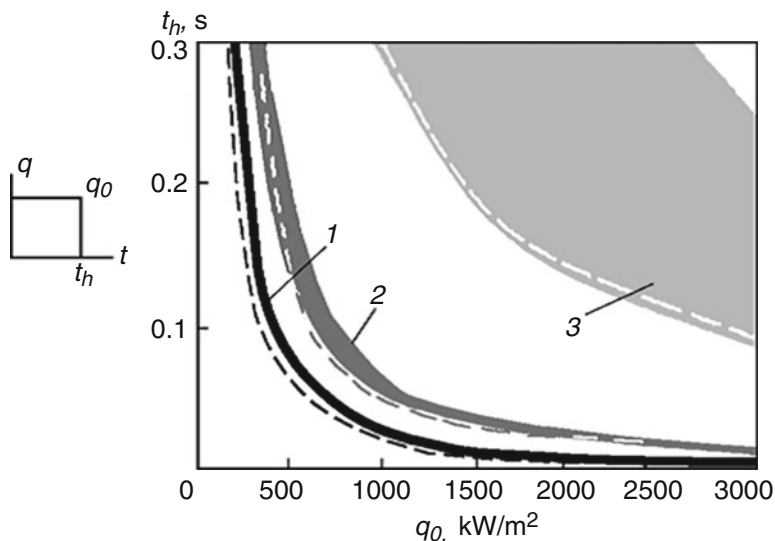
Fig. 3 Regions of the stability of ignition upon rectangular radiant flux action for propellants with $\alpha = 100\,000$ (*1*), 11 500 (*2*), and 1500 m^{-1} (*3*); dashed curves correspond to approximate calculation data

experiments conducted in the 1980s both in USSR and the USA [28, 29]. The diagram of Fig. 3 shows that, for heat flux q_o acting during time t_h, the stable transition to self-sustaining combustion proceeds only in the case when overheating after reaching the ignition instant (low boundary of ignition domain) does not exceed a critical value. The magnitude of admissible overheating time is very short for low transparent propellant ($\alpha = 100,000$ m^{-1}) and is much larger for transparent propellant ($\alpha = 1500$ m^{-1}). Here α is the coefficient in Beer-Lambert-Bouguer law of radiation attenuation.

In the case of exponentially decreasing function $q(t) = q_0 \exp(-t/t_e)$, a much larger transition stability can be realized because the exponential decay of the energy pulse, at the instant of the radiant flux cut off, only provides a small disturbance of the heat balance to the burning system. In this case, a specific response of the burning system is expected. Namely, when acting by small amplitude radiant flux, the stable transition to combustion can be realized even for nontransparent propellant (Fig. 4b). If the magnitude of radiant flux becomes higher than a certain level, the unstable ignition at small characteristic time t_e can be changed to stable one if t_e is increased. The physical reason for such behavior is rather simple. In the case of short t_e, the burning system is disturbed to a larger extent that for longer t_e. Thus, the recommended practice should be the following: design the ignition unit in such a way that, at the end of the ignition stimuli operation, the disturbance of temperature profile near the burning surface is reasonably small.

Some pioneering results were obtained by O. Leipunskii of the Semenov Institute of Chemical Physics (Moscow) in the 1940s, when studying the solid-propellant
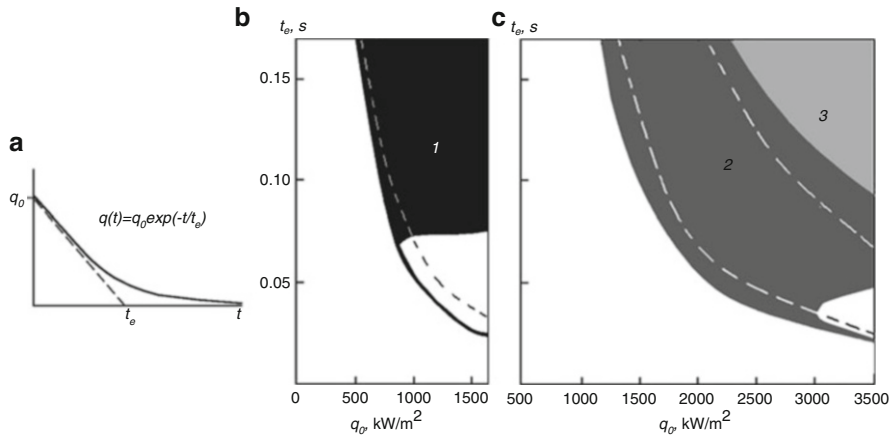
Fig. 4 Regions of stable ignition upon action of exponentially decreasing (**a**) radiant flux for $\alpha = 100{,}000$ (**b**) and $\alpha = 11{,}500$ m^{-1} (area *2* in **c**); *dashed curves* correspond to approximate calculation data

combustion in conditions of intensive gas blowing over the burning surface [30]. Much later, his discovery of the burning rate enhancement, after reaching a threshold value of blowing gas velocity, was named erosive burning in the scientific literature (Leipunskii called it "swelling effect"). The theoretical background of this phenomenon was given by V.N. Vilyunov, who gave an analytical solution of the problem and explained the burning rate enhancement by increased heat feedback from the turbulent gas flow to the burning surface when the gas velocity exceeds a certain limit value.

One may also mention the pioneering, and important for practice, results obtained in studies about metal particles' combustion performed under the leadership of A.F. Belyaev and P.F. Pokhil. They successfully investigated combustion of aluminum nanoparticles, incorporated in model solid propellants [31], well in advance of the foreign investigators.

4   Automatic Processing Systems in Russia

Owing to severe requirements of high accuracy in processing experimental information, and also because of the large volume of the processed information, in the late 1960s of the last century, the development of Automatic Processing Systems of Experimental Information (ASPEI) started. Such systems allowed partially squeezing information if the corresponding experimental curve was in admissible limits in relation to the average one. ASPEI allowed issuing all necessary graphic information and provided release of the report. ASPEI surely allocated a point and its vicinities where the deviation extended over admissible limits. It also

indicated nonstandard fluctuations of the curves of pressure, thrust, or flow rate. In certain cases, usually for research studies, other parameters (such as pressure drops, acoustic fluctuations, temperature of gaseous substances, especially in stagnant zones) were analyzed.

The necessity of an integrated approach to the SRM design process, including that of solid-propellant charge, led to the creation of SRM Automatic Systems of Design (ASD). These works had begun in the 1960s–1970s and the first options of SRM ASD were put in operation in 1972. When using such approach, the maximum distance for a particular rocket was calculated using parameter values chosen close to the boundary or within the range of parameter variation.

The variation of the component magnitude allowed one to find an extremum of the vector modulus. For example, if it was the flight range, reaching of its maximum was the goal. If it was the production cost of the motor, its minimum was defined. As a result, there were optimally designed SRMs, their constructive elements, processing equipment, and other objects.

Along with the above systems, there were needs of creating the Automatic Systems of Service of Scientific Research (ASSSR) and Automatic Systems of Service of Design Development (ASSDD). Works in this direction began in the 1960s, but actually automatic systems were created in the 1980s [32, 33] and allowed accelerating considerably the design process and elaboration of possible searching options.

Of course, everything was carried out on the basis of computers and mathematical models available at that time. In present times, these problems are solved in more correct statements and on the basis of contemporary models of physical and chemical processes, using the possibilities of modern computers with increased computer speed by many orders of magnitude (up to 9) and huge random access memory, with advanced and powerful mathematical software packages.

5 Guidelines for Solid Rocket Motor Development in Russia

The solid motors development became a sort of outcome of successful activity for Russian chemists, technologists, and engineers and was based on accomplishments of the scientists working in the field of processes of combustion and explosion.[2] Some data regarding the history of development of solid rockets in Russia and accomplishments achieved in the 1990s were summarized in the paper by Lipanov [34]. Information on achievements of the Russian synthetic chemists engaged in the search of perspective energetic materials was published in the work reported by Prof. Z. Pak at the AIAA Joint Conference in 1993 [35]. It was announced there that while searching the ways of decreasing the ecological damages from launch of

---

[2]See also chapter "The Russian Missile Saga: Personal Notes from a Direct Participant" by Manelis in this volume.

solid-propellant rockets, the Russian (Soviet) scientists developed solid propellants containing new ingredients, for example, ammonium dinitramide (ADN) as oxidizer and aluminum hydride as fuel. Thus, the theoretical specific impulse managed to be raised up to the value of about 2850 Ns/kg (at the pressure ratio of 70/1). The report [35] also contained new information on the main physical and chemical properties and kinetics of thermal decomposition of the prospective oxidizer. Unusual dependency of the solid-propellant (SP) burning rate on the oxidizer dispersity was for the first time noted. Contrary to what is known for AP-based formulations, this dependency for SP based on ADN turned out to be rising for increasing size of the oxidizer particles.[3] It was also stressed that, for manufacturing the modern composite SP, it is vital to use roundish particles of heterogeneous components. In particular, when modifying the shape of ADN crystals, the possibility was realized of increasing the SP loading with filler from 60 to 90 %. On the basis of the analysis of dinitramide anion properties, the conclusion was drawn on advantages of using nitrile oxide-based systems as the curing agents, since this provides the possibility of carrying out curing with a relatively high rate at the room temperature. It can also be mentioned that in this report, the specific proposals were made on optimization of the processes of SP disposal from the motors removed from arms (Pershing-2 and SS-20), in order to reduce the ecological damage.

More detailed discussions of the approaches to the SP design and manufacture developed in Russia were presented by Sakovich [36]. In this review, the important statement concerning the SP mass and energy characteristics was repeatedly formulated and proved. On the basis of the analysis of Tsiolkovsky's equation for the vehicle maximum velocity increment, while keeping constant the motor volume, the following expression is often used [37]:

$$I_s \rho^\lambda = \text{const}$$

For the majority of practical applications the values of the exponent lambda typically are equal to 0.7, 0.3, and 0.2 for the first, second, and third rocket stages, respectively. It follows that propellants used at the first stage of rockets have to possess the maximum density, whereas propellants at the top stages can have lower density, but enhanced specific impulse.

In order to increase the specific impulse, thermodynamic calculations show that it is necessary to use initial components with a high formation enthalpy which produce gaseous reaction products with low enthalpy. Real SP formulations may differ from the theoretically calculated ones due to the need to satisfy various and sometime contradictory requirements, including those providing the optimum rheological characteristics needed for SP manufacturing. In particular, it leads in practice to some excess quantities of binder as compared to the theoretical level. High-molecular mass polymeric binder in SP serves for providing not only an

---

[3]See also chapter "Effects of Dual Oxidizers on Composite Solid Propellant Burning" by Pang et al. in this volume.

acceptable rheology to manufacture charges but also the demanded mechanical charge properties. Thus, it is required that polymer had as high as possible concentration of hydrogen atoms and low (or zero) concentration of the oxidized atoms of carbon and similar elements. It is possible to give butyl resin as an example of rubber polymer of (CH_2) type. Different versions with introducing groups of atoms of C, H, and N were used in various Russian SP. Experience in designing the SP formulations led to the use of energetic (active) binder whose fraction in SP can be taken up to 15–20 % mass without decrease in a specific impulse.[4] To increase the binder energy, oxidizing groups of atoms can be introduced into its structure. An example is the copolymer of vinyl ether of ethylene glycol mononitrate and isoprene (CVEI). When developing the process of CVEI synthesis, a number of problems have been solved: catalytic vinylation and high cleaning of ethylene glycol mononitrate, acid-catalytic polymerization of the nitrate monomer, purification of CVEI, etc. An important requirement for the polymeric binder is the following: its molecule has to contain the minimum needed double-bond links, or active functional groups of atoms, which provide formation of a spatial structure. Unfortunately, a surplus of reactive elements in the molecular chains of polymer can decrease the chemical stability of SP.

Practical implementation for the binder requirements is provided when using low-molecular mass plasticizers which can comprise 70–80 % of the total binder mass. Of great interest are nitroester plasticizers like ethylene glycol dinitrate, nitroglycerin, and nitroisobutanetriol trinitrate. Wide use of nitroesters as plasticizers puts forward problems of developing the automated low-tonnage installations of continuous action which are carrying out nitration, separation of a target product, its washing, and stabilization. Promising plasticizers are aliphatic nitro amines.

As the curing agent as showed in special researches, it is expedient to use the quinol esters capable to form three-dimensional structures in the binder in the presence of a heterogeneous filler. These ethers affect double bonds in rubber, are capable to work at rather low temperatures, and give chemically stable compounds. Other class of the curing agents is represented by various epoxy materials. Hydantoic resin EN-10 is one of the best at which use the mechanical characteristics of SP are improved, in particular, due to better adhesion of the oxidizer crystals to the binder.

Upon developing the SP production technology, there appeared serious problems connected with lack of the data on high-filled systems rheology (up to 80 % volume content of filler). The problems of mathematical modeling of behavior of such systems, which allowed predicting their fluidity depending on structure and conditions of the environment, were solved. According to experimental data, the absolute values of rheological characteristics of SP strongly depend even on small changes in chemical composition and ratio of filler fractions. This dependency

---

[4]See also chapters "Synergistic Effect of Ammonium Perchlorate on HMX Thermal Stability and Combustion Behavior of Compositions with Active Binder" by Pivkina et al. and "Combustion of Solid Propellants with Energetic Binders" by Rashkovskiy et al. in this volume.

appears especially strong in the region of the maximum filler loading. Theoretically, the maximum filler loading, in the presence of three filler fractions with different grains, reaches approximately the value of 0.9825 that allows designing the SP formulations with a high filler loading. However in reality, it is necessary to deal with formation and destruction of coagulated structures which result from physical and chemical interaction of the molecules of binder and filler. Here the great effect can be reached due to the use of surfactants allowing reducing viscosity by two orders of value. The computer codes that provide the right choice of the component ratio and the mixing regimes and estimate the hydrodynamic resistance of processing equipment, allowing to minimize the temperature factors and visualizing the consecutive pictures of the motor case filling with the mass of SP, are developed for the mathematical description of the SP production process.

Specific demands for developing SP which possess the needed mechanical properties were formulated in [38]. It was shown that the volume of polymeric binder has to slightly exceed the volume of pores in solid fillers (oxidizer and metal fuel). The pore volume V_{por} is calculated as

$$V_{\mathrm{por}} = m_l/\rho_l = V_{\mathrm{fp}} - V_s,$$

where V stands for the volume, m for the mass, and ρ for the density. Subscripts l, fp, and s stand for liquid, free packing (loose), and solid states, respectively. It follows from this expression that the amount of liquid binder equals

$$m_l = \left(m_s\rho_l/\rho_{fp}\rho_s\right)\left(\rho_s - \rho_{fp}\right).$$

In practice, the value of $V_{\mathrm{por}} = 8$ % is reachable, but to satisfy a total complex of demands for mechanical SP properties, it is necessary to use an amount of liquid binder about two times larger. It means that the real formulations have compositions which differ from the optimal ones calculated on the basis of thermodynamical code. Keeping in mind these requirements and taking into account realistic SP properties, the authors of [38] estimated the SP-specific impulse gains while changing the values of the oxidizer ΔH_f formation enthalpy. The plots in Fig. 5 show the ΔI_s dependency on the oxidizer ΔH_f for different formulation types. The basic SP formulation contains "inert" binder of $(C_xH_y)_n$ type with $\Delta H_f = -354$ kcal/kg and ammonium nitrate as an oxidizer. As "energetic" binder, the compound with formula $(C_xH_yN_zO_m)_n$ is taken with $\Delta H_f = 42$ kcal/kg. The additional fuel is represented by Al or AlH_3.

These illustrative calculations show that, in the case of positive ΔH_f values, the role of metal in raising the I_s value diminishes and may even become negative. These data replotted in the form of $\Delta I_s(T_c)$ dependency, where T_c is the temperature in the combustion chamber, lay on the same straight line growing with T_c thus showing that the only effect of metals or hydride present in the formulation is to increase T_c. It follows from these considerations that in the future, counting on high-enthalpy oxidizer and using energetic binder, the SP designers may create formulations without metal and without chlorine-containing components. Such formulations will

Fig. 5 I_s increment vs. oxidizer ΔH_f. Curves *1*, *2*, and *4* correspond to energetic binders with AlH$_3$, Al, and without metal, respectively; curves *3* and *5* correspond to inert binder with Al and without metal
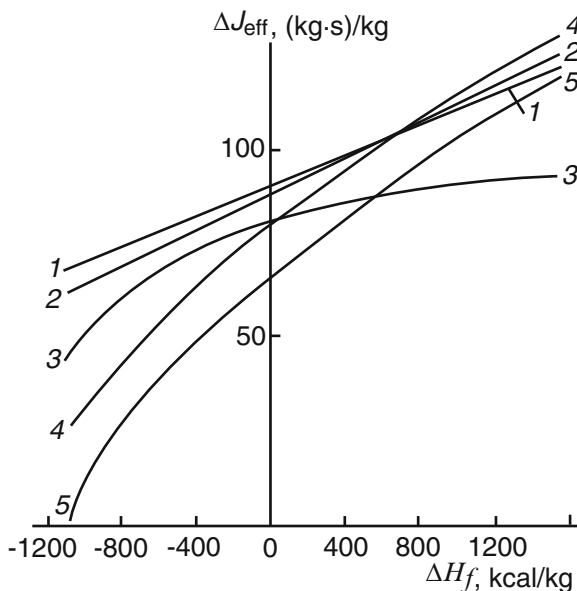
have the great advantage against the existing ones due to improved ecological properties and enhanced energetic efficiency because of the absence of two-phase losses for specific impulse.

6 Technical Characteristics of Selected Russian Solid Rocket Motors

At present time, the main organization which is engaged in Russia in design and development of solid-propellant strategic rockets is the Moscow Institute of Thermal Technology (MITT). It is a very professional research and development organization [39]. In particular, MITT was responsible for developing ICBM 15Zh42 which is the predecessor of the modern Topol-M ballistic missile. The Topol-M is a cold-launched, three-stage, solid-propellant, silo-based, or road-mobile ICBM. The Topol-M rocket (SS-27 Sickle B by NATO classification) has the motor case made by winding of strong and lightweight composites according to the "cocoon" scheme.

The overview of Topol-M assembled on the MZKT-79221 "Universal" 16-wheeled transporter-erector-launcher is shown in Fig. 6. The first flight test from the mobile launcher of the rocket took place on 27 September 2000 [40].

Some technical characteristics of Topol-M missile are presented in Table 1 along with the characteristics of several other Russian solid rockets.

Another rocket developed by MITT in recent years is a submarine-launched ballistic missile Bulava ("Mace"; the NATO reporting title is SS-NX-32) [41, 42].

Fig. 6 Rocket "Topol-M" http://army.lv/large-photos/topol-m.8424.jpg

Table 1 Technical characteristics of Russian solid rockets vehicles

Title	Purpose/staged	Range, km	Total mass, kg	Payload, kg	References
Topol-M (SS-27 Sickle B)	3-staged ICBM	11,000	46,100	1200	[40]
Yars (SS-27 Mod 2)	3-staged ICBM	12,000	49,000	1200	[41]
Bulava (SS-NX-32)	3-staged ICBM	8300	36,800	1150	[42, 43]
Iskander M/E (SS 21/26)	Short-range ballistic missile	280–500	3800	480	[44, 45]
Ovod (X-59)	Air-to-ground rocket	115–285	930	320	[46]
RVV-BD (K-37 M)	Air-to-air rocket	300	510	60	[47–49]
53T6 (SH-08/ABM-3A GAZELLE)	2-staged, interceptor missile	60	10,000		[50, 51]
Pechora-2A (ARC S-125M)	Antiaircraft missile system	35	980	72	[52, 53]
9K123 Khrizantema-S (AT-15 Springer)	Antitank-guided missile	6	46		[54, 55]
Hermes	Multi purposed, 2 staged missile	15–100	90	28	[56, 57]

This missile has three stages; the first and second stages use solid propellants, while the third stage uses a liquid one. Its launch weight makes 36.8 t and the payload mass equals 1150 kg. For this size of payload, the operational range reaches 8300 km. The length of the rocket is 11.5 m, while the first stage has a diameter of 2.0 m and a length of 3.8 m. The mass of the motor of the first stage is 18.6 t. The rocket is capable to start from submarines or from land-based silos. Bulava has a low flight

Fig. 7 ICBM "Bulava" https://www.google.ru/search

trajectory and due to this could be classified as a quasi-ballistic missile. An overview of Bulava is shown in Fig. 7.

It can be mentioned that some mid- and small-sized missiles are developed for working under severe operating conditions. For example, the working temperature ranges for the rocket 9M723K1 (Iskander M/E system) is from -50 to $+50\,^{\circ}$C and for the V-600P rocket (Pechora-2A system) is from -40 to $+50\,^{\circ}$C. The acceleration overload of the rocket V-600P in flight is equal to 6 g.

7 Disposal of Solid Rocket Motors in Russia

One has to keep in mind that utilization of military solid motors containing multi-ton charges of solid propellant costs enormous amounts of money and labor. This justifies the efforts that might be spent for the civilian conversion of military rockets. It has to be noted that the solid-propellant charge utilization is an urgent international problem. In particular, in accordance with START-2, about 400 ballistic missiles, which contain over 20,000 tons of solid rocket propellants, have to be eliminated in the Russian Federation.

The researchers in the Institute of Catalysis (Novosibirsk) and in FR & PC ALTAI (Bijsk) elaborated [58] a safe and environmentally acceptable process of chemical disruption of the propellant polymeric binder, followed by separation of the rest of the propellant components and their recycling into commercial products (AP, Al, and octogen). Processes of chemical disruption of cross-linked polymer binder in solid propellants of two types have been studied: the first one without ferrocene combustion catalyst and the other one containing ferrocene additive. Suitable disrupting (or destructive) mixture compositions were chosen and investigated. The active agent causing cleavage of polymer bonds, the nitric acid, is transported into the bulk of the propellant by means of a mixed solvent containing toluene (or benzene) and acetic acid. The kinetics of mixed solvent penetration into the composite propellant and kinetics of the destruction of solid propellants of two types have been studied. The feasibility of the proposed technology and efficiency

of process stages were proved by tests with large propellant samples (over 0.5 kg) in bench-scale experimental installations.

To study the efficiency of a new chemical disruption process, it was found desirable to develop nonintrusive techniques for measurement of the mass loss rate. This work was executed at the Institute of Chemical Kinetics and Combustion (Novosibirsk). The techniques were elaborated for this purpose based on registration of attenuation of penetrating X-rays or microwave radiation [59]. By means of an X-ray technique, the video images of the solid-propellant (SP) sample were recorded directly during the disruption process. The pulsed X-ray setup is characterized by a soft radiation (about 66 keV) and short pulse duration (5 ns), at a frequency of 50 Hz pulse repetitions. The very low radiation dose allows neglecting its effect on the process of SP disruption. By means of a microwave technique, the time dependency of intensity of the microwave radiation passing through the measuring waveguide cell is registered. The technique is based on recording the microwave attenuation by disrupting reactant mixture upon dissolution of the SP components. The safety in working with SP is provided by the low power of microwave radiation (30 mW) and placing the measuring cell far away from the reactor with SP and disrupting reactant mixture.

8 Conclusions

The authors presented information on different samples of military equipment of the Russian Army. For this reason, the data on design details of propellant charges, rocket motors, and solid-propellant formulations are usually not available. However, some output parameters (flying range of rockets, total mass, payload, and other characteristics) are available in the literature. The authors believe that the information collected in this article on Russian solid-propellant missile systems gives a certain idea of their level of perfection.

It is necessary to mention the potential use of rockets removed from the military service for launching satellites of small and medium weight. Examples of using liquid-propellant rockets for such purposes are well known. In particular, these are the "Dnepr" rocket (modified Voevoda rocket, SS-18 Satan by NATO classification) and the "Rokot" and "Strela" rockets (modified RS-18B rocket, SS-19 mod.2 "Stiletto" by NATO classification). At present time, 21 successful launches of Dnepr, 22 launches of Rokot, and 3 launches of Strela were performed. The satellite Kondor was delivered in orbit by the Strela rocket on 19 December 2014 [60].

References

1. Zabelin LV, Goryunova EA (2006) V.V. Bakhirev- sozdatel' sovremennoi boepripasnoi promyshlennosti (V. V. Bakhirev – the founder of the modern ammunition industry). Grif and Co, Tula
2. Sorkin RY (1983) The theory of intra-chamber processes in solid-propellant rockets (Solid rockets interior ballistics). Science, Moscow, 288 pp
3. Kalinin VV, Kovalyov YN, Lipanov AM (1986) Nestacionarnie processi i metodi proek-tirovania uzlov RDTT (Non-stationary processes and methods of design of the SRM units). Mechanical engineering, Moscow
4. Sorkin RY (1967) Gazotermodinamika raketnikh dvigatelei na tverdom toplive (Gaz thermo-dynamics of solid rocket motors). Science, Moscow
5. Shishkov AA (1974) Gazodinamika porokhovikh raketnikh dvigatelei (Gaz dynamics of powder rocket motors). Mechanical engineering, Moscow
6. Wimpress RN (1952) Vnutrennyaya ballistika porokhovikh raket- (Internal ballistics of powder rockets (translated from English by A.N. Rubashova). Foreign Literature, Moscow
7. Vilyunov VN (1960) K teorii erozionnogo gorenia porokhov (To the theory of erosive burning of gunpowder), Proc USSR Acad Sci 136(2):381–383
8. Vilyunov VN, Dvoryashin AA (1971) Regularities "N"-type propellant burning of gunpowder N in flow. Comb Expl Shock Waves 7(1):45–51
9. Zel'dovich YB (1942) On the theory of combustion for powders and explosives. J Exp Theor Phys (Russian) 12(11–12):498
10. Novozhilov BV (1965) J Appl Mech Tech Phys, No 6, 141 (Russian)
11. Zel'dovich YB, Leipunsky OI, Librovich VB (1975) Teoriya nestatsionarnogo gorenya of powder (The theory of nonstationary combustion of powder). Science, Moscow
12. Zarko VE, Beckstead MW (1996) Simulation of transient solid propellant combustion. Proc Zel'dovich Memorial 1:255–265, Moscow
13. Denison MR, Baum E (1961) A simplified model of unstable burning in solid propellants. ARS J 31:1112
14. Culick FEC (1968) AIAA J 6, (12), 2241
15. DeLuca LT (1990) Pure Appl Chern 62(5):825–838, IUPAC
16. Summerfield M, Caveny LH et al (1971) J Spacecr Rocket 8:251 (see also AIAA Paper 1970, 70)
17. Condon JA, Osborn JR, Glick RL (1976) 13th JANNAF combustion meeting
18. Nelson CW (1978) Response of three types of transient combustion models to gun pressuriza-tion. Combust Flame 32:317–319
19. Nelson CW (1979) Calculated transient combustion of solid propellants, Proc 10th interna-tional annual conference of ICT, Karlsruhe, pp 153–167
20. (a) Novozhilov BV (1973) Nestatsionarnoe gorenie tverdykh raketnykh topliv (Nonstationary combustion of solid propellants). Science, Moscow; (b) Novozhilov BV (1988) Theory of nonstationary combustion of condensed systems including finite relaxation times. Khim Fiz (Russian) 7:674–687
21. Novozhilov BV (1992) Theory of nonsteady burning and combustion stability of solid propellants by the Zel'dovich-Novozhilov method. In: DeLuca LT, Price EW, Summerfield M (Eds) AIAA progress in astronautics and aeronautics, Ch. 15, vol 143. AIAA, Washington, DC
22. King MK (1982) Modeling of pressure-coupled response functions of solid propellants. Nineteenth symposium (international) on combustion, Pittsburgh, 707
23. Frost VA, Yumashev VL (1976) Combust Expl Shock Waves 12:496
24. DeLuca LT (1984) Extinction Theories and Experiments. In: Kuo KK, Summerfield M (Eds), AIAA progress in astronautics and aeronautics, Ch. 12, vol 90. AIAA, New York, NY
25. Zarko VE, Gusachenko LK (2010) Critical review of phenomenological models for studying transient combustion of solid propellants. Int Journal Spray Combust Dynamics 2(2):151–167, Multi-Science Publishing, UK

26. Vilyunov VN, Zarko VE (1989) Ignition of solids. Elsevier Science Publishers, Amsterdam
27. Gusachenko LK, Zarko VE, Rychkov AD (2012) Ignition and extinction of homogeneous energetic materials by a light pulse. Combust Expl Shock Waves 48(1):73–80
28. Mikheev VF, Levashov YV (1973) Experimental study of the critical conditions for ignition and combustion of gunpowder. Fiz Goreniya Vzryva 9(4):438–441 [Comb Expo Shock Waves 9 (4), 506–510 (1973)]
29. DeLuca LT, Caveny LH, Ohlemiller TJ, Summerfield M (1976) Radiative ignition of double base propellants: II. Preignition events and source effects. AIAA J 14:1111–1117
30. Leipunskii OI, Kolesnikov VI, Marshakov VN (1964) Transient burning rate of powders. Proc USSR Acad Sci 154(4):907–909. See also "Theory of combustion of powders and explosives" (O.I. Leipunskii and Yu.V. Frolov, Eds. Science, Moscow, 1982)
31. Pokhil PF, Belyaev AF, Frolov YV et al (1972) Combustion of powdered metals in active media. Science, Moscow
32. Lipanov AM (1987) O problemno orientirovannom programnom komplekse pri issledovanii processov v gazogeneratorax (About the problem focused program system at research of processes in gas generators). Proc USSR Acad Sci 293(1):33–47
33. Lipanov AM (2002) Kratkaya istoriya sozdania tverdotoplivnikh raket v Rossii v 20 veke (Brief history of development of solid propellant rockets in Russia in XX century). Inst Appl Mech, Ural Div Russ Acad Sci, Izhevsk, 84 pp
34. Lipanov AM (2003) Historical survey of solid-propellant rocket development in Russia. J Prop Power 19(6):1067–1088
35. Pak Z (1993) Some ways to higher environmental safety of solid rocket applications. AIAA Paper 93–1755, 12 pp
36. Sakovich GV (1995) Design principles of advanced solid propellants. J Prop Power 11(4):830–837
37. Williams FA, Barrère M, Huang NC (1969) Fundamental aspects of solid propellant rockets, AGARDograph 116. Technivision Services, Slough, UK
38. Komarov VF, Shandakov VA (1999) Solid fuels, their properties, and applications. Combust Expl Shock Waves #2, 139–143
39. Portret na fone epokhy (2014) «Aleksandr Davidovich Nadiradze». 100 let so dna rogdenia (A portrait on era background. "Alexander Davidovich Nadiradze". 100 years since birth). RPM, Yaroslavl, 2014
40. Shevchenko SN (ed) (2007) Strategicheskie raketnie kompleksi nazemnogo bazirovania (Strategic missile systems of land basing). Military parade, Moscow
41. Mobilnui raketnui kompleks RS-24 "Yars". (Mobile Yars RS-24 missile system). (RIANOVOSTI. News line. Infographics. 11.04.2011)
42. Gertsev O (2007) Rabota po «Bulave» idet po planu. Interviu s Yu. Solomonovim. (Work on "Mace" goes according to the plan. Interview to Yu.Solomonov), All-Russian weekly newspaper "Military-Industry Courier", No. 34(200), 5.09.2007
43. Ballisticheskaia raketa «Bulava-30». (Ballistic missile "Bulava-30"), "Army Messenger", 01.11.2010
44. Uchayev VN (Ed) (2010) Polevaya academiya raketchikov (Field academy of rocketeers) 2nd edn. V.Ch. 422, 102–112
45. Pulin G (2008) Voorugennie sily: god peremen. (Armed forces: year of changes). Weekly newspaper "Military-Industry Courier" Moscow Issue 15(231), 16.04.2008
46. Markovsky V, Perov K (2006) Sovetskie aviacionnie raketi «vozdukh-zemlya». (Soviet aviation air-to-ground missiles). Eksprint, Moscow, 50 pp
47. Angelskii R, Korovin V (2005) Otechestvenie upravlaemie raketi «vozdux-vozdux». Chast' 1. Raketi maloi dalnosti. (Native air-to-air guided missiles. Part 1. Rockets of short range), "Equipment and Arms Yesterday, Today, Tomorrow" Magazine, no. 9
48. Karpenko AV (2014) Aviacionaya raketa sverkh bolshoi dalnosti klassa «vozdukh-vozdukh» KS-172. (Aviation "air-to-air" rocket of super long range KS-172). Military and technical collection "Bastion", St. Petersburg, 2.07.2014

49. Angelscii RD (2002) Otechestvennye upravlaemie raketi «vozdukh-vozdukh». (The native air-to-air guided missiles), Aircraft and astronautics, no. 1
50. Vpervie v mire. Interviu generalnogo directora NII RP S.M. Kurushkina. (For the first time in the world. Interview of the general director of the RP Scientific Research Institute S. M. Kurushkin), Arrow, No. 2 (2009)
51. Sergeyev VK (2012) Cherez ternii k ponimaniu. (Through thorns – to understanding). Electron Sci Technol Business, No. 5
52. Ganin S, Korovin V, Karpenko A, Angelskii R (2005) Sistema S-125. (S-125 system). "Equipment and Arms Yesterday, Today, Tomorrow" Magazine, No. 5, pp 8–10
53. Pervov M (2001) Zenitnoe raketnoe oruzhie protivovozdushnoi oboroni strani. (Antiaircraft rocket weapon of antiaircraft defense of the country). AviaRus-XXI, Moscow
54. Angelskii RD (2002) Otechestvenie protivotankovie kompleksi. Ilustrirovanii spravochnik. (Native anti-tank systemes. The illustrated reference book). AST "Astrel", Moscow, 192 pp
55. Karpenko AV, Ganin SM (2000) Otechestvennie aviacionnie takticheskie raketi. (Native aviation tactical missiles). "Bastion", Moscow, No. 1
56. Shipunov A, Kuznetsov V, Selkin V (2004) Koncepcia mnogocelevogo visokotochnogo orugia megvidovogo primenenia. (Concept of multi-target precision weapons of interspecific application). "Military parade", Moscow, January–February
57. Shipunov A, Dudka V, Zakharov L, Parfyonov Y (2000) Koncepcia PTRK tretiego pokolenia. (Concept of PTRK of the third generation). "Military parade", January–February, Moscow, No. 31
58. Ismagilov ZR, Malakhov VV, Sakovich GV et al (2003) Environmentally safe process for utilization of large-scale composite solid rocket propellant charges. In: Proceedings of the 34th international annual conference of ICT, P144 (14 pp), Karlsruhe, FRG
59. Perov VV, Zarko VE, Shandakov VA, et al (2003) Non-intrusive methods for studying mass loss kinetics in destruction of solid propellants. In: Proc 34th international annual conference ICT, P67 (14 pp), Karlsruhe, FRG
60. https://ru.wikipedia.org/wiki

The Contribution of the Semenov Institute of Chemical Physics to the Science of Combustion: A Historical Review

Alexander A. Berlin, Yury V. Frolov, and Yury G. Isaevich

Abstract The Semenov Institute of Chemical Physics was established in 1931 under the direction of Prof. N. N. Semenov, Nobel Prize Winner in Chemistry (1956). One of the main areas of scientific activity of the institute is the physics and chemistry of combustion, shock waves and detonation. This article is a historical review of the main theoretical and experimental approaches of scientists in the Semenov Institute to the study of combustion phenomena. This school was founded by Academicians N.N. Semenov and Ya. B. Zel'dovich. The self-ignition theory of N.N. Semenov, founded on the laws of heat transfer and heat release, formed the basis of "chemical kinetics" and produced solutions for the safe use of combustible materials. Along with D. Frank-Kamenetskii, he developed the classical theory of thermal explosion, thus integrating chemical kinetics with the theory of mass and energy transfer. The theory of combustion and gas flame propagation that was developed by Academician Ya. B. Zel'dovich, based on the kinetics of high-temperature reactions and heat balance equations, drove the main direction of combustion theory development in gas-phase and condensed systems. We discuss the evolution of these basic ideas in the work of successors, i.e. D. Frank-Kamenetskii, A. F. Belyaev, P. F. Pokhil, K. K. Andreev, K. I. Shchelkin, V. N. Kondrat'ev and others. The theoretical and experimental approaches are still under continuous development and improvement.

1 Introduction

Established in 1931, the Institute of Chemical Physics (ICP) of the Russian Academy of Science is the largest Russian scientific centre in the field of combustion processes. It has played a key role in many theoretical and experimental studies in

A.A. Berlin (✉) • Yu.V. Frolov
Semenov Institute of Chemical Physics, Kosygin St., 4, 119991 Moscow, Russia
e-mail: a7777@center.chph.ras.ru

Yu.G. Isaevich
Central Scientific Research Institute of Chemistry and Mechanics, Nagatinskaya St. 16a, 115487 Moscow, Russia

Russia since Academician N. N. Semenov laid the foundations of his school of research on combustion processes. This period saw the advent of the Soviet school of combustion research, headed by prominent scientists: N. N. Semenov, Ya. B. Zel'dovich, Yu. B. Khariton, D. A. Frank-Kamenetskii, A. F. Belyaev, P. F. Pokhil, K. K. Andreev, V. N. Kondrat'ev, B. P. Zhukov and others. Their fundamental studies of combustion and explosion kinetics became classic. A significant addition to the theory of combustion and explosion is developed by A. Nobel, P. Vieille, Bunsen, Chapman, Jouguet, Le Chatelier, N. Manson, M. Summerfield, B. Lewis, G. von Elbe, S.A. Arrhenius, Chilton, Damköhler, Fischbeck and others.

2 Semenov

Academician N. N. Semenov gained worldwide renown for his discovery of branched chain reactions, his general theories of processes and phenomena related to the chain mechanism of chemical reactions (including the concept of chain explosion) and his theory of thermal explosion and the determination of relationships between combustion, explosion and flame propagation.

Semenov started the systematic study of combustion in the 1920s. In 1926, Semenov and the members of his team Yu. Khariton and Z. Valta at the Laboratory of Electronic Chemistry, Leningrad Physicotechnical Institute, discovered and investigated in detail a number of novel, surprising effects that accompanied the reaction of phosphorus vapour with oxygen. They found that, when oxygen was introduced into a vessel containing phosphorus vapour, the oxidising phosphorus began to glow not immediately but after some critical oxygen pressure was reached. The ignition reaction had a lower pressure limit: no reaction took place in the system below the limit, and a violent reaction occurred, to the point of ignition, when the pressure exceeded the limit. Also they noticed that the pressure limit depended on the reactor diameter: it was higher in vessels of small diameter and lower at large diameters. In addition, there was a critical size of the system: reducing its size (diameter) to below the critical level prevented the reaction from accelerating to the point of explosion. Thus, they discovered a sharp transition of a chemical system from almost complete inertness to a violent explosive process.

In 1932, Semenov was elected member of the USSR Academy of Sciences for his outstanding scientific achievements (Fig. 1).

In addition to pursuing his main research areas, Semenov and his colleagues encountered a number of incorrect ideas about the combustion processes in publications of some European scientists and proposed their own, experimentally confirmed and scientifically substantiated data. For example, the theory of normal flame propagation relied on the idea that a burning layer ignited neighbouring cold layers through thermal conduction. The neighbouring layers were thought to ignite when heated to the self-ignition temperature, but the chemical nature and kinetics of the process were not considered. In the mid-1930s, Semenov and his co-workers formulated a general thermal theory of flame propagation in gases and the theory
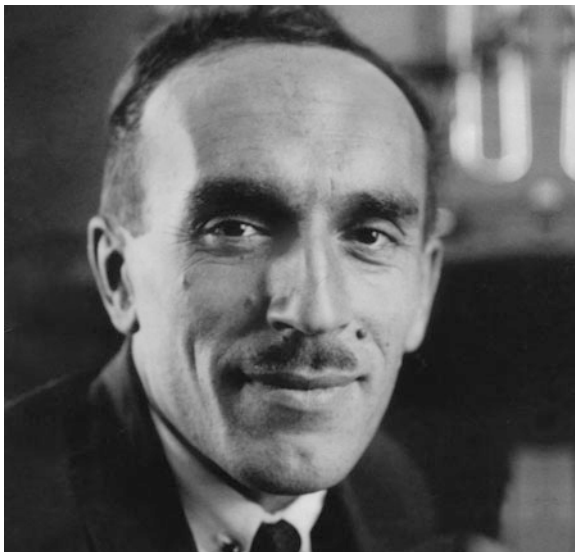
of the combustion of liquid and solid secondary explosives. This was verified using experimental data on the combustion of carbon monoxide + oxygen mixtures and liquid nitroglycol.

A kinetic treatment of combustion processes allowed Semenov to develop theoretical approaches for assessing the concentration limits of normal flame propagation. This phenomenon was interpreted in terms of the thermal loss in the wall of the tube through which a flame propagates. With mathematical formulation, it becomes obvious that the propagation speed cannot be lower than a certain level, which explains why there are concentration limits for flame propagation.

Led by Semenov, researchers at ICP examined the role of turbulence in the flame propagation process. To gain insight into this phenomenon, an experiment was carried out: helical wire placed in a glass tube containing a carbon monoxide + oxygen mixture increased the flame speed by about three orders of magnitude. Turbulent combustion theory builds on the premise that pulsation increases the flame front area. The total flame speed then increases with turbulence intensity.

As a flame propagates through a long tube, its speed increases. This gives rise to detonation combustion, a process in which ignition is initiated by the high temperature resulting from gas compression in a shock wave. The detonation velocity of near-stoichiometric combustible mixtures in wide tubes is independent of reaction kinetics. This is also suggested by classical detonation theory, according to which instantaneous combustion of a substance is possible in the shock front. This theory, however, fails to account for the facts that low-energy mixtures do not detonate at all and that high-energy mixtures do not detonate in narrow tubes. It is by investigating these examples that those researchers at ICP showed detonability to depend on chemical kinetics. According to their experiments, CO + air mixtures

do not detonate under ordinary conditions, whereas the addition of 1 % hydrogen makes them detonable. Based on those experiments, scientists at ICP developed a detonation theory that took into account reaction kinetics and became the basis for subsequent theoretical and experimental studies.

After Campbell and Bone discovered the so-called spinning detonation, it was studied in detail at ICP, which enabled an initial theoretical model for this effect to be constructed.

However, the most important of Semenov's discoveries is his theory of chain self-ignition.

The first approach to understanding the chain nature of combustion reactions was made by Semenov as early as 1926–1927. At that time, he noted that not every ignition was of a thermal nature: there was basically a different type of self-ignition, which Semenov referred to as chain self-ignition. Together with A. I. Shal'nikov, Semenov investigated the lower ignition limit (discovered by Khariton and Valta) of phosphorus. In the same years, he made an attempt to theoretically explain this effect under the assumptions that branched chain reactions were involved and that the ignition chain terminated on the wall of the vessel. The results were so important that branched chain reactions became one of the key research directions at ICP.

There is hardly any other modern scientific concept as popular among researchers as the concept of chain reaction. It is related to the ideas of self-propagating, self-sustaining and chemical and physical avalanche processes, in which weak stimuli cause considerable changes in the reaction system. Clearly, the extraordinary popularity of chain reactions was contributed in large measure by the discovery of the chain mechanism of uranium and plutonium fission, which enabled the practical use of huge nuclear energy resources.

The theory of chain reactions proposed by Semenov was verified experimentally by V. N. Kondrat'ev, E. I. Kondrat'eva, L. I. Avramenko and N. M. Emanuel. Their experiments corroborated Semenov's theoretical concepts: a branched chain process in a substance produces active species—free radicals—whose number rapidly increases over time because of the chain branching. The formation of just one free radical as a result of thermal motion initiates a chain-branching process, leading to fast reactions such as chain ignition and thermal transformations. Free atoms and molecular fragments act as free radicals in chemical chain reactions and neutrons in nuclear chain reactions.

To explain these phenomena, Semenov proposed a theory of branched chain processes. He assumed that phosphorus oxidation is a chain reaction with the feature that the interaction of an active centre with molecules may sometimes produce more than one new active centre, i.e. chain branching occurs. If the number of branching events exceeds the number of chain terminations, the reaction rapidly accelerates to rather high (explosive) rates. This mechanism of chain ignition was formulated by Semenov in his classic paper published in 1928: *On the Theory of Combustion Processes* [1].

In addition to the concept of chain branching, one of the key points of this theory is the concept of chain termination (loss of free radicals) on the wall of the reaction vessel and in the bulk of the reaction mixture. It has become clear that,

at low pressures, active species easily reach the wall of the vessel and disappear there, so a chain avalanche of chemical reactions is impossible and the system remains inert. With increasing pressure, it becomes more difficult for active species to reach the wall of the vessel; the number of bulk reactions increases and, under proper conditions, the number of chain-branching events exceeds the number of chain terminations, leading to chain ignition. The so-called critical diameter can be interpreted in a similar way: the larger the diameter of a vessel, the higher the probability that the number of branching events will exceed the number of chain terminations.

Many chain ignition reactions have not only a lower pressure limit, due to chain termination on the wall of the reaction vessel, but also an upper limit, associated with chain termination in the bulk. Above this limit, the number of chain terminations again exceeds the number of branching events, and the reaction rate drops sharply. The concept of chain termination in the bulk was also formulated by the renowned English kinetic chemist C. N. Hinshelwood, who was awarded the Nobel Prize in Chemistry jointly with Semenov in 1956.

In 1934 in his book *Chain Reactions* [2], which drew on both extensive theoretical work by Western scientists and his own experimental data, Semenov theoretically substantiated the branched chain nature of combustion, which has become a key area of research in modern theoretical chemistry. Semenov was also the author of chain interaction theory, which made it possible to explain many phenomena related to interaction between active species.

Extensive studies at ICP were aimed at identifying the chemical mechanism of various chain reactions. New ideas and concepts concerning the mechanism of chemical processes in general and chain reactions in particular were summarised by Semenov in his monograph *Some Problems of Chemical Kinetics and Reactivity* (1954) [3].

Many chemical processes have a chain nature, e.g. halogenation of organic compounds and polymerisation. Chlorinated derivatives of hydrocarbons are used as organic solvents, agrochemicals, fire-extinguishing agents, refrigerants, etc. Chain oxidation reactions produce synthetic fatty acids that replace edible fats in the manufacture of detergents and lubricants. Oxidation products include alcohols, ketones, aldehydes and peroxides, which find important applications in the chemical industry. Cracking, which offers the possibility of obtaining high-grade petrol, is also a chain process.

The theory of chain reactions allows one to find new effective ways of conducting chemical processes and develop novel principles for intensifying existing production facilities.

The potential extension of its concepts to the field of heterogeneous catalysis opens new prospects for the theory of chain reactions, as a number of chemical processes on the surface of solid catalysts follow a chain mechanism involving surface radicals. Analysis of such processes with the use of chain theory laws may be helpful in developing new approaches for controlling heterogeneous catalytic reactions.

3 Zel'dovich

Zel'dovich's scientific interests included the study of a very wide range of modern scientific problems. Merely listing them provides a detailed idea of this outstanding scientist: chemical physics, theory of combustion and explosion, nuclear physics, nuclear power, gas dynamics, hydrodynamics, particle physics, theory of gravitation, X-ray astronomy, high-energy astrophysics and cosmology.

In 1936, Zel'dovich defended his candidate of science dissertation, concerned with heterogeneous catalysis and adsorption on nonuniform surfaces, where he proposed the notion of a continuous distribution of regions of equal adsorption activity. In that work, Zel'dovich showed himself not only as a theorist but also as an experimentalist.

The relationship between diffusion and heat transfer processes, the influence of temperature and component concentrations on the rate of chemical reactions and the ignition temperature viewed as a variable rather than as a constant—all these ideas were formulated by Lewis and von Elbe in 1934, but they were addressed in detail (qualitatively and quantitatively) only by Semenov, Zel'dovich and Frank-Kamenetskii.

In 1939, Zel'dovich defended his doctoral dissertation in physics and mathematics, concerned with the theory of nitrogen oxidation during combustion and explosion and the temperature effect on this process. From then on, his creative efforts focused on a series of studies owing to which he is thought to be one of the founders of the Soviet school of research on combustion and explosion processes. He investigated liquid and solid explosives and analysed the combustion of gas mixtures, ignition and flame propagation. His scientific interests included the theory of gunpowder combustion, interior ballistics, shock and detonation waves and explosion gas dynamics. In each of these research directions, Zel'dovich obtained fundamental results that became classic. References to his results can be encountered in every publication—an original research article or a monograph (Fig. 2).

Zel'dovich treats combustion and detonation as complex, multifactorial processes involving chemical kinetics, thermodynamics, heat and mass transfer, gas dynamics and flow hydrodynamics. An important achievement was the notion of chemical reaction as a strong function of temperature. This made it possible to divide a flame into regions and identify a narrow chemical transformation zone near the maximum temperature and a broad heating zone, where chemical reactions were thought to be negligible.

In one of his works of that period, Zel'dovich proved that the law of mass action equations for a mixture of reacting ideal gases at complete thermodynamic equilibrium have a unique solution. In that work, he also proved that an approach to equilibrium has an exponential character and that a small change in parameters of a system leads to a small, continuous change in its equilibrium.

Frank-Kamenetskii's classic works on the theory of thermal explosion, concerned with the macrokinetics of chemical reactions under real conditions, in combination with the physical laws of heat and mass transfer, are of fundamental

Fig. 2 Ya. B. Zel'dovich at the early 1930s

importance. Using a system of differential equations, Zel'dovich and Frank-Kamenetskii solved two problems: thermal propagation of a flame and the so-called diffusion propagation, corresponding to an isothermal autocatalytic process. The strong temperature effect on the rate of chemical reactions made it possible to identify a narrow chemical transformation zone in a flame near the peak combustion temperature region and a broader heating zone, where the chemical reaction can be neglected. In each zone, the basic equations of the theory can be simplified, which allows one to integrate the equations and find the temperature and concentration distributions.

The analytical formula thus obtained for evaluating the flame speed is known as the Zel'dovich–Frank-Kamenetskii (ZFK) formula in the national and world scientific communities. It relates the flame speed to Arrhenius-type chemical kinetics and thus brings experiments with flames to the level of kinetic measurements. These provide important information (activation energy, order of reaction, pressure dependence, etc.) about chemical reactions at high temperatures and pressures. In the case of power plant fuel combustion, more than half of the energy is provided by the reaction $CO +1/2O_2 = CO_2$. Semenov initiated a detailed kinetic study of this reaction at high temperatures by flame speed measurements.

The heat conduction/diffusion theory of normal flame propagation, developed by Lewis, Zel'dovich, Frank-Kamenetskii and Semenov, served as the basis for further theoretical work aimed at gaining greater insight into chemical reactions in flames,

including multistep and chain transformations. The most consistent development of the theory was made by Hirschfelder, Curtis, von Karman, Millan and Spalding.

Heterogeneous exothermic ignition and extinction regimes were formulated by Zel'dovich and Frank-Kamenetskii.

Almost all of the studies carried out by Zel'dovich addressed fundamental issues in combustion, proposed solutions at the level of discoveries, obtained the recognition of the scientific community and received a number of honorary awards in the field of combustion, including the Bernard Lewis Gold Medal.

In 1946, Zel'dovich analysed for the first time the shock front structure in a gas with retarded excitation of some degrees of freedom [4]. Previously, Einstein and others investigated the effect of processes with slow relaxation (dissociation and excitation of internal degrees of freedom) on the sound propagation distance [5]. In Zel'dovich's work, their ideas are applied to a non-linear shock wave propagation process. Different compression modes are possible, depending on the wave amplitude: smooth or with a pressure discontinuity. Several years later, the process in question became the basis of the most effective approach to experimental investigation of high-temperature reaction kinetics in gases: with the use of shock tubes.

In the late-1950s, Zel'dovich proposed a qualitative picture of the shock wave structure with allowance for radiative heat exchange, which made it possible to qualitatively explain the observed luminescence behaviour of the front of strong shock waves and the emission in the early stage of fireball growth.

Together with Belyaev, Zel'dovich developed a theory of the combustion of volatile explosives and gunpowders, which is now generally accepted. This, of course, includes his work on the theory of inflammation and ignition of a gas by a hot surface, the theory of the combustion of unmixed gases and the concentration limits of gas combustion in vessels when a significant role is played by the thermal loss arising not so much from heat conduction as from thermal instability and a curved flame front.

The theory of gas combustion and flame propagation created by Zel'dovich (and his predecessors Lewis, Elbe and Kogarko) relying on the kinetics of high-temperature reactions and the thermal balance with the ambient medium made it possible to evaluate the heat effect, propagation speed and consequences of combustion.

Zel'dovich's work in the early 1940s remains basic to the theory of detonation and shock waves. As in the case of combustion, to analyse detonation he examined the high-temperature kinetics of chemical reactions. Zel'dovich, and independently W. Döring (Germany) and J. von Neumann (United States), created a detonation theory which mathematically substantiated the Chapman-Jouguet condition. In the literature, this theory is referred to as ZND.

In the same years, Zel'dovich suggested that, under nearly critical conditions, a rarefaction wave in a substance might propagate discontinuously, whereas a compression wave would propagate continuously, which was later confirmed by experiment. Zel'dovich's book *Theory of Shock Waves and Introduction to Gas Dynamics* [6] was a basic guide in the field of combustion physics.

In the late 1950s to early 1960s, a series of his publications [7–9] was concerned with the structure of shock waves, its response to radiative heat exchange and the theory of avalanche breakdown in gases exposed to nuclear radiation.

Zel'dovich's works on combustion and detonation made a great contribution to the defence capability of the Soviet Union, and he was awarded the 1943 USSR State Prize.

Together with Khariton, Zel'dovich was the author of pioneering work on steady state and explosive uranium fission (1939–1940). His "age theory" served the basis for calculating thermal reactors.

A decade later, Zel'dovich carried out a series of studies on the theory of elementary particles. In this time, he formulated laws of conservation of nuclear and neutrino charges, specified the key points of the universal theory of weak interaction and carried out a number of studies on the muon catalysis of nuclear reactions. In addition, he predicted new isotopes (^{8}He), performed pioneering work on the theory of heavy mesons, investigated the cause of black hole and neutron star formation and developed a theory of the formation of galaxies and the evolution of the hot universe.

His works on quarks and the estimation of the energy density in cosmological vacuum initiated the advent and development of a promising independent direction at the junction of elementary particle theory and cosmology.

Zel'dovich's contribution to cosmology obtained international recognition: in 1970, he was elected the first president of the Cosmological Commission, International Astronomical Union. He was awarded the Catherine Wolfe Bruce Gold Medal—the highest astronomical award—and the Gold Medal of the Royal Astronomical Society.

It should be emphasised that, having a deep scientific meaning, Zel'dovich's work is of great independent interest from the viewpoint of the development of mathematics. In particular, this refers to the theory of flares, which is regarded by mathematicians as an independent section of the general mathematical bifurcation theory. For beginners in physics and engineering, Zel'dovich wrote higher mathematics textbooks, highly appreciated by professional mathematicians [10–13].

In the last years of his life, Zel'dovich again turned to the theory of combustion and the theory of flame propagation in condensed mixtures. Flame propagation was represented as intermediate asymptotics in the general problem of the course of a chemical reaction at a finite rate and initial temperature.

Despite his immense workload, until the last days of his life Zel'dovich gave lectures to students, supervised postgraduates, had meetings with his many pupils, presented his work at conferences and symposia, reviewed books and advised on issues pertaining to both pure and applied science.

4 Belyaev

Prof. Belyaev went down in the history of combustion science by proposing a mechanism of combustion in condensed systems with a leading stage in the condensed phase: the high-temperature reaction in a flame begins in the solid, which is then dispersed to the gas flame zone. He was also the author of a new theory of the ignition and combustion of liquids, which initiated extensive theoretical and experimental studies in this field.

His first work, carried out in 1933–1934 under Khariton's guidance, was concerned with the mechanism of detonation propagation in vacuum (with lead azide as an example). An unexpected result was obtained: the probability of detonation propagation from one (active) charge to another (passive) depends on the separation between them and the area of the passive charge, and the process does not stop even when vacuum has optimal parameters. There was conclusive evidence that the shock wave was not the main detonation propagation source and that the assumption that detonation propagation through gaseous explosion products and the decomposition of several explosive molecules under their action had a thermal character should be discarded. It was clear that detonation propagation was due to microscopic (submicron-sized) fragments of the solid scattered upon the explosion of a lead azide active crystal.

In the next series of studies, Belyaev investigated the mechanism of combustion of explosives and gunpowders. He was sceptical about the theory proposed by Muraour at the beginning of the twentieth century that the energy released during the combustion of the surface layer of gunpowder as a result of impacts of heated molecules of combustion products is transferred to the underlying layer, activating the decomposition of its molecules. He was not convinced by Muraour's assertion that the combustion rate was a linear function of gas density or pressure. This relation implied that the decomposition process took place entirely in the condensed phase (Fig. 3).

Belyaev believed that the theory of combustion of volatile explosives should be developed proceeding from the following assumptions: (1) the combustion of explosives takes place in the gas phase; (2) when energy is deposited in the surface layer of an explosive capable of combustion under given conditions, the energy should go primarily to vaporisation of the explosive. The resulting vapour does not participate immediately in the reaction but after some necessary time for further heating. As a result, combustion is initiated not on the surface but some distance from the condensed phase. The vapour heating region is observed as a nonluminous, dark zone.

This approach allowed the thermal theory of flame propagation in gases, proposed previously by Frank-Kamenetskii and Zel'dovich, to be readily extended to the combustion of volatile explosives. Calculations of the flame structure and the combustion rate of explosives in this theory required knowledge of physical constants of substances, which Belyaev determined with high accuracy.

Fig. 3 A. F. Belyaev at the early 1930s

Analysing the combustion of liquid explosives, Belyaev noticed that the combustion of low-boiling point substances, such as methyl nitrate and nitroglycol, readily switched to detonation. He attributed this not to a chemical reaction in the explosive when it is heated to its boiling point, which would be logical at first glance, but to the physical process of boiling. The role of boiling reduces to vigorous agitation and scattering of the surface layer of the explosive—"injection" to the combustion zone, according to Belyaev's figurative expression. This disturbs combustion in parallel layers and leads to a strong increase in the vaporisation surface and an increase in the amount of the vaporising and burning explosive. Thus, the gas dynamic conditions under which the accelerated combustion products are removed lead to an extremely rapid local rise in pressure and, eventually, to a transition to the detonation regime.

These ideas had a logical continuation in analysis of the causes responsible for disturbance of steady combustion of condensed explosives. It was assumed that one possible reason for the disturbance of layer-by-layer combustion was penetration of the combustion front into pores of the condensed phase, the sharp increase in pressure in the pores and an overall increase in the amount of generated and burning gases.

Belyaev's view of the conditions of failure of steady combustion of liquid explosives has something in common with well-known results by Shchelkin [14], which demonstrate that roughness leads to strong tubulisation of the gas mixture and, as a consequence, to a sharp increase in combustion rate and a rapid transition from combustion to detonation.

In the years of World War II, when an urgent need emerged for gunpowders for the Katyusha rocket launchers, data on the laws of gunpowder combustion became a critical issue. The concepts formulated by Belyaev for volatile explosives turned out to be applicable for the most part to gunpowder combustion, with the decomposition of the surface layer of the condensed phase of gunpowder instead of vaporisation. Detailed studies of the heated gunpowder layer showed that the chemical reaction in the condensed phase was accompanied by only partial decomposition of the material. The rest of it, in the form of tiny particles, was brought directly into the gas phase. Pokhil discovered the role of particle size reduction in gunpowder combustion—one more fundamental phenomenon—along with the views of the heated layer and the heat transferred from the gas phase to the combustion surface.

For the sake of the defence industry, Belyaev began to study mixed explosives. Since the munition factories were very short of trinitrotoluene, Belyaev investigated ammonium nitrate-based surrogate explosives containing some amount of TNT. He proposed that, regarding detonation stability, there was no fundamental distinction between ammonium nitrate and other explosives. Its only distinctive feature is that its critical detonation diameter slightly exceeds the detonation diameter of the other explosives. This made it possible to answer the question of scientific importance whether ammonium nitrate detonates or only induced, decaying detonation can propagate in it.

Analysis of the relationship between the charge density, critical diameter and initiator power led Belyaev to warn many practitioners that there was the possibility, and danger, of failure of industrial explosives in bore holes because of the overdensification under the action of the explosion products penetrating the gap between the bore hole wall and charge. He proposed specific measures to prevent this dangerous effect.

Subsequently, Belyaev returned repeatedly to the influence of physical factors (density, initial temperature, composition and particle size of components) on the detonation stability of explosives, including mixtures based on ammonium perchlorate, a stronger oxidant than sodium nitrate.

Belyaev showed an illustrative example of pinpoint accuracy in his experiments: to ensure microscopic-scale local heating, he introduced a tiny wire (2–5 μm in diameter) into an explosive charge. As shown in those experiments, energy sources of 10^{-5} cal with an operation time of 10^{-9} to 10^{-5} s are needed to ensure detonation in explosives such as lead azide and nitrogen chloride.

In 1946, Belyaev successfully defended his doctoral dissertation, concerned with the combustion mechanism of explosives. Following that, he continued to study the effect of pressure on the combustion rate of priming explosives, evaluated the boiling point and heat of vaporisation of secondary explosives, determined detonation and combustion limits and investigated flameless combustion.

In the early 1950s, a transition to new research directions, related to the combustion behaviour of a more complex class of mixed powders, was planned at ICP. This was begun with experiments on the combustion of thermite compositions, which demonstrated that, in the absence of a gas phase in combustion products, the combustion rate was independent of total pressure. It was suggested that combustion products might contain metal nitrides.

Together with his co-workers, Belyaev studied in detail the combustion of rapidly burning picrates and began to investigate black powder, which was a prototype of mixed powders. He showed that the weak dependence of the combustion rate of black powder on pressure in the range 1–100 atm was the result of inappropriate averaging. Actually, the kinetics of chemical reactions underlying the combustion process vary with pressure: at pressures below 10 atm the combustion rate rises almost linearly with pressure. At higher pressures above 10 atm, the exponent in the combustion law $u = bp^v$ approaches zero. This is characteristic of mixed powders whose components differ in chemical and thermophysical properties and exhibit different behaviours in the combustion wave.

Considering Belyaev's works on mixed fuels, special mention should be given to his studies of the influence of the particle size and volatility of components on the combustion mechanism and rate. By merely changing the particle size of components, the combustion rate was varied from 1–2 to 100 mm/s and above (at pressures from 1 to 100 atm). At a sufficiently large particle size, the combustion rate is almost completely determined by the speed at which the chemical reaction propagates along grain boundaries in the oxidant and fuel. The combustion front had a "multiflame" structure and the combustion rate increased almost linearly with pressure. The effect of pressure was also strong at small particle sizes, of the order of 2–3 μm, but there was then an ideal mixing of the oxidant and fuel gasification products, and the flame front was essentially identical to that in the case of individual explosives: uniform and flat. In practice, an intermediate configuration is typically encountered, with a more complex dependence on pressure. The picture is much more complicated if a third component, e.g. a powder metal such as aluminium or magnesium, is added to the oxidant–fuel binary system.

A. F. Belyaev, P. F. Pokhil and co-workers studied not only the effect of powder metal additives on characteristics of combustion but also the ignition and combustion of metal particles in the gaseous products of interaction between a crystalline oxidant and polymer fuel. Subsequently, this research direction became independent and made it possible to develop a method for assessing the combustion efficiency of metalized fuels in combustion chambers of power plants [15].

In 1940, analysing conditions of steady combustion of explosives, Belyaev concluded that, at relatively slow combustion rates, the critical rate of gas formation upon the combustion of condensed systems, which would disturb the steady state, might be reached because the flame penetrated into pores in the charge.

In the 1960s, he returned to this issue and examined in detail the conditions of flame penetration into a single pore, the combustion behaviour of gas-permeable porous explosives and powders and the combustion–detonation transition, including that at a slow rate [16].

Belyaev's main theoretical views of combustion were summarised in 1967 in the fundamental book *Combustion of Heterogeneous Condensed Systems*, which he wrote together with N. A. Bakhman. The book continues to attract researchers' great interest and remains one of the most authoritative sources in the field of combustion [17].

For their works on combustion and explosion, Profs. Belyaev and Andreev were awarded the 1971 USSR State Prize.

References

1. Semenov NN (1928) On the theory of combustion processes. J Russ Phys Chem Soc Phys Sect 60: 271 (in Russian) (There is also a German variant: Semenov NN (1928) Zur Theorie des Verbrennungsprozesses. Z.fur Physik. Bd.48, N 7-8.- S.571–582)
2. Semenov NN (1935) Chemical kinetics and chain reactions. Clarendon, Oxford
3. Semenov NN (1958) Some problems of chemical kinetics and reactivity. Pergamon, London
4. Zel'dovich YB (1948) On the theory of flame propagation. Zh. Fiz. Khim. no. 1 (in Russian)
5. Einstein A (1920) Bemerkung zur Abhandlung von W. R. Hess: Theorie der Viscosität heterogener Systeme. Kolloidzeitschrift 27:137
6. Zel'dovich YB (1946) Theory of shock waves and introduction to gas dynamics. Akad, Nauk SSSR, Moscow
7. Zeldovich YB (ed) (1985) The mathematical theory of combustion and explosion, transl. from Russian by D. H.Weill, Consultants Bureau, New York
8. Zeldovich YB, Kornpaneets AS (1960) Theory of detonation. Academic, New York
9. Zeldovich YB, Raizer YP (1966) In: Hayes WD, Probstein RF (eds) Physics of shock waves and high-temperature hydrodynamic phenomena. Academic, New York
10. Zel'dovich YB (1963) Higher mathematics with application to physics. Fizmatgiz, Moscow
11. Zel'dovich YB, Myshkis AD (1967) Elements of applied mathematics. Nauka, Moscow
12. Zel'dovich YB, Myshkis AD (1967) Elements of mathematical physics. Nauka, Moscow
13. Zeldovich YB, Yaglom IM (1988) Higher math for beginning physicists and engineers. Prentice-Hall, Englewood Cliffs
14. Shchelkin KI (1947) Detonation onset in gases in rough tubes. Zh Teor Fiz 17(5):613–618
15. Pokhil PF, Belyaev AF, Frolov YV, Logachev VS, Korotkov AI (1972) Combustion of powdered metals in active media. Nauka, Moscow (See also FTD-MT-24-551-73 translate from Russian by Foreign Technology Division. Wright Patterson Air Force Base. Ohio. Oct. 1973.)
16. Belyaev AF (1975) Transition deflagration to detonation in condensed phases, Israel program for scientific translations. Springfield. Department of Commerce report TT-74-50028
17. Bakhman NN, Belyaev AF (1967) Combustion of heterogeneous condensed systems. Defence Technical Information Center, Ft Belvoir

The Russian Missile Saga: Personal Notes from a Direct Participant

George B. Manelis

Abstract The Institute of Chemical Physics (ICP) and The Institute of Problems of Chemical Physics (IPCP), Academy of Sciences of the USSR (AS USSR) played a decisive role in the creation and development of solid propellants under the guidance of N.N. Semenov. This article presents first-hand facts as eye witnessed by the author, deputy of Semenov on this topic. Study of combustion and explosion of explosives and gunpowders, thermal self-ignition and explosion, detonation, kinetics of thermal decomposition of explosives, and more were initiated at the ICP AS USSR from the beginning of its establishment in the 1930s, along with the creation of the theory of branched chain reactions. Initial studies mainly concerned processes in gases. Later, a full investigation started on the synthesis and study of high-energy materials that were potential components of explosives and propellants. At the end of the 1950s, the question of the creation of the intercontinental ballistic missile based on a solid fuel arose. In the middle of the 1960s, the theoretical foundations and the practical development ways of the solid composite propellants industry were established. The key role of the condensed phase reactions was clarified, thus allowing to control the combustion mechanism by means of catalysts or additives affecting the solid fuel. This was quite different from the theory developed by Summerfield in the USA and based on the controlling role of mass diffusion in the gas phase. By the end of the 1980s, energy, ballistic, and performance properties outran those available in the USA.

Nomenclature

ADN	Ammonium dinitramide
AP	Ammonium perchlorate
AS	Academy of Sciences
CPSU	Communist Party of the Soviet Union
DGTC	Department of General and Technical Chemistry

G.B. Manelis (deceased)
Institute of Problems of Chemical Physics, RAS, Chernogolovka,
Moscow Region 142432, Russia

GIPH   State Institute of Applied Chemistry Leningrad
ICP   Institute of Chemical Physics
MIC   Military-Industrial Commission
MIPT   Moscow Institute of Technical Physics
NIIPM   Research Institute of Polymer Materials
NKVD   People's Commissariat of Internal Affairs prior to KGB
SCP   Solid composite propellants
TSNIIHM   Central Research Institute of Chemistry and Mechanics
USSR   Union of Soviet Socialist Republics

1   Background

The Institute of Chemical Physics (ICP), Academy of Sciences of the USSR played a decisive role in the creation and development of rocket technology that uses solid composite propellants (SCP). The formulation and direction of this research were carried out by Nikolai Nikolayevich (N.N.) Semenov. This article does not pretend to be a complete summary of the history of the development of SCP in the USSR. It presents a lot of first-hand facts and their inevitably subjective assessment of a direct participant and eyewitness who was a deputy of N.N. Semenov on this topic.

The study of the processes of combustion and explosion of explosives and gunpowders, thermal self-ignition and explosion, theory of branched chain reactions, detonation, kinetics of thermal decomposition of explosives, mechanisms of thermal decomposition and sensitivity to mechanical impact of energetic materials, and investigation of a number of other related problems were initiated at the ICP AS USSR (Institute of Chemical Physics, Academy of Sciences of the USSR). The works of Yu.B. Khariton, Ya.B. Zel'dovich, D.A. Frank-Kamenetskii, O.M. Todes, V.N. Kondratyev, and many others on such topics have received worldwide recognition. As a result the School of Chemical Physics, established and headed for many years by N.N. Semenov, was formed and played a leading role in the world of energetic material research.

These studies were based mainly on processes occurring in gases, as the simplest objects, which allowed to formulate the first fundamental principles. At the same time, research into condensed systems began, underlying the peculiarities of the above processes in the condensed phase.

Thus, it was shown by A.F. Belyaev that the leading stage of combustion of many organic explosives occurs in the gaseous phase at the maximum temperature in accordance with the Zel'dovich theory whereby condensed explosives melt and vaporize thanks to heat feedback by conduction from the gas phase. This is known as Belyaev and Zel'dovich's combustion theory Through studying the combustion of mercury fulminate Belyaev also discovered the phenomenon of dispersion whose mechanism and significance were understood only much later. In addition, in the works of P.F. Pokhil, the formation of a "liquid-viscous" foam layer on the surface of

burning nitrocellulose-based propellants was revealed due to generation of gaseous products.

Before and during the Second World War (the Great Patriotic War in Russia), the main focus of the works conducted at the ICP AS USSR shifted toward missiles as well as the fuel and combustion of gunpowder in rocket engines. This was part of development of a new class of weapons such as the famous "Katyusha".

Since the war the Institute has been located in Kazan (Tatar Autonomous Republic, USSR), where the opportunities for extensive experimentation were virtually absent. Furthermore, a large group of employees headed by Ya.B. Zel'dovich were sent to Moscow and worked on the basis of SRI-6 (a classified institute later named as TSNIIHM – Central Research Institute of Chemistry and Mechanics).

Since 1944 onwards, a number of researchers at the ICP AS USSR have been involved in the creation of nuclear weapons. However, that is a separate issue.

Even before the war, a strong informal cooperation has been developed around the Institute of Chemical Physics AS USSR, with numerous academic institutions. These include Institute of Organic Chemistry (IOC), Academy of Sciences of the USSR; Leningrad Lensovet Technological Institute (LTI); Kazan Institute of Chemical Technology (KKhTI); Institute of General and Inorganic Chemistry (IGIC), Academy of Sciences of the USSR; Mendeleev Chemical Technology Institute (MChTI), *retsepturschikov* (slang meaning experts in making good compositions, technologists and ballistics), SRI-6 and SRI-125 (now the Federal Center of Dual Technologies "Soyuz"); SRI-130, later named Research Institute of Polymer Materials, Perm, GIPH – State Institute of Applied Chemistry in Leningrad, SRI – 1 (now the Moscow Institute of Heat Engineering), as well as a number of leading design offices. All of these institutions were involved in the solution of the respective tasks under the guidance of N.N. Semenov.

2   Investigating High-Energy Materials

In the second half of the 1950s, a very wide range of research was started under the overall direction of N.N. Semenov on the synthesis and study of high energetic materials that were potential components of explosives and propellants. All of these materials were directly delivered to Chemical Physics (ICP slang name). They were not just the new compounds, but also novel classes of substances which had not been previously considered and often, even a rough idea of their properties was not known. New techniques and devices were created during their study though. Furthermore, old ideas about safety were not good, but they were improved during the research as well as unfortunately due to the fact that there were accidents.

As an example, in order to investigate the critical parameters for thermal explosion and the boundary conditions, it was necessary to carry out experiments ending with explosions where the charge remained intact. The most dangerous operation was dismantling the unexploded charge, dissolution (according to instructions) in acetone and the burning of this solution.

As we did not trust the younger employees, we did it ourselves with Alexander Merzhanov (at the beginning of the 2000s, Academician, Director of the Institute

of Structural Macrokinetics and Materials Science Russian AS). We dismantled the 40 g charge of TNT which at that time was the most powerful known explosive and this charge posed a threat greater than a hand grenade.

Sasha (short name of Alexander) dismantled the sensors, while I carried out the operation of dissolution under the fume hood. As it turned out, this substance, contrary to others, reacted with acetone to produce an explosive substance. When trying to dissolve it, I noticed a beginning of a stormy reaction in a tiny fraction of a second and immediately threw the vessel containing the explosives deep into the fume hood. The charge exploded in the air. Fortunately for me, there were no metal parts but the detonation was full and all the glass turned into a fine dust. The shock wave also smashed the fume hood, and I was thrown to the floor. There was no serious damage due to the absence of any large fragments, but my appearance was quite scary. Glass dust like sandpaper scraped the skin on my face, neck, arms, and chest, and there was a lot of blood.

I was immediately transported to the First City Hospital in the institute's car, where small glass pieces were pulled out of my eyes, and everything else was "treated." I was bandaged up before being transported back to the Institute, as there was no need for hospitalization. At that moment I acquired a terrifying appearance. I looked like an revived Egyptian mummy. Only one eye and my mouth were not bandaged and my shirt was stained with blood and an antiseptic.

Having heard about the explosion, Fedor Ivanovich Dubovitskiy (from 1960 to the end of the 1980s was a head of the Branch of the Institute of Chemical Physics in Chernogolovka) came running to see me. After ensuring I had not been seriously injured, Fedor made the following decision: "There was no accident, the equipment will be repaired and replaced, but you, Jora (short form of George), should not come to the laboratory for 10 days, as you work at the library." A little later the head of the security department came, he saw the state of my health, looked at my exterior, breathed hard, and said: "While you are under bandages, do not approach to the institution closer than a kilometer." My question of "why?" was followed by a clear answer: "Now the Moscow International Festival of Youth and Students is held, there is a lot of foreigners, you will be noticed."

At the end of the 1950s the question of the creation of an intercontinental ballistic missile based on a solid fuel was put on the agenda. The country was faced with the choice of strategic scientific and technical direction, and this included whether to use solid or liquid propellants. The decision on the application of the solid-fuel missiles was mainly determined by solving the following main issues: This was to create them on the basis of ballistic powders as our country had a huge scientific, technical, and technological experience or on the basis of mixed SCP where the full range of work had to be started almost from the beginning. The main problems were a sharp increase in energy, the creation of construction and technology of the preparation of multi-tonnage charges, providing the proper ballistic parameters of fuels and combustion processes in engines, as well as the necessary stability and exploitation properties of fuels and charges for many years. It also involved the creation of new manufactory technologies. All this can only be achieved by performing a broad range of synthetic research, developing new technologies, and arranging appropriate facilities.

Of course, there were different points of view and therefore fierce debates started at all levels from the laboratories to the country's leadership in the country. Many leading designers insisted on creating a liquid propellant solution only to address strategic issues and so leaving solid-fuel applications for tactical problems on the basis of relatively small rockets. Among specialists in ammunition as well there was no unanimity either. Some of the leading and reputable scientists and industry leaders insisted on the priority development of ballistic powders. N.N. Semenov and his leading Institute of Chemical Physics of the USSR AS was at the center of these discussions at all levels. In the late 1950s and early 1960s, the Institute had deployed extensive research on all the key issues and organized several new laboratories. The Branch of ICP AS USSR in Chernogolovka was mainly reoriented from the problem of explosives to the problem of SCP. The major feature of this work was the priority of the fundamental and theoretical studies that ultimately led to quick success. This organization of work in the USSR radically differed to that in the USA, where most part of the work was carried out on full-scale experiments, while we used full-scale experiments only to test and to verify the calculations.

In the middle of the 1960s, the foundations of the theory and the ways of development of the SCP industry were formulated. In the works of Institute of Chemical Physics AS USSR, which were in close cooperation with academic institutions and industry organizations, a number of key scientific discoveries were made. These included establishing the key role of the reactions in the condensed phase, the partial evaporation of the components of fuels based on ammonium perchlorate (AP), the role of the fuel structure (grain size distribution of particles), and the chemical nature of the other components in the fuel combustion mechanism.

Once this was known it enabled the speed and peculiarities of combustion mechanism of the developed explosive compositions to be controlled by the introduction of catalysts and various additives as well as by changes in the structure of fuel and components in a wide range.

At that time, the USA actively developed another point of view (Granular Diffusion Flame theory by Summerfield[1]), based on the role of diffusion processes in the gas phase, which explained the importance of component dispersion, but it did not provide any explanation of the catalyst's action and the influence of chemical nature of the fuel components.

The theory of non-isothermal polymerization of the large propellant charges used in big rockets and methods of process optimization were developed, on the basis of which the corresponding process was organized. In this way, frontal polymerization was started and was later adopted in the polymer industry.

Early on, there were very promising improvements in the energetic characteristics of SCP. The very first recipe using an AP (ammonium perchlorate)-based binder and 7 % aluminum provided a sharp jump in energy performance compared with conventional propellants. It was shown that in this area significant advances are

---

[1]See chapter "Survey of Solid Rocket Propulsion in Russia" by Alexey M. Lipanov and V.E. Zarko in this volume.

possible and several ways of energy development were successfully implemented in the coming years[2].

In the first half of the 1960s, there were two major events which were important to the development of SCP and strategic missiles based on their technology. The first was a meeting of the Scientific Council on SCP, with a key report presented by N.N. Semenov. He collected and analyzed current works on SCP and suggested the ways for the development of science and industry in his report. Also included in this were remarks relating to the state of energy and ways to improve this significantly in the coming years, SCP combustion mechanism and control methods including technology relating to this, laws of combustion, theory and technology of production of large missile warheads, theoretical principals of stability and persistence with regards to missile charges, as well as methods of research.
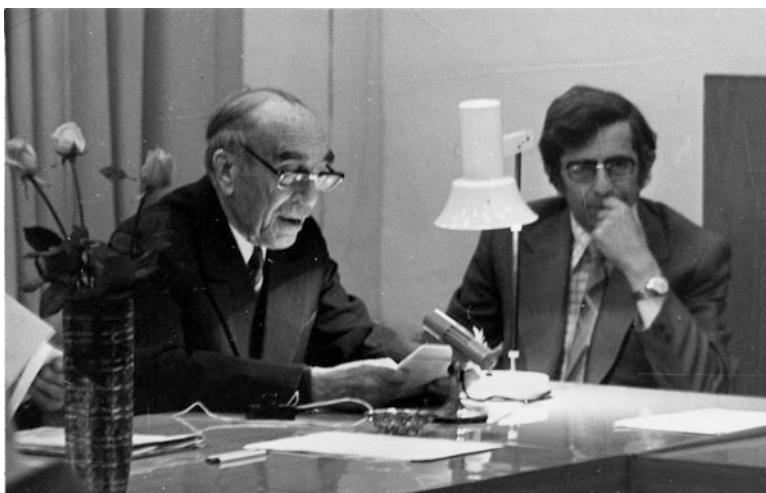

Chernogolovka, Moscow Region, Russia, about 1960: N.N. Semenov and George B. Manelis

Working with N.N. (Nikolai Nikolaevich Semenov, we informally called him N.N.) to prepare the report taught me a lot. He usually wrote reports himself, but in this case he attracted a lot of people to help. During the 1.5–2 months, he came to Chernogolovka and stayed in the hotel and we met him at the hotel. First he defined the issues that would be discussed in the report, and then since the morning we worked on a specific section.

We discussed what was known from the literature and what experiments, calculations, and ideas we had before a physical model and technological conclusions were formulated. All participants of the gathering were equal in the discussion regardless

[2]Similar advances were made at Atlantic Research and Aerojet, USA, in a 100 lb (about 442 N) rocket in early 1956.

of ranks and titles. The discussions were very serious and the well-known expression of N.N., "Bull****," sounded from the lips of different people at least one time per hour. By 10–12 pm we finally came to a consensus with respect to the theoretical issues and the proposed technical solutions . Completely exhausted, we went home, and an excited N.N. ran around the hotel looking for partners with the question, "Well who would like to play *Durak* with me?" ("Durak" means "fool" and it was the most popular card game in Russia). The next morning he handed me the written text of his section in order to decipher his handwritten text as well as for literary editing. Thus, the entire report was formed. N.N. was not used to read a written text for his presentations. During his speech, his thoughts were running ahead of his words, new arguments appeared, the sequence of presentation also underwent spontaneous changes, but the basic ideas and conclusions of the report held firmly in his head were brought to the listeners and readers.
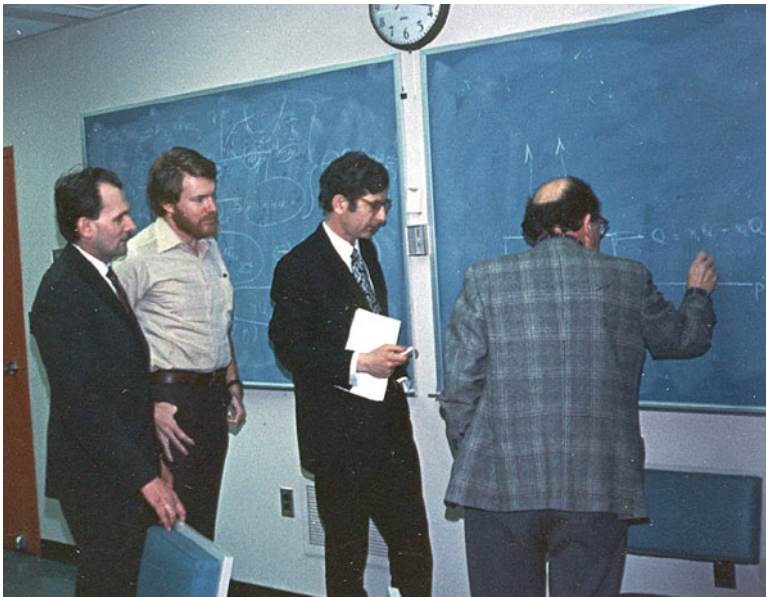
Princeton University, Forrestal Campus, SPLab, Princeton, NJ, USA: from left to right Yury V. Frolov, Leonard H. Caveny, George B. Manelis, and M. Summerfield

It was 1963 when the Commission of the Council of Ministers, chaired by Y.B. Khariton (academician, one of the founders of nuclear weapons, the chief designer and scientific director of the design department – 11, Arzamas), was established which essentially had to decide the destiny of SCP development in the USSR. It had to find answers for the key questions about the feasibility of the establishment of strategic missiles on SCP basis along with the liquid, and, if so, to formulate proposals for the development of science and industry.

A military industrial commission (MIC) was in charge of organizing the work of the Yu.B. Khariton Commission. It allocated offices in the Kremlin, invited business leaders and ministries and organized trips. Several staff members of MIC were delegated to the Yu.B. Khariton Commission . The volume and nature of work of the Commission can be illustrated by the following fact – one employee of MIC, Yu.N. Tsiomo, was charged to collect all available open domestic literature, as well as, if possible, all open foreign publications. Material was found to be so much and of such high level that after its analysis Yu.N. Tsiomo wrote and successfully defended his Ph.D. thesis on global trends in the creation of SCP which was under my supervision.

The commission included such prominent scientists as N.N. Semenov, Ya.B. Zel'dovich, S.P. Korolev, V.S. Shpak, B.P. Zhukov, D.I. Halperin, and many others. According to the suggestion of Nikolai Nikolaevich, I also was included in the commission. The commissioner worked for 2 years. During this time she visited almost all the organizations involved in this issue.

In addition to general reports and visits of members of the Commission to different places in the country, local meetings were held on specific issues where informal discussions of the problems were conducted. For example, one such meeting of a working group was organized in the office of N.N. devoted to the issue of the use of metals in the SCP, where in addition to N.N and Yu.B., also Ya.B. Zel'dovich, A.D. Sakharov, O.I. Leipunsky, F.I. Dubovitskiy, and your humble servant participated. As a result of a sharp debate, the main provisions were set out which determined both theoretical and practical ways to use metals in rocket propellants. It is very important to note the specific atmosphere during such meetings when, for example, my views were heard and discussed as carefully and respectfully as the point of view of N.N. and Ya.B. (as we informally called Yakov Borisovich Zel'dovich). After this discussion I was charged to write down everything on paper. In addition to the understandable satisfaction of the completion of a step of work, I experienced a great esthetic enjoyment from the highest intellectual and professional level of the discussion. It was a real feast of ideas, which were born in my presence and with my participation, even if my contribution was a minor one.

All the major issues were carefully examined. A huge literary material was gathered. In many cases, additional calculations as well as relevant experiments were carried out according to the instructions of the Commission. The conclusions of the committee contained also the issues of the report of Nikolai Nikolaevich.

After finishing the prolonged work of the Commission, Yu.B. charged D.I. (David Izrailevich) Halperin, the outstanding expert in gunpowder and founder and scientific leader of SRI-130 (Perm), and me with summarizing and writing the conclusions on the commission's work. We were given an office room in the Kremlin and we had worked there every day from the morning till night. Once, in the evening, over a glass of tea, D.I Halperin told me about his life. Here I want to mention only some details that are important for understanding the atmosphere and character of the people in those years. In 1937, D.I. Halperin was already known

at that time as an expert in gunpowder, and he was unexpectedly appointed as the chief of gunpowder department of the Weapons Ministry of the USSR. A couple of months later he was arrested and condemned as an enemy of the people. Since the NKVD (People's Commissariat for Internal Affairs – the prototype of the Ministry of State Security) were overloaded by the "work" (the mass arrests of innocent people in the late 1930s), he was not immediately sent to Kolyma (area at the northeastern Siberia with the most severe conditions for prisoners), but was held in Butyrka (prison in Moscow), waiting for deporting with other convicts.

During this time, it was decided to create so-called sharashkas. In the late 1930s the authorities realized that most of the experts who developed weapons had been convicted or shot. Instead of releasing innocent prisoners from jails, they created special enterprises, where convicts professionally worked in their field and continued to create new technologies. These organizations were called *sharashka*. Many prominent Soviet scientists and designers had passed through sharashka. Of course, such prisoners were more happy compared to the common prisoner. Although they were not free, they worked as specialists in normal labor conditions. They were also normally fed, but they lived and slept like prisoners.

D.I. Halperin was one of them, specializing in the creation of gunpowder, and was in essence an informal creative leader. After a series of ordeals, that *sharashka* was moved to Perm, where he developed the technology of gunpowder and the continuous production of the charges for the "Katyusha" as well as their implementation into production. In 1944, Halperin was called to the camp commander, who read him the act of clemency for D.I. Halperin. David Izrailevich remembered later: "Before I could wipe the sweat from my brow and catch my breath after this news, as the camp commander took from the same folder a second paper awarding DI Halperin with a Stalin Prize of 1st degree."

Another interesting fact. In our institute, there was a senior engineer who was a former security officer. His name was Moses Isaacovich Levichek and we all went on trips to Perm together where usually we were well hosted at a comfortable hotel. But on one trip, Halperin took Levichek to live in his apartment. We were really surprised, but were more amazed when we found out why. During the war, Levichek, NKVD [People's Commissariat for Internal Affairs, the predecessor of the KGB] officer, was the head of the same "sharashka," in which zek Halperin worked as a prisoner. Zek is a slang term meaning "prisoner" and prisoners were referred to as ZK or ZEKI. Halperin and Levichek developed a warm, friendly, relationship that lasted until death of Halperin. Paradox! But everything can happen in the life.

The Materials of Commission provided the basis for the Resolution of the Central Committee of the CPSU [communist party of the Soviet Union] and the Council of Ministers of the USSR identified the ways for developing of this new branch of science and technology over many years.

I was always astonished by the amazing ability of N.N., Yu.B. (Academician Yuliy Borisovich Khariton) and N.M. (Academician Nikolai Markovich Emanuel) to convey their thoughts to the reader or listener in a manner very close to their language. Their extended and short reports, as well as letters on the same topic, were written all over again each time and often used different arguments.

As an example, the General Report of the Commission of Yu.B. – a thick volume with hundreds of pages – was written by me and D.I. Halperin. Yu.B. also ordered me to prepare a document known as the short squeeze which was about ten pages long and was for executives of ministries, chief designers, heads of organizations, and enterprises. Meanwhile, Yu.B. wrote the one page documents for N.S. Khrushchev himself.

On the eve of his visit to N.S. Khrushchev, Yu.B and Smirnov (Deputy Prime Minister, Chairman of the MIC [Military-Industrial Commission]) were discussing the findings, the tactics of the conversation, and the arguments that they expected to use and there was a large group gathered in the waiting room. Among them were S.P. Korolyov (academician, chief creator of missiles) and some of the top missile designers, representatives of the various ministries, and some members of the committee, including myself. Our opponents were among others there as well.

We watched football during the long wait at the reception. Finally, Yu.B. and L.V. Smirnov went out of the office, obviously satisfied with the situation and each other. Turning to our opponents, L.B. Smirnov said, "All the time you hang noodles on my ears, when told me that it would burnt badly, but it burns so nice, that a real problem would be to put out a fire. It would be better to ask academicians (a nod to my side, although at that time I was only a PhD and Yu.B. winked at me). You claimed that the polymer binder would be spoiled during storage, and the charge would collapse, but really it could be explained simply – one polymer chain and the other polymer chain, and between them .... Your mother . . . ?!!!.Crosslinking!" (this is a literal translation of a Russian folk expression expressing a strong amazement like 'can you imagine?!' or 'mamma mia!' In Italian)."

I also have another example. We have long fought against the military, which at first demanded exploitation of missiles in a wide temperature range, as for conventional ammunition. To meet this requirement was possible in principle, but it resulted in a strong change in the composition of fuels, significantly lower energy and ballistic characteristics, as well as requiring a less efficient design of the charge. Neither the calculations nor the corresponding experimental results convinced the military. After detailed discussions N.N. sighed and said, "well, I have to appeal to the high-level boss." Shortly afterwards, N.N. presented our proposal to thermostat missiles at a high-level meeting. Briefly, his statement was as follows: "The demand for a wide temperature range will result in a heavy rocket and in the significant loss of its effectiveness. I have a blanket with electric heating at home. When the heating is turned off in the house in the spring or fall, I turn on this heating blanket for 10–15 min and sleep in a comfortable environment, despite of the cold in the apartment. Intercontinental missiles represent single-piece goods. Let's wrap it in something like this blanket. It would cost pennies compared to the cost of the rocket, and the efficiency and reliability dramatically would grow." As a result of this statement, the problem was resolved in a half an hour.

After this there were a number of organizational decisions that created a solid foundation for the development of the sector. Resolution of the Council of Ministers USSR had identified three leading organizations. The Institute of Chemical Physics of the Academy of Science USSR was assigned to be responsible for science, the

GIPH [State Institute of Applied Chemistry, in Leningrad] for technology of initial components and raw materials and finally the TSNIIHM dealt with fuels and charges technology.

An interministerial Coordination Council was established and chaired by the Minister of Engineering of the USSR, V.V. Bahirev. This Coordination Council included leading scientists, technologists, engineers, heads of organizations, and manufacturers. Deputy Minister of engineering L.V. Zabelin was approved as Deputy Chairman of the Board, being a brilliant organizer, scientist, and engineer and a great friend of our Institute. The Board of the Council included deputy ministers of key ministries involved in solving the problem, N.N. Semenov from the Academy of Sciences, as well as Deputy Chief of Main Directorate for Science, N.G. Rogov, and Professor George B. Manelis. The Bureau of the Council not only solved scientific and technical problems but also organizational issues, and so this enabled work to take place without undue interagency delay. The Council of AS USSR on SCP chaired by N.N. Semenov was included in the general system of guidance with F.I. Dubovitskiy and George B. Manelis as Vice-Chairmen.

By the end of the 1970s, many fundamental questions had been solved. As a result, new components were created and recipes of SCP of the first fuels generation were created. Additionally, the technologies and equipment for the production of fuels and charges were designed and there was collaboration with design offices for a robust creation and testing of the first Soviet ballistic missiles on solid fuel. At the same time, research and technological exploration continued with respect to a sharp increase in energy, ballistic, and exploitation parameters to create a second generation of fuels, which were based on the widely performed fundamental investigations.

3 Future High-Energy Materials

As already mentioned the possibilities of different classes of compounds as components of SCP had been widely studied. Studies on fluoro nitro compounds were carried out together with A.V. Fokin and members of his chair at the Military Academy of chemical protection. In our institute this topic was studied by a junior researcher (later Prof.) Vladimir Grebennikov. One day he received a notice to come to the recruitment office to serve in the army because there was not military department in the university where he studied. Our attempts to do something to get him back were unsuccessful. The last hope remained. I called to A.V. Fokin, who had recently been awarded the rank of general as a head of the Department of the Military Academy. Next morning the Volga (car) driven by a General, with professors and associate professors of his Chair as passengers, entered the military office in the yard of Noginsky (Noginsk – district center, Chernogolovka is in Noginsk district). The rank of military commissar, if my memory serves me properly, was not higher than a major.

A few hours later the phone rang and it was Fokin. He said it was not possible to cancel mobilization, as the order for the appeal was signed by the Minister of Defence and can be canceled only by himself. However, something was achieved behind the scenes. Volodya was called into the army and sent to serve in the utility services, serving for the Academy of chemical protection. And every morning, when the other soldiers were sent to peel potatoes, to clean sidewalks, to stand on the walk-through, Grebennikov went to the lab to continue his scientific work. We moved his installation and that's not all.

After about 6 months of service there was a meeting of the Academic Council of the Academy with the defense of a thesis. Chaired by Head of the Academy, Colonel-General. The first rows in the room were occupied by the generals and the next seats were taken by professors and associate professors, in rank to colonel and lieutenant colonels but there were less majors. During the debate on the defense, a hand was stretched at the back row. A green jacket with red piping could be seen but the shoulder straps are not visible. The Chairman gave the man with the outstretched hand the floor. And, to the great surprise of most present on the defense, a young ordinary soldier approached the tribune. His coat was unbuttoned; his left hand was in his pocket. In short, his speech was as follows – work, of course, is not bad, but some statements and conclusions are "bull****," it would have to do so-and-so. By the end of the speech of Grebennikova Head of the Academy stood, (as I was told by Fokin).At this moment employees of the department might have broken into a cold sweat and decided that now our Volodya would go to the guardhouse for his arrogance in the best case, and at worst – would be sent to somewhere in the Far East to the built battalion. But the replica of the Colonel-General sounded in a completely unexpected way: "That's our Soviet Army! Where even an ordinary soldier deeply versed in the complex issues of modern chemistry and could just tell senior in rank the right decision. Good for you! Where are you come from?" And our Grebennikov went to Chernogolovka on holiday instead of to the guardhouse.

The great successes in the development of the science and technology enabled the applications of SCP to be expanded widely. Not only were they used in inter-continental ballistic missiles but also in sea-based missiles, tactical and operational-tactical missiles, missile and air defense systems, as well as missile systems known as "air-land."

The Academy (headed by Mstislav Vsevolodovich Keldysh, and later Anatoly Petrovich Alexandrov) always paid a great attention to our work. For example, the Academy annually sent a large report, which also contained specific proposals for the near future. The President (of Academy) called me one day regarding with the report that I had prepared, and we worked alongside him all day. Evenings after the working day typically ended with traditional "Presidential tea" and 15 min chatting on free topics.

However, the styles of work of Keldysh and Alexandrov were completely different. It was like M.V. Keldysh had an analytical unit in his head as he worked with incredible speed. He carefully read every sentence, meticulously analyzed the results of the calculations and he also verified and compared the quantitative results.

A.P. Alexandrov was a man of totally different kind though. Anatoly Petrovich had a physical technical mentality and approach and was very congenial to our

institute as it had the same roots. His main focus was on the physical ideas. Anatoly Petrovich would read the introduction, conclusion, and findings and would modify the text with a pencil, trying to isolate and highlight the key issues. But he was not careful when reading the descriptive part as he would say, "Well, here everything is all right, I know you."

Two forecasts for the development of SCP and systems on their basis were presented in the following years, each of which took at least a year to prepare. Included were the common points of science and technology, the results of special experiments and calculations, and they concluded with a concrete plan of research developments and implementations in the industry. These projections were the basis of the relevant resolutions of the Central Committee of the CPSU and the Council of Ministers USSR. I'm still surprised that, despite their apparent adventurous nature and the presence of plenty of skeptics, they were fully implemented not only on scientific and technical merits but also on time.

Predictions were based on the use of a significant change in the chemical nature of fuels and access to new components. Bets were made on new classes of oxidizers and fuels. HMX synthesized in Germany before the Second World War was the only previously known compound. Others, such as ADN and aluminum hydride, were prepared in the laboratory in a gram scale. ADN and other salts of dinitramide acid were first synthesized in the Institute of Organic Chemistry AS USSR by VA Tartakovsky and his staff who quickly carried out all the complex physico-chemical studies and ballistic tests. A large complex of relevant branch institutes and industrial organizations was then involved for the development of industrial technology and related production of compounds such as ADN. Aluminum hydride was a somewhat more complicated case. The main characteristics of this compound were first calculated on the "tip of the pen" and a lot of time and effort were spent to develop a suitable method for the synthesis and organization of technology, as well as to provide the necessary stability. Work on the use of beryllium and its hydride were quickly completed to the recipes and charges, but were then frozen due to sanitary and environmental considerations. At the first stage, investigations on ADN and aluminum hydride were developed in parallel and competing directions However, as solutions to the many problems were found, it became possible to combine both compounds, yielding significant additional ballistic effect. These areas were pioneering and as for the formulation and implementation, were far ahead of Western studies, as confirmed even by American researchers in open publications.

Work on the use of HMX was developed in parallel with American developments in this field, but it was not possible to realize fully the theoretically expected effect because it was necessary to introduce a considerable amount of ammonium perchlorate to provide the ballistic characteristics. Exploitation properties of fuel and charges were about the same in the USA and the Soviet Union and were achieved approximately at the same time.

By the end of the 1980s energy, ballistic, and performance properties of SCP already outran that achieved in the USA. At the final stage of this work a very important role was played by N.M. Emanuel after his election as an academician-secretary DGTC (Department of General and Technical Chemistry) USSR. Presidents of the

AS USSR M.V. Keldysh and A.P. Alexandrov also expended much time and effort. Regular joint meetings of the Presidium of the AS USSR and the Collegium of the Ministry of Machine Building (it supervised the production of rocket fuel) of the USSR not only maintained a high academic level but also ensured prompt resolution of organizational issues.

Advanced development of Soviet works was recognized in the USA. So, after the writing of the START contract, signed by President Yeltsin, when some characteristics of domestic strategic missiles were disclosed, several articles were published in leading American journals, in which it was clearly stated "Russian overtaken us for 20 years, and it was so well organized that even the CIA knew nothing."

In hindsight, the work did not go as smoothly and easily as it seems now. In addition to the solving the new scientific and technical problems we had to fight constantly with numerous opponents at various levels to prove the obvious things. Then, when the opponents arguments were exhausted, they used a recurrent perennial question "why the Americans do not have it?" And the only answer put opponents to a standstill was a counter-phrase, "You should think more about why we have it!"

The successful development of this area along with obvious meaning for the country's defense led to results that had general scientific and technical values: There were significant developments in the understanding of the macrokinetics of chemical reactions, the theories of combustion of condensed energetic materials, self-ignition, explosions in condensed systems, and on-isothermal polymerization processes. The foundations of the theory of the solid phase reactions were laid and the methodology for the synthesis of multifunctional organic compounds was achieved along with the development of the rheology and mechanics of composite materials. On the basis of these studies, new classes of technologies were born that did not have a direct relation to gunpowder and explosives. These included SPS (self-propagating high-temperature synthesis) and filtration combustion, both for new material preparation and for the use of alternative fuels in the energy sector. This is not a complete list of new trends in science and technology, whose roots stretched back to the problem of SCP. One of the "side effects" of this trend was the creation of Research Center of Russian Academy of Sciences, Chernogolovka, the three most important achievements of N.N. Semenov and the creation of the theory of chain reactions and the school of Chemical Physics. Today this center is surely one of the leading research centers in the world.

The history of creation of solid propellants in the USSR has not been yet written. The author considers this attempt only as an occasion to attract the attention of serious investigators of the history of science and technology to this fantastically interesting, humanly very complex and versatile issue.

It is necessary to mention at least some of the people we have to thank for their talented and dedicating work. They are Deputy Chairman of the Council of Ministers USSR, Chairman of MIC L.V. Smirnov, Ministers of the USSR V.V. Bakhirev, V.V. Listov, and S.A. Zverev, and Deputies of Minister of Engineering L.V. Zabelin and V.N. Raevskii.

In the ICP Academy of Sciences USSR, the older generation should be mentioned. Along with N.N. Semenov and N.M. Emanuel are A.F. Belyaev, O.I. Leipunsky, F.I. Dubovitskiy, V.K. Bobolev, K.K. Andreev, S.G. Entelis, N.M. Chirkov, and P.F. Pokhil.

A.N. Dremin, A.G. Merzhanov, George B. Manelis, L.N. Stesik, and their students and colleagues G.N. Nazin, V.A. Strunin, L.P. Smirnov, A.V. Raevskii, Yu.I. Rubtsov, L.N. Erofeev, V.V. Barzykin, V.G. Abramov, B.V. Novozhilov, N.N. Bachmann, A.D. Margolin, Yury V. Frolov, V.I. Pepekin, and Yu. Lebedev are the "younger" generation that came to science in the years 1950–1960.

Manelis' house, Chernogolovka, Moscow Region, Russia, 1992: Summerfield at the table head and Manelis first on the right hand side.

Synthetic work was evolved by the efforts of S.S. Novikov, V.A. Tartakovsky, L.I. Bagal, L.T. Eremenko, B.V. Gidaspov, and A.F. Fokin. Recipe-engineering works and the provision of equipment were primarily associated with the names of V.A. Morozov and G.K. Klimenko (TSNIIHM), B.P. Zhukov, N.A. Krivosheeva, and Z.P. Pak (Federal Center of Dual Technologies' "Union").

In the city of Perm (NIIPM – Research Institute of Polymer Materials) there were the students and followers of D.I. Halperin – V.V. Moshev, N.G. Rogov, and L.N. Kozlov, and in Siberia (Altai ANIIHT Research Institute of Chemical Technology) – G.V. Sakovich, and Ya.F. Savchenko. Important and serious research, in addition to synthetic works, as was mentioned above, was conducted in Mendeleev MChTI, in the Artillery Academy (scientific school of I.V. Tishunin), in MIPT (Moscow Institute of Technical Physics).

There was also close collaboration with leading designers such as S.P. Korolev, V.P. Glushko, A.D. Nadiradze, and V.P. Makeyev, along with many others who also played an important role. This list could be endless, but the limited size of the paper and volume of human memory makes me stop here and apologize to those who were not mentioned here without any malicious intent.